FEB - FRESENIUS ENVIRONMENTAL BULLETIN
Founded jointly by F. Korte and F. Coulston
Production by PSP - Vimy Str. 1e, 85354 Freising, Germany in
cooperation with PRT-Parlar Research & Technology
Vimy Str 1e, 85354 Freising

Printed in Germany-ISSN 1018-4619

Fresenius Environmental Bulletin is abstracted/indexed in:
Biology & Environmental Sciences, BIOSIS, CAB International, Cambridge Scientific abstracts, Chemical Abstracts, Current Awareness, Current Contents/Agriculture, CSA Civil Engineering Abstracts, CSA Mechanical & Transportation Engineering, IBIDS database, Information Ventures, NISC, Research Alert, Science Citation Index (SCI), Scisearch, Selected Water Resources Abstracts

CONTENTS

ORIGINAL PAPERS

© by PSP Volume 31– No. 05/2022 pages 4644-4650 Fresenius Environmental Bulletin

DETERMINATION OF VARIABLE RATE FERTILIZER PERFORMANCE OF A ROW TYPE MACHINE

Ufuk Turker*, Ugur Yegul, M Baris Eminoglu, Babak Talepbour

Department of Agricultural Machinery and Technologies Engineering, Faculty of Agriculture, Ankara University, 06135 Aydinlikevler, Ankara, Turkey

ABSTRACT

Increasing profitability associated with reduction of environmental pollution and production costs made variable rate application unavoidable. Therefore, fertilizing according to the field demand and the ability to vary fertilizer rates on the go is regarded as one of the site-specific management tools. Variable-rate application machines tend to be more complicated and thus farmers must take into account how reliable the extra components and systems are. This study introduces a frugal variable rate granular fertilizer with features of simplicity that was modified on a row fertilizer machine. Interpolation accuracy, coefficient of variation, and response time as parameters to achieve a reliable variable rate fertilizing system were considered to evaluate the fertilizer applicator performance. According to the results, when interpolation accuracy was determined as 0.94 (R^2), the response times of low to high and high to low transition rate orders were estimated as 4.44s and 4.63s taking into account operation speed at 1 ms^{-1}, respectively. The coefficient of variation of fertilizer rates ranged from 6.44 to 26.25% and 10.45 to 81.3 for application rates from 0 to 150 kg/ha. Variation of fertilizer rate among the metering units in terms of coefficient of variation (CV) resulted from 10.11 to 36.15% and 11.15 to 117.89 % in increasing and decreasing transition order, respectively.

KEYWORDS:
Variable-rate fertilizer application, control system, response time

INTRODUCTION

There are many questions such as economic, agronomic, and technology-related questions when adopting a site-specific management program for crop production [1]. The cost of adopting, difficulties in integrating components, problems with data interpretation, and agronomic solutions were also some of the issues in adopting site-specific management based on spatial variability across farming zones rather than other PA tools such as automatic steering and yield monitoring [2]. Especially due to a high level of management information, data interpretation, and decision support process requirements, the implementation of variable rate application differs from other precision agriculture technologies. Like other innovations, relative advantage, compatibility, complexity, trialability, and observability are the five key attributes that can be used to explain a high proportion of possible reasons for low/variable adoption of PA technology [3].

Access to technical training, meeting, oral transmission, trust in technicians, and belief in the technology introduced by scientists are the factors affecting a change of technology use [4]. Generally, socioeconomic factors, agro-ecological factors, institutional factors, information sources, farmer perception, behavioral factors, technological factors are the main factors affecting the adoption of precision agriculture [5]. Because usefulness and ease of use are central aspects of technology adoption, it seems to be more effective to create a low-performance tool with few “useful” characteristics to attain a lower purchase price [6].

Currently, with continuing research on variable rate fertilization technology, Using map-based or sensor-based applications as two basic methods of implementing site-specific management (SSM) for the variable rate application with its unique benefits and limitations has been developed [1].

Previous studies on the development of variable rate granular fertilizers revealed that good application performance with high accuracy and short response time are the main aspects for evaluating the performance of a granular applicator [7,8,9]. Most of these studies have focused on fertilizing applicators and developed a way to determine fertilizer rate based on field sampling data was neglected. Therefore, the objective of this study was to develop and evaluate the alternative method to determine fertilizer rates and their application on row granular fertilizer. In this study, low cost and ease of use as two specific features were considered. Zalat et al [10] have studied the effect of method and time of fertilizer application on sugar beet productivity under two nitrogen fertilizer sources. Time and method of micronutrients application significantly affected all studied traits.

Khaled et al. [11] have also studied the effect of nitrogen and potassium rates and their interactions on some yield characters. They concluded that inceasing nitrogen rates declined NUE. This result indicates the importance of changing and controlling fertilizer amount during application.

MATERIALS AND METHODS

Test fertilizer and rate control equipment. A six-row hoeing fertilizer was used as a test machine. Generally, distributing mechanism for granular fertilizers is worked by changing the fertilizer outlet cross-sectional area existing under the fertilizer hopper. Plastic molded sheaves mounted on fertilizer shaft and replace by turning adjusting lever to right or left to achieve the desired flow rate. A linear actuator with position feedback was used to control adjusting lever replacement use in fertilizer norm changing (Figure 1).

FIGURE 1
Implemented flow rate control mechanism

Fertilizing rate determination. To obtain fertilizing rate based on predetermined field sampling IDW (Inverse Distance Weighting) interpolation method was implemented. The simplicity of the underlying principle, the speed in the calculation, the ease of programming, and reasonable results for many types of data are some of the advantages associated with inverse distance weighted interpolation [12]. The inverse distance weighting method used in this study uses a mathematical function known as Shepard´s method [13]:

$$F(x,y) = \sum_{i=1}^{n} w_i f_i \quad (1)$$

$$w_i = \frac{h_i^{-p}}{\sum_{j=1}^{n} h_i^{-p}} \quad (2)$$

where p is an arbitrary positive real number called the power parameter (typically $p = 2$) and hj are the distances from the dispersion points to the interpolation point, given by:

$$h_i = \sqrt{(x - x_i)^2 + (y - y_i)^2} \quad (3)$$

where *x, y* are the coordinates of the interpolation point and *xi, yi* are the coordinates of each dispersion point. For this method, the influence of a known data point is inversely related to the distance from the unknown location that is being estimated as nearby values contribute more to the interpolated values than distant observations [14]. C++ programming language was used for writing the required programs. The accuracy of the developed program was investigated by choosing 40 hypothetical points within the field. Interpolation was done based on pre-determined field sampling data and then compare with IDW interpolation values obtained from ArcMap 10 software as a referenced program.

Variable Rate Application Control System. The system used for controlling fertilizer application rate was developed in two different forms; manual and automatic forms. In both systems, a linear actuator arm mounted on the fertilizer outlet lever was provided by using a driving circuit comprising of ATMEGA328 based Arduino Uno board and relay circuit. Feedback signals from linear actuators were perceived by Arduino Uno to determine actuator position. Then a program load onboard combined two interpolation values and feedback signals and send out an essential command to relay circuit to perform the required fertilizer rate.

In the manual system, the desired fertilizer rate was determined by pressing the relative button. Five embedded button used on the control unit was in the number and color of anticipated classification in the interpolation program. The time of pressing buttons can also be determined by using a prescription map. System integrated with a GPS via tablet computer. The GPS location on each color of the prescription map is considered as the corresponding color on the buttons. So, the required fertilizer rate was applied when the relative colored button was pressed (Figure 2).

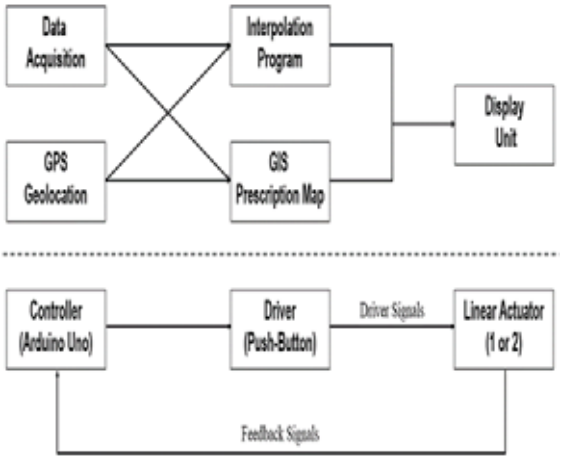

FIGURE 2
The block design of manual type variable rate fertilizer

In the automatic system, the same process was done with the exception that no operator intervention is required to apply fertilizer rates. By using

this system without the need for mapping software, predicted fertilizer rates were determined by interpolation program at GPS position were sent to control unit to provide linear actuator movement at the desired level (Figure 3).

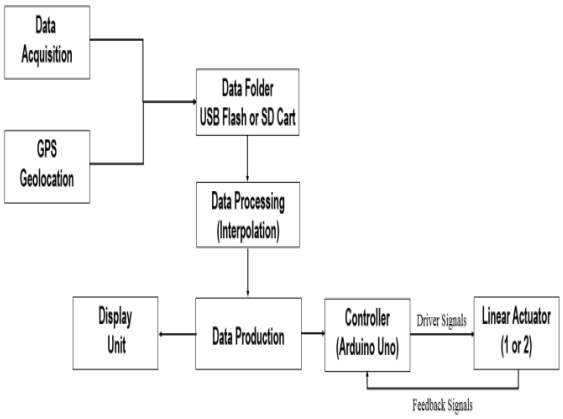

FIGURE 3
The block design of automatic type variable rate fertilizer.

A C++ software program was developed to integrate the function of the system component.

System performance evaluation. Performance evaluation of the developed system was carried out under different target fertilizer rates (0, 60, 90, 120, 150 kgN/ha) and 1 m/s as operation speed. Urea (46% N) was used as selected granular fertilizer and foam rubber surface was placed to determine the fertilizer performance for the different rate-setting and the transition from one rate to another. The calibration of fertilizer was done before installing the system component. A simulated field test was conducted to collect granular fertilizer from metering units for short intervals of travel to define the transition performance. 20-meter long distance was divided into 10 plots with a 1.65*2 m dimension. Two lines of collecting surface were used and fertilizer from each three metering units was collected into each line. Change of fertilizer rate was initiated at the first plot of the experiment line, and then samples collected from each plot were weighted to determine the application rate for each line. Test procedure to determine response time for different fertilizer rates was conducted at low to high transition order (increasing form) and high to low transition order (decreasing form). Considering 1 m/s as operation speed, where the application rate starts to change can be translated into time (Table 1).

The sigmoid equation was used to fit the data from the experiment to determine response time for both increasing and decreasing forms of fertilizer rate changing. A four-parameter logistic model estimated the sigmoidal behavior of the variable rate system response as follows [15]:

$$Y = d + \frac{a-d}{1+\left(\frac{X}{c}\right)^{b}} \qquad (4)$$

Where, Y=application rate, a=minimum rate, c=inflection point, d=maximum rate and X=distance.

Microsoft Excel-based XLSTAT extension procedure was used to determine model parameter estimates. The extracted sigmoid pattern of the model is used to interpret the application rate behavior.

RESULTS AND DISCUSSION

Interpolation accuracy. Hypothetical points selected from a field were used to investigate the developed interpolation program. The value of predetermined field sampling data was interpolated using IDW interpolation of spatial analyst toolbox as an ArcMap 10.2.2 software function. Figure 4 shows the best fit line relating the interpolated values from the developing program to ArcMap 10.2.2 software values. The result of linear regression was revealed a high coefficient of determination (R^2=0.95) between two variants that demonstrated the accuracy of the interpolation program.

TABLE 1
Descriptive statistics of fertilizer rate at different rate-setting

Transition order	rates, kg/ha	Mean, kg/ha	Percentage deviation, %	Down-the-row		Among metering units	
				STDEV, kg/ha	CV, %	STDEV, kg/ha	CV, %
Increasing rate (low to high)	0-60	52.25	-12.92	13.71	26.25	18.89	36.15
	60-90	87.39	-2.9	7.3	8.35	10.63	12.17
	90-120	112.93	-5.89	7.68	6.8	13.27	11.75
	120-150	144.54	-3.64	9.31	6.44	14.61	10.11
Decreasing rate (high to low)	150-120	123.68	+3.06	17.65	14.27	17.31	13.99
	120-90	99.46	+10.51	10.39	10.45	11.09	11.15
	90-60	69.15	+15.25	7.97	11.53	12.08	17.48
	60-0	18.99	+18.99	15.43	81.3	23.35	117.78

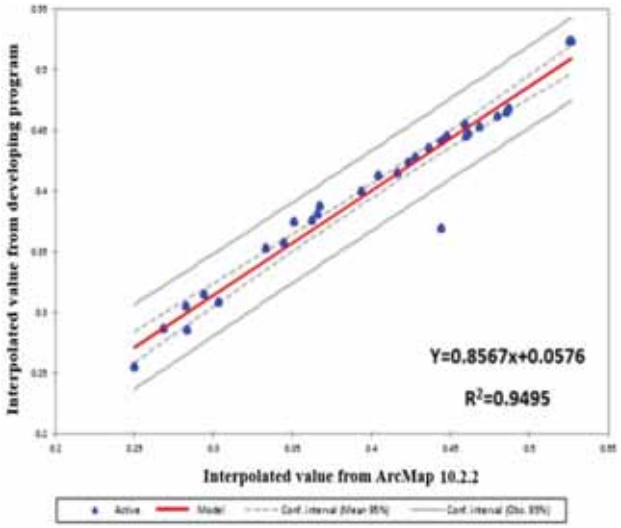

FIGURE 4
Linear regression relating the interpolated values from developing a program to ArcMap 10.2.2 software values

Application performance. Increasing and decreasing rate changing order as two transition orders were applied to evaluate application performance. The variability of the fertilizer delivered by each metering unit in terms of down-the-row and among metering units is summarized in Table 1. Statistical data in this table represent application data of test procedure from 10 plots with 1.65 * 2 m dimension.

Variation of fertilizer rates down-the-row for two series of pilots with 2 m length resulted in a coefficient of variation (CV), ranging from 6.44 to 26.25% and 10.45 to 81.3 for application rate from 0 to 150 kg/ha and 150 to 0 kg/ha as increasing and decreasing transition order, respectively. Variation of fertilizer rate among the metering units in terms of CV resulted from 10.11 to 36.15% and 11.15 to 117.89% in increasing and decreasing transition order, respectively. It seems that the system has better performance on increasing transition order in both down-the-row and among metering units in terms of coefficient of variation.

During the process of fertilization rate changing in the form of increasing to decreasing order, the calculated value related to CV was high at the beginning and end of shifts compared with other mid rates. Accumulation of fertilizer on downfall wickets at startup and incomplete wickets closure due to granules resistance at the end of rate changing was observed as the reason for CV percentage. Figures 5 and 6 present variations in fertilizer rate with distance for increasing and decreasing transition order, respectively. Mean values related to the different fertilizer rate-setting were demonstrated in each figure.

Time response. As a result of a simulated field test, all data from different fertilizer rate exchanges were used to investigate the sigmoidal behavior of the variable rate system. Generally, changes in fertilizer rate can be observed as an S-shaped diagram. So, to test the control system's ability to change the applied rate on the go, sigmoidal parameter estimation, R-squared values, and distance values at 95% confidence interval were determined (Table 2). Table 2 shows the summary results for sigmoidal model parameters estimation and time response values at increasing (low to high) and decreasing (high to low) transition order. As the results show, even though the signal of the fertilizer rate change was applied at the beginning of the first pilot (0 m), the rate changed after a few meters traveled. The traveled distance need to apply the desired rate represents the time needed for the actuator to overcome the mechanical friction of the system. The distance traveled before the complete change occurred at increasing rate order were about 9.01, 5.30, 4.78, 3.19 m for 0-60, 60-90, 90-120, 120-150 kg/ha rates, respectively. As the same, distance values determined for decreasing rate order were 4.53, 5.37, 3.91, and 9.44 m for 150-120, 120-90, 90-60, 60-0 kg/ha rates, respectively. Considering 1 m/s as operating speed, the values determined for distance corresponded to a system response time. It should be noted that because of increasing of fertilizer rate from 0 to 60 kg/ha and decreasing rate from 60 to 0 kg/ha were doubled, determining response time for first/last 30 kg will be possible by halving response time values obtained from above-mentioned fertilizer rates (0-60 and 60-0 kg/ha). The average values of response time were also determined as 4.44 and 4.63 s for increasing and decreasing transition orders, respectively.

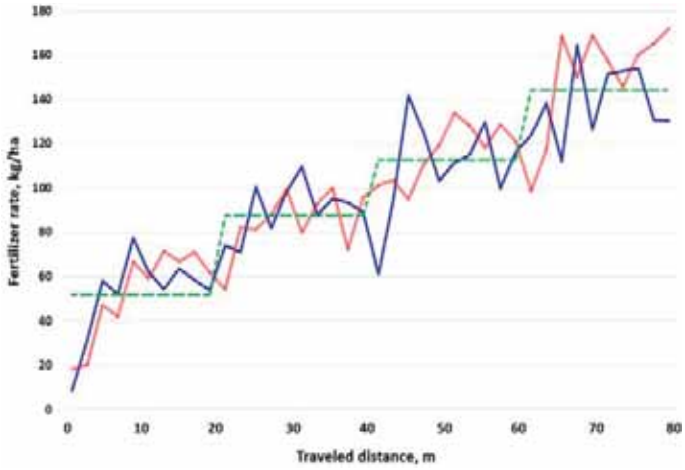

FIGURE 5

Variation in fertilizer rate with traveled distance at increasing transition order

(collected from the right hopper and collected from left hopper represents observed data and dashed line represent the mean value for each fertilizer rate)

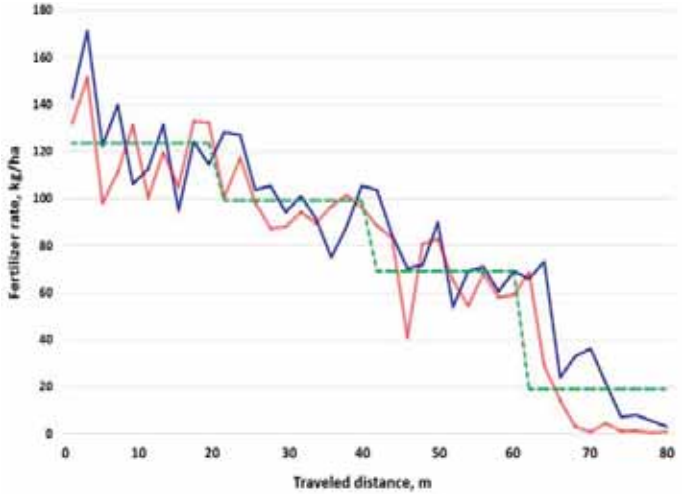

FIGURE 6

Variation in fertilizer rate with traveled distance at decreasing transition order

(collected from the right hopper and collected from left hopper represents observed data and dashed line represent mean value for each fertilizer rate)

TABLE 2

Sigmoidal model parameters estimation, R-square, and time response values for different fertilizer rates at two transition order

Transition Order	Exchange rate	Model Parameters				R^2	X*	Time Response*
		a	b	c	d			
	kg/ha	Estimate	Estimate	Estimate	Estimate		metre	second
Low to High	0 - 60	66.81	1.59	4.11	22.79	0.67	9.01	9.01
	60 - 90	94.19	4.01	4.17	62.65	0.60	5.30	5.30
	90 -120	118.67	11.47	4.04	81.27	0.47	4.78	4.78
	120 -150	152.45	4.59	4.41	110.51	0.42	3.19	3.19
High to Low	150 - 120	117.28	364.24	4.54	149.26	0.46	4.53	4.53
	120 - 90	93.89	22.142	5.76	118.22	0.57	5.37	5.37
	90 - 60	62.38	4.62	4.60	96.51	0.82	3.91	3.91
	60 - 0	-6.14	0.94	0.06	1874.42	0.88	9.44	9.44

* 95% confidence Interval

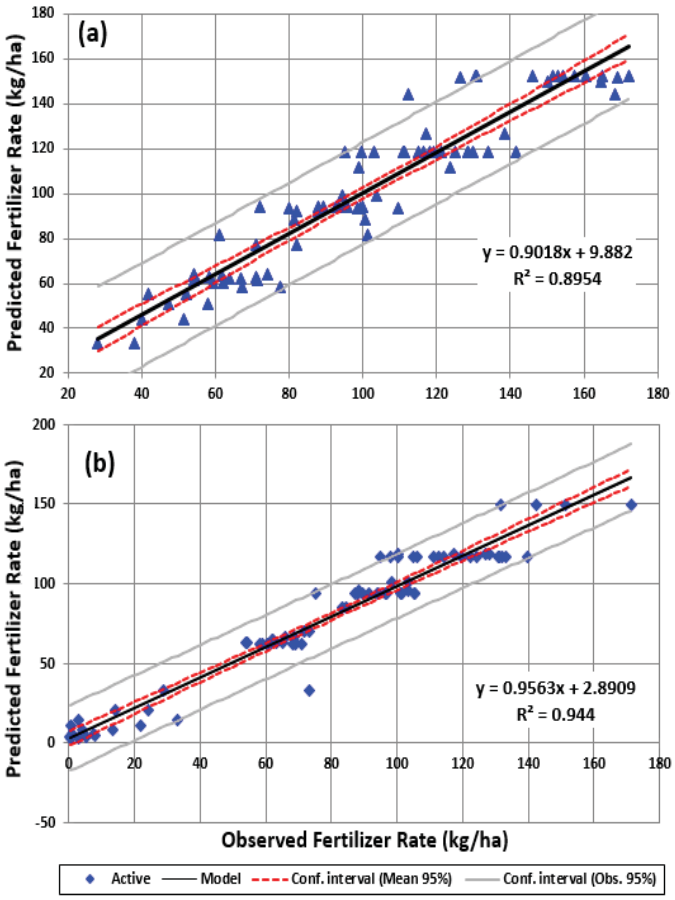

FIGURE 7
Relation between predicted and observed fertilizer rates during test procedure for increasing transition order (a) and decreasing transition order (b). The total number (n) of samples in each plot is 80

Figure 7 shows graphically the relationship between the predicted fertilizer rate using a logistic model (y) and the observed fertilizer rates (x). The simple linear regression model was established to evaluate comparing the predicted and the observed data during the test procedure. The parameters of the regression analysis showed that the model was able to satisfactorily predict the fertilizer rate in each transition order. As the results of regression analysis, the coefficient of determination was found as 0.89 and 0.94 for increasing and decreasing fertilizer rate, respectively. The results showed that the established model can be a suitable tool to investigate response time in the proffered system.

CONCLUSIONS

In this study, a cheap and simple solution to variable-rate granular fertilizing based on field sampling data was introduced. For this purpose, the system consisted of interpolation, control, and applicator adjustment systems with the beneficiary of geographic information system (GIS) implementation. The developed system was modified for a six-row hoeing fertilizer to change fertilizer rate on the go in both manual and automatic types. The manual type system allowed an operator to change the required fertilizing rate either from the prescription map or developed interpolation software. The automatic system was used a field sampling data document to apply the desired fertilizer rate properly at the right time of progress without any operator interference. A test procedure was carried out to evaluate the accuracy of interpolation software and the performance of the variable rate system across the field in terms of response time. Compared with professional software used for variable rate applications such as ArcMap, the accuracy of developed software by the Inverse Distance Weighting method was proved with a high coefficient of determination (0.95) from a linear regression model.

During a simulated field test, changing in fertilizer rates was followed by increasing and decreasing rates as transition orders in 20 m length distance with two series of 10 plots. To determine system response time, fertilizer rates were changed at the beginning of the predetermined distance to set a distance for the acquirable fertilizer rate. Taking into account operation speed at 1 m/s, the average values of response time were determined as 4.44 and 4.63 s for increasing and decreasing transition orders, respectively.

The developed system is not only used for the row fertilizer machine, but also it can be beneficial in all variable rate applicators such as seeders, centrifugal fertilizer distribution machines, and spreaders with changes in their distributor driving systems. Replacement of linear actuator with high speed and high power type and optimization of the opening and closing mechanism to overcome granular fertilizer particles in front of the wickets are recommended to improve variable rate system quality use in row hoeing fertilizer machines.

ACKNOWLEDGEMENT

The authors acknowledge Scientific and Technological Research Institution of Turkey Supporting Project number 113O226, 2015. The authors also would like to thank to Konya sugar research institute-Pankobirlik for their support.

REFERENCES

[1] Ess, D. R., Morgan, M. T., and Parsons, S. D. (2001) Implementing site-specific management: map-versus sensor-based variable rate application. Pub. No. SSM-2-W, Site-Specific Management Center, Purdue University. 1-9.

[2] Jochinke, D. C., Noonon, B. J., Wachsmann, N. G., Norton, R. M. (2007) The adoption of precision agriculture in an Australian broadacre cropping system—Challenges and opportunities. Field Crops Research. 104(1), 68-76.

[3] Robertson, M. J., Llewellyn, R. S., Mandel, R., Lawes, R., Bramley, R. G. V., Swift, L., O'Callaghan, C. (2012) Adoption of variable rate fertiliser application in the Australian grains industry: status, issues and prospects. Agriculture. 13(2), 181-199.

[4] Chi, T. T. N., and Yamada, R. (2002) Factors affecting farmers' adoption of technologies in farming system: A case study in Omon district, Can Tho province, Mekong Delta. Omonrice, 10, 94-100.

[5] Antolini, L. S., Scare, R. F. and Dias, A. (2015) Adoption of precision agriculture technologies by farmers: a systematic literature review and proposition of an integrated conceptual framework. IFAMA World Conference, USA. 1-17.

[6] Pierpaoli, E., Carli, G., Pignatti, E., and Canavari, M. (2013) Drivers of Precision Agriculture Technologies Adoption: A Literature Review. Procedia Technology. 8, 61-69.

[7] Bakdemir, B., Aydoğdu, B., Üngör, M,G., Atık, M and Sağlam N. (2018) Variable Rate Fertilizer Control System for Centrifugal Fertilizer Spreaders. Journal of Agricultural Faculty of Gaziosmanpasa University. 35(3), 319-329.

[8] Kim, Y. J., Kim, H. J., Ryu, K. H., Rhee, J. Y. (2008) Fertiliser application performance of a variable-rate pneumatic granular applicator for rice production. Biosystems Engineering. 100 (4), 498-510.

[9] Talha, Z., Tola, E., Al-Gaadi, K. A., and Kheiralla, A. F. (2011) Pneumatic System for Granular Fertilizer Flow Rate Control. Middle-East Journal of Scientific Research. 8(3), 688-693.

[10] Saad, S. Z., Abdelwahed, A.E. M., Rania, A.E. E., Yaser, M. H., Esmat, A., Khaled, A. A. (2021). Effect of method and time of micronutrients application on sugar beet productivity under two nitrogen fertilizer sources. Fresen. Environ. Bull. 30(7), 9135-9140.

[11] Khaled, A.A., Ragab, Y. A., Dalia, A. E., Mohamed, F. O. (2019) Effect of nitrogen and potassium fertilization on productivity and quality of sugarbeet plants at North delta region. Fresen. Environ. Bull. 30(7), 9135-9140.

[12] Hu, J. (1995) Methods of generating surfaces in environmental GIS applications. In 1995 ESRI User Conference Proceedings.

[13] Shepard, D. (1968) A two-dimensional interpolation function for irregularly-spaced data. In Proceedings of the 23rd ACM National Conference. 517-524.

[14] Azpurua, M. A., Ramos, K. D. (2010) A comparison of spatial interpolation methods for estimation of average electromagnetic field magnitude. Progress In Electromagnetics Research. 14, 135-145.

[15] Motulsky, H., Christopoulos, A. (2004) Fitting models to biological data using linear and nonlinear regression: a practical guide to curve fitting. Oxford University Press.

Received: **18.01.2018**
Accepted: **19.02.2022**

CORRESPONDING AUTHOR

Ufuk Turker
Department of Agricultural Machinery and Technologies Engineering,
Faculty of Agriculture, Ankara University,
Aydınlıkevler 06130 Ankara – Turkey

e-mail: uturker@agri.ankara.edu.tr

© by PSP Volume 31– No. 05/2022 pages 4651-4658 Fresenius Environmental Bulletin

ANTIOXIDANT AND ANTIMICROBIAL ACTIVITIES OF FIVE ENDEMIC *Hypericum* SPECIES IN TURKEY

Caglayan Unsal Gurer[1,*], Esra Eroglu Ozkan[1], Sukran Kultur[2], Nurten Ozsoy[3], Berna Ozbek Celik[4], Afife Mat[1]

[1]Department of Pharmacognosy, Faculty of Pharmacy, Istanbul University, 34116 Beyazit, Istanbul, Turkey
[2]Department of Pharmaceutical Botany, Faculty of Pharmacy, Istanbul University, 34116 Beyazit, Istanbul, Turkey
[3]Department of Biochemistry, Faculty of Pharmacy, Istanbul University, 34116 Beyazit, Istanbul, Turkey
[4]Department of Pharmaceutical Microbiology, Faculty of Pharmacy, Istanbul University, 34116 Beyazit, Istanbul, Turkey

ABSTRACT

Plants of the genus *Hypericum* are widely used in folk medicine for the treatment of gastric ailments, burns, inflammation, microbial infections, skin wounds and psycological disorders. Five endemic *Hypericum* species in Turkey (*H. kotschyanum* Boiss.*, H. scabroides* Robson & Paulter*, H. salsugineum* Robson & Hub.-Mor*, H. thymopsis* Boiss. *and H. uniglandulosum* Hausskn. ex Bornm.) were tested *in vitro* for antioxidant activity. Methanol-acetone extracts of the aerial parts of *H. salsugineum* and *H. scabroides* possessed significant activity which may be attributed to their strong reducing power, DPPH and superoxide radicals scavenging, metal chelating and lipid peroxidation inhibitory activities. The superoxide radical scavenging activity of *H. scabrides* (EC_{50}: 1.14 ± 0.046 mg/ml) and *H. salsugineum* (EC_{50}: 1.09 ± 0.096 mg/ml) were more remarkable than that of other three species. The antimicrobial study was carried out by microbroth dilution technique. The extracts showed good antibacterial activity against Gram-positive bacteria but no antifungal activity. Chloroform extract of the aerial parts of *H. scabroides* showed antibacterial activity against *Staphylococcus aureus* with a MIC value of 39.06 µg/ml.

KEYWORDS:
Hypericum, phenolic, flavonoid, antioxidant, antimicrobial

INTRODUCTION

The widespread use of traditional herbs and medicinal plants have been traced to the occurence of natural products with medicinal properties [1]. Recent findings have shown that many human diseases are associated with oxidative stress and several investigations have led to the research for dietary antioxidants. Many phytochemicals from plants, particularly phenolic compounds have been found to possess strong antioxidant activity and reduce the risks of degenerative diseases such as neurodegenerative, cardiovascular, aging diseases and cancer [2]. In recent years, the consumption of *Hypericum*-derived products has increased dramatically and presently they are one of the most consumed medicinal plants over the world [3, 4]. Several *Hypericum* species had been evaluated for their possible antioxidant activities [4-11]. *Hypericum pamphylicum* N.Robson & P.H. Davis collected from Antalya (Turkey) was studied for its biological activities and it has been shown that the methanol extract of the plant has antibacterial activity as well as antioxidant properties [12]. *H. uniglandulosum* Hausskn. ex Bornm., an endemic species from Turkey was investigated before and it has been shown that the methanol extract of the flowers of this species possesed high antioxidant activity [13]. The methanol extract of *H. capitatum* Choisy var. *capitatum* from Northwestern Turkey was found to be most active in scavenging of DPPH free radical and ABTS cation radical and CUPRAC assays together with the highest antibacterial activity against *Escherichia coli* [14].

Five species included in this study (*H. kotschyanum* Boiss.*, H. scabroides* Robson & Paulter *, H. salsugineum* Robson & Hub.-Mor*, H. thymopsis* Boiss. *and H. uniglandulosum* Hausskn. ex Bornm.) are growing wild and endemic to Turkey. A survey of the literature revealed that no studies have been undertaken on the potential antimicrobial and antioxidant activities of *H. kotschyanum*, *H. salsugineum* and *H. thymopsis*. Accordingly, our objective was to evaluate the antioxidant activity of methanolic extracts from these five *Hypericum* species, including antioxidant effect on Fe^{3+}/ ascorbate-induced lipid peroxidation in a liposome model system, scavenging effect on $DPPH^{\bullet}$ and superoxide radicals, reducing power and chelating activity in order to establish a relationship between their antioxidant activities and their effects against infectious agents.

MATERIALS AND METHODS

(1) Plant material. *Hypericum kotschyanum* (HK) was collected from Mersin in June 2007, *H. salsugineum* (HSa) was collected from Konya in

July 2005, *H. scabroides* (HSc) and *H. uniglandulosum* (HU) were collected from Erzincan in July 2006 and *H. thymopsis* (HT) was collected from Sivas in July 2005. Voucher specimens were identified by Ş. Kültür (Department of Pharmaceutical Botany, Faculty of Pharmacy, Istanbul University) and deposited in the Herbarium of the Faculty of Pharmacy, Istanbul University. The identification numbers of the voucher specimens *H. kotschyanum*, *H. salsugineum*, *H. scabroides*, *H. thymopsis* and *H. uniglandulosum* were ISTE 83979, ISTE 85341, ISTE 85343, ISTE 85342 and ISTE 85344, respectively.

(2) Preparation of extracts. The aerial parts of *Hypericum* species were dried at room temperature and powdered. Plant material (20 g) from each species was extracted with 200 ml of methanol and acetone in an ultrasonic bath for 30 minutes respectively and filtered. Methanol and acetone extracts were combined and the solvent was removed *in vacuo* at 40°C. The methanol-acetone extracts of each species were used for antioxidant activity assays.

Powdered aerial parts of *Hypericum* species (25 g) were extracted sequentially with petroleum ether, chloroform and methanol in a Soxhlet apparatus. The solvents were evaporated *in vacuo* and the resulting extracts were subjected to antimicrobial activity assays.

(3) Determination of total phenolic and flavonoid compounds. Total phenolics in the methanol-acetone extracts of *Hypericum* species were determined with Folin-Ciocalteu reagent according to the method of Slinkard and Singleton [15]. Total flavonoid content was determined by using a method described by Sakanaka et al. [16].

(4) Antioxidant activity on liposome peroxidation. Lipid peroxidation assay was based on the method described by Duh et al. [17]. Lecithin (300 mg) was suspended in 30 ml, 10 mmol/L phosphate buffer (pH 7.4). This suspension was then sonicated with a rod using a Ultrasonic Homogenizer (Bandelin, Berlin, Germany) at 30s intervals for 10 min until an opalescent suspension was obtained. The sonicated solution (10 mg/ml), $FeCl_3$, ascorbic acid and water solution of the plant extracts

(0.125 - 5 mg/ml) or reference antioxidants (0.016 – 2.5 mg/ml rutin, 0.004 - 0.0625 mg/ml BHT) were mixed to produce a final concentration of 3.08 mg liposome/ml, 123 µmol/L $FeCl_3$ and 123 µmol/L ascorbic acid. After 1 h incubation at 37ºC, the formation of lipid peroxidation products was assayed by the measurement of MDA levels on the basis of MDA reacted with thiobarbituric acid at 532 nm according to Buege and Aust [18].

(5) DPPH radical scavenging activity. The DPPH radical scavenging activity of the methanol-acetone extracts from *Hypericum* species was measured according to the procedure described by Brand-Williams et al. [19].

(6) Superoxide radical scavenging activity. The effects of the methanol-acetone extracts from *Hypericum* species and rutin on generation of superoxide radicals were determined by the nitroblue tetrazolium reduction method [20].

(7) Iron chelating activity. The extracts were assessed for their ability to compete with ferrozine for iron (II) ions in free solution. The chelating ability of ferrous ions by the methanolic extracts from *Hypericum* species was estimated by the method of Dinis et al. [21].

(8) Reducing power. The reducing powers of the methanol-acetone extracts from *Hypericum* species, rutin and BHT were determined according to the method described by Chung et al. [22].

(9) Statistical analysis. Results were expressed as the means of three replicates ± standard deviation. Statistical comparisons were performed with Student's *t*-test. Differences were considered significant at $p<0.05$. The correlation coefficient (r^2) between the parameters tested was established by regression analysis.

(10) Antimicrobial activity tests. Antimicrobial activity tests were performed on the extracts obtained from the aerial parts of *Hypericum* species (25 g) using solvents petroleum ether, chloroform and methanol in a Soxhlet apparatus.

Antimicrobial activity against *Staphylococcus aureus* ATCC 65538, *Staphylococcus epidermidis* ATCC 12228, *Escherichia coli* ATCC 25922, *Klebsiella pneumoniae* ATCC 4352, *Pseudomonas aeruginosa* ATCC 27853, *Proteus mirabilis* ATCC 14153 and *Candida albicans* ATCC 10231 were determined by the microbroth dilutions technique using the CLSI 2000 and 2006 recommendations [23, 24]. Mueller-Hinton broth for bacteria, RPMI-1640 medium for yeast strain were used as the test media. The extracts were dissolved in dimethylsulfoxide (DMSO, 10 mg/mL) before the test for antimicrobial activity. Serial two-fold dilutions ranging from 5000 to 4.9 µg/mL were prepared in medium. The inocula were prepared using a 4-6 h broth culture of each bacteria and 24 h culture of yeast strains adjusted to a turbidity equivalent to a 0.5 McFarland standard, diluted in broth media to give a final concentration of 5×10^5 cfu/mL for bacteria and 0.5×10^3 to 2.5×10^3 cfu/mL for yeast in the test tray. The trays were covered and placed in plastic bags to prevent evaporation. The trays containing Mueller-Hinton broth were incubated at 35ºC for 18-20 h and the trays containing RPMI-1640 medium were incubated at 35ºC for 46-50h.

The MIC was defined as the lowest concentration of compound giving complete inhibition of visible growth. All the microorganisms were obtained from American Type Culture Collection (ATCC), Manassas (VA), USA. Cefuroxime-Na and ceftazidime were used as positive control for the tested bacteria whereas clotrimazole was used as positive control for yeast.

RESULTS

(1) Extraction yield (Amount of total extractable compounds). The results presented in Table 1 showed that the amount of extractable compounds ranged from 61.54 to 74.93 mg/g dry plant material. *H. scabroides* and *H. salsugineum* extracts which showed similar values were found to have the highest amount of total extractable compounds whereas *H. uniglandulosum* produced the lowest yield.

(2) Extractable total phenolic and flavonoid amounts. Because phenolic compounds may contribute to overall antioxidant activities, the present study measured the total phenolic compounds using Folin-Ciocalteu reagent. The results given in Table 1 showed the amount of extractable phenolic compounds in *Hypericum* extracts, expressed in mg gallic acid equivalents (GAE) /g of dry weight. These values were greater than that detected in *H. perforatum* (0.55 ± 0.01 mg GAE/ 100 g of dry weight) [7], suggesting that these herbal drugs may serve as a dietary source of phenolic substances. Kizil et al. [6] reported that the total phenolic content of 1 mg *H. triquetrifolium* and *H. scabroides* ethanol extracts were equivalent to 267 and 333 µg gallic acid, respectively. Estimation of total phenolics revealed that *Hypericum* species are a rich sources of phenolic compounds. Thus, the results appear to be in reasonable agreement with the literature.

No significant differences (p>0.05) were found between the amount of total phenolic compounds in *H. uniglandulosum*, *H. kotschyanum* and *H. thymopsis*, while the amount of phenolics in *H. scabroides* and *H. salsugineum* were higher (p<0.05).

The amount of flavonoids in the total extractable compounds of *Hypericum* extracts, expressed in mg catechin equivalents/g dry weight were given in Table 1. Flavonoid amounts of *H. uniglandulosum* and *H. thymopsis* did not differ significantly (p > 0.05), however were significantly lower (p< 0.05) than flavonoid amounts of *H. scabroides* and *H. salsugineum* which were similar. The amount of flavonoids in *H. kotschyanum* was higher than that of *Hypericum uniglandulosum* and *H. thymopsis*, but lower than that of *H. scabroides* and *salsugineum*. There was high correlation between total phenolic and flavonoid contents (r^2 = 0.998, 0.997, 0.997, 0.999, and 0.986 for *H. uniglandulosum*, *kotschyanum*, *thymopsis*, *scabroides* and *salsugineum* extracts, respectively) amounts. The total phenol/extractable compounds ratio ranged from 10.9 % (*H. kotschyanum*) to 11.4 % (*H. salsugineum*). This suggested that there was a large amount (88.6 % to 89.1 %) of non-Folin-Ciocalteu reactive substances.

(3) Antioxidant activity on lipid peroxidation. The antioxidant activity of five *Hypericum* species was evaluated by the decrease of thiobarbituric acid reactive substances (TBARS) produced from lipid peroxidation of the soybean phosphatidylcholine (lecithin) liposomes induced by Fe^{3+}/ascorbate model system. The inhibitory effects of various amounts of *Hypericum* extracts on lipid peroxidation of liposomes are shown in Figure 1B. According to the obtained results, all *Hypericum* extracts act as antioxidant agents and reduce the production of TBARS. *H. uniglandulosum* (87.6 ± 0.35 %), *H. kotschyanum* (88.7 ± 0.54 %), *H. thymopsis* (92.5 ± 0.88 %), *H. scabroides* (82.6 ± 0.50 %) and *H. salsugineum* (92.0 ± 0.25 %) extracts, at 7.5 mg/ml, showed almost similar inhibitory effects on TBARS formation, which were comparable to that of rutin (89.3 ± 0.32 %) at 2.5 mg/ml and BHT (94.7 ± 0.10 %) at 0.0625 mg/ml.

TABLE 1
Total extractable compounds (EC), total phenolic compounds (PC) (as gallic acid equivalents) and total flavonoids (as catechin equivalents) in methanol extracts from *Hypericum* species

Extract	Yield from 20 g dry plant (g)	Yield % (w/w)	EC (mg /g DW)	PC (mg /g DW)	Flavonoid (mg /g DW)	PC/EC (%)
HU	1.2309	6.15	61.54^{a}	6.80 ± 0.22^{a}	2.48 ± 0.11^{a}	11.04
HK	1.3392	6.69	66.96^{b}	7.34 ± 0.28^{a}	5.19 ± 0.24^{b}	10.96
HT	1.2607	6.30	63.03^{a}	6.58 ± 0.092^{a}	3.46 ± 0.04^{a}	10.43
HSc	1.4987	7.49	74.93^{c}	8.52 ± 0.40^{b}	6.79 ± 0.07^{c}	11.37
HSa	1.4565	7.28	72.82^{c,d}	8.32 ± 1.34^{b,c}	6.25 ± 0.32^{c,d}	11.42

Values were the means of three replicates ± standard deviation.Values with different letters in the same column were significantly (p < 0.05) different. (HU: *Hypericum uniglandulosum*, HK: *H. kotschyanum*, HT: *H. thymopsis*, HSc: *H. scabroides*, HSa: *H. salsugineum*)

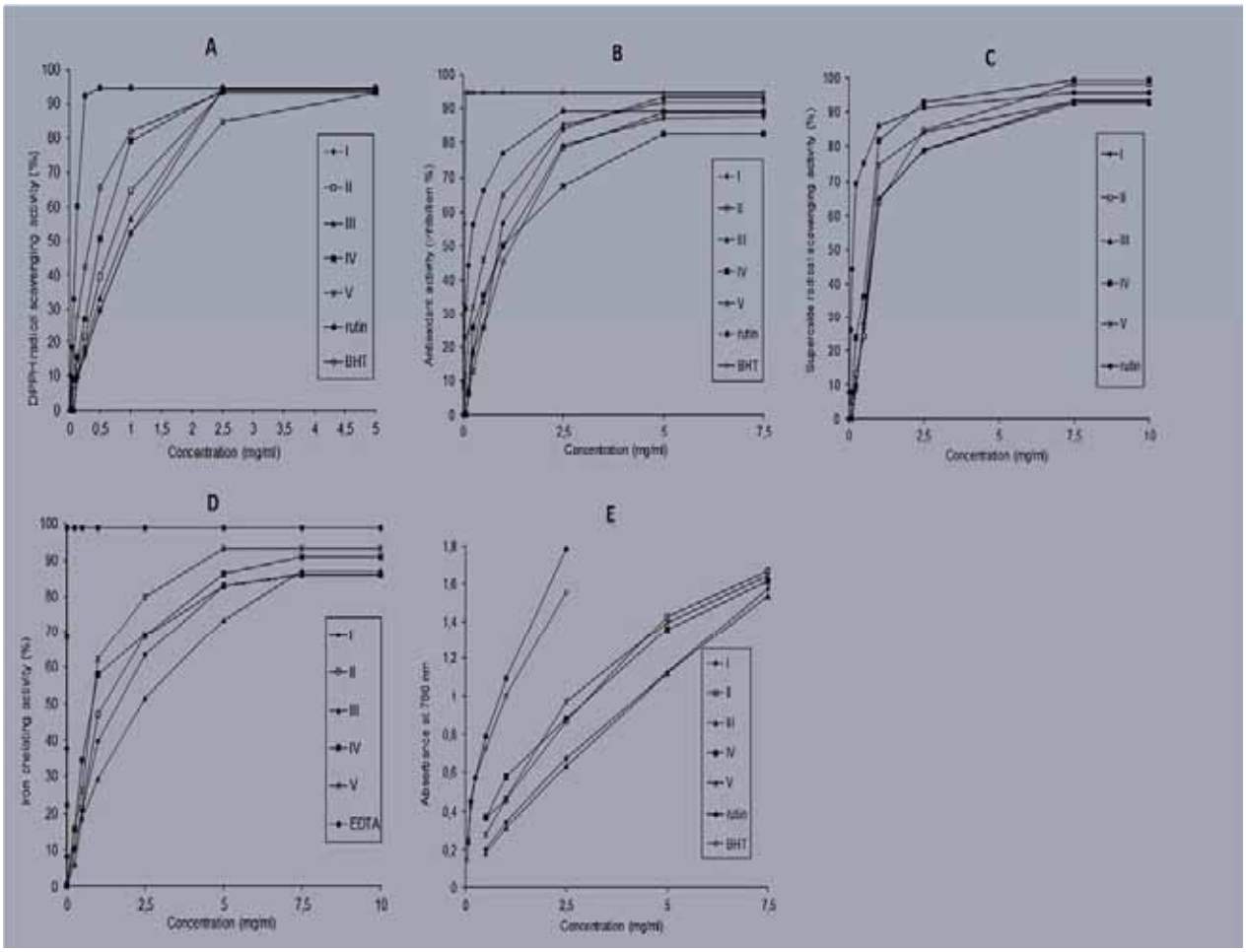

FIGURE 1

Antioxidant test results of the methanol extracts from *Hypericum* species.

A: DPPH radical scavenging activity, B: The inhibitory effect on TBARS formation, C: Superoxide radical scavenging activity, D: Iron chelating activity, E: Reducing power. Values are means ± SD (n = 3). I: *H. uniglandulosum*; II: *H. kotscyanum*; III: *H. thymopsis*; IV: *H. scabroides*; V: *H. salsugineum.*

Based on the EC_{50} values, *H. salsugineum* was the most efficient inhibitor with the lowest EC_{50} value of 1.5 ± 0.02 mg/ml. The antioxidant activities of *H. uniglandulosum*, *H. kotschyanum*, *H. thymopsis* and *H. scabroides* extracts were comparable, and less effective ($p < 0.05$) than that of *H. salsugineum*. None of the extracts were as effective lipid peroxidation inhibitors as the reference antioxidants, rutin and BHT. This results were consistent with the previous observation that *Hypericum* species showed good antioxidant activity *in vitro* [21]. Zou et al [8] found that the *H. perforatum* extract exhibited about 70.0 % inhibition effect at a concentration as low as 0.8 mg/ml, which was similar to that of α-tocopherol. Silva et al [4] reported that the EC_{50} value, determined for the *H. perforatum* inhibitory effect on lipid peroxidation, induced with ascorbate/Fe^{2+} was 26 μg dry weight biomass/ml. It was reported [6] that *H. triquetrifolium* and *H. scabroides* showed notable capacity to supress Fe^{2+}-induced lipid peroxidation in rat brain homogenate. With regard to the antioxidant activity, these five *Hypericum* species were less effective than *H. perforatum*.

(4) DPPH radical scavenging activity. The ability of the extracts to act as a free radical scavengers or hydrogen donors was revealed by DPPH radical scavenging assay. All *Hypericum* extracts showed the DPPH radical scavenging activity in a dose dependent manner. Figure 1A shows that at 2.5 mg/ml the methanolic extracts of *H. uniglandulosum* (94.1 ± 0.06 %), *H. kotschyanum* (93.5 ± 0.32 %), *H. thymopsis* (94.2 ± 0.09 %), *H. scabroides* (93.9 ± 1.02 %) and *H. salsugineum* (92.9 ± 0.47 %) did not differ in their DPPH radical scavenging activities ($p > 0.05$), which were comparable to that of BHT (93.5 ± 1.02 %) at the same concentration and rutin (93.6 ± 0.73 %) at 0.5 mg/ml. The results were in agreement with Kızıl et al [6] who reported the similar DPPH radical scavenging activity of 91.3 % and 82.6 % for *H. scabroides* and *H. triquetrifolium*, respectively.

From the effective concentrations (EC_{50}), it was seen that among the five extracts, *H. scabroides* and *H. salsugineum* showed the highest DPPH radical scavenging activities respectively due to their richest phenolic contents that may contribute to a similar

TABLE 2
Antioxidant properties of methanol-acetone extracts from *Hypericum* species expressed as EC_{50} values

Activity	*EC_{50} (mg/ml)						
	HU	HK	HT	HSc	HSa	Rutin	BHT
LPO inhibition	2.16 ± 0.026[a]	2.34 ± 0.049[b]	2.10 ± 0.061[a]	2.39 ± 0.020[b]	1.51 ± 0.026[d]	0.76 ± 0.038[e]	0.03 ± 0.001[f]
DPPH	1.55 ± 0.030[a]	1.49 ± 0.015[a]	1.62 ± 0.060[a]	1.14 ± 0.046[b]	1.09 ± 0.096[b]	0.15 ± 0.070[d]	0.96 ± 0.110[b]
Superoxide anion	3.09 ± 0.083[a]	3.27 ± 0.065[a]	3.06 ± 0.085[a]	2.36 ± 0.045[b]	2.70 ± 0.090[c]	0.56 ± 0.070[d]	N.d.
Reducing power	1.98 ± 0.100[a]	1.18 ± 0.049[b]	2.05 ± 0.070[a]	0.92 ± 0.051[c]	1.19 ± 0.015[b]	0.18 ± 0.010[d]	0.30 ± 0.015[e]
Chelation activity	2.75 ± 0.101[a]	2.57 ± 0.026[a]	3.31 ± 0.090[b]	1.74 ± 0.055[c]	1.61 ± 0.060[c]	EDTA: 0.006 ± 0.150[d]	

*EC_{50} value: The effective concentration at which the LPO inhibition was 50 %; DPPH and superoxide radicals were scavenged by 50 %; the absorbance was 0.5 for reducing power and ferrous ions were chelated by 50%, respectively. EC_{50} value was obtained by interpolation from linear regression analysis.Values were the means of three replicates ± standard deviation. Values with different letters in the same row were significantly ($p < 0.05$) different. N.d.: Not determined (HU: *Hypericum uniglandulosum*, HK: *H. kotschyanum*, HT: *H. thymopsis*, HSc: *H. scabroides*, HSa: *H. salsugineum*)

(p>0.05) antioxidant activities. The DPPH radical scavenging activities of *H. uniglandulosum, H. kotschyanum* and *H. thymopsis* were comparable (p>0.05) whereas significantly lower (p<0.05) than that of *H. scabroides* and *H. salsugineum*. EC_{50} values of all the extracts, in scavenging abilities on DPPH radicals, were significantly different (p<0.05) from the EC_{50} values obtained for rutin and BHT. These findings are in agreement with our observation on phenolic contents of the extracts and seem to suggest phenolics to be important contributors to the antioxidant activity.

Based on EC_{50} values, Kizil et al [6] reported the higher DPPH radical scavenging activity of *H. triquetrifolium* (IC_{50} = 39.0 µg/ml) and *H. scabroides* (IC_{50} = 33.8 µg/ml). It was reported that *H. perforatum* extract showed relatively high DPPH radical scavenging effect with an average IC_{50} value of 10.63 µg/ml [8]. It was evident that *H. perforatum*, *H. triquetrifolium* and *H. scabroides* extracts had the stronger effects on the DPPH radicals compared to *Hypericum* sp. extracts used in this study. It can be explained with the different phytochemical composition. It is known that only flavonoids of a certain molecular structure, particularly those with a certain hydroxyl position will determine the antioxidant properties [26].

Previous reports have shown that polyphenolic compounds are associated with antioxidant activity. Ivanova et al [1] reported that *H. perforatum* showed high antioxidant potencial with high TEAC value of 3.7 ± 0.14 mM/QE which corresponded to a high phenolics content (881.9 ± 6.68 µM QE). It was reported that *H. perforatum* ethanolic extract contain many phenolic compounds (hypericin, hyperforin and their derivatives, hydroxycinnamic acids, rutin, hyperoside, quercetin, chlorogenic acid, flavonols and flavones), suggesting that they could have important antioxidant properties [4, 8, 10]. Flavonoids, specifically quercetin and its glycoside derivatives, are a major class of compounds present in the *H. perforatum* total ethanolic extract, representing almost 57 % of the total phenols, whereas hydroxycinnamates represent up to 10 % [4]. The antioxidant activity of *H. androsaemum* infusion was also related to its phenolic content [9]. Some of the identified phenols in the *H. androsaemum* infusion extract were 3- and 5-*O*-caffeoylquinic acids, quercetin and glycosylated derivatives, also present in extracts of *H. perforatum*. It was interesting to note that the extract of *H. scabroides* was the most powerful DPPH scavenger but the least effective inhibitor of lipid peroxidation. These results suggested that the nature of biologically active constituents of *H. scabroides* may be different from those present in other extracts.

(5) Superoxide radical scavenging activity. Figure 1C shows the dose-response of superoxide radical scavenging activity of the extracts from *Hypericum* species by the PMS-NADH superoxide-generating system. It was found that at 7.5 mg/ml the *H. uniglandulosum, H. kotschyanum, H. thymopsis, H. scabroides* and *H. salsugineum* extracts exhibited 93.4 ± 0.25, 98.3 ± 0.36, 92.6 ± 0.39, 99.2 ± 0.20 and 93.2 ± 0.25 %, respectively, superoxide radical scavenging activity, which were comparable to that of rutin (95.8 ± 0.12) at the same concentration. BHT showed no detectable superoxide radical scavenging effect.

EC_{50} values, in scavenging abilities on superoxide radicals, were comparable for *H. uniglandulosum*, *H. kotschyanum* and *H. thymopsis* extracts but significantly lower (p< 0.05) than the EC_{50} values obtained for the *H. scabroides* and *H. salsugineum*. This data reinforced the greater antioxidant activity of the *H. scabroides* and *H. salsugineum* in the DPPH assay compared to other three extracts. However, those values were significantly lower (p<0.05) than the value of the reference antioxidant rutin. Table 2 shows that all five extracts are more efficient scavengers of DPPH radicals than of superoxide radicals. Hunt et al [11] evaluated the antioxidant effect of preparations of *H. perforatum* extracts against the superoxide anion. They postulated that the observed free radical scavenging effect could be related to its content in hypericin, among other com-

pounds. In accordance with Hunt et al [11] observations, the results imply that *Hypericum* extracts are superoxide scavengers and their capacity to scavenge superoxide may contribute to their antioxidant activity.

(6) Iron chelating activity. All the extracts demonstrated an ability to chelate iron (II) ions in a dose-dependent manner. Figure 1D shows that at 7.5 mg/ml *H. uniglandulosum* (86.1 ± 0.18 %), *H. kotschyanum* (86.2 ± 0.42 %) and *H. thymopsis* (87.2 ± 1.9 %) did not differ in their chelating abilities (p>0.05), however the extent of complexation by the extract of *H. scabroides* (91.9 ± 0.96 %) and *H. salsugineum* (93.2 ± 0.23 %) was significantly greater ($p < 0.05$) than those observed with the three other extracts. As can be seen from the EC_{50} values, the most effective iron chelators were *H. scabroides* and *H. salsugineum* extracts, followed by the extracts of *H. uniglandulosum* and *H. kotschyanum*, which were not significantly different ($p > 0.05$), while extract of *H. thymopsis* was the least effective. It was evident that the extracts did show the iron chelating activity and might be able to afford protection against oxidative damage by sequestring free iron (II) ions. *Hypericum* extracts investigated in this study showed relatively higher chelating ability compared to that obtained from ethanol extracts of *H. triquetrifolium* and *H. scabroides* [6]. These observations were in agreement with those of Zou et al [8], who showed that chelation of metal ions was the main action of *H. perforatum* extract.

There was high correlation between chelating activity and lipid peroxidation inhibitory (r^2 = 0.986, 0.995, 0.942, 0.987, and 0.992 for *H. uniglandulosum*, *H. kotschyanum*, *H. thymopsis*, *H. scabroides* and *H. salsugineum* extracts respectively), $DPPH^{\bullet}$ (r^2 = 0.969, 0.979, 0.926, 0.959, and 0.959 for *H. uniglandulosum*, *H. kotschyanum*, *H. thymopsis*, *H. scabroides* and *H. salsugineum* extracts, respectively) and superoxide (r^2 = 0.989, 0.968, 0.982, 0.962, and 0.957) radical scavenging activities of the five extracts. The combination of chelating and free radical scavenging activities thus decreases free radical generation and increases radical scavenging potential [27].

(7) Reducing power. Figure 1E shows the dose-response of the reducing powers of methanol-acetone extracts from *Hypericum* species. At 7.5 mg/ml *H. uniglandulosum*, *H. kotschyanum*, *H. thymopsis*, *scabroides* and *H. salsugineum* extracts showed strong reducing powers of 1.57 ± 0.012, 1.67 ± 0.007, 1.54 ± 0.036, 1.64 ± 0.026 and 1.64 ± 0.043 in terms of absorbance values at 700 nm, respectively, which were comparable to that of rutin (1.74 ± 0.021) and BHT (1.560± 0.028) at 2.5 mg/ml. From the EC_{50} values, it was seen that *H. scabroides* extract had the highest reducing power as shown by the lowest value of EC_{50}, followed by *H. kotschyanum* and *H. salsugineum* while the *H. uniglandulosum* and *H. thymopsis* extracts had the lowest reducing powers. It was observed that reducing power increased proportionally to the polyphenol content.

TABLE 3
Minimum inhibitory concentrations (µg/mL) of extracts from *Hypericum* species

		Microorganisms						
		Gram-positive bacteria		Gram-negative bacteria				Fungi
Species/ reference standard	Extract[a]	*Sa*	*Se*	*Kp*	*Pm*	*Ec*	*Pa*	*Ca*
Hypericum kotschyanum	PE	NA	1250	NA	NA	NA	NA	1250
	C	NA	1250	NA	NA	NA	NA	1250
	M	NA	1250	NA	NA	NA	NA	1250
Hypericum salsugineum	PE	156.2	625	NA	NA	NA	NA	NA
	C	78.12	625	NA	NA	NA	NA	NA
	M	625	625	NA	NA	NA	NA	NA
Hypericum scabroides	PE	78.12	625	NA	NA	NA	NA	NA
	C	39.06	625	NA	NA	NA	NA	NA
	M	312.5	625	NA	NA	NA	NA	NA
Hypericum thymopsis	PE	78.12	625	NA	NA	NA	NA	NA
	C	625	312.5	NA	NA	NA	NA	NA
	M	312.5	625	NA	NA	NA	NA	NA
Hypericum uniglandulosum	PE	312.5	625	NA	NA	625	NA	NA
	C	625	625	NA	NA	NA	NA	NA
	M	625	625	NA	NA	NA	NA	NA
Cefuroxime-Na		1.2	9.8	4.9	2.4	4.9		
Ceftazidime							2.4	
Clotrimazol								4.9

Sa: *Staphylococcus aureus*, *Se*: *Staphylococcus epidermidis*, *Kp*: *Klebsiella pneumoniae*, *Pm*: *Proteus mirabilis*, *Ec*: *Escherichia coli*, *Pa*: *Pseudomonas aeruginosa*, *Ca*: *Candida albicans*
PE: petroleum ether, C: chloroform, M: methanol. NA: not active.

Despite the extracts ability to reduce Fe^{3+}, none of the extracts were significantly better ($p< 0.05$) than the reference antioxidants, rutin (0.18 ± 0.01 mg/ml) and BHT (0.30 ± 0.015 mg/ml). All the extracts were capable of reducing Fe^{3+} to Fe^{2+}, and thus were capable of donating electrons. This results compared well with that reported for *H. triquetrifolium* and *H. scabroides* [6].

A strong correlation between reducing power and DPPH$^{\bullet}$, superoxide radical scavenging and antioxidant activity determined in liposome system was also identified. This may be due to components within the extracts acting via a common redox mechanism. This suggests that the extracts may act as free radical chain terminators transforming reactive free radical species into more stable nonradical products.

(8) Antimicrobial activity. The antimicrobial study was carried out by microbroth dilution technique and petroleum ether, chloroform, methanol extracts obtained from the aerial parts of *Hypericum* species were investigated. Based on the result (Table 3), *Hypericum* species extracts showed remarkable antibacterial activity but no activity was observed against *C. albicans*. Our findings correlate with the observations of previous screenings of medicinal plants for antimicrobial activity, where most of the active plant extracts showed activity against Gram-positive strains only [28].

Among these five extracts, the chloroform extract of *H. scabroides* showed the strongest activity against *Staphylococcus aureus* with a MIC value of 39.06 µg/ml. Petroleum ether extract of *H. scabroides* and *H. thymopsis* and chloroform extract of *H. salsugineum* showed moderate activity against *S. aureus* with a MIC value of 78.12 µg/ml. *H. uniglandulosum* has the minimum flavonoid content, accordingly its antibacterial activity is the lowest. Flavonoid-rich plant extracts from species of *Hypericum* have been reported to possess antibacterial activity [29]. Since the antimicrobial activity in other species of *Hypericum* genus has been found to be closely related to the levels of flavonoids and phenolic derivatives [30, 31, 32, 33], it is reasonable to assume that these compounds are responsible for the antimicrobial activity reported here.

CONCLUSIONS

In the present paper, we report the antimicrobial and antioxidant activities of five endemic *Hypericum* species; *H. kotschyanum* Boiss., *H. scabroides* Robson & Paulter, *H. salsugineum* Robson & Hub.-Mor, *H. thymopsis* Boiss. and *H. uniglandulosum* Hausskn. ex Bornm. On the basis of the biochemical characterization of the five extracts and on their antimicrobial activity, we could say that *H. scabroides* could be suitable for further investigations in pharmacy to be used as an extract which has antioxidant ant antibacterial properties.

ACKNOWLEDGEMENTS

This study was supported by The Research Fund of Istanbul University (Project No. 442 / 27122005).

REFERENCES

[1] Ivanova, D., Gerova, D., Chervenkov, T., Yankova, T. (2005) Polyphenols and antioxidant capacity of Bulgarian medicinal plants. Journal of Ethnopharmacology. 96, 145-150.

[2] Scalbert, A., Manach, C., Morand, C., Rémésy, C., Jiménez, L. (2005) Dietary polyphenols and the prevention of diseases. Critical Reviews in Food Science and Nutrition. 45, 287-306.

[3] Wills, R.B.H., Bone, K., Morgan, M. (2000) Herbal products: active constituents, modes of action and quality control. Nutrition Research Reviews. 13, 47-77.

[4] Silva, B.A., Ferreres, F., Malva, J.O., Dias, A.C.P. (2005) Phytochemical and antioxidant characterization of *Hypericum perforatum* alcoholic extracts. Food Chemistry. 90, 157-167.

[5] Eroğlu-Özkan, E., Mat, A. (2013) An overview on *Hypericum* species of Turkey. Journal of Pharmacognosy and Phytotherapy. 5(3), 38-46.

[6] Kizil, G., Kizil, M., Yavuz, M., Emen, S., Hakimoğlu, S. (2008) Antioxidant activities of ethanol extracts of *Hypericum triquetrifolium* and *Hypericum scabroides*. Pharmaceutical Biology. 46, 231-242.

[7] Wojdylo, A., Oszmianski, J., Czemerys, R. (2007) Antioxidant activity and phenolic compounds in 32 selected herbs. Food Chemistry. 105, 940-949.

[8] Zou, Y., Lu, Y., Wei, D. (2004) Antioxidant activity of a flavonoid-rich extract of *Hypericum perforatum* L. *in vitro*. Journal of Agricultural and Food Chemistry. 52, 5032-5039.

[9] Valentão, P., Fernandes, E., Carvalho, F., Andrade, P.B., Seabra, R.M., de Louredes Bastos, M. (2002) Antioxidant activity of *Hypericum androsaemum* infusion: scavenging activity against superoxide radical, hydroxyl radical and hypochlorous acid. Biological and Pharmaceutical Bulletin. 25, 1320-1323.

[10] Conforti, F., Statti, G.A., Tundis, R., Menichini, F., Houghton, P. (2002) Antioxidant activity of methanolic extract of *Hypericum triquetrifolium* Tura aerial part. Fitoterapia. 73, 479-483.

[11] Hunt, E.J., Lester, C.E., Lester, E.A., Tackett, R.L. (2001) Effects of St. John's wort on free radical production. Life Sciences. 69, 181-190.

[12] Eroğlu-Özkan, E., Özsoy, N., Özhan, G., Özbek-Çelik, B., Mat, A. (2013) Chemical composition and biological activities of *Hypericum pamphylicum*. Industrial Crops and Products. 50, 182-189.
[13] Türkoğlu, S., Türkoğlu, I., Çelik, S., Bahsi, M., Gür, S., Parlak, A.E. (2015) Some biological compounds, antioxidant and antimicrobial activities of endemic *Hypericum uniglandulosum.* Chemistry of Natural Compounds. 51(4), 615-619.
[14] Boğa, M., Ertaş, A., Eroğlu-Özkan, E., Kızıl, M., Çeken, B., Topçu, G. (2016) Phytochemical analysis, antioxidant, antimicrobial, anticholinesterase and DNA protective effects of *Hypericum capitatum* var. *capitatum* extracts. South African Journal of Botany. 104, 249-257.
[15] Slinkard, K., Singleton, V.L. (1977) Total phenol analysis: automation and comparison with manual methods. American Journal of Enology and Viticulture. 28, 49-55.
[16] Sakanaka, S., Tachibana, Y., Okada, Y. (2005) Preparation and antioxidant properties of extracts of Japanese persimmon leaf tea (kakinoha-cha). Food Chemistry. 89, 569-575.
[17] Duh, P.D., Tu, Y.Y., Yen, G.C. (1999) Antioxidant activity of water extract of Harng Jyur (*Chrysanthemum morifolium* Ramat). Food Science and Technology. 32, 269-277.
[18] Buege, J.A., Aust, S.D. (1978) Lipid peroxidation. Methodsin Enzymology. 52, 302-310.
[19] Brand-Williams, W., Cuvelier, M.E., Berset, C. (1995) Use of a free radical method to evaluate antioxidant activity. Food Science and Technology. 28, 25-30.
[20] Nishikimi, M., Rao, N.A., Yagi, K. (1972) The occurence of superoxide anion in the reaction of reduced phenazine methosulfate and molecular oxygen. Biochemical and Biophysical Research Communications. 46, 849-854.
[21] Dinis, T.C.P., Madeira, V.M.C., Almeida, L.M. (1994) Action of phenolic derivatives (acetoaminophen, salicylate and 5-aminosalicylate) as inhibitors of membrane lipid peroxidation and as peroxyl radical scavengers. Archives of Biochemistry and Biophysics. 315, 161-169.
[22] Chung, Y.C., Chen, S.J., Hsu, C.K., Chang, C., Chou, S.T. (2005) Studies on the antioxidative activity of *Graptopetalum paraguayense* E. Walther. Food Chemistry. 91, 419-424.
[23] Clinical and Laboratory Standards Institute (CLSI) (2000) Reference method for broth dilution antifungal susceptibility testing of yeasts, in: Approved Standard M-27-A. Wayne, Pennsylvania.
[24] Clinical and Laboratory Standards Institute (CLSI) (2006) Methods for dilution antimicrobial susceptibility tests for bacteria that grow aerobically, in: Approved Standard M7-A5, Wayne, Pennsylvania.
[25] Couladis, M., Badisa, R.B., Baziou, P., Chaudhuri, S.K., Pilarinou, E., Verykokidou, E. (2002) Antioxidant and cytotoxic activities of *Hypericum* species on brine shrimps and human cancer cell lines. Phytotherapy Research. 16, 719-722.
[26] Rice-Evans, C.A., Miller, N.J., Paganga, G. (1997) Antioxidant properties of phenolic compounds. Trends in Plant Science. 2, 152-159.
[27] Decker, E.A. (2002) Antioxidant mechanisms. In Akoh CC, editör. Food lipids: chemistry, nutrition and biotechnology. 2nd edition, Marcel Dekker Inc, New York. 517-542.
[28] Rabanal, R.M., Arias, A., Prado, B., Hernández-Pérez, M., Sánchez-Mateo, C.C. (2002) Antimicrobial studies on three species of *Hypericum* from the Canary Islands. Journal of Ethnopharmacology. 81, 287-292.
[29] Dall'Agnol, R., Ferraz, A., Bernardi, A.P., Albring, D., Nör, C., Sarmento, L., Lamb, L., Hass, M., von Poser, G., Schapoval, E.E.S. (2003) Antimicrobial activity of some *Hypericum* species. Phytomedicine. 10, 511-516.
[30] Bombardelli, E., Morazzoni, P. (1995) *Hypericum perforatum*. Fitoterapia. 66, 43-68.
[31] Ishiguro, K., Yamaki, M., Kashihara, M., Takagi, S., Koichiro, I. (1990) Sarothralin G: A new antimicrobial compound from *Hypericum japonicum*. Planta Medica. 56(3), 274-276.
[32] Jayasuriyab, H., Clark, A.M., Mc Chesney, J.D. (1991) New antimicrobial filicinic acid derivatives from *Hypericum drummondii*. Journal of Natural Products. 54(5), 1314-1320.
[33] Rocha, L., Marston, A., Potterat, O., Auxiliadora, M., Kaplan, C., Stoeckli-Evans, H., Hostettmann, K. (1995) Antibacterial phloroglucinols and flavonoids from *Hypericum brasiliense*. Phytochemistry. 40(5), 1447-1452.

Received: **15.01.2019**
Accepted: **19.02.2022**

CORRESPONDING AUTHOR

Caglayan Unsal Gurer
Department of Pharmacognosy,
Faculty of Pharmacy,
Istanbul University,
34116 Beyazit Istanbul – Turkey

e-mail: cunsal@istanbul.edu.tr

© by PSP Volume 31– No. 05/2022 pages 4659-4676 Fresenius Environmental Bulletin

ASSESSMENT OF SOME MAJOR CHEMICAL ELEMENTS IN SEDIMENTS OF AQUATIC SOURCES IN DRINI I BARDHË RIVER BASIN: A CASE STUDY OF SPATIAL DISTRIBUTION

Fisnik Laha[1], Fatbardh Gashi[1], Naser Troni[1,*], Stanislav Franciskovic-Bilinski[2], Halka Bilinski[2]

[1]Department of Chemistry, Faculty of Natural Sciences, M. Teresa 10, University of Prishtina, 10000 Prishtina, Kosovo
[2]Institute Ruđer Bošković", Division for Marine and Environmental Research, POB 180, HR-10002 Zagreb, Croatia

ABSTRACT

In Kosovo, the supply of potable water from water sources is represented by about 40%. This study represents the geochemical analyses of sediments, spatial and statistical analyses of major elements in sediments (fraction <63 μm) of water sources in Drini i Bardhë river basin. For better understanding of geochemical consistence of sediments ICP-MS was used and the amounts of P and S were determined by ICP-OES. By comparing the concentrations of Ba, Se and P elements with the existing criteria, it was found that 26 from 50 sample points exceed recommended norms, that cause low/significant toxic effects and 23 from 50 sample points include anomalies of analysed elements. In terms of statistical interpretation the average concentration of the studied elements have decreased in such order: Ca>Al>Mg>K>S>P>Na>Ba>Sr>Li> Rb>B>Ga>Cs>Be>Se. In terms of correlation analyses elements such as: Li, Be, Mg, P and Ba did not show significant positive correlation with any element. Cluster analysis of R-modality show a branch of dendogram linked with Ca, Al, Mg, S, K, P, Na, Ba, Sr, Cs, B, Ga, Se, Be, Rb and Li. Spatial distribution maps of major elements show that high concentration of Li, Ca and Ba were located mostly in the north part, high concentrations of B, Na, Mg, Sr and Cs were located in the north-east part, high concentrations of Be and Al were located in the north and south part and high concentrations of P, S, K and Rb were located mostly in the south-east part of the catchment basin. This high concentration of elements is impacted by the lithology of rocks and from minor influence of human activity (the case of P).

KEYWORDS:
Major elements, Sediments, Spatial distribution, ICP-MS and ICP-OES, Drini Bardhë river basin, Aquatic sources

INTRODUCTION

Sediment and water pollution by chemical elements is a crucial environmental and human problem and human activities may induce considerable changes in the physico-chemical properties of aquatic sediments and aquatic sources. Demographic growth, overall economic development has increased industrial and agro-productive capacities and producers in country level by posing an increased pressure on the use of groundwater. Groundwater resources represent one of the safest sources of potable water supply. In Kosovo, the supply of potable water from water sources is represented by about 40%. Sediments are integral parts of the aquatic environments because they help to determine the overall assessment of heavy metals in water vis-avis aquatic life and survivabilit [1]. Bottom sediments in all aquatic environments are reasonable and fact-finding sources of information on processes and mechanisms occurring in aquatic ecosystems [2]. Hydrological cycles, physico-chemical processes, and complex spatiotemporal variations enable remobilization of heavy metals from sediments into the water [3]. The concetration of heavy metals in exceeding norms in the environment can cause environmental and human health problems [4-6]. Studies on metals in rivers, lakes, fish and sediments have been a major environmental focus especially in the last decades [7]. Sediments (silt and clay) containing ecotoxic heavy metals and other inorganic and organic substances are important for studying water pollution, and therefore, their multidisciplinary research is essential for understanding different processes and to understand better the geochemical cycles of different trace elements [8]. The behavior of the metals in natural waters is determined by the water chemistry and sediment composition [9]. Heavy metals are regarded as serious pollution of aquatic ecosystem because of their environmental persistence and toxicity effects on living organisms [10]. Heavy metals are present mainly as suspended colloids or are fixed by organic and mineral substances [11] and the safe water gradually becomes scarce commodity, due to the mix up

of huge contaminants through natural processes like soil and rock weathering and anthropogenic activities such as industrial effluents, domestic sewage, garbage, over mining activities, explosive population etc. [12]. Metallic elements are environmentally stable and they can enter the living system through an aquatic medium cause acute adverse effects on human beings, animals and plants.

This work is a continuation of earlier studies of sediments in the area of nearby countries of Kosovo and Croatia [13-20]. The objective of this work is to determine the concentrations of some major chemical elements in sediments (fraction <63 µm) of aquatic sources and to create their spatial and temporal distributions maps in study area.

STUDY AREA

Description of the study area. Geographically Kosovo is located between 41°51'-43°16' N and 20°01'-21°48' E, and it is mainly situated on two plains; the Dukagjini plain (sea levels 330-550m) and the Kosovo Plain (sea levels 500-600m). Drini i Bardhë river basin is the biggest with surface of 4.289 km2 and takes the western part of Kosovo. This area consists of several small streams from the mountains, water flows into tributaries and Drini i Bardhë river. In geotectonic terms, Kosovo is located within the Dinaric Mountains and all three divisions of rocks, namely magmatic, sedimentary and methamorphic of Precambrian to Quaternary ages are present in the territory of Kosovo [21]. The sediments of the rivers in Kosovo are composed of alluvial deposits containing largely varying proportions of unconsolidated to semi consolidated sand and gravel materials [22]. In hydro-geological aspects, geological, lithological, structural and tectonic characteristics, the following areas of aquifers are distinguished in the study area: intergranular porous aquifers, porous cracks, karst porosity and waterless terrain [23].

MATERIALS AND METHODS

Sampling and sample preparation. In the study area, sediment samples were collected from 50 different locations during November 2018 - January 2019, in order to assess the concentration of some major elements and to create the spatial distribution of the analysed elements. The standard sampling method was used for sediment collection [24]. Sediment samples were taken from the bottom of aqua sources (in different depth) using the sediment sampler (model, Ekman grab) with package size 56x22x40cm [25]. According to the sampling procedure the sediment sampler was washed and dried with water before the next sampling. Sampling was realised at different points and 1-2 kg of sediment was collected to provide enough sediments of fraction under 63 µm. Fine fraction <63µm, is usually used in environmental studies and is easily transported. Each sampling point has been coded, the sampling material was collected in plastic bags and it was dried in the air for 21 days. Coarse materials were separated using a 40-mesh sieve, and afterwards a sieve "Fritsch" with 63 µm was used for the separation purpose. Results of 16 major elements for the sediment samples were compared with the existing criteria for sediment quality given by SMSP, Falconbridge NC, SAS [26]. The locations of sample points were determined by applying the global positioning system device, using a ''GARMIN'' GPS. The study area with sampling points and the details about sites are shown in Figure 1 and Table 1.

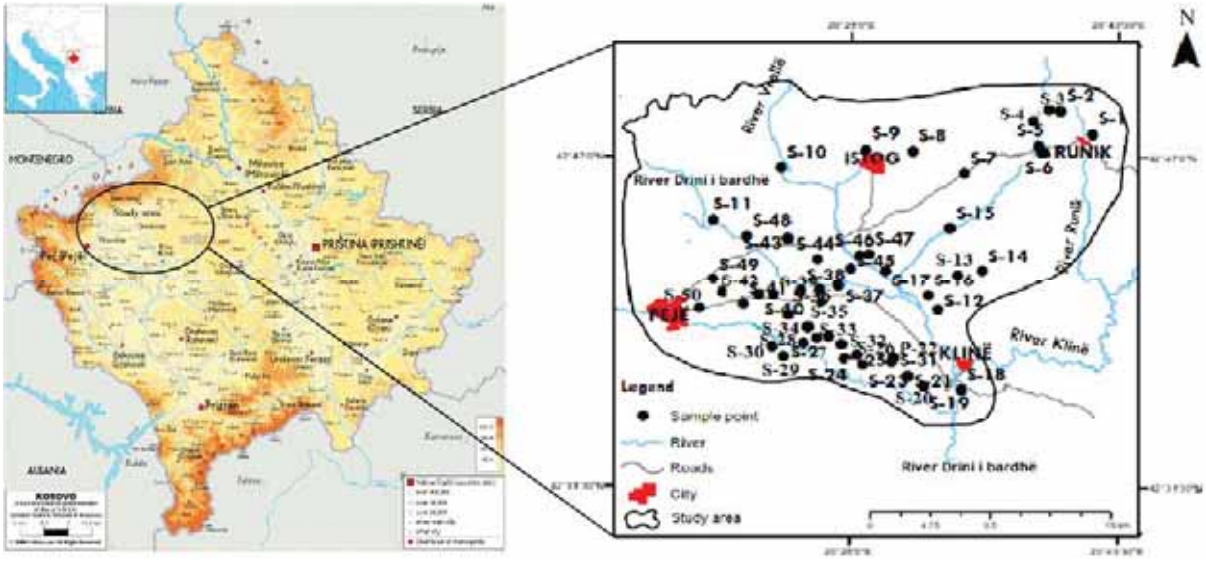

FIGURE 1
The investigated area with station points.

TABLE 1
Sampling stations, locality, coordinates (x and y) and sea level with detailed locality description.

Sample	Locality	Coordinate X	Coordinate Y	Sea level /m	Possible pollution sources
P1	Runik	427938	202933	721	Settlement, agriculture land
P2	Banjë e Runikut	424869	204008	766	Settlement, agriculture land
P3	Surigjan	4249112	2038904	680	Settlement, wastewater
P4	Cerkulez	4248422	2038347	684	Settlement, agriculture land
P5	Padalishtë	424731	203853	604	Settl., agric. land, wastewater
P6	Rakosh	4247316	203853	575	Settl., agric. land, wastewater
P7	Bellopojë	4246136	2034334	581	Settl., agric. land, wastewater
P8	Dubravë	4246754	2031355	549	Settlement, agriculture land
P9	Burimi - Istog	4274329	202886	560	Mountain tourism
P10	Burimi - Vrellë	424648	202397	509	Mountain tourism
P11	Radavc	4243635	2019644	593	Settlement, agriculture land
P12	Zllakuqan	4239467	2032678	439	Settlement, agriculture land
P13	Ranoc	4240855	2033738	466	Agriculture land, wastewater
P14	Leskoc	4241394	2034992	490	Settlement, agriculture land
P15	Osjan	4243409	2033467	493	Agriculture land, coal source
P16	Berkovë	4240275	2031954	438	Settlement, agriculture land
P17	Zabllaq	4241396	2029643	453	Settlement, agriculture land
P18	Gjurakovc	4242285	202905	477	Settlement, agriculture land
P19	Prekallë	4241837	2028288	485	Settlement, agriculture land
P20	Trubohovc	4241458	2027578	480	Settlement, agriculture land
P21	Staradran	4241751	2026059	492	Settlement, agriculture land
P22	Kashicë	4242709	2023831	515	Settlement, agriculture land
P23	Fusha e Pejës	4239513	2019206	525	Settlement, agriculture land
P24	Vitomiricë	4241141	2019667	549	Settlement, agriculture land
P25	Dubravë e Vogël	4243167	2022004	522	Settlement, agriculture land
P26	Klinë	423561	2034274	415	Agriculture land, wastewater
P27	Grabanicë	4235725	2032207	423	Settlement, agriculture land
P28	Drenoc	4236379	2031178	444	Settlement, agriculture land
P29	Poterq i ulët	4236373	2030825	431	Agriculture land, wastewater
P30	Poterq i epërm	423679	2030273	455	Agricult. land, wastewater
P31	Jabllanicë e Leshanit	4237089	2028447	446	Agricult. land, wastewater
P32	Kliqinë	4237292	2027433	448	Agriculture land, wastewater
P33	Leshan	4237685	2026971	463	Settlement, agriculture land
P34	Gllaviqicë	4238325	2026483	475	Settlement, agriculture land
P35	Gllaviqicë	4238287	202566	468	Settlement, agriculture land
P36	Vragoc	423774	2024783	490	Agriculture land, wastewater
P37	Millovanc	4237362	2024133	503	Settlement, agriculture land
P38	Gorozhdevc	4238014	2022916	506	Settlement, agriculture land
P39	Poterq	4236918	2029919	449	Settlement, agriculture land
P40	Jabllanicë	4237454	2028234	451	Agriculture land, wastewater
P41	Ramun	4238579	2024992	496	Settlement, agriculture land
P42	Llabjan	4239328	2024266	509	Agricult. land, Meat industry
P43	Lutogllavë	4239661	2025829	487	Agricult. land, garbage dump
P44	Ruhot	4240441	2026153	473	Settlement, agriculture land
P45	Terstenik	4240557	202722	460	Settlement, agriculture land
P46	Nabergjan	424041	2025084	489	Settlement, agriculture land
P47	Nabergjan i epërm	4240275	2023349	479	Settlement, agriculture land
P48	Nakull	423988	2022435	502	Settlement, agriculture land
P49	Bllagajë	424002	2021492	507	Agriculture land, wastewater
P50	Fusha e Pejës	423995	2020394	524	Settlement, agriculture land

ICP-MS and ICP-OES determination of major elements. The geochemical analysis of aquatic sediment samples has been done at „Actlabs“ laboratory in Canada, using the “Ultratrace 2” testing program. Regarding to the testing standard operation procedure, the sample preparation procedure started with 0.5 g of the aquatic sediment sample, dissolved in aqua regia at 90º C in a microwave digestion unit and after that the prepared solution was diluted and was chemically analyzed with a „Perkin Elmer SCIEX ELAN 6100“ ICP-MS instrument. For determination, the following reference materials

TABLE 2
Concentration of 16 elements in ppm (mg/kg) and % in sediment (fraction <63 µm) of 50 aqua sources.

Metal	Li	Be	B	Na	Mg	Al	P	S	K	Ca	Rb	Sr	Cs	Ba	Se	Ga
Unite	ppm	ppm	ppm	%	%	%	%	%	%	%	ppm	ppm	ppm	ppm	ppm	ppm
LOD*	0.1	0.1	1	0.001	0.01	0.01	0.001	0.001	0.01	0.01	0.1	0.5	0.02	0.5	0.1	0.02
P1	15.9	0.9	17	0.062	2.37	2.12	0.051	0.05	0.36	17.1	25.9	332	2.84	129	0.9	4.54
P2	15.4	1	12	0.026	0.46	1.52	0.086	0.773	0.3	15.7	36.3	533	35	222	1.8	3.55
P3	16.7	0.7	6	0.022	0.61	1.32	0.059	0.037	0.25	21.2	15	135	1.86	67	0.2	2.82
P4	24.4	1	7	0.029	0.86	2.92	0.032	0.351	0.28	10.2	24.3	222	1.88	81.9	0.3	6.64
P5	24.2	0.8	8	0.033	0.74	2.09	0.024	0.183	0.21	8.86	18.2	112	1.03	90.9	0.3	4.81
P6	29.9	1.3	4	0.029	0.33	3.06	0.032	0.004	0.26	1.17	22.9	84.5	1.61	216	<0.1	7.65
P7	41.1	1.1	6	0.029	0.69	3.25	0.06	0.011	0.3	0.57	19.5	40.8	2.55	107	<0.1	7.23
P8	44.4	1.5	7	0.032	0.75	3.7	0.046	0.016	0.4	4.63	27.5	52.9	3.83	123	<0.1	7.9
P9	16.3	0.9	6	0.019	0.41	1.29	0.059	0.022	0.19	23.4	15.8	92.5	3.63	68.3	0.3	2.83
P10	36.1	1	10	0.021	0.74	1.4	0.043	0.022	0.23	8.89	13.9	74.2	2.15	1090	0.1	<0.02
P11	32.7	0.9	6	0.028	0.68	2.49	0.066	0.033	0.24	1.7	16.4	35.5	2.19	102	0.1	6.15
P12	17.6	0.9	8	0.03	0.55	2.02	0.097	0.099	0.24	7.65	21.2	103	1.32	117	0.2	4.32
P13	16.6	0.9	6	0.024	0.47	2.06	0.062	0.107	0.22	6.81	16.8	88.8	1.29	90.8	0.3	4.53
P14	18.2	0.8	11	0.034	0.55	1.91	0.087	0.073	0.24	9.9	18.1	117	1.34	137	0.3	4.18
P15	23.7	1.2	11	0.025	0.52	2.6	0.07	0.032	0.45	3.05	31.7	62.6	2.49	164	<0.1	6.21
P16	29.1	1.2	9	0.023	0.63	2.06	0.126	0.04	0.26	6.56	21.8	136	1.92	292	0.3	3.81
P17	28.4	1.1	11	0.023	0.58	2.26	0.166	0.041	0.31	5.55	25.4	126	1.95	267	0.3	3.95
P18	30.2	1.4	7	0.029	0.5	3.01	0.072	0.027	0.38	3.37	28.2	80.6	1.99	205	<0.1	6.66
P19	20.9	1.1	11	0.035	0.36	2.14	0.099	0.347	0.27	3.14	25	59.7	1.62	152	0.7	4.61
P20	25.3	1.3	7	0.03	0.53	2.41	0.072	0.143	0.31	3.74	25.9	85.2	1.87	163	0.3	5.97
P21	25.9	1.1	7	0.026	0.64	2.37	0.112	0.095	0.23	3.28	24.4	66	2.18	218	0.2	4.47
P22	28.6	1.5	15	0.028	0.69	3.02	0.045	0.072	0.45	4.8	68.4	135	18.2	318	<0.1	5.48
P23	29.8	1.6	9	0.021	0.52	2.25	0.032	0.094	0.22	2.13	27.8	60.6	4.66	127	0.2	5.14
P24	25.3	0.9	5	0.019	0.59	1.39	0.035	0.011	0.12	14.9	9.8	472	1.24	111	<0.1	3.09
P25	29	3.4	5	0.022	0.8	1.6	0.026	0.036	0.12	1.57	12.2	41.9	1.64	106	<0.1	4.05
P26	19.8	0.9	5	0.022	0.61	1.5	0.054	0.037	0.17	7.38	14.5	185	1.36	98.7	0.2	3.69
P27	18.1	0.8	6	0.025	0.47	1.77	0.055	0.423	0.19	10.1	17.7	183	1.28	145	0.8	3.81
P28	24.3	1	6	0.027	0.56	2.01	0.085	0.075	0.2	2.68	19.9	57.8	1.93	173	0.2	4.39
P29	15.9	1	7	0.034	0.51	1.78	0.071	0.276	0.2	1.52	19.3	58.5	1.57	182	0.2	3.75
P30	17.8	0.9	7	0.031	0.54	2.33	0.077	0.128	0.2	3.98	18.1	139	1.45	206	0.2	3.97
P31	14	0.3	2	0.02	1.28	0.8	0.042	0.021	0.07	10.6	4	442	0.57	46.6	<0.1	2.08
P32	17.7	0.7	3	0.023	1.03	1.63	0.063	0.03	0.16	8.04	12.7	281	1.09	91	<0.1	3.35
P33	17.3	1.2	6	0.036	1.16	1.33	0.043	0.087	0.18	15.5	8.2	512	0.91	206	0.1	1.39
P34	24.4	1.2	2	0.023	0.53	3.02	0.037	0.015	0.35	0.29	23.4	17.8	1.44	157	0.2	6.59
P35	25.1	0.8	5	0.027	0.74	1.8	0.122	0.028	0.2	3.77	15.6	146	1.43	154	0.1	3.93
P36	22.2	1.9	9	0.051	1.21	1.97	0.055	0.172	0.3	13.5	12.8	311	1.02	370	0.1	1.2
P37	19.9	0.5	3	0.023	0.78	1.54	0.063	0.008	0.13	0.67	7.5	22.1	0.77	50.2	<0.1	3.33
P38	17	0.7	9	0.04	0.75	1.59	0.048	0.12	0.14	19.6	9.9	250	1.15	152	0.2	3.08
P39	22.1	1	4	0.026	0.54	2.37	0.064	0.05	0.24	1.39	19.5	38.5	1.44	141	<0.1	4.86
P40	16	1	24	0.077	0.55	2.02	0.14	1.122	0.24	4.52	19.6	97.1	1.52	175	0.6	7.17
P41	23.5	1	3	0.021	0.43	1.69	0.044	0.01	0.15	0.77	13.5	40.9	1.26	75.7	<0.1	4.24
P42	15.9	0.9	4	0.019	0.24	1.55	0.096	0.152	0.14	1.03	21.6	31.9	1.72	95.5	0.6	4.03
P43	22	0.6	3	0.023	0.64	1.38	0.06	0.032	0.15	9.41	12.7	132	1.11	76.8	<0.1	3.31
P44	28.9	1.1	8	0.025	0.67	2.2	0.107	0.045	0.42	2.16	25.8	80.8	1.97	136	0.2	5.29
P45	26.1	0.9	5	0.025	0.77	1.94	0.054	0.015	0.22	6.26	15	246	1.85	93.6	<0.1	4.49
P46	18.6	0.7	20	0.07	0.77	1.56	0.097	0.17	0.28	10.1	14.6	260	1.19	145	0.2	3.31
P47	25.1	0.9	5	0.02	0.73	1.71	0.053	0.015	0.21	10	14.3	284	1.55	106	<0.1	4.02
P48	19.8	0.7	5	0.022	0.74	1.42	0.063	0.041	0.19	9.16	14	274	1.19	94.5	0.2	3.36
P49	25.4	0.9	5	0.022	0.73	1.75	0.054	0.021	0.21	9.61	13.6	273	1.46	102	0.2	4.11
P50	23.1	0.8	8	0.033	0.8	1.74	0.079	0.085	0.22	9.86	14.8	211	1.61	157	0.5	3.58

*Limit of Detection

(RM) were used: USGS GXR-1, GXR-2, GXR-4 and GXR-6. Although the digestion of sediment samples is not total, its use is justified because the international standard methods for determining action limits are based on aqua regia leach [27].

Statistical assessment. Statistical assessment of this work such as: basic statistical parameters, 2D box plot diagrams for determination of anomalies for solution data, correlation coefficient and Q- and R-mode cluster analyses were performed using the program "Statistica 6" [28]. Multivariate statistics was used to assess the sources and distribution of major elements in natural aqua sediments in the study area. Outlier values are between 1.5 and 3 and extreme values above 3 standard deviations. The principal component analysis (PCA) is considered the main of the multivariate data analysis and it was first formulated by Pearson in statistics and after that it has been followed by Fisher and MacKenzie [29]. PCA was widely applied to reduce original variables of the contaminants and to analyze their sources. Correlation analysis was performed to find mutual dependence of elements. Statistical processing of chemical data and setting up the database, mainly for the purpose of achieving GIS maps, is an essential phase of sediment quality assessment. R-mode, clusters of variables, in our case chemical elements are desired. Cluster analysis of Q-modality was applied, in order to disaggregate it into more homogenous subsets [30], and it was performed to find groups which contain similar/different sediment samples.

Spatial and temporal distribution of elements in aqua sediments. The GIS mapping methodology was applied to create spatial distribution maps of major elements concentrations. The software "ArcView" version 10.1, was used for spatial distribution mapping of the analysed major elements in the study area [31].

RESULTS AND DISCUSSION

Chemical analyses of elements using ICP-MS and ICP-OES methods. The result of concentrations of major elements in the aquatic sediment, was determined by using ICP-MS and ICP-OES methods (Table 2).

Sediments from aqua sources were analyzed in a completely randomized design and the limit of detection of used methods for the elements is: Li 0.1 ppm, Be 0.1 ppm, B 1.0 ppm, Na 0.001 %, Mg 0.01 %, Al 0.01 %, P 0.001 %, S 0.001 %, K 0.01 %, Ca 0.01 %, Rb 0.1 ppm, Sr 0.5 ppm, Cs 0.02 ppm, Ba 0.5 ppm, Se 0.1 ppm and Ga 0.02 ppm.

Statistical analysis. The results of descriptive statistical analysis for chemical elements in sediment samples are presented in Table 3, and the value of each element is given as arithmetic mean, geometric mean, median, minimal and maximal concentration, variance and standard deviation based on the total concentration for each element. Using experimental data from Table 2, frequency histograms and 2D scatter box with plots diagrams [32] for selected elements are presented in Figures 2 and 3. The anomalous values (outliers and extremes) of elements in all sediment points are presented in Table 4. The relationship between the concentrations (mean values) of these elements was shown by performing correlation analysis and matrix for Pearson's correlation coefficients of selected variables and it is displayed in Table 5. The level of significance was set at $p < 0.05000$ for all statistical analyses. The clustering techniques R and Q-mode has often been applied to a wide variety of research issues [33-35]. Cluster analyses of R-mode, clusters

TABLE 3
Basic statistical analyses of 16 elements in fine sediment.

Variable	Descriptive statistics						
	Mean	Geometric	Median	Minimum	Maximum	Variance	Std. Dev.
Li /ppm	23.314	22.4866	23.3	14	44.4	43.51	6.5966
Be /ppm	1.038	0.9732	0.95	0.3	3.4	0.20	0.4421
B /ppm	7.5	6.5498	6.5	2	24	18.54	4.3059
Na /%	0.0293	0.0277	0.026	0.019	0.077	0.00	0.0120
Mg /%	0.687	0.6393	0.635	0.24	2.37	0.10	0.3178
Al /%	2.0132	1.9315	1.955	0.8	3.7	0.35	0.5927
P /%	0.0677	0.0618	0.061	0.024	0.166	0.00	0.0302
S /%	0.1179	0.0547	0.043	0.004	1.122	0.04	0.198
K /%	0.24	0.2252	0.225	0.07	0.45	0.01	0.0854
Ca /%	7.2354	4.8384	6.41	0.29	23.4	32.70	5.7181
Rb /ppm	19.5	17.717	18.1	4	68.4	92.22	9.6031
Sr /ppm	158.464	114.558	114.5	17.8	533	17069.33	130.6496
Cs /ppm	2.7224	1.7838	1.59	0.57	35	27.68	5.2614
Ba /ppm	163.89	136.9693	136.5	46.6	1090	22403.34	149.6775
Se /ppm	0.26	0.19	0.2	0.1	1.8	0.0848	0.29
Ga /ppm	4.34	3.74	4.08	0.02	7.9	2.595868	1.61

the variables and Figure 4 has shown mutual links between studied elements and observed that an element has the closest association with other elements. Cluster analysis of Q-modality was performed on the total set of elements (Table 2) and this analysis shows that sampling points were grouped in 4 clusters. The results of Q-modality cluster analysis, with the distances given in parenthesis and means for each clasters, are presented in Tables 6, 7 and 8.

Spatial and temporal distribution of elements in sediment from study area. Spatial and temporal distribution of elements such as: Li, Be, B, Na, Mg, Al, P, S, K, Ca, Rb, Sr, Cs, Ba, Se and Ga observed in all sediment samples are presented in Figure 5.

Discussion of ICP-MS and CV-AAS analyses. Geochemical data from Table 2 can be used for the assessment of sediment's quality and contamination by chemical elements. Results of chemical analyses were used to compare the obtained amounts of elements with the existing criteria for sediment quality by SMSP, Falconbridge NC, SAS, referred in further discussion.

Excessive concentration of Phosphorus (P) is the most common cause of eutrophication in freshwater lakes, reservoirs, streams, and in the headwaters of estuarine systems and the amount of P present in a sediment depends on both the external Phosphorus load and its release and retention in the sediments. Sediments act as a sink where P can be stored, and also as a source of P for the overlying water [36-38]. Anthropogenic sources of Phosphorus include sewage and industrial effluent, although diffused phosphorus is predominantly of agricultural origin [39]. Concentration values of Phosphorus in all samples were lower than the recommended norms from 2000 ppm that cause significant toxic effects, but our analyses showed that P in 25 sample points (P2, P7, P11-P21, P28-P30, P32, P35, P37, P39, P42, P44, P46, P48 and P50) exceeds the recommended norms from 600 ppm, that cause low toxic effects and make the aquatic life unsuitable.

The high concentration of P is probably due to natural (present in the earth's crust) and anthropogenic factors (excessive use of chemical fertilizers in agricultural lands in this area).

Selenium (Se) is present in Earth's crust, often in association with sulfur-containing minerals. Selenium is an essential trace element, and food such as cereals, meat and fish are the principal source of selenium in the general population. Levels in food also vary greatly according to geographical area of production [40]. Selenium is part of metal sulphide ores, where it partially replaces the sulfur. Bottom sediments are the dominant sink for Se in aquatic ecosystems via association with suspended particulate matter and subsequent deposition [41]. In our study, Se with concentration from 1.8 ppm (in the sample point P2), was found to be higher than recommended norms from 1 ppm (causing significant toxic effects), probably from the chemical composition of the earth's crust in that area.

Barium (Ba) is present as a trace element in both igneous and sedimentary rocks, and his compounds are used in a variety of industrial applications; however, Barium in water comes primarily from natural sources. Barium is surprisingly abundant in Earth's crust (as Barite ore), and high amounts of it may only be found in soils and in food (nuts, seaweed, fish and certain plants) [40]. The extensive use of Barium in the industry and human activities increases the release of barium in the environment. Our comparative analysis shows that Barium in two station points (P31 and P37) exceeds recommended norms from 60 ppm, that cause significant toxic effects. But only in the sample station P10 (1090 ppm), it exceeds recommended norms from 500 ppm, that norm means "removal of sediment from the water sources".

The average concentrations of Na, Mg and Ca in the present study were lower than the average value that was presented by Frančišković-Bilinski [18] for sediments of Kupa river drainage basin, Croatia. Sodium (Na) is correlated with terrigenous origin. Sodium exists in some forms of minerals such as: feldspars, sodalite and rock salt. Most salts of Na are highly water-soluble. Sodium (Na) was ranged 0.019-0.077 %, with the overage value from 0.0293 % and with highest value at sample point P40. Magnesium (Mg) and Calcium (Ca) occur in nature in various minerals: such as dolomites and high Mg-calcite and may be present in the amphiboles pyroxenes and such as limestone (calcium carbonate), gypsum (calcium sulfate), fluorite (calcium fluoride). Magnesium (Mg) was ranged 0.24-2.37 % with the arithmetic mean value from 0.687 % and the highest value at sample point P1 as a sign of rock Ni-mineral most as magnesium - iron silicates [42]. The statistical analysis shows a sample point P1 with extreme values of Mg and outlier values at sample point in P31, P33 and P36 as a sign of rock composition in that area. Calcium was ranged 0.29-23.4 % with the average value from 7.236%, standard deviation from 5.72% and highest value at sample point P9 as a sign of rock composition in that area. The statistical analysis shows a sample point P9 with outlier values of Ca and this is probably impacted from the consistence of the earth's lithology.

The average concentrations of Al, S, K, Rb, Sr, Li, Cs, Ga and Be in the present study were higher than average value that was presented by [18] in study of sediments of Kupa river drainage basin, Croatia. Aluminium (Al) is released to the environ-

ment mainly by natural processes, mainly from soil–water interactions, and the composition of the underlying geological materials [43]. Aluminium ranged 0.8-3.7 % with the arithmetic mean value from 2.0132% and the highest value is reached at station point P8. The statistical data on Figure 2 and 3 shows a sample point P8 with outlier values of Al and this is probably impacted by the consistence of the earth's lithology. Sulphur (S) ranged 0.004-1.122 ppm with the average value from 0.118 ppm and highest value from 1.122 ppm at sample point P40.

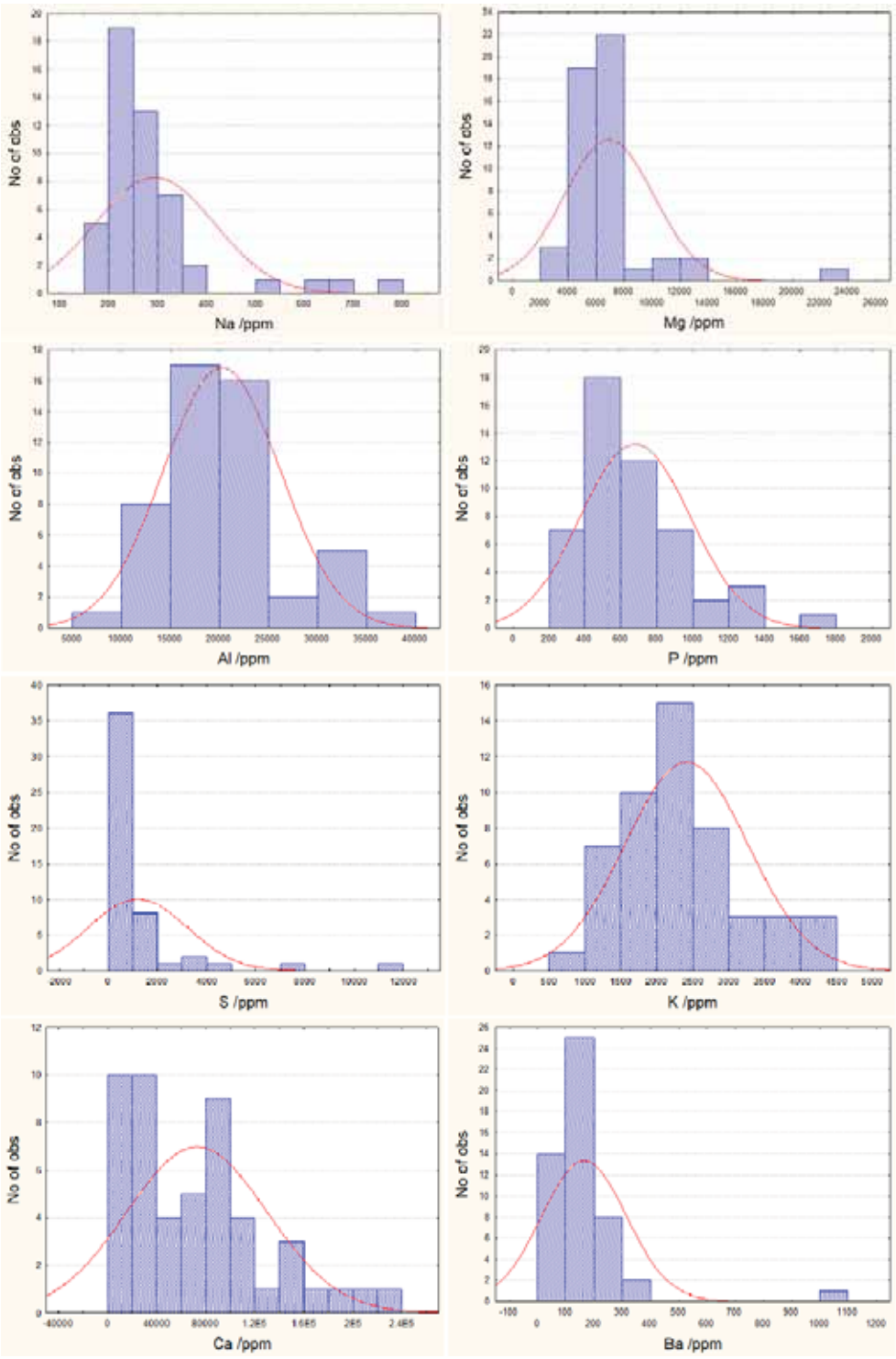

FIGURE 2
Frequency histograms of selected elements.

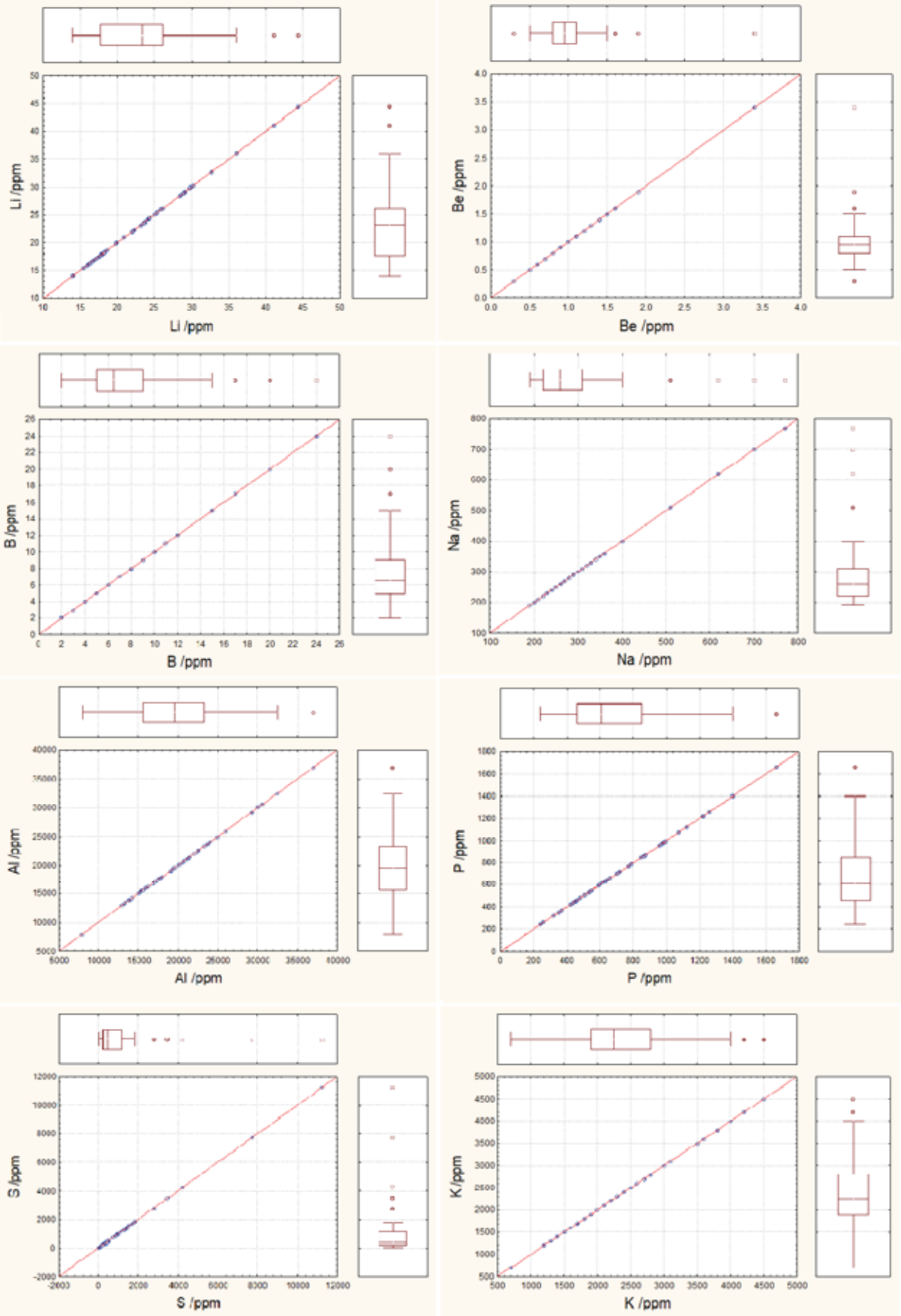
Li /ppm
Li /ppm
Be /ppm
Be /ppm
B /ppm
B /ppm
Na /ppm
Na /ppm
Al /ppm
Al /ppm
P /ppm
P /ppm
S /ppm
S /ppm
K /ppm
K /ppm

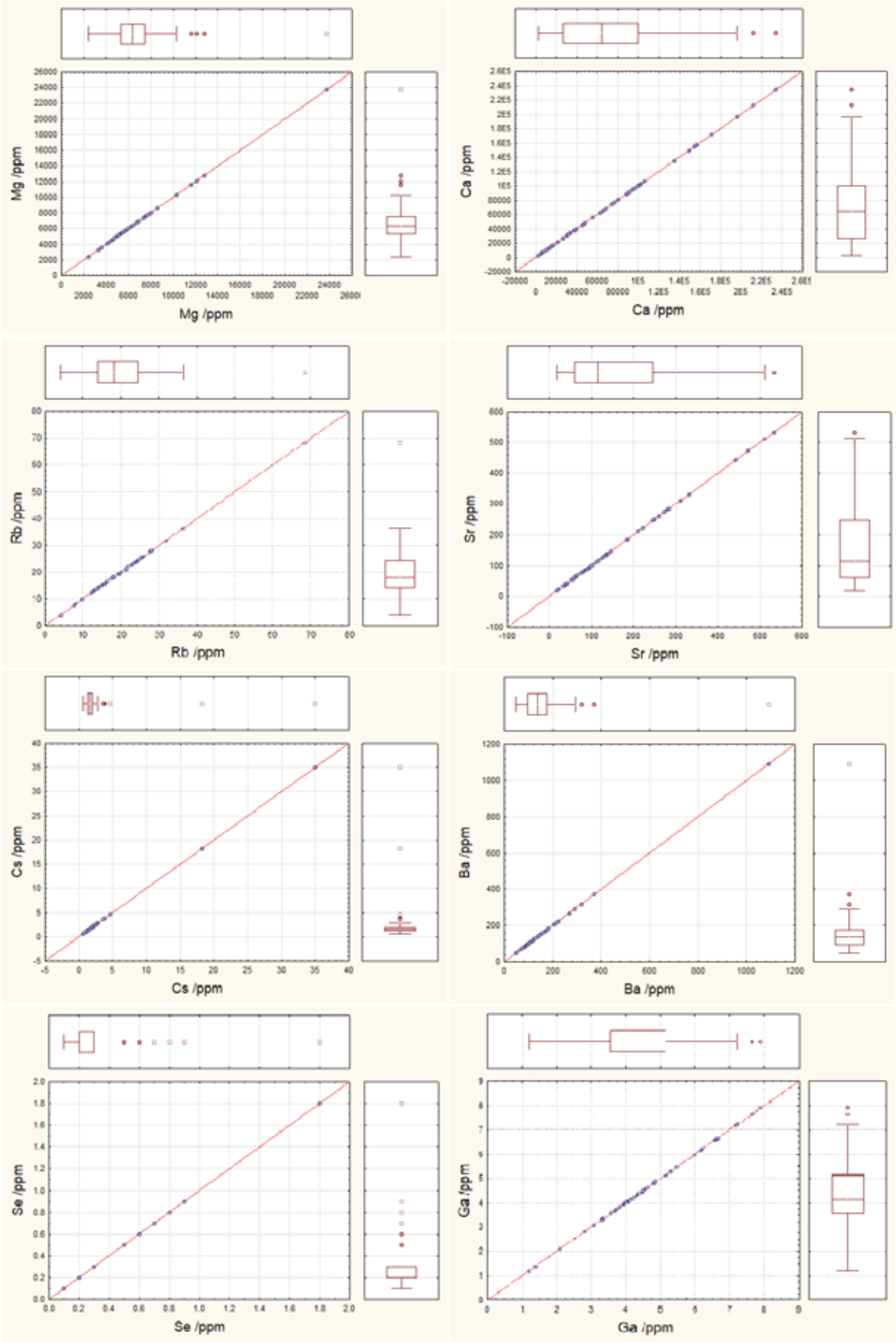

FIGURE 3
Scatterplot with plots diagrams of 16 elements.

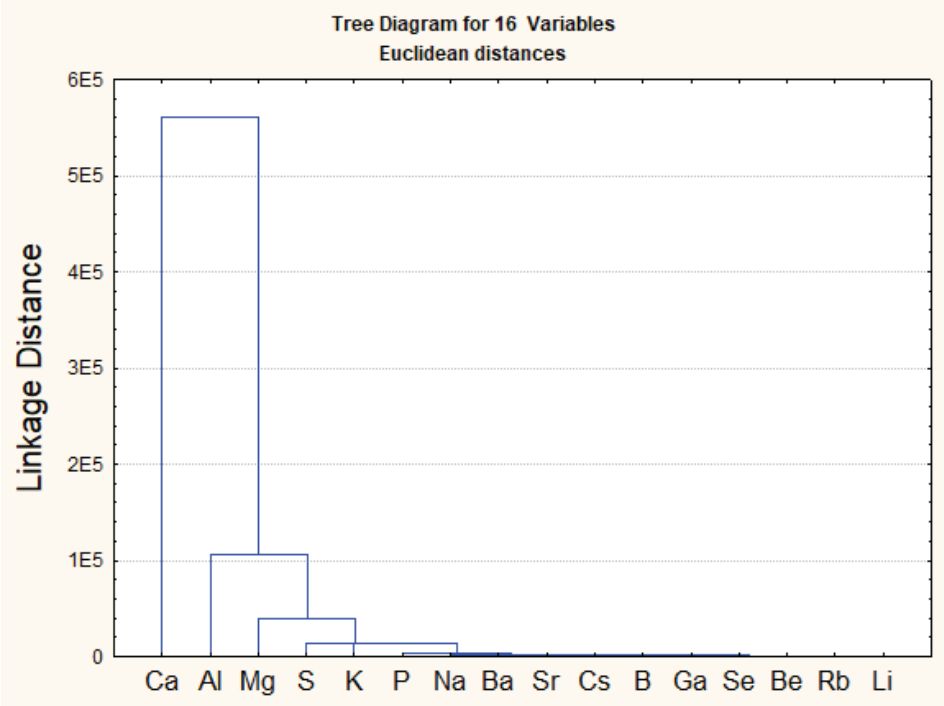

FIGURE 4
Cluster analysis R- mode, dendogram of studied 16 elements.

The statistical data from Table 2 and frequency histograms and 2D scatter box plot diagrams presen-ted in Figure 2 and 3 show sample point P2, P27 and P40 with extreme values of S and outlier values at sample point in P4, P18 and P19. This may be impacted from the consistence of the earth's lithology. Potassium (K) is correlated with terrige-nous origin and in our study it ranged 0.07-0.45 %, with the average value from 0.24% and highest value at sample point P22.

The analyses of frequency histograms (Figure 2) and 2D scatter box plot diagram (Figure 3), show outlier values at sample points P15, P22 and P44 impacted from the consistence of the earth's crust. The concentration of K in the present study was lower than the value presented by Mona et. al [44] of sediments of Edku and Mariut Lakes, North Egypt. Rubidium (Rb) is correlated with terrigenous origin and in our study it was ranged 4-68.4 ppm with the average value from 19.5 and highest value at sample point P22. The analyses of 2D scatter box plot diagram show an extreme value at sample point in P22 probably from the chemical composition of the earth's crust. Strontium (Sr) ranged 17.8-533 ppm with the average value from 158.46 ppm. Lithium (Li) is a tracer of weathering at the Earth's surface, ranged 14-44.4 ppm with the average value from 23.314 ppm. 2D scatter box plot diagram of Li show two outlier values at sample points P7 and P8 as sign of natural-geochemical pollution. Using comparative analysis, Cesium (Cs) ranged 0.57-35 ppm with the average value from 2.72 ppm, standard deviation from 5.26 ppm and highest value at sample point P2. Using experimental data from Table 2 and frequency histograms and 2D scatter box plot diagrams we found two sample points (P2 and P22) with extreme value of Cs and an outlier value at sample point in P8. Gallium (Ga) does not occur as a free element in nature, but as Gallium (III) compounds in trace amounts, in zinc ores and in bauxite. In our study, Gallium ranged <0.02-7.9 ppm with the average value from 4.34 ppm and highest value at sample point P8. Scatter box plot diagrams (Figure 3) show an outlier value at sample point in P6.

Beryllium (Be) does not occur as a free element in nature but in concentrated silicate minerals relative to sulfides and feldspar minerals relative to ferromagnesium minerals. In water, at pH 7.5 only a small amount of beryllium will be in a soluble form [45]. In our study, Be ranged 0.3-3.4 ppm with the average from 1.038 ppm. 2D scatter box plot diagram of Be show an extreme value at P25 and two outlier values at sample points P23 and P36 probably from the chemical composition of the earth's crust.Boron (B) is concentrated on Earth by the water-solubility of its more common naturally occurring compounds, the borate minerals. In natural waters, boron exists primarily as undissociated boric acid with some borate ions. In hight concentration boron ions may be adsorbed by soils and sediments and their adsorption is depended on the pH value [46,47]. Our results shows that B ranged 2-24 ppm with mean from 7.5 ppm. 2D scatter box plot diagram of B show an extreme value at P40 and two outlier values at sample points P1 and P46 probably from the chemical composition of the earth's crust and as a result of wastewater discharges, because borate compounds are ingredients of domestic washing agents [48].

TABLE 4
Sediment points with anomalous values (extreme and outlier) of chemical elements.

Sample points	Extreme values of elements (¤)	Outlier values of elements (o)
P1	Na, Mg, Se	B
P2	S, Cs, Se	Sr
P4	-	S
P6	-	Ga
P7	-	Li
P8	-	Li, Al, Cs, Ga
P9	-	Ca
P10	Ba	-
P15	-	K
P17	-	P
P18	-	S
P19	Se	S
P22	Rb, Cs	K, Ba
P23	-	Be
P25	Be	-
P27	S, Se	-
P31	-	Mg
P33	-	Mg
P36	-	Be, Na, Mg, Ba
P40	B, Na, S	Se
P44	-	K
P46	Na	B
P50	-	Se

TABLE 5
Matrix of Pearson's correlation coefficient between elements in aquatic sediments.

Variable	Marked correlations are significant at p < 0.05000 N=50 (Casewise deletion of missing data)															
	Li	Be	B	Na	Mg	Al	P	S	K	Ca	Rb	Sr	Cs	Ba	Se	Ga
Li	1.00	0.41	-0.10	-0.22	-0.12	0.64	-0.12	-0.35	0.40	-0.44	0.25	-0.38	-0.04	0.31	-0.37	0.44
Be	0.41	1.00	0.06	-0.00	-0.03	0.32	-0.18	-0.03	0.24	-0.27	0.26	-0.23	0.10	0.15	-0.10	0.20
B	-0.10	0.06	1.00	0.79	0.19	0.11	0.41	0.58	0.45	0.16	0.41	0.08	0.27	0.25	0.39	0.12
Na	-0.22	-0.00	0.79	1.00	0.39	0.09	0.25	0.52	0.24	0.15	0.03	0.14	-0.05	0.04	0.22	0.12
Mg	-0.12	-0.03	0.19	0.39	1.00	-0.14	-0.22	-0.15	0.05	0.37	-0.15	0.49	-0.10	0.02	0.03	-0.25
Al	0.64	0.32	0.11	0.09	-0.14	1.00	-0.01	-0.05	0.72	-0.51	0.60	-0.47	0.06	0.01	-0.13	0.84
P	-0.12	-0.18	0.41	0.25	-0.22	-0.01	1.00	0.32	0.17	-0.18	0.13	-0.16	0.03	0.05	0.24	0.04
S	-0.35	-0.03	0.58	0.52	-0.15	-0.05	0.32	1.00	0.04	0.07	0.17	0.15	0.40	0.02	0.67	0.14
K	0.40	0.24	0.45	0.24	0.05	0.72	0.17	0.04	1.00	-0.17	0.75	-0.21	0.31	0.20	0.11	0.53
Ca	-0.44	-0.27	0.16	0.15	0.37	-0.51	-0.18	0.07	-0.17	1.00	-0.23	0.66	0.16	0.00	0.27	-0.54
Rb	0.25	0.26	0.41	0.03	-0.15	0.60	0.13	0.17	0.75	-0.23	1.00	-0.21	0.61	0.15	0.26	0.48
Sr	-0.38	-0.23	0.08	0.14	0.49	-0.47	-0.16	0.15	-0.21	0.66	-0.21	1.00	0.31	-0.05	0.31	-0.47
Cs	-0.04	0.10	0.27	-0.05	-0.10	0.06	0.03	0.40	0.31	0.16	0.61	0.31	1.00	0.13	0.65	0.03
Ba	0.31	0.15	0.25	0.04	0.02	0.01	0.05	0.02	0.20	0.00	0.15	-0.05	0.13	1.00	-0.02	-0.35
Se	-0.37	-0.10	0.39	0.22	0.03	-0.13	0.24	0.67	0.11	0.27	0.26	0.31	0.65	-0.02	1.00	-0.01
Ga	0.44	0.20	0.12	0.12	-0.25	0.84	0.04	0.14	0.53	-0.54	0.48	-0.47	0.03	-0.35	-0.01	1.00

According to the findings of the present study, the concentration values show that the average value of 16 elements, in the sediments of aqua sources, in this study area follow this trend: Ca>Al>Mg>K>S>P>Na>Ba>Sr>Li>Rb>B>Ga>Cs >Be>Se.

Statistical interpretation of the results. The descriptive statistics of 16 major elements in the sediment, fraction under 63 mμ, are presented in Table 3 and the statistical values are given as arithmetic mean, geometric mean, median, minimal and maximal concentration, variance and standard deviation. Using experimental data from the Table 2 and box plot approach of Tukey, anomalous values (extreme and outlier) of all analyzed elements were determined. Analyzing the frequency histograms and scatter box plot diagrams (Figure 2 and 3), extreme and outlier values of measured elements were defined and they are presented in Table 4. Analyzing Table 4 we have noticed that 23 sample points include anomalies (outlier and extreme) values for the analyzed elements. Correlation Pearson's analysis of elements was calculated to see if some of the parameters were interrelated with each other. In terms of correlation analyses (Table 5) elements such as: Li, Be, Mg, P and Ba did not show significant positive correlation with any element. But, B was significantly positive correlated with Na (0.79), whereas Al was with K (0.72) and Ga (0.84). S showed significant positive correlation with Se (0.67), whereas K was with Al (0.72) and Rb (0.75). Ca showed significant positive correlation with Sr (0.66) whereas Cs was with Se (0.65).

TABLE 6
Members of 4 clusters and distances of samples from respective cluster center.

Cluster	Members of cluster (Q-mode) and distances from respective cluster center
Cluster 1 Cluster contains 9 cases	P8 (4987.885)* P12 (4143.869) P13 (2107.552) P16 (1510.226) P17 (1239.316) P22 (3594.026) P26 (3957.649) P40 (4491.849) P45 (1199.546)
Cluster 2 Cluster contains 14 cases	P4 (3177.052) P5 (2711.038) P10 (2611.084) P14 (818.7068) P27 (1277.807) P31 (3186.200) P32 (4630.059) P36 (9147.866) P43 (1516.313) P46 (743.1777) P47 (451.0308) P48 (1950.523) P49 (732.1495) P50 (120.5278)
Cluster 3 Cluster contains 7 cases	P1 (4844.965) P2 (6537.042) P3 (7558.003) P9 (13075.48) P24 (8305.399) P33 (6797.455) P38 (3534.898)
Cluster 4 Cluster contains 20 cases	P6 (3102.357) P7 (4553.085) P11 (1183.175) P15 (2567.122) P18 (3691.737) P19 (2752.325) P20 (4122.832) P21 2972.406) P23 (183.5928) P25 (2255.879) P28 (1600.421) P29 (1971.221) P30 (4708.081) P34 (4902.629) P35 (4372.159) P37 (4070.020) P39 (1791.155) P41 (3655.738) P42 (3339.006) P44 (578.6340)

* In parenthesis is the distance of a cluster member (sample) from the center of the respective cluster group.

Cluster analysis (CA) is another type of classification that clusters chemical elements (R-mode) and sample points (Q-mode) in terms of their similarities or differences. Cluster analysis (R-mode) shows a dendogram (Figure 4) where all sixteen chemical elements were grouped into one statistically significant cluster. Dendogram shows mutual links between studied variables and it could be observed that Ca has the closest association with Al. After that, Al has the closest association with Mg and they form one branch of the dendogram linked with the other one, in which S, K, P, Na, Ba, Sr, Cs, B, Ga, Se, Be, Rb and Li follows. These correlations are highlighted, suggesting similar sources and similar geochemical processes that could control the occurrence of these elements in analysed sediments (fraction under 63 μm).

CA of Q-modality was performed on the total set of geochemical data from Table 2 and samples were grouped in 4 clusters (Table 6). The results of Q-modality cluster analysis, with the Euclidian distance and means value of elements in each clusters are given in parenthesis (Tables 7 and 8). In case of 4 clusters, the cluster 1 contains 9 sample points, the cluster 2 contains 14 sample points, the smallest cluster 3 contains 7 sample points, and the biggest cluster 4 contains 20 sample points.

Spatial distribution of chemical elements in aqua sediments. Determination of major elements and their spatial variations is crucial for a better understanding of pollution sources. Spatial distribution maps of major chemical elements (Li, Be, B, Na, Mg, Al, P, S, K, Ca, Rb, Sr, Cs and Ba) are presented in Figure 5, and they show high concentration values of analyzed elements in different parts of the study area. By analyzing the created maps, the high concentrations of Li, Ca and Ba were located mostly in the north part, whereas the high concentrations of B, Na, Mg, Sr and Cs were located mostly in the north-east part of the catchment basin. Also the spatial maps, show that high concentrations of Be and Al were located mostly in the north and south part, whereas high concentrations of P, S, K and Rb were located mostly in the south-east part of the catchment basin.

TABLE 7
Euclidean Distances between 4 Clusters.

	Euclidean distances between 4 clusters Distances below diagonal Squared distances above diagonal			
Cluster Number	**No. 1**	**No. 2**	**No. 3**	**No. 4**
No. 1	0.00	95208780	931864800	96068970
No. 2	9757.50	0	433657700	380119500
No. 3	30526.46	20824	0	1624743000
No. 4	9801.48	19497	40308	0

TABLE 8
Means of major elements in 4 clusters.

Variable /ppm	Cluster Means			
	Cluster No. 1	**Cluster No. 2**	**Cluster No. 3**	**Cluster No. 4**
Li	25.18	22.06	17.7	25.32
Be	1.10	0.85	0.9	1.19
B	10.00	7.29	8.7	6.10
Na	315.56	304.29	320.0	265.00
Mg	6222.22	8064.29	9071.4	5555.00
Al	22866.67	17178.57	15085.7	22735.00
P	877.78	576.43	544.3	703.50
S	1721.11	1170.71	1571.4	804.50
K	2788.89	2100.00	2200.0	2505.00
Ca	60177.78	98735.71	182000.0	20990.00
Rb	25.58	14.69	17.3	20.91
Sr	129.98	226.87	332.4	62.53
Cs	3.69	1.32	6.7	1.89
Ba	175.01	195.26	136.5	146.52
Se	0.24	0.24	0.5	0.20
Ga	5.04	3.41	3.0	5.13

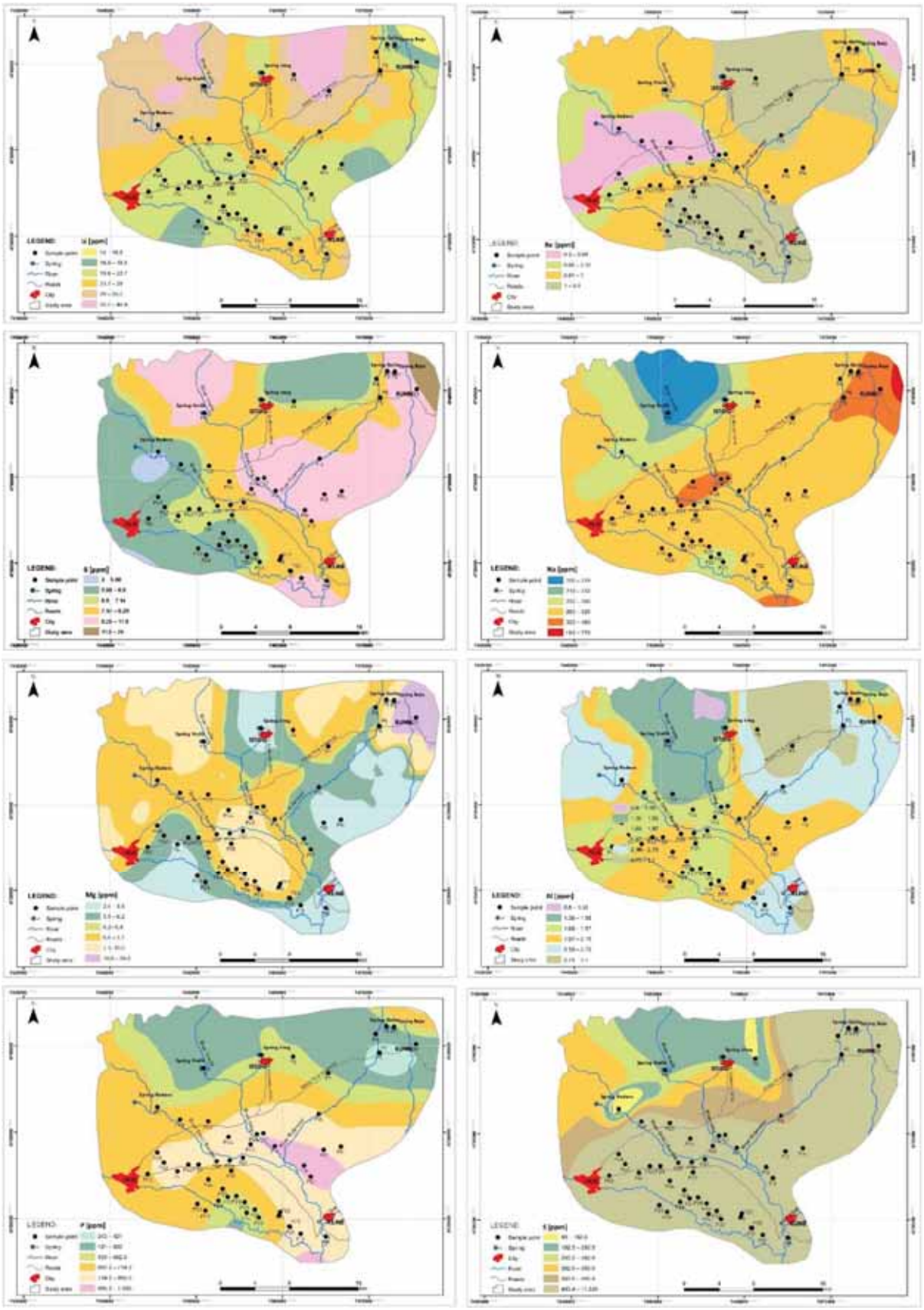

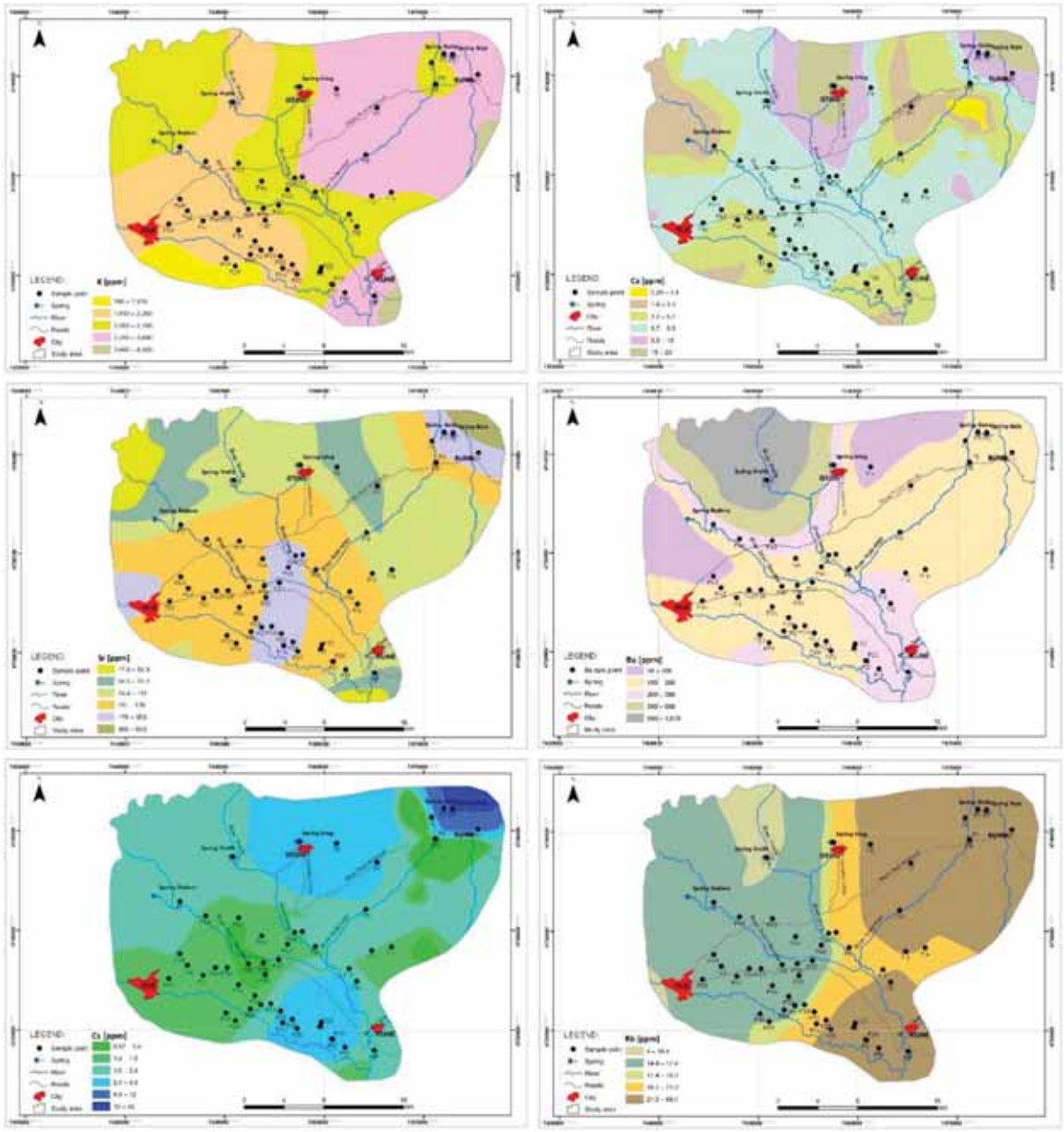

FIGURE 5
Spatial distribution of analysed elements in sediment of the study area.

CONCLUSIONS

This study represents the geochemical analysis, spatial and statistical analyses of major elements in sediments (fraction <63 µm) of water sources in Drini i Bardhë river basin. In terms of statistical interpretation the arithmetic mean concentrations of the studied elements have decreased in such order: Ca>Al>Mg>K>S>P>Na>Ba>Sr>Li>Rb>B>Ga>Cs >Be>Se. According with the existing criteria for sediment quality, Ba, Se and P in some sample stations exceed recommended norms that cause low or significant toxic effects and make unsuitable aquatic life. Using the frequency histograms and Scatter box plot diagrams, this study found that 23 sample points include anomalies (outlier and extreme) of measured elements.

In terms of correlation analysis elements such as: Li, Be, Mg, P and Ba did not show significant positive correlation with any element. But, B was significantly positive correlated with Na, whereas Al was with K and Ga. S showed significant positive correlation with Se whereas K was with Al and Rb. Ca showed significant positive correlation with Sr, whereas Cs was with Se. Cluster analysis of R-modality shows a Tree diagram where all elements were grouped into one statistically significant cluster and we observed that Ca has the closest association with Al. After that, Al has the closest association with Mg and they form one branch of the dendogram linked with S, K, P, Na, Ba, Sr, Cs, B, Ga, Se, Be, Rb and

Li. Results of cluster analysis Q-mode (in case of 4 clusters) show that cluster 1 contains 9 sample points, cluster 2 contains 14 sample points, the smallest cluster 3 contains 7 sample points, and the biggest cluster 4 contains 20 sample points.

Spatial distribution maps of major elements show high concentration values of analyzed elements in different parts of the study area. The high concentrations of Li, Ca and Ba were located mostly in the north part, the high concentrations of B, Na, Mg, Sr and Cs were located mostly in the north-east part, the high concentrations of Be and Al were located mostly in the north and south part and high concentrations of P, S, K and Rb were located mostly in the south-east part of the catchment basin. By comparing the concentrations of Ba, Se and P elements with the existing criteria, it was found that sample points P2, P7, P11-21, P28-32, P35, P37, P39, P42, P44, P46, P48 and P50 exceed recommended norms that cause low/significant toxic effects. Using scatter box plot diagrams, 23 sample points (P1, P2, P4, P6-10, P15, P17-19, P22, P23, P25, P27, P31, P33, P36, P40, P44, P46 and P50) include anomalies of analysed elements, probably impacted by the lithology of rocks and from minor influence of human activity (the case of P from the overuse of chemical fertilizers in agricultural lands in this area). The authors of this paper suggest that study will be a useful tool for the authorities who has responsibility for the natural resources.

ACKNOWLEDGEMENTS

This paper is a part of PhD Thesis of Fisnik Laha (supervised by Dr. Fatbardh Gashi). Colleagues from Department of Chemistry, Faculty of Natural Sciences, University of Prishtina “Hasan Prishtina”, are thanked for participation in this research. Part of this research and preparation of the manuscript was partly supported by University of Prishtina “Hasan Prishtina”, Kosovo.

REFERENCES

[1] Shukla, R., Sharma, Y.K. (2008) Heavy metal toxicity in environment. In: Environmental Monitoring and Management, Trivedi, A., K. Jaiswal, B.N. Pandey and S.P. Trivedi (Eds.). Alfa Publications. Delhi, India, 137–162. ISBN 978-81-907843-8-2.

[2] Andrews, S., Sutherland, R. (2004) Cu, Pb and Zn contamination in Nuuanu watershed, Oahu, Hawaii. Science of the Total Environment. 324, 1–3, 173–182.

[3] Hakanson, L. (1980) An ecological risk index for aquatic pollution control. a sedimentological approach, Water Research. 14(8), 975–1001.

[4] Fouladi Fard, F., Naddafi, K., Hassanvand, M. S., Khazaei, M., Rahmani, F. (2018) Trends of metals enrichment in deposited particulate matter at semi-arid area of Iran. Environ. Sci. Pollut. Res. Int. 25, 18737–18751.

[5] Yahaya, A., Adegbe, A.A., Emurotu, J.E. (2012) Assessment of heavy metal content in the surface water of Oke-Afa canal Isolo Lagos, Nigeria. Arch. Appl. Sci. Res. 4, 2322–2326.

[6] Shokrzadeh, M., Rokni, M.A., Galstvan, (2013) Lead, cadmium, and chromium concentrations in irrigation supply of/and Tarom Rice in Central cities of Mazandaran province-Iran. J. Mazandaran. Univ. Med. Sci. 23, 234–242.

[7] Ali, M.H., Fishar, M.R. (2005) Accumulation of trace metals in some benthic invertebrate and fish species relevant to their concentration in water and sediment of lake Qarun, Egypt. Egypt. J. Aquat. Res. 31 (1), 289–301.

[8] Halamić, J., Bukovec, D., Miko, S., Galović, L. (2001) A factor model of the relationship between stream sediment geochemistry and adjacent drainage basin lithology, Medvednica Mt., Croatia. Geologia Croatica. 54(1), 37-51.

[9] Mohiuddin, K.M., Otomo, K., Ogawa, Y., Shikazono, N. (2012) Seasonal and spatial distribution of trace elements in the water and sediments of the Tsurumi River in Japan. Environmental Monitoring and Assessment. 184(1), 265–279.

[10] Khalil, M.K.H., Radwan, A. M., El-Moselhy, K. H. M. (2007) Distribution of phosphorus fractions and some of heavy metals in surface sediments of Burullus lagoon and adjacent Mediterranean Sea. Egypt. J. Aquat. Res. 33 (1), 277–289.

[11] Kabata-Pendias A., Pendias H. (1986) Trace elements in soils and plants. CRC Press, Boca Raton. 26.

[12] Pandey, S.K., Tiwari, S. (2009) Physico-chemical analysis of ground water of selected area of Ghazipur city. A case study. Nature and Science. 7(1), 17-20.

[13] Gashi, F. Troni, N. Faiku, F. Ibrahimi, R. Laha, F. Kurteshi, K., Jusufi, F., Osmani, S., Hoti, F. (2014) Chemical determination of some elements in water of sitnica river (Kosovo) by ICP-MS technique. . Fresen. Environ. Bull. 23(1), 91-97.

[14] Gashi, F., Frančišković-Bilinski S., Bilinski, H. (2009) Analysis of sediments of the four main rivers (Drini i Bardhë, Morava e Binçës, Lepenc and Sitnica) in Kosovo. Fresen. Environ. Bull. 18(11), 1462-1471.

[15] Gashi, F., Frančišković-Bilinski, S., Bilinski, H., Troni, N., Bacaj, M., Jusufi, F. (2011) Establishing of monitoring network on Kosovo rivers: preliminary measurements on the four main rivers (Drini i Bardhë, Morava e Binçës, Lepenc and Sitnica). Env. Mon. Assess. 175, 279–289.
[16] Gashi, F., Stanislav Frančišković-Bilinski, S., Bilinski, H., Kika, L. (2016) Assessment of the effects of urban and industrial development on water and sediment quality of the Drenica River in Kosovo. Environ. Earth Sci. 75, 801.
[17] Frančišković-Bilinski, S. (2006) Barium anomaly in Kupa River drainage basin. Journal of Geochemical Exploration. 88, 106-109.
[18] Frančišković-Bilinski, S. (2007) An assessment of multielemental composition in stream sediments of Kupa River drainage basin, Croatia for evaluating sediment quality guidelines. Fresen. Environ. Bull. 16(5), 561-575.
[19] Frančišković-Bilinski, S. (2008) Detection of geochemical anomalies in stream sediments of the upper Sava River drainage basin (Slovenia, Croatia). Fresen. Environ. Bull. 17(2), 188- 196.
[20] Frančišković-Bilinski, S., Bilinski, H., Tibljaš, D., Rantitsch, G. (2005) Effects of mercury mining regions from NW Dinarides on quality of stream sediments. Fresen. Environ. Bull. 14(10), 913-927.
[21] Sikošek, B. (1971) Explanation for Geological map of Yougoslavia, scale 1:500000, Federal Geological Institute, Belgrade.
[22] Ivković, A., Šarin, A., Komatina, M. (1983) Explanation for the Hydrogeological Map of SFR Yugoslavia 1:500000, Federal Geological Institute, Belgrade.
[23] Çadraku, H. (2014) Quantitative and qualitative characterization of hydric resources in Dukagjini Basin, Kosovo, Doctoral thesis (in alabanien), Polytechnic University of Tirana, Fakulty of Geology and Mining, Tirana. (Accessed date: dibmin-fgjm.org/doktorata/DisertacioniHCadraku.pdf)
[24] The United States Geological Survey (USGS) (2018) Lakes and reservoirs; Guidelines for study design and sampling: U.S. Geological Survey Techniques and Methods, Book 9, Handbooks for Water-Resources Investigations, USA. 9-57.
[25] Ekman grab set. (Accessed date: en.eijkelkamp.com/products/sediment-samplers/tech-specs-ekman-grab.html)
[26] SMSP and FALCONBRIDGE NC SAS, (2005) Koniambo project, Environmental and Social Impact Assessment, Chapter 4 Mine, 4. Quality criteria for freshwater sediment. 2-7.
[27] Salminen, R., Tarvainen, T. (1997) The problem defining geochemical baselines. A case study of selected elements and geological materials in Finland. Journal of Geochemical Exploration. 60, 91-98.
[28] Statsoft, Inc. (2001) Statistica data analysis software system, ver. 6, The Statistics Homepage.
[29] Fisher, R., Mac Kenzie, W. (1923) Studies in crop variation. II. The manorial response of different potato varieties. Journal of Agricultural Science. 13, 311-320.
[30] Davis, J. C. (1986) Statistics and data analysis in geology, Second edition. John Wiley & Sons, New York.
[31] The software "ArcView" ver. 10.1. ArcGIS for desktop 10.1.
[32] Tukey, J.W. (1977) Exploratory data analysis. Reading: Addison-Wesley. 21-711
[33] Yuan, Z., Taoran, S., Yan, Z., Tao, Y. (2014) Spatial distribution and risk assessment of heavy metals in sediments from a hypertrophic plateau lake Dianchi, China. Environmental Monitoring and Assessment. 186, 1219–1234.
[34] Sundaray, S.K., Nayak, B.B., Lin S., Bhatta, D. (2011) Geochemical speciation and risk assessment of heavymetals in the river estuarine sediments—a case study: Mahanadi basin, India. Journal of Hazardous Materials. 186, 1837–1846.
[35] Ren, J., Shang, Z., Tao, L., Wang, X. (2015) Multivariate analysis and heavy metals pollution evaluation in Yellow River surface sediments. Polish Journal of Environmental Studies. 24 (3), 1041-1048.
[36] Schelske, C. L. (2009) Eutrophication: focus on phosphorus. Science. 324(5929), 722.
[37] Wang, L., Liang, T., Zhong, B., Li, K., Zhang. Q. (2014) Study on Nitrogen Dynamics at the Sediment–Water Interface of Dongting Lake, China. Aquat Geochem. 20(5), 1–17.
[38] Wang, Z., Gao, W., Cai, Y., Guo, H., Zhou, F. (2012) Joint optimization of population pattern and end-of-pipe control under uncertainty for Lake Dianchi water-quality management. Fresen. Environ. Bull. 21(12), 3693–3704.
[39] Withers, P.J.A., Sharpley, A.N. (2008) Characterisation and appointment of nutrient and sediment sources in catchments. J. Hyd. 350, 127-130.
[40] World Health Organization (WHO), (2008) Guidelines for Drinking-water Quality. Geneva. 1, 310.
[41] Presser, T.S., Sylvester, M.A., Low, W.H. (1994) Bioaccumulation of Selenium from Natural Geologic Sources in Western States and its Potential Consequences. Environ. Manage. 18, 423-436.
[42] Barałkiewicz, D., Siepak, J. (1999) Chromium, Nickel and Cobalt in Environmental Samples and Existing Legal Norms. Polish Journal of Environmental Studies. 8 (4), 201-208.
[43] World Health Organization (WHO) (2003) Aluminium in Drinking-Water, Background document for development of WHO Guidelines for Drinking-Water Quality. Geneva. 2-6.

[44] Mona, Kh.K., Gehan, M.E.Z., Mamdouh, A.F., Tarek O.S., Mohammed. A.Sh. (2013) Geochemistry of Some Major and Trace Elements in Sediments of Edku and Mariut Lakes, North Egypt. World Applied Sciences Journal. 24(3), 282-294.
[45] World Health Organization (WHO) (2009) Beryllium in drinking-water Background document for development of WHO Guidelines for Drinking-water Quality. 9-17.
[46] Rai, D., Zachara J.M., Schwab, A.P., Schmidt, R.L., Girvin, D. C., Rogers. J.E. (1986) Chemical attenuation rates, coefficients, and constants in leachate migration. Project 2198-1, vol. 1, Richland, WA, USA.
[47] Keren, R, Gast, R.G., Bar-Yosef, B. (1981) pH-dependent boron adsorption by Namontmorillonite. Soil Science Society of America Journal. 45, 45–48.
[48] Water quality—Determination of borate—Spectrometric method using azomethine-H. Geneva, International Organization for Standardization (ISO 9390:1990). 2-4.

Received: **24.04.2020**
Accepted: **24.05.2021**

CORRESPONDING AUTHOR

Naser Troni
Department of Chemistry
Faculty of Natural Sciences, M. Teresa 10
University of Prishtina
Prishtina, 10000 – Kosovo

e-mail: naser_troni@yahoo.com

© by PSP Volume 31– No. 05/2022 pages 4677-4683 Fresenius Environmental Bulletin

RESEARCH ON ENVIRONMENT DESIGN BASED ON GREEN AND ECOLOGICAL PERSPECTIVE

Yaping Liu*

North China University of Water Conservancy and Electric Power, School of Art and Design, Zhengzhou, Henan Province 450046, China

ABSTRACT

From the perspective of ecological civilization construction, this paper explores the research on interior environment design based the concept of green and harmonious ecology, discusses and studies the current situation of indoor environment decoration in China, and analyzes the main problems of green indoor environment design at present, such as unsatisfying the basic indoor physical conditions, over-decoration and the lack of green design concept by consumers. Based on the introduction of green and harmonious ecological concept design, this paper summarizes four main green and harmonious ecological indoor environment design concepts, and through the form of questionnaire survey, makes statistical analysis on consumers' preference for the four green interior design concepts, which is helpful for green interior environment designers to grasp the psychological dynamics of consumers and green design concepts in the future, find out the new trend of green interior design and design the indoor environment more in line with the needs of consumers.

KEYWORDS:
Ecological Civilization, Green and Harmonious, Environment Design, Green Design

INTRODUCTION

In recent years, with the rapid development of China's real estate, residents' demand for materials in the construction industry is increasing, and their requirements for green and healthy interior design environment are constantly improving [1]. With the development of real estate, residents' living quality and living environment are continuously improving, but at the same time, some ecological problems are exposed, such as light pollution and noise pollution. Besides, poor lighting and high energy consumption are major factors that seriously affect the indoor environment. Pollution cases caused by improper interior decoration design abound in China every year, such as fetal malformation caused by excessive toxic gases in decoration materials, excessive dependence on air conditioning caused by poor indoor ventilation, and excessive depression caused by long-term poor lighting environment [2-4]. Therefore, under the current environment of ecological civilization construction, it is the general trend to develop indoor environment design with green and harmonious ecological concept.

Research Status of Green Interior Environment Design. Before the end of the 20th century, people's pursuit of life mostly stayed at the material level, and the primary problem to be solved was food and clothing. Therefore, people had no concept of interior design. With the advent of the Internet era and the rapid development of national economy, people's living conditions have undergone fundamental changes, no longer staying at the material level, and the requirements for indoor environment comfort are getting higher and higher. Also, people pay more attention to the design style of indoor space and environmental protection concept [5]. In the future, the development of housing will pay more attention to the issues of green ecology and energy conservation. The era of interior decoration and design at the cost of environment has gradually become the past. With the introduction of green development concept, China's "Thirteenth Five-Year Plan" also pointed out that by 2020, green construction needs to reach half of the goal of new buildings. Furthermore, China is increasing efforts to develop green building professionals [6-7].

At present, more and more buildings in China have obtained China Green Building logo. For example, in 2016, Gezhouba Hongqiao Zijun Mansion established in China became the first building in Asia to pass the DGNB pre-certification standard, as shown in Figure 1. Its architectural features include: paying attention to ecological civilization construction, putting stress on green area, saving resources and space, improving the utilization rate of natural energy, minimizing and reducing environmental pollution, and creating a healthy and comfortable green indoor environment, which is a benchmark in the field of green building. At the same time, more and more consumers are aware of the importance of green environmental protection.

FIGURE 1
Gezhouba Hongqiao Zijun Mansion

FIGURE 2
Over-Decorated Interior Decoration

Existing Problems of Green Interior Environment Design. Green interior environment design is in its infancy in China, and the development time is still relatively short. At present, the green interior design system is not very mature, and there are various problems. In addition to the common indoor decoration material pollution, light pollution, noise pollution and other problems, there are also the following problems [8-10]:

(1) Unsatisfied basic physical conditions. At present, some interior design tends to pursue the so-called fashion and novelty. In the process of decoration, a large number of transparent glass, polished stone and aluminum alloy are widely used. They simply emphasize decorative materials and styles, lack of innovative and flexible design, not only ignore the basic physical conditions, but also use excessive non-renewable resources, which is contrary to the concept of ecological civilization construction. For example, in the lighting, simply pursuing luxury lamps while ignoring the lighting design of natural light, not only causes a lot of energy waste, but also easily causes light pollution [11].

(2) Over-decoration. With the economic development, China has gradually entered a well-off society. The development and popularization of the Internet, 5G and artificial intelligence have affected and impacted the residents' consumption concept in many aspects. Meanwhile, with the advent of the influencer economy era, consumers' consumption concept is easy to be influenced by Internet celebrities, which leads some consumers to blindly follow the trend and excessively pursue luxury and beauty. In the interior decoration, too much attention is paid to luxury decoration, which often leads consumers to buy more decoration materials and furniture. This

kind of decoration deviates from the purpose of indoor green decoration, and indoor space is congested and indoor air quality is difficult to be guaranteed due to excessive decoration. Excessive decoration not only causes a huge waste of resources, but also fail to protect the living environment [12]. As shown in Figure 2, too many furniture, murals and ornaments will make the hall look luxurious, but at the same time give people a feeling of congestion. There are many sofas and chairs in the hall, which reduces its whole space. In addition, too much furniture makes the indoor air quality difficult to guarantee. Therefore, the whole decoration deviates from the interior design concept of green and environmental protection.

(3) Lack of green interior design concept. At present, many consumers can't specifically describe the decorative style they want, and they don't know what the so-called green design is like. At the same time, as people are busy with their daily work, they often only have a one-sided understanding of green design through the Internet, advertising and other ways when buying or decorating houses, and they can't understand the purpose of green design concept clearly [13]. Moreover, for designers and constructors themselves, there is a shortage of talents with a background in education and training of green design concepts. Therefore, it is often difficult for so-called green interior designers in the market to come up with better solutions, and the construction workers also lack green construction technology, which is an important reason why green interior design is difficult to popularize nowadays [14].

Main Idea of Green Interior Environment Design. People-oriented, health and comfort are the essential concepts of green interior ecological design. While creating a comfortable living environment for human beings, it is necessary to reduce the waste of resources and environmental pollution as much as possible to achieve a green and harmonious sustainable development path. Therefore, the green interior environment design needs to focus on the following aspects [15-16]: (1) Advocate moderate consumption and decoration, avoid excessive decoration and waste, and it is not recommended to excessively follow the suggestions of the influencer, but to create a comfortable living environment to the maximum extent according to the individual economic ability of consumers. (2) Pay attention to natural aesthetics. In the process of interior design, make rational use of natural light, keep good ventilation, minimize the waste of resources caused by artificial light sources and reduce the dependence on air conditioning systems. Green interior design pays attention to the integration of indoor environment and nature. Effective integration with nature can bring lasting pleasure to people. (3) Adhere to the people-oriented, pay attention to the physiological and psychological needs of consumers, and make every effort to provide a comfortable living environment according to individual economic ability, so as to avoid the burden of excessive or unnecessary decorations on people's physical and mental health. (4) Pay attention to localization design. In the process of interior design, it is necessary to consider the harmony between man and nature and the influence of folk customs, adjust measures to local conditions, take local materials as far as possible, use advanced technology and innovative design to effectively integrate local elements, save resources and take into account the concept of sustainable development.

MATERIALS AND METHODS

Reasonable Layout of Interior Design Space. Reasonable indoor layout can not only avoid space congestion, but also ensure adequate ventilation and natural lighting. Reasonable zoning and visual adjustment can highlight the advantages of its decoration. Reasonable indoor division can achieve the purpose of expanding sensory space and realizing green environmental protection, which can not only maximize the use of space, but also avoid unnecessary decoration, save building materials and decorations, and avoid waste of resources and environmental pollution [17].

Reasonable Choice of Decoration Materials. Modern decoration materials and indoor furniture often contain a large amount of harmful substances such as formaldehyde, which poses a great threat to people's physical and mental health. Under the design concept of green harmony and ecology, nowadays young people pay more and more attention to whether the decoration materials themselves meet the requirements of green environmental protection. When choosing decoration materials, they will try their best to choose pollution-free natural stone and wood, or some natural materials that are nontoxic and harmless after simple modification, give full consideration to the green environmental protection of decoration materials and their impact on human health [18].

Reasonable Indoor Lighting Design. The sources of indoor lighting mainly include natural lighting and artificial light sources. In interior design, natural sunlight should be used as much as possible to provide light sources for the living room. For example, glass is used to introduce natural light into the room, and designers set up corresponding reflectors to achieve the purpose of natural lighting through the spatial layout and actual situation of the room [19]. Moreover, in the process of lighting design, it is necessary to comprehensively consider local sunshine time, spacing and orientation of buildings, light pollution caused by excessive lighting, etc.

Reasonable Indoor Greening Layout. People spend more than half of their time indoors every day. Therefore, the air quality of indoor environment has a great impact on the physical and mental health of human body. In the process of interior design, proper greening layout not only reflects the purpose of green environmental protection design, but also can use green plants to beautify the environment, purify air and reduce radiation. The green layout of indoor environment can effectively relieve people's life pressure and make them experience the comfort brought by green life [20-21].

Basic Information of Questionnaire Survey. The questionnaire survey relies on randomly distributing questionnaires among the people who need to carry out housing design and decoration, and carries out statistical analysis according to the questionnaire returned by consumers. The main content of the questionnaire is to investigate consumers' preference for the four green interior decoration modes. A total of 500 questionnaires were distributed and 367 valid questionnaires were recovered, with a recovery rate of 73.4%.

RESULTS AND DISCUSSION

Reasonable indoor layout can not only avoid space congestion, but also ensure good ventilation and sufficient natural lighting. Through questionnaire survey, this paper investigates the application of green residential design mode, and a total of 367 valid questionnaires are collected. There are four kinds of interior environment design modes with green and harmonious ecological concept: reasonable layout of interior design space, reasonable choice of decoration materials, reasonable indoor lighting design and reasonable indoor greening layout. This paper studies the distribution of four indoor environment design concepts among consumers of different ages and genders, and finds out the preference of consumers with different characteristics for green indoor environment design mode, so as to provide a clear direction for green indoor environment design.

Distribution of Different Green Interior Environment Design Concepts The 367 valid questionnaires were classified and counted to analyze the proportion of each kind of interior environment design concept. The statistical results are shown in Figure 3. The design concept of reasonable interior space layout accounts for the highest proportion (31.5%), which is the most popular design concept among consumers; the second most popular design concept among consumers is reasonable indoor greening layout (30.6%), which is close to the popularity of the most popular design concept.

Age distribution of Consumers with Different Green Interior Environment Design Concepts According to the general purchasing power law of consumers, the age stages of consumers who are engaged in interior decoration design are divided into 25-35 years old, 36-45 years old, 45-60 years old and over 60 years old. According to the results of 367 valid questionnaires, the design concepts of green indoor environment preferred by consumers of different ages were counted. The relationship between consumers at different ages and different green indoor environment design concepts is shown in Figure 4. Reasonable choice of decoration materials design concept is the most popular among consumers aged 25-35, reasonable greening layout design concept is the most popular among consumers aged over 60, while it is the least popular among consumers aged 45-60. Reasonable indoor lighting design concept accounts for a low popularity among consumers at different ages. This difference indicates that with the increase of age, consumers' demand for ecological concept will change.

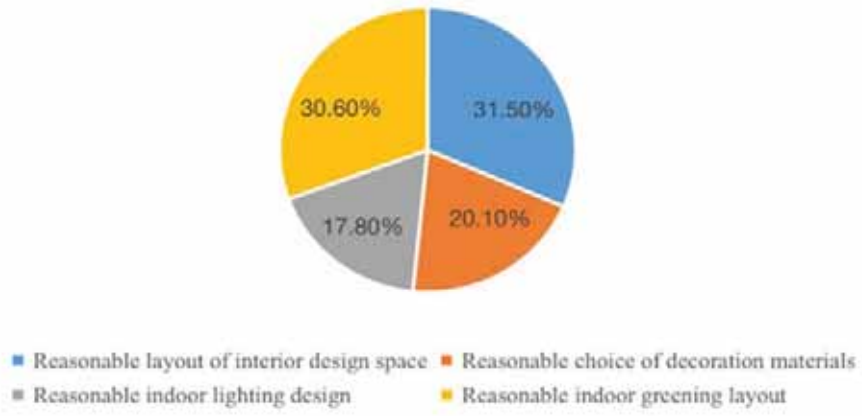

FIGURE 3
Distribution of Different Green Design Concepts

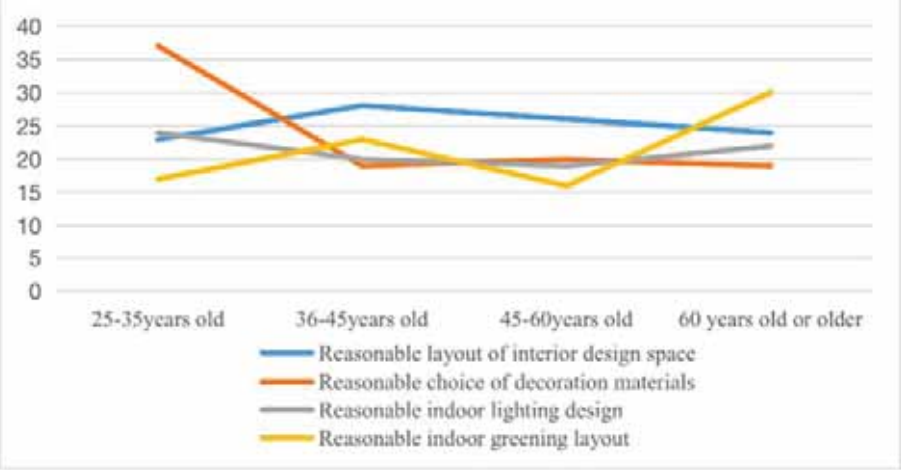

FIGURE 4
Age Distribution of Consumers with Different Green Interior Design Concepts

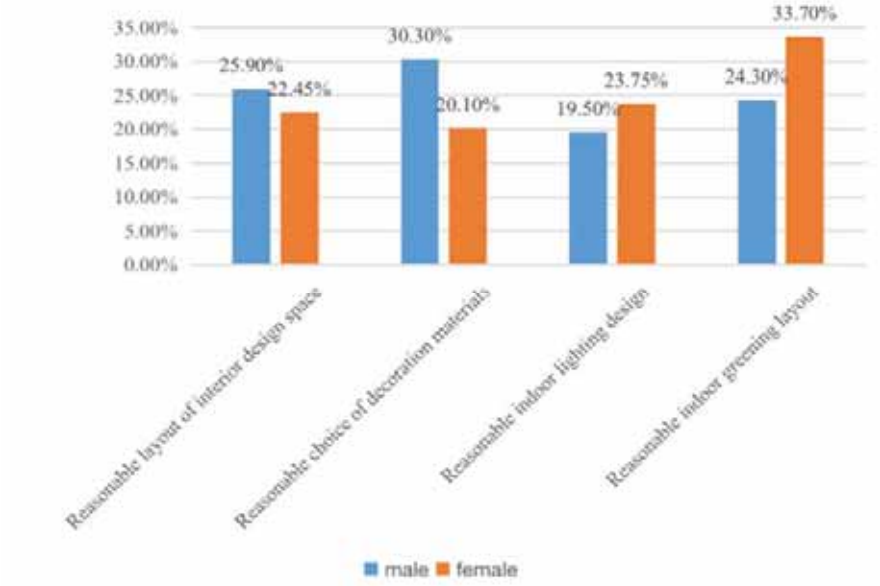

FIGURE 5
Gender Distribution of Consumers with Different Green Interior Design Concepts

Gender Distribution of Consumers with Different Green Interior Environment Design Concepts Considering the influence of gender on different green interior environment design concepts, according to the results of 367 valid questionnaires, the green interior environment design concepts preferred by consumers of different genders were counted. The gender distribution of different green interior environment design concepts was studied. As shown in Figure 5, the design concept of reasonable choice of decoration materials is the most popular among male consumers (30.30%), which is far higher than the demand of women for the concept of ecological unity (20.10%). The most popular among female consumers is the design concept of reasonable indoor greening layout (33.70%), which is far higher than the male demand for personalized multifunctional ecological concept (24.30%). The reason for this difference may be due to the gender differences between men and women, which leads to the differences in demand for green interior environment design concepts.

Based on the introduction of green and harmonious ecological concept design, this paper summarizes four main green and harmonious ecological interior environment design concepts, and analyzes consumers' preference for four green interior design concepts through 367 valid questionnaires. Among the consumers, the most popular green design concept is the reasonable interior space layout design concept, accounting for 31.5%; while the reasonable indoor lighting design concept is the least popular. In the study of the relationship between consumers of different ages and different green interior environment design concepts, reasonable choice of decoration materials design concept is most popular among

consumers aged 25-35, and reasonable greening layout design concept is most popular among consumers over 60 years old. In addition, among the consumers of different genders, the popular design concepts are also inconsistent. Among the male consumers, the most popular design concept is the reasonable choice of decoration materials (30.30%), which is far higher than the demand of women for the concept of ecological unity (20.10%); among the female consumers, the most popular design concept is the reasonable indoor greening layout design concept (33.70%).

CONCLUSIONS

This paper uses statistical methods to study and analyze the green interior design concept, combines ecological concept with indoor environment design, so as to integrate ecological concept into interior design. On the basis of introducing green and harmonious ecological concept design, four main green and harmonious ecological interior design concepts are summarized, and the consumers' preferences for four green interior design concepts are analyzed through 367 valid questionnaires. This paper provides a new idea for green interior design, so that the design is not limited to the traditional interior design relying on experience to analyze and judge, but based on the preference of consumers' design concept, so as to better provide a scientific judgment of design direction for designers.

REFERENCES

[1] Tang, X.F. (2018) Controllability analysis of indoor environment design based on green ecological residence. Northern Environment. 30(3), 134-135.

[2] Kubba, S. (2017). Handbook of green building design and construction indoor environmental quality. Publisher, City. 353-412.

[3] Kaymaz, I., Oguz, D. and Cengiz-Hergul, O.C. (2019) Factors influencing children's use of urban green spaces. Indoor and Built Environment. 28(4), 520-532.

[4] Wang, R., Liu, P., Qian, Y. (2018) Research on the implementation of technological measures for controlling indoor environmental quality in green residential buildings. Iop Conference. 113.

[5] Lee, L.S.H. and Jim, C.Y. (2017) Subtropical summer thermal effects of wirerope climber green walls with different air-gap depths. Building & Environment. 126(Dec.), 1-12.

[6] Tamiami, H., Khaira, F. and Fachrudin, A. (2018). Green design application on campus to enhance student's quality of life. Iop Conference. 309, 012022.

[7] Moya, T.A., Andy, V.D.D., Ottele, M. and Bluyssen, P.M. (2019). A review of green systems within the indoor environment. Indoor and Built Environment. 28(3), 298-309.

[8] Lee, J.Y., Wargocki, P., Chan, Y. H., Chen, L. and Tham, K.W. (2019) Indoor environmental quality, occupant satisfaction, and acute building-related health symptoms in green mark-certified compared with non-certified office buildings. Indoor Air. 29(1), 112-129.

[9] Aigbavboa, C. and Thwala, W.D. (2019) Performance of a green building's indoor environmental quality on building occupants in south africa. Journal of Green Building. 14(1), 131-148.

[10] He, Y., Kvan, T., Liu, M. and Li, B. (2018) How green building rating systems affect designing green. Building & Environment. 133(APR.), 19-31.

[11] Radwan, A. and Issa, M.H. (2017). An evaluation of indoor environmental quality and occupant well-being in manitoba school buildings. Journal of Green Building. 12(1), 123-141.

[12] Ponce, A. (2019) Critical success factors for indoor green walls. The Construction Specifier. 72(3), 22-27.

[13] Geng, Y., Ji, W., Wang, Z., Lin, B. and Zhu, Y. (2019) Response to the commentary on "a review of operating performance in green buildings: energy use, indoor environmental quality and occupant satisfaction" by john h. scofield. Energy and Buildings. 194(JAN.), 500-514.

[14] Yu, L., Wang, H., Wang, X. and Feng, G. (2017) Study on the measurement of indoor environment quality and enclosure structure thermal defects of green residential buildings in severe cold areas. Procedia Engineering. 205, 3373-3380.

[15] Mueller, W., Steinle, S., Juha Pärkkä, P.E. and Loh, M. (2019) Urban greenspace and the indoor environment: pathways to health via indoor particulate matter, noise, and road noise annoyance. Environmental Research. 180, 108850.

[16] Wei, W., Wargocki, P., Zirngibl, J., Jana Bendžalová. and Mandin, C. (2019) Review of parameters used to assess the quality of the indoor environment in green building certification schemes for offices and hotels. Energy and Buildings. 209, 109683.

[17] Hu, K., Fang, Z., Ji, Z. and Jiang, X. (2018) Analysis on actual measurement of indoor thermal and humidity environment of green office buildings in guangzhou area. Guangzhou Architecture. 046(006), 23-27.

[18] Chen, D. (2018) Research on the Application of Green Ecological Design Concept in Interior Design. Global Market Information Herald. 000(029), 152-153.

[19] Sun, Y. (2019) Indoor environment design based on ecological concepts. Modern Horticulture 380(08), 111-112.

[20] Akom, J.B., Sadick, A.M., Issa, M.H., Rashwan, S., Duhoux, M. (2018) The indoor environmental quality performance of green low-income single-family housing. Journal of Green Building. 13(2), 98-120.
[21] Turner, T.L., Stevinson, C. (2017) Affective outcomes during and after high-intensity exercise in outdoor green and indoor gym settings. International Journal of Environmental Health Research. 27(2), 106-116.

Received: **19.09.2020**
Accepted: **17.02.2021**

CORRESPONDING AUTHOR

Yaping Liu
North China University of Water Conservancy and Electric Power,
School of Art and Design,
Zhengzhou Henan Province 450046 – China

e-mail: niulixin998@163.com

© by PSP Volume 31– No. 05/2022 pages 4684-4691 Fresenius Environmental Bulletin

A STUDY ON SCALLION YIELD AND QUALITY IN ONION GENOTYPES ACCORDING TO HARVEST TIME

Atnan Ugur[1,*], Mustafa Ozgur Gural[2]

[1]Department of Horticulture, Faculty of Agriculture, Ordu University, 52200, Ordu, Turkey
[2]Giresun Directorate of Agriculture and Forestry, 28100, Giresun, Turkey

ABSTRACT

Green onion quality varies by genotype, ecology, harvesting period and production material. In the study performed as a greenhouse test, the pots were filled with peat:perlite mixtures (3:1 v/v) and 140 sets per m^2 were planted in the pots on 21st of October. The green onions were harvested in three periods (on 30th, 60th and 90th days) following planting of sets. Yield (kg/da), plant height (cm), white stalks length (cm), pyruvate content (µm/ml), and soluble solids content (g/100 g) were determined in the harvested plants. Yield values varied between 1072.33 and 3880.67 kg/da depending on genotypes. Bayramlı and Osmanbey genotypes yielded the highest yield values in second and third harvesting respectively. The following genotype heights were found out to be superior: Yayladalı and Osmanbey in terms of white stalks length, Bayramlı and Osmanbey in terms of low pyruvate content and Çalköy, Karaca-1 and Bayramlı in terms of soluble solids content. Use of productive and quality specialties obtained as per consumption purposes of green onion is significant in terms of agricultural production and sustainability.

KEYWORDS:
Allium cepa L., green onion, height, pyruvate, SSC

INTRODUCTION

Onion is a plant used for traditional medicine for centuries and frequently produced and consumed in great quantities across the globe. According to data of FAO, global onion and green onion production is 97.862.928 tons and 5.134.362 tons respectively. 2.131.513 tons of onion and 138.993 tons of green onion is produced in Turkey. Onion has been more popular in Asian and American cuisine in the recent years and its production volume has rapidly increased [1]. Onion draws interest with its unique test, mineral content and health improving effects and is one of the plants with a great economic significance [2-3]. Fresh leaves of the green onion contain antimicrobial, bioactive, allyl-root sulphide compounds in addition to being antioxidant and rich of A, B6, B9 (folic acid) and C vitamins [3-6]. These specialties are affected by the ecology of the place of growing in addition to genetic specialties [7]. Sulphurous compound content brings differences for the onions in terms of taste, aroma, smell and lachrymation [8]. The pyruvate content of onion provides more effective and definite results to determine its quality in terms of taste and aroma. The success of green onion production varies by production material, number and length of leaves, white stalks length, tuberization states, taste, aroma and fibre content [9]. Production of green onion by using set is preferred for both its growing period and homogenous production [10]. There is not sufficient data for assessment of yield and quality together in green onion growing. In our study, it was aimed to test the green onion production performances of the sets selected from different location by harvesting periods and certain quality parameters were determined.

MATERIALS AND METHODS

Plant material and equipment. The sets of the genotypes used in the study were supplied from the provinces of Ankara, Amasya, Tokat, Çorum and Samsun provinces. The names and place of supply of the genotypes and average diameter and weight of the sets are given in the Table 1.

Growing the plants and cultural procedures. The plants were grown under maximum/minimum temperatures of 27/14 °C in greenhouse conditions. As the growing pot, a plastic sowing pot of 75x16x18 cm and 17 liter volume was used. 3:1 v/v ratios of peat (Basissubsrat 2, Stender Group, Germany) and perlite (Akper Mining Co, Çankiri/Turkey) growing medium mixture was used in the study. The pots were filled with growing media mixture and the sets were manually potted on 21st of October. It was ensured that 1/3 of the sets would remain above the growing media while potting. 21 sets were planted in each pot in triangle planting pattern. All cultural procedures were fully performed during the study and thus it was ensured for the plants to reach harvesting sizes [10].

While fertilizing the plants, 12 kg pure nitrogenous fertilizer (26% N, calcium ammonium nitrate)

per decare was applied in three times, namely on 15th, 30th and 45th days, and equivalent dosages (on 30th and 45th days, 1.04 kg nitrogen per decare was supplied from potassium nitrate fertilizing). 10 kg phosphate fertilizer (42% P_2O_5, Triple superphosphate) per decare was applied once, namely on the 15th day following the planting. 16 kg potassium fertilizer (44% K_2O, potassium nitrate) per decare was applied twice, namely on the 30th and 45th days in equal dosages. The green onions were harvested three times, namely on 30th, 60th and 90th days following the planting. During the harvesting, the plants were removed with their roots and they were immediately brought to the laboratory after being roughly cleaned under tap water following the harvesting.

Measurements performed on green onions. In the study, the plant height, white stalks length, soluble solids content, pyruvate content and yield of the harvested plants was determined.

Plant yield (kg/da): The plants harvested from each parcel were weighted by an electronic scale with a precision of 1 g and thus yield per decare was calculated.

Plant height (cm): The distance between the root crown and longest leave edge was measured by a ruler in cm for 5 randomly-selected plants per parcel.

White stalks length (cm): The length of the white stalk section in between the root crown and beginning of the green section was measured by a ruler in cm for 5 randomly-selected plants per parcel.

Pyruvate content (µm/ml): The pyruvate content was determined by spectrophotometric analysis developed by Wall and Corgan [11] for 100 g randomly-selected plant sample per parcel.

Soluble Solids Content (g/100 g): 50 g plant sample randomly selected from each parcel was grinded in the blender and filtered by filter paper and SSC was determined by reading the filtered content through the manual refractometer.

Statistical analysis. The experiment was designed as a randomized parcel with three replicates. Each pot was regarded as an application repetition in the study. The data obtained was statistically analysed by using JMP 10 statistical software and analysis of variance was used to test for significant differences at a 0.05 level between genotypes were revealed in LSD multiple comparison test.

RESULTS AND DISCUSSION

This study, in which certain local genotypes were used for green onion production, was conducted under unheated greenhouses with plastic films. In the study, the sets of the local onion genotypes supplied from the fields in the provinces of Amasya, Samsun, Çorum, Tokat and Ankara were used. Certain yield and quality specialties of the plants harvested on 30th, 60th and 90th days following the set planting were determined in the study.

Plant yield. Plant yields of onion genotypes by harvesting period are given in the Table 2. As is seen from the Table 2, it was found out that there were statistically significant differences among the plant yield values of the onion genotypes by harvesting period ($p<0.001$). In terms of plant yield values, the genotypes were classified into 6 different groups. Bayramlı genotype had the highest plant yield value of 3329.67 kg/da and it was followed by Osmanlı genotype with a plant yield of 3162.11 kg/da. Examining the plant yield of green onion by harvesting period, the lowest yield was identified in the 1st harvest and 2nd and 3rd harvests led to significantly higher yields. In terms of genotype / harvesting period interaction, Bayramlı genotype had the highest plant yield of 3880.67 kg/da in the 2nd harvest and the lowest plant yields were obtained from the genotypes of Delfos, Çorum sarısı, Çorum kırmızısı-1 and Çorum kırmızısı-2 in the 1st harvest.

TABLE 1
Local names and place of supply of the onion genotypes and average diameter and weight of the sets

Name of genotypes	Place of supply	Average diameter (cm)	Average weight (g)
Bayramlı	Bayramlı village, Çarşamba/Samsun	2.8	13.4
Çalköy	Çalköy village, Vezirköprü/Samsun	2.6	9.4
Çorum kırmızısı-1	Bozboğa village, Çorum	2.3	9.6
Çorum kırmızısı-2	Deliler village, Çorum	2.3	8.4
Çorum sarısı	Bayat village, Çorum	2.4	8.4
Karaca-1	Yelpe village, Tokat	3.1	13.6
Yayladalı	Yayladalı village, Tokat	3.1	14.3
Banko	Karailyas village, Polatlı/Ankara	2.6	11.8
Delfos	Bayırlı village, Suluova/Amasya	2.4	8.5
Osmanbey	Deveci village, Suluova/Amasya	2.8	16.2

TABLE 2
Plant yields of onion genotypes by harvesting period (kg/da)

Genotypes	Harvest times			Genotype average
	1st harvest	*2nd harvest*	*3rd harvest*	
Bayramlı	2763.67 e	3880.67 a	3344.67 c	**3329.67 A**
Çalköy	1633.33 i	2308.33 f	2183.33 fg	**2041.67 D**
Çorum kırmızısı-1	1208.33 j	2074.67 fgh	2144.33 fg	**1809.11 E**
Çorum kırmızısı-2	1072.33 j	1747.33 hi	2072.33 fgh	**1630.67 E**
Çorum sarısı	1237.67 j	1864.00 ghi	2061.33 fgh	**1721.00 E**
Karaca-1	1669.33 i	2889.00 de	3158.33 cd	**2572.22 C**
Yayladalı	2032.67 fgh	3308.67 c	3763.67 ab	**3035.00 B**
Banko	1675.00 ı	2361.00 f	2311.00 f	**2115.67 D**
Delfos	1241.67 j	1872.33 ghi	1850.00 ghi	**1654.67 E**
Osmanbey	2114.00 fg	3502.67 bc	3869.67 a	**3162.11 AB**
Harvest average	***1664.80 B***	***2580.87 A***	***2675.87 A***	

$LSD_{genotype}$:203.35***, $LSD_{harvest}$:111.38***, $LSD_{genotype*harvest}$:352.20***

Taherlou [12] identified plant yields of 299 to 1534 kg/da for green onions grown by seed sowing in 6 different periods. The lower temperatures in Ankara and production by seed sowing might have led to development of the plants to a certain degree. Thus, it was expected that our study, conducted by planting set, would have higher yield values. Zambi [13] stated that yield values of green onion could be improved by boron applications (5306.46- 5856.11 kg/da) and the plant yield value of 4727.95 kg/da on 40th day following set planting increased up to 5488.90 kg/da and 6321.02 kg/da on 50th and 60th days respectively. The fact that the researcher planted 92.85% more sets per unit area compared to our study might have boosted yield values. Although average plant yield values were observed to increase as the harvesting period delayed, certain genotypes showed deterioration in certain quality-related characteristics following the 75th day. Zambi [13] also reported a similar observation. Especially increase in the age of plant and rise in competition for feeding and living space due to limited root section may lead to this result. As development rate of the genotypes by harvesting period differed from each other, fluctuations were observed in green onion yields.

Plant height. The plant height values of the onion genotypes by harvesting period are given in the Table 3. As is seen in the Table 3, the genotype and harvesting period brought along statistically significant differences for the plant height values ($p<0.001$). Osmanbey genotype yielded the highest average plant height values by an average height of 64.78 cm. Bayramlı genotype was ranked second with a plant height of 63.98 cm and Karaca-1 genotype followed those aforementioned with a plant height of 62.12 cm. Çalköy genotype yielded the lowest plant height of 55.27 cm. In terms of plant heights by harvesting period, 2nd harvest (64.66 cm) and 3rd harvest (63.33 cm) were included in the first group and 1st harvest was included in the second group statistically. As the harvesting period was delayed, the plant length increased as per natural course of plant development. This increase was maintained until 2nd harvest and a small decrease was observed in the 3rd harvest. We believe that the plant length was lower in the 3rd harvest compared to 2nd harvest as the initially formed leaves aged and dried backwards starting from its edge due to extension in the vegetation period. In terms of genotypes, Osmanbey yielded the highest plant height value of 64.78 cm. Bayramlı genotype was included in the 2nd group with a plant height of 63.9 8cm and Karaca-1 genotype was included in the 3rd group with a plant height of 62.12 cm following the first two genotypes.

These genotypes grew faster thanks to their larger sets and yielded higher plant heights compared to other genotypes. On the other hand, Çalköy and Çorum kırmızısı-2 genotypes showed a comparatively slower development especially until the first harvesting period due to having smaller sets. Accordingly, they yielded shorter green onions. No statistical correlation was found out for the changes in the plant height of onion genotypes by harvesting period in terms of genotype/harvesting interaction. The plant height values of the genotypes varied between 45.47 and 69.73 cm by harvesting period. The changes in the plant height values also affected yield values similarly. Bayoumi *et al*. [14] stated in a study analysing the effects of sulphur fertilizing and Trichoderma spp. biocontrol agent on the yield and quality of onion under the conditions of Egypt that the plant height varied between 55.4 and 79.7 cm. El-Awadi and Abd El Wahed [15], in their study conducted in Egypt on the effects of certain bioregulators on the green onion, stated that the plant height varied between 42.50 and 46.46 cm. Jilani *et al.* [16] stated in their study carried out in Pakistan and analysing the effect of plant density on yield and quality of onion, that the plant height varied between 47.18 and 53.88 cm. Taherlou [12], in his study conducted in Ankara under greenhouse conditions, obtained average plant height values of 29.2 to 49.2 cm for the green onions produced from seeds. Other than the findings of Bayoumi *et al.* [14], other researches yielded plant height values somewhat lower than our

TABLE 3
Plant height values of onion genotypes by harvesting period (cm)

Genotypes	Harvest times			Genotype average
	1st harvest	*2nd harvest*	*3rd harvest*	
Bayramlı	54.90	69.27	67.77	**63.98 AB**
Çalköy	45.47	60.63	59.70	**55.27 G**
Çorum kırmızısı-1	48.40	65.77	63.03	**59.07 DE**
Çorum kırmızısı-2	46.57	62.80	58.43	**55.93 FG**
Çorum sarısı	54.15	64.73	61.40	**60.09 CDE**
Karaca-1	54.63	67.93	63.80	**62.12 ABC**
Yayladalı	56.45	62.53	66.10	**61.69 BCD**
Banko	46.23	60.47	61.30	**56.00 FG**
Delfos	50.20	63.00	62.70	**58.63 EF**
Osmanbey	55.80	69.43	69.10	**64.78 A**
Harvest average	***51.28 B***	***64.66 A***	***63.33 A***	

$LSD_{genotype}$:2.78***, $LSD_{harvest}$:1.53***, $LSD_{genotype*harvest}$: ns.

results. It is possible that plant height values were lower than those in our study as average temperature was lower in Ankara, harvesting period was earlier and green onion was directly produced from sowing seeds. On the other hand, plant height values under the ecological conditions of Pakistan, having a warmer climate compared to ours, were also lower than our results. This might be caused by lower light exposure in our region and thus faster development of our plant. The different plant height values obtained in the study conducted in Egypt indicates that genetic structure is a significant factor for the plant height.

White stalks length. White stalks length values of onion genotypes by harvesting period are given in the Table 4. Statistically significant differences were found out among white stalks length values of the onion genotypes ($p<0.001$, Table 4). The genotypes were classified into four different statistical groups in terms of white stalks length. Yayladalı and Osmanbey genotypes yielded the highest white stalks length values. On the other hand, the lowest white stalks length values were found out for the genotypes of Çalköy, Çorum kırmızısı-2, Çorum sarısı and Delfos. Statistically significant differences were found out among white stalks length values by harvesting periods ($p<0.001$). For the onion genotypes, 3rd harvest period yielded the highest white stalks value with an average white stalks length of 10.04 cm. In terms of genotype / harvesting period interaction, no statistically significant difference were found out among white stalks length values and white stalks length of the genotypes by harvesting period varied between 5.30 and 10.53 cm.

Among the genotypes, Osmanbey and Yayladalı genotypes were revealed to have the longest axes. El-Awadi and Abd El Wahed [15] identified that white stalks length values of the green onion varied between 4.41 and 5.97 cm depending on the harvesting period and treatments. Our study yielded white stalks length values of 5.30 to 10.53 cm. As is the case for plant heights, white stalks length values of the plants were probably measured to be higher than the aforesaid study due to low light exposure in our region. On the other hand, it was also observed that white stalks length was correlated with set weight to a great extent. Ansari *et al.* [17] stated that there was a correlation between the size of set and plant height and bigger sets brought along higher plant height. El-Awadi and Abd El Wahed [15] suggested that white stalks length varied by harvesting period and delayed harvesting led to an increase in white stalks length. Zambi [13] stated that the white stalks length increased (5.89 to 7.01 cm) in green onions in late harvest, and similarly, the white stalks length increased with the increase in set size. It is a natural consequence that white stalks length of the plants increase as the vegetative development continues under appropriate ecological conditions. Considering white stalks length of the genotypes by harvesting periods, it was observed that white stalks length of the genotypes increased as the harvesting period delayed. White stalks length directly affects the yield of the plant. Having a higher white stalks length is a desirable specialty for green onion in terms of quality. In our study, plant development rate decelerated as the harvesting delayed. Decrease in change of white stalks length observed as we approached to tuberization period of the genotypes was another interesting finding of our study.

Pyruvate content. The change in pyruvate content of onion genotypes by harvesting period is given in the Table 5. It was observed that there was statistically meaningful differences among pyruvate contents of onion genotypes by the harvesting period ($p<0.001$). Yayladalı genotype yielded the highest pyruvate content of 0.30 µm/ml and it was followed by Çorum kırmızısı-2 genotype with a pyruvate content of 0.28 µm/ml. The lowest pyruvate content of 0.17 µm/ml was identified for Bayramlı genotype.

Examining pyruvate content of the onion genotypes by the harvesting period, 3rd harvest yielded the highest pyruvate content of 0.31 µm/ml. Considering the genotype/harvest interaction, Yayladalı (0.48

µm/ml) and Çorum kırmızısı-2 (0.44 µm/ml) genotypes were found out to have the highest pyruvate content in the 3rd harvest. The lowest pyruvate content of 0.09 µm/ml was found out in the 1st harvest for Bayramlı genotype. Pyruvate contents of the onion genotypes were identified to be 0.17 to 0.30 µm/ml. It was observed that the pyruvate content increased as the harvesting period was delayed. Average pyruvate content of green onions was identified to be 159% higher in the 3rd harvesting period compared to the 1st one. Pyruvate content is the indicator of bitterness of onions and used as an index showing the storage performance of bulb onion. Moreover, the onions with higher bitterness are preferred for dehydration procedures [18-19]. Although pyruvic acid content depends on genetic structure to a great degree, humidity content of the soil and climate conditions also affect it [20]. Short day onions have lower pyruvate content compared to long day ones [21]. However, sulphur and pyruvate content of the onion was not found out to be directly related [22-23]. It was understood that the genotypes with darker skins were bitter to those with lighter skins [24]. It is preferred for green onions to have lower bitterness in terms of quality. Poornima [25], in his study carried out in India to research effect of different sulphur and potassium dosages on yield and quality of onion and pepper grown together, stated that pyruvic acid values of bulb onion varied between 0.43 and 3.33 µm/g. It was observed that pyruvic acid content of bulb onion increased as the applied sulphur and potassium dosages increased. This study might have yielded higher pyruvate content values as only bulb onion was used as sample for pyruvate analysis, sulphur and other fertilizing practises were preferred et cetera. In the study on different potassium and sulphur rates by Díaz-Pérez *et al.* [26], pyruvate content did not differ greatly and was measured to be 2.42-3.26 mM. Bacon *et al.* [27] identified different pyruvate contents by onion genotypes (4.56 to 7.96 $\mu m.g^{-1}$), middle and lower/upper section of tuber (4.95 to 7.93 $\mu m.g^{-1}$) and internal and external sections (4.43 to 5.46 $\mu m.g^{-1}$). Simon [28] concluded a pyruvate content of 4.0-18.0 $\mu m.g^{-1}$ for the onions put under hybrid breeding programme and stated that pyruvate content varied up to 130% by years. These researches yielded quite higher results compared to our as they were performed on bulb onions.

TABLE 4
White stalks length values of onion genotypes by harvesting period (cm)

Genotypes	Harvest times			Genotype average
	1st harvest	*2nd harvest*	*3rd harvest*	
Bayramlı	6.70	9.70	10.23	**8.88 AB**
Çalköy	5.30	9.03	10.03	**8.12 C**
Çorum kırmızısı-1	5.70	9.73	10.27	**8.57 BC**
Çorum kırmızısı-2	5.77	9.13	9.40	**8.10 C**
Çorum sarısı	6.15	8.87	9.67	**8.23 C**
Karaca-1	6.70	9.80	10.20	**8.90 AB**
Yayladalı	7.45	9.77	10.37	**9.20 A**
Banko	6.50	8.77	9.90	**8.39 BC**
Delfos	6.43	8.83	9.80	**8.36 C**
Osmanbey	7.15	9.63	10.53	**9.11 A**
Harvest average	***6.39 C***	***9.33 B***	***10.04 A***	

$LSD_{genotype}$:0.52***, $LSD_{harvest}$:0.28***, $LSD_{genotype*harvest}$:ns.

TABLE 5
Pyruvate content of onion genotypes by harvesting period (µm/ml)

Genotypes	Harvest times			Genotype average
	1st harvest	*2nd harvest*	*3rd harvest*	
Bayramlı	0.09 j	0.24 efg	0.17 ghi	**0.17 E**
Çalköy	0.10 ij	0.26 c-f	0.29 b-f	**0.21 CD**
Çorum kırmızısı-1	0.12 ij	0.28 b-f	0.33 b	**0.24 BC**
Çorum kırmızısı-2	0.12 ij	0.29 b-f	0.44 a	**0.28 AB**
Çorum sarısı	0.16 hij	0.22 fgh	0.29 b-e	**0.22 CD**
Karaca-1	0.14 ij	0.24 def	0.32 bc	**0.23 CD**
Yayladalı	0.10 ij	0.31 bcd	0.48 a	**0.30 A**
Banko	0.13 ij	0.26 b-f	0.23 efg	**0.21 CD**
Delfos	0.14 ij	0.24 def	0.27 b-f	**0.22 CD**
Osmanbey	0.10 ij	0.23 efg	0.27 b-f	**0.20 DE**
Harvest average	***0.12 C***	***0.26 B***	***0.31 A***	

$LSD_{genotype}$:0.04***, $LSD_{harvest}$:0.02***, $LSD_{genotype*harvest}$:0.07***

TABLE 6
SSC contents of onion genotypes by harvesting period (g/100 g)

Genotypes	Harvest times			Genotype average
	1st harvest	*2nd harvest*	*3rd harvest*	
Bayramlı	2.97 k	4.77 fg	6.20 abc	**4.64 A**
Çalköy	2.83 kl	5.00 ef	6.37 ab	**4.73 A**
Çorum kırmızısı-1	2.77 kl	4.23 g-j	6.43 ab	**4.48 AB**
Çorum kırmızısı-2	2.37 l	5.10 ef	5.93 bcd	**4.47 AB**
Çorum sarısı	2.65 kl	4.23 g-j	6.10 abc	**4.33 BC**
Karaca-1	2.83 kl	4.67 fgh	6.50 a	**4.67 A**
Yayladalı	2.95 k	4.10 ıj	6.27 ab	**4.44 AB**
Banko	2.43 kl	3.77 j	5.50 de	**3.90 D**
Delfos	2.97 k	4.43 ghı	6.20 abc	**4.53 AB**
Osmanbey	2.57 kl	4.13 hıj	5.67 cd	**4.12 CD**
Harvest average	***2.73 C***	***4.44 B***	***6.12 A***	

$LSD_{genotype}$:0.31***, $LSD_{harvest}$:0.17***, $LSD_{genotype*harvest}$:0.53*

Soluble Solids Content (SSC). SSC contents of the onion genotypes by the harvesting period are given in the Table 6. It was observed that there were statistically significant differences among SSC values of the onion genotypes by the harvesting period ($p<0.001$). In terms of genotypes, Çalköy (4.73 g/100 g) genotype, Karaca-1 (4.67 g/100 g) genotype and Bayramlı (4.64 g/100 g) genotype yielded the highest SSC values and they were followed by Delfos, Çorum kırmızısı-1, Çorum kırmızısı-2 and Yayladalı genotypes included in the second group. Banko genotype yielded the lowest SSC of 3.90 g/100 g. Statistically significant differences were identified in SSC values by harvesting periods ($p<0.001$). As the harvesting period was delayed, SSC value of the onion genotypes increased. The highest average SSC value (6.12 g/100 g) was identified in the 3rd harvest. Considering in terms of genotype/harvest interaction, statistically significant differences were observed among SSC values ($p<0.05$). The highest SSC value of 6.50 g/100 g was measured for Karaca-1 genotype in the 3rd harvesting period. SSC value is considered as an indicator of quality for onions [28]. In our study, a difference of 19.74% was measured between the highest and lowest SSC values. Simon [28] stated that there was not a significant change (12.85%) in SSC value of onion lines over the years and that the SSC amounts of the lines varied between 7.0-16.7 g/100 g. The onions treated with potassium and sulphur of varying dosages by Díaz-Pérez *et al*. [26] yielded SSC values of 7.4-7.9%. Lee [29] measured the SSC value of onions, treated with organic fertilizers, to be 6.6-8.7%. Fatideh and Asil [30] stated that the SSC value was measured to be 11.85-13.59 g/100g varying by different irrigation and nitrogen levels. Our SSC values were lower probably because we studied on green onion. The fact that our SSC value increases by harvesting period supports this suggestion.

CONCLUSIONS

There is not sufficient data on modelling studies examining yield and quality of green onions by genotype and harvest times. Products of different quality are grown in temperate zones depending on the climate and growing conditions. In line with the demands of the market, a quality and highly effective production system compatible with consumption methods of green onion is targeted. In our study, the green onion production performances in different harvesting periods of the onion genotypes selected from different ecological regions were measured. As development rate of the genotypes were also different periodically, we obtained varying yield and quality characteristics. Selecting the appropriate genotype and harvesting period considering portioning sizes in instant salad mixes, endurance following the harvesting and bitterness is significant for economic and sustainable agricultural production. Although total output is also significant, selecting the harvesting period yielding the highest quality may provide higher revenue. Regarding sustainable production quality and higher yield; it is recommended to harvest the Bayramlı and Karaca-1 genotypes on the 60th day, harvest the Osmanbey and Yayladalı as late as possible and harvest other genotypes in between 45th and 75th days. It is significant to carry our studies on storage examining both genotypes and harvesting periods in order to maintain the quality of green onion in line with their post-harvesting areas of use. By this study, certain vegetative specialties and chemical contents of the high quality genotypes compatible with the demands of the market were identified for green onion production.

ACKNOWLEDGEMENTS

The authors thank the Ordu University Scientific Research Projects Coordination Unit for their support within the scope of the project numbered TF-

1234.

REFERENCES

[1] The Food and Agriculture Organization (FAO), (2019) Food and agriculture data. http://www.fao.org/faostat/en/#data/QC. (Date of access: 23.05.2019).

[2] Ashwini, M., Sathishkumar, R. (2014) Onion (Allium cepa) – Ethnomedicinal and therapeutic properties. In: Handbook of Medicinal Plants and Their Bioactive Compounds. (Ed. Nidhi Gupta) Research Signpost, Kerala, India. 27-34.

[3] Upadhyay, R.K. (2016) Nutraceutical, pharmaceutical and therapeutic uses of *Allium cepa*: A review. International Journal of Green Pharmacy. 10(1), 46-64.

[4] Augusti, K.T. (1990) Therapeutic and medicinal values of onions and garlic. In: Onions and Allied Crops. Vol. III. Biochemistry, Food Science and Minor Crops. (Eds. Brewster, J.L., Rabinowitch, H.D.) CRC Press, Boca Raton, Fla. 93-108.

[5] Wang, H., Li, J., Wang, Z., Zhang, X., Ni, Y. (2007) Modified method for rapid quantitation of S-alk(en)yl-L-cysteine sulfoxide in yellow onions (*Allium cepa* L.). J. Agric. Food Chem. 55, 5429-5435.

[6] Pellegrini, N., Miglio, C., Del Rio, D., Salvatore, S., Serafini, M., Brighenti, F. (2009) Effect of domestic cooking methods on the total antioxidant capacity of vegetables. Int. J. Food Sci. Nutr. 60(2), 12-22.

[7] Jones, M.G., Hughes, J., Tregova, A., Milne, J., Tomsett, A.B., Collin, H.A. (2004) Biosynthesis of the flavour precursors of onion and garlic. Journal of Experimental Botany. 55(404), 1903-1918.

[8] Augusti, K.T. (1996) Therapeutic values of onion (*Allium cepa* L.) and garlic (*Allium sativum* L.). Indian J. Exp. Biol. 34(7), 634-640.

[9] Hodges, L. (2004). Growing scallions (green onions) for market gardeners. Historical materials from University of Nebraska-Lincoln Extension. NebFacts04-607.

[10] Vural, H., Eşiyok, D., Duman, I. (2000) Culture vegetables-growing vegetables. Ege University Printing Office, Bornova, Izmir, Turkey, p. 31-48.

[11] Wall, M.M., Corgan, J.N. (1992) Relationship between pyruvate analysis and flavor perception for onion pungency determination. Hortscience. 27(9), 1029-1030.

[12] Taherlou, A. (2011) Salad vegetables growing for preparing mixed salad composition. Ankara University, Graduate School of Natural and Applied Science, Department of Horticulture, Ankara, Turkey.

[13] Zambi, O. (2015) Effect of set sizes and boron application on yield and quality of green onion (*Allium cepa* L.). Ordu University, Graduate School of Natural and Applied Science, Department of Horticulture, Ordu, Turkey.

[14] Bayoumi, Y., Taha, N., Shalaby, T., Alshaal, T., El-Ramady, H. (2019) Sulfur promotes biocontrol of purple blotch disease via Trichoderma spp. and enhances the growth, yield and quality of onion. Applied Soil Ecology. 134, 15-24.

[15] El-Awadi, M.E., Abd El Wahed, M.S.A. (2012) Improvement the growth and quality of green onion (*Allium cepa* L.) plants by some bioregulators in the new reclaimed area at Nobaria region. Egypt. New York Sci. J. 5(9), 114-120.

[16] Jilani, M.S., Ahmed, P., Waseem, K., Kiran, M. (2010) Effect of plant spacing on growth and yield of two varities of onion (*Allium cepa* L.) under the agro-climatic condition of DI Khan. Pakistan Journal of Science. 62(1), 37-41.

[17] Ansari, N.A., da Silva, J.A.T., Yazdani, N. (2009) Effect of onion set size and cultivar on production of green bunch onion (*Allium cepa*). Middle Eastern Russian J. Pl. Sci. Biotech. 3, 5-9.

[18] Jones, H.A., Mann, L.K. (1963) Onions and their allies. World Crops Books, Interscience publishers, Inc. New York. 286.

[19] Bartholomew, B.L. (1986) Onion growing in Queensland. Queensland Agricultural Journal. November-December. 315-325.

[20] Shekib, L.A., Shehata, A.A., El-Tabey, A. (1986) The effect of fresh Egyptian onions on some of its quality aspects. Alexandria J. Agr. Res. 31(2), 167-174.

[21] Randle, W.M., Bussard, M.L. (1993) Streamlining onion pungency analyses. HortScience. 28(1), 60.

[22] Randle, W.M., Bussard, M.L., Warnock, D.F. (1993) Ontogeny and sulfur fertility affect leaf sulfur in short-day onions. Journal of the American Society for Horticultural Science. 118(6), 762-765.

[23] Randle, W.M., Bussard, M.L. (1993) Pungency and sugars of short-day onions as affected by sulfur nutrition. Journal of the American Society for Horticultural Science. 118(6), 766-770.

[24] Gallina, P.M., Cabassi, G., Maggioni, A., Natalini, A., Ferrante, A. (2012) Changes in the pyruvic acid content correlates with phenotype traits in onion clones. Australian Journal of Crop Science. 6(1), 36-40.

[25] Poornima, K.S. (2007) Effect of potassium and sulphur on yield and quality of onion and chilli intercrops in a vertisol. Department of Soil Science and Agricultural Chemistry College of Agriculture, Dharwad University of Agricultura Sciences, Dharwad, India.

[26] Díaz-Pérez, J.C., Bautista, J., Bateman, A., Gunawati, G., Riner, C. (2016) Sweet onion (*Allium cepa*) plant growth and bulb yield and quality as affected by potassium and sulfur fertilization rates. HortScience. 51(12), 1592-1595.
[27] Bacon, J.R., Moates, G.K., Ng, A., Rhodes, M.J., Smith, A.C., Waldron, K.W. (1999) Quantitative analysis of flavour precursors and pyruvate levels in different tissues and cultivars of onion (*Allium cepa*). Food Chemistry. 64(2), 257-261.
[28] Simon, P.W. (1995) Genetic analysis of pungency and soluble solids in long-storage onions. Euphytica. 82, 1-8.
[29] Lee, J. (2010) Effect of application methods of organic fertilizer on growth, soil chemical properties and microbial densities in organic bulb onion production. Scientia Horticulturae. 124(3), 299-305.
[30] Fatideh, M.M., Asil, M.H. (2012) Onion yield, quality and storability as affected with different soil moisture and nitrogen regimes. South Western Journal of Horticulture Biology and Environment. 3(2), 145-165.

Received: **08.12.2020**
Accepted: **09.01.2022**

CORRESPONDING AUTHOR

Atnan Ugur
Department of Horticulture,
Faculty of Agriculture,
Ordu University,
52200 Ordu – Turkey

e-mail: atnanugur@gmail.com

© by PSP Volume 31– No. 05/2022 pages 4692-4698 Fresenius Environmental Bulletin

INHIBITORY EFFECT OF CILOSTAZOL ON OSTEOCLAST DIFFERENTIATION BY IN-VITRO AND IN-SILICO STUDIES

Syed Rizwan Abbas[1,*], Rizwan Taj Khan[2], Munazza Nazir[2], Asia Bibi[3], Nosheen Azhar[3], Syed Mubashir Sabir[4], Saima Shafique[5], Attiya Batool[6], Muhammad Ali Safder[1]

[1]Department of Biological Sciences; Karakoram International University, Gilgit, Pakistan
[2]Department of Botany; University of Azad Jammu and Kashmir, Muzaffarabad, Pakistan
[3]Department of Botany; Women University Bagh, Bagh, Pakistan
[4]Department of Chemistry; University of Poonch, Rawalakot, Pakistan
[5]Department of Plant Breeding and Molecular Genetics; University of Poonch, Rawalakot, Pakistan
[6]Department of Biotechnology; Virtual University, Pakistan

ABSTRACT

Cilostazol has been reported to reduce the osteoclast differentiation induced in (ApoE−/−) mice model via decreasing the ROS level. To prove this hypothesis 12 wks. old WT and ApoE−/− mice were performed Sham and ovariectomy (OVX) surgery and feed WT mice with normal diet (ND) and ApoE−/−mice model with Atherogenic diet (AD) for 8 Weeks. ApoE−/− mice were injected with I. P injections of Cilostazol (0.5mg/kg) for 8wk. After 8 Wks. Osteoclast differentiation, CROS and bone resorption were analyzed. Cilostazol reduced the osteoclast differentiation and CROS in ApoE−/− mice model with Atherogenic diet (AD). Cilostazol also reduced the bone loss in ApoE−/− mice but the results are not significant as compared to control. Our data highlight the potential role of Cilostazol for attenuating the osteoclast differentiation and bone resorption in ApoE−/− mice model via decreasing the ROS level. The Molecular docking studies between the Cilostazol and RANKL receptors proved that Cilostazol binds tightly to the receptors, showed the highest binding affinities of −7.3, −7.5, −7.7, −8.0, −8.3, and −10.0 kcal/mol. Cilostazol shall be excellent inhibitors against RANKL receptors.

KEYWORDS:
Cilostazol, osteoclast, ovariectomy, RANKL, ROS, Protein Docking

INTRODUCTION

Bone is a very rigid structure within the body that plays a very important role in protection and support. One of the unique processes in bone is remodelling by which old bone is replaced by the new bone [1]. There are two main cells in the bone which perform this process of remodelling, one is the osteoclast cell which resorbs the bone and another one is the osteoblast which forms the new bone [2]. Osteoclast cell attracted to the site of old bone and resorb it while at the same place osteoblast cells come and form the new bone. Bone remodelling is a physiological as well as a pathological phenomenon. If the osteoclast number has increased a condition developed which is called Post-menopausal osteoporosis in female while in male this condition is called Rheumatoid arthritis [3].

RANKL and MCSF are two very crucial cytokines that play a critical role in osteoclast differentiation. MCSF is a factor for survival and Proliferation while RANKL is a factor for the regulation of osteoclast formation [4, 5].

Receptor ligand interaction is very important in osteoclast differentiation and maturations, When RANKL binds to its receptor RANK it activates different signalling cascades in macrophages cells like NF-κB,c-Jun N-terminal kinase (JNK), p38, and extracellular signal-regulated, kinase (ERK) [6]. The crucial factor for osteoclast differentiation is (NFATc1) and that it is upregulated by RANKL through activation of the NF-κB and JNK/AP-1 signalling pathways [7].

Cilostazol, a vasodilation agent. It is used to treat arterial abstractions. It has an anti-inflammatory effect as well as good anti-atherogenic properties [8].

In the present study, we hypothesized the Cilostazol alleviate the ovariectomy-induced bone loss in (ApoE−/−) mice model treated with atherogenic diet by inhibiting osteoclastogenesis through the inhibition of ROS by using Ex. VIVO system.

MATERIALS AND METHODS

Detection of Intracellular Reactive Oxygen Species (ROS). By using the fluorescent probe 2',7'-dichlorofluorescein diacetate (H2DCFDA) (Molecular Probes), Intracellular ROS were identified. BMMs were treated with H2DCFDA and incubated at 37°C for 30 min. FACSCalibur flow cytometer used to measure the Reactive oxygen species.

Statistical Analysis. Values are expressed as means ± SEM. Pairs of groups were compared by Student's t-test and multiple groups by one-way ANOVA followed by Bonferroni posttests. A P value of less than 0.05 was considered statistically significant.

OC Differentiations. BMM were isolated from WT and (ApoE−/−) mice model. BMM cells were treated with cytokines like M.CSF and RANKL for Proliferations and osteoclast Differentiations. After 3 days when we get mature osteoclast. The osteoclast cells were stain with TRAP stain and count the total number of osteoclast.

Data and Databases. Structure of resveratrol obtained from PubMed in 3D structure and saved in SDF file. The X-ray crystallographic structure of the protein was obtained from the Protein Data Bank (PDB).

Docking Tools. PyRx free software was used for Ligand to Protein docking. For result visualization, Discovery studio was used.

Protein preparation. The crystal structures of RANKL Proteins were obtained from the protein data bank. The active sites of the proteins were identified using reference ligands already in the target site and proteins were prepared by using the receptor preparing tool PyRx.

Animals and Study Design. 12Wks old and (ApoE−/−) mice model were performed with OVX Surgery and treated with Atherogenic diet for 8 wks along with I.P injections of Cilostazol0.5mg/kg daily. Femur bones were analyzed for X-RAY analysis to check the resorption level. Bodyweight and weight gain are analyzed regularly.

RESULTS AND DISCUSSIONS

Cilostazol reduced weight gain and body weight after ovariectomy (OVX)-surgery in ApoE−/− mice model. 12wk(ApoE−/−) mice model with OVX surgery treated with Atherogenic diet along with I.P. Injections of Cilostazol (0.5mg/kg) for 8wk.with the treatment of Cilostazol reduced body weight and weight gain in ApoE−/− mice model (Figure 1).

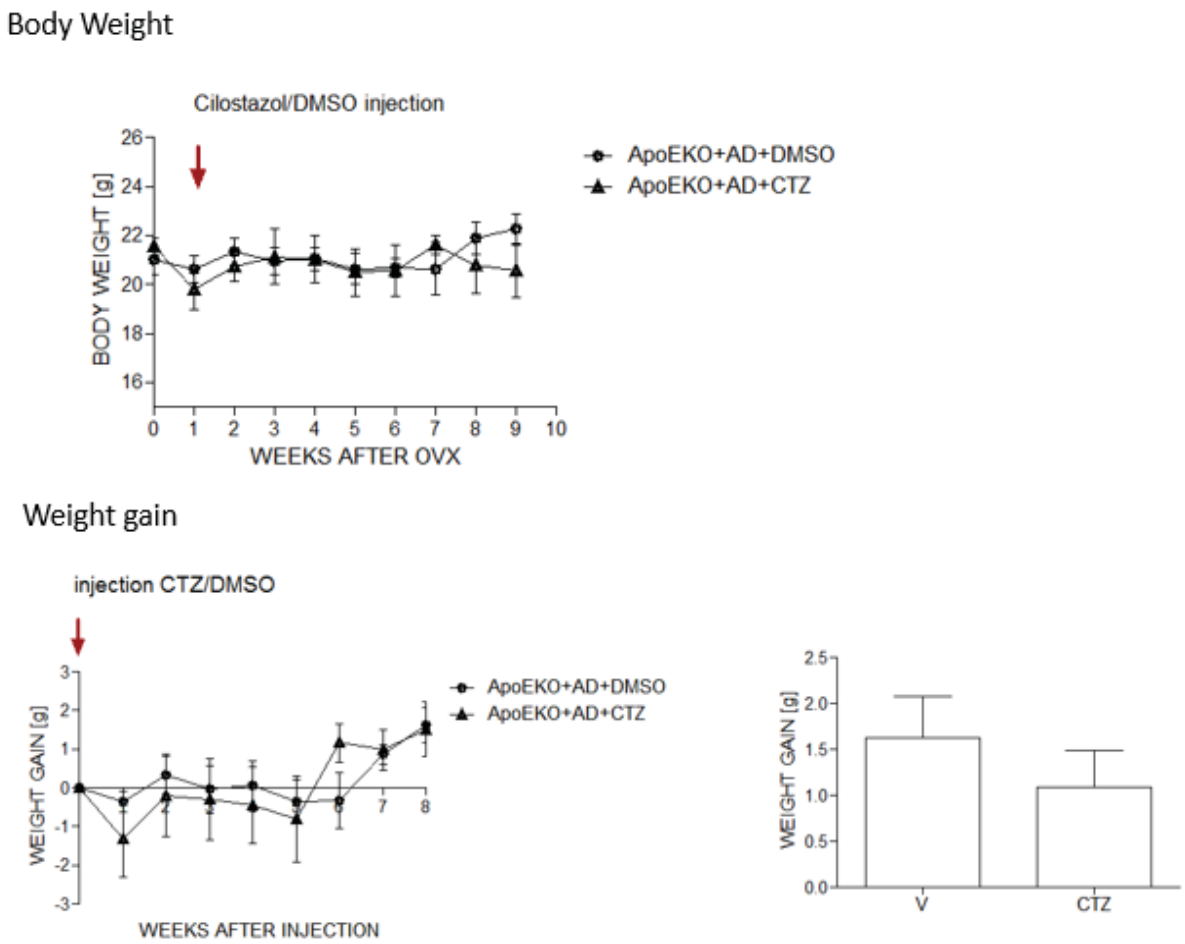

FIGURE 1
Body weight, Weight gain analysis of (ApoE−/−) mice model with OVX surgry treated with Atherogenic diet along with I.P. Injections of Cilostazol (0.5mg/kg) for 8wk.

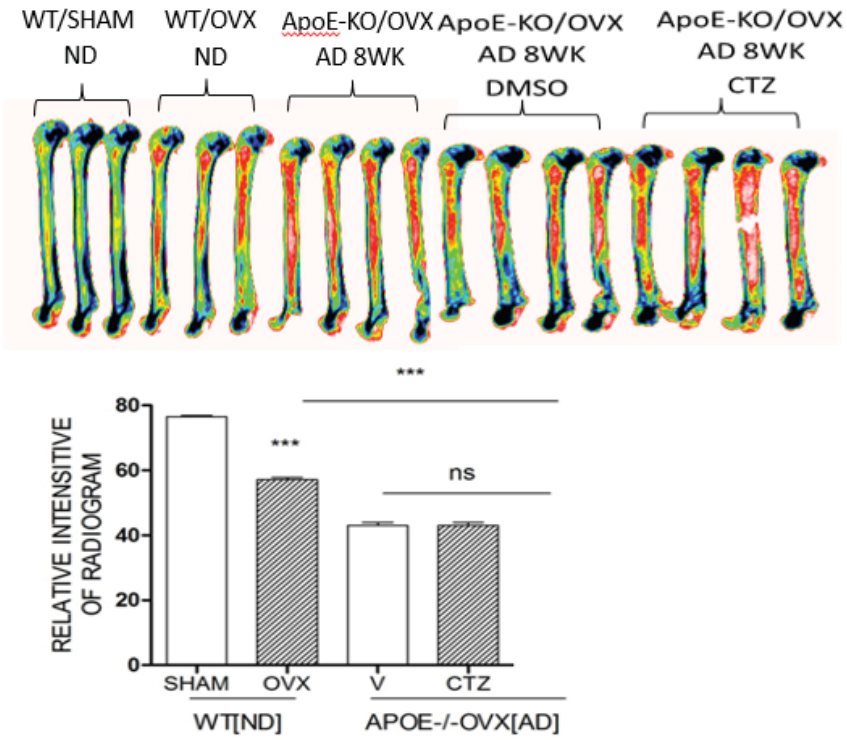

FIGURE 2

(ApoE−/−) mice model performed with OVX surgery were treated with Cilostazol.

Although the difference is not significant as compared to control but a slight decreased in the Relative intensity of Radiogram with the treatment of Cilostazol.

OC formation/BMM 3D

2014-5-16SET				
	SHAM	OVX	V	CTZ
1	194	216	351	251
2	123	270	331	281
3	161	294	342	288
4	124	280	254	236
AVERAGE	151	265	320	264
	0.57		1.21	0.83

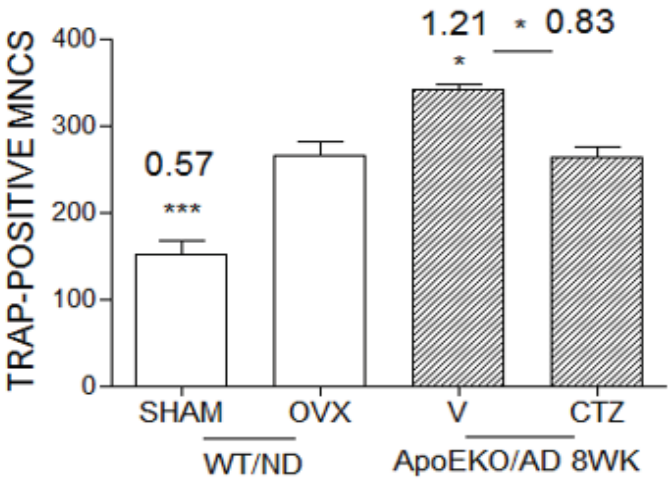

FIGURE 3

Cilostazol reduced the osteoclast differentiation in (ApoE−/−) mice model.

Cilostazol reduced ovariectomy (OVX)-induced bone loss in ApoE−/− mice model. 12 wk(ApoE−/−) mice model performed with OVX surgery were treated with Cilostazol I.P. injections (0.5mg/kg) along with Atherogenic Diet for 8 wk. Although the difference is not significant as compared to control a slight decrease in the relative intensity of the Radiogram with the treatment of Cilostazol (Figure 2).

Cilostazol reduced the osteoclast differentiation in (ApoE−/−) mice model. 12wk (ApoE−/−) mice model with OVX surgery treated with Atherogenic diet along with I.P. Injections of Cilostazol (0.5mg/kg) for 8wk.BMM were isolated from WT mice with Sham and OVX surgery while BMM isolated from (ApoE−/−) mice model treated with DMSO and Cilostazol treated with M.CSF and RANKL to get mature osteoclasts. The mature osteoclast was stained with TRAP staining to count the osteoclast having nuclear NO more than3. The results indicate the Cilostazol reduced osteoclast number in (ApoE−/−) mice model (Figure 3).

In this study, we have tried to illustrate that Cilostazol reduced the osteoclast number and to some extent decreased the bone resorption in Apoeko mice models performed with OVX surgery by inhibiting the ROS level which suggest the beneficial role of Cilostazol in the cure of pathological disorders like post-menopausal osteoporosis and Rheumatoid arthritis. Osteocalcin has a beneficial role in combating vascular dysfunctions in Atherosclerosis. Cilostazol attenuated Ovariectomy induced bone loss by inhibiting osteoclastogenesis. We have provided evidence that HFD-induced bone loss in adult ApoE-KO mice is the result of compromised osteoblast supply and bone formation. Ezetimibe potently reduces atherosclerosis and vascular Inflammation.

Protein Docking Results. After docking scores of cilostazol with receptors best efficacy is given in Table 1.

TABLE 1
Protein docking Scores of receptors with Cilostazol

	1JTZ	1S55	3ME2	3QBQ	4E4D	4GIQ	5BNQ	1IQA
Cilostazol	-8.3	-10	-7.6	-7.9	-7.3	-7.7	-7.5	-8.0

M signal

2014-5-21SET				
M	SHAM	OVX	OVX/V	OVX/CTZ
1	23.2	45.6	64.8	35.5
2	23.2	39.5	71.6	40.6
3	26	34.8	71.7	41.3
AVERAGE	24.1	40.0	69.4	39.1
	0.60		1.74	0.56

M+R signal

M+R	SHAM	OVX	OVX/V	OVX/CTZ
1	44.2	54.4	77.5	53.3
2	43	56	84.1	
3	42.9	59.4	82.2	54.7
AVERAGE	43.4	56.6	81.3	54.0
	0.77		1.44	0.66

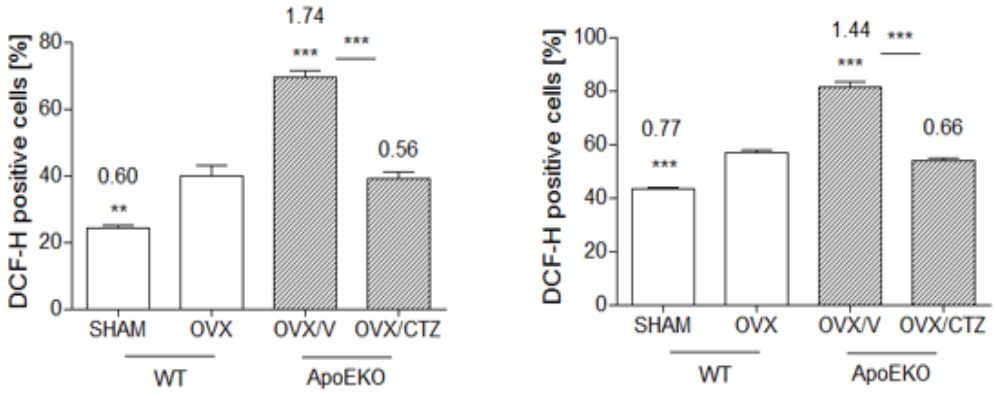

FIGURE 4
To find out the involvement of M or M+R signalling Apoeko Mice models were treated either with M or M+R and the total number of DCF Positive cells were counted

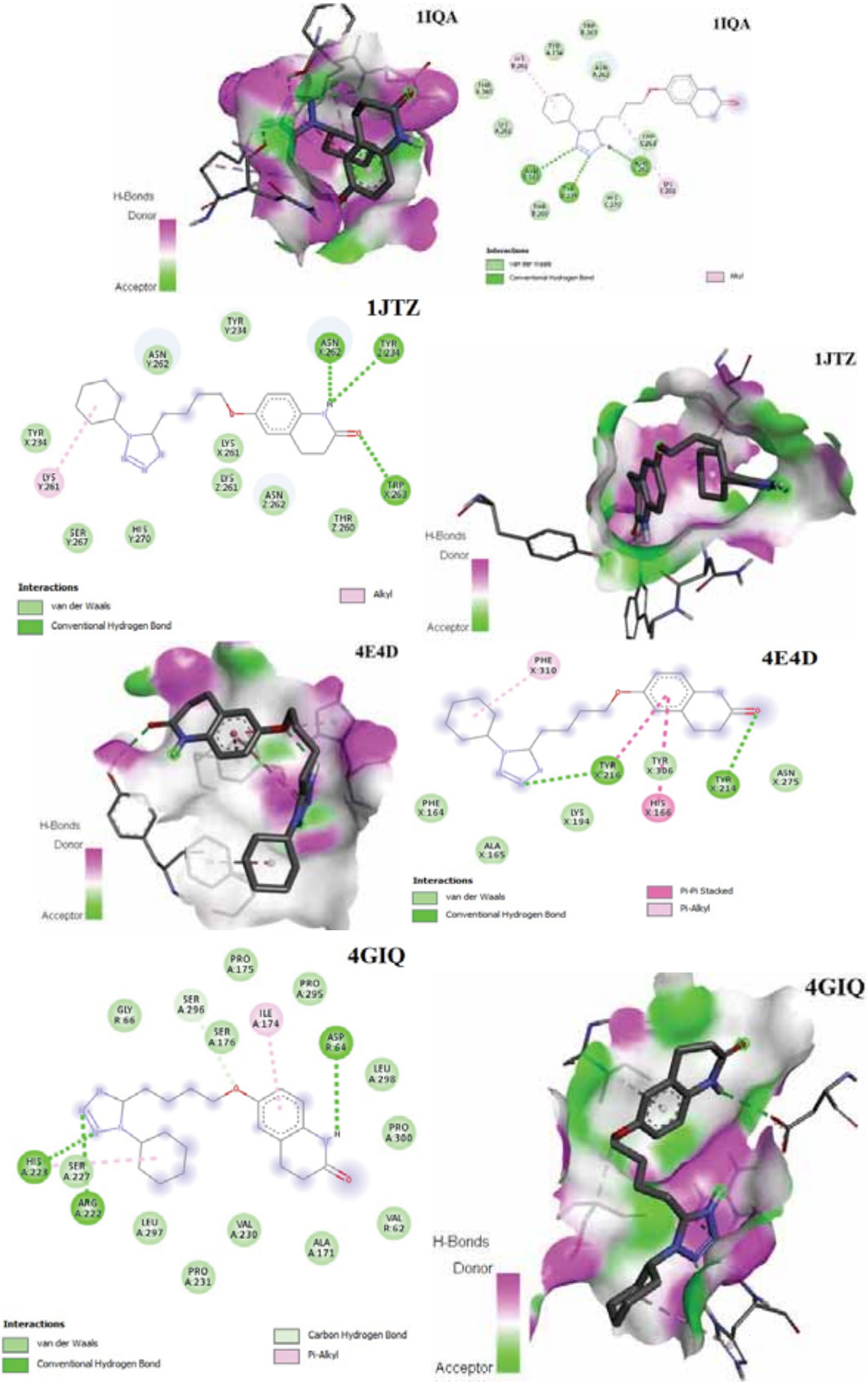
1IQA
1IQA
H-Bonds
Donor
Acceptor
1JTZ
1JTZ
TYR Y:234
ASN Y:262
TYR X:234
ASN X:262
TYR X:294
LYS X:261
LYS Y:261
LYS Z:261
TRP X:263
ASN Z:262
THR Z:260
SER Y:267
HIS Y:270
Interactions
van der Waals
Conventional Hydrogen Bond
Alkyl
H-Bonds
Donor
Acceptor
4E4D
4E4D
PHE X:310
TYR X:216
TYR X:306
TYR X:214
ASN X:275
PHE X:164
LYS X:194
HIS X:166
ALA X:165
H-Bonds
Donor
Acceptor
Interactions
van der Waals
Conventional Hydrogen Bond
Pi-Pi Stacked
Pi-Alkyl
4GIQ
4GIQ
PRO A:175
PRO A:295
SER A:296
GLY R:66
ILE A:174
SER A:176
ASP R:64
LEU A:298
PRO A:300
HIS A:228
SER A:227
ARG A:222
LEU A:297
VAL A:230
ALA A:171
VAL R:62
PRO A:231
H-Bonds
Donor
Acceptor
Interactions
van der Waals
Conventional Hydrogen Bond
Carbon Hydrogen Bond
Pi-Alkyl

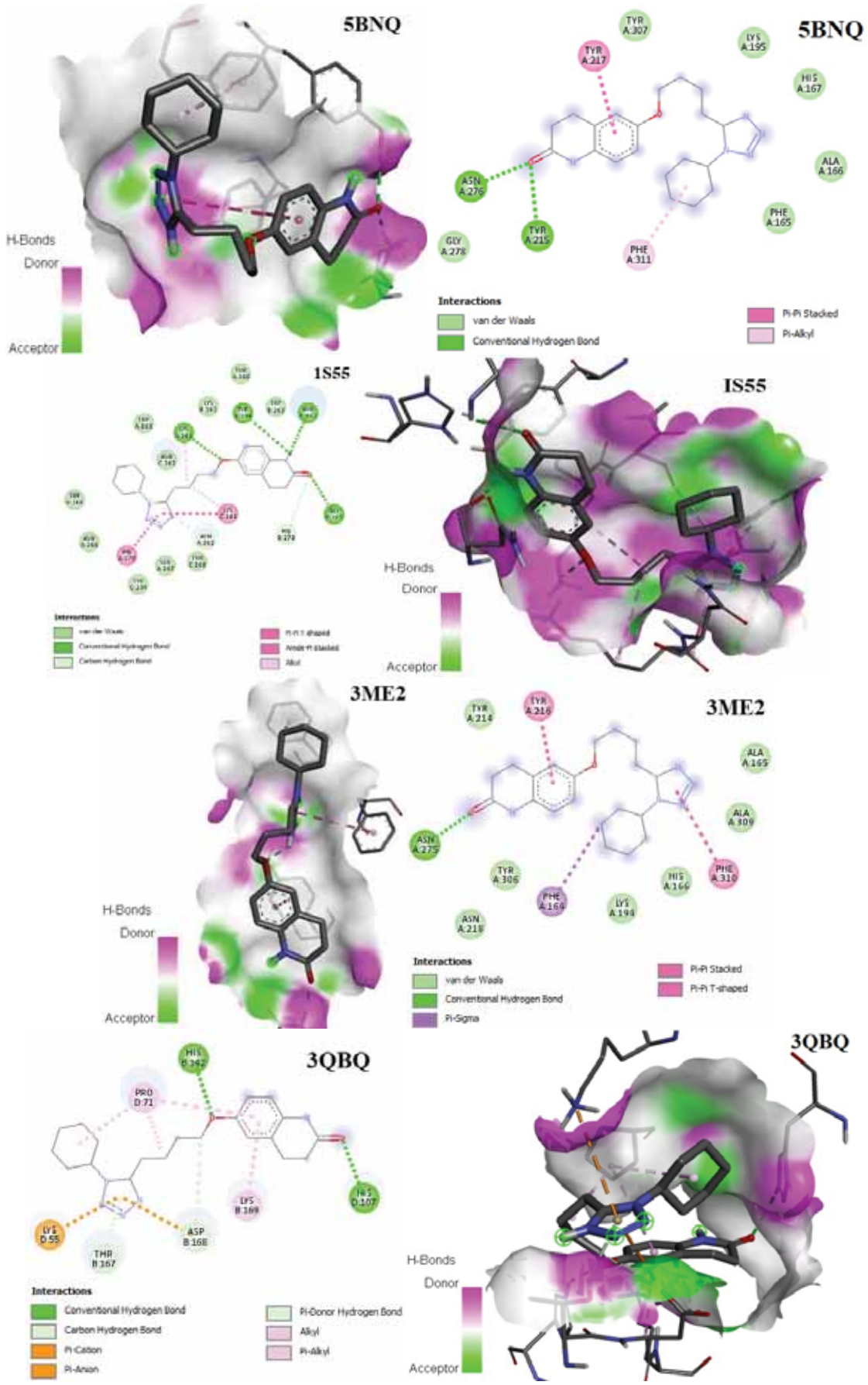

FIGURE 5
Molecular docking interaction in some complexes.

The Molecular docking studies between the Cilostazol and RANKL receptors proved that Cilostazol binds tightly to the receptors, showed the highest binding affinities of −7.3, −7.5, −7.7, −8.0, −8.3, and −10.0 kcal/mol. Cilostazol shall be excellent inhibitors against RANKL receptors Figure 5.

REFERENCES

[1] Weiner, S. and H.D. Wagner, H.D. (1998) The material bone: structure-mechanical function relations. Annual Review of Materials Science. 28(1), 271-298.

[2] Hadjidakis, D.J. and Androulakis, I.I. (2006) Bone remodeling. Annals of the New York Academy of Sciences. 1092(1), 385-396.

[3] Henriksen, K., Karsdal, M.A. and Martin, T.J. (2014) Osteoclast-derived coupling factors in bone remodeling. Calcified Tissue International. 94(1), 88-97.

[4] Tatsuo S., Naoyuki T., Nobuyuki U., Eijiro J., Matthew T. and T. J. Martin. (1999) Modulation of osteoclast differentiation and function by the new members of the tumor necrosis factor receptor and ligand families. Endocrine Reviews. 20(3), 345-357.

[5] Takayanagi H., Kim S., Takako K., Hiroshi N., Masashi I., Hiroki Y., Akio S., Miho I., Taeko Y., ., Erwin F. and Tadatsugu T. (2002) Induction and activation of the transcription factor NFATc1 (NFAT2) integrate RANKL signaling in terminal differentiation of osteoclasts. Developmental Cell. 3(6), 889-901.

[6] Boyle, W.J., Simonet, W.S. and Lacey, D.L. (2003) Osteoclast differentiation and activation. Nature. 423(6937), 337.

[7] Ogasawara, T., Katagiri, M., Yamamoto, A., Hoshi, K., Takato, T., Nakamura, K., Tanaka, S., Okayama, H. and Kawaguchi H. (2004) Osteoclast differentiation by RANKL requires NF-κB-mediated downregulation of cyclin-dependent kinase 6 (Cdk6). Journal of Bone and Mineral Research. 19(7), 1128-1136.

[8] Meru, A.V., Mittra, S., Thyagarajan, B. and Chugh A. (2006) Intermittent claudication: an overview. Atherosclerosis. 187(2), 221-237.

Received: **15.12.2020**
Accepted: **25.04.2021**

CORRESPONDING AUTHOR

Syed Rizwan Abbas
Department of Biological Sciences,
Karakoram International University,
Gilgit – Pakistan

e-mail: dr.syedrizwan@kiu.edu.pk

© by PSP Volume 31– No. 05/2022 pages 4699-4708 Fresenius Environmental Bulletin

COMPARISON OF DIFFERENT ANN (FFBP GRNN RBF) ALGORITHMS AND MULTIPLE LINEAR REGRESSION FOR DAILY STREAMFLOW PREDICTION IN KOCASU RIVER - TURKEY

Halil Ibrahim Burgan*

Akdeniz University, Department of Civil Engineering, 07070, Antalya, Turkey

ABSTRACT

Flow gauging stations in hydrological basins are mostly installed on main rivers. It is known that how difficult the prediction of daily flow with its stochastic and complicated structure. In this study, the application of time-lagged streamflow records of a gauging station is proposed as an accurate method for flow prediction. In this way, five time-lagged scenario is evaluated as daily streamflow prediction function station at Kocasu River, Turkey. At the first stage, typical three-layer feed forward back propagation (FFBP) neural networks is applied as an ANN method to reach the best time-lagged solution for the river. Additionally, other ANN algorithms as generalized regression neural networks (GRNN) and radial basis function (RBF) neural networks and also multiple linear regression (MLR) method are applied in order to comparison of the mentioned ANN and MLR techniques. Root mean square error (RMSE) and determination coefficients (R^2) are calculated to evaluate the performance of the techniques. According to the results, daily records of the station are sufficient to achieve high efficiency value which can be proposed as the most reasonable daily streamflow prediction model for Kocasu river, which is in the southern part of the Marmara Sea. The performance of FFBP algorithm for daily flow prediction studies is the best one in all other techniques. At the same time, these ANN algorithms can be used not only in flow prediction, but also they can be used for the purpose of water resources management in hydrological basins by estimating extreme events as floods and droughts.

KEYWORDS:
ANN, daily streamflow prediction, Kocasu river, multi linear regression, performance criteria

INTRODUCTION

Since a random variable takes dependent values in time successively, the generated time series by these values are known as stochastic process. Streamflow process modeling is important for water resources planning, operating and management studies. Specific modeling technique is important in decreasing the effects of extreme events as flood and drought. For the purpose of this, a lot of hydrological models are developed in order to simulate this complicated process. By producing simulations corresponding to a chosen historical streamflow series; they are required to resemble the historical data in respect of hydrologically important properties, such as runs of and low flow [1].

Auto-Regressive (AR), Auto-Regressive Moving Average (ARMA) or Auto Regressive Integrated Moving Average (ARIMA) from traditional black-box time series models such as are widely used techniques for estimation of hydrological time series [2–7]. These linear models are bottomed on an essential stationarity assumption and have restricted ability in terms of capturing characteristics of which is nonstationary and nonlinearity in streamflow data [8]. Of late years, new artificial intelligence (AI) techniques such as fuzzy logic, genetic programming, genetic algorithm and artificial neural networks (ANNs) have laid out enormous ability in modeling and predicting nonlinear streamflow time series [9–10]. AI techniques provide an effective approach to handling large amounts of complex and nonlinear data, especially when the underlying physical relationships are not fully understood. In other words, it does not require prior knowledge of the method to apply the AI technique.

ANN which is one of AI models has extensive usage in the fields of hydrology, hydraulics and water resources [11] or other subjects as to predict particulate matter in air [12] and hourly temperature [13]. There are more accomplished results of ANN application on streamflow prediction than traditional black box hydrological time series techniques [14–20]. A comprehensive literature of these papers was presented by Abrahart et al. [21]. As described hereinbefore, ANN techniques show better performances than traditional time series modeling approaches. There are only a few studies to assess the performance of different ANN algorithms in streamflow prediction. Kisi and Cigizoglu have compared three-layer feed forward back propagation (FFBP), radial

basis function (RBF) and generalized regression neural networks (GRNN) techniques in monthly and daily river flow prediction [22, 23]. They result indicated superiority of GRNN to the other ANN techniques in monthly flow and superiority of RBF to the others in daily flow forecasting.

The gradient descent and Levenberg–Marquardt (LM) algorithm FFBP algorithms are employed and suggested by Kisi and Cigizoglu in the most of ANN applications in hydrology and water resources [23]. The FFBP algorithms are very vulnerable to the selection of initial weight values. FFBP show better performance under different applications. The other problem comes across to FFBP application is the local minimum subject. All along the training stage, the networks are sometimes ambushed in local error minimum avoiding them from reaching the global minimum [24]. Therefore, current tendency is to determine and evaluate the performances of three different ANN algorithms (FFBP, GRNN and RBF) in daily streamflow prediction of Kocasu River, located in eastern South Marmara region (Turkey).

Seeing daily streamflow time series of Kocasu River in one successive gauging station, the time series are come into the FFBP-ANN technique to construct the predicted streamflow series. The best scenario will be chosen at this step based on performance analysis. In the second step, GRNN and RBF algorithms will also be employed to generate new ANN structures for the chosen scenario. An attempt also will be done to model the relationship between input and output time series by multiple linear regression (MLR) method. Eventually, three different ANN algorithms and MLR modeling results will be compared with each other in terms of accuracy and applicability.

MATERIALS AND METHODS

ANNs are soft computational methods that somebody uses input and output data sets to ascertain the system approach. Absolutely, they are nothing more than complicated version of regression or statistical (black-box) models. Supervised and unsupervised are chiefly two types of training mechanisms. A supervised algorithm involves an extraneous instructor to direct the training step however unsupervised methods are self-organizing networks. The full description of ANN algorithms is the subject of a number of studies. Accordingly, the following is limited to the concepts of the algorithms that are used in this study.

FEED FORWARD BACK PROPAGATION (FFBP)

FFBP networks are supervised training mechanisms which are known as general nonlinear approaches. The main objective of this algorithm is to minimize the estimate error by looking for a collection of link weights which cause the ANNs to produce outputs closer to their goals.

It usually consists of three components: i) a layer with a number of input nodes, ii) one or more hidden layers, iii) a number of output layer nodes. There are two architecture parameters of ANNs: the number of hidden layers and the number of nodes on each layer, computational nodes. Any differentiation of the input nodes takes place in the sample data sets. Only the weighted values are transmitted to the hidden layer nodes. In general, the hidden layer nodes accept weighted inputs from the input layer or a hidden previous layer, convert them and transfer the output to the next neighboring layer, normally a secret one or the output layer. The output layer consists of nodes that are sent to the recipient of the ANN and are sent to the secret layer outcome.

ANNs are complex design problems and are important to the development of ANNs. Typically, the number of nodes in the input and the output layer is decided from the problem. Calibration parameters are the number of hidden layers and the number of nodes within every hidden layer that can be changing in experiment to best fit measured, projected output data on the basis of the same input data. Such design decisions are learned during the training of the ANN, utilizing predefined (or measured) data sets, and above all the determination of the values of weights and thresholds of each relation.

The training phase may take a lot of time for preparation. When the ANN model achieves a given user performance level, it is considered complete. At this stage, the network will generate the necessary outputs for a defined series of inputs to achieve the desired statistical accuracy. For situations where no further preparation is deemed necessary, the weights for the test are usually calculated. External criteria can be used to interrupt the training period such as an evaluation loss rise in the validity level.

The FFBP algorithm first multiplies any input node by a correct weight, then introduces a constant value which is called the pre-defined transfer element, and finally enters the pre-defined transmission functions. For an output value for a FFBP 3-layer network, the expression is provided by (Eq. 1):

$$y_C = f_O\left[\sum_{j=1}^{M_N} W_{kj} \cdot f_h\left(\sum_{i=1}^{N_N} W_{ji} x_i + W_{jo}\right) + W_{ko}\right] \quad (1)$$

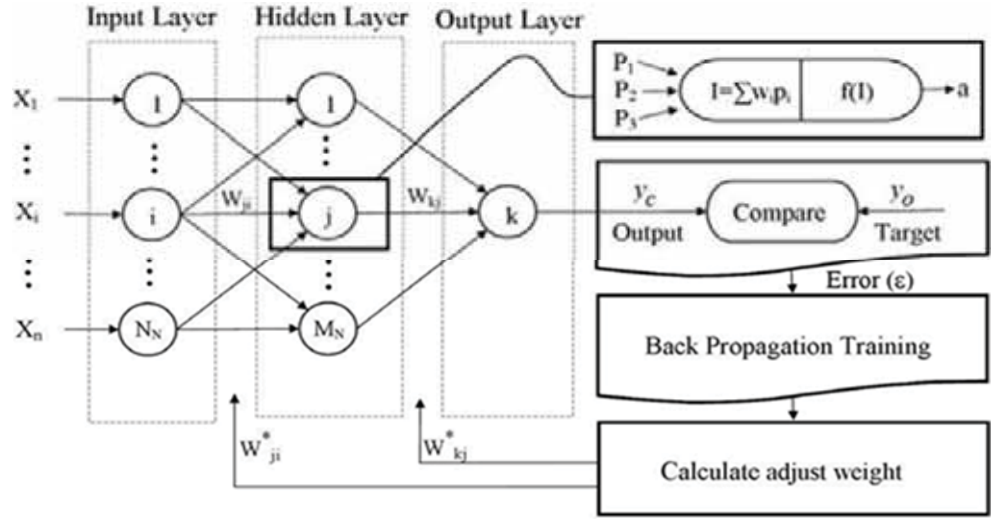

FIGURE 1
A three-layered FFBP network

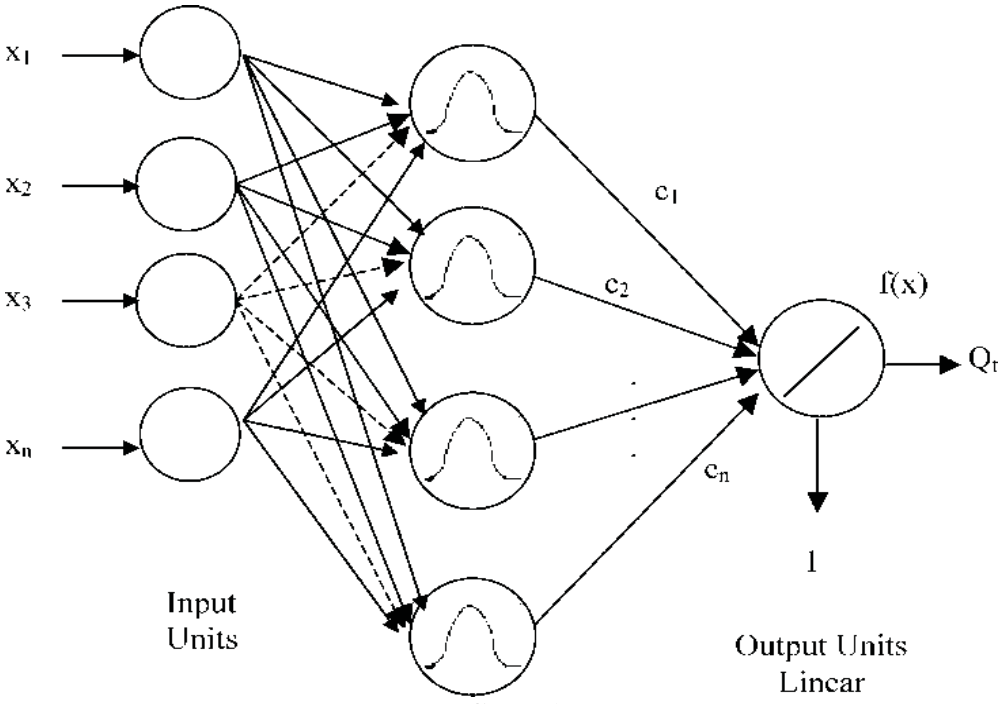

FIGURE 2
RBF structure used in the study

RADIAL BASIS FUNCTION NETWORKS

RBF is an artificial neural network of radial base features, real-assessed functions, the importance of which depends on the distance from the source as the activation functions. The RBF is composed of two layers with a linear mix of radial base functions as the output node. The radial base of the hidden layer provides a relevant non-zero response to the input stimulus only if the feedback is situated in a small region of the input field. This model is therefore often named a localized field receiving network. The relation between inputs and outputs is illustrated in Figure 2. Inputs transformation is important to counter the dimensionality curse in empirical modeling. Inputs transformation is important to counter the dimensionality curse in empirical modeling. After nonlinearing multi-dimensional inputs, the radial basis functions play a role as retrogressors, without taking into account the output area. The only customizable parameters are the weights of the regressor because the output layer uses a linear regressor. Therefore, these parameters can be defined using the less square linear approach, which provides a significant convergence benefit. The basic concept and algorithm of the RBF was described by Kisi and Cigizoglu [23].

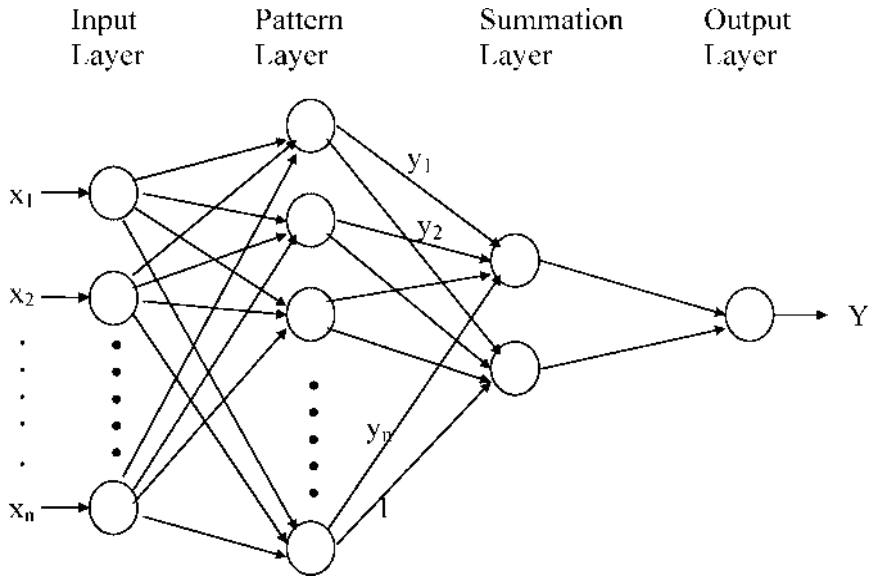

FIGURE 3
GRNN architecture schematic diagram

GENERALIZED REGRESSION NEURAL NETWORKS

The basics of the GRNN algorithm can be obtained in the literature [24]. A schematic of the GRNN was shown in Figure 3. It consists of four layers: input layer, pattern layer, summation layer, and output layer. In the first layer the number of input units equals the total number of parameters. The first layer is fully connected to the second, pattern layer, where each unit represents a training pattern and its output is a measure of the distance of the input from the stored patterns. The two neurons in the summation layer are linked to each pattern layer unit: S-summation neuron and D-summation neuron. The S-summation neuron calculates the number of weighted layer outputs, whereas the D-summation neuron calculates the unsightly neural template outputs.

The number of input neurons and the secret layers respectively are N_N and M_N. In the hidden and input layers, the weights are specific and their values during the network training process can be modified. W_{ji} is a weight in the hidden layer connecting the i^{th} neuron in the input layer and the j^{th} neuron in the hidden layer, W_{jo} is the bias for the j^{th} hidden neuron, f_h is the activation function of the hidden neuron, W_{kj} is a weight in the output layer connecting the j^{th} neuron in the hidden layer and the k^{th} neuron in the output layer, W_{ko} is the bias for the k^{th} output neuron, f_o is the activation function for the output neuron, x_i is i^{th} input variable for input layer and y_c , y_o are computed and observed output variables.

According to Figure 1 several three-layer feed forward back propagation (FFBP) networks with sigmoid transfer function in hidden layer and linear transfer function in output layer has been developed as a nonlinear modeling structure. The subscripts i, j and k in this figure denote the number of neurons in input layer, hidden layer and output layer, respectively and w is the applied weight by the neuron. FFBP networks at three tiers have been demonstrated to fulfill forecasting and simulation in all technical issues[11]. Following the modeling structure definition, we carried out the training process using the Levenberg-Marquardt algorithm with a useful toolbox available in the MATLAB® software. The training process automatically stops when generalization ceases improving, as indicated by an increase in the mean square error of the validation samples.

STUDY AREA AND DATA

The study area is the Kocasu River, located in Sakarya basin in Turkey (Figure 4). Sakarya basin covers 58160 km^2, which is approximately 7.46% of Turkey. The river located at 29°46'03" E- 40°15'18" N coordinates. It is near the Yenisehir-Bursa approximately 12 km. Average streamflow of Kocasu River is approximately 18.889 m^3/s. The daily streamflow data of the station (1222) on Kocasu River published in the water-year report by General Directorate of Electrical Power Resources Survey and Development Administration was used for prediction. The statistical characteristics of 29-year period (1952-2001) observed data of the station were given in Table 1.

Before training, in the ANNs models, the normalization was applied for the data. ANNs which make the data dimensionless and contain it within a certain range need to be normalized. The data set between 0 and 1 was used here by splitting the observational data by the average data detected. Normalization procedure is also mentioned by Burgan and Aksoy [25].

After training, the model that yields the best results in terms of the determination coefficient (R^2)

and root mean squared error (RMSE) are selected as the most efficient model. RMSE measures the root average of the squares of the errors and calculated by (Eq. 2):

$$RMSE = \sqrt{\frac{\sum_{i=1}^{n}(X_i^{obs} - X_i^{pre})^2}{n}} \quad (2)$$

Determination coefficient (R^2), returns a square of the Pearson product moment coefficient of correlation which can be interpreted as the proportion of the forecast variance compared to the empirical variance and calculated by (Eq. 3):

$$R^2 = \frac{\left(\sum_{i=1}^{n}(X_i^{obs} - X_{mean}^{obs})(X_i^{pre} - X_{mean}^{pre}) \right)^2}{\sum_{i=1}^{n}(X_i^{obs} - X_{mean}^{obs})^2 \sum_{i=1}^{n}(X_i^{pre} - X_{mean}^{pre})^2} \quad (3)$$

FIGURE 4
Location of study area (Kocasu River and gauging station)

TABLE 1
The daily statistical parameters of observed streamflow data

Statistical parameter	Kocasu - Rustumkoy (1222)	
	raw	normalized
Number of data (X)	17892	17892
X_{max} (m^3/s)	283	1
X_{min} (m^3/s)	0	0
X_{mean} (m^3/s)	18.26	0.0645
Standard Deviation (m^3/s)	20.39	0.0721
Coefficient of Skewness	2.71	0.0096

TABLE 2
Statistical parameters of data sets

Parameters	Entire data	Training set	Validation set
Number of data (X)	17892	14315	3577
X_{max} (m^3/s)	283	237	283
X_{min} (m^3/s)	0	0	0.034
X_{mean} (m^3/s)	18.26	18.55	17.08
Standard Deviation (m^3/s)	20.39	20.08	21.53
Coefficient of Skewness	2.71	2.53	3.38

TABLE 3
Performance (goodness of fitness) Comparison of ANNs and MLR results at validation stage

FFBP		RBF		GRNN		MLR	
R^2	RMSE	R^2	RMSE	R^2	RMSE	R^2	RMSE
0.823	9.08	0.748	10.83	0.753	10.73	0.798	9.70

Where X_i^{obs} = observed value of X, X_i^{pre} = predicted value X_{mean}^{obs} = mean value of observed data and n = number of observed data.

RESULTS AND DISCUSSION

As it mentioned Kocasu River has been selected for study area. The data record is composed of 17892 observations of the daily streamflow at the station. 80 and 20 percent of 17892 observations were selected for training and validation of the networks, respectively. The statistical parameters for each set, training set, testing set, and the entire data set are presented in Table 2.

According to Figure 5, the correlogram shows that 5 is enough for the time-lag. So, 5 time-lag is used to make models in this study.

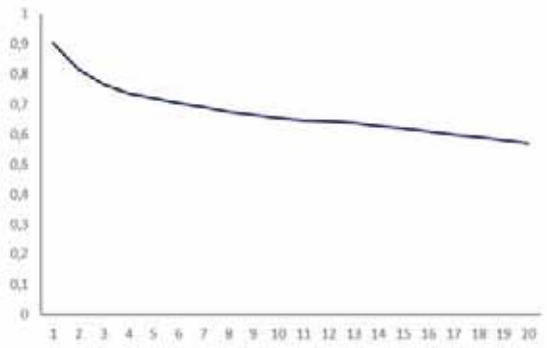

FIGURE 5
Correlogram of the data

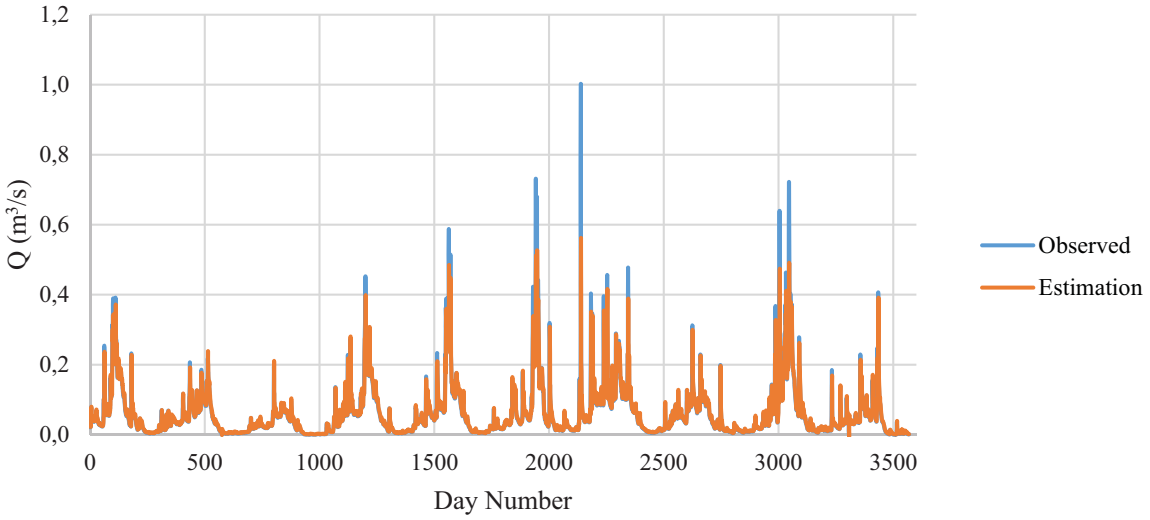

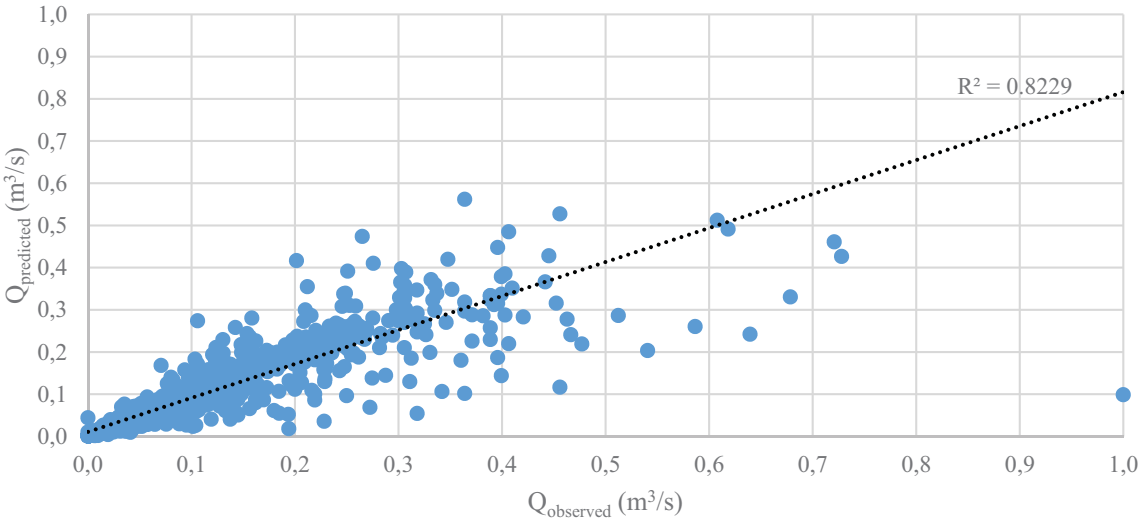
R² = 0.8229
Q predicted (m³/s)
Q observed (m³/s)

(a) FFBP

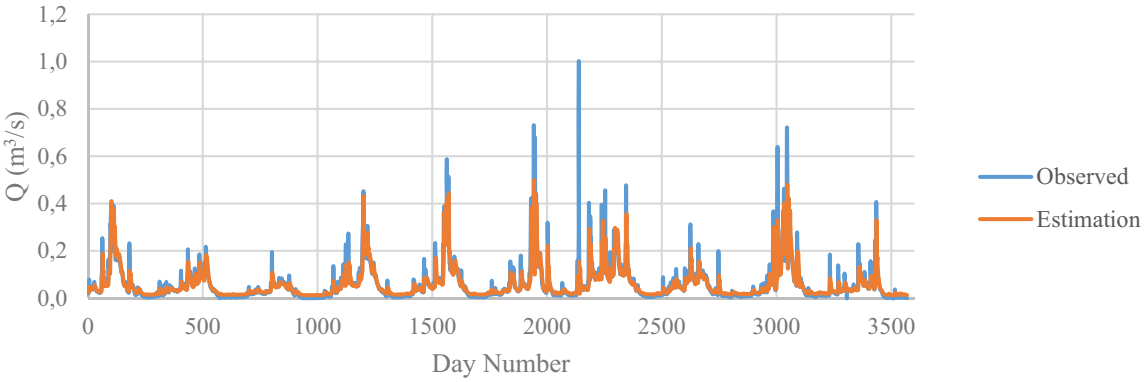
Q (m³/s)
Day Number
Observed
Estimation

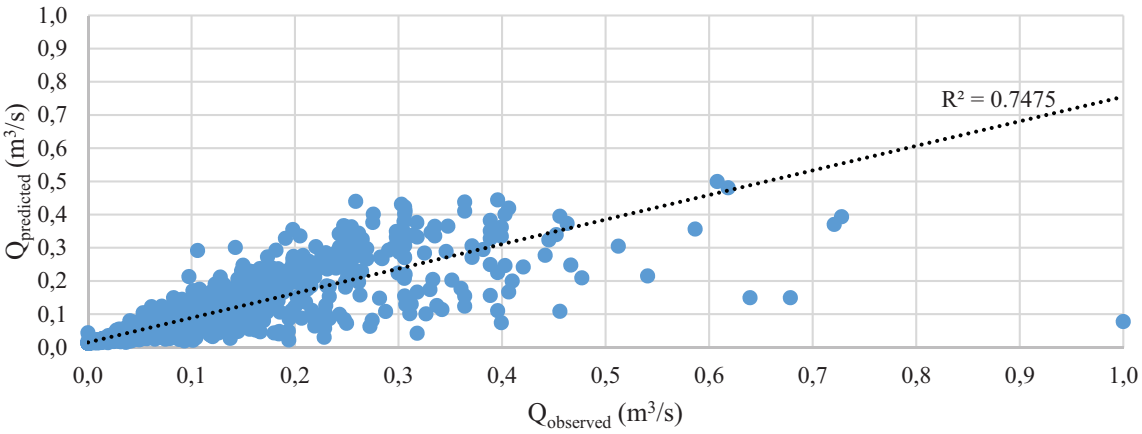
R² = 0.7475
Q predicted (m³/s)
Q observed (m³/s)

(b) RBF

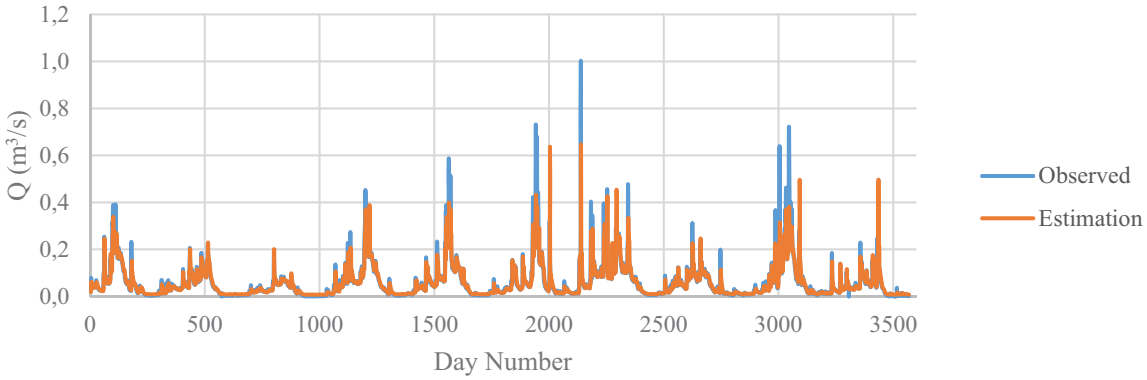
Q (m³/s)
Day Number
Observed
Estimation

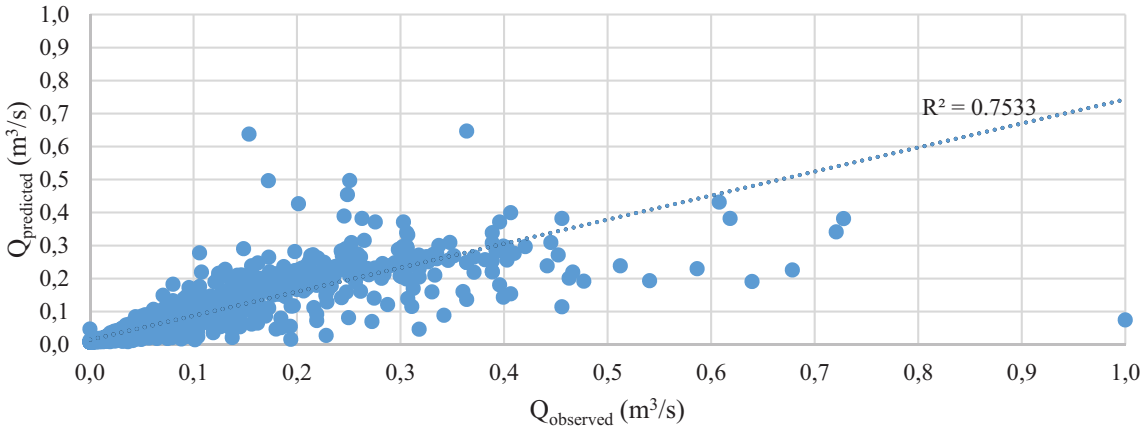
R² = 0.7533
Q predicted (m³/s)
Q observed (m³/s)

(c) GRNN

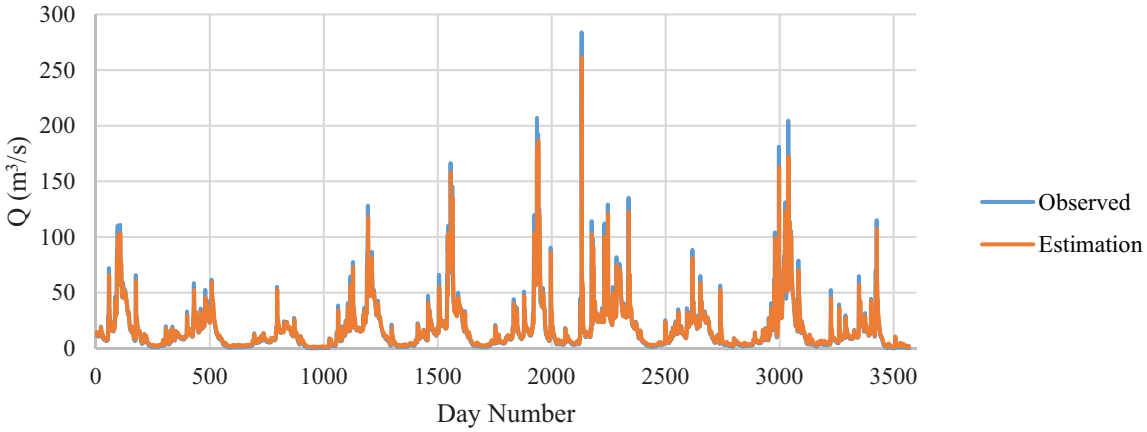
Q (m³/s)
Day Number
Observed
Estimation

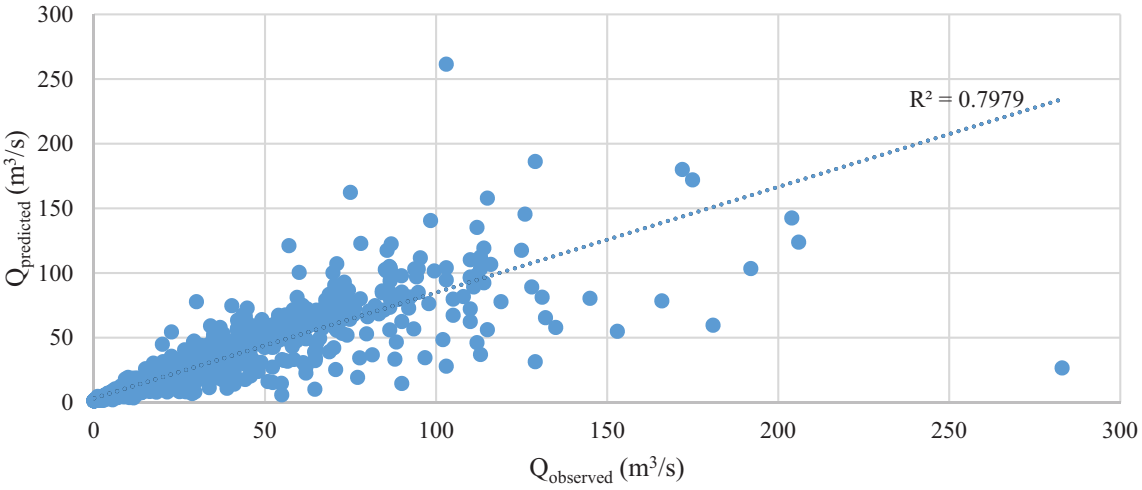

(d) MLR

FIGURE 6
Comparison of different techniques for validation period (a) FFBP, (b) RBF, (c) GRNN and (d) MLR.

COMPARISON OF ANN ALGORITHMS AND MLR TECHNIQUES' PERFORMANCES

In this part of the study, the focus is given to the performance comparison of the three ANN methods in prediction. The prediction results of different models compared to observed data for the validation time series are shown in Table 3 and Figure 6. They show the higher capability of FFBP method the proposed model in prediction.

CONCLUSIONS

In this study, five time-lagged streamflow prediction model based on records of gauging station located on the Kocasu River has been developed by FFBP technique and has been compared with each other. Then, two different ANN techniques, including GRNN and RBF, and classical MLR method were applied for comparison of different ANN and MLR techniques. In general, the forecasting performance of FFBP is found to be superior to the all techniques.

The performance level of the presented model shows the power and ability of lag-time based ANNs technique in daily streamflow prediction. Although our model efficiency seems to be acceptable, daily streamflow prediction based on time-lag analysis in combination with other AI techniques would be interesting to investigate.

REFERENCES

[1] Lawrence, A.J., Kottegoda, N.T. (1977) Stochastic Modelling of River flow Time Series. J. R. Stat. Soc. A Stat. 140(1), 1-31.

[2] Abrahart, R.J., See, L. (2000) Comparing Neural Network and Auto Regressive Moving Average Techniques for the Provision of Continuous River Flow Forecasts in Two Contrasting Catchments. Hydrol. Process. 14(11-12), 2157-2172.

[3] Baran, T., Bacanli, U.G. (2006) Evaluation of Goodness of Fit Criterion in Time Series Analysis. Tek Dergi. 17(84), 3987-4002.

[4] Guang-Te, W., Singh, V.P. (1994) An Autocorrelation Function Method for Estimation of Parameters of Autoregressive Models. Water Resour. Manag. 8, 33-55.

[5] Mondal, M.S., Wasimi, S.A. (2006) Generating and Forecasting Monthly Flows of the Ganjes River with PAR Model. J. Hydrol. 323(1-4), 41-56.

[6] Salas, J.D., Delleur, J.W., Yevjevich, V., Lane, W.L. (1980) Applied Modeling of Hydrologic Time Series. Water Resour. Publ. Littleton, Colorado.

[7] Tankersley, C., Graham, W., Hatfield, K. (1993) Comparison of Univariate and Transfer Function Models of Groundwater Fluctuations. Water Resour. Res. 29(10), 3517-3533.

[8] Nourani, V., Kisi, O., Komasi, M. (2011) Two Hybrid Artificial Intelligence Approaches for Modelling Rainfall–Runoff Process. J. Hydrol. 402(1-2), 41-59.

[9] Cigizoglu, H.K. (2004) Estimation and Forecasting of Daily Suspended Sediment Data by Multi-Layer Perceptrons. Adv. Water Resour. 27(2), 185-195.

[10] Cigizoglu, H.K., Kisi, O. (2005) Flow Prediction by Two Back Propagation Techniques using k-fold Partitioning of Neural Network Training Data. Hydrol. Res. 36(1), 49-64.

[11] ASCE TASK COMMITTEE (2000) Artificial Neural Networks in Hydrology II: Hydrologic Applications. J. Hydrol. Eng. 5(2), 124-137.

[12] Demir, G., Ozdemir, H., Ozcan, H.K., Ucan, O.N., Bayat, C. (2010) An Artificial Neural Network-based Model for Short-term Predictions of Daily Mean PM10 Concentrations. J. Environ. Prot. Ecol. 11(3), 1163-1171.
[13] Ilie, C., Lungu, M.L., Panaitescu, L., Ilie, M., Lungu, D., Nita, S. (2014) Simulating for Predicting the Hourly Dew Point Temperature using Artificial Neural Networks. J. Environ. Prot. Ecol. 15(3), 1101-1109.
[14] Besaw, L.E., Rizzo, D.M., Bierman, P.R., Hackett, W.R. (2010) Advances in Ungauged Streamflow Prediction using Artificial Neural Networks. J. Hydrol. 386(1-4), 27-37.
[15] Cigizoglu, H.K. (2003a) Estimation, Forecasting and Extrapolation of Flow Data by Artificial Neural Networks. Hydrolog. Sci. J. 48(3), 349-361.
[16] Cigizoglu, H.K. (2003b) Incorporation of ARMA Models into Flow Forecasting by Artificial Neural Networks. Environmetrics. 14(4), 417-427.
[17] Dolling, O.R., Varas, E.A. (2002) Artificial Neural Networks for Streamflow Prediction. J. Hydraul. Res. 40(5), 547-554.
[18] Kisi, O. (2005) Daily River Flow Forecasting using Artificial Neural Networks and Auto-Regressive Models. Turkish J. Eng. Env. 29(1), 9-20.
[19] Muhamad, J.R., Hassan, J.N. (2005) Khabur River Flow Modeling using Artificial Neural Networks. Al-Rafidain Eng. 13(2), 33-42.
[20] Ochoa-Rivera, J.C., Garcia-Bartual, R., Andreu, J. (2002) Multivariate Synthetic Stream Flow Generation using A Hybrid Model Based on Artificial Neural Networks. Hydrol. Earth Syst. Sc. 6(4), 641-654.
[21] Abrahart, R.J., Anctil, F., Coulibaly, P., Dawson, C.W., Mount, N.J., See, L.M., Shamseldin, A.Y., Solomatine, D.P., Toth, E., Wilby, R.L. (2012) Two Decades of Anarchy? Emerging Themes and Outstanding Challenges for Neural Network River Forecasting. Prog. Phys. Geog. 36(4), 480-513.
[22] Kisi, O. (2008) River Flow Forecasting and Estimation using Different Artificial Neural Network Techniques. Hydrol. Res. 39(1), 27-40.
[23] Kisi, O., Cigizoglu, H.K. (2007) Comparison of Different ANN Techniques in River Flow Prediction. Civ. Eng. Environ. Syst. 24(3), 211-231.
[24] Cigizoglu, H.K. (2005) Application of the Generalized Regression Neural Networks to Intermittent Flow Forecasting and Estimation. J. Hydrol. Eng. 10(4), 336-341.
[25] Burgan, H.I., Aksoy, H. (2018) Annual Flow Duration Curve Model for Ungauged Basins. Hydrol. Res. 49(5), 1684-1695.

Received: **04.01.2021**
Accepted: **31.01.2022**

CORRESPONDING AUTHOR

Halil Ibrahim Burgan
Department of Civil Engineering,
Akdeniz University,
07070 Antalya – Turkey

e-mail: burgan@akdeniz.edu.tr

© by PSP Volume 31– No. 05/2022 pages 4709-4715 Fresenius Environmental Bulletin

ENVIRONMENTAL IMPACT AND ENERGY SAVING OF LED LIGHTING IN UNIVERSITY BUILDINGS

Duygu Yigit Unlu*

Graduate School of Natural and Applied Sciences, Aksaray University, 68100, Aksaray, Turkey

ABSTRACT

Energy saving in lighting has been seen as an important issue in recent years due to the increasing energy demand and global warming. The university building which is big and old construction is one of the major energy consumer and CO_2 emitter. Energy efficiency systems are possible to use Light Emitting Diode (LED) technology. This study investigates the energy-saving potential and environmental effects of LED lighting applications indoor lighting. For this purpose, the study was carried out in Aksaray University Faculty of Engineering (AUFE), Aksaray, Turkey. The LED luminaires were designed instead of the Fluorescent Lamp in the AUFE building and calculated within the scope of energy efficiency and CO_2 emissions. According to the analysis of the result, it was found that the initial investment cost of LED lamps is 61% higher than that of fluorescent lamps however LED luminarias to save 59% of the annual electricity consumption and 74% of the total consumption cost. Also, it was seen that LED lighting contributes to the reduction of CO_2 emissions by 67% per year. Based on the result of the study despite the cost of LED luminaires it is economically and environmentally friendly.

KEYWORDS:
Energy-saving, public lighting, investment analyses, school lights, emission reduction

INTRODUCTION

Global warming has seriously threatened humanity in the last decade. The major reason for global warming is the use of fossil fuels and greenhouse gas emissions. The increase in greenhouse gas and CO_2 emissions with global warming also triggers climate change. Effective use of energy is the main way to reduce greenhouse gas emissions [1]. Many countries in the world are making joint efforts to reduce CO_2 emissions, energy-saving, and energy efficiency [2]. Electricity traditionally relies on the primary fossil fuel supplies [3] and these energy resources exert adverse environmental issues. Fossil fuel consumption produces the emissions of chemical pollutants and gases into the atmosphere; thus causing deterioration in environmental quality [4]. However, the need for electricity is increasing day by day and also, environmental well-being is often overlooked while producing electrical energy [5].

Statistics endorsed that the highest consumption and widely used of electricity is in the building sector. The global consumption of electricity increased last ten years [6] and it is evaluated that the buildings consume about 20% to 60% of the global electricity [7]. In the building, one of the important energy-consuming systems is lighting, ranging from 20% to 45% [8]. Also, lighting accounts for 15% of global energy consumption and 5% of global greenhouse gas emissions [9]. With the increase in electricity consumption in the world, the estimation of electricity consumption of plays an important role in the electricity management and control system. With the increase in electricity consumption, necessary precautions taken to reduce the electricity consumption in the electricity management and control system play an important role. Thanks to the improvements to be made in the lighting systems, around 30% energy savings can be achieved [10]. School buildings are among the large consumers of energy in the building sector [11] and a large contributor to energy saving in the school building is the schools are lightning [12]. Lighting products are essential for energy saving. They also consume a large number of resources and produce considerable harmful emissions such as greenhouse gas emissions in the world [13]. It has been stated that fluorescent lamps are generally preferred in the lighting of schools [14]. However, in recent years, it has been seen that LEDs have started to be preferred in the lighting of schools for their efficient, cheap, and flexible structure [15].

LED has become one of the most promising among the other lighting technologies due to high energy efficiency, lighting quality, durability, aesthetics, low cost of use, environmental awareness, safety, and creating livable cities, which are not possible in conventional lighting [16]. Compared with traditional lamps such as fluorescent lamps [17], LEDs have better optical efficiency and a longer lifetime. In addition, it has advantages such as lower power consumption, smaller emitting angle, mercury release, and less heat radiation than conventional lighting sources [18].

LED lights operate at a lower temperature and have less impact on the environment [19]. Recent

studies also emphasized that LED lighting design has been particularly to bring a clean and non-polluting lighting environment to the world [20]. The replacement of traditional lighting sources with LEDs is to reduce the electrical energy consumption for lighting purposes by 15% in 2020, by 40% in 2030, and up to 75% in 2035 according to recent predictions [21]. The low energy consumption of LEDs is shown as the most important benefit of the energy-saving programs [22] and this is due to the environmental friendliness [23]. LEDs have been already widely used in many indoor and outdoor locations and applications used as light sources [15, 24, 25].

Although university buildings are one of the most important components of energy consumption in many countries [26] there were limited studies focused on energy-saving in university buildings [27,28]. Most of the universities were older, had inefficient lighting technology, and consumed a lot of electrical energy. One of the major energy-consuming categories in any university building is lighting [29]. By achieving efficiency in university building lighting systems significant savings can be made and lighting products' impact on the environment can be decreased. For this reason, in this study, energy savings will be calculated by converting Fluorescent Lamp used in schools to LED lighting elements.

In this regard, AUFE was chosen as the sample case. The study plans to have the maximum benefit with the minimum total cost and examine the potential energy-saving and its environmental effects when energy-efficient indoor lighting was designed. In the study, it will be determined that a significant amount of electrical energy savings can be achieved by replacing the lighting elements and it is foreseen that the use of more environmentally friendly lighting elements will be widespread. Thanks to energy-saving practices, unnecessary expenditures will be prevented, and besides the more effective and efficient use of resources, it will contribute to the creation of cleaner environments.

MATERIALS AND METHODS

In the study, the LED luminarias designed instead of the Fluorescent Lamp replaced in the AUFE building was calculated within the scope of energy efficiency and CO_2 emissions. The selected area for the study is AUFE located in the Central Anatolian Region of Turkey. AUFE consists of a single building. When the distribution of the indoor areas of the building is examined, it consists of a total of 23521,70 closed areas, including the administrative area of 3609.71 m2, the classroom areas of 4287.77 m2, the laboratory areas of 3374.1 m2, the meeting and conference hall 568.97, the canteen 169.26 and the other areas 11511, 88 [30]. To determine the current status of the lighting systems, the data obtained from Aksaray University Directorate of Construction and Technical Affairs well as the field studies are used.

RESULT AND DISCUSSION

This study aimed to investigate the energy and CO_2 saving possibilities that can be obtained in lighting systems university buildings. As known that university building has often large indoor spaces, different parts such as well as educational and administrative buildings, and are used extensively throughout the year to late hours. For this reason, this study was carried out on the internal lighting system of a university building. According to the priority of the criteria such as initial investment cost, energy-saving, payback time, total cost, and CO_2 emissions demonstrated with the data. In the analysis, the unit price of electricity was taken as 0.36₺. It is assumed that the lighting panels are used 8 hours a day and 365 days a year.

The necessary information for the Fluorescent Lamp is stated in Table 1. Accordingly, when the features of the Fluorescent Lamp existing in AUFE were examined; there are a total of 2954 pieces of 4 different Fluorescent Lamp types, 72W, 36W, 20W, and 80W. The total power of these luminaires was calculated as 208kW. The unit prices of four different Fluorescent Lamp types vary between 35₺ and 65₺. A total of 8 bulbs were needed for the Fluorescent Lamp. Fluorescent Lamp lifespan was calculated as 2000 hours and lifetimes of 0.7 years by the manufacturer. It was seen that the initial investment cost of Fluorescent Lamp was 177.39₺, annual electricity consumption was 549.929 kWh, annual electricity consumption was 197.975₺, annual lamp consumption was 116,415₺ and the annual cost of Fluorescent Lamp is 314.389₺.

In the study, the use of 28W, 14W, and 30W LED fixtures instead of the Fluorescent Lamp were examined and shown in Table 2. The design was carried out with 2954 luminaires and the power of the LED luminaires was calculated as 80 kW in total. LED luminaires life given by the manufacturer was determined as 50000 hours and the service life is 17.1 years. It has been calculated that the initial investment cost of LED lamps is 458,346₺, annual electricity consumption is 225.85 kWh, annual electricity consumption is 81,306₺, and the annual cost of LED lamps is 81,306₺ in total. In addition, since there was no lamp in LED luminaires, it was not ant lamp consumption and lamp cost.

Table 3 includes the necessary information for the Fluorescent Lamp and LED luminaire equivalent tCO_2 emissions per year. The equivalent CO_2 emissions were calculated by using 329.91 equivalent gCO_2/kWh emission factor [31, 32]. The Fluorescent Lamp releases around 181 equivalent tCO_2 and the LED luminaire releases 75 equivalent tCO_2 for the

production of annually consumed energy. It can be said LED luminaries contribute to the reduction of CO_2 emissions. Accordingly, when compared with the Fluorescent Lamp and LED luminaire, it is possible to prevent the release of 106 equivalent tCO2 with the LED luminaire to the atmosphere.

The evaluation of the investment in which Fluorescent Lamps were converted to LED lamps was shown in Table 4. Accordingly, when the initial investment cost between Fluorescent Lamp and LED lamps is compared, it was seen that the difference was -280,956. According to the results obtained, it was determined that the initial investment cost of LED lamps was quite high. (Figure 1). However, the payback period of the investment was calculated by dividing the initial investment cost for conversion to LED by the cost difference between the two fixtures and was determined as 1.2 years. Considering the total electricity consumption, it was calculated that an annual average of 324,079 kWh of electricity will be saved with the use of LED luminaires. (Figure 2). It was observed that the amount of annual electricity savings resulting from the use of LED fixtures instead of fluorescent lamps was 116,669 and the total savings is 233,083. (Figure 3). At the end of the 17.1-year life of the LEDs, the total savings amount was determined as 9.589,534, considering the annual 10% increase in electricity unit prices. In the study, it was seen that LED lighting systems save 67% CO_2 per year (Figure 4).

TABLE 1
Fluorescent Lamp AUFE

Number of luminaires	Armature Power (kW)	Fixture Unit Price (₺)	Number of Luminaire Lamps	Unit Lamp Price (₺)	Lamp Life (Hour)	Lifespan (Years)	Initial Investment Cost (₺)	Annual Electricity Consumption (kWh)	Annual Electricity Consumption Cost (₺)	Annual Lamp Consumption Cost (₺)	Total Cost (₺)
2296	72	65	4	8	2000	0.7	177,39	549,929	197,975	116,415	314,389
125	36	55	2	8							
402	20	35	1	8							
131	80	55	1	8							

TABLE 2
Designed LED Lamps

Number of luminaires	Armature Power (kW)	Fixture Unit Price (₺)	Number of Luminaire Lamps	Unit Lamp Price (₺)	Lamp Life (Hour)	Lifespan (Years)	Initial Investment Cost (₺)	Annual Electricity Consumption (kWh)	Annual Electricity Consumption Cost (₺)	Annual Lamp Consumption Cost (₺)	Total Cost (₺)
2296	28	170	-	-	50000	17.1	458,346	225,85	81,306	-	81,306
125	28	205	-	-							
402	14	68	-	-							
131	30	115	-	-							

TABLE 3
CO_2 emissions

Lamp Type	Energy consumption (kWh/year)	CO_2 emission (tCO_2/year)
Fluorescent Lamp	549,929	181
LED luminaire	225,85	75
Differences	324,079	106

TABLE 4
Main characteristics of the Investment

Estimate	Value	%
Initial investment cost	-280,956	-61%
The payback time of investment	1.2 year	-
Annual Electricity Savings (kWh)	324,079	59%
Annual Total Savings (₺)	233,083	74%
Total Gain of Investment (₺) (end of the 17.1 years)	9,589,534	-
CO2 saving (tCO2/year)	106	67%

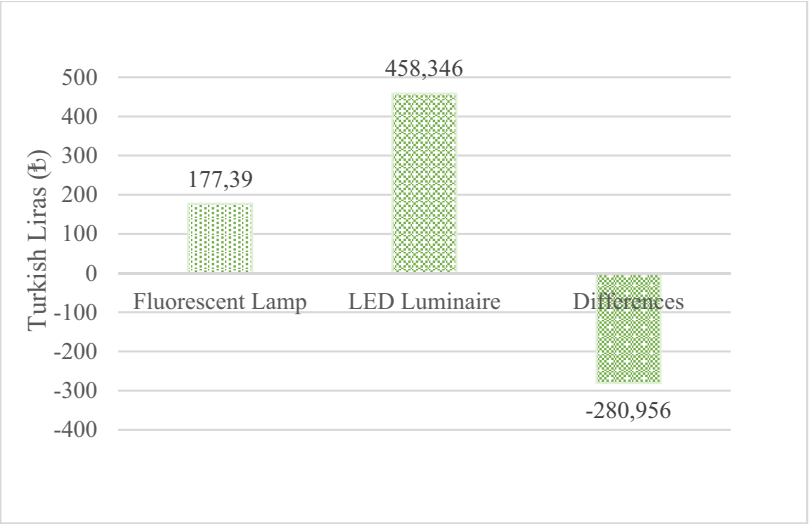

FIGURE 1
Initial Investment Cost

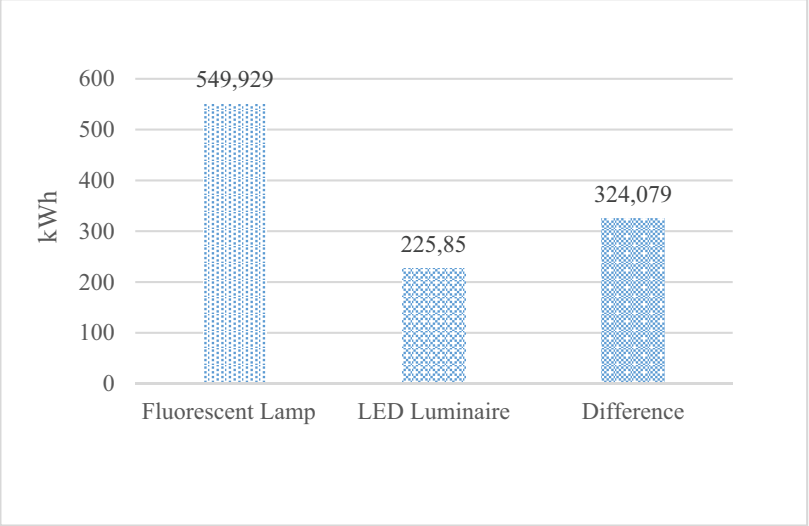

FIGURE 2
Annually Electricity Savings

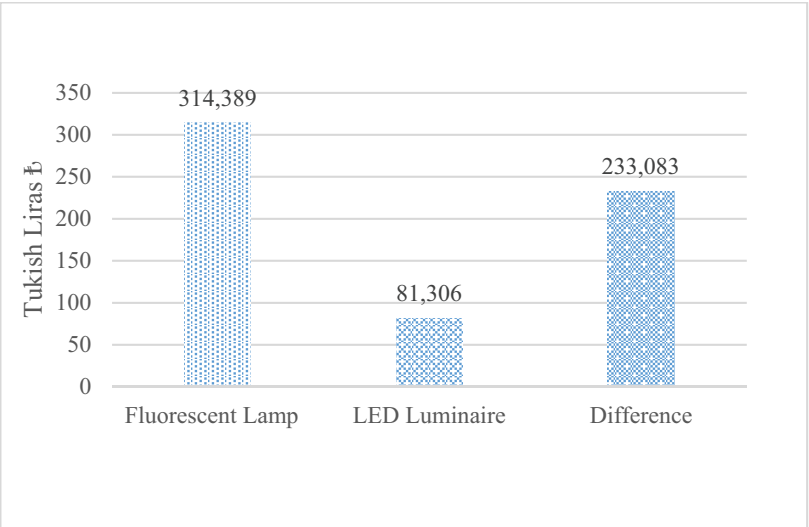

FIGURE 3
Annually Total Savings Cost

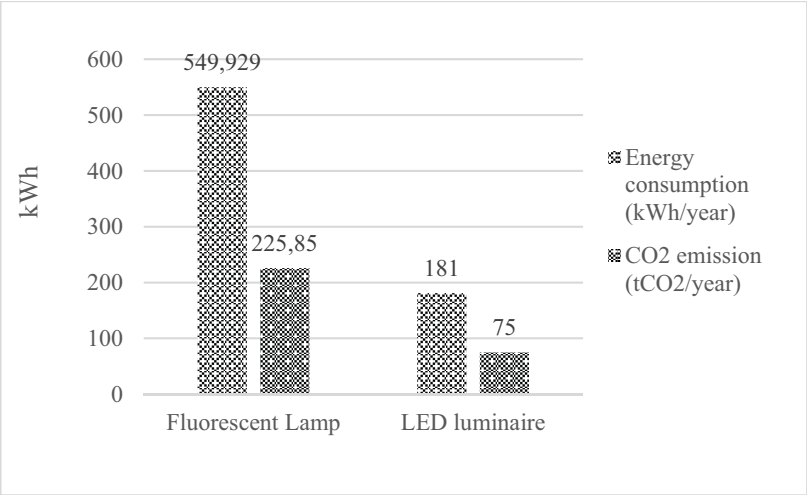

FIGURE 4
CO2 emissions

As a result of this study it was found that thanks to the LED lamps designed instead of fluorescent lamps, it was seen that 59% of the annual electricity consumption and 74% of the total consumption cost will be saved. Similar studies demonstrated that the investment of replacing the lighting devices with LEDs was evaluated economically [32] and energy savings up to 66% can be achieved by replacing lighting lamps with LEDs [31]. In another study where LED lamps and fluorescent lamps were compared in terms of energy efficiency, it was seen that less energy was consumed by using LED lamps instead of traditional lamps by maintaining the illuminance levels specified in the standards [33].

It was determined that the initial investment cost of LED lamps is 61% higher than that of fluorescent lamps, but the initial investment cost was paid off in a short period of 1.2 years. Fluorescent lamps cost less initially, they were not economical in the long term run due to their high energy consumption and maintenance expenditures [34]. Lamps with low initial investment costs wear out over time and lose their power and life. Although the initial cost of LED technology was high, it becomes preferable in terms of cost, since it does not lose its power and lighting effect in long years of use [35].

In the study, it was also found that LED lighting contributes to the reduction of CO_2 emissions by 67% per year. In a similar study conducted in Turkey in 2019, it was stated that LED lighting has benefits such as contributing to the reduction of CO_2 emissions and energy-saving [36]. The reduction in electrical energy consumption will result in less use of fossil fuels for electricity generation and indirectly release less carbon dioxide into the atmosphere. In this way, more energy savings can be achieved and an environmentally friendly outdoor lighting system design can be realized [24].

In the study, it was observed that the use of LED lighting systems in university buildings can provide important advantageous lighting thanks to their long life, cost, and energy-saving structures. Also, LED lighting systems contribute to environmental sustainability to reduce CO_2 emissions.

CONCLUSION

According to the results obtained from the study, LED lighting luminaries have been evaluated as energy-efficient lighting tools in the interior lighting of school buildings with their long lifetime, low maintenance costs, and energy-efficient structures. In addition, it was observed that LED lamps contribute to the reduction of CO_2 emissions and the creation of a more sustainable environment with their energy-efficient structures. By changing the traditional lighting devices in school buildings, the energy class of the school buildings will be increased and the energy performance of the building will be improved. It is important to use environmentally friendly lighting tools to prevent environmental pollution both while producing and consuming energy and to leave a cleaner and livable environment for future generations. In this context, LED lighting tools contribute to the creation of energy-efficient and clean environments thanks to their low energy consumption. As a result; LED lighting devices provide the optimum level of illumination with minimum energy cost and CO_2 emission. With LED lighting tools, energy-efficient and low CO_2 emission lighting can be provided in university buildings. Based on the results obtained from the research, studies can be carried out to design LED lighting areas in the interior lighting of other public buildings.

REFERENCES

[1] Ardavani, O., Zerefos, S. and Doulos, L.T. (2020) Redesigning the exterior lighting as part of the urban landscape: The role of transgenic bioluminescent plants in mediterranean urban and suburban lighting environments. Journal of Cleaner Production. 242, 118477.

[2] Zhou, J. and Bai, X. (2021) Study on Intelligent Space, Environment Planning and Design Based on Ecological Theory. Fresen. Environ. Bull. 30(1), 158-163.

[3] Sahin, M. (2019) A new approach for the estimation of depreciation factor and energy loss in lighting system. Fresen. Environ. Bull. 28(5), 3787-3794.

[4] Hanif, I., Raza, S.M.F., Gago-de-Santos, P. and Abbas, Q. (2019) Fossil fuels, foreign direct investment, and economic growth have triggered CO_2 emissions in emerging Asian economies: some empirical evidence. Energy. 171, 493-501.

[5] Murshed, M., Alam, R. and Ansarin, A. (2021) The environmental Kuznets curve hypothesis for Bangladesh: the importance of natural gas, liquefied petroleum gas, and hydropower consumption. Environmental Science and Pollution Research. 28(14), 17208-17227.

[6] Zhan, S. and Chong, A. (2021) Building occupancy and energy consumption: Case studies across building types. Energy and Built Environment. 2(2), 167-174.

[7] Ma, Y.X. and Yu, C. (2020) Impact of meteorological factors on high-rise office building energy consumption in Hong Kong: From a spatiotemporal perspective. Energy and Buildings. 228, 110468.

[8] Wagiman, K.R., Abdullah, M.N., Hassan, M.Y., Radzi, N.H.M. and Kwang, T.C. (2020) Lighting system control techniques in commercial buildings: Current trends and future directions. Journal of Building Engineering. 31, 101342.

[9] U.S. Department of Energy. (2015) Rise and shine: lighting the world with 10 billion LED bulbs. December 7, 2015. https://www.energy.gov/articles/rise-and-shinelighting-world-10-billion-led-bulbs. (Accessed 10 July 2021).

[10] Aqilah, N., Zaki, S.A., Hagishima, A., Rijal, H.B. and Yakub, F. (2021) Analysis on electricity use and indoor thermal environment for typical air-conditioning residential buildings in Malaysia. Urban Climate. 37, 100830.

[11] Zheng, T. (2020) Energy Consumptıon Analysıs of Green Town Public Buildings Based on Mathematical Regression Analysis Method. Fresen. Environ. Bull. 29(4a), 2792-2801.

[12] Doulos, L.T., Kontadakis, A., Madias, E.N., Sinou, M. and Tsangrassoulis, A. (2019) Minimizing energy consumption for artificial lighting in a typical classroom of a Hellenic public school aiming for near Zero Energy Building using LED DC luminaires and daylight harvesting systems. Energy and Buildings. 194, 201-217.

[13] Su, D., Casamayor, J.L. and Xu, X. (2021) An Integrated Approach for Eco-Design and Its Application in LED Lighting Product Development. Sustainability. 13(2), 488.

[14] Booysen, M.J., Samuels, J.A. and Grobbelaar, S.S. (2021) LED there be light: The impact of replacing lights at schools in South Africa. Energy and Buildings. 235, 110736.

[15] Gentile, N., Goven, T., Laike, T. and Sjoberg, K. (2018) A field study of fluorescent and LED classroom lighting. Lighting Research & Technology. 50(4), 631-650.

[16] Czyżewski, D. and Fryc, I. (2020) The Influence of Luminaire Photometric Intensity Curve Measurements Quality on Road Lighting Design Parameters. Energies. 13(13), 3301.

[17] Chen, M.J., Le, H.T., Le, L.T., Tseng, W.H., Lee, W.Y., Chen, S.Y. and Lee, H.Y. (2020) Design of Counter Beam Tunnel Lights for CIE 88: 2004 Regulation in Threshold Zone. International Journal of Optics. 6145638.

[18] Liao, H.Y., Chen, S.Y., Gao, W.L., Chang, F.C., Wen, C.C., Fang, Y.C. and Le, H.T. (2021) Design and Prototyping of Efficient LED Counter Beam Light with Free-Formed Surface for Meeting International Tunnel Lighting Standards. Energies. 14(2), 488.

[19] Loconsole, D., Cocetta, G., Santoro, P. and Ferrante, A. (2019) Optimization of LED lighting and quality evaluation of romaine lettuce grown in an innovative indoor cultivation system. Sustainability. 11(3), 841.

[20] Carli, R. and Dotoli, M. (2020) A dynamic programming approach for the decentralized control of energy retrofit in large-scale street lighting systems. IEEE Transactions on Automation Science and Engineering. 17(3), 1140-1157.

[21] Penning, J., Stober, K., Taylor, V., Yamada, M. (2014) Energy Savings Forecast of Solid-State Lighting in General Illumination Applications; Technical Report; U.S. Department of Energy: Washington, DC, USA.

[22] Phannil, N., Jettanasen, C. and Ngaopitakkul, A. (2018) Harmonics and reduction of energy consumption in lighting systems by using LED lamps. Energies. 11(11), 3169.

[23] Fryc, I., Czyżewski, D., Fan, J. and Gălăţanu, C.D. (2021) The Drive towards Optimization of Road Lighting Energy Consumption Based on Mesopic Vision-A Suburban Street Case Study. Energies. 14(4), 1175.

[24] Gorgulu, S. and Kocabey, S. (2020) An energy saving potential analysis of lighting retrofit scenarios in outdoor lighting systems: A case study for a university campus. Journal of Cleaner Production. 260, 121060.
[25] Ünlü, D.Y., and Şahin, N. (2021) High Energy Efficient and LED Lighting Vehicles in Lighting of Sports Halls. Bitlis Eren Üniversitesi Fen Bilimleri Dergisi. 10(1), 277-286.
[26] Wang, J.C. (2016) A study on the energy performance of school buildings in Taiwan. Energy and Buildings. 133, 810-822.
[27] Gamarra, A.R., Istrate, I.R., Herrera, I., Lago, C., Lizana, J. and Lechón, Y. (2018) Energy and water consumption and carbon footprint of school buildings in hot climate conditions. Results from life cycle assessment. Journal of Cleaner Production. 195, 1326-1337.
[28] Litardo, J., Palme, M., Hidalgo-León, R., Amoroso, F. and Soriano, G. (2021) Energy Saving Strategies and On-Site Power Generation in a University Building from a Tropical Climate. Applied Sciences. 11(2), 542.
[29] Zehra, F., Korkmaz, K.A. and Ahmeda, M.S. (2018) Sustainable Lighting System for University Buildings. Journal of Buildings and Sustainability. 1, 12-22.
[30] Aksaray University, Department of Construction and Technical Affairs. (2020) Annual Report for 2020. https://yapiisleri.aksaray.edu.tr/Faliyet-Raporu 13.06.2021 (Accessed 13 June 2021).
[31] Beccali, M., Bonomolo, M., Ciulla, G., Galatioto, A. and Brano, V.L. (2015) Improvement of energy efficiency and quality of street lighting in South Italy as an action of Sustainable Energy Action Plans. The case study of Comiso (RG). Energy. 92, 394-408.
[32] Campisi, D., Gitto, S. and Morea, D. (2018) Economic feasibility of energy efficiency improvements in street lighting systems in Rome. Journal of Cleaner Production. 175, 190-198.
[33] Perdahçı, C. (2018) Comparison of Led Lamp and Fluorescent Lamp in Metal Processing Plant Lighting. Fırat Üniversitesi Mühendislik Bilimleri Dergisi. 30(3), 105-113.
[34] Pulay, A. and Williamson, A. (2019) A case study comparing the influence of LED and fluorescent lighting on early childhood student engagement in a classroom setting. Learning Environments Research. 22(1), 13-24.
[35] Demir, H., Çıracı, G., Kaya, R. and Ünver, Ü. (2020) Energy Efficiency in Lighting: Yalova University Engineering Faculty Case Study. Uludağ University Journal of the Faculty of Engineering. 25(3), 1637-1652.
[36] Duman, A.C., and Güler, Ö. (2019) Techno-economic analysis of off-grid photovoltaic LED road lighting systems: A case study for northern, central and southern regions of Turkey. Building and Environment. 156, 89-98.

Received: **21.06.2021**
Accepted: **11.02.2022**

CORRESPONDING AUTHOR

Duygu Yigit Unlu
Graduate School of Natural and Applied Sciences,
Aksaray University,
68100 Aksaray – Turkey

e-mail: dyunlu68@gmail.com

© by PSP Volume 31– No. 05/2022 pages 4716-4724 Fresenius Environmental Bulletin

STUDY ON THE IMPROVEMENT OF TREE COMMUNITY TO OUTDOOR HUMAN WIND COMFORT

Xin Chen[1,2,*], Guangjun Gao[1,2]

[1]Key Laboratory of Traffic Safety on the Track of Ministry of Education, Central South University, Changsha Hunan 410075, China
[2]School of Traffic & Transportation Engineering, Central South University, Changsha Hunan 410075, China

ABSTRACT

With the continuous development of urbanization and the continuous growth of urban population, the urban environment is affected. An overheated environment will seriously affect the health of urban residents. The environment outside the building is the site most frequently used by urban residents, and finding ways to improve the environment outside the building has become the focus of recent research. The external environment characteristics of a building include related factors such as temperature, humidity, wind, and ambient radiation temperature. The changes of these factors not only depend on the spatial characteristics of the building itself, but are also closely related to the composition of the underlying surface surrounding the building. As an important part of the composition of the city, the tree community has a good effect on the improvement of the environment. Human comfort is an important index to evaluate the comfort degree of environment. This paper adopts the methods of field measurement and software analysis, and takes the tree community of the Olympic Forest Park as the research object to discuss the impact of the park tree community on human comfort. The research results show that during the high temperature period, the tree community has a certain cooling and humidification benefit relative to the surrounding environment. The maximum cooling intensity is 2.96°C, and the maximum humidification intensity is 8.34%. In addition, compared to the external environment of the park, the tree community could reduce the discomfort index.

KEYWORDS:
Tree community, city, environment, human comfort

INTRODUCTION

With the continuous growth of urban population and the continuous expansion of urban boundaries, the gradual conversion of the underlying surface of the city from natural to artificial, triggering a series of environmental problems. The benefits of urban heat islands result in a higher temperature in the urban environment than in the suburbs. The environment outside the building is the site most frequently used by urban residents, and finding ways to improve the thermal environment outside the building has become the focus of recent research [1]. The characteristics of the external thermal environment of the building include related factors such as air temperature, air humidity, and wind. The changes of these factors not only depend on the shape, structure, reflectivity and material of the building itself, but also on the surrounding underlays of the building [2]. The surface composition is closely related. An overheated environment will seriously affect human health. Extremely high temperature weather, especially continuous high temperature, will increase the mortality rate of the population. As an important part of the underlying surface composition, tree communities play a good role in improving the urban thermal environment through significant cooling and humidification effects [3-4].

Human comfort is a biometeorological index based on the principle of heat exchange between the human body and the near-earth atmosphere, to evaluate human comfort under different climatic conditions from a meteorological point of view. If the outdoor environment is too cold or too hot, it is not suitable for human metabolism, which will affect the normal work and life of human beings. Various countries have carried out research on human comfort for many years. In 1959, Thorn of the National Weather Service proposed the Discomfbrt Index (DI), which was widely used in summer comfort forecasting in the United States [5-6].

Different tree species have different cooling and humidification effects, so the discomfort measured under the tree is also different. Yan Hai conducted a research on 8 plant communities in Beijing and compared the effects of different plant communities on human comfort. The results showed that the 8 plants in the experiment can reduce the discomfort index to a certain extent compared with the control point, but the difference is not the same. Some scholars have studied and compared the cooling and humidification effects of 54 garden plants [7-8]. Finally, 14 species of trees, 5 kinds of shrubs, 5 kinds of herbaceous flowers and ground cover vegetation have better cooling and humidification effects. Scholars have also studied the cooling and humidification

benefits of white orchids and banyan trees with high canopy closure when the air temperature is 30°C. They found that each square meter of green coverage can cool the 10m thick atmosphere by 1.9°C and increase humidity by 3.3%, and can cool the atmosphere after 100m by 1.3°C and humidity by 2.4%. Different tree species have different cooling and humidification effects, so the discomfort measured under the tree is also different [9-10].

Greenbelt canopy structure has different characteristics such as total canopy coverage, total density, community importance value, and canopy closure. It has a certain regulating effect on the environmental temperature and humidity, thereby affecting the human comfort in the community [11]. Some scholars have studied the relationship between the structural characteristics of plant communities in Nanning and the local thermal environment and concluded that in tree-shaded land, the temperature decreases with the increase of the total canopy coverage, total density, and community importance of the plant community [12]. There is a significant negative correlation between them. In the gap, the stronger the light intensity, the higher the total average plant height of the plant community. However, the higher the wind speed, the smaller the average plant height.

In addition, the total canopy coverage decreases extremely significantly with the increase of the cooling effect value [13]. At the same time, the total density increases with the increase of the cooling effect value, especially the important value of the tree community and the cooling benefits, humidification benefits, and windshield. The effect values such as efficiency, shading benefit, etc. all show a very significant positive correlation. Some scholars used the temperature and humidity index to evaluate the human comfort of three different forest types in urban forests [14-15]. The results showed that in the summer and daytime, the three forest types have different degrees of cooling and humidification effects, but the role of birch forest is the largest. The highest cooling rate, and better comfort. Lin Ying conducted research on the community and human comfort in residential areas in Chongqing, and found that the plant communities in the green spaces of residential areas are beneficial to increase the comfort of the human body. Among them, the communities with large canopy closure can increase the comfort of the human body [16-17].

Some scholars have also combined human comfort with the green area or temporal and spatial distribution characteristics. Some researchers found that when the green area increases to a certain value, the increase in the area will not affect the comfort index, that is to say, the impact range is basically constant [18]. Other researchers found that human comfort has certain characteristics in temporal and spatial distribution, and it is closely related to topography and geographic elements. Different landform features affect the temperature, humidity and wind speed near the ground. Generally speaking, whether in winter or summer, areas with high vegetation coverage are more comfortable [19]. Coastal comfort is greater than inland areas, and wind speed plays a decisive role. Geographical factors related to human comfort mainly include road network density, altitude, and population density. Built-up areas and densely populated areas are more prone to thermal discomfort in summer [20].

However, through literature research, it is found that domestic research on the cooling effect of parks is often used to explain the mitigation of urban heat island effects, and is less integrated with human comfort. Taking the tree community of the Olympic Forest Park as the research object, we discuss the impact of the tree community on human comfort.

MATERIALS AND METHODS

(1) Research area. The Olympic Forest Park contains many tree communities and is located on Lincui Road, Chaoyang District, Beijing, which is 9,000 meters away from Tiananmen Square. The park occupies an area of 680ha, a green area of 478ha, a water surface of 67.7ha, and a green coverage rate of 95.61%. The Olympic Forest Park has a temperate continental semi-humid monsoon climate with four distinct seasons and concentrated precipitation. Spring is dry and windy, with a large temperature difference between day and night, the summer is hot and rainy, the autumn is sunny with little rain, which is suitable for cold and warm, and sufficient sunlight, and the winter is cold and dry, with more wind and less snow [21].

This experiment aims to explore the influence of tree communities on outdoor human wind comfort. Therefore, with the park as the center, a community is selected as the test site every 500m away from the park. Therefore, a total of 4 plots were selected for this experiment. In addition to the park as the control group, three plots were selected in the East District of Guo'ao Village, West District of Guo'ao Village, and Beijing Automation Engineering School. 12 measuring points were evenly arranged in each plot, totaling 48 measuring points. Then a total of 26 out-of-community control points were selected in the periphery of the 3 communities, with a total of 74 measurement points. In order to avoid the significant cooling effect caused by vegetation shadows and architectural shadows, all measuring points are arranged in a full-light environment, and there should be no large trees around the measuring points as much as possible.

(2) Measurement of environmental factors. A total of 4 environmental factors are measured, including air temperature, air relative humidity, and wind speed. The instrument used is TES-1314 anemometer. The measurement time is October 2017

and April 2018. The high temperature period of sunny and breezy weather is selected during the measurement, 13:00-15:00, and the atmospheric temperature reaches about 27°C. During the measurement, multiple people are used to measure at the same time to ensure that the time difference is small. In addition, a fixed temperature and humidity meter is used to measure the temperature and humidity of the day and used to correct other measurement data [22].

(3) Data processing and analysis. Using DI (Discomfort impact, discomfort index) index as the standard for evaluating comfort, the calculation formula is as Eq. 1:

$$DI = T - 0.55(1 - 0.01Rh) + （T - 14.5）\quad (1)$$

T is the air temperature (°C) and Rh is the relative humidity (%) of the air.

All samples are classified according to the distance to the park, and then we use SPSS software to perform one-way analysis of variance on the data to compare the differences between the groups. We calculate the correlation analysis between the park distance and each environmental factor, and establish the relationship between each factor and the distance to the park (Table 1).

(4) Simulation. The research uses FLUENT6.3 software to conduct a three-dimensional steady-state simulation of the outdoor wind environment in a residential area. 3D-CAD is used to model the project to be simulated. Some unimportant factors (such as unevenness on the surface of the building) are ignored when modeling, and the building is simplified to a cube with a regular shape. Although the simplified building will have a certain impact on the flow field around the building surface, it does not affect the parameter distribution in the mainstream field. The established geometric model is imported into the GAMBIT software, the geometric model is meshed and the boundary is set, the corresponding msh file is generated, and the FLUENT software is used for calculation and solution.

MATERIALS AND METHODS

(1) The impact of tree communities on the surrounding environment. In the spring and autumn seasons, when the atmospheric temperature reaches about 27°C, the tree community shows the benefits of cooling, humidifying and increasing wind relative to the surrounding environment, and this benefit is closely related to the distance of the tree community from the external environment. As shown in Figure 1, the abscissa represents the distance from the park's tree community to the external environment, and the ordinate represents the wind gain intensity of the park. On a street of 800m relative to the park, the average wind gain intensity of the park is 0.52m/s. On the street of 1200m to the park, the average wind gain intensity of the park is 0.98 m/s. On the street of 1600m to the park, the average wind gain intensity of the park is 1.53m/s.

TABLE 1
Discomfort index and feeling degree

Level	DI	Comfort intensity
1	<21.0	No one is uncomfortable
2	21.0-23.9	A small number of people feel uncomfortable
3	24.0-26.9	Many people feel uncomfortable
4	27.0-28.9	Most people feel uncomfortable
5	29.0-31.9	Almost everyone feels uncomfortable
6	>32.0	Risk of heat stroke

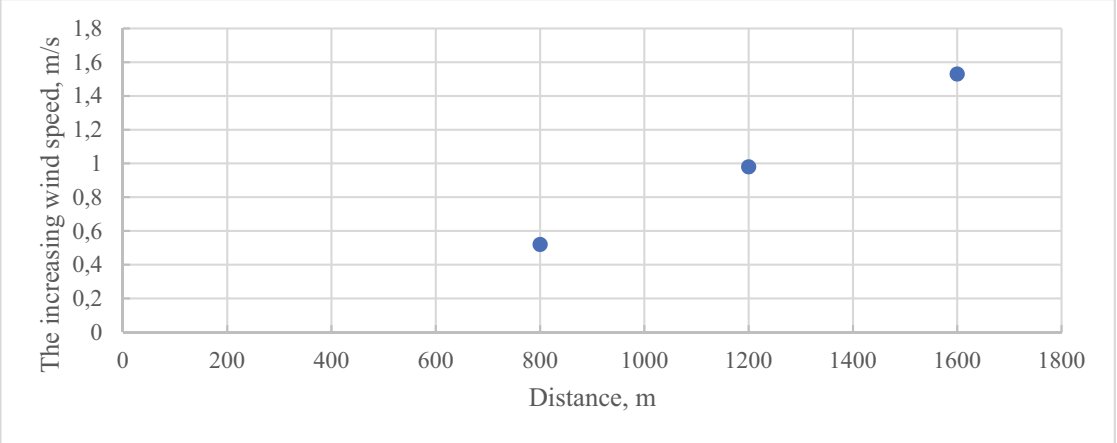

FIGURE 1
Park with respect to increasing wind strength of the external environment.

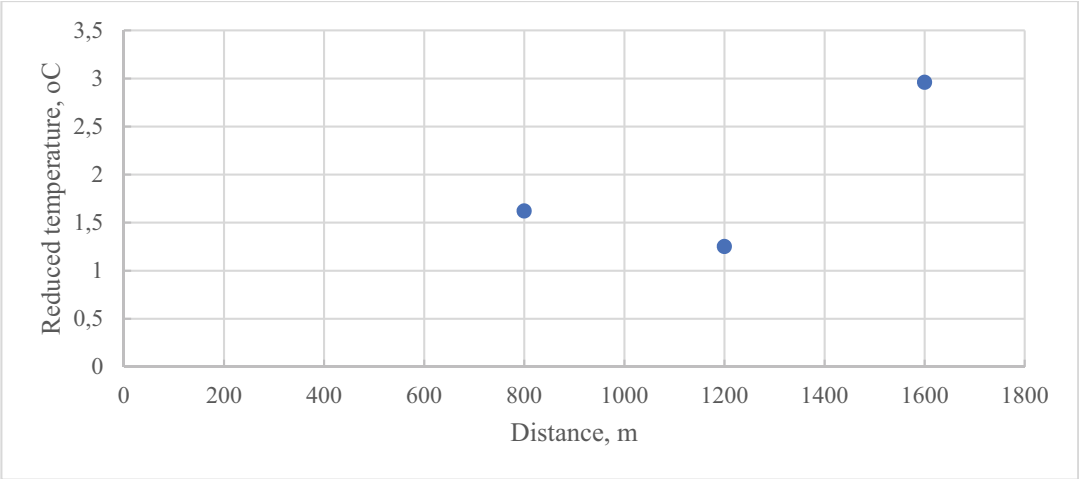

FIGURE 2
The cooling effect of the park relative to the external environment.

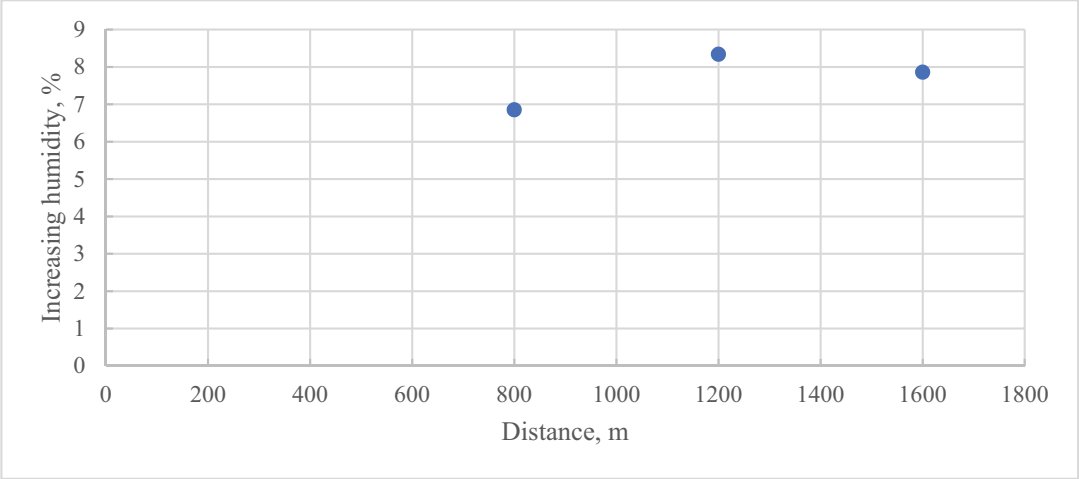

FIGURE 3
Humidification intensity of the park relative to the external environment.

TABLE 2
The correlation between the distance to the park and various environmental factors

	Wind speed	Temperature	Humidity	DI
Distance to the park	0.019	0.745**	-0.679**	0.656**
Sig.	0.925	0.000	0.000	0.000

Note: **. Means that the significance level is lower than 0.01, which means that the correlation is extremely significant; *means that the significance level is lower than 0.05, which means that the correlation is significant.

As shown in Figure 2, the abscissa represents the distance from the park to the external environment, and the ordinate represents the cooling intensity of the park. On a street 800m relative to the park, the average cooling intensity of the park is 1.62°C. On a street 1200m relative to the park, the average cooling intensity of the park is 1.25 °C, and the average cooling intensity of the park is 2.96 °C on a street 1600m relative to the park. As shown in Figure 3, the abscissa represents the distance from the park to the external environment, and the ordinate represents the humidification intensity of the park. On a street 800m relative to the park, the average humidification intensity of the park is 6.85%. On the street 1200m relative to the park, the average humidification intensity of the park is 8.34%, and the average humidification intensity of the park is 7.86% on the street 1600m relative to the park.

The correlation analysis between the various indicators of the 74 measuring points and the distance to the park shows that the temperature and the discomfort indexhave a very significant positive correlation with the distance. Humidity and distance show a very significant negative correlation (Table 2). There is no obvious correlation between wind speed and comfort index.

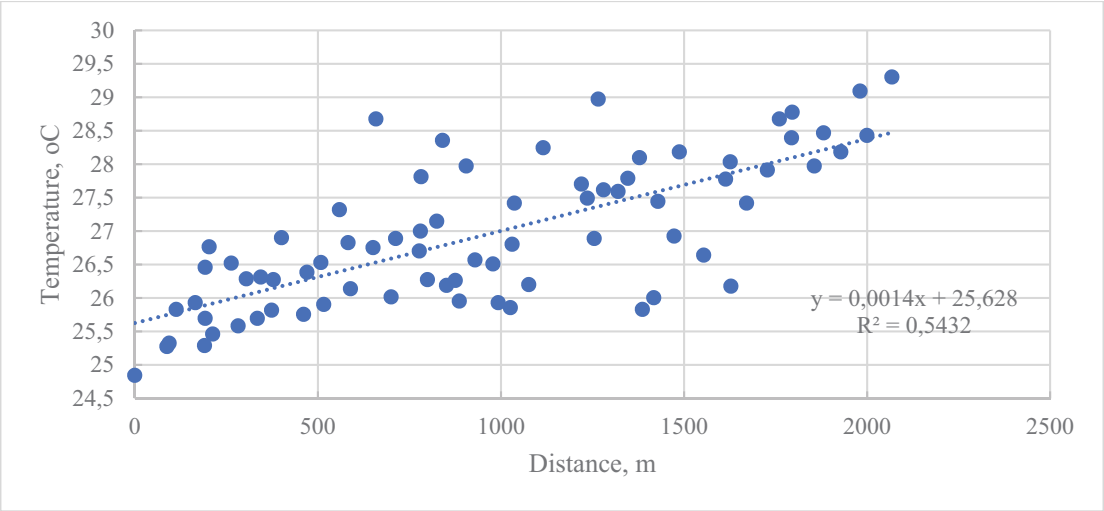

FIGURE 4
Unary regression scatter plot of temperature and distance.

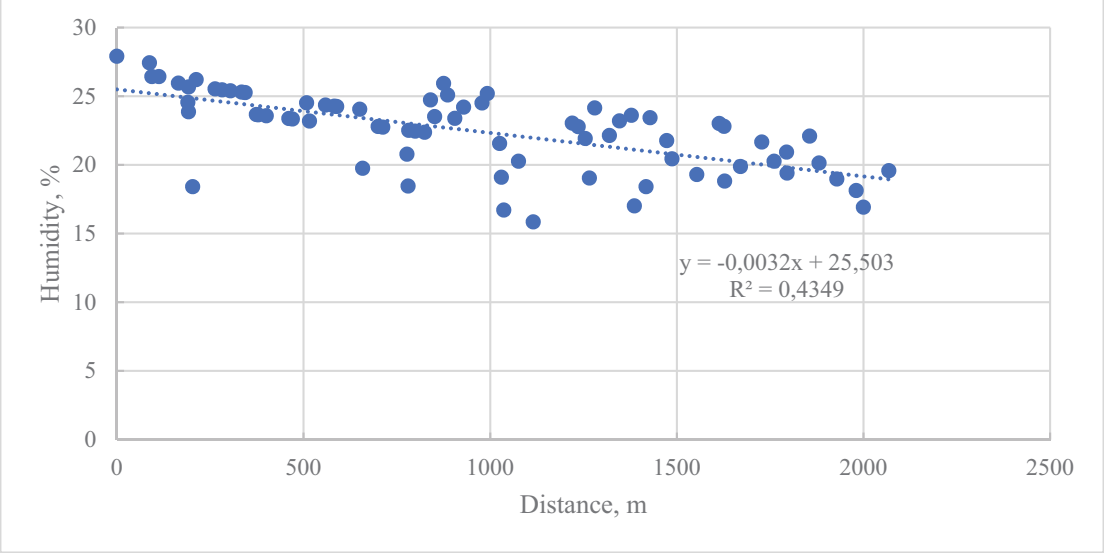

FIGURE 5
Unary regression scatter plot of relative air humidity and distance.

We use EXCE1 software to draw scatter plots of air temperature and relative humidity and distance to the park, add trend lines, and use SPSS19.0 software to perform unary regression analysis. The results are shown in Figure 4 and Figure 5. The regression equation is as Eq. 2 and Eq. 3:

$$T = 0.0014D + 25.628 \quad (2)$$

$$Rh = 0.0032D + 25.503 \quad (3)$$

In the formula, T is the air temperature (°C), D is the measuring point reaching the park, and Rh is the relative humidity of the air (%).

During the high temperature period of the measurement day, the average cooling intensity of the tree community was 1.94°C, of which the maximum cooling intensity was 2.96°C (compared to the sample point at a distance of 1600m from the park). This cooling intensity changes with the change of the reference point. If the reference point is farther from the park, the cooling intensity is greater, and vice versa. This is higher than Yan Hai's conclusion where he found that the maximum temperature drop of the tree community during the summer high temperature period is 1.8°C, and the average temperature drop is 0.6°C. The results are different which could be due to different distances. His measurement points are basically around 1000m in the park, and they are still within the scope of the park's cooling benefits. In this article, the measurement points outside the park are farther away. Wu Fei et al.'s research on green area and cooling intensity found that the cooling benefits of green areas above 5ha tend to be constant, and the maximum cooling intensity is about 3.2 degrees, which is slightly higher than the data obtained in this experiment. The reason may be that some of the measuring points in her study are located in the shade of trees, which will increase the cooling intensity of the park. In this experiment, the measuring points are all located in an open full-light area.

During the high temperature period of the

measurement day, the average humidification intensity of the tree community was 7.68%, of which the maximum humidification intensity was 8.34% (compared to the sample point 1200m away from the park). This humidification intensity changes with the change of the reference point. If the reference point is farther from the park, the humidification intensity is greater, and vice versa. This may be due to the large area of water in park, which leads to more water vapor evaporation in the park. Because of the large green area in the park, vegetation will have a certain degree of transpiration. Although the transpiration of vegetation on the measurement day will be less than in summer, the moisture in the soil will also have a certain evapotranspiration effect. In her research, Fei Wu found that the humidification intensity of green land with an area of more than 5 ha is between 4.3% and 5.6%, which is slightly lower than the maximum humidification intensity in this test. The reason may be that the water body in the park is larger. The amount of evapotranspiration is more, and the measuring point outside the park is farther away from the park in the cooling intensity. It is a measurement of the park's humidification intensity at a local scale, so the value will be slightly higher than the test value of Wu Fei and others.

During the high temperature period of the measurement day, the average wind gain intensity of the tree community was 1.01 m/s, of which the maximum wind gain intensity was 1.53 m/s (compared to the sample point at a distance of 1600 m from the park). Regarding wind speed, in this study, the wind speed in the park is the highest, reaching an average wind speed of 2.2m/s. This may be due to the fact that the selected spot in the park is close to the lake surface, and the specific heat capacity of water is greater than the specific heat capacity of impervious ground, and the temperature rises more slowly, resulting in temperature difference. The air will blow from the high-pressure area to the low-pressure area, so the wind speed at the water's edge will be higher. In addition, it may also be related to the surface roughness of the water and land. The surface roughness of the water body is low, so the velocity of the wind will increase slightly when the wind passes through the water body. This is similar to Xuan Chunyi's conclusion. The addition of water in summer can increase the wind speed in the downwind direction. The park will affect the surrounding environmental temperature through convection. In this study, it was found that the temperature of the measuring point has a very significant correlation with the distance to the park.

(2) The influence of tree community on human comfort. As shown in Figure 6, the abscissa represents the distance from the park to the external environment, and the ordinate represents the intensity of the park's discomfort index reduction (hereinafter referred to as DI reduction intensity). On a street 800 meters away from the park, the average DI of the park decreases with the intensity of 0.57. The average DI reduction intensity of the park is 0.18 on the street 1200m relative to the park, and the average DI reduction intensity of the park is 1.14 on the street 1600m relative to the park.

Since the discomfort index is closely related to temperature and humidity, the discomfort index and the distance from each measuring point to the park are analyzed by unary regression analysis and the EXCEL software is used to draw a scatter diagram. Figure 7 shows that the discomfort index is related to the distance to the park. And there is a positive correlation. The closer to the park, the lower the discomfort index and the higher the comfort level. The regression equation is as Eq. 4:

$$DI = 0.0006D + 21.021 \quad (4)$$

In the formula, DI represents the discomfort index, and D represents the distance from the measuring point to the park.

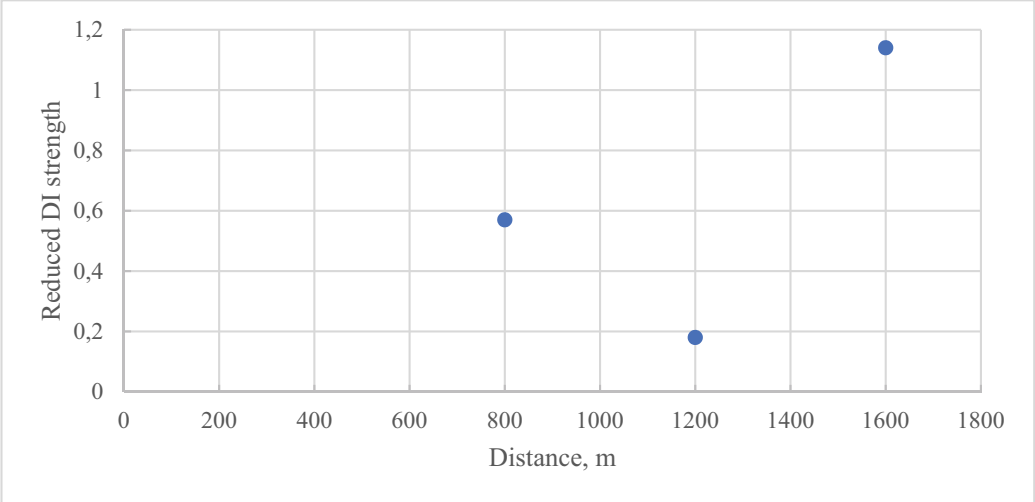

FIGURE 6
The intensity of the park's reduced DI index relative to the external environment.

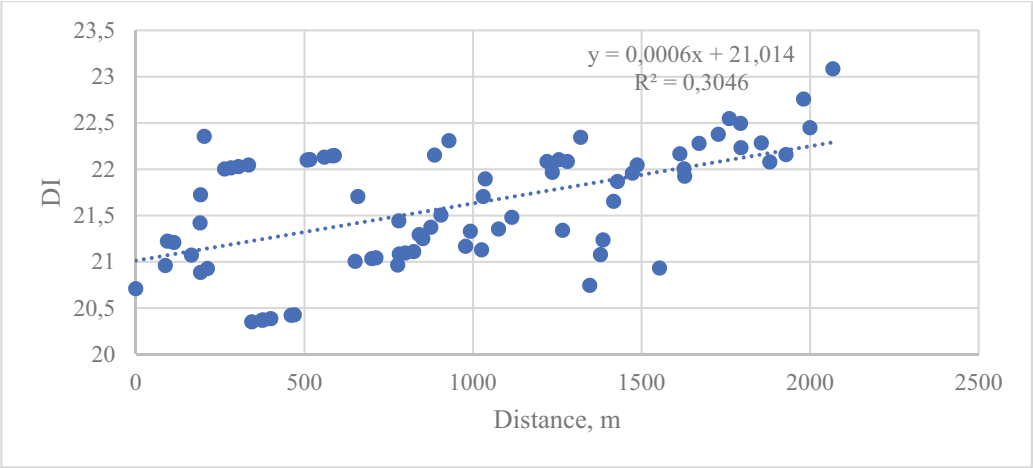

FIGURE 7
Univariate regression analysis of DI index and distance to the park.

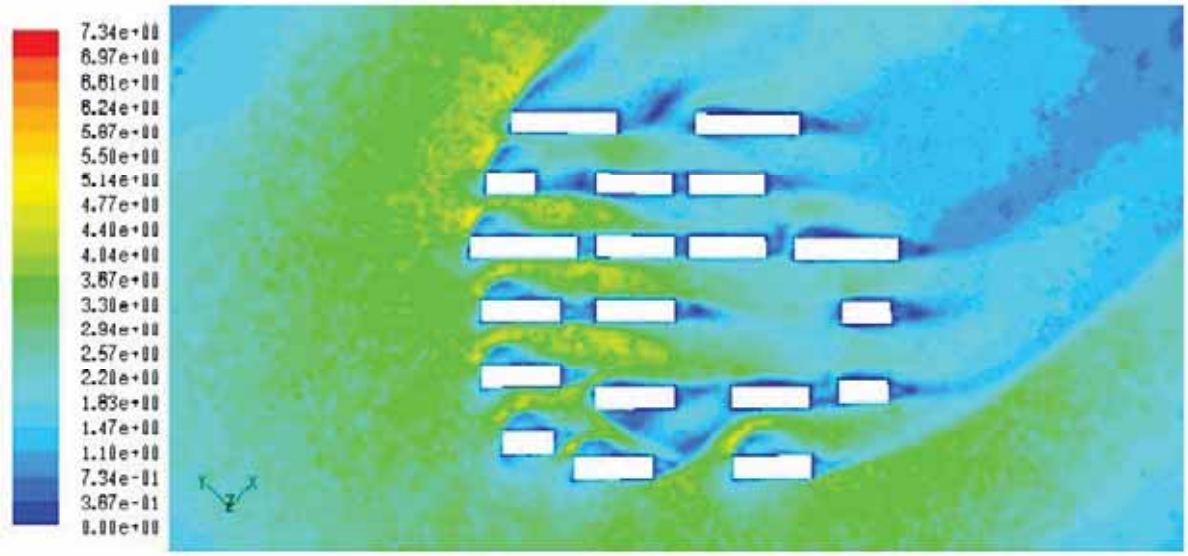

FIGURE 8
Simulation output of wind speed contours.

Due to its own cooling and humidification effect, the park also exhibits a certain effect of reducing the discomfort index during the high temperature period of the measurement day. The discomfort index in the park at 14:00 on the measurement day was 21.37, and the maximum discomfort index outside the park was 22.49. From Table 1, it can be seen that all of them belong to the range of discomfort felt by a small number of people, but they are different from the external environment of the park. In other words, the average reduction in discomfort index is 0.7, the maximum is 1.13, and the minimum can be reduced by 0.14. Since DI is affected by the combined effect of air temperature and relative humidity, and both temperature and humidity are closely related to the distance from the measuring point to the park, the DI index also has a significant correlation with the distance to the park when performing regression analysis. As the distance to the park increases, the discomfort index also increases.

(3) Simulation. The results of using Fluent software to simulate the wind speed of this district are shown in Figure 8. The experimental results show that the wind speed of the residential area is related to the distance from the tree community, which is consistent with the physical field test results.

CONCLUSIONS

(1) In this paper, when studying the impact of the tree community on the environment of the surrounding residential areas, the study is carried out when the temperature is higher at the end of spring. The results show that during the high temperature period of the measurement day, the average cooling intensity of the tree community is 1.94°C, of which the maximum cooling intensity is 2.96°C (compared to the sample point at a distance of 1600m from the park).

(2) The average humidification intensity of the tree community is 7.68%, of which the maximum

humidification intensity is 8.34% (compared to the sample point 1200m away from the park). Due to its own cooling and humidification effect, the park also exhibits a certain effect of reducing the discomfort index (DI) during the high temperature period in autumn. Compared with the external environment of the park, the average reduced discomfort index is 0.63 and the maximum is 1.14. Communities closer to the park have higher levels of comfort.

(3) In the research of this paper, all data are measured by actual measurement, the air temperature and humidity are constantly changing, and the wind speed is also somewhat random. Although various data adjustments have been made, there will still be errors. In addition, due to the difference in the basic environment between different communities, the different building materials and plant types, the materials of the impermeable ground, and the different reflectivity, etc., it will cause test errors and lead to low R^2 in the regression equation. Human comfort is a comfort index based on human feelings. The comfort indexes used in this test are all comfort indexes based on human skin feeling, and human feelings are more comprehensive feelings, not only including the cold and hot feelings of the skin, if we can combine people's visual and psychological feelings, we may get more conclusions about garden design.

ACKNOWLEDGEMENTS

This work was not supported by any funds. The authors would like to show sincere thanks to those techniques who have contributed to this research.

REFERENCES

[1] Ji, W., Zhao, B. (2014) Numerical study of the effects of trees on outdoor particle concentration distributions. Building Simulation. 7(4), 417-427.

[2] Gao, Y., Yao, R., Li, B., Turkbeyler, E., Luo, Q., Short, A. (2012) Field studies on the effect of built forms on urban wind environments. Renewable Energy. 46, 148-154.

[3] Yin, J.F., Zheng, Y.F., Wu, R.J., Tan, J.G., Ye, D.X., Wang, W. (2012) An analysis of influential factors on outdoor thermal comfort in summer. International Journal of Biometeorology. 56(5), 941-948.

[4] Shih, W.M., Lin, T.P., Tan, N.X., Liu, M.H. (2017) Long-term perceptions of outdoor thermal environments in an elementary school in a hot-humid climate. International Journal of Biometeorology. 61(1), 1-10.

[5] Rutty, M., Scott, D. (2015) Bioclimatic comfort and the thermal perceptions and preferences of beach tourists. International Journal of Biometeorology. 59(1), 37-45.

[6] Jamei, E., Rajagopalan, P., Seyedmahmoudian, M., Jamei, Y. (2016) Review on the impact of urban geometry and pedestrian level greening on outdoor thermal comfort. Renewable & Sustainable Energy Reviews. 54, 1002-1017.

[7] Katavoutas, G., Flocas, H.A., Matzarakis, A. (2015) Dynamic modeling of human thermal comfort after the transition from an indoor to an outdoor hot environment. International Journal of Biometeorology. 59(2), 205-216.

[8] Pantavou, K., Chatzi, E., Theoharatos, G. (2014) Case study of skin temperature and thermal perception in a hot outdoor environment. International Journal of Biometeorology. 58(6), 1163-1173.

[9] Leng, H.B., Yong-Hong, H.U., Zhou, X., Liu, W.W., Sun, C.J., Lian, Z.W. (2012) Effect of outdoor vegetation on human comfort and environmental satisfaction. Journal of Central South University (Science and Technology). 43(11), 4574-4580.

[10] Wu, F., Yang, X., Shen, Z. (2019) Regional and seasonal variations of outdoor thermal comfort in China from 1966 to 2016. Science of the Total Environment. 665, 1003-1016.

[11] Dmitry, B., Yaakov, G., David, P. (2018) The influence of climatocultural background on outdoor thermal perception. International Journal of Biometeorology. 62, 1873-1886.

[12] Imagawa, H., Rijal, H.B., Shukuya, M. (2016) Field survey on the comfort temperature and occupant behaviour in bedrooms. Journal of Environmental Engineering. 81(728), 875-883.

[13] Feng, Z., Ji, S., Zhu, J., Qian, Z., Yang, J. (2018) Study on the influence of semiconductive property for the improvement of nanogenerator by wave mode approach. Nano Energy. 52, 474-484.

[14] Zheng, S., Sun, G., Wang, P., Liu, Z., Jiang, J., Liao, X. (1994) Study of the improvement on the property and working life of freeman source. Review of Scientific Instruments. 65(4), 1329-1330.

[15] Fan, Z., Li, J., Li, C., Ma, K. (2005) Study on improvement of the laser uniformity transformation of over lapping-image waveguide cavity. Chinese Optics Letters. 3(1), 24-27.

[16] Huang, J. (2007) Prediction of air temperature for thermal comfort of people in outdoor environments. International Journal of Biometeorology. 51(5), 375-382.

[17] Vanos, J.K., Warland, J.S., Gillespie, T.J., Kenny, N.A. (2010) Review of the physiology of human thermal comfort while exercising in urban landscapes and implications for bioclimatic design. International Journal of Biometeorology. 54(4), 319-334.
[18] Mahmoodi, T., Iravani, M.R. (2012) Determination of bioclimatic comfort in Sirjan desert. Management Science Letters. 2(3), 769-774.
[19] Ono, T., Murakami, S., Ooka, R., Omori, T. (2008) Numerical and experimental study on convective heat transfer of the human body in the outdoor environment. Journal of Wind Engineering & Industrial Aerodynamics. 96(10-11), 1719-1732.
[20] Stathopoulos, T., Wu, H., Zacharias, J. (2004) Outdoor human comfort in an urban climate. Building & Environment. 39(3), 297-305.
[21] Honjo, T. (2009) Thermal comfort in outdoor environment. Global Environmental Research. 13(1), 43-47.
[22] Nagano, K., Horikoshi, T. (2011) New index indicating the universal and separate effects on human comfort under outdoor and non-uniform thermal conditions. Energy & Buildings. 43(7), 1694-1701.

Received: **08.07.2021**
Accepted: **08.02.2022**

CORRESPONDING AUTHOR

Xin Chen
Key Laboratory of Traffic Safety on the Track of Ministry of Education,
Central South University,
Changsha Hunan 410075 – China

e-mail: 2519933021@qq.com

© by PSP Volume 31– No. 05/2022 pages 4725-4733 Fresenius Environmental Bulletin

APPLICATION OF RAINWATER HARVESTING TO MUNZUR UNIVERSITY CAMPUS AND EXAMINATION OF CONTRIBUTIONS

Meral Korkmaz*

Civil Engineering, Faculty of Engineering, Munzur University, Tunceli, Turkey

ABSTRACT

The world is facing drought, and over time, water problems are becoming more serious. Agricultural land and green areas are gradually declining due to water scarcity. While the amount of available water is gradually decreasing, people's unnecessary use of water and water consumption are increasing. This, in turn, requires the accurate use of existing water resources and the realization of intelligent building systems as soon as possible. Despite this fact, none of the university's public buildings currently use systems such as the rainwater harvesting technique. The main aims of this research are to find effective results in terms of savings and to contribute to avoiding water shortages in the future.

It is important today to immediately begin making future housing with these systems and to integrate these intelligent systems into public buildings, especially incorporating the latest technologies. In this study, the advantages of zero-energy built roofs and rainwater harvesting systems on the Munzur University campus are evaluated.

KEYWORDS:
Rainwater Harvesting, Rainfall, Water storage, Trend analysis, Şen method.

INTRODUCTION

Unlike many of the techniques used today, rainwater harvesting (RWH) is not a new technique. It has been practiced by the people of Ur, the Nabataeans, and other peoples of the Middle East for 4,500 years. However, with the increasing population and urbanization, the need for water is increasing, and rain harvesting is needed. With the increasing need for water in urban areas, many studies have been carried out regarding the continuity and effective use of water resources. As global warming in the world manifests itself in a serious way, rainwater collection systems for the effective use of water have begun to stand out [1]. Harvested rainwater can be used in many applications that do not require potable water, such as garden irrigation, greenhouse, cultivation and agricultural cleaning. Further, harvested rainwater can be used as drinking water with the implementation of purification processes [2].

The use of rainwater by storing it in a tank before using it for various purposes is called rainwater harvesting. This system is widely used in most regions of the world that are experience suitable climatic conditions. The RWH system is generally used for indoor water use, agriculture, and environmental management. Generally, rainwater harvesting increases demand for RWH systems. Additionally, water consumption is increasing, and the need for water resources is increasing with climate change. Along with urbanization, green areas are reduced and reinforced, underground aquifers are blocked, streams are changed, and floods occur in short green areas. For this reason, little rain can be mixed into groundwater. As a result, there is also a large reduction in groundwater. By storing and using existing rainwater, a rainwater harvesting system can also reduce floods and drought, resulting in significant savings in air and soil moisture balance as well as in water-related energy consumption and greenhouse emissions. In addition to the positive environmental effects of RWH systems, there are many economic benefits to be gained by reducing water consumption in urban areas [3, 4, 5, 6]. Rainwater harvesting is also an easy and economical farming practice for regional farmers [7].

RWH systems consist of a roof with an impermeable surface, a storage tank (storage volume), and a transport system between the roof and the tank [3]. The only downside to RWH systems is that large water volumes of conditions of irregular rainfall may necessitate the use of a large water tank. It can also be difficult to install RWH roofs, and the quality of rooftop RWH represents another challenge. The collection, storage, and subsequent use of rainwater from roofs is a simple way to reduce the demand for both public water supplies and waste treatment plants. Rainwater tank capacity is one of the most important design parameters affecting system performance and cost. Therefore, a RWH system must be carefully considered and designed to provide appropriately-valued storage capacity in accordance with its location [8]. A large size tank may be a waste of resources (energy, time and money), while a small size tank may not be able to meet the required water

demand. Therefore, the needs of households, the characteristics of geographical locations, and the amount of precipitation are taken into account when designing a RWH system [9]. System design and planning in the RWH system are important in terms of affecting the initial investment cost and the repayment period of the system. Choosing a storage volume and a storage method suitable for the system reduces the initial investment cost of the request while increasing the operating rate as planned. With the right components, treatment technology, and location, the RWH system can reduce the water consumption of buildings by up to 40% [3].

Calculations were made by using precipitation data and roof areas measured during the RWH system design process for rainwater harvesting that can be obtained from the roof at the Munzur University Aktuluk campus, which has hard floor and roof surfaces in a high area. The aim of this study is to estimate the potential contribution of rooftop RWH to meet the drinking water demands of large public institutions and to establish links between rainwater harvesting, campus-level consumption, and individual consumption at an individual institution.

In this study, the precipitation data obtained from the Meteorology directorate were analyzed statistically. The return times of precipitation data are calculated by many researchers as in equations 1, 2 and 3 [10]:

$$P = \frac{m}{n} + 1 \text{ (Weibull)} \quad (1)$$

$$P = \frac{m-0,3}{n+0,4} \text{ (Chegodayev)} \quad (2)$$

$$P = \frac{m-0,5}{n+1} \text{ (California)} \quad (3)$$

All three equations are used in the probabilistic analysis of annual precipitation values. The annual precipitation values are arranged in descending order, and the probability of each annual precipitation value is calculated via the Weibull equation. Regarding notation:

P: Probability of each annual precipitation value;

N: Number of years in the time series;

m: Rank of annual precipitation rate value relative to all values included in the time series.

In this context, determining the appropriate storage volume and storage method when planning a RWH system for application in a structure is an important decision that needs to be made in the design stage of the system.

Because public institutions, such as universities, take up sizable roof areas, they can provide a great water yield and lead the way in bringing applications to the city level. At the same time, they can be an example of a change in practice that can eventually reach the roofs of houses and private institutions.

MATERIALS AND METHODS

Study Area. In this study, the rainwater harvesting system is located in the province of Tunceli (Aktuluk Campus), Turkey. Its geographical coordinates are 39° 02' 44" North, 39° 31' 02" East. Tunceli province is located in the Eastern Anatolia region of Turkey. Munzur University campus is in a location between a large creek and the Munzur River, as seen in Figure 1. The total campus area is 747013 m^2. The climate is harsh, and the average daily temperature is 13 ˚C. The water source of the city is provided from the dinar creek. Water is delivered from the Dinar Stream to the 500-ton warehouse in the campus with a submersible pump. Campus irrigation is done with two hydrophores. However, in recent years, due to the high rate of urbanization combined with industrial development, population growth, and a change in precipitation patterns, the water available to meet the water demand has decreased rapidly [11].

This study aims to investigate the potential amount of rainwater that can be collected from the roofs of the campus buildings for the irrigation of the green areas in Munzur University and also to determine the usability of harvested rainwater to meet the need for green area irrigation. The amount of rainwater that can be collected from the building roof surfaces is determined. Data measured over the past 60 years by precipitation measurement stations located around the study area were collected, and it was seen that the average annual precipitation amount was 876.7 mm. In the calculation of the water requirement of the green areas, the amount of water required for each irrigation was assumed to be 6 lt/m^2 [12].

Munzur University is an ideal example for which to study water conservation and rainwater harvesting measures, as the university experiences occasional water cuts. With the current study, an additional warehouse can be built for the university, and the water problems of appliances such as sinks and closets can be solved in the event of a water cut.

Rooftop Rainwater Harvesting. The data on the total roof area for the Aktuluk campus, where water conservation and rainwater harvesting will be carried out at Munzur University, were obtained from the Department of Construction. In this study, the total roof area of the university was calculated from the site plan of Munzur University Aktuluk Campus, shown in Figure 1, and the potential amount of harvestable rainwater was calculated. Table 1, Aktuluk Campus physical area is approximately 653,335 m^2. There are 13 completed buildings within the campus area, and the majority of the areas outside the buildings are green areas and roads.

Munzur University's total physical area information is given in Table 1. The RWH system will be applied to the Central Aktuluk campus area. Due to the facts that the study area of Munzur University

shown in Figure 1 is large and that there are buildings and green areas within the area, the current study area is divided into 10 separate parts (Figure 1). Each section area is given separately in Table 3.

Rainfall Data Analysis. The monthly averages of daily total rainfall values and their corresponding coordinates in the Tunceli province for the years 1980-2021 were obtained from the General Directorate of Meteorology. Considering the average values of past years in Table 4, the longest sun duration in the Tunceli province was 8.7 hours in July. In the table, the temperature and rainfall data for the Tunceli province are also given. The average temperature is 14.7 °C, and the average total rainfall is 876.7 mm.

FIGURE 1
Munzur University Aktuluk Campus

TABLE 1
Munzur University total physical area information (m^2)

Central / Districts	Closed area	Open area	Total (m^2)
Merkez	66567	586768	653335
Çemişgezek	1415	981,41	2396,41
Pertek	4486	81501	85977
Hozat	1589	1826	3415
Pülümür	1050	830	1880
Total (m^2)	75107	671906,41	747013

TABLE 2
Extreme maximum, minimum, average temperatures and radiation measured in long period [13]

Measurement Period (1960- 2020)	Jan	Feb	Mar	Apr	May	Jun	Jul	Aug	Sep	Oct	Nov	Dec	Annual
Average temperature (°C)	-2	-0.2	5.6	11.7	16.8	22.4	27.1	26.7	21.6	14.4	6.8	1	12.7
Average High Temperature (° C)	3	5	11.3	18.1	24	30.1	35.1	35.4	30.6	22.8	13.6	5.7	19.6
Average Lowest Temperature (°C)	-5.5	-4.1	1	6.2	10.2	14.5	18.9	18.5	13.4	8.2	2	-2.3	6.8
Average Sunbathing Duration (hours)	3.4	4.3	5.3	6.5	8.4	10.8	11.6	10.8	9.3	6.7	5	3.1	7.1
Average Rainy Number of Days	11.7	11	13.6	14.8	13.9	6.2	2.1	1.9	3.5	9.6	9.6	11.8	109.7
Highest Temperature (° C)	14.2	19.4	26	32.2	36.6	39	43.5	43.5	40.3	35.6	27	21.7	43.5
Lowest Temperature (°C)	-30.3	-29	-24.7	-7.1	-0.1	1	9.2	7.7	2.6	-4	-16.4	-25.6	-30.3
Monthly Total Precipitation Average Amount (mm)	130.6	107.4	113.9	106.5	72.7	18.2	5	4.7	16.7	62.8	101.4	136.8	876.7

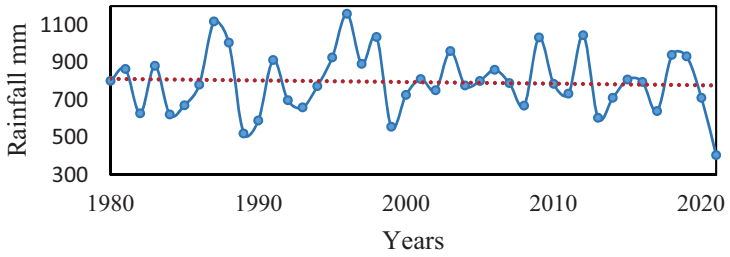

FIGURE 2
Average annual precipitation data for the 1980-2021 period

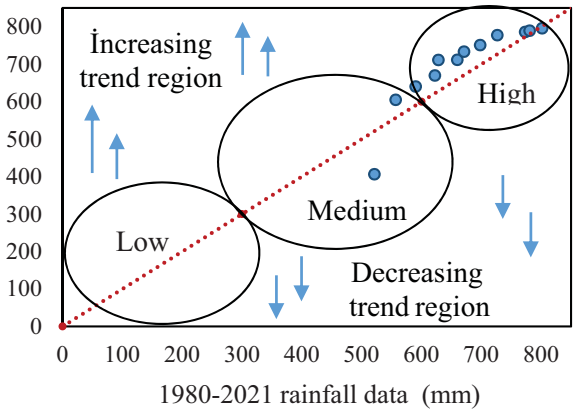

FIGURE 3
Annual average rainfall data for the 1980-2021 period Şen Method

The annual average rainfall data for the 1980-2021 period are taken from the General Directorate of the DMI. Looking at the trend of 42-year precipitation data in Figure 2, it is clear that the rainfall trend is variable. However, the average amount of rainfall has increased over time. This shows that the amount of rainfall will increase in the following years.

Figure 2 shows the changes in annual precipitation depth. The highest annual precipitation depth of 1159 mm was seen in 1996, and the lowest precipitation amount of 521 mm was seen in 1989. The collection and storage of rainwater will help ensure sustainability in the supply of water for domestic and other uses, given the seasonal variation of precipitation.

Trend analysis provides a view for meteorological, hydrological, and climatic variables as they relate to past and future time changes. Many researchers have used the Sen method in their work to determining trends in hydrological and meteorological variables [14, 15]. In this study, the Şen method was used to investigate the future trend of annual average rainfall in the Tunceli province. Before applying trend methods, the serial correlation was looked at to investigate whether the data were serially dependent. The Şen method was applied to the annual average rainfall data collected by meteorological stations between the years 1980 and 2021.

The annual average rainfall data for the 1980-2021 period were divided into two equal halves from the median year. Both sub-series were individually sorted from small to large. After that, the first sub-series (X_i) was sorted along the x-axis, and the second sub-series (X_j) was sorted on the y-axis of a Cartesian coordinate system. If the data are located along the 1:1 line, there is no trend. If the data are located in the lower triangle area of the 1:1 line, a decreasing trend is implied. If the data are located in the upper triangle area, it can be said that there is an increasing trend. The innovative feature of Şen's method can be interpreted over all data ranges [16, 17]. The average annual rainfall trend directions are given in Figure 3, according to the Şen trend analysis method. Clusters (low, medium, and high) providing visual results and trends in precipitation are also shown in the figure. A high trend is observed in the annual total rainfall parameter.

TABLE 3
Total Number of Buildings and Roof Area

Build	Aktuluk Campus	Total Construction Area (m^2)	*A* Total Roots Area (m^2)	*R* Average Rainfall (mm)	Total amount of rainwater collected from the roof of the university (m^3)	*CV*
1	Administrative Units Building	4745	1392	876.7	933.58	0.93
2	Ar-Ge Lab. Building	9699	2667.6	876.7	1789.09	1.79
3	Education Instructor. Building	7648	2439.4	876.7	1636.05	1.64
4	English Preparatory School Building	8994	2545.6	876.7	1707.27	1.71
5	Faculty of Engineering	11016	2765.3	876.7	1854.62	1.85
6	Housing Block A,B,C,D	1173*4	1164	876.7	780.67	0.78
7	Rector Administration Building	3132	1194.88	876.7	801.38	0.80
8	Home Rector	548	422	876.7	283.03	0.28
9	Central Cafeteria Building	4450	1750.4	876.7	1173.95	1.17
10	Indoor Sports Hall	3306	2353	876.7	1578.10	1.58
	Total	**58898**	**18694,18**		**12537.73**	

TABLE 4
42 years of total precipitation for analysis

m	Year	R mm	P(%)	m	Year	R mm	P(%)	m	Year	R mm	P(%)	m	Year	R mm	P(%)
1	1996	1159.5	1.5	12	1997	892	27.5	23	1986	780.8	53.6	34	1993	659.9	79.6
2	1987	1118	3.8	13	1983	881.7	29.9	24	2004	777.2	55.9	35	2017	640.4	82.0
3	2012	1045.2	6.2	14	1981	865	32.2	25	1994	773.3	58.3	36	1982	628.3	84.3
4	1998	1035.6	8.6	15	2006	860.7	34.6	26	2002	751	60.7	37	1984	622.5	86.7
5	2009	1032.6	12.8	16	2001	811.3	37.0	27	2011	733.2	63.0	38	2013	604.9	89.1
6	1988	1005.3	13.3	17	2015	808.7	39.3	28	2000	726.7	65.4	39	1990	590.2	91.4
7	2003	960.6	15.7	18	1980	801.6	41.7	29	2014	711.6	67.8	40	1999	556.9	93.8
8	2018	939.9	18.0	19	2005	801.2	44.1	30	2020	711.3	70.1	41	1989	521.2	96.2
9	2019	932.1	20.4	20	2016	795.8	46.4	31	1992	698.2	72.5	42	2021	405.9	98.5
10	1995	925.9	22.8	21	2007	789.4	48.8	32	1985	671.1	74.9				
11	1991	912.8	25.1	22	2010	785.8	51.2	33	2008	669.8	77.2				

Statistical variability. Monthly precipitation and annual precipitation (mm) were expressed as coefficients of variation (*CV*) using Eq. 4 [8]:

$$CV = \frac{Sd}{Mr} * 100 \quad (4)$$

where *CV* represents monthly, seasonal, or yearly coefficients of variation, *Sd* represents a mean monthly, seasonal, or yearly standard deviation, and *Mr* represents a monthly, seasonal, or yearly precipitation average.

Mean annual rainwater harvesting. For this study, the rainwater harvesting potential was calculated using the monthly balance approach. The mean monthly harvestable rainwater (Q_m), the mean monthly average rainfall (*R*), and the catchment areas of the roofs (*A*) were calculated as a function of the product of the percentage of roof area used for rainwater harvesting (β = 0.5 to represent 50% usage) and the runoff coefficient (*C*), as given in Eq. 5. The average rainfall "*R*", dependent roof area "*A*" as well as gutter and collection system leakage and overflow can be mathematically combined to representing a yield efficiency coefficient "β, C":

$$Q_m = R * A * \beta * C \quad (5)$$

The value of the runoff coefficient ranges between 0.80 to 0.9 for each building's roof top, each of which was constructed from concrete cement materials [17, 18, 19, 20, 21, 22]. The runoff coefficient of 0.85 was employed to account for evaporation loss and a possible first flush of the rooftop.

As shown in Table 2, although there are 13 completed buildings, there are buildings under construction within the campus. While the total area of the buildings in the campus is 58,898 m^2, the total roof area is 18694.18 m^2.

The Effect of Precipitation. A simple graphical method will be used to determine the probability and frequency of annual precipitation occurrence. It is first necessary to obtain annual precipitation totals from the relevant area. Where precipitation records are not available, data from nearby stations can be used with caution. It is important to obtain long-term records. Since the variability of precipitation in arid and semi-arid regions is important, the analysis was performed using long-term precipitation data. The annual totals in Table 4 are listed as m = 1 for the

largest value and m = 42 for the lowest value, and the data have been rearranged accordingly [23].

Finally, a curve is placed on the drawn observations such that the distance of the observations above or below the curve should be as close to the curve as possible (Figure 4). The curve can be a straight line. From this curve, it is also possible to obtain the probability of occurrence or exceedance of a precipitation value of a certain magnitude and to obtain the magnitude of the precipitation corresponding to a particular probability.

In the example above, the annual precipitation with a 67 percent chance of occurring is 680 mm (Figure 4). So, annual precipitation equals or exceeds 680 mm, 67 percent of the time (2 years out of every 3 years, on average). For a probability of exceedance of 33 percent, the corresponding value of the yearly rainfall is 900 mm (Figure 4).

The return period T (in years) can be obtained from the Eq. 6, since the probability of exceeding P (%) is known, and an example calculation is provided in Eq. 7-8:

$$T = \frac{100}{P} \ (years) \tag{6}$$

$$T_{67\%} = \frac{100}{67} = 1{,}5 \text{ years} \quad 680 \text{ mm} \tag{7}$$

$$T_{33\%} = \frac{100}{33} = 3 \text{ years} \quad 900 \text{ mm} \tag{8}$$

Here, on average, annual precipitation of 900 mm or more can be expected in just 1 year out of 3 years.

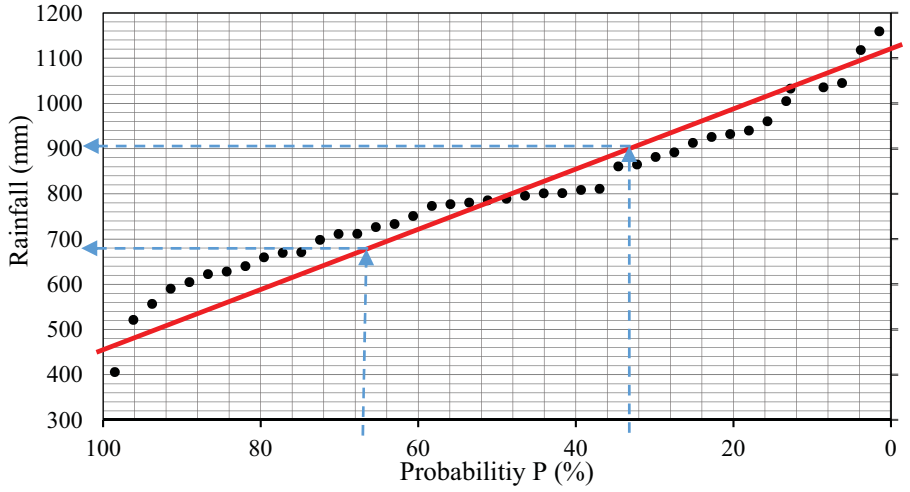

FIGURE 4
Regression line probability diagram for the observed annual precipitation total series

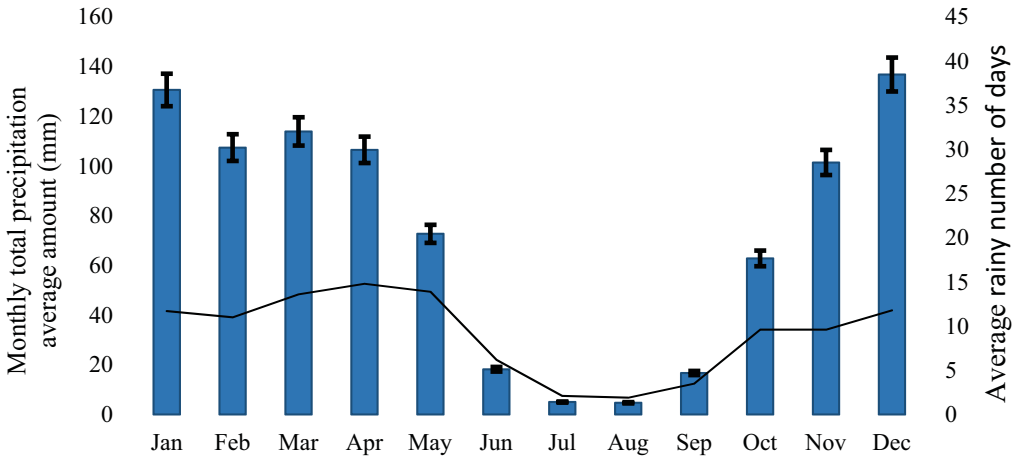

FIGURE 5
60 years (1960–2020), monthly mean precipitation depth (*R*), standard deviation (I), and average number of rainy days in the Tunceli province

RESULTS AND DISCUSSION

In this study, the Munzur University campus was evaluated to investigate the potential contribution of loft RWH from major public institutions. The roof areas of the buildings in the region were calculated, and the amount of rainwater to be collected from each building was calculated using the monthly precipitation data obtained from the Tunceli Regional Directorate of State Meteorology Affairs.

The monthly precipitation amount and the number of rainy days in the Tunceli province are shown in Figure 5. While precipitation depths of 106.5 and 76.7 mm were recorded in April and May, precipitation depths of 5 and 4.7 mm were recorded in July and August. From this, it can be seen that there is a high variability in the distribution of precipitation. Further, changes are expected in the distribution of future precipitation due to climate change. Given the fact that central water reservoirs are vulnerable to prolonged drought and climate change, roof rainwater harvesting can help reduce the vulnerability of the water supply in urban areas [24].

As seen in Table 3, harvested rainwater from the roofs of large public institutions such as universities corresponds to 12,537 m^3 of water. Institutions can use their own water resources in January and December when precipitation is abundant, and they can also store excess rainwater for later use. During the dry months (June to September), they can replenish their water supply via rooftop RWH, which saves irrigation water for institutions. This provides a maximum water requirement of 12537 m^3 during rainy months if each of the major public institutions is included in the roof RWH.

With rainwater harvesting, available water resources can contribute to minimizing water shortages, as current systems cannot withstand the long dry months and climate change. In addition, RWH will reduce the pressure on groundwater resources, as a significant amount of rainwater can be collected from roofs, which can result in potable water savings.

Many existing RWH systems are focused solely on conserving water without considering the other potential benefits associated with the multipurpose nature of RWH. RWH benefits many applications, including water conservation, storm water management, energy consumption management, and greenhouse gas management. However, improved modeling of these benefits is needed [25]. More work is needed to assess the cost and payback time of RWH, and low-cost systems need to be developed.

The role of maintenance on system performance has been established, though further research is needed on how system reliability can be improved. Such findings would allow for increased system uptake. It would also be helpful for the government to support new RWH projects.

The contribution of RWH to the monthly water consumption of the campus area is shown in Figure 6. For example, it could contribute 0,5% in July, 0.4% in August, 1.5% September. Most of the water needs of the campus area in April or May can be met by storing the water collected in the months of no irrigation.

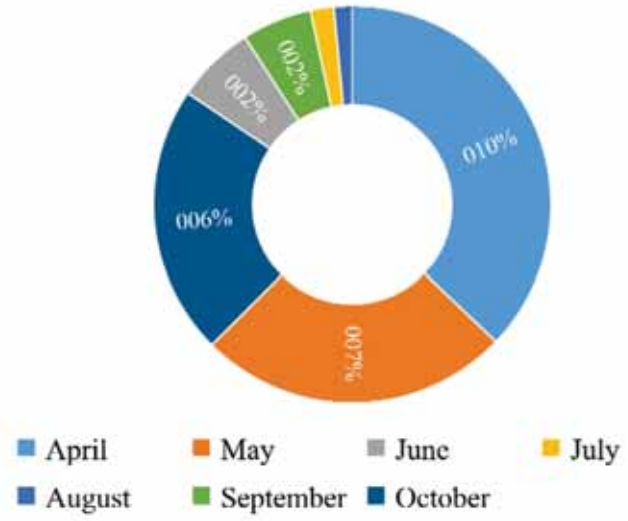

FIGURE 6
Rooftop RWH contribution to campus area irrigation water

CONCLUSION

In this study, the potential contribution of RWH on Munzur University campus roof areas was investigated. The roof areas of the buildings in the region were calculated, and the amount of rainwater to be collected from each building was also calculated from the monthly precipitation data obtained from the Tunceli Regional Directorate of State Meteorology Affairs. When precipitation data are examined, there is high variability, and changes to the underlying distribution of precipitation are expected in the future due to climate change. Considering this forecasted change in precipitation, it is seen that drought and climate change could increase over time. As a result, water harvesting from the roofs of large public institutions could contribute to the water supply in urban areas. The importance and impact of government incentive policy regulations on how RWH systems can be optimally designed and financially evaluated is emphasized. A RWH system can be useful in terms of the sustainable use of existing water resources, water conservation, rainwater storage, and green field irrigation. In this study, it has been calculated that an annual average of 12,537.73 m^3 of water can be stored. Accordingly, if irrigation is done every day, the amount of water collected from the roof areas will meet 9.8% of the total green area irrigation water need. With the current study, an additional warehouse can be built at the university and the water needs of the campus, such as sinks and toilet bowls, can be met in case of water interruption in the months when there is no irrigation. For this reason, the importance of collecting and using rainwater in buildings should be explained to all members of society and further researched. There are many beneficial aspects of RWH systems, especially in regards to water conservation, stormwater management, energy consumption management and greenhouse gas management. Further work is required to improve the modeling of these benefits.

ACKNOWLEDGEMENTS

The author gratefully acknowledges the Munzur University Construction Affairs Department for their contribution.

Data Availability. The data that support the findings of this study are available from the corresponding author upon reasonable request.

REFERENCES

[1] Sivanappan, R.K. (2006) Rain Water Harvesting, Conservation and Management Strategies for Urban and Rural Sectors. In National Seminar On Rainwater Harvesting and Water Management. 11(12), 1-5.

[2] Eren, B., Aygün, A., Likos, S., Damar, A.I. (2016) Rainwater Harvesting. Sakarya University Esentepe Campus Example. In 4th International Symposium On Innovative Technologies in Engineering and Science (Isites2016) 3-5 Nov 2016 Alanya/Antalya-Turkey, 1(1): 1–5.

[3] Temizkan, S., Kayili, M.T. (2021) Determination of optimum storage method in rainwater harvesting. Karabuk University Social Life Center Example. El-Cezeri Journal of Science and Engineering. 8(1), 102-116.

[4] Abdulla, F.A., Al-Shareef, A.W. (2009) Roof rainwater harvesting systems for household water supply in Jordan. Desalination. 243(1-3), 195-207.

[5] Campisano, A., Butler, D., Ward, S., Burns, M.J., Friedler, E., Debusk, K., Han, M., Urban, (2017) Rainwater harvesting systems. Research, Implementation and Future Perspectives, Water Research. 115, 195-209.

[6] Radhakrishna, B.P. (2003) Rainwater harvesting, A Time-Honoured Practice, Need for Revival. Current Science. 85(9), 1259-1261.

[7] Kuzucu, M. (2017) Effects of water harvesting techniques and using humic acid on soil moisture, Plant Evaporation, Growth and Yield in Pistachio Orchards in Southeastern of Turkey. Fresen. Environ. Bull. 26(12), 7521-7528.

[8] Adugna, D., Jensen, M. B., Lemma, B., Gebrie, G.S. (2018) Assessing the potential for rooftop rainwater harvesting from large public institutions. International Journal of Environmental Research and Public Health. 15(2):336, 1-11.

[9] Amin, M.T., Alazba, A.A. (2011) Probable sources of rainwater contamination in a rainwater harvesting system and remedial options. Australian Journal of Basic and Applied Sciences. 5(12), 1054-1064.

[10] Bayazıt, M., Şen, Z., Avcı, I. (2009) Hydrology Applications, Chapter 12-Statistical methods, İstanbul. 286 pages, 201-278.

[11] Kanno, G.G., Lagiso, Z.A., Abate, Z.G., Areba, A.S., Gondol, B.N., Temesgen, H., Aregu, M.B. (2021) Estimation of rainwater harvesting potential for emergency water demand in the era of covid-19. The Case of Dilla Town, Southern, Ethiopia. Environmental Challenges. 3:100077, 1-11.

[12] Küçüksayan, C., Gülez, S., Cengiz, B. (2011) Investigation of automatic irrigation system in landscape areas: The case of Ankara. Bartın Faculty of Forestry Journal. 13(19), 52-62.

[13] T.C. General Directorate of Meteorology (2021) http://www1.mgm.gov.tr/verideger-lendirme/yillik-toplam-yagis-ver-ileri.aspx?m=tunceli#sfB (Accessed date: 20.Nov.2021)
[14] Saplıoğlu, K. (2015) A new methodology for trend analysis: A case study in Burdur and Isparta, Turkey. Fresen. Environ. Bull. 24, 3344-3351
[15] Senocak, S. and Emek, M.F. (2017) A Case Study: Trend analysis of total annual rainfalls on eastern anatolia region in Turkey. Fresen. Environ. Bull. 26(10), 5858-5864.
[16] Karaburun, A. (2011) Trend analysis of long term spatially distributed precipitation in Marmara region between 1975- 2006. Fresen. Environ. Bull. 20(2a), 475-483.
[17] Köse, B. (2014) Phenology and ripening of Vitis Vinifera L. and Vitis Labrusca L. varieties in the maritime climate of Samsun in Turkey's Black Sea Region. South African Journal of Enology and Viticulture. 35(1), 90-102.
[18] Jamali, B., Bach, P.M., Deletic, A. (2020) Rainwater harvesting for urban flood management–an integrated modelling framework. Water Research. 171:115372, 1-11.
[19] Campisano, A., D'amico, G., Modica, C. (2017) Water saving and cost analysis of large-scale implementation of domestic rain water harvesting in minor Mediterranean Islands. Water. 9(12):916, 1-15.
[20] Quinn, R., Rougé, C., Stovin, V. (2021) Quantifying the performance of dual-use rainwater harvesting systems. Water Research. X, 10:100081, 1-12.
[21] Van Dijk, S., Lounsbury, A.W., Hoekstra, A.Y., Wang, R. (2020) Strategic design and finance of rainwater harvesting to cost-effectively meet large-scale urban water infrastructure needs. Water Research. 184:116063, 1-10.
[22] Bekar, M., Yalcinalp, E., Meral, A. (2020) Analysis of the contribution of rainwater recycling (RWR) to the campus area of KTU, Trabzon Turkey. Fresen. Environ. Bull. 29(4), 2112-2122.
[23] Rainfall-runoff analysis (2021), http://www.fao.org/3/u3160e/u3160e05.htm#TopOfPage (Accessed date: 20.Nov.2021)
[24] Aladenola, O.O., Adeboye, O.B. (2010) Assessing the potential for rainwater harvesting. Water Resources Management. 24(10), 2129-2137.
[25] Machad, N.A.L., Gonzalez, C.G.D., Barreto, W., Méndez, N., Machado, L.J.L., Pugo, M.G.S., Machado, V.V.M. (2020) Rainwater storage in urban environments using green roofs. La Granja. 32(2), 54-71.

Received: **08.08.2021**
Accepted: **16.10.2021**

CORRESPONDING AUTHOR

Meral Korkmaz
Civil Engineering Department
Faculty of Engineering
Munzur University
Tunceli – Turkey

e-mail: meralkorkmaz@munzur.edu.tr

© by PSP Volume 31– No. 05/2022 pages 4734-4742 Fresenius Environmental Bulletin

RESEARCH ON WIND COMFORT INDEX OF CHANGSHA CITY BASED ON THE COUPLING OF THERMAL AND MECHANICAL EFFECTS OF WIND

Guangjun Gao[1,2], Xin Chen[1,2,*], Jie Zhang[1,2], Feng Li[1,2]

[1]Key Laboratory of Traffic Safety on the Track of Ministry of Education, Central South University, Changsha Hunan 410075, China
[2]School of Traffic & Transportation Engineering, Central South University, Changsha Hunan 410075, China

ABSTRACT

The current outdoor wind comfort index is mainly to evaluate the impact of the mechanical effect of wind on human body. In the actual outdoor human wind comfort evaluation, it is necessary to establish an index that considers the thermal effect of wind at the same time. Firstly, the coupling method of thermal and mechanical effects of wind is proposed, and 16 kinds of coupling relations between Soligo wind comfort index and UTCI thermal climate index are established; Secondly, Taking Changsha City as the research area, the applicability of UTCI index was analyzed and corrected by field meteorological observation and TSV questionnaire survey; Finally, the wind comfort evaluation index of Changsha under the dual coupling effect of wind is established. The results show that: the scale of UTCI without heat stress in Changsha is revised from [+9,+26] to [+15.4,+32.4]. When the probability of wind speed exceeding the threshold in spring meets P ($v_{a,h=1.5}>2.5$)$\leqslant$20%, it can meet all the requirements of human body wind comfort under sitting, standing and walking behavior; when the probability of wind speed exceeding the threshold in autumn meets P($v_{a,h=1.5}>2.5$, $v_{a,h=1.5}<1.25$)$\leqslant$20%、P($v_{a,h=1.5}>3.8$, $v_{a,h=1.5}<1.25$)$\leqslant$20%, P($v_{a,h=1.5}>3.9$, $v_{a,h=1.5}<1.25$)$\leqslant$20%, it can meet the requirements of human body wind comfort under sitting, standing and walking behavior respectively; It is hot in summer and cold in winter, wind environment in these two seasons cannot meet the requirements of human comfort.

KEYWORDS:
Thermal effects of wind, mechanical effects of wind, wind comfort, UTCI, exceeding probability of threshold

INTRODUCTION

With the improvement of the living environment, the influence of outdoor wind environment on human comfort has been paid attention. The method of evaluating wind comfort has also become the focus of research. The existing evaluation methods at home and abroad are mainly divided into absolute wind speed threshold method and exceeding probability threshold method. In 1973, based on summing up all kinds of absolute wind speed thresholds, Penwarden [1] put forward the average wind speed 5m/s, 10m/s and 20m/s for comfortable, uncomfortable and dangerous wind speed limits. In 1983, Isyumov [2] first took the exceeding probability threshold method as the evaluation method of wind comfort index. After that, a variety of exceeding probability threshold evaluation indexes was proposed and became the mainstream method of wind environment evaluation [3-4]. Soligo points out that wind has dynamic effect and thermal effect on human comfort, and the transcendental probability threshold method only evaluates the dynamic effect of wind [5]. Some research scholars used the exceeding probability evaluation index to evaluate the influence of wind dynamic effect on human comfort [6-8], and others proposed set the typical working conditions to consider the dual effects of wind. However, the typical working conditions can not represent the overall wind comfort in the study area, so this paper studies the outdoor wind comfort evaluation index under the coupling of wind thermal and dynamic effects [9-10].

In addition, some scholars compare the indexes based on the law of Weibull distribution, and find that there is an overall convergence and different strictness among the indexes [11-12]. The difference is caused by test method and standard adaptability. People in different regions have different perception of wind comfort due to their long-term living environment. Therefore, this paper adopts the questionnaire survey method to modify the evaluation index regionally to make the evaluation results more objective.

MATERIALS AND METHODS

Coupling method of thermal and dynamic effects of wind. The dual effect coupling idea of wind is to establish the coupling relationship between outdoor thermal comfort index and outdoor

wind comfort exceeding probability threshold evaluation index. In all kinds of exceeding probability threshold evaluation index, Soligo index takes the average wind speed as the critical wind speed parameter, and the exceeding probability threshold of various activities is 20%, which is conducive to the application of end users [13].In this paper, we select Soligo index to evaluate the dynamic effect of wind, as shown in Table 1.In addition, because of the complexity of the outdoor environment, the international general outdoor thermal comfort evaluation index has not been formed at this stage. Some scholars have compared and analyzed various outdoor thermal comfort indexes, UTCI (Universal Thermal Climate Index) adopts Fiala human model, which can better reflect the overall and local physiological and thermal response of the human body [14-16]. In the research on thermal comfort in recent years, UTCI reflects the thermal feeling of human body outdoors and has good applicability, therefore, UTCI is selected to evaluate the thermal effect of wind.

The evaluation criteria of UTCI index are divided into 10 grades according to the intensity of heat (cold) stress, where [+ 9, + 26] is the standard comfort temperature. UTCI equivalent temperature is linear with air temperature (T_a), average radiation temperature (T_r), wind speed in 10m (v_a), water vapor pressure (p_a) and relative humidity (RH), as Eq. 1, Eq. 2:

$$v_a = v_{a,h=1.5}\left(\frac{10}{1.5}\right)^{\alpha} \quad (2)$$

In the formula (2), $v_{a,h=1.5}$ represents the wind speed at the pedestrian height of 1.5m; a represents the surface roughness of the area where the measuring point is located, value according to specification, a =0.22, as Eq. 3:

In the formula (3), T_g represents the black ball temperature; ε represents the black sphere reflectivity, ε= 0.95; D represents the diameter of the black ball, the parameters of measuring equipment can be checked.

The highest temperature in a day occurs at about 14:00. The sun shines directly on the ground, and the mean radiant temperature in this time period is also the maximum; the lowest temperature is before sunrise, the mean radiant temperature in this period is the minimum. The relative humidity changes little in the quarter, so we can take the average value. The average humidity is RH. In the real environment, the wind speed is incompletely stationary, so the UTCI index acquiescence minimum wind speed value is 0.5m/s. According to equation (2), 10m high wind speed v_a takes[0.76, i], where i is the wind speed threshold of Soligo index converted according to gradient wind. According to formula (1), (2), (3) and online computing platform (www.utci.org), we can get the UTCI value at the maximum mean temperature (radiant temperature) and UTCI value at the minimum mean temperature (radiant temperature). The following 16 type of working conditions can be obtained through the thermal effect coupling of wind:

(I)When T_a is minimum, v_a=[0.76,i], UTCI⊆[+9,+26]; When T_a is maximum, v_a=[0.76,i], UTCI⊆[+9,+26].

Then the wind comfort index under the coupling of wind thermal effect is P(v_a＞i)≤20%.

(II)When T_a is minimum, v_a=[0.76,i], UTCI⊄[+9,+26]; When T_a is maximum, v_a=[0.76,i], UTCI⊄[+9,+26].

Then the wind comfort under the coupling of wind thermal effect cannot be satisfied. If UTCI≥ +26, it indicates that the climate is hot all day, the thermal effect of wind cannot reduce human heat stress, it can take measures to increase the wind speed to i, or reduce the outdoor air temperature and radiant temperature all day; If UTCI≤+9, it indicates that the climate is cold all day, the thermal effect of wind will further increase cold stress, it can take measures to decrease the wind speed to 0m/s, or increase the outdoor air temperature and radiant temperature all day; If UTCI≤+9 when T_a is minimum, and UTCI≥+26 when T_a is maximum, it indicates that the climate is cold in the morning and at night, and the thermal effect of wind will further increase the cold stress, it can take measures to decrease the wind speed to 0m/s, or increase the outdoor air temperature and radiant temperature at night, however, it is hot at noon, and the thermal effect of the wind cannot eliminate human heat stress, it can take measures to increase the wind speed to i or reduce the outdoor air temperature and radiant temperature during the daytime.

(III)When T_a is minimum, v_a=[0.76,i], UTCI⊆[+9,+26]; When T_a is maximum, v_a=[0.76,i], UTCI⊄[+9,+26].

Then the wind comfort under the coupling of wind thermal effect cannot be satisfied. If UTCI≥ +26 when T_a is maximum, it indicates that the climate is comfortable in the morning and at night, however, it is hot at noon, it can take measures to increase the wind speed to i, or reduce the outdoor air temperature and radiant temperature during the daytime.

$$UTCI\left(T_a, T_r, v_a, p_a\right) = T_a + offset\left(T_a, T_r, v_a, p_a\right) \quad (1)$$

$$T_r = \left[\left(T_g + 273.15\right)^4 + \frac{1.10\times10^8 v_a^{0.6}}{\varepsilon D^{0.4}}\left(T_g - T_a\right)\right]^{1/4} - 273.15 \quad (3)$$

TABLE 1
Outdoor wind comfort index of Soligo

Behavior activities	Wind speed threshold /(m·s-1)	Exceeding probability /%
Sit	＞2.5	20
Stand	＞3.9	20
Walk	＞5.0	20

(IV)When T_a is minimum, v_a=[0.76,i], UTCI⊆[+9,+26]; When T_a is maximum, v_a=[0.76,i], UTCI∩[+9,+26] corresponding v_a=[c,i] .

Then the wind comfort index under the coupling of wind thermal effect is P(v_a＞i, v_a＜c)≤20%

(V) When T_a is minimum, v_a=[0.76,i], UTCI⊄[+9,+26]; When T_a is maximum, v_a=[0.76,i], UTCI⊆[+9,+26].

Then the wind comfort under the coupling of wind thermal effect cannot be satisfied. If UTCI≤+9 when T_a is minimum, it indicates that the climate is comfortable at noon, however, it is cold in the morning and at night, it can take measures to decrease the wind speed to 0m/s, or increase the outdoor air temperature and radiant temperature in the morning and at night.

(VI) When T_a is minimum, v_a=[0.76,i], UTCI⊄[+9,+26]; When T_a is maximum, v_a=[0.76,i], UTCI∩[+9,+26].

Then the wind comfort under the coupling of wind thermal effect cannot be satisfied. The reason is the same as (V).

(VII) When T_a is minimum, v_a=[0.76,i], UTCI∩[+9,+26] corresponding v_a=[0.76,b]; When T_a is maximum, v_a=[0.76,i], UTCI⊆[+9,+26].

Then the wind comfort index under the coupling of wind thermal effect is P(v_a＞b, v_a＜0.76)≤20%

(VIII) When T_a is minimum, v_a=[0.76,i], UTCI∩[+9,+26] corresponding v_a=[a,b]; When T_a is maximum, v_a=[0.76,i], UTCI∩[+9,+26] corresponding v_a=[c,d].

If b＞c, then the wind comfort index under the coupling of wind thermal effect is P(v_a＞b, v_a＜c)≤20%; If b≤c ,then the wind comfort under the coupling of wind thermal effect cannot be satisfied. It can take measures to control the wind speed in [a,b] in the morning and at night, and control the wind speed in [c,b] during the daytime.

(Ⅸ) When T_a is minimum, v_a=[0.76,i], UTCI∩[+9,+26]; When T_a is maximum, v_a=[0.76,i], UTCI⊄[+9,+26].

Then the wind comfort under the coupling of wind thermal effect cannot be satisfied. The reason is the same as (III).

(X) When T_a is minimum, v_a=[0.76,i], UTCI⊃[+9,+26] corresponding v_a=[a,b]; When T_a is maximum, v_a=[0.76,i], UTCI⊃[+9,+26] corresponding v_a=[c,d].

The reason is the same as (VIII).

(Ⅺ) When T_a is minimum, v_a=[0.76,i], UTCI⊃[+9,+26]; When T_a is maximum, v_a=[0.76,i], UTCI⊄[+9,+26].

Then the wind comfort under the coupling of wind thermal effect cannot be satisfied. The reason is the same as (III).

(Ⅻ) When T_a is minimum, v_a=[0.76,i], UTCI⊃[+9,+26] corresponding v_a=[a,b]; When T_a is maximum, v_a=[0.76,i], UTCI∩[+9,+26] corresponding v_a=[c,d].

The reason is the same as (VIII).

(XIII) When T_a is minimum, v_a=[0.76,i], UTCI⊃[+9,+26]; When T_a is maximum, v_a=[0.76,i], UTCI⊆[+9,+26] corresponding v_a=[c,d].

The situation does not exist.

(XIV) When T_a is minimum, v_a=[0.76,i], UTCI⊄[+9,+26]; When T_a is maximum, v_a=[0.76,i], UTCI⊃[+9,+26] corresponding v_a=[c,d].

Then the wind comfort under the coupling of wind thermal effect cannot be satisfied. UTCI≤+9, it indicates that the climate is cold in the morning and at night, the thermal effect of wind will further increase cold stress, it can take measures to decrease the wind speed to 0m/s, or increase the outdoor air temperature and radiant temperature in the morning and at night; however, it is comfortable at noon if control the wind speed in [c,d].

(XV) When T_a is minimum, v_a=[0.76,i], UTCI∩[+9,+26] corresponding v_a=[a,b]; When T_a is maximum, v_a=[0.76,i], UTCI⊃[+9,+26] corresponding v_a=[c,d].

The reason is the same as (VIII).

(XVI) When T_a is minimum, v_a=[0.76,i], UTCI⊆[+9,+26]; When T_a is maximum, v_a=[0.76,i], UTCI⊃[+9,+26].

The situation does not exist.

UTCI correction analysis based on linear regression method. UTCI is the universal thermal comfort index of outdoor human body in the world, the calculation principle is Fiala dynamic physiological response system model, which determines the comfort through the physiological responses of human body to environmental conditions, such as sweating, vasodilatation or contraction, metabolism and so on. People in different regions of the world have different perception of cold and heat because they live in different climatic environments all year round. Some scholars believe that the existing outdoor comfort evaluation indexes are calculated based on meteorological data, lacking the consideration of

subjective factors of activists in different regions [17-18]. Therefore, before using UTCI index to determine urban thermal comfort, its applicability should be judged first. This paper adopts the method of field measurement and questionnaire survey at the same time.

(1) Test site and conditions. We selected 4 sites in the downtown area of Changsha as the test sites to measure the air temperature (T_a/ ℃), relative humidity (RH/%), wind speed (v_a /m·s^{-1}) and black sphere temperature (T_g /℃). The measuring instrument adopts JT-IAQ-50 thermal comfort tester and CP-WDS2V101 integrated wind speed and direction measuring instrument. The height of the measuring instrument is 1.5m, and the space around the measuring points is more spacious. It avoids the sheltering of the black globe thermometer by building and plants.

Changsha is a subtropical monsoon climate, a typical hot summer and cold winter zone. In order to verify the calculation results of UTCI index in combination with the climate characteristics of Changsha in each season, we select October 17 and 18, 2019 as the measurement days in autumn, January 2 and 3, 2020 as the measurement days in winter, March 25 and March 26, 2020 as the measurement days in spring, and July 4 and 5, 2020 as the measurement days in summer. Considering the large daily climate change, the test period is from 13:00 to 15:00 (noon) and from 18:00 to 20:00 (sunset) on the measurement days. The measured data are shown in Table 2.

(2) TSV questionnaire. The questionnaire was filled in at the same time and place as the field measurement, and the staff guided the volunteers to fill in. Since the purpose of this test is to verify the applicability of UTCI index to evaluate the outdoor human comfort of Changsha City, in order to increase the reliability of the survey results, the following matters should be paid attention to: 1) make sure that volunteers are permanent residents in Changsha; 2) at the time of filling in the questionnaire, the volunteers had been in the outdoor area without sunshine for more than 30 minutes; 3) the proportion of volunteers is half of men and women. Age includes youth (20-32 years old), middle age (38-50 years old) and elderly people (60-72 years old); 4) other unconventional factors such as noise, rainstorm and hurricane have been eliminated during the test. According to the central limit theorem of Statistics, no matter what the overall distribution is, the average value of the sample from the population is larger than 30, which is approximately the average of the population, and the average value of the samples is normal distribution [19]. Therefore, 40 volunteers were called to fill in the questionnaires in 8 time periods, and 320 questionnaires were collected.

The questionnaire includes the basic information of the volunteers (gender, age) and the feeling of the current outdoor comfort. Adopting the TSV (Thermal Sensation Vote) thermo sensory voting method, but in order to correspond to the UTCI index level, we increase the extreme cold and extreme heat two scales. TSV is divided into 9 levels according to extreme cold (- 4), very cold (- 3), cold (- 2), cool (- 1), moderate (0), temperature (+ 1), heat (+ 2), very hot (+ 3) and extreme heat (+ 4). The voting results of each test period in four seasons are counted, and the results are shown in Figure 1.

RESULTS

Analysis of test results. We calculated the measured meteorological data of 16 test periods in 4 sites, and calculate the average local radiation temperature in each test period according to Formula (2), UTCI index value can be obtained from online computing platform. The results of TSV questionnaire reflect the comfort feeling of people at a specific time in the study city. The voting results can be determined by calculating the expected value E (x) through probability statistics, so as to obtain the TSV scoring results of 16 test periods. Carry out linear regression between the expected value E(x) of outdoor TSV and the UTCI index value at the corresponding time to analyze the applicability of UTCI index in the study city, as shown in Figure 2.

TABLE 2
Measured meteorological data of characteristic day

Date	Air temperature T_a/ ℃		Relative humidity RH/%		Wind speed v_a /m·s^{-1}		Black sphere temperature T_g/ ℃	
	Noon	Sunset	Noon	Sunset	Noon	Sunset	Noon	Sunset
20191017	14.3	14.4	78.7	81.7	4.5	2.4	20.7	17.2
20191018	22.2	18.3	77.5	75.2	2.6	2.1	27.2	21.3
20200102	4.5	4.0	98.2	98.4	6.4	4.7	6.8	4.7
20200103	4.6	4.6	98.3	97.6	4.7	3.1	7.4	5.2
20200325	25.9	24.9	73.2	76.4	2.9	4.7	29.6	27.5
20200326	21.4	22.7	76.2	73.4	4.7	3.8	26.2	25.8
20200704	37.6	32.5	62.3	65.6	1.7	1.3	49.1	38,2
20200705	36.7	31.3	60.3	63.7	5.6	4.2	47.2	37.5

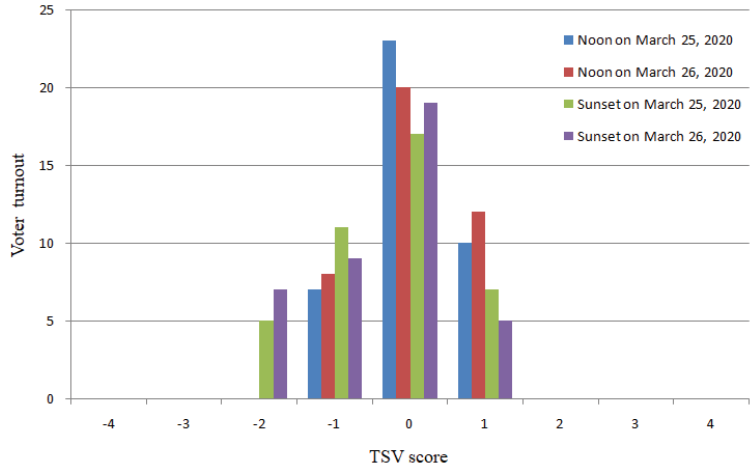

(a) Spring test day

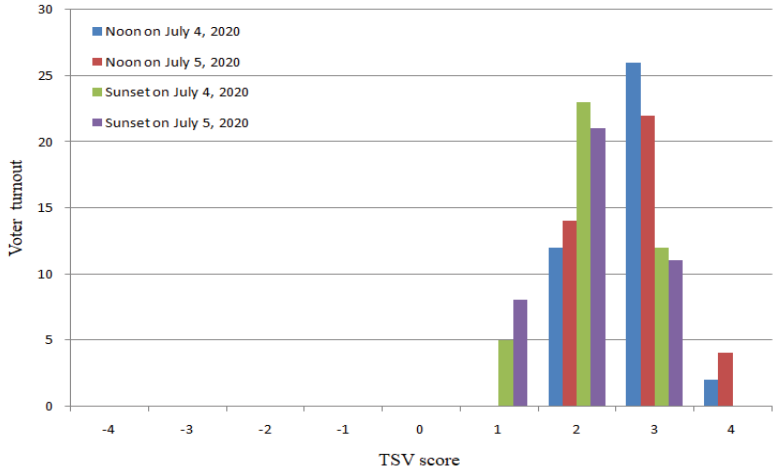

(b) Summer test day

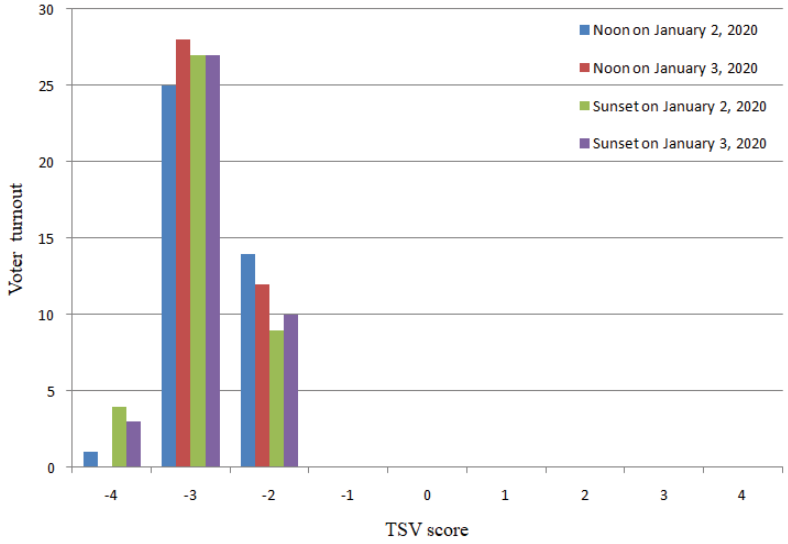

(c) Autumn test day

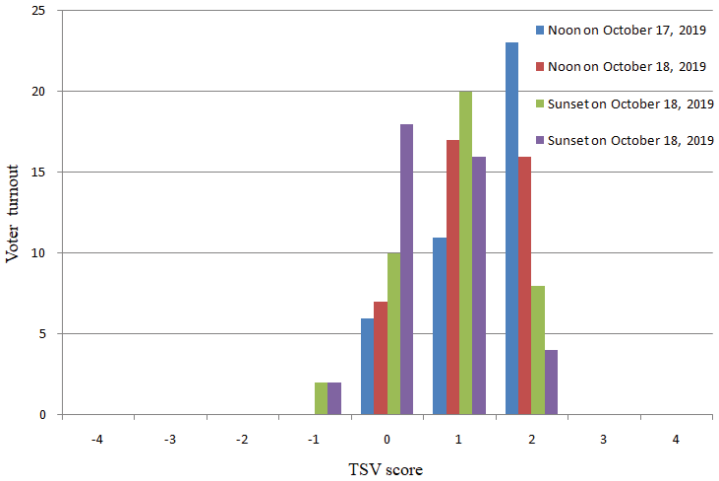

(d) Winter test day

FIGURE 1
Statistics of TSV questionnaire in different experimental periods.

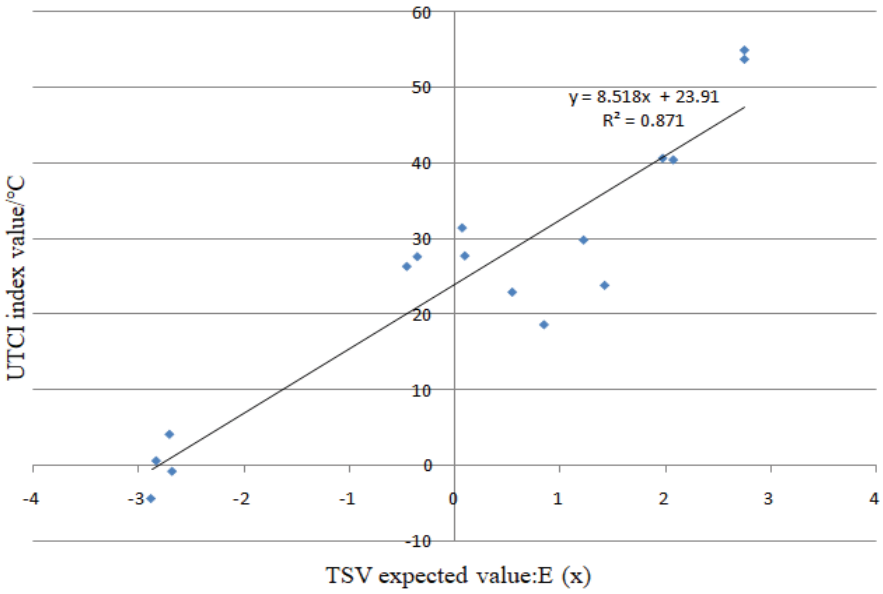

FIGURE 2
Correlation between outdoor TSV and UTCI in Changsha.

From the graph we can seen that the linear regression coefficient R^2=0.871 between TSV and UTCI, and the overall correlation is good. The UTCI index correction function of urban outdoor human comfort in Changsha is y = 8.518x + 23.91. According to this function, the revised UTCI scale range can be determined, that is, when meeting the regional comfort requirements TSV (- 1, + 1) of Changsha, the scale of UTCI index "no thermal stress" is revised from the original [+ 9, + 26] to [+ 15.4, + 32.4]. It can be seen from the data that the comfort zone value after the regional correction is greater than the original comfort zone value. Empirically, this is because Changsha is in the hot summer and cold winter zone. There are more about 85 days in summer when the daily average temperature is above 30℃, and the hot days that the temperature higher than 35℃ is about 30 days, the survey population is living in this characteristic environment all the year round, resulting in increased heat resistance to the climate; the average temperature in winter is 4-10 ℃. Although the overall temperature in winter is not low, however, the average relative humidity is as high as 77.3%. The regional population is sensitive to the wet and cold response of the climate.

Establishment of regional wind comfort index. According to the coupling method of thermal and dynamic effects of wind, we take Changsha City as the research area to establish the urban human wind comfort index. Firstly, according to the meteorological data recorded by the national meteorological station ([57687] Changsha station) in recent two years, we counted the meteorological extreme data related to UTCI index in four seasons of Changsha, then calculated the minimum and minimum UTCI

index of Changsha in each quarter, as shown in Table 3.

Wind speed v_a is taken from [0.76, i], i is the wind speed threshold of sit, stand and walk in Soligo index converted according to gradient wind, that is 3.8m/s、5.9 m/s、7.6 m/s. Through the online calculation platform, we can get the value range of UTCI index at the meteorological extreme value of each season in Changsha, and compare it with the revised UTCI comfort interval [+ 15.4, + 32.4] in Changsha. According to the 16 kinds of working conditions under the coupling of wind dual effect, we can eventually determine the urban human wind comfort index in each season and behavior state.

Spring (March to May). (1) Sitting behavior state: when T_a is minimum, v_a=[0.76,3.8], UTCI=[+15.4,+22.5]⊆[+15.4,+32.4]; when T_a is maximum, v_a=[0.76,3.8], UTCI= [+27.4,+32.0]⊆[+15.4,+32.4].

It belongs to (I) working condition, then the wind comfort index under the coupling of wind thermal effect is P(v_a＞3.8)≤20%

(2)Standing behavior state: when T_a is minimum, v_a=[0.76,5.9], UTCI=[+11.0,+22.5] ∩ [+15.4,+32.4],corresponding v_a=[0.76,3.8]; when T_a is maximum, v_a=[0.76,5.9], UTCI= [+27.4,+32.0]⊆[+15.4,+32.4].

It belongs to (IV) working condition, then the wind comfort index under the coupling of wind thermal effect is P(v_a＞3.8)≤20%

(3)Walking behavior state: when T_a is minimum, v_a=[0.76,7.6], UTCI=[+8.5,+22.5] ∩ [+15.4,+32.4],corresponding v_a=[0.76,3.8]; when T_a is maximum, v_a=[0.76,7.6], UTCI= [+23.3,+32.0]⊆ [+15.4,+32.4].

It belongs to (IV) working condition, then the wind comfort index under the coupling of wind thermal effect is P(v_a＞3.8)≤20%

Summer (June to August). (1)Sitting behavior state: when T_a is minimum, v_a=[0.76,3.8], UTCI=[+35.4,+39.4]⊄[+15.4,+32.4]; when T_a is maximum, v_a=[0.76,3.8], UTCI= [+44.2,+47.7]⊄ [+15.4,+32.4].

It belongs to (II) working condition, then the wind comfort under the coupling of wind thermal effect cannot be satisfied. UTCI≥+32.4, it indicates that the climate is hot all day, the thermal effect of wind cannot reduce human heat stress, it can take measures to increase the wind speed to 3.8m/s, or reduce the outdoor air temperature and radiant temperature all day.

(2)Standing behavior state: when T_a is minimum, v_a=[0.76,5.9], UTCI=[+35.4,+39.4]⊄ [+15.4,+32.4]; when T_a is maximum, v_a=[0.76,5.9], UTCI= [+44.2,+47.7]⊄[+15.4,+32.4].

It belongs to (II) working condition, then the wind comfort under the coupling of wind thermal effect cannot be satisfied. The reason is the same as sitting behavior state, it can take measures to increase the wind speed to 5.9m/s.

(3)Walking behavior state: when T_a is minimum, v_a=[0.76,7.6], UTCI=[+32.7,+39.4]⊄[+15.4,+32.4]; when T_a is maximum, v_a=[0.76,7.6], UTCI= [+42.2,+47.7]⊄[+15.4,+32.4].

It belongs to (II) working condition, then the wind comfort under the coupling of wind thermal effect cannot be satisfied. The reason is the same as sitting behavior state, it can take measures to increase the wind speed to 7.6m/s.

Autumn (September to November). (1)Sitting behavior state: when T_a is minimum, v_a=[0.76,3.8], UTCI=[+19.5,+26.0]⊆[+15.4,+32.4]; when T_a is maximum, v_a=[0.76,3.8], UTCI= [+29.3,+33.8] ∩ [+15.4,+32.4] ,corresponding v_a=[1.9,3.8].

TABLE 3
Meteorological extreme value data of each season in Changsha

Season	Maximum average temperature $T_{a,max}$/℃	Maximum mean radiant temperature $T_{r,max}$/℃	Minimum average temperature $T_{a,min}$/℃	Minimum mean radiant temperature $T_{r,min}$/℃	Relative humidity *RH*/%
Spring	22.0	52.6	13.0	37.9	79.3
Summer	32.0	81.1	27.0	67.9	77.0
Autumn	23.0	57.1	15.0	45.8	78.7
Winter	10.0	21.4	4.0	15.8	77.3

TABLE 4
Urban wind comfort index of human in Changsha City

Season	Sitting	Standing	Walking
Spring	P($v_{a,h=1.5}$＞2.5)≤20%		
Summer	Unable to meet, UTCI≥+32.4,the weather is hot all day		
Autumn	P($v_{a,h=1.5}$＞2.5, $v_{a,h=1.5}$＜1.25)≤20%	P($v_{a,h=1.5}$＞3.8, $v_{a,h=1.5}$＜1.25)≤20%	P($v_{a,h=1.5}$＞3.9, $v_{a,h=1.5}$＜1.25)≤20%
Winter	Unable to meet, UTCI≤+15.4,the weather is cold all day		

It belongs to (IV) working condition, then the wind comfort index under the coupling of wind thermal effect is P(v_a＞3.8,v_a＜1.9)≤20%

(2) Standing behavior state: when T_a is minimum, v_a=[0.76,5.9], UTCI=[+15.5,+26.0]⊆ [+15.4,+32.4]; when T_a is maximum, v_a=[0.76,5.9], UTCI= [+26.8,+33.8] ∩ [+15.4,+32.4] ,corresponding v_a=[1.9,5.9].

It belongs to (IV) working condition, then the wind comfort index under the coupling of wind thermal effect is P(v_a＞5.9,v_a＜1.9)≤20%

(3)Walking behavior state: when T_a is minimum, v_a=[0.76,7.6], UTCI=[+13.2,+26.0] ∩ [+15.4,+ 32.4] ,corresponding v_a=[0.76,6.0]; when T_a is maximum, v_a=[0.76,7.6], UTCI= [+25.6,+33.8] ∩ [+15.4,+32.4] ,corresponding v_a=[1.9,7.6].

It belongs to (IV) working condition, then the wind comfort index under the coupling of wind thermal effect is P(v_a＞6.0,v_a＜1.9)≤20%

Winter (December to February of the following year). (1)Sitting behavior state: when T_a is minimum, v_a=[0.76,3.8], UTCI=[-0.7,+9.3]⊄ [+15.4,+ 32.4]; when T_a is maximum, v_a=[0.76,3.8], UTCI= [+7.0,+15.0]⊄[+15.4,+32.4].

It belongs to (II) working condition, then the wind comfort under the coupling of wind thermal effect cannot be satisfied. UTCI≤+15.4, it indicates that the climate is cold all day, the thermal effect of wind will further increase cold stress, it can take measures to decrease the wind speed to 0m/s, or increase the outdoor air temperature and radiant temperature all day.

(2)Standing behavior state: when T_a is minimum, v_a=[0.76,5.9], UTCI=[-6.7,+10.8]⊄ [+15.4,+ 32.4]; when T_a is maximum, v_a=[0.76,5.9], UTCI= [+2.1,+15.0]⊄[+15.4,+32.4].

It belongs to (II) working condition, then the wind comfort under the coupling of wind thermal effect cannot be satisfied. The reason is the same as sitting behavior state.

(3) Walking behavior state: when T_a is minimum, v_a=[0.76,7.6], UTCI= [-10.5,+10.8]⊄ [+15.4,+ 32.4]; when T_a is maximum, v_a=[0.76,7.6], UTCI= [-0.9,+15.0]⊄[+15.4,+32.4].

It belongs to (II) working condition, then the wind comfort under the coupling of wind thermal effect cannot be satisfied. The reason is the same as sitting behavior state.

To sum up, according to the gradient wind principle of equation (2), converting the 10m high wind speed into the 1.5m pedestrian height wind speed, we can obtain the urban human wind comfort index of Changsha City. For details see Table 4.

CONCLUSIONS

(1) According to Soligo wind comfort index and UTCI thermal climate index, we establish 16 relationships under the coupling of wind dynamic effect and thermal effect. People in different regions live in a specific climate environment all year round, their perception of environmental comfort will be different. Taking Changsha City as the research area, the applicability of UTCI index was corrected by field meteorological observation and TSV questionnaire survey, the scale of UTCI index "no thermal stress" is revised from the original [+ 9, + 26] to [+ 15.4, + 32.4]. This is because Changsha is located in a hot summer and cold winter area, and the summer is hot, the survey population lives in this characteristic environment all year round, and their resistance to the hot climate is enhanced. Although the overall temperature in winter is not low, the average relative humidity is as high as 77.3%, and the regional population is sensitive to the wet and cold response of the climate.

(2) According to the dual effect coupling method of wind and based on the regionally revised UTCI index, establishing the outdoor human wind comfort evaluation index of Changsha. It can be seen from the index that Changsha is hot in summer and damp cold in winter. It is impossible to improve human outdoor comfort only from a single meteorological factor of wind environment.

(3) In summer in Changsha, the thermal effect of wind cannot eliminate human heat stress, it can use outdoor blower to increase the wind speed in the study area, or take some measures such as landscape fog spraying and plant shading to reduce the outdoor air temperature and radiation temperature. But the thermal effect of winter wind will further increase cold stress, it can reduce the wind speed relying on the wind resistance of plants, or take measures such as outdoor heater to increase outdoor air temperature to improve human comfort.

ACKNOWLEDGEMENTS

This work was not supported by any funds. The authors would like to show sincere thanks to those techniques who have contributed to this research.

REFERENCES

[1] Penwarden, A.D. (1973) Acceptable wind speeds in towns. Building Science. 8(3), 259-267.

[2] Isyumov, N., Poole, M. (1983) Wind induced torque on square and rectangular building shapes. Journal of Wind Engineering & Industrial Aerodynamics. 13(1), 183-196.

[3] Vardaxis, N.G., Bard, D., Waye, K.P. (2017) On the definition of acoustic comfort in residential buildings. The Journal of the Acoustical Society of America. 141(5), 3540-3540.
[4] Blocken, B., Roels, S., Carmeliet, J. (2004) Modification of pedestrian wind comfort in the silvertop tower passages by an automatic control system. Journal of Wind Engineering & Industrial Aerodynamics. 92(10), 849-873.
[5] Gerhardt, H.J., Kramer, C. (1992) Wind comfort and pollutant transport in a satellite city. Journal of Wind Engineering & Industrial Aerodynamics. 44(1-3), 2343-2351.
[6] Chen, P.Y., Tung, C.P., Lin, W.C., Li, Y.H. (2016) Spatial optimization procedure for land-use arrangement in a community based on a human comfort perspective. Paddy & Water Environment. 14(1), 71-83.
[7] Tolias, I.C., Koutsourakis, N., Hertwig, D., Efthimiou, G., Bartzis, J.G. (2018) Large Eddy Simulation study on the structure of turbulent flow in a complex city. Journal of Wind Engineering & Industrial Aerodynamics. 177, 101-116.
[8] Ratcliff, M.A., Peterka, J.A. (1990) Comparison of pedestrian wind acceptability criteria. Journal of Wind Engineering & Industrial Aerodynamics. 36(1-3), 791-800.
[9] Lopes, A., Saraiva, J., Alcoforado, M.J. (2011) Urban boundary layer wind speed reduction in summer due to urban growth and environmental consequences in Lisbon. Environmental Modelling & Software. 26(2), 241-243.
[10] Williams, C.J., Soligo, M.J., Côté, J. (1992) A discussion of the components for a comprehensive pedestrian level comfort criterion. Journal of Wind Engineering & Industrial Aerodynamics. 44(1), 2389-2390.
[11] Yardml, S., Ozer, D.G., Shahriary, A. (2020) Sustainable street architecture and its effects on human comfort conditions: Yazd, Iran. A|Z ITU Journal of Faculty of Architecture. 17(2), 113-122.
[12] Irwin, H. (1981) The design of spires for wind simulation. Journal of Wind Engineering & Industrial Aerodynamics. 7(3), 361-366.
[13] Toi, I., Lazi, L. (1998) Improved bora wind simulation using a nested eta model. Meteorology & Atmospheric Physics. 66(1-2), 1-10.
[14] Gobbi, M.F., Dorweiler, R.P. (2012) Simulation of wind over a relatively complex topography: application to the Askervein Hill. Journal of the Brazilian Society of Mechanical Sciences & Engineering. 34(4), 492-500.
[15] Tsichritzis, L., Nikolopoulou, M. (2019) The effect of building height and faade area ratio on pedestrian wind comfort of London. Journal of Wind Engineering and Industrial Aerodynamics. 191, 63-75.
[16] Huang, K.T., Yang, S.R., Matzarakis, A., Lin, T.P. (2018) Identifying outdoor thermal risk areas and evaluation of future thermal comfort concerning shading orientation in a traditional settlement. Science of the Total Environment. 626, 567-580.
[17] Stathopoulos, T., Storms, R. (1986) Wind environmental conditions in passages between buildings. Journal of Wind Engineering and Industrial Aerodynamics. 24(1), 19-31.
[18] Hercikova, E., Komarkova, P., Glombikova, V., Havelka, A., Kus, Z. (2018) Evaluation of thermal properties of textile structures under fast flowing air conditions. Vlakna a Textil. 25(4), 31-34.
[19] Papadopoulou, M., Raphael, B., Smith, I., Sekhar, C. (2016) Evaluating predictive performance of sensor configurations in wind studies around buildings. Advanced Engineering Informatics. 30(2), 127-142.

Received: **09.08.2021**
Accepted: **08.02.2022**

CORRESPONDING AUTHOR

Xin Chen
Key Laboratory of Traffic Safety on the Track of Ministry of Education,
Central South University,
Changsha Hunan 410075 – China

e-mail: 2519933021@qq.com

© by PSP Volume 31– No. 05/2022 pages 4743-4749 Fresenius Environmental Bulletin

*bla*KPC, *bla*NDM AND *bla*OXA-48 *Carbapenemases* AMONG *Klebsiella pneumoniae* IN HOSPITALIZED PATIENTS: FIRST REPORT FROM NORTHWEST PAKISTAN

Adil Khaliq[1], Hazir Rahman[1,*], Hina Khaliq[2], Zakir Khan[3], Taj Ali Khan[4], Raham Sher Khan[2], Muhammad Qasim[4], Khalid J Alzahrani[5], Yusuf Karatas[3]

[1]Department of Microbiology, Abdul Wali Khan University Mardan, Pakistan
[2]Department of Biotechnology, Abdul Wali Khan University Mardan, Pakistan
[3]Department of Medical Pharmacology, Institute of Health Sciences, Faculty of Medicine, Cukurova University, Adana, Turkey
[4]Department of Microbiology, Kohat University of Science and Technology, Kohat, Pakistan
[5]Department of Clinical Laboratories Sciences, College of Applied Medical Sciences, Taif University, P.O. Box 11099, Taif 21944, Saudi Arabia

ABSTRACT

Klebsiella pneumoniae causes infections especially in hospital environment. Emergence of antibiotics resistance among *K. pneumoniae* is a global concern. Resistance through Carbapenemase production reported in *K. pneumoniae.* The purpose of the study is to find the frequency of *K. pneumoniae*, related antibiogram, and phenotypic and molecular detection of carbapenemases. A total of 5475 samples were processed for culture, in which 1140 exhibited bacterial growth. Among 1140 culture positive samples, 110 isolates were *K. pneumoniae.* Phenotypic and molecular methods were used for detection of carbapenemases. All the isolates were resistant to Fosfomycin, cefotaxime, gentamicin and cloxacillin. 65.4% (n=72) isolates were resistant to meropenem and 57.2% (n=63) to imipenem. *bla*NDM gene was most prevalent (22.7%) followed by *bla*KPC (13.6%); however, *bla*OXA-48 was detected in one isolate. In the undertaken study, antibiotic resistance was increasingly observed in *K. pneumoniae* through carbapenemases. The current work will help to devise an appropriate antibiotic hospital policy to reduce K. *pneumoniae* resistance burden.

KEYWORDS:
Klebsiella pneumoniae, Hospitalized, Carbapenemase procuction, *bla*KPC*, bla*NDM*, bla*OXA-48

INTRODUCTION

Klebsiella pneumoniae is bacterial pathogen causing nosocomial infections. Aminoglycosides and third-generation cephalosporin are used to treat *K. pneumoniae* infections. The prevalence rate of *K. pneumoniae* among urinary tract infections is 90% with a resistance of 70% against cephalosporins [1]. Among health care facilities, resistance becomes higher up to 80-95% against cephalosporins and quinolones [2]. The emergence of antibiotics resistance limits the choice of available antibiotics to treat *K. pneumoniae* infections. *K. pneumoniae* resistance to cephalosporin and carbapenem is reported due to the production of carbapenemase [3]. Three classes of carbapenemase were detected, involving the emergence of class A *Klebsiella Pneumoniae* Carbapenemase, class B Metallo Beta-Lactamase and class D Oxacillinases [4]. The prevalence rate of carbapenemase-producing *K. pneumoniae* is causing global health threats against mankind [2]. Carbapenemase-producing *K. pneumoniae* were reported in Pakistan, throughout which the presence of NDM was explicitly high while the existence of KPC among *K. pneumoniae* was also reported [5]. The recent biochemical and molecular studies documented the presence of these mutative genes of *bla*KPC and *bla*MBL. Resistance against extended-spectrum cephalosporins are also found in *K. pneumoniae* either plasmid-mediated or chromosomally encoded [6]. There is ultimate concern regarding the high prevalence of carbapenemases in different parts of the world [7]. Limited data found on carbapenemase detection in *K. pneumoniae* from Pakistan. The undertaken study reported the prevalence of *blaK*PC*, bla*NDM and *bla*OXA-48 types of carbapenemase detection in *K. pneumoniae*. The finding of the current work may be helpful for further characterization of molecular drug resistance in *K. pneumoniae*.

MATERIALS AND METHODS

Sampling. The samples of urine, pus, sputum, and blood were collected from different wards and then processed for culture identification at Tertiary Care Hospital. The study duration was from January 2017 to December 2019.

Isolation and identification of *K. pneumoniae.* Samples were inoculated on MacConkey agar (Oxoid, UK). Biochemical identification of *K.*

pneumoniae was performed on API 20E (BioMerieux, USA).

Antibiotics susceptibility test. Antibiotics susceptibility evaluation were performed by Kirby Bauer disc diffusion method [8]. Isolates of *K. pneumoniae* were inoculated on Muller Hinton Agar (Oxoid, UK) while antibiotic disks were placed on plates aseptically. Antibiotic disks (Oxoid, UK) used in the study were ampicillin (AMP), amoxicillin-clavulanic acid (AMC), piperacillin-tazobactam (TZP), cloxacillin (OB), ampicillin-sulbactam (SAM), aztreonam (ATM), cephradine (CE), cefixime (CFM), cefotaxime (CTX), ceftriaxone (CRO), cefepime (FEP), cefoperazone-sulbactam (SCF), imipenem (IMI), doripenem (DR), ertapenem (ETP), meropenem (MEM), doxycycline (DO), amikacin (AK), gentamicin (CN), tigecycline (TG), ciprofloxacin (CIP), norfloxacin (NOR), levofloxacin (LEV), , moxifloxacin (MOX), nitrofurantoin (F), fosfomycin (FOS) and colistin (CT). The result was interpreted according CLSI (2018).

Phenotypic detection of carbapenemase production. Modified carbapenem inactivation method (MCIM) was done as described earlier [9]. All carbapenem-resistant *K. pneumoniae* isolates were subjected to carbapenemase production. Briefly, *K. pneumonia* isolates were suspended in 1ml of tryptic soya broth (Oxoid, UK) along with meropenem disc (10 µg) and incubated at 35°C. Meropenem disc was set on MHA inoculated with 0.5 McFarland of *Escherichia coli* (ATCC 25922) and incubated overnight at 37°C. In the case of *K. pneumoniae,* the result was interpreted as the presence of pinpoint colony in the range of 6-18mm zone of inhibition was considered as carbapenemase producer [10].

Phenotypic detection of KPC, NDM, and OXA-48 among *K. pneumoniae.* A combined disc method was used for KPC, NDM, and OXA-48 carbapenemase detection. These phenotypic tests were performed on MHA plates with imipenem discs having carbapenemase inhibitors. For *blaKPC* production, a single imipenem disc (10µg) and the second disc containing imipenem (10µg) with APBA (Acetyl phenylboronic acid, 600µg) on MHA streaked plate with *K. pneumoniae* [11]. For NDM production, *K. pneumoniae* was streaked on MHA plates. A combination of imipenem (10µg) with 0.5 M dehydrated EDTA while another disc containing single imipenem (10µg) was placed on MHA [12]. Oxacillinase (OXA) production was checked with a disc carrying temocillin (30µg) [13].

Molecular detection of *bla*KPC, *bla*NDM and *bla*OXA-48 carbapenemase. Boiling method was used for DNA extraction [14]. PCR amplification was performed using *bla*KPC*, bla*NDM *and bla*OXA-48 specific genes primers as described [15]. PCR amplification condition involved the first round of initial denaturation for 10 min at 94°C and then 36 cycles of denaturation at 94°C, annealing at 52°C and extension at 72°C. PCR product was resolved on agarose gel electrophoresis and visualized under UV light [16, 17].

RESULTS

A total of 1146 (20.9%) samples exhibited bacterial growth while remaining 4329 (79.1%) showed no growth. Among the culture positive samples, 110 (9.6%) isolates were positive for *K. pneumoniae.*

In sample demographics, *K. pneumoniae* isolates from female were 41 (37.2%) while from male were 69 (62.8%). It was observed that age group of 19-50 years encountered the most (n=60; 54.5%) with *K. pneumoniae* infections while the less prevalent (n=5; 4.5%) in 5-12 years of age.

K. pneumoniae (n=110) isolates exhibited increased susceptibility towards cefoperazone/sulbactam (n=105; 95.4%) and cefixime (n=99; 90%). Similarly, more susceptibility was observed against cephradine (83.5%) and amoxicillin-clavulanic acid (72.7%). The resistance towards gentamicin, cloxacillin and cefotaxime was significantly high (100%) (Table 1).

Modified carbapenem inactivation method showed that 31 *K. pneumoniae* isolates were carbapenemase producer while 79 (71.9%) were carbapenemase non-producer. Phenotypic detection showed that 10 (13.6%) *K. pneumoniae* isolates possessed KPC carbapenemase while 21 (22.7%) isolates of *K. pneumoniae* possess NDM carbapenemase. OXA was only detected in one (0.9%) sample (Figure 1, Table 2).

Molecular detection of carbapenemase through PCR showed that *bla*KPC was detected among 15 (13.6%) isolates while *bla*NDM was detected among 25 (22.7%) isolates. Simultaneously the occurrences of *bla*OXA-48 were detected in one isolate. The prevalence rate of *bla*KPC is remarkably low as compared to *bla*NDM both on phenotypic and molecular methods (Figure 2, Table 2).

DISCUSSION

Antibiotic resistance in *K. pneumoniae* is a major health threat that limits the treatment options. This study reported the increased resistance towards diverse classes of antibiotics. *K. pneumoniae* was 100% resistant to ampicillin, cloxacillin, cefotaxime and fosfomycin. cefotaxime was frequently used antibiotics among respiratory infections while fosfomycin was the drug of choice in UTIs. *K. pneumoniae* was susceptible > 90% to few antibiotics such as cefoperazone/sulbactam, ertapenem,

TABLE 1
Antibiotic susceptibility pattern of *K. pneumoniae*.

Antibiotics	Resistant N (%)	Sensitive N (%)
1. Bacterial cell wall inhibitors		
a. Beta-lactam drugs		
Cloxacillin	110 (100)	0 (0)
Ampicillin	110 (100)	0 (0)
Amoxycillin-clavulanic acid	20 (27.3)	80 (72.7)
Ampicillin-sulbactam	55 (50)	55 (50)
Piperacillin-tazobactam	27 (24.6)	83 (75.4)
b. Monobactam		
Aztreonam	11 (10)	99 (90)
c. Cephalosporins		
Cefixime	11 (10)	99 (90)
Cephradine	17 (16.55)	93 (83.5)
Ceftriaxone	93 (83.5)	17 (16.5)
Cefotaxime	110(100)	0 (0)
Cefepime	51 (46.3)	59 (53.7)
Cefoperazone-sulbactam	5 (4.6)	105 (95.4)
d. Carbapenem		
Imipenem	63 (57.6)	37 (42.4)
Ertapenem	10 (7.3)	100 (92.7)
Meropenem	72 (65.4)	38 (34.6)
Doripenem	0 (0)	110 (100)
2. Cell membrane inhibitors		
Colistin	11 (10)	99 (90)
3. Protein synthesis inhibitors		
a. Aminoglycosides		
Gentamicin	99 (90)	11 (10)
Amikacin	44 (40)	66 (60)
b. Tetracycline		
Doxycycline	94 (85.5)	16 (14.5)
4. DNA gyrase inhibitors		
Ciprofloxacin	60 (54.5)	50 (44.5)
Levofloxacin	70 (63.6)	40 (36.4)
Moxifloxacin	40 (36.4)	70 (63.6)
Norfloxacin	38 (34.6)	72 (65.4)
5. Others antibiotics		
Nitrofurantoin	55 (50)	55 (50)
Tigecycline	66 (60)	44 (40)
Fosfomycin	110 (100)	0 (0)

Note: The Resistance/Sensitive was calculated and interpreted as per criteria given in CLSI 2018.

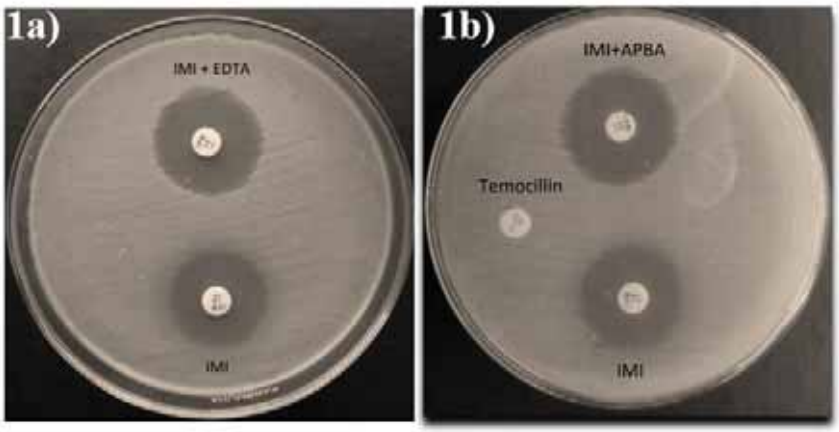

FIGURE 1
Phenotypic detection of KPC, NDM and OXA carbapenemase.
(1a) Shows MHA plate containing two discs IMI+EDTA combined and single IMI, combined disc showed slightly greater zone of inhibition (> 4 mm). (1b) shows MHA plate containing two discs IMI+APBA combined and single IMI, combined disc showed significantly greater zone of inhibition (>4 mm) than IMI alone. In the case of temocillin disc showed no zone of inhibition (< 10 mm).

TABLE 2
Detection of *bla*KPC, *bla*NDM and *bla*OXA-48 in *K. pneumoniae* isolates.

Methods	Carbapenemases								
	KPC N (%)		P value	NDM N (%)		P value	OXA-48 N (%)		P value
	Positive	Negative		Positive	Negative		Positive	Negative	
Phenotypic	10 (9.0)	100 (91.0)	0.288	21 (19.0)	89 (81.0)	0.507	1 (0.9)	109 (99.1)	1
Molecular	15 (13.6)	95 (86.4)	0.288	25 (22.7)	85 (77.3)	0.507	1 (0.9)	109 (99.1)	1

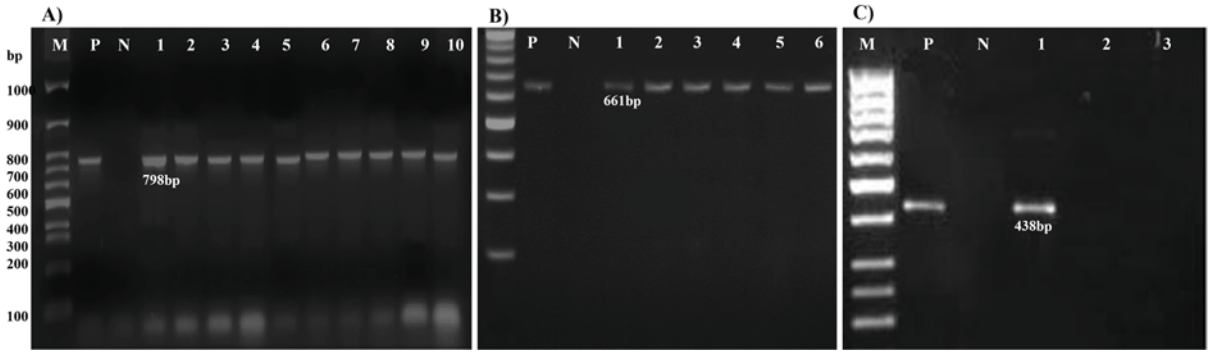

FIGURE 2
Molecular detection of *bla*KPC, *bla*NDM and *bla*OXA-48
A) Detection of blaKPC (798bp), B) Detection of blaNDM (621bp), C) Detection of blaOXA-48 (438bp) M: DNA marker, P: Positive control, N: Negative control, 1-10: Sample of *K. pneumoniae*.

aztreonam, cefixime and colistin. Many reports are published about the resistance of *K. pneumoniae* towards antimicrobial agents [18, 19].

The resistance is because of the production of carbapenemase which causes inactivation of beta-lactam by hydrolysis mechanism [20]. The reason for spreading resistance in developing countries is the misuse of antibiotics such as in Pakistan. However, resistance of *K. pneumoniae* against quinolone was relatively low as compared to cephalosporin ranging from 17-53%, according to surveillance report 10-40% of the resistance of *K. pneumoniae* towards quinolone [21]. As discussed before excessive and frequent use of cephalosporin leads to resistance which developed a trend to switch towards alternative therapy, aminoglycosides, and quinolone [22, 23]. Judicious use and structure dissimilarities are the reasons which overcome the resistance problem. Amoxicillin/clavulanic acid showed a lower picture of resistance rate as compared to other studies [24]. In some cases, carbapenem has excellent efficacy against *K. pneumoniae* infection. These antibiotics are not commonly used so least resistance is observed in *K. pneumoniae*. The *K. pneumoniae* in hospitalized patients was found highly resistant than non-hospitalized [2].

The *K. pneumoniae* isolates were proved resistant and significantly carbapenemase producers by confirmation on a phenotypic test [25, 26, 27]. MCIM was considered accurate for the detection of carbapenemase. The current study showed 28.1% of *K pneumoniae* carbapenemase producer which is in line with other study performed at Rawalpindi, which showed 29% of carbapenemase producer [10]. It is to mention that even one study reported 63% carbapenemase producing *K pneumoniae* [28]. Combined disk test confirmed KPC (n=16; 9%) and NDM (n=21; 19%) which considerably higher than the study performed in 2016 [5]. Another study phenotypically detected that the presence of Metallo beta-lactamase (MBL) was high in Pakistan [29, 30]. MBL is an emerging carbapenemase among the Indian and Pakistan subcontinent [31].

Carbapenemase among *K. pneumoniae* are reported in various region of Pakistan [31]. Molecular study detected KPC 13.6% (n=15) which is in line with previous work [5]. The prevalence of NDM was 22.7% (n=25) that agreed with the study conducted at Karachi [28]. NDM become an emerging threat for European countries due to active tourism causes carriers of NDM [31]. The presence of OXA-48 was recorded low in this region. Although previous study suggested the existence of OXA-48 in Pakistan [32]. Most of the patients visited to Pakistan were found with OXA-48 while hospitalized due to some infection [33].

CONCLUSIONS

The production of carbapenemase among *K. pneumoniae* is an emerging threat. Which causes difficult to treat life-threatening infections caused by *K. pneumoniae.* In the undertaken study resistance in *K. pneumoniae* was highly prevalent through NDM and KPC production. The PCR method detected more carbapenemase-producing isolates as compared to the phenotypic method. The findings of the study will help to understand the mechanism of antibiotics resistance among *K. pneumoniae*.

ACKNOWLEDGEMENTS

This work was supported by Taif University Researchers Supporting Program (project number: TURSP-2020/128), Taif University, Saudi Arabia.

REFERENCES

[1] Jamil, I., Zafar, A., Qamar, M.U., Ejaz, H., Akhtar, J., Waheed, A. (2014) "Multi-drug resistant Klebsiella pneumoniae causing urinary tract infections in children in Pakistan." African Journal of Microbiology Research. 8(4), 316-319.

[2] Amin, A., Ghumro, P.B., Hussain, S. and Hameed, A. (2009) "Prevalence of antibiotic resistance among clinical isolates of Klebsiella pneumoniae isolated from a Tertiary Care Hospital in Pakistan." Malaysian Journal of Microbiology. 5(2), 81-86.

[3] Paterson, D.L., Ko, W.C., Von Gottberg, A., Mohapatra, S., Casellas, J.M., Goossens, H., Mulazimoglu, L., Trenholme, G., Klugman, K.P., Bonomo, R.A. and Rice, L.B. (2004) "Antibiotic therapy for Klebsiella pneumoniae bacteremia: implications of production of extended-spectrum β-lactamases." Clinical Infectious Diseases. 39(1), 31-37.

[4] Helfand, M.S. and Bonomo, R.A. (2003) "β-Lactamases: a survey of protein diversity." Current Drug Targets-Infectious Disorders. 3(1), 9-23.

[5] Sattar, H., Toleman, M., Nahid, F. and Zahra, R. (2016) Co-existence of bla NDM-1 and bla KPC-2 in clinical isolates of Klebsiella pneumoniae from Pakistan. Journal of Chemotherapy. 28(4), 346-349.

[6] Tzouvelekis, L.S., Tzelepi, E., Mentis, A.F. and Tsakris, A. (1993) "Identification of a novel plasmid-mediated β-lactamase with chromosomal cephalosporinase characteristics from Klebsiella pneumoniae." Journal of Antimicrobial Chemotherapy. 31(5), 645-654.

[7] Podschun, R., Ullmann, U. (1998) "Klebsiella spp. as nosocomial pathogens: epidemiology, taxonomy, typing methods, and pathogenicity factors." Clinical Microbiology Reviews. 11(4), 589-603.

[8] Bauer, A.W. (1966) "Kirby Bauer method antimicrobial susceptibility testing by a standardized single disk method." American Journal of Clinical Pathology. 45(4), 493-496.

[9] Van der Zwaluw, K., de Haan, A., Pluister, G.N., Bootsma, H.J., de Neeling, A.J. and Schouls, L.M. (2015) "The carbapenem inactivation method (CIM), a simple and low-cost alternative for the Carba NP test to assess phenotypic carbapenemase activity in gram-negative rods." PloS One. 10(3), 1-13.

[10] Pierce, V.M., Simner, P.J., Lonsway, D.R., Roe-Carpenter, D.E., Johnson, J.K., Brasso, W.B., Bobenchik, A. M., Lockett, Z.C., Charnot-Katsikas, A., Ferraro, M.J., Thomson, R.B. (2017) "Modified carbapenem inactivation method for phenotypic detection of carbapenemase production among Enterobacteriaceae." Journal of Clinical Microbiology. 55(8), 2321-2333.

[11] Amjad, A., Mirza, I.A., Abbasi, S.A., Farwa, U., Malik, N. and Zia, F. (2011) Modified Hodge test: A simple and effective test for detection of carbapenemase production. Iranian Journal of Microbiology. 3(4), 189.

[12] Anwar, M., Ejaz, H., Zafar, A. and Hamid, H. (2016) "Phenotypic detection of metallo-beta-lactamases in carbapenem resistant Acinetobacter baumannii isolated from pediatric patients in Pakistan." Journal of Pathogens. 2016 (3) 1-66

[13] Tsakris, A., Poulou, A., Pournaras, S., Voulgari, E., Vrioni, G., Themeli-Digalaki, K., Petropoulou, D. and Sofianou, D. (2010) "A simple phenotypic method for the differentiation of metallo-β-lactamases and class A KPC carbapenemases in Enterobacteriaceae clinical isolates." Journal of Antimicrobial Chemotherapy. 65(8), 1664-1671.

[14] Van Dijk, K., Voets, G.M., Scharringa, J., Voskuil, S., Fluit, A.C., Rottier, W.C., Leverstein-Van Hall, M.A., Stuart, J.C. (2014) "A disc diffusion assay for detection of class A, B and OXA-48 carbapenemases in Enterobacteriaceae using phenyl boronic acid, dipicolinic acid and temocillin." Clinical Microbiology and Infection. 20(4), 345-349.

[15] Poirel, L., Walsh, T.R., Cuvillier, V. and Nordmann, P. (2011) "Multiplex PCR for detection of acquired carbapenemase genes." Diagnostic Microbiology and Infectious Disease. 70(1), 119-123

[16] Dashti, A.A., Jadaon, M.M., Abdulsamad, A.M. and Dashti, H.M. (2009) "Heat treatment of bacteria: a simple method of DNA extraction for molecular techniques." Kuwait Medical Journal. 41(2), 117-122.

[17] Ellington, M.J., Kistler, J., Livermore, D.M. and Woodford, N. (2007) "Multiplex PCR for rapid detection of genes encoding acquired metallo-β-lactamases." Journal of Antimicrobial Chemotherapy. 59(2), 321-322.

[18] Poirel, L., Walsh, T.R., Cuvillier, V. and Nordmann, P. (2011) "Multiplex PCR for detection of acquired carbapenemase genes." Diagnostic Microbiology and Infectious Disease. 70(1), 119-123.

[19] Padmini, N., Ajilda, A.A K., Sivakumar, N. and Selvakumar, G. (2017) "Extended spectrum β-lactamase producing Escherichia coli and Klebsiella pneumoniae: critical tools for antibiotic resistance pattern." Journal of Basic Microbiology. 57(6), 460-470.

[20] Versporten, A., Bolokhovets, G., Ghazaryan, L., Abilova, V., Pyshnik, G., Spasojevic, T., Korinteli, I., Raka, L., Kambaralieva, B., Cizmovic, L. and Carp, A. (2014) "Antibiotic use in eastern Europe: a cross-national database study in coordination with the WHO Regional Office for Europe." The Lancet Infectious Diseases. 14(5), 381-387.

[21] Subha, A. and Ananthan, S. (2002) "Extended spectrum beta lactamase (ESBL) mediated resistance to third generation cephalosporins among Klebsiella pneumoniae in Chennai." Indian Journal of Medical Microbiology. 20(2), 92.

[22] Shigemoto, N., Kuwahara, R., Kayama, S., Shimizu, W., Onodera, M., Yokozaki, M., Hisatsune, J., Kato, F., Ohge, H. and Sugai, M. (2012) "Emergence in Japan of an imipenem-susceptible, meropenem-resistant Klebsiella pneumoniae carrying blaIMP-6." Diagnostic Microbiology and Infectious Disease. 72(1), 109-112.

[23] McDanel, J., Schweizer, M., Crabb, V., Nelson, R., Samore, M., Khader, K., Blevins, A.E., Diekema, D., Chiang, H.Y., Nair, R. and Perencevich, E. (2017) "Incidence of extended-spectrum β-lactamase (ESBL)-producing Escherichia coli and Klebsiella infections in the United States: a systematic literature review." Infection Control & Hospital Epidemiology. 38(10), 1209-1215.

[24] Szymankiewicz, M., Wróblewski, M., Janicka, G., Sekowska, A., Wojda, M. and Kłyszejko, C. (2002). "Resistance of Klebsiella pneumoniae strains producing and not producing ESBL (extended-spectrum beta-lactamase) type enzymes to selected non-beta-lactam antibiotics." Medical Science Monitor. 8(3), 100-104.

[25] Fouzia, B. and Damle, A.S. (2015) "Genotypic detection of extended-spectrum β-lactamase-producing Klebsiella pneumoniae in a Tertiary care hospital." International Journal of Biomedical and Advance Research. 6, 91-7.

[26] Giske, C.G., Gezelius, L., Samuelsen, Ø., Warner, M., Sundsfjord, A. and Woodford, N. (2011) "A sensitive and specific phenotypic assay for detection of metallo-β-lactamases and KPC in Klebsiella pneumoniae with the use of meropenem disks supplemented with aminophenylboronic acid, dipicolinic acid and cloxacillin." Clinical Microbiology and Infection. 17(4), 552-556.

[27] Byun, J.H., Seo, Y., Kim, D., Kim, M., Lee, H., Yong, D., Lee, K. and Chong, Y. (2020) "An agar plate-based modified carbapenem inactivation method (p-mCIM) for detection of carbapenemase-producing Enterobacteriaceae." Journal of Microbiological Methods. 168, 105781.

[28] Laolerd, W., Akeda, Y., Preeyanon, L., Ratthawongjirakul, P. and Santanirand, P. (2018) "Carbapenemase-producing carbapenem-resistant Enterobacteriaceae from Bangkok, Thailand, and their detection by the Carba NP and modified carbapenem inactivation method tests." Microbial Drug Resistance. 24(7), 1006-1011.

[29] Sultan, B.A., Khan, E., Hussain, F., Nasir, A. and Irfan, S. (2013) "Effectiveness of modified Hodge test to detect NDM-1 carbapenemases: an experience from Pakistan." Journal Pakistan Medical Association. 63(8), 955-60.

[30] Pesesky, M.W., Hussain, T., Wallace, M., Wang, B., Andleeb, S., Burnham, C.A.D. and Dantas, G. (2015) "KPC and NDM-1 genes in related Enterobacteriaceae strains and plasmids from Pakistan and the United States." Emerging Infectious Diseases. 21(6), 1034.

[31] Qamar, M.U., Walsh, T.R., Toleman, M.A., Tyrrell, J.M., Saleem, S., Aboklaish, A. and Jahan, S. (2019) "Dissemination of genetically diverse NDM-1,-5,-7 producing-Gram-negative pathogens isolated from pediatric patients in Pakistan." Future Microbiology. 14(8), 691-704.

[32] Kumarasamy, K.K., Toleman, M.A., Walsh, T.R., Bagaria, J., Butt, F., Balakrishnan, R., Chaudhary, U., Doumith, M., Giske, C.G., Irfan, S. and Krishnan, P. (2010) "Emergence of a new antibiotic resistance mechanism in India, Pakistan, and the UK: a molecular, biological, and epidemiological study." The Lancet Infectious Diseases. 10(9), 597-602.

[33] Al-Zahrani, I.A. and Alasiri, B.A. (2018) "The emergence of carbapenem-resistant Klebsiella pneumoniae isolates producing OXA-48 and NDM in the Southern (Asir) province, Saudi Arabia. Saudi Medical Journal. 39(1), 23-30.

Received: **18.08.2021**
Accepted: **02.02.2022**

CORRESPONDING AUTHOR

Hazir Rahman
Department of Microbiology,
Abdul Wali Khan University Mardan,
Pakistan

e-mail: hazirrahman@awkum.edu.pk

© by PSP Volume 31– No. 05/2022 pages 4750-4758 Fresenius Environmental Bulletin

THE EFFECTS OF VERMICOMPOST APPLICATION ON ANTIOXIDANT ENZYMES OF CORN (*Zea mays* L.) GROWN AS A TEST PLANT IN SUGAR BEET SOIL SAMPLES

Tulay Dizikisa[1], Kadriye Uruc Parlak[2,*], Nesrin Yildiz[3]

[1]Agri Ibrahim Cecen University, Vocational Training School, Agri, Turkey
[2]Agri Ibrahim Cecen University, Faculty of Arts and Sciences, Agri, Turkey
[3]Ataturk University, Faculty of Agriculture, Dept. of Soil Science and Plant Nutrition, Erzurum, Turkey

ABSTRACT

Vermicomposting is a low-price, environmentally companionable practice in which organic remnant is processed to raise fertility in agriculture. Humic substances in vermicompost improve the chemical and physical properties of soils and promote plant growth. For the study, soil samples were taken from 10 different points from Eleşkirt district of Ağrı province. Grown in Sugar Beet Soils. Vermicompost was applied to the taken soils at 0, 2, 6 g to 1 kg of soil (0, 2, 6 g/ 1 kg /pot of soil). This work aims to determine the chlorophyll amount, antioxidant enzyme activity, and lipid peroxidation on Zea mays plants associated with vermicompost application. The results show that the application of vermicompost causes a decrease in catalase, ascorbate peroxidase, and guaiacol peroxidase enzyme activities and lipid peroxidation, but an increase in superoxide dismutase enzyme activity. Furthermore, vermicompost applications did not have a negative effect on plant growth. On the contrary, it increased plant growth.

KEYWORDS:
Vermicompost, Zea mays, Lipid Peroxidation, Antioxidant Activity, soil

INTRODUCTION

In recent years, the overuse of chemical fertilizers, herbicides, and pesticides has come to the fore in industrial agriculture. These chemicals cause deterioration of soils, biological resources [1, 2] and water resources anddecrease the quality of food products [3]. To overcome these problems and minimize the health risk, alternative methods based on sustainable agriculture and organic fertilizer use that prevent excessive nitrate accumulation in the soil are considered viable methods. Organic farming methods minimize environmental pollution and are an alternative farming practice that is highly economical in crop production [4]. Vermicomposting is an inexpensive and practicable method for appropriate and influential administration of livestock manure [5].

Vermicompost (VC) is a type of compost produced by non-thermophilic biodegradation by a red roundworm named *Eisenia foetida* [5]. Vermicompost may augment the capacity to maintain proper plant nutrients due to having superior porosity, aeration, water holding capacity, drainage, and microbial activity capacity [6]. With the application of vermicompost to the soil, microbial activities occurring in the soil are stimulated, nitrogen fixation increases the presence of nitrogen and phosphorus for plants, and no bad odors occur during the process. Phosphorus dissolves, thus, improve soil quality and nutritional conditions. Since vermicompost is wealthy in microbial action and involves antagonistic organisms to check herb pathogens, it is an influential biocontrol factor. It is, therefore a suitable material for applications in sustainable agriculture. Some studies demonstrate that the growth of many vegetables and fruits are affected by vermicompost applications in the glasshouse [7, 8] and in the field [9-11]. Zuo et al. [8] reported that vermicompost affects morphological properties and physiological and biochemical properties. In another similar study, vermicompost improved yield and fruit biomass in the pineapple plant and increased leaf count and height [12]. The reason for the growth of the plant with the application of vermicompost; nutrients, microbial biomass, biologically active substances, and increased water holding capacity of the soil [13, 14]. Vermicompost contains numerous plant organizers comprising humic acids, gibberellins, auxins, and microbial origin cytokinins [15]. In addition, the activities of soil enzymes such as phosphodiesterase, urease, arylsulfatase, and phosphormonoesterase increase with the applications of vermicompost [16, 17].

Maize (*Zea mays*), which is used to feed humans and animals, is one of the most valuable crops grown globally. Maize cultivation is carried out on approximately 160 million hectares in the world, resulting in 822 million tons of product [18]. Maize should be considered a food source and has an important role in the development of the national economy by creating an important raw material source for the domestic industry [19]. Maize in Turkey (600,000 hectares cultivated in) ranks third after wheat and barley. Previous studies have shown that

maize can be used as a bioindicator in ecotoxic evaluations of contaminated soils.

Although there are studies on the impacts of VC on field and greenhouse plants, there is no literature on the effect of VC on maize. To complete this part that we see incomplete in the literature; in this study, it was planned to determine the effect of fertilizer by taking soil samples from Ağrı Eleşkirt region, where sugar beet farming is intense, and growing corn plants with different vermicompost doses on these soils. For this purpose, soil sampling was made from 10 different points, and different amounts of vermicompost were applied to the soil to observe the change in soil fertility, corn development, and enzyme activity. Vermicompost fertilizer was obtained from a private company.

MATERIALS AND METHODS

Plant Materials and Experimental Design. To investigate the effects of vermicompost application on the biochemical properties of the corn plant, soil samples taken from Eleşkirt district of Ağrı province were tested in a heated greenhouse. The province of Ağrı is located approximately between 38˚ 59' - 40˚ 02' northern parallels and 42˚ 15' - 44˚ 36' east meridians, and the area of the province reaches 11,099 km². Ağrı was established at an altitude of 1640 m above sea level. While taking samples from the determined area, attention was paid to parameters such as color, slope, soil transport, depth, humidity, direction, and vegetation. Soil samples were collected based on root depth (from at least ten different points along zigzag lines in areas smaller than 20 da, since the sampling units are uniform), and the samples were mixed, put in bags and labeled, and then brought to the laboratory for analysis.

The experiment was carried out in the heated greenhouse like a pot experiment. The study was carried out in triplicate with ten different soils taken as a growing medium. Different amounts of vermicompost applications have been tested; corns were planted by mixing 1000 g soil per pot used and three doses of vermicompost (0 g, 2 g, and 6 g) homogeneously mixed with soil. During the experiment, the field capacity level was planned and irrigation was done every three days. The moisture content of the trial soils was adjusted to the field capacity moisture level.

After the plants were harvested, some parts were cleaned with pure water, and frozen at fluid nitrogen, and stored at -80 °C until further usage. Other samples were dried at 70 ◦C then plants were digested with 10 mL of intense HNO_3, using a Milestone Start microwave. Afterward, thevolume of every example was regulated to 25 mL using deionized water [20]. Specification of the element amounts in whole examples (triplicate) was achieved by Thermo ICP-MS. Physico-chemical properties of vermicompost and soil used in the experiment (Table 1 and Table 2).

TABLE 1
Physico-chemical properties of the applied vermicompost.

Properties	Vermicompost
pH	7.76
Electrical conductivity (dS m^{-1})	14,3
Organic matter (%)	52,9
Total N (%)	4,13
Na (%)	10,2
Ca (%)	7,11
P (%)	22,8
K (%)	14,3

TABLE 2
Physico-chemical properties of soil used in the experiment.

	pH	Organic matter (%)	Electrical conductivity (dS m^{-1})	Total N (%)	P (ppm)	K (ppm)
S1	6.61	1.60	124	0.10	13	65.50
S2	6.75	2.93	129	0.16	14	64.00
S3	6.81	3.17	155	0.18	12	61.00
S4	6.89	2.86	175	0.16	13	61.50
S5	6.67	3.14	150	0.20	15	64.00
S6	6.71	2.24	237	0.20	16	62.50
S7	6.83	2.56	222	0.17	16	60.50
S8	6.89	3.34	183	0.21	14	61.50
S9	6.83	2.11	163	0.20	15	63.50
S10	6.95	2.28	155	0.23	16	63.00

Determination of the Total Chlorophyll. The total chlorophyll amounts were detected considering the technique of Yang et al. [21]. Fronds (200 mg) were homogenized in 10 mL acetone (80%). The absorbance of the supernatant fraction of the homogenates centrifuged at 3000 rpm was deter-mined at 663.6 and 646.6 nm by UV–vis Spectrophotometer (Shimadzu V-1800). Total chlorophyll pigment concentration was calculated using the equality declared by Porra et al. [22].

Determination of Antioxidant Enzymes. Extraction for Enzyme Studies. Fresh plant piece (0.2 g) was homogenized with 2 mL of 50 mM potassium phosphate buffer (pH 7.0) involving 1% polyvinylpyrrolidone and 1 mM EDTA. The homogenate was centrifuged at 15,000 g for 25 minutes at 4° C [23]. The supernatants acquired after centrifugation were utilized in enzyme detection studies.

CAT (Catalase). CAT activity was carried out spectrophotometrically considering the method of Aebi [24] at 240 nm in enzyme extract (about 50 mg of protein) having 15 mM H_2O_2 and potassium phosphate buffer (150 mM, pH 7).

APX (Ascorbate peroxidase). The APX activity was detected by monitoring the absorption of ascorbate at 290 nm concerning the procedure of Nakano and Asada [25].

SOD (Superoxide dismutase). SOD activity was detected by gauging the inhibition of the photochemical degradation of nitroblue tetrazolium (NBT) [26].

GPOX (Gualkol Peroxidase). GPOX activity was carried out using a slightly modified version of the method [27]. GPOX activity was measured spectrophotometrically at 470 nm and was calculated using the extinction coefficient of 25.5 mM^{-1} cm^{-1}.

Statistical Evaluation of Results. Entire tests were replicated in triplicate. Worthes shown in the tables indicated the mean worthes ± standard error (SE) for every vermicompost concentration. ANOVA was made to verify the changefulness of the datum and the effectualness of the conclusions, and Tukey analyses were carried out to define substantial distinctions inter the practices. Distinct letters demonstrated importantly dissimilar worthes $P < 0.05$.

RESULTS AND DISCUSSION

Composition of Vermicompost. Worm humus has a very high organic matter content (52.9%), above the average value reported in other studies [28, 29]. The pH value of vermicompost we used was determined to be approximately 7.76. The fact that the pH values of the vermicompost are close to neutrality indicates the biological stabilization of the material used. In addition, the nutrient concentra-tions agree with values reported for cattle manure vermicomposts [29].

Morphological Parameters. It is thought that vermicompost increases the growth and yield of various species through direct or indirect beneficial effects and these benefits are in the form of long-term effects. Furthermore, using organic fertilizers such as vermicompost helps maintain soil fertility and has evident environmental benefits as it enables on-farm recycling of organic waste. However, it has been reported that repeated applications over several years are required to see the benefits of organic fertilizers on soil fertility. In our study with vermicompost, differences were observed in the agronomic properties of the corn plant with increasing doses of vermicompost applications. Significant increases were determined in values compared to the control. However, it was determined that the increase in corn plant height, fresh weight, and dry weight values in worm fertilizer application compared to the control was very important at the level of 1% (Table 3). These results we have obtained are in accordance with the findings of Jahan et al. [30].

Similarly, in the study conducted by [31], the result was that vermicompost increases the wet and dry weight of the pepper plant and has a positive effect on nutrient content supports our results. Zuo et al. [8] reported that leaf area, leaf number, and plant fresh-dry weight of strawberry increased on vermicompost applications. Leaf dry weight, chlorophyll content and the number of leaves of cucumber (*Cucumis sativus*) [32], leaf number, yield, and chlorophyll content of *Lactuca sativa* L. [7], chlorophyll and carotenoid contents of leaves of chickpea (*Cicer arietinum* L. cv. *pirouz*) [33] increased on using vermicompost.

Effects of Vermicompost in Plants Biochemical Parameters. The form of nitrogen (nitrate) that plants can take is more in vermicompost than conventional composted fertilizer. Nitrogen fertilizing improves daylight absorption by positively improving plant growth and leaf area index, thereby resulting in more dry matter and crops in the plant [34]. In this study, we conducted with different concentrations of worm manure. An increase was observed in the amount of chlorophyll in proportion to the increased amount of worm manure in corn. Similarly, increased chlorophyll concentrations were shown in chickpea and beans because of the treatment of vermicompost [33, 34]. The favorable impact of vermicompost application on chlorophyll amount is probably because of food elements such as Mg, N,

Fe, and P in the vermicompost, which play an important role in the photosynthetic structure and chlorophyll formation [34-36]. Mg joins in the photosynthetic pigment synthesis straightly. We determined that vermicompost applications importantly reduced the MDA content compared with the control (Table 4). The lowest MDA content was obtained in 2gr vermicompost applications. Statistically, the difference between applications and control can be seen. Zuo et al. [8] obtained similar results with us in their study with strawberries.

The fact that the MDA content decreases with increasing amounts of vermicompost in our study shows that vermicompost has a positive effect against aging by improving the activities of antioxidant enzymes.

Vermicompost contains some micronutrients such as Cu. Zn. Fe and Mn function as prosthetic groups of antioxidant enzymes. Antioxidant enzymes such as SOD, CAT, APX and GPOX play a significant role in destroying free radicals or making them less harmful [37]. An sended up O2 $^{\bullet-}$ level is the early step in the series reaction of antioxidative functions in cells [38]. SOD is a fundamental antioxidant enzyme that missions in plant stress reaction and transforms O_2^- into H_2O_2 reduction the toxic effect of free radicals [39]. In this study, we also tried SOD activity and determined important rises in SOD activity in complete vermicompost applications compared to control (Table 5). The highest SOD enzyme activity (1.1839 IU/mg protein) was obtained from S5 soil samples (2 g vermicompost application), and the lowest SOD enzyme activity (0.2378 IU/mg protein) was obtained from S1 soil samples (control group) (Table 5). The difference in SOD activity increased depend on the vermicompost amounts, soil structure, and different species of plants (Rahbarian et al. 2012).

Catalase, considered one of the iron-including proteins in plants, plays a significant role in removing and scavenging the manufactured H_2O_2 in peroxisomes. By decreasing the detrimental effects of ROS averts cell membrane degradation and helps the plant to survive [40-42]. Table 5 demonstrated that vermicompost amounts rise resulted in an important reduction in CAT and APX enzyme against with the control. The lowest cat activity was 0.001 IU / mg protein in 6 g application in S5 soil. Similarly the lowest APX activity was found as 0.01 IU / mg protein in 6 g application in S4 soil. Unlike CAT, APX is more interested in H_2O_2 so more specific places allow the removal of small amounts of H_2O_2 [43]. As in our study Rahbarian et al. [41] and Mirzamohammadi et al. [44] showed that an increase in vermicompost significantly reduced the CAT enzyme activities of chickpeas and mint compared to controls, but some researchers found there were increase in species such as lettuce and chickpea [33, 45].

TABLE 3
Mean values of growth characteristics in different vermicompost treatments

	Samples	Fresh weight (gr)	Dry weight (gr)	Plant Height (cm)
	0 gr	11.255	1.327	74.67
S1	**2 gr**	10.255	1.223	84.16
	6 gr	19.083	2.217	95.10
	0 gr	10.412	1.312	84.56
S2	**2 gr**	12.508	1.595	76.60
	6 gr	14.846	1.733	93.96
	0 gr	11.479	1.171	84.00
S3	**2 gr**	16.673	1.846	86.63
	6 gr	18.403	2.077	94.60
	0 gr	11.025	1.381	83.90
S4	**2 gr**	16.311	1.654	86.56
	6 gr	19.179	2.386	94.80
	0 gr	16.397	1.730	85.20
S5	**2 gr**	22.167	2.631	92.10
	6 gr	20.914	2.457	87.26
	0 gr	20.631	2.090	100.76
S6	**2 gr**	20.697	2.557	98.66
	6 gr	14.737	1.852	84.73
	0 gr	10.630	1.226	79.40
S7	**2 gr**	16.019	1.890	88.90
	6 gr	19.139	2.412	82.03
	0 gr	13.177	1.515	84.36
S8	**2 gr**	16.405	1.904	84.13
	6 gr	17.780	2.167	80.10
	0 gr	13.076	1.380	87.30
S9	**2 gr**	13.868	1.399	79.20
	6 gr	8.941	0.902	75.53
	0 gr	9.102	0.913	68.60
S10	**2 gr**	13.319	1.440	66.56
	6 gr	12.336	1.115	78.66

TABLE 4
Comparison of MDA (lipid peroxidation) and chlorophyll amounts of the maize affected by vermicompost

	Applied Vermicompost Amounts	*Total Chlorophyll (mg g^{-1} FW)*	*MDA (nmol g^{-1} FW)*
	0 gr	2,142±0,038	0,285±0,002
S1	**2 gr**	2,371±0,036*	0,185±0,001*
	6 gr	2,473±0,028*	0,258±0,001*
	0 gr	2,643±0,032	0,228±0,001
S2	**2 gr**	3,206±0,028*	0,187±0,003*
	6 gr	3,430±0,017*	0,212±0,001*
	0 gr	2,613±0,003	0,177±0,002
S3	**2 gr**	2,811±0,031*	0,157±0,000*
	6 gr	3,015±0,014*	0,159±0,000*
	0 gr	2,148±0,032	0,181±0,001
S4	**2 gr**	2,529±0,049*	0,174±0,000
	6 gr	3,122±0,037*	0,180±0,001
	0 gr	2,642±0,036	0,219±0,001
S5	**2 gr**	2,979±0,028*	0,180±0,002*
	6 gr	3,241±0,035*	0,192±0,001*
	0 gr	3,321±0,035	0,202±0,002
S6	**2 gr**	3,579±0,013*	0,184±0,004*
	6 gr	3,643±0,025*	0,193±0,001*
	0 gr	3,368±0,103	0,221±0,003
S7	**2 gr**	3,702±0,034*	0,177±0,002*
	6 gr	3,875±0,053*	0,190±0,002*
	0 gr	3,184±0,056	0,217±0,002
S8	**2 gr**	3,475±0,059*	0,163±0,004*
	6 gr	4,036±0,057*	0,184±0,001*
	0 gr	3,686±0,085	0,218±0,000
S9	**2 gr**	3,715±0,048	0,169±0,000*
	6 gr	4,206±0,067*	0,188±0,002*
	0 gr	3,126±0,185	0,199±0,001
S10	**2 gr**	3,439±0,065*	0,188±0,002*
	6 gr	4,391±0,019*	0,192±0,002

Comparison of control and treatment groups (ns and *: non significant and significant at 5% probability levels).

TABLE 5
Comparison of CAT, SOD, APX, and GPOX activities of the maize affected by vermicompost

	Applied Vermicompost Amounts	**CAT (unit mg^{-1} protein)**	**SOD (unit mg^{-1} protein)**	**APX (unit mg^{-1} protein)**	**GPOX (ΔA g^{-1} FW)**
	0 gr	0,011±0,000	0,237±0,077	0,194±0,001	5153,081±25,637
S1	**2 gr**	0,001±0,000*	0,658±0,176*	0,078±0,000*	5116,243±25,453
	6 gr	0,001±0,000*	0,493±0,196	0,053±0,000*	4073,650±20,266
	0 gr	0,015±0,000	0,491±0,009	0,091±0,000	6376,083±31,721
S2	**2 gr**	0,004±0,000*	0,947±0,130*	0,070±0,000*	4674,006±23,253
	6 gr	0,004±0,000*	0,750±0,196	0,012±0,000*	4438,057±22,079
	0 gr	0,025±0,000	0,509±0,135	0,127±0,001	4406,887±21,924
S3	**2 gr**	0,006±0,000*	0,810±0,204	0,079±0,000*	4125,412±20,524
	6 gr	0,005±0,000*	0,780±0,235	0,054±0,000*	4038,135±20,090
	0 gr	0,023±0,000	0,959±0,165	0,132±0,001	10097,790±50,237
S4	**2 gr**	0,010±0,000*	1,017±0,045	0,065±0,000*	5288,529±26,311
	6 gr	0,009±0,000*	0,978±0,100	0,009±0,000*	4607,887±22,924
	0 gr	0,014±0,000	0,605±0,123	0,123±0,001	5140,235±25,573
S5	**2 gr**	0,008±0,000*	1,183±0,047*	0,091±0,000*	5066,560±25,206
	6 gr	0,001±0,000*	0,898±0,072	0,062±0,000*	4292,975±21,358
	0 gr	0,014±0,000	0,858±0,005	0,183±0,001	5116,621±25,455
S6	**2 gr**	0,014±0,000	1,087±0,022	0,083±0,000*	4615,444±22,962
	6 gr	0,013±0,000	0,976±0,002	0,076±0,000*	4574,261±22,757
	0 gr	0,014±0,000	0,685±0,063	0,197±0,001	5633,289±28,026
S7	**2 gr**	0,011±0,000	1,173±0,083*	0,071±0,000*	4973,239±24,742
	6 gr	0,010±0,000*	1,137±0,043*	0,059±0,000*	4938,479±24,569
	0 gr	0,013±0,000	1,017±0,022	0,105±0,000	6108,775±30,391
S8	**2 gr**	0,009±0,000*	1,153±0,101	0,079±0,000*	4562,738±22,700
	6 gr	0,005±0,000*	1,100±0,104	0,015±0,000*	4521,367±22,494
	0 gr	0,009±0,000	0,765±0,132	0,091±0,000	5104,720±25,396
S9	**2 gr**	0,003±0,000*	1,110±0,084	0,087±0,000*	4988,540±24,818
	6 gr	0,003±0,000*	1,094±0,115	0,082±0,000*	4685,529±23,311
	0 gr	0,034±0,000	0,748±0,072	0,183±0,001	4857,626±24,167
S10	**2 gr**	0,008±0,000*	1,032±0,008	0,088±0,000*	4521,178±22,493
	6 gr	0,007±0,000*	0,962±0,145	0,032±0,000*	2962,672±14,739

Comparison of control and treatment groups (ns and * : non significant and significant at 5% probability levels).

TABLE 6
Correlation values between plant samples, enzymes, and morphological features

	Chl a	Chl b	Total Chl	MDA	CAT	AST	SOD	GPOX	Ca	Mg	Na	Cu	Zn	B	Mn	Mo	Ni	Pb	Cd	Co	Fresh Weight	Dry Weight	Plant Height	P
Chl b	0.892**																							
Total Chl	0.980**	0.964**																						
MDA	-0.302**	-0.266*	-0.295**																					
CAT	-0.232*	-0.230*	-0.238*	0.047																				
AST	-0.344**	-0.352**	-0.357**	0.378**	0.614**																			
SOD	0.604**	0.518**	0.582**	-0.634**	-0.169	-0.385**																		
GPOX	-0.422**	-0.454**	-0.448**	0.090	0.417**	0.381**	-0.015																	
Ca	0.282**	0.297**	0.297**	-0.344**	-0.067	-0.194	0.145	-0.223*																
Mg	0.113	0.075	0.100	0.069	0.024	-0.174	-0.182	-0.234*	0.270*															
Na	-0.496**	-0.360**	-0.450**	0.126	-0.098	-0.048	-0.455**	0.028	0.028	0.062														
Cu	-0.559**	-0.389**	-0.500**	0.178	-0.009	0.191	-0.583**	-0.071	0.067	0.062	0.732**													
Zn	-0.663**	-0.504**	-0.612**	0.197	0.011	0.061	-0.581**	0.050	0.013	0.096	0.831**	0.814**												
B	-0.456**	-0.364**	-0.428**	0.185	-0.109	-0.008	-0.412**	0.006	-0.014	0.097	0.727**	0.696**	0.709**											
Mn	-0.600**	-0.466**	-0.549**	0.310**	-0.086	-0.020	-0.555**	0.085	-0.061	0.131	0.838**	0.718**	0.829**	0.754**										
Mo	-0.627**	-0.476**	-0.578**	0.152	-0.012	-0.002	-0.549**	0.031	0.048	0.115	0.801**	0.794**	0.843**	0.711**	0.780**									
Ni	-0.277**	-0.243*	-0.270*	0.416**	-0.005	0.248*	-0.355**	-0.006	-0.172	0.021	0.105	0.229*	0.243*	0.210*	0.113	0.197								
Pb	-0.215*	-0.204	-0.216*	-0.110	-0.067	-0.023	-0.081	-0.081	0.081	-0.038	0.225*	0.236*	0.318**	0.087	0.171	0.155	0.010							
Cd	-0.351**	-0.258*	-0.320**	-0.190	-0.045	0.032	-0.240*	-0.142	0.089	-0.035	0.459**	0.517**	0.452**	0.338**	0.404**	0.465**	0.013	0.720**						
Co	-0.178	-0.124	-0.159	0.136	-0.163	0.022	-0.231*	-0.171	0.073	0.151	0.341**	0.491**	0.406**	0.536**	0.453**	0.395**	0.214*	0.078	0.242*					
Fresh Weight	0.085	0.088	0.089	-0.201	-0.306**	-0.340**	0.301**	-0.266*	-0.091	-0.139	-0.115	-0.138	-0.194	-0.094	-0.153	-0.140	-0.106	0.160	0.102	-0.075				
Dry Weight	0.041	0.062	0.052	-0.161	-0.289**	-0.360**	0.283**	-0.167	-0.124	-0.132	-0.049	-0.141	-0.133	-0.035	-0.095	-0.112	-0.084	0.148	0.064	-0.056	0.931**			
Plant Height	-0.148	-0.043	-0.106	-0.064	-0.153	-0.206	0.061	-0.031	-0.095	-0.056	0.141	0.078	0.082	0.082	0.157	0.179	-0.106	0.169	0.197	0.123	0.529**	0.529**		
P	0.040	0.019	0.032	0.053	-0.065	-0.168	-0.041	-0.033	0.052	0.012	0.089	0.054	0.049	0.113	0.148	0.188	-0.017	-0.030	-0.053	-0.015	-0.004	0.012	0.061	
N	0.103	0.130	0.117	0.147	-0.139	-0.038	0.068	-0.021	-0.085	0.105	-0.004	-0.176	-0.168	-0.058	-0.008	-0.126	0.011	-0.070	-0.110	-0.126	0.349**	0.381**	0.252*	0.033

Comparison of datum shows that all vermicompost treatments had more importantly reduced GPOX activity than the controls (Table 5). This tion of GPOX, CAT, and APX activities using vermicompost was presumed from the biological and physical construction of vermicompost. Correlation values

between plant samples, enzymes and morphological features are given in Table 6.

CONCLUSIONS

Vermicompost can be defined as a mixture of earthworm excrement. Moistened organic matter and microorganisms when added to the plant growing medium. Increases germination, growth flowering, fruit production and accelerates the development of various plant species. It regulates the substances necessary for plant growth and improves the soil structure. Thus it provides direct or indirect benefits. Mainly stimulating plant growth; it can vary depending on the biological properties of vermicompost. Growing conditions and the type of plant used. In this study. The amount of chlorophyll increased with the increasing amount of VC, and the highest amount of chlorophyll was obtained from 6 g. application. However, the highest MDA (lipid peroxidation) was observed in the control group, while the lowest MDA was obtained in 2 g VC applications. At the same time, there was a decrease in the CAT, APX and GPOX enzyme activities in corn. Vermicompost applications increased, while the SOD enzyme activity increased. It is thought that different vermicompost applications may have controlled the ROS reactions and the formation of lipid peroxidation by affecting the activity of some enzymes such as SOD, CAT, APX and GPOX in the antioxidant defense system.

Although positive response were obtained on plant enzyme activity and chlorophyll content with vermicompost fertilizer application, caution should be exercised at the point of recommendation since the electrical conductivity (salt content) of the selected vermicompost fertilizer is high. It was requested to contribute to sustainable soil fertility by reminding the vermicompost producer to check whether the water it uses is salty or not and to take precautions in this regard.

ACKNOWLEDGEMENTS

Ethics Approval and Consent to Participate: Not applicable.

Consent for Publication: Not applicable.

Author contributions. T.D. carried out the growth of plants and made soil analyzes, K.U.P. studied biochemical and molecular tests, N.Y. coordinated the study, K.U.P. wrote the manuscript; all authors commented on and improved the manuscript.

REFERENCES

[1] Ahmadpour, R. and Armand, N. (2020) Effect of ecophysiological characteristics of tomato (*Lycopersicon esculentum* L.) in response to organic fertilizers (compost and vermicompost). Notulae Botanicae Horti Agrobotanici Cluj-Napoca. 48(3), 1248-1259.

[2] Sahin, S. and Kurt, H. (2020) Effects of vermicompost applications on growth and phosphorus uptake of maize plants (Zea Mays L.). Fresen. Environ. Bull. 29(12), 11216- 11222.

[3] Gill, H.K. and Garg, H. (2014) Pesticide: environmental impacts and management strategies. Pesticides-toxic aspects. Intech. 8, 187-230.

[4] Padel, S., Röcklinsberg H. and Schmid, O. (2009) The implementation of organic principles and values in the European Regulation for organic food. Food Policy. 34(3), 245-251.

[5] Garg, P., Gupta, A. and Satya, S. (2006) Vermicomposting of different types of waste using *Eisenia foetida*: A comparative study. Bioresource Technology. 97(3), 391-395.

[6] Chaudhuri, P., Pal, T.K. Bhattacharjee, G., Dey, S.K. (2000) Chemical changes during vermicomposting (*Perionyx excavatus*) of kitchen wastes. Tropical Ecology. 41(1), 107-110.

[7] Papathanasiou, F., Papadopoulos, I., Tsakiris, I., Tamoutsidis, E. (2012) Vermicompost as a soil supplement to improve growth, yield and quality of lettuce (*Lactuca sativa* L.). J. Food Agric. Environ. 10(2), 677-682.

[8] Zuo, Y., Zhang, J., Zhao, R., Dai, H., Zhang, Z. (2018) Application of vermicompost improves strawberry growth and quality through increased photosynthesis rate, free radical scavenging and soil enzymatic activity. Scientia Horticulturae. 233, 132-140.

[9] Eo, J. and Park, K.C. (2019) Effect of vermicompost application on root growth and ginsenoside content of *Panax ginseng*. Journal of Environmental Management. 234, 458-463.

[10] Gholami, H., Raouf Fard, F., Saharkhiz, M.J., Ghani, A. (2018) Yield and physicochemical properties of inulin obtained from Iranian chicory roots under vermicompost and humic acid treatments. Industrial Crops and Products. 123, 610-616.

[11] Najar, I.A., Khan, A.B., Hai, A. (2015) Effect of macrophyte vermicompost on growth and productivity of brinjal (*Solanum melongena*) under field conditions. International Journal of Recycling of Organic Waste in Agriculture. 4(2), 73-83.

[12] Chaudhuri, P.S., Paul, T.K., Dey, A., Datta, M., Dey, S.K. (2016) Effects of rubber leaf litter vermicompost on earthworm population and yield of pineapple (*Ananas comosus*) in West Tripura, India. International Journal of Recycling of Organic Waste in Agriculture. 5(2), 93-103.

[13] Knapp, B.A., Ros, M., Insam, H. (2010) Do composts affect the soil microbial community?, in Microbes at work. Springer. 271-291.
[14] Warman, P., AngLopez, M. (2010) Vermicompost derived from different feedstocks as a plant growth medium. Bioresource Technology. 101(12), 4479-4483.
[15] Weber, J., Karczewska, A., Drozd, J., Licznar, M., Licznar, S., Jamroz, E., Kocowicz, A. (2007) Agricultural and ecological aspects of a sandy soil as affected by the application of municipal solid waste composts. Soil Biology and Biochemistry. 39(6), 1294-1302.
[16] Albiach, R., Canet, R., Pomares, F., Ingelmo, F. (2000) Microbial biomass content and enzymatic activities after the application of organic amendments to a horticultural soil. Bioresource Technology. 75(1), 43-48.
[17] Ros, M., Pascual, J.A., Garcia, C., Hernández, T., Insam, H. (2006) Hydrolase activities, microbial biomass and bacterial community in a soil after long-term amendment with different composts. Soil Biology and Biochemistry. 38(12), 3443-3452.
[18] Tariq, M., Esperanca, J.M., Rebelo, L.P. (2010) High-temperature surface tension and density measurements of 1-alkyl-3-methylimidazolium bistriflamide ionic liquids. Fluid Phase Equilibria. 294(1-2), 131-138.
[19] Hassan, A. (2000) Effect of plant population density on yield and yield components of eight Egyptian maize hybrids. Bulletin of Faculty of Agriculture, University of Cairo. 51(1), 1-16.
[20] Parlak, K.U., Yilmaz, D.D. (2012) Response of antioxidant defences to Zn stress in three duckweed species. Ecotoxicology and Environmental Safety. 85, 52-58.
[21] Yang, D.H., Webster, J., Adam, Z., Lindahl, M., Andersson, B. (1998) Induction of acclimative proteolysis of the light-harvesting chlorophyll a/b protein of photosystem II in response to elevated light intensities. Plant Physiology. 118(3), 827-834.
[22] Porra, R., Thompson, W., Kriedemann, P. (1989) Determination of accurate extinction coefficients and simultaneous equations for assaying chlorophylls a and b extracted with four different solvents: verification of the concentration of chlorophyll standards by atomic absorption spectroscopy. Biochimica et Biophysica Acta (BBA)-Bioenergetics. 975(3), 384-394.
[23] Parlak, K.U. (2016) Effect of nickel on growth and biochemical characteristics of wheat (*Triticum aestivum* L.) seedlings. NJAS-Wageningen Journal of Life Sciences. 76, 1-5.
[24] Aebi, H. (1984) Catalase in vitro, in Methods in enzymology. Elsevier. 121-126.
[25] Nakano, Y., Asada, K. (1981) Hydrogen peroxide is scavenged by ascorbate-specific peroxidase in spinach chloroplasts. Plant and Cell Physiology. 22(5), 867-880.
[26] Beauchamp, C., Fridovich, I. (1971) Superoxide dismutase: improved assays and an assay applicable to acrylamide gels. Analytical Biochemistry. 44(1), 276-287.
[27] Baycu, G., Tolunay, D., Ozden, H., Günebakan, S. (2006) Ecophysiological and seasonal variations in Cd, Pb, Zn, and Ni concentrations in the leaves of urban deciduous trees in Istanbul. Environmental Pollution. 143(3), 545-554.
[28] Pereira, M.G., Arruda, M.A. (2003) Vermicompost as a natural adsorbent material: characterization and potentialities for cadmium adsorption. Journal of the Brazilian Chemical Society. 14, 39-47.
[29] Jordao, C.P., Fialho, L.L., Neves, J.C.L., Cecon, P.R., Mendonça, E.S., Fontes, R.L.F. (2007) Reduction of heavy metal contents in liquid effluents by vermicomposts and the use of the metal-enriched vermicomposts in lettuce cultivation. Bioresource Technology. 98(15), 2800-2813.
[30] Jahan, F.N., Shahjalal, A.T., Paul, A.K., Mehraj, H., Jamal Uddin, A.F.M. (2014). Efficacy of vermicompost and conventional compost on growth and yield of cauliflower. Bangladesh Research Publications Journal. 10(1), 33-38.
[31] Küçükyumuk, Z., Gültekin, M., Erdal, İ. (2014) The effect of vermicompost and mycorrhiza on pepper plant growth and mineral nutrition. Ziraat Fakültesi Dergisi. 9(1), 51-58.
[32] Azarmi, R., Giglou, M.T., Hajieghrari, B. (2009) The effect of sheep-manure vermicompost on quantitative and qualitative properties of cucumber (*Cucumis sativus* L.) grown in the greenhouse. African Journal of Biotechnology. 8(19), 4953-4957.
[33] Hosseinzadeh, S.R., Amiri, H., Ismaili, A. (2018) Evaluation of photosynthesis, physiological, and biochemical responses of chickpea (*Cicer arietinum* L. cv. *Pirouz*) under water deficit stress and use of vermicompost fertilizer. Journal of Integrative Agriculture. 17(11), 2426-2437.
[34] Fernández-Luqueño, F., Reyes-Varela, V., Martínez-Suárez, C., Salomón-Hernández, G., Yáñez-Meneses, J., Ceballos-Ramírez, J.M., Dendooven, L. (2010) Effect of different nitrogen sources on plant characteristics and yield of common bean (*Phaseolus vulgaris* L.). Bioresource Technology. 101(1), 396-403.
[35] Karanatsidis, G., Berova, M. (2009) Effect of organic-N fertilizer on growth and some physiological parameters in pepper plants (*Capsicum annum* L.). Biotechnology & Biotechnological Equipment. 23(1), 254-257.

[36] Cheng, H., Xu, W., Liu, J., Zhao, Q., He, Y., Chen, G. (2007) Application of composted sewage sludge (CSS) as a soil amendment for turfgrass growth. Ecological Engineering. 29(1), 96-104.
[37] Ahmed, J., Shivhare, U., Sandhu, K. (2002) Thermal degradation kinetics of carotenoids and visual color of papaya puree. Journal of Food Science. 67(7), 2692-2695.
[38] Gill, S.S., Tuteja, N. (2010) Reactive oxygen species and antioxidant machinery in abiotic stress tolerance in crop plants. Plant Physiology and Biochemistry. 48(12), 909-930.
[39] Chen, C.Y., Wang, Y.F., Lin, Y.H., Yen, S.F. (2003) Nickel-induced oxidative stress and effect of antioxidants in human lymphocytes. Archives of Toxicology. 77(3), 123-130.
[40] Lokhande, R.S., Singare, P.U., Pimple, D.S. (2011) Study on physico-chemical parameters of waste water effluents from Taloja industrial area of Mumbai, India. International Journal of Ecosystem. 1(1), 1-9.
[41] Rahbarian, R., Khavari-Nejad, R., Ganjeali, A., Bagheri, A., Najafi, F., (2012) Study of Germination and Seedling Growth in Tolerant and Susceptible Chickpea (*Cicer arietinum* L.) Genotypes under Drought Stress. Iranian Journal of Field Crops Research. 10(3), 522-531.
[42] Ahmadi, S.A.K., Ebadi, A., Sodabeh Jahanbakhsh, S., Jahanfar Daneshian, J., Siadat, S.A. (2015) Changes in enzymatic and nonenzymatic antioxidant defense mechanisms of canola seedlings at different drought stress and nitrogen levels. Turkish Journal of Agriculture and Forestry. 39(5), 601-612.
[43] Radić, S., Babić, M., Skobić, D., Roje, V., Pevalek-Kozlina, B. (2010) Ecotoxicological effects of aluminum and zinc on growth and antioxidants in *Lemna minor* L. Ecotoxicology and Environmental Safety. 73(3), 336-342.
[44] Mirzamohammadi, H.K., Modarres-Sanavy, S.A.M., Sefidkon, F., Mokhtassi-Bidgoli, A., Mirjalili, M.H. (2021) Irrigation and fertilizer treatments affecting rosmarinic acid accumulation, total phenolic content, antioxidant potential and correlation between them in peppermint (*Mentha piperita* L.). Irrigation Science. 1-13.
[45] Kiran, S. (2019) Effects of vermicompost on some morphological, physiological and biochemical parameters of lettuce (*Lactuca sativa* var. *crispa*) under drought stress. Notulae Botanicae Horti Agrobotanici Cluj-Napoca. 47(2), 352-358.

Received: **21.09.2021**
Accepted: **11.02.2022**

CORRESPONDING AUTHOR

Kadriye Uruc Parlak
Faculty of Arts and Sciences,
Agri Ibrahim Cecen University,
Agri – Turkey

e-mail: uruckadriye@gmail.com

© by PSP Volume 31– No. 05/2022 pages 4759-4768 Fresenius Environmental Bulletin

MOLECULAR AND MORPHOLOGIC STUDY OF *Clinostomum complanatum* (DIGENEA CLINOSTOMIDAE) IN *Garra rufa* (DOCTOR FISH) FROM SOUTHERN TURKEY

Ifakat Tulay Cagatay[1,*], Baki Aydin[2], Yusuf Aktop[1], Hasan Emre Yilmaz[1]

[1]Department of Basic Sciences, Faculty of Fisheries, Akdeniz University, Antalya, Turkey
[2]Department of Aquaculture, Faculty of Fisheries, Akdeniz University, Antalya, Turkey

ABSTRACT

Clinostomum complanatum is a zoonotic parasite and can cause economic losses in fish farms. The parasite has been mostly reported in freshwater fish species but not in *Garra rufa* (Doctor fish) which is getting more popular for fish spa. This is the first report of yellow grub trematode *C. complanatum* infected with doctor fish (*G. rufa*) in the Southern Turkey. A total of 40 dead *G. rufa*, which were taken from a commercial firm, were examined. The parasite from fish were confirmed by morphologically and molecular methods (PCR and sequencing) using nuclear internal transcribed spacer gene marker (ITS 1). *G. rufa* were found to be infected by *C. complanatum*, with prevalence 90.0%, and a mean intensity of the infection 19.8. We observed that *C. complanatum* metacercariae were in the encysted form and excysted form in the infected fish, and the diameter of the metacercarial cysts was found to be between 0.15-2.3 mm. The parasites were measured as mean body length 4079±861 µm, mean body width 1463±244 µm, mean body length/body width 2.81±0.47. Internal transcribed spacer 2 (ITS2) gene were amplified for sequence and phylogenetic analyses and those sequences of metacercariae were also similar to the respective *C. complanatum* sequences in GenBank. Therefore, this study described the morphological characterization and molecular identification of *C. complanatum* for the first time from *Garra rufa* in Southern Turkey.

KEYWORDS:
Digenean trematode, doctor fish, metacercaria, molecular phylogeny, morphology

INTRODUCTION

According to the FAO (Food and Agriculture Organization) [1], world aquaculture production grew on average at 5.3 percent per year in the period 2001-2018, and attained a record high of 114.5 million tons in live weight in 2018. The growth momentum of the world aquaculture production will continue until 2050 [2]. Similarly, aquaculture industry has been growing rapidly in recent years in Turkey [3]. However, while this growth continues, the sector is reported to have deficiencies in adapting to environment and climate change [4]. Fish diseases in aquaculture have now emerged as significant threats to aquaculture sector. Diseases are caused by several infectious agents like bacteria [5-6], viruses [7], fungi [8], parasites [9-10]. Among all pathogens, parasites are the most important causal agents of diseases in fishes. Knowing the biology, life cycle and identification of the parasitic organisms is important in terms of creating solutions for the prevention, control and reduction of harmful species that affect farm fish species.

C. complanatum (Rudolphi, 1814) which is a member of the family Clinostomidae is well known as 'yellow grubs' trematodes because of their color, in freshwater fish species [11].The parasite has a complex life cycle involving 3 hosts. Freshwater snails are first intermediate host, fish and amphibians as second intermediate hosts which is located in head, brain, muscles, skin, fins and abdominal cavity of fish and birds as a definite host for *C. complanatum* [12-13-14-15-16-17-18]. Human can also be infected after eating raw fishes causing halazoune syndrome [19]. *C. complanatum* have a great attention due to its zoonotic potential to pathogenicity in its host and can cause economic losses in fish farms [10-19].

This parasite have been reported in almost all regions of the world in freshwater fish species such as *Perca fluviatilis* and *Squalius cephalus* from Turkey [11-20], *Barbus barbus, Barbus meridionalis* and *S. cephalus* from Italy [21], *Cobitise longatoides* from Ukraine [10], *Alburnoides bipunctatus* and *Capoeta gracilis* from Iran [22], *Carassius auratus* and *Microphysogo bioyaluensis* from Republic of Korea [23-24], *Hemibarbus labeo* and *Zacco platypus* from Taiwan [25], *Rhamdi quelen* from South Brazil [19]. *Carassius cuvieri* and *Rhodeus ocellatus* from Japan [26], *C. complanatum* has been reported to infecting humans as definite host [27-28-29-30-18]. Recently, studies on this parasite are of great importance, given the increase in zoonotic diseases.

G. rufa (Heckel, 1843) known as the doctor fish is a type of fish with a small (2.7-11.2 g body weight, 7.4-9.7 cm body length) and cylindrical body shape

[31]. This fish normally occur in Turkey, Syria, Iraq and Iran and in different freshwater habitats such as rivers, lakes and streams. *G. rufa* is famous for its ability to feed on the dead skin and hence have been used for the treatment of psoriasis and by the spa industry for pedicures, and this fish was first used in ichthyotherapy in 1989 [32-33]. In the last decade, *G. rufa* is getting more popular and commonly used for fish spa and fish pedicure in Turkey and most other countries [34]. Ireland, UK and Spain also using this fish for skin therapy [35]. It has been reported in the literature that pathogens such as *Aeromonas sobria* [36], *Citrobacter freundii* [6], *Streptococcus agalactiae* and aquatic birnavirus [37] and *Paradiplozoon bingolensis* [38] are registered in *G. rufa*.

Clinostomum species has been defined molecularly with using internal transcribed spacers (ITS), 5.8S rRNA, 18S rRNA and the mitochondrial gene cytochrome c oxidase I (COI) gene markers in different fish species in worldwide [39-21-40-25]. However, characterization of this parasite has not been performed using the ITS gene in *G. ruffa* to date. The ITS 1 and ITS2 regions were more suitable for taxonomic studies at the species level and have been used to discriminate species in at least 19 digenean families [41]. Especially, *C. cutaneum* and *C. phalacrocoracis* are better resolved by ITS rRNA than by 18S rRNA and COI [42]. Therefore, in this study, we report the first time, the morphological characterization and molecular identification of *C. complanatum* in doctor fish, *G. rufa* in Southern Turkey.

MATERIALS AND METHODS

Fish collection. A total of 40 dead *G. rufa* were taken between August to November 2019 from commercial firms in Southern Turkey. The fish samples were transferred to laboratory for parasitological examination and some specimens were also preserved in tubes with 100% ethanol for molecular analyses.

Fish dissection and morphometric analysis. Firstly, total length (cm) and weight (g) of all fish samples were measured. Secondly, surfaces of the samples were observed with naked eye for parasitic infection. Then, fins, skin and gills of the samples were monitored carefully under the stereo binocular microscope (Leica EZ4HD, Germany) with built in digital camera and dissected all parasites from fish skin. Next, visceral organs of fish were dissected and placed in petri dishes. All encysted and excysted metacercariae carefully retrieved and transferred to petri dishes contain approximately 1% saline solution to record their number and morphological examination of parasite. Morphological measurements of the parasites were taken in micrometers following [16]. Morphological measurements were made with a stereo binocular microscope with built in digital camera. Measurements based on 35 parasites are given in micrometer (µm) as mean±standard deviation (SD). The data were calculated in SPSS software (Version 23, IBM Corp., Armonk, New York, USA).

Parasitology terms used. The prevalence, mean intensity and mean abundance of each host species were calculated according to [43].

Molecular analysis. Genomic DNA from each parasite samples was extracted by using Qiagen Tissue&Blood Kit (Qiagen, USA) according to manufacturer's instructions. The DNA were then stored at –20 °C for further use. Nuclear internal transcribed spacer gene (ITS 1) (1000 bp) was amplified using ITS 1-TCCGTAGGTGAACCTGCGG and ITS 4-TCCTCCGCTTATTGATATGC primers as previously reported [44]. The PCR reaction for amplification was performed some modification of [44], in a total volume of 50 µL, containing 5 µL 10XPCR Buffer, 3 µL $MgCl_2$ (25 mM), 1 µL each primer (10 µM), 1 µL dNTP solution (10 mM), 0.5 µL Taq DNA polymerase (5 U/µL), 2 µL genomic DNA (100 ng) and 37.5 µL nuclease free sterile water. The PCR was performed under this conditions: 5 min at 95 °C, 5 cycles of 30 sec at 94 °C, 45 sec at 65 °C and 1 min at 72 °C, 30 cycles of 30 sec at 94 °C, 45 sec at 60 °C and 1 min at 72 °C followed by 10 min at 72 °C final extension step. PCR products were resolved on 1.5% agarose gel.

Amplicons were sequenced in both direction with ITS 1 and ITS 4 primers (Macrogen, Amsterdam, Netherlands). Sequencing chromatograms were screened and checked by eye in MEGA-X (Molecular Evolutionary Genetics Analysis) [45]. Forward and reverse sequences were assembled and aligned to create contig sequence. Our sequence was compared with Genbank nucleotide database by BLAST-n for determine the gene region and species. All ITS sequences about *Clinostomum* genus at Genbank were aligned with our sequence using ClustalW algorithm and the genetic distance was estimated using Kimura-2-Parameter (K2P) in MEGA-X.

Phylogenetic analysis, 37 sequences (including 15 species) were retrieved from Genbank (Table 1). The best nucleotide substitution model was determined by using jModelTest [46] under Akaike Information Criteria (GTR+G). Bayesian inference method was used for phylogenetic tree construction in MrBayes v3.2.6 [47]. The Markov Chain Monte Carlo (MCMC) runs were set to four chains and the analysis was carried out until the standard deviation of split frequencies fell under 0.01 (10.000.000 generations, sampling every 1000). The first 25% of trees were removed as burn-in and the consensus trees were visualized and coloured using Figtree v. 1.3.1 [48]. *Diplostomum spathaceum* was used as out group.

TABLE 1
ITS sequences and accession numbers of *Clinostomum* species which are retrieved from Genbank

Original ID	Final ID	Accession Number
Clinostomum complanatum	*C. complanatum*	MF741738.1
		MF741737.1
		MF741736.1
Clinostomum tilapiae	*C. tilapiae*	KY649351.1
		KY649353.1
		KY649356.1
Clinostomum brieni	*C. brieni*	MH238416.2
		MH238415.2
		MH238412.2
Clinostomum marginatum	*C. marginatum*	JF718641.1
		JF718635.1
		JN108032.1
Clinostomum phalacrocoracis	*C. phalacrocoracis*	KJ786982.1
		KJ786979.1
		KJ786978.1
Clinostomum heluans	*C. heluans*	MH159770.1
Clinostomum tataxumui	*C. tataxumui*	JX631140.1
		JX631139.1
		JX631138.1
Clinostomum poteae	*C. poteae*	MH282569.1
		MH282568.1
		MH282567.1
Clinostomum album	*C. album*	MH282564.1
		MH282563.1
		MH282562.1
Clinostomum attenuatum	*C. attenuatum*	KP150307.1
Clinostomum philippinense	*C. philippinense*	KP110570.1
Clinostomum detruncatum	*C. detruncatum*	KP110566.1
Clinostomum cutaneum	*C. cutaneum*	KP110565.1
		KP110564.1
		FJ609421.1
Clinostomum piscidium	*C. piscidium*	KY312848.1
		KY290511.1
		KY304779.1
Clinostomum giganticum	*C. giganticum*	KY312846.1
		KY319339.1
		KY304778.1
Diplostomum spathaceum	*D. spathaceum*	JX986847.1
Euclinostomum heterostomum	*E. heterostomum*	MT785768.1

RESULTS

Description of infections. A total of 36 out of 40 individuals of *G. rufa* (mean weight 2.1±0.2 g and total length 4.9±0.8 cm) were found to be infected by *C. complanatum*, with a prevalence 90.0%, and a mean intensity of the infection 19.8 (Table 2). After the morphological examination, it was observed that *C. complanatum* was in the encysted form (yellow grub) (Figures. 1a, 1c, 1d) and excysted form (Figure 1b) in the infected fish. The diameter of the metacercarial cysts was found to be between 0.15-2.3 mm. The number of parasites per host varied between 3 and 39. Among 713 *C. complanatum*, the peritoneal cavity was the most heavily infected (391 parasites, 54.8%), followed by the skin (235 parasites, 32.9%) and the head (87 parasites, 12.2%).

Morphological results. The major characteristics of the *C. complanatum* were that the body was oval, elongated, ventrally concave, dorsally convex, and white color (Figure 2). The results of morphological examination of the parasites were given in Table 3. *C. complanatum* body, 2666-5981 µm long and 849-2132 µm width. The ventral sucker (VS) located in the third of the parasite was larger than the

oral sucker (OS) (VS width/OS width=1.95±0.20). Sub-terminal oral sucker small, surrounded, length 210-325 µm and width 279-477 µm. Ventral suckers length 375-761 µm, ventral sucker width 457-908 µm. Distance between sucker 625-997 µm. Intestinal ceca run laterally to ventral sucker to posterior end of body and appears in yellow color.

Molecular analysis results. The ITS region (1000 bp) was sequenced successfully from all samples. The BLAST analysis of present sample was perfect matched with *C. complanatum* (99.78-100% per identity). The minimum value (changed between 0.000-0.009) of genetic distance was estimated between present sample and *C. complanatum* species. The maximum value (0.140) of genetic distance was estimated between present sample and *C. piscidium* (KY319340.1 and KY304779.1). BI tree was constructed by using Mr. Bayes v3.2.6 [47]. All species seperated clearly except *C. phillippinense* (KP110570.1) and *C. attenuatum* (KP150307.1). Present sample was clustered within *C. complanatum* species (99%). Bootstrap values of BI tree were changed between 64-100%.

TABLE 2
Infection status of *C. complanatum* metacercariae in some freshwater fish species

Fish species	Total number examined fish	Number of infected fish	Prevalence (%)	Min. / max. no of parasites per fish	Mean intensity	References
G. rufa	40	36	90	3-39	19.8	In this study
G. rufa	13	2	15	0-2	1.5	[15]
T. fasciatus	240	209	87.1	-	13.9	[51]
M. yaluensis	9	8	88.9	1-30	8.8	[23]
C. auratus	298	77	25.8	1-310	8.8	[23]
M. asiaticus	148	96	64.9	1-7	2.33	[14]
L. platymetopon	1666	1013	60.8	1-585	23.1	[13]
P. galeatus	951	104	10.9	1-85	5.4	[13]
C. carpio	9	1	11.1	1-14	14	[25]
Z. barbata	344	31	9	1-107	14.4	[25]

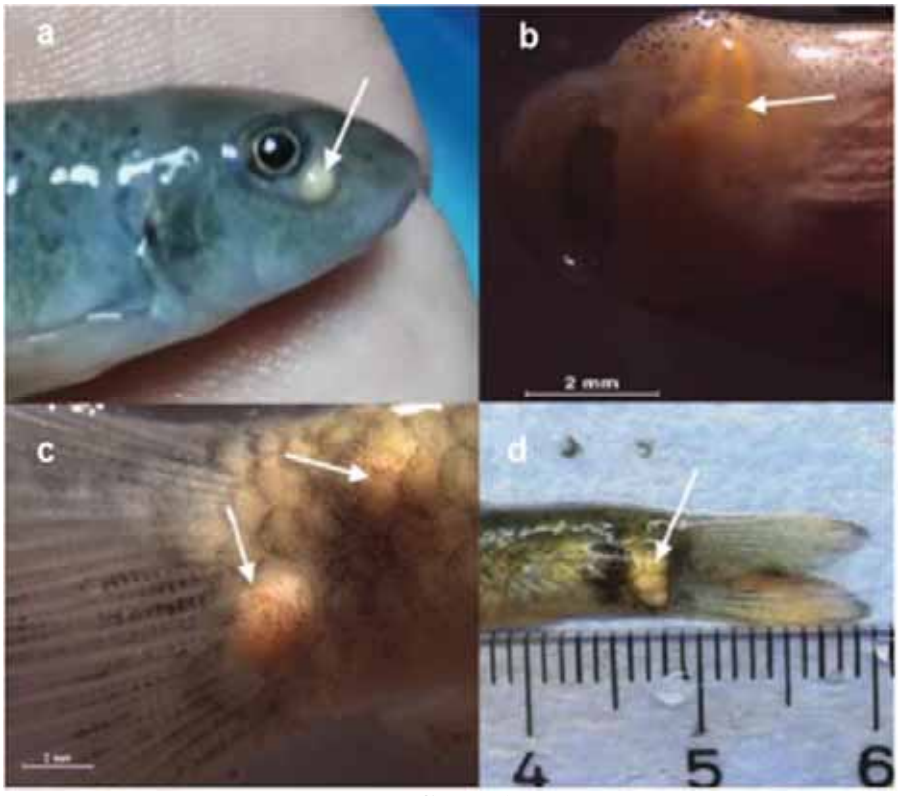

FIGURE 1
G. rufa* infected with *C. complanatum
(a) Encysted *C. complanatum* metacercariae in the head. (b) Excysted *C. complanatum* metacercariae in the gills. (c) and (d) Encysted *C. complanatum* metacercariae in the skin on the tail side of the body

TABLE 3
A comparison of the measured morphological values of metacercariae of *C. complanatum* in this study and other studies (µm)

	This study (n= 35)			(11) (n= 12)	(14) (n= 27)	(15) (n 16)	(21) (n= 11)
	Min	Max	(Mean ± SD)	Min-Max (Mean ± SD)	Min-Max (Mean ± SD)	Min-Max (Mean ± SD)	Min-Max (Mean ± SD)
Body length	2666	5981	(4079 ± 861)	3998 – 6718 (5108 ± 340)	2470 – 3287 (2924 ± 224)	1917 – 2700 (2331 ± 205)	4495 – 7874 (5741 ± 1223)
Body width	849	2132	(1463 ± 244)	1197 – 2131 (1697 ± 160)	1071 – 1507 (1273 ± 121)	646 – 1058 (851 ± 119)	1635 – 2434 (1934 ± 239)
Body length / Body width	1.75	5.13	(2.81 ± 0.47)	2.58 – 3.53 (3.04 ± 0.21)	1.85 – 2.68 (2.3 ± 0.20)	2.29 – 3.45 (2.77 ± 0.33)	2.20 – 4.37 (2.99 ± 0.66)
Oral sucker (OS) length	210	325	(269 ± 27)	243 – 319 (272 ± 11)	156 – 285 (212 ± 33)	143 – 231 (178 ± 26)	259 – 337 (294 ± 27)
OS width	279	477	(366 ± 56)	261 – 483 (336 ± 36)	235 – 390 (285 ± 36)	147 – 243 (193 ± 24)	284 – 507 (401 ± 74)
OS width / Body width	0.13	0.53	(0.26 ± 0.06)	-	0.16 – 0.34 (0.22 ± 0.04)	-	1.06 – 1.67 (1.36 ± 0.18)
Ventral sucker (VS) length	375	761	(537 ± 98)	581 – 821 (682 ± 36)	385 – 571 (457 ± 44)	336 – 449 (395 ± 34)	637 – 910 (795 ± 77)
VS width	457	908	(710 ± 114)	679 – 893 (763 ± 32)	430 – 672 (546 ± 59)	322 – 422 (379 ± 29)	766 – 952 (839 ± 60)
VS width / OS width	1.64	2.01	(1.95 ± 0.20)	1.84 – 2.60 (2.33 ± 0.16)	1.33 – 2.38 (1.93 ± 0.2)	1.63 – 2.45 (2 ± 0.24)	1.78 – 2.6 (2.1 ± 0.3)
Distance between sucker	625	997	(784 ± 123)	823 – 1012 (915 ± 28)	513 – 732 (632 ± 63)	356 – 583 (419 ± 31)	860 – 1115 (1020 ± 84)

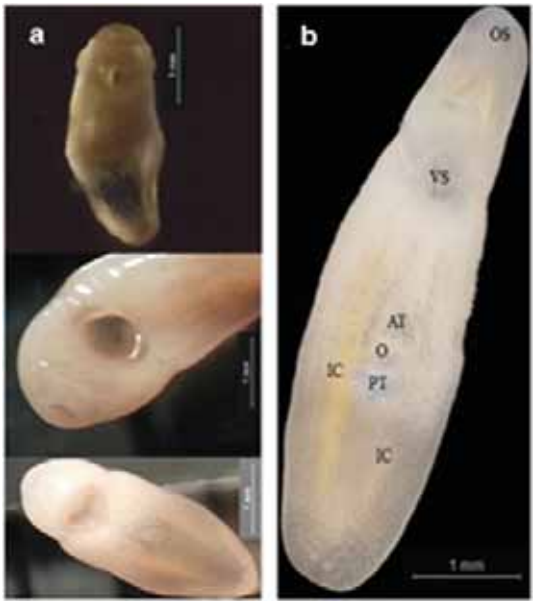

FIGURE 2
Metacercariae of *C. complanatum* from *G. rufa*. Various image of the parasite (a and b).
Abbr.: oral sucker (OS), ventral sucker (VS), anterior testis (AT), ovary (O), posterior testis (PT), intestinal caeca (IC)

DISCUSSION AND CONCLUSIONS

The biotic and abiotic factors of environments by global warming can affect the prevalence of Clinostomidae species [10]. Exact identification of parasite species is important for not only control of infections but also treatment. Although morphological features can be used to identify most *Clinostomum* species, this may be difficult in some specimen and larvae. Because of this difficulty in morphological identification, molecular methods have become useful to distinguish morphologically similar species [49-11]. Therefore, in this study, both morphological and molecular analysis was carried out and results showed that specimen was identified as *C. complanatum* (Digenea, Clinostomidae) from *G. rufa* in Southern Turkey.

The metacercariae of *C. complanatum* have been recorded in snails, birds and several freshwater fish species by a variety of authors (Table 4).

C. complanatum was found in total 23 species of freshwater fishes from the water systems in Korea, and is widely distributed in the world. *C. complanatum* was previously registered in Turkey from *Lepomis gibbosus, P. fluviatilis, Scardinius erythrophthalmus, Sander lucioperca, S. cephalus* [24-50-11-20]. *C. complanatum* was first reported in *G. rufa* from Gheshlagh River in Iran [15]. This parasite had not been reported in *G. rufa* from Turkey so far. *C. complanatum* was recorded for the first time in *G. rufa* in the present study, and results show that *G. rufa* is a suitable intermediate host for *C. complanatum*. It is seen in Table 2, infection status of *C. complanatum* in *G. rufa* and some freshwater fish species. We found the prevalence of infection was 90.0% in the current study. Similar to the our study, [51] and [23] reported quite high prevalence of infection of *Trichogaster fasciatus* from India and *Microphysogobio yaluensis* from Korea were 87.1% and 89.9%, respectively. [13] and [14] observed high prevalence of infection in *Loricariichthys platymetopon* (60.8%) and *Myxocyprinus asiaticus* (64.9%), respectively. But, some of studies stated

prevalence of infection was low rate [15-25]. Prevalence of infection in this parasite can be affected by various biotic and abiotic environmental factors such as climate [10-15]. In this study we observed that the *C. complanatum* were in the encysted form (yellow grub) (Figure 1a, 1c, 1b) and excysted form (Figure 1b) in the infected fish. But, [24] were observed *C. complanatum* only excysted form.

Our morphological features and measurement data of *C. complanatum* (Table 3) is consistent with the results of previous studies results [22-21-14-15-11]. *C. complanatum* length (2331±205 µm) and width 851±119 µm) in [15] study results appear to be smaller size than current study findings (4079±861 µm, 1463±244 µm, respectively). In current study, body length is minimum 2666 µm and maximum 5981µm, [11] have reported minimum 3998 µm and maximum 6718 µm, but [14] have reported minimum 2470 µm and maximum 3287 µm. The mean body length / width ratio in our specimen is 2.81±0.47, and this ratio seems to be similar to the data reported by previous study [21-14-11].

In our study, 1000 bp of the ITS gene region was replicated and compared with the data in the GenBank. The molecular identification and DNA sequences using the ITS gene marker here, determined the true identity of the metacercariae from *G. rufa* as *C. complanatum* (Figure 3). Our sample was clustered into *C. complanatum* species in the BI phylogenetic tree (99%). Several previous reports have indicated that in support of morphological data, the ITS gene, 18S rRNA, and mt-COI has been used in the detection of new species related to the genus of Clinostomum, molecular characterization of the species and in the investigation of the genetic relationship and variation between species [39-21-52-11].

TABLE 4
Records of *C. complanatum* metacercaria reported in different host species in the world

Host species	Country	References
Snails		
Galba pervia	China	[14]
Radix swinhoei	China	[14]
Amphibians		
Lissotriton vulgaris	Italy	[12]
Triturus carnifex	Italy	[12]
Fish		
Garra rufa	Iran	[15]
Garra rufa	Turkey	In this study
Perca fluviatilis	Turkey	[20]
Squalius cephalus	Turkey	[11]
Perca fluviatilis	Slovakia	[54]
Perca fluviatilis	Italy	[30]
Myxocyprinus asiaticus	China	[14]
Trichogaster fasciatus	India	[53]
Zacco spp.	Taiwan	[25]
Acrossocheilus paradoxus	Taiwan	[25]
Cyprinus carpio	Taiwan	[25]
Loricariichthys platymetopon	Brazil	[13]
Parauchenipterus galeatus	Brazil	[13]
Rhamdia quelen	Brazil	[19]
Acheilognathus rhombea	Korea	[23]
Microphysogobio yaluensis	Korea	[23]
Carassius carassius	Korea	[23]
Birds		
Ardea cocoi	Brazil	[13]
Phalacrocorax brasilianus	Brazil	[13]
Ardea purpurea	Iran	[17]
Egretta spp.	Iran	[17]
Nycticorax nycticorax	Iran	[17]
Ardeola bacchus	China	[14]
Egretta garzetta	China	[14]
Alcedo bengalensis	China	[14]

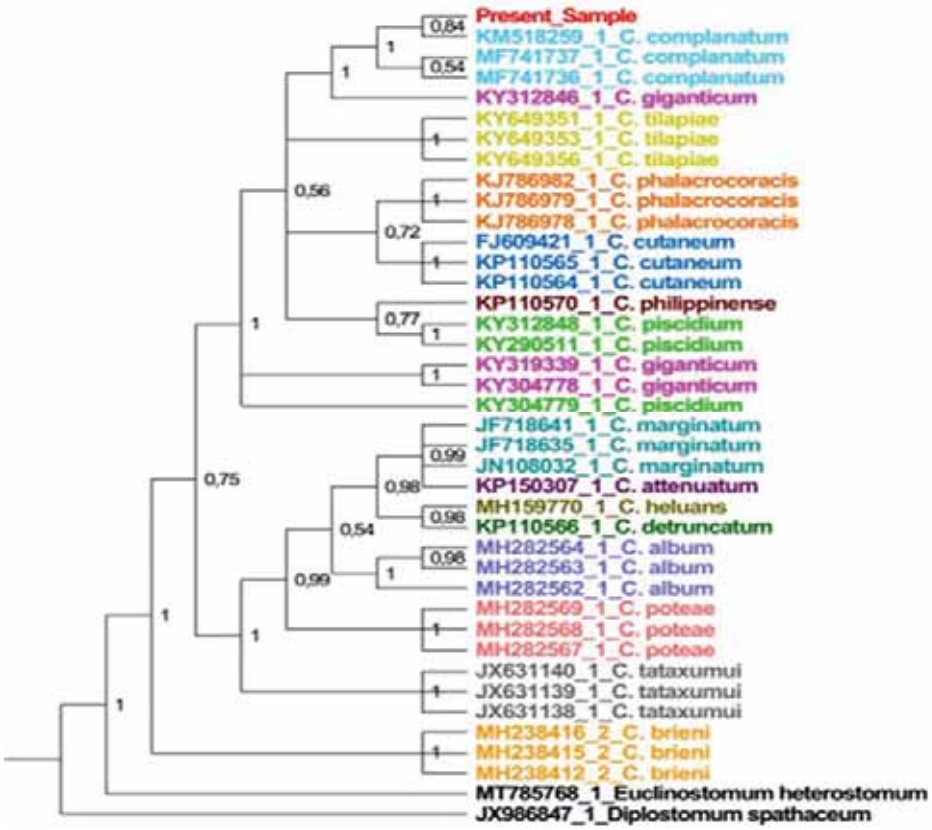

FIGURE 3
Molecular analysis using Bayesian phylogenetic tree based on ITS gene of *Clinostomum* species

It is stated that *C. complanatum*, a digenean trematode, is a fish-borne zoonotic parasite and is transmitted through the freshwater fish species [27-28-29-30-18]. [28] and [18] stated that human infections are known to be resulting from eating raw fish. *C. complanatum* was first reported from human in 1938, and 23 cases of human infection from Japan and Korea were reported by 2017 [29]. In Turkey, so far, there are no records of human infection by *C. complanatum* and it is clear that this situation may be largely from consumption habits of humans. In the last decade, *G. rufa* is getting more popular and commonly used for fish spa and fish pedicure. There has been no report that it infects humans through the skin in fish spa and fish pedicure. However, it may be more accurate for people with open wounds in skin to avoid contact with infected fish. Considering the increase of diseases from animals to humans in recent days, diagnosis and detection of the parasite is important as it may affect human health as well as aquatic ecosystem and necessary precautions should be taken with care. Infected fish should not be marketed, they should be quarantined immediately. Because, *C. complanatum* has caused loss to not only natural fish resources but also the aquaculture industry worldwide in recent years [14]. Also, there are few studies on the treatment of this parasite [53].

This study is the maiden attempt and the first report of molecular identification and morphological characterization of *C. complanatum* isolates in *G. rufa (doctor fish)* from Southern Turkey. It is understood that this parasite can be carried and transported to many points through international fish trade and piscivorous birds. Using infected fish for spa and fish pedicure can be potential risk for human transmission and infection with *C. complanatum*. In addition, if we do not pay attention and take necessary measures, we also think that there is a possibility of being seen in cultured fish. More studies are needed to prevent and treat this parasite in aquaculture environment.

ACKNOWLEDGEMENTS

Research approval was obtained from the Republic of Turkey Ministry of Agriculture and Forestry, Agricultural Research and Policy General Directorate with number 92190712-288.04-E.2293312.

REFERENCES

[1] FAO. (2020) The State of World Fisheries and Aquaculture. Sustainability in action. Rome.
[2] Engle, C.R., D'Abramo, L., Ponniah, A.G., Slater, M. (2017) Global Aquaculture 2050. Journal of the World Aquaculture Society. 48, 3-6.

[3] Candemir, S. and Dağtekin, M. (2020). Estimation of Turkey aquaculture production and proficiency index. Acta Aquatica Turcica. 16(3), 409-415.

[4] Brugère, C., Aguilar-Manjarrez, J., Beveridge, M.C.M. and Soto, D. (2019). The ecosystem approach to aquaculture 10 years on- a critical review and consideration of its future role in blue growth. Reviews in Aquaculture. 11, 493-514.

[5] Acar, U., Kesbiç, O.S., Yilmaz, S., Gültepe, N. and Türker, A. (2015). Evaluation of the effects of essential oil extracted from sweet orange peel (*Citrus sinensis*) on growth rate of tilapia (*Oreochromis mossambicus*) and possible disease resistance against *Streptococcus iniae*. Aquaculture. 437, 282-286.

[6] Baeck, G,W., Kim, J.H., Choresca, C., Gomez, D.K., Shin, S.P., Han, J.E. and Park, S.C. (2009) Mass mortality of doctor fish (*Garra rufa obtusa*) caused by *Citrobacter freundii* infection. Journal of Veterinary Clinics. 26, 150-154.

[7] Way, K., Haenen, O., Stone, D., Adamek M., Bergmann, S.M., Bigarré, L., Diserens, N., El-Matbouli, M., Gjessing, M.C., Jung-Schroers, V., Leguay, E., Matras, M., Olesen, N.J., Panzarin, V., Piačková, V., Toffan, A., Vendramin, N., Veselý, T. and Waltzek, T. (2017). Emergence of carp edema virus (CEV) and its significance to European common carp and koi *Cyprinus carpio*. Diseases of Aquatic Organisms. 126, 155-166.

[8] Gormez, O. and Diler, O. (2014). In vitro antifungal activity of essential oils from *Tymbra, Origanum, Satureja* species and some pure compounds on the fish pathogenic fungus, *Saprolegnia parasitica*. Aquaculture Research. 45, 1196-1201.

[9] Balta, F., Balta, Z.D. and Akhan, S. (2019). Seasonal distribution of protozoan parasite infections in rainbow trout (*O. mykiss*) farms in the eastern black sea of Turkey. Bulletin-European Association of Fish Pathologists. 39(1), 31-38.

[10] Fedorčák, J., Šmiga, Ľ., Kutsokon, I., Kolarčik, V., Koščová, L., Oros, M., Koščo, J. (2019). Parasitic infection of *Cobitis elongatoides* Băcescu&Mayer, 1969 by zoonotic metacercariae *Clinostomum complanatum* (Rudolphi, 1814). Journal of Fish Diseases. 42, 1677-1685.

[11] Şimsek, E., Yildirim, A., Yilmaz, E., Inci, A., Duzlu, O., Onder, Z., Ciloglu, A., Yetismis, G. and Pekmezci, G.Z. (2018) Occurrence and molecular characterization of *Clinostomum complanatum* (Trematoda: Clinostomidae) in freshwater fishes caught from Turkey. Parasitology Research. 117, 2117-2124.

[12] Caffara, M., Bruni, G., Paoletti, C., Gustinelli, A. and Fioravanti, M.L. (2014). Metacercariae of *Clinostomum complanatum* (Trematoda: Digenea) in European newts *Triturus carnifex* and *Lissotriton vulgaris* (Caudata: Salamandridae). Journal of Helminthology. 88, 278-285.

[13] Dias, M.L.G.G., Eiras, J.C., Machado, M.H., Souza, G.T.R. and Pavanelli, G.C. (2003). The life cycle of *Clinostomum complanatum* Rudolphi, 1814 (Digenea, Clinostomidae) on the floodplain of the high Paraná river, Brazil. Parasitology Research. 89, 506-8.

[14] Li, B.F., Liu., X.H., G H.L., Xie, C.Y, Cai, R.,Y., Hu, Z.C., Zhang, Y.G. and Wang, Z.J. (2018). The discovery of *Clinostomum complanatum* metacercariae in farmed *Chinese sucker*, *M. asiaticus*. Aquaculture. 495, 273-280.

[15] Maleki, L., Heidari, H., Ghaderi, E. and Rostamzadeh, J. (2018). Occurrence and description of *Clinostomum complanatum* (Rudolphi, 1819) metacercariae in freshwater fishes from Gheshlagh basin, West of Iran. Iranian Journal of Animal Biosystematics. 14, 91-103.

[16] Matthews, D. amd Cribb, T.H. (1998). Digenetic trematodes of the genus *Clinostomum* Leidy, 1856 (Digenea: Clinostomidae) from birds of Queensland, Australia, including *C. wilsoni* n. sp. from *Egretta intermedia*. Systematic Parasitology. 39, 199-208.

[17] Shamsi, S., Halajian, A., Tavakol, S., Mortazavi, P. and Boulton, J. (2013). Pathogenicity of *Clinostomum complanatum* (Digenea: Clinostomidae) in piscivorous birds. Research in Veterinary Science. 95, 537-539.

[18] Park, C.W., Kim, J.S., Joo, H.S. and Kim, J. (2009). A human case of *Clinostomum complan*atum infection in Korea. The Korean Journal of Parasitology. 47, 401-404.

[19] Vianna, R.T., Júnior, J.P. and Brandão, D.A. (2005). *Clinostomum complanatum* (Digenea, Clinostomidae) density in *Rhamdia quelen* (Siluriformes, Pimelodidae) from South Brazil. Brazilian Archives of Biology and Technology. 48, 635-642.

[20] Soylu, E. (2013). Metazoan parasites of Perch *Perca fluviatilis* L . from Lake Sığırcı, Ipsala, Turkey. Pakistan Journal of Zoology. 45, 47-52.

[21] Caffara, M., Locke, S.A., Gustinelli, A., Marcogliese, D.J. and Fioravanti, M.L. (2011). Morphological and molecular differentiation of *Clinostomum complanatum* and *Clinostomum marginatum* (Digenea: Clinostomidae) metacercariae and adults. The Journal of Parasitology. 97, 884-891.

[22] Aghlmandi, F., Habibi, F., Afraii, M.A. and Shamsi, S. (2018). Infection with metacercaria of *Clinostomum complanatum* (Trematoda: Clinostomidae) in freshwater fishes from Southern Caspian Sea Basin. Revista de Medicina Veterinaria. 169, 147-151.

[23] Chung, D.I., Kong, H.H. and Moon, C.H. (1995). Demonstration of the second intermediate hosts of *Clinostomum complanatum* in Korea. The Korean Journal of Parasitology. 33, 305-312.

[24] Sohn, W.M., Na, B.K. and Cho, S.H. (2019). Infection status with *Clinostomum complanatum* metacercariae in fish from water systems of nakdong-gang (River) in Korea. The Korean Journal of Parasitology. 57, 389-397.

[25] Wang, M.L., Chen, H.Y. and Shih, H.H. (2017). Occurrence and distribution of yellow grub trematodes (*Clinostomum complanatum*) infection in Taiwan. Parasitology Research. 116, 1761-1771.

[26] Aohagi, Y., Shibahara, T., Machida, N., Yamaga, Y. and Kagota, K .(1992). *Clinostomum complanatum* (Trematoda: Clinostomatidae) in five new fish hosts in Japan. Journal of Wildlife Diseases. 28, 467-469.

[27] Chung, D.I., Moon, C.H., Kong, H.H., Choi, D.W. and Lim, D.K. (1995). The first human case *of Clinostomum complanatum* (Trematoda: Clinostomidae) infection in Korea. The Korean Journal of Parasitology. 33, 219-223.

[28] Kitagawa, N., Oda Mayuko Totoki, T., Washizaki S. and Masamichi Kifune, T. (2003) Lidocaine spray used to capture a live *Clinostomum* parasite causing human laryngitis. American Journal of Otolaryngology and Head and Neck Surgery. 24, 341-343.

[29] Lee, G.S., Park, S.W., Kim, J., Seo, K.S., You, K.W., Chung, J.H., Moon, H.C. and Hong, G.Y. (2017) A case of endoscopically treated Laryngopharyngitis resulting from *Clinostomum complanatum* infection. The Korean Journal of Gastroenterology. 69, 177-180.

[30] Menconi, V., Manfrin, C., Pastorino, P., Mugetti, D., Cortinovis, L., Pizzul, E., Pallavicini, A. and Prearo, M. (2020) First report of *Clinostomum complanatum* (Trematoda: Digenea) in European perch (*Perca fluviatilis*) from an Italian Subalpine Lake: A risk for public health? International Journal of Environmental Research and Public. 17, 1389.

[31] Aydın, B. and Akhan, S. (2020). An alternative species for aquaculture: Doctor fish (*Garra rufa*). Atatürk University Journal of Agricultural Faculty. 51(2), 199-206.

[32] Grassberger, M., Hoch, W. (2006). Ichthyotherapy as alternative treatment forp with Psoriasis: A pilot study. Evidence based complement. Alternative Medicine. 3, 483-488.

[33] Özçelik, S., Polat, H.H., Akyol, M., Yalcin, A.N., Özçelik, D. and Marufihah M. (2020). Kangal hot spring with fish and psoriasis treatment. The Journal of Dermatology. 27, 386-390.

[34] Aydın, B., Akhan, S., Gümüş, E. and Özbaş, M. (2019). Anesthetic efficacy of clove oil and 2-phenoxyethanol on doctor fish, *Garra rufa* (Heckel, 1843). The Boletim Do Instituto De Pesca. 45(4), e506.

[35] Bhattacharya, S. (2016). Doctor fish *Garra rufa*: Health and risk. The Journal of Fish. 10, 1-3.

[36] Majtán, J., Černy, J., Ofúkana, A., Takáč, P., Kozánek, M. (2012) Mortality of therapeutic fish *G. rufa* caused by *Aeromonas sobria*. Asian Pacific Journal of Tropical Biomedicine. 2, 85-87.

[37] Ruane, N.M., Collins, E.M., Geary, M., Swords, D., Hickey, C. and Geoghegan, F. (2013). Isolation of *Streptococcus agalactiae* and an aquatic birnavirus from doctor fish *Garra rufa* L. The Iranian Journal of Veterinary Research. 66, 2-5.

[38] Civáňová, K., Koyun, M. and Koubková, B. (2013) The molecular and morphometrical description of a new diplozoid species from the gills of the *Garra rufa* (Heckel, 1843) (Cyprinidae) from Turkey including a commentary on taxonomic division of Diplozoidae. Parasitology Research. 112, 3053-3062.

[39] Acosta, A.A., Caffara, M., Fioravanti, M.L., Utsunomia, R., Zago, A.C. Franceschini, L. and Da Silva, R.J. (2016) Morphological and molecular characterization of *Clinostomum detruncatum* (Trematoda: Clinostomidae) Metacercariae infecting *Synbranchus marmoratus*. The Journal of Parasitology. 102(1), 151-156.

[40] Dzikowski, R., Levy, M.G., Poore, M.F., Flowers, J.R., Paperna, I. (2004) *Clinostomum complanatum* and *Clinostomum marginatum* (Rudolphi, 1819) (Digenea: Clinostomidae) Are separate species sased on differences in ribosomal DNA. The Journal of Parasitology. 90, 413-414.

[41] Nolan, M.J. and Cribb, T.H. (2005) The use and implications of ribosomal DNA sequencing for the discrimination of digenean species. Advances in Parasitology. 60, 101-163.

[42] Bowles, J., Blair, D. and McManus, D.P. (1995). A molecular phylogeny of the human Schistosomes. Molecular Phylogenetics and Evolution. 4, 103-109.

[43] Bush, A.O., Lafferty, K.D., Lotz, J.M. and Shostak, A.W. (1997) Parasitology meets ecology on its own terms. Revisited Journal of Parasitology. 83, 575.

[44] White, T.J., Bruns, T., Lee, S. and Taylor, J. (1990) Amplification and direct sequencing of fungal ribosomal RNA genes for phylogenetics, in: PCR Protocols. a Guide to Methods and Applications, Academic Press, New York. 315-322.
[45] Kumar, S., Stecher, G., Li, M., Knyaz, C. and Tamura, K. (2018) MEGA X: Molecular evolutionary genetics analysis across computing platforms. Molecular Biology and Evolution. 35(6), 1547-1549.
[46] Posada, D. (2008) jModelTest: Phylogenetic model averaging. Molecular Biology and Evolution. 25(7), 1253-1256.
[47] Ronquist, F., Teslenko, M., Van Der Mark, P., Ayres, D.L., Darling, A., Höhna, S., Larget, B., Liu, L., Suchard, M.A. and Huelsenbeck, J.P. (2012) Mrbayes 3.2: Efficient bayesian phylogenetic inference and model choice across a large model space. Systematic Biology. 61(3), 539-542.
[48] Rambaut, A. (2010) FigTree v1.3.1: Tree figure drawing tool. Website http//tree.bio.ed.ac.uk/software/figtree (Accessed date: 2021.7.01).
[49] Moszczynska, A., Locke, S.A., McLaughlin, J.D., Marcogliese, D.J. and Crease, T.J. (2009) Development of primers for the mitochondrial cytochrome c oxidase I gene in digenetic trematodes (Platyhelminthes) illustrates he challenge of barcoding parasitic helminths. Molecular Ecology Resources. 9, 75-82.
[50] Çolak, H.S. (2013) Metazoan parasites of fish species from Lake Sıgırcı (Edirne, Turkey). Turkish Journal of Veterinary And Animal Sciences. 37, 200-205.
[51] Khan, S., Ahmed, S., Serajuddin, M. and Saifullah, M.K. (2018) Variation in seasonal prevalence and intensity of progenetic metacercariae of *Clinostomum complanatum* infection in *Trichogaster fasciatus* fish. Beni-Suef University Journal of Basic and Applied Sciences. 7, 310-316.
[52] Locke, S.A., Caffara, M. and Marcogliese Fioravanti, M.L. (2015) A large-scale molecular survey of *Clinostomum* (Digenea, Clinostomidae). Zoologica Scripta. 44, 203-217.
[53] Rehman, A., Ullah, R., Jaiswal, N., Khan, M.A.H., Rehman, L., Beg, M.A., Malhotra, S.K. and Abidi, S.M.A. (2017) Low virulence potential and in vivo transformation ability in the honey bee venom treated *Clinostomum complanatum*. Experimental Parasitology. 183, 33-40.
[54] Juhásová, Ľ., Radačovská, A., Bazsalovicsová, E., Miklisová, D., Bindzárová-Gereová, M. and Králov-Hromadová, I. (2019) A study of the endohelminths of the European perch *Perca fluviatilis* L. from the central region of the Danube river basin in Slovakia. Zookeys. 47-58.

Received: **22.09.2021**
Accepted: **17.11.2021**

CORRESPONDING AUTHOR

Ifakat Tulay Çagatay
Department of Basic Sciences,
Faculty of Fisheries,
Akdeniz University,
Antalya – Turkey

e-mail: tulaycagatay@akdeniz.edu.tr

© by PSP Volume 31– No. 05/2022 pages 4769-4779 Fresenius Environmental Bulletin

BIODIVERSITY OF BEETLES FAUNA IN AGRICULTURAL ENVIRONMENTS FROM NORTHWESTERN ALGERIA

Mohammed Boutaiba Benklaouz[1,*], Fatiha Righi Assia[1], Amine Ghelamallah[2], Mouffok Elouissi[1]

[1]Biology Systems and Geomatics Laboratory, Faculty of Nature and Life Sciences, Mascara University 29000, Algeria
[2]Plant Protection Laboratory, Faculty of Nature and Life Sciences, Mostaganem University 27000, Algeria

ABSTRACT

Beetles provide valuable ecosystem services as biological pest control and soil fertilization. However, their community structure has not been completely elucidated. The current study was performed to make specific inventories of beetles in agricultural environments, provide fundamental information on their community structure and evaluate their diversity based on the seasonal climate of Northwestern Algeria. Regular sampling of beetle specimens was done by using the Barber pitfall traps and the yellow traps in four agroecosystems: one cereal field (CF), one citrus orchard (CO) and two potato fields (PT1 and PT2). A total of 205 species, belonging to 29 families, were recorded from the four studied environments. Tenebrionidae, carabidae and Scarabeidae were the most dominant families in terms of individuals and species. However, the Shannon-Wiener index and equitability presented their highest values in the CF (H'=3.63 and E=0.76). The biggest qualitative and quantitative similarities were recorded between the faunas of PT1 and PT2(S=0.57; J=0.40). The chi-squared test showed that the family abundances were dependent of the environments. The species number rates differed significantly among the seasons in the four studied environments. An important taxonomic diversity of the beetle community was found, which is highly related to environmental variables.

KEYWORDS:
Agricultural environments, Beetles, Biodiversity, Northwestern Algeria

INTRODUCTION

The biodiversity of insects acts directly on the dynamics and functioning of ecosystems by intervening at all levels of trophic chain [1]. The beetles are considered as one of the most important groups of insects which can shelter in cultivated fields. They represent one-third of the world's known insects [2]. Although polyphagy is the main feature of beetles feeding behavior, their biology features enable them provide valuable ecosystem services. This is the case of scarabaeinae as soil fertilization and biological pest control [3, 4], carabids and their effects on invertebrate pests [5], some Hybosoridae as predators [6] and Cetoniinae as pollinators and good bioindicators of environmental changes [7, 8]. In contrast, these include also a number of so-called phytophagous species which are responsible for crops damage (i.e., some melolonthids, rutelids and dynastines) whose larvae feed on roots that can act as important pests [9].

Biodiversity restoring is a key strategy in sustainable agriculture [10]. This one makes agroecosystems able to sponsoring their own soil fertility, crop productivity and protection through restoration of natural control of insect, diseases and nematodes [11]. However, various studies reported that the assembly of entomological fauna composition was influenced by several factors, including human-induced disturbances, such as destruction and fragmentation of natural habitats and the application of pesticides [12, 13].

In agricultural areas, Beetles fauna group can provide crucial ecosystem roles as biological pest control (predators) and soil fertilization (coprophagous). However, the heavy agricultural practices in cultivated areas could be the cause of their limited biodiversity and abundance [13]. Updated beetles inventories can provide important data on their biodiversity in order to adopt new strategies for their preservation. In Algeria, studies on beetles in agroecosystems are still incipient because most of them are not fully identified and their community structure is not completely elucidated. Therefore, this study was performed to make specific inventories of beetles in different agroecosystems and to provide fundamental information on their diversity and community structure based on seasonal climate of Northwestern Algeria.

MATERIALS AND METHODS

Study area. The present study was carried out at four different agroecosystems located in Mostaganem and Relizane areas, Northwestern Algeria. These regions were chosen given their high fertility and important agricultural production in this country. Our inventory has focused on three potential crops

grown in these two provinces: Potato fields (PT), cereal field (CF) and citrus orchard (CO). The surveys were conducted in four stations: Sirat 1 (35˚78′ 37″ N; 0˚15′ 98″ E; elvation: 42 m a.s.l), Sirat 2 (35˚76′19″ N; 0˚16′ 59″ E; elvation: 47 m a.s.l), Souaflias (35˚88′ 75″ N; 0˚35′42″ E; elvation: 284 m a.s.l) and Yellel (35˚75′ 36″ N; 0˚38′ 83″ E; elvation: 131 m a.s.l) (Figure 1). Based on the climatic data for the period 2000–2020 provided by the meteorological station of Mostaganem, the study area has a semiarid bioclimate. Precipitation was very irregular with large fluctuations; it was totaled 381.47 mm where November was the rainiest month with an average of 64.53 mm, while July was the driest month with 0.59 mm. The highest maximum temperature was recorded in July with 40.75 °C, whereas the lowest minimum temperature was recorded in January with 0.71 °C.

Sampling. The sampling of beetles fauna on the site was done regularly from 96 surveys distributed during two years, from March 2018 to February 2020, using the previously described techniques (Barber pitfall trap and yellow trap) [14]. Captured beetles were collected weekly and transferred to the laboratory, where they were counted and examined. Specimens were then sorted, labeled and identified with the help of specialists and identification keys.

Diversity analysis. For the diversity analysis of the beetle assemblages, several structural parameters and ecological indexes were calculated as previously described for the relative abundance (RA %) and centesimal frequency (Cf %) [15], Shannon-Weaver diversity index (H') [16], Equitability index (E) [17], Sorenson index (S) [18] and Jaccard index (J) [19].

Statistical analysis. The chi-squared test was used to test the dependency of the species richness and the relative abundances of the different families and the four agroecosystems. One way ANOVA with t-test were used to test the significance of differences between species number of the different stations and seasons. All data were presented as mean ± standard deviation. p values <0.05 were considered to be significant. Statistical calculations were performed using SPSS v21 software.

RESULTS

Composition and abundance of beetle community. A total of 4633 individuals classified into 29 different families, 69 subfamilies, 146 genera and 205 species, were identified in the four studied agroecosystems. The largest number of beetles was recorded in the CF with 1472 individuals and 114 species), followed by the CO with1266 individuals and 96 species, the PT2 with 1074 individuals and 82 species and finally by the PT1 with 821 individuals and 72 species) (Table 1; Figure 2).

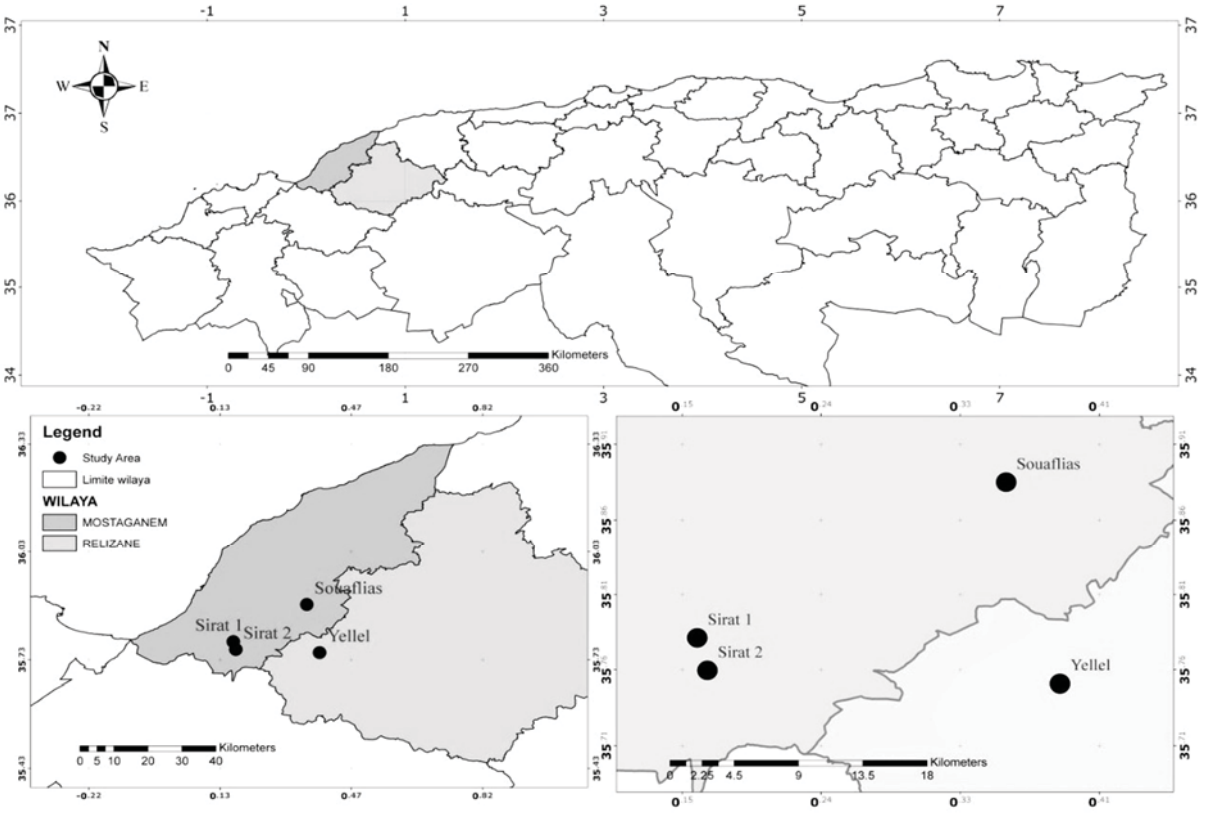

FIGURE 1
Study area localization

TABLE 1
Checklist of beetles recorded in the study (+ : present, - absent)

Family	Subfamily	Species	PT 1	PT 2	CF	CO
Carabidae	Harpalinae	*Harpalus oblitus* (Dejean, 1829)	+	+	+	+
		Harpalus tenebrosus (Dejean, 1829)	-	-	+	-
		Harpalus punctatostriatus (Dejean, 1829)	-	-	-	+
		Harpalus attenuatus (Stephens, 1828)	-	-	-	+
		Harpalus sp	-	+	-	+
		Ophonus opacus (Dejean, 1829)	-	-	-	+
		Ophonus cordatus (Duftschmid, 1812)	-	-	-	+
		Ophonus sp	-	-	-	+
		Poecilius quadricollis (Dejean, 1828)	-	-	+	-
		Poecilus purpurascens (Dejean, 1828)	+	-	-	-
		Poecilus sp1	+	+	-	-
		Poecilus sp2	-	+	-	-
		Graphipterus serrator (Forsskal, 1775)	-	-	+	-
		Platytarus faminii (Dejean, 1826)	-	-	+	-
		Amara aenea De Geer, 1774	-	-	-	+
		Amara rufipes (Dejean, 1828)	+	-	-	-
		Licinus punctatalus (Fabricius, 1792)	-	+	-	-
		Licinus silphoides (Rossi, 1790)	-	-	+	-
		Microlestes corticalis (Dufour, 1820)	-	+	-	+
		Microlestes sp	-	-	+	+
		Laemostenus algerinus (Gory, 1833)	-	-	-	+
		Sphodrus leucophthalmus (Linnaeus, 1758)	-	+	-	+
		Zabrus ignavus (Csiki, 1907)	+	-	-	-
		*Carterus calydonius (*P. Rossi, 1790)	-	-	-	+
		Carterus fulvipes (Latreille, 1817)	+	+	+	+
		Oedesis villosulus (Reiche, 1859)	-	+	-	+
		Chlaenius sp	-	+	-	+
		Agonum marginatum (Linnaeus, 1758)	-	-	-	+
		Calathus opacus (Luca, 1846)	-	+	-	+
		Calathus fuscipes algiricus (Gautier des Cottes, 1866)	+	+	-	-
		Calathus sp	-	-	+	+
		Myriochile melancholica (Fabricius, 1798)	-	-	-	+
	Cicindellinae	*Cicindela lunulata* (Fabricius, 1781)	-	-	+	-
		Cicindella sp	-	-	+	+
	Lebiinae	*Cymindis setifensis* (Lucas, 1842)	-	-	-	+
	Carabinae	*Carabus morbillosus* (Fabricius, 1792)	-	-	+	+
		Calosoma algiricum (Géhin, 1885)	-	-	+	-
		Calosoma inquisitor (Linné, 1758)	-	-	+	-
	Nebriinae	*Nebria andalusia* (Rambur, 1837)	-	-	+	+
		Notiophilus sp	-	+	-	+
	Scaritinae	*Distichus planus* (Bonelli, 1813)	-	-	+	-
		Dyschyrius chalybeus (Putzeys, 1846)	-	-	+	-
		Scarites sp	-	+	+	-
	Siagoninae	*Siagona europaea* (Dejean, 1826)	+	+		+
	Broscinae	*Broscus politus* (Dejean, 1828)	-	-	+	-
	Trechinae	*Pogonus chalceus* (Marsham, 1802)	+	+	-	-
		Notaphus varius (Olivier, 1795)	-	-	+	-
Scarabaeidae	Cetoniinae	*Tropinota squalida* (Scopoli, 1763)	+	+	+	+
		Aethiessa floralis (Fabricius, 1787)	-	+	+	-
		Oxythyrea funesta (Poda, 1761)	-	-	-	+
		Protaetia opaca (Fabricius, 1787)	-	-	-	+
	Melolonthinae	*Hoplia* sp1	+	+	+	-
		Hoplia sp2	-	-	+	-
		Hymenoplia sp	+	+	+	-
		Pachydema sp1	+	+	-	-
		Pachydema sp2	+	+	-	-
	Rutelinae	*Sphodroxia mauritanica,* (Lucas, 1846)	-	-	+	-
		Geotrogus deserticola (Blanchard, 1851)	-	-	+	-
		Anthoplia floricola (Fabricius, 1787)	-	+	+	-
		Hemichaetoplia pallidipennis (Gyllenhal, 1817)		+	+	+
	Scarabaeinae	*Euoniticellus pallens* (Olivier, 1789)	+	-	-	-
		Onitis alexis (Klug, 1835)	+	+	-	-
		Onthophagus(Trichonthophagus) maki (Illiger, 1803)	-	-	+	-

		Onthophagus(sensu stricto)tarus (Schreber, 1759)	-	-	-	+
		Scarabeus sp	-	-	+	-
		Pentodon algerinum (Herbst, 1789)	+	+	+	+
	Dynastinae	*Phyllognathus excavatus* (Forster, 1771)	+	+	+	+
		Oryctes nasicornis(L.) spp grypus (Illiger 1803)	-	-	-	+
	Orphninae	*Hybalus* sp	-	-	-	+
		Aphodius sp	+	+	+	-
	Aphodiinae	*Pleurophorus* sp	+	-	+	-
		Calamosternus granarius (Linnaeus 1767)	-	-	+	+
Cebrionidae		*Cebrio* sp	-	-	+	-
Anthicidae	Notoxinae	*Notoxus* sp1	-	+	-	-
		Notoxus sp2	-	-	+	-
Bostrichidae	Bostrichinae	*Apate monachus* (Fabricius, 1775)	-	-	+	-
		Acmaeodera adspersula (Illiger, 1803)	-	+	+	+
		Acmaeodera sp1	+	+	+	-
	Polycestinae	*Acmaeodera* sp2	-	+	+	-
		Acmaeodera sp3	+	-	+	-
		Acmaeodera sp4	-	+	-	-
		Acmaeodera sp5	-	+	+	-
Buprestidae		*Anthaxia scutellaris* (Gené, 1839)	+	-	+	+
	Buprestinae	*Anthaxia umbellatarum* (Fabricius, 1787)	-	-	+	-
		Anthaxia funerula (Illiger, 1803)	-	+	-	+
		Anthaxia sp*(Melanthaxia)*	-	-	+	
	Chrysochroinae	*Sphenoptera rauca* (Fabricius, 1787)	-	-	+	-
		Capnodis tenebrionis (Linnaeus, 1760)	-	-	+	-
	Agrilinae	*Trachys fabricii* (Schaefer, 1949)	-	-	-	+
		Trichoferus fasciculatus (Faldermann, 1837)	-	-	-	+
	Cerambycinae	*Stenopherus ater* (Linnaeus, 1767)	-	+	-	-
		Stenopterus mauritanicus (Lucas, 1849)	-	+	-	-
Cerambycidae		*Purpuricenus desfontainii* (Fabricius, 1792)	-	-	+	-
		Agapanthia cardui (Linnaeus, 1767)	+	-	-	-
	Lamiinae	*Agapanthia suturalis* (Fabricius, 1792)	+	+	-	-
		Niphona picticornis (Mulsant, 1839)	-	+	-	-
		Calamobius filum (Rossi, 1790)	-	+	-	-
		Galeruca interrupta (Illiger, 1802)	+	+	+	+
	Galerucinae	*Galeruca barbara* (Erichson, 1841)	+	+	+	+
		Altica ampelophaga (Guérin-Méneville, 1858)		+	+	+
Chrysomelidae	Cassidinae	*Cassida* sp	+	+	+	+
	Chrysomelinae	*Chrysolina* sp	+	-	+	+
		Cryptocephalus rugicollis (Olivier, 1791)	-	+	+	+
	Cryptocephalinae	*Lachnaia* sp	-	-	+	+
		Clytra sp	+	+	+	+
Cleridae	Clerinae	*Trichodes umbellatarum* (Olivier,1795)	+	-	+	+
		Hippodamia tredecimpunctata (Linnaeus, 1758)	-	-	+	-
		Hippodamia undecimnotata (Schneider, 1792)	+	+	-	-
		Hippodamia variegata (Goeze, 1777)	+	+	-	+
		Hippodamia sp	+	+	-	-
		Henosepilachna elaterii (Rossi, 1794)	-	-	+	-
Coccinellidae	Coccinellinae	*Scymnus apetzi* (Mulsant, 1846)	-	-	+	-
		*Scymnus interruptus (*Goeze, 1777)	-	+	-	+
		Scymnus sp1	-	-	+	-
		Scymnus sp2	-	+	-	-
		Coccinella algerica (Kovar, 1977)	+	+	-	-
		Coccinella sp	-	-	-	+
		Lixus algirus (Linnaeus, 1758)	-	-	+	+
		Lixus elegantulatus (boheman, 1842)	-	-	+	-
	Lixinae	*Lixus* sp	+	+	+	+
		Cleonus sp	+	-	-	-
		Larinus sp	-	-	+	-
		Sibinia primita (Herbst, 1795)	-	-	+	-
Curculionidae	Curculioninae	*Pachytychius* sp	-	+	-	+
		Mecinus janthinus (Germar, 1821)	-	-	-	+
	Rhynchophorinae	*Sphenophorus piceus* (Pallas, 1771)	-	-	+	-
	Bagoinae	*Bagous argillaceus* (Gyllenhal, 1836)	-	-	+	-
	Apioninae	*Apion* sp	-	-	+	-
	Baridinae	*Baris* sp	-	-	-	+
		Aulacobaris sp	-	-	+	-

		Sitona macularius (Marsham 1802)	-	-	+	-
	Entiminae	*Sitona* sp1	-	-	+	-
		Sitona sp2	+	-	+	-
	Hyperinae	*Donus salviae* (Schrank, 1789)	-	-	+	-
	Megatominae	*Anthrenus verbasci* (Linnaeus, 1767)	-	-	+	-
Dermestidae		*Dermestes* sp	-	+	+	-
	Attageninae	*Attagenus* sp1	+	-	-	-
		Attagenus sp2	-	-	+	-
	Cardiophorinae	*Cardiophorus* sp1	+	-	-	+
		Cardiophorus sp2	+	-	+	-
		Drasterius bimaculatus (Rossi, 1790)	-	+	-	+
Elateridae	Agrypninae	*Drasterius* sp1	-	+	+	+
		Drasterius sp2	-	+	-	+
	Elaterinae	*Agriotes sordidus* (Illiger, 1807)	+	-	-	+
		Agriotes pilosellus (Schönherr, 1817)	+	+	-	+
	Hypnoidinae	*Athous* sp	+	+	-	-
Endomychidae		*Dapsa pallescens* (Marseul, 1868)	-	+	-	-
Geotrupidae	Geotropinae	*Thorectes puncticollis* (Lucas, 1845)	-	-	+	-
Glaphyridae	Glaphyrinae	*Eulasia bombylius* (Fabricius, 1787)	-	-	+	+
		Saprinus sp1	+	+	+	+
Histeridae	Histerinae	*Saprinus* sp2	+	+	-	+
		Hister sp	-	-	+	-
Hybosoridae	Hybosorinae	*Hybosorus arator (*Illiger, 1803)	+	+	+	-
Hydrophilidae	Acidocerinae	*Helochares lividus* (Forster, 1771)	+	+	-	-
	Enochrinae	*Enochrus* sp	-	-	+	-
		Mylabris variabilis (Pallas, 1781)	+	-	-	-
		Mylabris sp	+	-	-	-
Meloidae	Meloinae	*Meloe cavensis* (Petagna, 1819)	-	-	+	-
		Meloe sp	-	-	+	-
		Berberomeloe sp	-	-	+	-
		Oenas afra	-	-	+	-
Melyridae	Dasytinae	*Dasytes virens* (Marsham, 1802)	-	-	+	+
		Dasytes sp	-	-	-	+
	Malachiinae	*Axinotarsus pulicarius* (Fabricius, 1777)	-	-	+	+
Mordellidae	Mordellinae	*Mordella* sp	-	-	+	+
Nitidulidae	Carpophilinae	*Urophorus humeralis* (Fabricius, 1798)	+	-	-	-
		Carpophilus sp	+	-	-	-
	Epuraeinae	*Epuraea* sp	-	-	+	-
Oedemeridae	Oedemerinae	*Oedemera lurida* (Marsham, 1802)	-	-	+	+
Prionoceridae		*Lobonyx aeneus* (Fabricius, 1787)	-	-	-	+
Scraptiidae	Anaspidinae	*Anaspis* sp	-	-	-	+
Silphidae	Silphinae	*Silpha puncticollis* (Lucas, 1846)	+	+	+	-
Staphylinidae	Staphylininae	*Quedius pallipes* (Lucas, 1846)	-	+	+	-
		Staphylinus olens (O. Müller, 1764)	-	+	-	+
	Oxytelinae	*Carpelimus corticinus* (Gravenhorst, 1806)	-	-	+	+
		Bledius sp	-	+	-	+
		Pimelia muricata (Olivier, 1795)	+	+	+	+
		Pimelia costata, (Waltal, 1835)	+	+	+	-
		Zophosis sp1	+	+	+	+
		Zophosis sp2	+	-	-	+
		Erodius sp	+	+	-	-
		Pachychila sp1	+	+	+	+
	Pimeliinae	*Pachychila* sp2	+	-	+	+
		Tentyria interrupta (Latreille, 1807)	-	+	-	+
		Akis sp	+	-	+	+
		Scaurus striatus (Fabricius, 1792)	+	-	+	+
Tenebrionidae		*Scaurus* sp1	+	+	-	-
		Scaurus sp2	+	-	+	-
		Asida sp	-	-	-	+
		Opatrum sabulosum (Linnaeus, 1758)	+		+	+
		Opatrum sp1	+	+	-	-
		Opatrum sp2	+	-	-	-
	Tenebrioninae	*Eledona agricola* (Herbst, 1783)	+	+	-	+
		Neopachypterus mauritanicus (Lucas, 1846)	-	-	-	+
		Dendarini sp	-	-	+	-
		Catomus sp	-	-	+	-
		Blaps sp groupe B gigas	-	-	+	+

	Diaclina fagi (Panzer, 1799)	+	+	-	-
	Tenebrio molitor (Linnaeus, 1758)	+	+	-	-
	Heliotaurus ruficollis (Fabricius 1781)	+	+	+	+
Alleculinae	*Heliotaurus* sp	+	-	-	+
	Hymenalia sp	-	+	-	+
Helopinae	*Raiboscelis* sp	-	-	+	+
Lagriinae	*Lagria villosa* (Fabricius, 1781)	-	-	+	+
	Lagria atripes (Mulsant & Guillebeau, 1855)	-	-	-	+

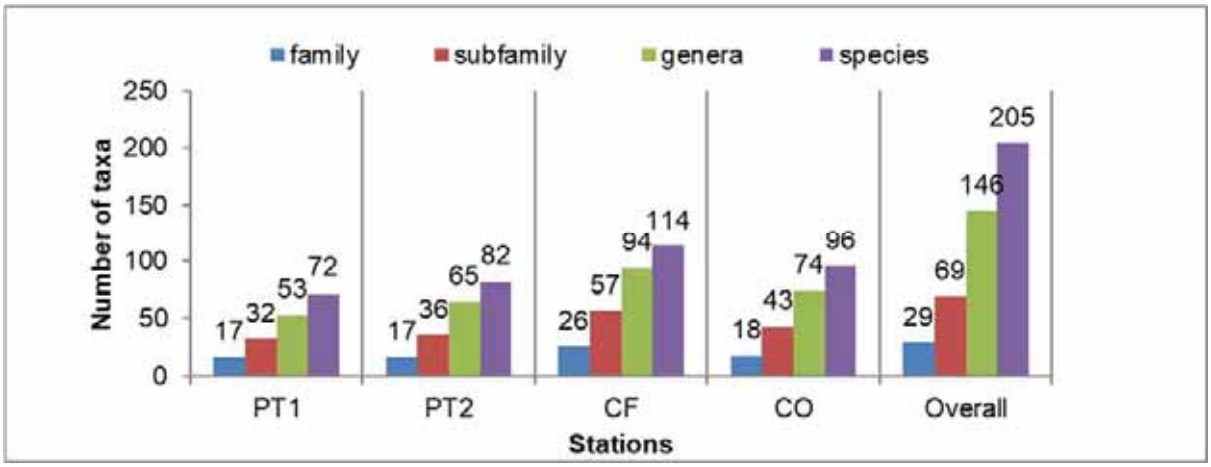

FIGURE 2
Total number of families, subfamilies, genera, and species of beetles for the four prospected agroecosystems

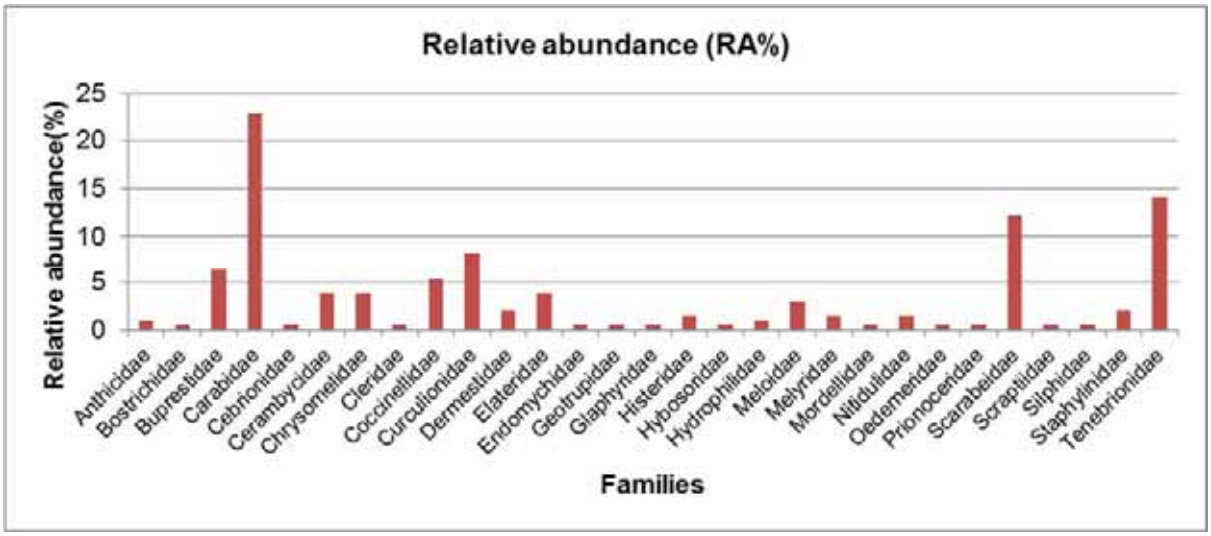

FIGURE 3
Relative abundance of various families recorded in the four agroecosystems

For the whole reported beetles, the highest number of species belonged to the Carabidae (22.92%), Tenebrionidae (14.14%) and Scarabaeidae (12.19%). The remaining species were distributed over the other families (Figure 3).

However, the tenebres were the most dominant family in term of individuals in the four studied crops, followed by Scarabaeidae in the CF and the PT and by Carabidae in the CO (Table 2). Buprestidae, Chrysomelidae, Coccinellidae, Curculionidae, Elateridae, Histeridae and Staphylinidae were also present in all the studied agricultural areas but with low frequencies. The Bostrichidae, Geotrupidae and Cebrionidae were reported only in the CF. Endomychidae was present only in the PT and Scraptiidae and Prionoceridae were reported only in the CO with one species for each (Table 2). Overall, the species

TABLE 2
Species richness and centesimal frequency of different beetles families in the four prospected agroecosystems

Families	Potato field 1			Potato field 2			Cereal field			Citrus orchard		
	N. sp*	N. ind**	C.fr (%)***	N. sp	N. ind	C.fr (%)	N. sp	N. ind	C.fr (%)	N. sp	N. ind	C.fr (%)
Anthicidae	-	-	-	1	5	0.47	1	1	0.07	-	-	-
Bostrichidae	-	-	-	-	-	-	1	1	0.07	-	-	-
Buprestidae	3	5	0.61	6	32	2.98	10	123	8.36	4	72	5.69
Carabidae	9	11	1.34	16	49	4.56	20	57	3.87	26	176	13.90
Cebrionidae	-	-	-	-	-	-	1	2	0.14	-	-	-
Cerambycidae	2	3	0.37	5	11	1.02	1	2	0.14	1	3	0.24
Chrysomelidae	5	40	4.87	6	49	4.56	8	92	6.25	8	108	8.53
Cleridae	1	2	0.24	-	-	-	1	21	1.43	1	1	0.08
Coccinellidae	4	59	7.19	6	45	4.19	4	8	0.54	3	18	1.42
Curculionidae	3	15	1.83	2	3	0.28	13	40	2.72	5	25	1.97
Dermestidae	1	1	0.12	1	3	0.28	3	10	0.68	-	-	-
Elateridae	5	25	3.05	5	62	5.77	2	12	0.82	6	49	3.87
Endomychidae	-	-	-	1	13	1.21	-	-	-	-	-	-
Geotrupidae	-	-	-	-	-	-	1	1	0.07	-	-	-
Glaphyridae	-	-	-	-	-	-	1	14	0.95	1	1	0.08
Histeridae	2	6	0.73	2	15	1.40	2	3	0.20	2	9	0.71
Hybosoridae	1	97	11.81	1	26	2.42	1	4	0.27	-	-	-
Hydrophilidae	1	3	0.37	1	7	0.65	1	6	0.41	-	-	-
Meloidae	2	2	0.24	-	-	-	4	139	9.44	-	-	-
Melyridae	-	-	-	-	-	-	2	24	1.63	3	20	1.58
Mordellidae	-	-	-	-	-	-	1	2	0.14	1	2	0.16
Nitidulidae	2	8	0.97	-	-	-	1	1	0.07	-	-	-
Oedemeridae	-	-	-	-	-	-	1	4	0.27	1	27	2.13
Prionoceridae	-	-	-	-	-	-	-	-	-	1	5	0.39
Scarabeidae	11	205	24.97	12	92	8.57	16	267	18.14	10	33	2.61
Scraptiidae	-	-	-	-	-	-	-	-	-	1	2	0.16
Silphidae	1	7	0.85	1	2	0.19	1	4	0.27	-	-	-
Staphylinidae	-	-	-	3	10	0.93	2	12	0.82	3	20	1.58
Tenebrionidae	19	332	40.44	13	650	60.52	15	622	42.26	19	695	54.90
Total	72	821	100	82	1074	100	114	1472	100	96	1266	100

*number of species, **number of individuals, ***centesimal frequency

TABLE 3
Structural parameters of beetle populations evaluated for each agroecosystem

Agroecosystems Parameters	Potato field 1	Potato field 2	Cereal field	Citrus orchard
S^{*}	72	82	114	96
H'^{**}	2.96	3.15	3.63	3.49
$H_{max}{}^{***}$	4.27	4.40	4.73	4.56
E^{****}	0.69	0.71	0.76	0.76

*Species richness, **Shannon diversity index, ***Maximal diversity, ****Equitability

richness (S) of the families and the relative abundance (RA%) were differents. The chi-squared test showed that the family abundances were dependent on the stations ($P < 0.0001$), while the species richness values of families were independent of the stations ($P = 0.60$).

Beetles diversity. The present study showed that the beetles diversity varied from one agroecosystem to another. In effect, the highest level of diversity and equitability was reported in the CF which considered as the most diversified and equitable environment (H'=3.63 bits; E=0.76). The CO was ranged in second position with a diversity of 3.49 bits and an equitability of 0.76. In addition, both of the PT1 and the PT2 showed the lowest values of diversity and equitability in comparison with the other studied environments (Table 3). Whereas, no statistically significant differences was observed between the species number rates in the four studied environments.

At season scale, all the prospected areas showed their highest values of diversity in spring and summer. The diversity levels observed were slightly less in autumn and very low in winter. Furthermore, the highest diversity values were noted in spring in the CF and CO with a Shannon- Weaver index of 3.60 and 3.47 bits, respectively, against both of the PT with 2.93 and 3.26 bits. However, beetles).

TABLE 4
Seasonal structural parameters of beetle populations for each agroecosystem

Agroecosystems	parameters	Spring	Summer	Autumn	Winter
Potato field 1	H' *	2.93	2.34	1.82	0.55
	H_{max} **	3.85	3.55	2.39	1.09
	E***	0.76	0.65	0.76	0.50
Potato field 2	H'	3.26	2.40	1.76	0.73
	H_{max}	4.12	3.61	2.48	1.60
	E	0.79	0.66	0.71	0.45
Cereal field	H'	3.60	3.01	1.96	1.44
	H_{max}	4.47	3.87	3.09	1.94
	E	0.76	0.77	0.63	0.74
Citrus orchard	H'	3.47	2.59	2.43	1.50
	H_{max}	4.24	3.80	2.83	1.79
	E	0.81	0.68	0.86	0.83

*Shannon diversity index, **Maximal diversity, ***Equitability

TABLE 6
Values of the Sorenson similarity index (above diagonal) and the Jaccard similarity index (below diagonal) between the beetles fauna of the four studied areas

Beetles fauna	BFPT1	BFPT2	BFCF	BFCO
BFPT1*	-	0.57	0.36	0.36
BFPT2**	0.4	-	0.34	0.46
BFCF***	0.22	0.20	-	0.41
BFCO****	0.22	0.29	0.26	-

BFPT1*: beetles fauna of the potato field 1, BFPT2**: beetles fauna of the potato field 2,
BFCF***: beetles fauna of the cereal field, BFCO****: beetles fauna of the citrus orchard.

community in the CO was the most equitable in comparison with the other studied environments. Equitability values in this perennial agroecosystem (CO) were 0.81, 0.86 and 0.83 in spring, autumn and winter, respectively (Table 4). The species number rates differed significantly among the seasons in the four studied environments (F=33.87; p<0.0001) (Table 5

TABLE 5
Result of the pairwise of species number between the different seasons

Seasons	Species number
Spring	66.75±8.54[a]
Summer	41.25±3.12[b]
Autumn	15.50±2.53[c]
Winter	5.25±0.85[c]
Anova	F=33.87 ; p<0.0001

a, b, c mean difference between groups

Similarity of the studied agroecosystems. Even though each sampling habitats had different conditions, both of Sorenson and Jaccard indexes showed high similarities between the beetles species inventoried in the both PT. However, slightly less similarities were noted between those of the CO, CF and the PT1 and a very low similarities were recorded between the CF and the PT2 (Table 6).

DISCUSSION

The most dominant beetle families reported in this study were Carabidae, Tenebrionidae and Scarabaeidae. These results were almost similar to several studies conducted on beetles fauna in different countries [20, 21, 1, 22]. In Algeria, a study carried out by Baghem [20] showed the dominance of the Carabidae family in CF conducted with conventional seeding in Eastern Algeria. Another study conducted by Daas et al [1] reported the dominance of Carabidae and Scarabeidae in two cork forests in Northeastern Algeria. However, a study on beetles diversity in the mobile dunes of Northeastern Morocco revealed that the Scarabaeidae and the Tenebrionidae were found as the most dominant families [21]. In a rural area in India, Tom and D Kaippallil [22] reported the dominance of Melolonthiidae family followed by Tenebrionidae. Generally, the entomological fauna is taxonomically dominated by the Tenebrionidae family [23], which is considered as one of the most diversified family in North Africa [24]. The abundance of the families recorded in the current study might be in relation with the abusive use of cow dung as organic manure in the study area and the availability of their habitats, overwintering sites and food resources.

Bouraada et al [21] suggested that the good species diversity is largely due to the coprophagous species, generally independent to the environment and closely linked to the presence of faeces, organic mat-

ter and plant cover for the species. Moreover, Carabids are abundant in temperate agroecosystems and play a pivotal role as biocontrol agents for weed seed and pest regulation. While there is good knowledge regarding their effects on invertebrate pests, direct evidence for seed predation in the field is missing [5].

The results obtained in this study showed that beetles population varied from one agroecosystem to another. The most diversified ecosystem was the CF, followed by the CO, the PT2 and finally by the PT1. A recent study conducted by Mohammedi et al [13] in agroecosystems in Northwestern Algeria reported that the largest number of insects was recorded in uncultivated field followed by CO, CF and PT. The difference observed between the various studied agroecosystems may be influenced by crops variation, microclimatic conditions and vegetation cover. It may also be due to the presence of some species originated from other surrounding habitats, where maintain abundant populations as previously suggested [25]. Furthermore, other factors including monoculture that are frequently invaded by pests can play a crucial role in the variation of insect abundance from one crop to another [26]. In addition, the richness of plant communities can also favor diversity of insects [27]. The differences in families of beetles were suggested to be influenced by different habitat association [22]. Moreover, climatic variations and applied agricultural techniques may also have an action on the diversity of species [20]. Likewise, there is an interaction between agriculture and biodiversity. i.e., some weeds such as Leguminosae, Umbelliferae and Compositae can play a crucial ecological role by harboring and supporting a complex of beneficial arthropods that help in suppressing pest populations [11].

The results of the present study showed that the CF was the most diversified and equitable environment. This study demonstrated also the presence of some forest species (i.e. *Sphrodroxia* sp.) in this agroecosystem. This can be explained by the vicinity of this area to a forest. Generally, more diversified resources for forest species are found at the edges of fields which are characterized by greater plant diversity [28]. Furthermore, the environments closer to natural provide food resources to generalist species [29]. Shannon-Weaver's Diversity index values revealed slightly low levels of diversity in the other prospected areas (PT1, PT2 and CO). This can be explained by the monoculture system applied in those regions that is not sufficient to attract most diversified species.

Perennial ecosystems and the annual crops have been suggested to lead to uniform environments, causing the resilience of the ecosystem and less biodiversity [30]. Other factors, including the expansion of monocultures and heavy agricultural practices at the expense of natural vegetation can also influence the instability of the agroecosystems, generating diversity weaknesses [13].

At the whole prospected cultivated fields, Beetles populations showed their highest values of diversity in spring and summer. However, the diversity observed was slightly less in autumn and very low in winter. The highest diversity was noted in winter at the CO while the lowest was reported at the PT. Under the same climatic conditions, Mohammedi et al [13] reported that the highest entomofauna diversity was found in uncultivated fields and the lowest one in CF in their study conducted in Northwestern Algeria. This diversity disturbance may be due to the intensification of cultural practices applied in the vegetable crops (PT). The presence of several layers exploitable by biological communities as overwintering sites and the creation of plant developments within the plot or border may also be the origin of plant diversity in orchards [31, 32]. Cultural practices and the heavy crop protection management strategy have also been considered as the main causes for devastating a natural balance within the PT, reducing faunal population [33].

The both Sorenson and Jaccard indexes showed high similarities between the beetles species inventoried in the PT1 and the PT2, and slightly less similarities between those of the CO and the other environments, but very low similarities between the CF and the PT2. Low values of similarity index have been suggested to be linked to great differences in richness, abundance and species dominance among the pairs of areas [29]. The degrees of similarities observed may be the result of the distance between the four study areas, the vegetation heterogeneity and the microclimatic conditions.

This is the first specific inventory providing fundamental information on community structure of beetles fauna in agroecosystems in Northwestern Algeria. Thus, the annual crop and the perennial ecosystem clearly appear as the agroecosystems favorable to the development of beetles fauna diversity. Nevertheless, vegetable crops environments constitute landscape in which a small number of species develop. The intensification of cultural practices in vegetable crops allows to the instability of these environments and reduces a necessary habitats and refuges to these species, leading to limited biodiversity and lost agricultural production. Furthermore, providing habitats and overwintering sites as the wild plants and natural hedges in the cultivated areas for beneficial species, like those found in this study (i.e., coprophagous Scarabeidae, Carabidae and coccinellidae) should be preserved from being devastated in order to adopt sustainable pest management strategies, support organic agriculture and improve productivity of our agroecosystems.

ACKNOWLEDGEMENTS

We are deeply grateful to Professor Hervé BRUSTEL (France) for specimens' identification.

We also thank the staff of the Regional Station of Plant Protection of Mostaganem for their technical assistance and the farmers for allowing us the collection of specimens.

REFERENCES

[1] Daas, H., Adjami, Y., Ghane, R., Viñolas, A., Ouakid, M.L., Tahraoui, A. (2016) Coleoptera inventory in cork oak stands of North-Eastern Algeria. Turkish Journal of Forestry. 17(special issue), 11-17. (in French).

[2] Zagatti, P., Horellou, A., Mari, A., Arnaboldi, F., Reisdorf, P. (2001) Atlas of beetles of the Massif Rambouillet and of the Regional Natural Park of the High Chevreuse Valley. Tom 1: 1990-2000, National Invertebrate Observatory. Office for Eco-entomological Information. Paris. (in French).

[3] Nichols, E., Spector, S., Louzada, J., Larsen, T., Amézquita, S., Favila, M.E. (2008) Ecological functions and ecosystem services provided by Scarabaeinae dung beetles. Biological Conservation. 141, 1461-1474.

[4] Carvalho, M.S.G. (2018) Functional characteristics, generals and food preference of dung beetle (Coleoptera: Scarabaeinae) in the Brazilian Cerrado. Doctoral Thesis of the Postgraduate Course in Zoology, Institute of Biological Sciences, University of Brasilia. (in Portuguese).

[5] Sint, D., Guenay, Y., Mayer, R., Traugott, M., Wallinger, C. (2018) The effect of plant identity and mixed feeding on the detection of seed DNA in regurgitates of carabid beetles. Ecology and Evolution. 8(28), 10834-10846.

[6] Huchet, J.B. (2014) Hybosoridae Erichson, 1847. In: The beetles of Reunion Island, Editors: Gomy Y, Lemagnen R and Poussereau J). Orphie, Saint Denis, Reunion. 238-240. (in French)

[7] Steenhuisen, S.L., Johnson, S.D. (2012) Evidence for beetle pollination in the African grassland sugarbushes (Protea: Proteaceae). Plant Systematics and Evolution. 298, 857-869.

[8] Touroult, J., Le Gall, P. (2013) Fruit feeding Cetoniinae community structure in an anthropogenic landscape in West Africa. Journal of Insect Conservation. 17, 23-34.

[9] Hayes, W.P. (1930) Morphology, Taxonomy, and Biology of Larval Scarabaeoidea. (Editors: Buchholz J T, Tanner F W and Zeleny C.) University of Illinois Urbana-Champaign.

[10] Altieri, M. (1994) Biodiversity and Pest Management in Agroecosystems. Haworth Press, New York. 185.

[11] Altieri, M. (1999) The ecological role of biodiversity in agroecosystems. Agriculture, Ecosystems & Environment. 74, 19-31.

[12] Escobar, F., Halffter, G., Arellano, L. (2007) From forest to pasture: an evaluation of the influence of environment and biogeography on the structure of dung beetle (Scarabaeinae) assemblages along three altitudinal gradients in the Neotropical region. Ecography. 30, 193-208.

[13] Mohammedi, A., Ali Arous, S., Kerrouzi, M. (2019) Entomofaunal diversity and similarity indices of different agroecosystems in northwest Algeria. Journal of Insect Biodiversity and Systematics. 5(2), 143-152.

[14] Benkhellil, M. (1991) Sampling and trapping techniques used in terrestrial entomology. Office des publications universitaires. Alger. 60. (in French).

[15] Dajoz, R. (1985) Precis of ecology. Ed. Bordas. Paris. 505. (in French).

[16] Barrantes, G., Sandoval, L. (2009) Conceptual and statistical problems associated with the use of diversity indices in ecology. Revista de Biologia Tropical. 57(3), 451–460.

[17] Blondel, J. (1979) Biogeography and ecology. Ed. Masson. Paris. 173. (in French).

[18] Magurran, A.E. (1988) Measuring biological Diversity. Blackwell science Ltd, UK copyright, designs and patents Act.

[19] Younes, G., Saporta, G. (2004) A methodology for partition comparison. Revue de Statistique Appliquée. 52, 97–120. (in French).

[20] Baghem, O. (2012) Effect of Cultivation Techniques on Faunistic Biodiversity of Cereals in the Semi-arid region. Mémoire Magister. Université de Sétif Algérie. 53. (in French).

[21] Bouraada, K., Chavanon, G., Essafi, M., El Ghadraoui, L., Benjelloun, M. (2016) Ecological diversity of the beetle population in the mobile dune ecosystems of the northern fringe and of the eastern region of Morocco. Ecologia Mediterranea. 42(1), 39-50. (in French).

[22] Tom, H., Kaippallil, J.D. (2016) preliminary study on the diversity of coleopterans in a rural area in Changanacherry, Kerala. Journal of Entomology and Zoology Studies. 4(5), 297-300.

[23] Bouraada, K., Chavanon, G., Chergui, H. (1999) Beetles population of dune fixed by perennial grasses in the eastern region of Morocco. Actes Institue Agronomique et Vétérinaire. 19, 219-230. (in French)

[24] Pierre, F. (1958) Ecology and entomological population in the living sands of the North-West. Biological Series n° 1, National Center for Scientific Research, France. 332. (in French)

[25] Gibrán, S.H., Gómez, B., Delgado, L., López, M.E.R., Chamé-Vázquez, E.R. (2018) Diversity of copronecrophagous beetles (Coleoptera: Scarabaeidae: Scarabaeinae) in the Selva El Ocote Biosphere Reserve, Chiapas, Mexico. Ecologia. 40(1), 144-160. (in Spanish).

[26] Dajoz, R. (2003) Precis of ecology. Ed. Dunod. Paris. 615. (in French).

[27] Hartley, E.E., Gaedner, S.M., Mitchell, R.J. (2003) Indirect effects of grazing and nutrient addition on the hemipteran community of heather moorlands: Moorland vegetation and insect community diversity. Journal of Applied Ecology. 40, 793–803.
[28] Aviron, S., Burel, F., Baudry, J., Collet, S. (2003) Long-term impacts of agricultural practices on carabid beetles communities in different landscape contexts. In: Proceedings of the days of the International Association for Landscape Ecology IALE, France, 2003. 91-97. (in French)
[29] Da Silva, P.G., Vaz-De-Mello, F.Z., Di Mare, R.A. (2013) Diversity and seasonality of Scarabaeinae (Coleoptera: Scarabaeidae) in forest fragments in Santa Maria. Rio Grande do Sul. Brazil. Anais da Academia Brasileira de Ciências. 85(2), 679-697.
[30] Lacoste, A., Salanon, R. (2001) Elements of Biogeography and Ecology. Nathan/HER, Paris. 318. (in French)
[31] Altieri, M., Schmidt, L.L. (1986) The dynamics of colonizing arthropod communities at the interface of abandoned, organic and commercial apple orchards and adjacent woodland habitats. Agriculture, Ecosystems & Environment. 16, 29-43.
[32] Rigamonti, I.E., Lozzia, G.C. (2002) Phytoseiid mites (Acari: Phytoseiidae) on apple tree and spontaneous flora under different environmental and cultural conditions in Valtellina (Lombardy, Northern Italy). Bollettino di Zoologia agraria e di Bachicoltura. 34, 53-70.
[33] Debras, J.F., Dussaud, A., Rieux, R., Dutoit, T. (2007) Prospective research on the role of hedges in Integrated Fruit Production, the case of Earwigs: Forficula auricularia L. et Forficula pubescens Gené. Reports of the Academy of Sciences. Comptes Rendus Biologies. 330, 664-667. (in French).

Received: **07.10.2021**
Accepted: **24.11.2021**

CORRESPONDING AUTHOR

Mohammed Boutaiba Benklaouz
Biology Systems and Geomatics Laboratory,
Faculty of Nature and Life Sciences,
Mascara University 29000 – Algeria

e-mail: mohamed.boutaiba@univ-mascara.dz

© by PSP Volume 31– No. 05/2022 pages 4780-4786 Fresenius Environmental Bulletin

THE INFLUENCE OF THE PROCESS PARAMETERS ON THE MICROSTRUCTURE OF Al-Cu-Mg-Ti ALLOYS

Biljana Zlaticanin*

University of Montenegro, Faculty of Metallurgy and Technology, 81000 Podgorica, Montenegro

ABSTRACT

Results presented in this paper contribute to investigation of the influence of process parameters on the microstructure of samples during solidification of AlCuMgTi alloys. In this aim the 20 samples was solidified by different growth rate. The growth rate has been very important factor in the crystallization process. Obtained results give us possibility to create the desired microstructure by growth parameters. The similar microstructure was observed for the very close values of growth rate.

KEYWORDS:
Al-Cu-Mg-Ti alloys, growth rate

INTRODUCTION

One of the growing industries is the production of aluminum, which requires attention and planning since emits dangerous pollutants such as particulate matter, SO_2, NO_x, dioxins, furans, mercury chloride and fluorine compounds [1]. Large amount of pollution is produced in the alumina production and the aluminum electrolysis units, which in the best case, for the production of one ton of final aluminum, emit 4.73, and 1.32 kg of sulfur dioxide, and nitrogen dioxide respectively [1]. Therefore, reducing pollutants is a key element in the sustainable development of the aluminum industry [2]. The main raw material for aluminium is bauxite, which is extracted from bauxite mines and processed into aluminium oxide at alumina plants. Aluminium metal is produced from aluminium oxide by an electrolytic process. In addition to alumina, the main raw materials are carbon anodes and aluminium fluoride. Aluminum production from bauxite mines needs more energy rather than other metals, which leads to large emissions of greenhouse gases [3]. It should also be noted that during the aluminum production process, hazardous compounds such as fluorine, sulfur dioxide, hydrogen sulfide, and polycyclic aromatic hydrocarbons are released into the air, leading to many chronic and acute epidemiological effects on human health [4-6]. Two successive process chains including preparing alumina (aluminum oxide) from bauxite rock and aluminum from raw alumina are performed to produce aluminum. Melting steps and processes associated with primary production (including mining, purifying, and anode production for refining) account for 90% of all contaminants [7].

The bauxite residue from the Bayer process is known as ‘red mud’ due to its distinctive colour. In alumina production, the disposal of bauxite residue saturated with caustic soda ("red mud") is the main problem, although emissions to the atmosphere of gases and particles from boilers, calcination furnaces and bauxite dryers may also be important. Worldwide, the most common method of disposal of red mud is to discharge it into deposit lakes constructed for this purpose. An alternative method, which has environmental advantages, is to pump back the sludge in order to recover and reuse the caustic solution. In older installations, however, this is usually not done for reasons of cost. Primary aluminium is produced through the electrolytic decomposition of alumina in a molten bath composed of cryolite and fluorides, in which the carbon anodes collect oxygen released from the decomposition of alumina. The liquid aluminium is deposited on the carbon coating of the crucible – the pot - which acts as the cathode [8]. Historically, it has been disposed of completely in landfills but due to the volume and hazardous, high-alkalinity nature, researchers have been looking into treating red mud as an infeed material to produce products with some value. Furthermore, the continued development of inert anodes and their imminent commercialisation in the primary industry is an exciting prospect especially considering the ability to mitigate a large proportion of the CO_2 produced. Solid waste in the aluminum smelting process includes dross, unused carbon, nondissolved alumina, and spent pot liners. The industry has made significant progress in finding solutions to reduce, re-utilize and/or eliminate most of the wastes involved in mining, anode production, electrolysis, cast house operations, and secondary aluminum production. A remaining challenge is the minimization and elimination of “red mud” that is a solid-waste byproduct of the bauxite refining process.

Industrial production world-wide of new metal is around 20 million tons per year. Features such as low weight, corrosion resistance, and high ductility have led to a greater tendency to use aluminum in the aerospace, automotive, transportation, construction,

beverage, and electrical industries [9-13]. Interest in the system AlCuMgTi alloys during the last decades was due to the wide use of these alloys in the industry and transportation. Depending on the casting conditions and alloy composition, microstructure, properties and characteristics of the aluminium alloys will be different. The cooling rate affects the structure of as-cast alloys in a well-established manner, i.e. the grain size, the dendrite arm spacing (DAS) and the size of structure constituents (both primary and eutectic) decrease with increasing the cooling rate [14]. Many techniques are available to investigate the solidification of metals and alloys. Some of them were standardized such as DTA and DSC.

MATERIALS AND METHODS

Twenty samples were prepared by melting raw materials. The experimental material was delivered in form of ingots and from these ingots were casted samples for experimental work into the metallic moulds. The designed compositions were synthesized by high-purity Al (99.5%), pure Cu and pure Mg. The chemical composition (in wt. %) of the Al and AlCuMg alloys was specified by quantometery analysis and the results are reported in Table 1. The solidification structure was modified by the addition of the AlTi5B1 master alloy to give alloys containing 0 to 0.3 mass. % titanium. The melting was carried out in a 20 kW electric resistance furnace using a graphite crucible, and the melting temperature was kept at 760±5 °C. For the fluxing of the melts, a TAL-2 as a mixture of potassium chloride and sodium chloride with a small addition of cryolite was used. It was added in the amount of about 2 % of the melt quantity and reacted at a temperature of 660 °C. The melts were degassed with hexachloroethane tablets in the amount approximately equal to 0.25 % of each melt quantity.

To study the variations in the mechanical properties with respect to cooling rate, the alloy was cast by conventional air-cooled and water-cooled methods. Properties of the materials have been investigated, eg: hardness and determination of compression strength. Hardness has been measured by use of the Brinell method. Hardness measurement for aluminium and AlCuMg alloys samples was performed using a Brinell hardness tester with a load of 62.5 kp (1kp = 9.80665 N), 2.5 mm diameter ball and a dwell time of 30 s. Compression strength of the samples have been tested on an electronic tensile testing machine of 10t. Special attention was given to an assessment of the different structural parameters by modern quantitative microstructure analysis, using an automatic device for quantitative picture analysis and linear measuring method, which was considered as more reliable, accurate and faster than conventional manual methods of microstructure analysis.

RESULTS AND DISCUSSION

Aluminum is used in many industries to make millions of different products and is very important to the world economy. Structural components made from aluminum are vital to the aerospace industry and very important in other areas of transportation and building in which light weight, durability, and strength are needed. The use of aluminum exceed that of any other metal except iron. Pure aluminum easily forms alloys with many elements such as copper, zinc, magnesium, manganese and silicon. As aluminium and its alloys are inert and non-reactive when employed correctly, potential health and safety impacts are extremely limited. This paper analyzes the influence of cooling rate on the structure and properties of pure aluminium and on the structure and properties of Al-Cu-Mg alloys. In Figure 1 there are represented the obtained significant structures for solidified samples at different cooling rates. When a liquid alloy solidifies in a mold, there can be up to three distinct zones in the microstructure (Figures 1-3). In contact with the wall, the chill zone is formed, in which the grains are fine, equiaxed and have a largely random crystallographic orientation. The nucleation of grains in this zone may be on the wall itself or on heterogeneities in the melt, and is driven by the chilling that occurs when the liquid first makes contact with the cold wall. The zone can be eliminated by heating the mold. As solidification

TABLE 1
Chemical composition of the investigated Al and AlCuMg alloys (in mass%)

Type of sample	% Al	%Ti	%Fe	%Si	%Cu	%Mg	%Zn	%Cr	%Mn
Al (0%Ti)	99.54	0.000	0.08	0.15	0.003	0.00	0.050	0.001	0.010
Al (0.05%Ti)	99.59	0.048	0.19	0.07	0.006	0.00	0.052	0.001	0.007
Al (0.10%Ti)	99.62	0.097	0.12	0.09	0.003	0.00	0.054	0.002	0.008
Al (0.15%Ti)	99.56	0.143	0.16	0.07	0.003	0.00	0.052	0.002	0.008
Al (0.30%Ti)	99.50	0.323	0.08	0.05	0.007	0.00	0.058	0.002	0.009
Al-Cu13-Mg2.5 (0% Ti)	81.08	0.000	0.12	0.08	13.15	2.50	0.078	0.002	0.008
Al-Cu13-Mg2.5 (0.05% Ti)	83.46	0.052	0.12	0.08	13.56	2.57	0.071	0.002	0.009
Al-Cu13-Mg2.5 (0.10% Ti)	83.82	0.103	0.12	0.08	13.46	2.35	0.070	0.002	0.008
Al-Cu13-Mg2.5 (0.15% Ti)	85.22	0.177	0.11	0.08	12.13	2.20	0.067	0.002	0.008
Al-Cu13-Mg2.5 (0.30% Ti)	84.07	0.298	0.12	0.08	13.01	2.28	0.069	0.002	0.009

continues towards the center of the casting, the grains become elongated, giving the columnar zone. For pure metals, the columnar zone continues to the center of the casting, but for impure metals and alloys there is often an equiaxed zone in the final stages of solidification (Figures 1-3), in which a random crystallographic orientation is restored. The casting temperature for both cooling rate were at 760°C, 735°C, 715°C and 680°C, respectively [15-16]. In casting alloys, nonuniform microstructures (mixed columnar and equiaxed) are undesirable, and mostly an entirely equiaxed microstructure is strongly preferred. Fully equiaxed structures can be obtained by adding nucleant particles to the melt.

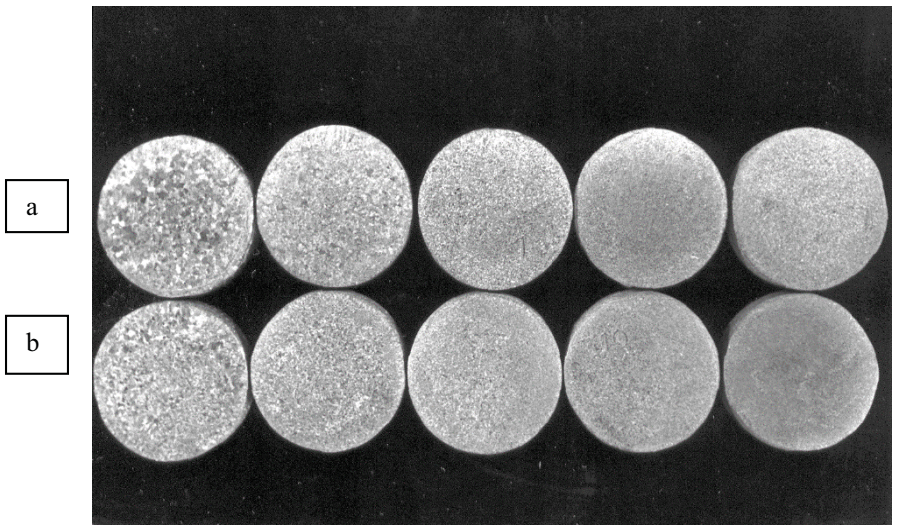

FIGURE 1
Macrostructure of Al samples (0%Ti, 0.05%Ti, 0.10%Ti, 0.15%Ti, 0.30%Ti, respectively) with different cooling rates: a) air-cooled, b) water cooled.

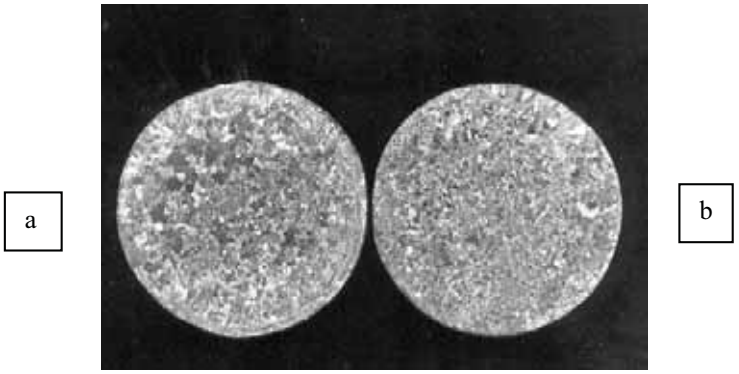

FIGURE 2
Macrostructure of Al (0wt.%Ti) samples with different cooling rates:
a) air-cooled, b) water cooled.

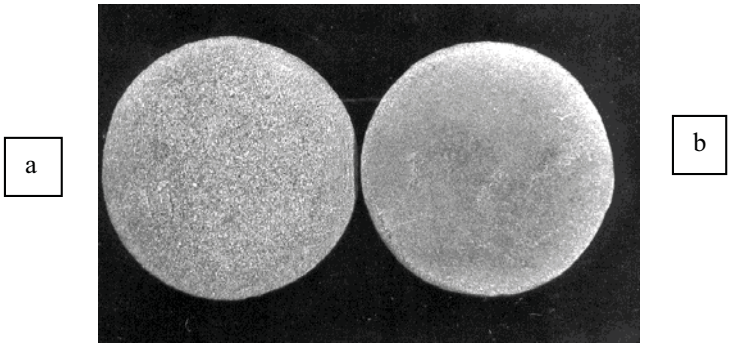

FIGURE 3
Macrostructure of Al (0.05wt.%Ti) samples with different cooling rates
a) air-cooled, b) water cooled.

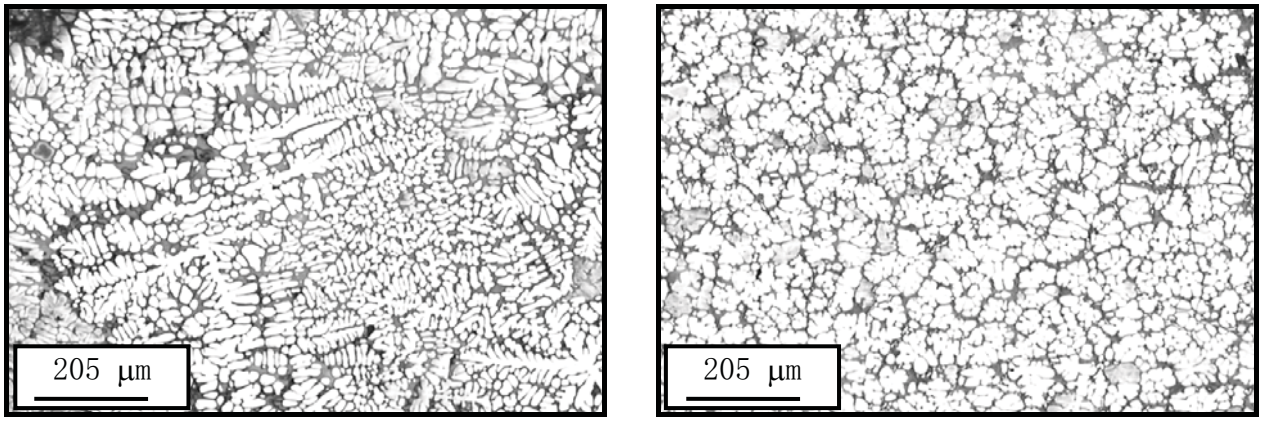

FIGURE 4
Microstructure of alloy: a) Al-Cu13-Mg2.5 (0%Ti), b) Al-Cu13-Mg2.5 (0.3%Ti).

TABLE 2
Effect of cooling rate and composition on the amount of eutectic

Type of sample	$V_{eutectic}$ (%)	
	air-cooled	water cooled
Al-Cu13-Mg2.5 (0% Ti)	24.9	29.8
Al-Cu13-Mg2.5 (0.05% Ti)	25.9	30.7
Al-Cu13-Mg2.5 (0.10% Ti)	26.7	31.3
Al-Cu13-Mg2.5 (0.15% Ti)	27.1	32.5
Al-Cu13-Mg2.5 (0.30% Ti)	27.8	33.4

TABLE 3
Hardness and compression strength of the Al and AlCuMg alloys obtained during the experiment

Type of sample	HBaverage		$\sigma_{0,2p}$ (N/mm^2)		σ_{mp} (N/mm^2)	
	air-cooled	water cooled	air-cooled	water cooled	air-cooled	water cooled
Al (0% Ti)	24.15	25.02	38.22	43.31	119.74	127.39
Al (0.05% Ti)	25.27	26.50	46.82	47.16	139.68	153.39
Al (0.10% Ti)	25.85	27.30	50.14	55.96	143.60	161.90
Al (0.15% Ti)	26.27	28.57	50.96	63.64	145.22	167.20
Al (0.30% Ti)	26.90	29.65	58.60	63.70	146.24	168.15
Al-Cu13-Mg2.5 (0% Ti)	107.75	136.50	280.25	361.78	557.96	670.06
Al-Cu13-Mg2.5 (0.05% Ti)	118.50	139.75	336.30	369.43	560.51	672.61
Al-Cu13-Mg2.5 (0.10% Ti)	123.50	142.50	351.60	371.97	583.44	675.16
Al-Cu13-Mg2.5 (0.15% Ti)	138.12	154.50	371.97	374.52	603.83	677.71
Al-Cu13-Mg2.5 (0.30% Ti)	149.25	157.50	382.16	377.07	619.11	680.25

Figure 4. shows the microstructure results obtained from a higher cooling rate, and that higher cooling rate produced finer grain size. The two important phases in the microstructure are the primary phase that solidifies first and the secondary phase that solidifies second. Figure 4a, show the dendritic microstructure of the alloys at higher cooling rate. The microstructure configurations consisted of dendrites and the interdendritc eutectic. The eutectic structure of this alloy with higher titanium content is presented in Figure 4b. The microstructure configurations for other alloys were similar. For all alloys, in both cooling rates, equilibrium eutectic is formed during solidification.

Phase-transformation temperatures and enthalpy of solidification of these alloys have been measured using differential scanning calorimetry. For the studied alloys, it has been found that with increasing cooling rate, liquidus temperature increases slightly, whereas solidus temperature decreases from 537.6°C to 506.3°C for Al-Cu13-Mg2.5 alloy. Enthalpy of solidification increases with increasing cooling rate, from -70.98 J/g to -46.75 J/g for Al-Cu13-Mg2.5 alloy. Besides, with increasing cooling rate, the secondary dendritic arm spacing decreases from 15.92 μm to 14.45 μm for Al-Cu13-Mg2.5 with 0.3%Ti (Figure 5). It is found that the volume fraction of eutectic increases with increasing cooling rate (Table 2). Also, the average values of the eutectic cell length were found to increase from 4.25 μm to 9.32 μm for Al-Cu13-Mg2.5 alloy with increasing cooling rate (Figure 6). Fast cooling rate condition produced smallest grain size, the sizes of the grains for the same content of titanium in the Al-Cu13-Mg2.5 are decreased from 73.12μm to 49.26 μm (Figure 7) and we obtain a fine, uniform grain structure, as shown in micrographs.

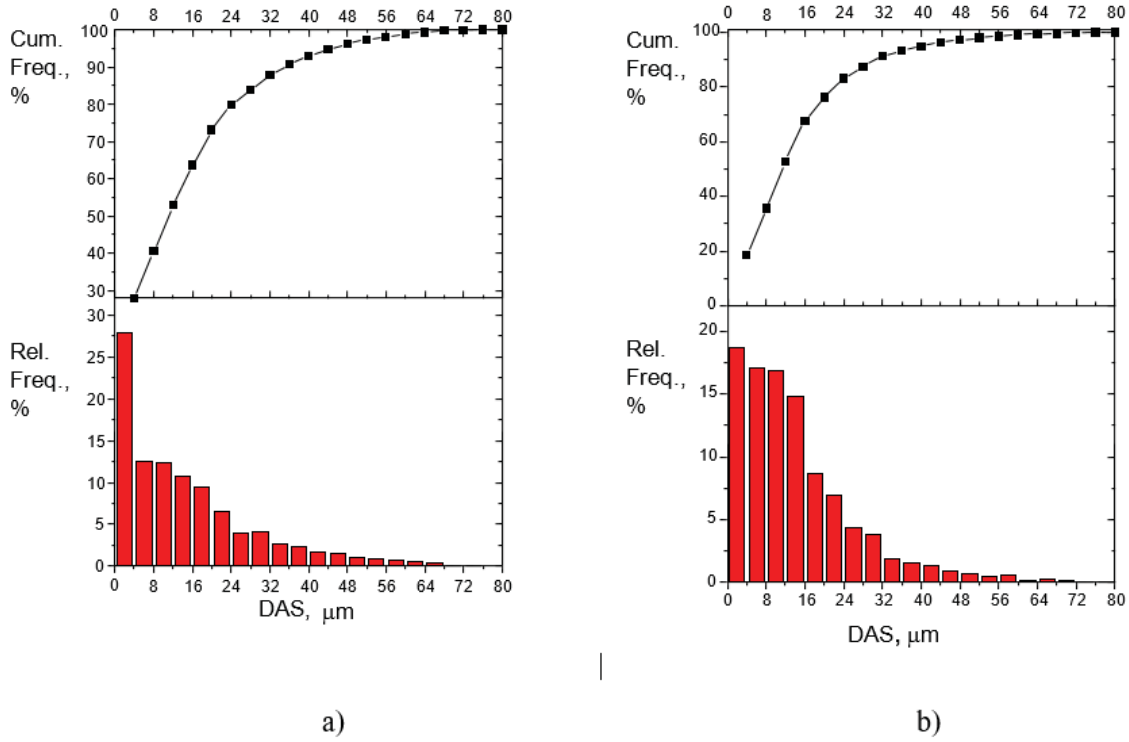

FIGURE 5
Dendrite arm spacing (DAS) for investigated Al-Cu13-Mg2.5 alloys: a) air-cooled, b) water cooled

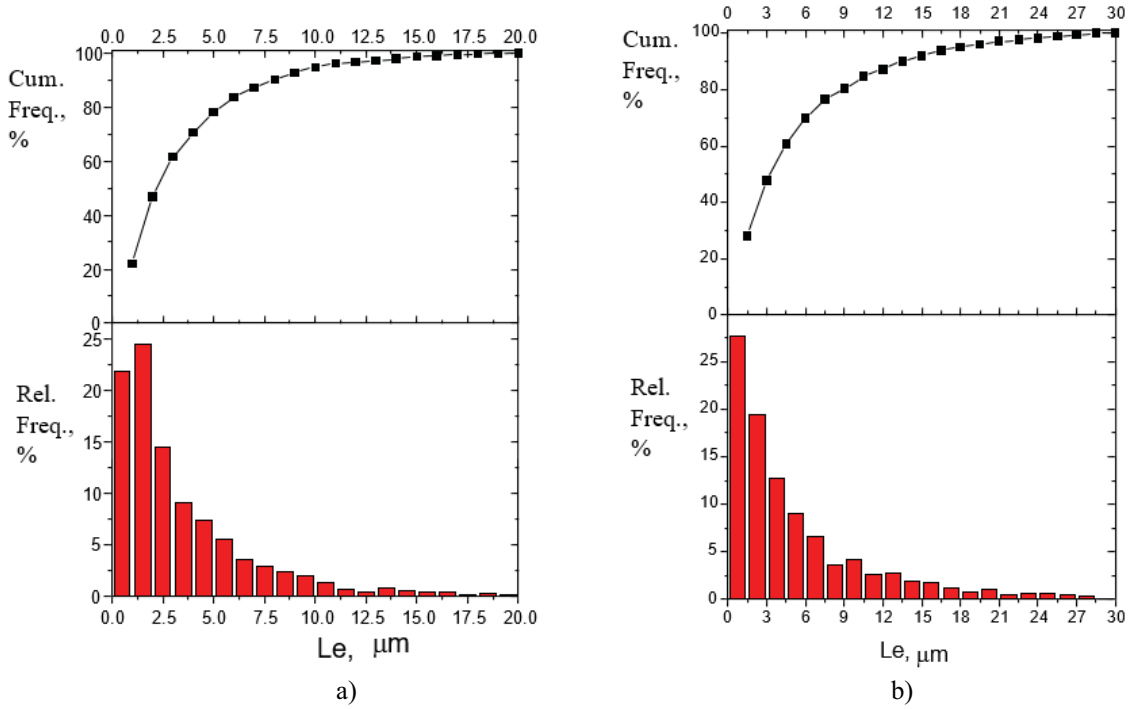

FIGURE 6
The linear intercept size of eutectic cells (Le) for investigated Al-Cu13-Mg2.5 alloys: a) air-cooled, b) water cooled

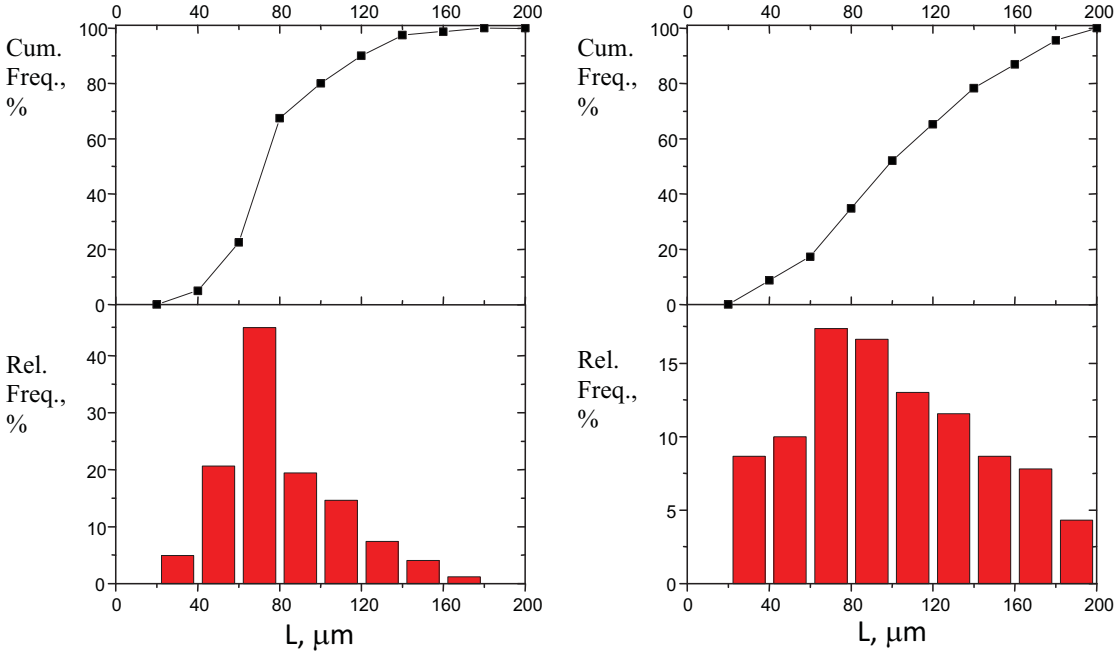

a) b)

FIGURE 7
Grain size for investigated Al-Cu13-Mg2.5 alloys: a) air-cooled, b) water cooled.

In this study the mechanical properties like compressive strength and hardness of both air-cooled and water cooled cast specimens were tested and the results were compared (Table 3). Increases in hardness and compressive strengths of the water cooled cast specimen have been encountered from the present work. This result reveals that increase in cooling rate leads to enhancement of the mechanical properties.

Alloy composition plays an important role in the environmental impact of the material. A key aspect is the fact that each alloying element presents different adverse effects on the environment. In conclusion, the alloy composition modifies not only the physical and mechanical properties of the alloy, but also its total environmental impact. The aluminum industry has taken a life-cycle approach to manufacturing and designing its products. This approach emphasizes responsibilities in managing products, services, and/or business operations throughout the entire life of the product—from product to recycling to new product. In the case of aluminum, this involves the management of resources, minimizing energy consumption, emissions and waste releases to the environment, while keeping a focus on the overall economic, social and environmental benefits that the products bring to society.

CONCLUSIONS

The effect of different process parameters during the solidification of the Al and AlCuMg alloys were examined. The microstructure and mechanical properties of cast products are greatly influenced by the cooling rate during their solidification. It is evident that the increase in cooling rate improves the mechanical properties of the cast alloy. The DAS decreases with increasing cooling rate, and the hardness and strength increase correspondingly. In addition, higher cooling rates produced a finer primary α-phase particle. As an elemental material, the basic properties of aluminum do not change with mechanical or physical processing. This means that aluminum is intrinsically sustainable: once produced, it can be recycled repeatedly without any loss in quality and reused in the manufacture of consumer and industrial products.

ACKNOWLEDGEMENTS

This work was not supported by any funds.

REFERENCES

[1] Abdollahi, J., Emrani, N., Chahkandi, B., Montazeri, A. and Gheibi, M. (2021) Environmental impact assessment of aluminium production using the life cycleassessment tool and multi-criteria analysis. Ann. Environ. Sci. Toxicol. 5, 059-066.

[2] Liu, G. and Muller, D.B. (2012) Addressing sustainability in the aluminum industry: a critical review of life cycle assessments. Journal of Cleaner Production. 35, 108-117.

[3] Norgate, T.E., Jahanshahi, S. and Rankin, W. J. (2007) Assessing the environmental impact of metal production processes. Journal of Cleaner Production. 15, 838-848.

[4] Li, X., Yang, Y., Xu, X., Xu, C. and Hong, J. (2016) Air pollution from polycyclic aromatic hydrocarbons generated by human activities and their health effects in China. Journal of Cleaner Production. 112, 1360-1367.

[5] Wannaz, E.D., Rodriguez, J.H., Wolfsberger, T., Carreras, H.A. and Pignata, M.L. (2012) Accumulation of aluminium and physiological status of tree foliage in the vicinity of a large aluminium smelter. Scientific World Journal. 32, 1-7.

[6] Ivanova, S.V. and Ryabchikova, I.A. (2019) Ecological human health risk in aluminum producing areas of Baikal region. In IOP Conference Series: Materials Science and Engineering. IOP Publishing. 687, 066013.

[7] Liu, G., Bangs, C.E. and Müller, D.B. (2013) Stock dynamics and emission pathways of the global aluminium cycle. Nature Climate Change. 3, 338-342.

[8] Anders, E.W., Andong, D., Gegan, Y., Jinchuan, Z. and Kaikun, W. (2020) On the Sustainable Choice of Alloying Elements for Strength of Aluminum-Based Alloys. Sustainability. 12, 1059-1068.

[9] Zhang, Y., Sun, M., Hong, J., Han, X. and He, J. (2016) Environmental footprint of aluminum production in China. Journal of Cleaner Production. 133, 1242-1251.

[10] Brough, D. and Jouhara, H. (2020) The aluminium industry: A review on state-of-the-art technologies, environmental impacts and possibilities for waste heat recovery. International Journal of Thermofluids. 1, 407-421.

[11] Wang, S. and Fan, C. (2019) Crystal Structures of Al2Cu Revisited: Understanding Existing Phases and Exploring Other Potential Phases. Metals. 9, 1037-1047.

[12] Türe, Y. and Türe, C. (2019) An assessment of using Aluminum and Magnesium on CO2 emission in European passenger cars. J. Clean. Prod. 2, 247-254.

[13] Mamur, H. and Candan, A.K. (2020) Detailed simulation of regenerative braking of BLDC motor for electric vehicles. Bilge International Journal of Science of Technology Research. 4, 63 – 72.

[14] Eskin, D., Du, Q., Ruvalcaba, D. and Katgerman, L. (2005) Experimental study of structure formation in binary Al–Cu alloys at different cooling rates. Materials Science and Engineering A. 405, 1-10.

[15] Zlaticanin, B., Radonjic, B. and Filipovic, M. (2004) Characterization of Structure and Properties of as-cast AlCuMg Alloys. Mater. Trans. 45, 440-446.

[16] Zlaticanin, B., Radonjic, B. and Marinkovic, Z. (2003) DSC Investigation of high-copper AlCuMg alloys. Materials and Technology. 37, 217-220.

Received: **08.10.2021**
Accepted: **06.02.2022**

CORRESPONDING AUTHOR

Biljana Zlaticanin
University of Montenegro,
Faculty of Metallurgy and Technology,
81000 Podgorica – Montenegro

e-mail: biljana@ucg.ac.me

© by PSP Volume 31– No. 05/2022 pages 4787-4792 Fresenius Environmental Bulletin

SIMULATION AND ANALYSIS OF SPATIAL-TEMPORAL CHARACTERISTICS OF URBAN SPATIAL EVOLUTION UNDER THE CONSTRAINT OF ECOLOGICAL SECURITY

Shan Cao*

Landscape Architecture School, Beijing Forestry University, Beijing 100083, China

ABSTRACT

The spatial and temporal characteristics of urban spatial evolution under the constraint of ecological security are studied, and the general situation of regional ecological environment is analyzed. The index system of regional ecological security is constructed, and the status of regional ecological security is obtained through the combination of these indexes and membership function. The elasticity coefficient and intensity coefficient of urban expansion are obtained by calculation, and the degree of interprovincial difference is obtained by calculating the Gini coefficient. The urban spatial center of gravity is calculated according to the gravity synthesis analysis method, and the spatial and temporal characteristics of the final urban spatial evolution are obtained by integrating these coefficients. The study area data was input into Matlab software to simulate the urban spatial evolution of the study area. Through analysis, 2010 to 2015 is the key period of the ecological security of the region, the degree of ecological security decreased, and the ecological security of the region has been greatly improved from 2015 to 2020. Under the constraints of ecological security and under the influence of economic factors, this region has witnessed stable urban spatial evolution after 2015, with small fluctuations in the future, indicating that this region has achieved good results in the evolution process to the suburbs. This study provides new ideas for future urban evolution and development.

KEYWORDS:
Ecological security, constraints, urban space, evolution, spatiotemporal characteristics, the simulation analysis

INTRODUCTION

Statistics show that more than 59% of the world's population live in urban areas. Urban areas are the most important living areas of mankind, and urbanization will also be the final form of social development [1]. With the continuous progress of human society, the process of urbanization is gradually increasing, urban land resources are becoming increasingly tense, and the contradictions between urban functional areas are gradually highlighted. To solve this problem, the city continues to expand to the surrounding areas, resulting in the evolution of urban space [2-3]. The evolution of urban space and the development of ecological environment interact with each other, and there are certain laws of mutual influence. Ecological protection promotes the long-term and sustainable development of cities. Domestic cities pay more and more attention to the development of urban green space concept, hoping to solve the ecological and environmental problems existing in cities [4]. In foreign studies, the United States was the first country to put forward the concept of urban evolution, put forward the idea of urban forest, formulated relevant laws and regulations, and classified urban ecological construction and environmental protection into the category of legal protection [5]; Canada, Japan and other countries also pay attention to green space protection in the process of urbanization. Government departments cooperate to supervise urban development and prevent urban disorderly development and improper expansion [6]. In the process of the development of China's urban law, it is mainly to expand the scope of the city to the suburbs. However, some studies show that the development of urbanization leads to excessive damage to the ecological environment, heat island effect, population expansion and other problems, resulting in the destruction of urbanization [7]. Therefore, in the future research, we should make a unified study on the evolution of urbanization and the balance of ecological environment, and regard them as a whole and develop in harmony [8].

With the sharp decline of biodiversity, the deterioration of ecological environment and the depletion of natural resources all over the world, all mankind has fallen into a survival crisis. Ecological security is classified into national security. The development of ecological security affects the overall national security and has become the key research direction of many researchers [9]. Among the existing studies, there are many fields related to ecological security, including water research, provincial and municipal ecosystem regulation and land use. The relevant research of some researchers focuses on the ecological security elements of multiple or a fixed

area, but in the actual environment, ecological security does not occur only in a moment, but a dynamic process [10]. China's investment in urbanization construction is increasing, but with the expansion of the city to the suburbs, the natural resources are over exploited, the ecological environment is under great pressure and gradually damaged, and the problem of ecological security is gradually exposed [11]. According to expert statistics, more than 300 million people will be transferred to cities in the next five years, changing the environment and social structure, and ecological security is also facing severe challenges. If cities want to achieve sustainable development, ecological security should be paid special attention to.

This paper focuses on the temporal and spatial characteristics of urban space evolution under the constraints of ecological security. Through a detailed analysis of the urban characteristics of the research area, this paper analyzes the internal relationship between urban space and ecological environment, so as to provide new theoretical support for the future development of the city.

MATERIALS AND METHODS

Overview of the study area. This paper takes a province in North China as the research object. The per capita land area of this province is about 30% of the land area owned by the national population. The province has developed rapidly in recent years, with rapid economic and population growth and accelerated urbanization. It is required that the province must have a large number of construction land to meet the current rate of economic and population growth. However, the urban scope is limited, the land use is limited, and the contradiction between supply and demand is becoming increasingly acute [12-14]. In the process of development, the province not only needs to meet the requirements of ecological sustainable development and cultivated land development, but also needs to implement the land demand for economic development. In other words, on the premise of paying attention to ecological protection and ensuring stable and rapid economic growth, the available land resources in the province are particularly scarce.

Because there are few water systems in the province, the water storage only accounts for 0.64% of the total water storage in the country. Due to the lack of water resources, water resources have become the main constraint factor in the region. In one city of the province, the per capita water resources reached only 122m^3 / person in 2019, accounting for about 5.51% of the country, resulting in serious water resource shortage [15].

Statistics show that because the province is located in the North China Plain, it receives cold air from the north to the north and convective warm air to the south, resulting in serious dust pollution in the region [16]. The province has developed industrial technology and high people's living standards. Almost every family has private cars. Although the living standards have improved, it has led to serious air pollution and increased urban emissions. In recent years, the problem of haze pollution in the province has been frequently reported in the newspapers. To alleviate this problem, the government has made many efforts, but with little effect. Industrial pollution, tail gas pollution and sand dust pollution have brought great pressure to the atmospheric environment of the province, and PM2.5 seriously exceeds the standard. According to the survey and statistics results of relevant departments in 2019, the dust content in the province is 9.34t, the nitrogen oxide content is 6.77t and the sulfur dioxide content is 5.68t, and the content of each pollutant exceeds the national average pollutant by 4 to 8 times [17,18].

Construction of evaluation index system. With the active promotion of the government and relevant departments, China's ecological environment has entered a new stage. Authoritative experts pointed out that the needs and characteristics of ecological environment improvement with Chinese characteristics should be fully considered when establishing the ecological environment evaluation index, the index system should be innovative, and the environmental ecological index should fully consider the air quality level [19]. Using the idea of experts, this paper not only considers the ecological benefits, but also takes the resource and environmental constraints into account when evaluating the ecological environment security of the research area, reflects the current ecological environment benefits, and constructs the ecological security evaluation index system. See Table 1.

When selecting indicators, the first level indicators are divided into ecological benefits and environmental benefits, in which environmental benefits can mainly reflect the living environment quality level of people in the study area, and environmental benefits are directly related to people's quality of life. With the improvement of living standards, people have higher and higher requirements for living comfort and health level, and the environmental benefits also reflect the people-oriented ecological civilization construction [20]. Measuring the economic development results obtained after the consumption of ecological resources in the study area requires the use of ecological benefits, which can also reflect the efficiency of the use of ecological resources in the study area. As an important indicator, it can measure whether the provincial capital development and economic development meet the green demand.

TABLE 1
Ecological security index system

Content	Primary index	Secondary index
Ecological security index system	Environmental benefit	Per capita public green space area / m^2
		Proportion of nature reserves in the Province /%
		Natural environmental pollution
		Forest coverage /%
		PM2.5 concentration
	Ecological benefit	Years of education per capita / (year / person)
		Land occupation per unit GDP / (km2 / 10000 yuan)
		Life expectancy per capita / year
		Water resource consumption per unit GDP / (t / 10000 yuan)
		Energy consumption per unit GDP / (t standard coal / 10000 yuan)

Ecological security evaluation model and temporal-spatial evolution method. (1) Calculate ecological security index. The boundary of security is very fuzzy, so the evaluation of ecological security is relative. The ecological security evaluation model selected in this paper is the fuzzy membership model. According to the evaluation index constructed above, the standard value of ecological security degree obtained from the evaluation is taken as the evaluation result, so as to obtain the ecological security degree of the study area. Equation (1) is the membership degree of ecological security:

$$U_{(j)} = \frac{1}{1+\left\{\frac{\sum_{i=1}^{m}\left[W_i\left(r_{ij}-1\right)\right]^p}{\sum_{i=1}^{m}\left(W_i * r_{ij}\right)^p}\right\}^{\frac{2}{p}}} \quad (1)$$

$U_{(j)}$ and $W_{(i)}$ represent the degree of ecological security and the weight of the i_{th} index respectively; p and r_{ij} represent the values of the distance parameter and the i_{th} index respectively. Select 2 Euclidean distance as the distance parameter, and the ranges of i and j are 1,2,3,..., n. The membership results of ecological security are obtained through calculation, and there is a positive proportional relationship between the membership and the degree of ecological security.

There is a spatial correlation between ecological security and the temporal and spatial characteristics of urban spatial evolution. Spatial autocorrelation analysis is used to show spatial dependence or explain the attributes of things [21]. Local and global indicators are indicators of military spatial autocorrelation, in which local indicators can reflect a geographical phenomenon in a small area in the study area, and can also reflect the attribute correlation degree of two adjacent areas; the global index is mainly to study the spatial relationship of a single element in the region. In this paper, local spatial autocorrelation index and global spatial autocorrelation index are used to analyze the spatial characteristics of regional ecological security. The global spatial autocorrelation index range is between 1 and -1. If the index is greater than 0, it is a negative correlation relationship. The spatial distribution correlation is affected by the absolute value. The greater the absolute value, the greater the correlation, showing strong aggregation. The closer the absolute value is to 0, the more random the spatial distribution is.

(2) Urban spatial evolution method. After obtaining the ecological security constraints, the spatial characteristics of urban spatial evolution are analyzed by indicators such as urban expansion elasticity coefficient and urban expansion intensity coefficient. The elastic coefficient of urban expansion is obtained:

The results of urban spatial expansion are obtained through the interaction between people and land. The rationality of the evolution of the city to the suburbs is expressed by the urban elasticity coefficient, which can reflect the outward expansion mode of the city from the side [22]. This coefficient can be obtained by dividing the annual growth rate of urban area after the completion of urban establishment by the annual average urban population growth rate. The critical value of urban expansion elasticity coefficient is 1.23. If it exceeds this critical value, it means that the urban expansion rate is too fast compared with the population growth rate; If it is lower than this critical value, it indicates that the urban expansion to the suburbs is low. The larger the expansion elasticity coefficient, the more sparse the outward expansion of the city, and vice versa.

The calculation method of urban expansion strength coefficient is: Through the urban expansion intensity coefficient, the speed and intensity of urban land use expansion in different time periods can be obtained, and the land area of spatial unit can be used when standardizing the annual average expansion speed. The land use area is calculated through the urban built-up area [23].

In the process of urban spatial evolution, the degree of inter provincial differences caused by spatial expansion is obtained by using Gini coefficient which can analyze distribution differences. By calculating that the Gini coefficient is between 0 and 1, there is a positive proportional relationship between the Gini coefficient and inter provincial differences [24]. The center of gravity of urban space is calculated according to the gravity synthesis analysis law, and the detailed coordinates of the center of gravity are obtained through calculation.

RESULTS

The data of the research area are imported into Matlab simulation software, and the development law and spatial characteristics of urban spatial evolution are analyzed in the simulation software.

Ecological security assessment results. Through the above research and analysis, the regional ecological security index is studied, and the analysis results are shown in Table 2.

The evolution of ecological security in the study area is shown in Figure 1. Figure 1 shows that in 2010, the ecological security of the whole central region of the study area was low. With the passage of time, the low-risk region gradually expanded, changed significantly every five years, and the ecological security continued to improve. Table 2 shows that the ecological security of the study area has decreased first and then increased in 10 years. The reasons for this are mainly due to the acceleration of urbanization, the increase of urban population, the obvious changes of ecological landscape types in the study area, the continuous expansion of cities to suburbs, a large number of construction needs occupy rural planting land, the trace of human life has a direct impact on the ecological environment, and the increasing pressure on the ecological environment, the stability of the ecosystem was destroyed, so the ecological security of the study area decreased in the five years from 2010 to 2015. After this happened, the government and relevant departments began to take measures, invest a lot of money and formulate policies to protect the ecological environment. Therefore, the ecological security has been improved in the five years from 2015 to 2020. Compared with the last five years, the change of ecological security in the first five years is more obvious. The first five years are the key process of urban spatial evolution.

Temporal-spatial characteristics of urban spatial evolution. In recent years, urbanization has developed more and more rapidly, and the urban construction area has gradually increased. Statistics show that the growth rate of urban space expansion has increased by 5.51% in recent 30 years. From the perspective of urban boundary, the urban construction area has increased nearly three times compared with the end of the 20th century. The change law of urban spatial expansion speed and expansion scale in recent 10 years is shown in Figure 2 and Figure 3.

TABLE 2
Ecological security index in different years

Particular year	2010	2015	2020
Minimum value	0.1349	0.1929	0.1653
Maximum	0.8291	0.7682	0.7733
Average value	0.4747	0.3989	0.3991
Variance	0.0281	0.0212	0.0224
Global spatial autocorrelation index	0.9129	0.8849	0.8814

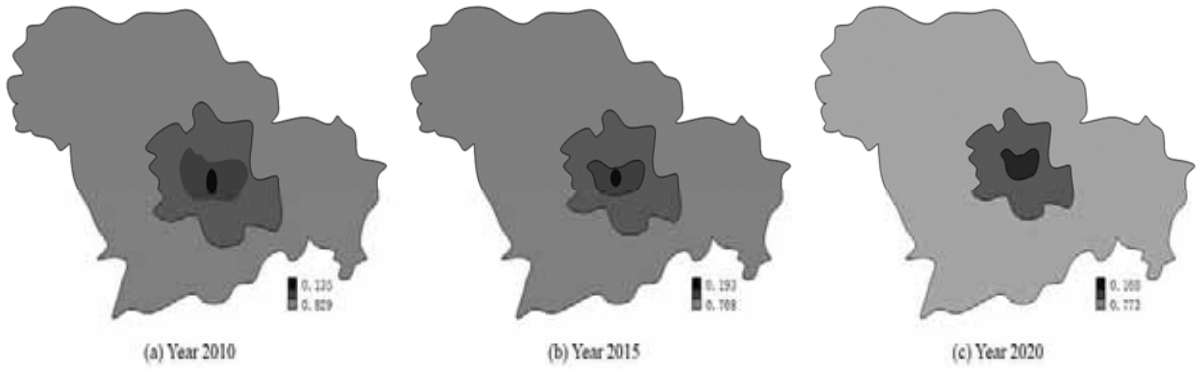

FIGURE 1
Evolution of ecological security.

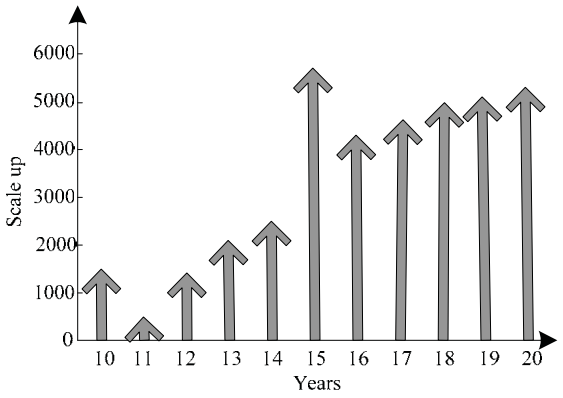

FIGURE 2
Urban expansion scale.

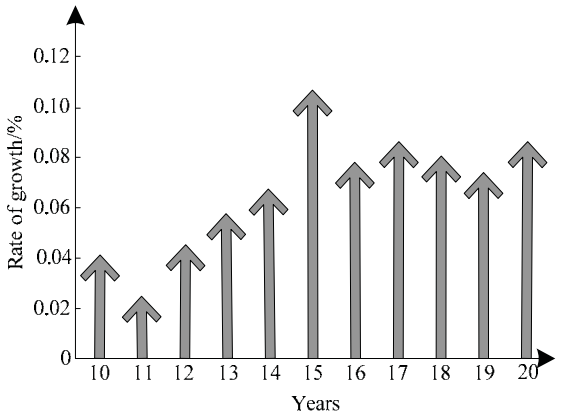

FIGURE 3
Urban expansion speed.

According to Figure 2 and Figure 3, the urban spatial evolution in the study area first showed a rapid decline, and then a rapid upward trend from 2012 to 2015. After that, the expansion evolution continued to fluctuate slightly in the next five years. The evolution law is a growth trend without linear relationship. On the whole, the speed of urban expansion is always consistent with the area. There was a sudden rise in the evolution of urban space in 2015. According to the analysis, in 2015, the government responded to the national call and implemented urban construction, with a new urban area of more than 1000 square kilometers. In 2011, there was a low point in urban expansion, which may be mainly due to the lag of urban development due to the impact of the economic environment. It can also be seen that the progress of regional economy also directly affects urban development.

CONCLUSIONS

This paper studies the temporal and spatial characteristics of urban spatial evolution under the constraints of ecological security through simulation software.

(1) The analysis shows that there is a non-linear relationship in the evolution of urban space to the suburbs, and the evolution law is sparse. The study shows that the urban evolution from 2010 to 2015 shows a steady rise, and has shown a steady development since 2015.

(2) The ecological security in the city is directly affected by the urban development, so the ecological security restricts the outward evolution of the city and the evolution of the city to the suburbs, resulting in the extension of human activities to the suburbs and the artificial destruction of the ecological landscape to varying degrees.

(3) Through research and analysis, the overall evolution law of the study area is obtained, and the future development direction of similar areas is also obtained. Urban spatial evolution should not only consider the constraints of ecological environment, but also comprehensively consider the state of regional economic development. In the process of urban evolution, we should pay attention not to negative population growth, but also to transform the local ecological environment and build a modern city suitable for living and business.

ACKNOWLEDGEMENTS

This research was jointly funded by the Industrial Cooperative Education Project Hosted by Ministry of Education of the People's Republic of China (grant no. 20210109602D) and the Beijing Natural Science Foundation (grant no. 9222022).

REFERENCES

[1] Liu, S., Huang, Y. (2020) Landscape Ecological Security Evaluation and Coupling Characteristics Analysis of Wanzhou District from the Perspective of "Sansheng Space". Research on Soil and Water Conservation. 143(06), 314-322.

[2] Zhu, L., Luo, Z., Wang, Q., Zhang, J. (2020) Temporal and spatial differences and evolution characteristics of urban land use efficiency in Gansu Province under environmental constraints. Research on Soil and Water Conservation. 141(04), 372-379.

[3] Wu, Z., Li, H. (2020) Research on the urban spatial layout of the southern Shaanxi River Valley based on the transfer of land use: Taking Shanyang County as an example. Planner. 318(18), 12-21.

[4] Li, P., Peng, Z. (2018) The mechanism of rapid transit on the development of residential space in the suburbs of metropolis - An analysis based on the perspective of temporal and spatial economic attributes. Urban Development Research. 200(4), 75-83.

[5] Li, H., Zhao, Y., Zheng, F. (2020) The framework of an agricultural land-use decision support system based on ecological environmental constraints. Science of the Total Environment. 717, 1-10.
[6] Chatterjee, S., Mukherjee, S. (2019) Estimation in tournaments and graphs under monotonicity constraints. IEEE Transactions on Information Theory. 65(6), 3525-3539.
[7] Jin, R. (2019) Study on the change of urban spatial structure based on the interaction relationship of geographical objects. Geography and Geo-Information Science. 35(3), 141.
[8] Wu, Y., Xi, Y., Tu, W., Zhu, Y., Li, R., Li, C. (2018) Landscape security assessment and spatial-temporal change in ecologically sensitive area: A Case study of Shiyan City, Hubei Province. Yangtze River. 49(23), 32-37.
[9] Mahmoodi, K., Ghassemi, H., Razminia, A. (2019) Temporal and spatial characteristics of wave energy in the persian gulf based on the era5 reanalysis dataset. Energy. 187(15), 115991.
[10] Han, Y., Deng, M. (2020) Spatial-temporal changes and influencing factors of ecological efficiency in Central Plains Urban agglomeration. Acta Ecologica Sinica. 40(14), 4774-4784.
[11] Xu, C., Zhu, S. (2019) Temporal and spatial movement characteristics of the Altyn Tagh fault inferred from 21years of Insar observations. Journal of Geodesy. 93(8), 1147-1160.
[12] Wei, G., He, Q., Zhu, X., Ouyang, X. (2019) Spatial-temporal evolution of urban flow in Zhejiang Province based on spatial interpolation. Arid Land Geography. 183(01), 217-224.
[13] Cheng, C., Hu, Y., Zhao, M. (2020) Research progress and Prospects of urban green spatial pattern and ecosystem service evaluation. Progress in Geography. 39(10), 1770-1782.
[14] Ghobadi, A., Cheraghi, M., Sobhanardakani, S., Lorestani, B., Merrikhpour, H. (2020) Hydrogeochemical characteristics, temporal, and spatial variations for evaluation of groundwater quality of hamedan–bahar plain as a major agricultural region, west of Iran. Environmental Earth Sciences. 79(18), 1-16.
[15] Yu, D., Liang, Z, Xiao, Z., Sun, C., Zheng, Y. (2020) Spatial-temporal characteristics of land ecological risk in Nanchang City based on landscape ecological thinking. Research of Soil and Water Conservation. 27(1), 213-220.
[16] Zhang, Y., Jia, Y. (2020) Spatialization of Time: The Research Path of the Spatio-temporal Relationship of Historical Cities -- Based on the Comparative Perspective of Chinese and Western Philosophy. Urban Development Studies. 27(7), 75-82.
[17] Li, C. (2020) Landscape design of the urban bus station based on the urban characteristics and ecological environment of smart city, China. Fresen. Environ. Bull. 29(4A), 3300-3307.
[18] Liu, W., Tao, Y., Bi, K. (2020) Exploring temporal and spatial evolution of the patent collaboration network: a case study of smart grid field in china. IEEE Transactions on Engineering Management. 99, 1-16.
[19] Hu, J. (2020) Comparison of building resilience in the international typical green building evaluation system based on the concept of ecological and environmental protection. Fresen. Environ. Bull. 29(8), 7147-7155.
[20] Yang, J., Wang, S., Gao, Y., Zhang, J. (2019) Analysis on the characteristics of urban spatial Interaction from the perspective of place: A Case study of The Sixth Ring Road of Beijing. Geography and Geo-Information Science. 35(06), 79-86.
[21] Wang, H., Yu, D., Zheng, J. (2018) Spatial-temporal variation characteristics of urban density in Xinjiang based on spatial econometric model. Journal of Natural Science of Hunan Normal University. 41(05), 5-13.
[22] Shafie, A. (2019) Comparison between TDMA and random multiple-access energy-harvesting networks under security constraints. IEEE Communications Letters. 23(2), 334-337.
[23] Chen, R., Poulsen, A., Schmidt, H. (2019) Spectral, spatial, and temporal characteristics of underwater ambient noise in the Beaufort sea in 1994 and 2016. The Journal of the Acoustical Society of America. 145(2), 605-614.
[24] Du, J., Ning, X., Liu, J, Qiu, S, Wang, H., Wang, C. (2019) Analysis of urban spatial expansion pattern and morphological characteristics based on remote sensing monitoring in Beijing. Areal Research and Development. 38(02), 75-80.

Received: **29.10.2021**
Accepted: **05.12.2021**

CORRESPONDING AUTHOR

Shan Cao
Landscape Architecture School,
Beijing Forestry University,
Beijing 100083 – China

e-mail: Caoshan@bjfu.edu.cn

© by PSP Volume 31– No. 05/2022 pages 4793-4799 Fresenius Environmental Bulletin

FEASIBILITY ANALYSIS OF ENTREPRENEURSHIP CONSIDERING ENVIRONMENTAL PERFORMANCE UNDER LOW-CARBON ECOLOGICAL VALUES

Gang Zhao[1,*], Zheng Liu[2]

[1]School of Business, Macau University of Science and Technology, Macau, 999078, China
[2]School of Economics, Sichuan University, Chengdu, Sichuan, 610000, China

ABSTRACT

Entrepreneurship is one of the power sources of China's economic development. With the increasingly mature low-carbon ecological values of the whole society, environmental performance, as an important factor affecting the feasibility of entrepreneurship, must be fully considered. Based on the analysis of low-carbon ecological values, this paper considers the entrepreneurial feasibility of environmental performance. According to low-carbon ecological values and the concept of environmental performance, environmental performance must be considered in entrepreneurial feasibility. Through the establishment of empirical analysis model, select the small and medium-sized entrepreneurial enterprises that have carried out or are carrying out entrepreneurial activities in the entrepreneurship Park of a city's economic and Technological Development Zone as the object of empirical analysis, and obtain the index information through questionnaires and interviews. The empirical analysis results show that the questionnaire title has high reliability. Under the low-carbon ecological values, various indicators of environmental performance have a significant impact on the entrepreneurial feasibility, that is, the environmental performance with low-carbon as the constraint determines the entrepreneurial feasibility. The carbon emission level in the environmental performance indicators has the greatest impact on the entrepreneurial feasibility, water consumption per unit product has the least impact on entrepreneurial credibility. This paper provides a theoretical reference for effectively using environmental performance to improve the feasibility of entrepreneurship.

KEYWORDS:
Low carbon ecology, consider environmental performance, entrepreneurial feasibility, entrepreneurial activities, significant imact, resource consumption level

INTRODUCTION

With the rapid development of economy and society, China has entered the stage of mass entrepreneurship. However, the prosperous economic behavior has also brought great damage to the natural environment [1]. Without the protection of scientific and reasonable environmental protection policies, the rapid economic growth has seriously damaged the ecological balance, that is, the best balance between ecological benefits and economic benefits can not be obtained. Green economy and green life are the inevitable trend of social development [2]. With the advent of the era of "mass entrepreneurship", entrepreneurship has gradually become an important choice for college graduates and many people. China has entered the wave of innovation and entrepreneurship. The state has formulated many incentive policies on innovation and entrepreneurship to actively support college students' entrepreneurship [3]. In recent years, with the improvement of people's awareness of environmental protection, the combination of low-carbon ecological concept and entrepreneurship has been recognized by relevant people from all walks of life. The combination of entrepreneurship and low-carbon ecological concept can improve the environmental performance of enterprises, give full consideration to low-carbon ecological values, promote entrepreneurs' innovation and entrepreneurship [4], and meet the concept of entrepreneurial ecological values.

With the gradual implementation of low-carbon values, enterprise environmental performance, as an important indicator to measure enterprises, has become the focus of academic research in recent years. At present, many researchers do not have a unified understanding of the research on low-carbon ecology and environmental performance in entrepreneurship. Jin et al. [5-6] studied environmental performance, economic performance and ecological consumption behavior, preliminarily defined the impact of environmental performance on economy, measured entrepreneurs' entrepreneurial feasibility from two aspects of accuracy and robustness, and provided help for the full study of entrepreneurial feasibility considering environmental performance under ecological values. However, the above related research is

not specific to the concept of low-carbon ecology. It is only from the perspective of environmental protection, and the research is not detailed enough.

Enterprises are the main body of social and economic activities. With the increase of resource pressure and the increasing problem of carbon emission in environmental problems, this paper fully considers the low-carbon ecological values, considers entrepreneurship, makes effective use of social resources and maintains the sustainable development of entrepreneurial enterprises. Low carbon and environmental benefits are important parts that entrepreneurs should pay attention to in the process of entrepreneurship. There is a high correlation between environmental benefits in entrepreneurship and economic benefits of enterprises. To analyze the entrepreneurial feasibility of considering environmental performance under low-carbon ecological values, we need to fully consider low-carbon ecological values and combine the economic benefits of enterprises with environmental benefits as an important index to evaluate entrepreneurial performance. The results show that there is a significant impact on environmental performance and entrepreneurial feasibility under low-carbon value. Under the low-carbon value, the improvement of environmental performance can not only improve the economic performance of the entrepreneurial process, but also ensure that enterprises give full play to their due social responsibility after entrepreneurship.

MATERIALS AND METHODS

Low carbon ecological values. Low carbon ecological values are the combination of low carbon ecological theory and low carbon ecosystem. It is an important subject to study the correlation of carbon emissions between different organisms and their surrounding environment. Low carbon ecology studies the relationship between animals, plants and carbon emissions in fixed areas. Low carbon values can reflect the interaction between different factors in the ecosystem, explore the functions of different organisms [7], and realize the effective unity of biological functions and carbon emissions. In recent years, the theory of low-carbon ecology has developed continuously, and many researchers have begun to do a lot of research on the theory of low-carbon ecology. There is a very high correlation between various elements in low-carbon ecology and carbon emissions. Low carbon ecosystem is a system with high openness, dynamics and development. All subjects in the system are interrelated and various factors restrict each other [8]. There is competition and action relationship. It has high carbon emission dynamics and balance. The application of low-carbon ecology theory in life has a high guiding role.

Based on the above ecological values, it can be seen that things have high levels and organic, and all things in the ecological values theory have high dynamics, balance and systematicness. The concept of ecological values has attracted the attention of many researchers, and its development is very rapid. At present, it has been applied to many countries and regions with global characteristics [9]. Low carbon ecological values have become an important aspect for entrepreneurs to consider when discussing the feasibility of entrepreneurship. Low carbon ecological values are not only applied in the industrial environment, but in many industries such as tourism and finance.

The research on innovation and entrepreneurship under the concept of low-carbon environment in China started late and is currently in the primary research stage. Under the concept of low-carbon ecological values, fully consider the impact of entrepreneurial feasibility, take "sustainable development" as the core goal of entrepreneurial feasibility, cultivate entrepreneurs' socio-economic innovation and entrepreneurial awareness and entrepreneurial level, make entrepreneurs fully consider carbon emission factors under ecological values and improve entrepreneurial feasibility.

Enterprise environmental performance. The concept of environmental performance in ISO14001 environmental management system is to fully consider environmental objectives, environmental policies and environmental indicators, and consider the impact of various factors related to the environment on the environment [10], and use the measurement method to clarify the management effect of various indicators in the environmental management system. The logical relationship of environmental performance is shown in Figure 1.

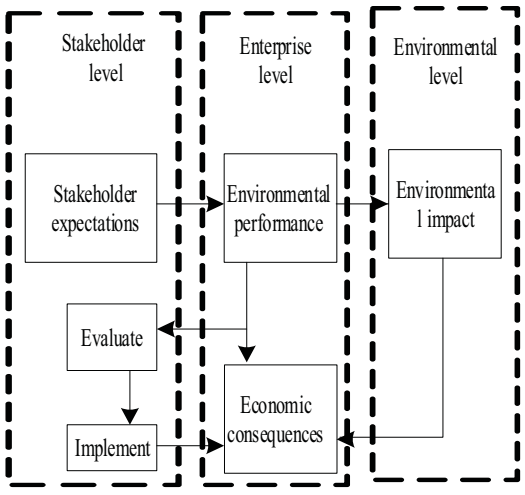

FIGURE 1
Logical relationship of environmental performance.

Environmental performance mainly includes enterprise level, environmental level and relevant

levels of stakeholders. The level of low-carbon ecological environment directly affects enterprise development, ecological environment protection and the relevant interests of stakeholders.

The environmental performance of enterprises mainly includes two parts: business performance and management performance. Business performance and management performance can respectively reflect the environmental performance related to enterprise operation and the management efforts made by enterprises to improve ecological and environmental protection. The subjects of business performance and management performance of enterprises are: managers of resource consumption level related to enterprise environment, and management procedures [11]. With full consideration of ecological values, enterprise supply chain management, new technologies in the business process and recyclable related products can be used to measure the environmental performance of enterprises. In the process of enterprise operation, many indicators of environmental pollution and impact, such as wastewater, waste, noise and radioactive substances, can be used as important business performance indicators to measure environmental performance. Under the concept of low-carbon ecological values, the enterprise's management performance indicators mainly include the formulated low-carbon environmental protection scheme, low-carbon environmental protection policies, the enterprise's compliance with laws and regulations related to ecological environment and the enterprise's financial situation [12]. The enterprise's carbon emission target, carbon emission management system and relevant strategic indicators of ecological and environmental protection can be used as important indicators to measure the enterprise's environmental performance.

With the national support for innovation and entrepreneurship and the attention to low-carbon ecological and environmental protection, when analyzing the feasibility of entrepreneurship under low-carbon ecological values, it is necessary to fully consider the environmental performance of enterprises. The environmental situation is deteriorating [13]. When starting a business, it is not only necessary to consider the economic interests of the enterprise, but also need to take the environmental performance as an important indicator to measure the entrepreneurial feasibility of entrepreneurs. The environmental responsibility of entrepreneurship and the economic interests of enterprises should be considered at the same time. In the future investment concept, environmental performance is extremely important [14]. The balance between environmental performance and economic interests is an important part for entrepreneurs to maintain the sustainable development of enterprises. The environmental performance of entrepreneurs can directly reflect the effectiveness of environmental management. Entrepreneurs realize the internal management of the enterprise through the environmental performance of the enterprise, which helps the enterprise formulate a scientific basis for the production plan and various environmental protection implementation plans [15], provides strategic support for the sustainable development of the enterprise, and can effectively analyze the entrepreneurial feasibility of the enterprise for entrepreneurs.

Research hypothesis. Under the concept of low-carbon ecological values, there is a high correlation between environmental performance and entrepreneurial feasibility. Different low-carbon indicators of environmental performance have a high impact on entrepreneurial feasibility. Combined with the above theoretical analysis, this paper puts forward the entrepreneurial feasibility verification hypothesis considering environmental performance under the low-carbon ecological values. It is assumed that environmental pollution control level, resource consumption level, water consumption of enterprise unit products, eco-environmental training level, environmental operation expenditure, enterprise innovation technology level, enterprise carbon emission target, enterprise carbon emission management level and other indicators have a positive impact on entrepreneurial feasibility, and they are numbered and matched one by one, designed experiments and analyzed the results.

Empirical research methods. (1) Research object of empirical analysis. Select the small and medium-sized entrepreneurial enterprises in the entrepreneurship Park of a municipal economic and Technological Development Zone as the empirical analysis object, and obtain the index information of small and medium-sized enterprises that have carried out or are carrying out entrepreneurial activities through questionnaires and interviews. The empirical research data is the data of 2019. The field survey and questionnaire survey are used to collect data and select samples [16]. A total of 200 questionnaires were recovered, and 180 valid questionnaires. (2) Measuring tools. Select Likert level 5 scale to formulate an empirical analysis questionnaire [17], and adjust the questionnaire measurement scale through expert survey method [18]. Select the middle and senior managers of start-up enterprises as the tested object. Spss22.0 and Amos 5.0 software were selected to statistically analyze the questionnaire.

RESULTS

Questionnaire scale test. The exploratory factors of environmental performance and entrepreneurial feasibility of the questionnaire measurement scale are analyzed, and the confirmatory factor analysis is carried out after the exploratory factor analy-

sis is completed [19]. The results of exploratory factor analysis are shown in Table 1.

Table 1 shows that the measurement variables in the questionnaire measurement scale designed for empirical analysis have high reliability. The KMO values of the measured variables are higher than 0.7 and the significance levels are lower than 0.005. The approximate chi square value meets the needs of empirical analysis.

The Amos software is used to carry out confirmatory factor analysis on the survey scale to verify the effectiveness of the designed empirical analysis model [20]. The goodness of fit results of confirmatory factor analysis are shown in Table 2.

Table 2 shows that the questionnaire and the fitting indexes in the empirical analysis model can meet the empirical analysis standards of the model, and verify that the structural validity of the questionnaire is credible.

TABLE 1
Exploratory factor analysis

Measurement variables	KMO	Approximate chi square value	Freedom	Significance
Entrepreneurial feasibility	0.785	945.61	11	0.001
Environmental pollution control level	0.815	815.64	12	0.002
Carbon emission level	0.823	826.64	7	0.002
Water consumption per unit product of the enterprise	0.865	784.65	8	0.001
Low carbon ecological environment training level	0.765	768.52	10	0.001
Environmental operating expenses	0.784	832.64	16	0.001
Enterprise innovation technology level	0.765	784.52	18	0.002
Enterprise carbon emission target	0.871	594.65	15	0.001
Enterprise carbon emission management level	0.751	486.52	17	0.001

TABLE 2
Model goodness of fit

Parameters	Environmental performance	Entrepreneurial feasibility
Standardized load	0.918	0.824
Fitness	0.886	0.915
Reference fit	0.852	0.916
Comparative fitness	0.935	0.945
Normalized root means square residual	0.005	0.003

TABLE 3
Correlation analysis results

Parameters	Entrepreneurial feasibility	Environmental pollution control level	Resource consumption level	Water consumption per unit product of the enterprise	Low carbon ecological environment training level	Environmental operating expenses	Enterprise innovation technology level	Enterprise carbon emission target	Enterprise carbon emission management level
Entrepreneurial feasibility	0.756	/	/	/	/	/	/	/	/
Environmental pollution control level	0.725	0.815	/	/	/	/	/	/	/
Carbon emission level	0.685	0.561	0.825	/	/	/	/	/	/
Water consumption per unit product of the enterprise	0.625	0.615	0.254	0.756	/	/	/	/	/
Low carbon ecological environment training level	0.526	0.536	0.715	0.625	0.786	/	/	/	/
Environmental operating expenses	0.385	0.564	0.625	0.284	0.648	0.748	/	/	/
Enterprise innovation technology level	0.856	0.645	0.751	0.584	0.612	0.581	0.825	/	/
Enterprise carbon emission target	0.705	0.715	0.458	0.615	0.751	0.658	0.645	0.865	/
Enterprise carbon emission management level	0.735	0.568	0.685	0.745	0.685	0.485	0.685	0.715	0.815

Reliability analysis and variable correlation analysis. The correlation analysis results and α reliability coefficient results of the measurement variables set in the statistical empirical analysis are shown in Table 3.

When the α reliability coefficient in correlation coefficient analysis is higher than 0.7, the set variables have high reliability [21]. Table 3 shows that the α reliability coefficient of each index in the empirical analysis model is higher than 0.7, indicating that the empirical analysis questionnaire has high reliability and can be applied to the entrepreneurial feasibility analysis considering environmental performance under low-carbon ecological values [5, 22]. Under the low-carbon ecological values, the relationship between environmental performance and various variables of entrepreneurial feasibility, and there is a high correlation between various indicators of environmental performance and entrepreneurial feasibility.

Regression analysis. To investigate the impact of different indicators of environmental performance on entrepreneurial feasibility under low-carbon and low-carbon ecological values, environmental performance and entrepreneurial feasibility are set as independent variables and dependent variables for regression analysis. The regression analysis results are shown in Table 4.

Table 4 shows that there are great differences in the impact of environmental performance indicators on entrepreneurial feasibility. The carbon emission level in environmental performance indicators has the greatest impact on entrepreneurial feasibility, and the water consumption per unit product of enterprises has the least impact on entrepreneurial feasibility.

The coefficient estimation results of the empirical analysis model of entrepreneurial feasibility considering environmental performance under low-carbon ecological values are shown in Table 5.

Table 5 shows that the model set in the empirical analysis has good goodness of fit. The research hypothesis verification results show that under the set low-carbon ecological values, various indicators of environmental performance have a significant impact on entrepreneurial feasibility, that is, environmental performance determines entrepreneurial feasibility. All the hypotheses proposed in the model are valid, and various indicators have varying degrees of impact on entrepreneurial feasibility. According to the results of empirical analysis, entrepreneurs can put forward improvement measures for the weak stage of entrepreneurial feasibility in the process of enterprise entrepreneurship, and fully consider the low-carbon ecological values, so as to ensure the smooth progress of entrepreneurship under the condition of high environmental performance.

TABLE 5
Regression analysis results

Research hypothesis	P	Hypothesis test results
Hypothesis 1	0.005	Establish
Hypothesis 2	0.002	Establish
Hypothesis 3	0.001	Establish
Hypothesis 4	0.003	Establish
Hypothesis 5	0.002	Establish
Hypothesis 6	0.004	Establish
Hypothesis 7	0.002	Establish
Hypothesis 8	0.003	Establish

TABLE 4
Regression analysis results

Measurement index Environmental pollution control level	Non standardized regression coefficient		Standardized regression coefficient	*t*	sig.
	B	Standardized mean square error	Beta		
Carbon emission level	0.895	0.059	0.685	5.615	0.001
Water consumption per unit product of the enterprise	0.385	0.052	0.594	2.615	0.002
Low carbon ecological environment training level	0.168	0.048	0.132	1.254	0.001
Environmental operating expenses	0.265	0.065	0.563	1.284	0.001
Enterprise innovation technology level	0.495	0.048	0.485	3.615	0.001
Enterprise carbon emission target	0.594	0.035	0.385	2.648	0.003
Enterprise carbon emission management level	0.385	0.028	0.394	1.645	0.002
Measurement index	0.352	0.019	0.285	1.584	0.001

CONCLUSIONS

Analyze the entrepreneurial feasibility considering environmental performance under low-carbon ecological values, fully consider the concept of low-carbon ecological values, and explore the impact of environmental performance on entrepreneurial feasibility. This paper selects small and medium-sized enterprises in an economic and Technological Development Zone as the object of empirical analysis. The eight low-carbon indicators of environmental pollution control level, resource consumption level, enterprise unit product water consumption, eco-environmental training level, environmental operation expenditure, enterprise innovation technology level, enterprise carbon emission target and enterprise carbon emission management level under environmental performance have a positive impact on entrepreneurial feasibility. After verification, the P values of various assumptions are 0.005, 0.002, 0.001, 0.003, 0.002, 0.004, 0.002 and 0.003 respectively, which are less than 0.005. The statistical results verify that there is a significant correlation between environmental performance and entrepreneurial feasibility.

Under the concept of low-carbon ecological values, considering environmental performance and improving entrepreneurial feasibility, we should actively cultivate innovative talents and optimize the green innovation and entrepreneurship system. The empirical analysis results show that cultivating entrepreneurs' green innovation and entrepreneurship concept under the condition of environmental performance is an important way to improve the feasibility of entrepreneurship. College graduates are an important core of green entrepreneurship. Colleges and universities should give full play to their guiding role, integrate the concept of green and low-carbon ecology into the innovation and entrepreneurship education of colleges and universities, and let college entrepreneurs establish scientific and reasonable green and low-carbon ecological values. By setting up green innovation and entrepreneurship practice courses to improve the entrepreneurship practice level of college students, college students can improve their sense of social responsibility and innovation quality through the innovation and entrepreneurship concept under low-carbon ecological values, and cultivate entrepreneurial talents to meet the needs of the society. In the process of enterprise entrepreneurship, it is necessary to fully consider the impact of environmental performance on enterprise entrepreneurship, establish an incentive entrepreneurship system, improve the innovation and entrepreneurship level of enterprises, fully consider low-carbon ecological values, jointly improve the entrepreneurial performance of enterprises from the two aspects of low-carbon ecological environment protection and enterprise income, and realize the sustainable development of enterprises. In the process of entrepreneurship, enterprises should establish good cooperative relations with relevant suppliers, customers and other stakeholders, and actively promote the healthy growth of enterprises by using good cooperative relations.

ACKNOWLEDGEMENTS

This work was not supported by any funds. We want to thank all the techniques who have helped this research and all the authors of the references.

REFERENCES

[1] Gu, J. (2019) Research on the relationship between entrepreneurs' professional values, resource patchwork and entrepreneurial performance. Scientific Research Management. 40 (11), 206-215.

[2] Hao, C., Zhao, Y., Dong, Z., Hu, R., Li, Z. (2019) "Twelfth Five-Year" Environmental Performance and Economic Development Coupling Analysis. Ecological Economy. 35(03), 185-190+209.

[3] Pechanec, V., Vondrakova, A., Sterbove, L., Cudlin, P. (2020) Environmental data visualization: Stocks of the stored carbon in Czechia. Fresen. Environ. Bull. 29(3), 1630-1636.

[4] Wang, H., Xiong, L., Li, Y. (2020) The impact of the entrepreneurial environment of the crowd-creation space on the performance of new ventures. Studies in Science of Science. 252(04), 100-111.

[5] Liu, C., Zhang, F., Zhang, H. (2020) Comparative analysis of off-site precast concrete and cast-in-place concrete in low-carbon built environment. Fresen. Environ. Bull. 29(3), 1804-1812.

[6] Wang, S., Zhou, H. (2019) Environmental values affect ecological consumption behavior - An empirical test based on intermediary variables. Soft Science. 238(10), 54-61.

[7] Chen, Z., Ma, L. (2020) Research on the relationship between the parent entrepreneurial environment and the performance of technology-based spin-offs - Based on the mediating role of entrepreneurial motivation. Soft Science. 250(10), 66-72.

[8] You, J., Zhang, Y. (2020) Research on the Impact of Corporate Social Responsibility and Environmental Performance on Environmental Performance Information Disclosure. China Coal. 522(01), 22-27.

[9] Wang, X., Zheng, J. (2020) The impact of government environmental subsidies on environmental performance from a macro and micro perspective. East China Economic Management. 283(07), 24-33.

[10] Li, W., Xu, E. (2020) Changes in the Institutional Environment and Performance of Startup Enterprises - An Empirical Study Based on the New Third Board Enterprises. Management Modernization. 228(02), 52-54.
[11] Chen, B., Yang, D. (2020) Research on the Impact of Work Values on Innovation Performance under the Background of Evaluation-based Performance Appraisal. Nanjing Social Sciences. 395(09), 64-71.
[12] Liu, Y., Huang, L., Lin, Q. (2019) Environmental Dynamics, Entrepreneurship Orientation and Corporate Performance: The Moderating Effect of Management Relationship. Research and Development Management. 31(05), 89-102.
[13] Guo, X., Hao, C., Wang, B. (2019) Environmental performance evaluation and influencing factors analysis of Hubei Province from a spatial perspective. China Environmental Science. 39(10), 4456-4463.
[14] Lin, N., Bao, J. (2020) Research on the Impact of Cultural Values on Farmers' Entrepreneurship Financing - Data Analysis from "China's Thousand Villages Survey". Foreign Economics and Management. 496(06), 39-55.
[15] Chen, W., Chi, Q., Qian, M., Xu, G. (2019) The impact of entrepreneurial resource sharing on college students' entrepreneurial performance - Based on a regulated intermediary model. Techno Economics. 38(06), 90-98.
[16] Zhou, Y., Shen, H. (2019) Supervision of environmental enforcement and corporate environmental performance: Evidence of quasi-natural experiment from talks on environmental protection. Nankai Business Review International. 11(5), 113-119.
[17] Channa, N., Hussain, T., Casali, G. (2021) Promoting environmental performance through corporate social responsibility in controversial industry sectors. Environmental Science and Pollution Research. 1, 71-75.
[18] Kalyar, M., Shoukat, A., Shafique, I. (2019) Enhancing firms' environmental performance and financial performance through green supply chain management practices and institutional pressures. Sustainability Accounting, Management and Policy Journal. 32(2), 1032-1038.
[19] Homroy, S., Slechten, A. (2019) Do Board Expertise and Networked Boards Affect Environmental Performance? Journal of Business Ethics. 158, 721-724.
[20] Chiarini, A. (2021) Industry 4.0 technologies in the manufacturing sector, Are we sure they are all relevant for environmental performance?. Business Strategy and the Environment. 15(6), 344-352.
[21] Yang, X. (2021) Study on the coordinated development of regional economic, tourism and ecology coupling: Taking Henan province as an example. Fresen. Environ. Bull. 30(1), 210-215.
[22] Majid, A., Yasir, M., Javed, A. (2019) Nexus of institutional pressures, environmentally friendly business strategies, and environmental performance. Corporate Social Responsibility and Environmental Management. 3, 79-85.

Received: **01.11.2021**
Accepted: **05.12.2021**

CORRESPONDING AUTHOR

Gang Zhao
School of Business,
Macau University of Science and Technology,
Macau 999078 – China

e-mail: 450085009@qq.com

© by PSP Volume 31– No. 05/2022 pages 4800-4806 Fresenius Environmental Bulletin

POSSIBLE ASSOCIATION OF TAS2R38 BITTER TASTE RECEPTOR WITH LARYNGEAL CANCER

Onur Bobusoglu[1], Senay Balci[1,*], Didem Derici Yildirim[2], Melis Yilmaz[3], Cengiz Ozcan[4], Lulufer Tamer[1]

[1]Mersin University Faculty of Medicine, Department of Medical Biochemistry, Mersin, Turkey
[2]Mersin University Faculty of Medicine, Department of Biostatistics, Mersin, Turkey
[3]Mersin University Faculty of Dental Medicine, Department of Endodontics, Mersin, Turkey
[4]Mersin University Faculty of Medicine, Department of Ear, Nose and Throat, Mersin, Turkey

ABSTRACT

It is reported that the bitter taste develops to protect people from the consumption of toxic compounds. Genetically, the alleles of the TAS2R38 gene are the main genetic markers of phenotypic variation in 6-n-propylthiouracil (PROP) taste sensitivity used to describe the ability to taste bitter compounds. TAS2R38 mutations and bitter taste responses have been found to be associated with many diseases, including alcoholism, obesity, thyroid function and cancer. Therefore, this study aims to investigate the role of bitter taste receptor genes or polymorphisms in these genes, which can be related to risk factors in head and neck cancers in laryngeal cancer.

Eighty-two individuals, 44 patients diagnosed with laryngeal cancer and 38 patients in control group, were included in this study. DNA isolation was performed from whole blood samples and analysis of TAS2R38 (rs713598, rs1726866, rs10246939) polymorphism from DNA samples was performed on RT-PCR.

While PAV was more common in patients with laryngeal cancer, AVI frequency was similar in both groups. The prevalence of heterozygous individuals was lower in the patient group ($p < 0.005$).

To our knowledge, this is the first study investigating the role of TAS2R38 with laryngeal cancer in the literature. Thus, further studies on the role of TAS2R38 in the diagnosis and treatment of the disease, including taste sensitivity tests shoud be conducted.

KEYWORDS:
Laryngeal cancer, TAS2R38, bitter taste, PAV, AVI

INTRODUCTION

The bitter taste can protect people from the consumption of toxic compounds [1]. Therefore, they have more specific receptors than other tastes, and bitter molecules can be detected at thresholds 1000 times lower than other tastes in some cases [2, 3]. Sensitivity to bitter tastes is variable within the population, and phenotypic and genotypic variability in bitter taste perception has been widely studied [4, 5]. Phenylthiocarbamide (PTC) is a chemical that imitates the bitter taste perception of isothiocyanates obtained from cruciferous vegetable [6]. 6- n-propylthiouracil (PROP) is a derivative of PTC. PROP is generally substituted for PTC in taste studies. The sensitivity spectrum of PTC/PROP is very wide. Some individuals have an intensely bitter taste (supertasters), while others have no taste at all (non-tasters). Most people, on the other hand, are between these two degrees (tasters) [7].

Type 2 taste receptors (T2Rs, TAS2Rs) are a member of the G protein-linked receptor class (GPCRs) involved in signal transduction on the cellular membrane, especially in response to bitter-tasting compounds [1,8,9]. T2R receptors are encoded by members of the TAS2R gene family and they encode approximately 25 different T2R isoforms [10]. Genetically, alleles of the TAS2R38 gene are the main genetic determinants of phenotypic variation in PROP taste sensitivity that is used to describe the ability to taste bitter compounds [11]. In humans, TAS2R genes are known to exist on chromosomes 5, 7 and 12, and TAS2R38 is found on chromosome 7. There are three non-synonymous single nucleotide polymorphisms (SNPs) encountered in the TAS2R38 bitter taste receptor gene, which are: reference SNP (rs) number 713598; rs1726866; rs10246939. Their amino acid substitutions are A49P (A49→P49), A262V (A262 →V262) and I296V (I296 →V296)). These SNPs lead to five haplotypes responsible for varying levels of phenotypic PTC/PROP sensitivity in humans. Due to the high level of linkage disequilibrium between A262V and I296V, the only variation is seen between A49P and A262V in practice. While the PAV haplotype corresponds to a greater sensitivity to certain bitter tastes, the AVI haplotype corresponds to insensitivity to bitter taste [12, 13]. There is also a moderate heterozygous effect. As a group, PAV/AVI heterozygotes have a significantly higher PTC taste threshold than PAV homozygotes. Thus, they are less sensitive to PTC [14].

These receptors are expressed in oral tissues

where the perception of the bitter taste of food or waterborne compounds begins and in other extraoral tissues, including the respiratory, genitourinary, gastro intestinal and nervous systems. T2Rs serve to separate beneficial or harmful exogenous and endogenous molecules and activate subsequent steps, such as the use or elimination of these stimuli. Therefore, in addition to regulating metabolism, it has been reported that they are also associated with disease risk [15, 16]. In addition, studies show that taste genes play a much wider role in human health. Recently, taste receptors have been shown to be expressed in several organs and tissues that are not directly involved in food intake or digestion, such as the lung, airway smooth muscle, nose and testis. Their response to harmful stimuli increases in the airways or they may play a role in spermatogenesis in the testis. These findings suggest that bitter taste perception may have a central role in organisms' homeostasis. Besides, they are only one of the functions performed by this gene cluster [17, 18].

TAS2R38 mutations and bitter taste responses are associated with alcoholism, smoking and many diseases, including obesity, thyroid function, colon polyps and types of cancer [3]. Moreover, in the study conducted by Mirza et al. [19], taste abnormalities were observed in patients with head and neck cancer, and it was suggested that these defects were caused by radiation exposure based on treatment. Laryngeal cancer, which constitutes 25% of head and neck region malignancies, constitutes 2-5% of all malignant tumors [20]. Although the incidence of laryngeal cancers in men is higher, increased smoking habits in women caused a decrease in the male/female ratio similar to lung cancer [21]. Many factors may play a role in the development of laryngeal cancer. These factors may be effective alone in cancer formation, or they may have a synergistic effect with other factors [22]. Studies have shown that the effects of these genes or the variability in these genes are quite extensive, apart from protection from toxic compounds. Therefore, this study aimed to investigate the role of bitter taste receptor genes or polymorphisms in these genes in laryngeal cancer.

MATERIALS AND METHODS

This study consisted of individuals with the larynx (patient group, n=44) and healthy (control group, n=38). Participants were selected from patients with a similar age range between the groups who applied to Mersin University Medical Faculty Hospital ENT Department. While determining the inclusion criteria of the participants in the patient group, attention was paid to that there was no other cancer history other than larynx ca and that treatment was not initiated and newly diagnosed. Apart from this, the pediatric group, patients diagnosed with any cancer other than laryngeal cancer and any systemic disease, patients with obesity or any substance addiction were excluded from this study. After DNA isolation from blood samples taken from individuals belonging to the patient and control groups to the tubes with EDTA and stored at +4°C, analysis of TAS2R38 (ThermoFisher, rs713598, rs1726866, rs10246939) polymorphism was performed on RT-PCR device (RocheLightCycler480) to investigate its role in laryngeal cancer. As a result of the data obtained, allele frequency, genotype distribution and risk ratio were calculated. In addition, disease risk was evaluated according to haplotype types. Whether the groups were in Hardy-Weinberg balance concerning genotype distribution was investigated. A chi-square test was used to investigate the relationship between two categorical variables. The exact test was used as the frequency percentage that was expected lower than 5 was greater than 20%. If a significant relationship was found, a pairwise ratio comparison was made. An independent sample t-test was used to compare the means of two independent groups. $p < 0.05$ was accepted as the statistical significance level. Analyses were made in Statistica v.13.3.1 program.

Before conducting this study, ethical approval was obtained from the ethics committee of the university (Decision No: 12/275, Date: 26.06.2019).

RESULTS

The study group consisted of 44 patients (average age: 58) and 38 controls (average age: 57). Of those included in this study, 67.1% were men, 32.9% were women. 84.1% of the patient group were male, while 15.9% of the control group were male and a statistically significant relationship was found between the gender and the group ($p<0.001$). The findings obtained in this study showed that the rate of males in the patient group was significantly higher than in the control group.

In this study, 3 SNPs of TAS2R38 taste receptor gene polymorphisms were studied to investigate their role in laryngeal cancer in the patient and control groups (Table 1). As shown in Table 2, no statistically significant difference was found between the groups concerning distribution of genotype and allele frequencies (rs102469; p=0.412, p=0.797), (rs713598; p=0.105, p=0.205), (rs1726866; p=0.727, p=0.917).

The importance of TAS2R38 for bitter taste perception was first shown by Kim et al. (12), and it was named PAV and AVI, which defined two common alleles with extremely different functional characteristics associated with threshold detection of PTC.

However, recent studies have revealed that TAS2R38 contains a wide range of genetic variation beyond the PAV and AVI alleles and contains 19 amino acid variants cataloged in populations worldwide up to date, which may underlie unrecognized

TABLE 1
SNP genotyping of TAS2R38 taste receptor gene

SNP ID	SNP Location	Polymorphism	Major/minor allele	MAF	SNP Type	Observed Codons	Observed Amino Acid
rs713598	229	C/G, Transversion Substitution	C/G	0.42	Missense Mutation	CCA, GCA	P,A 49
rs1726866	869	A/G, Transition Substitution	T/C	0.46	Missense Mutation	GCT, GTT	A,V 262
rs10246939		C/T, Transition Substitution	T/C	0.46	Missense Mutation	ATC, GTC	I,V 296

TABLE 2
Allele frequency and genotype data in groups

SNP ID	Genotype	Patient n (%)	Control n (%)	P Value
rs102469	**CC**	15 (34.1)	9 (23.7)	0.412
	CT	18 (40.9)	21 (55.3)	
	TT	11 (25.0)	8 (21.1)	
	Allele frequency			
	C	48 (54.5)	39 (51.3)	0.797
	T	40 (45.5)	37 (48.7)	
rs713598	**CC**	**10 (22.7)**	**9 (23.7)**	**0.105**
	CG	**12 (27.3)**	**18 (47.4)**	
	GG	**22 (50.0)**	**11 (28.9)**	
	Allele frequency			
	C	**32 (36.4)**	**36 (47.4)**	**0.205**
	G	**56 (63.7)**	**40 (52.6)**	
rs1726866	**AA**	11 (25.0)	8 (21.1)	0.727
	AG	17 (38.6)	18 (47.4)	
	GG	16 (36.4)	12 (31.6)	
	Allele frequency			
	A	39 (44.3)	34 (44.7)	0.917
	G	49 (55.7)	42 (55.3)	

functional and phenotypic diversity [23,24]. In this study, the PAV rate was 54.54%, the AVI rate was 32.95% and the rate of PAV/AVI presence was 20.5% in the patient group. In all individuals included in this study, the rate of presence of PAV was 53.05%, and the rate of AVI was 36.59%. There was no statistically significant relationship between haplotype and groups ($p=0.3110$). PAV/PAV was detected as 29.3% in all individuals, and PAV/AVI rate was 30.5%. When the pairwise ratio comparison was made between the groups, while the percentage of PAV/AVI presence was 20.5 in the patients, it was found as 42.1 in the control group, and the percentage of PAV/PVI presence was 2.6 in the patients and 18.2 in the control group, and a statistically significant difference was found between both rates ($p<0.05$) (Table 3).

DISCUSSION

To our knowledge, this is the first study with laryngeal cancer for the role of TAS2R38 in the literature. Bitter taste sensitivity, polymorphisms in the TAS2R38 gene and its association with many diseases, including alcoholism, obesity, COPD, asthma, coronary artery diseases, head and neck cancers, ovarian, prostate cancers and colon polyps, were investigated [25-27]. The underlying reason for its association with diseases is that the increased sensitivity to bitter taste, the change caused by preference and unwillingness, also affects dietary choices. The underlying reason for its association with diseases is that changes in preference and reluctance caused by the increased sensitivity to bitter taste also affect dietary choices. In addition, developing nutritional habits may affect the nutritional status later and increase the risk of long-term health and chronic diseases.

However, the interactions between taste and other dietary effects are complex, and the exact nature of the interactions cannot yet be fully explained [3]. It has been reported that individuals with increased sensitivity to bitter taste tend to avoid foods rich in antioxidants and nutrients with a bitter taste and maybe less healthy due to this. It is even assumed that the risk of many diseases, especially cardiovascular diseases, will increase, as there will be an increase in the consumption of sweet, fatty and low-nutritional foods instead of a bitter taste. It is also argued that those with very high sensitivity to bitter taste generally increase their taste acuity, which may cause a parallel decrease in sugar and fat intake. While the possible interactions between bitter taste and health remain complex, it is seen that non-

TABLE 3
Haplotype and diplotype distributions

		Control	Patient	Total
Haplotype				
PAV	n (%)	39 (51.32)	48 (54.54)	87 (53.05)
AVI	n (%)	31 (40.79)	29 (32.95)	60 (36.59)
AAV	n (%)	2 (2.63)	3 (3.41)	5 (3.04)
AVV	n (%)	1 (1.32)	--	1 (0.61)
PAI	n (%)	1 (1.32)	--	1 (0.61)
PVI	n (%)	2 (2.63)	8 (9.1)	10 (6.1)
	Total	76	88	164
Diplotype				
PAV/PAV	n (%)	10 (26.3)	14 (31.8)	24 (29.3)
AVI/AVI	n (%)	6 (15.8)	10 (22.7)	16 (19.5)
PAV/AVI*	**n (%)**	**16 (42.1)**	**9 (20.5)**	**25 (30.5)**
PAV/PVI*	**n (%)**	**1 (2.6)**	**8 (18.2)**	**9 (11.0)**
AAV/AVI	n (%)	1 (2.6)	0 (0.0)	1 (1.2)
AVI/AVV	n (%)	1 (2.6)	0 (0.0)	1 (1.2)
PAV/AAV	n (%)	1 (2.6)	3 (6.8)	4 (4.9)
PAV/PAI	n (%)	1 (2.6)	0 (0.0)	1 (1.2)
PVI/AVI	n (%)	1 (2.6)	0 (0.0)	1 (1.2)
	Total	38	44	82

*$p<0.05$

tasters who are less sensitive to bitter vegetables may consume more vegetables but also prefer more sweet and high-fat foods. Thus, the finding suggests that increased taste acuity can prevent excessive consumption in all food groups [27].

TAS2Rs are G protein-like receptors. GPCRs bind to taste receptors to which specific intracellular G proteins are coupled, and G α-gustducin is involved in sweet and bitter taste transduction. When stimulated with PROP or PTC, phosphodiesterase (PDE) is stimulated via the activated a-gustducin and cAMP is hydrolyzed. Decreased levels of cAMP may also raise intracellular Ca^{2+} and consequently promote neurotransmitter release. While this path is still uncertain, a second way is as follows. It activates the phospholipase C isoform β2 via the β and γ subunits of gustducin (described as Gβ3 and Gγ13). When inositol trisphosphate (IP3) is released, it binds to IP3 receptor type III and causes Ca^{2+} release. High Ca^{2+} levels activate transient receptor potential proteins (TRP) in the taste receptor and TRPM5, which is abundantly expressed in taste receptor cells involved in taste sensing. TAS2R38, which mediates taste responses of thioamides, including PTC and PROP, is the most extensively studied bitter receptor concerning both functional and epidemiological relationships [26].

In many diseases, the course of the disease can be completely different in patients with the same risk factors of the same age and same gender. In such cases, we encounter genetic differences. One of the genetic factors in diseases that develop in the upper respiratory tract is the bitter taste receptors. The ability to regulate congenital immunity, especially in the respiratory system, is increasingly dependent on bitter taste receptors, specifically TAS2R38 [28, 29]. When stimulated with known agonists of TAS2R38, such as PTC, low-level calcium responses occur in epithelial cells, which activate nitric oxide (NO) synthase and lead to strong intracellular NO production [30]. The effectiveness of this innate immune defense in the nasal and sinus mucosa differs due to the three most common polymorphisms in TAS2R38. Studies suggest that people affected by chronic rhinosinusitis are much less likely to have PAV/PAV homozygotes [31]. The expression of TAS2Rs in human airway smooth muscle (ASM) has recently been described. Stimulation with TAS2R agonists has been shown to cause relaxation of ASM. The dysfunction of ASM cells plays a crucial role in promoting the progression of diseases, such as asthma and COPD and contributing to the symptoms of these diseases [32].

In oncology, genetic factors come to the fore in following the course of the disease and the search for new treatments and new possibilities. Singh et al. examined the expression levels of TAS2Rs in high and low metastatic breast epithelial cells and non-cancerous cell lines. It is reported that the increase in expression levels may be functional because there is anincrease in intracellular calcium mobilization of bitter agonist kin after administration of dextromethorphan and phenylthiocarbamide. They found that the expression patterns of TAS2R 4 and TAS2R 14, in particular, were different in these cells, and there were decreased TAS2R4 levels and increased TAS2R14 levels in breast cancer clinical samples than non-cancerous controls. While activation of TAS2Rs with their relevant agonists causes physiological responses in metastatic breast cancer cells, it has been argued that this response is absent in non-

tumorigenic breast epithelial cells. The agonist activation of TAS2Rs induces anti-proliferative, pro-apoptotic, and anti-migration responses in highly metastatic breast cancer cells, and the signal network of the chemosensor TAS2R plays a role in inducing physiological responses in the metastatic breast cancer cell line [33].

In studies conducted in ovarian and prostate cancers, it has been reported that some TAS2R receptors are expressed in ovarian cancer and that the transcriptional regulation of these receptor genes differs in high-grade serous and low-grade serous ovarian cancer cell lines. It was found that the expression of TAS2R14 and TAS2R38 decreased in almost all ovarian cell lines, while TAS2R4 and TAS2R10 increased compared to control tissue samples. In prostate cancer cells, it was found that the expression of TAS2Rs, except TAS2R38, significantly reduced in PC3 cells [34].

The role of the TAS2R38 in pancreatic cancer has been studied in the literature. TAS2R38 has been reported to be expressed and localized in lipid droplets of tumor cells from pancreatic cancer patients and cell lines. Stimulation with N-acetyl-dodecanoyl homoserine and phenylthiourea leads to TAS2R38-mediated activation of key transcription factors. These results have shown the potential role of TAS2R38 in pancreatic cancer progression [35].

Yamaki et al. [36] conducted a genotyping study of TAS2R38 and TAS2R46 in hepato-pancreatic-biliary system cancers, with patients diagnosed with colorectal and gastric cancer. They reported that non-taster homozygotes (AVI/AVI) for TAS2R38 were more common in Japanese cancer patients, with cancer risk not associated with any TAS2R46 genotype. They reported that non-taster homozygotes (AVI/AVI) for TAS2R38 were more common in Japanese cancer patients, and cancer risk was not associated with any TAS2R46 genotype [36].

Some studies have hypothesized that individuals with the PAV/PAV diplotype may have a greater risk for cancer than the AVI/AVI group. However, some studies have also reported a trend towards an increased risk for colorectal cancer independent of dietary food intake in the AVI/AVI group and not in the PAV/PAV group. While the exact mechanism of this phenomenon has not yet been confirmed, it is attributed to the variable protein's less ability to neutralize and excrete potentially harmful chemicals from the gastrointestinal tract [37].

A49P, V262A, I296V and diplotypes were genotyped for determining the relationship between TAS2R38 polymorphism and gastric cancer and it was found that the AVI/AVI was not associated with consumption of food, alcohol or cigarettes, regardless of or dependent on gastric cancer phenotype, whereas the PAV/AVI diplotype significantly increased the risk of gastric cancer regardless of dietary intake. The TAS2R38 receptor encoded by the PAV/PAV variant is activated by bitter compounds containing only one thiourea moiety; the response to other bitter flavors is rather low. It has been reported that the TAS2R38 protein encoded by the AVI/AVI variant rarely responds to PTC and PROP, even to other bitter tastes as well as individuals with PAV/PAV. These data suggest that AVI carriers mediate a reaction to unknown bitter chemicals rather than impaired receptor activity. That is, both PAV/PAV and AVI/AVI can fully respond to each agonist and therefore have a greater ability to initiate protective mechanisms against potentially toxic chemicals in the gastrointestinal tract. However, the PAV/AVI heterozygous protein may be less active in detecting agonist molecules, resulting in longer exposure to carcinogenic chemicals. The findings suggest that TAS2R38 may be associated with stomach cancer risk in Koreans but that TAS2R38 diplotype does not affect dietary intake [38].

In the study involving laryngeal, hypopharyngeal, and pharyngeal tumor types, Tsutsumi et al. [39] examined the effects of chemotherapy and radiotherapy on the expression of the taste receptors in lingual mucosa samples. Although the bitter taste perception threshold remained unchanged, the lingual mRNA levels of TAS2R5 increased significantly after chemotherapy. In another study evaluating the differences in PTC response between the patient and healthy controls, genotyping has been performed for the TAS2R38 gene. It has been reported that there is no difference in genotype distribution and haplotype frequencies in healthy and patient groups; however, the frequency of subjects with the PAV/AVI diplotype in the patient cohort is lower than expected [40].

In this study, when evaluations were made in all of the included participants, similar to the studies conducted, the findings showed that 53.05% had PAV and 36.59% had AVI. While PAV was more common in the patient group, the frequency of AVI was similar in both groups. Although there was no significant difference between the groups due to the similarity in allele frequency and haplotype distribution in the groups, the frequency of heterozygous (PAV/AVI) individuals was lower in the patient group ($p<0.005$).

It has been determined that bitter taste receptors are in the mouth and in many tissues. Studies show that its stimuli and responses differ according to the tissue and cell it is located in. In particular, variations in TAS2R38 genes cause different responses even in diseases. Looking at the relationship between bitter taste and diseases, it is seen that different results are obtained due to reasons, such as geographical, population and race differences, whether nutrition is a risk for the disease. To our knowledge, these findings, which need to be confirmed in a larger population, are the first study for the role of TAS2R38 in laryngeal cancer. The data obtained through further studies, in which taste sensitivity test is added, can make a significant contribution to the literature.

ACKNOWLEDGEMENTS

This research project was partially supported Mersin University Scientific Research Projects Unit under grant number 2019-3-AP4-3809. (Not commercial)

Ethics approval. Ethical approval was obtained from the ethics committee of Mersin University (Decision No: 12/275, Date: 26.06.2019).

REFERENCES

[1] Meyerhof, W., Batram, C., Kuhn, C., Brockhoff, A., Chudoba, E., Bufe, B., Appendino, G., Behrens, M. (2010) The molecular receptive ranges of human TAS2R bitter taste receptors. Chem. Senses. 35(2), 157-170.

[2] Meyerhof, W. (2005) Elucidation of mammalian bitter taste. Rev. Physiol. Biochem. Pharmacol. 154, 37-72.

[3] Beckett, E. L., Martin, C., Yates, Z., Veysey, M., Duesing, K., Lucock, M. (2014) Bitter taste genetics–the relationship to tasting, liking, consumption and health. Food Funct. 5(12), 3040-3054.

[4] Feeney, E., O'Brien, S., Scannell, A., Markey, A., Gibney, E.R. (2011) Genetic variation in taste perception: does it have a role in healthy eating? Proc. Nutr. Soc. 70, 135–143.

[5] Lambert, J. D., VanDusen, S. R., Cockroft, J. E., Smith, E. C., Greenwood, D. C., Cade, J. E. (2019) Bitter taste sensitivity, food intake, and risk of malignant cancer in the UK Women's Cohort Study. Eur. J. Nutr. 58(5), 2111-2121.

[6] Drewnowski, A., Henderson, S.A., Shore, A.B. (1997) Taste responses to naringin, a flavonoid, and the acceptance of grapefruit juice are related to genetic sensitivity to 6-n-propylthiouracil. Am. J. Clin. Nutr. 66, 391–397.

[7] Lucchina, L.A., Curtis, V.O.F., Putnam, P., Drewnowski, A., Prutkin, J.M., Bartoshuk, L.M. (1998) Psychophysical measurement of 6-n-propylthiouracil (PROP) taste perception. Ann. NY. Acad. Sci. 855, 816–819.

[8] Chandrashekar, J., Mueller, K. L., Hoon, M. A., Adler, E., Feng, L., Guo, W., Ryba, N. J. (2000) T2Rs function as bitter taste receptors. Cell. 100(6), 703-711.

[9] Mueller, K. L., Hoon, M. A., Erlenbach, I., Chandrashekar, J., Zuker, C. S., Ryba, N. J. P. (2007) The receptors and coding logic for bitter taste. Nature. 434, 225-229.

[10] Kim, U., Wooding, S., Ricci, D., Jorde, L. B., Drayna, D. (2005) Worldwide haplotype diversity and coding sequence variation at human bitter taste receptor loci. Hum. Mutat. 26(3), 199-204.

[11] Bufe, B., Breslin, P. A., Kuhn, C., Reed, D. R., Tharp, C. D., Slack, J. P., Kim, U., Drayna, D., Meyerhof, W. (2005) The molecular basis of individual differences in phenylthiocarbamide and propylthiouracil bitterness perception. Curr. Biol. 15(4), 322-327.

[12] Kim, U., Jorgenson, E., Coon, H., Leppert, M., Risch, N., Drayna, D. (2003) Positional cloning of the human quantitative trait locus underlying taste sensitivity to phenylthiocarbamide. Science. 299, 1221-1225.

[13] Drewnowski, A., Rock, C.L. (1995) The influence of genetic taste markers on food acceptance. Am. J. Clin. Nutr. 62, 506–511.

[14] Kim, U.K., Drayna, D. (2005) Genetics of individual differences in bitter taste perception: lessons from the PTC gene. Clin. Genet. 67(4), 275-280.

[15] Jaggupilli, A., Singh, N., Upadhyaya, J., Sikarwar, A. S., Arakawa, M., Dakshinamurti, S., Chelikani, P. (2017) Analysis of the expression of human bitter taste receptors in extraoral tissues. Mol. Cell Biochem. 426(1-2), 137-147.

[16] Shaik, F. A., Singh, N., Arakawa, M., Duan, K., Bhullar, R. P., Chelikani, P. (2016) Bitter taste receptors: extraoral roles in pathophysiology. Int. J. Biochem. Cell Biol. 77, 197-204.

[17] Schembre, S. M., Cheng, I., Wilkens, L. R., Albright, C. L., Marchand, L. L. (2013) Variations in bitter-taste receptor genes, dietary intake, and colorectal adenoma risk. Nutr. Cancer. 65(7), 982-990.

[18] Dotson, C. D., Wallace, M. R., Bartoshuk, L. M., Logan, H. L. (2012) Variation in the gene TAS2R13 is associated with differences in alcohol consumption in patients with head and neck cancer. Chem. Senses. 37(8), 737-744.

[19] Mirza, N., Machtay, M., Devine, P. A., Troxel, A., Abboud, S. K., Doty, R. L. (2008) Gustatory impairment in patients undergoing head and neck irradiation. Laryngoscope. 118(1), 24-31.

[20] Halperin, E.C., Perez, C.A., Brady, L.W. (2008) Principles and practice of radiation oncology. 5th ed, 2008, 730.

[21] Rosenberg, S.A., Hellman, S., De Vita, V.T. (2001) Cancer: principles and practice of oncology. Lippincott Williams &Wilkins.

[22] Jemal, A., Bray, F., Center, M. M., Ferlay, J., Ward, E., Forman, D. (2011) Global cancer statistics. CA Cancer J. Clin. 61(2), 69-90.

[23] Wooding, S., Kim, U.K., Bamshad, M.J., Larsen, J., Jorde, L.B., Drayna, D. (2004) Natural selection and molecular evolution in PTC, a bitter-taste receptor gene. Am. J. Hum. Genet. 74(4), 637-646.

[24] Campbell, M.C., Ranciaro, A., Froment, A., Hirbo, J., Omar, S., Bodo, J.M., Nyambo,, T., Lema, G., Zinshteyn, D., Drayna, D., Breslin, P.A.S., Sarah A Tishkoff, S.A. (2012) Evolution of functionally diverse alleles associated with PTC bitter taste sensitivity in Africa. Mol. Biol. Evol. 29(4), 1141–1153.
[25] Smail, H.O. (2019) The roles of genes in the bitter taste. AIMS Genet. 6(4), 88-97.
[26] Jeruzal-Świątecka, J., Fendler, W., Pietruszewska, W. (2020) Clinical role of extraoral bitter taste receptors. Int. J. Mol. Sci. 21(14), 5156.
[27] El-Sohemy, A., Stewart, L., Khataan, L., Fontaine-Bisson, B., Kwong, P., Ozsungur, S., Cornelis, M. C. (2007) Nutrigenomics of taste–impact on food preferences and food production. Nutrigenomics-Opportunities in Asia. 60, 176-182.
[28] Carey, R.M., Lee, R.J., Cohen, N.A. (2016) Taste receptors in upper airway immunity. Adv. Otorhinolaryngol. 79, 91-102.
[29] Rowan, N. R., Soler, Z. M., Othieno, F., Storck, K. A., Smith, T. L., Schlosser, R. J. (2018) Impact of bitter taste receptor phenotype upon clinical presentation in chronic rhinosinusitis. Int. Forum Allergy Rhinol. 8(9), 1013-1020.
[30] Carey, R. M., Workman, A. D., Yan, C. H., Chen, B., Adappa, N. D., Palmer, J. N., Kennedy, D.W., Lee, R.J., Cohen, N. A. (2017) Sinonasal T2R-mediated nitric oxide production in response to Bacillus cereus. Am. J. Rhinol. Allergy. 31(4), 211-215.
[31] Lee, R.J., Cohen, N.A. (2015) Role of the bitter taste receptor T2R38 in upper respiratory infection and chronic rhinosinusitis. Curr. Opin. Allergy Clin. Immunol. 15(1), 14-20.
[32] Deshpande, D. A., Wang, W. C., McIlmoyle, E. L., Robinett, K. S., Schillinger, R. M., An, S. S., Sham, J.S.K., Liggett, S. B. (2010) Bitter taste receptors on airway smooth muscle bronchodilate by localized calcium signaling and reverse obstruction. Nat. Med. 16(11), 1299-1304.
[33] Singh, N., Shaik, F. A., Myal, Y., Chelikani, P. (2020) Chemosensory bitter taste receptors T2R4 and T2R14 activation attenuates proliferation and migration of breast cancer cells. Mol. Cell Biochem. 465(1), 199-214.
[34] Martin, L. T., Nachtigal, M. W., Selman, T., Nguyen, E., Salsman, J., Dellaire, G., Dupré, D. J. (2019) Bitter taste receptors are expressed in human epithelial ovarian and prostate cancers cells and noscapine stimulation impacts cell survival. Mol. Cell Biochem. 454(1), 203-214.
[35] Gaida, M. M., Mayer, C., Dapunt, U., Stegmaier, S., Schirmacher, P., Wabnitz, G. H., Hänsch, G. M. (2016) Expression of the bitter receptor T2R38 in pancreatic cancer: localization in lipid droplets and activation by a bacteria-derived quorum-sensing molecule. Oncotarget. 7(11), 12623-12632.
[36] Yamaki, M., Saito, H., Isono, K., Goto, T., Shirakawa, H., Shoji, N., Satoh-Kuriwada, S., Sasano, T., Okada, R., Kudoh, K., Fuyuhiko, Motoi F., Unno, M., Komai, M. (2017) Genotyping analysis of bitter-taste receptor genes TAS2R38 and TAS2R46 in Japanese patients with gastrointestinal cancers. J. Nutr. Sci. Vitaminol. (Tokyo). 63(2), 148-154.
[37] Schembre, S.M., Cheng, I., Wilkens, L.R., Albright, C.L., Le Marchand, L. (2013) Variations in bitter-taste receptor genes, dietary intake, and colorectal adenoma risk. Nutr. Cancer. 65, 982–990.
[38] Choi, J. H., Lee, J., Choi, I. J., Kim, Y. W., Ryu, K. W., Kim, J. (2016) Genetic variation in the TAS2R38 bitter taste receptor and gastric cancer risk in Koreans. Scientific Reports. 6(1), 1-8.
[39] Tsutsumi, R., Goda, M., Fujimoto, C., Kanno, K., Nobe, M., Kitamura, Y., Abe, K., Kawai, M., Matsumoto, H., Sakai, T., Takeda, N. (2016) Effects of chemotherapy on gene expression of lingual taste receptors in patients with head and neck cancer. Laryngoscope. 126 (3), E103-E109.
[40] Melis, M., Grzeschuchna, L., Sollai, G., Hummel, T., & Tomassini Barbarossa, I. (2019) Taste disorders are partly genetically determined: role of the TAS2R38 gene, a pilot study. Laryngoscope. 129(9), E307-E312.

Received: **01.11.2021**
Accepted: **05.12.2022**

CORRESPONDING AUTHOR

Senay Balci
Department of Medical Biochemistry,
Mersin University Faculty of Medicine,
Mersin – Turkey

e-mail: sbfidanci@hotmail.com

© by PSP Volume 31– No. 05/2022 pages 4807-4815 Fresenius Environmental Bulletin

STABILITY ANALYSIS OF SURROUNDING ROCK IN THE OPERATION PROCESS OF GOB-SIDE ENTRY RETAINING IN MAIN ROADWAY UNDER COAL MINING ENVIRONMENT

Qi Wang[1,*], Dongxu Guo[2]

[1]College of Mining, Liaoning Technical University, Fuxin, 123000, China
[2]College of Materials Science and Engineering, Liaoning Technical University, Fuxin, 123000, China

ABSTRACT

The deformation and collapse of the roadway in the coal mining process affect the normal underground mining of coal, threaten the lives of underground workers, and damage the underground operating environment. Related research failed to carry out critical analysis and exploration on the stability laws and mechanisms of underground main lanes. Based on this, by considering the creep characteristics of the soft coal seam, the force status of the surrounding rock of the main roadway in the Cartesian coordinate system is analyzed. At the same time, the influence of creep on the stability of the surrounding rock of the main roadway is compared and researched, and the influence of the direction and stress characteristics of the main roadway on the deformation of the main roadway is explored. The research has found that neglecting the creep of the surrounding rock of the muddy soft coal seam will significantly underestimate the deformation of the surrounding rock of the main roadway. When considering the creep characteristics of the surrounding rock, the deformation of the roadway is 1.29 times that when the creep characteristics are neglected. In addition, research also found that the stability of the surrounding rock will be significantly worsened when the direction of the main roadway gradually changes from north- south to east-west. When the direction of the roadway is east-west, the longitudinal space of the roadway is compressed by more than 41.33%. Finally, the research believes that the greater the difference between the in-situ stress components, the greater the possibility of instability of the surrounding rock of the roadway. When the minimum horizontal principal stress changes from 5.00MPa to 3.45MPa, the maximum deformation of the roadway will increase from 1.37m to 1.74m.

KEYWORDS:
Soft coal seam mining, main roadway, gob-side entry retaining, surrounding rock deformation, simulation analysis

INTRODUCTION

Although the global greenhouse effect and climate change are becoming more and more serious, and initiatives such as carbon reduction have been put on the agenda of countries around the world, fossil fuels are still the most stable and cheapest energy sources at present and in the near future [1]. According to data from the U.S. Energy Information Administration (EIA), the energy provided by fossil fuels currently accounted for more than 80% of all energy consumption [2-4]. Even by 2050, this proportion will still be as high as 66% [5]. Moreover, as the most easily exploited, processed and utilized energy source among fossil fuels, coal resources occupies a pivotal position. The reason for choosing coal as an important energy source under the premise of ignoring its environmental impact is mainly its stable energy output and controllability of utilization (compared to nuclear energy) [6]. At present, the share of coal in the domestic energy market once exceeded 70%, and this proportion will not change much in the future [7]. However, during the development of coal, safety accidents such as the deformation of the surrounding rock of the roadway often occur, which poses a threat to the safety of underground workers and the stable operation of equipment [8]. For this reason, carrying out research on the stress and deformation of roadways can not only improve the production efficiency of coal mines, but also avoid unnecessary loss of life and property.

The technology of gob-side entry retaining is a new type of coal-pillar-free mining technology commonly used in coal mines. It is gradually replacing the traditional coal-pillar roadway mining and is favored by coal mining enterprises [9]. There is no coal pillar support in the operation area during the use of the technology of gob-side entry retaining and the working face is directly used as the roadway wall to support the roof and floor and the overlying layer. Soft coal seams are medium-quality coal seams with extremely soft texture and extremely low strength, which are extremely common in the Lianghuai mining area in our country. Soft coal seams are usually shallow in the longitudinal direction, and they are

weakly compacted by gravity. Very slight engineering disturbances may cause their stability to be severely damaged [10]. At the same time, soft coal seams are usually very high in mud content and have outstanding water-absorbing swelling characteristics. They are prone to collapse and deformation under the action and influence of stress concentration around the roadway [11]. In addition, the creep characteristics of muddy soft coal seams are usually very significant. Under the action of extremely strong stress concentration, they may protrude and stick together (ie creep). This will seal the workers and equipment inside the roadway on the working surface, and cause extremely strong damage to workers and coal mining equipment. In addition, the main roadway carries the functions of the export of the finished coal and the ventilation input. The main roadway being sealed due to creep deformation will directly cause the gas content in the underground working environment exceed the standard [12-13]. For this reason, carrying out theoretical and experimental analysis related to the stability of the surrounding rock of the soft coal seam main roadway has strong engineering significance, and can provide theoretical support for avoiding and weakening the occurrence of malignant production accidents due to the sudden deformation of the roadway wall.

At present, domestic and foreign experts and scholars have conducted extensive research on the force and deformation (ie stability) of coal seam roadways, and have made certain academic progress. Chin et al. [14] used the ABAQUS platform to analyze the impact of coal compaction during coal mining on the subsequent development of the coal seam by using the finite element method. This method can be used to quantitatively evaluate the economic benefits and safety risks brought by coal compaction deformation to guide safe production in coal mines. Hall et al. [15] carried out a series of experimental researches related to coal seam deformation caused by rock compressibility in the process of soft coal mining, and found that coal seam deformation would cause a series of geological disasters and harm the underground coal mining environment. The top-cutting and pressure relief operation can effectively alleviate this safety accident caused by the deformation of the surrounding rock. Morita et al. [16] analyzed the characteristics and laws of deformation and permeability changes of soft coal seams under the temperature range of 70° F~280° F and different loading paths through experiments, and analyzed the evolution characteristics of rock characteristics during coal seam deformation. The research can provide engineering guidance for the design of support operations to prevent roadway deformation. Silva et al. [17] used the 3D finite element model to analyze the bolt support damage caused by the deformation of the soft coal seams in the coal mining process through the ABAQUS platform. The field application shows that the bolt support scheme designed based on this research can guarantee a longer bolt life. Although all the mentioned researches are helpful to understand the roadway deformation and failure mechanism in the process of soft coal seam mining, the current research still has the problems and deficiencies: (1) There are very few relevant researches considering the impact of creep on surrounding rock and roadway deformation, which affects the accuracy of the analysis results. (2) There is a lack of analysis and research on the stress and deformation of surrounding rock in the mining process of muddy soft coal seams under complex stress conditions.

Based on this, taking the roadway wall of the main roadway in the muddy loose soft coal seams as the research object, and considering the creep characteristics of the soft coal seams, the stress status of the surrounding rock of the main roadway in the Cartesian coordinate system is analyzed. At the same time, the influence of creep on the stability of the surrounding rock of the main roadway is comparatively researched, and the influence of factors such as the direction and stress status of the main roadway on the deformation of the main roadway is explored. It is hoped that through research, a feasible engineering plan can be put forward to avoid the collapse and deformation of the transportation lane in the process of soft coal seams mining.

MATERIALS AND METHODS

The numerical analysis process of the stress and deformation of the surrounding rock of the muddy soft coal seam main roadway involves two physical fields: the deformation field (also called the stress field) and the seepage field. Among them, the deformation field equations mainly include the stress analysis equations, creep equations and constitutive equations of the surrounding rock of the roadway, while the seepage field only involves the single-phase seepage of pore water. At the same time, in order to carry out relevant numerical simulations, the assumptions are made: (1) The seepage flow of water in the coal seam satisfies Darcy's law. (2) The deformation of the soft coal seam conforms to the theory of small solid deformation, that is, it is believed that the external force and load on the object do not change with its deformation. (3) Assume that the top section of the main roadway is regularly round.

Mechanics analysis of surrounding rock of main roadway. During the development of muddy soft coal seam, the deformation of the surrounding rock of the roadway must first be analyzed for the stress distribution state around the roadway. Figure 1 shows the schematic diagram of the distribution of the micro-element stress state of the surrounding rock of the main roadway. Based on the basic principles of static analysis, the micro-element whose

width and thickness of the surrounding rock of soft coal seam roadway are both *dr* is used for mechanical analysis. The stress spatial distribution of the micro-element of the roadway surrounding rock in polar coordinates [18] is shown in Equation (1).

In the formula, σ_r, σ_θ, $\tau_{r\theta}$ are the radial stress, circumferential stress and tangential stress of the micro-element, respectively, MPa. λ is the ratio of horizontal stress to vertical stress, dimensionless. R is the radius of the roadway, m. r is the distance from the center of the roadway to the surrounding rock micro-element, m. θ is the circumferential angle in the polar coordinate system, °.

The stress-strain relationship of the surrounding rock of the roadway in the soft coal seam mining process follows the Moore-Coulomb criterion [19], and the Mohr-Coulomb criterion can be expressed as:

$$\tau = C + \sigma_n \tan\varphi \tag{2}$$

In the formula, C is the cohesive force, MPa. φ is the internal friction angle, °. σ_n and τ_n are the normal stress and shear stress, respectively, MPa.

When the stress of any micro-element of the surrounding rock exceeds the strength of the soft coal seam, the surrounding rock of the soft coal seam roadway will be damaged and deformed in varying degrees, triggering coal mining safety accidents and affecting the normal development and safe construction of subsequent coal mining operations.

In addition, the statics equation of the rock skeleton in the deformation field is [20]:

$$\begin{cases} \dfrac{\partial\sigma_x}{\partial x}+\dfrac{\partial\tau_{xy}}{\partial y}+\dfrac{\partial\tau_{xz}}{\partial z}+f_x=0 \\ \dfrac{\partial\sigma_y}{\partial y}+\dfrac{\partial\tau_{xy}}{\partial x}+\dfrac{\partial\tau_{yz}}{\partial z}+f_y=0 \\ \dfrac{\partial\sigma_z}{\partial z}+\dfrac{\partial\tau_{xz}}{\partial x}+\dfrac{\partial\tau_{xz}}{\partial y}+f_z=0 \end{cases} \tag{3}$$

In the formula, σ is normal stress, MPa. τ is shear stress, MPa. f is fluid force, MPa. subscripts x, y, and z represent three directions respectively.

The fluid-solid coupling modeling and analysis of the stability of the surrounding rock of the main roadway strictly follows the effective stress principle [21], which can be expressed as:

$$\sigma_{ij} = \sigma_{ije} - \alpha P\delta_{ij} \tag{4}$$

In the formula, σ_{ije} is the effective stress tensor, MPa. P is the pore pressure, MPa. α is the Biot coefficient.

As mentioned earlier, the creep characteristics of muddy soft coal seams are extremely strong, and it is particularly necessary to consider its creep characteristics. Therefore, creep and slow and time-varying deformation are important characteristics of soft coal seams. The creep characteristic equation of mussy soft coal seam can be calculated by the Formula (5):

$$\varepsilon_{ij} = \frac{1}{2}\left(u_{i,j} + u_{j,i}\right) \tag{5}$$

The constitutive equation of muddy soft coal seam. Due to the extremely strong plasticity of soft coal seams, the conventional Mohr-Coulomb criterion and other constitutive relationship models cannot truly describe its mechanics and deformation behavior. The constitutive equation is a formula used to reflect the relationship between stress and strain, and its accuracy directly relates to the safety of soft coal seams mining. For this reason, the exploration of mechanical experiments related to soft coal seams is of great significance for the true description and analysis of its deformation. Taking into account the non-reusable characteristics of rock samples in the process of mechanical experiments, four rock samples were sampled from the soft coal seams in the Lianghuai mining area. The characteristics of the four rock samples are shown in Table 1. This part uses the three-axis mechanical characteristic experimental instrument shown in Figure 2 to carry out the relevant mechanical analysis.

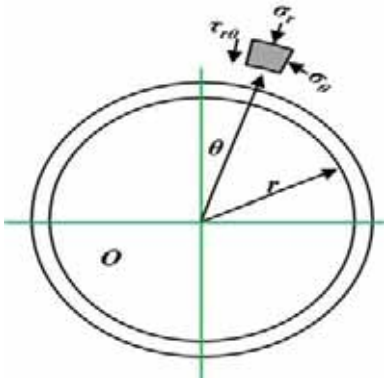

FIGURE1
The static mechanics model of the micro-element of the surrounding rock of the soft coal seam main roadway.

$$\begin{cases} \sigma_r = \dfrac{\gamma H}{2}\left[(1+\gamma)\left(1-\dfrac{R^2}{r^2}\right)+(1-\lambda)\left(1-\dfrac{4R^2}{r^2}+\dfrac{3R^4}{r^4}\right)\cos 2\theta\right] \\ \sigma_\theta = \dfrac{\gamma H}{2}\left[(1+\gamma)\left(1+\dfrac{R^2}{r^2}\right)-(1-\lambda)\left(1+\dfrac{3R^4}{r^4}\right)\cos 2\theta\right] \\ \tau_{r\theta} = -\dfrac{\gamma H}{2}(1-\lambda)\left(1+\dfrac{2R^2}{r^2}+\dfrac{3R^4}{r^4}\right)\sin 2\theta \end{cases} \tag{1}$$

TABLE 1
Characteristic parameters of soft coal seam samples

Number	Porosity /%	Permeability /mD	Length /mm	Diameter /mm	Strength /MPa	Elastic Modulus /GPa
1	10.25	1.25	50.43	24.34	540	1.21
2	10.34	1.54	51.27	25.61	567	1.34
3	11.21	1.10	48.65	27.64	584	1.26
4	9.84	1.23	49.43	25.13	532	1.57

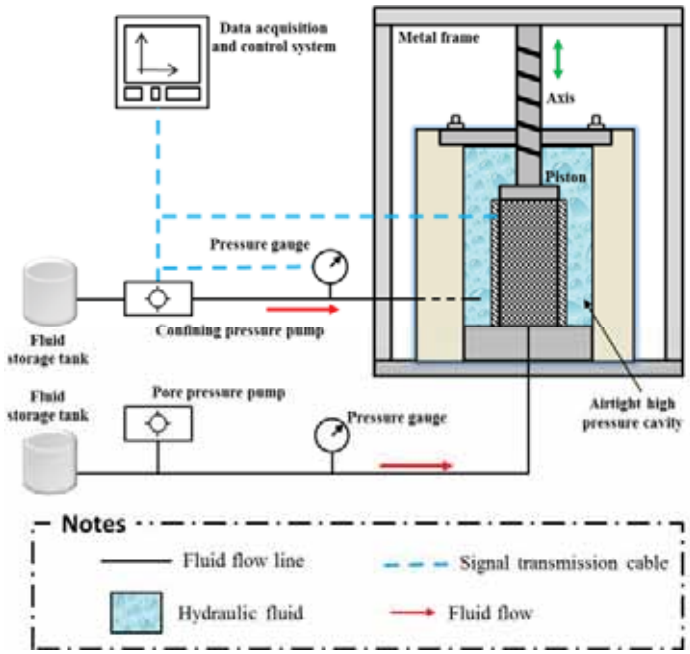

FIGURE 2
Servo three-axis mechanical characteristic experiment instrument.

As shown in Figure 2, the three-axis mechanical characteristic experiment instrument was mainly composed of three parts: axial pressure loading system, confining pressure loading system, and control and data collection system. The main function of the axial pressure loading system was the axial pressure loading of the coal sample. The axial pressure loading was mainly realized by the axial piston, and the axial pressure loading limit of the experimental instrument can reach 150KN (ie 400MPa). In addition, the confining pressure loading system was controlled by two servo pumps, and the confining pressure loading limit was 50MPa. During the experiment, the stress measurement was realized by the stress sensor, and the measurement accuracy of the stress sensor was 0.50N. In addition, the deformation of the rock sample during the experiment was measured by two sets of strain gauges attached symmetrically on the cross section, and the measurement accuracy of the strain gauges was 0.02mm. After analysis, the measurement accuracy and measurement limit of the experimental equipment met the requirements of this experiment. At the same time, the servo three-axis mechanics experimental instrument shown in Figure 2 can also research the influence of the stress sensitivity of coal on its physical parameters.

Through porosity and permeability testing experiments, it was found that most of the soft coal seams rock samples are muddy rocks with high porosity and low permeability, which average porosity and average permeability were 10.41% and 1.28mD, respectively. Although such a rock layer is beneficial to prevent water inrush accidents during coal mining, it is very unfavorable to the efficient development of resources such as coalbed methane. At the same time, the experimental results of the triaxial mechanical properties of the four soft coal seams showed that the strength of the soft coal seams is low, and the average compressive strength and average elastic modulus were only 555.75MPa and 1.345GPa, respectively. In this case, a constitutive relationship equation for soft coal seams is constructed based on the experimental data of mechanical properties:

$$\nu_i = -0.188\sigma_a - 0.00781 \times \log(\sigma_{max}) + 0.2804 \quad (6)$$

In the formula, ν_i is the linear Poisson's ratio, and σ_a and σ_{max} were the average effective stress and the maximum effective stress, respectively.

Percolation equation. The soft coal rock contains water and a small amount of methane (gas), and the filling of the two pore fluids can also share the

framework stress [22]. For this reason, the seepage equation of pore water and gas can be expressed as:

$$\begin{cases} \varphi S_g v_{rg} = -\dfrac{K_{rg}}{\mu_g}[K]\left(\nabla P_g + \rho_g g\right) \\ \varphi S_w v_{rw} = -\dfrac{K_{rw}}{\mu_w}[K]\left(\nabla P_w + \rho_w g\right) \end{cases} \quad (7)$$

In the formula, φ is porosity, S is saturation, V is seepage velocity, K is permeability, μ is fluid viscosity, P is partial pressure, ρ is fluid density, and g is gravity acceleration. The subscripts g and w are methane gas and water, respectively.

RESULTS AND DISCUSSION

Model discretization and solution. Numerical simulation of the stability of surrounding rock during coal mining requires the discrete time and space of the mathematical model. Among them, the continuity equation of the skeleton is obtained based on the static equilibrium equation, so the continuity equation of the skeleton has only a discrete equation in space and no discrete form in time [23]. Its discrete form can be written as: (Eq 8)

$$\iiint_V \{\varepsilon^*\}^T \{\sigma\}^T dV = \iiint_V \{u^*\}^T \{F\} dV + \iint_\Gamma \{u^*\}^T \{T\} dS \quad (8)$$

In the formula, $\{\varepsilon^*\}$ is the virtual strain, $\{\sigma\}$ is the total stress of the micro-element, $\{F\}$ is the force and external load of the micro-element, $\{T\}$ is the surface force of the micro-element, $\{u^*\}$ is the virtual displacement.

In addition, based on the Galerkin finite element method [24], the discrete weak integral form in space represented by the methane phase can be expressed as:

$$\sum_i [Q]^e \{P_g\}^e = \sum_i \{f\}^e \quad (9)$$

Similarly, based on the Galerkin finite element method, the discrete form of the methane phase in the time domain is written as:

$$[Q]_{n+1}^j \{P_g\}_{n+1}^{j+1} = \{f\}_{n+1}^j \quad (10)$$

The continuity equation of the water phase has a similar form in the discrete form in time and space.

The influence of creep on the stability of surrounding rock. In order to analyze the stability of the surrounding rock of the soft coal seams main roadway during coal mining, a numerical simulation physical model as shown in Figure 3 is constructed.

As shown in Figure 3, the model is a 2D square section with a side length of 10m, and the main roadway is located in the middle of the model. In addition, the height of the rectangle at the bottom of the roadway is 2.5m, and the radius of the top semicircle is 2.0m. In order to improve the accuracy of the simulation, the surrounding rock surrounding the roadway was meshed during the grid division, and finally 64,000 CPE4P-type grid cells were obtained. The CPE4P-type grid unit can simultaneously simulate the deformation field and seepage field in the coal mining process. In addition, during the simulation process, the edge of the roadway and the outer boundary of the model should be restrained at the same time during the Geostatic stress balance analysis step, and the overburden pressure should be applied at the upper boundary. In the second analysis step, the normal constraint on the edge of the roadway needs to be lifted.

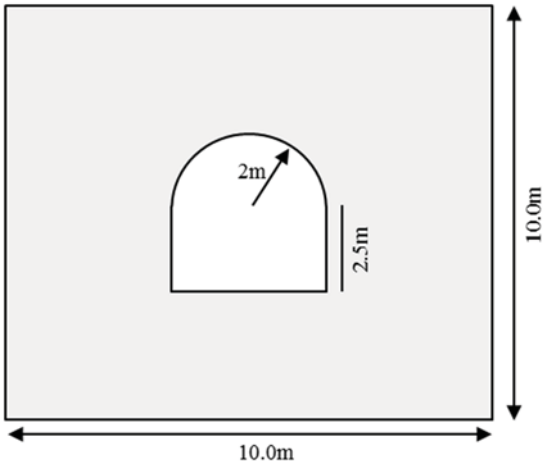

FIGURE 3
Physical model of surrounding rock stability analysis during coal mining operation of gob-side entry retaining of main roadway.

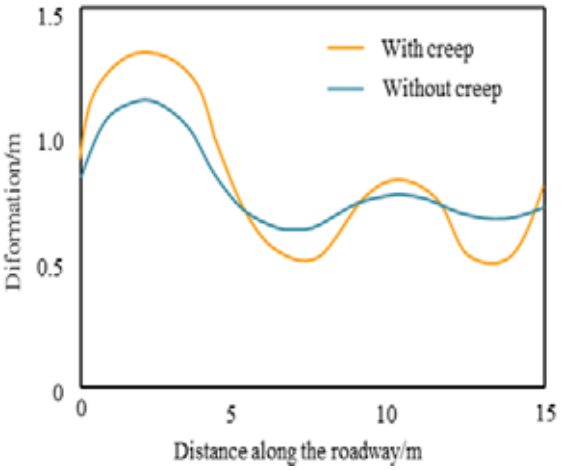

FIGURE 4
Distribution of deformation status of surrounding rock with and without considering the creep of surrounding rock.

Using the numerical simulation physical model shown in Figure 3, the influence of creep on the deformation and stability of the surrounding rock of the roadway was analyzed. Figure 4 shows the deformation distribution curve of the surrounding rock along the edge of the roadway. From Figure 4, we can find that regardless of whether the creep of soft coal seams is considered, the maximum displacement of the roadway appears at the top of the roadway. In addition, the horizontal deformation is smaller than the vertical deformation measured in the lower rectangular roadway. In addition, from Figure 4 we can also find that when the creep characteristics of soft coal seams are ignored, the deformation of surrounding rocks will be significantly underestimated. When ignoring the creep characteristics of the soft coal seam, the maximum deformation of the roadway is 1.07m, while when considering the creep characteristics of the soft coal seams, the maximum deformation is 1.38m, which is 1.29 times the former. This shows that when we take the creep characteristics of soft coal into account, we can more accurately simulate the real deformation of the main roadway during coal mining. This is mainly because the rock that does not consider the creep characteristics can accumulate the excess energy generated by the deformation, and considering the creep can release the energy released by the deformation more completely [25]. But what may happen is that the rock that does not consider creep may appear instantaneous failure due to excessive accumulation of energy, while the deformation of the rock that considers the creep characteristics is gradual.

The influence of the direction of the main roadway on the deformation of the roadway. From Equation (1), it can be seen that the stress distribution of surrounding rock will affect the stability of surrounding rock, while the stress distribution of surrounding rock is greatly affected by the direction of the roadway. According to geological convention, the azimuth angle of the north-south roadway is 0°, and the azimuth angle of the east-west roadway is 90°. For this reason, the situation of roadway deformation under different roadway direction conditions is analyzed, and the results are shown in Figure 5. We can find that as the direction of the roadway gradually changes from north-south to east-west, the deformation of the main roadway in the soft coal seams is increasing. When the direction of the main roadway is north-south, the maximum deformation of the roadway is 1.37 m. However, as the azimuth angle of the roadway increases, when the azimuth angle of the roadway is 30° and 60°, the maximum deformation of the roadway increases to 1.45 m and 1.59 m, respectively. As the azimuth angle of the roadway continues to increase, when the direction of the roadway is completely changed to east-west, the maximum deformation of the roadway quickly becomes 1.86 m. At this time, the space in the direction of the roadway height has been compressed by 41.33%.

From Figure 5b, we can understand the mechanism of the roadway deformation gradually changing with the direction of the roadway. It can be found from Figure 5b that as the azimuth angle of the roadway continues to increase, the stress on the surrounding rock of the roadway will gradually decrease. As the azimuth angle of the roadway gradually increased from 0° to 90°, the stress on the surrounding rock of the roadway gradually decreased from 5.08 MPa to 1.72 MPa. With the azimuth angle of the roadway gradually increases, although the stress concentration effect in the surrounding rock will gradually increase, the load that the surrounding rock can withstand is gradually reduced, which leads to the gradual increase in deformation [26]. Therefore, in order to ensure the stability of the roadway in the soft coal seams mining process, it is recommended to arrange the roadway as far as possible in the north-south direction while ensuring the convenience of other constructions.

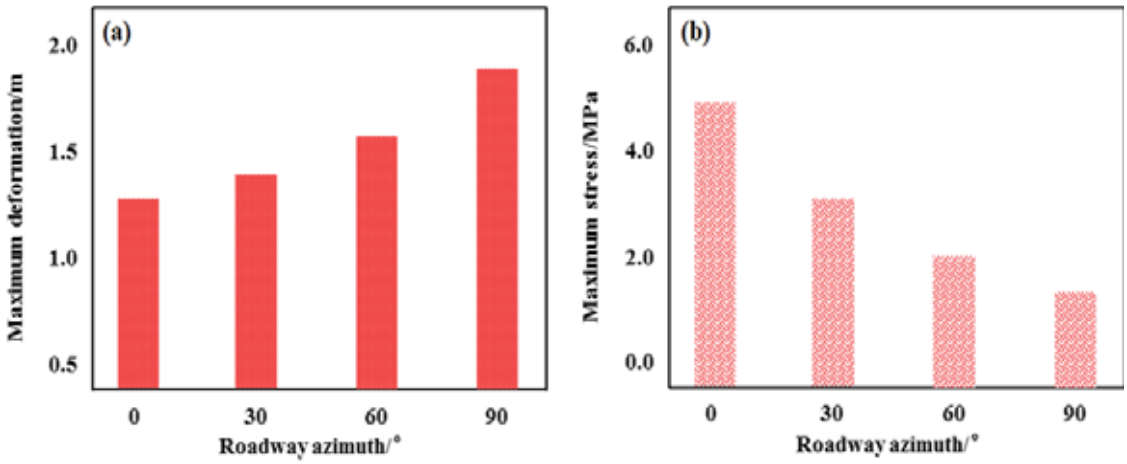

FIGURE 5

Roadway deformation and stress conditions under different roadway direction conditions.

Notes: (a) Maximum deformation, (b) Maximum stress.

TABLE 2
Research status and research results

γ	Maximum horizontal principal stress/MPa	Minimum horizontal principal stress/MPa	Maximum deformation/m	Plastic strain
1.00	5.00	5.00	1.37	0.034
1.15	5.00	4.35	1.44	0.067
1.30	5.00	3.85	1.57	0.109
1.45	5.00	3.45	1.74	0.177

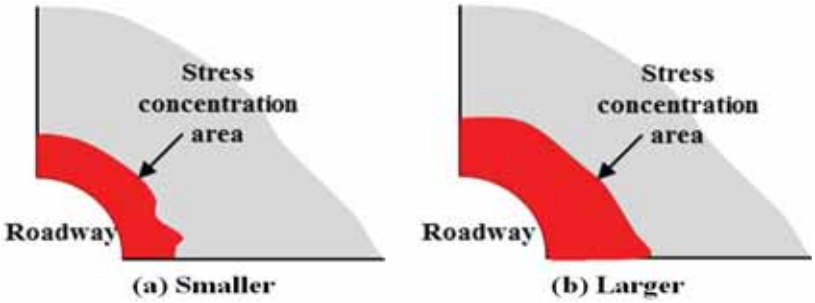

FIGURE 6
The distribution of stress concentration areas around the roadway under different in-situ stress distribution conditions.

The influence of in-situ stress distribution of surrounding rock on roadway deformation. Surrounding rock stress will also affect the deformation and stress of the roadway. For this reason, the deformation of the roadway under different in-situ stress conditions is researched, as shown in Figure 6. It should be noted that, for the convenience of research, the ratio of the maximum horizontal principal stress to the minimum horizontal principal stress is defined as the stress difference coefficient γ. From its definition, it can be found that as the stress difference coefficient increases, the difference between the maximum and minimum horizontal principal stresses will gradually become stronger. In this paper, the stress coefficient γ is changed by fixing the maximum horizontal principal stress (5.00MPa) and changing the minimum horizontal principal stress. Table 2 shows the research status of this part.

It can be found from Table 2 that as the difference between the in-situ stress components increases, the stability of the roadway will gradually become worse, the amount of deformation will gradually increase, and the plastic strain will gradually become stronger. When the stress difference coefficient is 1.00, the maximum and minimum horizontal principal stresses are both 5.00 MPa, and the maximum deformation and maximum plastic strain of the roadway are 1.37 m and 0.034, respectively. However, as the difference between the in-situ stress components increases, the stability of the roadway will become worse significantly. When the stress difference coefficient γ becomes 1.45, the minimum horizontal principal stress has become 3.45 MPa. At this time, the maximum deformation and the maximum plastic strain of the roadway increase to 1.74 m and 0.177, respectively [4, 27]. The influence of the in-situ stress difference on the deformation and stability of the roadway can be shown in Figure 6. We can find that the influence of the difference in in-situ stress on the stability of the transportation roadway is mainly due to the different stress concentration areas around the roadway under different in-situ stress distribution conditions [28]. When γ is small, the stress concentration area around the roadway is smaller, and the surrounding rock deformation and yield are weaker. On the contrary, when γ is large, the stress concentration area around the roadway is larger and the degree is more serious, and the surrounding rock deformation and yield are also extremely significant.

Therefore, based on the results of the research, it is found that in order to ensure the stability of the main roadway during the mining process of the muddy soft coal seams, the preliminary in-situ stress exploration should be done. In this case, according to the stress conditions of different blocks, corresponding engineering measures can be designed to reduce the influence of excessive in-situ stress differences on the stability of the roadway.

CONCLUSIONS

Soft coal seams are usually soft in texture. And roadway collapse accident is extremely prone, causing damage to the underground working environment and casualties. In order to avoid similar accidents, this paper analyzes the influence of the creep of soft coal seams on the stability of the surrounding rock of the main roadway through numerical simulation, and discusses the law and mechanism of the influence of the difference in the direction of the main roadway and the in-situ stress on the deformation of the surrounding rock. The main conclusions reached are:

(1) The creep of soft coal seams will aggravate the deformation and destruction of the roadway. Ignoring its creep characteristics in the process of mechanical analysis can easily underestimate the instability and stability of the roadway surrounding rock during coal mining. When ignoring the creep characteristics of the soft coal seams, the maximum deformation of the roadway is 1.07m, and when considering the creep characteristics of the soft coal seams, the maximum deformation is 1.38 m, which is 1.29 times the former.

(2) In the process of the direction of the main roadway is gradually changing from north-south to east-west, the stability of the surrounding rock will be significantly worsened, and the amount of deformation will be significantly increased. When the direction of the main roadway is north-south, the maximum deformation of the roadway is 1.37m. However, when the direction of the roadway is completely changed to east-west, the maximum deformation of the roadway quickly becomes 1.86m, and the longitudinal space of the roadway is compressed by more than 41.33%.

(3) The difference in in-situ stress will affect the stability of surrounding rock during coal mining by affecting the stress concentration around the roadway. Moreover, the greater the difference in in-situ stress, the greater the possibility of instability and collapse of the surrounding rock of the roadway. When the maximum horizontal principal stress and the minimum horizontal principal stress are both 5.00 MPa, the maximum deformation and maximum plastic strain of the roadway are 1.37 m and 0.034, respectively. However, when the minimum horizontal principal stress has become 3.45 MPa, the maximum deformation and maximum plastic strain of the roadway increase to 1.74 m and 0.177, respectively.

ACKNOWLEDGEMENTS

This study was supported by the Grant No.51874158 received from the National Natural Science Foundation of China and Liaoning Provincial Key R&D Guidance Plan (No.2019JH8/10100050) and Liaoning Education Fund No. LJ2019FL003.

REFERENCES

[1] Zhao, J., Zhou, L., Ma, J., Li, Y. (2016) Numerical simulation study of fracturing wells for shale gas with gas–water two-phase flow system under desorption and diffusion conditions. Journal of Natural Gas Geoscience. 1(3), 251-256.

[2] Jin, L. (2017) Experimental and numerical modeling of fluid injection into unconsolidated formations. Georgia: Georgia Institute of Technology. 32-35.

[3] Yan, M., Deng, J., Yu, B., Li, M., Zhang, B., Xiao, Q., Tian, D. (2020) Comparative study on sanding characteristics between weakly consolidated sandstones and unconsolidated sandstones. Journal of Natural Gas Science and Engineering. 76, 1-12.

[4] He, M., Chen, S., Guo, Z. (2017) Control of surrounding rock structure for gob-side entry retaining by cutting roof to release pressure and its engineering application. Journal of China University of Mining Technology. 46(5), 959-969.

[5] St-Pierre, L., Hassani, F., Radziszewski, P., Ouellet, J. (2009) Development of a dynamic model for a cone bolt. International Journal of Rock Mechanics and Mining Sciences. 46(1), 107-114.

[6] Bazrafshan, E., Mostafapoor, F. (2011) Survey of medical waste characterization and management in Iran: a case study of Sistan and Baluchestan Province. Waste Management & Research. 29(4), 442-450.

[7] Lee, B., Moure-Ersaso, R. (2004) Alternatives for treatment and disposal cost reduction of regulated medical wastes. Waste Management. 24(2), 143-151.

[8] Chen, X., Li, L., Guo, Z., Chang, T. (2019) Evolution characteristics of spontaneous combustion in three zones of the goaf when using the cutting roof and release pressure technique. Energy Science & Engineering. 7(3), 710-720.

[9] Wang, H., Guan, Z., Shi, Y., Chen, W., Liu, Y., Zhang, B., Liang, D., Wang, X. (2018) Modeling and analyzing the motion state of bottom hole assembly in highly deviated wells. Journal of Petroleum Science and Engineering, 170, 763-771.

[10] Stan, M., Avram, L. (2015) Experimental study on the model of the correlation between the movement of the drilling string with big diameter of drill and effects on the oil rigs. Journal of Petroleum Exploration and Production Technology. 5, 295-303.

[11] Chin, L., Thomas, L. (1999) Fully Coupled Analysis of Improved Oil Recovery by Reservoir Compaction. In: Proceedings of SPE Annual Technical Conference and Exhibition, 3-6 October, Houston, Texas. 101-108.

[12] Hall, H. (1953) Compressibility of Reservoir Rocks. Journal of Petroleum Technology. 5(1), 17-19.

[13] Sugiharti, L. (2014) A Regional Income Convergence Process in East Java (Indonesia): Do Spatial Dependence and Spatial Regimes Matter?". The Journal of Economic Literature. 76(17), 97-107.

[14] Hossain, M., Santhanam, A., Nik, N., Omar, A. (2011) Clinical solid waste management practices and its impact on human health and environment: A review. Waste Management. 31(4), 754-766.

[15] Wen, H., Yu, Z., Fan, S., Zhai, X., Liu, W. (2017) Prediction of spontaneous combustion potential of coal in the gob area using CO extreme concentration: A case study. Combust. Sci. Technol. 189, 1713-1727.
[16] Morita, N., Gray, K., Sroujl, F. and Jogi, P. (1992) Rock-Property Changes During Reservoir Compaction. SPE Formation Evaluation. 7(3), 197-205.
[17] Silva, F., Debande, G., Pereira, C. and Plischke, B. (1990) Casing Collapse Analysis Associated With Reservoir Compaction and Overburden Subsidence. In: Proceedings of European Petroleum Conference, 21-24 October, The Hague, Netherlands. 19-24.
[18] Huang, Z. (2020) Optimization and practice of key parameters for pressure relief in gob side entry driving of thick coal seam. Xuzhou: China University of Mining and Technology (Thesis). 72-76.
[19] Bu, R. (2020) Study on the stability control of thick coal seam roadway cutting top unloading and anchoring in conjunction with surrounding rock. Xuzhou: China University of Mining and Technology (Thesis). 45-52.
[20] Guo, D., Gao, L., Zhang, Y., Wang, W., Zhang, H., Fang, G., Zhang, Y., Huang, Z., Li, J. (2019) Experimental study on pore structure and fractal characteristics of tectonic coal. Fresen. Environ. Bull. 28(11), 8282-8291.
[21] Zhang, Y. (2020) Study on key roof cutting parameters and surrounding rock control of goaf retaining roadway without side entry filling and pressure relief in deep mine. Huainan: Anhui University of Science and Technology (Thesis). 66-71.
[22] Chen, Y., Ding, Q., Yang, X., Peng, Z., Xu, D., Feng, Q. (2013) Application countermeasures of non-incineration technologies for medical waste treatment in China. Waste Management & Research. 31(12), 1237-1244.
[23] Yao, Y., Wei, M., Kang, W. (2021) A review of wettability alteration using surfactants in carbonate reservoirs. Advances in Colloid and Interface Science. 294, 102477.
[24] Abdul, R., Abdul, R., Munir, A., Abbas, A., Zhang, D. (2019) The effect of carbon dioxide emission and the consumption of electrical energy, fossil fuel energy, and renewable energy, on economic performance: Evidence from Pakistan. Environmental Science and Pollution Research. 26(21), 21760-21773.
[25] Gong, J., Caldas, C. (2010) Computer Vision-Based Video Interpretation Model for Automated Productivity Analysis of Construction Operations. Journal of Computing in Civil Engineering. 24, 252-263.
[26] Chen, Z., Yuan, Y., Zhu, X., Liu, Y. (2020) Occurrence of unconventional natural gas in coal-bearing strata in Ordos Basin, China. Fresen. Environ. Bull. 29(4A), 3254-3260.
[27] Li, Q., Liu, L., Yu, B., Guo, L., Shi, S., Miao, L. (2021) Borehole enlargement rate as a measure of borehole instability in hydrate reservoir and its relationship with drilling mud density. Journal of Petroleum Exploration and Production. 11(3), 1185-1198.
[28] Cecati, C., Citro, C., Piccolo, A., Siano, P. (2011) Smart operation of wind turbines and diesel generators according to economic criteria. IEEE Transactions on Industrial Electronics. 58(10), 4514-4525.

Received: **10.11.2021**
Accepted: **03.01.2022**

CORRESPONDING AUTHOR

Qi Wang
College of Mining,
Liaoning Technical University,
Fuxin 123000 – China

e-mail: wq133350283@vip.qq.com

© by PSP Volume 31– No. 05/2022 pages 4816-4822 Fresenius Environmental Bulletin

SPATIAL STRATIFIED HETEROGENEITY OF RECLAMATION AND GEOGRAPHIC DETECTION OF ITS DISTANCE FACTORS

Yixin Dai, Peng Qin*

School of Resources and Environment, Qingdao Agricultural University, Qingdao 266109, P.R. China

ABSTRACT

Wetland is the most sensitive type of land use/cover to human disturbances. In recent years, the intensity of human activities in coastal areas have continued to strengthen, the coastal wetland ecosystems have continued to be at risk. This paper discussed reclamation that threatens coastal wetlands. The purpose of the research is to understand spatio-temporal heterogeneity and the relationship between distance factors and reclamation area. We used the Geodetector to quantify the effects of factors on the distribution and found out that the distance to coastline is the most determinant factor. So, the distance to coastline was selected as the main factor to explore the probability of reclamation occurrence. It was observed that the incidence of reclamation fluctuated along with the distance to coastline in all situations and there is a higher frequency of reclamation in 4 and 3 scales. This finding can provide scientific suggestions for decision-making of reclamation planning and ecosystem protection.

KEYWORDS:
Sea reclamation, distance factors, spatial autocorrelation, Geographic detection, Jiaozhou Bay

INTRODUCTION

Coastal wetlands which are an important ecological element of coastal regions are the interface between terrestrial and marine ecosystem [1], [2]. Due to the development of coastal cities and global climate change, the number of coastal wetlands with ecological and economic value in the world has decreased significantly in recent decades [3], [4]. With the expansion of urban land, the loss of the wetland in the city has lost more than 30% in the world[5], [6].Over 70 percent of global net permanent water loss occurred in the Middle East and Central Asia, linked to drought and human actions [7]. Despite that, since the 20th century, the economic center of coastal countries in the world has shifted to coastal areas, and more than half of the world's population has lived within 100km of the coastline [8]. The direct or indirect interference of human activities on the coastal ecosystem and coastline is the main reason for the dramatic changes of coastline and the increasing disasters in the coastal zone [9], [10]. Large-scale human reclamation has changed the natural properties of the Gulf coastline and the area and tidal capacity of the Bay, resulting in the deterioration of the natural environment of the bay[11]. For instance, the cooling-effect is being eliminated due to the simplified shape of the wetland [12].

Jiaozhou Bay is the "mother's Bay" of Qingdao. Its deep-water and wide port is a rare natural good port on the east side of the bay, which plays an extremely important role in the development of Qingdao[13][14]. Substantial wetland degradation lead to productivity decline, habitat loss, landscape fragmentation, etc., which has a negative impact on human health, regional climate and ecological stability[1], [13]. Over the years, many scholars have studied Jiaozhou Bay. Based on the charts of different times in Jiaozhou Bay, Bian and colleagues summed up the changes of total water area and total shoreline length in the past 130 years by means of human-computer interaction [15]. Wang et al. studied the evolution and control factors of the coastline in the area around Jiaozhou Bay by investigating the historical changes of the coastline[16]. Ma et al. carried out remote sensing analysis and quality evaluation on the dynamic change of Jiaozhou Bay wetland, and provided scientific basis for the protection, restoration and reconstruction of Jiaozhou Bay wetland[17].

MATERIALS AND METHODS

Qingdao is a typical pilot city of new urbanization guided by tourism. After the reform and opening up, the urban land expanded rapidly [18]. With the development of Qingdao, the area around Jiaozhou Bay has been developed rapidly. More and more natural scenes are replaced by man-made projects [17]. Satellite remote sensing data is becoming an efficient means of monitoring and management of the wetland resources [19]. Scientists have been carrying out quantitative research on shoreline movement and coastal zone change in Jiaozhou Bay(Figure 1), using historical charts and image remote sensing to

monitor shoreline attributes and location changes and calculate the growing land area[14], [20]. However, there are few systematic studies on the spatiotemporal distribution characteristics of contraction in different directions and influencing factors of wetland degradation and land reclamation in Jiaozhou Bay in recent 40 years. If allowed to develop, human activities will continue to approach the sea, not only the wetland area will gradually shrink and disappear, but also the tidal capacity and area of Jiaozhou Bay will be reduced, resulting in ecological environment deterioration, and the port shipping of Jiaozhou Bay will be affected [17]. Accordingly, it is of great significance to understand the temporal and spatial changes of reclamation in Jiaozhou Bay and the influencing factors for the scientific planning and rational development of the coastline resources.

Therefore, taking Jiaozhou Bay as a case study, with the support of Geographic Information System （GIS）technology, this research studied the shrinkage and attrition of Jiaozhou Bay from 1973 to 2018. Remote sensing image of coastline was used to analyze spatiotemporal distribution of reclamation and wetland degradation in Jiaozhou Bay. Remote sensing data were listed in Table 1. Three kinds of distance are selected as the influencing factors, including the distance to barycenter, distance to the bay mouth and distance to coastline, which was quantified by using Geodetector. The study will help to better understand the risk of wetland degradation and land reclamation in different time and space.

This part describes Lorenz curves, spatial autocorrelation model and geographical detector. The geographical detector includes four detectors, such as the risk detector, factor detector, ecological detector, and interaction detector. In this study, we use the factor detector to examine the determinant powers of different influencing factors for spatial heterogeneity of reclamation in Jiaozhou Bay. After factors were validated, risk detector was used to explore the incidence of reclamation fluctuated along with the distance to coastline in all situations.

FIGURE 1
The location of Jiaozhou Bay.

TABLE 1
Data source information

Year	Data source	Resolution (m)
19731117	Landsat image (MSS)	78
19801002	Landsat image (MSS)	78
19851102	Landsat image (TM)	30
19901015	Landsat image (TM)	30
19950420	Landsat image (TM)	30
20000916	Landsat image (TM)	30
20050602	Landsat image (TM)	30
20101006	Landsat image (TM)	30
20181028	Landsat image (OLI)	15

Lorenz curves. The Lorenz curve method is mainly used to analyze the degree of concentration and dispersion of geographical things in spatiotemporal and the change of such concentration and dispersion[21]. It provides a method to directly compare the actual regional distribution data with the standard distribution data. In this article, we use Lorenz curve to estimate temporal distributions of reclamation in Jiaozhou Bay. Taking the periods as the horizontal axis and the area of reclamation as the vertical axis. Mark the one-to-one corresponding points on the coordinate axis on the graph, and each point is connected into a curve. When the areas are evenly distributed, they are represented as a diagonal line starting from the origin. The more convex the curve is, the more concentrated the area is in some periods, and vice versa.

Spatial autocorrelation model. In order to describe the spatial distributing characteristics of reclamation in Jiaozhou Bay, spatial autocorrelation was adopted to detect spatial association and heterogeneity, which has been widely applied in many natural and social researches [22], [23]. Spatial autocorrelation includes a measure of global and local autocorrelation, and the local Moran's I can be used to explore the regional spatial distribution of the agglomeration degree [23]. We used a set of weighted features, identified statistically significant hot spots and cold spots using the Getis-Ord Gi* statistic. And there are 3 types: hot spots, cold spots and other spots [24], [25]. In this study, the area of reclamation was detected to explore the spot heterogeneity.

Geographical detector. The Geodetector model is a spatial analysis model based on the theory of spatial differentiation[26]. There are four models, including the risk detector, factor detector, ecological detector and interaction detector, which can detect the stratified heterogeneity of a responding variable and the determinant power of an impact factor[4], [27], [28]. In this study, we examined the distance factors for the distribution of the reclamation area. The factor detector is measured according to the following q-statistic:

$$q = 1 - \frac{\sum_{h=1}^{L} N_h \sigma_h^2}{N\sigma^2}$$

Here, h=1, 2…, L, the variable Y (or factor X) is composed of L grade, N_h is denoted as the number of units in stratum h and N stands for the number of units in study area, σ_h is denoted as the variance of Y in stratum h and σ stands for the variance of Y in study area, the p value is used to identify the responsible for factors. The value range of q is [0, 1]. The bigger q-statistic, the stronger impact of factors. Reclamation usually occurs alongside the coastline. Because of the high cost, it is difficult and complicated to construct an island, which is not adjacent to the continent. So, we speculated that the reclamation had a strong correlation with the distance. For distances, three types of distance were selected to be factors, including the distance to barycenter, distance to the bay mouth and distance to coastline. The barycenter was calculated by the data in 1973 as well as coastline was extracted. The bay mouth has never been changed, so the midpoint of the mouth's line was as the start of measurement. The area of reclamation is what we want to explain by the factors. The three factors were classified into seven scales separately by the distance. We settle the area of reclamation as the dependent variable Y, the factors including the distance to coastline, distance to barycenter and distance to the bay mouth as independent variables X.

RESULTS AND DISCUSSION

Temporal variation of reclamation. The distribution of reclamation area in different stages are measured by using Lorenz Curve (Figure 2). Specifically, the most frequent reclamation activities occurred from 1985 to 1995, which occupied the 42.69% of the whole reclamation area. Contrast, the reclamation activities were not so outstanding at the beginning and end of the entire period. The area only account for 12.84%. The reclamation trend looks like a mountain with two peaks. The first point is at the stage of 1985-1990 while the second is at that of 2005-2010.

Spatial variation of reclamation. The standard deviational ellipse was used to depict directional distribution. From the long axis, we can see that the reclamation areas were mainly along with the line from northeast to southwest. According to the shorter axis, the areas show an aggregation characteristic. In terms of spatial characteristics, the results show that regions classified as hot spots (Figure 3), with the proportion of 56.31%, were mainly concentrated in the northeast and southwest of the bay that have more reclamation activities, particularly in the estuaries of Moshui, Xiaomao and Dagu rivers. Conversely, regions classified as cold spots with the proportion of 13.61%, were mainly near the bay mouth, particularly distributed in the fringe of old town. Other regions with the proportion of 30.08%, were identified as neither hot nor spots, scattered the whole Jiaozhou Bay.

Detection of spatial heterogeneity. Geodetector was used to assess the affection of distance. Factor detector and Risk detector were chose to analyzed the factor deeply [28]. The factor detector was used to identify the responsibilities of different factors, the degree of spatial stratified heterogeneity is measured by a q-statistic method to test its significance. Risk detector was used to compare the difference of average values between sub-regions.

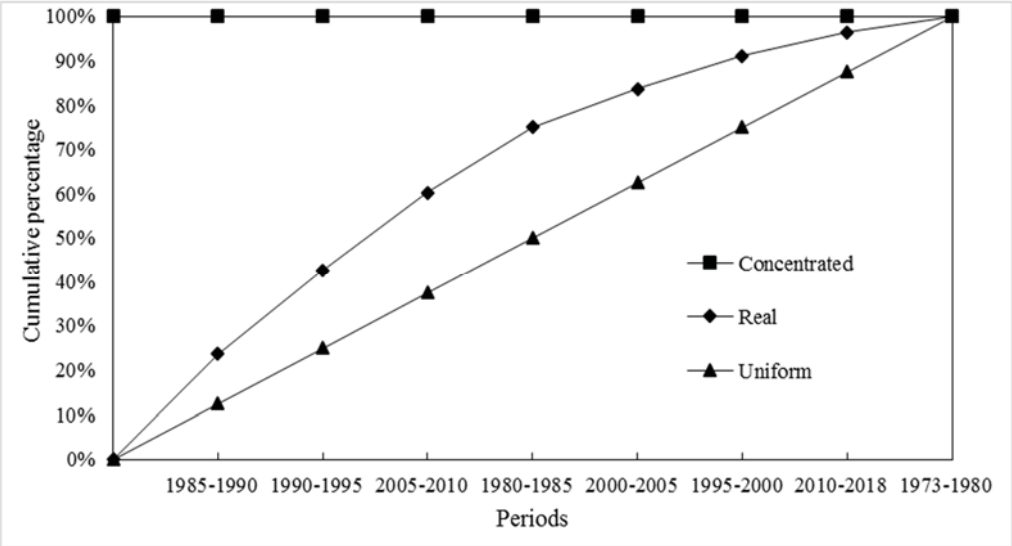

FIGURE 2
Lorenz curve of temporal distribution of reclamation in Jiaozhou Bay.

TABLE 2
The result of factor detector about distance factors of reclamation

Variables		q statistic	p value
All spots			
Distance to	Coastline	0.10	0.00
	Barycenter	0.04	0.02
	Mouth	0.03	0.14
Hot spots			
Distance to	Coastline	0.15	0.19
	Barycenter	0.06	0.83
	Mouth	0.04	0.89
Other spots			
Distance to	Coastline	0.13	0.01
	Barycenter	0.07	0.17
	Mouth	0.05	0.32
Cold spots			
Distance to	Coastline	0.12	0.01
	Barycenter	0.05	0.25
	Mouth	0.08	0.12

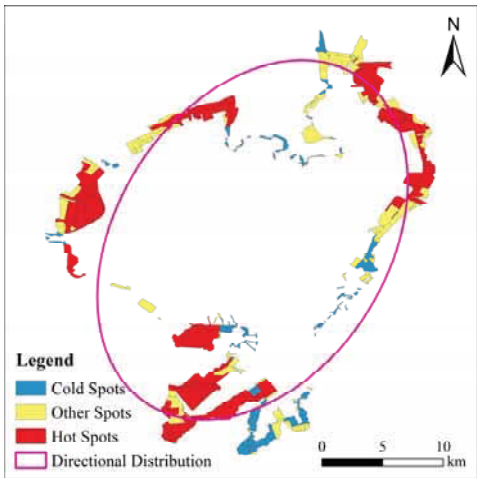

FIGURE 3
The spatial distribution of reclamation in the study area.

In all spots, Geo-Detector results reveal that the q value of distance to coastline is 0.10, and that of distance to barycenter is 0.04 with the p value of 0.02 (Table 2). The p value of both is significant ($p<0.05$), but the p value of distance to mouth is 0.14, which more than 0.05. Similarly, in other and cold spots, the p value of distance to coastline is significant ($p<0.05$). Even if all factors are not significant ($p<0.05$) in hot spots, the results show that the factor of distance to coastline has the greatest power for reclamation distribution. The distance to coastline with the highest q value in all situations that illustrates it has the most significant impact than the other factors.

The reclamation risk is more related to the factor of distance to coastline (Figure 4). In order to explore the probability of reclamation occurrence, the risk detector was used to monitor the variation in different scales of the factor. We examine the impact of

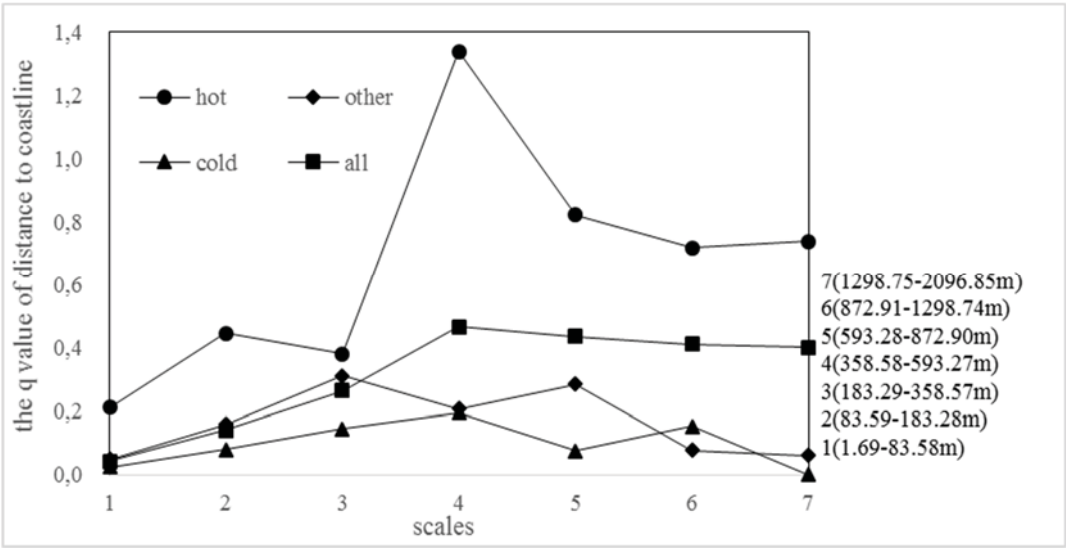

FIGURE 4
Comparison of the effects of distance to coastline on the reclamation in hot, other, cold and all spots

distance to coastline on reclamation. The incidence of reclamation fluctuated along with the distance to coastline in all situations. The values reached the peak in 4 scale except for that in other spots with the peak in 3 scale. So, there are a higher frequency of reclamation in 4 and 3 scales. But what can drop the more attention is that the q value is from 0.10 to 0.15, which shows that the affection is limited.

Over the past 45 years, With rapid and large-scale city construction, land reclamation has become a major threat to coastal wetland degradation [5], [19]. The situation is worse for Jiaozhou Bay, a relatively closed bay. There are different risks of wetland degradation or land reclamation in different time and space. In this study, temporal distribution was described or explained by Lorenz curve. The spatial autocorrelation was used to identify the study area into hot, cold and other spots respectively. Then, we used Geodetector to quantified the effects of three factors on reclamation. In previous studies, correlation analysis between the coastline length and the change in bay area shows that both have a strong connection[14]. Obviously, in our studies, the distance that corresponded to reclamation incidence was different. Hot spots tended to reported a higher correlation between distance and reclamation areas. The hotspots of reclamation were generally areas with frequent coastline expansion[29]. So, the coastline fluctuations are also strongly linked to the distance. In the factor detector, parts of samples were chosen to analyze individually. But the number of factor categories in different spots is same with that in whole spots[30]. There may be different regularity in classification. We have a test about it, the distinction was not so obvious. The q statistic is not so different in different parts.

Alternatively, in the urbanization process, the reclamation shows different characteristic. From the Lorenz curve, the reclamation intensity changed obviously with time, which is high correlated to urbanization concentrated occurred from 1985 to 2010 [18], [31]. That shows a strong time correlation between urbanization and reclamation. Generally, the greater the intensity of urbanization, the greater the intensity of reclamation. Undoubtedly, urbanization enriches the types of coastline so that the influence of coastline types could not be ignored[32].The estuary coastline formed by the river flowing can be utilized easily rather than the other coastline types, such as bedrock, sandy coastline and artificial shorelines. The cost of reclamation is more in some coastline types, which were generally far from urban with inconvenient transportation. The objective conditions lower down the desire of reclamation. In the last ten years, the intensity of reclamation has decreased outstandingly, which influenced by the reforestation policy and implementation of returning farmland to sea. In some countries, such as Netherland, ecological policies were opposed by farmers who have benefitted in the reclamation[33]. In China, farmers who lose aquaculture ponds will receive substantial compensation [34].

Many studies have paid more attention on the coastline[14], [16], [33]. But the polygon changes were the results of line, while the line change is confined. The coastline is emerged in the environment to be a whole. The evolution of driver force was induced by the line change[35]. Jiaozhou Bay was a big wetland patch. Its evolution is corresponding to the shrinkage and jaw models validated in forest, farmland and desert [36].This two models were introduced into wetland in this study shows that shrinkage started from the edge of gulf. Land transformation started form all round is one type of jaw model. This pattern had the least ecological impact [35]. Although there is a bridge, the closed corridor has no exchange of substance and energy with the gulf.

CONCLUSIONS

The spatiotemporal dynamics of reclamation from 1973 to 2018 in Jiaozhou Bay were described in this study. The hot spots were mainly distributed in the estuaries, while the cold spots were concentrated in the fringe of old town. To detect the influences of reclamation, the three distance factors were selected. It is obvious to seen that the distance to coastline is the most important factors effect, and it also varies in different spots. A good comprehension for the heterogeneity of the distance's effect on the reclamation distribution was captured, which can be served as beneficial references for measures from government. Generally, estuaries have higher ecological value, where have more restricted actions. Reclamation activities can be better planned based on effects of distance factors in this study.

ACKNOWLEDGEMENTS

This research was funded by Shandong Provincial Natural Science Foundation, China (ZR2017BD030), 2020 Shandong University Student Innovation Training Project and supported by the scholarship from Visiting Scholar Fund by Qingdao Agricultural University.

REFERENCES

[1] Hu, T., Liu, J., Zheng, G., Zhang, D., Huang, K. (2020) Evaluation of historical and future wetland degradation using remote sensing imagery and land use modeling. L. Degrad. Dev. 31(1), 65–80.

[2] Meng, W., Hu, B., He, M., Liu, B., Mo, X., Li, H., Wang, Z., Zhang, Y. (2017) Temporal-spatial variations and driving factors analysis of coastal reclamation in China. Estuar. Coast. Shelf Sci. 191, 39–49.

[3] Davidson, N.C. (2014) How much wetland has the world lost? Long-term and recent trends in global wetland area. Mar. Freshw. Res. 65(10), 936–941.

[4] Chen, H.W., Lin, H.C., Chuang, Y.H., Sun, C.T., Chen, W.Y., Kao, C.Y. (2019) Effects of environmental factors on benthic species in a coastal wetland by redundancy analysis. Ocean Coast. Manag. 169 (March 2018), 37–49.

[5] Yamazaki, D., Trigg, M.A. (2016) Hydrology: The dynamics of Earth's surface water. Nature. 540, 348–349.

[6] Rojas, C., Munizaga, J., Rojas, O., Martínez, C., Pino, J. (2019) Urban development versus wetland loss in a coastal Latin American city: Lessons for sustainable land use planning. Land use policy. 80 (September 2018), 47–56.

[7] Pekel, J.F., Cottam, A., Gorelick, N., Belward, A.S. (2016) High-resolution mapping of global surface water and its long-term changes. Nature. 540, 418–422.

[8] Primavera, J.H. (2006) Overcoming the impacts of aquaculture on the coastal zone. Ocean Coast. Manag. 49(9/10), 531–545.

[9] Qin, P., Zhang, Z. (2021) Evolution of wetland landscape disturbance in Jiaozhou Gulf between 1973 and 2018 based on remote sensing. Eur. J. Remote Sens. 54(Sup2), 145–154.

[10] Hou, X., Wu, T., Hou, W., Chen, Q., Wang, Y., Yu, L. (2016) Characteristics of coastline changes in mainland China since the early 1940s. Sci. China Earth Sci. 59(9), 1791–1802.

[11] Li, D., Tang, C., Hou, X., Zhang, H. (2019) Rapid morphological changes caused by intensive coastal development in Longkou Bay, China. J. Coast. Res. 35(3), 615–624.

[12] Xue, Z., Hou, G., Zhang, Z., Lyu, X., Jiang, M., Zou, Y., Shen, X., Wang, J., Liu, X. (2019) Quantifying the cooling-effects of urban and peri-urban wetlands using remote sensing data: Case study of cities of Northeast China. Landsc. Urban Plan. 182 (October 2018), 92–100.

[13] Mao, D., Wang, Z., Wu, B., Zeng, Y., Luo, L., Zhang, B. (2018) Land degradation and restoration in the arid and semiarid zones of China: Quantified evidence and implications from satellites. L. Degrad. Dev. 29(11), 3841–3851.

[14] Zhou, C., Li, G., Shi, J. (2010) Coastline Change of Jiaozhou Bay over the Lsat 150 Years. Period. Ocean Univ. China. 40(7), 099–106.

[15] Bian, S., Hu, Z., Feng, A., Xia, D. (2001) An Exploration on the Natural Morphology and the Siltation and Erosion Development of the Jiaozhou Bay in Recent 130 Years. J. Oceanogr. Huanghai Bohai Seas. 19(3), 46–53.

[16] Wang, W., Zhang, S., Ji, Y. (2006) Evolution and Controlling Factor of the Circum-Jiaozhou Bay Coastline. Mar. Geol. Lett. 22(9), 7–10.

[17] Wang, F., Wang, X., Song, N. (2021) Biochar and vermicompost improve the soil properties and the yield and quality of cucumber (*Cucumis sativus* L.) grown in plastic shed soil continuously cropped for different years. Agr. Ecosyt. Enron. 315: 107425.

[18] Qin, P., Guo, D. (2016) A study on the Expansion of the Urban Land Use in Qingdao. China Popul. Resour. Environ. 26(5), 401–404.

[19] Ghosh, S., Das, A. (2019) Urban expansion induced vulnerability assessment of East Kolkata Wetland using Fuzzy MCDM method. Remote Sens. Appl. Soc. Environ. 13, 191–203.

[20] Wang, Y., Gao, S., Jia, J. (2000) Sediment Distribution and Transport Patterns in Jiaozhou Bay and Adjoining Areas. Acta Geogr. Sin. 55(4), 449–458.

[21] Dong, L., Liang, H. (2014) Spatial analysis on China's regional air pollutants and CO_2 emissions: Emission pattern and regional disparity. Atmos. Environ. 92, 280–291.
[22] Gu, H., Fan, W., Liu, K., Qin, S., Li, X., Jiang, J., Chen, E., Zhou, Y., Jiang, Q. (2017) Spatiotemporal variations of typhoid and paratyphoid fevers in Zhejiang Province, China from 2005 to 2015. Sci. Rep. 7(1), 1–11.
[23] He, Y., Zhou, G., Tang, C., Fan, S., Guo, X. (2019) The spatial organization pattern of urban-rural integration in urban agglomerations in China: An agglomeration-diffusion analysis of the population and firms. Habitat Int. 87 (August 2018), 54–65.
[24] Wu, Y., Hu, K., Han, Y., Sheng, Q., Fang, Y. (2020) Spatial Characteristics of Life Expectancy and Geographical Detection of Its Influencing Factors in China. Int. J. Environ. Res. Public Health. 17(3), 906–921.
[25] Ord, J.K., Getis, A. (2001) Testing for local spatial autocorrelation in the presence of global autocorrelation. J. Reg. Sci. 41(3), 411–432.
[26] Tang, C., Yang, C., Cai, S., Ye, H., Duan, L., Zhang, Z., Shi, Z., Lin, K., Song, J., Huang, X., Zhang, H., Yang, J., Cai, P. (2019) Analysis of the relationship between electromagnetic radiation characteristics and urban functions in highly populated urban areas. Sci. Total Environ. 654, 535–540.
[27] Fan, H., Wang, J., Hu, M., Li, Z., Jiang, X., Wang, J. (2020) Spatiotemporal assessment of marine environmental monitoring programme based on DIN concentration in the Yangtze River estuary and its adjacent sea. Sci. Total Environ. 707, 1-8.
[28] Wang, J., Li, X., Christakos G., Liao, Y., Zhang, T., Gu, X., Zheng, X. (2010) Geographical detectors-based health risk assessment and its application in the neural tube defects study of the Heshun Region, China. Int. J. Geogr. Inf. Sci. 24(1), 107–127.
[29] Wu, T., Hou, X. (2015) Spatial-temporal characteristics of coastline in Jiaozhou Bay during the period of 1944-2012. Science & Technology Review. 33(2), 28–34.
[30] Zhang, X., Xu, C., Xiao, G. (2020) Spatial heterogeneity of the association between temperature and hand, foot, and mouth disease risk in metropolitan and other areas. Sci. Total Environ. 713, 1–6.
[31] Miao, X., Qin, P. (2016) The response research of land use transition in Qingdao. J. Qingdao Agric. Univ. Sci. 33(4), 261–267.
[32] Ye, X., Ji, Y., Zheng, Q., Wu, Y., Hua, F., Lin, Z. (2009) Fractal Analysis of the Coastline Changes of the Jiaozhou Bay. Adv. Mar. Sci. 27(4), 495–501.
[33] Sun, H., Zhang, L., Liang, J. (2013) Integration of Water and Land: The Ecological Concept of Land Reclamation in the Netherlands. Urban Plan. Int. 28(1), 80–86.
[34] Zang, Z., Zou, X., Zuo, P., Song, Q., Wang, C., Wang, J. (2017) Impact of landscape patterns on ecological vulnerability and ecosystem service values: An empirical analysis of Yancheng Nature Reserve in China. Ecol. Indic. 72, 142–152.
[35] Forman, R.T.T. (2019) Towns, Ecology, and the Land. Cambridge University Press, Cambridge,1-585.
[36] Forman, R.T.T. (1995) Land Mosaics: The ecology of landscapes and regions. Cambridge University Press, Cambridge,1-656.

Received: **11.11.2021**
Accepted: **04.01.2022**

CORRESPONDING AUTHOR

Peng Qin
School of Resources and Environment,
Qingdao Agricultural University,
Qingdao 266109 – P.R. China

e-mail: pqin@qau.edu.cn

© by PSP Volume 31– No. 05/2022 pages 4823-4832 Fresenius Environmental Bulletin

COMPARISON OF SIMULATED PYROLYSIS EXPERIMENTS OF CRUDE OIL AND KEROGEN: A CASE STUDY OF JURASSIC SHAXIMIAO FORMATION

Xianfeng Wang, Hongming Dai*, Yanyou Li, Wei Luo, Yuhuan Zhu

Southwest Petroleum University, School of Geoscience and Technology, Chengdu 610500, China

ABSTRACT

The hydrocarbon generation of Jurassic crude oil and kerogen samples from Sichuan Basin was simulated under two different linear heating procedures of 20℃/h and 2℃/h in a confined closed system (sealed gold tubular-autoclave-system). The experimental data was recorded in detail during the experiment. The hydrocarbon generation behavior of crude oil and kerogen was described based on the gaseous hydrocarbon component data obtained in the experiment, and the similarities and differences in hydrocarbon generation evolution were analyzed. The results show that the hydrocarbon generation process of different source rocks can be divided into three parts. The hydrocarbon generation range of kerogen is wider, the hydrocarbon generation range of crude oil cracking gas is more concentrated, and the main gas generation stage of crude oil is later than that of kerogen. Through the comparative analysis of hydrocarbon generation process of crude oil and kerogen, this paper aims to deepen the understanding of hydrocarbon generation of crude oil and kerogen under the condition of deep burial and hope to provide reference for the study of gas accumulation in over-mature areas.

KEYWORDS:
Hydrocarbon generation, Closed system, Thermal simulation reaction

INTRODUCTION

With the deepening of oil and gas exploration, the exploration objectives of oil and gas have been extended from shallow to deep and from new to old. Many important achievements have been made in the exploration of deep and ultra-deep oil and gas resources worldwide, and deep oil and gas exploration will be an important development trend of the oil and gas industry in the future [1]. Current studies show that most of the deep natural gas is related to oil cracking gas. Therefore, a deeper understanding of kerogen and hydrocarbon generation behavior of oil cracking under deep buried conditions is undoubtedly of great theoretical and practical significance to the identification of natural gas genetic types and the study of gas accumulation in over-mature areas [2,3].

The reaction process of hydrocarbon source rock organic matter forming oil and natural gas is a complex thermal and kinetic process under the comprehensive action in a long geological period [4,5]. The discriminant relation between hydrocarbon generation behavior and thermal maturity in the past is an empirical formula calculated based on different measured data (corresponding to the basic geological conditions of different areas and the differences of hydrocarbon generation parent material and its migration, accumulation and loss history) [6-9].If the source rock can be cracked directly using a thermal simulation experiment, which uses a closed experimental environment to replace the actual deep buried environment, a continuous pressure replaced the overlying formation pressure, and a continuous heating replace the geothermal gradient, the hydrocarbon generation process of the source rock under a long geological condition can be simulated in a short time [10-15]. In this paper, mudstones and oil sandstone of Shaximiao Formation of Jurassic Well Qinglin-1 in central Sichuan were selected to systematically investigate the generation behavior and difference of kerogen cracking gas and oil cracking gas, so as to deepen the understanding of hydrocarbon generation law in deep areas and provide guidance for identifying the source and origin of natural gas.

MATERIALS AND METHODS

The Jurassic mudstone and oil sandstone samples were taken from the Shaximiao Formation core of Well Qinglin-1. The Sichuan Basin was dominated by lacustrine environment in the Jurassic. Well Qinglin-1 was located in the middle of Sichuan (Figure 1) [16,17]. Mudstone samples are dark gray and lumpy-light gray, and the sample surface does not show texture. When cold and dilute HCl drops onto the surface, it can react and generate bubbles (Figure 2A). The oil sandstone is dark gray and has an odor when struck. Its interior is oily and shiny, and can be ignited when exposed to an open fire (Figure 2B).

GEOCHEMICAL CHARACTERISTICS OF SAMPLES

The samples used in the thermal simulation experiment and the study of hydrocarbon generation kinetics have the characteristics of low maximum pyrolysis temperature (T_{max}) and high TOC content, indicating that the samples obtained have low maturity and rich organic matter content, which meet the basic needs of thermal simulation experiment samples. The basic geochemical parameters of the experimental samples are shown in Table 1.

Figure 3 shows the characteristics of biomarker compounds in the two samples. In pentacyclic triterpenes, C_{29} hopane is the main peak of the two types of samples, and C_{31}-C_{35} liters of hopane series distribution is complete. C_{35} hopane > C_{34} hopane. Gammacerane is more abundant. Pregnane is more abundant, C_{29} regular steranes were predominant in the sample.

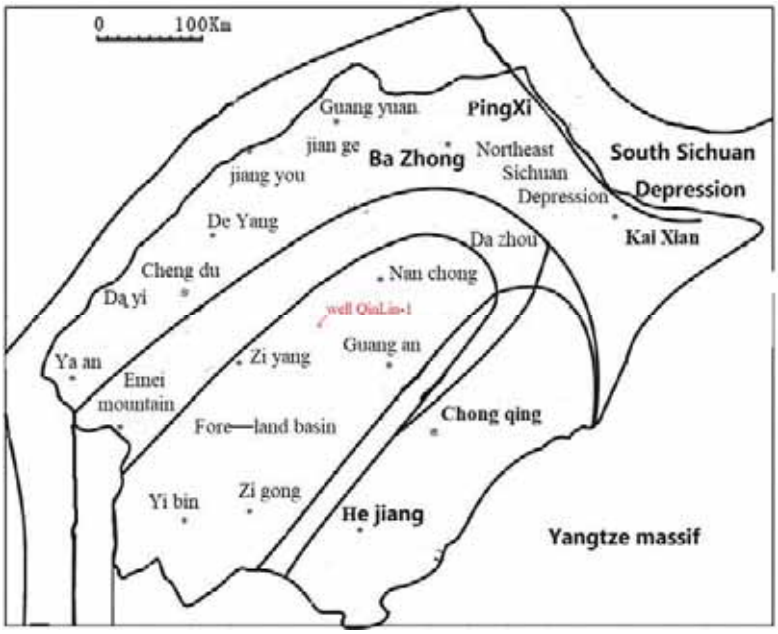

FIGURE 1
Geographical location map of well Qinglin-1

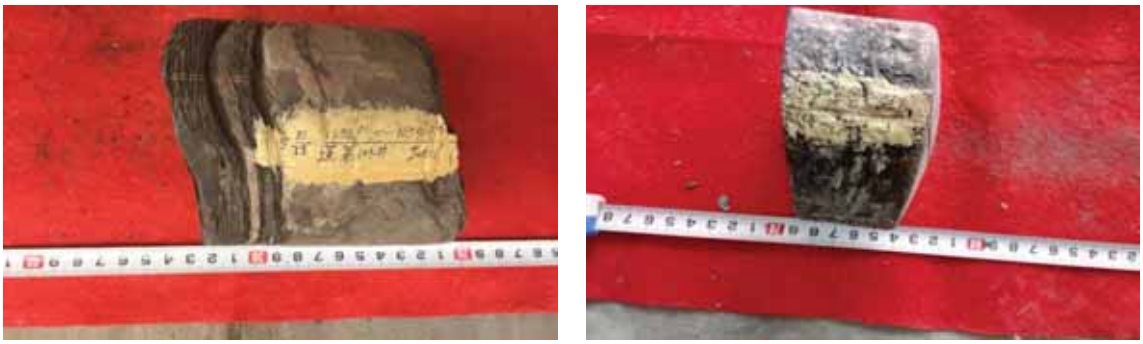

（A） （B）

FIGURE 2
Cores of mudstone and oil sandstone samples from Shaximiao Formation in well Qinglin-1
(A) mudstone; (B) oil sandstone

TABLE 1
Pyrolysis parameters of mudstone and oil sandstone samples from Well Qinglin-1

Sample	W /‰		T_{max}/°C	Hydrogen index I_H/‰	Oxygen index I_O/‰	W_{TOC}/%
	S_1	S_2				
Oil	19.14	354.53	418	1101.03	48.45	58.01
Kerogen	24.39	195.80	433	137.04	0.896	73.68

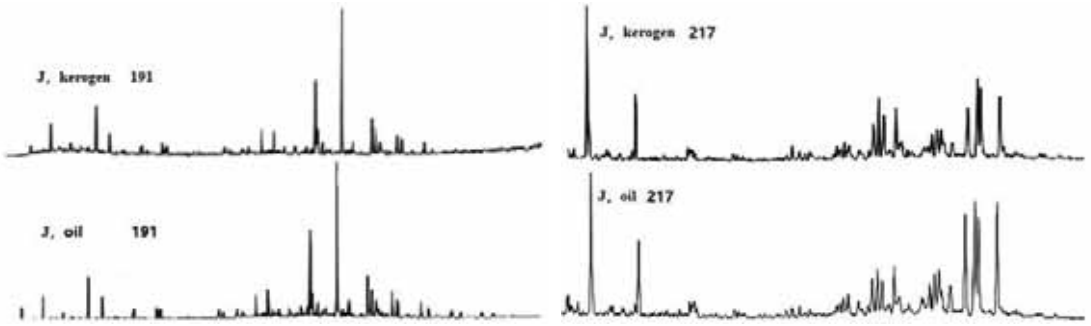

FIGURE 3
Biomarker compounds of crude oil and kerogen

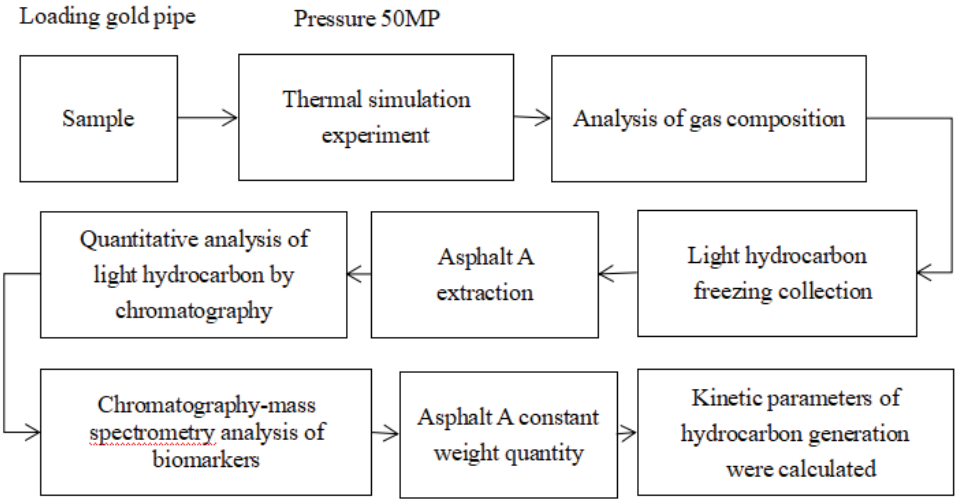

FIGURE 4
Experimental flow chart

EXPERIMENTAL PROCESS

According to the above organic geochemical studies, the hydrocarbon generation parent materials obtained in this paper are all from the stratigraphic period to which they belong. These two kinds of samples are ideal objects for thermal simulation in the study of hydrocarbon generation characteristics during thermal cracking.

Kerogen and crude oil preparation:

(A) The selected mudstone was crushed and soaked in hydrochloric acid. After heating with hydrochloric acid and hydrofluoric acid for 8h, they were separated and washed with deionized water. After repeated treatment, washed with distilled water to neutral, dried to prepare kerogen.

(B) The selected oil sandstone was extracted with reagent (methylene chloride: methanol = 97:3) for 24 hours, and then prepared into crude oil samples after deasphalting.

According to the basic program of hydrocarbon generation kinetics, the samples were first treated, and then the thermal simulation experiment was carried out by high-pressure closed method. Then the hydrocarbon was generated and analyzed by thermal simulation experiment. The experimental process is shown in Figure 4:

At the beginning of the experiment, the samples were put into a gold tube and sealed under the condition of continuous argon gas. This was to ensure that the experiment would not be adulterated with air, which would cause errors in the experiment. In order to simulate the overlying pressure of samples in the limited formation space, the gold tube containing the sample is placed under the high pressure condition of continuous water filling. The water pressure deforms the gold tube and then exerts pressure on the sample. In the experiment, the samples were heated at 20℃/ h and 2℃/ h respectively (the temperature error of several experiments was less than 1℃). The pressure conditions were controlled as 5MP (the pressure fluctuation was less than 0.5mp). The data ranged from 100℃ to 600℃. After heating, the gas products in the gold tube are released into a vacuum system connected online with GC7890 gas chromatograph. Data of gas products are obtained by testing. The simulation diagram of the experimental device is shown in Figure 5.

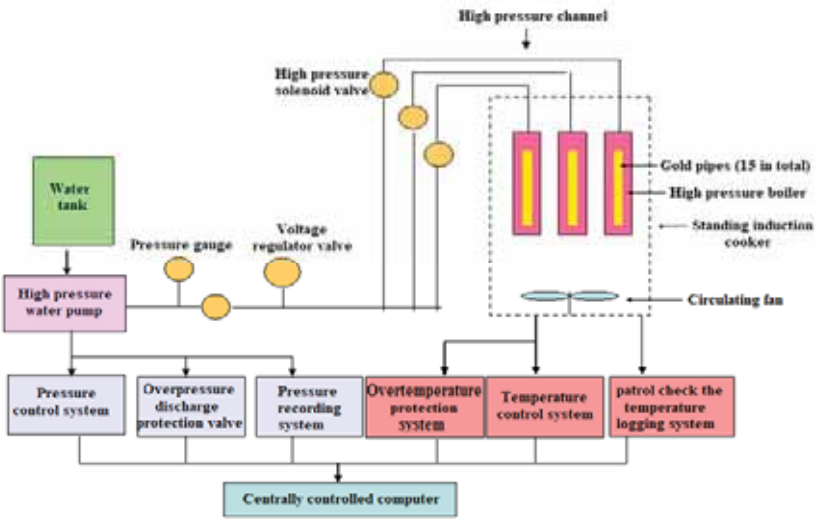

FIGURE 5
Schematic diagram of gold tube simulation experiment

TABLE 2
Data of crude oil and kerogen products changing with temperature

T (℃)	Methane		Ethane		Propane		Isobutane		Butane	
Product(mg/g)	20℃/h	2℃/h	20℃/h	2℃/h	20℃/h	2℃/h	20℃/h	2℃/h	20℃/h	2℃/h
289.5(kerogen)	0.1	0.1	0.0	0.1	0.005	0.014	0.002	0.004	0.001	0.003
311.0(kerogen)	0.1	0.3	0.0	0.1	0.013	0.027	0.004	0.013	0.005	0.011
336.2(kerogen)	0.3	1.2	0.1	0.5	0.025	0.111	0.009	0.023	0.008	0.024
360.5(kerogen)	0.6	3.7	0.2	1.3	0.114	0.506	0.017	0.055	0.019	0.044
393.2(kerogen)	3.2	9.9	1.1	2.9	0.374	0.900	0.056	0.128	0.054	0.156
411.4(kerogen)	6.4	23.4	2.0	5.2	0.673	1.469	0.120	0.202	0.130	0.244
435.6(kerogen)	14.0	37.3	3.8	5.6	1.281	1.194	0.189	0.228	0.279	0.265
457.6(kerogen)	24.5	52.7	5.3	4.8	1.552	1.134	0.230	0.178	0.288	0.160
480.5(kerogen)	39.1	70.2	5.8	3.1	1.590	0.335	0.246	0.038	0.259	0.014
504.5(kerogen)	58.3	88.9	4.7	1.4	0.958	0.065	0.143	0.008	0.092	0.002
528.7(kerogen)	76.4	102.3	3.2	0.7	0.290	0.026	0.028	0.000	0.008	0.000
554.2(kerogen)	91.2	112.1	1.7	0.5	0.067	0.009	0.000	0.000	0.002	0.000
578.7(kerogen)	102.6	123.3	0.8	0.3	0.020	0.002	0.000	0.000	0.000	0.000
600.7(kerogen)	111.3	127.1	0.6	0.2	0.009	0.014	0.000	0.004	0.000	0.000
288.0(oil)	0.0	0.6	0.0	0.1	0.000	0.001	0.000	0.010	0.000	0.000
312.7(oil)	0.0	2.0	0.0	0.2	0.001	0.287	0.001	0.067	0.000	0.001
336.0(oil)	0.5	6.2	0.1	2.2	0.001	0.752	0.007	0.209	0.000	0.065
360.0(oil)	1.1	9.4	0.3	4.1	0.201	2.224	0.063	0.462	0.001	0.251
384.0(oil)	4.2	20.8	1.4	9.1	0.848	4.741	0.158	0.766	0.071	0.652
408.0(oil)	9.4	34.0	4.0	14.2	2.306	8.029	0.362	1.133	0.228	1.065
432.0(oil)	18.8	55.7	8.1	19.7	4.896	11.21	0.757	1.441	0.690	1.131
456.0(oil)	31.7	88.5	12.5	24.5	7.400	12.42	1.060	2.105	0.959	0.251
480.0(oil)	51.7	116.3	18.1	23.9	10.37	9.542	1.496	0.742	1.039	0.033
504.0(oil)	78.9	141.9	23.5	20.8	11.48	6.012	2.099	0.045	0.282	0.014
528.1(oil)	107.2	168.2	23.9	10.7	9.220	3.015	0.719	0.003	0.031	0.000
552.5(oil)	139.2	180.2	20.7	5.9	6.350	1.261	0.081	0.000	0.014	0.000
576.1(oil)	167.3	187.5	12.0	2.3	3.210	0.861	0.003	0.000	0.000	0.000

RESULTS

Product Characteristics of Kerogen and Crude Oil. The contents of gaseous hydrocarbon components produced by crude oil and kerogen in the experiment are shown in table 2, and the data of each product obtained in the experiment are plotted.

This experiment consists of two different linear heating processes, with slightly different product yields at different heating rates. The conversion and yield of each product are shown in Figure 6 and Figure 7. Due to the complementary relationship between time and temperature, the reaction rate of each product at a slower heating rate (2°C/h) is higher. The experimental conditions with a fast heating rate will make the product conversion curve lag compared with the experimental conditions with a slow heating rate. The reason for this phenomenon is that the sample pyrolysis reaction is insufficient due to insufficient reaction time.

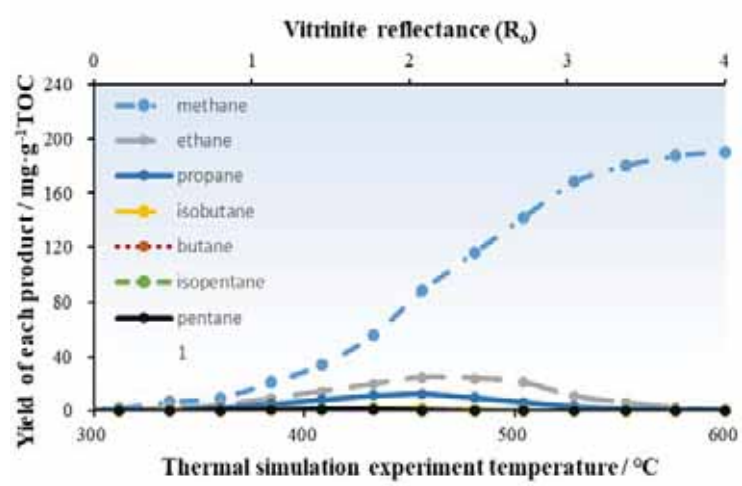

(A)

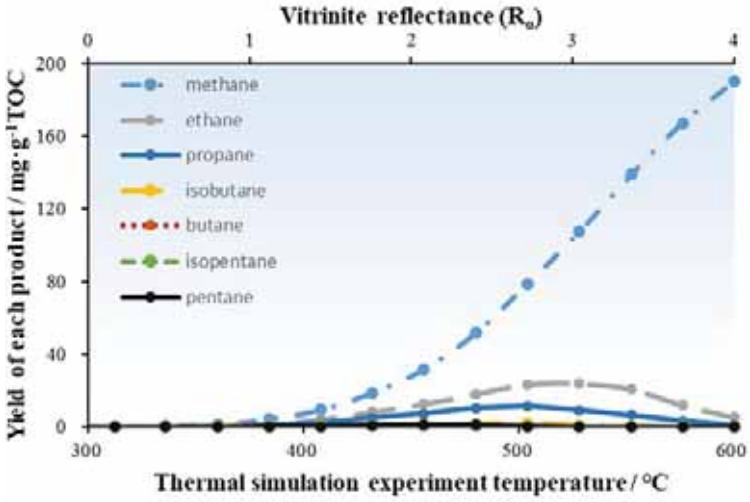

(B)

FIGURE 6

Relationship between oil cracking gas yield and temperature

(A) Heating rate of 20℃/h; (B) The heating rate is 2℃/h

The methane product yields of the two kinds of samples increased sharply with the increase of the experimental temperature from 400℃, reaching a maximum of 187.54 ml/g TOC. The ethane and heavy hydrocarbon gases with carbon number above increased first and then decreased, and ethane peaked at about 480℃. The higher the carbon numbers of heavy hydrocarbon gases, the lower the temperature corresponding to the peak.

The yield of C_1 was similar with $C_{1\text{-}5}$, and the yield of the product increased with thermal evolution. At the high to over mature stage, the increase of yield gradually slows down until no change at all. The maximum yield of total gaseous hydrocarbons is maintained at the thermal evolution temperature corresponding to the maximum yield of $C_{2\text{-}5}$, and the methane yield is relatively low at this time. The dramatic increase of C_1 production was consistent with the rapid disappearance of $C_{2\text{-}5}$, and the change of methane in the product was smaller than that of $C_{2\text{-}5}$. The reason for this phenomenon is that the heavy hydrocarbon gas is partly cracked into methane and partly converted into coke during the cracking process. This phenomenon further indicates that the increase of methane production is closely related to the massive pyrolysis of $C_{2\text{-}5}$. Methane gas doesn't come from just one source，which is not simply produced directly from source rocks. It is the hydrocarbon generating organic matter preferentially cracking into liquid hydrocarbon or heavy hydrocarbon gas, and then under the condition of heating gradually cracking into the most stable organic matter in thermodynamic sense—methane.

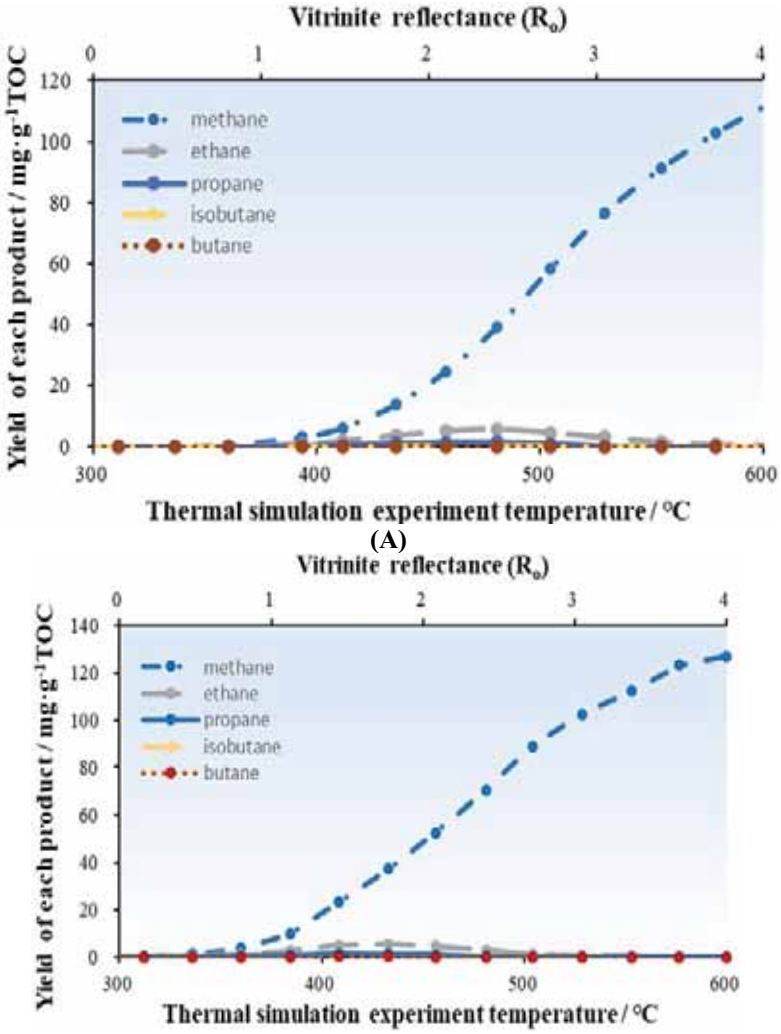

FIGURE 7

Relationship between yield and temperature of kerogen cracking gas

(A) Heating rate of 20℃/h; (B) The heating rate is 2℃/h

Study On Hydrocarbon Generation Model. As shown in Figure 8, according to the change of the yield of hydrocarbon compounds in the simulated experiment, the experimental process can be divided into three stages:

(a) When the temperature is less than 393℃, it is the main stage of oil generation, which corresponds to the stage of thermal catalytic oil and gas generation in the actual geological process. With the increasing of the experimental temperature, when the temperature reaches the critical temperature of hydrocarbon generation, the sample will begin to produce hydrocarbons violently. At this stage, a large number of liquid hydrocarbons of medium and low molecular weight are generated, and the yield of methane and $C_{2\text{-}5}$ gaseous hydrocarbons is basically zero.

(b) When the pyrolysis temperature rises, the temperature ranges from 393℃ to 481℃ (lower heating rate may make this range larger) is the main primary gas generation stage, which corresponds to the stage of pyrolysis and moisture gas generation in the actual geological process. At this stage, the temperature has already exceeded the critical temperature for the decomposition of most liquid hydrocarbons. At the same time, the C-C bonds of a large number of liquid hydrocarbons break, the alkanes above C_{25} almost disappear, and the hydrocarbons of low mass increase rapidly. The source of products in this stage is partly the direct pyrolysis of samples at high temperatures and partly the pyrolysis of liquid hydrocarbons formed in the previous stage.

(c) When the temperature is higher than 481℃, the evolution of organic matter has entered the overmature stage, and the hydrocarbon generation potential at this stage is gradually exhausted, and the gaseous hydrocarbon components evolve into dry gas. At this stage, all the products will gradually split into methane, which is considered the most stable organic substance in thermodynamic studies.

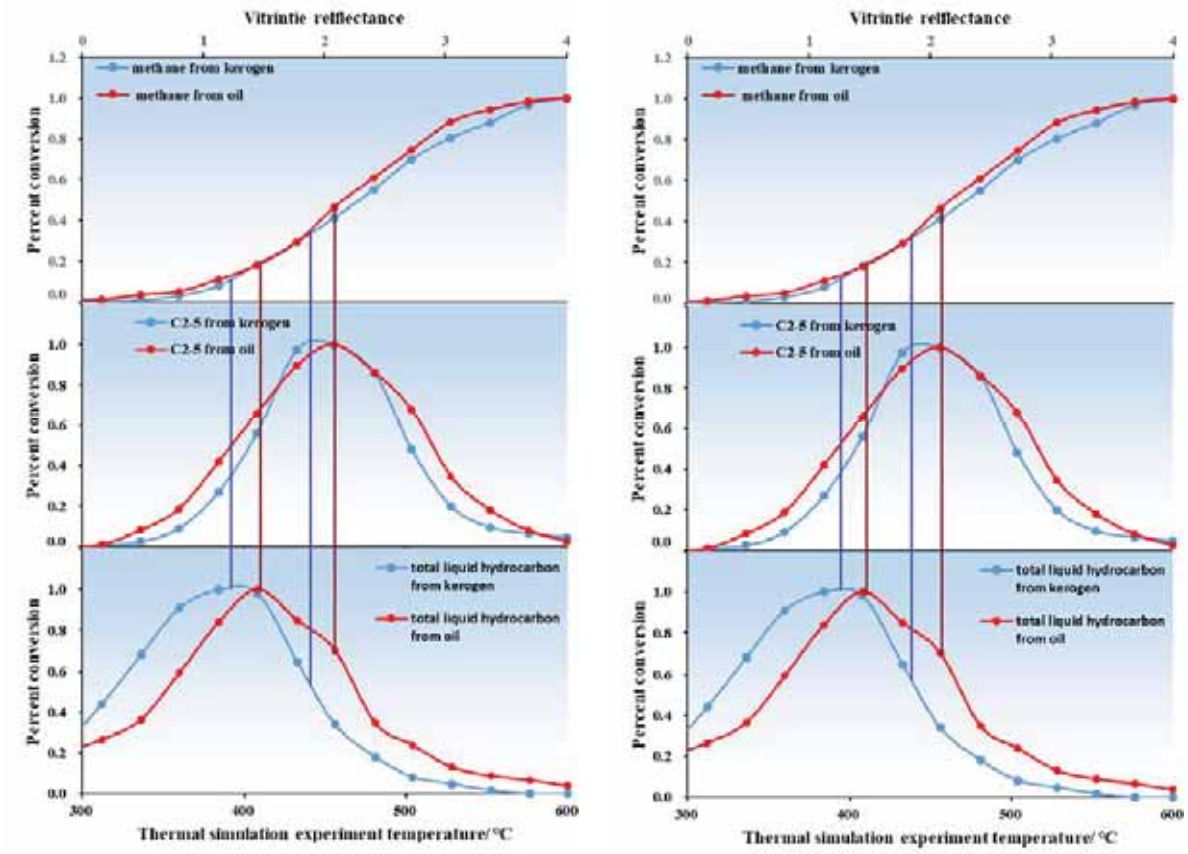

（A） （B）

FIGURE 8
Relationship between kerogen and crude oil cracking gas conversion and temperature
(A) Heating rate of 20℃/h; (B) Heating rate is 2℃/h

From the comparison of crude oil and kerogen pyrolysis, it can be seen that both the methane generation rate of crude oil and the pyrolysis of heavy hydrocarbon gas and liquid hydrocarbon lag behind that of kerogen, and this phenomenon is more obvious under the condition of slower heating rate. The reason for this phenomenon is related to the abundance of groups with low activation energy in kerogen which are easy to decompose into gaseous hydrocarbons. With the increase of maturity (experimental temperature), the liquid hydrocarbon products begin to crack to produce gas in large quantities, and the production of gaseous hydrocarbon products increases obviously, and the proportion of methane in gaseous hydrocarbon gradually increases, and the gas generation rate of crude oil samples accelerates obviously at this stage. The production peak of C_2H_6 and C_3H_8 produced by kerogen is earlier than that of oil samples, which is related to the earlier initiation of kerogen into the cracking of liquid hydrocarbon products. Finally, the total output value of gaseous hydrocarbons increases rapidly, and the oil samples in this stage accumulate more macromolecular hydrocarbon gas than crude oil samples, so the pyrolysis rate of kerogen is faster.

DISCUSSION

By studying the drying coefficient of gaseous hydrocarbon products, the evolution characteristics of pyrolytic gas generation of different hydrocarbon generation parent materials can be compared. The drying coefficient of natural gas is generally expressed by $C_1/\sum C_{2\text{-}5}$ and ln (C_1/C_2)—ln (C_2/C_3) [18,19]. As shown in Figures 9 and 10, the source rocks contain heteratomic groups, in which C-S and C-O bonds have lower bond energies than C-C bonds. Therefore, methane is first cleaved and non-hydrocarbon components are generated. After that, a large number of heavy hydrocarbon gases are generated, which is the reason for the observed decrease in dryness coefficient in early experiments. Kerogen generally has a higher dryness coefficient than crude oil. The temperature corresponding to the minimum dryness coefficient of pyrolysis gas is roughly similar, that is, the stage when condensate associated gas is generated. At this stage, once the thermal temperature and lithostatic pressure exceed the saturated vapor pressure of the gaseous hydrocarbon, the gasified products will be dissolved in the liquid hydrocarbon. As the pyrolysis temperature continues to rise, a large

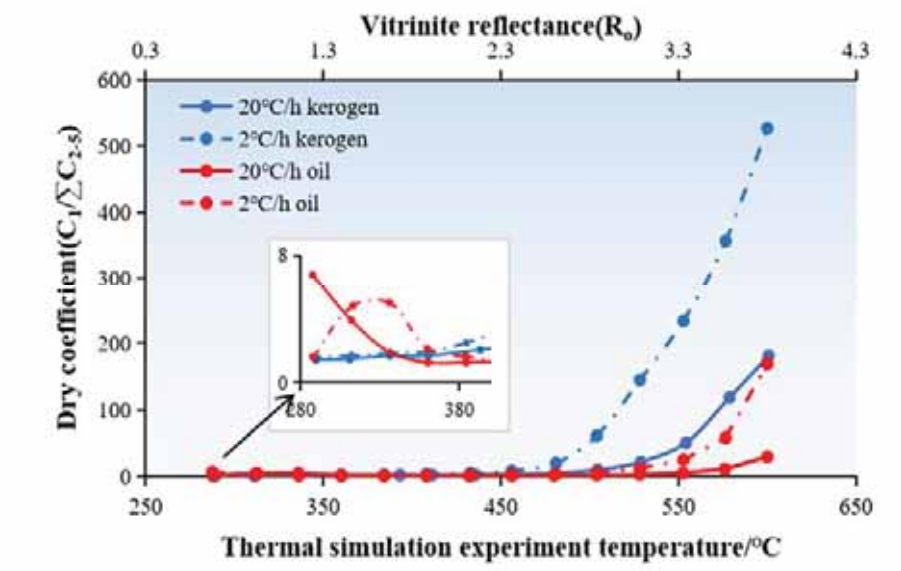

FIGURE 9
Drying coefficient curves of different hydrocarbon-generating parent materials

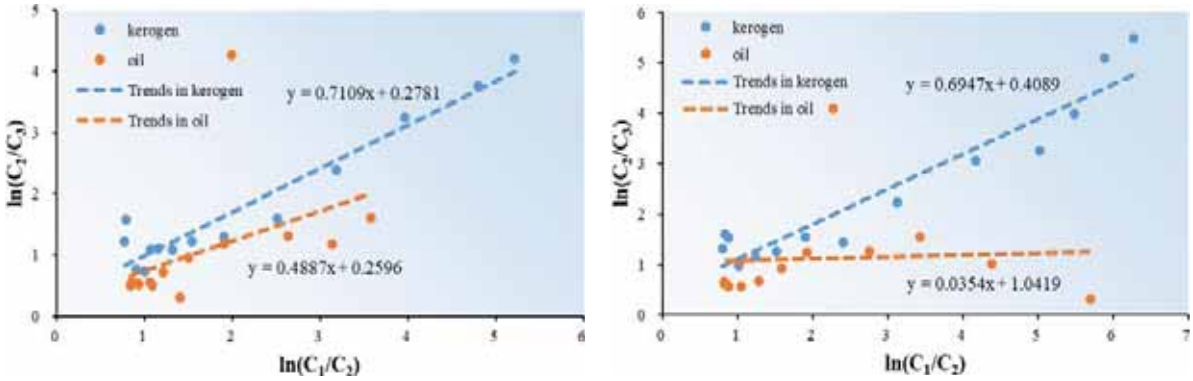

（A） （B）

FIGURE 10
Comparison of ln (C$_1$/C$_2$)—ln(C$_2$/C$_3$) of crude oil and kerogen cracking gas
(A) Heating rate of 20°C/h; (B) Heating rate is 2°C/h

number of liquid hydrocarbon and heavy hydrocarbon gas will begin to thermal cracking, and the overall evolution to dry gas composition, kerogen drying coefficient is obviously higher.

As the pyrolysis process of organic matter goes on, the ratio of methane to ethane increases slowly during the first pyrolysis process of organic matter, but remains stable during the second pyrolysis process. On the contrary, the ratio of ethane to propane remains constant during the first pyrolysis process, but increases rapidly during the second pyrolysis process. Kerogen tends to react more violently in primary pyrolysis than crude oil, which is more obvious at lower heating rates. This means that kerogen has a wider range of hydrocarbon generation and will react before crude oil at low thermal evolution. In addition, kerogen still retains a certain hydrocarbon generating capacity at the high to over-mature stage when crude oil has stopped cracking or is almost exhausted. This may be a way to distinguish crude oil cracking gas from kerogen cracking gas. The natural gas formed by kerogen cracking shows a rapid increase in ln(C$_1$/C$_2$). The formation process of kerogen cracking gas shows the characteristics of rapid increase of ln(C$_1$/C$_2$), and the drying coefficient of kerogen cracking gas is larger in high-over-mature area. The formation of crude oil cracking gas is characterized by the rapid increase of ln(C$_2$/C$_3$).

CONCLUSIONS

(A) According to pyrolysis experiments, the methane production of different hydrocarbon generating parent materials shows a trend of continuous increase, and other hydrocarbon gases all have a gas generation peak, and then the production begins to decline, which is related to the pyrolysis of heavy hydrocarbon gases into methane and non-hydrocarbon gases at high temperature. The time-temperature compensation effect is proved by different linear heating rates.

(B) According to the process of hydrocarbon

generation thermal simulation experiment, the hydrocarbon generation process can be divided into three stages: thermal catalytic oil generation stage dominated by the generation of liquid hydrocarbon substances, wet gas generation stage dominated by the rapid increase in the content of heavy hydrocarbon gas thermal cracking, and over mature stage of organic matter evolution dominated by the generation of methane. In these three stages, the different hydrocarbon generation behaviors of kerogen and crude oil cracking gas are described in detail.

(C) According to the comparison of hydrocarbon generation between kerogen and crude oil, kerogen is more severe in the initial hydrocarbon generation reaction, and the hydrocarbon generation threshold of kerogen is lower than that of crude oil, and the evolution interval of hydrocarbon generation is wider, while the cracking interval of crude oil is more concentrated. Kerogen still retains a certain hydrocarbon generating capacity at high to over mature stage.

REFERENCES

[1] Lu, S. (2010) The kinetics of hydrocarbon isotope fractionation of natural gas and its application. Petroleum Industry Press. 1-165.

[2] Guo, X., Hu, D., Huang, R., Wei, Z. (2020) Progress and prospect of deep and ultra-deep natural gas exploration in the Sichuan Basin. Natural Gas Industry. 40 (05), 1-14.

[3] Li, W., Hu, G., Zhou, J. (2015) Asphalt characteristics and gas accumulation mechanism of Sinian reservoir in Tongwan paleo-uplift, Sichuan Basin. Natural Gas Industry. 35(6), 14-23.

[4] Dai, J. (1993) Characteristics of hydrocarbon and hydrogen isotopes of natural gas and identification of various types of natural gas. Natural Gas Geoscience. 2(3), 140.

[5] Stahl, W. J., Carey, B. D. (1975) Source-rock identification by isotope analyses of natural gases from fields in the Vol Verde and Dclawere Basins, West Texas. Chememical Geology. 16(4), 257-267.

[6] Liu, B., Liu, Y., Liu, Y. (2020) Prediction of low-maturity shale oil produced by in situ conversion: a case study of the first and second members of Nenjiang Formation in the Centeal Depression, southern Songliao Basin, Northeasy China. Petroleum Geology & Experiment. 42(4), 15-27.

[7] Tang, Q., Zhang, M., Zhang, T., Liu, J., Yu, M. (2014) Kinetic pyrolysis simulation of hydrocarbon generation in shale system: A case study on Pearl River Mouth Basin, China. Geochimica. 43(5), 518-528.

[8] Zhao, H., Ma, Z., Zhen, L., Tan, J., Li, Q., Wang, Z., Ning, C. (2020) Geochemical characteristics of hydrocarbon products under thermal simulation of temperature and pressure co-control in finite space. Natural Gas Geoscience. 31(1), 73-83.

[9] Tian, H., Xiao, X., Li, X., Xiao, Z., Shen, J., Liu., D. (2007) Comparison of gas generation and carbon isotope fractionation of mathane from marine kerogen- and crude oil-cracking gases. Geochimica. 36(1), 71-77.

[10] Li, X., Ya, J., Xiao, D. (2019) Kinetic analysis of hydrocarbon generation based on saline lacustrine source rock and kerogen samples in the western Qaidam Basin, China. Original article. (34), 1045-1053.

[11] Wang, Y., Wang, Z., Zhao, C. (2007) Kinetics of hydrocarbon gas generation from marine kerogen and oil: implications for the origin of natural gases in the Hetianhe gasfield, Tarim basin, NW China. 30(4), 339-356.

[12] Zheng, H., Zhang, Y., Jiang, F., Yang, Y., Zhu, S. (2019) Dynamic analysis of hydrocarbon generation and prediction of favorable areas for coal and rock in Huimin area, China. Journal of Chengdu University of Technology (Science & Technology Edition). 46(1), 64-69.

[13] Li, J. (2005). Study of carbon isotopes fractionation during the process of natural gas generation. Daqing Petroleum Institute. Northeast Petroleum University and Lu, S., Daqing.

[14] Zhao, Z., Zhong, N., Li, Y., Zhang, P. (2006) Application of hydrocarbon generating chemical kinetics in the Puguang gas field, NE Sichuan Basim. Petroleum Exploration & Development. 33(6).

[15] Zhang, Q.X., Li, W.J., Zhang, B. (2012) Characteristics and Kinetics of Gaseous Hydrocarbon Generation from Pyrolysis of Crude Oil under High Pressure and High Temperature. Advanced Materials Research. 361, 579-583.

[16] Xiao, F., Wero, T., Wang, X., Guan, X., Wu C. J. (2020) Research on the sequence stratigraphy of the Shaximiao Formation in Chuanzhong-Chuanxi area, Sichuan Basin. Natural Gas Geoscience. 31(9), 1216-1224.

[17] Lu, B. (2015) Shale gas reservoir evaluation of Da'anzhai member in Ziliujing Formation of Lower Jurassic in Eastern Sichuan Basin. Chengdu University of Technology and Zhen, R., C., Chengdu.

[18] Qian, M., Jiang, Q., Li, Z., Li, M., Ma. Y., Shen, B., Yang, Y. (2017) A study on the compositional kinetics of shale hydrocarbon generation under an open system: Taking the Bonan Subsag as an example. Geochimica. 46(2), 149-157.

[19] Wang, Z., Wang, Y., Wu, B. (2016) Characteristics of gas generation and the application of hydrocarbon generation kinetics from low-maturity asphalt in Northwestern Sichaun Basin. Acta Petrolei Sinica. 37(3), 748-753.

Received: **11.11.2021**
Accepted: **04.01.2022**

CORRESPONDING AUTHOR

Hongming Dai
School of Geoscience and Technology,
Southwest Petroleum University,
Chengdu 610500 – China

e-mail: 1026598698@qq.com

© by PSP Volume 31– No. 05/2022 pages 4833-4840 Fresenius Environmental Bulletin

EXPERIMENTAL STUDY ON BLENDING RATIO OF HIGH PERFORMANCE NANOGEL COMPOSITES

Xiang Chen, Anxiang Song, Rui Wang, Xue Wang, Yuanchen Guo*, Yan Sun, Miao Tian, Xinzhou Liu

College of Civil Engineering, Chongqing Three Gorges University, Chongqing 404100, China

ABSTRACT

Ultra-fine cement and nano-silica (NS) are used to prepare high-performance cementitious composite materials (hereinafter referred to as composite materials) to solve the problems of low strength and poor fluidity of cement-based cementitious materials. The orthogonal test is used to determine the flow of composite materials. Tests on properties and strength are carried out. The influence of water to binder ratio, micro-silica fume, fly ash, nano-silica and water reducing agent on the fluidity of composite materials and the mechanical strength of different ages are studied, and the test results are analyzed. The results show that the content of micro-silica fume and water to binder ratio have the most significant influence on the composite material, the content of fly ash and NS are more significant, and the water reducing agent has little effect on the performance of the composite. Under the premise of comprehensively considering the fluidity and the strength of different ages, the optimal ratio is obtained as the water to binder ratio 0.34, microsilica 10%, fly ash 30%, NS 3.5%, and water reducing agent 2.0%.

KEYWORDS:
Nanogel composite, orthogonal test, strength, fluidity, optimal ratio

INTRODUCTION

As can be seen from the microscopic analysis of cement stone, the proportion of calcium silicate hydrate (C-S-H) gels with particle size exceeding 10nm in the hydration products is more than 50%, which belongs to the category of nanoscale. Therefore, the modification of cement-based materials based on nanoscale has caused extensive research [1-4]. In the meantime, due to small size and special properties, nanomaterials can be added to cement materials as admixtures. Common ones include nano-SiO_2 (NS) [5], carbon nano-tubes (CNTs) [6], nano-graphene [7] and nano-$CaCO_3$ (NC) [8], which can effectively improve the deficiency on the performance of cement materials from different aspects.

Among many types of nanomaterials, nano-SiO_2 (NS) is the most widely used in cement and concrete for the following reasons [9-12]:

(1) Excellent Pozzolanic effect. The mechanism of its left use is that the following chemical reactions occur in the hydration reaction process: $SiO_2+Ca(OH)_2 \rightarrow$C-S-H, which can promote the production of more C-S-H gel, and then play a role in compacting the slurry structure and improving the performance of cement-based materials.

(2) Produce nucleation effect. Nano-SiO2 in the dispersed cement slurry has a dual function, not only can be used as the crystal nucleus to promote the generation of more hydration products, but also significantly increase the crystallization site due to the characteristics of large specific surface area.

(3) It has filling effect. Nano silica particles can make up for the deficiency of the original system, can fill the pores formed by the cementitious system, and form a tight cement stone structure.

Due to the three effects above, nano-SiO_2 (NS), while playing the role of filling and crystal nucleus, can react with raw materials and improve the structure of interface transition zone [13], which plays an important role in significantly improving the properties of cement-based materials and is widely used in the preparation of construction engineering materials.

At present, domestic and foreign scholars have conducted a large number of studies on the application and performance of nanomaterials. Mohseni E et al. [14] have studied the influence of single and composite effects of nano-SiO_2, nano-Al_2O_3 and nano-TiO_2 on the related properties of self-compacting mortar containing fly ash. Zhang Yan et al. [15] used the coupling effect of NS and CNTs to develop cement-based surface strengthening materials based on nano-modification. Zhou L M et al. [16] optimized the interface structure and cement stone structure by adding nano-SiO_2 into polymer modified mortar. Gao X et al. [17] found that nanometer SiO_2 particles in HPNCC play the roles of filling and catalyzing, so as to improve the interface binding ability between matrix and fiber, and further enhance its mechanical properties.

Senff and Bernal[11][18] found that the fluidity of mortar in cement materials decreased with the addition of nanoparticles, the main reason that is the small particle size of nanomaterials reduced the free water content of slurry, and proposed that more water-reducing agent should be added after the addition of nano-SiO_2 to meet the workability requirements of mortar.

Although common cement materials can meet some engineering needs, they still need to be improved in the engineering with higher requirements on strength, flow performance and permeability[19-22]. This paper mainly makes use of the excellent hydration activity and small fineness of ultrafine cement and combines with the fine aggregates such as nano silica, fly ash and micro silicon powder to prepare composite materials, so as to improve the microscopic pores of composite materials and enhance the properties of composite materials. The effects of water to binder ratio, fly ash, silica powder, water-reducing agent and nano-silica content on the fluidity and mechanical properties of nano-cementitious composite materials were studied by orthogonal test, and the maximum influence range of each influencing factor on different indexes and the optimal combination of fluidity and mechanical properties were obtained.

MATERIALS AND METHODS

Ultrafine cement: The ultrafine cement used in the test adopts a kind of ultrafine Portland cement independently developed by Angong Group of Singapore.D50<7 m, specific surface area 500-700 m2/kg.

Nanometer silicon dioxide: Beijing Deke Island Gold Technology Co., LTD provides nanometer silicon dioxide, component: 60.084, density: 2.2g/cm3, purity: 99.9%. Other technical indicators are shown in Table 1.

Micro silicon powder and fly ash: micro god in Wuhan science and technology development co., LTD., provide micro silicon powder and I grade fly ash, its chemical composition as shown in table 2 and table 3 respectively.

Orthogonal experimental design. In order to explore the influence of water-binder ratio (A), fly ash (B), micro-silica powder (C), nano-silica (D) and water-reducing agent content (E) on the fluidity of composite materials and their flexural and compressive strength at 7d and 28d, the L25(55) orthogonal tests were conducted. The corresponding factor-level is shown in Table 4.

Preparation and curing conditions of specimens. In this experiment, JJ-160 cement mortar mixer was used to stir the mixture. Firstly, the stirring pot and the blades were wiped. Ultra-fine cement, fly ash, micro-silicon powder, nano-silicon dioxide and other powder materials were dry mixed for 60s at a slow speed. Then, water and water-reducing agent were evenly mixed and added.

TABLE 1
Technical index of NS

Type	Appearance	mean grain size /(nm)	specific surface area /(m^2/g)	PH	Fusion point/℃	Boiling point/℃	Rigidity	Thermal conductivity/ (W/(m.k))
DK-SO_2-30	White powder	30	200	5-7	1723	2230	4.5	4

TABLE 2
Chemical composition of micro silicon powder

Composition	CaO	SiO_2	Al_2O_3	MgO	K_2O	SO_3	BaO	Fe2O3	Cl-1
Content/%	0.16	92.24	1.29	0.52	0.3	0.26	0.2	0.16	0.009

TABLE 3
Chemical composition of Fly ash

Composition	CaO	SiO_2	Al_2O_3	MgO	SO_3	K_2O	Na_2O	Fe_2O_3	TiO_2	P_2O_5
Content/%	6.66	42.34	25.84	1.17	0.95	1.05	1.13	5.46	1.07	0.38

Note: Water reducing agent, polycarboxylate superplasticizer is used. Water, drinking water.

TABLE 4
Factors-level table

Level \ Factor	Water to binder ratio	Fly ash/%	Microsilica /%	NS/%	water reducing agent /%
1	0.34	30	10	1.5	1.0
2	0.36	35	15	2.5	1.5
3	0.38	40	20	3.5	2.0
4	0.40	45	25	4.5	2.5
5	0.42	50	30	5.5	3.0

TABLE 5
Mixture proportion and test results of Composite material

Num	Water to binder ratio	Fly ash	Microsilica	NS	Water reducing agent	Fluidity /mm	7d		28d	
							Bending strength /MPa	Compressive strength /MPa	Bending strength/MPa	Compressive strength/MPa
S1	0.34	30%	10%	1.5%	1.0%	173	7.8	39.1	10.4	73.5
S2	0.34	35%	15%	2.5%	1.5%	199	6.9	45.7	7.1	52.8
S3	0.34	40%	20%	3.5%	2.0%	211	6.0	38.9	6.2	65.3
S4	0.34	45%	25%	4.5%	2.5%	263	6.3	30.2	6.4	60.0
S5	0.34	50%	30%	5.5%	3.0%	225	6.4	31.4	6.6	49.5
S6	0.36	30%	15%	3.5%	3.0%	283	7.2	39.2	7.4	44.4
S7	0.36	35%	20%	4.5%	1.0%	154	3.9	32.4	5.8	46.3
S8	0.36	40%	25%	5.5%	1.5%	158	5.7	31.0	6.1	45.0
S9	0.36	45%	30%	1.5%	2.0%	274	6.9	27.1	7.1	51.1
S10	0.36	50%	10%	2.5%	2.5%	350	7.7	36.0	7.8	49.0
S11	0.38	30%	20%	5.5%	2.5%	220	5.9	36.8	6	40.8
S12	0.38	35%	25%	1.5%	3.0%	338	5.2	33.3	6.9	37.4
S13	0.38	40%	30%	2.5%	1.0%	211	5.9	35.6	7.9	43.7
S14	0.38	45%	10%	3.5%	1.5%	221	5.6	36.9	5.8	51.2
S15	0.38	50%	15%	4.5%	2.0%	245	5.5	32.2	6.5	44.7
S16	0.4	30%	25%	2.5%	2.0%	258	7.6	31.2	7.7	39.8
S17	0.4	35%	30%	3.5%	2.5%	305	6.9	27.9	7.1	39.1
S18	0.4	40%	10%	4.5%	3.0%	315	7.1	39.3	7.2	39.8
S19	0.4	45%	15%	5.5%	1.0%	180	4.6	29.5	5.1	42.8
S20	0.4	50%	20%	1.5%	1.5%	289	5.4	32.7	6.4	39.0
S21	0.42	30%	30%	4.5%	1.5%	229	4.4	42.3	5.7	42.7
S22	0.42	35%	10%	5.5%	2.0%	229	7.7	37.6	7.8	41.4
S23	0.42	40%	15%	1.5%	2.5%	400	6.0	36.9	7.4	34.2
S24	0.42	45%	20%	2.5%	3.0%	415	4.7	32.3	4.9	38.5
S25	0.42	50%	25%	3.5%	1.0%	221	4.4	35.7	4.5	36.2

Test contents and methods. Its fluidity and mechanical properties were tested according to different mix ratios. The fluidity and mechanical properties of composite materials (flexural strength and compressive strength) shall be implemented according to relevant specifications of cement cementitious materials.

This experiment adopts the six factors, five levels of orthogonal test table, the corresponding factors - level according to table 3 for orthogonal experimental design, test for composite material under different ratio of fluidity and mechanical strength, further analysis of water to binder ratio, fly ash, micro silicon powder, NS and water reducing agent on the properties of composite materials, in order to get the optimal mixture ratio. The test ratio and test results are shown in Table 5.

The range analysis. Range analysis method: R method for short. Kjm is the sum of test indexes corresponding to the level of factor m in column j and $\overline{K_{jm}}$ is the average value of test indexes. According to the size of K_{jm}, the optimal level of factor J and the horizontal combination of each factor can be judged, which is the optimal combination. R_j is the range of factors in column j, that is, the difference between the maximum and minimum average index values at each level of factors in column j, as Eq. 1.

$$R_j = \max(\overline{K_{j1}}, \overline{K_{j2}}, \ldots \overline{K_{jm}}) - \min(\overline{K_{j1}}, \overline{K_{j2}}, \ldots \overline{K_{jm}}) \quad \text{(Eq. 1)}$$

R_j reflects the variation range of the test index when the level of the factor in column j changes. The larger R_j is, the greater the influence of this factor on the test indicators is, and therefore the more important it is. So according to the magnitude of R_j, we can judge the priority of the factors.

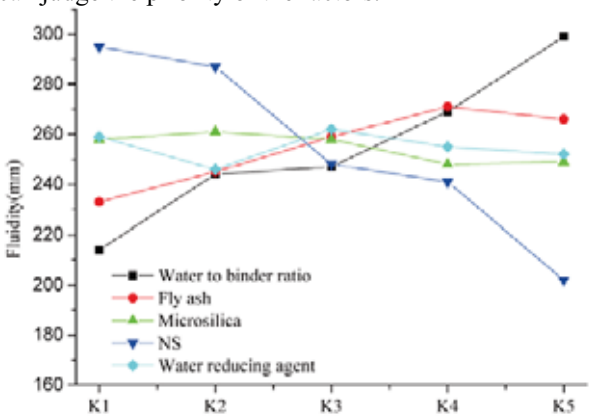

FIGURE 1
Fluidity effect curve

RESULTS AND DISCUSSION

Analysis of fluidity test results. The results of fluidity range analysis are shown in Table 6. It can be seen from Table 6 that NS content has the greatest influence on fluidity, while micro silicon powder content has the least influence.It can be seen from the fluidity effect curve (Figure 1) that the fluidity of composite materials increases with the increase of fly ash content and water to binder ratio. In contrast, microsilica powder

TABLE 6
The range analysis of fluidity/mm

Influence factor		Water to binder ratio	Fly ash	Microsilica	NS	Water reducing agent
Fluidity	K1	214	233	258	295	259
	K2	244	245	261	287	246
	K3	247	259	258	248	262
	K4	269	271	248	241	255
	K5	299	266	249	202	252
	R	85	37	14	92	16

Note: K_i is the average value of test indexes corresponding to the each level of every factor.
R:Range

and NS have a gradual decrease in fluidity due to the constant increase of mixing amount, among which the fluidity curve of micro-silicon powder is relatively gentle. The trend of fluidity curve corresponding to the amount of water-reducing agent shows a trend of first decreasing and then increasing. By adding an appropriate amount of NS into cement-based materials, the pores of the slurry can be filled with its extremely small particle size, increasing the amount of free water and achieving the lubrication effect [23], which is conducive to improving the fluidity of the slurry. Secondly, the influence of water to binder ratio is also significant. The larger the water to binder ratio is, the more water there is, the higher the fluidity will be. Fly ash content is in the third place in the primary and secondary factors. Due to its special microbead effect, it significantly improves the fluidity of composite materials. Water reducer and micro - silicon powder are in the bottom. From the test data, it is found that when the fluidity is lower than 173mm, the fluidity is generally insufficient and vibration compaction is difficult, which is not conducive to the practical application of the project. When the fluidity is 173-211mm, the fluidity is better and compacted, which is beneficial to the construction. When the fluidity is greater than 211mm, more bubbles appear in the specimen, which is not conducive to the development of mechanical strength. If the flow is too large or too small, other properties of composite materials will be affected. NS dosage and water to binder ratio can be used as important evaluation indexes for the fluidity of composite materials during the test.

7d Analysis of strength test results. According to the range analysis results on day 7 (Table 7), it can be seen that the amount of micro-silicon powder has the greatest influence on the bending strength of day 7, while the amount of water-reducing agent has the least influence. The content of fly ash and silica powder is an important factor influencing the compressive strength of 7d, while NS content has the least influence.According to the analysis in Figure 2 (a), the curve chart of flexural strength corresponding to micro-silicon powder, water-reducing agent content and water to binder ratio in the composite material shows an overall trend of decline first and then rise with the continuous increase of horizontal factors. Although fly ash can increase the workability of the slurry, with the increase of fly ash content in the slurry, its early strength has a great impact, and the overall trend of decline; With the increase of NS dosage, the flexural strength increases first and then decreases. Therefore, the optimal ratio of flexural strength for 7 days is 0.34 water to binder ratio, 10% micro-silicon powder, 30% fly ash, NS2.5%, and 2.5% water-reducing agent.

It can be seen from Figure 2 (b) that the increase of water to binder ratio and micro-silica powder content has the same influence law on the compressive strength, which presents an overall trend of first decreasing and then increasing. However, as the dosage of water-reducing agent and NS increases gradually, the overall effect curve shows a trend of first rising and then falling. With the increase of fly ash content there is a downward trend. Therefore, the optimal ratio of compressive strength for 7d is 0.34 water to binder ratio, 10% micro-silicon powder, 30% fly ash, 2.5% NS and 1.5% water-reducing agent.

In summary, when the water to binder ratio of the composite is 0.34, the content of micro-silicon powder is 10%, the content of fly ash is 30%, and the content of NS is 2.5%, the mechanical properties are optimal at the age of 7 days. At this time, 1.5% or 2.5% of the water reducer is taken. When 1.5% of the water reducer is taken, the bending strength on day 7 is 4.0% lower than that on day 7, and the compressive strength on day 7 is 5.3% higher than that on day 7, so 1.5% of the water reducer is taken. Therefore, the optimal ratio of mechanical properties for 7d is 0.34 water to binder ratio, 10% micro-silicon powder, 30% fly ash, NS2.5% and 1.5% water-reducing agent.

Analysis of 28d strength test results. According to the range analysis results on 28 days (Table 8), it can be seen that the dosage of micro silicon powder and the dosage of water-reducing agent are the factors that have the largest and the smallest influence degree on the bending strength on 28 days respectively. The water to binder ratio had a significant influence on the compressive strength of 28d, while NS content was not an important factor.

It can be seen from Figure 3 (a) that as the water to binder ratio and fly ash content in the composite material increase continuously, the curve shows an overall downward trend with a small increase in the

middle. With the increase of micro silicon powder content, water-reducing agent content and NS content, the curve shows a trend of decreasing first and then increasing. Therefore, the optimal ratio of the flexural strength for 28 days is 0.34 water to binder ratio, 10% micro-silicon powder, 30% fly ash, NS1.5% and 2.5% water-reducing agent.

It can be seen from Figure 3 (b) that there is a negative correlation between the water to binder ratio of the composite and its corresponding compressive strength. The compressive strength curve corresponding to fly ash content shows a trend of first rising and then falling with the increase of horizontal factor. The increase of micro silicon powder content, NS content and water-reducing agent content shows similar curve trend, which first decreases and then slows down. Therefore, the optimal ratio of 28d compressive strength is 0.34 water to binder ratio, 10% micro-silicon powder, 45% fly ash, NS3.5% and 1.0% water reducer.

TABLE 7
The range analysis of 7d strength/Mpa

Influence factor		Water to binder ratio	Fly ash	Microsilica	NS	Water reducing agent
Bending strength	K1	6.68	6.58	7.18	6.26	6.12
	K2	6.28	6.12	6.04	6.56	6.24
	K3	5.62	6.14	5.18	6.02	5.58
	K4	6.32	5.62	5.84	5.44	6.50
	K5	5.44	5.88	6.10	5.90	5.90
	R	1.24	0.96	2.00	1.12	0.66
Compressive strength	K1	37.06	37.72	37.78	33.82	32.50
	K2	33.14	35.38	36.70	36.16	36.92
	K3	34.96	36.34	34.62	35.72	36.00
	K4	32.12	31.20	32.28	35.28	35.06
	K5	36.96	33.60	32.86	33.26	33.76
	R	4.94	6.52	5.50	2.34	4.42

Note: K_i is the average value of test indexes corresponding to the each level of every factor.
R:Range

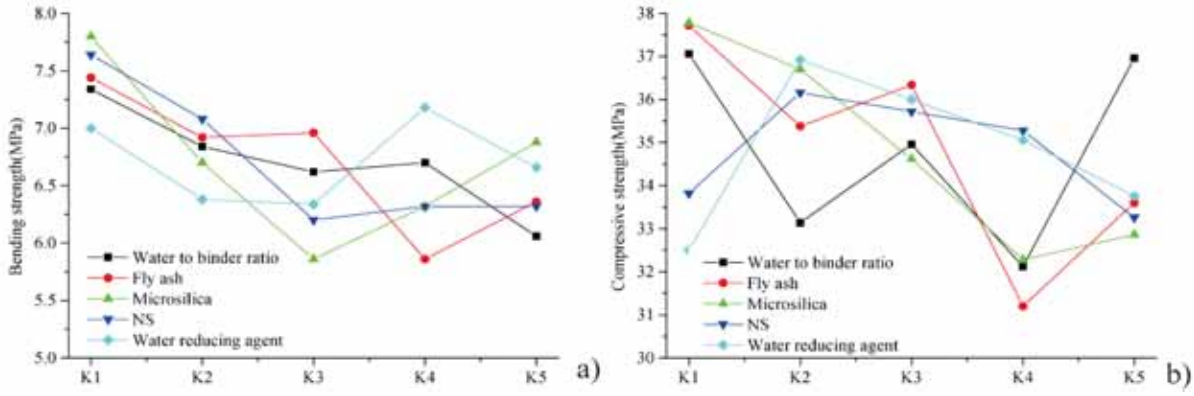

FIGURE 2
7d intensity effect curve: a) Bending Strength, b) Compressive Strength

TABLE 8
The range analysis of 28d strength/MPa

Influence factor		A	B	C	D	E
Bending strength	K1	7.34	7.44	7.80	7.64	7.00
	K2	6.84	6.92	6.70	7.08	6.38
	K3	6.62	6.96	5.86	6.20	6.34
	K4	6.70	5.86	6.32	6.32	7.18
	K5	6.06	6.36	6.88	6.32	6.66
	R	1.28	1.58	1.94	1.44	0.84
Compressive strength	K1	60.22	48.24	50.98	47.04	48.16
	K2	47.16	43.40	43.78	44.76	44.14
	K3	43.56	45.60	45.98	47.24	47.44
	K4	40.10	48.72	43.68	46.70	45.70
	K5	38.60	43.68	45.22	43.90	44.20
	R	21.62	5.32	7.30	3.34	4.02

Note: K_i is the average value of test indexes corresponding to the each level of every factor.
R:Range

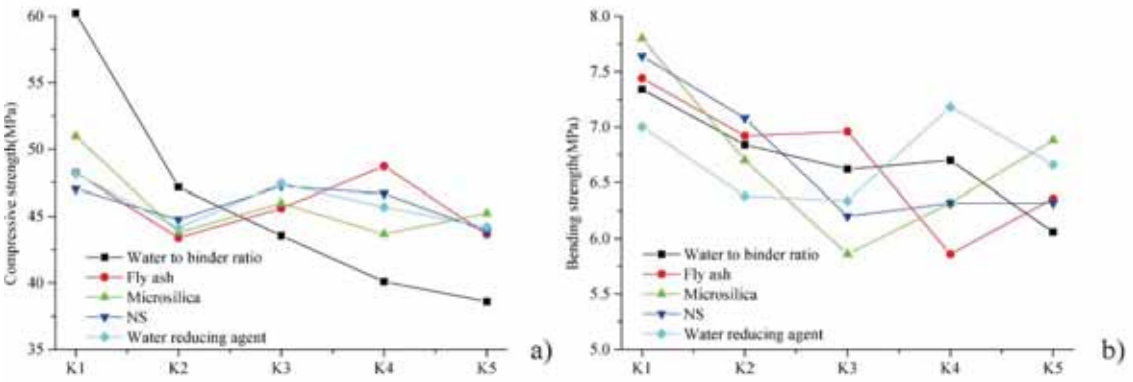

FIGURE 3
28d intensity effect curve: a) Bending strength, b) Compressive strength

Through the above comprehensive analysis, when the water to binder ratio of the composite material is 0.34 and the micro-silica powder content is 10%, the flexural strength and compressive strength corresponding to 28d can reach the optimal value. In 28 d flexural strength, compressive strength of the primary and secondary factors of sorting the second and third respectively, dosage of fly ash are more significant influence, 30% or 45% dosage of fly ash, select 30% dosage of fly ash on mechanical properties of the composites were analyzed, and the analysis found that the flexural strength is more than 45% 27.0%, but compressive strength is less than 45% 1.0%, so take 30% dosage of fly ash; At 28d, the primary and secondary factors of the compressive strength and flexural strength of NS content were ranked the third and fifth respectively. At this time, the NS content was 1.5% or 3.5%. When the NS content was 1.5%, the flexural strength was 23% more than that of 3.5%, but the compressive strength was 0.5% less than that of 3.5%, so the NS content was 1.5%. At 28d, the primary and secondary factors of anti-bending and compressive strength of water reducer were ranked the fifth and the fourth respectively. At this time, the water reducer content was taken as 2.5% or 1.0%. When the water reducer content was taken as 2.5%, the bending strength was 2.6% higher than that of 1.0%, but the compressive strength was 5.1% lower than that of 1.0%, so the water reducer content was taken as 1.0%. Therefore, the optimal ratio of 28d flexural strength and compressive strength is 0.34 water to binder ratio, 10% micro-silicon powder, 30% fly ash, NS1.5% and 1.0% water reducer.

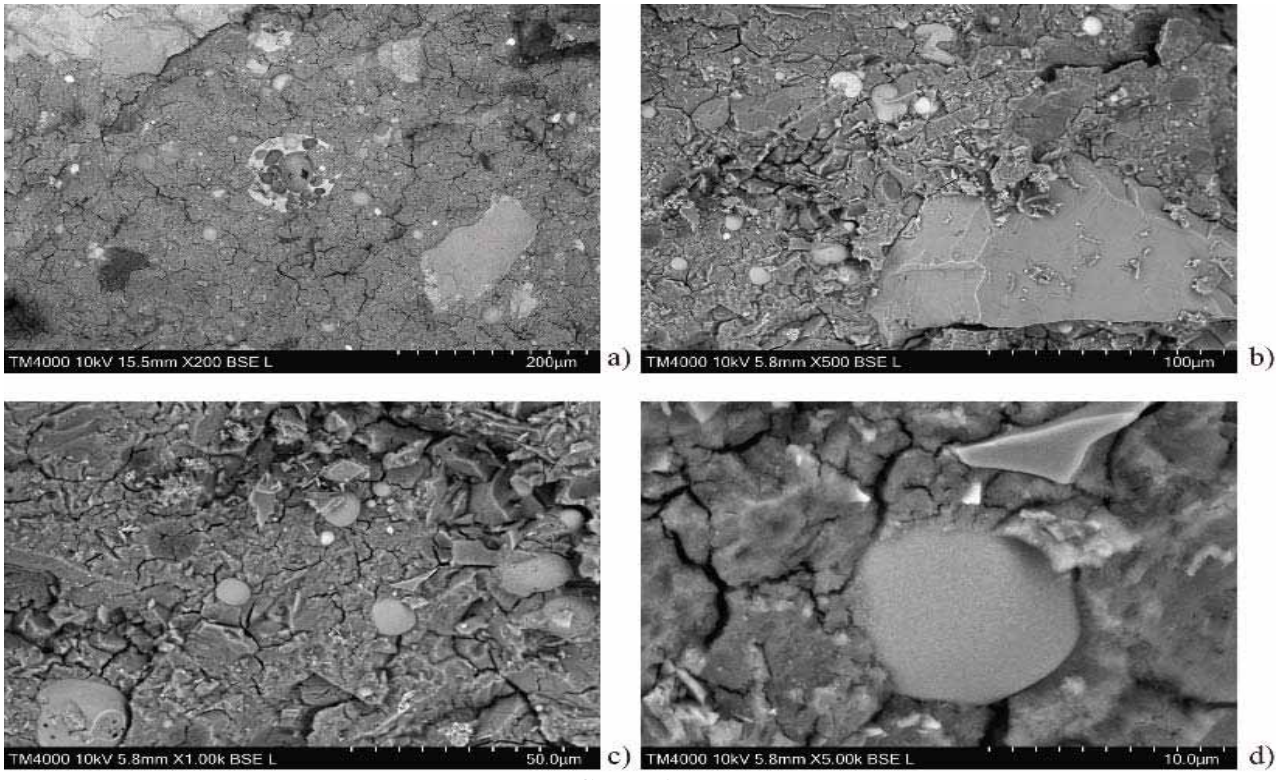

FIGURE 4
SEM micrographs of mortar mix at 56 days

Micro-Analysis. As the Figure 4 shows of the SEM picture results of 28 days after hydration. When the hydration reaches 28 days, the hydration amorphous products generated fill into the cracks to reduce the crack and make the texture more dense and compact. It is rare to see pure fly ash sphere exposed on the substrate surface. By analyzing the microstructure, it can be seen that silica powder, NS and fly ash can increase the efficiency and densification of the microstructure of hardened cementitious slurry, and the synergistic effect of multi-components can significantly improve the durability of the material, which has a good application prospect.

Comprehensive analysis of composite properties. Based on the analysis above, the best combination of strength of 7d and 28d can be obtained. 7d: water to binder ratio 0.34, micro-silicon powder 10%, fly ash 30%, NS2.5%, and water-reducing agent 1.5%.28d: Water to binder ratio 0.34, micro-silicon powder 10%, fly ash 30%, NS1.5%, water-reducing agent 1.0%. Considering that the composite material should have appropriate fluidity, the water to binder ratio 0.34, micro-silicon powder 10%, fly ash 30%, NS3.5% and water-reducing agent 2.0% were selected.

CONCLUSION

In this paper, ultra-fine cement is selected as the main cement material, supplemented by mineral admixtures and nanomaterials, and orthogonal experimental design is adopted to study the effects of water to binder ratio, fly ash, micro-silicon powder, water-reducing agent and NS content on the corresponding fluidity and strength of composite materials, and the following conclusions are drawn:

(1) Under the premise of considering the strength of 7d, strength of 28d and fluidity, the optimal ratio was obtained through 25 groups of mixing ratio: water to binder ratio 0.34, 10% micro-silicon powder, NS3.5%, 2.0% water reducer and 30% fly ash.

(2) NS content and water to binder ratio have a great influence on the fluidity of composite materials. During the test, it is found that the greater the fluidity is, the lower the flexural strength and compressive strength will be. In order to facilitate the construction and ensure the strength, the fluidity should be controlled within 173-211mm.

(3) The influence of fly ash and NS content on the flexural strength of 28d is much higher than the compressive strength;At different ages of 7d and 28d, the content of water-reducing agent in the composite material has a greater influence on the compressive strength than the flexural strength.

(4) In general, water to binder ratio and micro-silicon powder content have the most significant influence on the composite material, NS and fly ash content are relatively significant, and water-reducing agent has little influence on the performance of the composite material. With the continuous update of the manufacturing technology, the appearance of ultra-fine aggregates will become one of the focus of the research. The excellent properties of nanomaterials also provide new directions and ideas for the further improvement of the properties of high-performance cementitious composite materials, and their application prospect is very broad.

ACKNOWLEDGEMENT

This project was supported by the National Natural Science Foundation Project of China (52078089), Chongqing Wanzhou District Technology Innovation and application development project (wzstc-2019031), Basic science and frontier technology research project of CQ (cstc2017jcyjAX0085), Scientific and Technological Research Program of Chongqing Municipal Education Commission (K201901201,KJQN201901233, KJQN202001210 and KJQN201901240), Chongqing Talents Program(CQYC201905086), Chongqing Undergraduate Innovation Training Program (202110643015, SXAPGC19YB11P and YJSKY2007).

REFERENCES

[1] Gunasekara, C., Zhou, Z. Y., Law, D.W., Sofi, M., Setunge, S., Mendis, P. (2020) Microstructure and strength development of quaternary blend high-volume fly ash concrete. Journal of Materials Science. 55(15), 6441-6456.

[2] Anković, K., Stanković, S., Bojović, D., Stojanović, M., Antić, L. (2016) The influence of nano-silica and barite aggregate on properties of ultra high performance concrete. Construction and Building Materials. 126(NOV.15), 147-156.

[3] Ghafari, E., Costa , H., Júlio, E., Portugal, A., Durães, L. (2014) The effect of nanosilica addition on flowability, strength and transport properties of ultra high performance concrete. Materials and Design. 59(jul.), 1-9.

[4] Hosseini, P., Abolhasani, M., Mirzaei, F., Anbaran, M. R.K., Khaksari, Y., Famili, H. (2018) Influence of Two Types of Nanosilica Hydrosols on Short-Term Properties of Sustainable White Portland Cement Mortar. Journal of Materials in Civil Engineering. 30(2), 04017289.

[5] Silvestre, J., Silvestre, N., Brito, D, J. (2016) Review on concrete nanotechnology. European Journal of Environmental and Civil Engineering. 20(3/4),455-485.

[6] Lu, Z.Y., Hou, D.S., Ma, H.G., Fan, T.Y., Li, Z.J. (2016) Effects of graphene oxide on the properties and microstructures of the magnesium potassium phosphate cement paste. Construction and Building Materials. 119, 107-112.
[7] Camiletti, J., Soliman, A.N., Nehdi, M. L. (2013) Effects of nano- and micro-limestone addition on early-age properties of ultra-high-performance concrete. Materials and Structures. 46(6), 881-898.
[8] Maria, S., Gdoutos, K., Metaxa, S.Z., Shah, S.P. (2010) Highly dispersed carbon nanotube reinforced cement based materials. Cement and Concrete Research. 40(7), 1052-1059.
[9] Kong, D.Y., Du, X.F., Wei, S., Zhang, H., Yang, Y., Shah, S.P. (2012) Influence of nano-silica agglomeration on microstructure and properties of the hardened cement-based materials. Construction and Building Materials. 37, 707-715.
[10] Güneyisi, E., Gesoglu, M., Al-Goody, A., İpek, S. (2015) Fresh and rheological behavior of nano-silica and fly ash blended self-compacting concrete. Construction and Building Materials. 95(Oct.1), 29-44.
[11] Bernal, J., Reyes, E., Massana, J., León, N., Sánchez, E. (2018) Fresh and mechanical behavior of a self-compacting concrete with additions of nano-silica, silica fume and ternary mixtures. Construction and Building Materials. 160(JAN.30), 196-210.
[12] Jiang, H.Q., Yi, H.S., Erol, Y., Liu, S.W, Qiu, J.P. (2020) Ultrasonic evaluation of strength properties of cemented paste backfill: Effects of mineral admixture and curing temperature. Ultrasonics. 100, 105983-105983.
[13] Li, G. S., Gao, G., Zhu, J.P., Feng, C.H. (2018) Research progress of nano material in cement based material. New Chemical Materials. 46(06), 15-19.
[14] Mohseni, E., Miyandehi, B.M., Yang, J., Yazdi, M.A. (2015) Single and combined effects of nano-SiO 2 , nano-Al 2 O 3 and nano-TiO 2 on the mechanical, rheological and durability properties of self-compacting mortar containing fly ash. Construction and Building Materials. 84(1), 331-340.
[15] Zhang, Y., Li ,X.G., Cheng, Y.F., Liu, H. Q. (2017) Study on the Cooperative Effect of Nano-silica and Carbon Nanotubes as Additives of Cement-based Materials. Materials Reports. 31(A02), 410-412.
[16] Zhou, L.M., Wang, C., Li, D.L., Yin, J.Q., Zhang, H.B., Luo, Y.L. (2014) Influence of nano-SiO_2 on polymer-modified cement-based materials. Journal of Shenzhen University: Science and Engineering. 31(3), 227-232.
[17] Gao, X., Li, H.Q,. Xu, L.S.(2013) Compressive Strength and Flexural Properties of High Performance Nano-Binder Cementitious Composites. Applied Mechanics & Materials. 275-277, 2064-2068.
[18] Senff, L., Hotza, D., Lucas, S., Ferreira, V.M., Labrincha, J, A (2012). Effect of nano-SiO 2 and nano-TiO 2 addition on the rheological behavior and the hardened properties of cement mortars. Materials Science & Engineering A. 532(Jan.15), 354-361.
[19] Ehsan, G., Mahdi, A., Hugo, C., Eduardo, J. (2015) Influence of nano-silica addition on durability of UHPC. Construction and Building Materials. 94, 181–188.
[20] Li, L.G., Huang, Z.H., Zhu, J., Kwan, A.K.H., Chen, H.Y. (2017) Synergistic effects of micro-silica and nano-silica on strength and microstructure of mortar. Construction and Building Materials. 140(JUN.1), 229-238.
[21] Rupasinghe, M., Nicolas, R.S., Mendis, P., Sofi, M., Ngo, T. (2017) Investigation of strength and hydration characteristics in nano-silica incorporated cement paste. Cement and Concrete Composites. 80, 17-30.
[22] Shaikh, F.U.A., Supit, S.W.M., Sarker, P.K. (2014) A study on the effect of nano silica on compressive strength of high volume fly ash mortars and concretes. Materials and Design. 60, 433-442.
[23] Huang, C.L., Wang, D.M., Tian, H.W.(2018) Research Progress of the Effect of Nanosilica on the Fluidity of Cement-based Materials. Materials Review. 458-461,465.

Received: **12.11.2021**
Accepted: **04.01.2022**

CORRESPONDING AUTHOR

Yuanchen Guo
College of Civil Engineering,
Chongqing Three Gorges University,
666 Tianxing Road, Wanzhou District,
Chongqing City – China

e-mail: gyc1982@aliyun.com

© by PSP Volume 31– No. 05/2022 pages 4841-4850 Fresenius Environmental Bulletin

SOURCE APPOINTMENT AND ECOLOGICAL RISK ASSESSMENT OF HEAVY METALS IN DUST FROM COPPER-SILVER MINING AREAS BASED ON PMF

Chen Meng[1,2,3], Naiping Song[1,2,3,*], Jianmin Yue[2], Yun Ma[1], Daoqing Chang[1,2,3]

[1]Breeding Base for State Key Laboratory of Land Degradation and Ecological Restoration in Northwest China, Ningxia University, Yinchuan 750021, China
[2]Key Laboratory for Recovery and Restoration of Degraded Ecosystem in North-western China of Ministry of Education, Ningxia University, Yinchuan 750021, China
[3]College of ecological environment, Ningxia University, Yinchuan 750021, China

ABSTRACT

To understand pollution importance, risks, and sources of heavy metals in dust-fall materials around the Leixin copper-silver mining area in Ningxia, 30 sample sites were set within 2 km of the mining area. The dust-fall materials were collected in April, June, and August of 2020; the levels and pollution characteristics of eight heavy metals carried by the dust were determined. The potential ecological risk indexes evaluated the regional ecological risk, and the positive matrix factorization (PMF) model analyzed the source analysis of all eight heavy metals in the dust from the mining area. Those results showed that: 1) The over-standard rates of Cd, As, Cu, Ni, Cr, Hg, Pb, and Ag in atmospheric dust within 2 km with tailings pile at the center were 81.3%, 52.1%, 47.9%, 40.6%, 30.2%, 1.1%, 37.5%, and 100%, respectively. All eight metals showed high variation within the region. There were a variety of pollution sources in this area; 2) the average geo-accumulation indexes for Cu, Ni, Cr, and Pb all exceeded 5, which indicated a state of extreme pollution. All samples in the study area presented high potential ecological risks, among which the ecological risk levels of Cr, Ni, As, Pb, and Cd elements were minor, though the high accumulation of Hg and Cu caused extremely high ecological risks. 3) PMF results showed that the proportion of heavy metals in the dust from the copper and silver mining area was: Industrial activity (32.2%) > copper and silver tailings pollution (22.8%) > atmospheric dust (21.8%) > mixed pollution (18.4%) > transportation (4.8%). Among those, Pb came primarily from transportation, Cu and As were due to accumulation from copper and silver tailings, Cd and Hg came primarily from atmospheric dust. Ni and Cr came from industrial activities such as mining, while Hg, As, and Ag were primarily due to myriad pollution sources such as household waste, agriculture, and plastic film mulching. Both mining and open-pit accumulation of tailings caused heavy metal pollution in the mining region dust. By analyzing the distribution characteristics and sources of heavy metal levels in the dust fall and its risk assessment, the main factors influencing the wind erosion diffusion pollution of open-pit tailings were found. These results will provide the scientific basis for ameliorating heavy metal pollution and safeguarding environmental safety.

KEYWORDS:
PMF, heavy metal source analysis, ecological risk assessment, metal mining area

INTRODUCTION

Heavy metal pollution caused by industrial production, coal burning, atmospheric deposition, transportation, and household waste disposal is an important problem that restricts construction of ecological environments [1-3]. Heavy metal pollutants represent the primary soil contaminants, degrade with difficulty, possess high toxicity, and tend to bioaccumulate [4]. As the main source and indirect carrier of pollutants [5], atmospheric dust not only pollutes the environment, but also introduces heavy metal pollutants into soils, waterways, and other environments. In doing so, these pollutants enter the food chain with plants and pose significant threats to ecological safety and human health [6]. Recently, studies on falling atmospheric dust have focused primarily on urban streets; however, relatively few studies have been conducted on heavy metal pollution caused falling dust in tailing accumulation areas. As a result, the characteristics, risk assessment, and source apportionment of heavy metal pollutants in dust fall materials in tailing accumulation areas merit attention for the prevention and control of heavy metal pollution, agricultural economy, and sustainable ecological environment development.

Positive matrix factorization (PMF) is a commonly used model for heavy metal source apportionment [7-8]. Currently, PMF sees wide use in the source apportionment of atmospheric dust, water pollution, soil pollution, and sediments [9]. Com-

pared with previous heavy metal source apportionment methods, PMF increases the readability and interpretability of source apportionment results by adding factor fraction and non-negative load constraints [10]. The study results implied that PMF analyzed the pollution sources well, and gave the contribution rate of each heavy metal element [11]. Currently, research on using PMF for heavy metal source apportionment has focused mostly on urban atmospheric loading belts [12], mining soils [13], water sediments [14], and farmland soils [15]. In contrast, relatively few studies have been reported on heavy metals in dusts from mine areas and tailing accumulation areas.

In this study, levels of Cd, As, Cu, Ni, Cr, Hg, Pb, and Ag in the Yaoxianzi copper-silver mining area in Ningxia were determined. By calculating the geo-accumulation index, the potential ecological risk index, and using PMF to perform heavy metal source apportionment, the risk assessment of heavy metal pollution in the study area was conducted. Our study provides the scientific basis and data support for tailings heap treatment, human health protection, and regional environmental pollution prevention and control.

MATERIALS AND METHODS

Overview of the study area. Our study area was located in the Leixin copper-silver mining area in Yaoxianzi area, Zhongwei, Ningxia Province. The mining area is located at the northern foot of Xiangshan in Zhongwei, Ningxia Province. It features a typical continental arid climate, with hot summers, cold winters, and windy sand. The average annual temperature is 8.5 °C, and most of the rainfall occurs in May. The topographic relief is large and the altitude ranges from 1550–1744 m (elevation change, 194 m). The soil in this area is alkaline, the wind direction comes primarily from the south, and the wind speed is high, frequently exceeding 10 m/s and reaching speeds up to 21 m/s. Vegetation in the study area is dominated by dwarf shrubs and herbaceous plants, with low biodiversity and a fragile ecological environment that includes red sand, cat's head thorn, and hog's hair cabbage. The main fruit crop is the selenium arene melon.

Dust fall collection and heavy metal determination. In February 2020, according to the land use pattern, topographic features, and the falling direction of pollutants in the study area, a total of 34 sample points were laid out in different directions within 2 km of the tailing accumulation reservoir. Three dust removal cylinders were placed at each sample site at 5 m intervals. The dust removal cylinders were PVC pipe, 20 cm tall, and an inner diameter of 15 cm. All the dust removal cylinders were placed at least 10 cm above the ground. GPS marked the geographic coordinates of each point (Figure 1); the environmental conditions, topographic features, and vegetation coverage of each sample point were investigated and recorded. The dust fall materials were collected every two months (April, June, and August) in 250 x 180 mm Ziplock bags, marked and repeated, sealed, and brought back to the laboratory for processing. Plant residues and other impurities were removed using a 2 mm nylon screen. Approximately 0.5 g of the samples were weighed and ground with an agate mortar for later use. Levels of Cd, As, Cu, Ni, Cr, Hg, Pb, and Ag in the dust material were determined by inductively coupled plasma-mass spectroscopy (ICP-MS). The detection limits for each element were 0.007, 0.016, 0.013, 0.034, 0.013, 0.0002, 0.008, 0.019 ug/L, respectively.

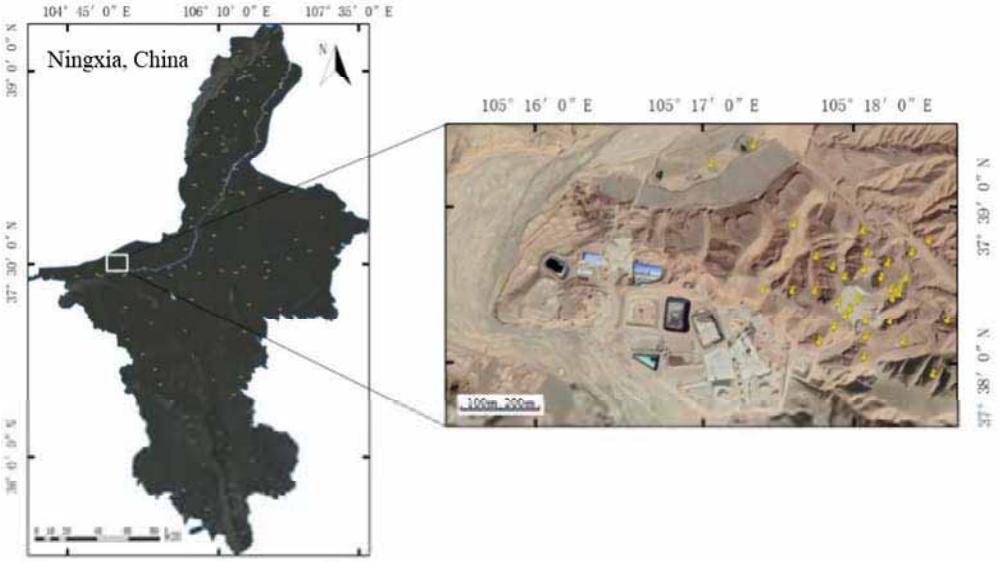

FIGURE 1
Study area and location of sampling points

Geo-accumulation index. Muller proposed the geo-accumulation index method [16] in 1969. According to the heavy metal level measured and the soil background value of the area, the geo-accumulation index was calculated and graded [17]. The geo-accumulation index quantitatively evaluates the heavy metal level in sediments and also reflects the influence of human activities on changes to those levels [18-19]. The equation for that calculation appears Eq 1:

$$Igeo=\log2[Ci/K\cdot BEn] \quad (1)$$

Where I_{geo} is the geo-accumulation index, C_i is the measured concentration of element *i* in the sample, BEn is the background value of soil heavy metals in Ningxia [20-21], K is the adjustment coefficient, usually 1.5. Table 1 shows the geo-accumulation pollution level.

Potential ecological risk index. Hakanson proposed the potential ecological risk index. In addition to considering heavy metal levels and background values, the biological toxicity intensity was also taken as an evaluation index [22-23]. This method reflects the impact of a particular heavy metal pollutant on the environment very well, and also reflects the comprehensive impact of various heavy metal pollutants on the environment. Equations for those calculations appear Eq 2, 3, 4:

$$C_f^i=C_s^i/C_n^i \quad (2)$$

$$E_r^i=T_r^i \cdot C_f^i \quad (3)$$

$$RI=\sum_{I=1}^{m} E_r^i \quad (4)$$

Where E_r^i is the ecological risk index of heavy metal *i,* and T_r^i is the toxicity response coefficient of heavy metal *i*. The response coefficients of Cd, As, Cu, Ni, Cr, Hg, and Pb are 30, 10, 5, 5, 2, 40, and 5, respectively [24]. C_f^i is the pollution index of heavy metal *i*, RI is the composite potential ecological risk index of heavy metals, C_s^i is the measured value of heavy metal *i*, and C_n^i is the background value of heavy metal *i*. The ecological risk degree is shown in Table 2.

PFM model. PMF is a multivariate factor analysis technique and first proposed by Paatero in 1994 [25]. The PMF model divides the measured element matrix into a factor contribution matrix and a factor distribution matrix. Based on the source of each heavy metal, the contribution rate of each pollution source factor is determined and is suitable for unknown pollution source appointment. Furthermore, PMF also manages lost data [26]. Currently, this model enjoys broad use in pollution source appointment. The formula appears Eq 5:

$$X_{ij}=\sum_{k=1}^{p} (G_{ik} \times F_{kj}) + E_{ij} \quad (5)$$

In which X_{ij} is the measured amount of the j^{th} component in the i^{th} sample, G_{ik} represents the contribution of the k^{th} pollution source to sample *i*, F_{kj} represents the amount of the j^{th} element in the source factor K, E_{ij} is the residual matrix, and P is the number of pollution sources.

The PMF model processes the sample concentration data several times through the least square and iterative methods to obtain two optimal matrices G and F, which minimizes the objective function Q (defined Eq 6).

$$Q=\sum_{i=1}^{n}\sum_{j=1}^{m}\left(\frac{E_{ij}}{U_{ij}}\right)^2 \quad (6)$$

Where, U_{ij} is the uncertainty of the i^{th} element in sample *j*, which is calculated as follows: (Eq 7, 8)

$$U_{ij} = 5/6 \times MDL \quad \text{(Concentration<MDL)} \quad (7)$$

Where, 'error fraction' is the measuring precision, 'concentration' is the heavy metal content, and 'MDL' is the detection limit of the determination method.

TABLE 1
Pollution degree classification of geo-accumulation index

Geo-accumulation Index Igeo	Pollution degree	Pollution level
≤0	A	No pollution
0~1	B	light to moderate pollution
1~2	C	moderate pollution
2~3	D	Moderate to strong pollution
3~4	E	intense pollution
4~5	F	intense to extremely intense pollution
＞5	G	extremely intense pollution

TABLE 2
Ecological risk coefficient and potential ecological risk index classification standards

ecological risk index E_r^i	Risk level	Potential ecological risk index RI	Risk level
E_r^i ＜ 40	light	RI ＜ 150	light
40 ≤E_r^i＜ 80	moderate	150 ≤ RI ＜ 300	moderate
80 ≤E_r^i＜ 160	high	300 ≤ RI ＜ 600	high
160 ≤E_r^i ＜ 320	higher	RI ≥ 600	higher
E_r^i ≥ 320	Extremely high		

$$U_{ij} = \sqrt{(error\ \ fraction \times concentration)^2 + (0.5 \times MDL)^2} \quad \text{（concentration>MDL）(8)}$$

TABLE 3
Analysis of heavy metal content in dust falling material

Types of heavy metals	National background value/(mg/kg)	Maximum/ (mg/kg)	Minimum/ (mg/kg)	Average/ (mg/kg)	SD/ (mg/kg)	CV/ %	Exceeded ratio/%	secondary standard
Cd	0.097	0.53	0.05	0.17	0.09	51	81.3	0.6
As	11.2	138.83	3.67	18.85	24.68	130	52.1	25
Cu	22.6	1478.21	6.68	92.00	230.92	251	47.9	100
Ni	26.9	317.01	6.83	81.87	75.07	91	40.6	190
Cr	61	473.30	13.20	127.70	110.33	86	30.2	250
Hg	0.07	0.37	0.01	0.04	0.04	119	1.1	3.4
Pb	26	132.59	9.76	33.38	30.19	90	37.5	350
Ag	0.108	4.44	0.22	0.79	0.90	114	100	—

RESULTS

Analysis of heavy metal elements in dust fall materials. The levels of eight different heavy metals were determined by ICP-MS. Table 3 shows the statistical analysis for the heavy metal element characteristics. These metal levels fluctuated greatly, 0.05–0.53, 3.67–138.83, 6.68–1478.21, 6.83–317.01, 13.20–473.30, 0.01–0.37, 9.76–132.59, and 0.22–4.44 mg/kg for Cd, As, Cu, Ni, Cr, Hg, Pb, and Ag, respectively. All eight metals around the tailings exceeded the standards set forth by the national secondary standard for soil background levels. The over-standard rate of each element (the ratio of over-standard sample points to total sample points) was 81.3%, 52.1%, 47.9%, 40.6%, 30.2%, 1.1%, 37.5%, and 100% for Cd, As, Cu, Ni, Cr, Hg, Pb, and Ag, respectively. The average levels of Cu, Ni, Cr, Pb, and Ag exceeded the standard by factors of 4.07, 3.04, 2.09, 1.28, and 7.31, respectively. Obviously, heavy metal levels in the dust fall material significantly exceed the standards.

The coefficient of variation reflects the dispersion of heavy metal levels; if it exceeds 0.5 (or 50%), it indicates a non-uniform spatial distribution caused by the pollution of exogenous substances [19]. Higher coefficient values indicate a greater influence by human activities and a larger pollution problem [27-28]. In this study area, the variation coefficients of Cd, As, Cu, Ni, Cr, Hg, Pb, and Ag were 51%, 130%, 251%, 91%, 86%, 119%, 90%, and 114%, respectively, all of which exceeded 50%, some by a significant margin. Based on the variation degree standard, all heavy metal elements in the study area were high variation, indicating the area was affected by obvious external pollution sources [29].

Geo-accumulation index and ecological risk analysis. Table 4 shows the descriptive statistical characteristics of the geo-accumulation index, the ecological risk index, and the potential ecological risk index for heavy metals falling from dust from the copper-silver tailings accumulation area. The geo-accumulation indexes of Cd, Hg and Ag were all below 0, which indicates a Class A index and no pollution. Accumulation in the dust fall is low, as is the potential pollution risk to the study area. However, the geo-accumulation indexes of Cu, Ni, Cr and Pb in dust fall were all above 5, which indicated a G class index, extremely intense pollution, and high-level accumulations in the dust. Based on the ecological risk index, Cd, Ni, As, Pb, Cu, and Hg all cause ecological risks. Among them, levels of Cd (7%), As 3%), Cu (4%), and Hg (40%) in samples cause high ecological risks. Cu content in 2% samples and Hg content in 4% samples causes high ecological risk. Potential ecological risk indexes in the study area ranged from 414.71–10435.10 and all sample sites showed high risks. In short, heavy metal pollution in dust from around the copper-silver tailings pile caused higher potential ecological risks, and the largest heavy metal contribution came from Hg, Cu, Cd, As, Ni, and Pb.

Correlation analysis of heavy metal levels in dusts. Pearson correlation analyses were conducted on eight heavy metal levels in the dust around the tailing accumulation area of the Leixin copper-silver mine (Figure 2). There was a significant correlation between As, Cu, Hg, Ag, Cd and other heavy metal elements in the dust, which indicated they likely came from the same source. However, Pb had a significant relationship with Cd but a low correlation with other elements. This suggested that Pb may come from a different source than the other elements.

Although correlation analysis reflects the relationship between heavy metals, determination of the different sources requires additional analysis.

TABLE 4
Descriptive statistical characteristics of soil heavy metal accumulation index, ecological risk index, and potential ecological risk index

Index	Types of heavy metals	Maximum/ (mg/kg)	Minimum/ (mg/kg)	Average/ (mg/kg)	SD/ (mg/kg)	CV/%	Kurtosis	Skewness	class/proportion
Index Igeo	Cd	-4.64	-8.06	-6.45	0.72	-0.11	-0.42	-0.07	A/100%
	As	10.22	4.98	6.79	1.04	0.15	2.81	1.61	A/1.04%, G/98.96%
	Cu	14	6.22	8.52	1.57	0.18	3.22	1.83	G/100%
	Ni	12.42	6.88	9.91	1.27	0.13	-0.86	0.22	G/100%
	Cr	14.19	9.02	11.8	1.19	0.1	-0.83	0.21	G/100%
	Hg	-8.29	-13.49	-12.02	0.83	-0.07	4.94	1.51	A/100%
	Pb	10.38	6.62	7.94	1.07	0.14	-0.65	0.79	G/100%
	Ag	-1.36	-5.66	-4.29	0.94	-0.22	2.96	1.71	A/100%
E_r^i	Cd	139.28	12.93	44.59	22.74	0.51	3	1.37	A/46%, B/47%, C/7%
	As	107.87	2.85	14.65	19.18	1.31	9.86	3.19	A/92%, B/5%, C/3%
	Cu	443.11	2	27.58	69.22	2.51	19.72	4.31	A/89%, B/2%, C/4%, D/3%, E/2%
	Ni	61.18	1.32	15.8	14.49	0.92	1.44	1.45	A/92%, B/8%
	Cr	16.01	0.45	4.32	3.73	0.86	1.33	1.41	A/100%
	Hg	1136.88	30.78	108.7	130.02	1.2	42.14	5.94	A/10%, B/42%, C/40%, D/4%, E/4%
	Pb	43.96	3.24	11.07	10.01	0.9	1.66	1.62	A/95%, B/2%
	Ag	-	-	-	-	-	-	-	-
RI		10435.10	414.71	3109.06	3210.25	1.03	4.18	2.03	higher/100%

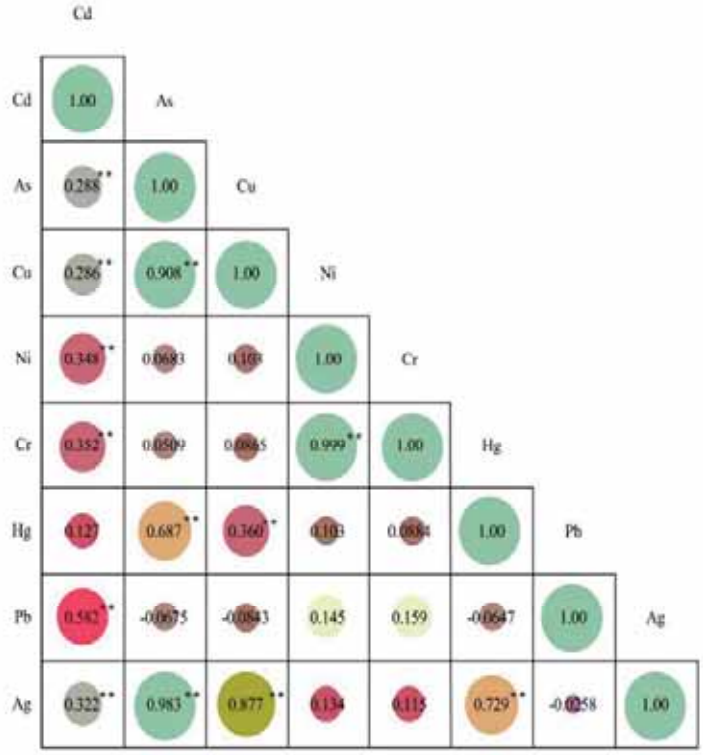

FIGURE 2
Correlation Coefficient of Dust Falling Heavy Metal

Note: **. when P＜0.01, it means significant correlation.

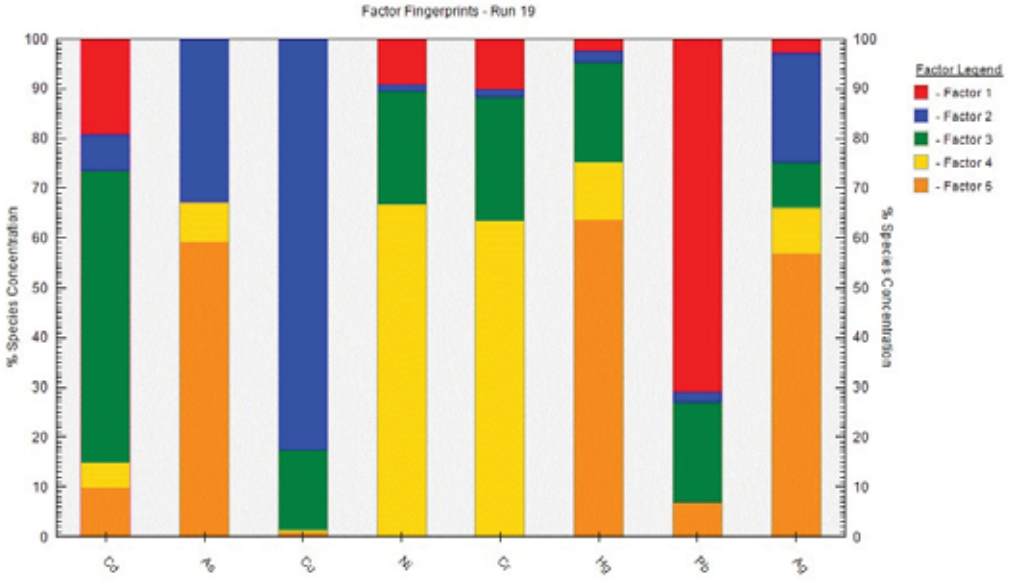

FIGURE 3
Factor fingerprint before rotation

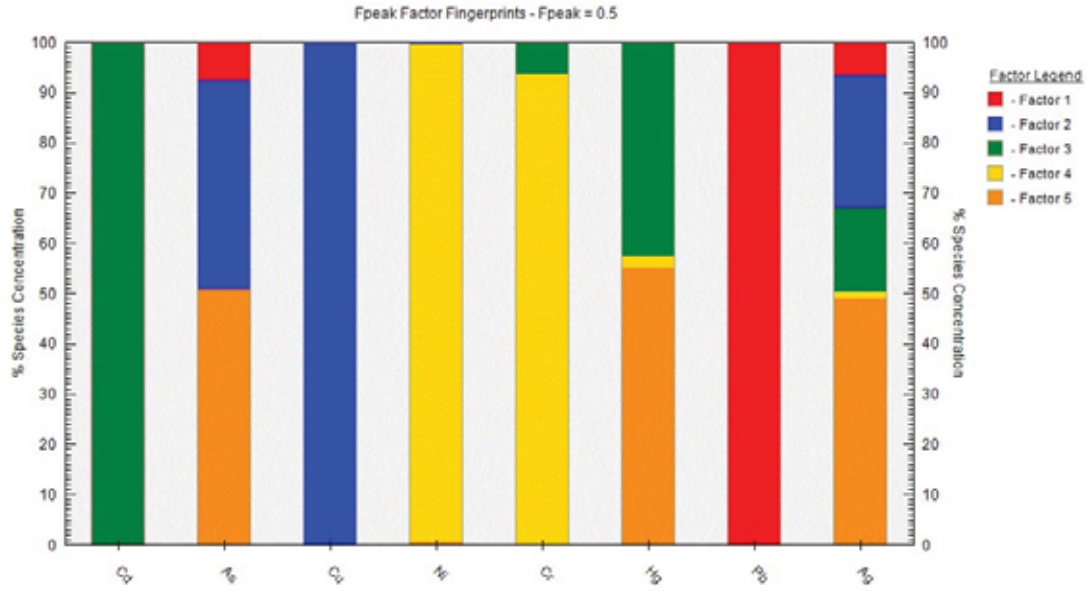

FIGURE 4
Factor fingerprint after rotation

Source appointment of heavy metals in dust fall based on PMF model. In order to further analyze the sources of all eight heavy metals in the dust, PMF determined the source appointment for each metal. Two sets of files were needed for the PMF model to run, the heavy metal concentration file and the heavy metal concentration uncertainty file, used to determine the signal-to-noise ratio (S/N) of the data. In this study, the S/N levels for all metals were greater than 2 and were defined as strong. Except for Hg, the linear fitting correlation coefficients (r^2) for both theoretical and measured values of Cd, As, Cu, Ni, Cr, Pb, and Ag were all above 0.96, which showed a strong correlation [30]. Before running the model, determination of the appropriate factor number by Q_{robust}/Q_{true} under multiple iterative operations was necessary. When the measured Q most closely approximated the theoretical value, that indicated the optimal factor number [31-32]. In this study, the factor number was between 3–7. Through multiple iterative operations, when the factor number was 5, Q_{robust} and Q_{true} were the closest. All residual values calculated were between –3 and 3, indicating that heavy metals in the dust fall were well-distributed by PMF. Therefore, the factor number was set to 5, and the fingerprint is shown in Figure 3 was obtained using that factor number. Figure 4 shows the fingerprint after rotation.

As shown in Figure 4, the problem of contributing factor sources after rotation dropped, which helped the determination of pollution source types for all five factors. The main loading element of Factor 1 is Pb (100%) element. Many studies have shown [33-36] that transportation is the main source of Pb. Large motor vehicles such as trucks and excavators enter the study area, which readily leads to the accumulation of Pb. The characteristics of heavy metals in the dust showed the variation coefficient of Pb was 90%, which indicated an obvious exogenous interference. Therefore, Factor 1 was traffic.

The main loading elements of Factor 2 were Cu (100%), As (41.5%), and Ag (26.4%). Research has shown that metal mining causes heavy metal pollution [14], and Cu was the main source of copper mining [37]. The study area primarily occupied the copper-silver tailings sand leakage accumulation area, so Cu and Ag are related to mining and solid waste leakage accumulation activities. Correlation analysis results in the dust showed that As and Cu, Ag and As, and Cu and Ag have strong correlations ($r > 0.75$). Therefore, the main source of heavy metals in Factor 2 comes from copper-silver tailings sand leakage accumulation. Wang et al. [38] found high levels of As in the mineral waste residue. In addition, heavy metals contained in the leak-filled and accumulated tailings diffused into the surrounding soil [39], which resulted in soil heavy metal levels that exceeded standards. Therefore, the open pit accumulation of tailing sand causes serious pollution in the surrounding dust.

The main loading elements of Factor 3 were Cd (100%), Hg (42.6%) and Ag (16.6%). Studies have implied that fertilizers and poultry manure contain large amounts of Cd [40-41]. Therefore, Cd is generally a sign of agricultural pollution. Cd enters the soil primarily via agricultural irrigation, fertilizer use, and atmospheric dust fall [42], and agricultural lands such as corn and watermelon fields were included in the study area. The source of Hg was complex, and atmospheric dust fall was one way for Hg to enter the soil. Therefore, the transport of pollutants from agricultural irrigation and fertilizer use in nearby areas via atmospheric dust remains the primary source of the three metals in Factor 3.

The main loading elements of Factor 4 were Ni (99.1%) and Cr (93.8%). The correlation analysis results showed a strong correlation between Cr and Ni, which indicated that Ni and Cr came from the same source. Accumulations of Ni and Cr relate to fossil fuels, chemical fertilizer fuel, industrial waste discharges, and industrial raw material use [43-45]. The heavy metal characteristics showed that Ni and Cr levels in the soil were 3.04 and 2.09 times higher than background values, respectively. These results showed that industrial activities in the mining area caused accumulations of Ni and Cr, and the variation coefficients of Ni and Cr were 91% and 86%, which indicated they were influenced by human activities. Therefore, the two heavy metals in Factor 4 came primarily from nearby industrial activities.

The main loading elements of Factor 5 were Hg (55.3%), As (50.9%) and Ag (49.0%); the source of Hg is complex and generally attributed to a variety of sources. The variation coefficient of Hg in this study area was 119%, indicating that Hg came from human sources. Previous studies [46] demonstrated that the ore contains Hg and produces during smelting of non-ferrous metals, which will be discharged into the atmosphere, and adsorbed by the soil through atmospheric dust so that Hg accumulates in the soil. The study area is a copper-silver mining area that engages in non-ferrous metal smelting activities. Therefore, Hg comes from atmospheric deposition. Bilali et al. [19] found that As may be related to industrial wastewater discharge. The study area was a tailings accumulation area, wastewater and sewage are discharged during ore mining, which results in the accumulation of As. Therefore, the three heavy metals in Factor 5 come from compound pollution sources that include atmospheric deposition and industrial wastewater discharge of pollutants in the smelting process of non-ferrous metals.

Using the fingerprint, the contribution rate of each pollution factor was calculated. Among those rates, the rate of industrial activities (32.2%) > copper-silver tailings pollution contribution (22.8%) > atmospheric dust pollution contribution (21.8%) > mixed pollution contribution (18.4%) > traffic pollution contribution (4.8%). Heavy metal levels were high in the dust near the study area, all caused by man-made factors such as industrial activities, crop planting, household garbage, and transportation. Most of that (59.8%) came from non-ferrous metal mining activities and the open-pit accumulation of tailing sand. As a result, it is necessary to carry out regional environmental remediation and pollution diffusion prevention after industrial mining activities.

CONCLUSIONS

(1) The heavy metal levels in the study area were higher than national background values. The average levels of Cu, Ni, Cr, Pb, and Ag were 4.07, 3.04, 2.09, 1.28, and 7.31 times higher than national soil background values, respectively. The variation coefficients for all elements surpassed 50%, indicating obvious external interferences. The excavation of copper-silver mines and the open-pit accumulation of copper-silver tailing sand led to significant excesses of Cu and Ag ions as well as several other heavy metals.

(2) The geo-accumulation index indicated that Cd, Hg and Ag showed no pollution; however, Cu, Ni, Cr and Pb showed very high levels of pollution. The ecological risk index E_r^i showed that risks due to Cr, Ni, As, Pb and Cd were negligible, but risks due to Hg and Cu were very high. Near the metal

tailing sand accumulation area, pollutants diffused via atmospheric dust deposition, which significantly increased the ecological risk in the region.

(3) Correlation analysis and source apportionment through PMF showed that 100% of Pb elements came from transportation. The proportions of Cu and As in the copper-silver tailings accumulation were 100% and 41.5%, respectively. Pollutants from watermelon and vegetable planting activities around the area were transported by atmospheric dust and contributed 100% Cd and 42.6% Hg. Ni and Cr came primarily from industrial sources, and their contribution rates were 99.1% and 93.8%, respectively. Compound pollution sources were the main sources of Hg, As and Ag, and their contribution rates were 55.3%, 50.9% and 49.0%, respectively. Obviously, human activities caused all heavy metal pollution in the study area. Non-ferrous metal mining, open-pit stacking, transportation, wastewater discharge and other activities contributed at least 59.8% of the heavy metal sources, which contributed the most to the excessive dust laden with heavy metals and the subsequent ecological risk increase. Controlling unreasonable metal mining and open-pit stacking tailings to reduce heavy metal diffusion and improving the regional ecological sustainability remains a clear objective.

ACKNOWLEDGEMENTS

Funding: The National Key Research and Development Project of China (2018YFC1802906) supported this study.

REFERENCES

[1] Hua, Z., Wang, Z., Zhang, Y., Hu, Z. (2012) The effects of the Qinghai–Tibet railway on heavy metals enrichment in soils. Science of the Total Environment. 439(NOV.15), 240-248.

[2] Yang, Q., Li, Z., Lu, X., Duan, Q., Huang, L., Bi, J. (2018) A review of soil heavy metal pollution from industrial and agricultural regions in China: Pollution and risk assessment. Science of the Total Environment. 642, 690–700.

[3] Anna, B., Christophoros, C., Lambrini, P., Katerina, G., Argyrios, P., Elena, M., Konstantinos, F. (2017) Characterization, heavy metal content and health risk assessment of urban road dusts from the historic center of the city of Thessaloniki, Greece. Environmental Geochemistry and Health. 39(3), 611-634.

[4] Mehdinia, A., Ramezani, M., Jabbari, A. (2017) Preconcentration and determination of lead ions in fish and mollusk tissues by nanocomposite of Fe3O4@graphene oxide@polyimide as a solid phase extraction sorbent. Food Chem. 15(237), 1112-1117.

[5] Sun, J., Yu, R., Yan, Y., Hu, G., Qiu, Q., Jiang, S., Cui, J., Wang, X., Ma, C. (2020) Isotope tracers for lead and strontium sources in the Tieguanyin tea garden soils and tea leaves. Chemosphere. 246, 125638. Epub 2019 Dec 16. PMID: 31891843.

[6] Kicińska, A., Bożęcki, P. (2018) Metals and mineral phases of dusts collected in different urban parks of Krakow and their impact on the health of city residents. Environ. Geochem. Health. 40(1), 473-488. Epub 2017 Mar 14. PMID: 28293749; PMCID: PMC5797563.

[7] Park, M., Lee, T., Lee, E., Kim, D. (2019) Enhancing source identification of hourly PM 2.5 data in Seoul based on a dataset segmentation scheme by positive matrix factorization (PMF). Atmospheric Pollution Research. 10(4), 1042-1059.

[8] Chen, X., Lu, X. (2018) Contamination characteristics and source apportionment of heavy metals in topsoil from an area in Xi'an city, China. Ecotoxicol. Environ. Saf. 30(151), 153-160. Epub 2018 Jan 12. PMID: 29334637.

[9] Li, Y., Chen, H., Teng, Y. (2020) Source apportionment and source-oriented risk assessment of heavy metals in the sediments of an urban river-lake system. Science of the Total Environment. 140310.

[10] Kim, E., Hopke, P., Pinto, J., Wilson, W. (2005) Spatial variability of fine particle mass, components, and source contributions during the regional air pollution study in St. Louis. Environ. Sci. Technol. 2005 Jun 1. 39(11), 4172-9. PMID: 15984797.

[11] Xu, X., Zhang, H., Chen, J., Li, Q., Wang, X., Wang, W., Zhang, Q., Xue, L., Ding, A., Mellouki, A. (2018) Six sources mainly contributing to the haze episodes and health risk assessment of PM2.5at Beijing suburb in winter 2016. Ecotoxicol. Environ. Saf. 2018 Dec 30. 166, 146-156. Epub 2018 Sep 25. PMID: 30265878.

[12] Tian, Y., Shi, G., Han, B., Wu, J., Zhou, X., Zhou, L., Zhang, P., Feng, Y. (2015) Using an improved Source Directional Apportionment method to quantify the PM(2.5) source contributions from various directions in a megacity in China. Chemosphere. 2015 Jan. 119, 750-756.

[13] Cheng, W., Bian, Z., Lei, S. (2019) Spatial distribution and source identification of heavy metals in surface soil of large open-pit coal mine based on PMF model, The 17th Annual Conference of Chinese Society of Mineralogy, Petrology and Geochemistry, Hangzhou, Zhejiang, China.1.

[14] Kuang, H. (2020) Pollution Characteristics, Risk Assessment and Souce Apportionment of Heavy Metals in Sediments and Soils of Poyang Lake Area. NanChang University.(in Chinese with English abstract)

[15] Dong, L., Hu, W., Huang, B., Liu, G., Ming, K., Kuang, R. (2015) Source appointment of heavy metals in suburban farmland soils based on positive matrix factorization. China Environmental Science. 35(07), 2103-2111. (In Chinese with English abstract)
[16] Muller, G. (1969) Index of Geoaccumulation in Sediments of the Rhine River. GeoJournal. 2(3), 109-118.
[17] Zhang, Y., Zhang, L., Cheng, H., Sun, H., Cui, X. (2020) Soil cadmium pollution and crop health risks in a mining area of southern China. Journal of Agro-Environment Science. 12, 1-16. (In Chinese with English abstract)
[18] Zhou, F., Wang, X., Zhao, X., Li, X., Huang, T., Sun, Q. (2020) Heavy metal distribution and pollution evaluation of rivers along mining area in Lujiang County, Anhui Province. Environmental Chemistry. 39(10), 2792-2803. (In Chinese with English abstract)
[19] Bilal, L., Abdugheni, A., Shi Q. (2019) Pollution and source identification of heavy metals in surrounding soils of Eastern Junggar Coalfield based on PMF model. Transactions of the Chinese Society of Agricultural Engineering. 35(09), 185-192. (In Chinese with English abstract)
[20] Yin, Y., Yong, J., Tao, J. (1988) Research on the background values of nine harmful elements in the main soils and food crops in Ningxia. Journal of Agro-Environment Science. 06, 1-4. (In Chinese with English abstract)
[21] Wei, F., Yang, G., Jiang, Z., Liu, Z., Sun, B. (1991) Basic statistics and characteristics of background value of soil elements in China. Environmental Monitoring in China. (01), 1-6. (In Chinese with English abstract)
[22] Lars, H. (1980) An ecological risk index for aquatic pollution control. a sedimentological approach. Hakanson Lars. 14(8), 975-1001.
[23] Kusin, F., Azani, N., Hasan, S., Sulong, N. (2018) Distribution of heavy metals and metalloid in surface sediments of heavily-mined area for bauxite ore in Pengerang, Malaysia and associated risk assessment. Catena. 165.
[24] Qiu G., Chen H. (2020) Trend and Risk Assessment of Heavy Metal Pollution in Sediments of Hengyang Section of Leishui. Journal of Hebei University of Environmental Engineering. 30(06), 22-27. (In Chinese with English abstract)
[25] Gholizadeh M, Melesse A., Reddi L. (2016) Water quality assessment and apportionment of pollution sources using APCS-MLR and PMF receptor modeling techniques in three major rivers of South Florida. Science of the Total Environment. 566-567.
[26] Wu J., Wu Z., Holländer R. (2012) The application of Positive Matrix Factorization (PMF) to eco-efficiency analysis. Journal of Environmental Management. 98.
[27] Zhu, J. (2012) The Research on the Eco-Remediation of Heavy Metals Contaminated Soils in Huayuan Pb/Zn Mine Area of Xiangxi. Hunan Agricultural University. (in Chinese with English abstract)
[28] Li, L., Shao, L., Li, Y. (2020) Characteristics and risk assessment of heavy metal pollution in soil of a polymetallic mine in Xinjiang. Environment and Development. 32(08), 23-26. (in Chinese with English abstract)
[29] Hu, X., Zhang, Y., Luo, J., Jian T. (2011) Bioaccessibility and health risk of arsenic, mercury and other metals in urban street dusts from a mega-city, Nanjing, China. Environmental Pollution. 159(5), 1215-1221.
[30] Ning, C., Li, G., Wang, Y., Li, B., Tian, L., Wang S. (2017) Evaluation and source apportionment of heavy metal pollution in Xihe watershed farmland soil. Journal of Agro-Environment Science. 36(03), 487-495. (In Chinese with English abstract)
[31] Chai, L., Wang, X., Ma, L., Cheng, Z., Su, L., Wang, Y. (2020) Sources appointment of heavy metals in cultivated soils of Lanzhou based on PMF models. China Environmental Science. 40(09), 3919-3929. (in Chinese with English abstract)
[32] Callén, M., De la Cruz, M., López, J., Navarro, M., Mastral, A. (2009) Comparison of receptor models for source apportionment of the PM10 in Zaragoza (Spain). Chemosphere. 76(8).1120-1129.
[33] Zhang, W., Yu, L., Hu, G., Hu, Q., Wang, X. (2016) Geochemical Characteristics and Source Apportionment of Rare Earth Elements in the Dustfall of Quanzhou City. Huan jing ke xue. 37(12). 1-10. (in Chinese with English abstract)
[34] Wang, Z., Zhang, J., Watanabe, I., Hirozaku, O. (2018) Concentrations and Sources of Heavy Metals in Soil near Railway and Road. Ecology and Environmental Sciences. 27(02), 364-372. (in Chinese with English abstract)
[35] Pant, P., Harrison, R.M. (2012) Critical review of receptor modelling for particulate matter: A case study of India. Atmospheric Environment. 49.
[36] Hjortenkrans, D., Bergbäck, B., Häggerud, A. (2006) New Metal Emission Patterns in Road Traffic Environments. Environmental Monitoring and Assessment. 117(1-3), 85-98.
[37] Zhang, H., Jiang, Y., Ding, M., Xie, Z. (2017) Level, source identification, and risk analysis of heavy metal in surface sediments from river-lake ecosystems in the Poyang Lake, China. Environmental Science and Pollution Research, 24(5):1-15.

[38] Wang, F., Huang, Y., Wang, X., Gao, Z., Fa, X., Bao, Q., Ying, H., Qiao, M., Jin, S. (2015) Ecological risk assessment of heavy metals in surrounding soils of tungsten ores: Comparison of different evaluation methods. Environmental Chemistry. 34(02), 225-233. (in Chinese with English abstract)
[39] Liu, H., Ge, C., Shen, Q., Huang, Y., Zhang, S. (2019) Source apportionment of heavy metals in reclaimed soil of iron mine wasteland. Journal of Agro-Environment Science. 38(02), 317-324. (in Chinese with English abstract)
[40] Nicholson, F., Smith, S., Alloway, B., Carlton-Smith, C., Chambers, B. (2003) An inventory of heavy metals inputs to agricultural soils in England and Wales. Science of the Total Environment. 311(1). 205-219.
[41] Liu, R., Li, S., Wang, X., Wang, M. (2005) Contents of Heavy Metal in Commercial Organic Fertilizers and Organic Wastes. Journal of Agro-Environment Science. (02), 392-397. (in Chinese with English abstract)
[42] Tang, S., Jiang, K., Huang, J., Tan, J., Long, J., Hou, H., Peng, P. (2020) Analysis of Cadmium Balance Source in Soil-rice System in a Certain Area of Xiangxiang City. Journal of Soil and Water Conservation. 34(02), 365-371. (in Chinese with English abstract)
[43] Wu, J., Lu, J., Li, L., Min, X., Luo, Y. (2018) llution, ecological-health risks, and sources of heavy metals in soil of the northeastern Qinghai-Tibet Plateau. Chemosphere, 2018, 201(jun.):234.
[44] Yang, S. (2020) Apportionment of Heavy Metals in Soil Using UNMIX Model. China University of Geosciences. (in Chinese with English abstract)
[45] Zhao, L., Xu, Y., Hou, H., Shangguan, Y., Li, F. (2014) Source identification and health risk assessment of metals in urban soils around the Tanggu chemical industrial district, Tianjin, China. Science of the Total Environment. 468-469.
[46] Sun, Y., Chen, Y. (2013) Study on pollution sources, cause of mercury pollution and its control technical roadmap in China. Environmental Chemistry. 32(06), 937-942. (in Chinese with English abstract)

Received: **12.11.2021**
Accepted: **04.01.2022**

CORRESPONDING AUTHOR

Naiping Song
Breeding Base for State Key Laboratory of Land Degradation and Ecological Restoration in Northwest China,
Ningxia University,
Yinchuan 750021 – China

e-mail: songnp@163.com

© by PSP Volume 31– No. 05/2022 pages 4851-4862 Fresenius Environmental Bulletin

MULTI-SCALE EXPERIMENTAL STUDY OF THE MECHANICAL PROPERTIES OF CHEMICALLY IMPROVED EXPANSIVE SOILS WITH POLLUTION FREE SOIL STABILIZERS

Yanfang Wang[1,*], Chuanxin Liu[2], Dawei Sun[3]

[1]Jinling Institute of Technology, Nanjing, Jiangsu, China
[2]Jiangsu Transportation Institute, NanJing, Jiangsu, China
[3]Shandong Fushilan Ecological Technology Co., Ltd, Zibo, Shandong, China

ABSTRACT

Expansive soils are widely distributed around the world, and their swelling properties in the presence of water and shrinking properties in the absence of water have caused many environmental geological disasters in terms of slope instability.Even for extremely gentle slopes, it is only just a matter of time for instability due to the existence of expansive soils that are highly influenced by the water environment.For the above reasons, many scholars at home and abroad have proposed many modification methods for expansive soils, among which soil stabilizers are favored to improve the water stability and mechanical strength of expansive soils by chemically changing the molecular structure of hydrophilic minerals in expansive soils.In this paper, the environmentally friendly concentrated MB-148 CA soil stabilizer is selected to improve the physical and mechanical properties of expansive soils. Soil basic characteristics test, wetting-drying cycle test, unconfined compressive strength test and environmental scanning electron microscope test were carried out to analyze the change law of specific indexes such as plasticity index, free expansion rate and linear expansion force. The effects of wetting-drying cycles on the evolution of fissure characteristics and mechanical properties of expansive soil improved by soil stabilizer were studied. The selected soil stabilizer has significant effect on improving expansive soil. Its optimal dilution concentration is 1:200, and the most suitable maintenance period is 3 days. The mechanical properties of soil stabilizer improved expansive soil are significantly better than that of plain expansive soil and slightly lower than that of cement improved expansive soil. With the increase of the number of wetting-drying cycles, some minerals in the soil are argillized and precipitated, and the porosity and pore diameter of the soil gradually increase. However, the addition of soil stabilizer can slow down the argillization and precipitation of mineral components in the soil, and inhibit the pore expansion rate of expansive soil. Therefore, the anti-crack ability of soil stabilizer improved expansive soil is better than that of cement improved expansive soil. The research results show that the ionic soil stabilizer selected in this paper is more effective in modifying the expansive soil, with higher water stability and no pollution to the environment, and is a suitable chemical modification method to be popularized and applied in the treatment of expansive soil slopes.

KEYWORDS:
Soil stabilizer, Chemical improvement, expansive soil, wetting-drying cycles, microstructure, crack

INTRODUCTION

Expansive soil is a kind of high liquid limit and high plasticity clay composed of strong hydrophilic minerals such as montmorillonite, illite, etc. [1, 2], which has strong expansive and shrinkage characteristics, multiple fissures and strength degradation, easily triggering geological hazards and bringing many adverse effects to the engineering environment. Therefore, how to improve the expansive soils have been the research hotspot of domestic and foreign scholars.[3~7].In terms of inorganic improvement materials, lime, cement, fly ash, alkali slag and sand are common physical or chemical improvements, with lime and cement being the most widespread.[8~12].However, both of them are incapable of long-term prevention and control of the deterioration effects of water environment changes on expansive soils due to their poor water stability, resulting in some limitations in environmental adaptability.It is worth noting that the mechanism of fiber reinforced modified expansive soil is similar to that of reinforced soil, using the occlusal force between fiber and soil particles to restrain the deformation of the soil, so that the physical and mechanical properties of the expansive soil can be improved to a certain extent, which is also more common in recent years.[13~14]. But as the high polymer fiber material tends to be hardly degradable, fearing to cause

physical pollution to the soil environment,and organic fibers are degradable but have insufficient long-term durability. Therefore, fiber reinforced improvement also is not the optimal improvement means for expansive soils. In terms of biological improvement, it makes use of the characteristics of biological enzyme surfactant attached to the surface of clay minerals to reduce the liquid surface tension and hydrophobize the surface of clay minerals,and destroy the hydration film on the surface of minerals or make it thinner, with promoting the adhesion of particles to become larger, improving the shear strength of soil, and reducing the expansion and contraction of soil. This biochemical improvement method has a certain degree of reversibility, the improvement effect is vulnerable affected by the mineral composition of the water environment, as well as the disadvantage of poor water stability. In terms of chemical improvement, ionic soil curing agents are used to improve expansive soils, which can increase the maximum dry density, compaction, and CBR values, as well as improve the swelling-shrinkage behaviors and long-term water stability of expansive soils. [15, 16], and are gradually gaining popularity among research scholars.

In recent years, the domestic and abroad scholars have conducted a lot of research with remarkable results around the evolution of physical and mechanical properties of expansive soils under wetting-drying environments with the help of geotechnical tests, electron microscopy microscopy scanning equipment and computer digital image processing techniques.[17~20].The above-mentioned studies initially explored the physicochemical properties of modified expansive soils under wetting-drying cycles, but the modified materials were mostly inorganic materials, etc. Few studies involving chemical modification of expansive soils (such as ionic soil stabilizers, etc.) have been reported.

In view of the above approaches , the concentrated MB-148 CA soil stabilizer was selected to improve the mechanical properties of swelling soil, and the basic soil properties test, wetting-drying cycle test, unconfined compressive strength test and scanning electron microscope test were carried out to analyze the change law of plasticity index, free swelling rate, linear swelling force and other specific indexes, and to study the effect of dry and wet cycle on the evolution law of fracture properties, mechanical properties and microstructure evolution law of swelling soil improved by soil stabilizer, and the research results can provide scientific basis for the application of ionic soil stabilizer in swelling soil engineering.

MATERIALS AND METHODS

The investigated expansive soils and stabilizer. The investigated expansive soils and stabilizer. The soil investigated in this study was taken from the test section of landslide remediation project in Ningming area of Guangxi, and the sampling depth was about 2.0-3.0 metre. The appearance of the soil material was grayish white. Table 1 gives the physical and mechanical parameters of the expansive soil, and according to 《GB50112-2013 Technical Specification for Construction in Expansive Soil Areas》, the soil material taken has medium expansion and contraction.

Soil stabilizer. The soil stabilizer used in this study was the concentrated MB-148 CA soil stabilizer provided by MICAVA International, which contains cationic active organic thio compounds in its main components and can form a protective oil layer on the surface of soil and clay particles, thus reducing the ionic movement and ion exchange between soil and water molecules and eliminating the water adsorption of soil particles, which is non-toxic, non-hazardous and non-polluting and has been widely used in improving the conventional high liquid limit soft soils.

Test methods. The Optimal dilution ratio test. In order to determine the effect of concentrated MB-148 CA soil stabilizer to improve the expansive soil in Guangxi and its most suitable dilution concentration, take certain soil stabilizer and deionized water at 1:100; 1:150; 1:200; 1:250; 1:300; 1:400 (all for volume ratio), equipped with diluted solution, as test reserve soil stabilizer.To comparatively study the improvement effect of soil stabilizer on expansive soil, the test was equipped with soil samples at the optimum moisture content of expansive soil, which were：(1) Vegetated expansive soil mixed at optimum moisture content and then sealed and resting for one day;(2) expanded soil mixed with 5% (mass ratio) cement and maintained for seven days to form the cement soil; (3) The above-mentioned soil stabilizers diluted in different volume ratios are mixed with the expansive soils, and the soils are sealed and resting for one, three and seven days respectively after mixing well.After the soil is prepared, the liquid-plastic limits, free expansion rate and expansion force tests are conducted on expansive soil, cement soil and soil stabilizer improved soil with various concentrations respectively, and the best dilution concentration of soil stabilizer is determined based on these test results.The expansion force test was carried out by the soil samples with the maximum dry density as the controlling index and preparing specimens of Φ63.1 mm×20 mm for the determination of expansion force.

Unconfined compressive strength test. A total of 54 triaxial specimens with Φ39.1 mm×80 mm were prepared for three groups of plain expansive soil, cement soil and improved soil, with18 specimens in each group, and the comparative study of unconfined compressive strength deterioration

performance under dry and wet cycling conditions was conducted.The test apparatus is TSZ-10 type triaxial instrument.In the drying process, the specimens were loaded into the modified drying molds and placed in an oven for low-temperature drying, with the temperature set at 40° C. The moisture content of the dried specimens was controlled to be 4%.During the wetting process, the specimens were loaded into a triaxial saturator, pumped for 4 h and treated with full water for 24 h to reach a saturated water content of 31%.Weighing method was used to obtain the sample mass at each moment, and the collection frequency was 2 h/time at the beginning of the drying stage, and 0.1 h/time when the critical saturation of the sample was approached.Every time the wet and dry cycle is completed, three specimens in each group are removed for lateral limit compressive strength test, and the remaining specimens enter the next wet and dry cycle until the end of the test. Test a total of five wet and dry cycles.The specific sample preparation and pumping saturation device is shown in Figure 2.

Fissure acquisition test. Three groups of Φ 110mm×63.1mm specimens (plain expansive soil, cement soil and improved soil), 8 specimens in each group and 24 specimens in total, were prepared for the comparative study of the fine fracture evolution of the specimens under the conditions of dry and wet cycles.The test sample preparation, saturation and picture acquisition device is shown in Figure 1.

The process of wet and dry cycle of specimen, temperature, moisture content control and the number of cycles are the same as the unconfined compressive strength test. 2 specimens are taken out for each completed wet and dry cycle, and high-definition digital camera is used to complete the collection of specimen surface fracture photos to observe the evolution law of soil surface fracture generation, propagation and expansion.The background processing, grayscale processing, binarization processing and fracture skeletonization processing were performed on the specimen fracture photos by using Image-J and Photoshop software to finally extract the fracture width and length values of the specimens under different dry and wet cycles, and then find out the apparent average fracture rate and average fracture width of the specimens.The effect of soil curing agents on the improvement of swelling soils was studied comparatively by describing the variation curves of mean fractality and mean fracture width values of specimens with the number of wet and dry cycles.

TABLE 1
Physical properties of expansive soils

Properties	Value
Optimum moisture content, w_{opt} (%)	22.3
Maximum dry unit weight, γ_{dmax} (kN/m^3)	16.1
Specific Gravity, G_S	2.73
Liquid limit,LL(%)	58.5
plastic limit,PL(%)	24.8
Plasticity Index,PI	33.7
Free swelling ratio, δ_{ep} (%)	60
Swelling force, P(kPa)	175

（a）Drying molds （b）Specimen saturation device

FIGURE 1
Saturation device for experimental sample preparation

（a）Sample making molds （b）Specimen saturation device （c）Image acquisition device

FIGURE 2
Test apparatus

（a）Placement of specimens （b）Electroplated metals （c）Finished plating of specimens （d）Sample observation

FIGURE 3
SEM scanning flow of soil samples

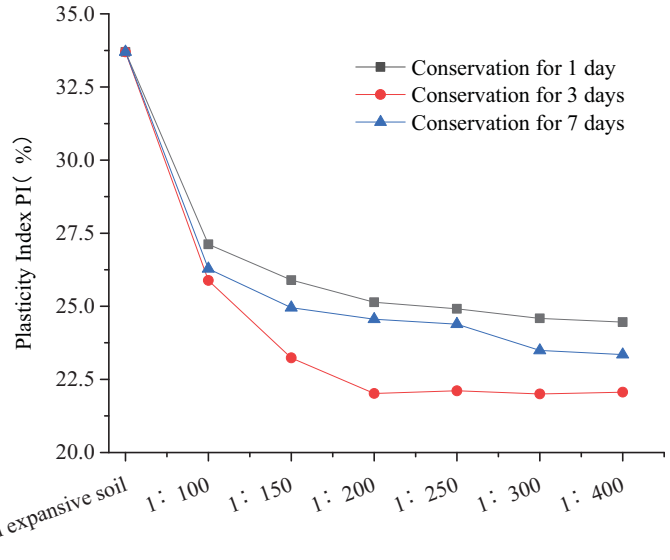

FIGURE 4
Plastic exponent change of expansive soil before and after soil stabilizer improvement

TABLE 2
Limits of liquid plastic in different curing days of expansive soil modified by soil stabilizer

Dilution ratio	Conservation for 1 day		Conservation for 3 days		Conservation for 7 days	
	Plastic limits (%)	Liquid limits (%)	Plastic limits (%)	Liquid limits (%)	Plastic limits (%)	Liquid limits (%)
Plain expanded clay	24.80	58.50	24.80	58.50	24.80	58.50
1：100	28.15	56.07	28.95	54.03	29.12	55.40
1：150	28.24	53.98	28.08	53.08	28.47	53.42
1：200	27.64	54.22	29.08	50.36	27.77	52.32
1：250	28.12	54.46	29.55	50.13	28.67	53.06
1：300	28.80	54.10	29.52	50.81	28.27	51.76
1：400	28.19	53.60	29.14	50.26	28.65	52.00

Microstructure tests. In parallel with the above fine fracture observation test, at the end of the "wet" step during the wet and dry cycle, one specimen in the saturated state was taken out and cut into a long strip of soil 2 cm long, 1 cm wide and 1 cm high with a wire saw, and a groove of nearly 0.5 mm was cut in the middle part to prepare the desired SEM specimen. The required SEM specimens were prepared.After the specimens were cut out and air-dried in a natural air-drying condition without disturbance or abrasion, the specimens were scanned using an environmental scanning electron microscope (FEI-Quanta250) to obtain photographs of the ESEM images of the soil.To maximize the representativeness of the images obtained and to ensure the numerical accuracy of the quantitative analysis of soil microporosity, three sets of parallel specimens were selected for each sample to obtain microscopic photographs. The specific steps are shown in Figure 3.

RESULTS

Basic characteristics test. (1) Liquid plastic limit. Table 2 shows the summary of liquid limit, plastic limit and plasticity index of the specimens. It can be seen that the liquid limit and plastic limit of the swelling soil were reduced to different degrees after the soil stabilizer was incorporated.When the soil stabilizer dilution volume is relatively small, the liquid limit, plastic limit to reduce the degree of faster, with the volume ratio increases, the liquid limit, plastic limit reduction is not obvious, making the plasticity index has a rebound trend.The curves of plasticity index versus dilution ratio are plotted in Figure 4. It can be seen that when the soil stabilizer dilution volume ratio is 1:200, the plasticity index of the swelling soil obtains the lowest value, and the suitable dilution concentration of soil stabilizer for improving swelling soil is considered to be 1:200, and 3 days is the suitable maintenance age of soil stabilization improver.

Free expansion rate. Soil stabilizers with different dilution concentrations were used to improve the swelling soil, and air-dried samples were taken after 3 days of maintenance to determine the free swelling rate, and the test results are shown in Figure 5.It can be seen that the soil stabilizer can reduce the free swelling rate of the swelling soil to some extent, but the effect is not as obvious as that of cement. As the dilution volume ratio of the soil stabilizer solution decreases, the reduction of the free swelling rate of the specimen slows down. When the dilution volume ratio of the solution is around 1:200, the value of the free swelling rate of the soil is relatively stable.

Expansion force. Soil stabilizers with different dilution concentrations were used to improve the swelling soil, and air-dried samples were taken after 3 days of maintenance to determine the swelling force, and the test results are shown in Figure 6.It can be seen that the soil stabilizer can reduce the expansion force of expansive soil as well as cement, but the improvement effect is slightly lower than that of cement.At the same time, the stabilizer dilution concentration is different, the degree of reducing the soil expansion force is different, when the solution dilution volume ratio is larger, the specimen expansion force is smaller, and vice versa, the larger.This reduction rate is relatively stable at a volume ratio of 1:200.

In summary, the selected soil stabilizer can reduce the thickness of the water-binding film of swelling soil, make the distance between mineral particles decrease, enhance the bond strength between soil particles, improve the compaction performance of swelling soil, reduce the free swelling rate of swelling soil agent swelling force value, but the actual effect is affected by the dilution concentration of soil stabilizer.Based on the above test results, it can be seen that the free swelling rate and swelling force of the swelling soil improved by soil stabilizer are relatively stable around the dilution volume ratio of 1:200 of soil stabilizer, and the lowest value of plasticity index of the specimen is also obtained at 1:200 and 3 days of maintenance. Therefore, the optimal dilution volume ratio of soil stabilizer was set to 1:200 in the subsequent tests.

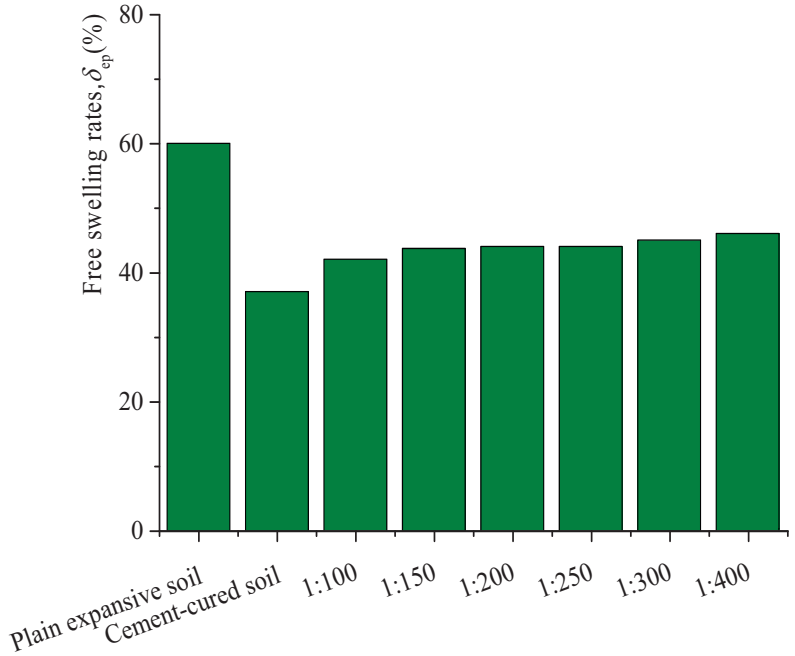

FIGURE 5
Histogram of free expansion rate

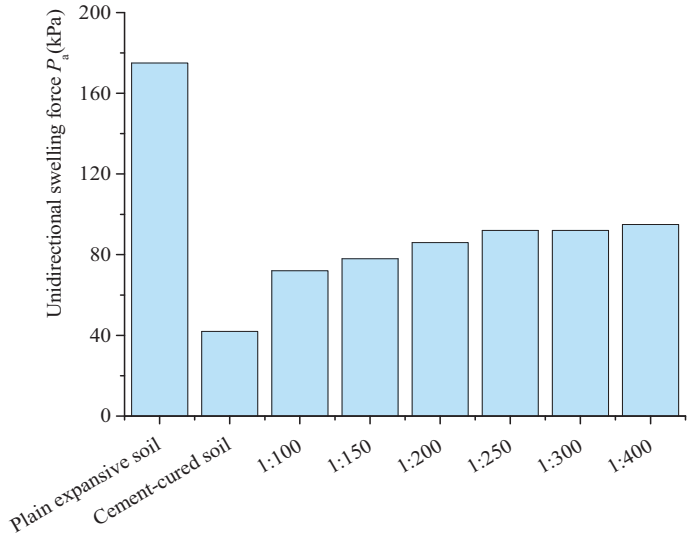

FIGURE 6
Histogram of expansive force of soil sample

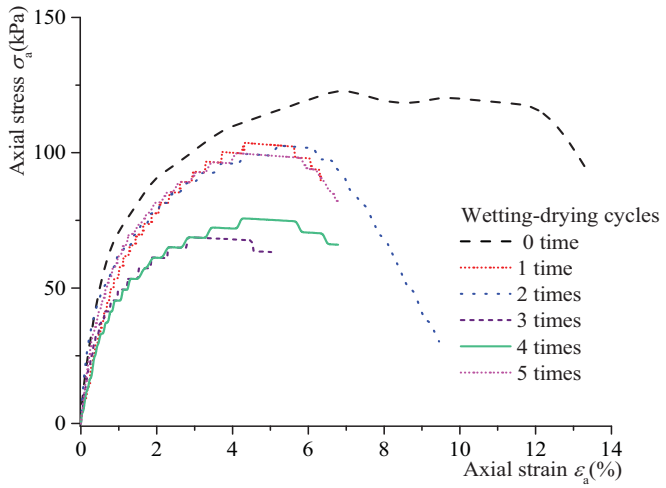

FIGURE 7
Stress-strain curve of plain expansive soil

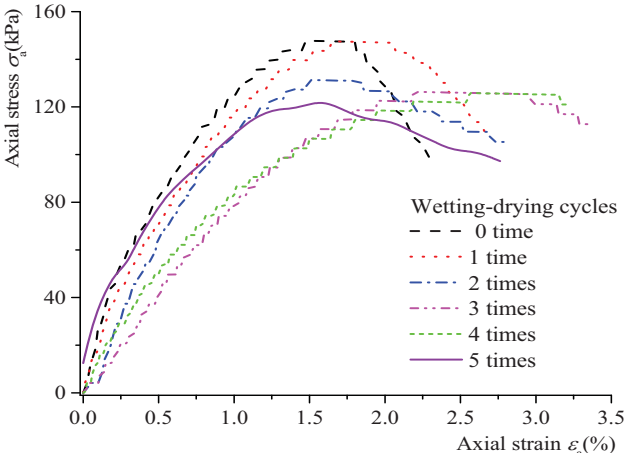

FIGURE 8
Stress-strain curve of cement-treated soil

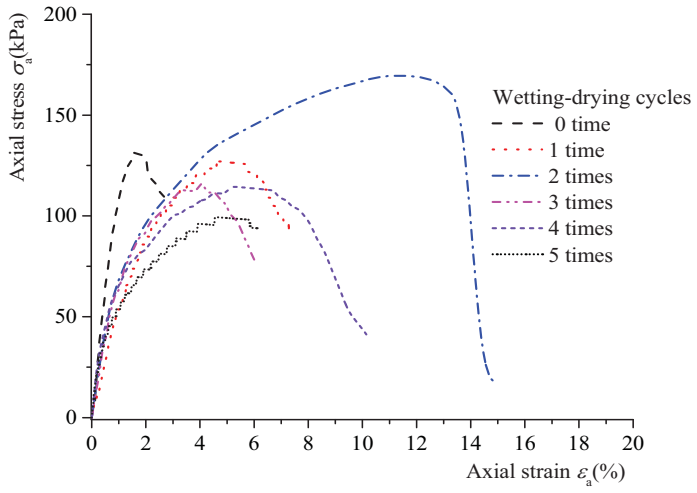

FIGURE 9
Stress-strain curve of solidified soil

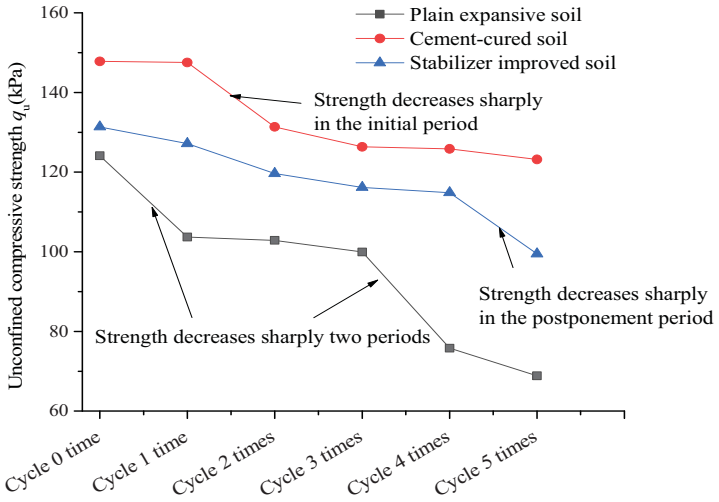

FIGURE 10
Relationship between q_u and wet-dry cycles

Unconfined compressive strength. Figures 7, 8, and 9 show the stress-strain relationship curves of the plain expansive soil, cement-amended soil, and soil stabilizer-amended soil under different cycle times, respectively. It can be seen that the stress-strain relationship curves of the plain expansive soil, cement-amended soil and soil stabilizer-amended soil are all characterized by strain softening. Based on this, the variation process of unconfined compressive strength with the number of wet and dry cycles was plotted in Figure 10.It can be seen that the mixing of stabilizer can improve the unconfined compressive strength of expanded soil, which indicates that stabilizer has some effect in improving the mechanical strength of expanded soil, but the degree of improvement is not as good as that of cement curing agents.Under the conditions of dry and wet cycles, the unconfined compressive strengthqu of all three soils gradually decreases with the increase of the number of cycles, and the mechanical strength of the vegetal swelling soil is most obviously affected by the effect of dry and wet cycles.The mechanical strength of vegetated expansive soil and cement soil decreases fastest when dry and wet cycles 1~2 times, and the rate of strength deterioration is basically stable after 3 times of dry and wet cycles. The deterioration of mechanical strength of soil stabilizer will also receive the effect of wet and dry cycle, but this trend is not as obvious as that of cement soil, and its lateral limitless compressive strength is gradually decreasing in general, and will not deteriorate as sharply as that of swelling soil (0~1 time) or cement soil (1~2 times) before 4 times of wet and dry cycle.In comparison, the strength of the soil stabilizer-improved expansive soil shows a uniform deterioration law during the dry and wet cycles, which makes it less likely to have sudden instability accidents and more conducive to engineering treatment; the soil stabilizer-improved expansive soil shows a certain resistance to dry and wet deterioration.

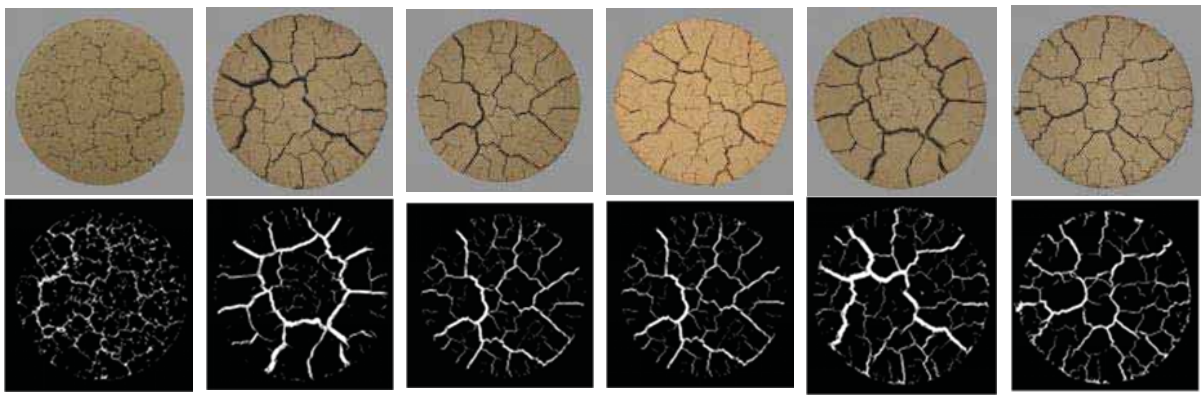

（a）wet-dry cycles 0 time （b）wet-dry cycles 1 time （c）wet-dry cycles 2 times （d）wet-dry cycles 3 times （e）wet-dry cycles 4 times （f）wet-dry cycles 5 times

FIGURE 11

Development law of sample cracks under different wet-dry cycles conditions

Surface fractures of Specimen. Background processing, grayscale processing, binarization processing and fracture skeletonization of specimen fracture photos were performed using Image-J and Photoshop software.Define the average fracture rate of the specimen as the ratio of the projected fracture area to the initial total area of the specimen (without considering the specimen body shrinkage); the average fracture width is the ratio of the total fracture area to the total fracture length.Therefore, the fracture width and length values of the specimens under different number of wet and dry cycles were extracted, and then the average fracture rate and average fracture width of the specimen surface were solved.Figure 11 shows the fracture ratio of the vegetative swelling specimens after graying and binarization under 5 dry and wet cycles.

Only the fracture evolution diagram of the vegetated swelling soil is given in the limitation of space. It can be seen that the vegetated swelling soil undergoes several wet and dry cycles, and the appearance changes significantly, mainly the protrusion of fractures, the increase of body shrinkage effect and the degradation of integrity.The specific features are: the soil structure is relatively dense and the appearance integrity is high when it has not experienced dry and wet cycles; after 1 dry and wet cycle effect, the specimen edge body shrinkage effect is revealed, fine fissures emerge, mainly concentrated in the central part of the specimen, the overall fissure rate, fissure length and fissure width are intensified; after 3 dry and wet cycles, the fissure rate continues to be prominent, the fissure length is intensified, the fissure width is intensified, the local extension to the edge of the specimen, and the mineral mud precipitation on the surface of the specimen; after 5 dry and wet cycles, the fissure development becomes stable, the fissure rate, fissure length and fissure width on the surface of the specimen are close to the limit value.Therefore, the fissure development pattern of swelling soil under dry and wet cycle conditions can be divided into 3 stages, i.e., the starting stage (0~1 dry and wet), the development stage (3~5 dry and wet), and the stabilization stage (after 5 dry and wet).

The image processing of the fracture photos of the three specimens under each dry and wet cycle condition was carried out by using Image-J and Photoshop software, and the fracture parameter values of each specimen under each dry and wet cycle number were extracted, and the average fracture rate and average fracture width of each specimen under different dry and wet cycle numbers were solved, and the relationship curves with the number of dry and wet cycles were plotted in Figures 12 and 13, respectively.

From Figure 12 and Figure 13, it can be seen that with the increase of the number of wet and dry cycles, the development of fissures in expansive soils is a gradual process, with the fissures developing faster in the early stage and then slowing down and gradually stabilizing. With the increase of the number of wet and dry cycles, the average fissure of the specimen was the first to increase and then tended to stabilize, among which the first three times, the average fissure rate increment was 3.02%; accounting for more than 50% of the overall increase. The increase during the last three dry and wet periods was weak. For the average gap width, with the increase of dry and wet times, the overall shows a rapid increase first and then tends to slow down, and finally steps into a stable state, and the increase is mainly concentrated in the first three dry and wet periods, which can develop to an average gap width of about 5 mm, accounting for more than 80% of the overall increase. The analysis should be that there are more fine secondary fractures in the soil at the end of dry and wet, which will inevitably inhibit the increase of the average gap width. Secondly, the repeated drying and shrinking of the specimen itself will also "squeeze" the existing fissures, so that the unstable particles at the side walls will crumble into the fissures and reduce the fissure width again.

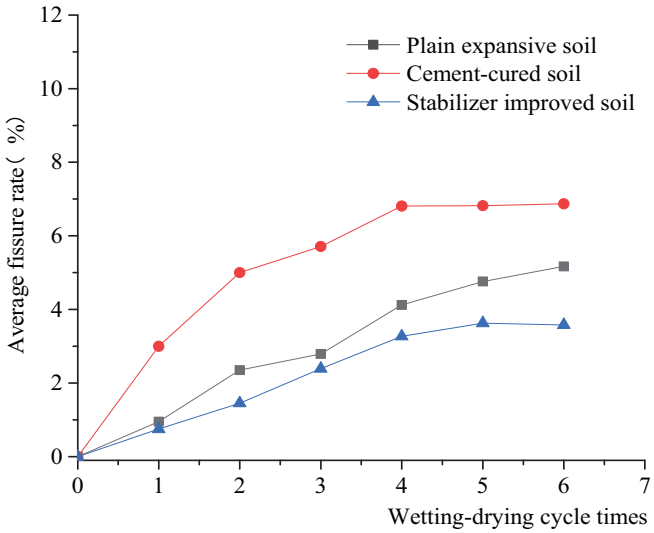

FIGURE 12
Development law of average crack rate of soil samples under different wet-dry cycles

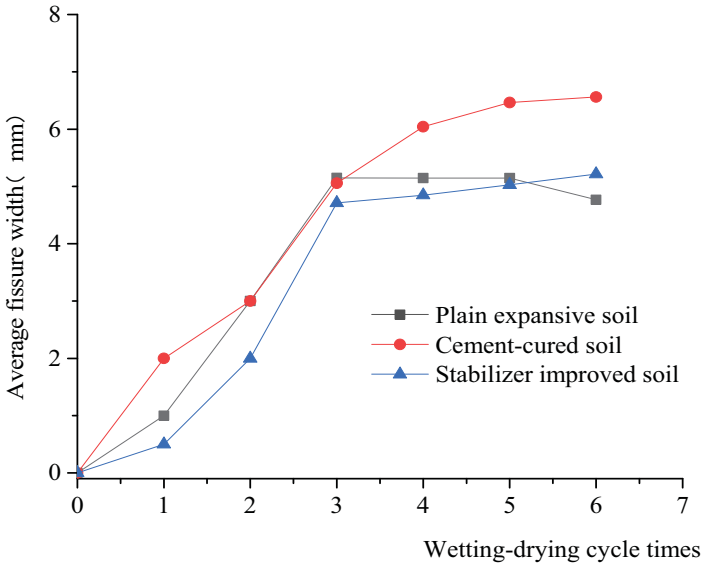

FIGURE 13
Development law of average gap width of soil samples under different wet-dry cycles

From the mechanical point of view, in fact, the specimen fissure development under dry and wet cycle conditions is a kind of tension damage. Once the main fissure is formed, the deformation restriction perpendicular to the direction of the main fissure is lifted and the corresponding strain energy is released, while the strain energy parallel to the direction of the main fissure development continues to accumulate and the strength of the tensile stress field continues to increase, and when it exceeds the tensile strength of the soil, a new sub-level fissure is formed and is perpendicular to the main fissure. Thereafter, the strain energy perpendicular to the direction of the sublevel fracture (originally parallel to the direction of the main fracture) is released and the stress field is readjusted until a new fracture is induced by another concentration.

Microstructure of specimens. Figure 14, Figure 15 and Figure 16 show the microstructure characteristics of the triaxial specimens under different numbers of wet and dry cycles, respectively. It can be seen that the microstructural characteristics of the three specimens are agglomerated, laminated and flocculated in order. Among them, the hydroclay soil is mainly agglomerated, the soil body after soil stabilizer improvement is mostly stacked, and the vegetal swelling soil is mainly oriented flocculation symptoms. Under the action of dry and wet cycles, the pore space between soil particles expands continuously, and the porosity and pore diameter of soil body become larger gradually. The author believes that the reason is that the internal mineral composition of the specimen is gradually muddied and pre-

cipitated under the action of dry and wet cycles, resulting in changes in the particle structure and interparticle pore structure of the soil body. At the same time, it can be found that the mudification precipitation is more serious in the vegetated swelling soil, which indicates that the soil stabilizer can slow down the mudification precipitation of the mineral components inside the soil, thus playing a role in inhibiting the expansion rate of the swelling soil pores and slowing down the development of fissures.

CONCLUSIONS

(1) According to the plastic limit index, free swelling rate, and swelling force and other parameters, the best dilution concentration volume ratio of soil stabilizer improved swelling soil in Guangxi is 1:200, and the most suitable maintenance period is 3 days.

(2) Soil stabilizer can significantly improve the strength of swelling soil, and the lateral limitless compressive strength of soil stabilizer improved swelling soil will not deteriorate sharply under the action of dry and wet cycles, and it has the characteristic of uniform decay.

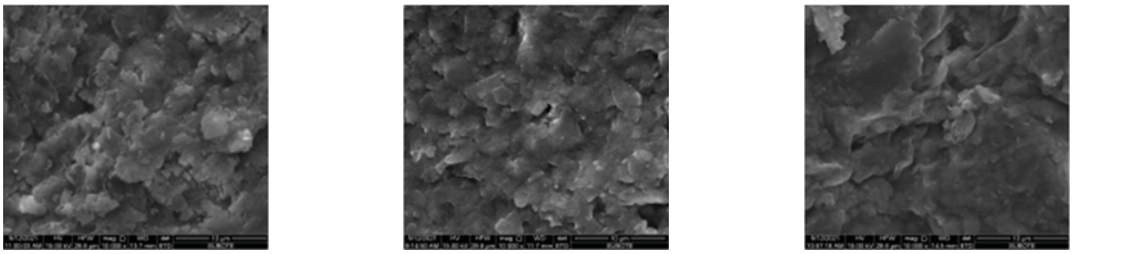

（a）being mainly agglomerated of Cement soils　（b） being mainly in stacked flakes of Improved soils　（c）being mainly in flocculated form of plain expansive soils

FIGURE 14
Particle structure characteristics of three soil samples

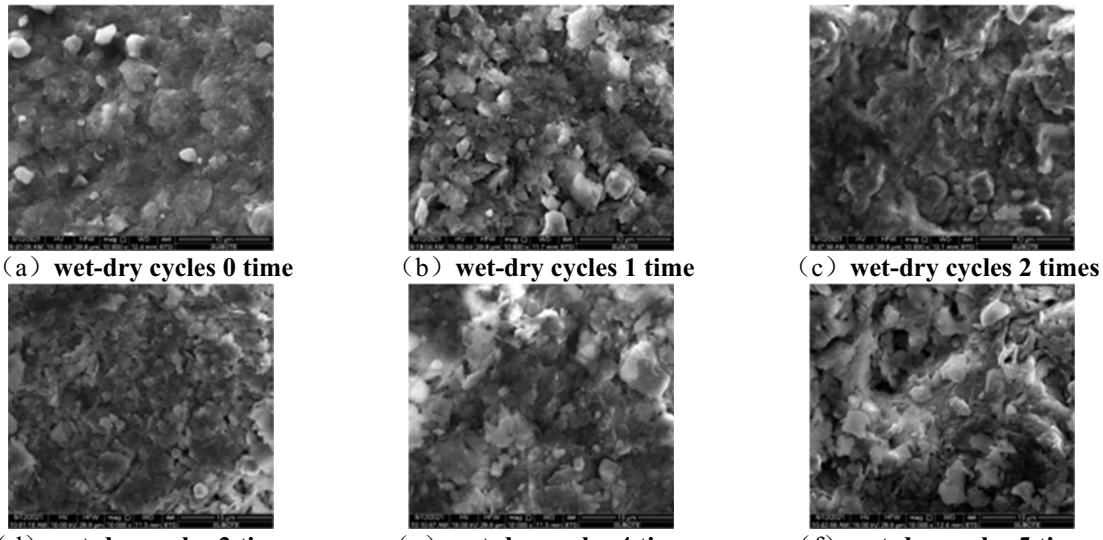

（a）**wet-dry cycles 0 time**　（b）**wet-dry cycles 1 time**　（c）**wet-dry cycles 2 times**

（d）**wet-dry cycles 3 times**　（e）**wet-dry cycles 4 times**　（f）**wet-dry cycles 5 times**

FIGURE 15
The pore structure characteristics of stabilizer treated soil with wet-dry cycles

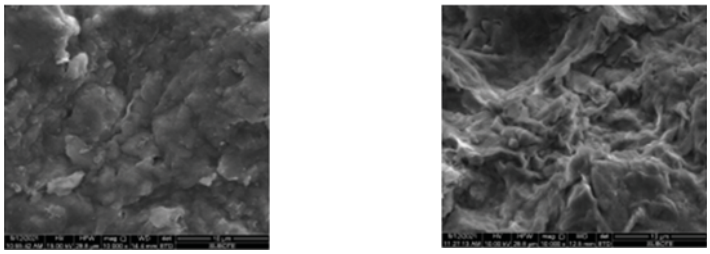

（a）**wet-dry cycles 1 time**　（b）**wet-dry cycles 10 times**

FIGURE 16
Microstructure of plain expansive soil after 1 and 10 wet-dry cycles

(3) The deterioration of vegetated swelling soil, soil stabilizer-amended soil, and cement-amended soil after experiencing dry and wet cycles is characterized by prominent fissures, increased body shrinkage effect, and degradation of integrity. Under the action of wet and dry cycles, the specimen fissure development pattern is divided into the starting stage (0~1 times of wet and dry), the development stage (3~5 times of wet and dry), and the stabilization stage (after 5 times of wet and dry).

(4) With the increase of the number of wet and dry cycles, some minerals inside the soil body muddied and precipitated, and the porosity and pore size of the soil body gradually became larger. The addition of soil stabilizer can slow down the mudification and precipitation of mineral components inside the soil, which has a certain effect on suppressing the expansion rate of pore space of swelling soil and slowing down the development of fissures. It can be concluded that soil stabilizer is slightly lower than cement in mechanical strength enhancement of expansive soils, but significantly better than cement in inhibiting fissure expansion.

ACKNOWLEDGEMENTS

The authors would like to acknowledge the support of the National Key Research and Development Program of China (No.2019YFC1509800); the National Natural Science Foundation of China (No.51908278); the Natural Science Foundation of Jiangsu higer Education institution of China (No.19KJD410002); the high-level talent scientific research of Jinling Institute of Technology (No.jit-b-202017).

REFERENCES

[1] Liu, T.H. (1997) Expansive soil problems in engineering construction. Beijing: China Building Industry Press. (In Chinese).

[2] Cheng, Z.L., Gong, B.W. (2015) Expansive soil slope. Beijing: Science Press. (In Chinese)

[3] Lu, D.J., Chen, S., Luo, H., Dai, Z.J., Li,Y.F., Chen, P.(2014)Study of failure characteristics and evolution mechanism of canal slope of Nanyang expansive soil. Rock and Soil Mechanics. 35(1), 189-196. (In Chinese with English abstract)

[4] Yang, G.L., Wang, Y.H., Li, X.M. (2005) Experimental study of engineering characteristic of expansive soils in the expressway of Xiangtan-Shaoyang. Journal of Railway Science and Engineering. 2(1), 62-67. (In Chinese)

[5] Yang, J., Tong, L., Zhang, G.D., Chen, H.P.. (2014) Effect of initial moisture content and improved material amount on shear strength of expansive soil. Advances in Science and Technology of Water Resources. 34(03), 39-43+49.

[6] Wang, D.X., Wang, H.W., Zou, W.L., Xu, X.Y.. (2019) Study of durability of dredged sludge solidified with reactive Mg0-fly ash. Rock and Soil Mechanics. 40(12), 4675-4684.

[7] Zheng, X.J., Xu, Y.F. (2021) Strength characteristics of GMZ bentonite saturated with salt solutions. Chinese Journal of Geotechnical Engineering. 43(04), 783-788.

[8] Chen, Y.Q., Liao, X.H., Fang, X.Q., XU, D., Wen, C.P.. (2018) Experimental study on the formulation of expansive soil modifiers. China Science paper. 13(13), 1445-1451.

[9] Zhuang, X.S., Yu, X.Y. (2015) Experimental study on strength of expansive soil treated by lime-basalt fiber.China Civil Engineering Journal. 48(S1), 166-170.

[10] Wen, C., Wang, J. (2018) Stress-strain characteristics of bioenzyme-treated expansive soil based on SHEN Zhujiang selasto-plastic model with double yield surfaces. 37(04), 1011-1019.

[11] Lei, W. (2014) Development and application of a new ionic soil stabilizer. Wuhan: China University of Geosciences. (Wuhan). (In Chinese)

[12] Xin, H. (2015) An improved experimental study on new soil treatment agent for expansive soil. Southwest University of Science and Technology Master degree thesis.)

[13] Yang, H.P., Zhang, R., Zheng, J.L. (2006) Variation of deformation and strength of expansive soil during cyclic wetting and drying under loading condition. Chinese Journal of Geotechnical Engineering. 28(11), 1936–1941. (In Chinese)

[14] Cai, Z.Y., Zhu, R., Huang, Y.H., Zhang, C., Guo, W.L. (2020) Centrifugal model tests on deterioration process of canal under cyclic action of coupling wetting-drying and freeze-thaw. Chinese Journal of Geotechnical Engineering. 42(10), 1773-1782. (In Chinese)

[15] Wei, X., Wang, G.(2014) Modeling swell-shrink behavior of compacted expansive clays subjected to cyclic drying and wetting. Chinese Journal of Geotechnical Engineering. 36(08), 1423-1431. (In Chinese)

[16] Chen, T.L., Zhou, C., Wang, G.L.. (2018) Centrifuge model test on unsaturated expansive soil slopes with cyclic wet-dry and inundation at the slope toe. International Journal of Civil Engineering. 18(10), 1341-1360.

[17] Cai, Z., Zhu, X., Huang, Y., Zhang, C.. (2019) Influences of freeze-thaw process on evolution characteristics of fissures in expensive soil. Rock and Soil Mechanics. 40(12), 4555-4563. (In Chinese)

[18] Tang, C.S., Shi, B., Liu, C., Wang, B., Gao W.. (2007) Developing law and morphological analysis of shrinkage cracks of clay soil at different temperature. Chinese Journal of Geotechnical Engineering. 29(5), 743-749. (In Chinese)
[19] Liu, K., Ye, W., Gao, H., Dong, Q.. (2020) Multi-scale effects of mechanical property degradation of expansive soils under drying-wetting environments. Chinese Journal of Rock Mechanics and Engineering. 39(10), 2148-2159.
[20] Wang, B., Shi, B., Cai, Y., Tang, C.S.. (2008) 3D visualization and porosity computation of clay soil SEM image by GIS. Rock and Soil Mechanics. 29(1), 251-255. (In Chinese)

Received: **16.11.2021**
Accepted: **18.02.2022**

CORRESPONDING AUTHOR

Yanfang Wang
Jinling Institute of Technology,
Nanjing Jiangsu – China

e-mail: chenkai20200313@163.com

© by PSP Volume 31– No. 05/2022 pages 4863-4871 Fresenius Environmental Bulletin

HYDRO-THERMAL COUPLING NUMERICAL SIMULATION FOR OPTIMAL EXPLOITATION OF SANDSTONE GEOTHERMAL RESERVOIR IN MINGHUAZHEN FORMATION YANCHENGUPLIFT

Mingkun Zhao[1,2], Yajun Sun[1,*]

[1]School of Resources and Geosciences, China University of Mining and Technology, Xuzhou 221116, China
[2]Henan Provincial Coal Geological Survey and Research Institute, Zhengzhou450052, Henan

ABSTRACT

Geothermal resources of large sedimentary basins have both reproducibility and depletion, it is necessary to study the reinjectionability of geothermal reservoirs. A series of hydro-thermal numerical simulation are carried out in order to realize the sustainable development and utilization of the geothermal resources based on the full analysis of geothermal geological conditions in Yancheng Uplift and four sets of reinjection test data from WELL TM1

A calibrated numerical simulation model was used to simulate and analyze its geothermal recovery and reinjection balance. The conclusions are as follows: the maximum natural reinjection rate in WELL TM1 is 633.48m^3/d, and the maximum mining influence radius is 1200m. The reinjection rate is much smaller than extraction. The reinjection increases with the decrease of the temperature of the reinjection water, and the permeability decreases gradually with time. The sustainable development of geothermal resources in Yancheng uplift requires the well pattern layout method of "One Production with Two Reinjection". The distance between the production and reinjection wells is 300m.

KEYWORDS:
Yancheng Uplift, sedimentary basin, reinjection, numerical simulation

INTRODUCTION

Geothermal energy is a sustainable and environment-ally friendly energy. However, geothermal resources have both reproducibility and exhaustion. Geothermal resources rely on fluids (mainly groundwater) to carry heat energy for utilization, but geothermal fluids (groundwater) are not inexhaustible and inexhaustible.

The hugely thick pores-fissuretype geothermal reservoirs of Lower Neogene formation in the Cenozoic sedimentary basins, whose lithology is sandstone and mudstone, is currently the main target for geothermal exploitation in North China. The development methods mostly adopt the unsustainable "Direct Exploitation and Direct Discharge". With the rapid growth of geothermal development, some negative reaction has been showed out, such as the imbalance of heat and water volume, the continuous decline of water level, the decline of resources, and the continuous increase of exploitation costs [1-2]. At the same time, it also bring a series of environmental problems such as land subsidence and surface water pollution. In order to slow the decline of groundwater head [3], ensure the sustainable development of geothermal resources and protect the geological environment [4], it is generally believed that the exploitation mode of "production with reinjection" is an important means [5-7].

Numerical simulation technology has been studied since the 1950s and is an important method for quantitative evaluation and prediction of geothermal water quantity and quality [8-10]. It can be used to evaluate reinjection the geothermal system and study the changing trend of groundwater level and its environmental impact under various development scenarios [11-12]. So the groundwater numerical model has become an indispensable tool for current geothermal resources and environmental impact assessment.

This study is based on the results of different forms of reinjection tests conducted in geothermal WELL TM1. With the hydro-thermal coupling simulation, a geological model of the Yancheng Uplift geothermal system is established and its production and reinjection balance are analyzed to provide a basis for the dynamic management and optimal allocation of geothermal resources [13-15].

MATERIALS AND METHODS

T Geothermal reservoir conceptual model: The study area is located in Zhoukou Sag, south part of North China Depression, Bohai Bay Basin [16-17]. It is a sedimentary basin type layered geothermal reservoir. WELL TM1 is near thenorth boundary Fault

of Yancheng Uplift, Yichuan-Xiangcheng-Mengmiao Fault (F1) and Changcun Fault (F4) which is a secondary Fault of F1. However, these Faults didn't cut off the Cenozoic strata, and have no obvious impact on the continuity of groundwater flow field in the Minghuazhen Formation geothermal reservoir. The stratum around the well is high in the west and low in the east. The stratum distribution around Well TM1 is shown in Figure 1.

In summary, the geothermal field in the study area is a low-temperature conduction geothermal system, and the main geothermal reservoir is a layered porous reservoir of the Minghuazhen Formation of Neogene.

Under the mechanism of heat flow refraction, the heat flow from deep earth gathers in the upper part of the structure and forms the geothermal abnormal area [18]. The heat flow transfers upward mainly in form of heat conduction, and its value is about 60mW/m^2, the highest geothermal gradient in the uplift area is 4.1℃/100m, and the average is 3.6℃/100m.

Geothermal reservoir can be divided by strata, such as Neogene Minghuazhen Formation, Guantao Formation, Paleocene and Cambrian, form a multilayer structure that is superimposed on each other [19]. The deeper, the temperature increases and the resources can be divided into two reservoirs of warm water and warm-hot water. The temperature at the bottom of the Minghuazhen Formation is about 60℃, which can be named low-temperature geothermal reservoir. The Minghuazhen geothermal reservoir is continuously distributed, with good porosity and permeability, strong water storage capacity, and good heat supply capacity. The geothermal reservoir can be generalized into a hydrogeological model of a confined aquifer with homogeneous, isotropic, and infinite boundaries on the plane, and there is no cross-flow between the reservoirs (There is a relatively water-resistant mudstone layer above and below) [20].

The caprock includes the upper strata of Minghuazhen Formation and the Quaternary strata. The lithology is mainly clay, silt, silty fine sand, fine sand and medium sand layer. It has poor permeability and low thermal conductivity, making it a good water and heat-insulating roof [21]. The conceptual model of the geothermal system is shown in Figure2.

Hydro-thermal couplingnumerical model: In order to obtain pattern parameters such as production rate and well spacing of the study area, this simulation establishes a numerical model around WELL TM1 in order to use well data for correction. The model is 6km long from east to west, 6km wide from north to south, with a total area of 27km^2.

1. Top boundary. According to the shallow temperature measurement results, the depth of the constant temperature zone is 22m and the temperature of the constant temperature zone is 16.6℃. The top boundary is set as a constant temperature and a constant pressure boundary. The temperature is 16.6℃, and the pressure is atmospheric pressure, 1.013E5Pa.

2. Bottom boundary. Based on the foregoing analysis, the study area is a conductive geothermal system and the deep heat flow is mainly transferred upward in form of heat conduction. According to the definition of terrestrial heat flow before the redistribution of heat flow, the vertical heat flow of the earth remains unchanged. Therefore, the bottom boundary of the model is set as a constant heat flow boundary. According to regional data, the heat flow value is about 60mW/m^2.

3. Lateral boundary. At present, there are only few geothermal wells in the study area and the amount of geothermal production is small, so there does not cause too much disturbance to the formation pressure and the pressure field basically maintains the normal hydrostatic pressure. The model boundary is far away from WELL TM1, and the geothermal extraction will not affect the pressure of the boundary, so the lateral boundary is set as the constant pressure boundary.

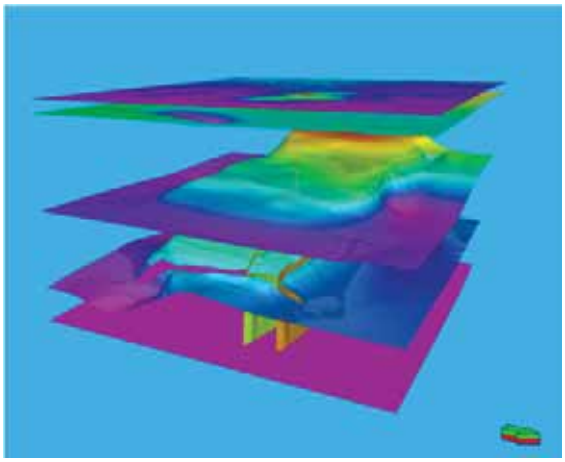

FIGURE 1
The stratum distribution around Well TM1

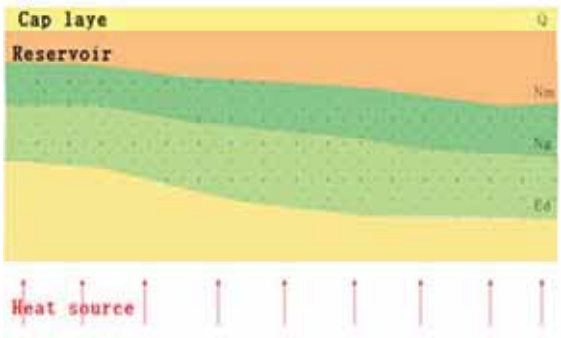

FIGURE 2
Conceptual model diagram of geothermal field

TABLE 1
Detailed information of reinjection well

Hashtag	TM1
Well depth (m)	1402.48
Drill model	GZ-2600
Completion method	Gravel filling, clay ball to stop water
Destination layer	Nm
Maximum angle of well (°)	1.67
Wellhead steady flow temperature (°C)	58
Water volume (m^3/h)	50.84

TABLE 2
Casing of reinjection well

Well section (m)	Outer diameter of casing (mm)	thickness (mm)	Filter tube position
0-310m	273mm	7.92	
310-1060m	139.7mm	7.85	1054.40-1348.11m
1060-1402.48m	159mm	17.5	

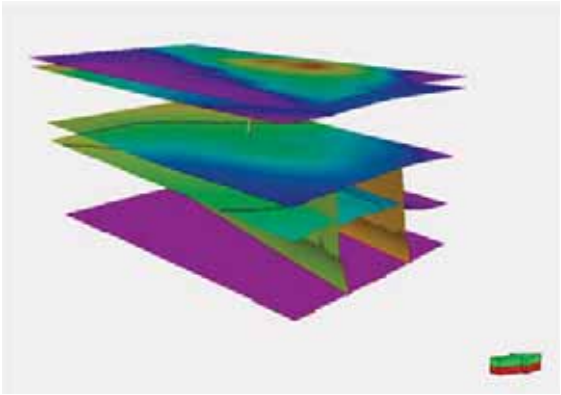

FIGURE 3
Model vertical layer map

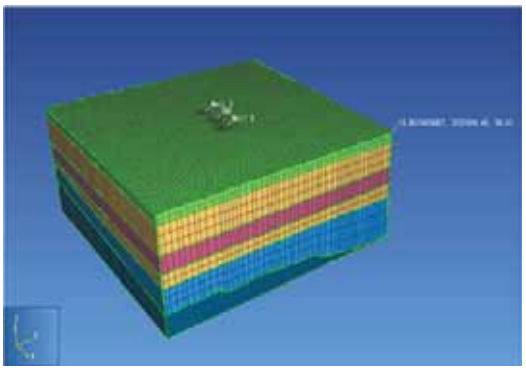

FIGURE 4
Model meshing diagram

The geometry model is established according to the aforementioned geothermal field conceptual model. From the Quaternary to the upper part of Minghuazhen Formation, it is treated as caprock, and the lower part of Minghuazhen Formation is the target geothermal reservoir and also the main simulation layer. The bottom depth of the model is 2600 meters deep. Each layer is derived from the geological model and can reflect the actual stratum distribution, as shown in Figure 3.

When meshing the main simulation layer, the lower part of Minghuazhen Formation is divided into 8 layers, each layer is 50 m thick.

After splitting, there are 74,428 active grids (Figure 4).

The natural state inversion and exploitation history calibration were performed in the model, and the ground temperature conditions set by the adjusted model were in line with reality.

Overview of Well TM1: The TM1 well was completed at a depth of 1402.48m and was drilled using a GZ-2600 rig.

Detail information of Well TM1 is shown in Table 1, 2.

The water intake section of Well TM1 is the Neogene Minghuazhen Formation (Nm) at depth of 1061.65～1345.53m. There are 21 layers of aquifer with a total thickness of 118.52m. It is a complete penetration of well under pressure. The static water level is 86.76m. When the pumping test water level drops by 63.54m, the water inflow is 50.84m^3/h, the water temperature is 58℃ and the unit water inflow is 0.8001 m^3/h.m.

RESULTS

Reinjection test of Well TM1. From September 22th to October 9th, 2019, four groups of natural reinjection tests and two groups of water level recovery tests were carried out in the WELL TM1. Before the rereinjection test, it was measured that the static water level of the well was 92.17m and the liquid surface temperature was 19.4℃. During the test, mechanical flow meters and thermometers were used to measure changes in flow and temperature, and automatic water level meters were used to record water level depth data.

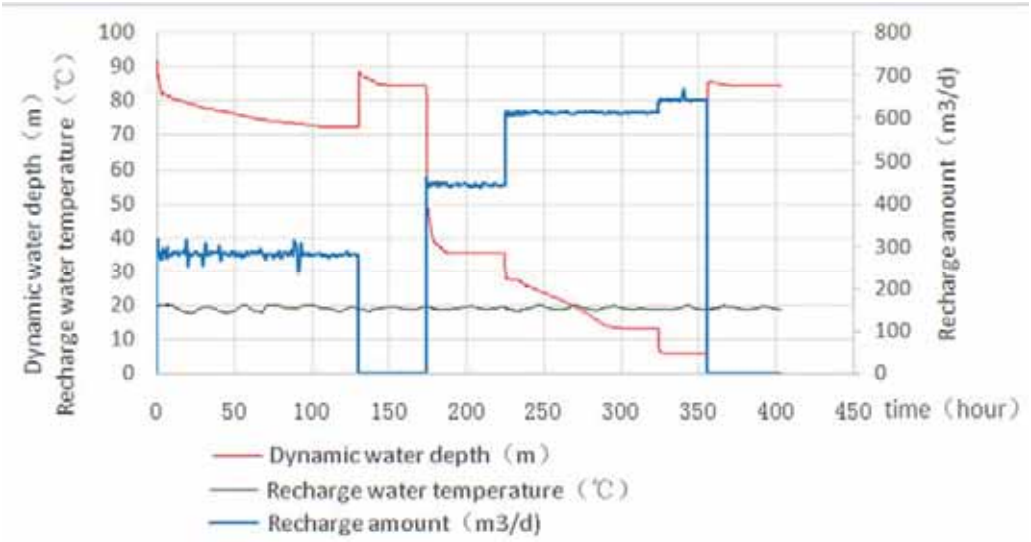

FIGURE 5
Time curve of natural reinjection test in Well TM1

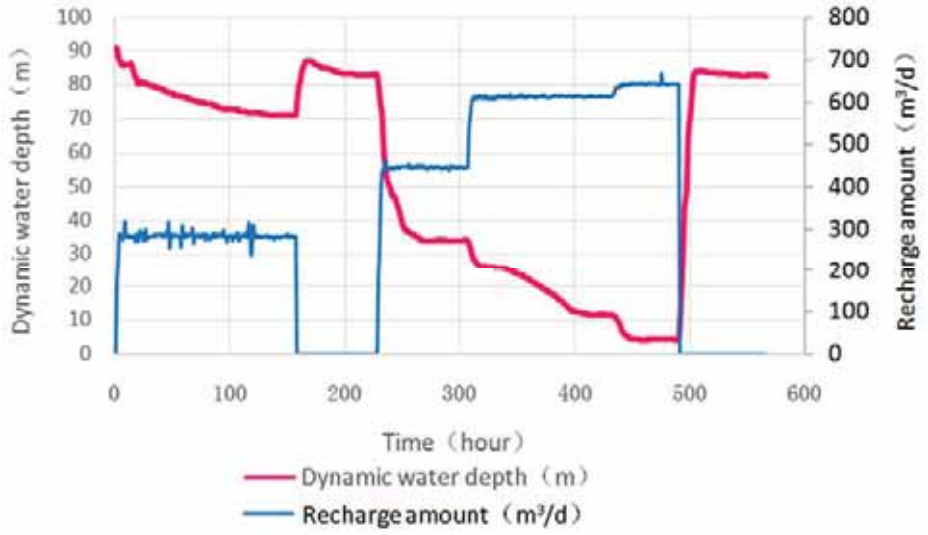

FIGURE 6
Corrected duration curve of reinjection test in WELL TM1 (25℃)

Shallow aquifer is used as reinjection water sources (quaternary water sources), and WELL TM1 is used as reinjection wells for interlayer reinjection. In order to ensure the quality of the reinjection water, the WH-SLB50/5-1 large flow filter is used to filter the reinjection water. The filter is designed for a flow rate of 60-80m³/h and the filtration accuracy is 2μm. The duration curve of this reinjection test is shown in Figure 5

Determination of reinjection rate: In the process of data compilation, uniform temperature correction is required to eliminate the influence of wellbore effect. Due to the conduction and diffusion characteristics of heat, the temperature and depth of the fluid in geothermal wells can be considered to be a linear relationship, and the corrected water level can be calculated according to the following formula.

$$h_c = H - \frac{(\rho_m + \rho_h) \times (H - h_s)}{2\rho_c} \quad (4\text{-}1)$$

$$h_c = H - \frac{\rho_m \times (H - h_d)}{\rho_c} \quad (4\text{-}2)$$

In the formula：

h_c---- Buried depth of water level after correction (m)；

H---- Buried depth of midpoint of water intake section (m) ；

h_s---- Buried depth of static water level (m) ；

h_d---- Dynamic water depth (m) ；

ρ_c---- Density of reinjection fluid (kg/m³) ；

ρ_h---- Density corresponding to heat storage temperature (kg/m³) ；

ρ_c---- Density corresponding to the corrected temperature (kg/m³) 。

The water source for this reinjection is Quaternary cold water, and the reinjection water temperature is about 19℃. According to the current situation of local geothermal utilization, the temperature of geothermal tail water is set at 25℃, and the test data are calibrated on the basis of the temperature. After calibration, the reinjection test duration curve is shown in Figure 6. The depth of the corrected static water level of Well TM1 is 96.62m.

1. Basic parameters. The basic parameters of the WELL TM1 reinjection test after corrected the same temperature (25℃) are shown in Table 3.

The calculation formula of of water injection osmotic coefficient (K_c) and coefficient of hydraulic conductivity(T_c) are as follows.

$$K_c = 0.366 \times \frac{Q_r}{s_r M} \lg \frac{R_r}{r_w} \quad (3)$$

$$R_r = 10 s_r \sqrt{K_c} \quad (4)$$

$$T_c = K_c M \quad (5)$$

In the formula:

K_c---- Geothermal reservoir injection permeability coefficient corrected to 25℃ (m/d) ；

T_c---- Thermal storage water injection conductivity corrected to 25℃ (m^2/d) ；

Q_r---- Stable reinjection rate of reinjection wells (m^3/d) ；

S_r---- The difference between the steady water level of the wellbore fluid during the reinjection test and the static water level before the test (m) ；

M---- Vertical thickness of heat storage (m) ；

R_r---- Reinjection influence radius (m) ；

r_w---- Well radius (m) 。

When T=25℃, according to the basic parameters of TM1 well reinjection test, it can be calculated by formulas (3), (4) and (5):

K_c^1=0.1217 m/d，$T_c^1=K_c^1 \cdot M$=14.424 m^2/d

K_c^2=0.0788 m/d，$T_c^2=K_c^2 \cdot M$=9.339 m^2/d

K_c^3=0.0795 m/d，$T_c^3=K_c^3 \cdot M$=9.422 m^2/d

K_c^4=0.0767 m/d，$T_c^4=K_c^4 \cdot M$=9.090 m^2/d

At 25℃, calculating the test data of WELL TM1, the average value of the reinjection permeability coefficient and hydraulic conductivity is calculated: K_c is 0.0783m/d and T_c is 9.284m^2/d.

2. Determination of reinjection rate. There injection water head increases with the increase of the reinjection amount, and the increase is greater than the increase in the reinjection rate. The reinjection test data shows that the reinjection volume is positively correlated with the reinjection head rise, which is roughly in line with the linear function relationship (Figure 7). According to the calculation, water level of the Minghuazhen Formation geothermal reservoir is 96.62m, the maximum natural geothermal reinjection rate (the dynamic water level is 5m) is 633.48 m^3/d, which is 26.40m^3/h.

TABLE 3
TM1 well reinjection test basic parameter table (corrected temperature 25℃)

Project	First stage	Second stage	Third stage	Fourth stage
Stable reinjection (m^3/d)	281.9	445.84	612.02	641.95
Stable dynamic water level after correction (m)	71	34	11.6	4.1
Water level rise (m)	25.62	62.62	85.12	92.62
Static water level after correction (m)	96.62			
Effective thickness of water intake section (m)	118.52			
Well radius (m)	0.062			

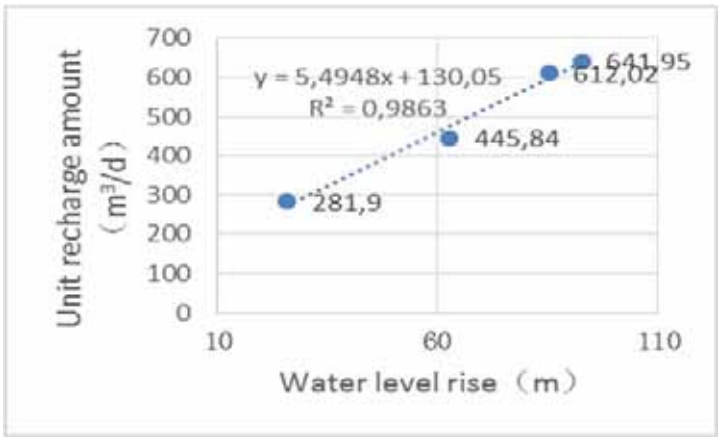

FIGURE 7
Relationship between unit reinjection volume and water head rise in WELL TM1

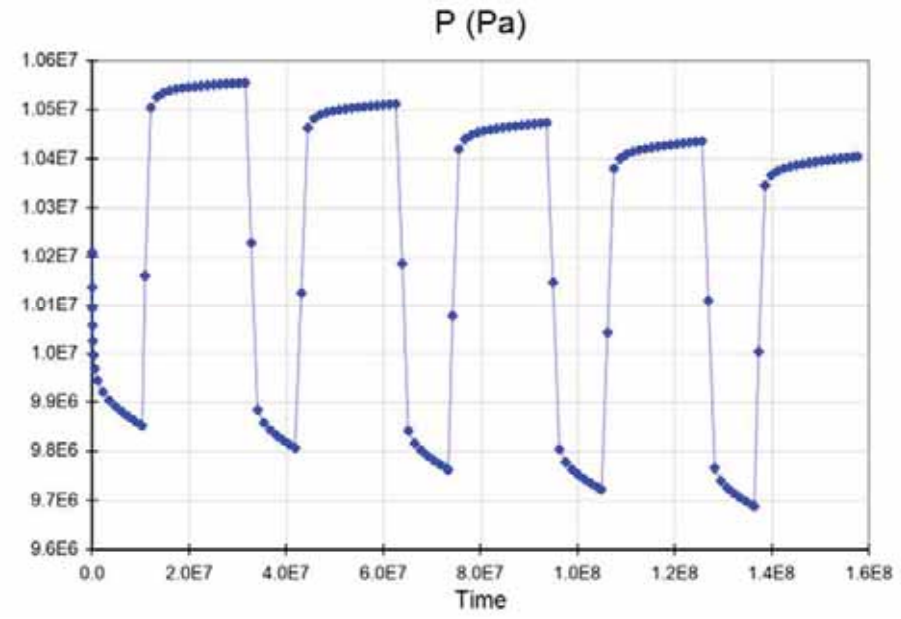

FIGURE 8
Pressure change of WELL TM1

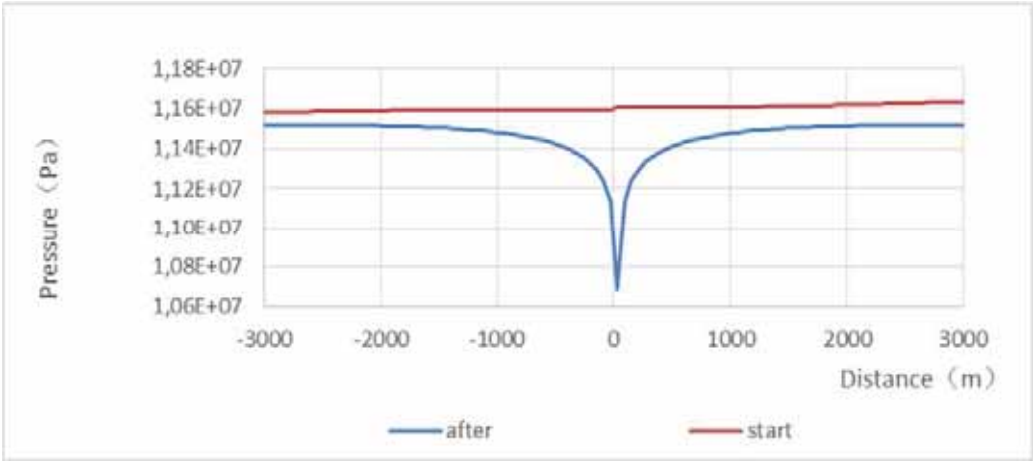

FIGURE 9
Pressure distribution curve around WELL TM1 at the end of the heating season

Optimization plan for mining and reinjection determined by simulation method: According to the pumping test data of WELL TM1, the water output is 50.84m^3⁄h, and the temperature of the wellhead is 58℃. The annual heating season in Northern China is from November 15th to March 15th next year, which is recorded as 122 days, and the water intake is 50m^3/h. Run the model for ten years to observe the pressure changes in the WELL TM1.

When the model has been running for five years, the pressure change of TM1 well is shown in Figure 5-13. During the heating season, the pressure around the well decreases due to pumping, but after the heating season was over, the water level recovered quickly and the pressure basically recovered, but it dropped slightly every year.

At the end of the heating season (March 15th next year), the cumulative pumping capacity from single well is the largest, and the pressure influence range is also the largest. Figure 9 shows the pressure distribution at the top (-1060) of the water intake section of the WELL TM1 at the end of the heating season. It can be seen that there is a falling funnel around the geothermal well, and the influence radius is about 1200 meters.

The single well reinjection rate is 25m^3/h, and the single well production rate is 50m^3/h. The reservoir permeability is 30mD, porosity is 0.20. It shows the pressure distribution between the production well and the reinjection well in Figure 10. Compared with no reinjection condition, for the action of reinjection water, the pressure around the reinjection well increases, and it can effectively replenish the pressure funnel around the exploitation well.

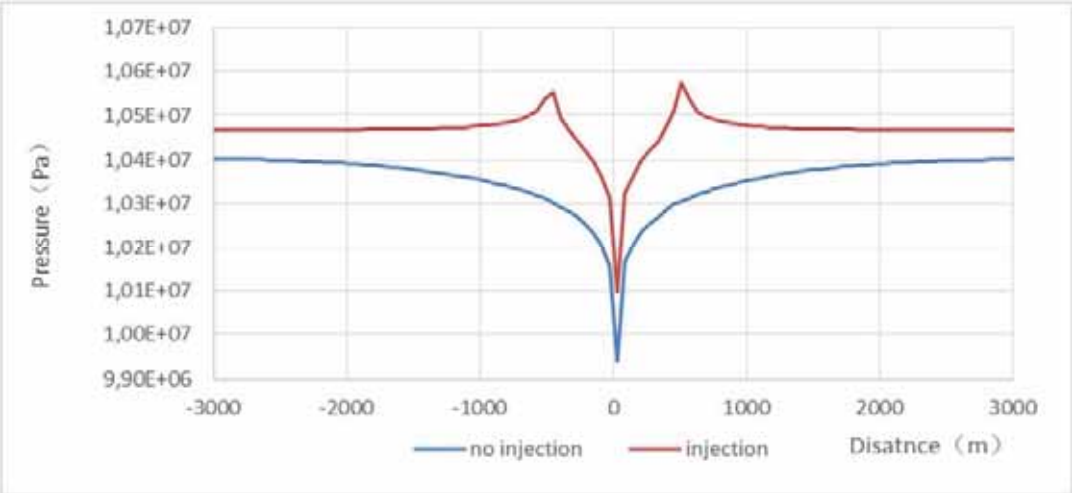

FIGURE 10
Pressure distribution between extraction and irrigation wells before and after reinjection

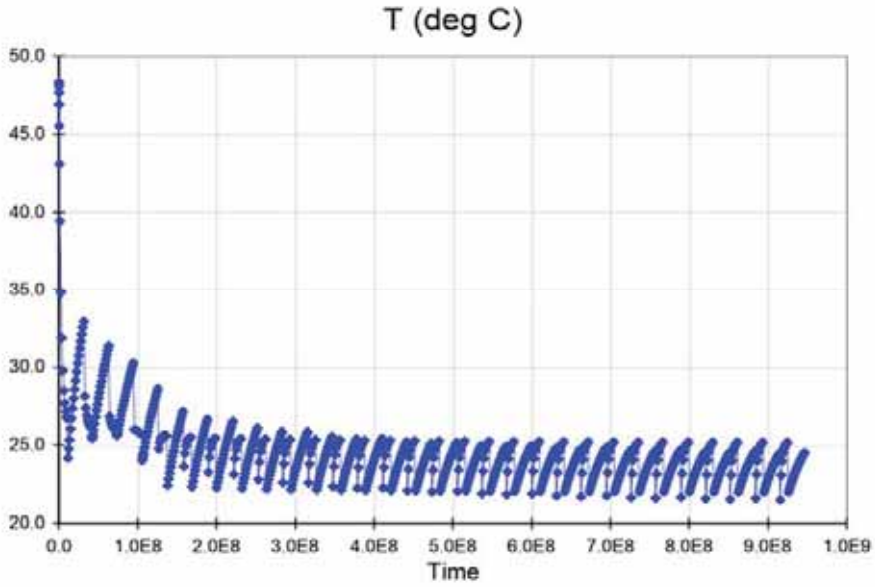

FIGURE 11
Temperature change over time in the reinjection well section

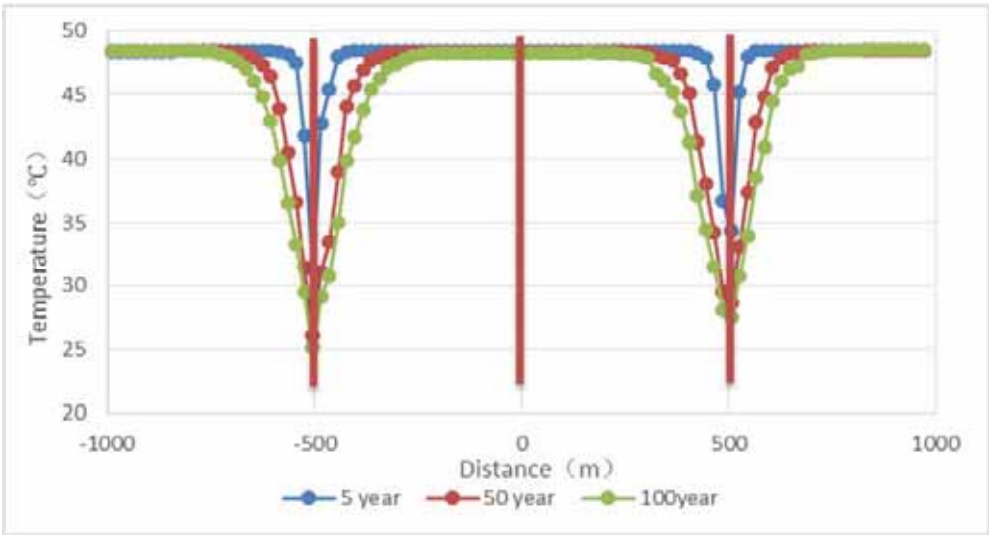

FIGURE 12
Temperature change over time in the reinjection well section

It shows the temperature change in the reinjection well in Figure 11. Due to the long-term injection of cold water, the temperature in the reinjection well drops continued until it reaches the reinjection temperature. During the non-heating period, the reinjected cold water absorbs the heat in the surrounding rock and the temperature rises slightly, but it is far from returning to the initial temperature. Therefore, the temperature influence range around the reinjection well is gradually expanded. It shows the temperature influence range with time around the reinjection well in Figure 12.

Generally for comprehensive utilization of medium and low temperature geothermal fields, the service life should be more than 100 years. As is shown in Figure 12, without regard to other changes of the exploitation scenario, the range of $\Delta t>1°C$ around the reinjection well is 230.75 m after 100 years.

Considering the heterogeneity of the reservoir and other factors, it is recommended that the distance between the production and reinjection well should is about 300m.

CONCLUSIONS

1. According to the results of the reinjection test of WELL TMI, the permeability coefficient of reinjection gradually decreases with the increase of reinjection time.

2. When the reinjection water temperature is 25℃, the maximum reinjection rate of single well is about 633.48m^3/d; at 19℃, the maximum reinjection volume is 641.04m^3/d. When the temperature of the reinjection water becomes lower, the reinjection rate increases, which means that after the temperature decreases, the increase in water density has a greater positive effect on reinjection than the negative effect caused by an increase in viscosity.

3. When the geothermal reservoir is reinjected, the reinjected water enters the reservoir for the action of the pressure difference between the reinjection head and the reservoir. The viscosity of water increases with decreasing temperature, so the reinjection rate at low temperature is smaller than the amount of production.

4. To achieve 100% reinjectionin Yancheng Uplift, the well pattern of "One Production with Two Reinjection" needs to be adopted. The distance between the production and reinjection well is 300m.

ACKNOWLEDGEMENTS

Thanks to Dr. Duan Zhongfeng from China University of Petroleum (Qingdao) for his careful guidance on this article.

REFERENCES

[1] Wang, K. (2019) Research on thermal storage and irrigation in Yanjin area based on TOUGH2 numerical simulation software. Ground Water. 041(001), 14-16.

[2] Wang, C., Wang, F. (2007) Discussion on the controlling of artificial reinjection of groundwater to the land subsidence. Shanxi Architecture. 33(033), 142-143.

[3] Bi, E. (1998) Geochemical modeling of the mixing of geothermal water and reinjection water: A case study of Laugaland low-temperature geothermal field in Iceland. Earth Science-Journal of China University of Geosciences. 36(6), 631-634.

[4] Wu, L.L., Meng, F.Q., Dong, Y.L., Liu, Q., Liu, Y.F. (2017) Experimental study on karst geothermal reservoir reinjection in Yuncheng county of Shandong province. Shandong Land and Resources. (06), 38-42.

[5] Liu, J. (2003) The status of geothermal reinjection. Hydrogeology & Engineering Geology. (3), 100-104.

[6] Zhu, H.L., Liu, X.M., Yang, F., Yang, H.J., Wang, X.Y. (2011) Analysis and study on geothermal reinjection test of deep groundwater in Kaifeng. Journal of Henan Polytechnic University (Natural Science). 30(02), 215-219.

[7] Tian, L.F., Zhu, X., Wang, L.M., Du, P., Peng, F.Q., Pang, Q.Q. (2020) Long-term trends in water quality and influence of water recharge and climate on the water quality of brackish-water lakes: a case study of Shahu lake. Journal of Environmental Management. 276,111290.

[8] Li, H.Q., Xing, G.P., Wang, C. (2015) Simulation study on effects of storm water reinjection on deep confined aquifer water quality. Bulletin of Soil and Water Conservation. 35(01), 139-142.

[9] Kolditz, O., Bauer, S., Bilke, L., Böttcher N., Delfs, J., Fischer, T., Görke, U., Kalbacher, T., Kosakowski, G., McDermott, C., Park, C., Radu, F., Rink, K., Shao, H., Sun, F., Sun, Y., Singh, A., Taron Walther, J., Wang, W., Watanabe, N., Wu, Y., Xie, M., Xu, W., Zehner, B.(2012) OpenGeoSys: An Open-Source Initiative for Numerical Simulation of Thermo-Hydro-Mechanical/Chemical (THM/C) Processes in Porous Media. Environmental Earth Sciences. 67(2), 589-599.

[10] Beier, R., Smith, M., Spitler, J. (2011) Reference data sets for vertical borehole ground heat exchanger models and thermal response test analysis. Geothermics. 40(1), 79-85.

[11] Pang, Z. (1987) The influence of groundwater movement on the ground temperature field-a review of research progress. Hydrogeology and Engineering Geology. (03), 30-34.

[12] Yasuhara, H., Kinoshita, N., Ohfuji, H., Lee, D., Nakashima, S., Kishida, K. (2011) Temporal alteration of fracture permeability in granite under hydrothermal conditions and its interpretation by coupled chemo-mechanical model. Applied Geochemistry. 26(12), 2074-2088.
[13] Yamamoto, H. (2008) PetraSim: A Graphical User Interface for the TOUGH2 Family of Multiphase Flow and Transport Codes. Ground Water. 46(4), 525-528.
[14] Pang, Z., Kong, Y., Pang, J., Hu, S., Wang, J. (2017) Research on geothermal resources and development and utilization of Xiongan New Area. Bulletin of the Chinese Academy of Sciences. (11), 1224-1230.
[15] Kong, Y., Pang, Z., Shao, H., Kolditz, O. (2014) Recent studies on hydrothermal systems in China: a review. Geothermal Energy. 2(1), 1-12.
[16] Yang, Y.D. (2020) Evaluation of geothermal resources in Zhoukou Depression (Zhoukou Section). China Energy and Environmental Protection. 42(06), 121-125.
[17] Zhang, C.Q. (2011) Development and utilization status of geothermal resources in Luohe City. Henan Water Conservancy and South-to-North Water Diversion. 3(06), 10-12.
[18] Xu, L., Liu, M. (2004) General situation of geothermal resources in Henan Province. Coal Geology of China. 16(1), 33-35.
[19] Lu, Y.B., Zhang, G.B., Chen, Y. (2010) Current situation of development and utilization of geothermal resources in Henan and the issue study. Exploration Engineering (Rock & Soil Drilling and Tunneling). 3(10), 35-39.
[20] Hunt, T., Bowyer, D. (2007) Reinjection and gravity changes at Rotokawa geothermal field, New Zealand. Geothermics. 36(5), 421-435.
[21] Seibt, P., Kellner, T. (2003) Practical experience in the reinjection of cooled thermal waters back into sandstone reservoirs. Geothermics. 32(4-6), 733-741.

Received: **16.11.2021**
Accepted: **09.01.2022**

CORRESPONDING AUTHOR

Yajun Sun
School of Resources and Geosciences,
China University of Mining and Technology,
Xuzhou 221116 – China

e-mail: kun20200101@163.com

© by PSP Volume 31– No. 05/2022 pages 4872-4879 Fresenius Environmental Bulletin

EFFECT OF HEAVY METAL CONTAMINATED SOIL ON FORAGE QUALITY BASED ON ENVIRONMENTAL PROTECTION

Ao Sun[1,3], Lihua Wen[1], Wu Song[1], Jianbo Li[1,3], Fang He[1], Haobang Li[1], Yang Luo[1], Cheng Huan[1], Yun Long[3], Kangle Yi[1,3,*]

[1]Hunan Institute of Animal Husbandry and Veterinary Medicine, Changsha 410131, China
[2]Hunan De Nong Animal Husbandry Group Co. Ltd., 416400, China
[3]Xiangxi Yellow Cattle Engineering Technology Center, Hunan Xiangxi, 416000, China

ABSTRACT

The development of industrial and agricultural technology, especially the progress of industrial civilization, industrial production and automobile exhaust will emit a large number of heavy metal elements, resulting in serious soil heavy metal pollution. The polluted soil has a serious impact on the growth and quality of forage grass. To study the impact of heavy metal contaminated soil on forage quality is very important for the safe production of forage. In view of this problem, this paper first analyzes the experimental design and experimental steps of the impact analysis of heavy metal contaminated soil on forage quality, takes the common forage bullwhip as the research object of forage, and takes the heavy metals copper, cadmium and lead as the research object of heavy metals. It is proposed to evaluate the forage quality by measuring the growth characteristic index, mature nutrient index and heavy metal accumulation index of bullwhip, and the determination method of relevant indexes is put forward. Single factor analysis showed that the three kinds of heavy metal contaminated soil were not conducive to the growth of forage grass. With the increase of soil heavy metal pollution, the growth characteristics of forage were seriously affected, and the average plant height (PH) and average biomass (DW) gradually decreased. The average plant height decreased from 44cm to about 12cm, and the average biomass decreased from 70g to about 20g. Compared with the control group, the average plant height and average biomass of forage in the polluted soil decreased by more than 70%. With the increase of soil heavy metal pollution, the content of Forage Crude Protein (CP) decreased gradually, the proportion of CP decreased by about 50%, the content of neutral detergent fiber (NDF) increased gradually, the accumulation of heavy metals in forage increased gradually, and the forage quality decreased continuously. Through experimental analysis, it can provide reference for forage safety production.

KEYWORDS:
Heavy metal contamination, soil, forage quality, growth characteristics, heavy metal accumulation

INTRODUCTION

Soil is the foundation of agricultural civilization and the basis of human survival and development. However, with the continuous progress of industrial and agricultural technology, due to the unreasonable development and utilization of natural resources, a large number of waste batteries, solid wastes, waste water, waste gas and other heavy metals are discharged, resulting in heavy metal pollution to the soil. The soil polluted by heavy metals destroys the physical and chemical properties of the original soil, seriously affects agricultural and animal husbandry production, has a more serious impact on animal husbandry, and the soil polluted by heavy metals is difficult to improve and eliminate in the short term [1-3].

At present, the grassland polluted by heavy metals in China has exceeded 60%, which has seriously affected the quality of forage grass and the stable development of animal husbandry. For example, the soil in Xiangjiang River Basin of Hunan Province is seriously polluted by heavy metals, and the main pollutants include copper, cadmium and lead. In the process of animal husbandry and livestock breeding, forage safety is the primary factor. The polluted soil has an adverse impact on the growth and quality of forage grass, which further affects the health quality of livestock and human dietary safety. Domestic and foreign scholars have done a lot of research on the impact of heavy metal polluted soil on forage quality, but the research on the evaluation index of forage quality in heavy metal polluted environment is insufficient [4-8].

To solve this problem, this paper first analyzes the experimental design and steps of the impact of heavy metal contaminated soil on forage quality. Taking common forage bullwhip as the research object of experimental forage and heavy metals copper, cadmium and lead as the research object of heavy

metals, this paper puts forward the evaluation of forage quality by measuring the growth characteristic index, mature nutrient index and heavy metal accumulation index of bullwhip, and puts forward the determination method of relevant indexes. The effects of three kinds of heavy metal contaminated soil on the average plant height (PH), average biomass (DW), crude protein (CP) content, neutral detergent fiber (NDF) content and the accumulation of heavy metals in forage were obtained by single factor analysis. The effects of heavy metal contaminated soil on forage quality were analyzed to provide reference basis for forage safety production.

MATERIALS AND METHODS

Test object and design. (1) Test analysis object. The development of social economy, especially the development of industrial civilization, industrial production and automobile exhaust will emit a large number of heavy metals. In industrial and agricultural production, heavy metals are generally metal elements with a density of more than 4.5g/cm3, such as cadmium, lead, copper, iron, zinc, nickel and cobalt [9-10]. Heavy metals are easy to settle and accumulate in the soil, causing heavy metal pollution in the soil and affecting the soil quality, especially the forage quality of animal husbandry. In this paper, copper (Cu), cadmium (Cd) and lead (Pb) were used as the analysis objects of heavy metals, and the commonly used forage bullwhip was used as the analysis object of forage. Bullwhip is a gramineous plant with lush stems and leaves and large yield. It is the most widely planted forage variety in China. Therefore, the study on the growth quality of Bullwhip in heavy metal polluted soil environment has a strong reference.

(2) Experimental design. To analyze the impact of heavy metal contaminated soil on forage quality, potted bullwhip was used for experimental analysis. The experimental soil was taken from a farm in Hunan as the experimental matrix soil. After disinfection and air drying, stones and other impurities were screened out to test its physical and chemical properties [11], as shown in Table 1.

The experimental matrix soil is the basis for the comparison of the whole experiment. To analyze the effects of heavy metals copper (Cu), cadmium (Cd) and lead (Pb) on forage quality, $CuSO_4 \cdot 5H_2O$, $CdCl_2 \cdot 2.5H_2O$ and $Pb(NO_3)_2$ were added to the salt solution to prepare the corresponding heavy metal solutions with different concentrations. The concentrations of copper (Cu) are 50, 100, 150, 200, 250 and 300 (mg/l), cadmium (Cd) are 5, 10, 20, 30, 40 and 50 (mg/l), and lead (Pb) are 100, 200, 300, 500, 600 and 800 (mg/l). The soil polluted by heavy metals is simulated by pouring heavy metal solutions of different concentrations into the matrix soil [12-13]. To ensure the accuracy of the test, strict test steps are formulated, as shown in Figure 1.

TABLE 1
Physical and chemical properties of test substrate soil

Indicator name	Content
Organic matter (%)	1.2
Total nitrogen (%)	0.13
Available P (mg/kg)	36.1
Available K (mg/kg)	86.9
Cu base value (mg/kg)	26.55
Cd Base value (mg/kg)	0.65
Pb base value (mg/kg)	21.05

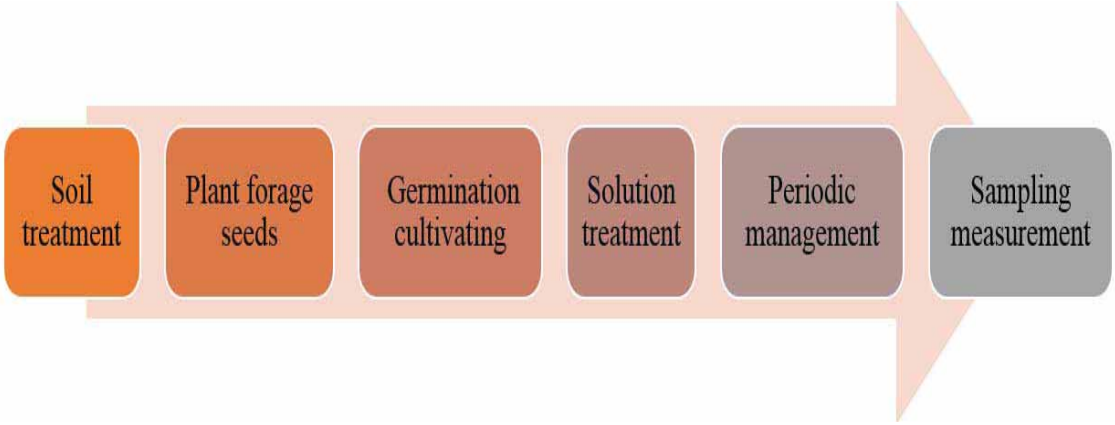

FIGURE 1
Test steps for the effect of heavy metal contaminated soil on forage quality.

In the figure above, the test steps mainly include six steps. Firstly, the soil collected from the farm was disinfected and air dried, and the standard soil was quantitatively loaded into different test pots, with a total of 31 pots, of which 1 pot was marked as the control group, and the other 30groups were divided into six groups, corresponding to the soil polluted by different heavy metal concentrations. The weight of each pot was 5kg, so as to ensure that the test was not disturbed by soil factors. After the soil treatment, the seeds of bullwhip shall be screened, disinfected and classified to screen the same full seeds. 50 seeds shall be evenly sown in each test basin to ensure that the test is not affected by seed factors. Then put all experimental groups in the environment with the same humidity and temperature, pour the same amount of water every day, evenly grow 3-4 leaves in the forage in all experimental pots, screen and treat the seedlings in all experimental pots, leaving 40 evenly growing seedlings. After the seedling cultivation treatment, the forage potted plants of the three experimental groups were poured with 300ml solution of different concentrations of heavy metals, and the control group was poured with the same amount of clean water. Then, all forage potted plants shall be managed regularly to maintain the normal growth of forage under the same external conditions, and finally the relevant data shall be measured according to the requirements.

Method for determination of forage quality. To analyze the effects of heavy metal contaminated soil on forage quality, this paper mainly measured the growth characteristics of bullwhip, the nutrient indexes after maturity and the accumulation indexes of heavy metals. The determination methods of relevant indexes are:

(1) Test method for growth characteristic index. The growth characteristic indexes of forage mainly include plant height and biomass, in which plant height is the height from forage soil surface to plant top. During the study, the average plant height of all plants in the pot culture after pouring heavy metal solution for 60 days was measured as the evaluation standard [14-15].

The biomass index of forage is determined by harvesting the forage after 60 days, cleaning all complete plants to remove the soil, drying at 105°C, and the average dry weight (DW) after drying is used as the biomass evaluation index of forage.

(2) Forage quality test method. The quality evaluation of forage grass is mainly carried out by analyzing the content of main nutrients. For forages, especially gramineous forages such as bullwhip, the content of crude protein (CP) and neutral detergent fiber (NDF) can be evaluated. The higher the content of crude protein (CP), the higher the forage quality, and the higher the content of neutral detergent fiber (NDF), the lower the forage quality [16-18].

Among them, crude protein (CP) represents the percentage of crude protein (CP) in dry matter in forage, which can be tested by Kjeldahl method. The content of crude protein (CP) is calculated by multiplying the total nitrogen in forage by the coefficient. The coefficients of different forages are slightly different. The commonly used value is 6.25 [19] in the calculation process of this paper. Neutral detergent fiber (NDF) represents the percentage of neutral detergent fiber in dry matter, which can be measured and analyzed by aikom fiber analyzer.

(3) Test method for heavy metal accumulation. For the evaluation of forage quality, in addition to the above nutrient content, the accumulation of heavy metals in forage is also an important factor affecting forage quality. The high content of heavy metals will do great harm to the growth and quality of livestock, as well as its consumers. In this paper, atomic fluorescence spectrometry is used to detect the accumulation of heavy metals in forage. This method has been widely used in the measurement of heavy metal content in forage. The content of elements to be measured is determined by measuring the fluorescence emission intensity of atomic vapor of elements to be measured excited by radiation energy. The calculation formula of heavy metal accumulation in forage is [20-22]:

$$X = \frac{(C - C_0) \times V \times 1000}{DW \times 1000 \times 1000} \quad (1)$$

In the formula, X is the accumulation of heavy metals in forage, mg/kg; C is the measured concentration of digestive solution of forage sample, ng/ml; C_0 is the concentration of the measuring reagent used, ng/ml; V is the total volume of digestive solution of the measured sample, ml; DW is the dry weight of forage sample, g.

RESULTS

Effect of heavy metal pollution on growth characteristics. The effects of heavy metal contaminated soil on forage quality were analyzed by single factor impact analysis method. Through the above test methods, bullwhip was taken as an example. Among them, the growth characteristic indexes of forage mainly include average plant height (PH) and average biomass (DW). The statistics of forage plant height (PH) and average biomass (DW) cultured with different concentrations of heavy metal copper (Cu) solution are shown in Figure 2.

In the above figure, the addition concentrations of heavy metal copper solution are 0, 50, 100, 150, 200, 250 and 300 (mg/l) respectively. When the concentration of heavy metal copper solution was 50 mg/l, the average plant height increased slightly compared with the control group, from 44cm to

48cm. Then, with the increase of the concentration of heavy metal copper solution, the average plant height and average biomass decreased gradually after 60 days. When it reached 300 mg/l, the average plant height decreased to 15cm and the average biomass decreased from 70g to 21g. Therefore, the increase of soil heavy metal copper pollution is not conducive to the growth of forage. The plant height (PH) and average biomass (DW) of forage grass cultured with cadmium (CD) solution of different concentrations are counted, as shown in Figure 3.

After 60 days, the average plant height and average biomass decreased gradually with the increase of heavy metal cadmium concentration. The average plant height decreased from 44cm to 12cm, and the average biomass decreased from 70g to 20g. Therefore, the increase of soil heavy metal cadmium pollution is not conducive to the growth of forage grass. The plant height (PH) and average biomass (DW) of forage grass cultured with different concentrations of heavy metal lead (Pb) solution are counted, as shown in Figure 4.

After 60 days, the average plant height and average biomass decreased gradually with the increase of heavy metal lead concentration. The average plant height decreased from 44cm to 13cm, and the average biomass decreased from 70g to 16g. Therefore, the increase of soil heavy metal lead pollution is not conducive to the growth of forage grass.

The above experiments showed that the three kinds of heavy metal pollution were not conducive to the growth of forage. With the increase of soil heavy metal pollution, the growth characteristics of forage were seriously affected. The average plant height (PH) and average biomass (DW) gradually decreased with the increase of pollution. Compared with the control group, the average plant height and average biomass of forage decreased by more than 70%.

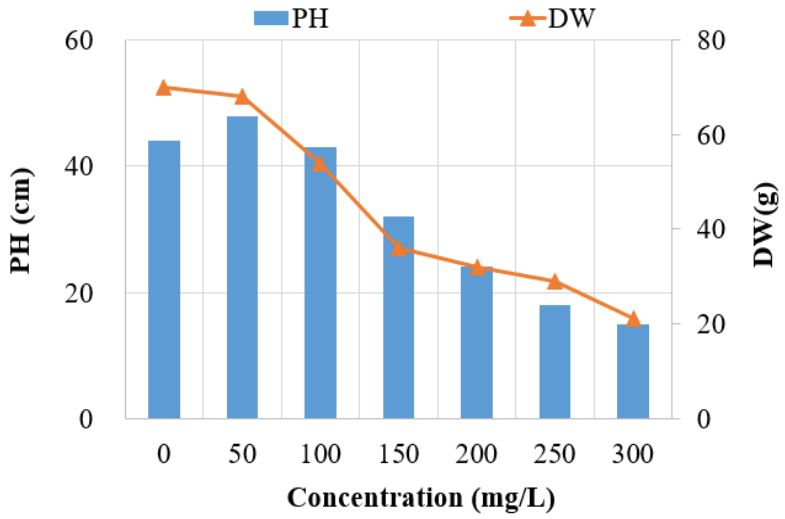

FIGURE 2
Effects of heavy metal copper on forage growth characteristics.

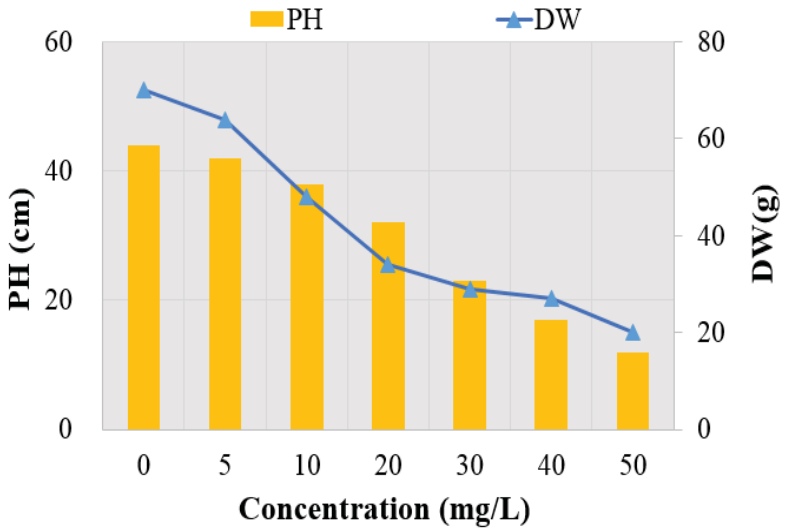

FIGURE 3
Effects of heavy metal cadmium on forage growth characteristics.

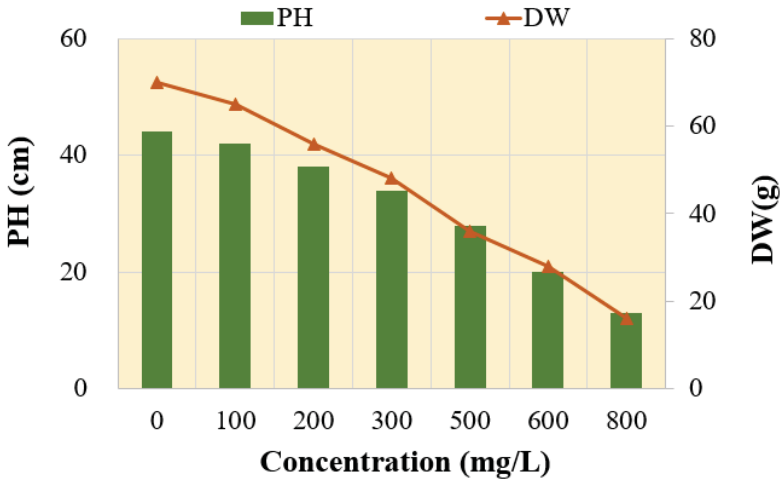

FIGURE 4
Effects of heavy metal lead on forage growth characteristics.

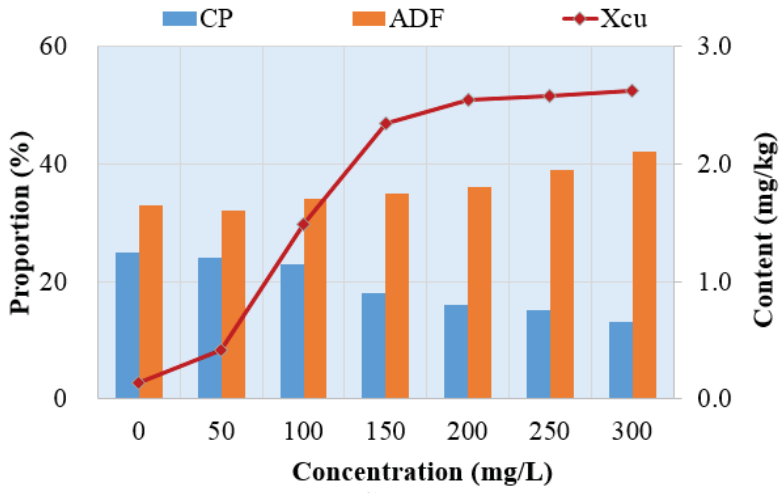

FIGURE 5
Effect of heavy metal copper on forage quality.

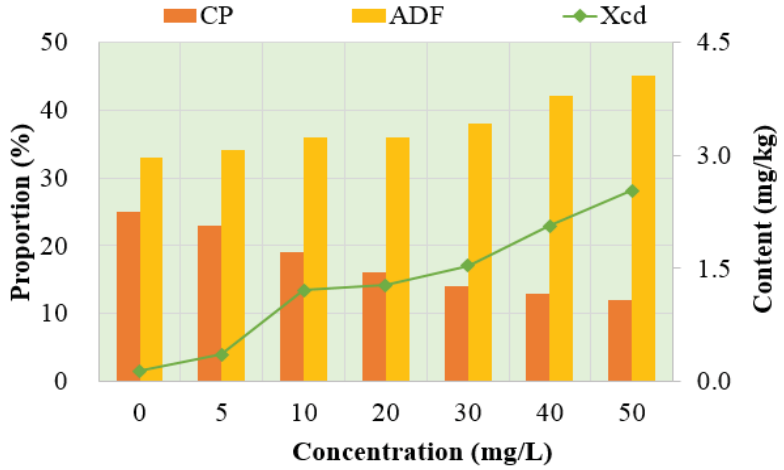

FIGURE 6
Effects of cadmium on forage quality.

Effect of heavy metal pollution on forage quality. In this paper, the quality of forage was evaluated by analyzing the content of crude protein (CP), neutral detergent fiber (NDF) and the accumulation of heavy metals in forage. The contents of Forage Crude Protein (CP), neutral detergent fiber (NDF) and the accumulation of heavy metals in forage (Xcu) cultured in soil polluted by heavy metal copper are counted, as shown in Figure 5.

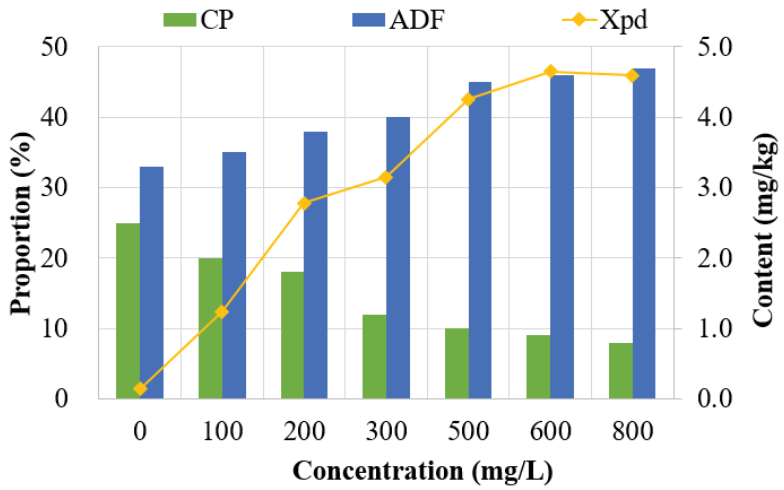

FIGURE 7
Effect of heavy metal lead on forage quality.

With the increase of soil heavy metal copper concentration in the experiment, the content of Forage Crude Protein (CP) gradually decreased, the content of crude protein (CP) decreased from 25% to 13%, the content of neutral detergent fiber (NDF) gradually increased from 33% to 42%, and the accumulation of heavy metal copper in forage gradually increased from 0.14mg/kg to 2.62mg/kg, which increased nearly 20 times, seriously affecting the growth quality of forage. It is generally believed that the accumulation of heavy metals exceeding 1mg/kg will have adverse effects on livestock eating the forage. The above analysis showed that with the increase of soil heavy metal copper concentration, the forage quality decreased continuously, and even could not be eaten. The contents of Forage Crude Protein (CP), neutral detergent fiber (NDF) and the accumulation of heavy metals in forage (Xcd) after culture with different concentrations of heavy metal cadmium (CD) solution are counted, as shown in Figure 6.

With the increase of soil heavy metal cadmium concentration in the experiment, the content of Forage Crude Protein (CP) gradually decreased from 25% to 12%, the content of neutral detergent fiber (NDF) gradually increased from 33% to 45%, and the accumulation of heavy metal cadmium in forage gradually increased from 0.14mg/kg to 2.53mg/kg, nearly 16 times, indicating that the forage quality decreased with the increase of soil heavy metal cadmium concentration. The contents of Forage Crude Protein (CP), neutral detergent fiber (NDF) and the accumulation of heavy metals in forage (Xpd) cultured with different concentrations of heavy metal lead (Pb) solution are counted, as shown in Figure 7.

With the increase of soil heavy metal lead concentration in the experiment, the content of Forage Crude Protein (CP) gradually decreased from 25% to 8%, the content of neutral detergent fiber (NDF) gradually increased from 33% to 47%, and the accumulation of heavy metal lead in forage gradually increased from 0.14mg/kg to 4.59mg/kg, nearly 30 times, indicating that the forage quality decreased with the increase of soil heavy metal lead concentration.

The above experimental analysis showed that the three kinds of heavy metal pollution not only reduced the growth characteristics of forage, but also had a serious impact on the quality of forage. The content of Forage Crude Protein (CP) decreased gradually with the increase of soil heavy metal pollution. Generally speaking, the proportion of CP decreased by about 50%. The content of neutral detergent fiber (NDF) increased gradually, and the forage quality decreased continuously. At the same time, compared with the control group, the accumulation of heavy metals in the forage gradually increased, and the accumulation of three types of heavy metal pollution increased by more than 16 times. Too high accumulation would endanger the quality of livestock eating the forage, and then endanger human health.

CONCLUSIONS

(1) This paper analyzes the experimental design and steps of the impact of heavy metal polluted soil on forage quality. Taking common forage bullwhip as the research object of experimental forage and heavy metals copper (Cu), cadmium (Cd) and lead (Pb) as the research object of heavy metals, this paper puts forward the evaluation of forage quality by measuring the growth characteristic index, mature nutrient index and heavy metal accumulation index of bullwhip, and puts forward the determination method of relevant indexes.

(2) Single factor analysis showed that the three kinds of heavy metal contaminated soil were not conducive to the growth of forage grass. With the increase of soil heavy metal pollution, the growth characteristics of forage grass were seriously affected,

and the average plant height (PH) and average biomass (DW) gradually decreased. The average plant height decreased from 44cm to about 12cm, and the average biomass decreased from 70g to about 20g. Compared with the control group, the average plant height and average biomass of forage grass decreased by more than 70%.

(3) Three kinds of heavy metal pollution not only reduce the growth characteristics of forage, but also have a serious impact on the quality of forage. With the increase of soil heavy metal pollution, the content of Forage Crude Protein (CP) decreased gradually, the proportion decreased by about 50%, and the content of neutral detergent fiber (NDF) increased gradually. Compared with the control group, the accumulation of heavy metals in the forage gradually increased, the forage quality continuously decreased, and the excessive accumulation was harmful to the livestock eating the forage, and then to human health.

ACKNOWLEDGEMENTS

Authors acknowledge the funding provided by 'Construction of Modern Agricultural Industrial Technology System in Hunan Province (Hunan Financial Agriculture Guide 2019 [97])', 'Xiangxi Yellow Cattle Engineering Technology Center. (2019TP2010)','Research and demonstration on key technologies of straw resources utilization in feed (2021NK4171)', 'Study on Breeding of Ramie with High protein and Low Anti-nutritional factor and Key technology of feeding Xiangxi cattle(2022NK2017)','Construction and demonstration of key technology system for large-scale green breeding of high-quality beef cattle(2022NK2025).

REFERENCES

[1] Huang, Y., Huang, Y., Yu, G., Diao, W., Sun, Q. (2011) Research Progress on Absorption and Accumulation of Heavy Metals in Vegetables. The Yangtze River Vegetable. 1(10), 1-6.
[2] Dong, Z., Chen, J. (2013) Effect of Salt Stress on Germination of Different Wheat Varieties. Seed World. 25(8), 38-42.
[3] Ozkan, A., Uygur, V. (2019) Determination of heavy metal concentrations in agricultural lands of Amik plain with MP-AES. Fresen. Environ. Bull. 28(1), 416-425.
[4] Pestana, M., Formoso, M. (2007) Mercury Contamination in Lavras Do Sul, South Brazil: A Gegacy from Past and Recent Gold Mining. Environmental Management. 103(2), 275-287.
[5] Christos, N., Ilias, Z., Vasileios, M. (2010) Heavy Metal Pollution Associated with an Abandoned Lead-Zinc Mine in the Kirki Region. Environmental Management. 85(1), 307-312.
[6] Ashraf, M., Maah, M., Yusoff, B. (2010) Heavy Metals Accumulation in Plants Growing in Extend Mining Catchment. Environmental Science Technology. 8(2), 401-416.
[7] Hidalgo-Moreno, J., Nuflez, R., Garcia, J., Ramirez, R., Larios, N., Ben, Z. (2020) Genetic diversity and population structure of Boer and Nubian goats in Mexico. Small Ruminant Research. 103(2), 187-192.
[8] Sebastien, H., Jessica, W., Bachar, C. (2012) Network Analyses Structure Genetic Diversity in Independent Genetic Worlds. Environmental Management. 107(1), 127-132.
[9] Casler, M., Pedersen, J., Undersander, D. (2003) Forage Yield and Economic Losses Associated with the Brown-Midrib Trait in Sudangrass. Crop Science. 43(3), 782-789.
[10] Huang, R. (2018) Research Progress on Plant Tolerance to Soil Salinity and Alkalinity in Sorghum. Journal of Integrative Agriculture. 17(4), 739-746.
[11] Bohemen, H., Janssen, V., Leak, W. (2003) The Influence of Road Infrastructure and Traffic on Soil, Water, and Air Quality. Environmental Management. 31(1), 50-68.
[12] Hjortenkrans, D., Bergback, B., Haggerud, A. (2006) New Metal Emission Patterns in Road Traffic Environments. Environmental Monitoring and Assessment. 117(3), 85-98.
[13] Huang, Y., Huang, Y., Yu, G., Diao, W., Sun, Q. (2011) Research Progress on Absorption and Accumulation of Heavy Metals in Vegetables. The Yangtze River Vegetable. 1(10), 1-6.
[14] Cai, K., Yu, Y., Zhang, M., Kim, K. (2019) Factors affecting the bioavailability of heavy metals in soil-corn systems in the Taiang Mountains Front Plain. Fresen. Environ. Bull. 28(8), 5795-5810.
[15] Li, Y., Xie, N., Zhao, H. (2011) Analysis of Vegetative Growth and Feeding Quality of Gordon Grass. Grassland Journal. 19(5), 813-820.
[16] Jia, C., Qian, Z., Tu, S. (2017) Nutrient Value Index of Roughage and Evaluation Method. Grass Science. 34(2), 415-427.
[17] Dong, W., Zhang, G., Zhang, H., Sun, S. (2019) Study on Production Performance and Feeding Value of Different Cultivars of High Grass in Ningxia Yellow Irrigation Area. Chinese Journal of Grassland. 40(1), 42-46.
[18] Chen, Z., Shi, M., Wang, Q., Li, Y. (2008) Determination of Protein Content in Food by Kjeldahl Method. Xinjiang Animal Husbandry. 10(5), 22-29.
[19] Chen, L., Shi, J., Wang, Y., Zhang, L., Feng, J. (2015) Adaptability Evaluation of Grass Productivity in Alpine Region. Grassland Journal. 15(2), 1-2-196.

[20] Guo, Y., Li, W., Yang, H., Qian, Y. (2011) Effects of Heavy Metal Combined Pollution on Antioxidant Enzyme Activities of Brassica Juneau. Journal of Soil and Water Conservation. 19(5), 813-820.
[21] Wang, Y., Xiao, L., Li, S., Wang, J. (2010) Effects of Pb and Cd Combined Pollution on Physiological and Biochemical Characteristics of Soil and Rice Leaves. Chinese Agricultural Science Bulletin. 16(2), 359-364.
[22] Liu, F., Sun, Z. (2019) Comprehensive Performance and Nutritional Value Evaluation of Different Forage Sorghum Varieties. Animal Husbandry and Feed Science. 40(9), 51-59.

Received: **17.11.2021**
Accepted: **09.01.2022**

CORRESPONDING AUTHOR

Kangle Yi
Hunan Institute of Animal Husbandry and Veterinary Medicine,
Changsha 410131 – China

e-mail: 23404504@qq.com

© by PSP Volume 31– No. 05/2022 pages 4880-4887 Fresenius Environmental Bulletin

HEALTH RISK ASSESSMENT TO FLUORIDE IN DRINKING GROUNDWATER OF RURAL RESIDENTS LIVING IN A FLUORIDE ENDEMIC AREA OF NORTHWEST OF ANHUI PROVINCE - CHINA

Yuqing Wang[1], Chen Cui[1], Yunhu Hu[1,*], Mu You[2], Wentie Zhang[1]

[1]School of Chemistry and Materials Engineering, Huainan Normal University, Huainan 232001, China
[2]School of Biology Engineering, Huainan Normal University, Huainan 232001, China

ABSTRACT

Due to excessive fluoride in groundwater, endemic fluorosis in drinking water is widespread in northwest of Anhui Province, China. A total of 104 shallow groundwater samples from groundwater sources were collected to evaluate the potential health risk of fluoride through ingestion and dermal pathway for infant, child, teen and adult age groups using a health risk assessment model recommended by USEPA. The range of fluorine in groundwater in the study area is 0.65-2.31. The highest fluorine average concentration in groundwater is Taihe and Jieshou, and the lowest average concentration is Yingshang. The results from health risk assessment indicate the infant and child population groups are more vulnerable to fluoride health hazards than teen and adult population groups. Fluoride may cause harmful effect on the residents' health in the order of: Infants > Teenagers > Children > Adults. And ingestion pathway was the main route of fluoride exposure health risk. Necessary measures should be taken to provide safe (defluorinated) drinking water, especially to infants and children to stay away from the harm of fluoride, drinking low fluoride water is an effective way to control fluorosis.

KEYWORDS:
Fluoride, Groundwater, Health risk, endemic area

INTRODUCTION

Groundwater is one of the important water sources for agricultural irrigation, industry and residents' life, and has been widely developed and utilized[1]. For the characteristics of wide distribution and stable water quantity, which plays an important role in China's water resources, and its quantity and quality have received extensive attention[2]. Drinking water is not only the basis of human survival and economic development, but also an important medium to spread diseases[3]. Groundwater is the main source of drinking water in rural areas of China, fluoride in groundwater is one of the factors threatening the safety of rural drinking water[4].

Fluorine is one of the elements widely distributed in nature, and it is also an important trace element necessary for life[5]. It plays an important role in maintaining the metabolism of calcium and phosphorus, nerve conduction and cell enzyme activity[6, 7]. However, excessive intake of fluoride is harmful to human health[8]. The international food and Agriculture Organization (FAO), the International Atomic Energy Agency (IAEA) and the World Health Organization (WHO) have defined fluorine as " the element with potential toxicity, but may have essential functions for human body at low doses"[9]. It is generally believed that fluoride has the characteristics of bilateral threshold concentration on human health, and it will affect human health when the intake is lower or higher than the threshold range[10]. Drinking water lower than 0.50 mg / L for a long time is easy to cause fluoride deficiency and dental caries[11], drinking water higher than 1.00 mg / L is defined as high fluoride water[12]. Overdose of fluorine will lead to endemic fluorosis, a systemic chronic cumulative poisoning caused in a specific natural environment, which seriously endangers human health. Drinking water for a long time is easy to cause fluoride content exceeding a certain standard and lead to dental fluorosis, osteo fluorosis and other symptoms[13]. In order to ensure the safety of drinking water, the standard of fluoride in drinking water is 1.0 mg / L [14]in China and 1.5 mg / L in the World Health Organization[15].

Fuyang City is located in the northwest of Anhui Province, which belongs to the Huang Huai alluvial plain. Urban and rural residents take groundwater as the main drinking water source. Urban residents use tap water as their living water source, and rural residents use domestic water wells to extract groundwater for use. Due to the excessive fluorine concentration in groundwater, dental fluorosis and skeletal fluorosis are one of the common geochemical diseases in Fuyang. Tao[16] has reported that the average prevalence of dental fluorosis and skeletal fluorosis in the endemic fluorosis area was 74.79%

and 8.28%, respectively, which seriously harmed people's health. There are many studies[17-19] on the characteristics of fluorine content in groundwater in this area. The results show that the fluorine content in groundwater is generally high. The formation, migration and enrichment process of fluorine in groundwater in this area is complex, which is controlled by both environmental geological conditions and geochemical effects[20]. The existence of fluorine-containing materials and specific geochemical environment are the basic conditions for the formation of fluorine in groundwater in the area, and a good storage environment is the necessary condition for the enrichment of fluorine in water. The prevalence of fluorosis not only seriously endangers the health of the masses in the disease area, but also restricts the economic development and social progress of the disease area. However, there are few reports on the health risk assessment of fluoride in groundwater. The health risk assessment of fluoride is of great significance to control and eliminate endemic fluorosis in the study area.

In this study, the health risk assessment model recommended by the U.S. Environmental Protection Agency (USEPA)[21] was used to assess the drinking water health risk of fluoride in the shallow groundwater of Fuyang city through the sample collection and analysis, assessed the potential risks from fluoride by ingestion and dermal pathway for infants, children, teenagers and adults age group, so as to provide scientific basis for ensuring the drinking water safety of the people and carrying out the prevention and control of endemic fluorosis in the area.

MATERIALS AND METHODS

Study areas. Fuyang is located in the northwest of Anhui Province with latitudes of 114°52′ - 116° 49′ E and longitudes of 32° 25′ - 34° 04′ N, respectively. It governs three districts (Yingzhou, Yingquan and Yingdong district), four county (Taihe, Linquan, Funan, Yingshang county) and one city (Jieshou city) with a total area of 10118 km^2. With a large population density of 10.77 million, 41.75% live in cities and towns and 58.25% in rural areas. Groundwater is the main water source in the area and plays an important role in the development of social and economic. Treated water was supplied by the form of tap water pipelines in cities and towns, and rural areas directly exploit groundwater. The annual average precipitation is 963 mm, of which the annual precipitation in June, July, and August.

Samples collection and analysis. Groundwater is the main water resource of the residents in the study area，which applied for drinking, bathing and other domestic purposes. A total of 112 groundwater samples were collected from domestic wells with depth of 10-25m. The locations of the sampling sites are shown in Figure 1. To ensure the representativeness of sample collection，one well is selected for each town and without factories and mining enterprises near the sampling point. The sampling container is a polyethylene plastic bottle which has been cleaned with distilled water in advance. The water sample is discarded 5 minutes before sampling, and then the sampling bottle is moistened three times with the sample groundwater. The samples were kept at 4°Cand take it back to the laboratory for testing as soon as possible. The content of fluoride was measured using a Spectrophotometer (DR/5000, USA) with the limits of determination (LOD) and quantification (LOQ) were 0.10 mg/L and 0.37 mg/L, separately. The reliability, accuracy and precision of the analytical results were determined by standardization, routine blank determination and spiked analysis[22]. The quality control was achieved by analysis of duplicate samples and calculation of the recovery rate (98 ± 2%) of fluoride added/digested samples[10].

Health risk assessment. Health risk assessment can quantitatively evaluate the potential adverse health effects of various pollutants to human health. The assessment model recommended by the United States Environmental Protection Agency was widely used for quantitative assessment of possible human health risks from exposure to various hazardous substances in the environment[23]. Generally, human exposure to fluoride in groundwater through 3 main pathways including oral ingestion, dermal absorption and inhalation contact[13, 24]. In this study，the most dominant potential exposure pathways of oral ingestion and dermal absorption were considered to evaluate the human health risk of fluoride in groundwater for infants (<1 year), children (1-10 years), teens (11-20 years), and adults (21-72 years) populations. Fluoride is a non carcinogenic risk factor, only non carcinogenic risk was considered in this study. The daily exposure to fluoride in groundwater can be calculated using the following equation Eqs. (1) and (2) [25], respectively.

$$I_{CDI} = \frac{C \cdot IR \cdot EF \cdot ED}{BW \cdot AT} \quad (1)$$

$$I_{CDD} = \frac{C \cdot SA \cdot K_P \cdot ET \cdot EF \cdot ED \cdot CF}{BW \cdot AT} \quad (2)$$

Where I_{CDI} and I_{CDD} are the chronic daily intake of fluoride (mg/kg/day) through oral ingestion and dermal absorption. The parameters used for the calculation of non carcinogenic risk values are obtained from previous literatures [4, 26-28] are listed in Table 1. Hazard quotient (HQ) is the value of non-carcinogenic risks from fluoride exposure through oral ingestion and dermal absorption exposure routes were calculated by dividing the total daily intake of fluoride (I_{CDI} and I_{CDD}) by the reference dose (*RfD*). In absence of particular guideline for HI in China, the USEPA recommended *RfD* for fluoride (0.06 mg/kg·day)[29]. To calculate the fluoride risk, hazard quotient (HQ) was determined using Eqs. (3), (4).

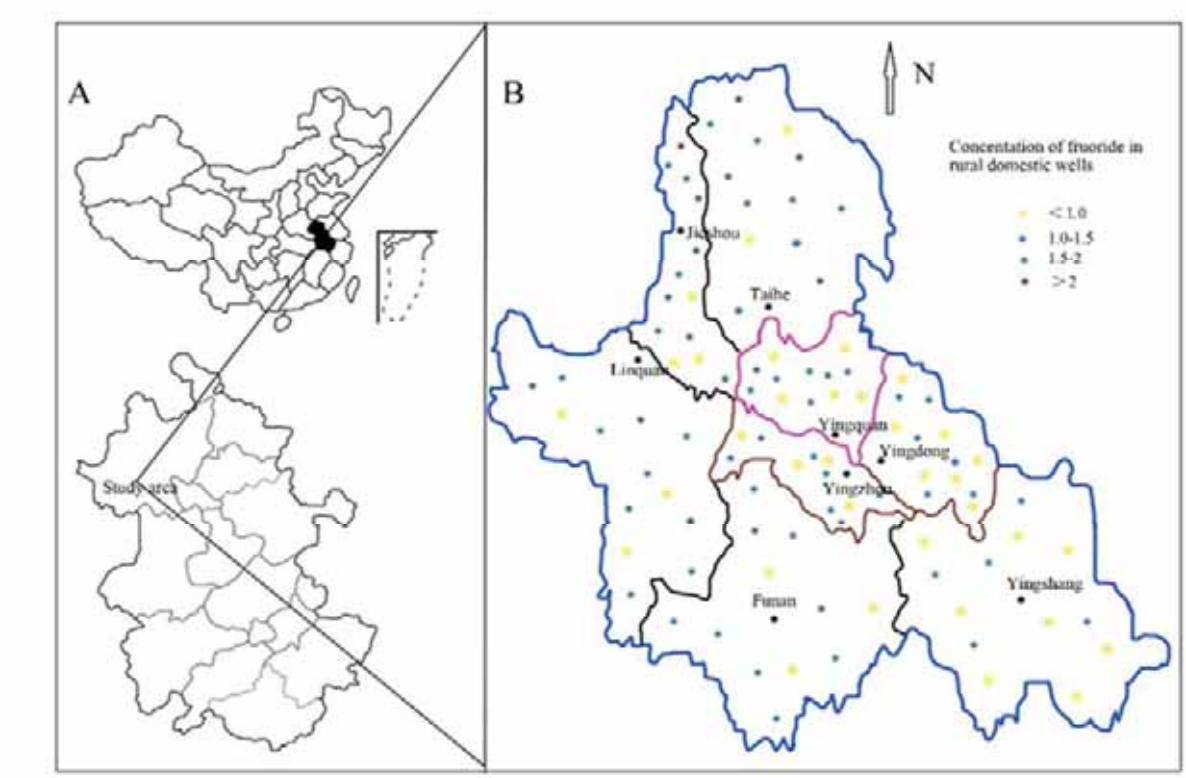

FIGURE 1
Location of sampling sites.

TABLE 1
Key parameters for calculate the health risk of fluoride by ingestion and dermal absorption pathways

Parameters	Infants	Children	Teenagers	Adults
C(Concentration of fluoride, mg/L)	Fluoride concentration in this study			
IR (Ingestion rate, L/d)	0.8	0.85	2	2.5
EF (Exposure frequency, d/year)	365	365	365	365
ED (Exposure duration, year)	6	6	6	30
BW (Body weight, kg)	10	15	50	78
AT (Average time, d)	2190	2190	2190	10950
SA (Exposed skin area, cm^2)	4500	10500	15700	19500
K_p (Dermal permeability coefficient for water)	0.001	0.001	0.001	0.001
ET (Exposure time, h/d)	0.54	0.54	0.54	0.71
CF (Unit conversion factor, L/cm^3)	0.001	0.001	0.001	0.001

$$HQ_{\mathrm{CDI}} = \frac{I_{\mathrm{CDI}}}{RfD} \quad (3)$$

$$HQ_{\mathrm{CDD}} = \frac{I_{\mathrm{CDD}}}{RfD} \quad (4)$$

In this study, HQ represents the fluoride intake non carcinogenic risk from fluoride in groundwater, and was calculated using Eq. (5)

$$HQ = HQ_{\mathrm{CDI}} + HQ_{\mathrm{CDD}} \quad (5)$$

According to the standard recommendations of non carcinogenic risk from USEPA, when HQ>1, which indicates the potential health risk exceeds the acceptable level of residents. HQ≤1is considered that there will be no adverse health effects or the potential health risk within an acceptable range for people[30].

RESULTS AND DISCUSSION

Fluoride concentration. The average concentration and over standard rate of fluorine in groundwater in the study area are shown in Table 2. The range of fluorine in groundwater in the study area is 0.65-2.31, and the concentration order is Taihe > Jieshou >Yingdong > Funan > Yingquan > Yingzhou > Linquan > Yingshang. The average fluorine concentration in drinking water in the study area is1.20mg / L, The highest fluorine average concentration in groundwater is Taihe and Jieshou, 1.52mg/L and 1.33 mg/L, separately. The lowest average concentration is Yingshang, 0.98mg/L. The exceeding rate of fluorine in groundwater in different regions is different. Among them, Taihe County has the highest over standard rate of 49.6%, followed by

Jieshou City, with 47.9%, For comparison, a study conducted by Wu&Ye[31] in Fuyang city, reported the same conclusion that the fluorine exceeding standard rate of rural drinking water in Fuyang City is generally at the national medium level, but Taihe and Jieshou are relatively serious. The fluorine concentration in groundwater generally shows a downward trend from northwest to Southeast. The fluorine in groundwater in the study area mainly comes from fluorine-containing minerals. The fluorine enrichment in shallow groundwater is affected by geographical environment or hydrogeological conditions, and the main control factor is evaporation concentration[17, 18, 32].

Human health risk assessment by ingestion pathway. Figure 2 illustrate the values of *HI* Comparison of mean fluoride concentrations in groundwater samples. The HQ_{CDI} values of fluoride ranged from 1.24 to 2.08 (mean 1.62) and from 0.88 to 1.47 (mean 1.15), from 0.62 to 1.04 (mean 0.81), from 0.50 to 0.83 (mean 0.65) for infants, teenagers，children, and adults, respectively. The results indicate that fluoride may cause harmful effect on the residents' health in the order of: Infants > Teenagers > Children > Adults. Whereas for fluoride, HQ_{CDI} values in 100%, 75%，12.5% and 0% of sample locations are above the acceptable USEPA limit of 1 for infants, teenagers, children and adults, respectively.

According to the HQ_{CDI} values, infants and children who ingest fluoride through drinking water carry serious health risk than any other age groups. The causes of the phenomenon maybe infants are more sensitive receptors and more vulnerable face higher health risks, and they have lower body weight and ingestion rate compared to other age groups.

TABLE 2
The fluoride concentration in groundwater in study area expressed as means, min and max.

Location of Sample Collection	MIN	MAX	AVER	Proportion exceeding Chinese standard	Proportion exceeding WHO Standard
Taihe	0.92	2.31	1.56	84.62%	69.23%
Funan	0.92	1.56	1.19	76.92%	15.38%
Linquan	0.89	1.85	1.31	76.92%	30.77%
Yingshang	0.65	1.27	0.93	38.46%	-
Jieshou	0.89	2.14	1.41	76.92%	38.46%
Yingquan	0.84	1.86	1.14	61.54%	15.38%
Yingzhou	0.82	1.48	1.12	69.23%	-
Yingdong	0.86	1.24	1.04	46.15%	-

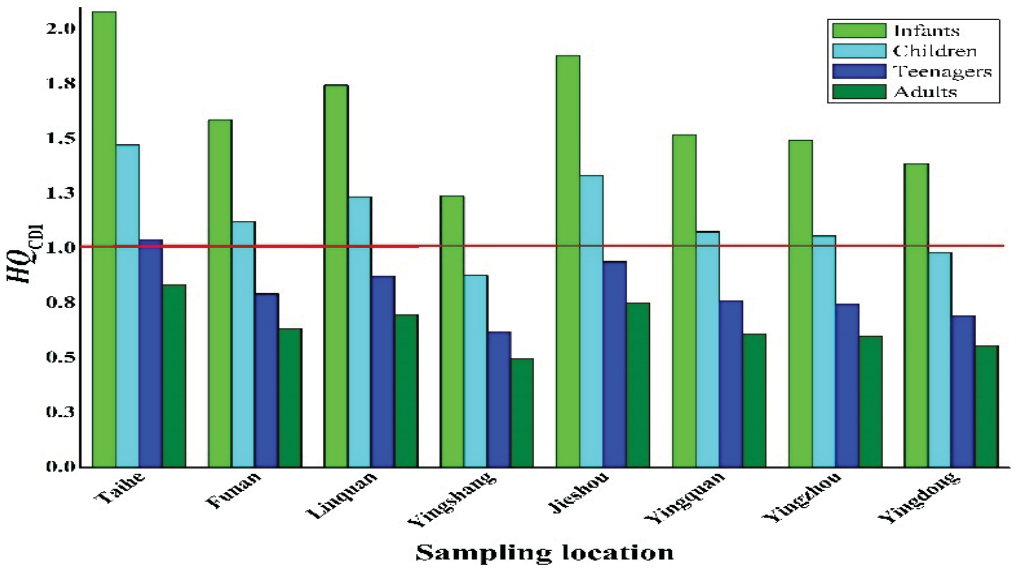

FIGURE 2
Statistical graph of fluoride noncarcinogenic risk by ingestion pathway.

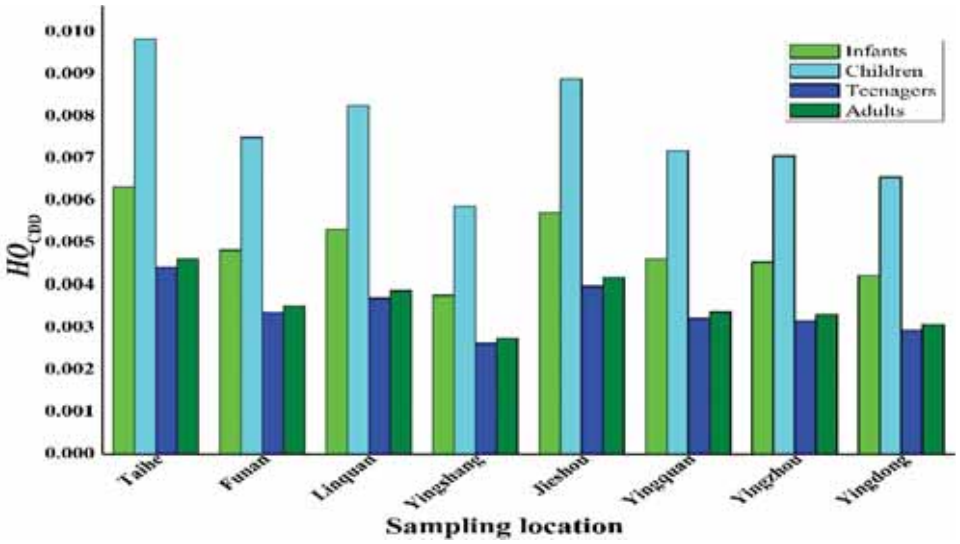

FIGURE 3
Statistical graph of fluoride noncarcinogenic risk by dermal pathway.

Human health risk assessment by dermal pathway. The values of HQ_{CDD} through dermal pathway were calculated separately for different age groups and depicted in Figure 3. The mean values of *HI* from fluoride in groundwater for infants, teenagers，children, and adults were 3.77×10^{-3}-6.32×10^{-3}(mean 4.91×10^{-3}), 5.86×10^{-3}-9.83×10^{-3}(mean 7.64×10^{-3}), 2.63×10^{-3}-4.41×10^{-3}(mean 3.43×10^{-3}) and 2.75×10^{-3}-4.62×10^{-3} (mean 3.59×10^{-3}), respectively. The order of health risk of fluoride in groundwater to different age groups: Teenagers > Infants > Adults > Children. All the values of HQ_{CDD} by dermal route is far less than 1, which indicates that the health risk of fluoride by dermal pathway is very small than that of ingestion pathway.

Total non-carcinogenic risk. The total non-carcinogenic risk of fluoride in groundwater was presented in Figure 4. The mean values of *HQ* from fluoride in groundwater for infants, teenagers，children, and adults were 1.24 - 2.09 (mean 1.62), 0.88-1.48 (mean 1.15), 0.62 - 1.04 (mean 0.81) and 0.50 - 0.84 (mean 0.65), respectively. The total non-carcinogenic health risk is higher than the threshold value of human health risk, and the value of human health for infants and children is higher than teenagers and adults. Infants and children are more sensitive receptors and the minors are also vulnerable to dental and skeletal fluorosis. The value of total non-carcinogenic risk of fluoride and health risk assessment by ingestion route has the same order: Infants > Teenagers > Children > Adults. Measures should be taken to protect infants and children from the health risks of fluoride and to strengthen the prevention and control of endemic fluorosis.

It indicates that the total risk of fluoride in the two exposure pathway is approximately equal to the health risk of ingestion route. The contribution rate of non-carcinogenic risk caused through Ingestion pathway accounted for 99.7%. The HQ_{CDD} in the study area was lower than the threshold, and ingestion pathway was the main route of fluoride exposure. The result is in agreement with the conclusions of some studies[13, 23, 33, 34]. Therefore, the quality control of drinking groundwater should be the primary approach to lessen the health risk of fluoride. Human health is closely related to drinking water. High quality water is an important guarantee for people's health. Groundwater in the study area is rich in fluorine ions. Residents take groundwater as drinking water source, so centralized water supply must be adopted to provide low fluorine water and ensure the safety of daily drinking water.

Uncertainty analysis. In this study, the risk assessment method of human health exposure to pollutants in drinking water of the U.S. Environmental Protection Agency was adopted. The exposure route only considered the average drinking water intake and direct contact, and did not consider other toxic substances and exposure routes, such as inhalation in the form of steam and dietary intake. In fact, the health risk of fluorine was underestimated.

In addition, the exposure risk of fluorine is also closely related to the lifestyle, water use habits and occupation of local residents. Many parameters are involved in the water environment health risk assessment model, such as personal life span, daily average drinking water intake and human quality, which come from previous studies and are not necessarily consistent with local residents. Basic research should be strengthened to improve the accuracy of health risk assessment. Therefore, the research on groundwater fluorine health risk assessment in this paper is preliminary and will be further improved in the future work.

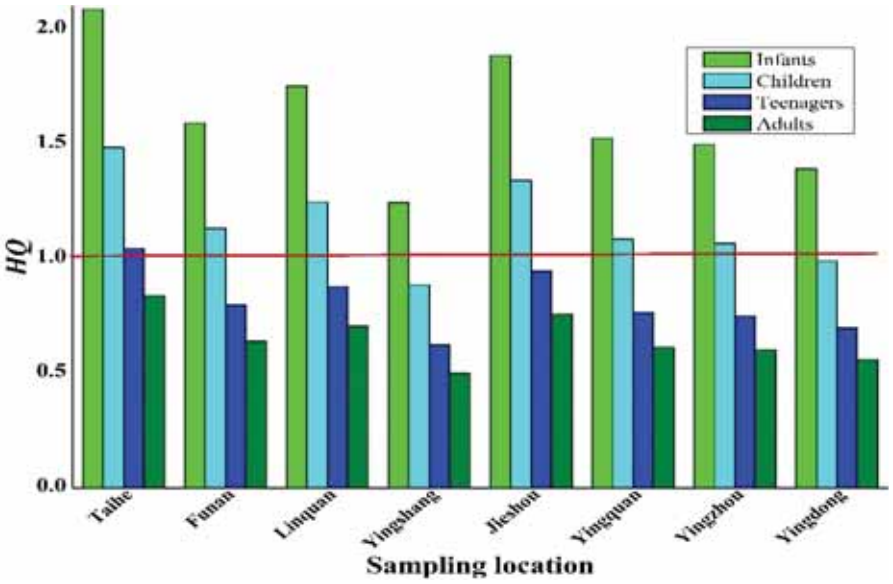

FIGURE 4
Statistical graph of total fluoride noncarcinogenic risk.

CONCLUSIONS

In this study，fluoride endemic areas of northwest of Anhui Province, concentration of fluoride was analysised in shallow groundwater, and Probabilistic risks to groundwater fluoride by ingestion pathway and dermal pathway was characterized for infant, child, teen and adult four age groups using a health risk assessment model recommended by USEPA.

The range of fluorine in groundwater in the study area is 0.65-2.31, and the concentration order is Taihe > Jieshou >Yingdong > Funan > Yingquan > Yingzhou > Linquan > Yingshang. The highest fluorine average concentration in groundwater is Taihe and Jieshou, and the lowest average concentration is Yingshang. The results from health risk assessment indicate the infant and child population groups are more vulnerable to fluoride health hazards than teen and adult population groups, Special attention should be paid to infants and young children to stay away from the harm of fluoride in groundwater. The order of total non-carcinogenic risk of fluoride and health risk assessment: Infants > Teenagers > Children > Adults. Further observation revealed that ingestion pathway was the main route of fluoride exposure health risk, drinking low fluoride water is an effective way to control fluorosis.

Local administrative departments should increase investment in water improvement and fluorine reduction projects, implement rural drinking water safety projects, implement centralized water supply, regularly detect water quality, and reduce the fluorine content of high fluorine groundwater through effective fluorine removal technology, so as to ensure the safety of rural drinking water. In addition, increase the width and intensity of health education on fluorosis, improve the people's awareness of fluorosis and understand its harm, and let the villagers actively participate in this work to jointly control the prevalence of local fluorosis.

ACKNOWLEDGEMENTS

This work was financially supported by the Key Program for Science and Technology Development of Anhui Province (No. 1908085MD113), the Postdoctoral Science Foundation of Anhui Province (No. 2020B438), scientific research project of Huainan Normal University (No. 2020XJZD003 ， 2021XJZD019), scientific research project of Anhui Provincial Department of Education (kj2021a0958), science and technology plan project of Huainan Municipal Government ([2021] 67). We acknowledge editors and reviewers for polishing the language of the paper and for in-depth discussion.

REFERENCES

[1] Hu, Y., Zhongbing, D., Guijian, L. (2017) Characterization and quality of groundwater in Huaibei, China. Fresen. Environ. Bull. 26(4) , 2541-2549.

[2] Wu, C., Wu, X., Qian, C., Zhu, G. (2018) Hydrogeochemistry and groundwater quality assessment of high fluoride levels in the Yanchi endorheic region, northwest China. Applied Geochemistry. 98, 404-417.

[3] Soleimani, H., Nasri, O., Ghoochani, M., Azhdarpoor, A., Dehghani, M., Radfard, M., Darvishmotevalli, M., Oskoei, V., Heydari, M. (2020) Groundwater quality evaluation and risk assessment of nitrate using monte carlo simulation and sensitivity analysis in rural areas of Divandarreh County, Kurdistan province, Iran. International Journal of Environmental Analytical Chemistry. 1-19.

[4] Narsimha, A., Rajitha, S. (2018) Spatial distribution and seasonal variation in fluoride enrichment in groundwater and its associated human health risk assessment in Telangana State, South India. Human and Ecological Risk Assessment: An International Journal. 24(8), 2119-2132.

[5] Yuan, L., Fei, W., Jia, F., Jun-Ping, L., Qi, L., Fang-Ru, N., Xu-Dong, L., Shu-Lian, X. (2020) Health risk in children to fluoride exposure in a typical endemic fluorosis area on Loess Plateau, north China, in the last decade. Chemosphere. 243, 125451.

[6] Yan, J., Chen, J., Zhang, W., Ma, F. (2020) Determining fluoride distribution and influencing factors in groundwater in Songyuan, Northeast China, using hydrochemical and isotopic methods. Journal of Geochemical Exploration. 217, 106605.

[7] Yadav, K. K., Kumar, S., Pham, Q. B., Gupta, N., Rezania, S., Kamyab, H., Yadav, S., Vymazal, J., Kumar, V., Tri, D.Q., Talaiekhozani, A., Prasad, S., Reece, L. M., Singh, N., Mauryal, P. K., Cho, J. (2019). Fluoride contamination, health problems and remediation methods in Asian groundwater: A comprehensive review. Ecotoxicol. Environ. Saf. 182, 109362.

[8] Zhao, L., Yu, C., Lv, J., Cui, Y., Wang, Y., Hou, C., Yu, J., Guo, B., Liu, H., Li, L. (2021) Fluoride exposure, dopamine relative gene polymorphism and intelligence: A cross-sectional study in China. Ecotoxicol. Environ. Saf. 209, 111826.

[9] Maheshwari, R. C. (2006). Fluoride in drinking water and its removal. Journal of Hazardous materials, 137(1), 456-463.

[10] Mridha, D., Priyadarshni, P., Bhaskar, K., Gaurav, A., De, A., Das, A., Joardar, M., Chowdhury, N.R., Roychowdhury, T. (2021) Fluoride exposure and its potential health risk assessment in drinking water and staple food in the population from fluoride endemic regions of Bihar, India. Groundwater for Sustainable Development. 13, 100558.

[11] Zhang, L., Zhao, L., Zeng, Q., Fu, G., Feng, B., Lin, X., Liu, Z., Wang, Y., Hou, C. (2020) Spatial distribution of fluoride in drinking water and health risk assessment of children in typical fluorosis areas in north China. Chemosphere. 239, 124811.

[12] Yang, N., Liu, J., Liao, A., Wang, W., Zheng, H., Lin, J., Wei, G.U. (2017) Distribution and formation factors of high fluoride deep groundwater in typical area of north Anhui Province. Hydrogeology & Engineering Geology. 44(3), 33-41. (In Chinese).

[13] Hu, Y., You, M., Liu, G., Dong, Z. (2021) Spatial distribution and potential health risk of fluoride in drinking groundwater sources of Huaibei, Anhui Province. Sci. Rep. 11(1), 1-11.

[14] Sacrifice. (2017) Chinese standard for groundwater quality (GB/T14848-2017).

[15] Edition, F. (2011) Guidelines for Drinking-water Quality WHO Chron. 38, 104-108.

[16] Tao, A. (2001) Investigation on the causes of fluorosis in Erlang Township, Taihe County. Occupation and Health. 17(5), 102-103. (In Chinese).

[17] Hu, Y., Xia, C., Dong, Z., Liu, G. (2016) Geochemical Characterization of Fluoride in the Groundwater of the Huaibei Plain, China. Analytical Letters. 50(5), 889-903.

[18] Hu, Y., Fuhai, Z., Zhiyuan, N., Zhongbing, D., Guijian, L. (2015) Hydrochemical characteristics of groundwater in centralized drinking water sources and its quality assessment in northern Anhui province. Journal of University of Science and Technology. 44(11), 913-920, 925. (In Chinese).

[19] Wang, W., Xu, G., He, X. (2010) Distribution and analysis of factors influencing three nitrogen compounds in groundwater of Huaibei Plain. Water Resources Protection. 26 (2) , 46-48.

[20] Mukherjee, I., Singh, U.K. (2020) Fluoride abundance and their release mechanisms in groundwater along with associated human health risks in a geologically heterogeneous semi-arid region of east India. Microchemical Journal. 152, 104304.

[21] EPA. (2011) Exposure Factors Handbook: 2011 Edition.

[22] Das, A., Das, S.S., Chowdhury, N.R., Joardar, M., Ghosh, B., Roychowdhury, T. (2020) Quality and health risk evaluation for groundwater in Nadia district, West Bengal: An approach on its suitability for drinking and domestic purpose. Groundwater for Sustainable Development. 10, 100351.

[23] Hu, Y., You, M., Liu, G., Dong, Z. (2021) Distribution and potential health risk of nitrate in centralized groundwater sources of Wanbei Plain, Central China. Journal of Water Supply: Research and Technology-Aqua. 70(5), 684-695.

[24] Adeyeye, O.A., Xiao, C., Zhang, Z., Yawe, A.S., Liang, X. (2021) Groundwater fluoride chemistry and health risk assessment of multi-aquifers in Jilin Qianan, Northeastern China. Ecotoxicol. Environ. Saf. 211, 111926.

[25] Yadav, K., Raphi, M., Jagadevan, S. (2021) Geochemical appraisal of fluoride contaminated groundwater in the vicinity of a coal mining region: Spatial variability and health risk assessment. Geochemistry. 81(1), 125684.
[26] Zhang, Q., Xu, P., Qian, H., Yang, F. (2020) Hydrogeochemistry and fluoride contamination in Jiaokou Irrigation District, Central China: Assessment based on multivariate statistical approach and human health risk. Sci. Total Environ. 741, 140460.
[27] Mukherjee, I., Singh, U.K., Patra, P.K. (2019) Exploring a multi-exposure-pathway approach to assess human health risk associated with groundwater fluoride exposure in the semi-arid region of east India. Chemosphere. 233, 164-173.
[28] Mondal, N.K., Pal, K.C., Kabi, S. (2012) Prevalence and severity of dental fluorosis in relation to fluoride in ground water in the villages of Birbhum district, West Bengal, India. Environmentalist. 32(1), 70-84.
[29] Bhattacharya, P., Adhikari, S., Samal, A.C., Das, R., Dey, D., Deb, A., Ahmed, S., Hussein, J., De, A., Das, A., Joardar, M., Panigrahi, A. K., Roychowdhury, T., Santra, S. C. (2020) Health risk assessment of co-occurrence of toxic fluoride and arsenic in groundwater of Dharmanagar region, North Tripura (India). Groundwater for Sustainable Development. 11, 100430.
[30] Liu, J., Peng, Y., Li, C., Gao, Z., Chen, S. (2021) A characterization of groundwater fluoride, influencing factors and risk to human health in the southwest plain of Shandong Province, North China. Ecotoxicol. Environ. Saf. 207, 111512.
[31] Wu, R., Ye, D. (2008) Investigation on fluoride concentration in rural water and current situation of water improvement and fluoride reduction in Fuyang City. Chinese Journal of Disease Control. 12(6), 608-610. (In Chinese).
[32] Li, J., Wang, Y., Zhu, C., Xue, X., Qian, K., Xie, X., Wang, Y. (2020) Hydrogeochemical processes controlling the mobilization and enrichment of fluoride in groundwater of the North China Plain. Sci. Total Environ. 730, 138877.
[33] Shalyari, N., Alinejad, A., Hashemi, A.H.G., RadFard, M., Dehghani, M. (2019) Health risk assessment of nitrate in groundwater resources of Iranshahr using Monte Carlo simulation and geographic information system (GIS). MethodsX. 6, 1812-1821.
[34] Zhai, Y., Zhao, X., Teng, Y., Li, X., Zhang, J., Wu, J., Zuo, R. (2017) Groundwater nitrate pollution and human health risk assessment by using HHRA model in an agricultural area, NE China. Ecotoxicol. Environ. Saf. 137, 130-142.

Received: **21.11.2021**
Accepted: **09.01.2022**

CORRESPONDING AUTHOR

Yunhu Hu
School of Chemistry and Materials Engineering,
Huainan Normal University,
Huainan 232001 – China

e-mail: huyunhu@ustc.edu.cn

© by PSP Volume 31– No. 05/2022 pages 4888-4894 Fresenius Environmental Bulletin

DESIGN OF GREEN ECOLOGICAL PUBLIC ENVIRONMENT BUILDING BASED ON BIM TECHNOLOGY

Wenli Wang*, Shuting He, Panyao Zou

School of Traffic Engineering, Wuhan Technical College of Communications, Wuhan Hubei 430065, China

ABSTRACT

The application of BIM technology in the design of green and ecological public environment buildings is an inevitable choice. Through the application principles of BIM green ecological public environment building design, detailed research on the practical application of BIM technology is carried out, with the purpose of making better use of the value of BIM technology in the energy-saving design of green buildings, improving the design level of green ecological public environment buildings, and achieving the energy-saving result. In this paper, through the application of BIM simulation analysis software, we design the natural lighting, natural ventilation, spatial pattern, and compare the performance before and after design. The research results show that after the design by using the BIM technology, the annual load of heating, ventilation and air conditioning was reduced from 34280KWh/year to 26350KWh/year, a reduction of more than 23%. The air velocity increased from 0.4m/s to 0.9m/s and carbon emissions have been reduced from 5621kg/year to 4651kg/year.

KEYWORDS:
BIM technology, green ecological public environment, energy-saving design

INTRODUCTION

In modern building design, the concept of green building energy-saving design is deepened, especially the public environment building energy-saving design puts forward higher standards. In this case, more attention must be paid to the green building energy-saving design. The main purpose of the application of green building energy-saving design is to help building construction save more resources, reduce energy consumption, coordinate the relationship with the environment, and ensure that the building design is reasonable and truly protects the environment. We actively apply green materials and use energy-saving technology to realize the sustainable development of construction enterprises [1-2]. The active application of BIM technology in the energy-saving design of green buildings provides more technical convenience for the design, especially the visualization and three-dimensional design, which helps the energy-saving design of green buildings to achieve comprehensive design detail control and achieve more ideal energy-saving design effects.

During the application of BIM technology, 3D information data is used to describe the specific structure and design situation of the building project, obtain more detailed design information, objectively analyze design information and performance, and effectively sort out the construction process, construction operation, construction quality and completion. The relationship between inspection and acceptance is of great significance to the design of green building energy conservation. The application of BIM technology in the energy-saving design of green buildings accurately identifies the construction process, objectively sorts out the connections among them, comprehensively organizes and analyzes the construction data, and presents the analysis results in various forms. If there are changes in some factors in the architectural design, the BIM system can quickly capture and automatically analyze the changes, and quickly provide the latest data analysis results. This not only achieves the timeliness and accuracy of data analysis, but also ensures the integrity of the architectural design [3-5].

BIM technology has the following principles [6-8]: 1) the application must adhere to local conditions, combine the surrounding environment of green buildings, geological conditions and climate, and analyze the characteristics of the ecological environment. In-depth survey of geology and hydrology, scientifically collate relevant data, and provide a more comprehensive and accurate application basis for BIM technology. Designers should also pay attention to ecological environment protection and minimize the impact of architectural design on the ecological environment. According to the energy-saving design of green buildings, all design content and parameters of designers must follow normative principles. After the energy-saving design is completed, it will be submitted to a special department for inspection and review in a timely manner to ensure that all energy-saving designs comply with the ecological environment protection and building construction regulations, which is a prerequisite for successful subsequent construction. 2) The application

of BIM technology implements relevant design standards, highlights the pertinence of energy-saving design based on specific conditions, and scientifically coordinates the relationship between construction engineering and the environment based on energy-saving and ecological protection, in order to effectively implement energy-saving design work and the realization of the efficiency of energy-saving design. The principle of operability is mainly reflected in the specific operation of BIM technology application, the application of three-dimensional digital technology, timely information modeling of energy-saving design, and simulation technology to visually present the design results, providing help for designers to improve design information and accurate design data. 3) We demonstrate the design model in a digital format, which is convenient for designers to master the engineering structure and energy-saving design, discover the insufficiency of energy-saving design in time, and adjust the design content scientifically. Under the requirements of operability principles, scientific parametric design is carried out, data and information collation is more timely and accurate, and the specific structural status of energy-saving design is presented in time, and the hidden correlation in parameters is objectively analyzed. With the assistance of virtual state space and distributed design, we can further optimize the energy-saving design of green buildings [9-14]. In this paper, the application of simulation analysis based on BIM technology in green ecological public environment building design-atrium design is the research direction. Through the transformation of examples and the use of BIM simulation analysis software, the BIM technology-assisted green design and performance optimization are described.

MATERIALS AND METHODS

(1) Research object. The case public environmental building (library courtyard) is located in a community in Chongqing. The main orientation of the building is 17.2° west-north, and the north side of the building is a residential road, and the surrounding vegetation is in good condition (Figure 1). The scale of the building is about 6,500 square meters. The reading area and library are located on the 1st and 3rd floors of the building, and the rest are office buildings. The main entrance of the building is on the west side. The building was built earlier, and its configuration functions are increasingly unable to meet the development needs of contemporary educational buildings. Through detailed field research and questionnaire surveys, it is found that the library's utilization efficiency of natural lighting and natural ventilation is low which mainly depends on equipment. The adjustment has caused a large amount of energy consumption. At the same time, the courtyard-style layout has the space to transform it into an atrium, so it was selected as the research object of the renovation to explore the green design of the building atrium under the typical climate conditions of Chongqing area method.

(2) The existing problems of the research objects and the goals of the transformation design. Through the preliminary investigation and starting from the green design, the key issues to be solved in the renovation design are put forward: 1) Update the function of the building space, create a pleasant landscape environment, and a comfortable, open and bright communication space; 2) By designing the building atrium, the reflection system and the surface treatment of the walls in the atrium to enhance the natural lighting in the room and improve the indoor light environment; 3) Using the heat and wind pressure of the atrium to organize effective natural ventilation, assist necessary mechanical ventilation, and improve the indoor air quality of the reading room.

Using the simulation analysis of BIM technology, based on the strategy of passive green renovation design, we explore the design method of saving building energy consumption in the process of building use [15-17]. The goal of the transformation of this article is to: 1) On the basis of keeping the existing buildings unchanged, we update the function of the building courtyard to adapt to the changes in building function requirements, and at the same time make corresponding adjustments to the spatial form of the building courtyard.

2) Improve the utilization efficiency of building atrium for natural lighting and natural ventilation, reduce the energy consumption of indoor equipment lighting and ventilation, and discuss the design and construction of atrium with natural lighting and natural ventilation on the basis of meeting the requirements of green energy saving; 3) Reasonable use of energy-saving retrofit technologies that have been verified through actual tests and effectively reduce building energy consumption and carbon footprint.

FIGURE 1
Research object.

(3) Research methods. We use BIM software as the technical means of simulation analysis for the reconstruction of this case and establish an information model of the existing building before the reconstruction design through ArchiCAD18 [18-19]. With the use of Eco-Designer to evaluate the overall building green building, the building can be further discovered on the basis of research and analysis. Based on the existing problems, compared with the plan after applying the renovation design strategy, it is concluded that the rationality of the design strategy used in the building can be achieved for the purpose of green energy-saving renovation [20-21].

RESULTS

(1) BIM technology assists the design of the atrium space form transformation. The library courtyard is located in the center of the building, and the courtyard can be directly reached through the main entrance of the building. The north and south sides of the courtyard are the main building, the 1-3 floors are the reading room and the library, and there is no building room on the east side. A large number of tall evergreen plants are planted inside the courtyard, which severely obstructs the natural lighting and natural ventilation of the reading rooms on both sides. At the same time, there is a lack of public activity and communication space in the overall building, and the existence of the courtyard does not affect it too much.

The auxiliary design of the space form of the atrium mainly includes the following contents: 1) Extend the building on the east side of the courtyard, which not only enables the reading area on each floor to have a public activity space, but also blocks the direct sunlight in the summer morning, effectively preventing the heat from spreading to the reading area. 2) Arrange a space for rest and communication in the courtyard, and at the same time adjust the indoor microclimate by setting up water bodies and planting plants. The water body in the atrium not only plays a role in maintaining humidity, but the larger heat capacity of the water body also plays a significant role in regulating the constant indoor temperature water body. In summer, it absorbs heat during the day to lower the temperature, and in winter, the heat absorbed during the day is used at night which can raise the temperature. In this way, "one-in and one-out" can generate a thermal pressure difference in the atrium air, which promotes indoor thermal pressure ventilation, thereby enhancing air convection and improving the indoor wind environment. In addition to viewing the plants in the atrium, they can also absorb carbon dioxide, toxic gases, and dust through photosynthesis to purify the indoor air and improve indoor air quality. At the same time, the transpiration of the plants can release water and maintain the humidity in the atrium.

(2) BIM technology assists natural lighting renovation design. The lighting status of the reading room inside the building is not good. The building on the south side is higher than the north side, blocking the natural light on the north side. The tall plants on the south side also have a certain impact on the natural lighting inside. At the same time, the deepening of the building and the interference of bookshelf arrangement and interior decoration have worsened the attenuation of light, causing the indoor area far away from the lighting windows to be weakly illuminated. Even in the daytime, artificial lighting can only be used to enhance the indoor illuminance (Figure 2).

The contents of the natural lighting auxiliary design mainly include: 1) Renovate the wall materials in the atrium, replace the original red tiles with white paint with better reflection effect, and increase the diffused lighting in the room; 2) Set up a fixed mirror on the top of the atrium. The prism skylight is adjusted, and the mirror hanging in the atrium forms a reflective system similar to the Genzyme center, which spreads the light to the greatest extent. The use of a reflective system can increase the illuminance value at the far window, shorten the daylight depth in disguised form, improve the uniformity of indoor illuminance, and reduce direct glare from the window (Figure 3).

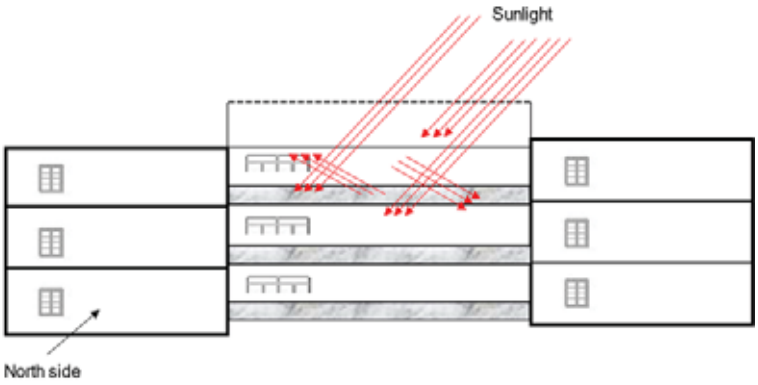

FIGURE 2
Building daylighting after adding reflective system.

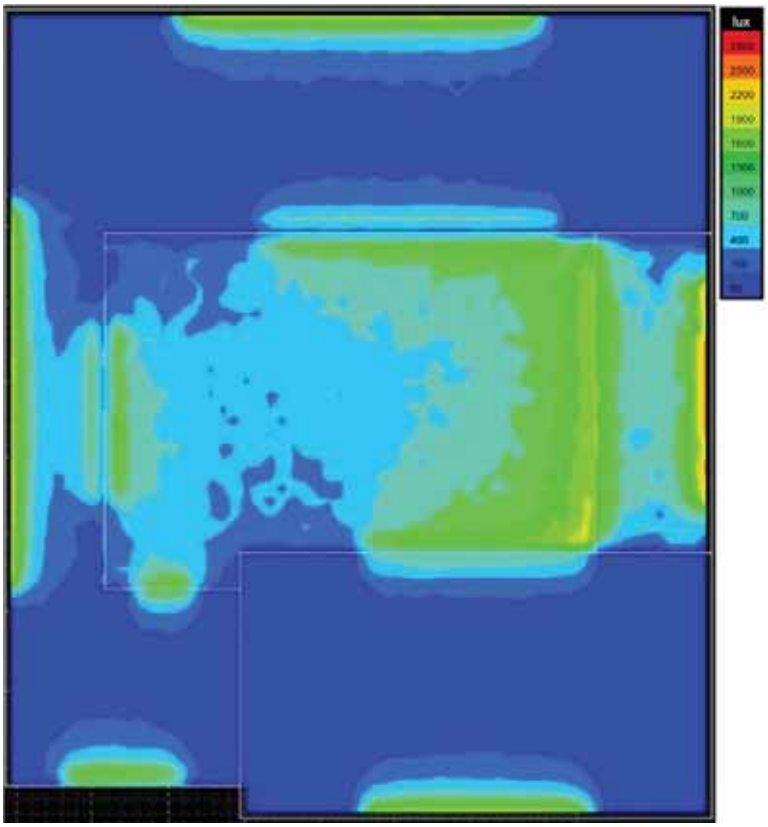

FIGURE 3
Daylighting analysis of the first floor after the renovation design.

In ECOTECT, the natural lighting simulation analysis of the BIM model before and after the renovation design is carried out, and the indoor natural lighting illuminance map of the first floor of the building is obtained (Figure 3). With the same window area and position, after transforming the courtyard into an atrium, adding a reflective system inside the atrium and changing the material of the inner wall, the natural illuminance value of the reading area is increased, and the illuminance is more uniform. It can be seen intuitively from the analysis results that the natural lighting situation in the reading area has been greatly improved, and the natural illuminance value has increased from 413.5 lux to around 913.6 lux.

(2) BIM technology assists natural ventilation transformation design. Quiet winds are common in this area, with an average wind speed of 1.4m/s in summer and 1.2m/s in winter. In China, where the summer is hot and the winter is cold, the wind environment is very poor. The prevailing wind direction in summer is southwest wind. The south side of the reconstructed building is taller, blocking the natural wind in the reading room on the north side, resulting in poor indoor ventilation and poor indoor thermal environment. Therefore, in summer, air conditioning is mostly used to increase the building energy consumption. In order to strengthen the building's thermal pressure ventilation capacity, the exhaust vents of the building atrium are set higher than the roof, the area of the exhaust vents is increased, and the ceiling of the atrium is inclined at an angle to increase the chimney effect of the atrium building. The wind pressure ventilation simulation analysis is performed on the buildings before and after the renovation, and the results are shown in Figures 4 and 5, respectively. From the analysis results, we can see that the ventilation effect of the indoor reading room on the south side is good before the renovation, and the air flow rate is fast, while the ventilation effect of the reading room on the north side is not good. After the courtyard was transformed into an atrium, the air flow rate on the south side is more even, the ventilation effect on the north side is obviously improved, and the air velocity is increased from 0.4m/s to 0.9m/s.

(3) BIM technology assists energy-saving renovation design. Choosing different materials as the inner maintenance wall materials of the atrium, and analyzing the energy consumption of its BIM model, we can obtain the corresponding building energy consumption assessment report, and intuitively compare from the aspects of cost, service life and energy saving. In the renovation design, aerated concrete blocks are selected as the material of the inner atrium enclosure structure. In the design of building atrium energy saving, reducing the heat transfer coefficient of doors and windows is also an important measure in the design. Therefore, the choice of window materials is very important.

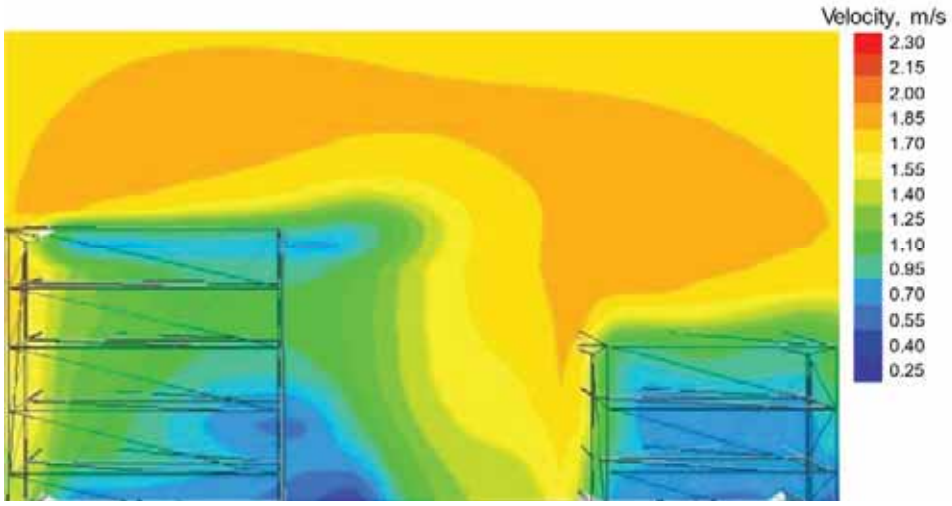

FIGURE 4
Building ventilation analysis before renovation design.

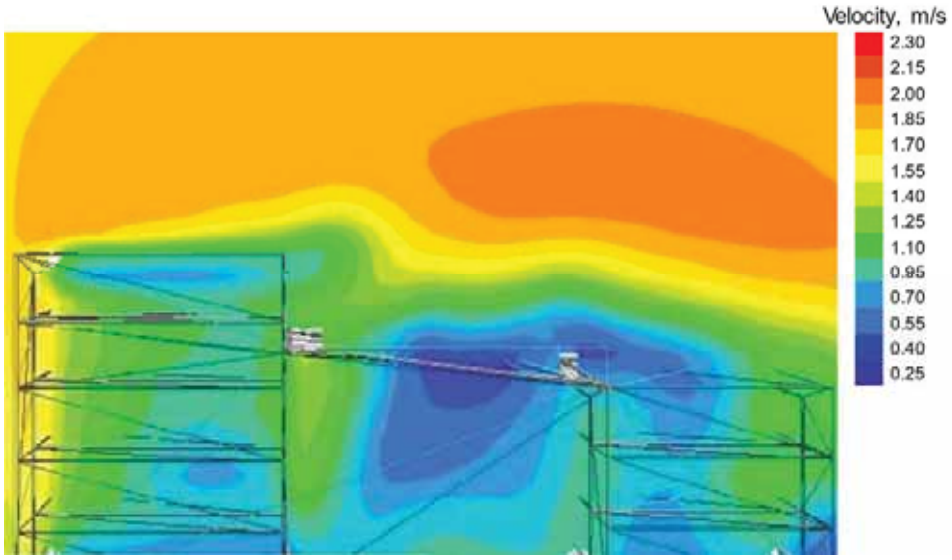

FIGURE 5
Building ventilation analysis after renovation design.

Consider the following aspects in the design: 1) Use plastic heat-insulating aluminum alloy window frame profiles; 2) Use low heat transfer coefficient glass materials; 3) Use doors and windows with good sealing performance. We adopt heat recovery ventilation equipment and passive solar energy design, rationally use waste heat and waste heat to solve the building's heating and domestic hot water needs. By establishing a building information model for the buildings before and after the renovation and using Eco-Designer to evaluate the carbon footprint and energy of the building, a comparison chart of the building carbon footprint and monthly energy balance is obtained as a reference for the evaluation of the renovation effect. The energy consumption during the operation of the building has been effectively controlled, and the carbon emissions have also been reduced. The energy consumption has been reduced from 82360 kwh/year to 76320 kwh/year, and the carbon footprint has also been reduced from 5621kg/year to 4651kg/year. The problem of summer ventilation and winter heating of the building mainly dealt with in the renovation design is solved. From the energy balance sheet of the project, the ability of the building to dissipate heat through natural ventilation in summer has been strengthened, and the effect of solar heating in winter is also obvious, which can effectively reduce the use of air-conditioning equipment, so that building energy consumption can be controlled.

(4) Comprehensive analysis. In this case, a library courtyard is transformed into a building atrium. The renovation design involved two types of indicators in the green evaluation system: energy conservation and energy use, and indoor environmental quality. Therefore, this paper conducts green evaluation and analysis for these two types of indicators and uses BIM technology to conduct a green evaluation and analysis.

Energy saving and energy utilization. The reconstructed building meets the requirements of control items for energy saving and energy utilization, and some of the requirements for scoring items have been improved: 1) Building and envelope structure. The enclosure structure is made of 200mm aerated concrete blocks, and the heat transfer coefficient K value is 0.79W/(m^2-K). The heat transfer coefficient of external walls in hot summer and cold winter areas is specified in the "Design Standard for Energy Conservation of Public Buildings" G50189 as K<1.0. After the transformation, the thermal performance of the envelope structure has increased by more than 10%. 2) Heating, ventilation, and air conditioning. Through the passive solar energy design and ventilation design transformation of the atrium, the annual load of heating, ventilation and air-conditioning was reduced from 34280 KWh/year before the transformation to 26350KWh/year, which was a reduction of more than 23%. 3) Comprehensive utilization of energy. Reasonably exhaust the energy recovery system and solar energy in the renovation design to meet the demand for heating and domestic hot water.

Indoor environmental quality. The reconstructed building meets the requirements for the control items of indoor environment quality, and the indoor light environment and visual field and indoor air quality required by the scoring items have been improved: 1) Indoor light environment and visual field. The main functional rooms of the building have good outdoor vision, and the evaluation score is 3 points. During the renovation of the library, the main function rooms can see the outdoor natural landscape through the external windows without obvious visual disturbance. The daylighting coefficient of the main functional rooms meets the requirements of the current national standard "Building Daylighting Design Standard" GB 50033. Before and after the renovation of the library, the proportion of the area where the daylighting coefficient of the reading room on the first floor meets the standard requirements exceeded 70%. The transformation improves the indoor natural lighting effect of the building: a. the main function room has reasonable measures to control glare. b. The area where the lighting coefficient of the inner zone meets the lighting requirements if the proportion reaches 60%. The atrium of the building has increased the diffuse and reflected light of the reading room through the renovation of the inner wall surface material and the addition of a reflective system, thereby reducing glare. At the same time, the lighting coefficient of the reading room meets the lighting requirements of more than 60% of the area. 2) Indoor air quality. The transformation improves the optimization of building space, plane layout and structural design, and improves the effect of natural ventilation. In the case, the design increases the exhaust vents of the building atrium, increases the area of the exhaust vents, strengthens the thermal pressure ventilation capacity of the building, tilts the ceiling of the atrium to a certain angle, and increases the chimney effect of the atrium, thereby improving the effect of air pressure ventilation. The air velocity is increased from 0.3m/s to 0.8m/s.

Innovation. 1) This design applies building information modeling (BIM) technology for auxiliary design in the planning and design stage. 2) This design carries out calculation and analysis of building carbon emissions and take measures to reduce the intensity of carbon emissions per unit of building area. The case simulates and calculates the building carbon emissions before and after the library renovation through energy evaluation and analysis. By using the design strategies, the carbon emissions are reduced from 5621kg/year to 4651kg/year.

CONCLUSIONS

(1) With the advancement of modern science and technology, the rapid development of digital technology and existing results will serve as the research foundation of this research. The BIM technology derived from the close integration of digital technology and architectural design has had a huge impact on architectural design. The combination of BIM technology and green building design will provide a brand-new design model for architectural design and provide solutions to related problems in current architectural design.

(2) In this case, research and simulation analysis are carried out based on the current situation and main problems of the library building. Combined with the typical climate of the area, we determine the appropriate courtyard renovation design strategy. In the renovation, the method of using BIM technology is used to assist the design of the green atrium, focusing on the use of passive green design strategies, and exploring green and energy-saving building design strategies.

ACKNOWLEDGEMENTS

This work was not supported by the Guiding Project of Science and Technology Research Plan of Hubei Provincial Department of Education (B2019428). The authors would like to show sincere thanks to those techniques who have contributed to this research.

REFERENCES

[1] Cheng, T.C., Cheng, C.H., Huang, Z.Z., Liao, G.C. (2011) Development of an energy-saving module via combination of solar cells and thermoelectric coolers for green building applications. Energy. 36(1), 133-140.

[2] Chen, X., Yang, H. (2015) Combined thermal and daylight analysis of a typical public rental housing development to fulfil green building guidance in Hong Kong. Energy & Buildings. 108(4), 420-432.

[3] Wu, T., Jeng, T., Pan, C., Lu, C. (2016) BIM applications in green building design-a case study from Taiwan. Journal of the Chinese Institute of Civil and Hydraulic Engineering. 28(2), 139-151.

[4] Abhinaya, K.S., Kumar, V., Krishnaraj, L. (2017) Assessment and remodelling of a conventional building into a green building using BIM. International Journal of Renewable Energy Research. 7(4), 1675-1681.

[5] Alsulaili, A.D., Al-Matrouk, M.F., Al-Baghli, R.A., Al-Enezi, A.F. (2020) Environmental and economic benefits of applying green building concepts in Kuwait. Environment, Development and Sustainability. 22(4), 3371-3387.

[6] Lu, Y., Wu, Z., Chang, R., Li, Y. (2017) Building Information Modeling (BIM) for green buildings: A critical review and future directions. Automation in Construction. 83, 134-148.

[7] Uddin, M.N., Wei, H.H., Chi, H.L., Ni, M., Elumalai, P. (2021) Building information modeling (BIM) incorporated green building analysis: An application of local construction materials and sustainable practice in the built environment. Journal of Building Pathology and Rehabilitation. 6(1), 1-25.

[8] Shin, T.S. (2017) Building information modeling (BIM) collaboration from the structural engineering perspective. International Journal of Steel Structures. 17(1), 205-214.

[9] Chang, Y.T., Hsieh, S.H. (2020) A review of building information modeling research for green building design through building performance analysis. Journal of Information Technology in Construction. 25, 1-40.

[10] Schlueter, A., Geyer, P. (2018) Linking BIM and design of experiments to balance architectural and technical design factors for energy performance. Automation in Construction. 86, 33-43.

[11] Singh, V., Gu, N., Wang, X. (2011) A theoretical framework of a BIM-based multi-disciplinary collaboration platform. Automation in Construction. 20(2), 134-144.

[12] Yan, W., Culp, C., Graf, R. (2011) Integrating BIM and gaming for real-time interactive architectural visualization. Automation in Construction. 20(4), 446-458.

[13] Yang, Q.Z., Zhang, Y. (2006) Semantic interoperability in building design: methods and tools. Computer-Aided Design. 38(10), 1099-1112.

[14] Sayary, S.E., Omar, O. (2021) Designing a BIM energy-consumption template to calculate and achieve a net-zero-energy house. Solar Energy. 216(4), 315-320.

[15] Zamanian, M.K., Pittman, J.H. (1999) A software industry perspective on AEC information models for distributed collaboration. Automation in Construction. 8(3), 237-248.

[16] Aram, S., Eastman, C., Sacks, R. (2013) Requirements for BIM platforms in the concrete reinforcement supply chain. Automation in Construction. 35(35), 1-17.

[17] Knight, D.M. (2012) BIM object creation. ASHRAE Journal. 54(11), 74-75.

[18] Xu, S. (2021) Study on environmental performance evaluation of green building based on BIM technology. Fresen. Environ. Bull. 30(5), 4911-4920.

[19] Jiang, H.Y. (2020) Research on information design of green ecological building on ecological perspective. Fresen. Environ. Bull. 29(7), 5004-5011.

[20] Li, H.S. (2020) Analysis of application advantages in interior design based on traditional building information modeling technology. Fresen. Environ. Bull. 29(7), 5564-5569.

[21] Liu, P., Li, Y., Wang, D.D. (2021) Research on green elderly apartment design based on the concept of ecological environment. Fresen. Environ. Bull. 30(6B), 7321-7328.

Received: **21.11.2021**
Accepted: **09.01.2022**

CORRESPONDING AUTHOR

Wenli Wang
School of Traffic Engineering,
Wuhan Technical College of Communications,
Wuhan Hubei 430065 – China

e-mail: wangqiaohua22@163.com

© by PSP Volume 31– No. 05/2022 pages 4895-4912 Fresenius Environmental Bulletin

CONSTRUCTION AND APPLICATION OF THE "ARTIFICIAL HABITAT ISLAND" DESIGN MODEL BASE ON THE RESEARCH THROUGH DESIGN FOR BUILT ENVIRONMENT IN SEMI-ARID MICROSCALE GREEN SPACE

Jingmao Wang[1,*], Yunyun Li[2], Du Han[1], Liyixuan Fan[1], Jiale Qi[1], Yifan Luo[1]

[1]College of Architecture, Xi'an University of Architecture and Technology, Xi'an 710055, Shaanxi, China
[2]Xi'an Longfor Properties Co. Ltd., Xi'an 710069, Shaanxi, China

ABSTRACT

Urban nature is of vital importance for human well-being in an increasingly urbanized world. How to use fragmented urban green space characteristics to meet the ecological function and landscape activity needs efficiently and economically is an urgent design research problem to be solved. This study promoted the theory and practice of community ecology into the design of urban environment base the carrier as artificial habitat island, demonstrated the correlation and interoperability of the types of built environment habitats and plant community organization, and explored the different design models and correlation between habitats and design elements base the research through design. The research proposed five "Artificial Habitat-Island" optimization design models for five environmental green space categories in semi-arid microscale green space, and summarized the "Artificial Habitat-Island" designing process of construction and management maintenance evaluating landscape full life circle. Using hierarchical analysis to make a comprehensive assessment of "Artificial Habitat-Island" to verify its application function value, the G1, G3, B3 and B7 prominently enhanced ecological and landscape benefits. Not only had good regional landscape characteristics, its management and maintenance cost were also lower. "Artificial Habitat-Island" provided a new experimental medium of both ecological and experimental value in small-scale urban space, effectively improved the value of the built environment landscape with using stable and high-quality local plant community, which was more conducive to the study of manual intervened groundcover plant community composition.

KEYWORDS:
Landscape full life circle, Planting community Composition, Design model, Habitat-site design, Analytic Hierarchy Process

INTRODUCTION

Compared with the natural habitat, the city green space is more fragmented, there are a large number of small patch green space, become an important part of the urban habitat network system with protecting urban biodiversity [1]. According to the spatial and temporal distribution characteristics of sunshine and hydrologic process under artificial intervention, variety types of habitat-sites and different spatial patterns are formed in the artificial green space in the built environment. It is an important content of low-impact development in systematic and sustainable urban green space construction to compose the plant community based on the zonal characteristics of plant, and effectively intervene its succession process to achieve the relative steady state. In an increasingly urban world, addressing human needs in the urban context is most essential [2]. The manifold ecosystem services are offered by urban greenspaces for improving human well-being and health, urban vegetation can positively influence social contact among neighbors [3] and allows people to maintain a connection with the natural world [4]. Even commonplace nearby nature, such as planting with community and habitats, can have positive effects on human well-being and is well appreciated by the public [5]. At also the considerable economic resource is presented by urban vegetation presents with increasing the market values of properties [6]. Some study indicate that vegetation can improve the soil nutrient, enzyme activities, and microorganisms in the surface soil of the reclamation area and remit subsidence area soil alkalinization, which is of great significance for the ecosystem restoration in coal mining subsidence land [7]. Some plants have tolerance to specific metal [8], so they can be adopted in phytoremediation of oil-contaminated soil [9].

The research aimed to demonstrate not only the vitality and richness of urban vegetation design by introducing a medium or carrier to improve urban diversity, but to explore the role of small-scale physical design interventions and carrier in enriching such

an environment and also the effect these changes have on the behavior of green space users. Unregulated space can successfully function as an attractive outdoor environment and green space does not need to be built to be a park or a playground [10-11]. But we need the medium or carrier to establish the urban habitat-site design in the urban microscale greenspace, so as to the "artificial habitat island" design pattern is a typical design pattern that mainly focuses on aesthetic features and supplemented by ecological functions. The core idea is to integrate the ground cover community into the urban built environment and improve its ecological and landscape functions on the basis of the theory of habitat construction. After systematic theory research, this study built in urban environment to carry out the "artificial habitat island" experimental research, and proves that the model can adapt to diverse fields design requirements diversification and heterogeneity of habitat conditions, with the popularization and application of the built environment in urban value, through the reasonable design can improve the community habitat adaptability, aesthetics and functionality [14-15].

Plant communities are open and complex systems. The practice of community design that simulates nature is a problem of resistance to solutions, and nature research is an effective way to explore solutions to irrational problems. The design and construction disciplines and the natural ecology part have different core knowledge areas and thinking research methods, and the "Research through Design" (RTD) method is to clearly specify the goals and action process research. However, the design has no epistemological function, so that the academic work of architecture or landscape architecture has to be used in other academic fields, and the content and methods of these disciplines must be applied. The characteristics of complex knowledge provide an alternative procedure for applied research, creating a highly relevant research system with landscape architecture practice. Scientific logic, and the use of specific ecosystems for guidance [17]. Through Peripheral research and wisdom to explore the applicability of plant community design patterns with inherent ecological mechanisms.

"Artificial Habitat Island" is a kind of landscape design based on the theory of habitat construction, which integrates the site habitat and stable high quality plant community. In the construction of urban small-scale habitat network, it is the product of transforming a small ecological patch into artificial landscape design based on site design [1] [18]. It has a clear boundary and a variety of types according to the characteristics of different sites, which can meet the heterogeneity of habitat patches. Moreover, it has a variety of alternative plant communities and indicator species patterns, which can flexibly increase urban biodiversity and ecological connectivity.

MATERIALS AND METHODS

Study sites and Scheme design. The research was carried out at the Center Green Galley and Baima River Park, which is the Associated Experimental Base in Xi Xian New Area, Shaanxi Province, semi-arid northern China. The construction of "artificial habitat island" is mainly divided into two categories. The first category is the reconstruction of the existing green space. The second category is the construction of habitat island in the green space to be built. The transformation of the existing green space mainly refers to the beautification and upgrading of the completed urban green space by using the habitat island. In view of this situation, Habitat Island needs to consider the construction situation and style of the current green space in the scheme design, and integrate with the current landscape. In addition, when Habitat Island is used in the green space to be built, it can be considered as an important landscape element in the overall green space design, so that Habitat Island can better play its ecological and landscape functions.

Habitat construction of "artificial habitat island" includes site habitat zoning and optimization. Understanding the habitat conditions of the site was the first step in the design：the light, water and soil conditions of the site were simulated and analyzed with computer software to classify the different habitat types. Secondly, according to the habitat needed by the ground cover plant community, the selected site habitat conditions were optimized, including the improvement of water conditions and soil conditions. The scheme design of "artificial habitat island" mode needs to consider both the site habitat type and the goal of landscape construction, which includes graphic design, interface design, species collocation and ground cover selection.

Soil treatments. Turn the soil: There is often a large amount of construction waste and compaction or hardening of the soil in the construction sites of the "artificial habitat island". Deep tillage or deep loosening tillage is an effective way to deal with these problems, which can preserve the natural soil layer of the original land and create a channel for air, water and roots to contact. If there is too much brick and gravel in the soil, it should be ploughed several times to remove it.

Plant community construction. It is very important to choose the time of plant community establishment. Reasonable time of plant establishment is beneficial to improve the survival rate of plants and save the amount of watering. Ground cover communities are often planted in spring and autumn in Xi 'an area, the best planting time of spring is from mid-March to mid-April, and autumn is in November. Construction and planting should be carried out as soon as possible after the site is fully prepared. On

the one hand, weeds can be prevented from invading the bare ground, and on the other hand, soil degradation caused by sunshine and extreme temperature changes can be avoided. In terms of planting weather, cloudy days are preferred; planting before and after rainfall is beneficial to the survival of seedlings and can reduce the need for irrigation. If it is built on sunny days, it should be avoided during periods of strong sunlight.

Construction layout and arrange the seedlings: Ideally, the designer is the best candidate for plant arrangement on the site. Layout should be carried out under the guidance of the designer, which is more conducive to establishing the connection between design and implementation and ensuring the effect of planting [18]. Layout and placement of seedlings specifically includes determining the location, density and spacing of seedlings. In order to determine the position of the seedlings more accurately, the grid method can be used, and the size of the grid should be a multiple of 1m×1m (Figure 1a, b). Water the plant after construction: The first task after the construction is finished is watering. The point of first watering is not just to moisten the soil, but to fill the air gaps in the soil with sediment. Watering time should be in the afternoon, at this time the ground and plant temperature difference are reduced, can avoid the stimulation of plant roots and the obstruction of water absorption (Figure 1c; Figure 1d).

Data observation and analysis. This study used Analytic Hierarchy Process to establish A functional and landscape dominant ground cover evaluation system respectively, and the evaluation model consisted of three levels: target layer(A), criterion layer(B) and factor layer(C) [20].

1) Construction of judgment matrix and Single hierarchical arrangement. Single hierarchical arrangement means to calculate the weight of each evaluation factor by comparing the importance scale in pairs according to the constructed judgment matrix. In the process of using the Analytic Hierarchy Process, the constructed judgment matrix transforms qualitative problems into quantitative problems, and there may be some errors in this process.

2) Consistency check. The eigenvector value and eigenvector of each matrix were solved by the EIG function of MATLAB, and the consistency index of the matrix was calculated by the following formula.

$$\sqrt{CI = \frac{\lambda_{\max} - n}{n-1}} \quad \text{(Formula 1)}$$

Formula：CI—Consistency index；$\lambda_{\max}$ —Maximum eigenvalue of the judgment matrix；n—The matrix order.

The consistency ratio of each matrix is calculated by Eq. 3.2

$$\sqrt{CR = \frac{CI}{RI}} \quad \text{(Formula 2)}$$

Formula：CR—Consistency ratio；RI—Average random consistency index.

FIGURE 1
Construction and application process of artificial habitat islands in urban spaces
(a) the layout process of the vegetation design, (b) construction of plant community, (c) maintenance and management of habitat island, (d) establishment and observation.

TABLE 1
Random consistency indices of RI

n	1	2	3	4	5	6	7	8	9
RI	0	0	0.58	0.9	1.12	1.24	1.32	1.41	1.45

FIGURE 2
Typical optimization model of "artificial habitat island" in different spaces.

When Cr <0.1, it is generally considered that the inconsistency of the matrix is within the allowable range, and its eigenvectors can be normalized as weight vectors (Table 1).

3) Total taxis of hierarchy and Quantification and grading of evaluation indexes and calculation of comprehensive evaluation indexes. The calculation formula of comprehensive evaluation score is:

$$S = \sqrt{\sum_{j=1}^{m}\left(\sum_{i=1}^{n} C_i M_i\right) B_j} \quad \text{(Formula 3)}$$

Evaluation indexes and weights. Geographical and climatic conditions of Xi Xian New Area, as well as the specific functional requirements of "artificial habitat island", "artificial habitat island" is taken as the first-level evaluation index (A), and ecological benefit (B1), landscape benefit (B2) and economic benefit (B3) are taken as the second-level evaluation index in the Analytic Hierarchy Process (AHP).

RESULTS

Evaluation analysis and result in Bioretention Facilities "artificial habitat island" of park green space. Park green space is mainly composed of large area concentrated area green space and part of core green space, which has important ecological function in built environment. Due to the large area of park green space, it is an important patch of urban habitat system, which can promote the improvement of urban biodiversity, and at the same time, it is an important communication space for the built environment by providing leisure activities for residents around the built environment. In addition, users have higher requirements for aesthetics, so the landscape function of the park green space is very prominent (Figure 2a and Figure 3). Therefore, for the "artificial habitat island" in the park green space, it not only emphasizes its ecological function, but also has higher requirements for its landscape aesthetics. Water features are usually arranged in the core area of the park green space. Such central water features not only assume important landscape functions, but also play a role in regulating rain and flood. Around the core water feature is an excellent location to lay out a wetland type "artificial habitat island". Most of the park green space is open, or enclosed by the vertical space of trees. There are fewer buildings and sufficient illumination. Therefore, according to the illumination conditions, the park green space is mainly divided into sun habitat and plant shade habitat. Based on the above factors, there are three typical "artificial habitat island" types in park green space: ecotype "artificial habitat island" in park green space, landscape "artificial habitat island" in park green

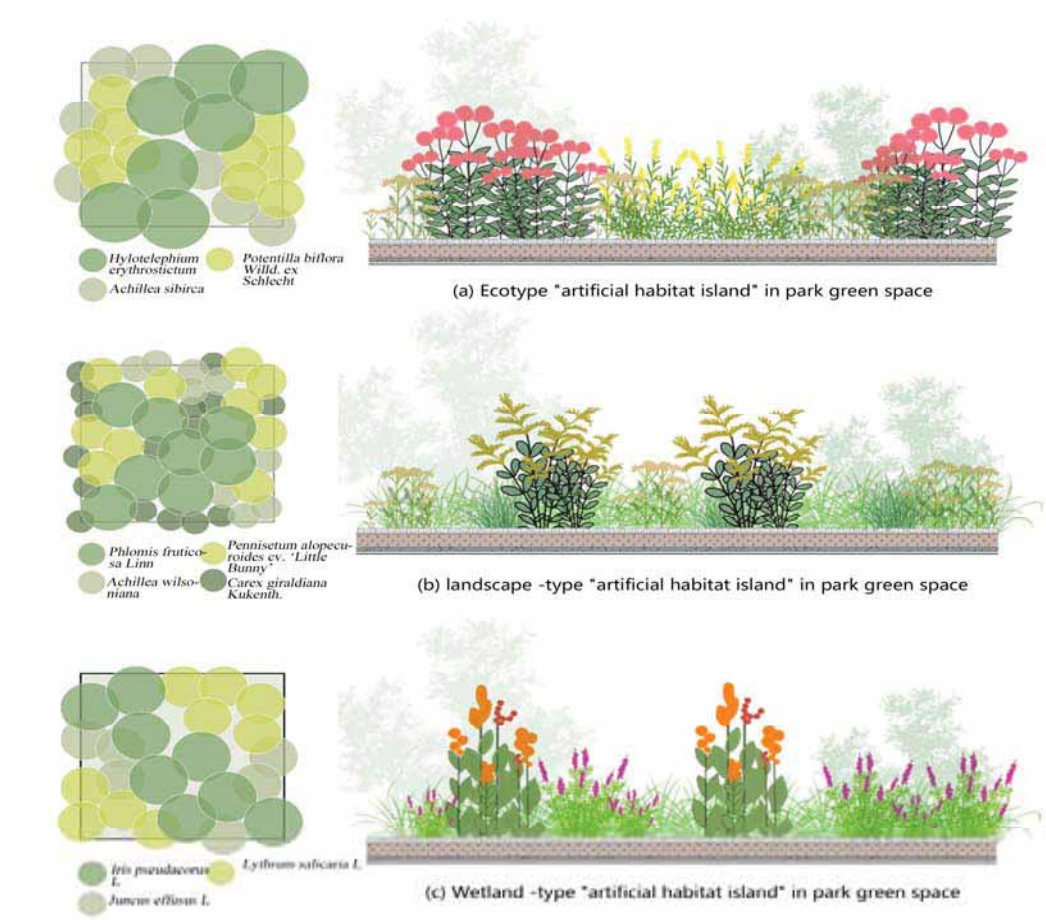

FIGURE 3
The design and composition of community structure samples in different types of "artificial habitat islands" in park green space.

space and wetland “artificial habitat island” in park green space (Table 2).

Evaluation analysis and result for “artificial habitat island” of attached to the green space in residential land. The function and location of the habitat construction of the green space attached to residential land are mostly determined by the use function of the building, its position in the built environment, and the relationship between its entrance and exit and green space. Important buildings in the built environment are located in the main entrance or the focal point of landscape vision, so the surrounding green space generally requires higher landscape image, which needs to focus on aesthetic function (Figure 2b and Figure 4). In addition, the large volume of the building has a strong impact on illumination. The south side is the sunny habitat, and the north side is the shady habitat. The rainwater falling on the roof of the building and the equipment drainage caused the hydrological change of the green space, so the appropriate position was selected to lay out the wetland “artificial habitat island”. Based on the above factors, there are two typical types of “artificial habitat island” in park green space: Landscape type “artificial habitat island” in the green space attached to residential land and rain-flood type “artificial habitat island” in the green space attached to residential land” (Table 3).

Evaluation analysis and result for “artificial habitat island” of attached green space in road and transportation land. Attached green space of road and transportation land can be divided into lane separation green space and green space beside the sidewalk. Due to the special characteristics of strip space, attached green space of road and transportation land is the most important corridor system in the urban habitat green space system, so its ecological function is particularly important. Attached green space of road and transportation land also have the important function of the rain flood regulation: “artificial habitat island” in the green space of the divider can initially purify and collect rainwater from the road surface and parking lot, alleviate the problem such as urban waterlogging. in the configuration of habitat island plants, the plants with water tolerance and purification function should be selected to create characteristic wet habitat island landscape. The belt green space on both sides of the road is an important urban interface, which plays a demonstra-

tion role in landscape construction and as an important object of urban greenway construction, meets people's needs for sports and leisure. The light condition of the attached green space of the road and transportation land is less affected by the buildings, and is mainly affected by the shadow formed by the street trees, which is dominated by the shade habitat of plants (Figure 2c and Figure 5). Based on the above factors, there are three typical types of "artificial habitat islands" in the green space attached to the land for roads and traffic facilities: rain flood type-"artificial habitat island" in the attached green space of road and traffic facilities land, landscape type-"artificial habitat island" in the attached green space of road and traffic facilities land and ecological type-"artificial habitat island" in the attached green space of road and traffic facilities land (Table 4).

TABLE 2
Typical patterns of "artificial habitat island" in park green spaces

Pattern Type	Scene features	Habitat types	Plant community types	Vertical structure	Plant community fabric
Ecotype "artificial habitat island" in park green space	It needs a large area of lawn or under-forest green space to enhance the ecological function	sun dry-land, plant dry land	Ecological improvement-dominated ground cover plant community	Structure layer Season theme layer Season theme layer	*Hylotelephium erythrostictum* *Achillea sibirca* *Potentilla biflora Willd. ex Schlecht.*
landscape - type "Artificial habitat island" in park green space	It needs a large area of lawn or under-forest green space to enhance the landscape function	sun dry-land, plant dry land	Landscape -dominant ground cover plant community	Structure layer Season theme layer Season theme layer Ground cover	*Phlomis fruticosa Linn.* *Achillea wilsoniana* *Pennisetum alopecuroides cv. 'Little Bunny'* *Carex giraldiana Kukenth.*
Wetland Type-"Artificial Habitat Island" of Park Green Space	It is a wetland adjacent to a water feature or a green area that undertakes the function of rain and flood regulation	Plant wetland, Building wetland; Building dry-land, Plant dry land	runoff intercepting and purification-dominated Ground cover plant community	Structure layer Season theme layer Season theme layer	*Iris pseudacorus L.* *Juncus effusus L* *Lythrum salicaria L.*

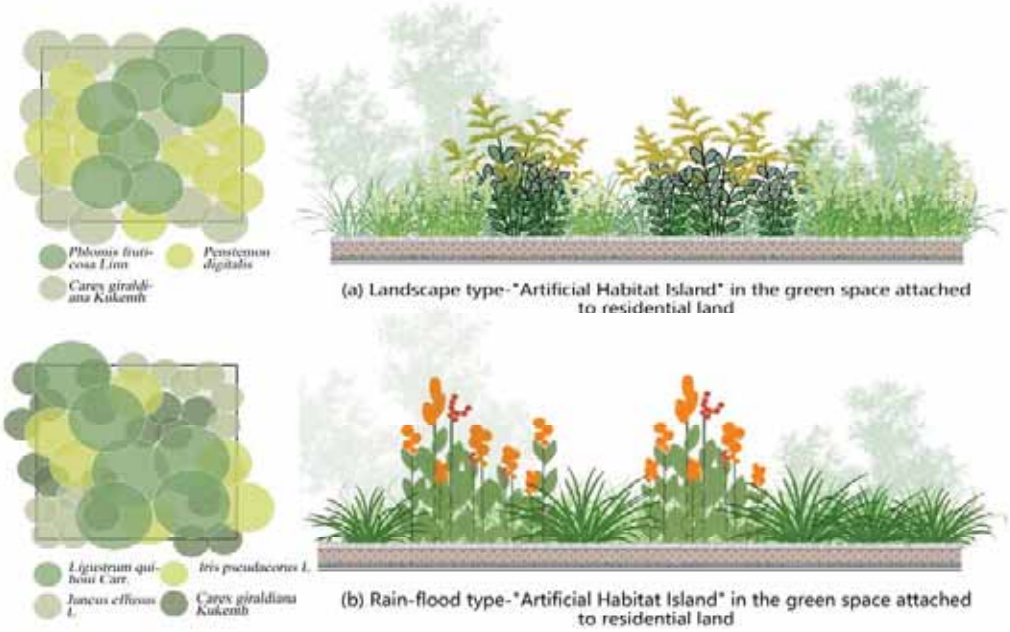

FIGURE 4
The design and composition of community structure samples in different types of "artificial habitat islands" in the green space attached to residential land.

TABLE 3
Typical pattern of "artificial habitat island" with green space attached to residential land

Pattern Type	Scene features	Habitat types	Plant community types	Vertical structure	Plant community fabric
Landscape type-"Artificial Habitat Island" in the green space attached to residential land	The residential land with higher landscape demand is attached to green space	Sun dry-land, Building-shade-dry land, Plant-shade-dry land	Landscape - dominant ground cover plant community	Structure layer Season theme layer Season theme layer	*Phlomis fruticosa Linn* *Carex giraldiana Kukenth.* *Penstemon digitalis*
Rain-flood type-"Artificial Habitat Island" in the green space attached to residential land"	Periodic wetland landscape created by using and purifying building drainage	Sun dry-land, Building-shade-dry land, Plant-shade-dry land	Runoff intercepting and purification-dominated Ground cover plant community	Structure layer Season theme layer Season theme layer Ground cover	*Ligustrum quihoui Carr.* *Juncus effusus L* *Iris pseudacorus L.* *Carex giraldiana Kukenth.*

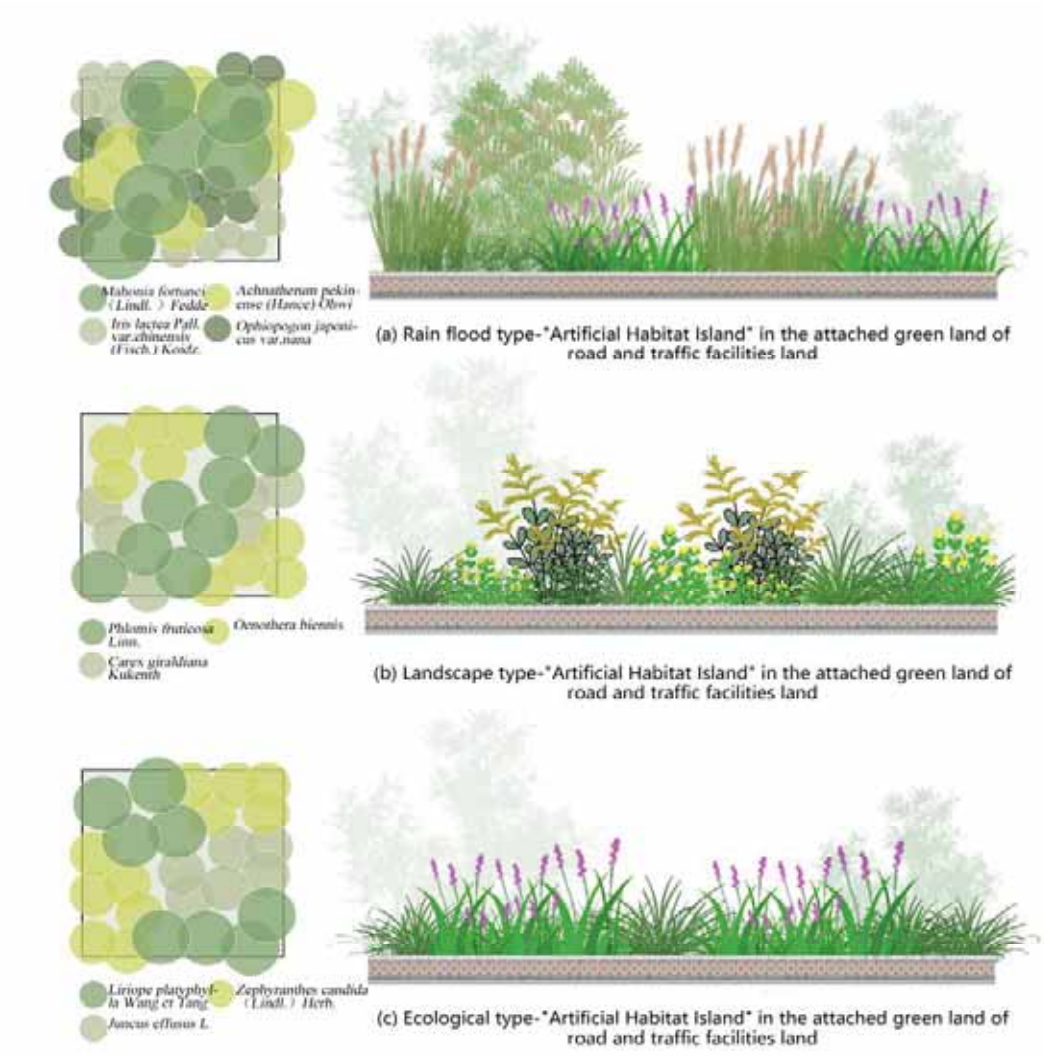

FIGURE 5
The design and composition of community structure samples in different types of "artificial habitat islands" in the attached green space of road and traffic facilities land.

TABLE 4
Typical pattern of "artificial habitat island" attached to the land for roads and transportation facilities

Pattern Type	Scene features	Habitat types	Plant community types	Vertical structure	Plant community fabric
Rain flood type-"Artificial Habitat Island" in the attached green land of road and traffic facilities land	Affiliated green space for roads and transportation facilities that undertake the function of rainwater storage and purification	Plant-shade-dry land, Sun dry-land,	Ecological improvement-dominated ground cover plant community	Structure layer Season theme layer Season theme layer Ground cover	*Mahonia fortunei (Lindl.)Fedde* *Iris lactea Pall. var.chinensis (Fisch.) Koidz.* *Achnatherum pekinense (Hance) Ohwi* *Ophiopogon japonicus var.nana*
landscape type-"Artificial Habitat Island" in the attached green land of road and traffic facilities land	An important part of streetscape and urban interface space	Sun dry-land, Plant-shade-dry land,	Landscape - dominant ground cover plant community	Structure layer Season theme layer Season theme layer	*Phlomis fruticosa Linn.* *Carex giraldiana Kukenth.* *Oenothera biennis*
Ecological type-"Artificial Habitat Island" in the attached green land of road and traffic facilities land	The most important corridor system in the urban habitat green space system	Building-shade-dry land, Plant-shade-dry land	Runoff intercepting and purification-dominated Ground cover plant community	Structure layer Season theme layer Season theme layer	*Liriope platyphylla Wang et Tang* *Juncus effusus L* *Zephyranthes candida (Lindl.)Herb.*

Evaluation analysis and result for "artificial habitat island" in square green space. The square green space provides a large area of activity for the built environment. Due to the large flow of people, and most of the squares are important urban identity space, and important city image display window, so there are higher requirements for its landscape function. In order to meet the needs of its activity site, the green space of the square is not suitable to appear in the form of a large area of park green space during the construction process. Instead, the green space should be scattered into small green patches, which are arranged around or inside the square in strips or blocks. These green spaces become important small patches of habitat and bear important ecological functions. These small patches of habitat are surrounded by large areas of hard pavement, forming a small catchment unit. Through the site design, surface rainwater can be collected to create a wetland habitat type of small area. Since the square space lacks the vertical spatial division element, Habitat Island can also become an important means of spatial organization (Figure 2d and Figure 6). Taking into account the above factors, there are four typical types of "artificial habitat island" in square green space: ecological type - "artificial habitat island" in square green space, landscape type - "artificial habitat island" in square green space, rain-flood type - "artificial habitat island" in square green space and spatial type - "artificial habitat island" in square green space (Table 5).

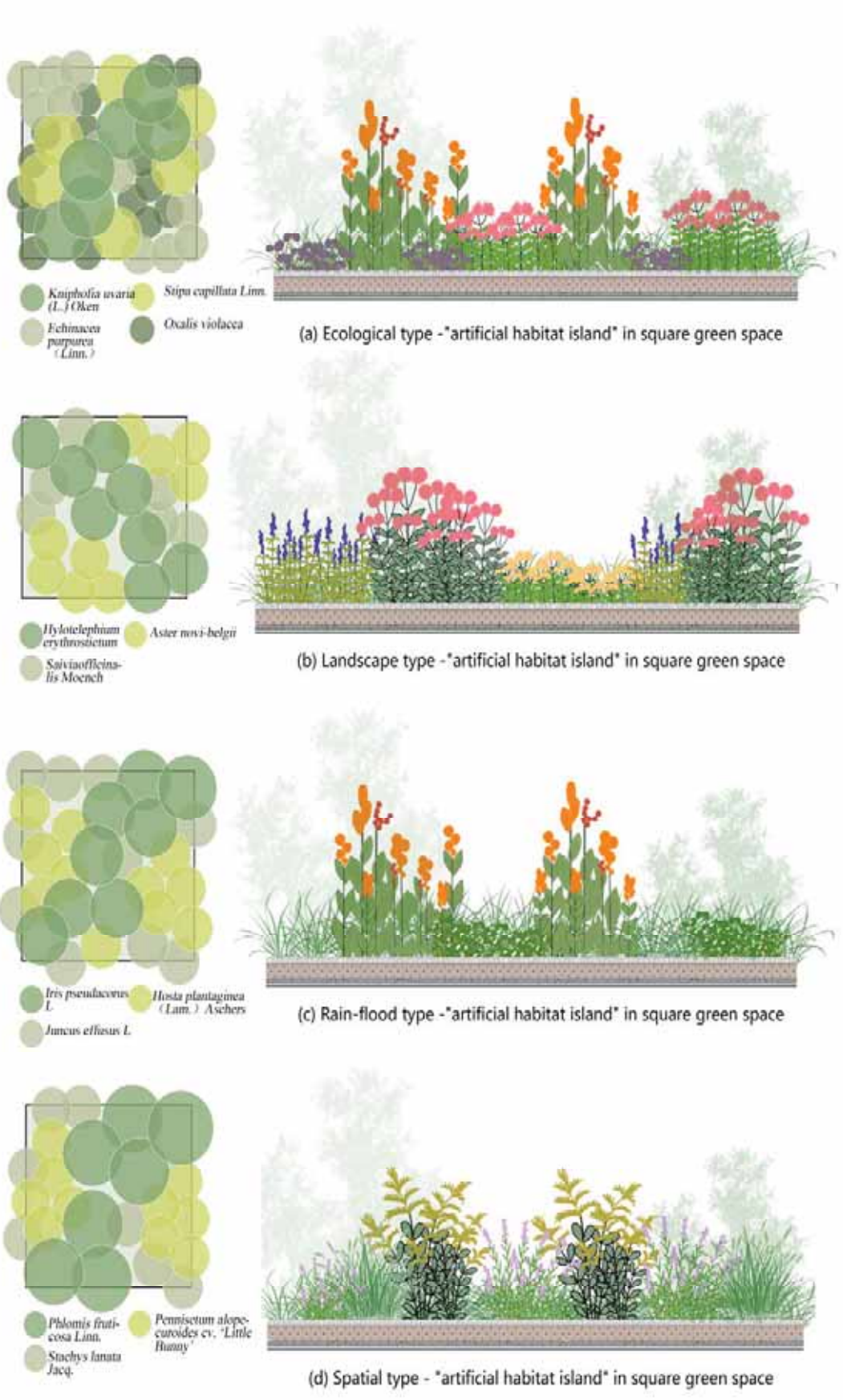

FIGURE 6
The design and composition of community structure samples in different types of "artificial habitat islands" in square green space.

TABLE 5
Typical pattern of "artificial habitat island" in square green space

Pattern Type	Scene features	Habitat types	Plant community types	Vertical structure	Plant community fabric
Ecological type - "artificial habitat island" in square green space	Small patches of habitat in a large hard space	Sun dry-land	Ecological improvement-dominated ground cover plant community	Structure layer Season theme layer Ground cover Ground cover	*Kniphofia uvaria (L.) Oken* *Echinacea purpurea (Linn.) Moench* *Stipa capillata Linn.* *Oxalis violacea*
Landscape type - "artificial habitat island" in square green space	It is an important city logo space and an important city image display window	Sun dry-land, Plant-shade-dry land	Landscape - dominant ground cover plant community	Structure layer Season theme layer Season theme layer	*Hylotelephium erythrostictum* *Saiviaofficinalis* *Aster novi-belgii*
Rain-flood type - "artificial habitat island" in square green space	A small area of wetland habitat that collects infiltrated water from the hard pavement of the square	Plant wetland, Building wetland; Building-shade-dry land, Plant-shade-dry land	Runoff intercepting and purification-dominated Ground cover plant community	Structure layer Season theme layer Season theme layer	*Iris pseudacorus L.* *Juncus effusus L* *Hosta plantaginea (Lam.)Aschers*
Spatial type - "artificial habitat island" in square green space	Vertical space division elements become an important means of spatial organization	Sun dry-land, Building-shade-dry land, Plant-shade-dry land	Spatial division-dominated ground cover plant community	Structure layer Season theme layer Season theme layer	*Phlomis fruticosa Linn.* *Stachys lanata Jacq.* *Pennisetum alopecuroides cv. 'Little Bunny'*

Evaluation analysis and result for "artificial habitat island" in boundary green space. Boundary green space is generally the belt green space or block green space in the negative space of built environment. The "artificial habitat island" in the boundary green space is the least disturbed among all types, so its ecological benefit is higher than other types. The aesthetic requirements of such habitat islands are not very high, so more ecological and economical methods can be adopted. Most of the "artificial habitat islands" in the boundary green space also play an important role in space enclosure and division. If the display function of the habitat construction site is taken into account, the boundary green space near the entrance and exit can be selected for habitat construction (Figure 2e and Figure 7). Multiple habitat types can exist at the same time in such sites. Considering the above factors, there are two typical types of "artificial habitat island" in boundary green space: ecological type and spatial type (Table 6).

The weight analysis of each index for evaluating landscape benefit of "artificial habitat island". Base on evaluation in Table 7, it can be concluded that the importance of the criterion layer is ranked as follows: ecological benefits> landscape benefits> economic benefits; the importance of indicators is ranked as: habitat adaptability> community stability Characteristic> Coordination with external environment> Species richness> Plant landscape temporal richness> Special functionality> Native soil> Plant ornamental characteristic richness> Management and protection requirements> Purchase cost. In order to make the evaluation result more objective and credible, the author uses mathematical methods to evaluate the "artificial habitat island". Among the above ten evaluation indicators, they are classified according to their ability and performance. The author divides the entire evaluation index into three

levels, of which the first level is assigned five to four points, the second level is assigned three to two points, and the third level is assigned one point. The detailed evaluation criteria are shown in Table 8.

The comprehensive index of ten "artificial habitat islands" and five Xi Xian New Area were calculated by the analytic hierarchy process (AHP) (Table 9), and they were ranked according to the comprehensive index. It can be clearly seen that the index values of the "artificial habitat island" are high, indicating that it has initially achieved the ecological, aesthetic and economic design objectives. At the same time, compared with the non - "artificial habitat island" green space, we can also see the obvious advantages. Using hierarchical analysis to make a comprehensive assessment of "Artificial Habitat-Island" to verify its application function value, the G1, G3, B3 and B7 prominently enhanced ecological and landscape benefits. Not only had good regional landscape characteristics, its management and maintenance cost were also lower (Table 10).

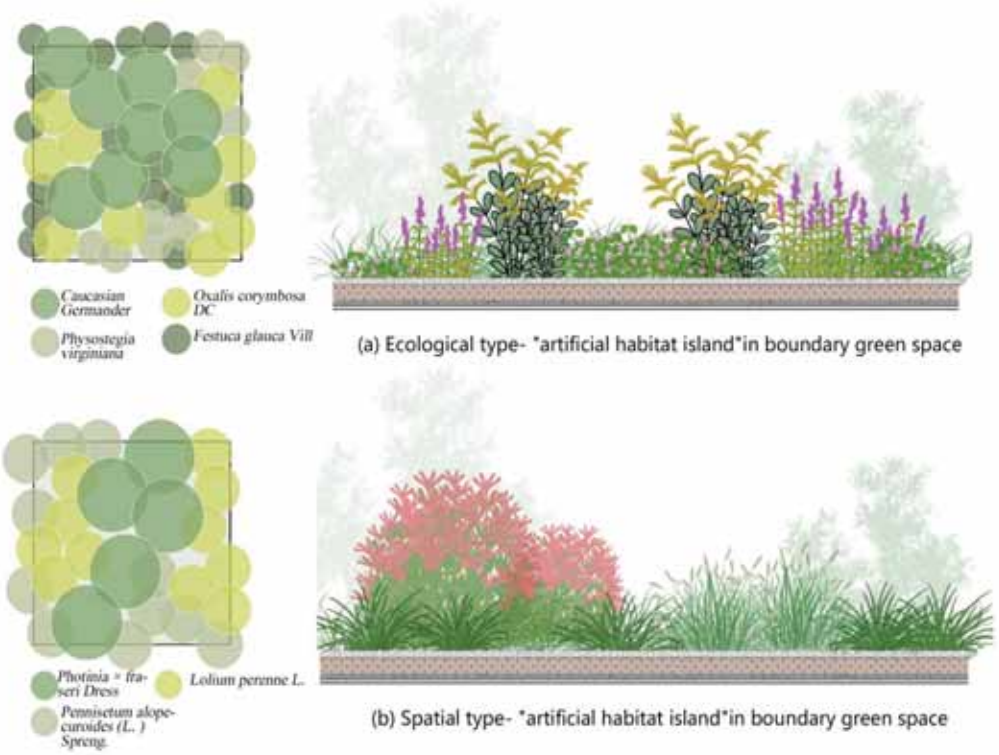

FIGURE 7
The design and composition of community structure samples in different types of "artificial habitat islands" in boundary green space.

TABLE 6
Typical pattern of "artificial habitat island" in boundary green space

Pattern Type	Scene features	Habitat types	Plant community types	Vertical structure	Plant community fabric
ecological type- "artificial habitat island"in boundary green space	Minimal human disturbance, larger area, and highest ecological benefit	Sun dry-land	Ecological improvement-dominated ground cover plant community	Structure layer Season theme layer Season theme layer Ground cover	*Caucasian Germander* *Physostegia virginiana* *Oxalis corymbosa DC.* *Festuca glauca Vill*
spatial type- "artificial habitat island "in boundary green space	It plays an important space enclosing and dividing boundary space	Sun dry-land, Plant-shade-dry land	Spatial division-dominated ground cover plant community	Structure layer Season theme layer Season theme layer	*Photinia × fraseri Dress* *Pennisetum alopecuroides (L.) Spreng.* *Lolium perenne L.*

TABLE 7
The total ranking of appraisal scale on "artificial habitat island"

Target layer	Criteria layer	Single weights	Evaluating factors	Single weights	Total single weights
"Artificial habitat island" A	Ecological benefits B_1	0.6738	Habitat adaptability C_{11}	0.5124	0.3453
			Special functionality C_{12}	0.0936	0.0630
			Community stability C_{13}	0.2798	0.1885
			Species richness C_{14}	0.1142	0.0770
	Landscape Benefits B_2	0.2255	plantscape time diversity C_{21}	0.2970	0.0670
			Coordination with the external environment C_{22}	0.5396	0.1217
			Richness of ornamental characteristics of plants C_{23}	0.1634	0.0369
	Economic benefit B_3	0.1007	Rural Native C_{31}	0.5936	0.0598
			Acquisition cost C_{32}	0.1571	0.0158
			Management demand C_{33}	0.2493	0.0251

TABLE 8
The quantitative classification of the evaluation indexes for the "artificial habitat island"

Characteristics of plants	Evaluation indexes	Grades(Score)		
		Grade 1 (5-4 point)	Grade 2(3-2point)	Grade 3 (1 point)
Ecological benefits	Habitat adaptability C_{11}	All the plants grow well	Plants growth status: general	Some plants are dead
	Special functionality C_{12}	With more than 2 functions	Only with 1 function	With no function
	Community stability C_{13}	No weed invasion, no exposed soil	Less weed invasion, part of the soil exposed	A large number of weeds invasion, more exposed soil
	Species richness C_{14}	Plant species are abundant and there are obvious signs of insect activity	Many plant species and a few signs of insect activity	The plant species is single and there is no obvious sign of insect activity
Landscape Benefits	plantscape time diversity C_{21}	High plantscape time diversity	General plantscape time diversity	Poor plantscape time diversity
	Coordination with the external environment C_{22}	High Coordination with the external environment	General Coordination with the external environment	Poor Coordination with the external environment
	Richness of ornamental characteristics of plants C_{23}	High Richness of ornamental characteristics of plants	General Richness of ornamental characteristics of plants	Poor Richness of ornamental characteristics of plants
Economic benefit	Rural Native C_{31}	Native species	Non-native species, Accessible	Non-native species, unobtainable
	Acquisition cost C_{32}	≤20 yuan/m2	>20yuan /m2 and ≤ 50 yuan /m2	>50 yuan /m2
	Management demand C_{33}	Extensive management	Semi-extensive management	Fine management

TABLE 9
Index Weight in the indexes of ecological benefit evaluation for assessment on "artificial habitat island"

Indexes of ecological benefits	Habitat adaptability C_{11}	Special functionality C_{12}	Community stability C_{13}	Species richness C_{14}	Weight	Consistency check
Habitat adaptability C_{11}	1	5	3	3	0.5124	
Special functionality C_{12}	1/5	1	1/4	1	0.0936	λ_{max} =4.1468
Community stability C_{13}	1/3	4	1	3	0.2798	*CI*=0.050，*RI*=0.9 *CR*=0.0550<0.1
Species richness C_{14}	1/3	1	1/3	1	0.1142	

TABLE 10
Analysis of Comprehensive Index Evaluation of "artificial habitat island"

Type	NO.	Name of the green space	The evaluation index										Comprehensive indexes
			C_{11}	C_{12}	C_{13}	C_{14}	C_{21}	C_{22}	C_{23}	C_{31}	C_{32}	C_{33}	
"Artificial habitat island"	1	Green corridor 1	5	3	4	5	5	5	4	5	3	5	4.6175
	2	Green corridor 3	5	3	4	3	5	5	3	5	2	3	4.3606
	3	Green corridor 7	3	1	5	5	5	5	3	5	3	4	4.1436
	4	Green corridor 11	5	2	3	4	5	5	3	5	3	5	4.1979
	5	Baimahe park 3	5	3	4	4	5	3	3	5	3	4	4.0926
	6	Baimahe park 7	3	1	5	5	3	3	3	5	3	4	3.805
	7	Baimahe park 12	3	1	5	5	5	5	3	5	2	4	4.1278
	8	Baimahe park 17	5	3	4	3	5	5	3	5	3	2	4.0738
	9	Baimahe park 20	2	3	5	5	5	5	3	5	3	4	3.9877
	10	Baimahe park 24	4	4	4	4	3	3	3	5	2	3	4.2877
Green space of non-"artificial habitat island"	1	Green space in Tongyi Road	1	1	1	3	5	5	3	5	4	4	2.6244
	2	Green space in the West Cloud Valley	3	1	1	3	5	5	3	5	2	3	3.0675
	3	Green space in the cultural tourism town named Book of Songs	4	3	3	3	5	5	3	3	4	4	3.6297
	4	Green space in the residential area named Fengximeijun	3	1	1	3	3	5	3	5	2	3	2.9967
	5	Green space in Shaanxi institute of international trade and commerce	2	1	3	4	3	5	3	5	3	4	2.6244

The study summarized "artificial habitat islands" schema types: "artificial habitat island" of park green space, "artificial habitat island" of attached to the green space in residential land, "artificial habitat island" of attached green space in road and transportation land, "artificial habitat island" in plaza green space, "artificial habitat island" in boundary green space, according to the typical characteristics of each type to carry on the design pattern

of generalizations. Then, the design process and construction management are elaborated to better guide its application. At the same time, the comprehensive evaluation of "artificial habitat island" is completed, which lays a foundation for the application and promotion of "artificial habitat island". This result has a guiding significance for the practical application of the "artificial habitat island" design pattern in urban built environment.

DISCUSSION

The application of different the Bioretention Facilities design model. In the urban built environment green space, there are a large number of fragmented green space patches of urban habitat with high heterogeneity. Traditional urban green space landscape design and construction methods have been unable to meet the ecological, functional and aesthetic requirements of such space. If the "artificial habitat island" design pattern can be applied into practice in this kind of site, it will not only make efficient and economical use of the fragmented urban habitat green space, but also give full play to the ecological function of these sites, improve the diversity of species in the city, and enhance their landscape function.

The "artificial habitat island" design pattern with aesthetic function as the main and ecological function as the auxiliary was selected from the multi-solution design pattern, and an experimental study was carried out in the urban built environment site. In the experimental study, the problems to be explored in the design mode were selected, and the design problems were converted into variables and substituted into the experiment in combination with the conditions of the experimental site [21]. The implementation was carried out through three links: site preparation, experiment construction and experiment management. Based on the data obtained from the experimental observation, the relationship between the design variables and the analysis variables and the evaluation variables were analyzed in the experimental results, and the successful design patterns were screened through the evaluation variables. The design method and implementation approach of "artificial habitat island" are the ultimate goal of the experimental research. The design method can guide the design of "artificial habitat island", and the implementation approach can guide the implementation of "artificial habitat island". The design mode that can be directly selected can be directly applied in the site conditions of similar urban built environment.

The evaluation and design method for the Bioretention Facilities. In this study, a design model of "artificial habitat island" based on the theory of habitat construction was proposed, this pattern is built in urban green space habitat environment of small scale network building, on the basis of research results, preliminary response of the habitat patches ecological design and complement, and based on the natural environment of west salty district built environment characteristics and landscape greening construction demand, carries on the experimental study. This paper tries to propose a variety of feasible "artificial habitat island" design methods and models according to the characteristics of urban built environment in Xi Xian New Area. The important innovation of this study is to solve the integration problem of plant community directly applied in urban environment. "Artificial habitat island" has the characteristics of multi-scale, multi-shape, and a variety of alternative plant community patterns, which can be duplicated, combined and coupled to different types of urban green space. Combining multi-scale and multi-form artificial structures as the carrier of "plant community" can improve the ornamental value of plant community, and also build a bridge for plant community landscape to intervene in urban public space [22].

The effect of different plant community and soil optimization. In terms of plant fabric, "artificial habitat island" uses ground cover plant communities that mimic natural habitats. Not only does such a fabric result in a good diversity of urban species, but in the long run, they can achieve a stable state through their own succession [23]. However, in the initial design, construction, management and maintenance of such community fabric, staff with a better understanding of plant community fabric should be involved. "Artificial habitat island" uses a large number of native plants in plant selection. Although they have better habitat adaptability and landscape effect than traditional horticultural plants, they are not available in the nursery stock market at present, making them difficult to purchase and use. This has also become a huge challenge for the promotion and use of "artificial habitat island".

The importance of community planting management and maintenance. The management of ground cover community is not mechanically copied, but a process of re-creation. After the establishment and planting, with the development and succession of the community, the constituent species interact with each other and choose the appropriate ecological niche [18], and the plane positions of species even change in a longer period of time [24]. At the same time, the number of species and the composition of species in the community will also change with time, and maintaining the diversity of species in the community is also one of the objectives of management. Managers need to respond to the dynamic changes of the community at any time and adjust the parts to adapt to the whole. The traditional way of maintaining individuals in management is no longer

suitable for the management of the ground cover community. It emphasizes more on the creative management of the whole, so management is a process of re-creation. The management and maintenance of the community can be divided into two stages according to the succession process of the community. The first stage is from the completion of self-establishment to the complete closure of the canopy. According to experimental observations, it will take about 1.5 years to complete this stage, and the core goal of management in this stage is to maintain the survival of the species and reduce the interference of invasive weeds. The second stage is after the complete closure of the canopy. In this stage, the stability and anti-invasion of the community increase, and the frequency of management and maintenance can be reduced accordingly. The management content is to intervene in the occurrence of abnormal conditions such as water shortage and lodging.

1) Layer management. Different layers of plant communities play different roles in ecological functions and aesthetic characteristics. The significance of structure layer and ground cover layer is to maintain the stability of the community, the value of seasonal theme layer is to enhance the aesthetic degree of the community, and the goal of ground cover layer is to enhance the anti-invasion of the community. Hierarchical management is a more clear and effective way, which can continue the goal of stratified design, and is conducive to maintaining the overall landscape framework of the community, while taking into account the ecological function of the community.

The management of the structure layer should preserve its position as the building species in the community and its function as the skeleton at the visual level. Structure layer plants are generally divided into two types: one is evergreen plants, whose aboveground biomass can be accumulated across the year; the other is a wilted, non-lodging plant whose biomass is re-accumulated each spring. The dominance of the former tends to increase continuously in the community, which leads to the imbalance of interspecific relationships. It is necessary to prune the former in early spring. The advantages of the latter are easily threatened by other plants, especially the plants that germinate earlier and grow faster in spring, such as Penstemon digitalis *'Husker Red', Heuchera micrantha,* etc., can indirectly maintain their advantages by restricting their neighboring plants.

The season theme layer is the main body of the visual change of the community, and the maintenance of its flowering amount and flowering period in the community is the core goal of management to maintain its color and texture to have sufficient influence [25].The threat of season theme plants is mainly due to the imbalance of interspecific relationships caused by the increase of competitiveness of other species, and the advantages of competitors often manifest themselves in one or more of three ways: overabundance, height and coverage. In general, the more plants in the seasonal theme layer are not the better. When the dominance of plants in the seasonal theme layer is greater than expected, it can be limited by pruning.

Ground cover is the base of the community, and it is the background of the upper plants in the community from the perspective of aesthetic characteristics. From the perspective of ecological function, its significance is to enhance the community's resistance to invasion. Therefore, the goal of ground cover management is to maintain and enhance its ground cover in order to reduce the blank ecological niche in the community. In a dynamic community structure, adequate growth space should be reserved for ground cover. The margins of communities and the empty spaces between plants are the most vulnerable areas for weed invasion. It is important to enhance the coverage of these areas through management.

2) Water. The two stages of management employ different watering strategies. In the first stage, when the community is in the critical period of development, the main purpose of watering is to ensure that the plants are fully adapted to the site conditions. Regular watering can be adopted, with a frequency of 1 to 2 times per month. In the second stage, the adaptability and stability of the community were enhanced, and the principle is watering when water was needed. Managers need to be on the lookout for "signs" of plant dehydration, such as wilting leaves or a slight hardening of the soil surface. The amount of watering should be based on the phenological changes of the community. The amount of watering should be increased in the growing period and decreased in the dormant period. Sprinkler irrigation and diffuse irrigation are two kinds of watering methods. The former has the advantage of saving water, but it is easy to make plants lodging when spraying, while the latter is on the contrary. From March to May of each year, the community is in the growing period, and its height is low and it is not easy to lodging. Therefore, sprinkler irrigation can be used, and after that, flood irrigation should be used. The time, amount and method of watering are not invariable, and managers should make timely adjustments according to different communities, different years and different rainfall conditions, and explore the optimal watering strategy in continuous practice.

3) The weeding. Weeding is the key and difficult point in the management stage. In different stages of management, the succession state of the community was different, the composition of weed species and the resistance to invasion of the commu-

nity were also different, so different weeding strategies were needed. In the first stage, newly established plants are vulnerable and lack the roots and resources to compete with other invasive plants. Therefore, the goal of weeding at this stage is to contain weeds at the budding stage. The smaller the weed plant, the easier it is to remove, and the less it affects the community. The time of weeding should be after rainfall or watering. At this time, the soil is wet and weeds can be pulled out by roots, but soil compaction and soil surface damage caused by trampling should be avoided. If weeds are controlled at this stage, the community structure tends to be complete, laying a good foundation for the succession and development of the next stage. In the second stage of management, the community canopy begins to close, the community species composition tends to be stable, the ecological niche and available resources left for weed plants are reduced, and the community resistance to invasion is enhanced [26-27]. The number of weeds will decrease during this period, but the species composition will take on new characteristics. Therefore, the weeding task at this stage is to control the perennials. In the community with gravel cover, once the weed invasion will increase the difficulty of cleaning, it should be detected in time and removed as soon as possible. Every year from April to October is the peak period of weed germination, is also the key period of weeding. Ideally, with the increase of succession time, the structure of the community becomes more stable and weeds become less and less. At this time, the community has been on the right track and weeding frequency can be appropriately reduced.

Summing up the occurrence rules of weeds in different habitats and communities in management is beneficial for managers to improve the efficiency of weed identification and removal [4]. Weed species are affected by habitat conditions. Of course, "weed" is a relative term. Sometimes weeds can fill the empty ecological niche in the community without interfering with the overall landscape effect of the community. In this case, selective weeding strategies can be adopted to retain some less invasive species, which is conducive to filling the spatial niche and improving the species diversity of the community.

4) The clip. Pruning is not a necessary management method. It is necessary to prune when a plant is taller than expected and affects the aesthetic characteristics of the community. The higher parts should be cut off, but the budding and flowering periods should be avoided. Second, some plants can be cut off when they proliferate too much and pose a threat to other plants. Third, some plants with thin and soft stalks should be cut off when they lodging due to wind or human factors. There is no specific time limit for pruning, depending on the circumstances.

CONCLUSIONS

In all, the theories and methods related to habitat construction and artificial ground cover plant community fabric design were comprehensively studied. The new carrier technique was constructed and applicated to transform the plant design model ang concluded five “AHI” optimization models in five kinds urban green space. Using hierarchical analysis to make a comprehensive assessment of “Artificial Habitat-Island” to verify its application function value, the G1, G3, B3 and B7 prominently enhanced ecological and landscape benefits. Not only had good regional landscape characteristics, its management and maintenance cost were also lower. In the construction of urban small-scale habitat network, it is the product of transforming a small ecological patch into artificial landscape design based on site design. It has a clear boundary and a variety of types according to the characteristics of different sites, which can meet the heterogeneity of habitat patches. Moreover, it has a variety of alternative plant communities and indicator species patterns, which can flexibly increase urban biodiversity and ecological connectivity. It combines multi-scale and multi-form artificial structures as the carrier of "plant community", builds a bridge for plant community landscape to intervene in urban public space, and effectively improves the ornamental value of built environmental landscape. Because it uses stable and high-quality native plant community, it not only has good regional landscape characteristics, but also has lower management and maintenance cost. In addition, “artificial habitat island” provides a new experimental method with both ornamental and experimental value in small scale urban space, which is more conducive to the study of artificial ground cover community fabric. It is wise to put forward a variety of feasible “artificial habitat island” design methods and models according to the characteristics of urban built environment in semi-arid green space.

The new carrier technique was constructed and applicated to transform the plant design model ang concluded five “AHI” optimization models in five kinds urban green space. Using hierarchical analysis to make a comprehensive assessment of “Artificial Habitat-Island” to verify its application function value, the G1, G3, B3 and B7 prominently enhanced ecological and landscape benefits. Not only had good regional landscape characteristics, its management and maintenance cost were also lower. In the construction of urban small-scale habitat network, it is the product of transforming a small ecological patch into artificial landscape design based on site design. It has a clear boundary and a variety of types according to the characteristics of different sites, which can meet the heterogeneity of habitat patches. Moreover, it has a variety of alternative plant communities and indicator species patterns, which can flexibly increase urban biodiversity and ecological

connectivity. At the same time, it combines multi-scale and multi-form artificial structures as the carrier of "plant community", builds a bridge for plant community landscape to intervene in urban public space, and effectively improves the ornamental value of built environmental landscape. Because it uses stable and high-quality native plant community, it not only has good regional landscape characteristics, but also has lower management and maintenance cost. In addition, “artificial habitat island” provides a new experimental method with both ornamental and experimental value in small scale urban space, which is more conducive to the study of artificial ground cover community fabric.

ACKNOWLEDGEMENTS

This research was financially supported by the National Natural Science Foundation of China (Youth Foundation, No. 31800604), the National Natural Science Foundation of China (General Foundation, No. 51878531), and the Scientific Research Program Funded by Shaanxi Provincial Education Department (Program No. 19JK0480). The authors would like to thank all the students in Hui Liu’s studio of Xi'an University of Architecture and Technology who helped with field investigation and data collection.

Data availability statement. Data, associated meta-data, and calculation tools are available from the corresponding author (airainmail@126.com).

REFERENCES

[1] Forman, R. (2014) Urban Ecology: Science of Cities. New York: Cambridge University Press.
[2] Young, R.F. (2010) Managing municipal green space for ecosystem services. Urban Forestry & Urban Greening. 9(4), 313-321.
[3] Sullivan, W.C. (2004) Forest, savanna, city: evolutionary landscapes and human functioning. Urban Place: Reconnecting with the Natural World. Cambridge: The MIT Press, MA. 237–253.
[4] Dunn, R.R., Gavin, M.C., Sanchez, M.C., Solomon, J.N. (2006) The pigeon paradox: dependence of global conservation on urban nature. Conservation Biology. 20, 1814-1816.
[5] Largo-Wight, E. (2011) Cultivating healthy places and communities: evidenced- based nature contact recommendations. International Journal of Environmental Health Research. 21(1), 41-61.
[6] Saphores, J.D., Li, W. (2012) Estimating the value of urban green areas: A hedonic pricing analysis of the single-family housing market in Los Angeles, CA. Landscape & Urban Planning. 104(3-4), 373-387.
[7] Wu, Z., Sun, L., Li, Y., Sun, Q. (2020) Shifts in Vegetation-Associated Microbial Community in the Reclamation of Coal Mining Subsidence Land. Environmental Engineering Science. 37(12), 838.
[8] De Marco, R., da Silva, R.F., Andreazza, R., Da Ros, C.O., Scheid, D.L., Bertollo, G.M. (2016) Copper phytoaccumulation and tolerance by seedlings of native Brazilian trees. Environmental Engineering Science. 33(3), 176.
[9] Liu, R., Jadeja, R.N., Zhou, Q., Liu, Z. (2012) Treatment and remediation of petroleum-contaminated soils using selective ornamental plants. Environmental Engineering Science. 29(6), 494.
[10] Unta, A.L., Bell, S. (2014) The impact of small-scale design interventions on the behaviour patterns of the users of an urban wasteland. Urban Forestry & Urban Greening. 13(1), 121-135.
[11] Wang, J.M., Liu, H., Wu, X.H., Li, C.S., Wang, X.L. (2017) Effects of different types of mulches and legumes for the restoration of urban abandoned land in semiarid northern China. Ecological Engineering. 102(5), 55-63.
[12] Koppler, M.R., Hitchmough, J. (2015) Ecology Good, Aut-ecology Better; Improving the Sustainability of Designed Plantings. Journal of Landscape Architecture. 10(2), 82–91.
[13] Wang, J.M., Liu, H., Zhang, S., Guo, F., Li, Y.Y. (2019) The resilience research of the plant and soil optimization design base on the habitat-site design in semiarid green space. Environmental Monitoring and Assessment. 191(4), 1–16.
[14] Xiang, W.N. (2018) Pasteur's quadrant: an appealing ecophronetic alternative to the prevalent Bohr's quadrant in ecosystem services research. Landscape Ecology. 33(1), 171.
[15] Li, C.S., Liu, H., Yang, Y.T., Li, Y.Y. (2019) Plant Community Design Approaches for Fragmented Green Space Habitats in Northwest China Arid Cities. Journal of Landscape Architecture. 26(2), 88-93.
[16] Jin, J. (2008). Engineering bid evaluation model based on normalization. J. Changshu Institute of Technology. 23(4), 39-43.
[17] Knapp, S., Kuhn, I., Schweiger, O., Klotz, S. (2008). Challenging urban species diversity: contrasting phylogenetic patterns across plant functional groups in Germany. Ecology Letters. 11(10), 1054–1064.

[18] Wang, C.Y., Wu, B.D., Jiang, K., Zhou, J.W., Liu J., Lv, Y.N. (2019) Canada goldenrod invasion cause significant shifts in the taxonomic diversity and community stability of plant communities in heterogeneous landscapes in urban ecosystems in East China. Ecological Engineering. 127(2), 504–509.
[19] Hitchmough, J., Fleur, M.D.L. (2006) Establishing North American prairie vegetation in urban parks in northern England: Effect of management and soil type on long-term community development. Landscape & Urban Planning. 78(4), 386–397.
[20] Rittel, H.W.J., Weber, M.M. (1973) Dilemmas in a General Theory of Planning. Policy Sciences. 4(2), 155–169.
[21] Daniels, B., Zaunbrecher, B., Paas, B. (2018). Assessment of urban green space structures and their quality from a multidimensional perspective. Science of the Total Environment. 615, 1364–1378.
[22] Xu, K.Y., Ye, W.H. (2003) Community invasiveness and environmental stress. Journal of Tropical and Subtropical Botany. 11(1), 75–82.
[23] Kühn, I., Brandl, R., Klotz, S. (2004) The flora of German cities is naturally species rich. Evolutionary Ecology Research. 6(5), 749–764.

Received: **23.11.2021**
Accepted: **11.01.2022**

CORRESPONDING AUTHOR

Jingmao Wang
College of Architecture,
Xi'an University of Architecture and Technology,
Xi'an 710055 Shaanxi – China

e-mail: airainmail@126.com

© by PSP Volume 31– No. 05/2022 pages 4913-4922 Fresenius Environmental Bulletin

ANALYSIS OF DECOMPOSITION CHARACTERISTICS OF SULFUR HEXAFLUORIDE IN PARTIAL DISCHARGE ENVIRONMENT

Tianxiang Lei[1,2,*], Fangcheng Lv[1,2], Jiaomin Liu[1], Jiahao Feng[3], Ruien Zhang[4,5], Yunan Zhao[4,5]

[1]State Key Laboratory of Alternate Electrical Power System with Renewable Energy Sources, North China Electric Power University, Baoding Hebei 071003, China
[2]Hebei Provincial Key Laboratory of Power Transmission Equipment Security Defence, North China Electric Power University, Baoding Hebei 071003, China
[3]State Grid Shijiazhuang Electric Power Supply Company, Shijiazhuang Hebei 050000, China
[4]Electric Power Research Institute of Hainan Power Grid Co., Ltd., Haikou Hainan 570311, China
[5]Key Laboratory of Physical and Chemical Analysis for Electric Power of Hainan Province, Haikou Hainan 570311, China

ABSTRACT

The safe and reliable operation of Gas Insulated Switchgear (GIS) equipment is very important to the entire power grid. Early detection and timely treatment of GIS equipment internal insulation defects is the main way to prevent large-scale power outages. Partial discharge (PD) monitoring is one of the most important ways to find insulation defects. SF_6 gas decomposes under PD to generate a series of characteristic products. By detecting the types of gas decomposition components in GIS and their content changes, the PD inside GIS equipment can be effectively monitored. This method is not subject to complex electromagnetic interference on site and has become the focus of research in this field. In this paper, an experimental platform for SF6 decomposition under partial discharge caused by free particles is designed, and a 240-hour partial discharge experiment under 5 voltage levels is carried out. Studies have shown that the decomposition products of SF_6 under the action of GIS partial discharge include CO_2, CF_4, H_2S and SO_2. These four decomposition products can be used to reflect the decomposition of SF_6 inside the GIS chamber, and the content of decomposition products and gas production. The rate increases with the increase of the applied voltage and the extension of the experiment time. When CO_2 and SO_2 are generated inside the GIS gas chamber, there may be an initial insulation failure. If H_2S and CF_4 are generated inside the GIS gas chamber, the failure is more serious and should be repaired in time.

KEYWORDS:
SF_6 decomposition, partial discharge, insulating environment, gas chromatograph, gas Insulated Switchgear

INTRODUCTION

Sulfur hexafluoride (SF6) is a colorless, odorless, non-toxic, non-flammable and chemically stable gas under normal temperature and pressure [1]. It has high electrical strength and good physical and chemical properties. The arc extinguishing capacity of SF_6 is more than 100 times that of air, and its electric strength is about 2.5 times that of air in a uniform electric field [2-3]. Due to the excellent performance of SF_6 gas, gas insulation has become an important development trend of high-voltage insulation equipment. With the development of economy and society, the requirements for reliability and compactness of equipment in the power system continue to increase [4-6]. GIS (Gas Insulated Switchgear) equipment instead of traditional open electrical equipment has gradually become the main direction of power grid construction. Compared with traditional open electrical equipment, GIS filled with SF_6 gas as insulation and arc extinguishing medium has the advantages of small footprint and space, safe and reliable operation, and long maintenance period, and is widely used in power equipment [7-8].

The GIS in operation may have discharge or overheating faults due to some internal defects that may occur during equipment manufacturing, installation, and operation. Although SF_6 is chemically stable, it will decompose to produce SF_2, SF_4, SF_5 and other low-fluorine sulfides under the action of electric discharge or overheating. If the SF_6 gas is pure, the above-mentioned low-fluorine sulfides will be compositely reduced to SF_6 gas. However, there will inevitably be a small amount of impurities such as air, moisture, etc. in the actual GIS equipment. At this time, if the GIS equipment has a discharge or overheating failure, the low fluorine sulfide generated by decomposition will be combined with the trace air, moisture, and other components in the GIS equipment. The impurity reacts chemically to generate SOF_2, SO_2F_2, SO_2F1_0, H_2S, SO_2, CF_4, HF and other components.

Partial Discharge (PD) is the main cause of internal insulation failure in GIS, and it can characterize the insulation status of equipment [9]. Long-term PD poses a threat to the safe operation of GIS, causing insulation failures in operating equipment, and even power outages in the system. In the process of manufacturing, installation, and transportation, GIS will inevitably have various defects, such as burrs, electrode potential floating caused by poor contact or loose parts, metal particles, etc., as well as corrosion and insulation aging during operation [10-14].

The above-mentioned defects will distort the internal electric field of the GIS to varying degrees, thereby causing the local electric field to increase and cause partial discharge. A lot of operating experience shows that with the increase of the operating time of GIS equipment, there are latent insulation faults inside, which often lead to major accidents. As the higher the operating voltage level, the greater the loss of power outage and the higher the maintenance cost [15-17]. Therefore, it is of great practical significance to evaluate the early insulation status of GIS equipment.

Many researchers have found that SF_6 undergoes various physical and chemical reactions under PD, and is affected by other multiple factors, making its decomposition components such as product type, gas production rate, content, etc. quite different [18]. The research of the decomposition process is very difficult. However, through continuous research by scholars from various countries, it is found that the decomposition process is mainly affected by factors such as discharge energy, micro water and oxygen content, discharge type, electrode material and adsorbent [19]. Based on 220kV AC single-phase GIS, this paper designs an experimental platform for SF_6 decomposition under partial discharge caused by free particles and carries out a 240-hour partial discharge experiment under 5 voltage levels to obtain changing law of the type, content and rate of SF_6 decomposition products with the voltage and test time. The research results of this paper provide an important basis for identifying the characteristics of PD faults and ensuring the safe and stable operation of the power grid.

MATERIALS AND METHODS

(1) Experimental platform design. In this experiment, 220kV AC single-phase GIS is used with single-pole, double-break structure, and CYA6-3 hydraulic spring operating mechanism, which integrates the spring's mechanical energy storage and hydraulic drive and control. The air chamber of GIS circuit breaker is completely isolated from other air chambers with two basin-type insulators. The experiment in this article is carried out in the air chamber of single-phase GIS circuit breaker. The volume of the air chamber is about 3000L. The schematic diagram of the experimental platform is shown in Figure 1.

The power supply in the experimental platform is a 220V AC power supply. The voltage regulator is an inductive voltage regulator with a voltage regulation range of 0 to 250 volts. The test transformer is a step-up transformer with a rated capacity of 50kVA and a rated voltage of 100kV. The protection resistance value is 10kΩ, which is used to protect the GIS gas chamber. What needs to be explained here is that the field voltage is applied to the GIS bushing, which is simplified in the schematic diagram of the experimental platform in this article.

The GIS gas chamber itself has a gas valve for charging and taking gas into the gas chamber, and a pressure sensor is installed at the GIS gas valve to sense the SF_6 gas pressure in the GIS gas chamber. When determining the gas composition in the gas chamber in the experiment, after reducing the voltage of the experimental system to 0, we connect the gas valve to the PDA600 (WANDI®) component detector with a special plastic tube, slowly open the gas valve, and analyze the PDA600 component. The instrument automatically measures the type and content of the components in the gas chamber. The PDA600 component detector consumes about 2L of gas in one measurement process, and the entire experimental process needs to be measured 10 times. The process consumes about 20L of SF6 gas, which has little effect compared with the 3000L gas of 5 atmospheres in the GIS chamber. Therefore, we can think that during the whole experiment, the SF_6 gas pressure in the GIS gas chamber is constant.

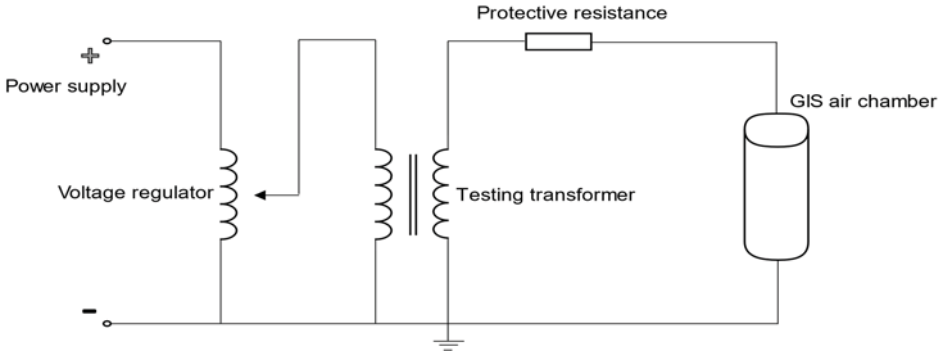

FIGURE 1
Schematic diagram of the experimental platform.

(2) Free particle discharge model. During the operation of GIS, the sources of free particles inside the air chamber are: metal particles generated during the manufacturing and installation process but not cleaned in the later stage, and vibration generated during the operation and switching operation of the GIS, making adjacent metal parts rub against each other, resulting in some metal particles. We can regard the GIS gas cell as a structure similar to a coaxial cylinder, and its internal electric field is slightly uneven. The metal particles produced during the operation of the GIS will induce electric charges in the electric field and will be displaced and jumped under the traction force of the electric field, resulting in partial discharge.

In this paper, small size stainless steel particles are used to simulate the free particles inside the GIS. Several small size stainless steel particles are purchased in the market. Before each experiment, 9g small size stainless steel particles are placed on the inner wall of the GIS. After connecting the experimental device, we slowly increase the experimental voltage until a stable partial discharge signal can be detected by a high-speed oscilloscope. The experimental voltage at this time is the initial discharge voltage U0 of the free particles. Under the conditions of this experimental platform, the initial discharge voltage U0 of free particles is 36kV.

(3) Experimental method. In this paper, the 240-hour partial discharge experiment of SF_6 decomposition under the five voltage levels of 1.3U0, 1.6U0, 1.9U0, 2.2U0, and 2.5U0 is carried out. The experimental steps are as follows:

1) Clean the air chamber of the GIS with absolute ethanol, place the free particle defect model, slowly use the vacuum pump to vacuum the air chamber of the GIS, and leave it for 24 hours to fully volatilize a small amount of moisture and other impurities in the air chamber of the GIS.

2) Slowly use the vacuum pump again to evacuate the GIS gas chamber that has been placed for 24 hours, and then use the SF_6 gas bottle to slowly fill the GIS circuit breaker gas chamber with 5 atmospheres of pure SF6 gas and use the PDA600 component analyzer to test the moisture and other impurities in the GIS air chamber in the initial state. If the moisture content exceeds 150μL/L, start again from the first step.

3) Connect the experimental circuit, slowly adjust the voltage regulator to the required experimental voltage and carry out the SF_6 decomposition experiment under the effect of partial discharge at this voltage level.

4) At 8 o'clock every morning, slowly reduce the voltage of the experimental platform to 0kV, and then use the PDA600 component analyzer to determine the composition and content of the decomposition products inside the GIS gas chamber. Pay attention to the recovery of the measured gas during this process and avoid direct contact the exhausted gas during the experiment on site.

5) After 240 hours of experiment at one voltage level, remove the experimental wiring, use the SF_6 gas recovery device to recover the gas in the gas chamber, and then perform the experiment at another voltage level according to the above steps until the five voltage level experiments are completed.

SF_6 decomposition experiments under partial discharge are carried out under five voltage levels of 1.3U0, 1.6U0, 1.9U0, 2.2U0, and 2.5U0. The SF_6 decomposition products detected in the GIS gas chamber under the experimental conditions in this article are CO_2, CF_4, H_2S and SO_2.

(4) Analysis of gas production rate of decomposition products. The internal faults of gas-insulated equipment often start with latent faults with lower energy. At the beginning of the latent fault, the content of gas products inside the gas-insulated equipment is not particularly high, but there is a very rapid gas production rate. Therefore, the generation rate of gas products can more intuitively reflect the fault nature and development process of initial faults. The analysis of the gas generation rate of gas products is of great significance for the early detection and early treatment of internal faults in gas-insulated equipment.

The gas production rate V_i is used to describe the formation of SF_6 decomposition products under the action of partial discharge. The calculation formula of the gas production rate v_i is as shown in formula 1:

$$Vi = \frac{C_{i2} - C_{i1}}{t_2 - t_1} \quad (1)$$

In the formula, V_i is the gas production rate of characteristic product i, in units of (μL/L)/day; C_{i1} is the concentration value of gas product i measured for the first time, and C_{i2} is the concentration value of gas product i measured for the second time.The unit of both is μL/L; t_1 is the time of the first measurement of SF_6 decomposition products, t_2 is the time of the first measurement of SF_6 decomposition products, and the units of both are days.

RESULTS

(1) Concentration analysis of SF_6 decomposition products. 1) Analysis of CO_2 concentration characteristics. As shown in Figure 2, the CO_2 concentration inside the GIS varies with the experimental time and applied voltage. As the experiment time increases, the CO_2 concentration will gradually increase. As the applied voltage increases, the CO_2 concentration will gradually increase, and the higher the applied voltage, the faster the CO_2 concentration will increase. When the applied voltage reached $2.5U_0$, the experiment was carried out for 240 hours, and the concentration of CO_2 inside the experimental system reached the highest value, which was

16.8μL/L.

In the experimental system used in this article, there are unavoidable impurities such as H_2O and O_2 inside the SF_6 gas which are charged into the GIS. In addition, the stainless-steel material of the GIS shell and the center conductor inevitably contains a lot of impurities. When the applied voltage reaches or exceeds the initial discharge voltage, the effect of the high-energy electric field causes a small amount of H_2O and O_2 in the experimental system to decompose to produce the O element. The stainless-steel material will also produce the C element under the action of the high-energy electric field. There will be a chemical reaction between C and O element, forming CO_2.

Since the experimental system in this article is a completely closed structure, as the experiment time increases, the generation of CO_2 will continue, making the concentration of CO_2 inside the experimental system continue to increase with the increase of the experiment time. As the applied voltage increases, the electric field energy at the fault point will increase. The C element produced on the surface of the stainless-steel material and the O element produced by the decomposition of H_2O and O_2 molecules will also increase. The CO_2 generated by the chemical action of the C and O elements will also increase.

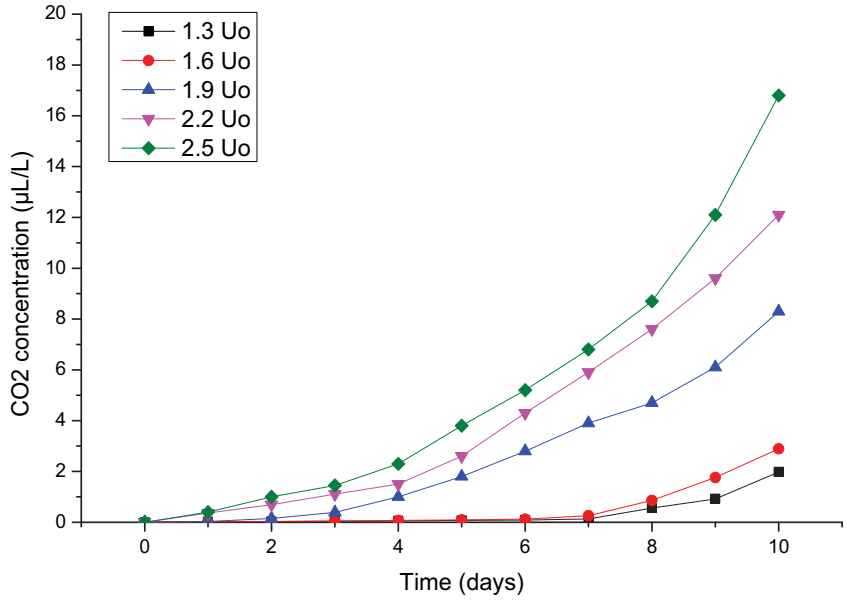

FIGURE 2
CO_2 concentration characteristic curve.

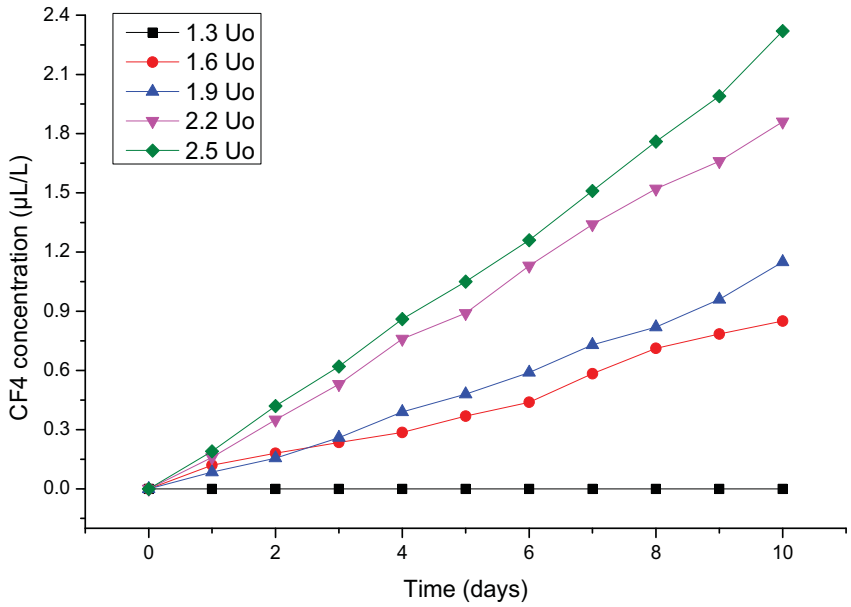

FIGURE 3
The CF_4 concentration characteristic curve.

2) CF_4 concentration characteristic analysis. As shown in Figure 3, the CF_4 concentration inside the experimental GIS varies with the experimental time and applied voltage. As the experiment time increases, the concentration of CF_4 will gradually increase. As the applied voltage increases, the concentration of CF_4 will also gradually increase. When the applied voltage is $2.5U_0$, the concentration of CF_4 in the experimental system reaches the highest value after 240 hours of experiment, which is 2.32μL/L.

In the experimental system used in this article, the GIS shell and center conductor are made of stainless steel, which will inevitably contain a small amount of C element. When the applied voltage reaches or exceeds the initial discharge voltage, the stainless-steel material will produce C element under the action of the high-energy electric field, the SF_6 molecule will crack to produce the F element. The C element and the F element will undergo a chemical reaction, thus forming CF_4.

Since the experimental container in this paper is a completely closed structure, as the experiment time increases, the generation of CF_4 will continue, making the CF_4 concentration inside the experimental system increase with the increase of the experiment time. In addition, with the increase of the applied voltage, the electric field energy at the fault point will increase, and the C element free from the surface of the stainless-steel material and the F element generated by the decomposition of SF6 molecules will also continue to increase. The CF_4 generated by the chemical action of the C and F elements will gradually increase.

The C element in the two C-containing compounds, CF_4 and CO_2, comes from the metal material in GIS. We compare the concentration curves of the two C-containing compounds, CO_2 and CF_4 under the same experimental conditions, and we can know that when the applied voltage reaches $1.3U_0$, CO_2 is produced. When the applied voltage reaches $1.6U_0$, a small amount of CF4 is produced. Moreover, under the same experimental conditions, the concentration of CF_4 in the experimental system is always lower than the concentration of CO_2, that is, under the same experimental conditions, the difficulty of generating CF_4 is higher than that of CO_2. When the insulation fault is severe, CF_4 starts to be generated inside the GIS. If it is detected that the C-containing compound, CF_4, is contained in the GIS gas chamber on the spot, it indicates that the internal insulation fault of the GIS has been serious, and the corresponding maintenance work should be arranged in time.

3) Analysis of H_2S concentration characteristics. As shown in Figure 4, the H_2S concentration inside the experimental system varies with the experimental time and applied voltage. When the applied voltage reaches $1.6U_0$, H_2S can be gradually detected in the experimental system. With the increase of the experiment time, the concentration of H_2S will gradually increase, and with the increase of the applied voltage, the concentration of $_{H2S}$ will also gradually increase. The higher the applied voltage, the faster the concentration of H_2S will increase. When the applied voltage is $2.5U_0$, after 240 hours of experiment, the concentration of H_2S in the experimental system reaches the highest value, which is 1.55μL/L.

In the experimental system used in this article, there is inevitably a small amount of impurities such as H_2O inside the SF6 gas that are filled into the GIS. When the applied voltage reaches or exceeds the initial discharge voltage, the effect of the high-energy electric field causes a small amount of H_2O in the experimental system to decompose to produce H element, and the SF_6 molecule is also cracked under the action of high-energy electric field to produce S element. The S element and H element will undergo a chemical reaction, forming H_2S.

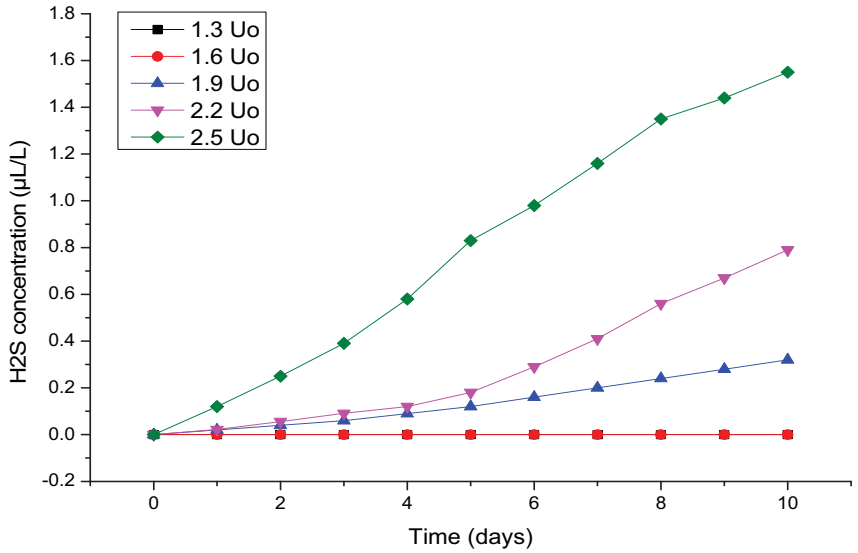

FIGURE 4
H_2S concentration characteristic curve.

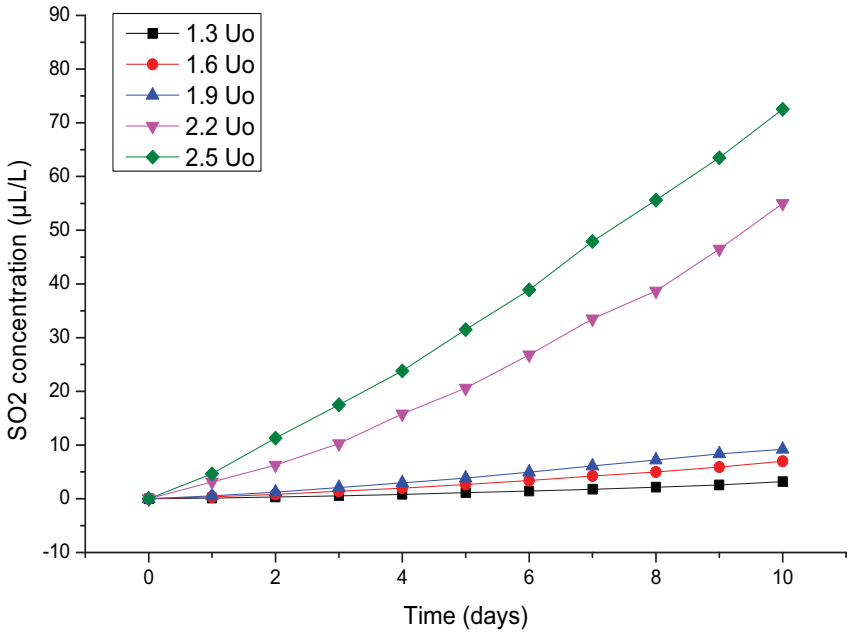

FIGURE 5
SO_2 concentration characteristic curve.

As the experimental time increases, the generation of H_2S will continue, so that the H_2S concentration in the experimental system will continue to increase with the increase of the experimental time. As the applied voltage increases, the electric field energy at the fault point will increase. The H element generated by the decomposition of H_2O in the experimental system and the S element generated by the decomposition of SF_6 molecules will continue to increase. These elements will also generate H_2S through chemical action. Since the applied voltage required to generate H_2S is relatively high, and under the same experimental conditions, the H_2S content in the experimental system is small, which means that the H_2S generation conditions are more stringent. If the H_2S gas is detected inside the GIS gas chamber on site, it indicates that the insulation fault inside the GIS gas chamber has been serious, and relevant maintenance work should be arranged in time.

4) Analysis of SO_2 concentration characteristics. As shown in Figure 5, the SO_2 concentration in the experimental system varies with the experimental time and applied voltage. With the increase of the experiment time, the concentration of SO_2 will gradually increase. With the increase of the applied voltage, the concentration of SO_2 will gradually increase, and the higher the applied voltage, the faster the concentration of SO_2 will increase. When the applied voltage is $2.5U_0$, after 240 hours of experiment, the concentration of SO_2 in the experimental system reaches the highest value, which is 72.25μL/L.

In the experimental system used in this article, a small amount of impurities such as H_2O and O_2 are inevitably present in the SF6 gas filled into the GIS. When the applied voltage reaches or exceeds the initial discharge voltage, the effect of the high-energy electric field causes the small amount of H_2O and O_2 in the experimental system to decompose to produce O element, and the SF_6 molecule will also crack under the action of high-energy electric field to produce S element. The S element and O element will undergo a chemical reaction, forming SO_2.

As the experiment time increases, the generation of SO_2 will continue, so that the concentration of SO_2 in the experimental system will continue to increase with the increase of the experiment time. With the increase of the applied voltage, the electric field energy at the fault point will increase. The O element produced by the decomposition of H_2O and O_2 in the experimental system and the S element produced by the decomposition of SF_6 molecules will continue to increase. These chemical elements generate SO_2 through chemical action, increasing the SO_2 content. Therefore, the concentration of SO_2 will continue to increase as the applied voltage increases.

(2) Analysis of gas production rate of SF_6 decomposition products. 1) Analysis of CO_2 gas production rate. Figure 6 shows the variation of the CO_2 gas production rate in the experimental system with the applied voltage and experimental time. With the increase of the applied voltage, the gas production rate of CO_2 will increase obviously, and the gas production rate of CO_2 will gradually increase with the increase of the experiment time. When the applied voltage was $2.5U_0$, after 240 hours of experiment, the gas production rate of CO_2 inside the experimental system reached the highest value, which was 4.86 (μL/L)/day.

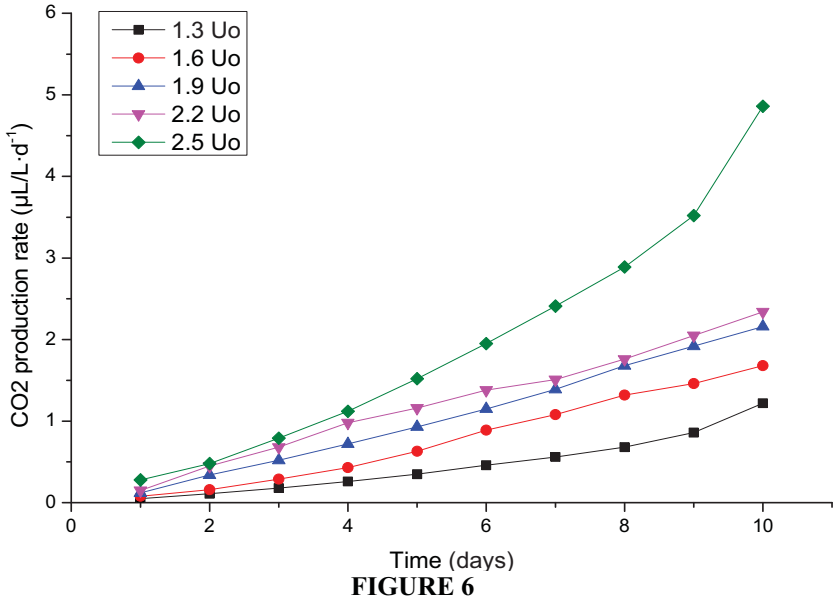

FIGURE 6
CO_2 gas production rate curve.

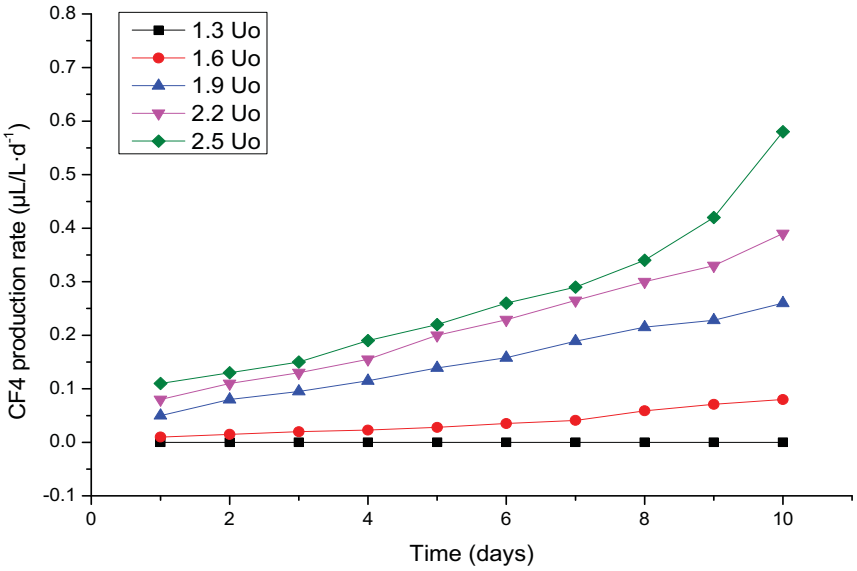

FIGURE 7
CF_4 gas production rate curve.

From the chemical reaction kinetic theory, we can know that when the reactants increase rapidly in the process of a chemical reaction, the chemical reaction rate will increase significantly. As the applied voltage increases, the electric field energy at the fault point increases rapidly, and more chemical bonds are broken. Correspondingly, the C and O elements produced will also increase rapidly, and the rate of CO_2 generation will increase. The cumulative effect of the experimental time is also another reason for the increase of the CO_2 gas production rate inside the experimental system.

2) CF_4 gas production rate analysis. As shown in Figure 7, the gas production rate of CF_4 in the experimental system varies with the applied voltage and experimental time. With the increase of the applied voltage, the gas production rate of CF_4 will increase obviously, and the gas production rate of CF_4 will gradually increase with the increase of the experiment time. When the applied voltage is $2.5U_0$ and the experiment is carried out for 240 hours, the gas production rate of CF_4 inside the experimental system reaches the highest value, which is 0.58 (μL/L)/day.

Similar to the above analysis of the CO_2 generation rate, as the applied voltage increases, the electric field energy at the fault point increases rapidly, the C and F elements generated by chemical bond breakage increase rapidly, and the generation rate of CF_4 also increases. The cumulative effect of the experimental time is also another reason for the increase of the CF_4 gas production rate in the experimental system.

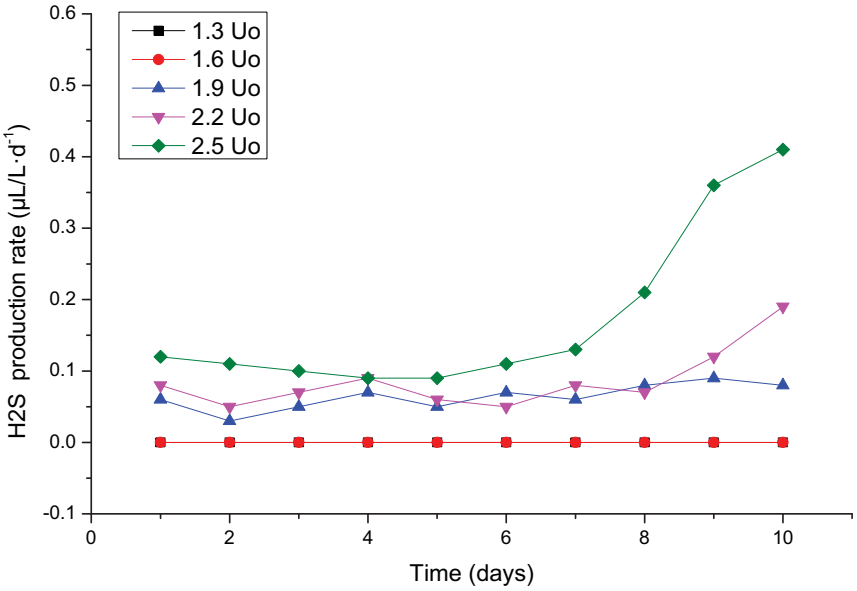

FIGURE 8
H_2S gas production rate curve.

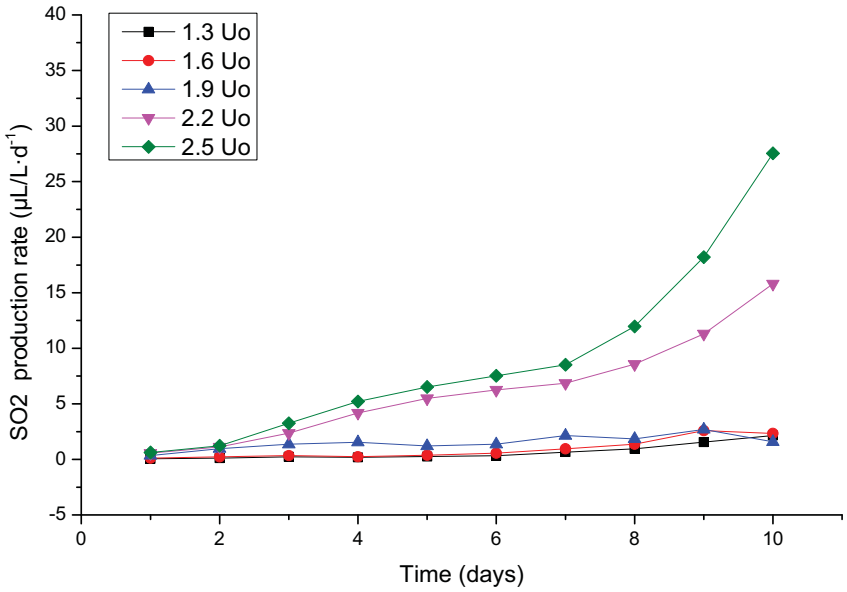

FIGURE 9
SO_2 gas production rate curve.

3) Analysis of H_2S gas production rate. Figure 8 shows the variation of the H_2S gas production rate in the experimental system with the applied voltage and experimental time. As the applied voltage increases, the gas production rate of H_2S will increase slowly. As the experiment time increases, the gas production rate of H_2S will also increase slowly. However, the overall value of the gas production rate is relatively small. When the applied voltage is $2.5U_0$ and the experiment is carried out for 240 hours, the gas production rate of H_2S in the experimental system reaches the highest value, which is 0.41 (μL/L)/day.

H_2S gas production rate curve. With the increase of the applied voltage, the electric field energy at the fault point increases rapidly, the H and S elements produced by the rupture of chemical bonds also increase rapidly, and the generation rate of H_2S also accelerates. The cumulative effect of the experimental time is also another reason for the increase of the H_2S gas production rate in the experimental system.

4) Analysis of SO_2 gas production rate. Figure 9 shows the variation of the SO_2 gas production rate in the experimental system with the applied voltage and experimental time. With the increase of the applied voltage, the gas production rate of SO_2 will

increase slowly. As the experiment time increases, the gas production rate of SO_2 will also increase slowly, and the overall value of the gas production rate is relatively large. When the applied voltage is $2.5U_0$, after 240 hours of experiment, the gas production rate of SO_2 inside the experimental system reaches the highest value, which is 27.55 (μL/L)/day.

With the increase of the applied voltage, the electric field energy at the fault point will increase rapidly, the O and S elements produced by the rupture of chemical bonds will increase rapidly, and the rate of formation of SO_2 will also increase. In addition, the cumulative effect of the experimental time is also the reason for the increase in the rate of SO_2 gas production inside the experimental system.

When a partial discharge occurs inside the GIS, the high-energy electric field at the fault point causes the SF_6 molecules to decompose to produce S and F elements. A small amount of H_2O and O_2 in the experimental system will decompose to produce H and O elements, and the GIS shell and the conductor is stainless steel, which will decompose to produce C elements. The chemical reactions between these elements will produce four decomposition products of CO_2, CF_4, H_2S, and SO_2. The concentration of these decomposition products and the rate of gas production will increase with the increase of the applied voltage and the extension of the experiment time. Studies have shown that these four decomposition products can reflect the decomposition of SF_6 inside the GIS chamber and the severity of discharge faults. If CO_2, CF_4, SO_2, and H_2S are detected in the on-site GIS gas chamber, it means that there is insulation defect or insulation cracking inside the GIS gas chamber. The staff shall conduct state assessment and maintenance on the operating conditions of the GIS.

CONCLUSIONS

(1) There are four types of SF_6 decomposition products under the action of partial discharge: CO_2, CF_4, H_2S and SO_2. These four types of decomposition products can reflect the decomposition of SF_6 inside the GIS gas chamber and the severity of discharge faults. The content and gas production rate of the four decomposition products of CO_2, CF_4, H_2S and SO_2 all increase with the increase of the applied voltage and the extension of the experiment time, and these four decomposition products all satisfy the relationship: $SO_2>CO_2>CF_4>H_2S$.

(2) When CO_2 and SO_2 are generated inside the gas chamber of the on-site GIS, the substation staff should pay attention to it. At this time, there may be an initial insulation failure inside the GIS. The conditions for the generation of H_2S and CF_4 are relatively harsh. If these two products are produced, the reaction will be more serious, and the maintenance work should be carried out in time.

ACKNOWLEDGEMENTS

This work was not supported by any funds. The authors would like to show sincere thanks to those techniques who have contributed to this research.

REFERENCES

[1] Christophorou, L.G., Olthoff, J.K., Van Brunt, R.J. (1997) Sulfur hexafluoride and the electric power industry. IEEE Electrical Insulation Magazine. 13(5), 20-24.

[2] Aziz, R.A., Slaman, M.J., Taylor, W.L., Hurly, J.J. (1991) An improved intermolecular potential for sulfur hexafluoride. Journal of Chemical Physics. 94(2), 1034-1038.

[3] Reed, A.E., Weinhold, F. (1986) On the role of d orbitals in sulfur hexafluoride. Journal of the American Chemical Society. 108(13), 3586-3593.

[4] Kiang, T., Zare, R.N. (1980) Stepwise bond dissociation energies in sulfur hexafluoride. Journal of the American Chemical Society. 102(12), 361-364.

[5] Yang, X., Moravej, M., Babayan, S.E., Nowling, G.R., Hicks, R.F. (2005) High stability of atmospheric pressure plasmas containing carbon tetrafluoride and sulfur hexafluoride. Plasma Sources Science & Technology. 14(3), 412-418.

[6] Liebermann, R.W., Lowke, J.J. (1976) Radiation emission coefficients for sulfur hexafluoride arc plasmas. Journal of Quantitative Spectroscopy & Radiative Transfer. 16(3), 253-264.

[7] Kobayashi, S., Horide, A. (1992) Development and field test evaluation of optical current and voltage transformers for gas insulated switchgear. IEEE Transactions on Power Delivery. 7(2), 815-821.

[8] Metwally, L. (2004) Status review on partial discharge measurement techniques in gas-insulated switchgear/lines. Electric Power Systems Research. 69(1), 25-36.

[9] Gui, Y., Zhang, X., Zhang, Y., Qiu, Y., Chen, L. (2016) Study on the characteristic decomposition components of air-insulated switchgear cabinet under partial discharge. AIP Advances. 6(7), 868-871.

[10] Mizuno, K., Tsutsumi, M., Matsumura, M., Yagi, Y. (2002) Development of highly reliable control systems for the gas-insulated switchgear. IEEE Transactions on Power Delivery. 11(1), 219-226.

[11] Khan, Q., Refaat, S.S., Abu-Rub, H., Toliyat, H.A. (2019) Partial discharge detection and diagnosis in gas insulated switchgear: state of the art. IEEE Electrical Insulation Magazine. 35(4), 16-33.

[12] Filho, J.R., Teixeira, J.A., Sans, M.R., Martinez, M.B. (2016) Very fast transient overvoltage waveshapes in a 500-kV gas insulated switchgear setup. IEEE Electrical Insulation Magazine. 32(3), 17-23.
[13] Bojic, P. (2002) A high-speed earthing switch in gas-insulated metal enclosed switchgear. IEEE Transactions on Power Delivery. 17(1), 117-122.
[14] Suehiro, J., Zhou, G., Hara, M. (2005) Detection of partial discharge in SF6 gas using a carbon nanotube-based gas sensor. Sensors & Actuators B Chemical. 105(2), 164-169.
[15] Nikonov, V., Bartnikas, R., Wertheimer, M.R. (2001) The influence of dielectric surface charge distribution upon the partial discharge behavior in short air gaps. IEEE Transactions on Plasma Science. 29(6), 866-874.
[16] Bui, A., Khedim, A., Loubiere, A., Kourdi, M.B. (1991) Aging of zinc oxide varistors subjected to partial discharges in sulfur hexafluoride. Journal of Applied Physics. 69(2), 1036-1040.
[17] Winstead, C., Mckoy, V. (2004) Low-energy electron collisions with sulfur hexafluoride, SF6. The Journal of Chemical Physics. 121(12), 5828-5835.
[18] Shuaibov, A.K., Shevera, I.V. (2002) Emission from a sulfur-hexafluoride volume discharge induced by attachment instability. Technical Physics. 47(11), 1473-1476.
[19] Zheng, Y.Y., Zhu, Y.L. (2020) Study on partial discharge signal denoising of transformer. Fresen. Environ. Bull. 29(4A), 2707-2710.

Received: **23.11.2021**
Accepted: **11.01.2022**

CORRESPONDING AUTHOR

Tianxiang Lei
State Key Laboratory of Alternate Electrical Power System with Renewable Energy Sources,
North China Electric Power University,
Baoding Hebei 071003 – China

e-mail: 1182101032@ncepu.edu.cn

© by PSP Volume 31– No. 05/2022 pages 4923-4929 Fresenius Environmental Bulletin

QUANTITATIVE RESEARCH ON SOIL ORGANIC MATTER BASED ON HYPERSPECTRAL REMOTE SENSING AND GENETIC ALGORITHM

Zhenyu Dong[1,2], Ni Wang[1,2,*], Jiancang Xie[1,2], Quanxi Wang[1,2], Zihan Guo[1,2]

[1]State Key Laboratory of Eco-hydraulics in Northwest Arid Region, Xi'an University of Technology, Xi'an, 710048, China
[2]Institute of Water Resources and Hydroelectric Engineering, Xi'an University of Technology, Xi'an 710048, China

ABSTRACT

Soil organic matter (SOM), as an important index for evaluating soil fertility, has important guiding significance for the evaluation of farmland quality. This study takes farmland soil in the Guanzhong Plain of Shaanxi Province as the research object, and uses ASD Fieldspec4 to obtain its spectral reflectance. The first-order differential, the second-order differential, and the reciprocal logarithm are used to reduce noise, and the genetic algorithm is combined to obtain the spectral characteristic bands. Based on this, the random forest (RF) algorithm is used to establish the SOM prediction model of the study area. The results show that: Compared with the original reflectance, first deviation (FD), second deviation (SD) and logarithm of reciprocal (Log) effectively reduce the impact of noise and improve the signal-to-noise ratio; the characteristic bands acquired based on Genetic algorithm (GA) are mainly in the visible light range, mainly located at 401-449nm. The SOM prediction model established based on GA-FD-RF has the best effect, with coefficient of determination (Rv^2), root mean square error (RMSE) and the ratio of performance to deviation (RPD) are 0.87, 1.35 and 3.23, respectively. This study provides a scientific basis for the rapid monitoring of SOM content in the Guanzhong Plain.

KEYWORDS:
Farmland Soil, Spectroscopy, Spectral feature extraction, Genetic algorithm, Random forest

INTRODUCTION

Soil organic matter (SOM) is an important reference index for evaluating soil quality and soil fertility, and it is also one of the main sources of crop nutrition, which can provide the nutrients needed for crop growth [1-3]. In the past, the determination of soil organic matter content can be obtained through field sampling and chemical experiments [4]. Although this method has high accuracy, it has a long cycle, high cost, small practical area and damage to the soil, which cannot meet the current demand for precision agriculture. With the in-depth study of soil hyperspectral [5, 6], it is found that soil organic matter exhibits unique spectral response characteristics in the visible-near infrared region. Hyperspectral technology has the advantages of large amount of information, time-saving, labor-saving, and pollution-free, and it provides an effective means for high-efficiency and real-time estimation of soil organic matter content [7, 8]. Shang et al through comparative analysis of model accuracy under different spectral transformations, variable screening methods and modeling methods, machine learning is determined to be the best estimation model for SOM content in Yinchuan Plain, with Rc^2 and RPD being 0.74 and 2.08, respectively [9]. Yu Huan et al. took the hilly farmland soil in Gangcheng District as the research object, and the study showed that the first-order differential R' is the best hyperspectral transformation method, and the 7 bands of 706, 1002, 1359, 1415, 1886, 1914 and 2221 nm are the soil organic matter content. In the significant band, the random forest model has the highest accuracy. The verification sample set R^2 and RPD are 0.73 and 1.87 to realize the rapid monitoring of the organic matter content in the hilly area of the region [10]. Guo Yunkai et al. took the heavy metals iron (Fe), arsenic (As), and chromium (Cr) of cultivated soil in a certain area of Yueyang County as their research attributes, and proposed a genetic algorithm (GA) optimized support vector machine (SVM) heavy metal content inversion model. The results show that the correlation between the second-order differential transformation spectrum and the content of each heavy metal is the most prominent overall; the three heavy metals have common sensitive characteristics in the visible light bands of 490 nm, 500 nm, 510 nm and 530 nm; after the GA algorithm optimizes the SVM parameters, compare SVM The regression model, the prediction accuracy has been significantly improved, the verification set R2 of heavy metals Fe, As and Cr are 0.968, 0.821 and 0.976, respectively [11]. The results can provide a new reference for the application of remote sensing technology to retrieve the heavy metal content of cultivated soil. In order to improve the accuracy of convolutional neural network modeling of soil element content spectroscopy, Liu Lanjun et al.

proposed a convolutional neural network soil nitrogen content spectral analysis model optimized by particle swarm algorithm. The smoothing and standard normal transformation are used to reduce the influence of noise on modeling, and the particle swarm algorithm is used to optimize the convolution kernel parameters, learning rate, number of iterations and other hyperparameters of the designed convolutional neural network. The research results show that the PSO-CNN modeling method has higher prediction accuracy. The coefficient of determination, root mean square error and relative analysis error of the test set are 0.9707, 0.8818, 5.88, respectively [12]. This research takes the farmland soil in the Guanzhong Plain of Shaanxi Province as the research object. After the soil samples are air-dried, ground, and sieved, the ASD Fieldspec 4 surface object spectrometer is used to collect the spectral numbers, and the SG nine-point smoothing, first-order differential, second-order differential, and the reciprocal logarithm performs spectral noise reduction on it and improves the signal-to-noise ratio. The genetic algorithm was used to extract the spectral characteristic bands of soil organic matter, and random forests were used to establish soil organic matter quantitative model pairs. The aim was to establish an estimation model of farmland soil organic matter content in the Guanzhong Plain and provide a theoretical basis for the quantitative assessment of large-scale farmland organic matter.

MATERIALS AND METHODS

Sample collection and data processing. From July to September 2019, soil sample collection points were arranged based on remote sensing images and farmland distribution locations, and the global positioning system was used to record the location of the sampling points, and a total of 121 soil samples were collected. During the collection, the sampling area was divided according to 1km×1km, and the five-point method was used for sampling. The top soil was mainly (0-20 cm), and the five soil samples were evenly mixed into one sample. The collected soil samples were air-dried in the laboratory to remove the grass roots and gravels, and then passed through a 2 mm sieve after being ground for spectral data collection and SOM content determination. Among them, the $K_2Cr_2O_7$-H_2SO_4 oxidation method is used to determine the soil organic matter content [13], and the ASD FieldSpec® 4 ground feature spectrometer collects the hyperspectral spectrum of the soil samples.

Data preprocessing. In the process of soil spectrum collection, in addition to the influence of environmental factors, the instrument itself will also have certain accuracy errors. These factors cause a lot of noise in the collected spectrum information, which in turn affects the accuracy of the data. In order to ensure the accuracy of the correlation and later model establishment and verification, it is necessary to eliminate the spectral data that has a greater impact, and then preprocess the eliminated spectral data [14-16]. Due to the large noise in the 350~399nm and 2450~2500nm wavebands, it is removed and only the soil spectral reflectance in the 400~2450nm waveband is retained. Savitzky-Golay (SG) nine-point smoothing method is used to smooth the spectral curve, reduce noise and improve signal-to-noise ratio [17]. In order to highlight the characteristics of the soil spectrum, this study uses the f first deviation (FD), second deviation (SD) and logarithm of reciprocal (Log) to perform spectral transformation on the smoothed original curve of the soil spectrum to further reduce the influence of noise on the spectral data [18]. After pretreatment, the correlation between the spectrum and soil organic matter can be effectively improved, and the signal-to-noise ratio can be enhanced.

Spectral feature extraction. Genetic Algorithm (GA) is an adaptive global optimization algorithm, based on the theory of biological evolution, drawing lessons from natural selection and genetic mechanisms, and selecting, crossing, and mutating each individual in the group [19, 20]. With continuous genetic iteration, variables with better objective function values can be retained, and poorer variables can be eliminated, and finally the global optimal result can be obtained, which can improve the accuracy and stability of the analysis results. When selecting the soil organic matter hyperspectral characteristic bands, each wavelength point of the spectrum is regarded as an individual in the population, and the PLS cross-check root mean square error RMSECV is used as the fitness function. The population size was set as 30, the maximum number of iterations was 100, the crossover probability was 0.5, and the mutation probability was 0.01, so as to realize the selection of characteristic bands.

Organic matter prediction model. Random forest (RF) is a major branch of machine learning. It is an optimization of traditional decision tree models. This algorithm has high accuracy and is not easy to fit. When solving nonlinear or large data problems Shows unique advantages. It uses the randomness of sample selection to have the advantage of cross-validation [21, 22]. When the number of decision trees is large enough, it can basically ensure that each sample is used as a training sample and a test sample, effectively avoiding overfitting. The coefficient of determination (R^2), root mean square error (RMSE), and RPD are used to evaluate the stability and accuracy of the model.

The Unscrambler® X 10.4 (64-bit) and MATLAB 2021a (MathWorks, Natick, MA, USA)

TABLE 1
Statistics of SOM content in the study area

Sample	Sample	Maximum (g/kg)	Minimum (g/kg)	Mean (g/kg)	SD (g/kg)	CV
Total	121	14.26	3.15	8.42	1.45	0.17

Note: SD, Standard error; CV, Coefficient of Variation

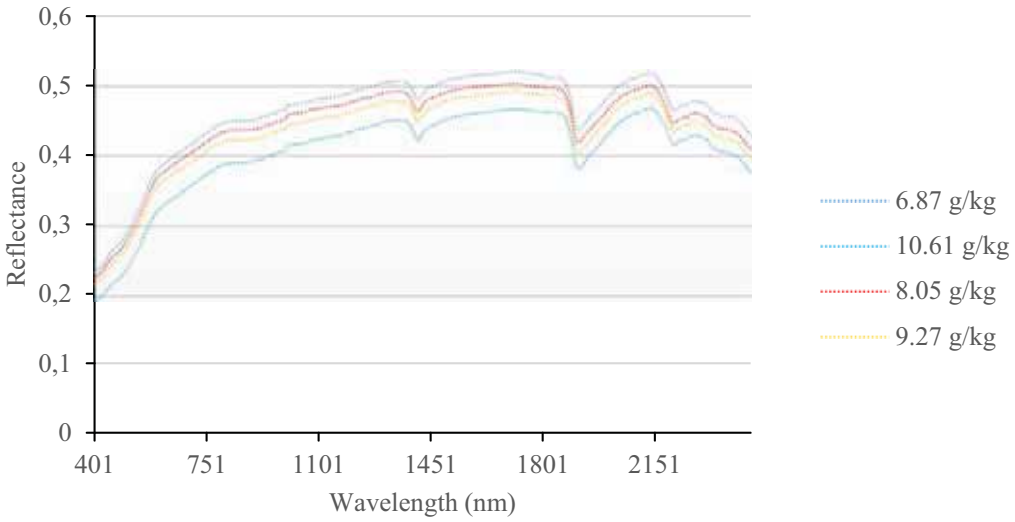

FIGURE 1
Spectral curve characteristics of different SOM content

were used for spectral data preprocessing, feature extraction and model building.

RESULTS

Spectral characteristic analysis of SOM content. The statistical information of the organic matter content of the soil samples in the study area is shown in Table 1. The SOM content of the study area is between 3.15~14.26 g/kg, the maximum, minimum and average values being 14.26 g/kg and 3.15 g/kg, 8.42 g/kg, respectively. The standard deviation is 1.45 g/kg, and the coefficient of variation is 17%.

In the range of 400~2450 nm, 4 kinds of soil measured spectral reflectance curves with different SOM content were randomly selected. After comparison, it was found that the overall trend of the spectral curves was the same. There were 3 obvious spectra near 1420, 1930 nm and 2200 nm. The absorption peak, but the depth and area of the absorption peak are different, which is mainly caused by water and clay minerals. In the whole band, with the increase of organic matter content, the overall spectral reflectance shows a downward trend, showing a negative correlation (Figure 1).

Comparative analysis of different processing spectra. In order to reduce the spectral noise and improve the signal-to-noise ratio, this study uses Savitzky-Golay (SG) smoothing, first-order differential, second-order differential, and reciprocal logarithmic transformation preprocessing (Figure 2). The transformation results show that the first derivative transformation of the spectrum can eliminate the influence of different backgrounds and noises, and can more quickly show the inflection point of the spectrum and the maximum and minimum reflection bands. There are five significant reflection peaks at 570nm, 1417nm, 1923nm, 2213nm, and 2257nm. (Figure 2a). After the second-order differential transformation, the number of reflection and absorption characteristics is significantly different from the first-order differential. There are obvious reflection peaks at 1409nm, 1902nm and 2201nm, and the remaining characteristic peaks are not obvious (Figure 2c). After the reciprocal logarithmic transformation of the original reflectivity, the curve trend has a negative correlation with the original reflectance curve (Figure 2d).

Selection and analysis of the best band based on GA. After four transformations of R, FD, SD and Log(1/R), GA is used to select the spectral characteristic bands. The results are shown in Figure 3. Comparative analysis shows that the characteristic bands selected based on GA-R are 2010nm, 591 nm, 427 nm, 1780 nm, 1132 nm, 416 nm, 431 nm, 2500 nm, 429 nm, 424 nm, 425 nm, 410 nm, 418 nm, 421 nm, 417 nm, 409 nm, 423 nm, 401 nm, 406 nm, 432 nm, 414 nm, 403 nm, 428 nm, 402 nm, 408 nm, 413 nm, 411 nm, 405 nm, 420 nm, 435 nm.

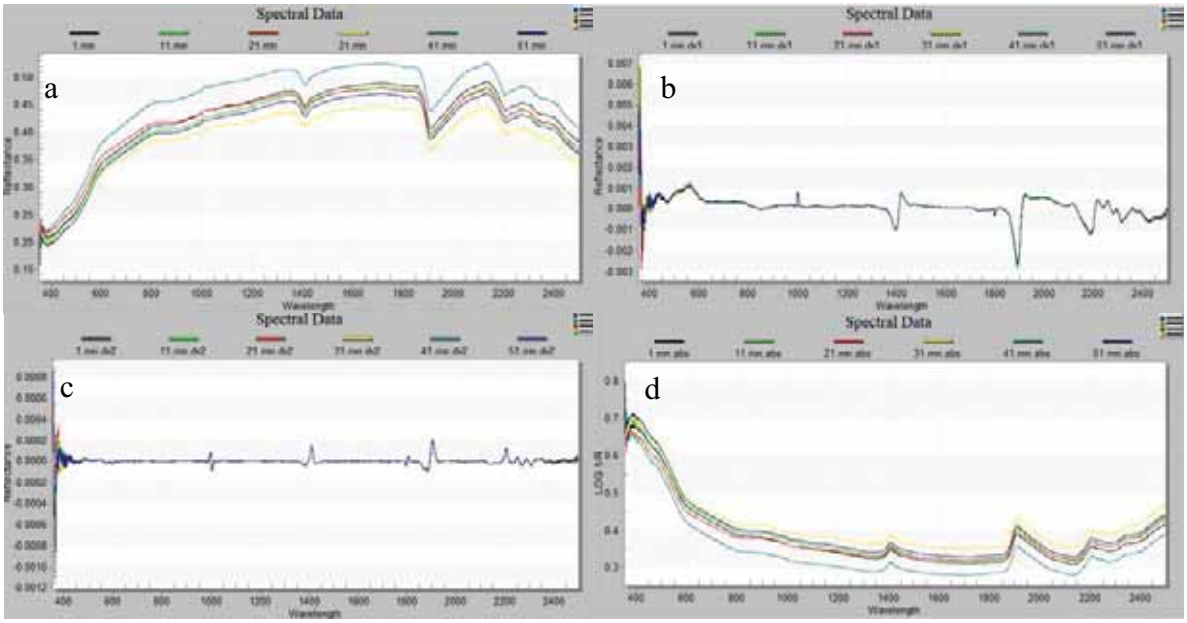

FIGURE 2
Comparative analysis of different processing spectra

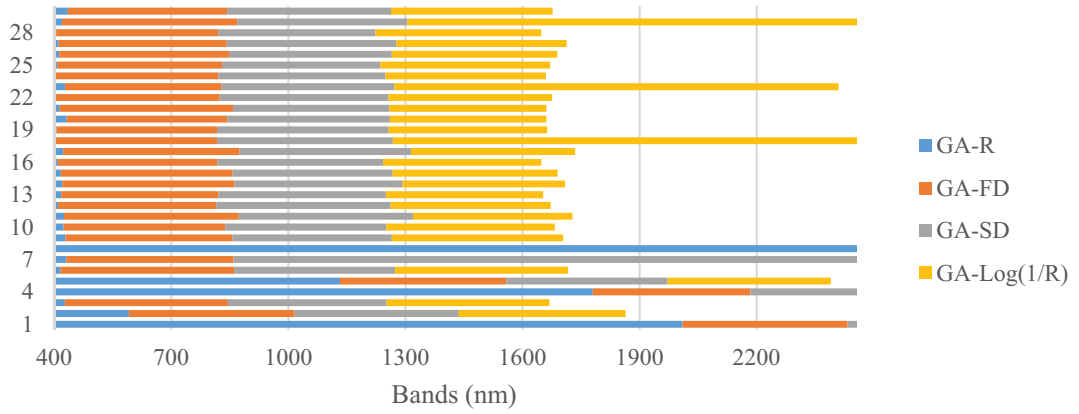

FIGURE 3
Different preprocessing feature band selection based on GA

In order to further compare the difference of feature selection after different differential transformations, take FD as an example for comparison. Except for 1746nm, its characteristic bands are all in the visible light band, that is, within the range of 401-449nm. This shows that after the first-order differential transformation, it not only effectively improves the response relationship between organic matter and spectrum, but also reduces the effect of noise.

SOM prediction model and comparative analysis. The characteristic band of the organic matter spectrum selected based on GA can improve the estimation accuracy of the SOM estimation model. In this study, the spectral variables selected by GA-R, GA-FD, GA-SD and GA-Log(1/R) were used as independent variables, and SOM was used as the modeling dependent variable. The SOM estimation model was constructed in combination with the RS model. From Table 2, it can be concluded that the modeling set and prediction set based on GA-R have poor results. The modeling set Rc^2 and RMSE are 0.51 and 3.75, and the prediction set results Rv^2, RMSE and RPD are 0.43, 4.24 and 1.38, respectively.

But after FD and SD transformation, its modeling and prediction effect is significantly improved. Among them, the model based on GA-FD has the best prediction effect. Rc^2 and Rv^2 are 0.91 and 0.87, respectively, indicating that the model has good predictive ability. The validation set RMSEP and RPD are 1.35 and 3.23, respectively, indicating that the model is stable (Figure 4). The accuracy of the SOM content nonlinear estimation model established in this paper based on the four pre-processing is better than the linear model. This is mainly because the RS model has a strong self-learning ability in data-driven, and can accurately obtain extremely complex nonlinear features in the soil spectrum.

TABLE 2
Cubist-based soil organic matter prediction statistics.

	Pretreatments	Calibration		Validation		
		Rc^2	RMSEC	Rv^2	RMSEP	RPD
RS	GA-R	0.51	3.75	0.43	4.24	1.38
	GA-FD	0.91	1.25	0.87	1.35	3.23
	GA-SD	0.79	1.98	0.78	2.17	2.35
	GA-Log(1/R)	0.55	3.28	0.54	3.75	1.97

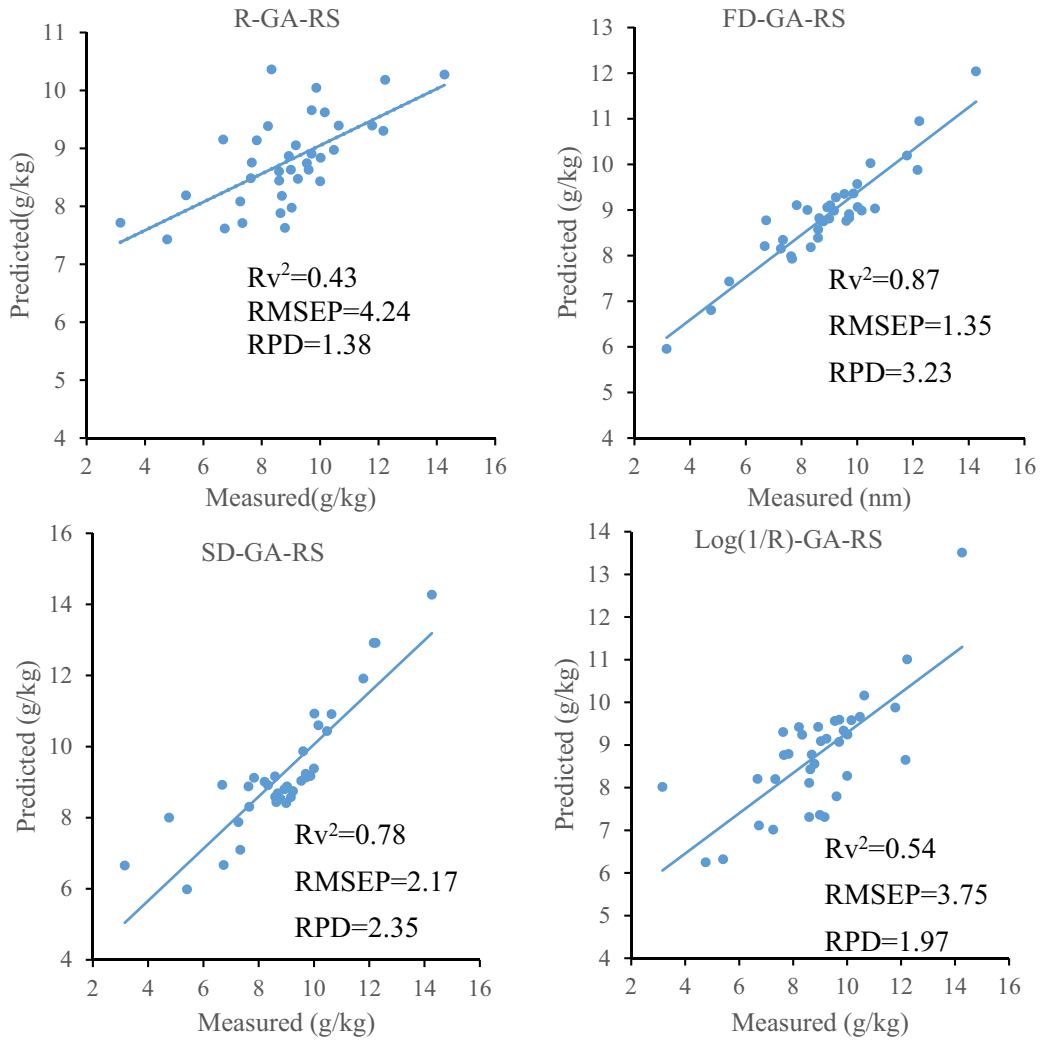

FIGURE 4
Scatter plot of SOM content prediction based on different preprocessing

CONCLUSIONS

This study takes farmland soil in the Guanzhong Plain as the research object, selects 4 spectral processing methods, combines GA to select spectral features, and combines RS to quantitatively estimate SOM. The results show that GA-FD effectively extracts the spectral characteristics of organic matter, and the SOM content model based on RS has the best prediction effect. Rc^2, Rv^2, RMSE and RPD are 0.87, 1.35 and 3.23, respectively. This model has strong quantification ability for SOM. In the spectral feature selection algorithm, this study uses GA to screen. Therefore, in the follow-up research, we continue to use different screening algorithms for comparison, and try to use the depth school spectrum processing method to further highlight the subtle differences between the soil spectra, and establish the SOM estimation model with the best accuracy and stability.

ACKNOWLEDGEMENTS

Funding: This work was supported by the National Natural Science Foundation of China (Grant No. 51979221) and Research Fund of the State Key

Laboratory of Eco-hydraulics in Northwest Arid Region，Xi'an University of Technology (Grant No. 2019KJCXTD-5).

REFERENCES

[1] Guo, Y., Zhao, R., Zeng, Y., Shi, Z. and Zhou, Q. (2018). Identifying scale-specific controls of soil organic matter distribution in mountain areas using anisotropy analysis and discrete wavelet transform. Catena. 160, 1-9.

[2] Mcfarlane, K.J., Schoenholtz, S.H., Powers, R.F. and Perakis, S.S. (2010). Soil organic matter stability in intensively managed ponderosa pine stands in California. Soil Science Society of America Journal. 74(3), 979-992.

[3] Gregory, S., Lauzon, J.D., O'Halloran, I.P. and Heck, R.J. (2006). Predicting soil organic matter content in southwestern ontario fields using imagery from high-resolution digital cameras. Canadian Journal of Soil Science. 86(3), 573-584.

[4] Chen, Y.Y., Qi, K., Liu, Y.L., He, J.H. and Jiang, Q.H. (2015). Transferability of hyperspectral model for estimating soil organic matter concerned with soil moisture. Spectroscopy & Spectral Analysis. 35(6), 1705.

[5] Ramirez-Lopez, L., Behrens, T., Schmidt, K., Stevens, A., Demattê, J.A.M. and Scholten, T. (2013). The spectrum-based learner: a new local approach for modeling soil vis-nir spectra of complex datasets. Geoderma. 195, 268-279.

[6] Tsakiridis, N.L., Theocharis, J.B., Symeonidis, A.L. and Zalidis, G.C. (2021). Improving the predictions of soil properties from vnir–swir spectra in an unlabeled region using semi-supervised and active learning. Geoderma. 387, 114830.

[7] Nascimento, C.M., Mendes, W., Quionez, N., Poppiel, R.R. and Demattê, J.A.M. (2021). Soil degradation index developed by multitemporal remote sensing images, climate variables, terrain and soil atributes. Journal of Environmental Management. 277, 1-9.

[8] Ripalda, J.M., Buencuerpo, J. and García, I. (2018). Solar cell designs by maximizing energy production based on machine learning clustering of spectral variations. Nature Communications. 9(1), 5126.

[9] Shang, T.H., Mao, H.X., Zhang, J.H., Chen, R.H., Wang, F., Jia, K.L. (2021) Hyperspctral estimation of soil organic matter content in Yinchuan plain, China based on PCA sensitive band screening and SVM modeling. Chinese Journal of Ecology. 40(12), 4128-4136.

[10] Yu, H., Liu, J., Liu, Y.Q., Gu, Z.P., Wang, A.L. (2021). Estimation of Soil Organic Matter Content of Cultivated Land in Hilly Regions with Hyperspectral. Journal of Shandong Agricultural University (Natural Science Edition). 52(4), 648-653.

[11] Guo, Y.K., Zhang, S.A., Xie, X.F., Xie, Q. (2021) The Hyperspectral Inversion Method of Heavy Metal Contents in Cultivated Soils Based on GA-SVM. Chinese Journal of Soil Science. 52(4), 968−974.

[12] Liu, L.J., Zhai, Y.Q., Zheng, J.J., Fan, P.P., Deng, L. (2021). Visible/Near infrared spectroscopy modeling of soil nitrogen content based on PSO-CNN. Optical Technique. 47(04), 438-455.

[13] Vicente, F., Santos, A., Sagüillo, E.G., Ángel, M., Martínez-Villacorta, R.J.M. and Romero, A. (2012) Diuron abatement in contaminated soil using fenton-like process. The Chemical Engineering Journal. 183(none), 357-364.

[14] Santana, F.D., Souza, A.D. and Poppi, R.J. (2018). Green methodology for soil organic matter analysis using a national near infrared spectral library in tandem with learning machine. Science of the Total Environment. 658, 895-900.

[15] Zhang, Z., Zhang, Y., Ying, L., Sun, C. and Zhang, H.F. (2019). Machine-learning based spectral classification for spectroscopic single-molecule localization microscopy. Optics Letters. 44(23), 5864.

[16] Daniel, K.W., Tripathi, N.K., Honda, K. and Apisit, E. (2004). Analysis of vnir (400-1100 nm) spectral signatures for estimation of soil organic matter in tropical soils of Thailand. International Journal of Remote Sensing. 25(3), 643-652.

[17] Tian, Y., Zhang, J., Yao, X., Cao, W. and Zhu, Y. (2013). Laboratory assessment of three quantitative methods for estimating the organic matter content of soils in china based on visible/near-infrared reflectance spectra. Geoderma. 202, 161-170.

[18] Zeng, R., Zhao, Y.G., Li, D.C., Wu, D.W., Wei, C.L. and Zhang, G.L. (2016). Selection of "local" models for prediction of soil organic matter using a regional soil vis-nir spectral library. Soil Science. 181(1), 13-19.

[19] Palaniappan, R., Paramesran, R. (2003). Using genetic algorithm to identify the discriminatory subset of multi-channel spectral bands for visual response. Applied Soft Computing Journal. 2(1), 48-60.

[20] Shi, T., Chen, Y., Liu, H., Wang, J. and Wu, G. (2014). Soil organic carbon content estimation with laboratory-based visible-near-infrared reflectance spectroscopy: feature selection. Applied Spectroscopy. 68(8), 831-837.

[21] Bao, Y., Meng, X., Ustin, S., Wang, X. and Tang, H. (2020). Vis-swir spectral prediction model for soil organic matter with different grouping strategies. Catena. 195, 104703.
[22] Kristie, W., Daniel, G. and Jennifer, R. (2018). Using bi-seasonal worldview-2 multi-spectral data and supervised random forest classification to map coastal plant communities in everglades national park. Sensors. 18(3), 829.

Received: **24.11.2021**
Accepted: **11.01.2022**

CORRESPONDING AUTHOR

Ni Wang
State Key Laboratory of Eco-hydraulics in Northwest Arid Region,
Xi'an University of Technology,
Xi'an 710048 – China

e-mail: wangni@xaut.edu.cn

© by PSP Volume 31– No. 05/2022 pages 4930-4938 Fresenius Environmental Bulletin

RESERVOIR CHARACTERISTICS AND ACCUMULATION ANALYSIS OF CHANG 7 MEMBER IN HESHUI BLOCK ORDOS BASIN

Yanlong Liu*

Department of Geology, Northwest University, Xi'an Shaanxi 710069, China

ABSTRACT

The Chang 7 member of the Heshui block in the Ordos Basin is the main oil-bearing formation discovered in recent years. In order to clarify the reservoir characteristics and main controlling factors in this area, the methods of casting thin section, scanning electron microscope, high pressure mercury intrusion, and reservoir physical properties are used to clarify the reservoir characteristics and main controlling factors in this area. The reservoir characteristics and main controlling factors of the Chang 7 member in the Heshui block are studied. Research shows that the rock types of Chang 7 Member are feldspar lithic sandstone and lithic feldspar sandstone, followed by feldspar sandstone and lithic sandstone. There are many types of reservoir interstitials. The main clay minerals are illite, chlorite, etc. and the cements include carbonate minerals, siliceous minerals, and occasionally sulfate minerals. The cuttings are mainly sedimentary rock cuttings and volcanic rock cuttings, with few metamorphic rock cuttings. The reservoir porosity of the Chang 7 Member in the Heshui block is about 3%-12%, with an average of about 8.2%, and the permeability is less than 0.3mD, indicating that this reservoir is a low-porosity and low-permeability reservoir. The pore types are mainly dissolved pores and intergranular pores. The throat radius is small, mainly sheet-like throats and pipe string throats. Sedimentation plays an innate control effect on the reservoir, and diagenesis such as early reservoir compaction, illite cementation, and carbonate cementation play a destructive effect on the reservoir. This article has a guiding role in the evaluation results of Chang 7_1 and Chang 7_2 reservoirs in the study area, which are the oil exploration of the Chang 7 member of the Triassic.

KEYWORDS:
Ordos Basin, reservoir characteristics, Yanchang Formation, oil and gas reservoirs

INTRODUCTION

With the increase in demand for oil and gas and the decline in conventional oil and gas production in various countries around the world, unconventional oil and gas have gradually received attention from various countries, and the increased research on unconventional reservoirs has promoted the progress of petroleum theory [1-3]. The Bakken Formation in the Williston Basin in North America is the most representative basin in the large-scale development of tight oil abroad [4-5]. The tight oil in the Yanchang Formation in the Ordos Basin and the Lucaogou Formation in the Junggar Basin are key areas for tight oil exploration in China [6-7]. According to current exploration discoveries, the bottom of the Chang 7 Member of the Ordos Basin mainly develops a set of thick and stable oil shale rich in organic matter. The middle and upper parts mainly develop dark mudstone, but the thickness is relatively small and the continuity is poor. Oil shale and dark mudstone are the oil source foundation of Chang 7 Member [8-11].

The current research on tight reservoirs mainly includes two aspects: macroscopic characteristics (petrophysical characteristics and physical characteristics) and microscopic characteristics (mainly pore structure characteristics) [12-14]. The lithology of tight reservoirs is mainly two types of silt sandstone and carbonate rock, with low composition maturity and structural maturity. The depositional environment of tight oil development at home and abroad is different, which leads to the difference in the lithology of tight reservoirs. The Ordos Basin is a continental lacustrine basin [15-16]. The Yanchang Formation mainly develops tight sandstone reservoirs. The rock types mainly include lithic feldspar sandstone and feldspathic lithic sandstone, which have certain particularities.

Generally, the porosity and permeability of tight reservoirs are extremely low, the porosity is less than 12%, and the overburden matrix permeability is less than 0.1mD. For example, the porosity of the tight reservoirs of the Bakken Formation in North America is mainly distributed between 7% and 12%. The permeability varies greatly, mainly between 0.01mD and 10mD. The tight reservoirs of the Yan-

chang Formation in the Ordos Basin have lower porosity and permeability. The porosity is mainly distributed between 6% and 12%, and the permeability is mainly Less than 0.3mD, belonging to a typical tight sandstone reservoir. In the diagenesis process, after the tight sandstone reservoir undergoes strong mechanical compaction and cementation, the physical properties of the reservoir become poor and the heterogeneity is extremely strong [17-19]. Therefore, the pore structure is an important factor that determines the physical properties of the reservoir and the oil and gas productivity [20].

The main oil layers of the Yanchang Formation in the Heshui block of the Ordos Basin are Chang 6 and Chang 8. However, with the drilling of the Chang 7 Member to obtain industrial oil and gas resources, the research on Chang 7 has gradually gained attention. The Chang 7 reservoir has the basic conditions for the formation and development of tight sandstone reservoirs. The current exploration shows that the formation has a large amount of oil and gas resources and is a key formation for future exploration. In this paper, petrology, sedimentology, and other theoretical methods are used to analyze the reservoir characteristics of the Chang 7 member of the Heshui block, and to discuss the main factors that form the oil and gas resources, so as to provide a basis for the oil and gas exploration in the block.

MATERIALS AND METHODS

(1) Regional location. The study area is located in the southwest of the Yishaan Slope of the Ordos Basin. The regional tectonic background is a gentle west-dipping monoclinic, with locally developed nose-like structures and not developed faults. The geographical location starts from Qingcheng in the north, Ning County in the south, Luoshan Mansion in the east, and Qingyang in the west (Figure 1). Among them, there are abundant oil and gas resources in Qingcheng, Huanxian, Heshui, Huachi and other places. The sedimentary strata in the study area are relatively stable, and the Yanchang Formation is divided into 10 sets of oil layer groups. The focus of this study is the Chang 7 oil layer group.

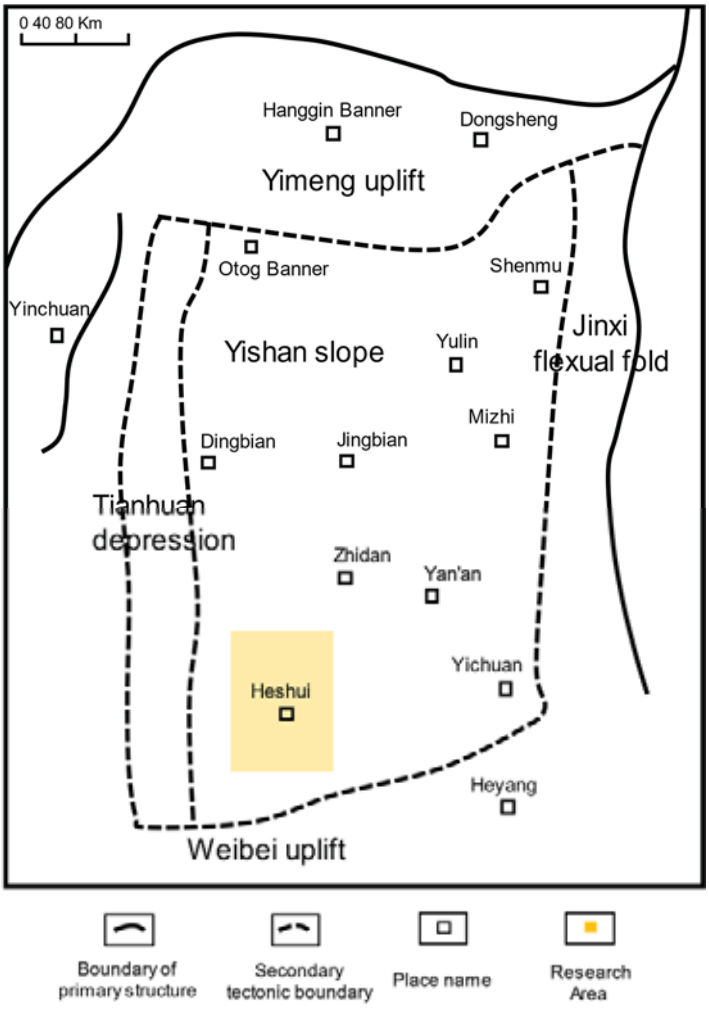

FIGURE 1
Regional location map of Heshui block.

(2) Experimental equipment and materials. Experimental instruments: X-ray diffractometer (RigakuD/Max-2500), ZHM-1B grinding machine (ZHM-1A), sample press (ZHY-501), rock porosity casting instrument (JS-4), Quattro ESEM scanning electron microscope (Thermo Scientific), full diameter core permeability tester (DYX-1), rock cutter (DQ1-4), automatic specific surface area and pore size distribution tester (MiniX), Zeiss Primotech polarizing microscope, core holder, etc. Auxiliary materials include emery, epoxy resin, curing agent, coloring agent, fir glue, etc.

Experimental materials: The samples in the test and analysis are all from the core drilling of the Chang 7-layer series in the study area. The lithology and thin slices to be tested are made according to the experimental method. The thin section production process first selects representative rock samples and washes the samples. During the production process, the vacuum state should be maintained, and the cast thin sections shall be cut and numbered. After rough grinding and fine grinding, the thickness is 0.03mm, and the label is used for identification.

RESULTS

(1) Petrology characteristics. The feldspar lithic sandstone and lithic feldspar sandstone of the Chang 7 member of the Heshui block account for 90%, and the feldspar sandstone and lithic sandstone account for 10%. Clay minerals mainly include illite and chlorite, carbonate minerals mainly include calcite, iron calcite, iron dolomite, iron-bearing minerals mainly include hematite, pyrite, and siliceous minerals include quartz, chalcedony. Analysis of a large number of rock slices shows that the quartz content is the highest, accounting for about 46.7% of the total composition, the average content of feldspar is about 26.5% of the total composition, and the content of cuttings is about 27.8% of the total composition (Figure 2).

Sedimentary rock debris content is relatively high in the debris component, with the highest average content accounting for 46.2% of the total debris composition. Metamorphic rock debris is the second, accounting for 39.3% of the total debris composition. Volcanic rock debris content is the lowest, accounting for about 14.5% of the total composition of cuttings. The volume fraction of interstitial material is about 18.1%, of which illite is about 9.98%, iron dolomite is about 2.39%, siliceous is about 1.23%, and iron calcite is about 1.89%. The sum of the metamorphic rock cuttings and sedimentary rock cuttings accounted for 85%, and volcanic rock debris accounts for about 15%.

The mudstone color of Chang 7 Member in the study area is mainly gray and dark, indicating that the sedimentary water body is deeper, reflecting that it was in a reducing environment when it was deposited. The grain size of sandstone is mostly fine grains, followed by medium grains and coarse grains, showing quiet hydrodynamic conditions. For sorting, etc., the roundness is mainly sub-circular-sub-angular. There are many types of sedimentary structures in the study area. In addition to bedding structures and layer erosion structures, there are also biological disturbance structures, wormholes, and gravity flow structures (Figure 3).

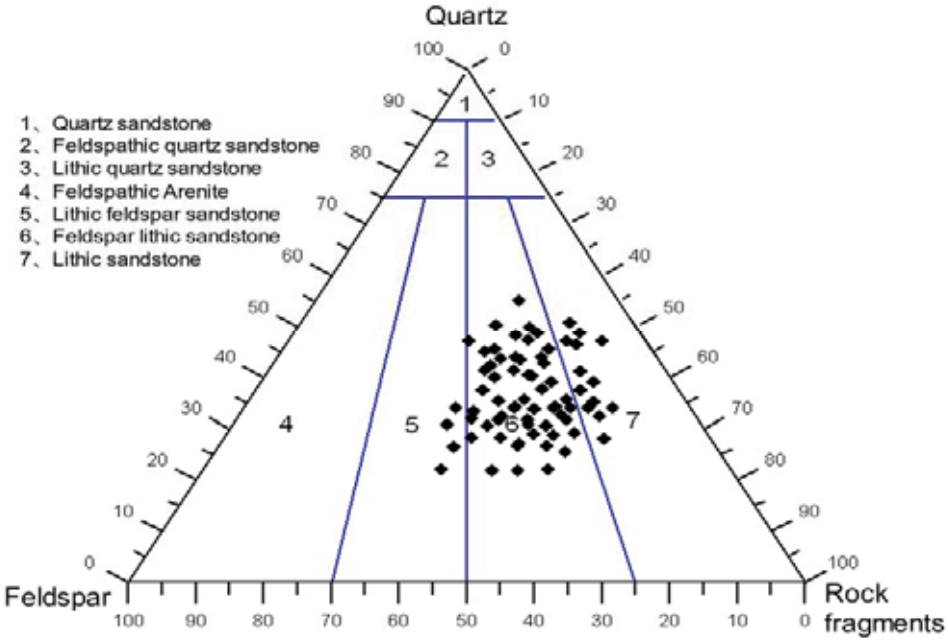

FIGURE 2
Triangle diagram of sandstone composition of Chang 7 Member in Heshui block.

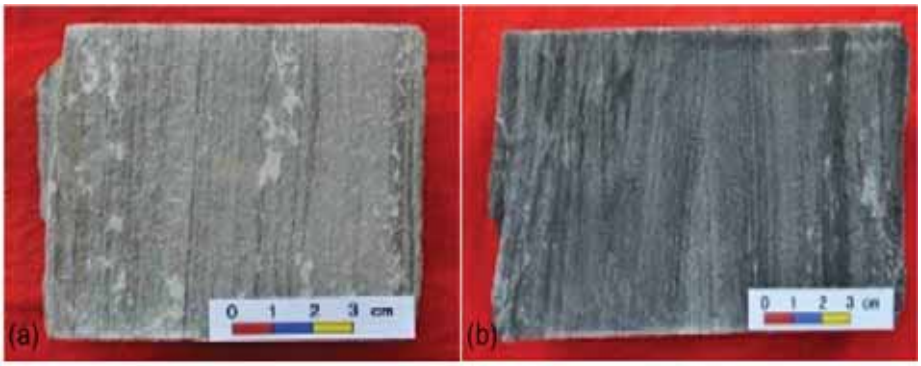

FIGURE 3
Core samples of Chang 7 Member in Heshui block (a, parallel bedding; b, plate-like cross bedding).

TABLE 1
The analysis statistics of the core physical properties of the Chang 7 member in the Heshui block

Member	Number of samples	Porosity (%)			Permeability(mD)		
		Minimum	Maximum	Mean	Minimum	Maximum	Mean
Chang 7_1	2682	0.26	16.78	9.65	0.01	20.72	0.24
Chang 7_2	1832	0.78	15.78	9.07	0.01	19.63	0.20
Chang 7_3	652	0.68	15.28	8.15	0.01	6.23	0.19

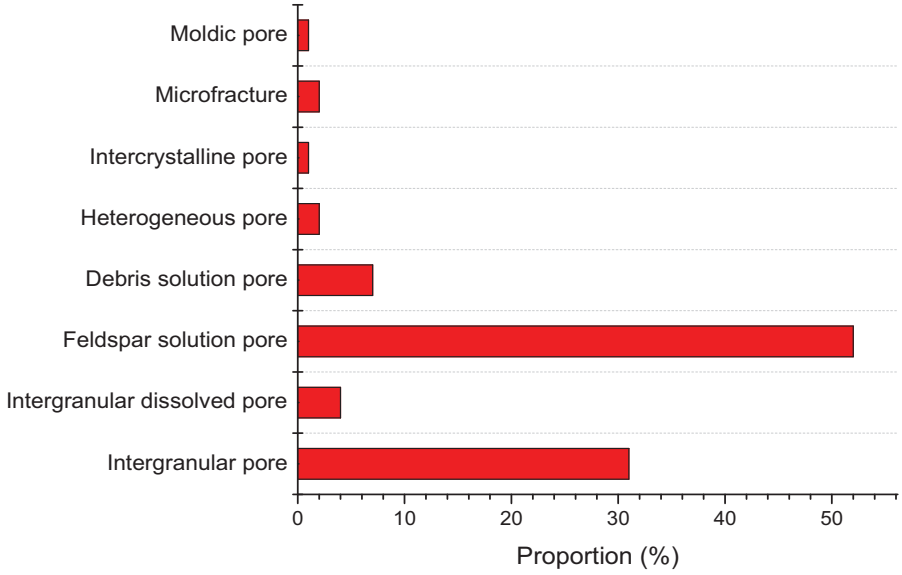

FIGURE 4
Statistics of the proportion of pore types in the Chang 7 member of the Heshui block.

(2) Reservoir physical properties and pore structure characteristics. 1) Reservoir physical characteristics. The reservoir porosity of the Chang 7 Member in the Heshui block of the Ordos Basin is about 0.26%-16.78%, with an average of about 8.2%. The permeability is lower than 0.3mD, with an average of about 0.11mD, of which the permeability of 63.7% samples is 1.0mD (Table 1). Through the analysis of the porosity and permeability of the three layers of the Chang 7 Member, it is believed that the entire Chang 7 Member is a low-porosity and low-permeability tight reservoir, in which the permeability shows the characteristics of Chang 7_1> Chang 7_2> Chang 7_3. The sedimentary environment of Chang 7_3 is dominated by semi-deep lake to deep lake, and the lithology is dominated by shale and oil shale, which is a set of source rocks. Chang 7_1 and Chang 7_2 develop multi-stage delta and gravity flow sandstone, and the physical properties of the reservoir are better.

2) Pore type. It can be seen from Figure 4 that the proportion of feldspar dissolved pores in the Chang 7 sandstone in the Heshui block of the Ordos Basin is the highest, followed by intergranular pores, lithic dissolved pores, intergranular dissolved pores, miscellaneous base dissolved pores, microcracks, miscellaneous base dissolved pores, and mold pores. The dissolved pores of feldspar include dissolved

pores in feldspar grains and dissolved pores between feldspar grains. The feldspar content in the study area is high, and feldspar generally develops cleavage, so dissolution pores in the inter-granular feldspar grains distributed along the joint and fracture surfaces are common. The intragranular dissolution is often accompanied by intergranular dissolution pores, with a certain degree of connectivity (Figure 5). Micro-fractures are usually formed due to tectonic movement. On the one hand, they are directly connected to the storage space, and on the other hand, they provide migration channels for atmospheric fresh water and acidic water, actively improving the storage space.

3) Pore structure. The mercury intrusion analysis results of the sandstone in the Chang 7 member of the Heshui Formation in the Ordos Basin show that the Chang 7_1 displacement pressure is 3.1628MPa, the median pressure is 12.68Mpa, and the median radius is 0.083μm. The Chang 7_2 displacement pressure is 3.0670Mpa, the median pressure 10.17Mpa, and the median radius 0.092μm. For Chang 7_3, the displacement pressure is 3.4509Mpa, the median pressure 13.13Mpa, and the median radius is 0.212μm. According to the pore structure classification and evaluation criteria of the reservoir, the pore structure of the Chang 7 member can be divided into four categories:

Type I pore structure: Mercury injection curve has obvious platform structure, good pore throat connectivity, sortability, roughness, drainage pressure>2.0Mpa, median radius>0.20μm, maximum tribute saturation> 90%, mercury removal efficiency> 35%, porosity> 12%, permeability> 0.50mD (Figure 6a).

Type II pore structure: Mercury injection curve has an obvious platform structure, relatively poor pore throat connectivity, equal-to-poor sorting, partial roughness, medium displacement pressure (2.0～3.0Mpa), median radius>0.05μm. The maximum mercury inlet saturation> 80%, the mercury removal efficiency> 30%, the porosity is 10% to 12%, and the permeability is 0.20 to 0.50mD (Figure 6b).

Type III pore structure: the mercury injection curve platform structure is not obvious, a small amount is developed in the study area, the pore throat connectivity, sorting property is poor, the fineness is high, the displacement pressure is high (3.0 ～ 4.0MPa), the median radius is <0.05μm, the maximum mercury saturation>40%, mercury removal efficiency>30%, porosity 8%-10%, permeability 0.1-0.2mD (Figure 6c).

Type IV reservoirs are compact, with porosity <8%, permeability <0.1mD, drainage pressure>4.0Mpa, and median pressure>12Mpa, making it the worst reservoir in the study area (Figure 6d).

(3) Main controlling factors of reservoir. 1) Sedimentation. Sedimentary facies determine the macroscopic spatial distribution and vertical lithological combination characteristics of reservoir sand bodies. Sedimentary microfacies from different provenances exhibit different rock types, grain structures and combinations, which in turn affect the type of reservoir diagenesis. Turbidite fans developed in the Chang 7 Member of the study area, mainly developed three types of sedimentary microfacies between the turbidite water channel, the front edge of the turbidite water channel, and the turbidite water channel. The coarser particles are deposited in the turbidite channel, the relatively fine particles are deposited in the front edge of the turbidite channel, and the finest particles are deposited in the turbidite channel. The statistical results of the physical properties of different sedimentary microfacies in the study area show that the physical properties of turbidite channel sedimentary microfacies reservoirs (the average porosity is 10.62%, the average permeability is 0.24mD)> sedimentary microfacies at the front edge of turbidite channel (the average porosity is 9.36%, the average permeability is 0.2mD)> the sedimentary microfacies between the turbidite channels (the average porosity is 8.19%, the average permeability is 0.08mD), so sedimentation has an important control on the reservoir(Table 2).

TABLE 2
Statistical comparison of physical properties of different sedimentary microfacies reservoirs in the Chang 7 member of the Heshui block

Sedimentary microfacies	Lithology	Porosity			Permeability		
		Number of samples	Data range	Average	Number of samples	Data range	Average
Turbidite waterway	Fine sandstone	3321	3.28～34.62	10.62	3321	0.01～17.59	0.24
Turbidite channel front	Fine sandstone, silty mudstone, argillaceous siltstone	2315	1.83～28.73	9.36	2315	0.01～16.73	0.2
Turbidite waterway in between	Argillaceous siltstone, silty mudstone	2389	1.63～25.31	8.19	2389	0.003～15.28	0.08

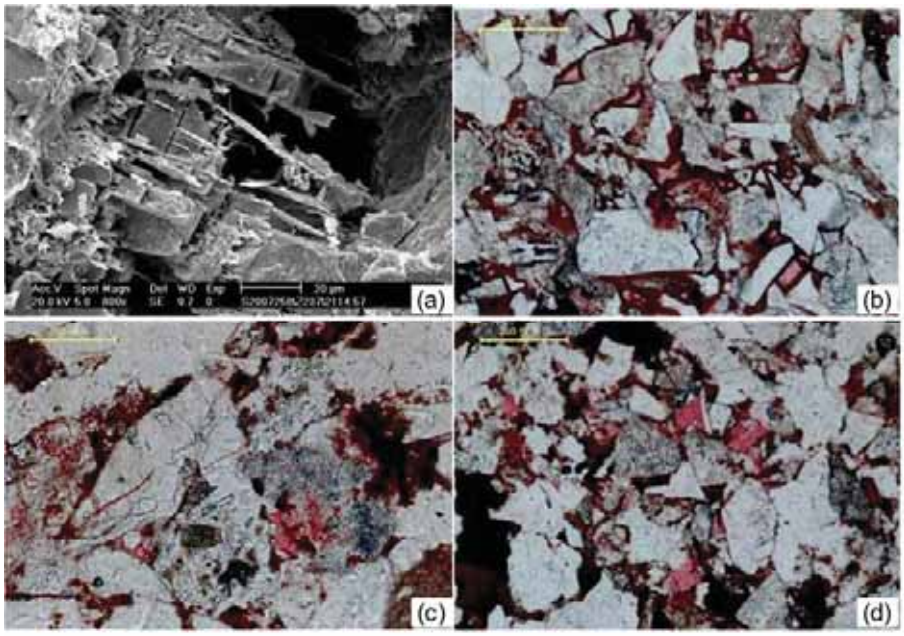

FIGURE 5
Pore microstructure of Chang 7 member in Heshui block (a, feldspar intragranular dissolved pores, 2124.75m; b, residual intergranular pores, 2018.65m; c, diagenetic fractures and dissolved pores, 2014.5m; d, intergranular dissolved pores, 1632.30m).

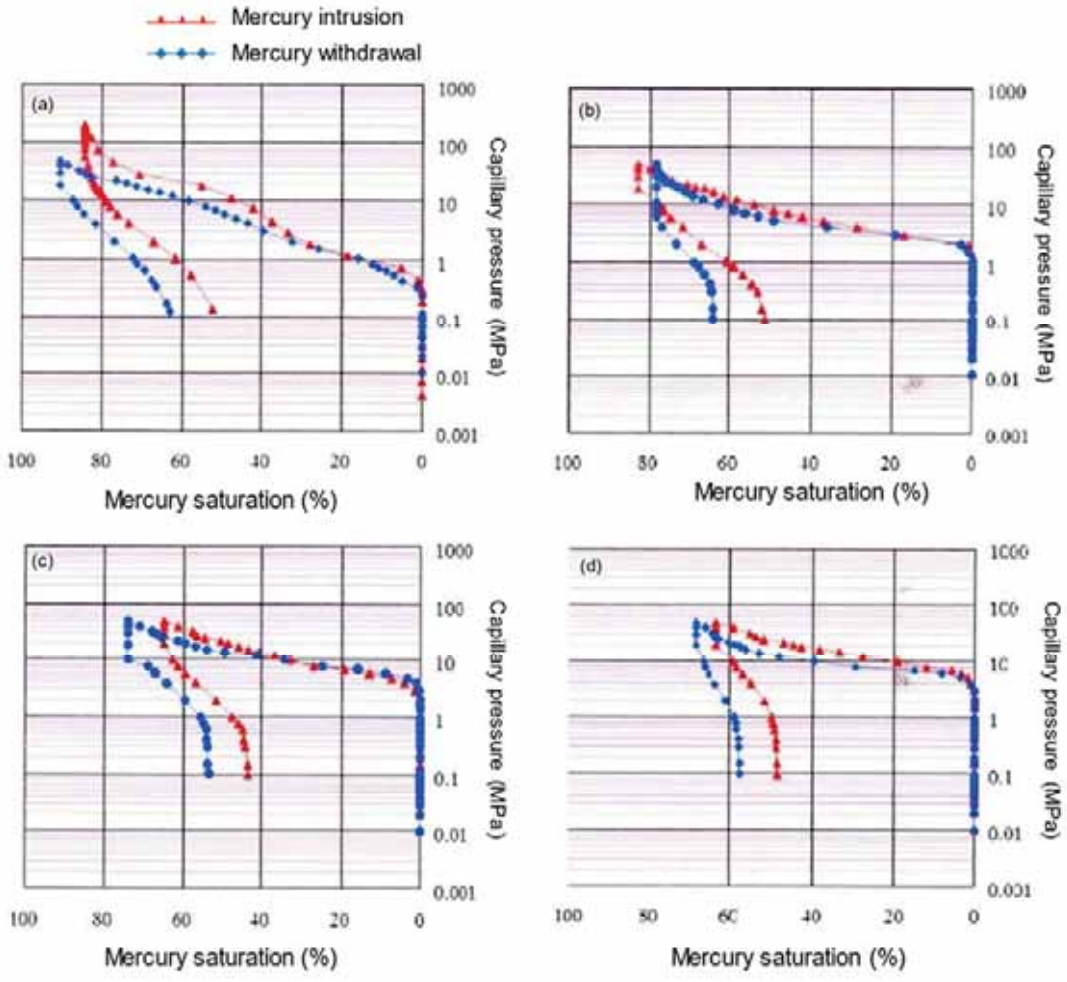

FIGURE 6
The mercury injection curve of the capillary curve of the Chang 7 segment in the Heshui block.

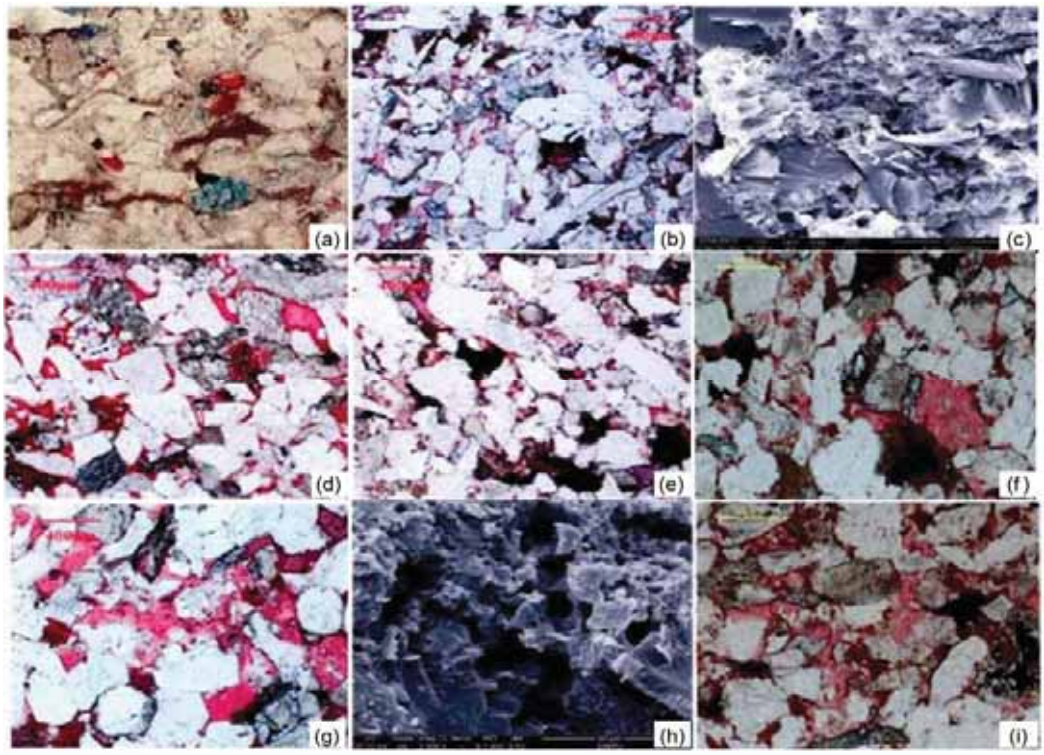

FIGURE 7

The microstructure of different types of diagenesis in the Chang 7 member of the Heshui block

(a, mica compaction deformation, Chang 7_1 section; b, directional distribution of clastics, Chang 7_1 section; c, illite cementation, Chang 7_1 section; d, chlorite cementation, Chang 7_1 section; e, secondary quartz, Chang 7_1 section; f, iron calcite cement, Chang 7_1 section; g, dissolved pore, Chang 7_1 section; h, feldspar dissolved pore, Chang 7_2 section; i, chlorite cement, Chang 7_2 section).

2) Diagenesis. Diagenesis has a great influence on physical properties during the formation of a reservoir. Therefore, a clear understanding of the diagenetic experience and pore evolution characteristics of the reservoir is conducive to clarifying the formation mechanism of its reservoir space and can provide theoretical guidance for favorable reservoir prediction bodies. There are many types of diagenesis in the Chang 7 Member of Heshui in the Ordos Basin, mainly including compaction, cementation and dissolution.

The compaction developed in the early Chang 7 member. The rock types in the study area are dominated by feldspar lithic sandstone and lithic feldspar sandstone, which are rich in various types of debris such as metamorphic rocks and volcanic rocks. Since the plastic particle component in the debris component has weak compaction resistance, it is prone to bending, torsion, deformation, and directional arrangement. The original pore loss during the compaction process is relatively large, and the early mechanical compaction will reduce the original pore Up to 21%. The primary pores of sandstone are greatly reduced, which has a destructive effect on the reservoir. When the pressure on the particle contact point exceeds the pressure of the normal fluid, increasing the contact point or surface of the particles with the formation temperature will cause the candle to dissolve, which will make the contact point of the particles closer, having a certain destructive effect on the reservoir space and seepage capacity.

Cementation is a major role in the transformation of sediments into sedimentary rocks. The main types of cementation in the Chang 7 Member of Heshui are siliceous cementation, carbonate cementation, and clay mineral cementation, which all have a destructive effect on the reservoir. The SiO_2 in the siliceous cementation mainly comes from the transformation of clay minerals and the dissolution of carbonate rocks. The siliceous cement is mainly composed of secondary enlarged cementation and pore-filled cementation. Carbonate cements are mainly dolomite, iron dolomite, and iron calcite cements. Calcite is divided into two stages and the late calcite is more common than early calcite. The cementation of clay minerals is mainly illite and chlorite. Observed under scanning electron microscope, it is found that the illite cement is hair-like and lamella-like and is distributed between the intergranular pores in the form of pores and bridges. Chlorite cements are produced in two forms in the reservoir. One type of chlorite is filled in the pores of the reservoir in the form of interstitials to reduce the storage space of the reservoir and the other type of chlorite is cemented on the surface of detrital particles. The second type of chlorite cement is more common in the study area.

The Heshui block has a strong dissolution effect, which is of great significance to improve the storage performance and seepage capacity of the reservoir. It is common that the dissolution of feldspar, cuttings and other particles produces intragranular dissolved pores, or the dissolution of intergranular filling clay and carbonate minerals produces intergranular dissolved pores and interstitial dissolved pores, which greatly improves the physical properties of the reservoir and is of great significance to the formation of relatively high porosity and high permeability reservoirs in the study area. The microscopic analysis of the cast thin section shows that the higher the dissolved porosity, the better the physical properties. Observed under the scanning electron microscope, the candle dissolution often occurs at the long right cleavage seam or cracked seam, forming intra-granular honeycomb-shaped dissolved pores or mold pores. A large number of dissolved pores between the grains developed after the dissolution between the grains and the physical properties of the reservoir are relatively good (Figure 7).

3) Tectonic influence. The study area is structurally stable, and no large-scale tectonic movement has occurred, but diagenesis and local small tectonic movements have caused many micro-fractures in the study area. In low-permeability sandstone reservoirs, fractures not only serve as oil and gas storage spaces, but also increase the seepage capacity of the reservoir, resulting in heterogeneity of reservoir physical properties. In the Heshui block, where the fractures develop, the permeability is higher than that of the matrix pores. The core observation shows that the porosity and permeability values at the depth of 1437.5m～1444.5m are low, the porosity is less than 5%, and the permeability is less than 0.01mD. However, the core permeability at a depth of 1438.4 m where fractures are developed is obviously higher, at 0.12 mD, which is significantly higher than that at the point where there are no fractures. Micro-fractures improve the pore throat system of tight reservoirs, increase the matrix permeability of the reservoir, and have an important impact on the physical properties of the reservoir.

The above research shows that sedimentation, diagenesis, and tectonics have an important control effect on the reservoirs in the study area. Deep pool flow deposits are widely developed in the Heshui block, and the sediment particles are relatively fine. Due to the strong compaction and pressure solution in the later stage, and the complex cementation, the reservoirs in the study area are dense. The lower the interstitial content in the original sediments, the higher the quartz content, the better the sortability, the stronger the candle dissolution and the more developed fractures, which is easier to form a relatively high-porosity and high-permeability reservoir. Therefore, the content of interstitial materials, the content of quartz, the sorting property, the dissolution candle effect and the development of fractures have an important control effect on the development of the relatively high porosity and high permeability reservoirs in the study area.

CONCLUSIONS

(1) The rock types in the study area are mainly feldspar lithic sandstone and lithic feldspar sandstone, and the interstitial materials are mainly illite, carbonate cement and siliceous. The reservoir porosity of the Chang 7 Member is about 3% to 12%, with an average of about 8.2%, and the permeability is less than 0.3 mD, with an average of about 0.11 mD. The entire Chang 7 Member is a tight reservoir with low porosity and low permeability.

(2) Sedimentation in the study area has an innate control effect on the reservoir. Diagenesis includes compaction, dissolution, and cementation, among which dissolution is widespread in the study area. The lower the interstitial content, the higher the chlorite film content, the stronger the dissolution, and the better the physical properties of the reservoir with more developed fractures.

(3) The detrital particles of the interval with good oil content are coarser, the dissolution is strong, the pores are more developed, the sorting ability is better, and the reservoir physical properties are better. Reservoir physical properties have an important impact on the oil-bearing properties of the reservoir and restrict the degree of hydrocarbon enrichment.

ACKNOWLEDGEMENTS

This work was not supported by any funds. The authors would like to show sincere thanks to those techniques who have contributed to this research.

REFERENCES

[1] Yang, Z., Zou, C., Wu, S., Tao, S., Yuan, X. (2015) Characteristics of nano-sized pore-throat in unconventional tight reservoir rocks and its scientific value. Journal of Shenzhen University Science and Engineering. 32(3), 257-265.

[2] Burtman, V., Fu, H., Zhdanov, M.S. (2014) Experimental study of induced polarization effect in unconventional reservoir rocks. Geomaterials. 4(4), 117-128.

[3] Li, Q., Xing, H., Liu, J., Liu, X. (2015) A review on hydraulic fracturing of unconventional reservoir. Petroleum. 1(1), 8-15.

[4] Chen, Z., Osadetz, K.G., Jiang, C., Li, M. (2009) Spatial variation of Bakken or lodgepole oils in the Canadian Williston Basin. AAPG Bulletin. 93(6), 829-851.

[5] Tao, L., Chang, Y., Guo, X., Liu, B., Jian, W.U. (2013) Influence factors of single well's productivity in the Bakken tight oil reservoir, Williston Basin. Petroleum Exploration & Development. 40(3), 383-388.
[6] Yao, J., Deng, X., Zhao, Y., Han, T., Chu, M., Pang, J. (2013) Characteristics of tight oil in Triassic Yanchang Formation, Ordos Basin. Petroleum Exploration & Development. 40(2), 161-169.
[7] Wei, B., Wei, H.H., Chen, Q.H., Zhao, H. (2003) Sediment provenance analysis of Yanchang Formation in Ordos Basin. Journal of Northwest University (Natural Science Edition). 33(4), 447-450.
[8] Guo, Y., Liu, J., Yang, H., Liu, Z., Zhang, Y. (2012) Hydrocarbon accumulation mechanism of low permeable tight lithologic oil fields in the Yanchang Formation, Ordos Basin, China. Petroleum Exploration & Development Online. 39(4), 447-456.
[9] Jian, Y., Yang, Y., Du, J. (2010) Sedimentation during the transgression period in Late Triassic Yanchang Formation, Ordos Basin. Petroleum Exploration & Development. 37(2), 181-187.
[10] Fu, J., Deng, X., Zhang, X. (2013) Relationship between deepwater sandstone and tight oil of the Triassic Yanchang Formation in Ordos Basin. Journal of Palaeogeography. 15(5), 624-634.
[11] Dou, W.T., Tian, J.C., Xu, X.R., Zhu, P., Deng, X.Q. (2005) Diagenetic facies study on Chang 6-8 oil formations of Triassic Yanchang Formation in Ordos Basin, China. Journal of Chengdu University of Technology (Science and Technology Edition). 32(2), 129-132.
[12] Shi, B., Fei, Z., Yan, Z., Jing, H., Lei, Z. (2014) Hydrocarbon accumulation conditions of Chang7 section, Yanchang Formation, Ordos Basin. Petroleum Geology & Experiment. 36(3), 285-290.
[13] Wen, H., Zheng, R., Chen, H., Fang, Y., Li, H. (2007) Characteristics of Chang 6 sandstone reservoir in Baibao-Huachi region of Ordos Basin. Acta Petrolei Sinica. 28(4), 46-51.
[14] Ma, X. (2005) Discussion on characteristics and reservoiring mechanism of deep basin gas in Upper Paleozoic in Ordos Basin. Oil & Gas Geology. 26(2), 230-236.
[15] Wang, D., Liao, Q.X., Wan, J.H., Wang, D., Chen, L.Z., Wang, M.C., Zhang, N. (2020) Study on microscopic reservoir characteristics and accumulation factors of tight oil reservoirs in Ordos Basin, China. Fresen. Environ. Bull. 29(4), 2475-2482.
[16] Zhang, T.J., Zhang, G., Zhang, L.S. (2020) Micropore structure characteristics of tight oil reservoirs in the Yanchang Formation in the Ordos Basin, China. Fresen. Environ. Bull. 29(4A), 3212-3222.
[17] Ma, L.J., Ma, L., Liu, T., Ha, J., Yu, Y. (2020) Source rock characteristics and hydrocarbon generation environment analysis of Chang 7 member in southeast area of Ordos Basin, China. Fresen. Environ. Bull. 29(12A), 11301-11310.
[18] Lyu, Q.Q., Luo, S.S., Xi, M.L. (2019) Classification scheme of lithofacies of fine grained sedimentary rocks in Chang 7 oil bearing formation, Ordos Basin, China. Fresen. Environ. Bull. 28(11), 8018-8030.
[19] Yang, J.M., Leng, F., Yu, H.S., Zhao, Y.P. (2021) Micro-pore structure characteristics of the Chang 6 member sandstone reservoir in Huangjiang Oilfield Ordos Basin China. Fresen. Environ. Bull. 30(5), 5377-5384.
[20] Wang, Z.Q., Liu, Q.Y., He, X., Zhang, C. (2021) Four-property relationship and determination of effective reservoir standard for the Chang 6 member of Huanjiang Oilfield in Ordos Basin, China. Fresen. Environ. Bull. 30(4), 3846-3854.

Received: **25.11.2021**
Accepted: **11.01.2022**

CORRESPONDING AUTHOR

Yanlong Liu
Department of Geology,
Northwest University,
Xi'an Shaanxi 710069 – China

e-mail: dongheng4466@126.com

© by PSP Volume 31– No. 05/2022 pages 4939-4950 Fresenius Environmental Bulletin

RESEARCH ON THE SPATIAL-TEMPORAL CHARACTERISTICS AND INFLUENCING FACTORS OF PM2.5 IN JIANGXI PROVINCE

Xiaoqiang Tu*, Chun Fu

School of Management, Nanchang University, Nanchang, Jiagnxi, 330031, China

ABSTRACT

At present, the research on PM2.5, the primary pollutant in smog, focuses on macro-scales such as urban agglomerations and economically developed provinces, but less on the financially underdeveloped regions in Mid-Eastern China. The research object of this paper is Jiangxi, an underdeveloped territory in Mid-Eastern China. By collecting PM2.5 concentration data from 2010 to 2015, this paper analyzed the temporal and seasonal variation of PM2.5 and studied spatial-temporal characteristics of PM2.5 by using spatial autocorrelation analysis, using the geographical detector models identified as the main influencing factors of PM2.5 concentration change. The results showed that: (1) the concentration of PM2.5 in Jiangxi province was the highest in winter and the worst pollution, followed by spring and autumn, and the best air quality in summer; (2) the spatial-temporal distribution of PM2.5 is quite different, the heavily polluted northwestern Jiangxi and the better air quality southern Jiangxi show a significant "diagonal" delivery, but the middle zone is not substantial; (3) Natural factors' temperature and socioeconomic factors' GDP are the leading factors that cause the PM2.5 concentration to change, and the interaction between the factors has greatly affected PM2.5 concentration changes.

KEYWORDS:
PM2.5, spatial-temporal, geographic detector, Jiangxi

INTRODUCTION

Delicate Particulate matter in the atmosphere, including PM2.5(Particulate matter with aerodynemic diameter ≤2.5μm)particle size small, area is large, vigorous activity, the long residence time in the air, attached with toxic and harmful substances [1], which has a significant impact on air quality and human health, causing great attention of the public and the scientific community. Some scholars have studied PM2.5 since the 1990s; the United States established the relevant standard: National Ambient Air Quality Standards (NAAQS) for PM2.5 in 1997, which was later incorporated into the international standards. In 2006, the World Health Organization (WHO) issued the "Air Quality Guidelines" (AQG) and determined the standard value of PM2.5 [2].In 2012, China issued the "Ambient Air Quality Standards" (GB3095-2012) and set the limit standard of PM2.5 [3]. At the same time, many scholars have conducted in-depth studies from different perspectives. Focusing on chemical composition and source analysis [4], spatial and temporal characteristics [5] [6], driving factors [7] [8], spatial differentiation [9] [10], estimation and prediction [11], pollution prevention and control [12] [13]. In terms of research methods, there are autocorrelation analysis, regression analysis, Grey Relation Analysis (GRA), etc., which seldom reveal the influence of spatial differentiation and interaction between variables on the change of PM2.5. In terms of research scale,macroscales such as the whole country, the Yangtze River Delta, the Pearl River Delta, and Beijing-Tianjin-Hebei regions, the mesoscale focus on economically developed or heavily polluted provinces, for example, Beijing, Chongqing, Guangdong, and Zhengzhou have rarely researched on the underdeveloped areas of Mid-Eastern China, especially in 2013, severe smog weather hit the Mid-Eastern regions of China[14]. Air pollution research is even more necessary.

This paper takes Jiangxi Province in China as a research area. It used a spatial autocorrelation method to explore the Spatio-temporal pattern of PM2.5 concentration changes in Jiangxi Province. It used the geographic detectors model for diagnosing the dominant factors that affect PM2.5 concentration changes in natural and socioeconomic factors. Explores natural factors interactions with socioeconomic factors that have a profound effect on PM2.5 concentration changes. The research results can provide scientific decision-making suggestions for the improvement of local atmospheric environmental quality.

STUDY AREA

Jiangxi (Figure 1), referred to as "Gan" for short, is located in the southeast of China, economic

division belongs to the central region. It is the central hinterland of the Yangtze River Belt Economic Zone, the Pearl River Delta Economic Zone, and the West Coast Economic Zone. It has jurisdiction over eleven prefecture-level cities including Nanchang, Jiujiang, Jingdezhen, Shangrao, Yingtan, Yichun, Xinyu, Pingxiang, Fuzhou, Ji'an, Ganzhou. In recent years, Jiangxi has adhered to the concept of innovation and green development, and the three industrial structures have been adjusted from 9.2: 48.1: 42.7 to 8.6: 46.6: 44.8.

MATERIALS AND METHODS

Data Sources. The PM2.5 concentration raster data comes from the global atmospheric Data published by the Atmospheric Composition Analysis Group of the Dalhousie University—China Regional Data (Http://fizz.phys.dal.ca/~atmos/martin/ ? page_id = 140), the collection period is from 2010 to 2015, which used to analyze the long-term sequence analysis of PM2.5 concentration and the study of influencing factors. To diagnose the influence of natural elements and socioeconomic factors on the dominant factors of PM2.5 concentration changes and the effects of interactions between factors on PM2.5 concentration changes, based on the complete collection of data in 2015, the natural elements and socioeconomic factors collected in this paper the deadline is 2015. Natural factor data includes elevation, precipitation, temperature, geography, vegetation raster data. Socioeconomic factors such as GDP, population density raster data from the Data Center of the Institute of Geographic Sciences and Resources and Environment of the Chinese Academy of Sciences (Http: // www.resdc.cn/), other socioeconomic factors such as the secondary industry value and the number of industrial enterprises are derived from the "2015 Statistical Yearbook of Jiangxi Province" and performed spatial interpolation into raster data by ArcGIS software. Based on the data collected above, constructed a 3km*3km raster by ArcGIS to extract the grid data of each impact factor and PM2.5 concentration grid.

No PM2.5 concentration seasonal data available from the PM2.5 concentration grid; this study uses monthly statistical historical data from the China Air Quality Online Monitoring and Analysis Platform (https://www.aqistudy.cn/historydata/). The period time is December 2014. Month-November 2017, according to the local weather conditions, the spring, summer, autumn, and winter seasons are March to May, June to August, September to November, and December to February. Revealed the seasonal variation of PM2.5 concentration in Jiangxi with the average annual level.

Methodology. This article mainly studies the spatiotemporal characteristics of PM2.5 concentration changes, diagnoses the dominant factors that affect PM2.5 concentration changes, and the influence of various factors on the PM2.5 concentration changes.

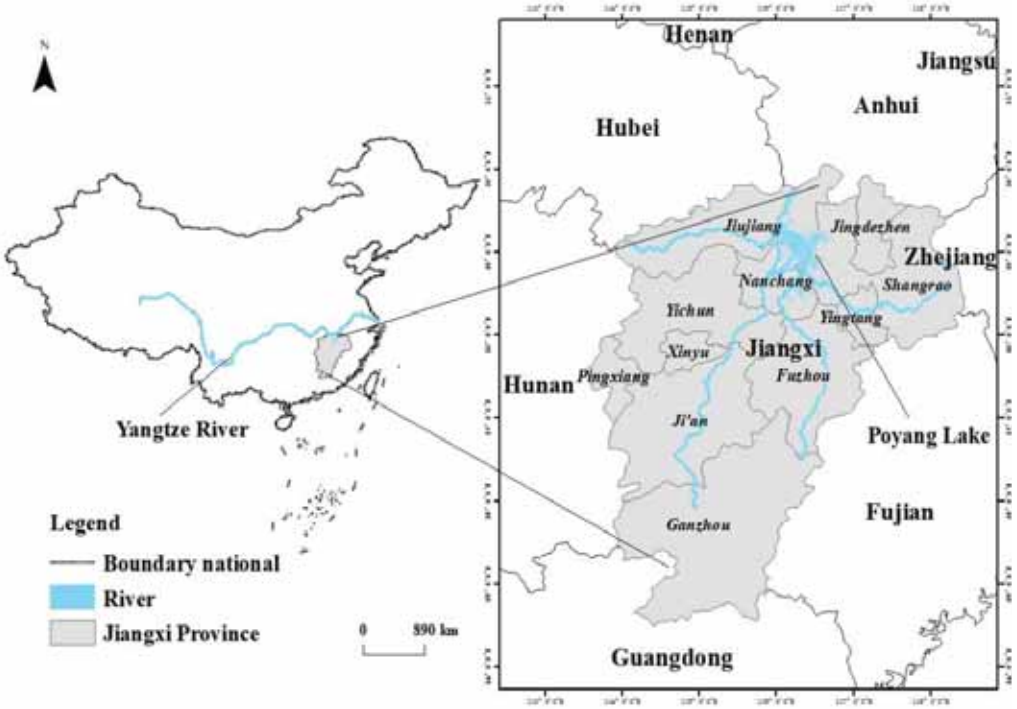

FIGURE 1
Geographic location of Jiangxi Province and 11 cities3.Materials and Methods

TABLE 1
Detection of interaction

Interaction	Result
$q(X_1 \cap X_2) < Min(q(X_1), q(X_2))$	Non-linear attenuation
$Min(q(X_1), q(X_2)) < q(X_1 \cap X_2) < Max(q(X_1), q(X_2))$	Single factor non-linear attenuation
$q(X_1 \cap X_2) > Max(q(X_1), q(X_2))$	Two-factor enhancement
$q(X_1 \cap X_2) = q(X_1) + q(X_2)$	independence
$q(X_1 \cap X_2) > q(X_1) + q(X_2)$	Non-linear enhancement

q(X1), q(X2) are the q values of the influence of factors X1 and X2 on Y, respectively. Max (q (X1), q (X2)) means to take the maximum value, Min(q (X1), q (X2))means to take the minimum, q (X1) + q (X2) means the sum of the q value of two factors, q(X1∩X2) means the interaction effect of factors X1 and X2

(1) Spatial evolution analysis of PM2.5 concentration. The first law of geography shows that geographical things or attributes are related to each other in spatial distribution. There are clustered, random, and regular distributions, and the closer the distance, the higher the correlation [15]. PM2.5 quickly moves with the atmosphere and spreads, causing pollution in related adjacent areas, spatial autocorrelation analysis characterizes the spatial linkage of PM2.5 between cities in Jiangxi. Spatial autocorrelation analysis includes global spatial autocorrelation analysis and local autocorrelation analysis. Global autocorrelation analysis refers to the spatial distribution of the same attribute value in the overall range of a specific area and commonly used the index Moran'I measure. The calculation formula is Eq 1:

$$I = \frac{\sum_{i=1}^{n}\sum_{j=1}^{n} W_{ij}(x_i - \bar{x})(x_j - \bar{x})}{S\sum_{i=1}^{n}\sum_{j=1}^{n} W_{ij}}. \quad \text{(Eq 1)}$$

$$S = \frac{1}{n}\sum_{i=1}^{n}(x_i - \bar{x})^2. \quad \text{(Eq 2)}$$

Where n is the number of spatial units in the study area, x_i and x_j are the attribute values of the i and j regions, W_{ij} is the spatial weight of the pixel; the range of value of *Moran ' I* is [-1,1]. When I>0, usually indicates spatial autocorrelation is positive, the closer the value is 1, the stronger the spatial autocorrelation. When I<0, typically shows the spatial autocorrelation is negative in the observations, the smaller the I value, the weaker the spatial autocorrelation. When I=0, regional spatial distribution is random. In other words, there is no spatial dependence between variables.

Local spatial autocorrelation describes the spatial correlation between an individual spatial unit and other adjacent spatial units in the study area, expressed using local *Moran'I*. The calculation formula is Eq 3:

$$I_i = \frac{1}{S^2}\sum_{i=1}^{n}\sum_{j=1}^{n} W_{ij}(x_i - \bar{x})(x_j - \bar{x})... \quad \text{(Eq 3)}$$

Where S is the same as Equation (2), other parameters have the same meaning as Equation (1) and (2). Four types of Spatial cluster include: Hight-Hight clusters (means that areas with the high value of PM2.5 concentration cluster each other); Low-Low cluster (implies that regions with the low amount of PM2.5 concentration cluster each other); Low-Hight cluster (means those cluster areas with the low value of PM2.5 concentration with high concentration); Hight-Low cluster (means those cluster areas with the high value of PM2.5 concentration with low concentration)

(2) Analysis of driving factors of PM2.5 concentration. Due to the existence of stratified spatial heterogeneity, an explanatory variable has an essential influence on the response variable, and the spatial distribution of the explanatory variable and the response variable are similar or consistent. The study uses the geographic detector model [16] to reveal the driving mechanism of PM2.5 concentration change and the degree of influence of various factors interaction on PM2.5 concentration change. There are four detectors in the geography detector.

The factor detector detects the degree to which the explanatory variables (selected natural factors and socioeconomic factors) explain the change in PM2.5 concentration, measured by q value. The calculation formula is Eq 4:

$$q = 1 - \frac{\sum_{h=1}^{L} N_h \sigma_h^2}{N\sigma^2} \quad \text{(Eq 4)}$$

In Equation, L is the stratification of factor X, that is, classification or partition, N_h and N are the number of units in layer h and the entire region, σ_h^2 and σ^2 are the variances of layer h and the entire region Y, q is the explanatory power, its value range is [0,1], the larger the value, the stronger the explanatory power of factor X to Y , which is the dominant factor.

The interaction detector explained whether the evaluation factors X_1 and X_2 will work together to enhance or weaken the explanatory power of the single evaluation factor to the dependent variable, or whether the impact of the evaluation factor on the dependent variable is independent of each other. The two factors (X_1 and X_2) interact in the following categories (Table 1).

RESULTS

Regularity of Time Change. Regularity of Pm2.5 Concentration. From the PM2.5 raster data, the mean value of PM2.5 concentration of each city was extracted by year to obtain the mean value of PM2.5 concentration of Jiangxi province and its cities from 2010 to 2015(Figure 2). Generally speaking, the mean value of PM2.5 concentration in Jiangxi showed a trend of fluctuation and decline, from 40.32μg/m³ (mean value of PM2.5 concentration by year) in 2010 to the lowest 35.64μg/m³ in 2015, which may be related to the strict implementation of the air pollution prevention and control action plan in Jiangxi province. During 2010-2015, the mean value of PM2.5 concentration by year in 2012 (37.74μg/m³) was higher than that in 2011 (36.85μg/m³), in 2013 (37.74μg/m³) was the same as in 2012 (37.74μg/m³), but reached the highest in 2014 (42.30μg/m³). Referring to the mean annual limit of PM2.5 concentration (35.00μg/m³) in the World Health Organization (WHO) and China's "Ambient Air Quality Standards" (GB3095-2012), the mean annual limit of PM2.5 concentration in 2010-2015 was all higher than the mean annual limit. Still, as mentioned above, the overall trend of decline was shown, the annual mean of PM2.5 concentration in Jiangxi province was close to the mean annual limit in 2015(35.64μg/m³).

From the perspective of various cities in Jiangxi Province, the annual mean PM2.5 concentration of overall trend has declined and fluctuated. All 11 cities in Jiangxi fell to its lowest point in 2015, from the broken line in Figure 2. Pingxiang City, Jiujiang City, Nanchang City, and Jingdezhen City have significant fluctuations, and their annual mean highest and lowest PM2.5 concentration, in turn, is 47.70μg/m³(in 2011) ~ 37.87μg/m³ (in 2015), 46.89μg/m³ (in 2014) to 39.05μg/m³(in 2012), 47.49μg/m³(in 2014) to 38.00μg/m³(in 2011), 42.91μg/m³(in 2014) to 32.52μg/m³(in 2012). It is also the four cities with a high PM2.5 concentration and severe pollution throughout the year, the mean PM2.5 concentration in the six years (from 2010 to 2015) were 44.09μg/m³, 42.76μg/m³, 41.33μg/m³ and 37.13μg/m³, respectively, which were all higher than the mean annual limit. From the broken line in Figure 2, it can be seen that Ganzhou City, Shangrao City, Fuzhou City, Yingtan City, Ji'an City have relatively stable fluctuation, and their annual mean highest and lowest PM2.5 concentration, in turn, is 30.27μg/m³(in 2014) ~ 26.02μg/m³(in 2015), 40.71μg/m³(in 2014) to 34.11μg/m³(in 2011), 35.44μg/m³(in 2014) to 30.10μg/m³(in 2015), 41.40μg/m³(in 2014) to 35.72μg/m³(in 2012), 39.05μg/m³(in 2014) to 33.38μg/m³ (in 2015). According to the GB3095-2012 average limit standard, only Ganzhou City and Fuzhou City reached the standard, accounting for 18.18%, and the proportion of non-compliance was as high as 81.81%, the Ganzhou City of the annual average value of PM2.5 concentration is lower than the annual average limit (35.00μg/m³).

Seasonal Variation of Pm2.5 Concentration. Unable to obtain the PM2.5 data from the PM2.5 concentration raster data, this paper uses monthly statistical historical data from the China Air Quality Online Monitoring and Analysis Platform (https://www.aqistudy.cn/historydata/), the data period is From December 2014 to November 2017. According to the classification of local meteorological conditions, the four seasons of spring, summer, autumn, and winter are March to May, June to August, September to November, and December to February of the following year, respectively. Calculate the average PM2.5 concentration in the four seasons to reveal the seasonal variation of PM2.5 in Jiangxi Province. The results show that (Figure 3), the change of PM2.5 concentration in Jiangxi shows a significant seasonal pattern and spatial characteristics: PM2.5 concentration value is highest in winter, pollution is the worst, spring and autumn are the second. Air quality in summer is the best. The most serious pollution in winter is Pingxiang City, Jiujiang City, Yichun City, and Nanchang City, the annual mean of PM2.5 concentrations are 82.89μg/m³(in Pingxiang City), 67.00μg/m³(in Jiujiang City), 65.44μg/m³(in Yichun City), and 62.89μg/m³(in Nanchang City), the pollution levels in spring (mean 41.27μg/m³) and autumn (mean 42.76μg/m³) decreased significantly. However, the average concentration is still more significant than the annual average limit (35.00μg/m³), In summer, the PM2.5 concentration value in Jiangxi province generally falls within the range of the annual average limit, especially in Yingtan City (mean 23.67μg/m³) and Nanchang City (23.44μg/m³) is best.

Analysis of Spatial Agglomeration Characteristics. GeoDa was used to perform spatial autocorrelation tests on the annual mean values of PM2.5 concentrations in Jiangxi from 2010 to 2015 (Table 2). The autocorrelation Z-value test shows that the spatial distribution of PM2.5 concentration in Jiangxi from 2010 to 2015 with significant spatial clustering characteristics($p=0.001<0.05$), the PM2.5 concentration of cities in Jiangxi prefecture-level cities is affected by both themselves and neighboring

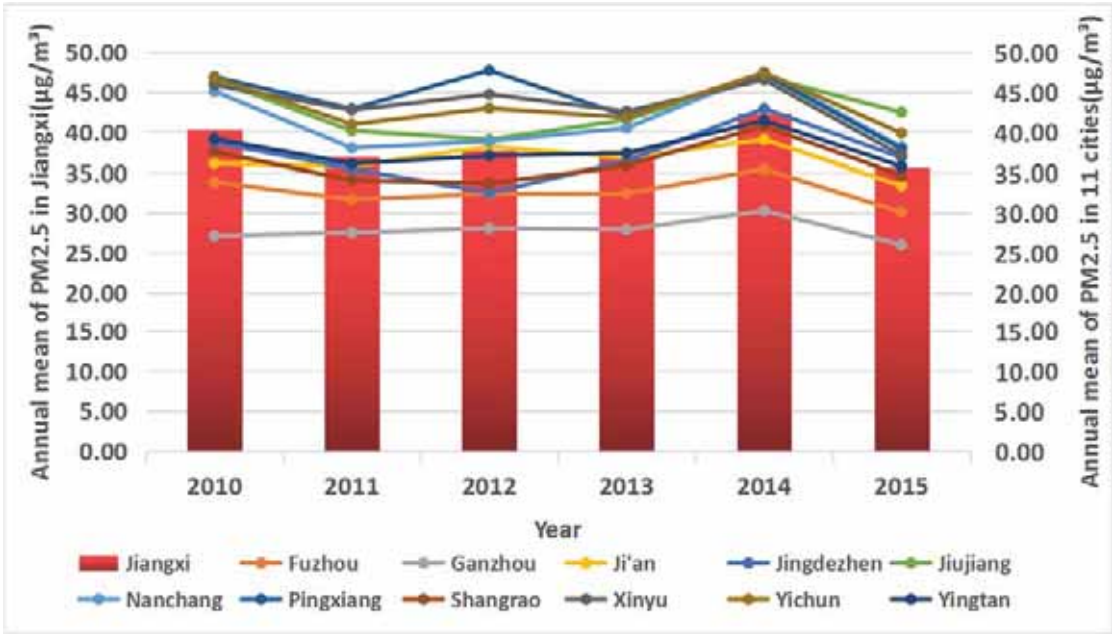

FIGURE 2
The Annual Mean of PM2.5 in Jiangxi Province and 11 Cities from 2010 to 2015

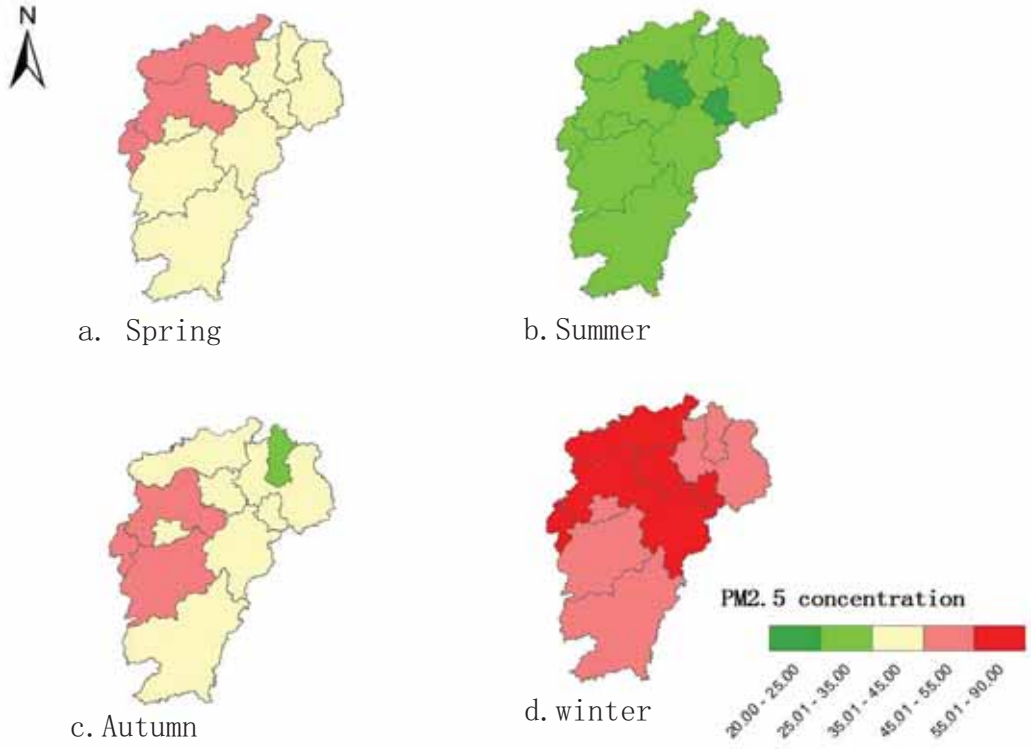

FIGURE 3
Seasonal variation of PM2.5 concentration in Jiangxi Province

TABLE 2
Autocorrelation test of PM2.5 concentration in Jiangxi from 2010 to 2015

Year	6-year mean	2010	2011	2012	2013	2014	2015
Moran's I	0.994***	0.995***	0.991***	0.992***	0.992***	0.994***	0.994***
p	0.001	0.001	0.001	0.001	0.001	0.001	0.001

***Passed 99% significance test

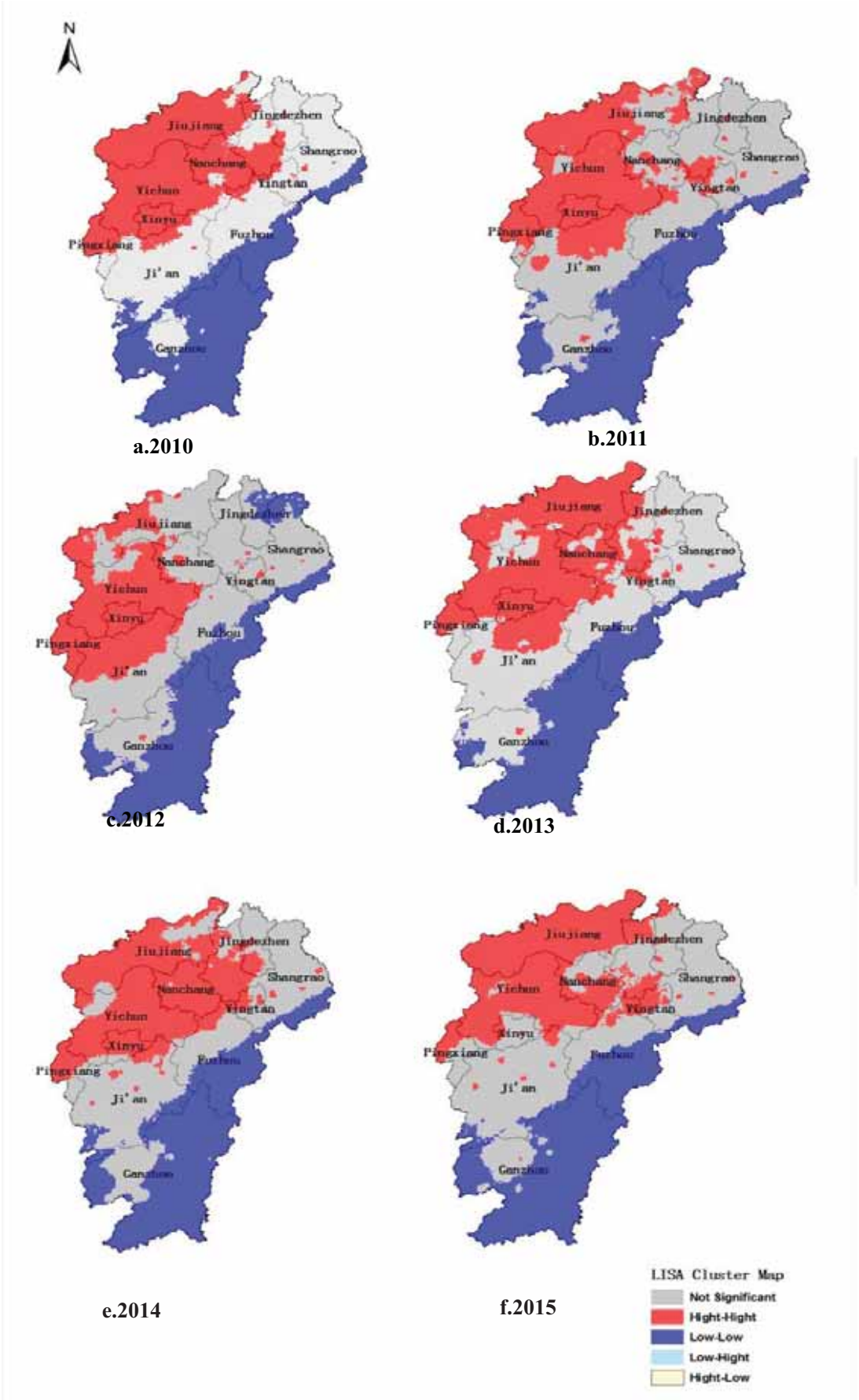

FIGURE 4
Cluster diagram of PM2.5 LISA in Jiangxi Province from 2010 to 2015

cities [17], and it shows a positive correlation distribution characteristic, that is, high-high or low-low clustering. Therefore, in PM2.5 governance requires concerted efforts.

To explore the more detailed spatial relationship between the research object and its neighbors, the k-nearest neighbor's method was used to construct a spatial weight matrix with a value of 6 to detect the spatial clustering area of PM2.5 in Jiangxi from 2010 to 2015, and draught the LISA (Local Indicators of Spatial Association) cluster diagram (Figure 4). The results show that the regional differences in PM2.5 concentration in Jiangxi from 2010 to 2015 are quite substantial. From figure 4, there is significant two-level differentiation between the heavily polluted areas and the areas with better air quality, which shows a "diagonal" distribution, and the middle zone is not significant. The areas with heavy PM2.5 pollution are mainly distributed in northwestern Jiangxi, while the areas with better air quality are mainly distributed in southeastern Jiangxi. At the same time, cities of PM2.5 concentration in northwestern Jiangxi have a high-high concentration spatial feature, and cities in southeast Jiangxi have a low-low, the aggregated spatial characteristics indicate that PM2.5 pollution in a specific area has strong spatial linkage.

According to the standard value of GB3095-2012 (PM2.5 concentration value, 35μg/m ^{3}), Pingxiang City, Xinyu City, Northwest Ji'an, Yichun City, Nanchang City, Jiujiang City, Yingtan City, belong to areas with high annual average PM2.5 concentration ((Both are over 40μg/m^3), and the highly polluted areas exhibit high-height (HH) accumulation spatial distribution characteristics, indicating that PM2.5 pollution in these areas and adjacent areas are more serious, probably because these areas have more developed industries [18]. It is located in the southeast of Shangrao City in northern Jiangxi, southeast of Fuzhou and southeast Ji'an in central Jiangxi, and the annual average concentration of PM2.5 in Ganzhou is lower than 35μg/m^3 , which belongs to the area with low PM2.5, that is, the area with better air quality, the spatial distribution characteristics are Low-Low (LL) clusters, indicating that these areas and their neighboring areas have better air quality, benefiting from forest cover [19]. The 2016 annual forest land change survey and forest resource data update results show that Ganzhou has a forest coverage rate of 76.23%, ranking second in the country. Comparing the LISA clustering chart from 2010 to 2015 (Figure 4), the high-high cluster area and the low-low cluster area both increased and decreased. Jiujiang City, Nanchang City, and Yingtan City, which belong to the high-high cluster area, were in 2011. The weather quality improved considerably in 2012, but air management showed enormous pressure in 2013 and 2014. The areas near Ganzhou City, which belongs to the low-low concentration region, and the southeast area of Shangrao also had varying degrees of change. It is worth noting that the air quality in many urban areas shows massive changes, and the PM2.5 concentration value is increased to varying degrees, which has a relatively stable relationship with the changes in land use in recent years [20] [21]. Especially Construction land, the continuity of construction land is high, PM2.5 concentration tends to be high.

Driving Factor Impact Analysis. The change of PM2.5 is affected by various factors, and the degree of influence will also be different. Geographical detectors model were used to detect the driving factors that affect the changes of PM2.5. GDP, population density, secondary industry value, number of industrial enterprises, construction land were selected from the socio-economic factors; Elevation, precipitation, temperature, vegetation, geography were selected as natural factors. Passed the significance test, and obtained p value (Figure 5). In descending order by q, temperature (0.33) > elevation (0.31) > precipitation (0.25) > GDP (0.240) > population density (0.238) > secondary industry value (0.22) > number of industrial enterprises (0.15) >geography (0.13) > construction land (0.05) > vegetation (0.04), it can be seen that the influence of natural factors is greater than the socioeconomic factors.

Natural Factor Driving Analysis. (1) Temperature factor (q = 0.33): Among the selected natural factors, the temperature factor has the greatest effect on PM2.5. PM2.5 concentration changes generally show seasonal characteristics in summer and non-summer seasons [23]. Low temperature is very helpful for increasing PM2.5 concentration [24] [25]. The province's average annual maximum temperature is "middle-high, north-south low," and the annual minimum temperature is "south high-north low" [26], and the PM2.5 concentration coincides with it. On the contrary, the highest annual average PM2.5 concentration in the province occurs in winter (average annual 67.6μg/m^3), followed by autumn, and the lowest in summer, and winter, Xinyu, Yichun, Pingxiang, and other places are heavily polluted areas.

(2) Elevation factors (q = 0.31) have an essential influence on the accumulation and dissipation of atmospheric pollutants such as PM2.5 [27], which can change the PM2.5 concentration through meteorological conditions [28], Such as basins, basins have poor atmospheric fluidity and high humidity, which readily form aerosols, which is not conducive to the diffusion of pollutants [29]. Hills and mountains dominate the Elevation in Jiangxi, and the basins and valleys are widely spread, mountains surround the eastern, southern and western parts of Jiangxi on three sides, and the north is the Poyang Lake plain. Therefore, the Elevation also plays a vital role in the change of PM2.5 in Jiangxi

(3) Precipitation factor (q = 0.25). Precipitation

plays a role in scouring, diluting, and removing atmospheric pollutants. According to research, the average PM2.5 concentration decreases with every 1 mm increase in rainfall [30]. Jiangxi belongs to the subtropical monsoon region with abundant rainfall throughout the year. In general, the spatial distribution of precipitation in Jiangxi is larger than that in northern Jiangxi. Spring and summer are the seasons with the most abundant precipitation, and autumn and winter are less [31], which explains to some extent the Spatial distribution of PM2.5 concentration changes in high-high clusters in northern Jiangxi and low-low clusters in southern Jiangxi.

(4) Geography factors (q=0.13) and vegetation factors (q=0.04) have a certain effect on PM2.5 concentration, but the influence is weaker than the first three natural factors, which also shows that geography and vegetation have a certain degree of digestion or absorption of PM2.5 [32].

Socioeconomic Factors Driving Analysis. (1) GDP factor (q = 0.24) is the leading factor in the socioeconomic factors. The reason is that the economic development model at that time was still extensive development. Zhou Yejing et al. [33] used the method of system dynamics to predict that under the development model of "ensuring the economy and neglecting the environment", GDP growth will inevitably lead to aggravation of atmospheric pollution. Statistics on the proportion of GDP of the secondary industry in each city in 2015, located in hight-hight cluster areas of Nanchang City (401.18 billion yuan, 54.5%), Xinyu City (94.68 billion yuan, 55.8%), Jiujiang City (190.94 billion yuan, 53.3%), and Pingxiang City (91.23 billion yuan,56.7%), Yichun City (162.102 billion yuan, 51.7%), Yingtan City (63.926 billion yuan, 59.4%), Jingdezhen City (91.239 billion yuan, 56.7%). The proportion of the secondary industry is generally higher than 50%, located in Low-low cluster areas of Ganzhou City (1973.87 billion yuan, 44.1%), Shangrao City (165.515 billion yuan, 48.7%), and located in insignificant areas of Ji'an City (132.552 billion yuan, 49.5%), Fuzhou City (110.514 billion yuan, 54.5%), of the majority less than 50%. From which we can see that transforming economic growth patterns, accelerating economic transformation and upgrading, and innovating development models, increasing governance at the source of pollution [7], and committing to the development of green GDP Model will inevitably make economic development and concentration consistent EKC, inverted U-shaped relationship [34].

(2) The impact of population density factor (q=0.238) on PM2.5 is second only to GDP factor, which indicates that the higher the population density, the human activities will cause factors such as dust and exhaust emissions to cause a significant increase in PM2.5 concentration, especially in central urban areas. Observing the LISA clustering chart, it was found that most of the downtown areas in various regions belong to high-high PM2.5 pollution areas, which are located in high-high areas such as Nanchang City (737Person / cubic kilometer), Pingxiang City (496Person / cubic kilometer), Yingtan City (324Person / cubic kilometer), and Xinyu City (369Person / cubic kilometer), the population density is relatively large.

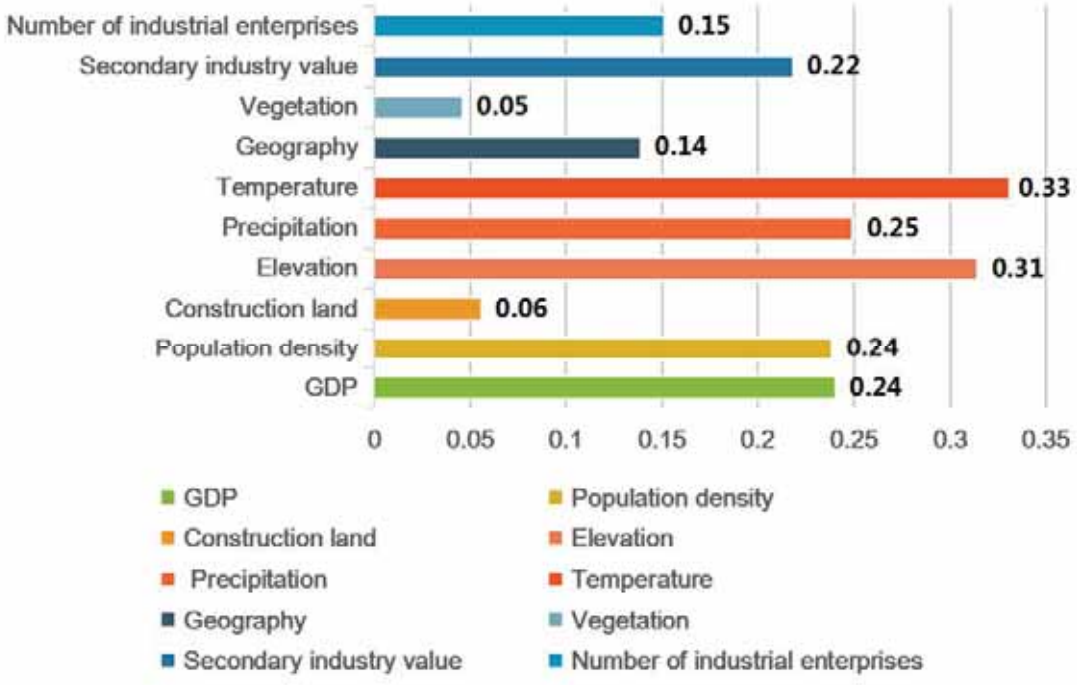

FIGURE 5
Explanatory power of PM2.5 concentration influencing factor (q value) in Jiangxi Province

TABLE 3
Two-factor interaction detector values of 2015

Factor	GDP	Population density	Construction land	Elevation	Precipitation	Temperature	geography	Vegetation	Secondary industry value	Number of industrial enterprises
GDP	0.24									
Population density	0.47	0.24								
Construction land	0.26	0.25	0.06							
Elevation	0.43	0.43	0.33	0.31						
Precipitation	0.52	0.52	0.29	0.52	0.25					
Temperature	0.60	0.57	0.40	0.84	0.63	0.33				
geography	0.35	0.33	0.17	0.38	0.39	0.65	0.14			
Vegetation	0.27	0.25	0.09	0.33	0.28	0.39	0.16	0.05		
Secondary industry value	0.54	0.54	0.28	0.49	0.47	0.49	0.36	0.26	0.22	
Number of industrial enterprises	0.45	0.49	0.21	0.45	0.41	0.46	0.30	0.20	0.41	0.15

(3) The factor of secondary industry value (q=0.22), the number of industrial enterprises (q=0.15), and the factor of construction land (q=0.05) all have positive effects on the increase of PM2.5 concentration. The increase in the proportion of industrialization and the increase in the number of enterprises with industrial pollution properties will contribute to the discharge of various pollutants, which will lead to aggravation of air pollution [35][36]. Yingtan, known as the "copper capital of China," and Xinyu, known as the "steel city," are highly industrialized and belong to the high-high cluster area. The increase in construction land has affected PM2.5 concentration changes to some extent [37].

Factor Interaction Detection Analysis. The concentration of PM2.5 is not the result of the interaction of a single factor, but the result of the interaction of multiple factors. They were using the interactive detector in the geographic detector to detect the interaction of factors, revealing the law. Interaction detection was performed, and the detection results are shown in Table 3. Among the socioeconomic factors, the interaction results of the GDP factor and other factors (population density, construction land, the gross output of the secondary industry, and the number of industrial enterprises) were: 0.47, 0.26, 0.54, and 0.45, respectively, which satisfies the two-factor enhancement, indicating the interaction effect has a more significant impact on PM2.5 concentration. The most noteworthy is that the interaction between GDP, population density, and secondary industry value or the number of industrial enterprises has a non-linear enhancement effect, so optimizing the industrial structure and promoting the development of a green economy will significantly help reduce PM2.5 concentration.

CONCLUSIONS

This article analyzes the spatiotemporal characteristics and driving factors of PM2.5 concentration changes in Jiangxi in order to provide a scientific decision basis for improving the quality of the atmospheric environment in the region. The research results show that:

(1) The change of PM2.5 concentration in Jiangxi showed significant seasonal patterns and spatial characteristics. PM2.5 concentration is highest in winter, and pollution is most dangerous, followed by spring and autumn, and air quality is best in summer. The overall PM2.5 concentration in Jiangxi showed a downward trend from 2010 to 2015 but fluctuated significantly during the period. The heavily polluted cities such as Pingxiang, Jiujiang, Nanchang, and Jingdezhen fluctuated significantly, while the best air quality in Ganzhou City, Fuzhou City, is relatively stable. In 2014, the PM2.5 concentration in 11 cities increased to a higher level. However, it fell to the lowest level in 2015, the reason for the decline is likely to be related to the implementation of the "State Council's Notice on Printing and Distributing Action Plan for Air Pollution Prevention and Control," and strict governance from the source " "Four Dusts" (dust at construction sites, roads, transportation, and storage yards), "three clouds of smokes" (food fume, barbecue fume, dense smoke from garbage incineration), "three gases" (motor vehicle exhaust, industrial waste gas, coal combustion) Boiler flue gas), straw burning in the open air is

strictly prohibited, concentrated fireworks and firecrackers in the main urban area are strictly prohibited. The industry's emission reduction tasks are mainly promoted. The above series of measures have effectively improved air quality

(2) The regional differences in PM2.5 concentrations in Jiangxi are quite substantial. The heavily polluted northwestern Jiangxi region and the southeast Jiangxi region with good air quality show a significant "diagonal" distribution, and the middle zone is not significant. The areas with massive pollution show high-high aggregation characteristics, and the areas with better air quality show low-low aggregation characteristics, indicating that pollution has a robust spatial linkage. It is suggested that a regional coordination mechanism should be established for the treatment of PM2.5 pollution, and strengthen Communicate and cooperate on pollution control measures to form a joint force for pollution control and avoid fighting on their own.

(3) Geographic detectors are used to detect the influencing factors that drive PM2.5 concentration changes. Natural factors have a greater influence on PM2.5 concentration changes than socioeconomic factors. Among natural factors, air temperature (q = 0.33)> elevation (q = 0.31)> precipitation (Q = 0.25)> geography (q = 0.13)>> Vegetation (q = 0.04), temperature is the dominant factor; among socioeconomic factors, GDP (q = 0.240)> population density q = 0.238)> secondary industry value (q = 0.22)> Number of industrial enterprises (q = 0.15)> Construction land (q = 0.05), GDP is the dominant factor. In the detection of interactions among factors, among the socioeconomic factors, the interaction between GDP factors and other factors satisfies a two-factor enhancement, indicating that the interaction between GDP and other factors has a greater impact on PM2.5 concentration, so the industrial structure is optimized and promoted. The development of the green economy; among natural factors, the interaction between air temperature and topography, air temperature and geography is linearly enhanced, indicating that the interaction greatly affects PM2.5 concentration changes, indicating that Jiangxi has a unique natural environment, protect the environment, and make good use of it. Taking advantage of the natural environment, focusing on economic development methods, promoting the optimization and upgrading of the industrial structure, and establishing a resource-saving and environment-friendly society, the governance of PM2.5 will be at a higher level.

REFERENCES

[1] Wang, W., Tang, D.G., Liu, H.J., Yue, X., Ding, Y. (2000) Research on Corrent Pollution Sataus and Pollution Characteristics of PM2.5 in China.Research of Environmental Sciences. (01), 1-5.

[2] WHO. (2005) Air quality guidelines:global update2005.Bonn:WHO Regional Office for Europe. 173-190.

[3] Ministry of environmental protection. (2012) GB 3095—2012 National ambient air quality standards. Beijing: China Environmental Science Press. 2-6.

[4] Sun, Y., Zhuang, G., Tang, A., Wang, Y., An, Z.S. (2006) Chemical characteristics of PM2.5 and PM10 in haze fog episodes in Beijing. Environmental Science & Technology. 40(10), 3148-3155.

[5] Jin, Q., Fang, X., Wen, B., Shan, A.D. (2017) Spatial-temporal variations of PM2.5 emission in China from 2005 to 2014. Chemosphere. 183, 429-436.

[6] Ye, W., Zhongyu, M.A., Xiuzhen, H.A. (2018) Spatial-temporal patterns of PM2.5 concentrations for 338 Chinese cities. Science of the Total Environment. 631-632, 524-533.

[7] Yang, M., Wang, Y. (2017) Spatialtemporal characteristics of PM2.5 and its influencing factors in the Yangtze River Economic Belt. China Population, Resources and Environment. 27(1), 91-100.

[8] Han, L. (2018) Relationship between urbanization and urban air quality: An insight on fine particulate dynamics in China. Progress in Geography. 37(08), 1011-1021.

[9] Xu, S., Zhang, W., Li, Q., Zhao, B., Wang, S., Long, R. (2017) Decomposition Analysis of the Factors that Influence Energy Related Air Pollutant Emission Changes in China Using the SDA Method. Sustainability. 9(10), 1742.

[10] Pinto, J.P., Lefohn, A.S., Shadwick, D.S. (2004) Spatial variability of PM2.5 in urban areas in the United States. Journal of the Air & Waste Management Association. 54(4), 440-449.

[11] Cao, C., Jiang, W., Wang, B., Fang, J.H., Lang, J.D., Tian, G., Jiang, J.K., Zhu, T.F. (2014) Inhalable microorganisms in Beijing's PM2.5 and PM10 pollutants during a severe smog event. Environmental Science & Technology. 48(3), 1499-1507.

[12] Han, W., Tong, L., Chen, Y., et al. (2018) Estimation of High-Resolution Daily Ground-Level PM2.5 Concentration in Beijing 2013–2017 Using 1 km MAIAC AOT Data. Appl. Sci. 8, 2624.

[13] Wang, Z., Liang, L., Lin, X. (2017) Mode summary of air pollution in Beijing- Tianjin- Hebei urban agglomeration and evaluation of treatment effects. Environmental Science. 38(10), 4005-4014.

[14] Tian, S., Pan, Y., Liu, Z., Wen, T., Wang, Y. (2014) Size-resolved aerosol chemical analysis of extreme haze pollution events during early 2013 in urban Beijing, China. Journal of Hazardous Materials. 279, 452-460.

[15] Tobler, W.R. (1970) A computer movie simulating urban growth in the Detroit region. Economic Geography. 46, 234-240.
[16] Wang, J.F., Xu, C.D. (2017) Geodetector: Principle and prospective. Acta Geographica Sinica. 72(01), 116-134.
[17] Liu, H., Sun, Y., Chen, M. (2017) Dynamic correlation and causes of urban haze pollution. China Population, Resources and Environment. (3), 74-81.
[18] Chen, L., Zhou, Y., Yao, L.Y., Wang, W., Sheng, J., Liu, L., Huang, H.Y. (2015) Modeling studies of industrial sector contributions to PM2.5 pollution in different districts of Tianjin. China, Environmental Science. 35(01), 33-39.
[19] Yang, K., Yang, Y., Zhu, Y., Cen, L., Meng, C. (2016) Social and economic drivers of PM2.5 and their spatial relationship in China. Geographical Research. 35(06), 1051-1060.
[20] Yang, H.O., Chen, W.B., Liang, Z.F. (2017) Relationship of PM2.5 concentration and land use type in nanchang city based on LUR simulation. Transaction of the Chinese Society of Agricultural Engineering. 33(06), 232-239.
[21] Bin, Z., Shan, X., Troy, S., Xin, F. (2016) Effect of Land Use and Cover Change on Air Quality in Urban Sprawl. Sustainability. 8(7).
[22] Yang, W.Y., Liu, Y.F., Liu, Y.L., Zi-Hao, A.N., Yin, C.H. (2019) Investigating the effect of urban landscape pattern on PM2.5 concentration based on LUR model:A Chang-Zhu-Tan urban agglomeration case study. Resources and Environment in the Yangtze Basin. 28(09), 2251-2261.
[23] Zhu, Q.R., Liu, Y.H., Xu, W.J. (2013) Analysis on the pollution characteristics and influence factors of PM2.5 in Guangzhou. Environmental Monitoring in China. 29(02), 15-21.
[24] Wang, Z.B., Fang, C.L., Xu, G., Pan, Y. (2015) Spatial-temporal characteristics of the PM2.5 in China in 2014. Acta Geographica Sinica. 70(11), 1720-1734.
[25] Zhang, Z.H. (2014) Research on spatial and temporal variation characteristics, factors and source apportionment of PM2.5. Hangzhou: Zhejiang University.
[26] Li, B., Ping, K., Zhan,M., Zhang, Y., Wang, H. (2017)Analysis on the temperature variation in Jiangxi province during 1961-2015. Meteor Disaster Reduction Res. 40(3), 184-192.
[27] Zhou, L., Wu, J., Jia, R.J., Liang, N., Zhang, F.Y., Ni, Y., Liu, M. (2016) Investigation of temporal-spatial characteristics and underlying risk factors of PM2.5 pollution in Beijing-Tianjin-Hebei area. Research of Environmental Sciences. 29(04), 483-493.
[28] Huang X., Shao T., Zhao J., Cao J., Song Y. (2019) Spatio-temporal Differentiation of Ozone Concentration and Its Driving Factors in Yangtze River Delta Urban Agglomeration. Resources and Environment in the Yangtze Basin, 28(06), 1434-1445.
[29] Ji, L., Chen, C., Wang, N.N. (2014) Comparison and analysis on characteristics and causes of PM2.5 pollution in typical central cities of China. Journal of Catastrophology. 29(04), 230-234.
[30] Zhou, S.D., Ouyang, W.Q., Ge, J.H. (2017) Study on the main influencing factors and their intrinsic relations of PM2.5 in Beijing-Tianjin-Hebei. China Population, Resources and Environment. 27(04), 102-109.
[31] Bin, Z., Wu, Y., Qiu, L. (2013) Variation characteristics and accuracy of precipitable water vapor from ground-based GPS remote sensing in Jiangxi. Plateau Meteorology. 32(05), 1503-1509.
[32] Zhou, M., Kuang, Y., Yun, G. (2020) Analysis of Driving Factors of Atmospheric PM2.5 Concentration in the City of Guangzhou based on Geo-Detector. Research of Environmental Sciences. 33(02), 271-279.
[33] Zhou, Y., Zhou, J., Xiao, R. (2016) System Dynamics Modeling for Prediction of Impacts on GDP and PM2.5 by Regional Air Pollutants Emission Reduction. Environmental Science &Technology. 39(04), 161-167.
[34] Wang, Y. (2015) Sociological perspectives on air pollution: a cross-national analysis of social determinants of fine particulate matter (PM2.5).Sociological Review of China. 3(03), 53-67.
[35] Li, X., Song, M., An, Q. (2013) The heterogeneity research of the impact of China's Economic growth on environmental pollution. Nankai Economic Studies. (05), 96-114.
[36] Qin, M., Liu, X.Y., Tong, Y.T. (2016) Does urban sprawl exacerbate haze pollution: An empirical study of fine particles (PM2.5) in Chinese cities. Finance and Trade Economics. (11), 146-160.
[37] Xu, G., Jiao, L.M., Xiao, F.T., Zhao, S.L., Zhang, X. (2016) Applying land use regression model to estimate spatial distribution of PM2.5 concentration in Beijing-Tianjin-Hebei region. Journal of Arid Land Resources and Environment. 30(10), 116-120.

Received: **25.11.2021**
Accepted: **11.01.2022**

CORRESPONDING AUTHOR

Xiaoqiang Tu
School of Management,
Nanchang University,
Nanchang, Jiagnxi, 330031 – China

e-mail: ren2005zhe@163.com

© by PSP Volume 31– No. 05/2022 pages 4951-4957 Fresenius Environmental Bulletin

In vitro ANTIMICROBIAL ACTIVITY AND BIOCHEMICAL COMPOSITION OF *Hibiscus syriacus* FROM TURKEY

Kerem Canli[1,2,*], Mustafa Eray Bozyel[3], Atakan Benek[4], Dilay Turu[1], Mustafa Ali Yakan[1], Ergin Murat Altuner[4]

[1]Department of Biology, Faculty of Science, Dokuz Eylul University, Buca, Izmir, Turkey
[2]Fauna and Flora Research and Application Center, Dokuz Eylul University, Buca, Izmir, Turkey
[3]Department of Biology, Faculty of Arts and Science, Canakkale Onsekiz Mart University, Canakkale, Turkey
[4]Department of Biology, Faculty of Science and Arts, Kastamonu University, Kastamonu, Turkey

ABSTRACT

Hibiscus syriacus is an ornamental plant, and it also has uses in traditional medicine. This study aimed to investigate *in vitro* antimicrobial activity and the biochemical composition of *Hibiscus syriacus*. In this study, the biochemical composition of ethanol extracts of *H. syriacus* flowers (HSFEt) and *H. syriacus* leaves (HSLEt) was analyzed by GC-MS. The antimicrobial activity was investigated using a disk diffusion test against 39 bacteria (including 11 multidrug-resistant strains) and 2 fungi strains. 21 and 12 components were identified in HSFEt and HSLEt, respectively. The main component is 2,3-Dihydroxypropyl stearate in both extracts. HSFEt and HSLEt have antimicrobial activity against most of the tested microorganisms. It has been detected the highest activities against *Staphylococcus aureus* ATCC 25923 (ST11) with a 15 mm, *Staphylococcus aureus* (CI1) and *Staphylococcus aureus* MRSA+MDR (MDR9) with a 14 mm inhibition zones in HSFEt, and *Staphylococcus aureus* ATCC 25923 (ST11) with an 11 mm inhibition zone in HSLEt. All these results showed that *H. syriacus* has antistaphylococcal potential.

KEYWORDS:
Hibiscus syriacus, disk diffusion, GC-MS, ethanol extract, antistaphylococcal

INTRODUCTION

The use of medicinal plants for the treatment of diseases before chemical drugs is an ancient order that took place with the transition of mankind to a sedentary life. Herbal medicines constitute a significant part of the customs of rural communities in developing countries [1].

According to WHO reports, 80% of the population in developing countries relies on non-chemical drugs, usually of plant origin, to ensure the sustainability of their health. It is noted that usually at least 25% of the active substances of drugs produced pharmacologically by modern methods are obtained from plants. In addition, the active substances of many synthetically produced drugs are also structural analogs of chemicals isolated from plants for the first time. The demand for plants used as pharmaceutical raw materials is increasing at a high level in both developed and developing countries due to their low cost, low side effects compared to synthetic drugs, very low toxicity, and being produced organically [2].

Medicinal plants are a natural source of compositions that can be used against many diseases today [3]. These plants contain many chemicals and active substances of a wide variety that have significant effects on humans [1]. Chemicals such as flavonoids, alkaloids, terpenoids, tannins, berberine, quinine, and emetine synthesized by plants are used quite widely in maintaining health and treating most diseases [4].

The reason why it has become increasingly difficult to treat infections in recent years is the increase of microorganisms with multiple antibiotic resistances. Drug resistance gradually increases in bacteria that develop resistance to all known antibiotics and is passed on from generation to generation. That is why it is recommended to use medicinal plants as an alternative to synthetic drugs, and some of them are even used as antimicrobials [5]. It is believed that the therapeutic properties of plants are due not to a single active substance, but the mutual interaction of a large number of compositions. Therefore, it is noted that herbal compositions provide a more effective healing process against resistant microorganisms that are difficult to kill with a single synthetic drug [6, 7]. This circumstance pushes researchers to study the compositions of active substances obtained from plant extracts that have an inhibitory property [8].

Essential oils, tannins, alkaloids, and bitter substances are the active substances usually used in plant metabolism. They strengthen the body's defense systems, support the functioning of organs, and promote healing. Thus, they have a positive effect on the functioning of certain organs and tissues in the organism. Throughout the history of mankind, many diseases such as diabetes, jaundice, shortness of breath have been tried to be treated using plants [9].

Although the possible effects vary according to the active ingredients, it is known that most essential oils have effects such as antimicrobial, carminative, choleretic, sedative, diuretic, and antispasmodic [5, 10].

Hibiscus syriacus is a native species of Southern China and Taiwan. Nowadays it is widely cultivated as ornamental plants and hedges in Japan, Korea, Malaysia, and other warm-temperate and subtropical regions of the world. It is called Common Hibiscus, Rose of Sharon, and Shrub Althea. It has antimicrobial, antioxidant, anticancer, antiulcer, anti-aging, and wound healing properties. Flowers decoction or infusion is used as a diuretic, stomachic, and ophthalmic in traditional medicine. It is also used for treating itches, other skin ailments, dizziness, dysentery, and bloody stools with much gas. In addition, leaves are used as a diuretic, stomachic, and expectorant [11].

We have determined that the antimicrobial activity of *H. syriacus* against a wide range of microorganisms, including multidrug-resistant strains, has not been adequately studied at the end of the literature review. Therefore to avoid toxic effects and to serve as the basis for plant-based drug molecule determination studies in the later stages, ethanol was preferred as a solvent when preparing plant extract in this study.

In this study, we investigated *in vitro* antimicrobial activity and the biochemical composition of HSFEt and HSLEt.

MATERIALS AND METHODS

Plant samples. *H. syriacus* samples were collected from near Faculty of Arts and Science, Canakkale Onsekiz Mart University, Canakkale, Turkey (40°6'39" N, 26°25'7" E) and identified by Dr. Bozyel. The plant aerial parts were placed in sample bags and transported to our laboratory. The samples were air-dried at room conditions. The voucher specimens were deposited at the Fauna and Flora Research and Application Center, Dokuz Eylül University, Buca, Izmir, Turkey (Personel herbarium number FFDEU-ERA1734).

Active compound extraction. Dried *H. syriacus* flowers and leaves samples were ground to obtain a fine powder, to increase the surface area for extraction. The active compounds were extracted by ethanol (Sigma Aldrich) through shaking at room conditions for two days [12]. After filtering through filter paper (Whatman No.1), the ethanol in the extract was evaporated at 45°C under vacuum by using a rotary evaporator (Heidolph Hei-Vap Value HL/HB-G1) [13]. The remnant was weighed and an extract stock was prepared for each plant using a defined volume of ethanol, and 50 µL, 90 µL, and 200 µl of the extracted stock of HSFEt and 50 µL, 100 µL, and 200 µl of the extracted stock of HSLEt were transferred to empty sterile antibiotic disks. The disks were loaded with 5.78, 10.41, and 23.13 mg of HSFEt and 1.15, 2.3, and 4.6 mg of HSLEt, respectively.

Antimicrobial activity. The disk diffusion test, which was described previously in detail by Yakan et al. [14] was used for testing the antimicrobial activity of HSFEt and HSLEt against 11 standard (ST), 11 multidrug-resistant (MDR), 10 clinical isolated (CI), and 7 food isolated (FI) bacteria, and 1 standard (ST) and 1 clinical isolated (CI) fungi strains. The incubation conditions for microorganisms excluding fungi strains were 37°C for 24 hours, but 27°C for 48 hours for *C. albicans* and *C. tropicalis*. Inoculum for each microorganism was prepared in 0.9% sterile saline solution and the turbidity of all inocula was adjusted by comparing with 0.5 McFarland standard. The Petri dishes containing disks, on which the ethanol extract was loaded, incubated according to the suitable time-temperature combinations mentioned above, and the inhibition zones were observed and recorded in millimeters. Empty antibiotic disk and ethanol-loaded disk were used as negative controls. A wide range of antibiotics was used as positive controls.

GC-MS Analysis. The biochemical composition of HSFEt and HSLEt were determined by GC-MS analysis according to the protocol given in previous studies [15].

Statistics. All tests were applied as triplicates. One-way analysis of variance (ANOVA), which is a parametric method was performed ($P = 0.05$) [16]. Pearson correlation coefficient was determined for any possible correlation between the intensity of antimicrobial activity and concentration. Statistical analysis was performed using R Studio (version 3.3.2) [17].

RESULTS AND DISCUSSION

Antimicrobial activity. The data obtained from the study about the inhibition zone diameters are shown in Table 1. According to the results, negative controls show no activity [18]. Additionally, statistical analysis verified that the differences between the results of three replicates of each extract volume were statistically non-significant ($p>0.05$). In addition, obtaining a Pearson correlation coefficient of 0.1986 and 0.1703 presented a very weak positive correlation between the antimicrobial activity and the volumes of extracts used. Also, thirteen antibiotics in standard, food isolated, and clinical isolated strains (Table 2) and thirty-three antibiotics in multidrug-resistant strains were used as positive controls (Table 3).

TABLE 1
Antimicrobial activity of HSFEt and HSLEt

Lab. Code	Microorganisms	HSFEt			HSLEt		
		50 µL*	**90** µL*	**200** µL*	**50** µL*	**100** µL*	**200** µL*
ST1	*Bacillus subtilis* DSMZ 1971	11,00 ± 0,00	7,00 ± 0,00	8,00 ± 0,00	8,00 ± 0,00	8,00 ± 0,00	9,00 ± 0,00
ST2	*Candida albicans* DSMZ 1386	10,00 ± 0,00	10,00 ± 0,00	10,00 ± 0,00	-	-	-
ST3	*Enterobacter aerogenes* ATCC 13048	-	-	-	-	-	-
ST4	*Enterococcus faecalis* ATCC 29212	7,00 ± 0,00	8,00 ± 0,00	8,00 ± 0,58	-	-	7,00 ± 0,00
ST5	*Escherichia coli* ATCC 25922	-	-	7,00 ± 0,00	-	-	-
ST6	*Listeria monocytogenes* ATCC 7644	11,00 ± 0,00	11,00 ± 0,00	11,00 ± 0,00	8,00 ± 0,00	8,00 ± 0,00	9,00 ± 0,00
ST7	*Pseudomonas aeruginosa* DSMZ 50071	-	7,00 ± 0,00	9,00 ± 0,00	-	-	-
ST8	*Pseudomonas fluorescens* P1	7,00 ± 0,00	8,00 ± 0,00	10,00 ± 0,00	-	-	-
ST9	*Salmonella enteritidis* ATCC 13076	-	7,00 ± 0,00	8,00 ± 0,00	-	-	7,00 ± 0,00
ST10	*Salmonella typhimurium* SL 1344	-	-	-	-	7,00 ± 0,00	7,00 ± 0,00
ST11	*Staphylococcus aureus* ATCC 25923	15,00 ± 0,00	9,00 ± 0,00	12,00 ± 0,58	10,00 ± 0,00	11,00 ± 0,00	11,00 ± 0,00
ST12	*Staphylococcus epidermidis* DSMZ 20044	11,00 ± 0,00	12,00 ± 0,00	13,00 ± 0,00	-	-	-
FI1	*Enterococcus durans*	8,00 ± 0,00	9,00 ± 0,00	9,00 ± 0,00	8,00 ± 0,00	8,00 ± 0,00	8,00 ± 0,00
FI2	*Enterococcus faecium*	10,00 ± 0,00	11,00 ± 0,00	12,00 ± 1,15	9,00 ± 0,00	10,00 ± 0,58	10,00 ± 0,00
FI3	*Klebsiella pneumoniae*	-	-	-	-	7,00 ± 0,00	7,00 ± 0,00
FI4	*Listeria innocua*	7,00 ± 0,00	8,00 ± 0,00	9,00 ± 0,00	-	-	-
FI5	*Salmonella infantis*	-	-	-	-	-	-
FI6	*Salmonella kentucky*	-	-	-	-	-	-
FI7	*Escherichia coli*	-	-	-	-	-	-
CI1	*Staphylococcus aureus*	14,00 ± 0,00	14,00 ± 0,00	14,00 ± 0,00	9,00 ± 0,00	9,00 ± 0,00	10,00 ± 0,58
CI3	*Staphylococcus hominis*	-	-	-	-	-	-
CI4	*Staphylococcus haemolyticus*	-	-	-	-	-	-
CI5	*Staphylococcus lugdunensis*	-	-	-	-	-	-
CI6	*Shigella boydi*	-	-	-	-	-	-
CI7	*Acinetobacter baumannii*	-	-	-	-	-	-
CI8	*Shigella flexneri*	-	-	-	-	-	-
CI9	*Staphylococcus aureus*	-	-	-	-	-	-
CI10	*Enterococcus faecalis*	-	-	-	-	-	-
CI11	*Klebsiella pneumoniae*	-	-	-	-	-	-
CI12	*Candida tropicalis*	-	-	-	-	-	-
MDR1	*Escherichia coli*	-	-	-	-	-	-
MDR2	*Klebsiella pneumoniae*	-	-	-	-	-	-
MDR3	*Acinetobacter baumannii*	-	-	-	-	-	-
MDR4	*Enterobacter aerogenes*	-	-	-	7,00 ± 0,00	7,00 ± 0,00	7,00 ± 0,00
MDR5	*Serratia odorifera*	-	-	-	-	-	-
MDR6	*Proteus vulgaris*	-	7,00 ± 0,00	8,00 ± 0,00	-	-	-
MDR7	*Streptococcus pneumoniae*	7,00 ± 0,00	8,00 ± 0,00	10,00 ± 0,00	7,00 ± 0,00	7,00 ± 0,00	8,00 ± 0,00
MDR8	*Staphylococcus aureus* MRSA	9,00 ± 0,00	7,00 ± 0,00	12,00 ± 0,00	-	-	-
MDR9	*Staphylococcus aureus* MRSA+MDR	11,00 ± 0,00	13,00 ± 0,00	14,00 ± 0,58	-	-	-
MDR10	*Providencia rustigianii*	-	-	-	-	-	-
MDR11	*Achromobacter* sp.	-	-	-	-	-	-

"-": No information, *: The data is given as the mean values of three replicates with standard errors

TABLE 2
Positive controls against all strains except MDR strains

Lab. Code	1	2	3	4	5	6	7	8	9	10	11	12	13
ST1	30	26	36	44	34	37	38	41	36	44	20	52	42
ST2	12	13	-	-	-	-	-	-	-	-	-	-	-
ST4	12	8	19	14	-	19	29	14	-	-	15	28	29
ST5	22	20	7	18	-	22	-	6	6	6	6	16	12
ST6	28	24	27	24	11	25	-	23	-	-	23	34	32
ST7	15	22	18	-	-	9	-	-	-	-	-	-	-
ST8	13	12	19	10	8	22	-	14	-	-	16	26	26
ST9	21	15	24	23	-	28	27	16	-	16	-	28	31
ST10	24	15	35	22	-	27	27	13	-	14	-	26	21
ST11	21	14	22	31	24	21	16	25	22	29	16	30	27
ST12	22	20	34	37	35	33	26	24	26	32	21	45	32
FI1	11	13	24	36	30	8	29	28	22	26	24	37	32
FI2	28	15	28	40	30	11	31	32	24	33	26	43	34
FI3	19	23	30	-	-	22	6	6	6	6	-	9	6
FI4	13	15	18	14	-	23	-	13	-	-	16	28	33
CI1	22	18	23	-	-	-	-	-	-	-	-	-	-

"-": No activity; 1: Gentamicin; 2: Tobramycin; 3: Ciprofloxacin; 4: Cefazolin; 5: Clindamycin; 6: Chloramphenicol; 7: Ceftriaxone ; 8: Ampicillin; 9: Cephalothin; 10: Cefuroxime; 11: Vancomycin; 12: Amoxicillin/Clavulanic acid; 13: Trimethoprim/Sulfamethoxazole

TABLE 3
Positive controls against MDR strains

Lab. Code	1	2	3	4	5	6	7	8	9	10	11	12	13	14	15	16	17
MDR4	16	18	32	11	-	31	32	-	-	18	-	-	30	15	33	15	-
MDR6	11	11	42	-	9	22	23	9	-	20	-	9	30	10	37	32	12
MDR7	10	8	42	-	9	22	26	9	-	19	9	10	8	10	40	31	15
MDR8	-	7	-	-	45	27	8	12	-	-	26	11	24	14	-	11	12
MDR9	22	21	27	26	38	30	19	22	28	31	19	25	30	15	-	23	23

"-": No activity; 1: Gentamicin; 2: Tobramycin; 3: Ciprofloxacin; 4: Cefazolin; 5: Clindamycin; 6: Chloramphenicol; 7: Ceftriaxone ; 8: Ampicillin; 9: Cephalothin; 10: Cefuroxime; 11: Vancomycine; 12: Amoxicillin/Clavulanic acid; 13: Trimethoprim/Sulfamethoxazole; 14: Clarithromycin; 15: Aztreonam; 16: Piperacillin/Tazobactam; 17: Ampicillin/Sulbactam

TABLE 3 (Continued)
Positive controls against MDR strains

Lab. Code	18	19	20	21	22	23	24	25	26	27	28	29	30	31	32	33
MDR4	31	8	8	-	-	8	29	14	-	28	9	13	25	8	8	30
MDR6	25	13	-	24	11	8	26	12	12	26	16	-	12	8	-	22
MDR7	27	11	-	24	13	9	29	10	10	30	13	9	13	8	-	14
MDR8	8	-	-	9	40	19	14	-	-	9	7	8	23	-	-	-
MDR9	19	36	17	21	33	18	25	9	20	56	20	8	17	-	8	22

"-": No activity; 18: Ceftazidime; 19: Rifampicin; 20: Oxacillin; 21: Piperacillin; 22: Linezolid; 23: Teicoplanin; 24: Amicasin; 25: Polymyxin B; 26: Cefoxitin; 27: İmipenem; 28: Sulbactam/Cefoperazone; 29: Colistin sulfate; 30: Furazolidone; 31: Optochin; 32: Bacitracin; 33: Cefotaxime.

According to Table 1, HSFEt shows antimicrobial activity against 18 of 41 strains. One of them has high susceptibility (≥ 15 mm), ten of them have moderate susceptibility (14-10 mm), and seven of them have low susceptibility (9-7 mm). HSLEt has antimicrobial activity against 12 of 41 strains. Three of them have moderate susceptibility (14-10 mm) and nine of them have low susceptibility (9-7 mm) [19]. The most susceptible gram-positive bacteria strain is ST11 with a 15 mm inhibition zone and the gram-negative bacteria strain is ST8 with a 10 mm inhibition zone in HSFEt. The most susceptible gram-positive bacteria strain is ST11 with an 11 mm inhibition zone and the gram-negative bacteria strains are ST9, ST10, FI3, and MDR4 with a 7 mm inhibition zone in HSLEt. In additionally the HSFEt has shown highly effective results against ST12, FI2, CI1, MDR8, and MDR9. Also, the HSLEt has shown highly effective results against ST1, ST6, FI1, FI2, CI1, and MDR7.

ST5 has more effective results than Ampicillin, Cephalothin, Cefuroxime, and Vancomycin, while ST8 showed more effective results than Clindamycin in HSFEt. ST11 showed more effective results than Gentamicin, while FI1 and FI2 have more effective results than Chloramphenicol in HSFEt. It was determined that MDR7 and MDR8 are more effective than 8 antibiotics, and MDR9 is more effective than 3 antibiotics in HSFEt. Only FI3 showed more effective results than Ceftriaxone, Ampicillin, Cephalothin, Cefuroxime, and Trimethoprim/Sulfamethoxazole in HSLEt. According to these results, it is observed that HSFEt has a higher antimicrobial activity than HSLEt.

Punasiya et al. [20] reported the antimicrobial activity of dichloro-methane, isopropyl alcohol, and petroleum ether extracts of *Hibiscus syriacus* leaves against *B. cereus* (MTCC 430), *E. coli* (MTCC433), *K. pneumoniae* (MTCC432), and *S. aureus* (MTCC 3160). Petroleum ether and isopropyl alcohol extracts showed antimicrobial activity against these strains. According to our results, HSLEt is more effective against *S. aureus* (ST11) than petroleum ether extract of *H. syriacus* leaves.

Panaitescu and Lengyel [21] showed the antimicrobial activity of aqueous, ethanol 50%, and ethanol 96% extracts of flowers of *Hibiscus sabdariffa* against *E. coli* ATCC 25922, *E. cloacae* ATCC 13047, *K. pneumoniae* ATCC 13833, *S. typhimurium* ATCC 14028, *S. aureus* ATCC 29213, and *Y. enterocolitica* ATCC 9610. When we compared two studies with each other, it appears that HSFEt has high antimicrobial activity against similar strains as *E. coli* ATCC 25922 and *S. aureus* ATCC 29213.

Mak et al. [22] investigated the antimicrobial activity of aqueous and ethanolic extracts of flowers of *Hibiscus rosa-sinensis* against *B. cereus*, *B. subtilis*, *E. coli*, *K. pneumonia*, *L. monocytogenes*, *S. typhimurium*, *S. enteritidis*, and *S. aureus*. The ethanolic extract showed antimicrobial activity against only *S. aureus*. Our results presented that HSFEt is more effective results against *S. aureus*. In the light of all these results, it has been determined that both HSFEt and HSLEt have a high antimicrobial potential.

Biochemical composition of HSFEt and HSLEt. The major components of HSFEt and HSLEt, which were observed higher than 1%, and their composition percentages are given in Table 5

TABLE 4
Biochemical composition of HSFEt

No	Retention Time	Components	Formula	Molecular Weight (g/mol)	Area (%)
1	22.028	Nonanoic acid	$C_9H_{18}O_2$	158.238	1.79
2	22.739	Ethyl nonanoate	$C_{11}H_{22}O_2$	186.291	1.61
3	41.705	Palmitic acid	$C_{16}H_{32}O_2$	256.424	12.18
4	42.389	Ethyl palmitate	$C_{18}H_{36}O_2$	284.477	2.59
5	45.785	Linoleic acid	$C_{18}H_{32}O_2$	280.445	9.81
6	45.915	Linoleic acid	$C_{18}H_{32}O_2$	280.445	7.76
7	45.843	Ethyl linoleate	$C_{20}H_{36}O_2$	308.499	6.20
8	46.551	Ethyl linolenate	$C_{20}H_{34}O_2$	306.483	1.74
9	54.762	2-Methoxyaniline	C_7H_9NO	123.152	1.69
10	59.694	2,3-Dihydroxypropyl stearate	$C_{21}H_{42}O_4$	358.556	20.38
11	59.911	2,3-Dihydroxypropyl stearate	$C_{21}H_{42}O_4$	358.556	2.10
12	63.697	1-Heptacosene	$C_{27}H_{54}$	378.718	1.03
13	63.961	1-Tetracosanol	$C_{24}H_{50}O$	354.653	2.64
14	64.087	Eicosane	$C_{20}H_{42}$	282.547	1.04
15	68.563	UNKNOWN	-	-	1.50
16	71.483	UNKNOWN	-	-	2.57
17	73.040	UNKNOWN	-	-	1.15
18	74.769	UNKNOWN	-	-	6.18
19	75.483	UNKNOWN	-	-	1.60
20	76.950	UNKNOWN	-	-	1.05
21	78.936	UNKNOWN	-	-	1.36

"-": No information

TABLE 5
Biochemical composition of HSLEt

No	Retention Time	Components	Formula	Molecular Weight (g/mol)	Area (%)
1	43.578	Palmitic acid	$C_{16}H_{32}O_2$	256.424	4.74
2	47.868	Phytol	$C_{20}H_{40}O$	296.531	1.97
3	48.697	Linoleic acid	$C_{18}H_{32}O_2$	280.445	3.71
4	48.882	α-Linolenic acid	$C_{18}H_{30}O_2$	278.430	4.81
5	49.574	Ethyl linolenate	$C_{20}H_{34}O_2$	306.483	1.25
6	60.714	2-Methoxyaniline	C_7H_9NO	123.152	4.14
7	67.986	2,3-Dihydroxypropyl stearate	$C_{21}H_{42}O_4$	358.556	50.33
8	68.182	2,3-Dihydroxypropyl stearate	$C_{21}H_{42}O_4$	358.556	6.21
9	85.784	UNKNOWN	-	-	3.01
10	89.536	UNKNOWN	-	-	5.17
11	90.202	β-Amyrin acetate	$C_{32}H_{52}O_2$	468.754	1.95
12	91.856	UNKNOWN	-	-	1.89

"-": No information

and 6, according to the data obtained from the GC-MS analysis. According to Table 4, 2,3-Dihydroxypropyl stearate (22.48%), Linoleic acid (17.57%), and Palmitic acid (12.18%) are major components in the biochemical composition of HSFEt. According to Table 5, 2,3-Dihydroxypropyl stearate (56.54%), α-Linolenic acid (4.81%), and Palmitic acid (4.74%) are major components in the biochemical composition of HSLEt.

CONCLUSIONS

H. syriacus is a medicinal plant with antimicrobial activity. HSFEt and HSLEt showed antimicrobial activity against 18 and 12 microorganism strains, respectively. Purification and further studies are recommended to determine whether the antimicrobial activity is caused by a single known biochemical compound, such as 2,3-Dihydroxypropyl stearate, or by a synergistic effect. Besides, some compounds found in the extracts are not matching with the library. As a reason for that, this medicinal plant is proposed to contain some unknown molecules and they should be identified and their 3D structure should also be determined. The unknown compounds, which consist of 15.41% and 10.07%, respectively, should be analyzed in detail. Also, the mode of action(s) of the extract should be determined in further studies.

ACKNOWLEDGEMENTS

The authors acknowledge the Dokuz Eylül University Scientific Research Coordination Unit for funding this research (project number 2018.KB.FEN.021).

Author contributions KC and EMA planned the study. KC, MEB, AB, DT, MAY, EMA designed, performed the experiments, and analyzed the results. MEB conducted literature retrieval and drafted the manuscript. KC and EMA supervised the experiments, critically reviewed and edited the manuscript. All authors read and approved the final manuscript.

REFERENCES

[1] Njume, C., Afolayan, A.J. and Ndip, R.N. (2009) An overview of antimicrobial resistance and the future of medicinal plants in the treatment of *Helicobacter pylori* infections. Afr. J. Pharmacy and Pharmacol. 3(13), 685-699.

[2] Sekar, S. and Kandavel, D. (2010) Interaction of plant growth promoting rhizobacteria (PGPR) and endophytes with medicinal plants–new avenues for phytochemicals. J. Phytol. 2(7), 91-100.

[3] Vital, P.G., Velasco Jr, R.N., Demigillo, J.M. and Rivera, W.L. (2010) Antimicrobial activity, cytotoxicity and phytochemical screening of *Ficus septica* Burm and *Sterculia foetida* L. leaf extracts. J. Med. Plant Res. 4(1), 058-063.

[4] Hussain, T., Arshad, M., Khan, S., Sattar, H. and Qureshi, M.S. (2011) *In vitro* screening of methanol plant extracts for their antibacterial activity. Pak. J. Bot. 43(1), 531-538.

[5] Yarnell, E. and Abascal, K. (2004) Botanical treatment and prevention of malaria: part 2-selected botanicals. Altern. Complement. Ther. 10(5), 277-284.

[6] Shanthi Sree, K.S., Yasodamma, N. and Paramageetham, C.H. (2010) Phytochemical screening and *in vitro* antibacterial activity of the methanolic leaf extract: *Sebastiania chamaelea* Müell. Arg. Bioscan. 5(1), 173-175.

[7] Mohd Nazri, N.A.A., Ahmat, N., Adnan, A., Syed Mohamad, S.A. and Syaripah Ruzaina, S.A. (2011) *In vitro* antibacterial and radical scavenging activities of Malaysian table salad. Afr. J. Biotechnol. 10(30), 5728-5735.

[8] Dash, BK., Sultana, S. and Sultana, N. (2011) Antibacterial activities of methanol and acetone extracts of Fenugreek (*Trigonella foenum*) and Coriander (*Coriandrum sativum*). Life Sci. Med. Res. 27, 1-8.

[9] Faydaoğlu, E. and Sürücüoğlu, M.S. (2011) History of the Use of Medical and Aromatic Plants and their Economic Importance. Kastamonu Univ. J. Forest. Fac. 11(1), 52-67 (Turkish).

[10] Maksimović, Z.A., Đorđević, S. and Mraović, M. (2005) Antimicrobial activity of *Chenopodium botrys* essential oil. Fitoterapia. 76(1), 112-114.

[11] Lim, T.K. (2014) *Hibiscus syriacus*. In: Lim, T.K. (ed.) Edible Medicinal and Non Medicinal Plants. Springer. Dordrecht. 8, 374-380.

[12] Canli, K., Yetgin, A., Akata, I. and Altuner, E.M. (2016) *In vitro* antimicrobial activity screening of *Rheum rhabarbarum* roots. Int. J. Pharm. Sci. Invent. 5(2), 1-4.

[13] Canli, K., Bozyel, M.E. and Altuner, E.M. (2017) *In vitro* antimicrobial activity screening of *Maclura pomifera* fruits against wide range of microorganisms. Int. J. Pharm. Sci. Invent. 6(8), 19-22.

[14] Yakan, M.A., Bozyel, M.E., Benek, A., Turu, D. and Canli, K. (2021) Investigation of *in vitro* antimicrobial activity of ethanol extracts obtained from *Asparagus acutifolius*. Int. J. Acad. Appl. Res. 5(1), 126-129.

[15] Canli, K., Cetin, B., Altuner, E.M., Türkmen, Y., Üzek, U. and Dursun, H. (2014) *In vitro* antimicrobial screening of *Hedwigia ciliata* var. *leucophaea* and determination of the ethanol extract composition by gas chromatography/mass spectrometry (GC/MS). J. Pure Appl. Microbiol. 8(4), 2987-2998.

[16] Canli, K., Bozyel, M.E., Benek, A., Yetgin, A., Akata, I. and Altuner, E.M. (2021) Screening of *in vitro* antimicrobial activity of *Sedum hispanicum* ethanol extract and determination of its biochemical composition. Fresen. Environ. Bull. 30(02), 869-875.

[17] Canli, K., Bozyel, M.E., Benek, A., Yetgin, A., Senturan, M. and Altuner, E.M. (2020) Chemical composition and *in vitro* antimicrobial activity of *Matthiola tricuspidata* ethanol extract. Fresen. Environ. Bull. 29(10), 8863-8868.

[18] Bozyel, M.E., Canli, K., Benek, A., Yetgin, A. and Altuner, E.M (2021) Biochemical composition and *in vitro* antimicrobial activity of endemic *Helichrysum arenarium* ssp. aucheri ethanol extract. Fresen. Environ. Bull. 30(11A), 12614-12619.

[19] Canlı, K., Yetgin, A., Benek, A., Bozyel, M.E. and Altuner, E.M. (2019) *In vitro* antimicrobial activity screening of ethanol extract of *Lavandula stoechas* and investigation of its biochemical composition. Adv. Pharmacol. Sci. 1-6.

[20] Punasiya, R., Joshi, A., Sainkediya, K., Tirole, S., Joshi, P., Das, A. and Yadav, R. (2011) Evaluation of anti bacterial activity of various extract of *Hibiscus syriacus*. Res. J. Pharm. Technol. 4(5), 819-822.

[21] Panaitescu, M. and Lengyel, E. (2017) Monitoring the antibacterial activity of *Hibiscus sabdariffa* extracts. Manag. Sustain. Dev. 9(1), 31-34.

[22] Mak, Y.W., Chuah, L.O., Ahmad, R. and Bhat, R. (2013) Antioxidant and antibacterial activities of Hibiscus (*Hibiscus rosa-sinensis* L.) and Cassia (*Senna bicapsularis* L.) flower extracts. J. King Saud Univ. Sci. 25(4), 275-282.

Received: **25.11.2021**
Accepted: **11.01.2022**

CORRESPONDING AUTHOR

Kerem Canli
Department of Biology,
Faculty of Science,
Dokuz Eylul University,
Buca Izmir – Turkey

e-mail: biyoloji@gmail.com

© by PSP Volume 31– No. 05/2022 pages 4958-4966 Fresenius Environmental Bulletin

RESEARCH ON THE COUPLING RELATIONSHIP BETWEEN ECOLOGICAL ENVIRONMENT QUALITY AND ECONOMIC DEVELOPMENT OF CHENGDU CITY BASED ON EKC MODEL

Wen Wu*

School of Finance, Chengdu Jincheng College, Chengdu Sichuan 610097, China

ABSTRACT

Based on the environmental Kuznets curve, this article uses Chengdu's 2005-2018 empirical data as a sample to establish a model to conduct an empirical analysis of the relationship between Chengdu's economic growth and environmental quality. In the empirical analysis stage, first we comment on the economic development trend of Chengdu. Then, the income is selected as the economic factor, and water pollutant discharge, gas pollutant discharge, solid waste discharge, etc. are selected as environmental quality indicators. We perform regression analysis on indicators and environmental indicators to study the coupling relationship between economic development and environmental quality changes in Chengdu. The discharge of industrial wastewater showed a slow downward trend from 2005 to 2010. In 2012, the discharge of industrial wastewater rose sharply, and after 2014, the discharge of wastewater decreased again. The emissions of SO_2 and industrial dust showed a downward trend as a whole. From 2005 to 2008, the discharge of solid waste showed an increasing trend. After 2011, the emissions of solid waste showed a downward trend, and after 2015, the emissions remained stable. At present, the Kuznets curve in Chengdu falls within the win-win range. It shows that the environment and economy of Chengdu are currently in a stage of coordinated development.

KEYWORDS:
Ecological environmental quality, economic development, environmental Kuznets curve, Chengdu

INTRODUCTION

The revolution in modern industry has changed the relationship between mankind and the natural environment. Especially since the mid-20th century, with the rapid development of science and technology and the rapid development of the world economy, the phenomenon of humans "conquering" the world has appeared all over the world, and humans have become a very important leader in the global ecosystem [1-4]. It is worth mentioning that in the short course of recent decades, environmental problems are no longer unique to a certain country or several countries but have become problems faced by all countries in the world [5]. Environmental problems have also evolved from simple problems to complex problems that are more harmful and difficult to solve [6-8]. Many global environmental problems (such as the greenhouse effect, the destruction of the ozone layer, and the sharp decline of biodiversity) have begun to emerge. It has an ever-increasing impact on the economy, politics, technology and trade of a country and the international community [9-10].

At present, the research on the relationship between environmental quality and economic growth at home and abroad is mostly carried out on the basis of the environmental Kuznets curve (EKC), mainly from verifying the existence of the inverted curve and exploring new curve characteristics [11-13]. Many scholars have established models to conduct empirical tests on them from different angles and using horizontal or vertical data from different countries and regions [14]. Usually the researchers select some environmental quality indicators and use regression analysis to study the changes of these indicators with the growth of per capita income. The more commonly used environmental quality indicators include SO_2, suspended particulates, smoke, NO, CO, CO_2, COD, pathogenic bacteria, and heavy metals [15-16].

Research models usually abstract economic factors as income. Some environmental quality indicators use emissions, and some use environmental degradation indexes. Due to the different data used in various studies, the empirical studies of the EKC hypothesis have different conclusions [17-19]. The environmental Kuznets curve has also received the attention of domestic academic circles, and some scholars have successively carried out empirical research on China's EKC [20-21]. For example, some scholars used national-level longitudinal historical data to test China's EKC. The results show that the relationship between China's economic development and the level of environmental pollution has shown weak EKC characteristics [22-23]. Some scholars

conducted a horizontal regression analysis of the relationship between pollution emissions from 1982 to 1997 in China's 30 provinces, municipalities, and autonomous regions and the level of regional economic development, showing that China's water pollution is in the declining stage of the EKC curve [24-25].

The research of this article intends to start from the reality of Chengdu's economic development and environmental problems, and deeply analyze the relationship between the two. Taking Chengdu's empirical data from 2005 to 2018 as a sample, a model is established to analyze the coupling relationship between Chengdu's economic growth and changes in the quality of the ecological environment.

MATERIALS AND METHODS

Since the "harmony-contradiction-harmony" relationship between environment and economic development is shown as an inverted curve on the number line, it is similar to the results of Kuznets' research. In the early 1990s, the inverted U-shaped relationship between environmental quality and economic growth was put forward, and the hypothesis of environmental Kuznets curve was put forward. As the economy grows, the environment will deteriorate first and then improve. That is, in the lower stage of economic development, because the level of economic activity is low, the level of environmental pollution is also low. After the economic take-off, resources consumption exceeds the regeneration of resources, and the environment is deteriorating. In the rapid stage of economic development, economic structure changes, polluting industries stop production or are transferred, the accumulation of economic development can be used to control the environment, and people's environmental awareness has also strengthened.

This relationship was later confirmed by statistical data from a large number of western economists. EKC refers to that the environmental quality is still at a good level in the initial stage of economic development, and as the economic development begins to deteriorate, it gradually improves when the economy is more developed, and when the economy reaches a certain level (per capita GDP is higher than a certain level), there will be a turning point—environmental quality and economic development have entered a phase of positive correlation. Therefore, the development model implied by EKC is the development model of "pollution first, governance later." Generally speaking, this environmental quality is inverted with economic growth. EKC reveals the relationship between environmental pollution and economic development in two aspects: one is the "dilemma" positive correlation, and the other is the "win-win" negative correlation. From the history of developed countries, as the per capita income level increases from low to high, the pollution index increases, and the relationship between the economy and the environment is in the "dilemma" range. When the per capita income reaches a certain level, the pollution index declines, and the relationship between the economy and the environment is in a "win-win" range.

RESULTS

(1) Comment on the economic development of Chengdu from 2005 to 2018. Since one variable in the Kuznets curve is per capita GDP, it is necessary to comment on the economic development of Chengdu from 2005 to 2018.

1) Economic aggregate situation. From 2005 to 2018, the total GDP of Chengdu increased from less than 237.101 billion yuan to 1.5344 billion yuan, an increase of more than six times (Figure 1). Per capita GDP increased from 17782 yuan to 96982 yuan. Chengdu's GDP has shown a continuous growth trend, and per capita GDP has increased year by year (Figure 2).

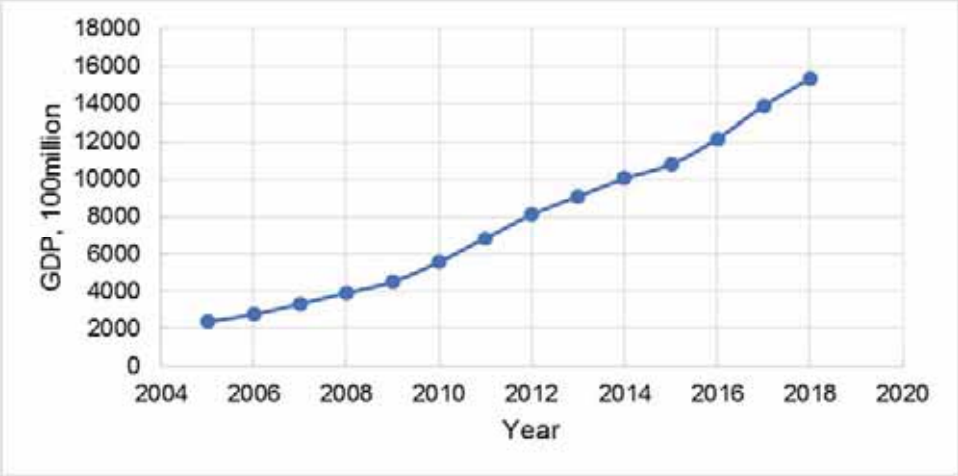

FIGURE 1
Changes in Chengdu's GDP over time.

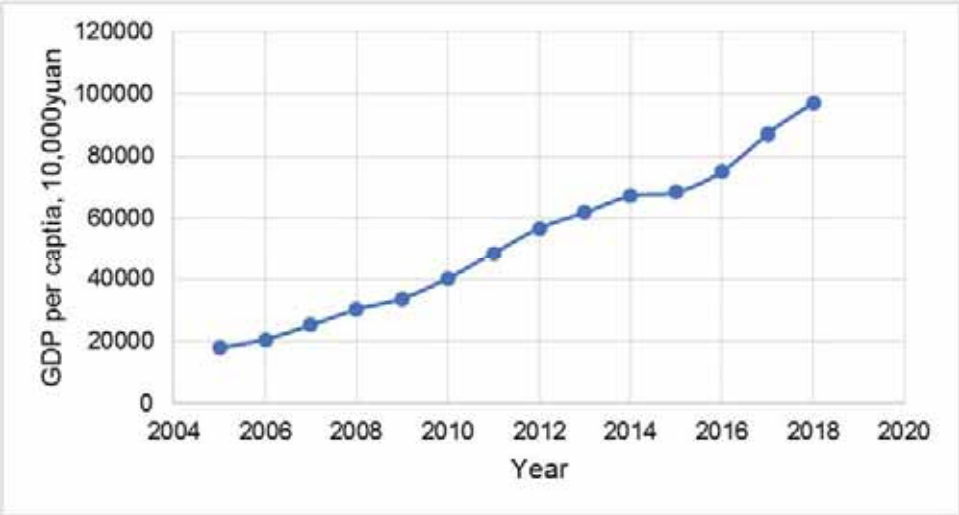

FIGURE 2
Changes in Chengdu's GDP per capita over time.

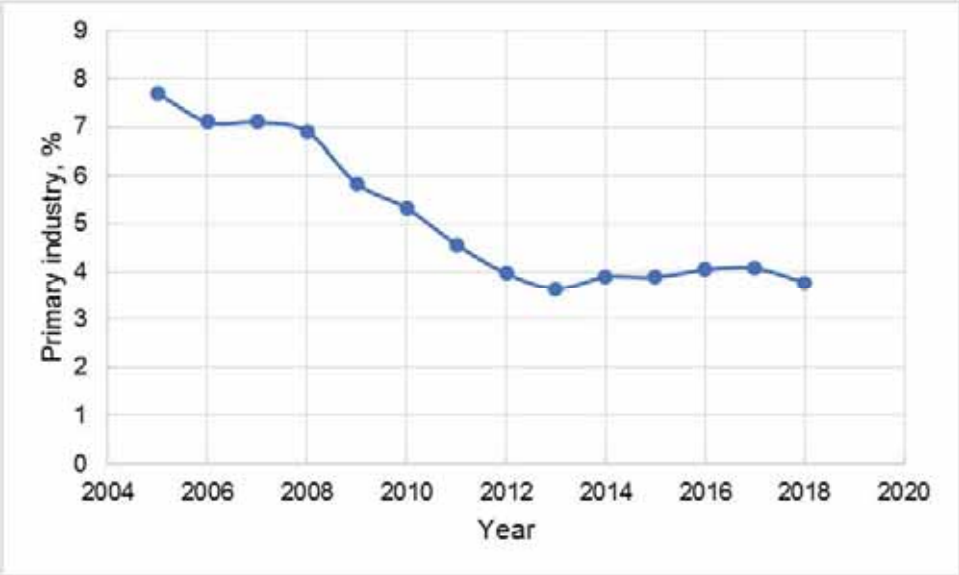

FIGURE 3
Trend chart of the proportion of the primary industry in the total GDP.

2) Change trend of industry proportion. There are two possible explanations for the appearance of the Environmental Kuznets Curve (EKC): First, the changes in the industrial structure in the process of economic growth, from a clean agricultural economy to a severely polluted industrial economy to a clean service industry economy which leads to the emergence of the EKC phenomenon. Second, in the first stage of industrialization, pollution increases rapidly. Increasing material output has a greater priority than protecting the environment, and people prefer employment and income compared with clean air. Rapid economic growth inevitably causes excessive consumption of natural resources and serious environmental pollution, which has brought great pressure to the environment.

But at this stage of economic development, people do not have more resources to protect the environment, so that they ignore the negative impact of environmental pollution on sustainable economic growth. In the next stage of industrialization, as the economy grows, people begin to pay attention to environmental problems, and they have the ability to solve environmental problems, and the pollution level drops accordingly. Changes in the proportion of GDP are also analyzed. According to the obtained relevant economic data, the change trends of the primary, secondary, and tertiary industries are drawn as shown in Figures 3-5.

From the perspective of changes in the internal structure of the industry, the proportion of the output value of the primary industry was in a declining trend from 2005 to 2013, from 7.7% in 2005 to 3.63% in 2013. After that, the proportion of its primary industry remained stable. Generally speaking, for Chengdu, the employment in the primary industry is relatively small, indicating that there is less dependence on the primary industry.

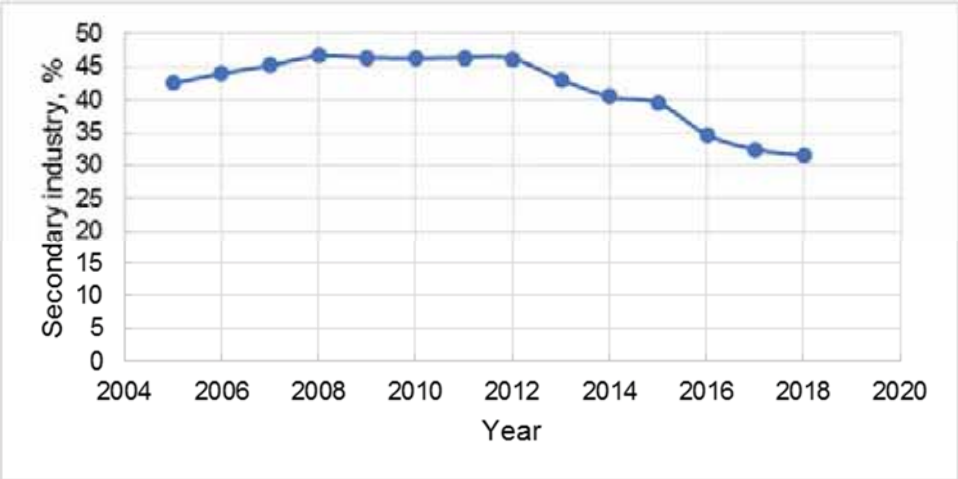

FIGURE 4
Trend chart of the proportion of the secondary industry in the total GDP.

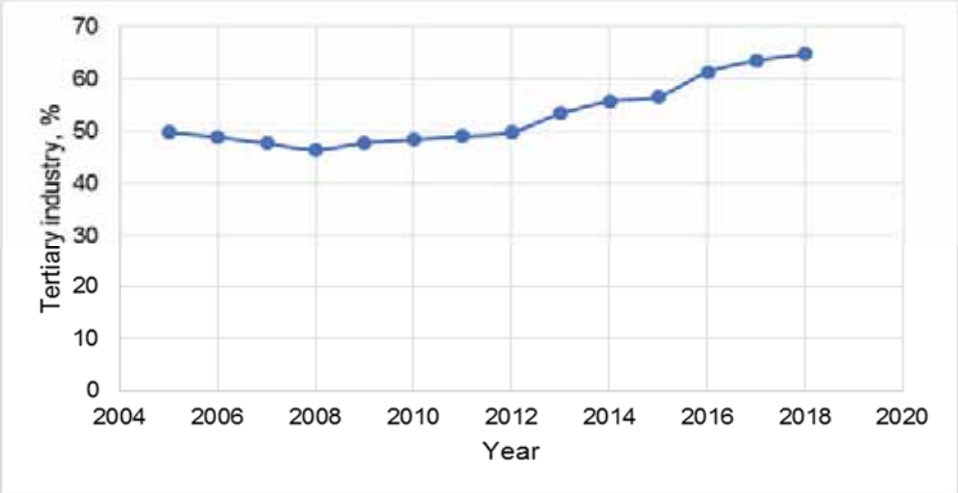

FIGURE 5
Trend chart of the proportion of tertiary industry in total GDP.

The proportion of the secondary industry in the total GDP has experienced a slow rise, reaching 46.17% at the highest, and then there has been a process of small fluctuations and declines (Figure 4). This is due to the gradual establishment of Chengdu's industrial system as the capital investment in industry increases, and the secondary industry has experienced a period of steady growth. In the later period, due to the slowing down of the industrial development speed, the proportion of the tertiary industry relatively increased, and the proportion declined.

From 2005 to 2012, the output value of the tertiary industry accounted for about 50% of the total GDP. After that, the proportion of the tertiary industry showed a gradual increase, from 53% in 2013 to 63.7% in 2018, an increase of 10% (Figure 5).

(2) Selection of environmental index system. The empirical analysis in this section is based on the environmental Kuznets curve, taking Chengdu's 2005-2018 empirical data as a sample, we establish an econometric model, and apply regressing analysis of major environmental indicators and per capita GDP to study the relationship between Chengdu's economic growth and environmental quality changes. The selection of indicators mainly considers the needs of research purposes and the availability of data. Some studies select ecological quality indicators and participate in the study of the relationship with economic growth. This is a very good research trend and deserves the attention of researchers in this field. But at present, there are still many immature factors in the use of ecological quality as an indicator to study. First, the current ecological quality indicator system is in the qualitative description or semi-qualitative and semi-quantitative stage, and it is difficult to accurately and objectively determine its impact on the entire contribution value of environmental quality. At the same time, environmental pollution causes the decline of environmental quality, part of which is reflected by the impact on ecological quality, and some environmental quality indicators and ecological quality indicators have overlapping networks. Therefore, when establishing the model in this paper, based on the principles of objectivity and

quantification, economic factors are abstracted as income, and water pollutant discharge, gas pollutant discharge, and solid waste discharge are selected as environmental quality indicators. We carry out regression analysis on relevant economic indicators and environmental indicators and study the correlation between economic development and environmental quality changes in Chengdu. The sample data comes from the "Chengdu Statistical Yearbook" and "China Statistical Yearbook" of each year and strive for the reliability and scientificity of the original data sources.

(3) Time series relationship between water environment indicators and GDP per capita. Water environment is the number one problem that needs to be solved in the ecological construction of Chengdu. Figure 6 shows the time series relationship between industrial wastewater discharge and per capita GDP in Chengdu. As shown in Figure 6, the discharge of industrial wastewater showed a slow downward trend from 2005 to 2010. In 2012, the discharge of industrial wastewater rose sharply, and after 2014, the discharge of wastewater decreased again.

(4) Time series relationship between atmospheric environmental indicators and GDP per capita. With the rapid economic development, energy consumption has increased rapidly. The coal-based energy structure and outdated combustion technology have led to relatively serious air pollution in some areas. Controlling air pollution and improving environmental quality have become an important part of the road to sustainable development. This section uses industrial SO_2 emissions and smoke and dust emissions as indicators and uses Chengdu's 2005-2018 time series data to study the correlation between the atmospheric environmental quality and the level of economic development.

1) Time series relationship between SO_2 emissions and GDP per capita. As the most typical representative of exhaust gas, SO_2 emissions have a great impact on people's living environment. Sulfur dioxide is mainly produced by burning coal and fuel oil and other sulfur-containing substances. The massive emission of sulfur dioxide has made the city's air pollution aggravated. Sulfur dioxide has a strong irritation to the human conjunctiva and upper respiratory tract mucosa, which can damage the breathing apparatus tube and cause bronchitis, pneumonia, and even pulmonary edema, respiratory paralysis. In addition, the massive emission of sulfur dioxide will cause the formation of “acid rain”. Environmental monitoring data show that due to the increase of acidic substances in the atmosphere, the cloud water over most of the province is becoming acidic. If it is not controlled, the area of acid rain area will continue to expand, and the harm to humans will also increase day by day. Figure 7 shows that SO_2 emissions show a downward trend as a whole. In 2005, SO_2 emissions were 122,697 tons. By 2018, SO_2 emissions were 11,181 tons, a reduction of more than 90%.

2) Time series relationship between industrial smoke (dust) emissions and GDP per capita. Smoke and dust are solid particles emitted during coal combustion and industrial production. As another typical representative of industrial waste gas, its emission is closely related to people's living environment. Soot particles will not only be deposited in the lungs but can also directly enter the blood to reach various parts of the human body, causing various respiratory diseases. Toxic smoke and dust will destroy human health and even life. Figure 8 shows that from 2005 to 2018, industrial dust emissions showed a downward trend. In 2005, the discharge of industrial dust was 189,361 tons. By 2018, the discharge of industrial dust was reduced to 9,936 tons, a reduction of more than 95% (Figure 8).

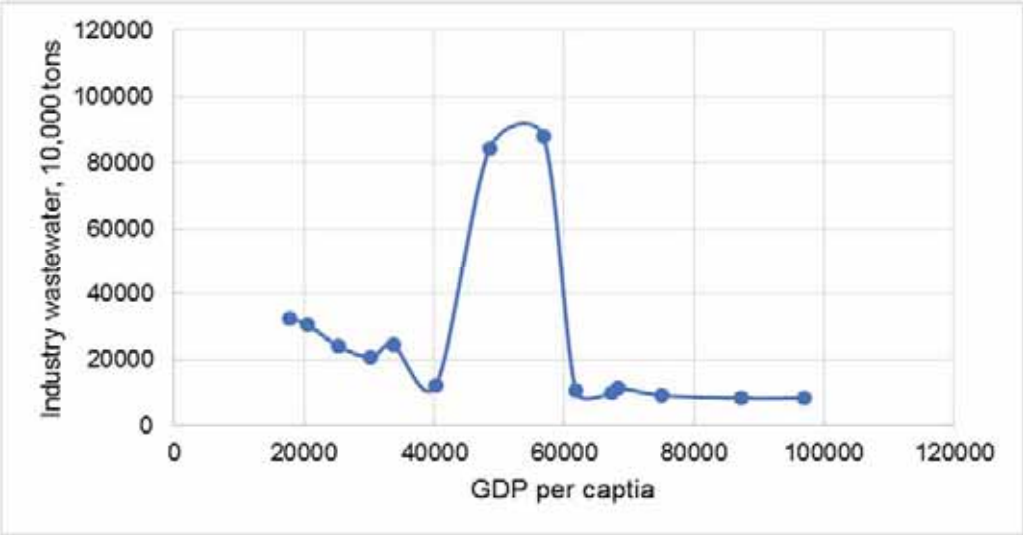

FIGURE 6
Kuznets curve of total wastewater discharge.

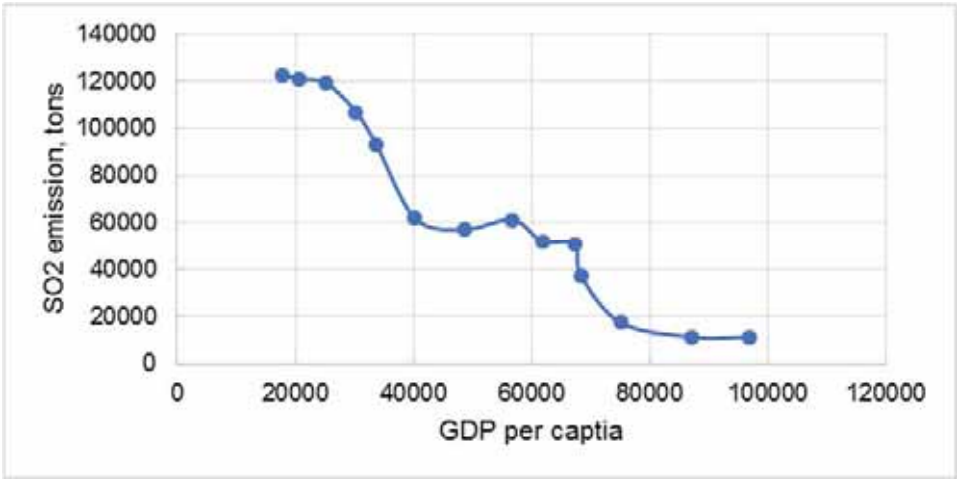

FIGURE 7
Kuznets curve of SO_2 emissions.

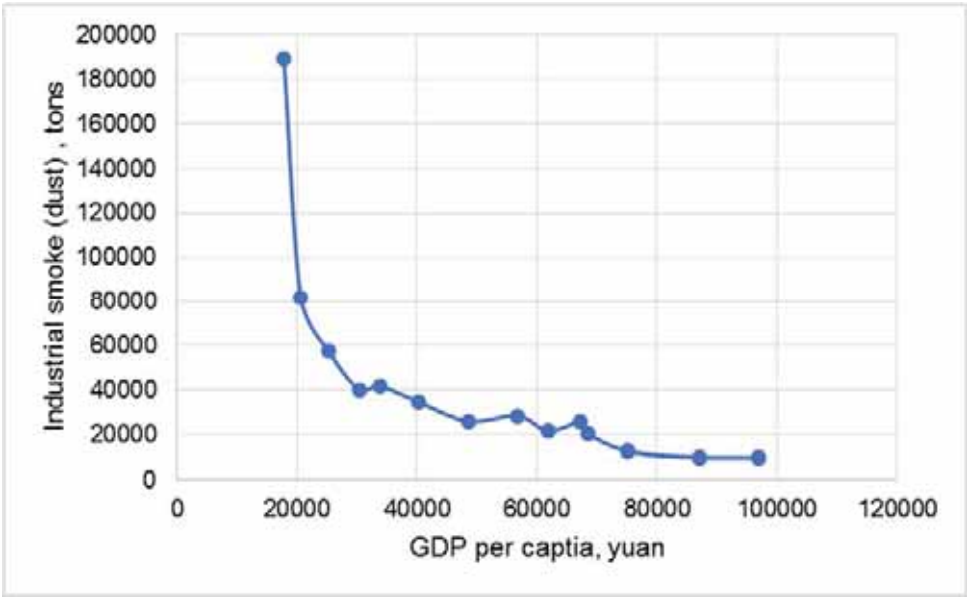

FIGURE 8
Kuznets curve of industrial dust emission.

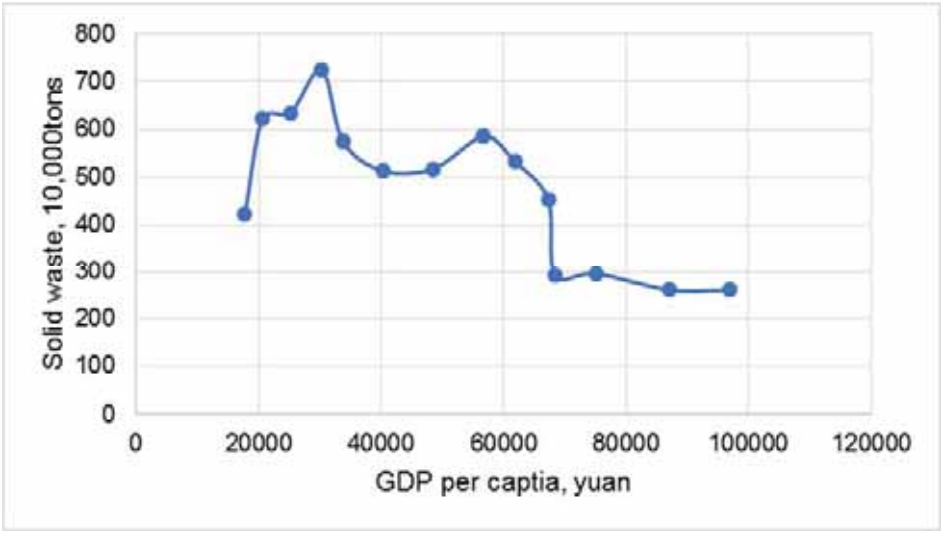

FIGURE 9
Kuznets curve of industrial solid waste emissions.

(5) Time series relationship between industrial solid waste discharge and GDP per capita. Chengdu is rich in mineral resources. Since the 1990s, various construction undertakings in Chengdu have achieved great development, especially in basic industries such as ferrous metal industry, non-ferrous metal industry, chemical industry, coal industry, thermal power industry and building materials industry. At the same time, the above-mentioned industrial sectors also produced a large amount of solid wastes during the production process, such as tailings, metallurgical slag, coal liver stone, coal slag, fly ash, and chemical slag. The solid waste generated by the industrial sector is dumped in mining areas, suburbs, or discharged into rivers, causing various harms to the soil, water bodies, atmosphere, and biological communities, destroying the ecological balance to varying degrees. Figure 9 shows that the discharge of solid waste shows a certain volatility over time. From 2005 to 2008, the discharge of solid waste showed an increasing trend. After 2011, the emissions of solid waste showed a downward trend, and after 2015, the emissions remained stable.

(6) Suggestions. In accordance with the principle of "regional economic development must be unified with environmental carrying capacity, and regional economic development must be coordinated with environmental protection", the environmental protection measures and environmental access of different regions should be taken in accordance with local conditions, and development patterns with their own characteristics have been gradually formed. We need to obtain funds through multiple channels to increase investment in environmental science and technology innovation, increase support for environmental science and technology and research conditions, and build a basic platform for environmental science and technology. We need to do a good job in the finishing work of the city's pollution source survey and soil pollution survey and manage and use the results of major provincial surveys. We also need to take measures to encourage and support the independent innovation of environmental protection enterprises and the introduction and digestion of advanced and applicable environmental protection high-tech technologies at home and abroad, so as to improve the core technical capabilities and market competitiveness of environmental protection enterprises.

We need to give full play to the role of industry associations and other intermediary organizations, improve and standardize the environmental protection consulting service market, establish unified and standardized environmental protection market operation rules, and actively implement a professional qualification system in accordance with national requirements. We must strengthen environmental protection publicity and education, continuously enhance the resource awareness and environmental awareness of the whole society, guide the public, social organizations, and the news media to pay attention to and supervise the environmental behavior of enterprises, and create an environment for the whole society to participate in environmental protection. Focusing on the requirement to be a pioneer in the construction of ecological civilization in the country, we have carried out in-depth environmental sunshine actions, green creation actions, and green dissemination actions. We need to strengthen the training and education of environmental protection laws and regulations and environmental protection responsibilities of leading cadres at all levels, improve the awareness of law-abiding by leading cadres at all levels, and clarify environmental protection responsibilities. Only by doing this can we improve the environment of the Chengdu better.

CONCLUSIONS

(1) Chengdu's GDP has shown a continuous growth trend, with per capita GDP increasing year by year. For Chengdu, the employment in the primary industry is relatively small, indicating that there is less dependence on the primary industry. The proportion of the secondary industry in the total GDP has experienced a slow increase at the beginning and then a slight fluctuation and decline. After 2013, the proportion of the tertiary industry has shown a gradual increase.

(2) The discharge of industrial wastewater showed a slow downward trend from 2005 to 2010. In 2012, the discharge of industrial wastewater rose sharply, and after 2014, the discharge of wastewater showed a downward trend. The overall SO_2 emissions showed a downward trend. In 2005, SO_2 emissions were 122,697 tons. By 2018, SO_2 emissions were 11,181 tons, a reduction of more than 90%. From 2005 to 2018, the emissions of industrial dust showed a downward trend. In 2005, the discharge of industrial dust was 189,361 tons. By 2018, the discharge of industrial dust was reduced to 9,936 tons, a reduction of more than 95%. From 2005 to 2008, the discharge of solid waste showed an increasing trend. After 2011, the emissions of solid waste showed a downward trend, and after 2015, the emissions remained stable.

(3) After 2015, the Kuznets curve in Chengdu fell within the win-win range. It shows that after 2015, human activities in Chengdu can improve the quality of the environment on the one hand, and at the same time obtain economic profits. The environment and economy in Chengdu develop in harmony.

ACKNOWLEDGEMENTS

This work was not supported by any funds. The authors would like to show sincere thanks to those techniques who have contributed to this research.

REFERENCES

[1] Fu, B.J., Zhuang, X.L., Jiang, G.B., Shi, J.B., Lu, Y.H. (2007) Environmental problems and challenges in China. Environmental Science & Technology. 41(22), 7597-7602.
[2] Ogri, O.R. (2001) A review of the Nigerian petroleum industry and the associated environmental problems. Environmentalist. 21(1), 11-21.
[3] Cox, M. (2011) Advancing the diagnostic analysis of environmental problems. International Journal of the Commons. 5(2), 346-363.
[4] Vanderpost, C. (1995) Population change and environmental problems in the Mid-Boteti region of Botswana. GeoJournal. 35(4), 521-529.
[5] Onokerhoraye, A.G. (1976) Urban environmental problems and planning strategies in Tropical Africa: the example of Nigeria. Annals of Regional Science. 10(2), 24-35.
[6] Mazurski, K.R. (1998) Environmental problems in the Sudetes, Poland. Geojournal. 46(3), 271-277.
[7] Marale, S.M. (2012) Shifting role of ecology in solving global environmental problems: selected practical tools. Environment, Development and Sustainability: A Multidisciplinary Approach to the Theory and Practice of Sustainable Development. 14(6), 869-884.
[8] Coates, J.F. (1991) The sixteen sources of environmental problems in the 21st century. Technological Forecasting and Social Change. 40(1), 87-91.
[9] Yedla, S. (2006) Dynamics of environmental problems in Mumbai. Clean Technologies and Environmental Policy. 8(3), 182-187.
[10] Kim, I.K. (1994) The environmental problems in urban communities and the protection of the environment in Korea. Korea Journal of Population & Development. 23(1), 63-76.
[11] Norway, E.F. (1998) Factoring the environmental Kuznets curve. Discussion Papers. 35(2), 126-141.
[12] Berrens, R.P., Hui, L., Grijalva, T. (2007) Economic growth and environmental quality: a meta-analysis of environmental Kuznets curve studies. Economics Bulletin. 17(5), 1-11.
[13] Mills, J.H., Waite, T.A. (2009) Economic prosperity, biodiversity conservation, and the environmental Kuznets curve. Ecological Economics. 68(7), 2087-2095.
[14] Cole, M.A. (2004) Trade, the pollution haven hypothesis and the environmental Kuznets curve: examining the linkages. Ecological Economics. 48(1), 71-81.
[15] Agras, J., Chapman, D. (1999) A dynamic approach to the environmental Kuznets curve hypothesis. Ecological Economics. 28(2), 267-277.
[16] Luzzati, T., Orsini, M. (2009) Investigating the energy-environmental Kuznets curve. Energy. 34(3), 291-300.
[17] Dinda, S. (2005) A theoretical basis for the environmental Kuznets curve. Ecological Economics. 53(3), 403-413.
[18] Bertinelli, L., Strobl, E. (2005) The environmental Kuznets curve semi-parametrically revisited. Economics Letters. 88(3), 350-357.
[19] Khanna, N., Plassmann, F. (2004) The demand for environmental quality and the environmental Kuznets curve hypothesis. Ecological Economics. 51(3/4), 225-236.
[20] Chimeli, A.B., Braden, J.B. (2005) Total factor productivity and the environmental Kuznets curve. Journal of Environmental Economics & Management. 49(2), 366-380.
[21] Tsurumi, T., Managi, S. (2010) Decomposition of the environmental Kuznets curve: scale, technique, and composition effects. Environmental Economics & Policy Studies. 11(1-4), 19-36.
[22] Hartman, R., Kwon, O.S. (2002) Sustainable growth and the environmental Kuznets curve. Journal of Economic Dynamics & Control. 29(10), 1701-1736.
[23] Meng, Y., Pu, J., Zhao, W.J., Sun, G.J., Chen, W.K. (2021) The relationship between air quality and economic growth based on the environmental Kuznets curve -taking Sichuan province as an example. Fresen. Environ. Bull. 30(7A), 9355-9362.
[24] Leng, J.F., Yuan, L.D. (2021) An empirical analysis of the environmental Kuznets curve in the Huaihe River Basin. Fresen. Environ. Bull. 30(7), 9355-9362.
[25] Yue, Y., Ying, Y.R. (2021) Analysis of china's environmental Kuznets curve from the perspective of PM2.5 index. Fresen. Environ. Bull. 30(5), 5262-5269.

Received: **26.11.2021**
Accepted: **11.01.2022**

CORRESPONDING AUTHOR

Wen Wu
School of Finance,
Chengdu Jincheng College,
Chengdu Sichuan 610097 – China

e-mail: yujingjing3333@163.com

© by PSP Volume 31– No. 05/2022 pages 4967-4974 Fresenius Environmental Bulletin

HIGH EFFICIENCY TOPOGRAPHIC SURVEY ON RESERVOIR BY UAV TILT PHOTOGRAMMETRY

Hongbao Dai[1], Jiying Xu[2,3,*]

[1]School of Environment and Surveying Engineering, Suzhou University, Suzhou, 234000, Anhui, China
[2]School of Resources and Geoscience, China University of mining and technology, Xuzhou, 221116, Jiangsu, China
[3]National Engineering Research Center of Coal Mine Water Hazard Controlling (Suzhou University), Suzhou, 234000, Anhui, China

ABSTRACT

The UAV tilt photogrammetry is a method that can be used to obtain large-area and high-precision 3D point cloud data after remote sensing and 3D laser scanning, which has the advantages of low labor intensity, high efficiency and little impact on the environment. It is widely used in various fields, and is in the trial stage in reservoir measurement. In this research, Guniubei reservoir was taken as the study area. The RTK (real-time dynamic difference technology) was used to obtain the coordinates of ground control points. The aerial photogrammetry were carried out by Dajiang spirit 4 UAV (unmanned aerial vehicle), with 35 photo control points and 42 check points, and then 3D model of reservoir was established. Evaluated by mean square error, M_S and M_H of root control points were 0.051m and 0.065m respectively, and the M_H of the detail points was 0.098m, which all met the accuracy requirements. For the tidal-flat area, the safety of UAV photogrammetry was much higher than that of manual field measurement. The outcomes of this research provide basis for comprehensive efficient topographic survey and reservoir capacity of hydraulic engineering.

KEYWORDS:
UAV, Photogrammetry, Guniubei Reservoir, Accuracy evaluation

INTRODUCTION

Water conservancy project is the basic industry of social and economic development, which has the functions of flood control, water storage and irrigation, water supply, power generation, fish culture and so on, so as to promote the development of national economy and ensure the safety of people's property [1]. The Surveying reservoir is the key step of water conservancy design, which can obtain high-precision geographic information and provides an important basis for the reinforcement and safety appraisal of reservoir [2,3].

The traditional artificial field measurement of reservoir has some problems, such as high labor intensity, high cost, easy to be affected by the field environment, etc. For the disordered beach around the reservoir, the surveyors were not easy to reach due to high and steep slope and numerous trees, leading to low efficiency [4]. In recent years, unmanned aerial vehicle (UAV) technology has been widely used in meteorological monitoring , land use survey, large-scale surveying and mapping and other fields [5,6]. The UAV photogrammetry completes the photographing of the ground in the air, which is almost not limited by the terrain, reducing the workload and difficulty of the field work. In addition, UAV flight has low requirements for landing site selection, and good weather conditions can ensure the timeliness and continuity of data acquisition [7]. The application of UAV photogrammetry can solve the problems of difficult implementation and incomplete scope due to wide area and complex environment [8]. However, the application UAV photogrammetry on reservoir topographic survey remains unclear, which need to be solved urgently.

The objectives of this paper are as follows: (1) to obtain image by aerial photography with spirit 4 UAV and construct 3D model by Context Capture Master software, (2) to evaluate the accuracy and efficiency of UAV and manual measurement (GPS-RTK). The outcomes of this research provide basis for comprehensive topographic survey and reservoir capacity of hydraulic engineering.

MATERIALS AND METHODS

Study Area. The Guniubei reservoir is located about 9.4km southwest of Tongcheng City, Anhui Province, China (Figure 1). It is a key medium-sized water conservancy and hydropower project in Anhui Province, which mainly focuses on irrigation and possess comprehensive benefits of flood control, power generation, urban water supply, breeding and tourism. The rainwater collection area of the reservoir is 125km^2, with total capacity 75.93 million m^3 and the flood regulation capacity 25.93 million m^3, and the dead capacity is 0.041 million m^3. The climate of the study area is subtropical humid, characterized by mild, abundant rain, sufficient light, four

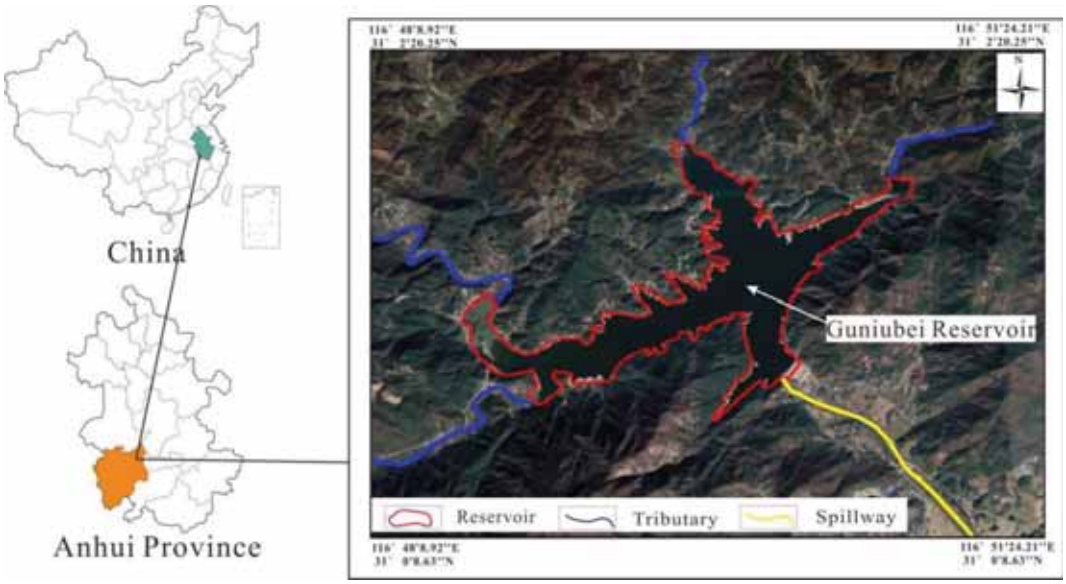

FIGURE 1
Geographical location map of the study area.

$$X - X_0 = -f\frac{a_1(X-X_S)+b_1(Y-Y_S)+c_1(Z-Z_S)}{a_3(X-X_S)+b_3(Y-Y_S)+c_3(Z-Z_S)}$$
$$Y - Y_0 = -f\frac{a_2(X-X_S)+b_2(Y-Y_S)+c_2(Z-Z_S)}{a_3(X-X_S)+b_3(Y-Y_S)+c_3(Z-Z_S)} \quad (1)$$

distinct seasons, suitable for the growth for variety of crops. with annual average temperature 15.8°C, the annual average precipitation 1326.9 mm, annual average sunshine hours 1903.34 hours, the sunshine percentage 43%, and annual average frost free period 246 days.

Principle of Photogrammetry. The UAV photogrammetry technology is to obtain high-resolution digital images as the target, unmanned aircraft as the flight platform, high-resolution digital camera as the sensor, using 3S technology, and finally obtain small area, true color, large-scale, strong current aerial remote sensing data [9]. Then, the processing and matching of image are carried out by computer software, the corresponding image points and coordinates are automatically identified, the three-dimensional coordinates of the object are determined by analytic photogrammetry, and the geographic information such as digital elevation model, orthophoto digital image, graphic contour map and orthophoto map with contour line are output [10]. The calculation formula [11] is as follows (1), (2) and (3).

$$\frac{X}{X_A - X_S} = \frac{Y}{Y_Y - Y_S} = \frac{Z}{Z_Z - Z_S} \quad (2)$$

$$R^T = \begin{bmatrix} a_1 & b_1 & c_1 \\ a_2 & b_2 & c_2 \\ a_3 & b_3 & c_3 \end{bmatrix} \quad (3)$$

In the formulas, f represents the inner orientation element. Both X_0 and Y_0 are exterior orientation elements [12]. The rotation orthogonal matrix R^T is imported from the input X, Y, Z into the collinear equation to get the actual ground data, and then introduce multiple groups of photos to obtain the highest precision 3D model [13].

Data Processing. The image of the study area was obtained by aerial photography with spirit 4 UAV (Dajiang, China), the 3D model was constructed by Context Capture Master software (Bentley), and the digital orthophotomap was made with CASS software [14]. Moreover, 42 check points in the study area were selected, and the accuracy and efficiency of UAV model and manual measurement (GPS-RTK) were compared. The research was shown in Figure 2.

RESULTS AND DISCUSSION

Preparation of Aerial Photogrammetry. In view of high and steep slope of the Guniubei reservoir, with the maximum gradient 80°and maximum drop 270 m, so the flight route was designed by layers and blocks. In order to obtain better images, the center of each block was selected as the flight site. Consideration elevation of the reservoir was relative higher, the wind speed was strong and changes frequently, therefore the difficulty coefficient of this

aerial survey was great, it was adjusted in time according to the field weather, wind speed, wind direction and other conditions.

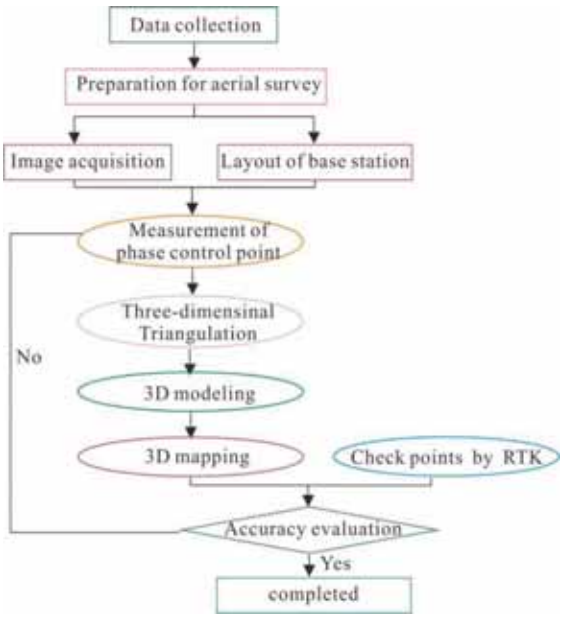

FIGURE 2
Flow chart of data processing

Control Surveying. In order to unify the 3D model to CGC2000 coordinate system, control surveying should be carried out firstly [15]. In general, the layout of control points follow the principle of "more around, less inside", with 3-5 image control points per square kilometer. Combined with the actual terrain, 35 photo-control points and 42 check points were set up in the study area, and the coordinates of control points under CGC2000 coordinate system were obtained through RTK, as shown in Figure 3.

UAV Image Acquisition. The Dajiang spirit 4 UAV was used to obtain the image of the study area. The detailed process was as follows: with Google image as the base map, the waypoint data was generated after inputting parameters, and the planned route was uploaded to the UAV flight control system [16]. In order to meet the accuracy requirements of reservoir survey, the design height of this aerial survey was set to 110m, 16 routes and 10 sorties were arranged, the overlap of heading and side direction was 80%, and the horizontal flight speed was 6m/s. The results of aerial survey showed that 2276 images were obtained from 5 cameras, with the image size of 5472 × 3678 pixels, and the average ground resolution of tilt image was 2.08cm.

3D Modeling and Post Processing. According to the control surveying and UAV images, the context capture master software was used to process the indoor data [17,18] and the three-dimensional model of the study area can be obtained according to the flow chart shown in Figure 4.

The compilation of topographic map mainly includes the extraction and processing of Geomorphic elevation and surface feature data. The 3D EPS software was commonly applied to extract the geomorphic elevation data. After loading the real 3D model obtained by aerial photo processing and extracting elevation, the overall 3D modeling of the study area were established, as shown in Figure 5a. Moreover, some key details of the 3D model, such as the dam and tidal flat, were also shown in Figure 5b, c, d.

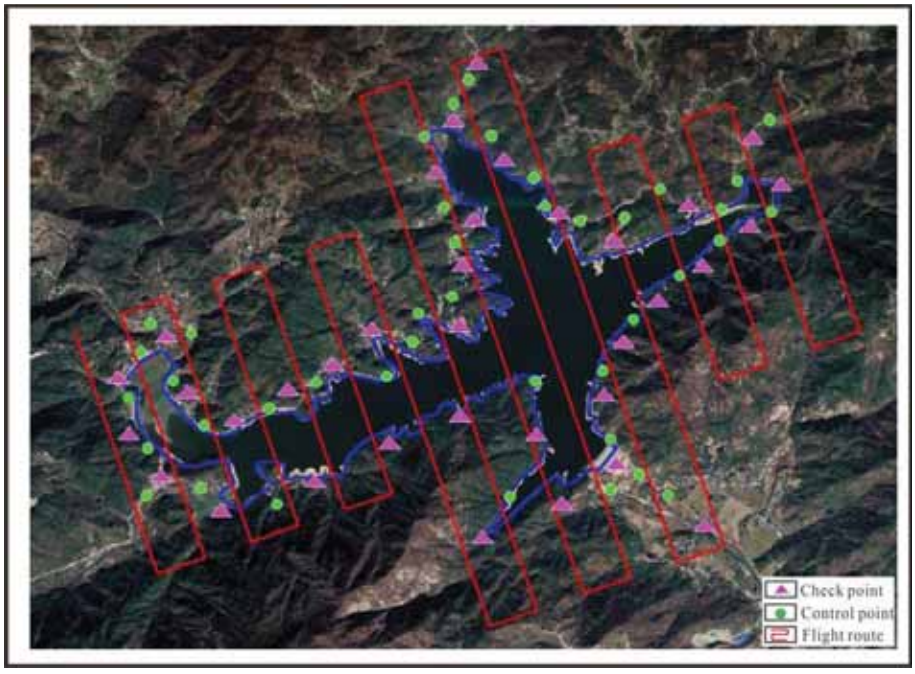

FIGURE 3
Layout of route, control points and check points

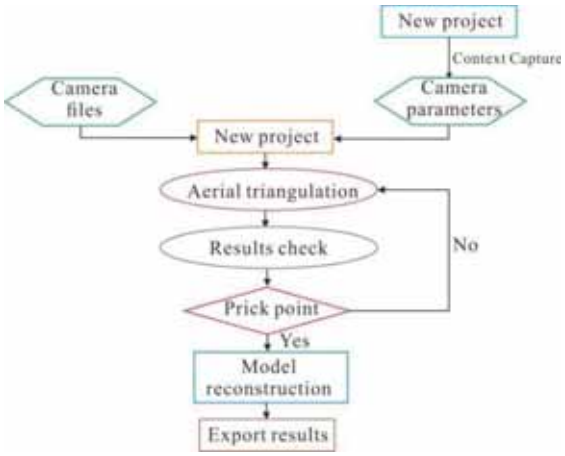

FIGURE 4
Flow chart of 3D modeling.

The surface feature data were extracted by Cass software. After loading the DOM obtained aerial photo processing, the elevation point and surface feature data were merged and then plotted to generate contour lines and completed topographic map [19], as shown in Figure 6.

Model Accuracy Evaluation. Mean square error is a useful way to analysis the accuracy of measurement, composing of M_S (plane) and M_H (elevation). The calculation formula of M_S and M_H [20] are follows (4), (5) and (6).

$$M_S = \sqrt{\frac{\sum(\Delta S)^2}{n}} \quad (4)$$

$$M_H = \sqrt{\frac{\sum(\Delta H)^2}{n}} \quad (5)$$

$$\Delta S = \sqrt{(\Delta X)^2 + (\Delta Y)^2} \quad (6)$$

In the formulas, the Δ s is the plane distance error, Δ x, Δ y and Δ h are the absolute error of three-dimensional coordinates respectively, and n represents the number of measuring points. Based on the manual measurement data (RTK) and 3D model measurement data (UAV), M_S and M_H can be calculated.

Evaluation of Root Control Surveying. A total of 42 root level accuracy check points (Figure 3) were measured in this study, which aim to check the plane and elevation accuracy of topographic map. According to the accuracy requirements of field survey, 3D coordinates of check points were obtained by RTK. Meanwhile, another coordinates also extracted from 3D modeling for the same 42 check points. The field surveying data were subtracted from the corresponding 3D model measurement data, and the absolute errors of the Δ x, Δ y, Δ h and Δ s were calculated, which were shown in Table 1.

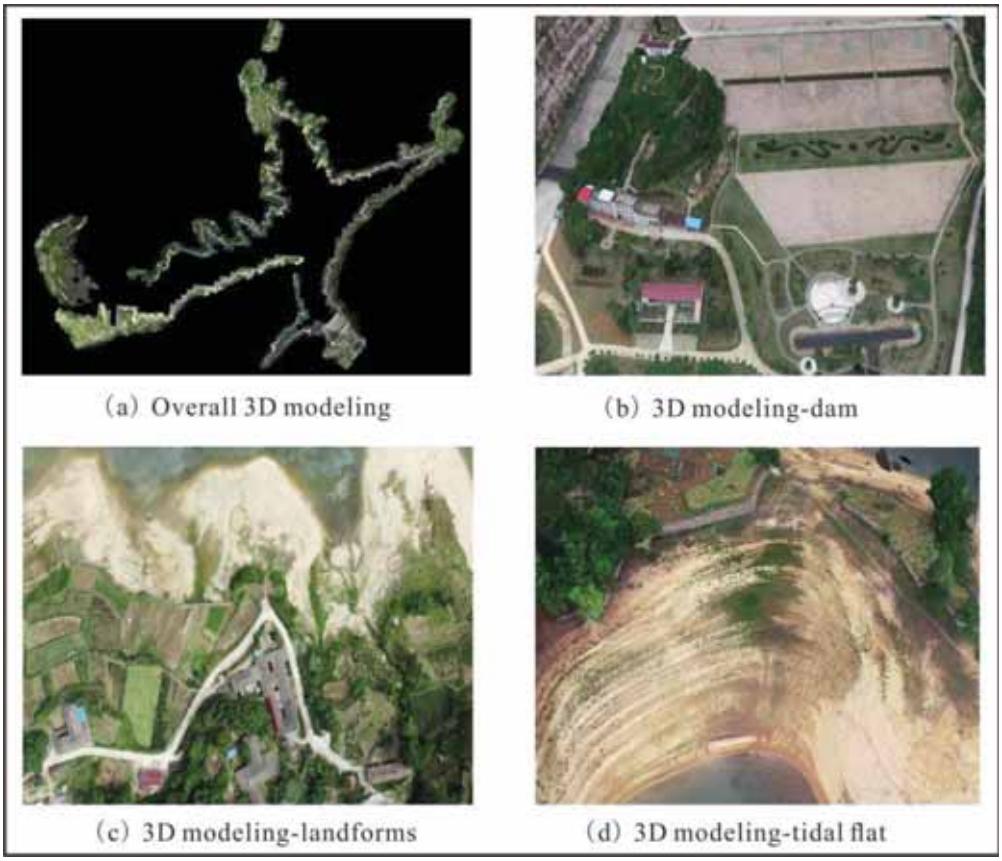

FIGURE 5
3D model of Guniubei reservoir

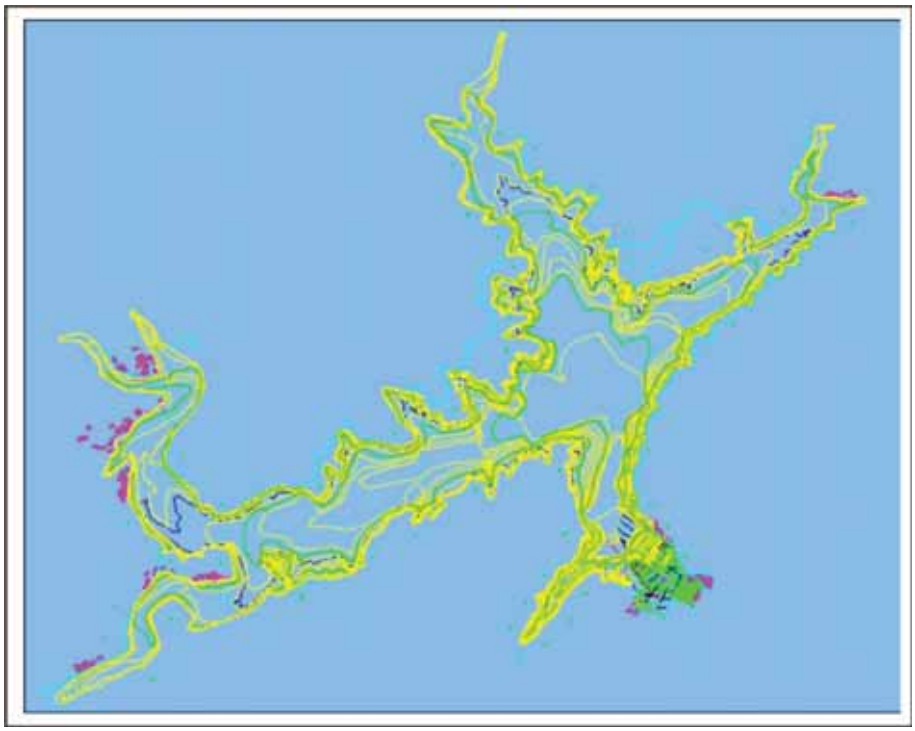

FIGURE 6
Topographic map of Guniubei reservoir

TABLE 1
Accuracy calculation results based on Root Control Surveying

point	△X (m)	△Y (m)	△H (m)	△S (m)	point	△X (m)	△Y (m)	△H (m)	△S (m)
1	-0.028	0.019	0.052	0.034	22	0.012	0.037	-0.066	0.039
2	0.043	0.037	0.030	0.057	23	0.046	-0.024	0.064	0.052
3	0.017	-0.034	-0.081	0.038	24	0.008	0.026	0.093	0.027
4	-0.021	0.056	0.049	0.060	25	0.028	0.045	0.074	0.053
5	0.039	0.015	0.068	0.042	26	0.047	0.026	0.038	0.054
6	0.048	0.026	0.079	0.055	27	-0.024	0.040	0.032	0.047
7	-0.043	0.013	0.083	0.045	28	0.036	0.002	0.070	0.036
8	0.047	0.022	0.005	0.052	29	0.015	0.072	0.039	0.074
9	0.016	0.042	0.075	0.045	30	0.036	0.041	-0.072	0.055
10	0.047	0.051	0.044	0.069	31	0.046	-0.020	0.058	0.050
11	0.051	-0.017	-0.067	0.054	32	0.012	0.033	0.107	0.035
12	-0.027	-0.033	0.063	0.043	33	0.032	0.029	0.088	0.043
13	0.023	0.015	0.078	0.027	34	0.041	0.013	0.052	0.043
14	0.052	0.016	0.059	0.054	35	-0.013	0.064	0.014	0.065
15	-0.027	0.030	0.023	0.040	36	0.060	0.016	0.084	0.062
16	0.041	-0.018	-0.015	0.045	37	0.029	0.016	0.053	0.033
17	0.036	0.062	0.055	0.072	38	0.031	0.055	-0.058	0.063
18	0.057	0.031	0.024	0.065	39	0.054	-0.036	0.072	0.065
19	-0.049	-0.021	-0.087	0.053	40	0.016	0.014	0.087	0.021
20	-0.047	0.050	0.043	0.069	41	0.036	0.019	0.068	0.041
21	0.023	0.028	0.092	0.036	42	0.025	0.038	0.070	0.045

According to the Specifications for aerophotogrammetric office operation 1:500, 1:1000, 1:2000 topographic map (GB7930-87) [21], M_S and M_H of 1:1000 topographic map in mountainous and hilly areas of root point should be less than 0.1m and 0.1m respectively. The calculated results of M_S and M_H for the study area were 0.051m and 0.065m respectively, suggesting plane and elevation accuracy met the specification requirements.

Elevation Accuracy Based on Detail Points. During water conservancy and hydropower survey, elevation accuracy play an more important role than

plane accuracy, so it is necessary to check the elevation accuracy by another method. In this study, 100 detail points were evenly selected from the Guniubei reservoir, and then RTK survey was carried out to obtain each elevation data. Moreover, the elevation data of these 100 detail points were extracted from the built 3D model. Finally, the two groups of data were subtracted to get △h, which were shown in Table 2.

According to the Specifications for aerophotogrammetric office operation 1:500, 1:1000, 1:2000 topographic map (GB7930-87) [21], M_H of 1:1000 topographic map in mountainous and hilly areas of detail point should be less than 0.3m. The calculated results of M_H was 0.098m, implying elevation accuracy met the specification requirements again.

Efficiency analysis. The workload of UAV and manual measurement(RTK) was compared and listed in Table 3,which mainly included the geographic coordinates of beach, dam and surrounding landform. It can be seen from Table 3 that UAV needed 4 surveyors and 2 days in total, and manual measurement (RTK) needs 7 surveyors and 9 days in total. Therefore, the work efficiency of UAV was greatly improved compared with manual measurement. In addition, for tidal-flat area with many trees and disordered places, the surveyors were generally not easy to reach, existing high security risks, so the application of UAV measurement also improved safety.

CONCLUSIONS

Main conclusions obtained from this research are listed as follows:

(1) In this paper, UAV photogrammetry technology was applied to the reservoir survey, which has the advantages of high precision, high efficiency and high safety factor, and was also a simple and effective method to obtain the reservoir terrain.

(2) According to the RTK manual measurement and UAV images, the 3D model of the reservoir area was established by using context capture. The M_S and M_H of the root Control surveying were 0.051m and 0.065m respectively, and the M_H of the detail points was 0.098m, which all met the accuracy requirements.

ACKNOWLEDGEMENT

This research was funded by the Key natural science research projects of Suzhou University(2020yzd03, 2020yzd07, 2019yzd01) , National Natural Science Foundation of China (41773100) and Funding projects for research activities of academic and technological leaders of Anhui Province (2020D239).

TABLE 2
Elevation accuracy results based on detail points

point	△H (m)	point	△H (m)	point	△H (m)	point	△H (m)
1	0.099	26	-0.05	51	0.075	76	0.113
2	0.077	27	0.11	52	0.113	77	0.057
3	-0.034	28	0.139	53	0.082	78	-0.054
4	0.096	29	0.12	54	-0.029	79	0.076
5	0.115	30	0.084	55	0.101	80	0.125
6	0.126	31	0.078	56	0.15	81	0.096
7	0.13	32	0.116	57	0.131	82	0.074
8	0.052	33	0.085	58	0.095	83	-0.037
9	0.122	34	-0.026	59	0.057	84	0.093
10	0.091	35	0.104	60	0.127	85	0.112
11	-0.07	36	0.153	61	0.096	86	0.123
12	0.11	37	0.134	62	-0.115	87	0.127
13	0.125	38	0.098	63	0.115	88	0.049
14	0.106	39	0.06	64	0.13	89	0.119
15	0.07	40	0.13	65	0.111	90	0.088
16	0.032	41	0.099	66	0.113	91	-0.073
17	0.102	42	-0.112	67	0.057	92	0.107
18	0.071	43	0.118	68	-0.054	93	0.122
19	-0.04	44	0.133	69	0.076	94	0.103
20	0.09	45	0.114	70	0.125	95	0.067
21	0.139	46	0.116	71	0.096	96	0.029
22	0.115	47	0.06	72	0.074	97	0.099
23	0.119	48	-0.051	73	-0.037	98	0.068
24	0.041	49	0.079	74	0.093	99	-0.043
25	0.111	50	0.128	75	0.112	100	0.087

TABLE 3
Workload table of manual measurement and UAV

No	UAV				manual measurement			
	Field survey		Indoor work		Field survey		Indoor work	
	Surveyor	day	Surveyor	day	Surveyor	day	Surveyor	day
beach					1	2		1
dam	2	1	2	1	2	2	2	1
surrounding landscape					2	2		1
total	2	1	2	1	5	6	2	3

REFERENCES

[1] Cao, J., Yuan, B. and Bai, Y. (2021). Simulation Study on Image Characteristics of Typical GPR Targets in Water Conservancy Projects. Geofluids. 3, 1-13.

[2] Huang, H.F., Long, J.J., Lin, H.Y., Zhang, L., Yi, W. and Lei, B.J. (2017). Unmanned Aerial Vehicle Based Remote Sensing Method for Monitoring a Steep Mountainous Slope in the Three Gorges Reservoir, China. Earth Science Informatics. 10 (3), 287-301.

[3] Jeongbae, J. and Won, C. (2020) Prediction Accuracy of Reservoir Break Flood Simulation Model Using Finite Volume Method and UAV. International Journal of Agricultural & Biological Engineering. 13 (6), 7-15.

[4] Smerdon, B. D., Mendoza, C. A. and McCann, A. M. (2005). Quantitative Investigations of the Hydraulic Connection between a Large Reservoir and a Buried Valley Aquifer in Southern Alberta. Canadian Geotechnical Journal. 42 (5), 1461-73.

[5] Wang, J., Lan, Y.B., Zhang, H.H., Zhang, Y.L., Wen, S., Yao, W.X. and Deng, J.J. (2018) Drift and Deposition of Pesticide Applied by UAV on Pineapple Plants under Different Meteorological Conditions. International Journal of Agricultural & Biological Engineering. 11 (6), 5-12.

[6] Xu,W.C., Lan, Y.B., Li, Y.H., Luo, Y.F. and He, Z.Y. (2019). Classification Method of Cultivated Land Based on UAV Visible Light Remote Sensing. International Journal of Agricultural & Biological Engineering. 12 (3), 103-9.

[7] Meng, L.X., Yang, L., Ren, S.Y., Tang, G.G., Zhang, L., Yang, F. and Yang, W. (2021) An Approach of Linear Regression-Based UAV GPS Spoofing Detection. Wireless Communications & Mobile Computing. 5, 1-16.

[8] Kaviyarasu, A., Saravanakumar, A., and Logavenkatesh, M. (2021). Software in Loop Simulation based Waypoint Navigation for Fixed Wing UAV. Defence Science Journal. 71(4), 448-455.

[9] Esposito, G., Mastrorocco, G., Salvini, R., Oliveti, M. and Starita, P. (2017) Application of UAV photogrammetry for the multi-temporal estimation of surface extent and volumetric excavation in the Sa Pigada Bianca open-pit mine, Sardinia, Italy. Environmental Earth Sciences. 76(3), 1-16.

[10] Ulvi, A. (2021). Documentation, Three-Dimensional (3D) Modelling and visualization of cultural heritage by using Unmanned Aerial Vehicle (UAV) photogrammetry and terrestrial laser scanners. International Journal of Remote Sensing. 42(6), 1994-2021.

[11] Dai, W.Q., Li, H., Zhou, Z. Stephanie, C., Lu,C.Z., Zhao,K., Zhang, X.Y., Yang, H.T. and Li, D.Y. (2018). UAV Photogrammetry for Elevation Monitoring of Intertidal Mudflats. Journal of Coastal Research. 85 (3), 236-40.

[12] Wang, F.Y., Zhao, M.Y., Wang, M.C., Zhang, J.Q. and Zhou, K. (2020) Application of UAV Photogrammetry in mine geological environment survey. Journal of Jilin University (Earth Science Edition) 50(3), 194-202.

[13] Jeong, E.Y., Park, J.Y. and Hwang, C.S. (2018) Assessment of UAV Photogrammetric Mapping Accuracy in the Beach Environment. Journal of Coastal Research. 85 (5), 176-80.

[14] Vacca, G., Furfaro, G. and Dessì, A. (2018). The Use of the UAV Images for the Building 3D Model Generation. International Archives of the Photogrammetry, Remote Sensing & Spatial Information Sciences. 42(4), 217-223.

[15] Nesbit, P. R., and Hugenholtz, C.H. (2019) Enhancing UAV-SfM 3D Model Accuracy in High-Relief Landscapes by Incorporating Oblique Images. Remote Sensing. 11(3), 239.

[16] Castaldi, F., Pelosi, F., Pascucci, S., and Casa, R. (2017) Assessing the potential of images from unmanned aerial vehicles (UAV) to support herbicide patch spraying in maize. Precision Agriculture. 18(1), 76-94.

[17] Nakano, K., Suzuki, H., Tamino, T. and Chikatsu, H. (2016) On Fundamental Evaluation Using Uav Imagery and 3D Modeling Software. International Archives of the Photogrammetry, Remote Sensing & Spatial Information Sciences. 41(B5), 93-97.

[18] Murtiyoso, A., Koehl, M., Grussenmeyer, P. and Freville, T. (2017) Acquisition and Processing Protocols for Uav Images: 3D Modeling of Historical Buildings Using Photogrammetry. ISPRS Annals of Photogrammetry, Remote Sensing & Spatial Information Sciences. 4(2W/2), 163-170.

[19] Rasmussen, J., Azim, S., Boldsen, S. K., Nitschke, T., Jensen, S. M., Nielsen, J. and Christensen, S. (2021) The challenge of reproducing remote sensing data from satellites and unmanned aerial vehicles (UAVs) in the context of management zones and precision agriculture. Precision Agriculture. 22(3), 834-851.
[20] Puliti, S., Astrup, R., and Talbot, B. (2018) Tree-Stump Detection, Segmentation, Classification, and Measurement Using Unmanned Aerial Vehicle (UAV) Imagery. Forests. 9(3), 102.
[21] China National Bureau of Standards. (1988) Specifications for aerophotogrammetric office operation 1:500, 1:1000, 1:2000 Topographic Map. GB7930-87.

Received: **27.11.2021**
Accepted: **11.01.2022**

CORRESPONDING AUTHOR

Jiying Xu
National Engineering Research Center of Coal Mine Water Hazard Controlling (Suzhou University),
Suzhou 234000 Anhui – China

e-mail: jiyingxu1986@163.com

© by PSP Volume 31– No. 05/2022 pages 4975-4982 Fresenius Environmental Bulletin

EXPERIMENTAL STUDY ON TREATMENT EFFICIENCY OF CONSTRUCTED WETLAND TAKING ZHENGDONG NEW DISTRICT PARK AS AN EXAMPLE

Hua Zhang*

Zhengzhou Shengda University, Zhengzhou, Henan 450000, PR China

ABSTRACT

Constructed wetlands are a kind of sewage treatment technology with simple process equipment and low energy consumption. The intermittent influent vertical flow constructed wetlands have positive effects on the control of pollutants and are widely used. Currently, most wetland parks have low wastewater treatment efficiency. This study analyzes the treatment efficiency of a constructed wetland by experimental simulation of a pond sewage treatment system. This study also investigates how to construct a wetland system that meets the water quality requirements, treatment effects, growth of plants, and changes in various water quality indicators. Research shows that the TN, NH_4^+-N, TP, and COD in effluent are high in the early stage of a test wetland operation and slightly higher than the surface water environmental quality standard V. The effluent quality of test wetlands after operation can reach the surface water environmental quality standard V. Total phosphorus and COD can meet the surface water environmental quality standard IV, and the effluent NH_4^+-N can meet the surface water environmental quality standard III.

KEYWORDS:
Constructed wetland, efficiency, scenery design, water body, water treatment, sewage

INTRODUCTION

With the rapid development of society, economy, population growth, improvement in living standards, and urbanization. The scarcity of water and the increasing water pollution has restricted the country's implementation of sustainable development strategies. Constructed wetlands are artificial ecosystems that simulate the function of natural wetlands. They provide a water purification effect, an ability to remove N, P, and other pollutants, simple process equipment, convenient operation and maintenance management, low energy consumption, strong plasticity of system configuration, and strong adaptability to load changes. The project infrastructure and operating costs are low, the effluent is biologically safe, the ecological and environmental benefits are significant, the wastewater can be recycled, and it has numerous landscape values. The substrate is an important part of subsurface flow in constructed wetlands, and plays vital direct and indirect roles in water purification [1, 2]. The differences in the physical and chemical properties of the substrate microenvironment between the matrix voids formed by different materials and particle sizes have a significant impact on the community structure of the biofilm formed by bacteria and other microorganisms [3, 4]. This, in turn, has an impact on the sewage purification function of the biofilm [5]. The growth of a biofilm significantly reduces the permeability coefficient of the system to water, but the effect on the porosity of the matrix can be ignored [6]. Other studies have shown that plant roots only occupy 3%-5% of the matrix pores, which has little effect on porosity [7].

Low-efficiency oxygen supplementation is a key factor in inhibiting the removal of ammonia and nitrogen pollutants in sewage [8]. A typical feature of sewage treatment plant tailwater is relatively low concentrations of carbon and nitrogen [9]. Insufficient capacity [10] can result in poor denitrification and has become a difficulty in the advanced treatment of wastewater plant tailwater [11]. For this reason, domestic and foreign researchers have proposed the addition of exogenous carbon sources to wetlands [12]. Through comparative studies, they found that adding denitrified carbon sources to wetlands significantly increased the nitrogen removal rate. Chang et al. [13] used carnation stalks as an additional carbon source in the pilot test to achieve an average nitrate/nitrogen removal rate of 51.8%. However, due to the relatively low carbon and nitrogen in the wastewater treatment plant tailwater, they were unable to provide sufficient carbon for denitrification [14, 15]. There was still a gap between the final effluent total nitrogen and the surface IV standard. Sun et al. [16] showed that under a hydraulic load of 0.25 $m^3/(m^2 \cdot d)$, the removal rate of CODCr by adding biochar and an activated carbon layer to the wetland reached 93.8%, and the effluent CODCr concentration was 2.81 mg/L. When the hydraulic

load was low, the higher DO content in the water created favorable conditions for the reaction of aerobic microorganisms and was more conducive to the degradation of CODCr. Constructed wetlands are an imitation ecological water treatment process composed of plants, substrates, and associated microorganisms. Since the 20th century, they have been widely used in the denitrification treatment of various types of sewage and wastewater [17].

Most of the various types of sewage and wastewater treated by constructed wetlands have low carbon to nitrogen ratios. The main nitrogen removal pathway in constructed wetlands is the nitrification-denitrification by microorganisms, and the amount of nitrogen removed accounts for more than 60% [18, 19]. The denitrification process of traditionally constructed wetland requires a carbon source. However, the carbon provided by plant root secretion and corruption alone is not sufficient to maintain the heterotrophic denitrification process in constructed wetlands [20]. When traditionally constructed wetlands treat pollution and wastewater with low carbon-nitrogen ratios, they lack sufficient electron donors which hinder the heterotrophic denitrification process [21]. The whole autotrophic denitrification process directly converts NH_4^+-N into nitrogen and NO_3-N which has low mud yield and reduces the cost of nitrogen removal. It is suitable for the treatment of high ammonia nitrogen and low carbon sewage [22]. Hu et al. [23] used an up-flow tidal operation to shorten the emptying stagnation time through intermittent recirculation, and the removal rate of total inorganic nitrogen reached more than 80% when BOD5/ρ(TN) was less than 0.2. Wang et al. [24] found that different split ratios had different degrees of enrichment of anammox bacteria. When the split volume ratio is 1:1, the enrichment effect of anammox bacteria was optimal. Jin et al. [25] found that reducing the drainage rate short-cut the nitrification and anammox process. When the drainage volume flow rate was 0.5 L/min, the wetland denitrification effect was maximized. Liu et al. [26] uniformly mixed elemental sulfur and limestone in a volume ratio of 1:1, the average removal rates of TN and NO_3-N were 81.0% and 98.5%, respectively, when HRT was 12 h. Park et al. [27] found the suitable mass ratio of filler sulfur to limestone was 3:1 and the average removal efficiency of NO_3-N was 66.6%. Elemental sulfur was more economical as a wetland filler. Gao et al. [28] found that the addition of $Na_2S_2O_3$ increased the abundance of autotrophic denitrifying flora, stimulated the growth of plants, and could control the production of the greenhouse gas nitrous oxide (N_2O) and the content of SO_4^{2-} in the effluent. Xu et al. [29] used $Na_2S_2O_3$ as the electron donor for the autotrophic denitrification process in the wetland, and the TN and SO_4^{2-} content of the effluent met the surface water environmental quality level V standard.

In this paper, new wetlands were constructed in the Zhengdong New District Wetland Park to test their ability to function as sewage treatment systems. This work investigates how to construct wetlands that can meet water quality standards and promote the growth of plants. Various water quality indicators were measured before and after passing through the constructed wetlands and the results provide a reference for the future design, operation, and management of constructed wetland systems.

MATERIALS AND METHODS

Natural conditions of test site. Zhengdong New District Wetland Park is mainly used to purify the water in Ruyi Lake, with a rated daily treatment capacity of up to 20,000 tons [18]. After the water in Ruyi Lake flows through the wetland park, the water quality is improved. The park covers an area of 40,000 square meters (60 acres) and has three ponds. Pond 1 is connected to multiple ditches and receives sewage from various sources, pond 2 is connected to pond 1 and 3 # Pond and 2# pond are connected. The untreated domestic sewage flows into these three ponds. This continuous discharge of sewage over many years has resulted in pond water that is of poor quality, has high turbidity, low transparency, and concentrations of organic matter, nitrogen, and phosphorus that exceed the standards [25, 26]. In their eutrophic state, the water quality of these ponds has not reached the landscape water requirements. In particular, the pollution of No. 1 pond is the most serious. The constructed wetland in this experiment was built on the east side of No. 1 pond, and the sewage from this pond was used as the inflow for the constructed wetland.

Experimental method. Samples of water flowing in and out of the wetland system were collected and analysed according to the Water and Wastewater Inspection Analytical method [23]. Several water quality indicators were measured: COD was measured using the potassium dichromate method, TN was measured using potassium persulfate oxidation-UV spectrophotometry, TP was measured using antimony spectrophotometry, NH_4^+-N was measured using sodium reagent spectrophotometry, SS was measured using filter paper. pH was measured using a PHB-4 portable pH meter, and ORP was measured with a waterproof ORP instrument.

Experimental device. In this experiment, six artificial wetlands were constructed, numbered 1#, 2#, 3#, 4#, 5#, 6#. The six sets of constructed wetland systems were operated in parallel. The raw water was pumped by a centrifugal pump from the end of the pond near the constructed wetland in the Zhengdong New District Wetland Park to all six of the constructed wetlands. The length and width of

each wetland system were uniform, with a length of 10 m and a width of 1 m. The depth was determined according to the depth of the substrate set in the experiment. Filled with gravel, the bottom slope was 0.5%. The inlet water was extracted from the No. 1 pond by a high-power water pump and distributed to each wetland through the main water pipe. The water was distributed evenly to each wetland by a PVC perforated cloth pipe with a diameter of DN50. The outlet water was collected by a PVC perforated outlet pipe with a diameter of DN50. After that, the water merged into a sump with a length of 6 m, a width of 1 m, and a height of 1.5 m. The water then flowed out of the sump and into the No. 2 pond. The bottom surface of the wetlands was concrete and the surrounding bricks and mortar were plastered. The parameters of each constructed wetland are described in Table 1.

RESULTS AND DISCUSSION

The civil construction of the wetlands commenced in September 2019 and was completed in October 2019. After planting, the test wetland was filled with water for two weeks, emptied and then the test pond water was injected to allow it to grow adaptively. After another two weeks the wetlands were emptied again and the test commenced. The trial proceeded from early November to late April 2020. Water samples were collected at 9 am, 4 to 5 times per month. During the test, the plants grew well, the temperature was between 10 °C and 21 °C, and the influent flow was adjusted by a flow meter. To compare the treatment effects in each wetland system, the flowmeters were adjusted to 4 m^3d^{-1} at the beginning of the test and operated continuously. The selected plants were transplanted in October 2019, with planting densities of six and nine plants/m^2. After planting, the entire system began to operate. During the operation and monitoring period, the six constructed wetlands were found to have a good treatment effect on the pond wastewater. From the average value of the effluent concentration, TN, NH_4^+-N, TP, and COD were all lower than the influent water. The values of all other water quality indicators, except TN, increased to the standard levels.

Apparent treatment effect and plant growth. As shown in Figure 1, the turbidity of the effluent from the constructed wetlands was significantly lower than the turbidity of the influent and decreased with time since construction. The constructed wetlands adopted a continuous flow operation mode, and sewage flowed in continuously from outside. The plants in the constructed wetland grew well. By the end of the experiment, the canna had bloomed, and the cattail leaves were green and plump. No plant mortalities were observed throughout the experiment. The height of the canna and cattail planted in each wetland increased from 20-62 cm and It grew from 30-102 cm to 55-154 cm and 124-220 cm at the later stage of the test and grew 35-92 cm and 9-118 cm on average. Figure 2 shows the distribution of artificial wetland plants numbered 1-6 and the growth of plants before and after the inflow of sewerage.

TABLE 1
Design parameters of experimental constructed wetland

Exp.	Area/m^2	Length/m	Particle size/mm	Bottom slope/°	Matrix depth	Planting density/Tree·m^{-2}
1#	10	10	20-80	0.5	0.6	6
2#	10	10	20-80	0.5	0.6	9
3#	10	10	20-80	0.5	1	9
4#	10	10	20-80	0.5	1	9
5#	10	10	20-80	0.5	1.5	6
6#	10	10	20-80	0.5	1.5	9

FIGURE 1
Water inlet and outlet effects in early stage of constructed wetland treatment

FIGURE 2
Plant growth diagram of Constructed Wetland

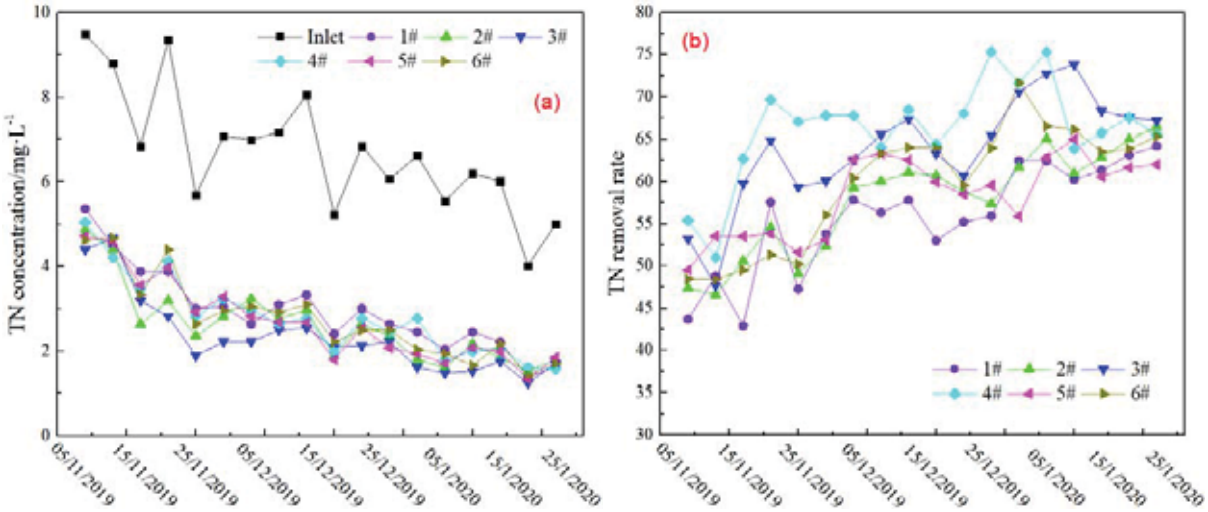

FIGURE 3
TN concentration and its removal rate of constructed wetland system

TN removal efficiency of constructed wetland system. The removal of nitrogen in constructed wetland system mainly depends on the absorption and assimilation of plants and the decomposition and transformation of microorganisms. Firstly, inorganic nitrogen is absorbed and removed by plants as a nutrient element. Secondly, plants transport oxygen to the wetland bed through plant roots through photosynthesis. In addition, water carrying and atmospheric reoxygenation form the distribution of aerobic in the surface layer, anoxic in the deep layer and anaerobic in the bottom layer of the wetland bed, aerobic around plant roots, anoxic in areas far away from roots and anaerobic in further areas, There are many aerobic, anoxic and anaerobic microenvironments in the system, which leads to the spatial differences of micro ecosystem, and creates good conditions for microbial nitrification and denitrification. The way of nitrogen removal is as follows: the organic nitrogen in the water is transformed into ammonia nitrogen by heterotrophic microorganisms (ammonifying bacteria), and then the nitrifying bacteria convert ammonia nitrogen into nitrite nitrogen and nitrate nitrogen in an aerobic environment. The inorganic nitrogen is removed from the water through the denitrification of denitrifying microorganisms and the absorption of plant roots. Physical interception, precipitation and ion exchange of wetland bed are also important processes of nitrogen removal in constructed wetland.

It can be seen from Figure 3 that when the TN concentration of influent water varied between 4 mg/L-9. 5 mg/L, the effluent concentration was 1.5 mg/L~5. 5 mg/L. The removal rate was 40-80%. After three months of operation, the effluent TN reached class V of the water standard. According to the average concentration of influent, the influent COD/TN = 10.2 > 65 eliminated the impact of the insufficient source. The possible reasons are: (1) the wetland influent TN concentration was too high and the underflow wetland had limited nitrogen consumption capacity, and (2) the microbial diversity of the treatment system was not very high. Likely, the populations of nitrifying and denitrifying bacteria were not fully developed, and their effects were weak, resulting in a poor denitrification capacity of the wetland system. With an increase in wetland operating time, the removal rate of TN by each system steadily increased.

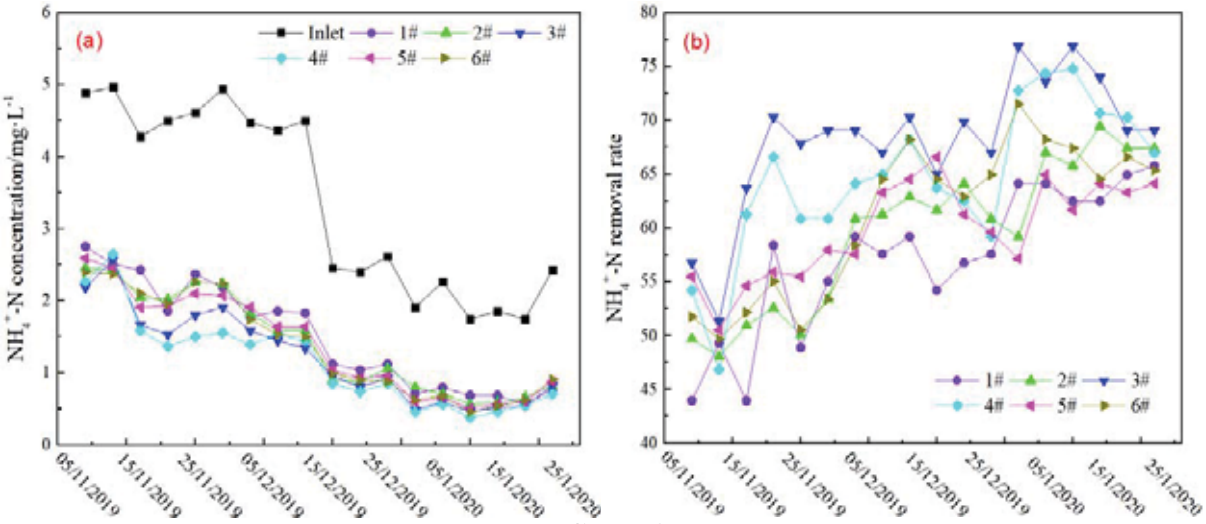

FIGURE 4
NH_4^+-N concentration and its removal rate of constructed wetland system

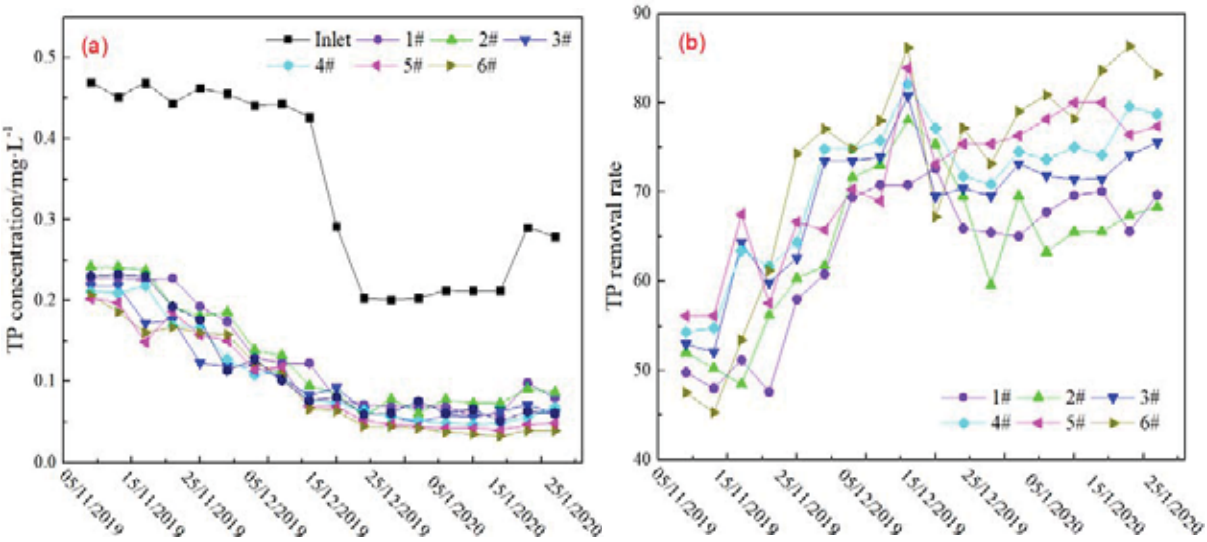

FIGURE 5
TP concentration and its removal rate of constructed wetland system

Removal efficiency of NH_4^+-N by constructed wetland system. It can be seen from Figure 4 that, when the influent NH_4^+-N concentration changed from 2 mg/L-5 mg/L, the effluent concentration was 0.5 mg/L-2.8 mg/L. The removal rate was 40-80%. After 35 days of operation, the effluent NH_4^+-N reached class V. After two months of operation, the effluent reached class III. The effluent NH_4^+-N concentration and removal rate was found to have a similar trend to the TN effluent concentrations. The removal rate gradually increased from approx. 50% in the early stage to approx. 70% over time, and then slowly decreased to approx. 60% in the later stage.

TP removal efficiency of constructed wetland system. The removal of phosphorus in constructed wetland system is mainly through three aspects: normal assimilation of microorganisms or absorption of plants; Uptake of phosphorus accumulating bacteria; Physicochemical action of matrix. The most important one is the adsorption of phosphorus by matrix. From Figure 5, it can be seen when the TP concentration of the influent changed from 0.2 mg/L-0.47 mg/L, the effluent concentration was 0.1 mg/L-0.25 mg/L. From November 25, 2019, the effluent TP concentration stabilized below 0.2 mg/L. After 25 days of operation, the effluent reached class V. After 50 days of operation, the effluent reached class IV. The removal rate of the subsurface flow in each constructed wetland system showed a slow upward trend over time.

COD removal efficiency of constructed wetland system. COD represents the reducing substances in water. In the environment with sufficient oxygen, the COD value is low. Therefore, generally speaking, in the constructed wetland that can fully

provide oxygen, the removal rate of COD is relatively high. The chemical oxygen demand estimates the amount of oxygen consumed by the water. In an environment with sufficient oxygen, the COD value is low. Therefore, in general, the removal rate of COD would be relatively high in constructed wetlands that can provide insufficient oxygen. It can be seen from Figure 6(a) that when the COD concentration of the influent from each wetland changed between 45 mg/L-73 mg/L, the concentration of the effluent was 20 mg/L-45 mg/L. After ten days of operation, the effluent reached class V. After two months of operation, the effluent reached class IV. As shown in Figure 6(b), the COD removal rate of each constructed wetland system was 35%-62%, which was lower than the 61%-94% reported by Fossey et al. [30]. This is may be because the COD concentration of the wetlands in this experiment were lower than that of the sewage generally used for the treatment of constructed wetlands. Studies have shown that when the COD concentration is lower than 50 mg/L, the removal is more difficult. During the entire operation period of the current study, when the influent COD concentration was around 50 mg/L or lower than 45 mg/L, the removal rate dropped slightly.

SS change of inlet and outlet water of constructed wetland system. The removal of SS occurred due to sedimentation in the filler gaps, and the interception and filtration between the filler and the plant rhizosphere. With the growth of the wetland plant root systems, the increased contact between the roots and the particulate matter reduced the particle pollution with the continuous interception of materials, the void ratio between the wetland substrates decreased, and the ability to intercept suspended particulates increased. It can be seen from Figure 7(a) that when the influent SS concentration changed from 30 mg/L-70 mg/L, the effluent SS of each wetland system was 2 mg/L-30 mg/L, as shown in Figure 7(b). The removal rate of SS by the wetland systems was 55%-97%, showing a steady upward trend.

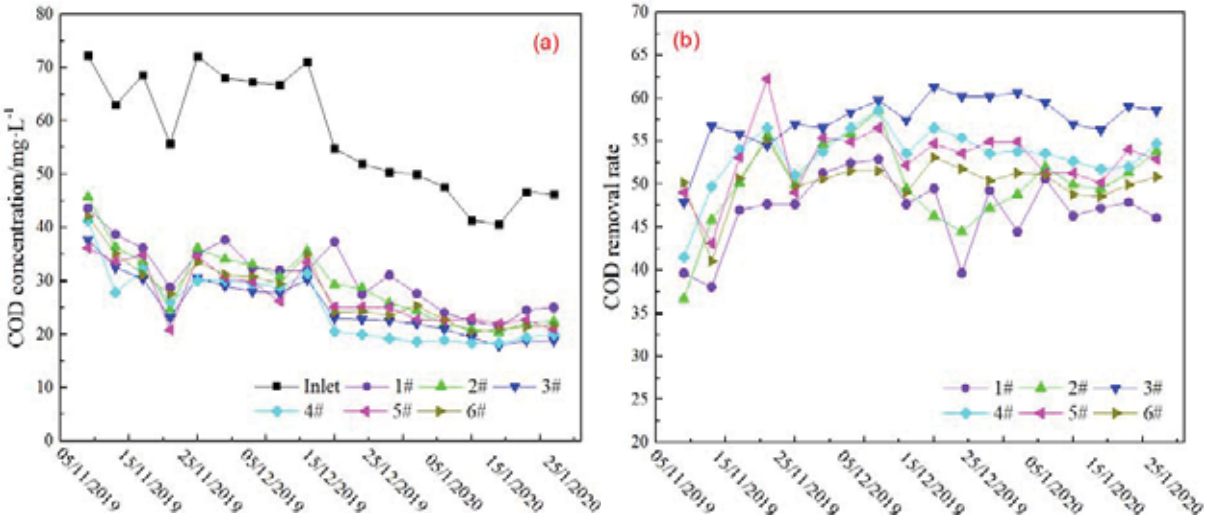

FIGURE 6
COD concentration and its removal rate of constructed wetland system

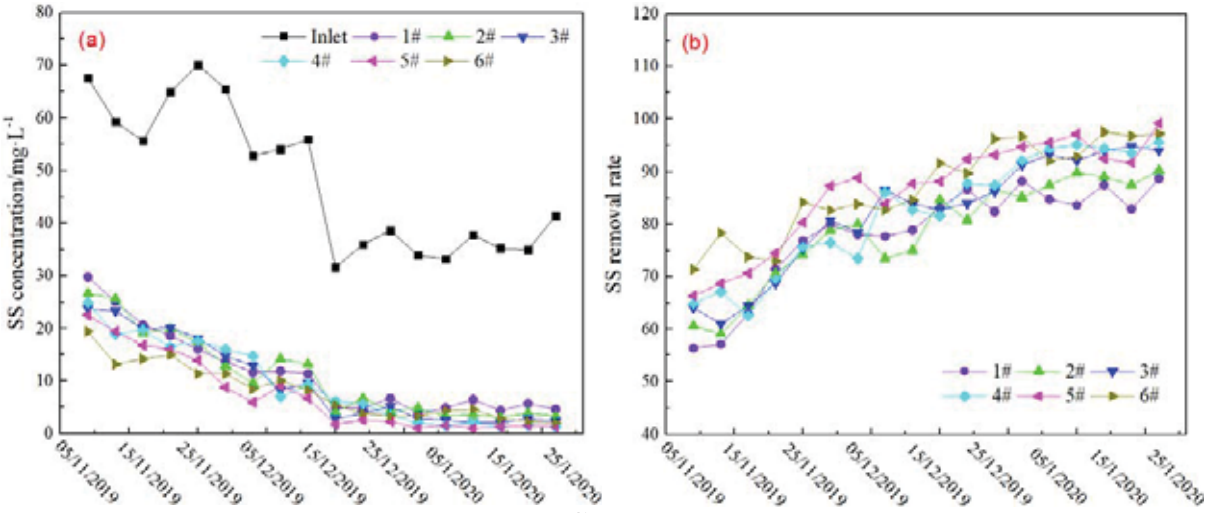

FIGURE 7
SS concentration and its removal rate of constructed wetland system

CONCLUSIONS

This study used subsurface flow constructed wetland technology to study the treatment efficiency of constructed wetlands in the wetland park of Zhengdong New District. The treatment effects and influencing factors of the constructed wetland treatment system was compared and the following conclusions were obtained: the average removal rate of the underflow constructed wetland system in this test was 49%-88% following the treatment of polluted influent. In the early stage of the test wetland operation, the effluent TN, NH_4^+-N, TP, and COD were slightly higher than the surface water environmental quality standard V. In the later stage of operation, the effluent water quality reached standard V, meeting effluent requirements. Effluent TP and COD met the quality standard IV and effluent NH_4^+-N met quality standard III. The cattail wetland had a higher removal effect for TN, NH_4^+-N and COD than the canna wetland while the TP removal effect was higher in the canna wetland.The underflow wetland with a depth of 1.5 m had a 10% higher removal rate of TP and SS than the underflow wetland with a depth of 0.6 m.

ACKNOWLEDGEMENTS

This study was no funds supported.

REFERENCES

[1] Ramirze, S., Torrealba, G., Lameda, E., Molina, Q.L., Sierra, M.C. (2019) Investigation of pilot-scale constructed wetlands treating simulated pre-treated tannery wastewater under tropical climate. Chemosphere. 23(4), 496-504.

[2] Liu, F.F., Fan, J., Du, J., Shi, X., Zhang, J., Shen, Y. (2019) Intensified nitrogen transformation in intermittently aerated constructed wetlands: removal pathways and microbial response mechanism. Science of the Total Environment. 65(10), 2880-2887.

[3] Zheng, X., Jin, M., Zhou, X., Wei, C., Dan, L., Yuan, Z. (2019) Enhanced removal mechanism of iron carbon micro-electrolysis constructed wetland on C, N, and P in salty permitted effluent of wastewater treatment plant. Science of the Total Environment. 64(9), 21-30.

[4] Long, Y., Zhang, Z., Pan, X., Guo, X., Li, Q.W. (2016) Substrate influences on archaeal and bacterial assemblages in constructed wetland microcosms. Ecological Engineering. 94(8), 437-442.

[5] Xu, R., Zhang, Y., Liu, R., Cao, Y., Wang, G., Ji, L. (2019) Effects of different substrates on nitrogen and phosphorus removal in horizontal subsurface flow constructed wetlands. Environmental Science and Pollution Research. 26(16), 229-238.

[6] Zhou, Y., Luo, S., Yu, B., Zhang, T., Jin, L., Zhang, Y. (2018) A comparative analysis for the development and recovery processes of different types of clogging in lab-scale vertical flow constructed wetlands. Environmental Science and Pollution Research. 25(2), 4073-4083.

[7] Teixeira, D.L., Matos, A.T., Pinebtel, D.E., Matos, M. (2018) The influence of plant roots on the clogging process and the extractive capacity of nutrients/pollutants in horizontal subsurface flow constructed wetlands. Ecological Engineering. 12(10), 54-60.

[8] Zheng, X.H., Zhuang, L.L., Zhuang, J., Cheng, D.B. (2020) Advanced oxygenation efficiency and purification of wastewater using a constant partially unsaturated scheme in column experiments simulating vertical subsurface flow constructed wetlands. Science of the Total Environment. 70(3), 1192-1203.

[9] Cheng, S.P., Wang, Y.Y., Wang, J. Cai, J. (2019) Advances and prospect in the studies on constructed wetlands. Journal of Lake Sciences. 31(6), 1489-1498.

[10] Pawet, M., Wojciech, D., Beata, K. (2018) Application of SS-VF bed for the treatment of high Concentrated Reject Water from Autothermal Termophilic Aerobic Sewage Sludge Digestion. Journal of Ecological Engineering. 19(4), 103-110.

[11] Fu, G.P., Huang, S., Lin, K., Li, C.D., Liu, G.L. (2017) Effect of plant-based carbon sources on denitrifying microorganisms in a vertical flow constructed wetland. Bioresource Technology. 224(6), 214-221.

[12] Tao, M.N., Tao, Z.K., Wang, Y. (2018) Study on enhanced nitrogen removal in microbial fuel cell integrated with constructed wetlands. Applied Chemical Industry. 47(10), 2212-2216.

[13] Chang, J.J., Liu, H., Luo, T., Xiang, G.G. (2016) Nitrate removal and negative effects of subsurface constructed wetlands adding flower straws as carbon source. Chinese Journal of Environmental Engineering. 10(9), 5313-5318.

[14] Wang, B.D., Song, X.S. (2019) Application of four solid carbon sources for high-effective nitrogen removal in constructed wetland. Journal of Donghua University. 45(3), 444-450.

[15] Zhang, R.X., Jiao, Y., Fu, J.X., Liu, R., Liang, L., Xu, X. (2018) Effects of hydraulic loading rate on the migration and transformation of pollutants in subsurface flowing wetlands. Environmental Pollution & Control. 40(7), 748-754.

[16] Sun, Y.P., Zhou, P.C., Yuan, M.Z., Shi, L.L. (2019) Effect of hydraulic loading on the degradation of the simulated tail water from wastewater treatment plant by improved vertical flow constructed wetland. Chinese Journal of Environmental Engineering. 30(7), 1-11.
[17] Wu, S., Kuschk, P., Brix, H. (2014) Development of constructedwetlands in performance intensifications for wastewater treatment: a nitrogen and organic matter targeted review. Water Res. 255(7), 5740-5755.
[18] Zhao, L.F., Zhu, W., Zhao, J., Zu, Q.Q. (2017) Nitrogen removal mechanism of constructed wetlands in the treatment of polluted river water with low C/N ratio. Acta Scientiae Circularae. 23(11), 1821-1827.
[19] Lu, S.Y., Jin, X.C., Yu, G. (2016) Nitrogen removal mechanism in constructed wetlands. Acta Ecologica Sinica. 112(8), 2670-2677.
[20] Gagnon, V., Chazarenc, F., Comeau, Y., Brisson, J. (2016) Influence of macrophyte species on microbial density and activity in constructed wetlands. Water Science & Technology. 56(3), 249-254.
[21] Zhi, W., Ji, G.D., Heng, F.G. (2014) Quantitative response relationships between nitrogen transformation rates and nitrogen functional genes in a tidal flowconstructed wetland under C/N ratio constraints. Water Research. 6(4), 32-41.
[22] Zhang, H.T., Zheng, P., Canon, M.T. (2013) Research progress of process. Industrial Water Treatment. 33(8), 1-5.
[23] Hu, Y.S., Zhao, X.H., Zhao, Y.Q. (2014) Achieving high-rate autotrophic nitrogen removal via Canon process in a modified single bed tidal-flow constructed wetland. Chemical Engineering Journal. 237(2), 329-335.
[24] Wang, Z., Huang, M.L. (2017) Enhancing nitrogen removalvia the complete autotrophic nitrogen removal over nitrite process ina modified single-stage tidal flow constructed wetland. Ecological Engineering. 10(3), 170-179.
[25] Jing, H.Z. (2018) Effects of drainage rate on Canon effect in tidal flow constructed wetlands. China Environmental Science. 38(6), 2182-2192
[26] Liu, D.N., He, S.B., Zhou, W.L., Zhao, Z.L. (2014) Nitrogen removal in a vertical flow constructed wetland enhanced by sulfur autotrophic denitrification. China Water and Wastewater Engineering. 30(3), 14-18.
[27] Park, J.H., Kim, S.H., Delaune, R.D. (2015) Enhancement of nitrate removal in constructed wetlands utilizing a combined autotrophic and heterotrophic denitrification technology for treating hydroponic wastewater containing high nitrate and low organic carbon concentrations. Agricultural Water Management. 16(2), 1-14.
[28] Gao, L., Zhou, W.L., Wu, S.Q., He, S., Huang, J., Zhang, X. (2018) Nitrogen removal by thiosulfate-driven denitrification and plant uptake in enhanced floating treatment wetland. Science of the Total Environment. 621(15), 1550-1558.
[29] Xu, J.H., He, S.B., Wu, S.Q., Huang, J.C., Zhou, W.L., Chen, X.C. (2016) Effects of HRT and water temperatureon nitrogen removal in autotrophic gravel filter. Chemosphere. 14(7), 203-209.
[30] Fossey, M., Rousseau, A.N. (2016) Assessing the long-term hydrological services provided by wetlands under changing climate conditions: a case study approach of a Canadian watershed. Journal of Hydrology. 124(11), 1287-1302.

Received: **27.11.2021**
Accepted: **23.01.2022**

CORRESPONDING AUTHOR

Hua Zhang
Zhengzhou Shengda University,
Zhengzhou Henan 450000 – PR China

e-mail: mrcfpn@163.com

© by PSP Volume 31– No. 05/2022 pages 4983-4994 Fresenius Environmental Bulletin

CAR INTERIOR DESIGN AND MATERIAL POLLUTION IMPACT ANALYSIS ON THE CAR'S INTERIOR ENVIRONMENT

Mingfei Wang*

Graduate School, Sejong University, Seoul 05006, South Korea

ABSTRACT

With the familyization of automobiles, the social problems caused by automobile pollution have become more and more serious. In addition to exhaust gas pollution affecting people's daily life, the problem of in-vehicle pollution has also become more and more serious affecting people's health. Inevitably, a lot of materials, including leather, plastic products, are used in the interior design of automobiles. Among the many factors that affect the air quality in the car, car interior materials are an important source of pollution for the air quality in the car. Environmental pollution caused by vehicle interior design materials should be emphasized. In this paper, acetylacetone spectrophotometry and gas chromatography are used to determine the pollutants in the air in the car, and the influence of the car made time, ventilation mode, temperature, driving state, vehicle type, and humidity on the air quality in the car is analyzed. Studies have shown that the main air pollutants in cars are formaldehyde, benzene, toluene, and xylene. With the prolongation of the made time of cars, the concentration of air pollutants in cars decays. The concentration of pollutants in the car under the airtight window will stabilize after about 25 to 30 days. Opening windows for natural ventilation can rapidly reduce the concentration of pollutants in the car, and the highest concentration of pollutants reaches when the internal circulation of the air conditioner is turned on. When the temperature inside the car rises by 10°C, the concentration of pollutants in the car increases by approximately 1-2 times. Compared with the static state, the concentration of air pollutants in the car decreases when the car is running. With the increase of humidity, the concentration of formaldehyde in the car increases, and the concentration of benzene series decreases. The research results of this article provide an important reference for the protection of air pollution in the car.

KEYWORDS:
Material pollution, air environment, car interior design, air pollution inside the car

INTRODUCTION

With the increasing number of civilian cars, cars have gradually become one of the main living spaces for people. Compared with the attention paid to automobile exhaust pollution, the pollution in automobiles is often ignored by us. At present, the international community has included car pollution and indoor pollution as one of the five major factors that endanger the physical and mental health of all human beings [1-3]. In order to meet consumers' requirements for comfort and sensory, automobile manufacturers continue to pursue more complex interior design, using more new processes and new materials, such as composite materials and adhesives [4-5]. A large number of toxic and harmful substances endanger the health of drivers and passengers.

Carpets, seats, plastic parts of dashboards, roof felts and glue used in decoration of automobile interior parts are the main sources of air pollution inside automobiles [6-7]. The narrow space of the car and the good airtightness of the car make the harmful gas in the car more harmful to the human body than the harmful gas in the indoor. The harmful gases contained in automobile decoration materials mainly include benzene, formaldehyde, acetone, trichloroethylene, etc [8-11]. These harmful gases have a serious impact on the immune system, nervous system and reproductive system of the human body, and even cause cancer [12-14]. The elderly and people with weakened immune systems are more vulnerable to threats.

The mass concentration of pollutants released by car interiors is particularly affected by ambient temperature, and increases sharply as the temperature rises [15-16]. The main reason is that the release of volatile substances such as organic solvents, additives and additives contained in the materials of car interiors increases with the increase of temperature. Studies have shown that if the temperature increases by 10°C, the mass concentration of pollutants will also increase by a factor of nearly double. The interior pollution caused by interior materials of the new cars is more serious than that of old cars. The mass concentration of pollutants produced in car interiors decreases with the increase of vehicle

usage time, but the degree of reduction of different pollutants is different [17-18].

Different air exchange rates have a great relationship with the degree of influence on the mass concentration of pollutants. During driving, if you drive with the windows fully opened or use enough air-conditioning outside air to be introduced into the car, the mass fraction of pollutants in the car will be significantly reduced. According to the survey, generally after 30 minutes of air exchange, the mass fraction of pollutants in the car will be reduced to 1/10 of the original level, or even lower.

For the research on air pollution in cars, many researchers have achieved some results. For example, they have studied the sources of pollution in cars and found that interior materials are likely to cause air pollution in cars. Due to the relatively small space in the car and the relatively large amount of decorative materials in the car, the concentration of air pollution in different types of cars varies with different influencing factors. In order to explore the characteristics of car interior air pollution in the environment of different influencing factors. In this paper, the pollutants in the air in the car are measured, and the influence of different influencing factors on the main pollutants in the air in the car is analyzed to provide a basis for controlling the air pollution in the car.

TABLE 1
Models and vehicle numbers of cars used in the experiment

Model	Experiment number
Car	1-5
Business car	6,7
SUV	8,9

MATERIALS AND METHODS

(1) Experimental vehicle. The cars used in the experiment are all new cars, 5 sedans, 2 off-road vehicles, and 2 commercial vehicles, provided by an automobile company in Tianjin, China, as shown in Table 1.

(2) Experimental instruments and reagents. Experimental instruments include gas chromatograph (TRACE 1300 Mainframe), high temperature blast drying oven (CYH1113), circulating water multipurpose vacuum pump (SHZ-95B), electronic balance (ME204E), glass instrument airflow dryer (), spectrophotometer Meter (KQ-B), water bath constant temperature oscillator (SHZ-82), etc.

Experimental reagents include carbon disulfide, benzene, toluene, p-xylene, meta-xylene, o-xylene, formaldehyde, ammonium acetate, glacial acetic acid, acetylacetone, hydrochloric acid, sodium hydroxide, potassium iodate, iodine, starch, thiosulfuric acid sodium etc.

(3) Experimental analysis test method. The experiment process refers to the GB/T18883-2002 indoor air quality standard to determine the pollutants in the air in the car. The determination of formaldehyde adopts acetylacetone spectrophotometry. Formaldehyde collection method is to use a porous glass plate absorption tube to collect formaldehyde in the air. The principle is that when the formaldehyde-containing air passes through the absorption liquid, the measured components around the bubble and the absorption liquid interface quickly dissolve in the rising process of the bubble. In the absorption liquid, the concentration of the measured component on the interface decreases rapidly due to the chemical reaction with the absorption liquid. The measured component in the bubble diffuses to the interface in time, and the absorbing liquid continuously absorbs the measured component into the liquid phase. After the formaldehyde gas is absorbed by water, it reacts with acetylacetone in the acetic acid-ammonium acetate buffer solution of pH=6. Under the conditions of boiling water bath, a stable yellow compound is rapidly formed, measured at a wavelength of 413nm.

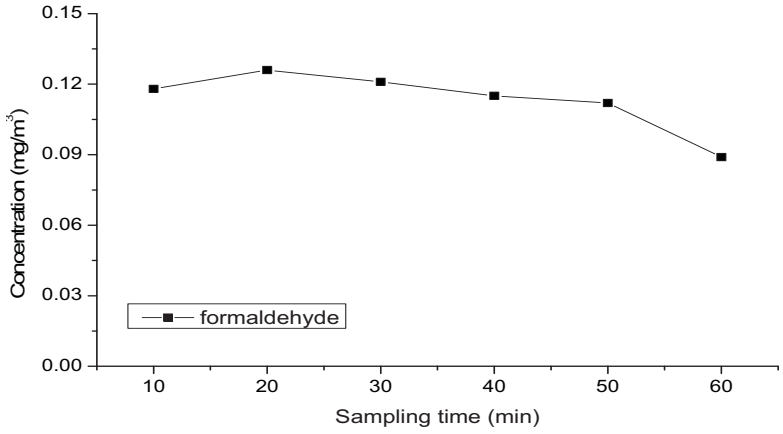

FIGURE 1
The relationship between formaldehyde concentration and sampling time.

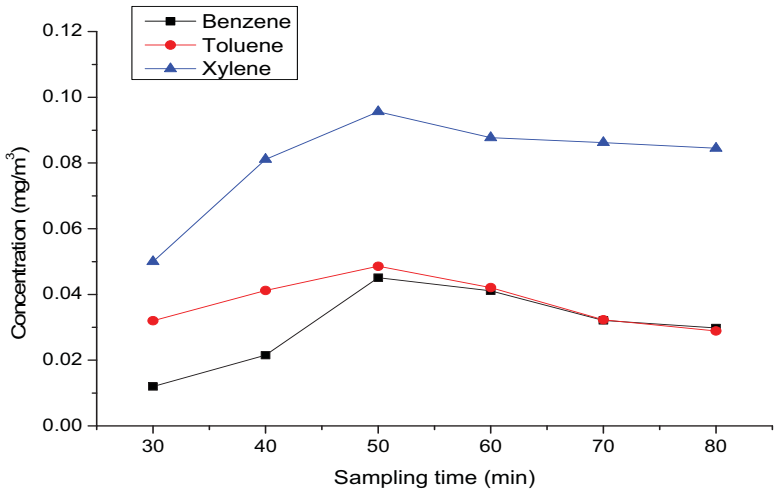

FIGURE 2
The relationship between the concentration of benzene series and sampling time.

The benzene series are determined by gas chromatography. Benzene series are sampled with solid adsorbent. The sampling principle is to fill the solid adsorbent (activated carbon) in a glass tube. When the air is drawn through the adsorption column, the oxygen, nitrogen and carbon dioxide in the air flow out first due to their weak adsorption and high in content while some components with strong adsorption remain on the adsorbent. After bringing it back to the laboratory, we desorb it with a solvent before performing the measurement. Benzene, toluene and xylene in the air are collected by activated carbon tube, extracted by carbon disulfide, and then separated by a chromatographic column and detected by a hydrogen flame ionization detector. The retention time is qualitatively and the peak area is quantified.

RESULTS

(1) The influence of sampling time on the concentration of pollutants. Taking into account that the volume of air in a car is much smaller than the volume of indoor air, the time to collect air samples in a car is different from the sampling time of indoor air. Referring to the indoor air pollutant determination standard, the sampling flow rate is 0.5L/min. The sampling time of formaldehyde is 10min, 20min, 30min, 40min, 50min, 60min, respectively, and the sampling time of benzene series is 30min, 40min, 50min, 60min, 70min, 80min, respectively. By comparing the pollutant concentration measured under different sampling time, the best sampling time can be determined.

It can be seen from Figure 1 and Figure 2 that the maximum concentration of pollutants is determined when the formaldehyde is collected for 20 minutes, and the concentration of pollutants is the maximum when the benzene series is collected for 50 minutes. It shows that the formaldehyde will be saturated at 20 minutes and the benzene series will be saturated at 50 minutes. The absolute amount of pollutants in the sampling tube remains unchanged as the sample time continues, the analysis sample will be too large and the concentration of pollutants will be lower. Thus, the best sampling time for formaldehyde is 20min, and the best sampling time for benzene series is 50min.

(2) The main pollutants in the air in the car. It has been experimentally determined that the SO_2, CO, CO_2, NO_2, O_3, etc. in the car do not exceed the standard. At the same time, combined with the GB/T18883-2002 indoor air quality standard to determine the air pollutants in the car, this article focuses on the investigation of formaldehyde, benzene, toluene, and xylene. According to the above-mentioned test method, the concentrations of formaldehyde, benzene, toluene, and xylene in the car are measured with the windows are closed. The temperature maintains at about 30°C, the engine was not started, and the air conditioner was not turned on. The results are shown in Table 2.

It can be seen from Table 2 that the air pollutants in the car contain formaldehyde, benzene, toluene, and xylene. The detection rate of the pollutants is 100%. Formaldehyde, benzene, toluene, and xylene all exceed the standard. The degree of pollution of pollutants is closely related to the degree of use of the interior of the car. The leather, peach wood, electroplating, metal, paint, engineering plastics, etc. selected for the interior of the vehicle will volatilize harmful gases such as benzene, formaldehyde, acetone, and xylene. The higher the degree of interior use, the more serious the pollution. From the above table, it can be seen that compared with the air in the car, the air pollutants in the commercial vehicle are obviously more serious than in the car. The air in the off-road vehicle is good, and the pollutants in the car do not exceed the national standard.

TABLE 2
Measurement results of the concentration of pollutants in the car in a closed state

No.	Days after the vehicle is completed, day	Temperature, ℃	Formaldehyde, mg/m^3	Benzene, mg/m^3	Toluene, mg/m^3	Xylene, mg/m^3
1	9	30	0.12	0.06	0.07	0.18
2	10	27	0.15	0.06	0.04	0.08
3	12	25	0.08	0.09	0.08	0.23
4	13	33	0.10	0.11	0.12	0.12
5	18	26	0.14	0.08	0.09	0.26
6	18	24	0.18	0.09	0.38	0.36
7	21	23	0.16	0.11	0.15	0.29
8	27	31	0.11	0.04	0.09	0.16
9	32	29	0.09	0.05	0.11	0.11
GB/T 18883-2002	/	/	0.10	0.11	0.2	0.2

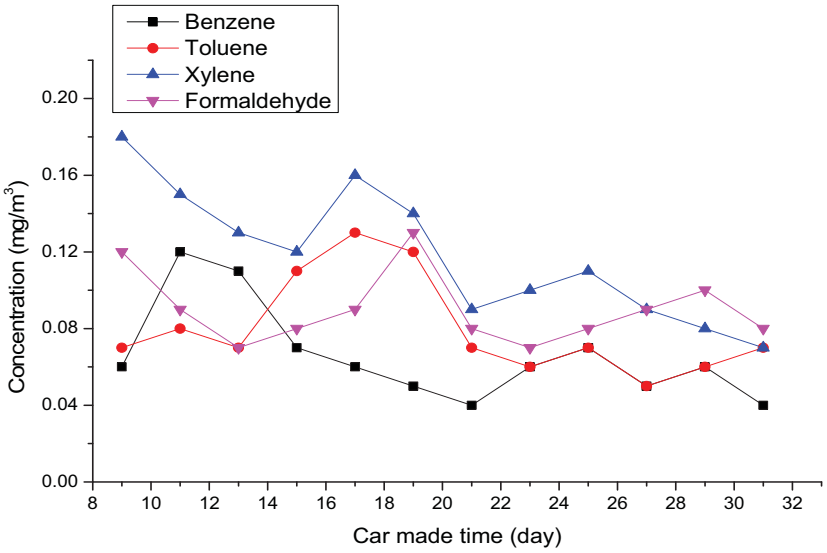

FIGURE 3
Variation of pollutant concentration with time.

Excessive formaldehyde is related to the adhesive used in the car. Most of the adhesive is urea-formaldehyde resin, which is formed by the polymerization of formaldehyde and urea. The free formaldehyde contained in it and the formaldehyde produced during degradation can be released and pollute the interior of the car. At present, most interior materials such as solvent-based coatings, adhesives and other materials use toluene and xylene instead of benzene as solvents in their production process, so that most interior materials used in the car will release benzene to the surrounding environment under certain conditions. Therefore, the use of solvent-based adhesives should be reduced or avoided, and green interior materials should be used.

(3) The changing law of air pollutants in cars. 1) The impact of vehicle made time on air pollutants in the vehicle. Changes in air pollutants in the same car under a closed car window with the time it is made. For most materials in the car, the rate of release of pollutants decreases with time. Cars of different ages have different levels of pollution, and new cars tend to have more pollution than old cars. The experiment measured the relationship of the air pollutant concentration in the car with time when the window is closed. The temperature in the car is kept at about 30°C, the engine is not started, and the air conditioner is not started, and the experimental results are shown in Figure 3.

It can be seen from Figure 3 that with the increase of the time, the pollutant concentration has a downward trend as a whole. The air pollutant concentration in the car will not change much after it is made for 21 days. Therefore, when the new car leaves the factory, it should be placed a period of time to reduce the air pollutants in the car to the equilibrium point. It can also be seen from the figure that the concentration of pollutants fluctuates. Humidity, weather conditions and other factors also affect the concentration of air pollutants in the car.

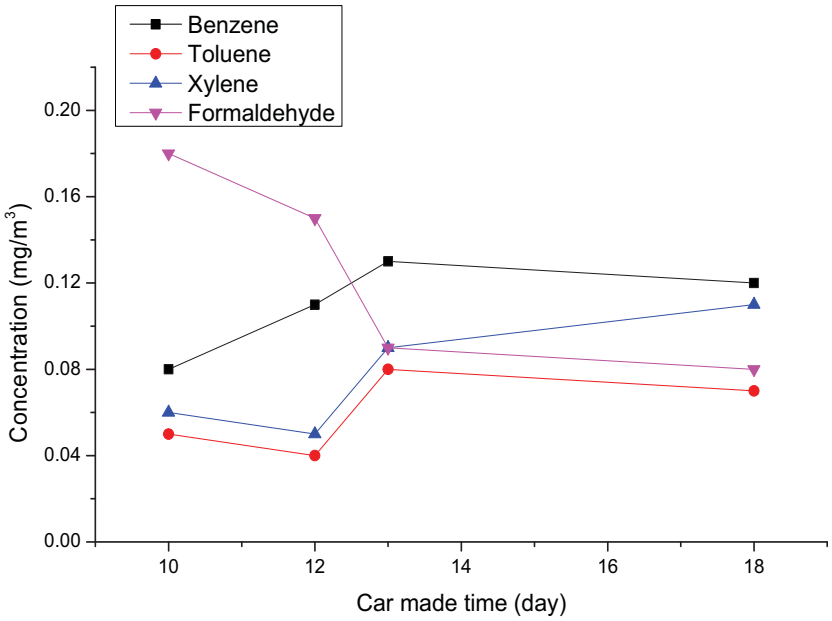

FIGURE 4
Air pollutant concentrations in cars at time (measured in the morning).

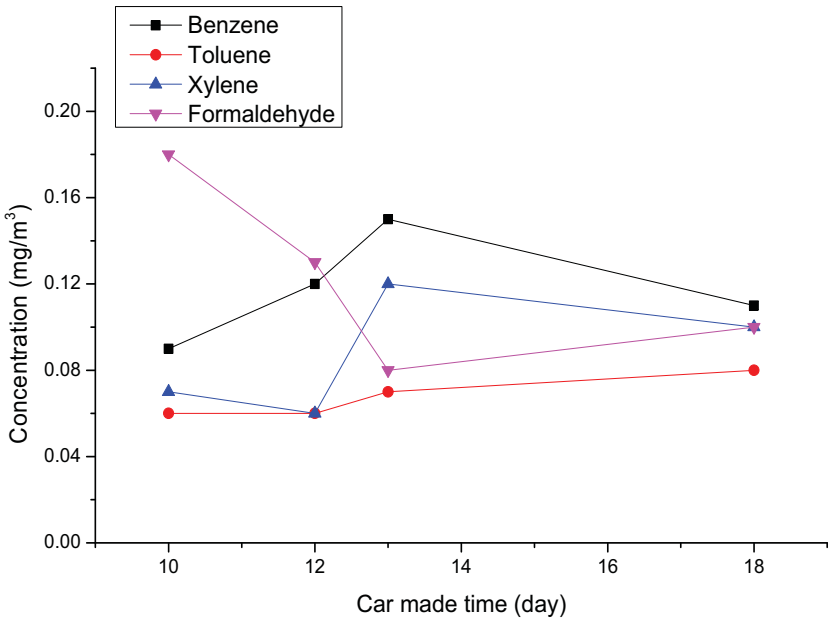

FIGURE 5
Concentrations of air pollutants in cars at different time (measured in the afternoon).

We try to understand the change of air pollutant concentration in different cars of the same vehicle type under the closed windows with the time of. We investigate the air pollutant concentration in the car at different times of the same vehicle after it is made. When the windows are closed, the internal temperature is kept at about 30℃, the engine and the air conditioner are not started, the concentration of air pollutants of NO.2-5 with the increasing time is determined (Figure 4 and Figure 5).

It can be seen from Figure 4 and Figure 5 that the formaldehyde concentration of the same type of car decreases with the extension of time, which is the same as the change of formaldehyde pollutants in the same car. The results of the morning measurement and the afternoon measurement did not change much. This is because these air samples are collected in the car garage, and the environmental factors in the garage do not change much in one day. Figure 5 shows the increase in the concentration of benzene series even after 18 days which is due to the fact that the windows of the car have been sealed. Therefore, in order to reduce the air pollution in the car, it is very important to keep a good ventilation state in the car.

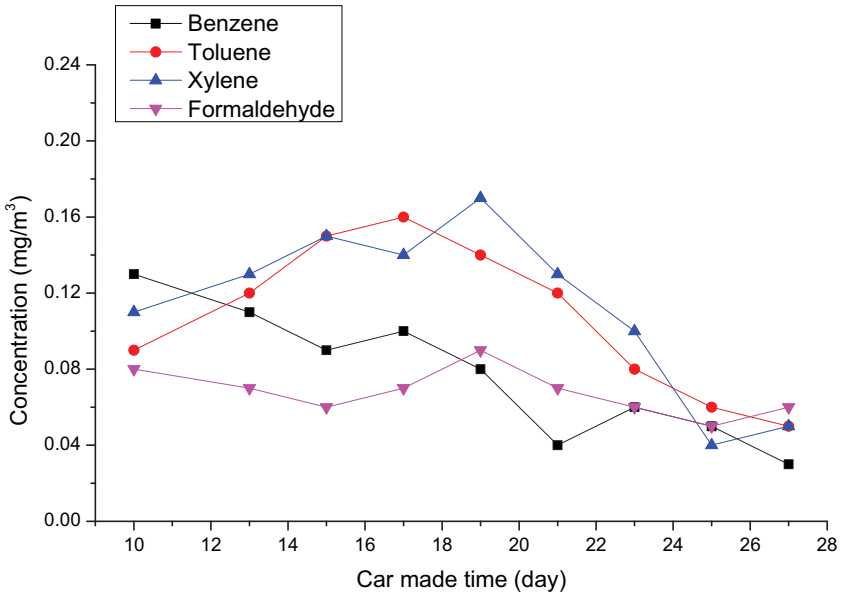

FIGURE 6
Changes in pollutant concentration with offline time under the window.

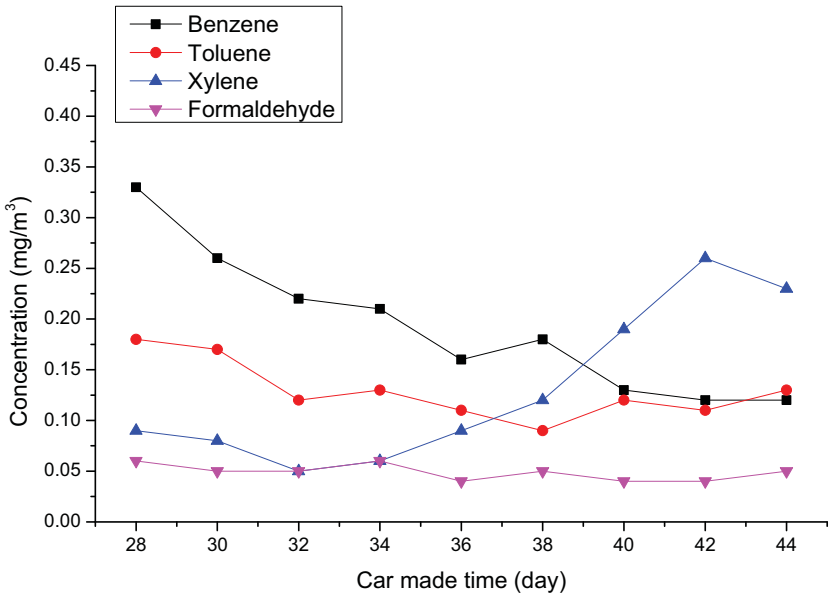

FIGURE 7
Changes in the concentration of air-conditioning pollutants with time.

In order to investigate the change of pollutants in the car with time when the window is opened, the experiment measured the concentration of air pollutants in the car when the window is opened, the temperature in the car is kept at about 32℃, and the air conditioner is not turned on. It can be seen from Figure 6 that compared with the case of closed windows, the air pollutant concentration in the car decreases faster with the extension of time. The reason is that the air inside and outside the car cannot be exchanged when the windows are closed and opening the window can obviously increase the air exchange rate of the car. The higher the air exchange rate, the lower the concentration of gaseous pollutants in the car.

In the case of car No. 1 in the air conditioner internal circulation, the air conditioner is set to a temperature of about 30 degrees, and the pollutant concentration in the car changes with the time. It can be seen from Figure 7 that with the extension of time, the pollutant concentration decline rate is slower, and the concentration tends to be stable. This may be due to the fact that the air exchange rate is zero under the internal circulation of the air conditioner, and the air flow rate in the car is large. The air flow in the car makes the interior materials of the car more likely to release formaldehyde, benzene, and other pollutants. After a period of time, the car will be polluted. The concentration of the substance reaches a balance.

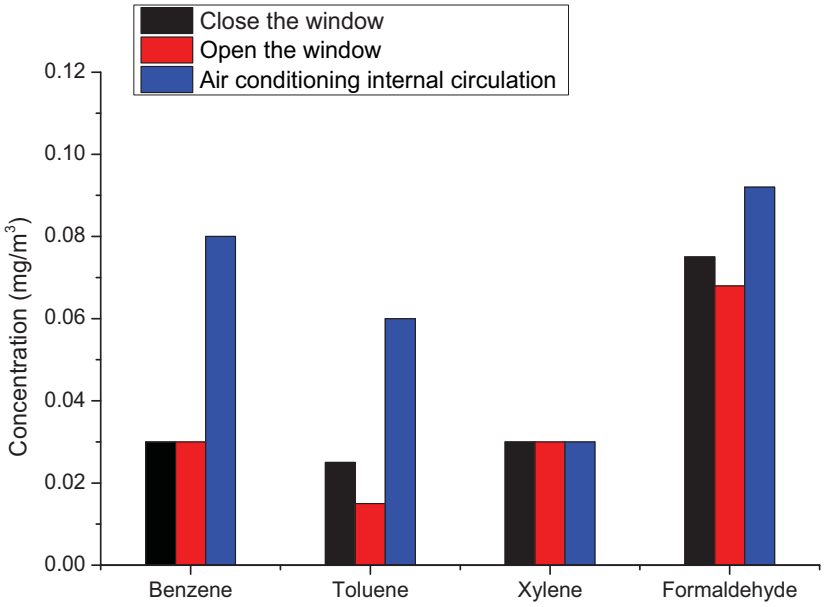

FIGURE 8
Changes in the concentration of pollutants under different ventilation conditions on September 12.

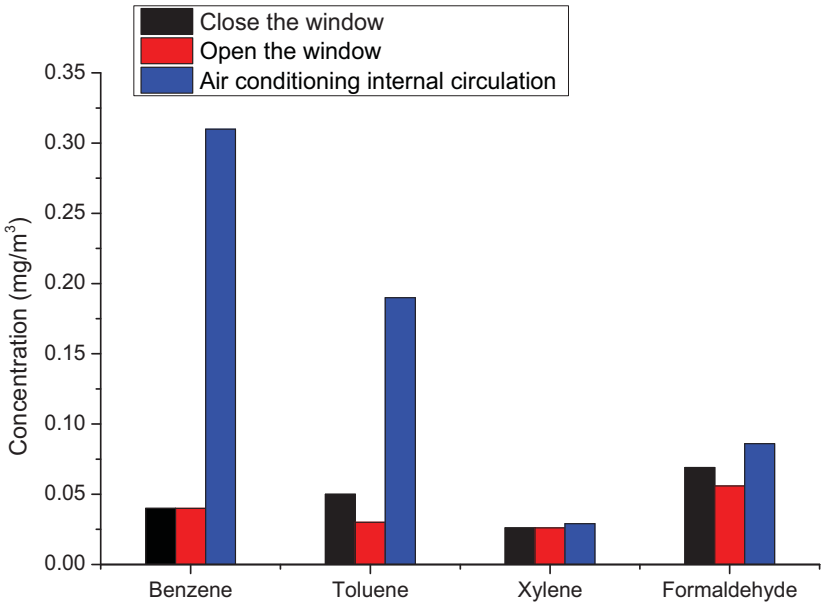

FIGURE 9
Changes in the concentration of pollutants under different ventilation conditions on September 17.

By examining the changes of the air pollutant concentration in the car with the time under the three situations of closing the window, opening the window, and turning on the air conditioner internal circulation, it can be seen that the air pollutant concentration in the car with the window open increases with the time and the reduction is the most obvious.

2) The influence of ventilation methods on the concentration of air pollutants in cars. Cars are mainly manifested in different air flow rates and air exchange rates under different ventilation modes. The air flow on the surface of the material helps the diffusion of gaseous pollutants. If the air is in a static state, the concentration of the interface layer between the material and the air will increase, which will affect the migration of gaseous pollutants inside the material and reduce the release rate of gaseous pollutants in the material. In addition, if the car is separately air-conditioned for internal and external cycles, the air exchange rate is different. The higher the air exchange rate, the lower the indoor concentration of gaseous pollutants. Therefore, it is necessary to investigate the relationship between the concentration of pollutants and the way of ventilation. The experiment measured four conditions of car No. 1 in static air (closed windows),

natural ventilation (open windows), air-conditioning internal circulation, and air-conditioning external circulation. The temperature in the car is maintained at about 33°C, and the pollutant concentration in the air under ventilation modes is derived.

It can be seen from Figure 8 and Figure 9 that compared with the two situations of opening and closing the window, the concentration of pollutants in the air in the car is significantly higher when the internal circulation of the air conditioner is turned on. The concentration of pollutants increases when the internal circulation of the air conditioner is turned on. The reason is that when the internal circulation of the air conditioner is turned on, the air exchange rate is zero, and the air flow rate in the car increases, which increases the concentration of pollutants. From Figure 10, it can be seen that when the air conditioner is externally circulated, the air in the car can be exchanged with the outside fresh air, and the concentration of air pollutants in the car is lower than the concentration when the internal circulation of the air conditioner is turned on. When the car is opened for natural ventilation, using fresh air outside the car to dilute the air pollutants in the car can reduce the concentration of air pollutants, which is the fastest way to improve the air quality in the car.

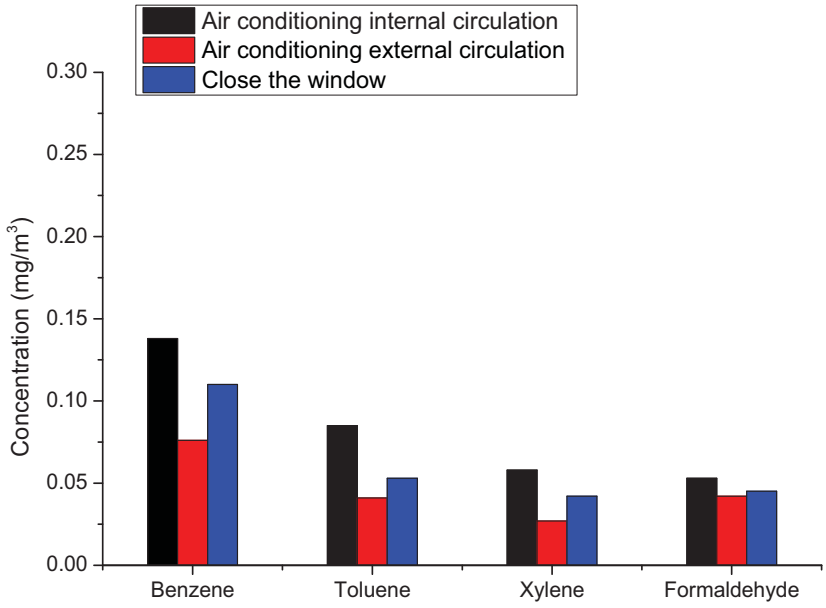

FIGURE 10
Changes in the concentration of pollutants under different ventilation conditions on September 20.

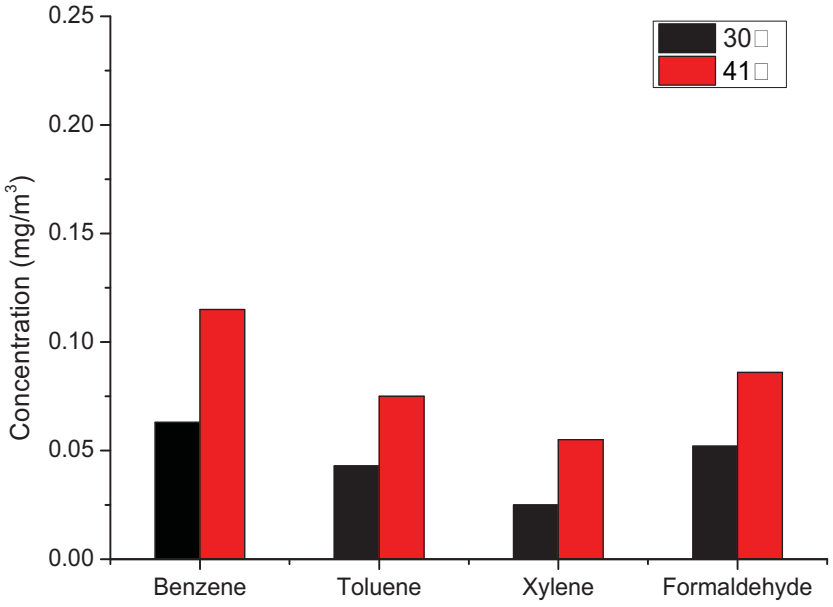

FIGURE 11
Changes in the concentration of air pollutants in the car at different temperatures on September 25.

3) The influence of temperature on the concentration of air pollutants in cars. Temperature will affect the vapor pressure of gaseous pollutants, the diffusion coefficient and the balance between the material and the gas phase, affecting the diffusion of pollutants inside the material and the migration from the surface of the material to the air layer. The concentration of pollutants in the car increases sharply with the increase of temperature. The main reason is that the release of harmful gases from the materials in the car increases with the increase of temperature. The experiment measures the relationship between the air pollutant concentration in the car and the temperature change of the same car when the windows are closed, the air conditioner is not turned on, and the engine is not started. Since there are many factors that affect the concentration of air pollutants in the car, it is designed to collect different air samples in the same car on the same day to reduce experimental errors. With the windows closed and the air conditioner not turned on, the experiment determined the pollutant concentration of car No. 1 at different temperatures on September 25 and September 26.

It can be seen from Figure 11 and Figure 12 that the air pollutant concentration in the car is not the same when the temperature is 30°C. This may be due to the fact that it is not measured on the same day and is affected by weather conditions and humidity. Comparing the measured concentration data on the same day, the results show that the pollutant concentration increase by 10°C with temperature, and formaldehyde, benzene, toluene, and xylene become 1.59 times, 1.76 times, 1.77 times, and 2.17 times, respectively.

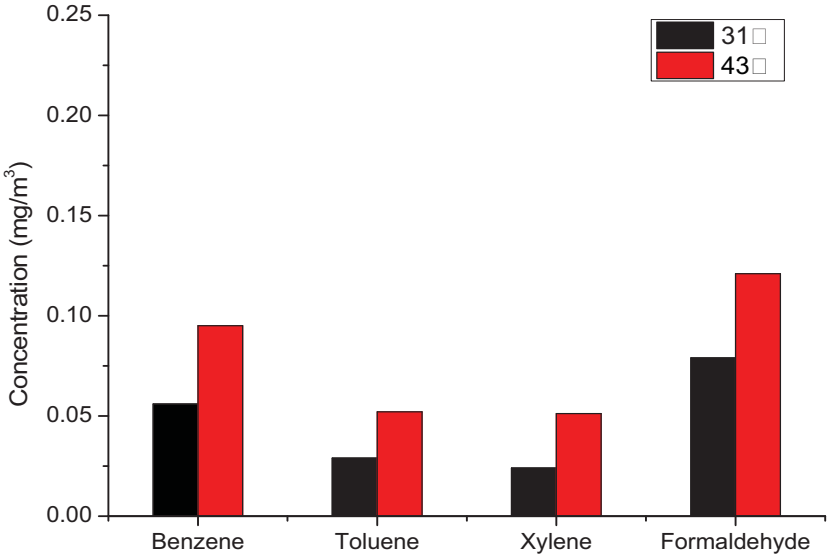

FIGURE 12
Changes in the concentration of air pollutants in the car at different temperatures on September 26.

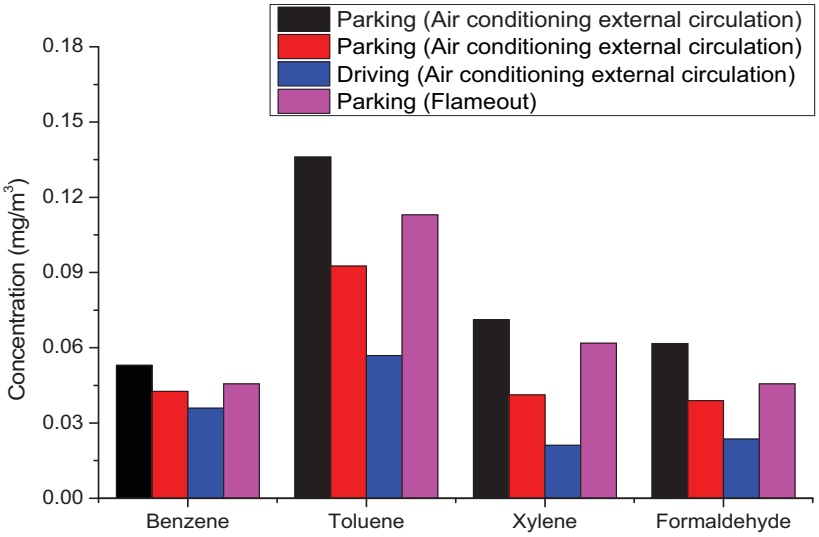

FIGURE 13
Changes in pollutant concentration during static and driving on September 25.

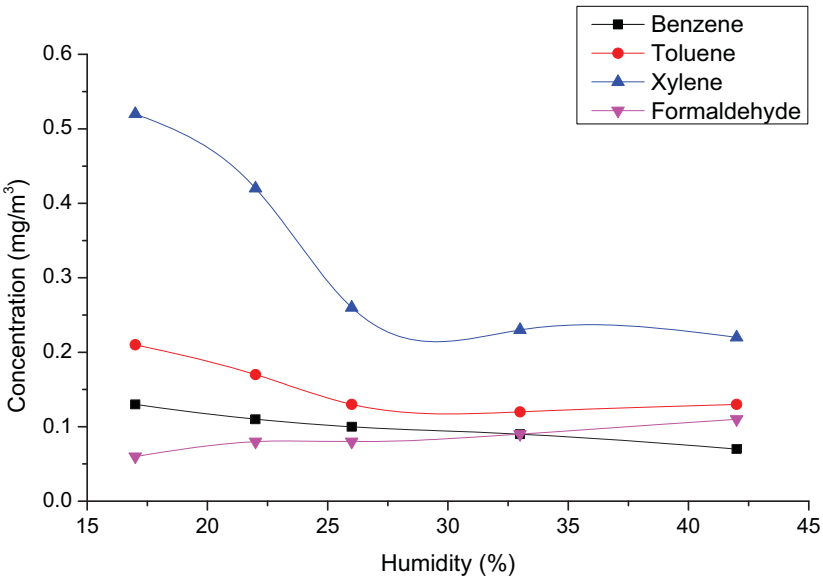

FIGURE 14
Changes in the concentration of air pollutants in the car with humidity.

4) The impact of driving status on the concentration of air pollutants in the car. To investigate the changes in the concentration of air pollutants in the car under static and driving conditions. The experiment collects the air samples of the car in the four states of static non-activated air conditioning, static air-conditioning internal circulation, static air-conditioning external circulation, and driving. It can be seen from Figure 13 that the concentration of air pollutants in the car is the largest when static air-conditioning internal circulation is on, and the concentration decreases in the order of static air-conditioning external circulation, driving, and air-conditioning external circulation. Compared with the static state, turning on the internal circulation of the air conditioner increases the air flow rate in the car. The air flow on the surface of the interior material helps the diffusion of gaseous pollutants, and the air exchange rate under the internal circulation is zero, which increases the concentration of pollutants. Under static external circulation, the air inside and outside the car is exchanged, and the pollutant concentration is lower than static. When the engine is started, the air conditioner is circulated, and the air exchange rate inside and outside the car increases, making the concentration of pollutants in the car the lowest. Therefore, the driving method of starting the car with the air-conditioning internal circulation is very unfavorable to the air quality in the car and should be avoided as much as possible.

5) The influence of humidity on the concentration of air pollutants in cars. Humidity affects the vapor pressure of gaseous pollutants, the diffusion coefficient, and the balance between the material and the gas phase. It not only affects the diffusion of pollutants inside the material, but also affects the migration from the surface of the material to the air layer. When the windows are closed, the engine is not started, the air conditioner is not started, and the temperature is stabilized at about 32 degrees. The relationship between the concentration of pollutants and the relative humidity in the No. 1 car is investigated, and the results are shown in Figure 14. It can be seen that with the increase of humidity, the concentration of formaldehyde increases slightly, and the concentration of benzene series decreases, which is similar to the increase of the concentration of formaldehyde released by wood-based plywood to the ambient air with the increase of humidity. When the humidity increases, the weakly acidic water vapor in the ambient air will react with the free dimethanol oligomers in the urea-formaldehyde resin to form formaldehyde. In addition, it can also promote the hydrolysis of the urea-formaldehyde resin to release formaldehyde. Adhesives used in automotive interior materials use toluene and xylene as solvents in the production process, and the increase in humidity may reduce the release of benzene series in the adhesive.

CONCLUSIONS

(1) By detecting the air in cars, off-road vehicles and commercial vehicles, the results show that the air pollutants in the cars are mainly formaldehyde, benzene, toluene and xylene. The effect of sampling time on the concentration of pollutants shows that the sampling time of formaldehyde is 20 minutes, and the sampling time of benzene series is better when the sampling time is 50 minutes.

(2) The time has a greater impact on the air pollution concentration in the car. Compared with

closing the window and opening the air-conditioning internal circulation, when the window is opened, the air pollutant concentration in the car decays most obviously with the extension of the time, followed by the closed window.

(3) The ventilation method has a significant impact on the air pollution concentration in the car. When the windows are opened for natural ventilation, the air exchange rate is increased, and the air pollutants in the car can be reduced. The air pollutant concentration in the car is the lowest. The pollutant concentration is the highest when the air conditioner is internally circulated.

(4) Temperature has a greater impact on the air pollution concentration in the car. When the temperature increases by 10°C, the formaldehyde, benzene, toluene, and xylene in the car become 1.59 times, 1.76 times, 1.77 times, and 2.17 times, respectively. The concentration of air pollutants in the car is the largest under static air conditioning internal circulation. The influence of humidity on the concentration of pollutants in the car is not obvious. With the increase of humidity, the concentration of benzene series in the air in the car has a downward trend, and the concentration of formaldehyde increases slightly.

ACKNOWLEDGEMENTS

This work was supported by the 2020 Heilongjiang Provincial Philosophical Social Science Plan (20YSE287); and the 2021 Heilongjiang Provincial Educational Science “14th Five-Year Plan” (GJB1421413).

REFERENCES

[1] Weinhold, B. (2001) Pollutants lurk inside vehicles. Environmental Health Perspectives. 109(9), 422-427.

[2] Deng, D.Y., Shao, R.T., Chen, S.J. (2006) Carbon dioxide pollution inside vehicle and ventilation modes. Environmental Science & Technology. 29(11), 94-95.

[3] Leung, P.L., Harrison, R.M. (1999) Roadside and in-vehicle concentrations of monoaromatic hydrocarbons. Atmospheric Environment. 33(2), 191-204.

[4] Park, J.H., Spengler, J.D., Yoon, D.W., Dumyahn, T., Ozkaynak, H. (1998) Measurement of air exchange rate of stationary vehicles and estimation of in-vehicle exposure. J. Expo. Anal. Environ. Epidemiol. 8(1), 65-78.

[5] Ye, X., Guo, X., Shi, H., Lin, S., Cen, Z. (2007) In-car air pollution of formaldehyde and its affecting factors. Environmental Pollution & Control. Environmental Pollution & Control. 29(4), 309-311, 315.

[6] Huang, L.Y., Lin, S.M. (2008) Emission and determination of VOC in car. Hebei Chemical Engineering and Industry. 145(5), 73-75.

[7] Liu, X., Yaozong, X.U., Shujie, X.U., Zhuang, M., Liu, W., Center, A.D. (2015) Situation and management policy about China's car VOC. Environment and Sustainable Development. 40(5), 26-29.

[8] Jing, W., Li, H., Liang, Y., Zhang, J., Shen, L., Chen, L. (2016) Headspace method analysis of VOC in car seat foam. Chemical Propellants & Polymeric Materials. 14(3), 75-78.

[9] Zhang, C.Z., Zhang, J.P., Zhao, H., Shi, J. (2014) An investigation of the harm of car interior pollution on human healthy. Journal of Qingdao University (Engineering & Technology Edition). 29(1), 105-110.

[10] He, X.F., Wang, G.S. (2009) Survey of air pollution inside cars. Journal of Environment and Health. 26(4), 341-343.

[11] Qian, L., He, X. (2015) Research on the air pollution inside saloon car and its release in winter. Shanghai Measurement and Testing. 42(3), 6-9.

[12] Jian, Z., Chen, L. (2010) Sampling analysis of vehicle volatile organic compounds and the control strategy for VOC. Straits Science. 12, 152-156.

[13] Bo, L.A., Xiang, Y.A., Hm, A., Di, L.A., Qh, A., Mi, T.B. (2019) Health risk assessment and source apportionment of VOCs inside new vehicle cabins: a case study from Chongqing, China – Science Direct. Atmospheric Pollution Research. 10(5), 1677-1684.

[14] Li, L., Hao, F. (2014) Determination of 7 kinds of benzene series in car air by ATD-GC-MS method. Environment and Development. 26(8), 27-32.

[15] Tong, J.W., Wang, Y., Jun, L.I. (2010) Benzene series compounds pollution inside passenger cars in Tangshan. Journal of Environment & Health. 196(1), 76-82.

[16] Chen, X., Zhang, G., Dai, J. (2010) Mass concentration characteristics of in-car benzene and its derivatives. Automotive Engineering. 32(11), 1006-1010, 1001.

[17] Liu, H., Liu, S.Q., Shi, T.X. (2013) Analysis on pollution status and influencing factors of benzene series pollutants in domestic cars in Guangzhou. Journal of Medical Pest Control. 29(7), 718-720, 724.

[18] Zhang, H.L., Chen, H.Y., He, L.F., Guo, Y., Chen, H.J. (2017) Investigation on air pollution in car and cognitive behavior of drivers in Zhongshan City. Occupation and Health. 33(19), 2703-2705, 2709.

Received: **27.11.2021**
Accepted: **23.01.2022**

CORRESPONDING AUTHOR

Mingfei Wang
Graduate School,
Sejong University,
Seoul 05006 – South Korea

E-mail: 13298891566@163.com

© by PSP Volume 31– No. 05/2022 pages 4995-5003 Fresenius Environmental Bulletin

CO_2 SUPPRESSION OF METHANE/ AIR EXPLOSION FLAME AND PRESSURE COUPLING ANALYSIS

Xinna Zhu, Junyi Zhou*, Zhengchao Guo, Xuelin Zhang

College of Civil Engineering, Chongqing Three Gorges University, Chongqing 404100, China

ABSTRACT

In the process of storage, transportation and use of clean energy such as natural gas and coal-bed methane, explosions often occur. The technology of inert gas explosion suppression based on CO_2 and N_2 has always been the focus of scholars. The popularization of CO_2 dilution natural gas technology to reduce NO_x emission, as well as the utilization of landfill gas and biogas dominated by methane and CO_2, makes the study on the explosive characteristics of methane and CO_2 mixture appear to be particularly important.

In order to study the coupling law of flame and pressure of methane/air explosion under the action of CO_2, experiments of suppressing methane/air explosion with different volume fraction of CO_2 were carried out in a square plexiglass duct. The influence of methane/air premixed gas explosion flame propagation and explosion pressure under different volume fraction of CO_2, as well as the coupling between explosion flame and pressure, were analyzed. The results show that with the increase of CO_2, the flame temperature, flame speed, explosion overpressure peak, and the time to reach the peak of overpressure all show a decreasing trend. CO_2 affects the combustion reaction rate from three aspects of dilution, thermal diffusion and chemical kinetics. The reduction of combustion reaction rate leads to three types of flame structure evolution, namely "non-tulip" flame, "tulip" flame and "buoyancy" flame, and also leads to three types of explosion overpressure evolution. They are "three-peak structure and the second peak is the maximum peak", "three-peak structure and the first peak is the maximum peak" and "two-peak structure and the first peak is the maximum peak" respectively. During the formation of tulip flame, the flame structure dominates the flame propagation speed and explosion pressure.

KEYWORDS:
Methane, carbon dioxide, explosion flame, pressure, couple

INTRODUCTION

Clean energy, such as natural gas and coal-bed methane, is widely used in industry and life. During the process of storage, transportation and use of these gases, explosion accidents often occur. For example, the gas explosion in a residential building in Magnitogorsk, Chelyabinsk Prefecture, Russia, on December 31, 2018, killed 39 people [1], and the natural gas explosion accident occurred in Shiyan City, Hubei Province, China, on June 13, 2021, causing 26 deaths and 138 injuries [2]. For one part, the technology of inert gas explosion suppression based on CO_2 and nitrogen is always the key research. For another, CO_2 dilution natural gas technology for reducing NO_x emissions has been promoted [3], and landfill gas and biogas dominated by methane and CO_2 has been used [1]. So the research of the mixture of methane and CO_2 explosive is particularly important.

In the field of methane and CO_2 mixed gas explosion, a lot of studies have been conducted through experimental and numerical simulation. In terms of explosive limit, Kondo [4] and Qu Zhongwei et al. [5] Respectively experimentally or numerically determined the explosion limits of CH_4/CO_2/air mixtures with different ratios. In terms of explosion overpressure, Zhang Yingxin et al. [6] experimentally studied the influence of different volume fractions of CO_2 on CH_4/air explosive overpressure in a medium-sized explosive experimental device. Li et al. [7] experimentally measured the maximum overpressure and overpressure rise rate of mixed gas with different proportions of CH_4/CO_2/ air in a square vessel. In terms of flame behavior, Zheng et al. [8] experimentally studied the flame structure characteristics of $CH_4/O_2/CO_2$ mixtures during the explosion process using a directional pipeline. Hugo et al. [9] experimentally studied the characteristics of CH_4/CO_2/air explosion flame in a micro reactor. In terms of flame propagation kinetics and mechanism, Jia Baoshan et al. [10] numerically investigated the reactants, free radicals and total methane consumption rate during the explosion process of CH_4/CO_2/air mixtures, and explained the explosion suppression mechanism of CO_2. Duva et al. [11] experimentally studied the influence of CH_4/air laminar combustion speed with CO_2 addition in a cylindrical combustion chamber, and elaborated the influence mechanism of CO_2 from the aspects of dilution

effect, thermal diffusion effect and chemical kinetics effect.

However, the current studies on the explosive characteristics of methane/air/CO_2 mixtures only focus on the explosion limit, explosion overpressure, flame structure, flame propagation dynamics and explosion mechanism. But the coupling of explosion flame and overpressure is seldom reported. The purpose of this study is therefore to investigate the explosion behavior of methane/air with the effect of CO_2 addition in a small circular open duct. In this study, the methane/air mixtures with stoichiometric ratio and six volume fractions (0,4%,8%,12%,16% and 20%) of CO_2 in mathane fuel are selected. In the experiment, flame structure, flame speed and overpressure are obtained and the coupling of explosion flame and overpressure is analyzed. This work may help to ensure the safety utilization of methane in the industry.

EXPERIMENTAL SET-UP

The sketch of experimental setup is shown in Figure 1, which is mainly composed of four parts: an explosion duct, gas distribution system, ignition system and data acquisition system [12]. The explosion duct is 0.84m long with a cross-section of 120mm × 120mm, producing an aspect ratio of 7. A small round discharge vent, which is closed by the PVC membrane with an inner diameter of 40mm, is mounted at the right end of the duct. After ignition, the explosion shock wave breaks through and acts as a discharge. The gas distribution system is composed of three mass flow controllers, a CH_4 cylinder, a CO_2 cylinder and a air compressor. The ignition system consists of a high frequency pulse igniter mounted in the center of the left end and the ignition pressure is about 6KV. The data acquisition system consists of high-speed camera, overpressure transducer, photoelectric transducer and data acquisition card. The process of explosion flame evolution is captured by a HighSpeedStar4G height camera produced by Lavision in Germany, and the acquisition frequency is 2000 frame/s. A MD-HF overpressure transducer is used to record the overpressure-time history, and installed on the upper wall on the left side of the duct. A RL-1 photoelectric transducer is used to mark the ignition time, which is located at the outside of the duct and points to the spark igniter. A USB-1608FS plus data acquisition card is used to collect overpressure and photoelectrical data during the process of explosion.

MATERIALS AND METHODS

Experiments are conducted for methane/air mixtures with one equivalent ratio(1.0) and five CO2 volume fractions (0%, 4%, 8%, 12%, 16% and 20%). The CO2 and methane used in the experiment are produced by Jining XieLi Special Gas Co. Ltd. and the purity exceeds 99.99%. Each of the tests is repeated at least 3 times so as to guarantee the accuracy of experimental results.

RESULTS AND DISCUSSION

Effect of CO_2 addition on the explosion flame. 1. Effect of CO_2 addition on the explosion flame temperature The typical effects of CO_2 volume fraction varying on explosion flame propagation of the stoichiometric ratio methane/air is presented in Figure 2. The flame color with 0% CO_2 volume fraction first changes from light blue (16.5ms) to cyan green (37.5ms) and then yellow (52ms). Finally, the flame front changes to cyan green and the burned area at the end of the flame changes to light blue (74ms). The color from light blue to cyan green and then yellow is a process in which the temperature of the flame gradually increases [13-14], so it can be seen that the temperature of the flame first increases and then decreases. At the beginning of the explosion, the combustion reaction rate is slow, and the heat released is less, so the temperature of the combustion products is lower; As the flame spreads, the combustion reaction rate gradually increases with releasing a large amount of heat, which gradually increases the temperature of the combustion products; However, the flame contacting the duct wall increases the heat dissipation rate during the combustion process, and the PVC membrane on the right side of the duct is ruptured to reduce the concentration of the premixed combustible gas, so the temperature of the combustion product decreases again. The methane/air flame color that is added low CO_2 is mainly cyan green.When the CO_2 volume fraction is high, which is 12%, 16%, 20%, the flame is mainly light blue. As expected, the methane/air/CO_2 mixtures flame temperature would decrease with the increases of CO_2.

2. Effect of CO_2 addition on the explosion flame structure. The explosion flame propagation process in a closed duct has been divided into four stages, hemisphere flame, finger flame, the skirt of flame touching the sidewalls,tulip shaped flame [15]. Duct aspect ratio and laminar flame propagation speed are two key factors for the formation of tulip shaped flame [16-17]. In this experiment, the aspect ratio of the duct remains the same, but the components of the methane/air/CO_2 mixtures are different, and different mixing components produce different laminar flame propagation velocities. In Figure 2, as CO_2 volume fraction increases, there is a big difference in the flame evolution process. The laminar flame speed decreases with CO_2 fraction increases in methane/air mixture, and therefore the flame propagation time decreases as CO_2 fraction increases.

When the volume fraction of CO_2 is 0%, 4% and 8% respectively, the flame only goes through two stages of hemisphere flame and finger flame without forming tulip flame; When the volume fraction of CO_2 is 12%, 16% respectively, the flame goes through four stages of hemisphere flame, finger flame, the skirt of flame touching the sidewalls, tulip shaped flame; When the volume fraction of CO_2 is 20%, the buoyant flame is dominant, this phenomenon can be attributed to the buoyancy effect [7, 18-19].

3. Effect of CO_2 addition on the flame speed. In this experiment, the flame front position is defined as the distance between the flame leading. When the flame spreads in hemisphere flame and finger flame, the flame front in the center of the duct is considered to be the leading tip; When the flame spreads in oblique plane flame, tulip shaped flame and buoyant flame, the flame front close to the upper sidewall is considered to be the leading tip. Figure 3(a) presented the measured flame front positions of methane/air under the action of different volume fraction of CO2. The flame front position gradually increases at the same time with the increase of CO2 volume fraction. This result can be attributed to the flame propagation time in the pipeline becomes longer as the laminar flame speed decreases.

The flame speed can be calculated based on the flame front positions in Figure 3(a). Figure 3(b) showed the flame speed of methane/air under the action of different volume fraction of CO_2. The flame speed is the difference in position between the two time points divided by the time interval between the two time points. The flame speed changes with time in a similar way under different volume fraction of CO_2. When the volume fraction of CO_2 is less than 16%, the flame speed increases exponentially due to the acceleration of finger shaped flame after ignition, which is caused by the rapid expansion of combustion products [20]. The flame acceleration process ends when the flame contacts the sidewall and the PVC membrane on the right side is broken. When the volume fraction of CO_2 is 0%, 4%, and 8%, as the flame approaches the right side of the tube, the flame speed produced a brief acceleration due to the nozzle limits energy release. When the volume fraction of CO_2 is 12% and 16%, the flame propagation speed increases slowly in the later stage due to the formation of "tulip" flame. This view will be verified in the follow-up section of the flame and pressure coupling analysis of methane/air explosion under the action of CO_2 in Section 3. When the volume fraction of CO_2 is 20%, the flame always travels smoothly at a small speed. As shown in Figure3(b) and Table 1, with the increase of CO_2, the slope of linear fitting in the rising phase of flame speed gradually decreases, that is flame front propagation acceleration presenting a downward trend. When CO_2 volume fraction is 12%, 16% and 20%, the slope of linear fitting decreases from 0.38 without inhibitor to 0.20, 0.08 and 0.001 respectively. This also indicates that low concentration of CO_2 has no obvious suppression effect, while high concentration of CO_2 has a good suppression effect [21].

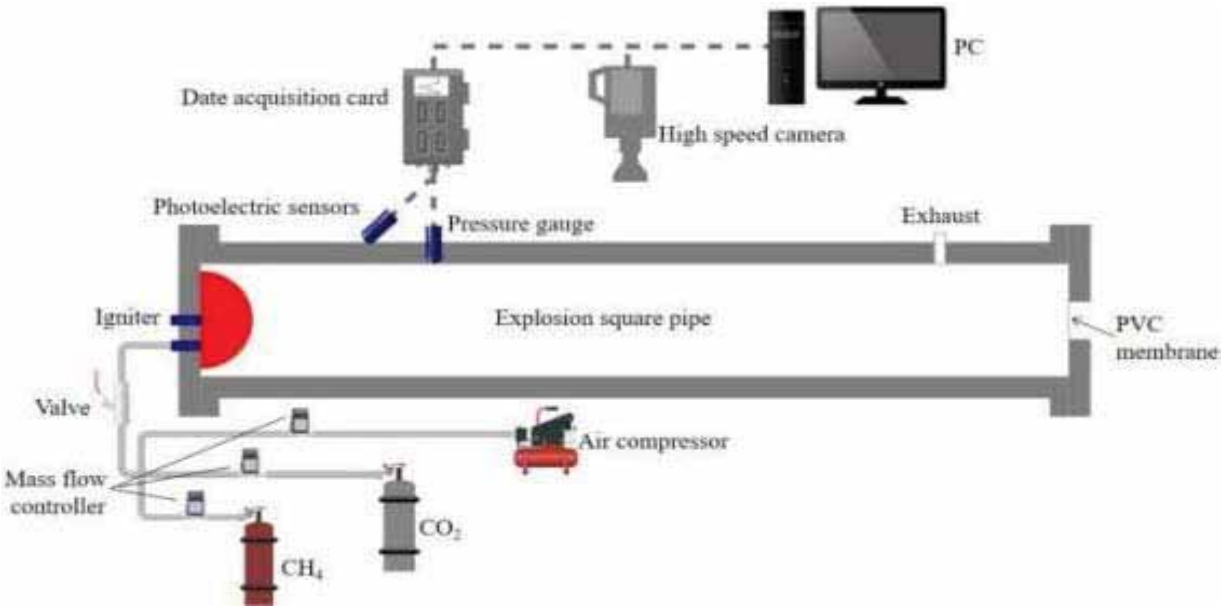

FIGURE 1
Schematic diagram of carbon dioxide explosion suppression experimental system

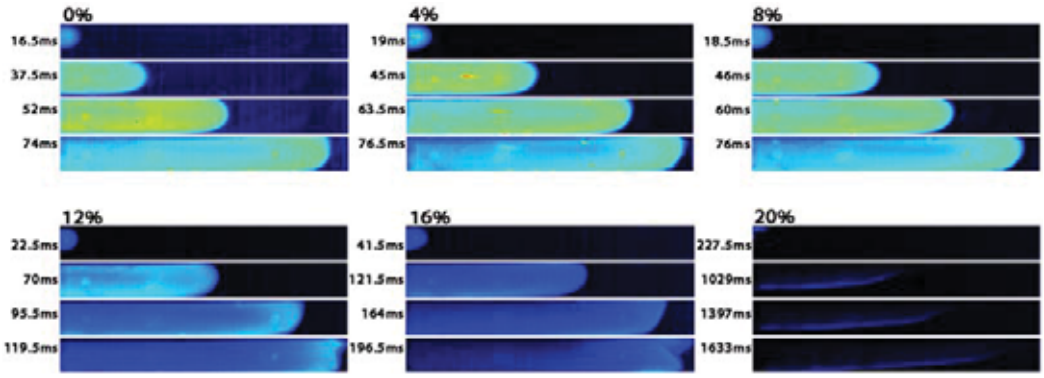

FIGURE 2
Propagation process of explosive flame under different volume fraction of carbon dioxide

TABLE 1
Linear fitting formula of flame front propagation velocity rising stage and time

Volume fraction of CO_2	Linear fitting formula	Correlation coefficient R^2
0%（No inhibitor）	V=0.38038t-1.06189	0.95691
4%	V=0.37977t-0.97162	0.96821
8%	V=0.36093t-1.13501	0.97994
12%	V=0.20368t-0.90358	0.95327
16%	V=0.07647t-0.38488	0.93111
20%	V=0.000845t+0.01543	0.76119

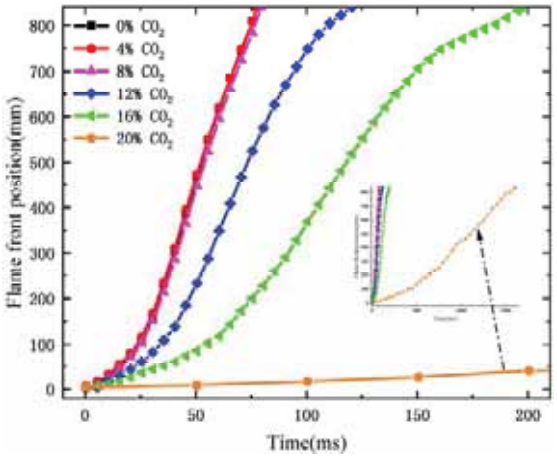

(a)

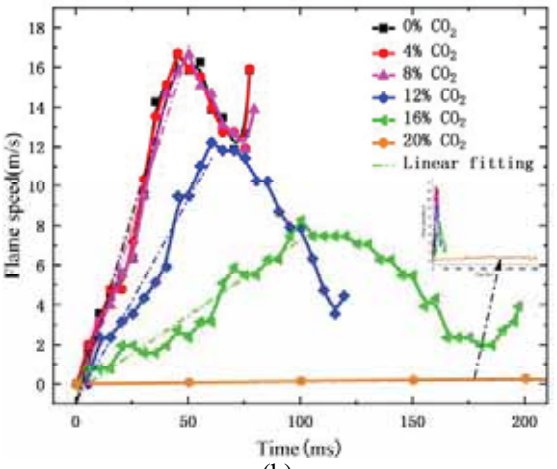

(b)

FIGURE 3
Variation of flame front position and flame propagation velocity under the action of different volume fraction of carbon dioxide

Effect of CO_2 addition on the overpressure history. 1. Effect of CO_2 addition on the evolution of overpressure. Figure 4 shows the change rule of overpressure and instantaneous overpressure rise rate with time of methane/air without inhibitor (0% CO_2). After ignition, the combustion products are heated and expand, the overpressure increases exponentially due to the dramatic growth of flame surface area. When the precursor shock wave exceeds maximum pressure of the PVC membrane, the PVC membrane breaks and the unburned gas begins to leak. When the pressure lost is equal to the pressure increased by combustion, the first peak P1 occurs [22-23]. Subsequently, the leakage loss pressure of the unburned gas is greater than the increasing pressure of the combustion generation. Hence, the pressure curve presents a temporary downward trend. As the flame spreads, the volumetric generation rate of burnt gas induced by combustion increases further and exceeds the leakage loss pressure, thus resulting in a continuous rise in the pressure again. With the consumption of unburned gas and the heat dissipation caused by flame contact with the duct sidewalls, the combustion rate of premixed combustible gas begins to decrease, and the volume generation rate of combustion products begins to decline. The pressure lost by the relief of the unburnt gas is equal to the pressure of combustion growth again. Thus, the second peak value P_2 appears. Subsequently, the leakage loss pressure is greater than the increasing pressure in the combustion process, and the pressure curve shows a downward trend. As the reaction progresses, after the premixed flame spreads to the end of the duct, the flame continues to burn at a relatively low

speed. When the negative pressure area at the circular vent hole moves towards the duct under the drive of the reflux gas, the overpressure rises in a small range and the third peak, P_3, appears [24].

The explosion overpressure histories of methane/air with CO_2 addition are presented, as shown in Figure 5. Six working conditions present three types of overpressure curves. Combined with Table 2, it can be seen that the overpressure curve of the first type appears when the volume fraction of CO_2 is 0%, 4%, 8% and 12%. The first type presents a typical three-peak structure, and the maximum overpressure peak is P_2. The second type of pressure curve appears when the volume fraction of CO_2 is 16%, which also presents a three-peak structure, but the maximum overpressure peak is P_1. The third type of pressure curve appears when the volume fraction of CO_2 is 20%, but it shows a double peak structure, and the maximum overpressure peak is also P_1.

Before the appearance of P_2, the increased pressure of combustion during flame propagation is greater than the pressure lost by the relief of the unburnt gas. After the appearance of P2, the increased pressure of combustion during flame propagation is less than the pressure lost by the relief of the unburnt gas. Therefore, P2 is the embodiment of the reaction intensity of premixed gas, which is defined as the maximum overpressure peak P_{max} [25]. As the volume fraction of CO_2 increases, the reaction intensity of the premixed gas gradually decreases. The maximum overpressure peak P_2/P_{max} diminishes significantly with CO_2 increasing, and it goes from greater than P_1 to less than P_1.

Although both the first and second types of pressure curves appear P_3, the first type of pressure curve P_3 is caused by the return of fresh air outside the pipe to the explosion pipe, which increases the overpressure value from negative pressure to close to normal pressure. The second type of pressure curve P_3 is the result of the formation of the "tulip" flame. This view will be verified in the follow-up section of the flame and pressure coupling analysis of methane/air explosion under the action of CO_2 in Section 3.

2. Effect of CO_2 addition on the peak overpressure（P_{max}）. The peak overpressure and the time required to reach the peak overpressure are presented in Figure 6. As the volume fraction of CO_2 increases, the peak overpressure gradually decreases, and the time required to reach the peak overpressure shows an overall upward trend. Under the action of low concentration of CO_2, that is, when the volume fraction of CO_2 is 4% and 8%, the peak overpressure and the time required to reach the peak overpressure change less than those without inhibitor (0% CO_2). When the volume fraction of CO_2 is 12%, 16%, and 20%, the rate of decrease in the peak overpressure and the increase rate of the time required to reach the peak overpressure are both large. When the volume fractions of CO_2 were 12%, 16%, and 20%, the peak overpressure dropped from 29.2KPa to 14.9KPa, 7.6KPa, 1.6KPa respectively, which decreased by 48.9%, 73.9%, and 94.54% respectively; The time required for the peak overpressure value increased from 54.6ms to 67.3ms, 101.1ms, and 1060.8ms respectively, which was extended by 23.2%, 85.23%, and 1842.94% respectively.

Coupling analysis of flame and pressure of premixed gas under different volume fraction of CO_2. The flame propagation is closely related to the overpressure. Figure 8 shows the coupling of flame propagation and overpressure under the action of different volume fractions of CO_2. Before the PVC membrane failure, the combustion belongs to the constant-volume combustion stage. As the reaction progresses, the burning rate and the flame surface continue to increase, and the flame front velocity increases exponentially. Especially, the overpressure value continues to increase. After the PVC membrane failure, it belongs to the constant pressure combustion stage. The overpressure value is determined by the combustion reaction rate and the vent rate. At this time, the combustion speed and the flame speed is still increasing, and the combustion reaction rate is greater than the explosion vent rate, which making the overpressure value increase again. As the combustion reaction progresses, the concentration of the combustion reactant decreases, the flame contacts the side wall of the pipe, and the heat loss increases, which reduces the combustion reaction rate and flame front velocity, and the detonation rate plays a dominant role, leading to the decline of the overpressure value.

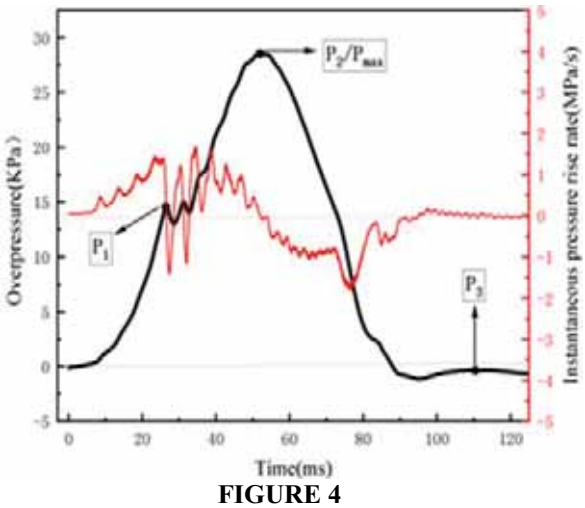

FIGURE 4
Variation of explosion pressure with time without inhibitor (0%)

TABLE 2
Pressure curve peak types under different volume fractions of carbon dioxide

Type	Volume fraction of CO_2	Number of peak overpressure	Peak overpressure
The first type	0%	3	P_2
	4%	3	P_2
	8%	3	P_2
	12%	3	P_2
The Second type	16%	3	P_1
The third type	20%	2	P_1

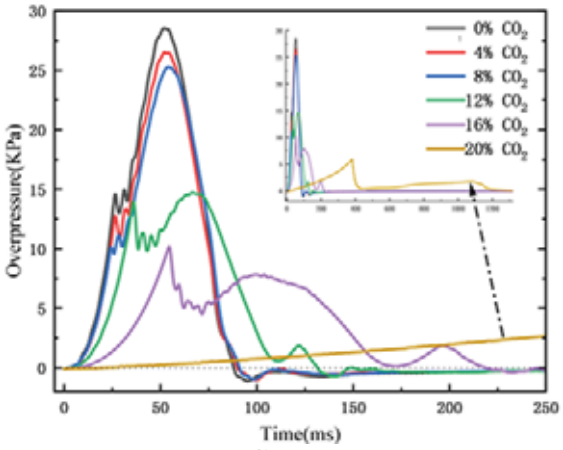

FIGURE 5
Pressure variation with time under the action of different volume fractions of carbon dioxide

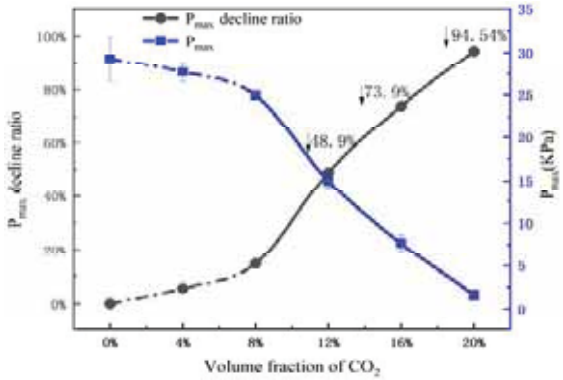

(a) Peak and decreasing rate of explosion overpressure

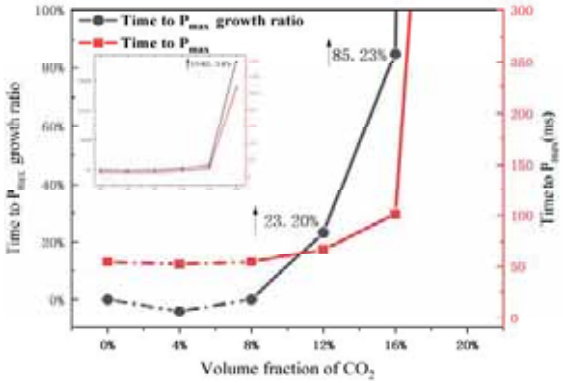

(b) Time to peak and increasing rate of overpressure

FIGURE 6
Variation rule of overpressure peak under different volume fraction of carbon dioxide

When the CO_2 volume fraction is small, as shown in Figure 7(a), at the end of the flame propagation, the front speed has a short and small increase. This is due to the fact that when the flame approaches the right side of the pipe, the energy release is restricted by the nozzle, which causes the energy to accumulate and a short acceleration process. After the flame passes through the vent hole, the overpressure value also increases slightly, which is caused by the fresh air outside the duct entering the inside of the duct [26]. When the CO_2 volume fraction is large, as shown in Figure 7(b), at the end of flame propagation, the flame speed and overpressure both show different increasing trends. This is due to the flame structure changing from "inclined flat plate" to "tulip-like". Meanwhile, the flame surface increases and the combustion reaction rate increases [27]. When the CO_2 volume fraction is close to the upper explosion limit, as shown in Figure 7(c), the flame front always propagates at a relatively low speed due to the low combustion speed, and the whole explosion process is dominated by buoyant flames.

The addition of CO_2 mainly affects the combustion reaction rate from three aspects: dilution, thermal diffusion, and chemical kinetics [11, 28]. Dilution effect always dominates, followed by thermal effect [29]. Under the action of high concentration of CO_2, the influence of chemical kinetics is higher than that of thermal effect [30]. First, CO_2 acts as a diluent, reducing the concentration of fuel and oxidizer, and reducing the burning rate; Second, CO_2 is an effective heat sink and radiator, and CO_2 increases the specific heat capacity of the mixture [29] and increases the radiant heat loss [31]. At the same time, it reduces the flame temperature and the combustion reaction rate. CO_2 reduces the thermal diffusivity and Lewis of the mixture (Lewis is the ratio of thermal diffusivity to mass diffusivity) [32-33], which reduces the transport performance of the mixture and reduces the combustion reaction rate.Thirdly, CO_2 on the one hand participates in the combustion elementary reaction of methane/air, and on the other hand accelerates the gas phase destruction rate of free radicals as a stable third body, thus reducing the combustion reaction rate [11,34]. As shown in Figure 7. the increase of the CO_2 volume fraction reduces the combustion reaction rate, which makes the flame structure, explosion overpressure and flame front propagation speed appear different rules.

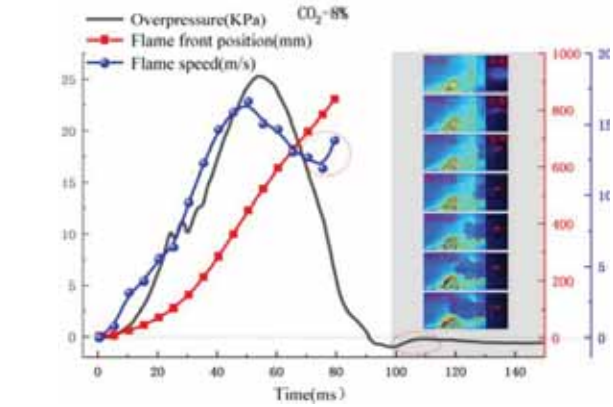

(a) "non-tulip" flame

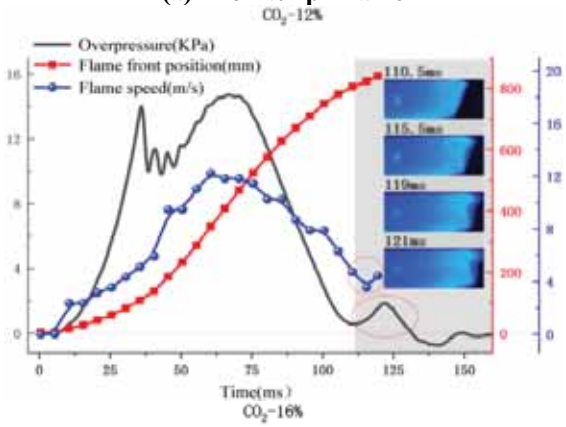

(b) tulip" flame

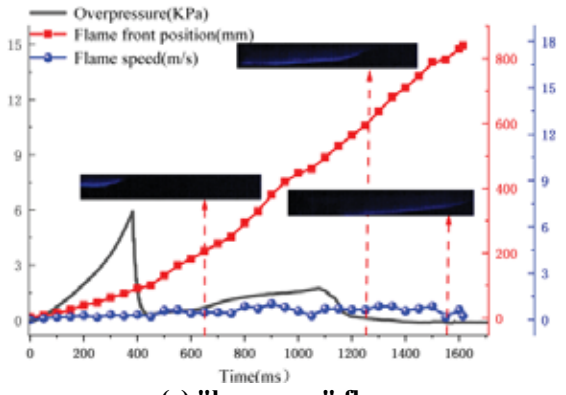

(c) "buoyancy" flame

FIGURE 7

Coupling relationship between flame propagation and pressure of methane explosion under the action of different volume fractions of carbon dioxide

CONCLUSIONS

In this paper, the explosion behavior of stoichiometric ratio methane/air under the effect of six volume fractions (0, 4, 8, 12, 16% and 20%) of CO_2 addition in a small circular open duct is investigated.

1. The typical effects of CO_2 volume fraction varying on explosion flame propagation process can be observed in all cases. With the CO_2 volume fraction increasing, the color of flame changes from cyan green to light blue indicating that the flame temperature decreases gradually, and there are three types of explosion flame propagation process: "non-tulip" flame, "tulip" flame and "buoyancy" flame. The slope of linear fitting in the rising stage of flame speed gradually decreases with the CO_2 volume fraction increasing. that is, the acceleration in the growth stage of flame front propagation presents a downward trend.

2. With the CO_2 volume fraction increasing, the maximum peak of overpressure and the time to reach the maximum peak of overpressure all show a decreasing trend.There are three types of explosive overpressure evolution, which are "three-peak structure with the second peak being the maximum peak", "three-peak structure with the first peak being the maximum peak" and "two-peak structure with the first peak being the maximum peak".

3. The CO_2 mainly affects the rate of combustion reaction from three aspects: dilution, thermal diffusion and chemical kinetics. The combustion reaction rate decreases with the CO_2 volume fraction increasing, and then changes the flame structure evolution process and the variation law of overpressure. The dominant effect of flame structure on flame speed and explosion overpressure can be clearly observed during the formation of tulip flame.

ACKNOWLEDGEMENTS

This research was funded by science and technology project of Chongqing Education Commission (KJQN202001202, KJQN201901229, KJQN201901202).

REFERENCES

[1] Shen, Y. (2019) Numerical Simulation Analysis of Leakage and Diffusion of Buried Low Pressure Natural Gas Pipeline. Beijing University of Civil Engineering and Architecture.

[2] Dong, X.B. (2021) An explosion at a residential building in Shiyan city, Hubei Province, killed 25 people. Oriental Sword. (08), 8-9.

[3] Xie, M.K., Fu, J.Q., Zhang, Y.X., Shu, J., Ma, Y.J., Liu, J.P., Zeng, D.J. (2020) Numerical analysis on the effects of CO_2 dilution on the laminar burning velocity of premixed methane/air flame with elevated initial temperature and pressure. Fuel. 264(03), 116858.1-116858.11.

[4] Kondo, S., Takizawa, K., Takahashi, A., Tokuhashi, K. (2006) Extended Le Chatelier's formula for carbon dioxide dilution effect on flamma-bility limits. Journal of Hazardous Materials. 138(1), 1-8.

[5] Qu, Z.W., Yan, S.L., Li, X.C. (2016) Effect of inert gas to gas explosion limits of methane/air premixed. Explosive Materials. 45(2), 11-15.

[6] Zhang, Y.X., Wu, Q., Liu, C.H., Jiang, B.Y., Zhang, B.Y. (2017) Experimental study on coal mine gas explosion suppression with inert gas N_2/CO_2. Explosion and Shock Waves. 37(05), 906-912.

[7] Li, M.H., Xu, J.C., Wang, C.J., Wang, B.Z. (2019) Thermal and kinetics mechanism of explosion mitigation of methane-air mixture by N_2/CO_2 in a closed compartment. Fuel. 255(11), 115747.1-115747.9.

[8] Zheng, L.G., Du, D.P., Wang, J., Dou, Z.G., Wang, X., Jin, H.W., Wang, Y. (2019) Study on premixed flame dynamics of $CH_4/O_2/CO_2$ mixtures. Fuel. 256(11), 115913

[9] Chouraqui, H., Dayma, G., Ribert, G., Halter, F., Chauveau, C., Dagaut, P. (2021) Experimental and numerical studies of the diluent influence (N_2, Ar, He, Xe) on stable premixed methane flames in micro-combustion. Proceedings of the Combustion Institute. 38(4), 6753-6761.

[10] Jia, B.S., Wen, H.Y., Liang, Y.T., Wang, X.Y. (2013) Mechanism characteristics of CO_2 and N_2 inhibiting methane explosions in coal mine roadways. Journal of China Coal Society. 38(03), 361-366.

[11] Duva, B.C., Chance, L.E., Toulson, E. (2020) Dilution effect of different combustion residuals on laminar burning velocities and burned gas Markstein lengths of premixed methane/air mixtures at elevated temperature. Fuel. 267(03), 117153.

[12] Pei, B., Yu, M.G., Chen, L.W., Wang, F.H., Yang, Y., Zhu, X.N. (2016) Experimental study on the synergistic inhibition effect of gas-liquid two phase medium on gas explosion. Journal of Loss Prevention in the Process Industries. 49(12), 797-804.

[13] Ning, G.X., Yi, X.J., Zeng, Y.A., Liu, H.T. (2002) Pseudo-color Encoding and Processing for lmages of Infrared Focal Plane Array. Infrared Technology. 24(02), 57-59.

[14] Ma, Q.J., Zhang, Q., Chen, J.C., Huang, Y., Shi, Y.T. (2014) Effects of hydrogen on combustion characteristics of methane in air. International Journal of Hydrogen Energy. 39(21), 11291-11298

[15] Clanet, C., Searby, G. (1996) On the "tulip flame" phenomenon. Combustion & Flame. 105(1-2), 225-238.

[16] Matalon, M., Metzener, P. (1997) The propagation of premixed flames in closed tubes. Journal of Fluid Mechanics. 336(336), 331-350.

[17] Dunn-Rankin, D., Sawyer, R.F. (1998) Tulip flames: changes in shape of premixed flames propagating in closed tubes. Experiments in Fluids. 24(2), 130-140.

[18] Zhang, Q., Li, W., Liang, H.M. (2012) Effect of spark duration on explosion parameters of methane/air mixtures in closed vessels. Safety Science. 50(9), 1715-1721.

[19] Mitu, M., Prodan, M., Giurcan, V., Razus, D., Oancea, D. (2016) Influence of inert gas addition on propagation indices of methane-air deflagrations. Process Safety and Environmental Protection. 102(05), 513-522.

[20] Bychkov, V., Akkerman, V., Fru, G., Petchenko, A., Eriksson, L.E. (2007) Flame acceleration in the early stages of burning in tubes. Combustion and Flame. 150(4), 263-276.

[21] Wang, T. (2014) Experimental and Numerical Studies on Methane Explosion and The Suppression Effect of CO_2 in Vessel. Xi'an University of Science and Technology.

[22] Yang, K., Hu, Q.R., Sun, S.H., Lv, P.F., Pang, L. (2019) Research progress on multi-overpressure peak structures of vented gas explosions in confined spaces. Journal of Loss Prevention in the Process Industries. 62(11), 103969.

[23] Cooper, M.G., Fairweather, M., Tite, J.P. (1986) On the mechanisms of pressure generation in vented explosions. Combustion & Flame. 65(1), 1-14.

[24] Luo, Z.M., Wang, T., Cheng, F.M., Song, Y., Wu, K. (2015) Experimental and numerical studies on the suppression of methane explosion using CO_2 in a mini vessel. Explosion and Shock Waves. 35(003), 393-400.

[25] Ibrahim, S.S., Masril, A.R. (2001) The effects of obstructions on overpressure resulting from premixed flame deflagration. Journal of Loss Prevention in the Process Industries. 14(3), 213-221.

[26] Wang, S.M., Li, X.D., Cai, Y.X., Li, G.Q., Qi, S. (2021) Explosion venting dynamics of fuel vapor-air premixed gas based on small scale experiments. CIESC Journal. 72(09):4961-4972.

[27] Xiao, H.H., Sun, J.H., Chen, P. (2014) Experimental and numerical study of premixed hydrogen/air flame propagating in a combustion chamber. Journal of Hazardous Materials. 268(15), 132-139.

[28] Chan, Y.L., Zhu, M.M., Zhang, Z.Z., Liu, P.F., Zhang, D.K., Yan, J., Shamim, T., Chou, S.K., Li, H. (2015) The Effect of CO_2 Dilution on the Laminar Burning Velocity of Premixed Methane/Air Flames. Energy Procedia. 75(06), 3048-3053.
[29] Benedetto, A.D., Sarli, V.D., Salzano, E., Cammarota, F., Russo, G. (2009) Explosion behavior of $CH_4/O_2/N_2/CO_2$ and $H_2/O_2/N_2/CO_2$ mixtures. International Journal of Hydrogen Energy. 34(16), 6970-6978.
[30] Hu, X.Z., Yu, Q.B., Liu, J.X. (2016) Chemical effect of CO_2 on the laminar flame speeds of oxy-methane mixtures in the condition of various equivalence ratios and oxygen concentrations. International Journal of Hydrogen Energy. 41(33), 15068-15077.
[31] Song, Y.Y. (2012) Study on Oxy-Fuel Combustion Charactristic of Oil-fired Boiler. Shandong University.
[32] Khan, A.R., Anbusaravanan, S., Kalathi, L., Velamati, R., Prathap, C. (2017) Investigation of dilution effect with N_2/CO_2 on laminar burning velocity of premixed methane/oxygen mixtures using freely expanding spherical flames. Fuel. 196(01), 225-232.
[33] Qiao, L., Gan, Y., Nishie, T., Dahm, W.J.A., Oran, E.S. (2010) Extinction of premixed methane/air flames in microgravity by diluents: Effects of radiation and Lewis number. Combustion and Flame. 157(8), 1446-1455.
[34] Luo, Z.M., Yang, Y., Cheng, F.M., Wang, T., Chang, Z.C., Su, B., Zhang, M. (2020) Experimental study on explosion limits parameters of propylene with dilution of nitrogen and carbon dioxide. CIESC Journal. 71(04), 1922-1928.

Received: **28.11.2021**
Accepted: **11.01.2022**

CORRESPONDING AUTHOR

Junyi Zhou
College of Civil Engineering,
Chongqing Three Gorges University,
Chongqing 404100 – China

e-mail: junyi202111@126.com

© by PSP Volume 31– No. 05/2022 pages 5004-5014 Fresenius Environmental Bulletin

APPLICATION OF AVO TECHNOLOGY IN SEISMIC IDENTIFICATION OF TIGHT SANDSTONE GAS

Xinran Tian*

College of Geophysics and Petroleum Resources, Yangtze University, Wuhan, Hubei 430100, P.R. China

ABSTRACT

For the tight sandstone gas reservoir with low porosity and permeability, it is difficult to be effectively identified by conventional processing and interpretation techniques. It is necessary to give the prompt of seismic identification of tight sandstone gas through forward modeling in seismic identification technology, and find out the seismic identification technology of tight sandstone gas suitable for this area through inversion and comprehensive application of various seismic attributes of pre-stack inversion. In this paper, the He-8 member of the main gas-bearing horizon in X block of tight sandstone gas field is taken as the targeted area. According to its geological and seismic characteristics, the DEM-Gassmann-Brie petrophysical model is used to simulate the velocity and density of tight sandstone gas, and the AVO forward modeling and analysis is conducted. Further, we discuss the influence of porosity, gas saturation and gas-bearing sandstone thickness on the AVO anomaly type of tight sandstone gas, and compare the AVO response difference between tight and conventional sandstone gas. The results show that tight sandstone gas is easy to identify in post-stack seismic data, and it will be enhanced with the increase of porosity, gas saturation and thickness, which can provide theoretical basis and prompt for the identification of tight sandstone gas from subsequent actual seismic data.

KEYWORDS:
Tight sandstone gas, AVO analysis, forward modeling, pre-stack inversion, seismic identification

INTRODUCTION

Tight sandstone reservoir is an unconventional oil and gas reservoir with great oil and gas exploration potential. However, due to the characteristics of low porosity, low permeability, compactness and thin interbedding, its exploration and development has always been a difficult problem. Due to its huge exploration and development potential, scholars have conducted in-depth research on the seismic exploration. In the seismic exploration field of tight sandstone gas, there are massive technologies were developed, such as AVO technology [1,2], three-dimensional seismic exploration technology [3], seismic inversion technology [4], seismic attribute technology [4], multi-wave and multi-component seismic exploration technology [5,6], three-dimensional coherent body technology [7], etc. Among which, AVO technology is a seismic exploration technology that uses the variation characteristics of seismic reflected wave amplitude with offset to identify lithology and detect oil and gas. AVO forward modeling method can directly identify lithology and hydrocarbon bearing property in actual seismic records, and AVO inversion method is an important means to quantitatively predict lithology and hydrocarbons. Especially for the tight sandstone gas field with a low porosity and low permeability, the conventional processing interpretation techniques are difficult to effectively identify them.

As an important part of seismic exploration technology for tight sandstone gas, seismic identification technology for gas-bearing property of tight sandstone reservoir has made great progress on the basis of a large number of studies. At present, the common technical methods for seismic identification of tight sandstone gas include: bright spot technology [8], AVO technology, P-wave Proni absorption filtering technology [9,10], P-wave attenuation and velocity divergence (AVD) technology [11], P-wave dynamic energy spectrum (DR) technology [12], P-wave multi-scale frequency and absorption technology [13], P-wave profile direct comparison method [14], P-wave velocity ratio method [15], absorption coefficient method, etc. As a relatively perfect theory of lithology identification and fluid prediction technology, AVO and pre-stack seismic inversion technology is based on Zoeppritz equation [16]. Koefoed et al. [17,18] simplified the equation and proved its significance in lithology and fluid expression, the role of Zoeppritz equation began to be valued. Nolet et al. [19] simplified the equation to an equation, and then Shuey et al. [20] derived the approximate formula based on Zoeppritz equation, which introduced Poisson's ratio for the first time, so that the approximate formula has great advantages in reflecting the difference between lithology and fluid of underground media, and promotes the development of AVO technology. Smith et al. [21-25] introduced different elastic parameters into their respective derived approximate expressions. The P-wave

reflection coefficients are expressed by approximate expressions of various elastic parameters, which enriches the application of AVO and pre-stack seismic inversion techniques. AVO technology uses the variation characteristics of reflection amplitude with offset for oil and gas detection and reservoir description. Whether the amplitude relative relationship of prestack gathers is correct or not directly affects the accuracy and correctness of analysis. In order to obtain the information related to lithology and oil-gas potential from seismic data, it is necessary to ensure that the concentrated reflection amplitude of prestack seismic trace is less affected by non geological factors. Therefore, the correct recovery of reflection amplitude, especially the amplitude loss related to offset, is not only the basis of AVO technology, but also the key to seismic oil and gas detection.

In this paper, the geological models that can reflect the underground geological characteristics of the region are constructed, and the seismic response is simulated and calculated according to the propagation theory of seismic waves, that is, the model seismic forward modeling. In order to obtain the seismic data characteristics of tight sandstone gas in the targeted area, the seismic records are forwarded, AVO technology is used to compare and analyze their seismic records, which provides theoretical basis and tips for the identification of tight sandstone gas in subsequent actual seismic data.

MATERIALS AND METHODS

Methods. In this paper, we establish the DEM-Gassmann-Brie rock physics model of tight sandstone and conventional sandstone based on the Sun et al. [26, 27], as shown in Figure 1. The method to determine the type of gas-bearing sandstone based on the position of gas-bearing sandstone top interface in P-G crossplot is adopted [18]. In which, the P-G crossplot is divided into four quadrants, and the horizontal coordinate is AVO intercept P and the ordinate is AVO slope G. The type of gas-bearing sandstone is determined by the positive and negative values of P and G at the top interface, as shown in Figure 2. For a limited time window, mudstone tends to be distributed along a clear background trend. The top interface reflection of gas-bearing sandstone tends to be distributed below the background trend, while the bottom interface reflection tends to be distributed above the background trend. The position of the top interface reflection of the four types of gas-bearing sandstones in the P-G crossplot has been indicated in the map. The specific relative wave impedance characteristics and seismic characteristics of the four types of gas-bearing sandstones are as follows: AVO anomaly of type 1 gas-bearing sandstone, AVO anomalies of type 2 gas-bearing sandstone, AVO anomalies of type 3 gas-bearing sandstone and AVO anomalies of type 4 gas-bearing sandstone [28, 29]. Due to the characteristics of low porosity, low permeability, low gas saturation and thin layer, tight gas-bearing sandstone is more difficult and complex in seismic identification than conventional gas-bearing sandstone. Nevertheless, it is necessary to analyze the AVO anomaly types of tight sandstone gas in theory. This is also the reason for the forward modeling research on the influence of different factors on the seismic response of tight sandstone gas.

Physical properties of tight sandstone reservoir. In order to study the influence of porosity, gas saturation and gas-bearing sandstone thickness on the seismic response of tight sandstone gas by forward modeling, according to the physical properties of tight sandstone reservoir, the following geological models are designed: variable porosity, variable gas saturation and variable gas-bearing sandstone thickness geological model of tight sandstone gas with mudstone surrounding rock. Among them, the geological model of variable porosity is the alternate layer structure of surrounding rock (mudstone) and gas-bearing sandstone. The thickness of surrounding rock is 40m, the thickness of gas-bearing sandstone layer is 10m and the gas saturation is 50%. From shallow to deep, the porosity of gas-bearing sandstone layer is 3%, 5%, 7%, 9%, 11%, 13%, 15%, 17%, 19%, 21%, 23%, 25% respectively. The geological model of variable gas saturation is the alternate layer structure of surrounding rock (mudstone) and gas-bearing sandstone. The thickness of surrounding rock is 40m, the thickness of gas-bearing sandstone layer is 10m and the porosity is 9%. From shallow to deep, the gas saturation of gas-bearing sandstone layer is 0%, 10%, 20%, 30%, 40%, 50%, 60%, 70%, 80%, 90% and 100% respectively. The geological model of variable thickness of gas-bearing sandstone is the alternate layer structure of surrounding rock (mudstone) and gas-bearing sandstone.The thickness of surrounding rock is 40m, the gas saturation of gas-bearing sandstone is 50% and the porosity is 9%. From shallow to deep, the thickness of gas-bearing sandstone is 2m, 4m, 6m, 8m, 10m, 12M, 14m, 16m, 18m and 20m respectively.

Forward geological model. In the forward geological model of tight sandstone gas, nine wells in the study area are selected. The average P-wave velocity and density of mudstone and dry sandstone layers in He-8 member of each well are calculated by using logging data and well stratification results interpreted by logging. Then the average density, average P-wave velocity and average S-wave velocity of the mudstone layer in He-8 member of the 9 wells are calculated, and the final results are the density, P-wave velocity and S-wave velocity of the mudstone layer in each geological model. On this basis, the P-wave velocity and density of gas-bearing sandstone with different porosity and gas saturation can be predicted by DEM-Gassmann-Brie rock physics model.

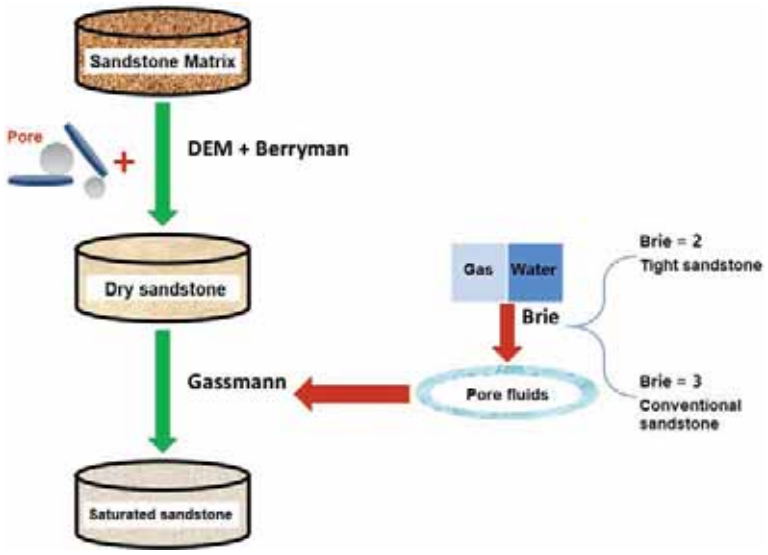

FIGURE 1
DEM-Gassmann-Brie rock physics model of tight sandstone and conventional sandstone

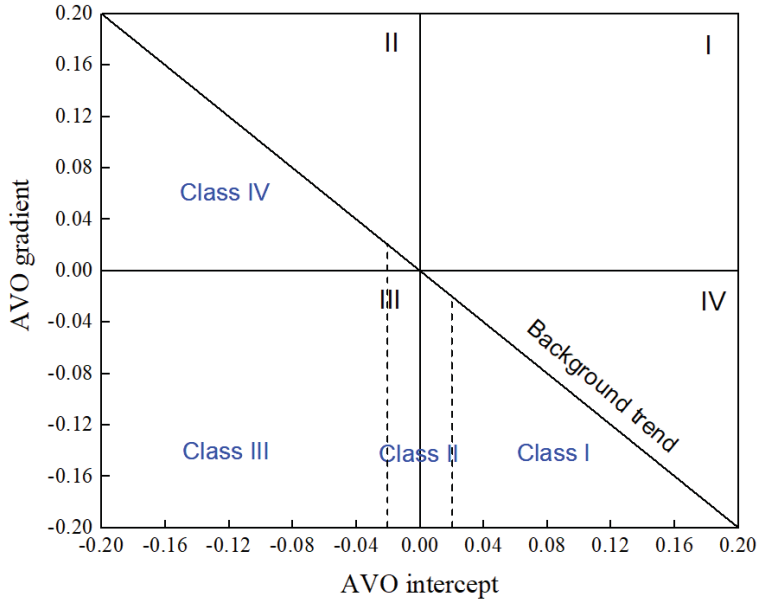

FIGURE 2
P-G (AVO intercept - AVO slope) crossplot containing four quadrants (I-IV)

TABLE 1
Calculation of P-and S-wave velocity and density of mudstone layer in the model

Exp.	Density (g/cm^3)	P-wave velocity (m/s)	S-wave velocity (m/s)
1	2.5841	4385.5038	2362.5386
2	2.5929	4427.2193	2353.6603
3	2.5872	4262.5137	2276.3085
4	2.5990	4211.3417	2284.0435
5	25853	4316.9891	298.0256
6	2.5860	4256.0383	2227.2726
7	2.5914	4308.7453	2313.3329
8	2.5905	4359.4203	2336.8422
9	2.5808	4279.4825	2303.1217
Average value	2.5886	4311.9171	2306.1273

Through the above process, the parameters of each geological model can be determined. Table 1 shows the calculation process of P-and S-wave velocity and density.

RESULTS AND DISCUSSION

Through the P-wave velocity and thickness of the geological model, the two-way travel time corresponding to the top interface of each gas-bearing sandstone layer in the model is calculated, and the accurate position of the top interface of the gas-bearing sandstone layer in the forward angular gather time axis is found. Then the reflection amplitude of the top interface of each gas-bearing sandstone layer in the pre-stack angular gather can be extracted, and the curve that changes with incident angle can be obtained, namely AVO curve. By calculating the intercept and slope of these AVO curves, the influence of different factors on the seismic response of tight sandstone gas is analyzed, and the difference between the seismic response of tight sandstone gas and that of conventional sandstone gas is compared. This paper analyzes the influence of porosity, gas saturation and gas sandstone thickness on AVO characteristics of tight gas sandstone.

Porosity. By extracting the reflection coefficient of the top interface of gas-bearing sandstone (seismic record is the convolution of reflection coefficient and seismic wavelet, when the influence of wavelet is not considered, the variation trend of reflection amplitude with offset is the same as that of reflection coefficient with offset, so it is called reflection amplitude below), two curves of reflection amplitude with incident angle can be obtained, as shown in Figure 3 and Figure 4. For the tight sandstone gas geological model with variable porosity, the reflection amplitude at the top interface of gas-bearing sandstone is generally negative, and for a certain incident angle, with the increase of porosity, the reflection amplitude generally increases negatively. When the surrounding rock is mudstone, with the increase of porosity, the curve of reflection amplitude changing with the incident angle (less than 35°) (hereinafter referred to as the curve) shows a trend of monotonic decrease, decrease after increase, and monotonic increase on the whole, and in the porosity range of general tight sandstone gas (3%~12%), the curve is monotonically decreasing.

In order to further analyze the effect of porosity on AVO response of tight sandstone gas, the P-G crossplot of variable porosity geological model of tight sandstone gas is made as shown in Figure 4. It can be seen that for the geological model with variable porosity, as a whole, with the increase of porosity, the AVO intercept P of the top interface of gas-bearing sandstone gradually decreases, while the AVO slope G gradually increases. When the surrounding rock is mudstone, with the increase of porosity, the position of the corresponding point (hereinafter referred to as the point) in the P-G crossplot of the top interface of the gas-bearing sandstone presents the

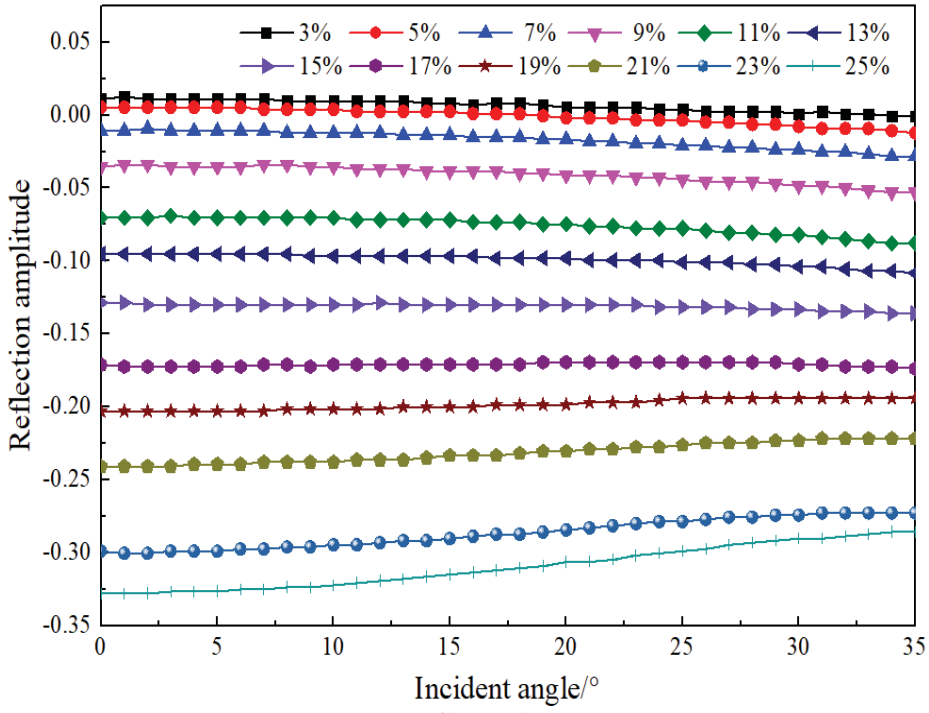

FIGURE 3
Reflection amplitude of gas bearing sandstone top interface with incident angle

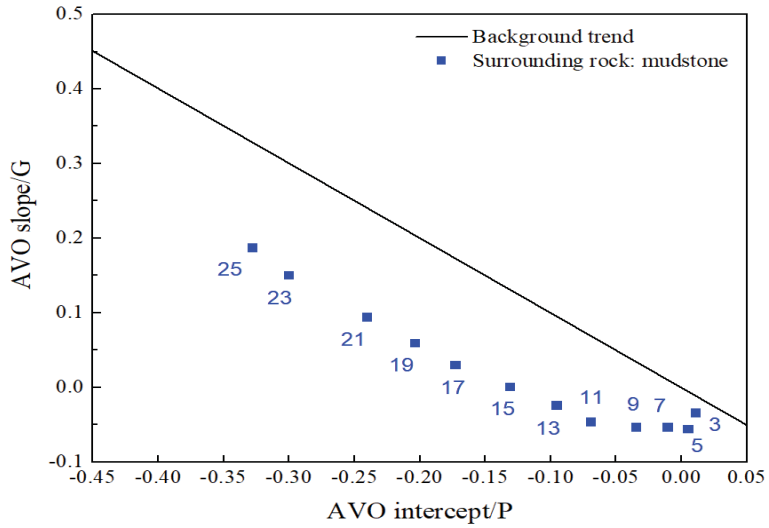

FIGURE 4
P-G crossplot of tight sandstone gas reservoir model with variable porosity

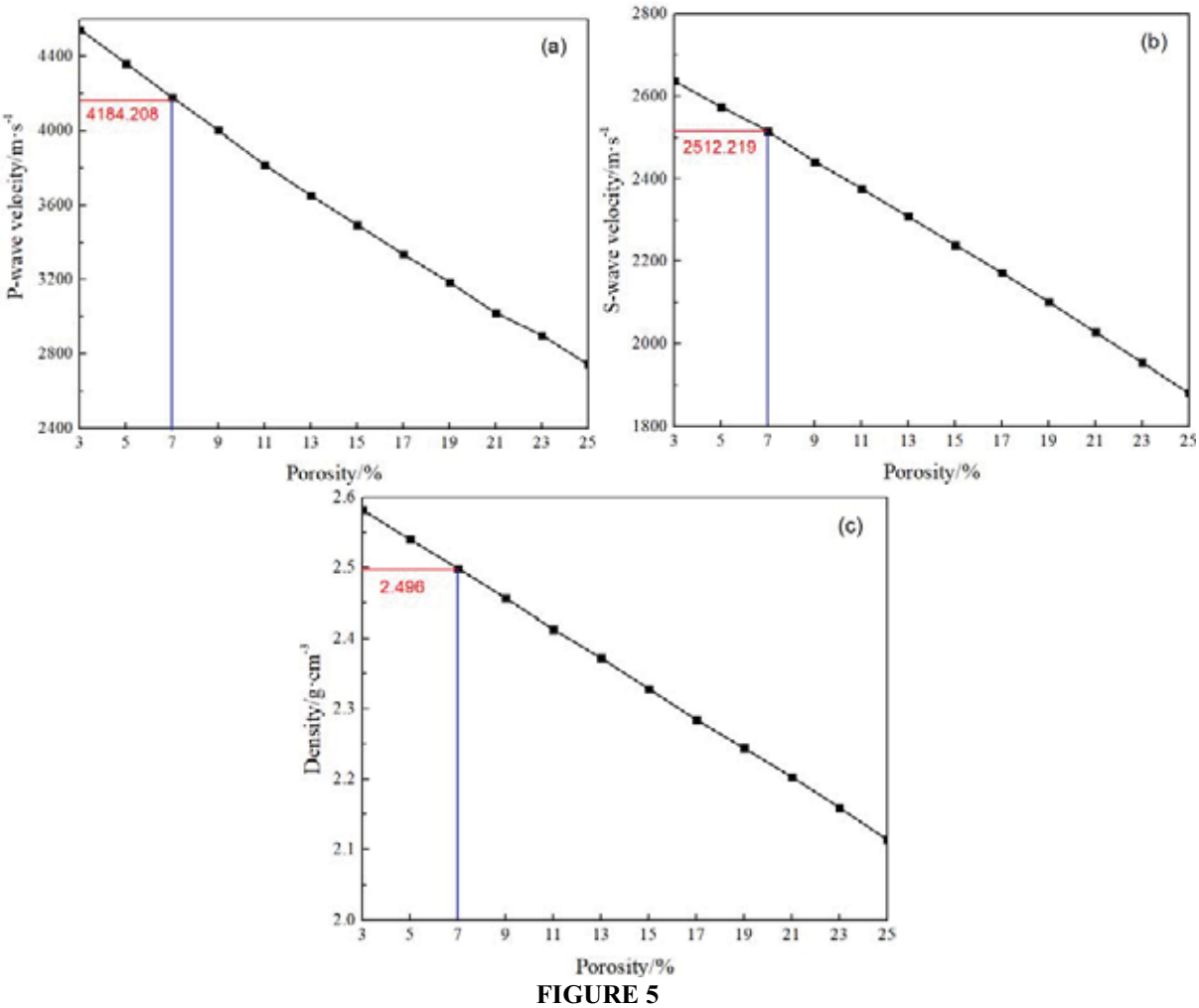

FIGURE 5
P, S-wave velocity, and density of tight gas-bearing sandstone with porosity

change trend of quadrant II - quadrant III - quadrant IV, and the distance between the point and the background trend gradually increases. In the porosity range of general tight sandstone gas (3%~12%), there is a change from quadrant II to quadrant III. When the porosity is more than 7%, the AVO intercept of the top interface of gas-bearing sandstone is less than -0.02.

For the variable porosity geological model of tight sandstone gas reservoir, it can be seen that the

AVO anomaly type of tight sandstone gas has a trend of 2 - 3 - 4. When porosity is more than 7%, AVO anomaly type of tight sandstone gas changes from 2 to 3. When porosity is more than 15%, AVO anomaly type of tight sandstone gas changes from 3 to 4. Within the porosity range of general tight sandstone gas (3%~12%), the AVO anomaly type of tight sandstone gas changes from 2 to 3. With the increase of porosity, the distance between the point corresponding to the top interface of gas-bearing sandstone in P-G crossplot and the background trend gradually increases, which means that the identification of tight sandstone gas in post-stack seismic data is gradually enhanced. According to Figure 5, for the parameters of the variable porosity geological model of tight sandstone gas with mudstone as the surrounding rock, the tight sandstone gas easy to identify on the post-stack seismic data has the following elastic characteristics: P-wave velocity is less than 4184.208 m/s, S-wave velocity is less than 2512.219 m/s, and density is less than 2.496 g/cm^3.

Gas saturation. By picking up the reflection amplitude of the top interface of gas-bearing sandstone, two curves of reflection amplitude varying with incident angle can be obtained, as shown in Figure 6 and Figure 7. For the geological model of tight sandstone gas with variable gas saturation, the reflection coefficient at the top interface of gas-bearing sandstone is generally negative, and for a certain incident angle, with the increase of gas saturation, the reflection amplitude generally increases negatively. When the surrounding rock is mudstone, the curve of reflection amplitude varying with incident angle (less than or equal to 35°) always shows a trend of monotonic decrease. In order to further analyze the influence of gas saturation on AVO response of tight sandstone gas, the P-G crossplot of tight sandstone gas geological model with variable gas saturation is made as shown in Figure 7. It can be seen that for the geological model with variable gas saturation, as a whole, with the increase of gas saturation, the AVO intercept P of gas sandstone top interface gradually decreases. When the surrounding rock is mudstone, the point corresponding to the top interface of gas-bearing sandstone in P-G crossplot (hereinafter referred to as point) is always in quadrant III. With the increase of gas saturation, the AVO slope G of the top interface of gas-bearing sandstone decreases gradually, and the distance between the point and the background trend increases gradually. When the gas saturation is more than 18%, the AVO intercept of the top interface of gas-bearing sandstone is less than -0.02.

Based on the above analysis, the following conclusions can be drawn for the geological model of tight sandstone gas with variable gas saturation: (1) when the model is a geological model of variable gas saturation with mudstone as the surrounding rock, the AVO anomaly type of tight sandstone gas has a trend of 2 - 3. When the gas saturation is more than 18%, the AVO anomaly type of tight sandstone gas changes from 2 to 3. In the gas saturation range of general tight sandstone gas (30%~55%), the AVO anomaly type of tight sandstone gas is type 3. (3) With the increase of gas saturation, the distance between the point corresponding to the top interface of gas-bearing sandstone in P-G crossplot and the background trend gradually increases, which means that the recognition of tight sandstone gas on post-stack seismic data is gradually enhanced. Because the typical "bright spot" sandstones with type 3 of AVO anomaly are easy to identify on the post-stack seismic data, and the gas saturation range of the general tight sandstone gas is 30%~55%. Therefore, for the parameters of variable gas saturation geological model of tight sandstone gas with mudstone as surrounding rock, tight sandstone gas with gas saturation (more than 18%) is easy to be identified on post-

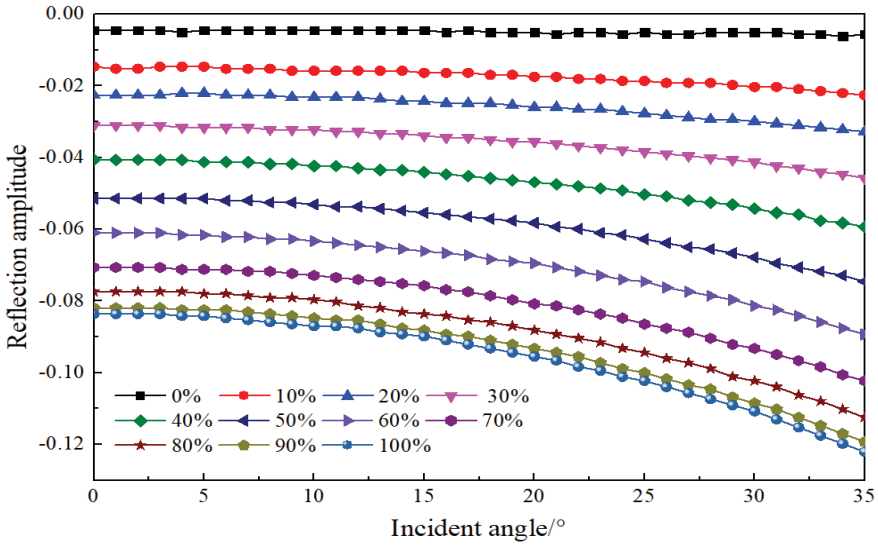

FIGURE 6
Reflection amplitude at the top interface of gas-bearing sandstone with incident angle

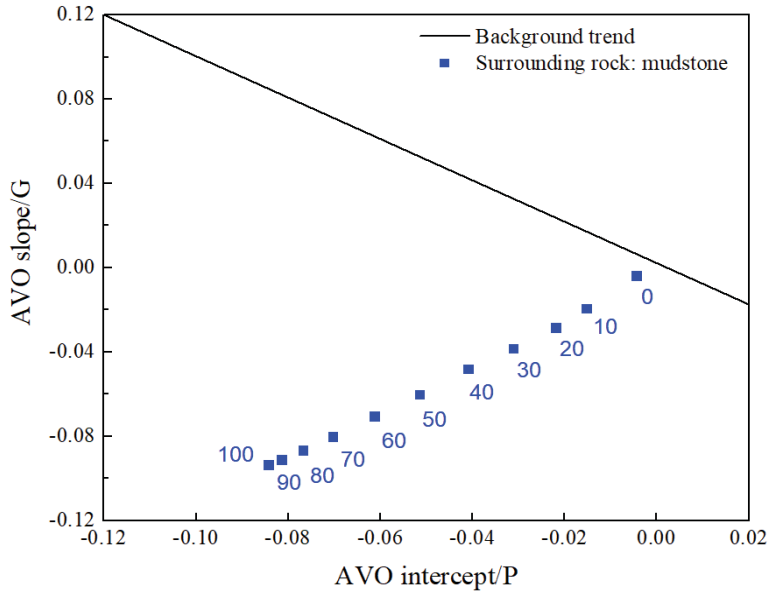

FIGURE 7

P-G crossplot of tight sandstone gas reservoir model with variable gas saturation

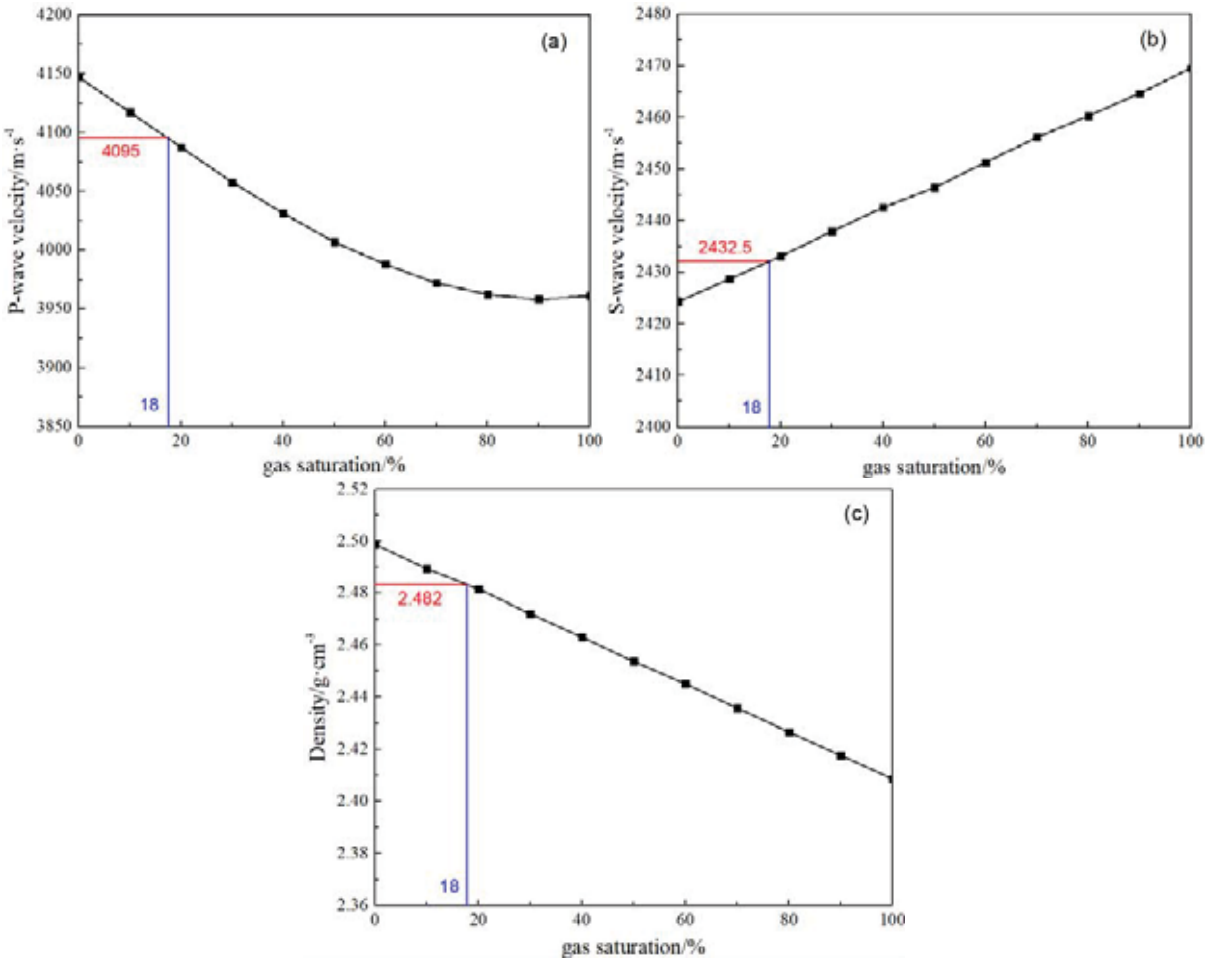

FIGURE 8

P, S-wave velocity, and density of tight gas-bearing sandstone with gas saturation

stack seismic data. According to Figure 8, for the parameters of the geological model of variable gas saturation of tight sandstone gas with mudstone as surrounding rock, the tight sandstone gas easy to be identified on post-stack seismic data has the following elastic characteristics: P-wave velocity is less than 4095 m/s, S-wave velocity is less than 2432.5 m/s, and density is less than 2.482 g/cm^3.

Thickness of gas-bearing sandstone. It can be seen from Figure 9 that for the geological model of tight sandstone gas with variable thickness of gas-bearing sandstone, the reflection coefficient at the top interface of gas-bearing sandstone is generally negative, and for a certain incident angle, with the increase of gas-bearing sandstone thickness, the reflection amplitude generally increases negatively. When the surrounding rock is mudstone, with the increase of the thickness of gas-bearing sandstone, the curve of the reflection amplitude changing with the incident angle (less than or equal to 35°) gradually changes from the trend of monotone increasing to the trend of monotone decreasing on the whole. Moreover, within the thickness range of gas-bearing sandstone (less than or equal to 10 m) of general single-layer tight sandstone gas, the trend of the curve gradually changes from monotone increasing to monotone decreasing. Through the P-G crossplot of tight sandstone gas geological model with variable gas-bearing sandstone thickness shown in Figure 10. For the geological model of variable gas-bearing sandstone thickness, as a whole, with the increase of gas-bearing sandstone thickness, the AVO intercept P of gas-bearing sandstone top interface gradually decreases. When the surrounding rock is mudstone, with the increase of gas-bearing sandstone thickness, the position of the corresponding points (hereinafter referred to as points) in the P-G crossplot of gas-bearing sandstone top interface shows a trend of quadrant IV - quadrant III. AVO intercept G of gas-bearing sandstone top interface decreases gradually, and the distance between the overall point and the background trend increases gradually. Within the

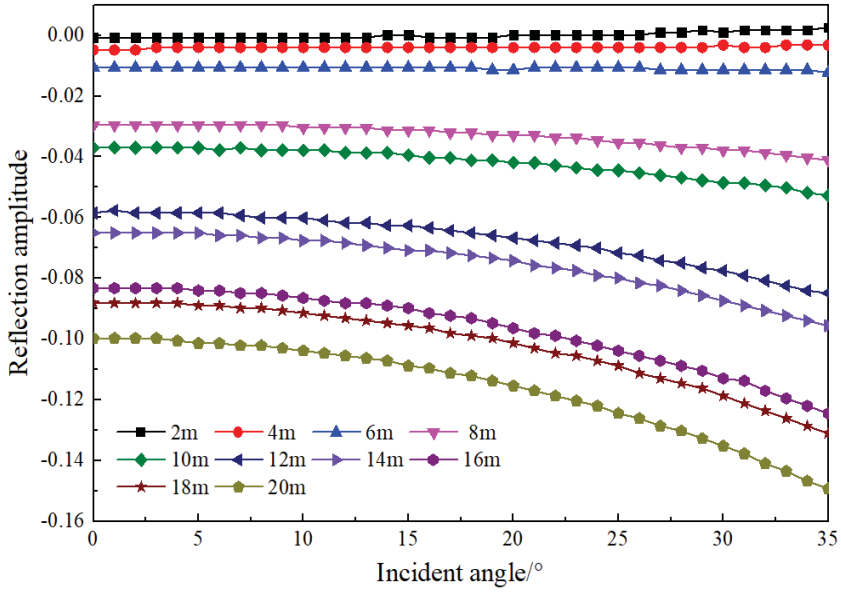

FIGURE 9

Reflection amplitude at the top interface of tight sandstone gas with incident angle

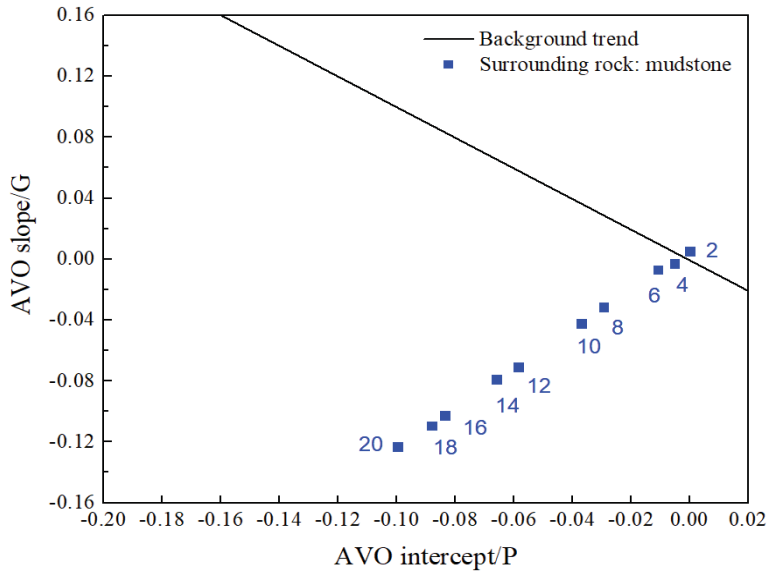

FIGURE 10

P-G crossplot of tight sandstone gas reservoir model with variable thickness

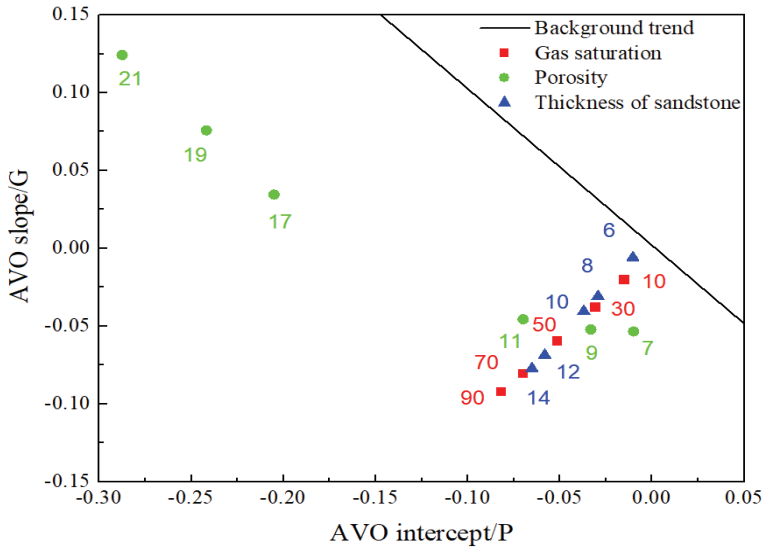

FIGURE 11
P-G crossplot of variable gas saturation, porosity and thickness of sandstone

thickness range (less than or equal to 15m) of gas reservoir (including single-layer gas reservoir and gas reservoir group) in the study area, the position of the point changes from quadrant IV to quadrant III. When the thickness of gas-bearing sandstone is more than 7m, AVO intercept at the top interface of gas-bearing sandstone is less than -0.02.

That is to say, when the model is a geological model of variable gas-bearing sandstone thickness with mudstone as surrounding rock, the AVO anomaly type of tight sandstone gas has a trend of 4 - 3. When the thickness of gas-bearing sandstone is more than 7m, the AVO anomaly type of tight sandstone gas changes from 4 to 3. The AVO anomaly type of tight sandstone gas change from 4 to 3 within the thickness range (less than or equal to 15m) of the gas layer (including single layer and gas group) in the study area. With the increase of gas-bearing sandstone thickness, the distance between the point corresponding to the top interface of gas-bearing sandstone in P-G crossplot and the background trend increases gradually, which means that the recognition of tight sandstone gas on post-stack seismic data is gradually enhanced. The sandstone with type 3 of AVO anomaly is a typical "bright spot" sandstone which is easy to identify on the post-stack seismic data. Therefore, for the parameters of the variable gas-bearing sandstone thickness geological model with mudstone as surrounding rock, the tight sandstone gas with thickness more than 7 m is easy to be identified on post-stack seismic data.

Seismic response analysis of tight sandstone gas. According to the research results of Si et al. [27] in the pore space of tight sandstone gas, the fluid mixture tends to be more heterogeneous plaque distribution. This leads to the fact that the variation trend of P-wave velocity of tight sandstone gas with gas saturation is most consistent with the Gassmann-Brie theoretical results when the Brie coefficient is 2. The change of P-wave velocity of tight sandstone gas with gas saturation is close to a linear decreasing trend. As shown in Figure 11, the point corresponding to the tight sandstone gas layer in the P-G crossplot is far from the background trend. In summary, tight sandstone gas reservoir is easy to be identified on post-stack seismic data.

CONCLUSIONS

(1) For the variable porosity geological model of tight sandstone gas, it can be seen that with the increase of porosity, the distance between the point corresponding to the top interface of gas-bearing sandstone in P-G crossplot and the background trend gradually increases, which means that the identification of tight sandstone gas in post-stack seismic data is gradually enhanced. According to the AVO forward modeling and analysis results of the geological model constructed with reference to the actual situation of He-8 member in the study area, tight sandstone gas is easy to identify in post-stack seismic data.

(2) When the model is a variable gas saturation geological model with mudstone as the surrounding rock, with the increase of gas saturation, the distance between the point corresponding to the top interface of gas-bearing sandstone in P-G crossplot and the background trend gradually increases, which means that the recognition of tight sandstone gas on post-stack seismic data is gradually enhanced. Because the typical "bright spot" sandstones with type 3 of AVO anomaly are easy to identify on the post-stack seismic data, and the gas saturation range of the general tight sandstone gas is 30%~55%. Tight sandstone gas with gas saturation more than 18% is easy to be identified on post-stack seismic data.

(3) When the model is a geological model of variable gas-bearing sandstone thickness with mudstone as surrounding rock, with the increase of gas-bearing sandstone thickness, the distance between the point corresponding to the top interface of gas-bearing sandstone in P-G crossplot and the background trend increases gradually, which means that the recognition of tight sandstone gas on post-stack seismic data is gradually enhanced. Therefore, the tight sandstone gas with thickness more than 7 m is easy to be identified on post-stack seismic data.

(4) According to the AVO forward modeling and analysis results of the geological model constructed with reference to the actual situation of He-8 member in the study area, tight sandstone gas has strong identifiability in post-stack seismic data. According to the distribution of P-G crossplot of tight sandstone in different gas saturation, porosity and thickness, it can be seen that the point corresponding to tight sandstone gas layer in P-G crossplot is far from the background trend. That is, tight sandstone gas layers are easily identified on post-stack seismic data.

ACKNOWLEDGEMENTS

This work was no fund supported.

REFERENCES

[1] Hajra, S., Mukhopadhyay, A. (2015) Reflection and refraction of seismic waves incident obliquely at the boundary of a liquid-saturated porous solid. Bulletin of the Seismological Society of America. 72(5), 1509-1533.

[2] Shan, R., Bian, A.F., Yu, W.H., Qu, Z. (2017) Pre-stack full waveform inversion for reservoir prediction. Oil Geophysical Prospecting. 46(4), 629-633.

[3] Yang, R., Yan, P., Wu, N., Sha, Z., Liang, J. (2014) Application of avo analysis to gas hydrates identification in the northern slope of the South China Sea. Acta Geophysica. 62(4), 802-817.

[4] Yang, R.Z., Zhao, Z.G., Peng, W.J., Gu, Y.B., Wang, Z.G., Zhuang, X.Q. (2013) Integrated application of 3D seismic and microseismic data in the development of tight gas reservoirs. Applied Geophysics. 10(2), 157-169.

[5] Huang, J., Gao, X., Wang, W. (2014) Application and development of fullwaveform inversion research in the seismic exploration. Journal of Geo-Information Science. 16(3), 396-401.

[6] Yang, R.Z., Zhao, Z.G., Peng, W.J., Gu, Y.B., Wang, Z.G., Zhuang, X.Q. (2013) Integrated application of 3d seismic and microseismic data in the development of tight gas reservoirs. Applied Geophysics. 27(2), 32-37.

[7] Varypae, A.V., Sanina, I.A., Chulkov, A.B., Kushnir, A.F. (2019) Application of robust phase algorithms for seismic emission detection in the area of blasting operations in mines. Seismic Instruments. 55(2), 136-147.

[8] Rajmohan, N., Prathapar, S.A., Jayaprakash, M., Nagarajan, R. (2014) Vertical distribution of heavy metals in soil profile in a seasonally waterlogging agriculture field in eastern ganges basin. Environmental Monitoring and Assessment. 43(6), 668-672.

[9] Dai, J.X., Qin, S.F., Hu, G.Y. (2019) Major progress in the natural gas exploration and development in the past seven decades in China. Petroleum Exploration and Development. 46(6), 29-39.

[10] Wang, X.W. (2012) Application of AVO technique in prediction of tight sandstone reservoirs. Journal of Oil and Gas Technology. 12(11), 56-62.

[11] Ling, L., Da, T., Yu, J.W., Li, H.L., Wei, S., Hong, M.L. (2018) Favorable area prediction of tight sandstone: a case study of the he8 formation in the Kangning area, eastern Ordos Basin, China. Journal of Petroleum Science and Engineering. 17(5), 430-443.

[12] Dai, J., Liao, F., Ni, Y. (2013) Discussion on the gas source of the Triassic Xujiahe formation tight sandstone gas reservoirs in Yuanba and Tongnanba, Sichuan Basin. Petroleum Exploration & Development. 40(2), 268-275.

[13] Wang, X.W. (2012) Application of AVO technique in prediction of tight sandstone reservoirs. Journal of Oil and Gas Technology. 11(1), 172-178.

[14] Jia, Y., Wei, S., Shi, Y. (2017) Prediction of enrichment zones of natural gas in deep off-shore layer based on AV attributes. Ship Building. 58(1), 210-215.

[15] Adeoti, L., Adeleye, K.O., Itsemode, A., Bello, M.A. (2015) Fluid prediction using AVO analysis and forward modelling of deep reservoirs in faith field, Niger delta, Nigeria. Arabian Journal of Geosciences. 8(6), 1-18.

[16] Zoeppritz, K. (1919) On the reflection and propagation of seismic waves. Gottinger Nachrichten. 1(5), 66-84.

[17] Koefoed, O. (1955) On the effect of Poisson ratios of rock strata on the reflection coefficients of plane waves. Geophysical Prospecting. 3(4), 381-387.

[18] Bortfeld, R. (1961) Approximations to the reflection and transmission coefficients of plane longitudinal and transverse waves. Geophysical Prospecting. 9(4), 485-502.

[19] Nolet, G. (1980) Quantitative seismology, theory and methods. Earth Science Reviews. 17(3), 296-297.

[20] Shuey, R.T. (1985) A simplification of the Zoeppritz equations. Geophysics. 50(4), 609-614.
[21] Smith, G.C., Gidlow, P.M. (1987) Weighted stacking for rock property estimation and detection of gas. Geophysical Prospecting. 35(9), 993-1014.
[22] Yin, X.Y., Zong, Z.Y., Wu, G.C. (2013) Improving seismic interpretation: a high-contrast approximation to the reflection coefficient of a plane longitudinal wave. Petroleum Science. 21(4), 466-476.
[23] Fatti, J.L., Smith, G.C., Vail, P.J. (2014) Detection of gas in sandstone reservoirs using AVO analysis: A 3-D seismic case history using the Geostack technique. Geophysics. 59(9), 1362-1376.
[24] Zhang, Y., Huang, Y., Yue, Y., Chao, J., Huo, F., Yin, C. (2018) A compact fluorescent probe based on o-phthalaldehyde for ultrasensitive detection of hydrazine in gas and solution phases. Sensors and Actuators. 73(8), 944-950.
[25] Han, D.H., Ru, W.Z., Guo, Q., Shen, T.L. (2011) Study of prestack elastic parameter consistency inversion methods. Applied Geophysics. 19(9), 107-119.
[26] Gray, D., Goodway, B., Chen, T. (2012) The theory and application of DEM-Gassmann rock physics model for complex carbonate reservoirs. Leading Edge. 31(2), 152-158.
[27] Luo, Y., Huang, H., Jakobsen, M., Yang, Y., Zhang, J., Cai, Y. (2019) Prediction of porosity and gas saturation for deep-buried sandstone reservoirs from seismic data using an improved rock-physics model. Acta Geophysica. 17(4), 1011-1019.
[28] Castagna, J.P., Swan, H.W., Foster, D.J. (1998) Framework for AVO gradient and intercept interpretation. Geophysics. 63(3), 948-956.
[29] Rutherford, S.R., Williams, R.H. (1989) Amplitude-versus-offset variations in gas sands. Geophysics. 54(6), 680-688.
[30] Higgs, K.E., Higgs, H., Zwingmann, A. (2007) Diagenesis, porosity evolution, and petroleum emplacement in tight gas reservoirs, Taranaki Basin, New Zealand. Journal of Sedimentary Research. 77(12), 1003-1025.
[31] Fu, H., Tang, D., Hao, X., Chen, X., Cui, L., Ma, Y. (2012) Characteristics of tight sandstone reservoir and accumulation process of gas pool. Fault-Block Oil & Gas Field. 19(1), 47-50.
[32] Zou, C.N., Zhu, R.K., Wu, S.T., Yang, L. (2012) Types, characteristics, genesis and prospects of conventional and unconventional hydrocarbon accumulations: taking tight oil and tight gas in China as an instance. Acta Petrolei Sinica. 33(2), 173-187.

Received: **28.11.2021**
Accepted: **31.01.2022**

CORRESPONDING AUTHOR

Xinran Tian
College of Geophysics and Petroleum Resources,
Yangtze University,
Wuhan Hubei 430100 – P.R. China

e-mail: jackzheng1@126.com

© by PSP Volume 31– No. 05/2022 pages 5015-5023 Fresenius Environmental Bulletin

DEVELOPMENT, FECUNDITY AND POPULATION PARAMETERS OF *Tuta absoluta* (MEYRICK) (LEPIDOPTERA: GELECHIIDAE) ON DIFFERENT SOLANACEAE HOST PLANTS

Baran Aslan[1,*], Ali Kemal Birgucu[2]

[1]Burdur Mehmet Akif Ersoy University, Burdur Food Agriculture and Livestock Vocational School 15030 Burdur, Turkey
[2]Isparta University of Applied Sciences, Agriculture Faculty, Plant Protection Department 32260 Isparta, Turkey

ABSTRACT

Tomato leaf miner [*Tuta absoluta* (Meyrick) (Lepidoptera: Gelechiidae)] is a major pest of tomato and damage to the other cultivated Solanaceae family plants. In this study, the effects of three host plants from Solanaceae (including the species *Solanum lycopersicum* L., *Solanum melongena* L. and *Nicotiana tabacum* L.) on the life table parameters of *T. absoluta* were determined. All of the experiments were conducted in climatic cabins with 25±1ºC, relative humidity 65±5% and 16L: 8D hour photoperiod. Pre-adult development times, lifespan, pupal period, adult longevity and fecundity of females were also designated. As a result from the experiments, *S. lycopersicum* was determined the most susceptible species among the studied plants, as expected. According to the life table parameters, *N. tabacum* was determined as the most effective host plant for intrinsic rate of increase (r), net reproductive rate (R_0), mean generation time (T), gross reproduction rate (GRR), population doubling time (DT) and finite rate of increase (λ). Additionally, *N. tabacum* was also effective of on egg and larval development, total longevity and fecundity of the *T. absoluta*. Life table parameters of the pest reared on *S. melongena* has been observed between the other two species. For determining the life curves of the pest on studied host plants, Weibull distribution model was applied on age specific survival rates (l_x) and significant differences were observed on the three host plants. Findings from the study can be useful for agricultural practices of the studied plants and helps to developing an integrated pest management strategy in the future.

KEY WORDS:
Tuta absoluta, tobacco, eggplant, tomato, life table

INTRODUCTION

The tomato leaf miner, *Tuta absoluta* (Meyrick) (Lepidoptera: Gelechiidae), is the main pest in field and greenhouse tomato growing areas. Because of causing very serious damage, the pest is on the A1 quarantine list of EPPO. *T. absoluta* was first described in Peru (1917), then spread to Africa continent and still causes a high percentage of yield reduction on tomato plants [1,2]. In 2006, tomato leaf miner was first recorded in Europe (Spain) and in a very short time spread to all Mediterranean countries [3]. Since 2008, the pest presence has been reported in many European and African countries, consecutively. Nowadays, *T. absoluta* is also found in almost all South America, the majority of European countries, all Africa continent, Middle East countries and Arabian peninsula, west Asian countries, especially India, Bangladesh and Myanmar [4].

Although *T. absoluta* is known as the tomato leaf miner, it can also cause damage to many different Solanaceae plants like; pepper (*Capsicum annuum* L.), eggplant (*S. melongena* L.), tobacco (*Nicotiana tabacum* L.), potato (*S. tuberosum* L.), pepino (*S. muricatum* Aiton), black nightshade (*S. nigrum* L.) [5,6,7]. Additionally, *S. elaeagnifolium* L., *S. bonariense* L., *S. sisymbriifolium* Lamarch, *S. saponaceum* Welwitsch, *Lycopersicum puberulum* Phil, *Physalis peruviana* L., *Datura ferox* L., *D. stramonium* L., *Nicotiana glauca* Graham are also included non cultivated Solanaceae family plants [8,9,10]. The pest develops on many plants belonging to different families; *Convolvulus arvensis* L. in Convolvulaceae, *Chenopodium album* L. in Chenopodiaceae, *Vicia faba* L., *Phaseolus vulgaris* L., *Medicago sativa* L. in Fabaceae, *Beta vulgaris* L., *Spinacia oleracea* L. in Amaranthaceae, *Malva* sp. in Malvaceae and *Citrullus lanatus* (Thunb.) Matsum.& Nakai in Cucurbitaceae [11,6].

Tuta absoluta adults can fly great distances but sometimes they drift by the wind [12]. In suitable climatic conditions like greenhouses, the pest survives and reproduces in all year [13,14]. This species has seven life stages (egg, four larval stages, pupae and adult) and only larvae stages feeds on all plant parts except roots [15]. Adult females lay eggs on the leaves, stems and petioles of the host plants and emerged larvae open galleries in the leaf epidermis tissue [16-18]. In addition to these galleries, pest can

also feed in the fruit and body of the host plants [19,20]. Due to these damages, *T. absoluta* causes 80-100% in crop losses [21-23].

A life table is a table that shows, for each age, the probability of an organism of that age to die before its next birthday [24]. Life table studies give an important data such as growth, survival and fecundity about the pests. This information answers the question of the biological performance how influenced via the host plant. The purpose of this study was constructed to clear these questions on the Solanaceae host plants including the species *Solanum lycopersicum*, *Solanum melongena* and *Nicotiana tabacum*. Among them the life table of *T. absoluta* on *N. tabacum* was studied for the first time in this study. In addition, Weibull distributions were created by using on an age-specific survivor rate (l_x) of *T. absoluta* on these different hosts.

MATERIAL AND METHODS

Plant and Pest Culture Rearing. Host plants and *Tuta absoluta* (Meyrick) (Lepidoptera: Gelechiidae) population were grown in two different climatic cabins (25±1ºC, 65±5% RH, and 16L:8D) in Isparta University of Applied Sciences, Agriculture Faculty, Plant Protection Department, Isparta, TURKEY.

Solanum lycopersicum (cv Depar), *Solanum melongena* (cv Anamur) and *Nicotiana tabacum* (cv White Burley) were grown together. Eggplant plants were supplied as seedlings, tomato and tobacco seeds were sized using standard seedling growing techniques, and then they were transplanted into 15×9 cm pots (4 L) containing a mixture of peat+perlite (1:1). While irrigation and maintenance procedures were applied to all seedlings grown, no chemical fertilizers or pesticides were used. In case of any disease or pest contamination, the damaged part of the plant was destroyed; if the damage spread to the whole plant, it was immediately removed from the plant growing cabin.

Rearing of *Tuta absoluta.* Larvae and pupae samples were collected from tomato growing greenhouses and were placed in a climate room with 25±1 °C temperature, 65±5% R.H., and 16/8 light/dark conditions. To get a stock culture, healthy individuals were reared on tomato plants at least for three generations and then used in experiments.

Survival experiments. The leaf of the host plant which the egg is desired to be laid on, were left in plastic boxes of 10×8×8 cm covered with net, containing 20 adults of *T. absoluta*. The only stem part of these leaves were covered with cotton and placed in Eppendorf tubes containing water. Leaves with eggs were replaced with clean leaves, and the eggs laid leaves were transferred into petri dishes. The leaf particles with eggs were left on the studied host plants leaves on the 4th day. In order to follow up the larvae for daily; the leaves with the larvae were taken into petri dishes covered with a net and the petiole entrance part of dishes were cut (covered with a sponge). Each larva was determined as a separate replication and all treatments were carried out with 30 replications. The development and survival of pest were checked daily, and the data were saved to the Excel work sheets. The sexes of individuals were distinguished at the pupae stage as male or female. Adults were left in net covered plastic boxes with clean host plant leaves, including one female and at least two males. For adults feeding, a 5% sugar-water solution soaked in blotting paper was left in the boxes. The host plants leaves were removed from the boxes, the laid eggs were counted, and clean leaves of the same host plant species were transferred to boxes daily. The experiments were continued until the last adult death. Survival experiments were performed in a climate chamber.

Life Table Analyses. The life tables were constructed with daily data according the theory of age stage, two-sex life table [25,26]. According to this theory, calculated parameters are; age-specific survival rate (l_x), fecundity rate (m_x), net reproductive rate (R_0) $R_0 = \sum_{x=0}^{\infty} l_x \, . m_x$ (female/female), intrinsic rate of increase (r), $1 = \sum_{x=0}^{\infty} \left(e^{-r(x+1)} \sum_{j=1}^{m} f_{xj} s_{xj}\right)$ (female/female/day), mean generation time (T), $T_o = \frac{\ln R_0}{r_m}$ (day), gross reproduction rate (GRR), $GRR = \sum m_x$ (larvae/female), finite rate of increase (λ), $1 = \sum_{x=0}^{\infty} \left(\lambda^{-(x+1)} \sum_{j=1}^{m} f_{xj} \, s_{xj}\right)$ (larvae/female/day) [27] and population doubling time (DT) $T_2 = \frac{\ln 2}{r_m}$ (day) [28].

The mean and standard errors of (r) values computed on the data obtained from these populations, to be used in a comparison test, were calculated by the Bootstrap re-sampling method with the estimates 100.000 times [29-33]. Tukey multiple comparison tests [34] were applied after One-Way ANOVA for these pseudo-r_{mj} values of the intrinsic rates. Statistical analyses were performed using IBM® SPSS® Statistics (Version 20.0, August 2011, SPSS Inc., Chicago, IL, USA) and MS Excel 2010 (Version 14.0) package programs.

A two-parameter Weibull distribution model was used to describe the l_x of individuals on all host plant species [35-38]. The parameters of this distribution model's formula include:

$$S_p(x) = e^{\left[-\left(\frac{x}{b}\right)^c\right]} \qquad x, b, c > 0$$

The probability of survival at x age $S_p(x)$ "x" is the female's age in days, "b" is a scale parameter, and "c" is a shape parameter. The parameters and the coefficients of determination R^2 were obtained using

SigmaPlot® (Version 11.0, Systat Software, Inc., San Jose California, USA) package program.

RESULTS

The data obtained on the development times of the pre-adult biological stages of *Tuta absoluta* (Meyrick) (Lepidoptera: Gelechiidae) on three different hosts are given in Table 1. When the biological periods are examined separately, the egg periods of *T. absoluta* on *Nicotiana tabacum*, *Solanum lycopersicum* and *Solanum melongena* were respectively 5.70, 5.63, 5.43 days, and was found to be statistically insignificant.

The longest development period of the first larval stage of *T. absoluta* was completed on *N. tabacum* species with 8.30 days and the shortest was on *S. lycopersicum* completed with 3.90 days. On *S. melongena*, it was completed in 4.17 days. As a result of the statistical analysis, it was determined that the effect of the hosts on the first stage larvae of the tomato leaf miner was significant. Similarly, the effect of the hosts in the 2nd larval period was also found to be statistically significant, *N. tabacum* has the highest value with 6.33 days. In the third larval stage, each host plant were statistically separated into three different groups and again listed from longest to shortest as *N. tabacum*, *S. melongena* and *S. lycopersicum*, respectively (with 7.73, 6.10, 5.13 days). However, it was determined that in the 4th larval period the difference between *N. tabacum* (8.90days) and *S. melongena* (9.03 days) species were insignificant, while the shortest development was observed on *S. lycopersicum* (7.40 days) and statistically separated from the others. Considering the pupal development times, the order was determined as *N. tabacum* (11.63 days), *S. melongena* (9.17 days), *S. lycopersicum* (9.13 days) highest to lowest, respectively. The lifespan of *T. absoluta* was determined the longest on *N. tabacum* (49.04 days) and the shortest on *S. lycopersicum* (35.90 days), while on *S. melongena* with 39.10 days ranking among the other two species. The difference between the three host plants was found significant (P<0.05) (Table 1).

Figure 1 gives age-specific survival rates (l_x) and fecundity (m_x) curves of the life table. In the life table curves, although l_x values decrease rapidly in *S. lycopersicum* species, wavy view is shown in m_x. The curve of *S. melongena* was similar, and changes were observed in m_x proportionally to l_x values. The curve in *N. tabacum* showed differences from the other two host species. Despite the rapid decrease in l_x, m_x remained at a low level, but peaked especially after the 64th day, and then a very rapidly decrease was observed (Figure 1).

In this study, no statistical differences were found in terms of adult pre-oviposition period (APOP) and adult female longevity of *T. absoluta* on examined hosts. However, in terms of oviposition periods, *N. tabacum* had the lowest value (3.73 days) and was statistically separated from the other two host plants. In the post oviposition period the order was very different, *S. melongena* was determined as the shortest duration with a value of 0.70 days. Adult male longevity was observed to vary between 7.37 days and 10.06 days on the three host plants, and no statistical difference were found between *S. melongena* and *N. tabacum* species (Table 2).

When fecundity of *T. absoluta* females reared on different host plants was examined, the highest egg numbers were determined on *S. lycopersicum* (8.06 and 89.08 eggs/female, respectively) daily and total. The lowest daily and total fecundities were observed on *N. tabacum* (3.78 and 35.25 eggs/female, respectively) (Table 3).

TABLE 1
Pre-adult development periods and total longevity (days*) of *Tuta absoluta* on *Solanum lycopersicum*, *Solanum melongena* and *Nicotiana tabacum.*

	S. lycopersicum	*S. melongena*	*N. tabacum*
n	30	30	30
Egg	5.63±0.09 [a]	5.43±0.09 [a]	5.70±0.09 [a]
L_1	3.90±0.09 [b]	4.17±0.08 [b]	8.30±0.15 [a]
L_2	4.70±0.17 [b]	5.20±0.16 [b]	6.33±0.26 [a]
L_3	5.13±0.11 [c]	6.10±0.16 [b]	7.73±0.36 [a]
L_4	7.40±0.23 [b]	9.03±0.34 [a]	8.90±0.55 [a]
n	30	30	27
Pupal Period	9.13±0.43 [b]	9.17±0.27 [b]	11.63±0.29 [a]
Lifespan	35.90±0.46 [c]	39.10±0.51 [b]	49.04±0.91 [a]
Total Longevity	40.31±0.49 [b]	43.10±0.80 [b]	54.13±2.23 [a]

*Different letters in each line shows significant differences among biological period at 5% level. (Tukey's HSD test, p>0.05).

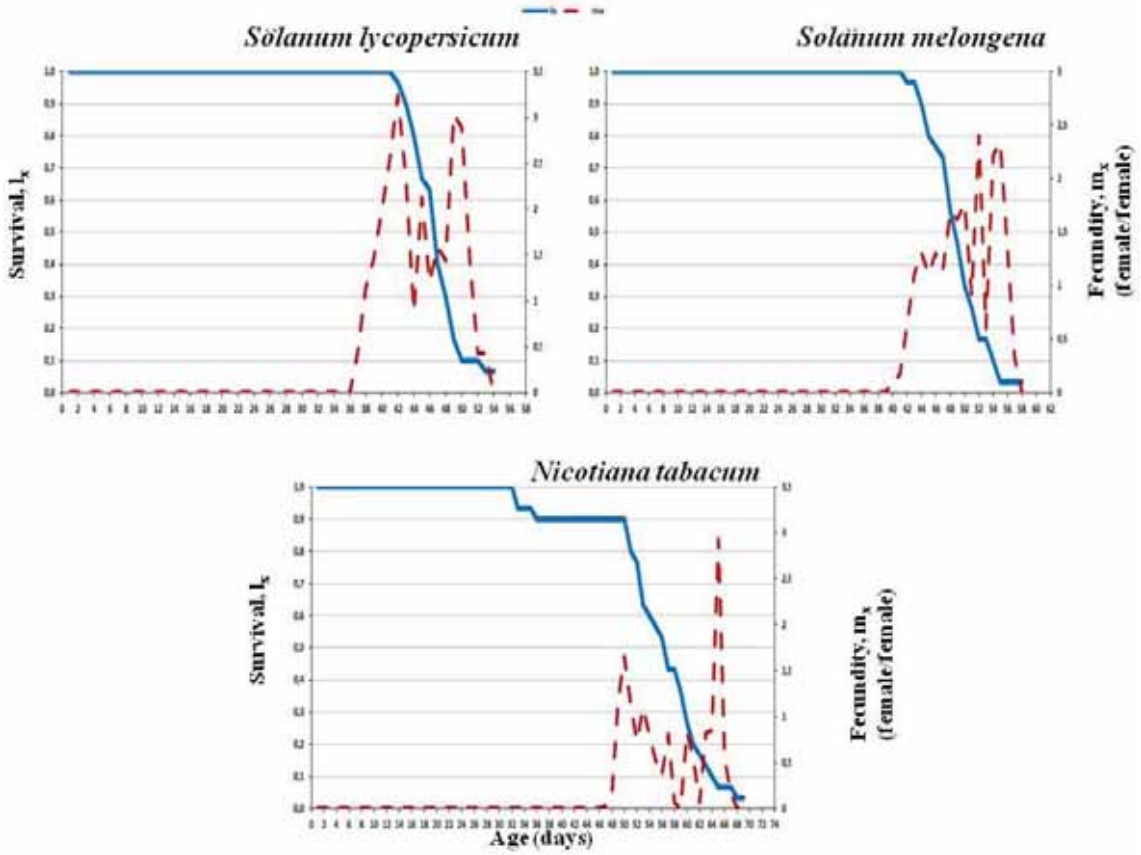

FIGURE 1
Age-specific survival rates (l_x) and fecundity (m_x) curves of *Tuta absoluta* individuals reared on *Solanum lycopersicum*, *Solanum melongena* and *Nicotiana tabacum*.

TABLE 2
Female pre-oviposition (APOP), oviposition, post-oviposition periods and adult (female, male) longevity (days*), of *Tuta absoluta* on *Solanum lycopersicum*, *Solanum melongena* and *Nicotiana tabacum.*

	n	APOP**	Oviposition period	Post-oviposition period	Adult longevity		
					Female	n	Male
Solanum lycopersicum	13	1.46±0.1 [a]	6.92±0.80 [a]	2.31±0.35 [a]	10.69±0.7 [a]	17	10.06±0.3 [a]
Solanum melongena	10	1.20±013 [a]	9.50±0.72 [a]	0.70±0.30 [b]	11.40±0.5 [a]	20	8.15±0.2 [b]
Nicotiana tabacum	11	1.36±0.31 [a]	3.73±0.79 [b]	1.64±0.34[ab]	9.25±0.45 [a]	16	7.37±0.3 [b]

*Different letters in each column shows significant differences among biological period at 5% level. (Tukey's HSD test, p>0.05),
**APOP: Adult pre-oviposition period.

"The intrinsic rate of increase (r_m)", which is one of the most important parameters showing the population increase, was found the highest on *S. lycopersicum* with 0.068 and the lowest on *N. tabacum* with 0.037. *S. melongena* species was placed between the other two species with a value of 0.048. These obtained values were found to be statistically significant. As seen in Table 3, "net reproductive rate (R_0)" was determined the highest with 17.788 (female/female) on *S. lycopersicum*, besides 9.277 and 7.049 (female female) observed on *S. melongena* and *N. tabacum* species, respectively. According to mean generation time (T) values, the highest to lowest arrangement were *N. tabacum*, *S. melongena* and *S. lycopersicum* with 52.498, 46.204 and 42.063 days, respectively. When gross reproductive rate (GRR), population doubling time (DT) and finite rate of increase (λ) were calculated, similar results were obtained, the ranking from susceptible to resistance were again *S. lycopersicum*, *S. melongena* and *N. tabacum*, respectively (Table 3).

TABLE 3
Fecundity and the population parameters (mean±SE)* of *Tuta absoluta* on *Solanum lycopersicum*, *Solanum melongena* and *Nicotiana tabacum.*

		Solanum lycopersicum	*Solanum melongena*	*Nicotiana tabacum*
n		13	10	11
Fecundity (eggs/female)	**Daily**	8.06 ± 0.78 [a]	6.69 ± 0.85 [a]	3.78 ± 0.60 [b]
	Total	89.08 ±12.98 [a]	79 ±60 ±12.93 [a]	35.25±5.61 [b]
The intrinsic rate of increase, r_m (day^{-1})		0.068 ±0.004 [a]	0.048 ±0.002 [b]	0.037 ±0.002 [c]
Net reproductive rate, R_0		17.788 ±0.158 [a]	9.277 ±0.071 [b]	7.049 ±0.065 [c]
Mean generation time, T (day)		42.063	46.204	52.498
Gross reproductive rate, GRR		28.644	22.112	15.386
Population doubling time, DT (day)		10.129	14.377	18.634
Finite rate of increase, λ (day^{-1})		1.071	1.049	1.038

* Differences between the intrinsic rate of increase and finite rate of increase (± standard errors) with different letters in the same lines are statistically significant. (Tukey's HSD test, p>0.05)

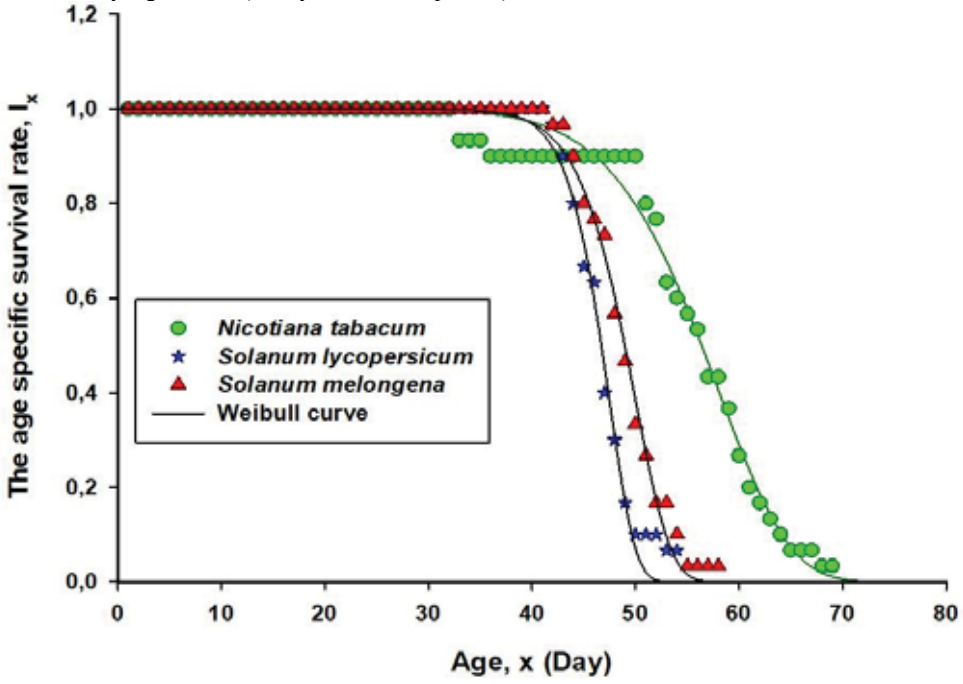

FIGURE 2
Weibull distribution models applied on the age-specific survival rate (l_x) of *Tuta absoluta* on *Solanum lycopersicum*, *Solanum melongena* and *Nicotiana tabacum*.

From the obtained results, Weibull distribution models were applied to the age-specific survival rate of *Tuta absoluta* reared on different host plants. When the model was examined, *S. lycopersicum* was ranked as having the lowest age (day). Looking at the model again, the l_x distribution of *T. absoluta* on *S. melongena* is close to that of *S. lycopersicum*. Unlike the other two host species, the age-specific survival rate distribution of *N. tabacum* appears to be very different (Figure 2).

Among the studied species, the highest b value was in *N. tabacum*, the lowest was in *S. lycopersicum*. When c values are examined, the order was different; the highest to lowest were *S. lycopersicum*, *S. melongena* and *N. tabacum*, respectively. Considering the values taken by the parameter c determines that the shape of the slope in the modelling, c > 1 shows the developing populations, c = 1 shows the stable populations, and c < 1 shows the regressed populations [35,36]. When these c values are examined, it is observed that *T. absoluta* populations represented an increasing population on all examined host plants (Table 4).

DISCUSSION

This study was conducted to determine the population parameters how effected *Tuta absoluta* (Meyrick) (Lepidoptera: Gelechiidae) reared on different Solanaceae host plants. For this purpose, *Solanum lycopersicum*, *S. melongena* and *Nicotiana tabacum* host plants from the family Solanaceae were selected. Among the host plants, *N. tabacum* was studied for the first time in terms of its effect on the life table parameters of *Tuta absoluta*.

TABLE 4
Weibull distribution model's parameters applied on the age-specific survival rate (l_x) of *Tuta absoluta* on *Solanum lycopersicum*, *Solanum melongena* and *Nicotiana tabacum.**

	b	c	R^2	RSS
Solanum lycopersicum	47.583 ± 0.091	19.693 ± 0.894	0.992	0.040
Solanum melongena	50.145 ± 0.083	15.467 ± 0.483	0.995	0.027
Nicotiana tabacum	58.645 ± 0.189	9.320 ± 0.349	0.987	0.087

* The values of parameters b and c are given with their standard errors (P<0.0001). RSS: residual sum of squares

There were not significant differences between the host plants in terms of egg period and values changed between 5.43 to 5.70 days. Hatching time takes 4-5 days in *T. absoluta* [39] and this result is similar to the values gained in this study. When the larval developments are compared, the shortest time observed on S. *lycopersicum* and the longest on *N. tabacum*. Lifespan were 35.90 days on *S. lycopersicum*, 39.10 days on *S. melongena* and 49.04 days on *N. tabacum* plants. In another study about the *T. absoluta* population parameters, lifespan were obtained 24.67days on *S. lycopersicum* and 27.57 days on *S. melongena* [40]. The differences might be attributed to that study was performed in greenhouse conditions.

Results of APOP and adult female periods showed no significant differences but the different life stages were all significant on all host plants. Different values have been reported for female longevity; 10-15 days [41], 10-22 days [42] and 18 days [43]. Female longevity ranged 9.25 to 10.69 in this study and results are similar with the majority.

Whenever fecundity of *T. absoluta* females reared on different host plants compared, there were no significant differences on *S. lycopersicum* and on *S. melongena*, but the value obtained on *N. tabacum* was statistically different from others. The number observed from *S. lycopersicum* were determined as a daily average number of 8.06 (eggs/female) and 89.08 (eggs/female) of total. Female *T. absoluta* fecundity ranged from 60 to 120 eggs [42], similarly, but another study reported that females laid an average of 132.7 eggs [44]. This result is much higher than the values obtained; this may be due to the females' mate with only one or two males in our study. In addition, the obtained data showed that fecundity values of *T. absoluta* on *N. tabacum* were very low in both daily and total (3.78 and 35.25, respectively).

Intrinsic rate of increase (*r*) values one of the most important parameters showing the population increase, were ranked the highest to lowest as *S. lycopersicum* (0.068 day^{-1}), *S. melongena* (0.048 day^{-1}) and *N. tabacum* (0.037 day^{-1}). *N. tabacum* has the lowest *r* value that was a result of the lowest fecundity and as well as the longest total longevity. The life table of *T. absoluta* was determined on different tomato varieties in the other studies. They found the *r* as 0.14 (without variety name) [42], 0.132 (without variety name) [43], 0.173 (Torry), 0.169 (Newton), 0.159 (Caracas) and 0.150 (Şimşek) [45]; 0.091 (Fallato), 0.074 (Grandella) and 0.095 (Isabella) females/females/day [39]. Similar results reported the obtained values as 0.14 on *S. lycopersicum* (Santa Clara) and 0.08 on *S. melongena* (Comprida Roxa) on different Solanaceae hosts [40]. These values are higher than what we obtained on all three host plants, differences might be occurred due to the different cultivars and experimental conditions.

According to net reproductive rate (R_0) and mean generation time (T) values, the most suitable host plant for the *T. absoluta* was determined as a *S. lycopersicum*. According to the other life table parameters sorting of suitable host plants continues as *S. melongena* and *N. tabacum*. In our study, the highest λ value was determined on *S. lycopersicum* and the lowest on *N. tabacum*. Researchers calculated the λ value as 1.15 on *S. lycopersicum* and 1.09 on *S. melongena* in their studies [40]. Population parameters of *T. absoluta* have not been studied before on *N. tabacum*, therefore we could not compare the obtained data. However, when the obtained results were evaluated together, it was concluded that *N. tabacum* is not a suitable host for *T. absoluta*.

The longest development periods were determined on *N. tabacum* in all the larval stages, pupae stage, development time, and longevity. Also the lowest values were observed in fecundity values in both daily and total egg numbers on *N. tabacum*. In life table parameters, *N. tabacum* was determined as the most effective host species in terms of *r*, R_0, T, DT, GRR and λ values. As expected, *S. lycopersicum* was determined as the most suitable host.

Considering all these results, it was found that *N. tabacum* had negative characteristics for reproduction and survival of *T. absoluta* compared with the other two host plants in this study. The results clearly demonstrate that tomato leaf miner is capable of laying eggs on all host plants, but there are differences observed on the population parameters between the hosts. These differences could be related to insect feeding deterrents present in host plants assessed. But, more studies must be performed and evaluated to find that what is causing these differences of morphological defence against the pest. Moreover, achievable results will be considered as candidates for use in integrated management programs of the tomato leaf miner.

REFERENCES

[1] Sylla, S., Brévault, T., Bal, A.B., Chailleux, A., Diatte, M., Desneux, N. and Diarra, K. (2017) Rapid Spread of the Tomato Leafminer, *Tuta absoluta* (Lepidoptera, Gelechiidae), an Invasive Pest in Sub-Saharan Africa. Entomologia Generalis. 36(3), 269-283.

[2] Biondi, A. and Desneux, N. (2019) Special Issue on *Tuta absoluta*: Recent Advances in Management Methods Against the Background of an Ongoing Worldwide Invasion. Journal of Pest Science. 92(4), 1313-1315.

[3] Bayram, Y., Duman, M., Buyuk, M. and Mutlu, Ç. (2017) Efficiency of Pheromone Water Traps and Life Cycle of *Tuta Absoluta* (Lepidoptera: Gelechiidae) in Diyarbakir Province, Turkey. Fresen. Environ. Bull. 26(12A), 8146-8153.

[4] EPPO. (2021) European and Mediterranean Plant Protection Organization (EPPO) Global Database. https://gd.eppo.int/taxon/GNORAB/hosts. (Access Date: 15.09.2021.)

[5] Mohamed, E.S.I., Mahmoud, M.E.E., Elhaj, M.A.M., Mohamed, S.A. and Ekesi, S. (2015) Host plants Record for Tomato Leaf Miner *Tuta absoluta* (Meyrick) in Sudan. European and Mediterranean Plant Protection Organization Bulletin. 45(1), 108–111.

[6] Cherif, A. and Verheggen, F. (2019) A Review of *Tuta absoluta* (Lepidoptera: Gelechiidae) Host Plants and Their Impact on Management Strategies. Biotechnologie, Agronomie, Société et Environnement. 23(4), 270-278.

[7] Erler, F., Kirisik, M. and Topuz, E. (2020) Comparable Study on Different Colored Sticky Traps for Catching of Adult *Tuta absoluta* (Meyrick) (Lepidoptera: Gelechiidae). Fresen. Environ. Bull. 29(09), 7349-7354.

[8] Tropea Garzia, G. (2009) *Physalis peruviana* L. (Solanaceae), a Host Plant of *Tuta absoluta* in Italy. IOBC/WPRS Bulletin. 49, 231-232.

[9] Portakaldalı, M., Öztemiz, S. and Kütük, H. (2013) A New Host Plant for *Tuta absoluta* (Meyrick) (Lepidoptera: Gelechiidae) in Turkey. Journal of Entomological Research Society. 15(3), 21-24.

[10] Al Antary, T., Alhawamdeh, A.S. and Katbeh-Bader, A.M. (2019) The Susceptibility of Three Tomato Cultivars and Efficacy of Three Insecticides in Controlling the Broad Tomato Leafminer, *Tuta absoluta* (Meyrick) (Lepidoptera: Gelechiidae) in the High Lands of Jordan. Fresen. Environ. Bull. 28(11A), 8694-8701.

[11] Abdul-Ridha, M., Alwan, S.L, Helal, S.M. and Aziz, K.A. (2012) Alternative Hosts of South American Tomato Moth *Tuta absoluta* (Gelechiidae: Lepidoptera) in Some Tomato Farms of Najaf Province. Euphrates Journal of Agricultural Science. 4(4), 130–137.

[12] Van Deventer, P. (2009) Leaf Miner Threatens Tomato Growing in Europe. Fruit and Vegetable Technologies. 9(1), 10-12.

[13] Desneux, N., Luna, M.G., Guillemaud, T. and Urbaneja, A. (2011) The Invasive South American Tomato Pinworm, *Tuta absoluta*, Continues to Spread in Afro-Eurasia and Beyond: The New Threat to Tomato World Production. Journal of Pest Science. 84(4), 403–408.

[14] Santana, P.A., Kumar, L., Da Silva, R.S. and Picanço, M.C. (2019) Global Geographic Distribution of *Tuta absoluta* as Affected by Climate Change. Journal of Applied Entomology. 92(4), 1373–1385.

[15] Öztemiz, S. (2012) The tomato leafminer [*Tuta absoluta* Meyrcik (Lepidoptera: Gelechiidae)] and its biological control. Journal of Agriculture and Nature. 15(4), 47-57 (in Turkish).

[16] Picanço, M.C., Bacci, L., Crespo, A.L.B., Miranda, M.M.M. and Martins, J.C. (2007) Effect of Integrated Pest Management Practices on Tomato Production and Conservation of Natural Enemies. Agricultural and Forest Entomology. 9(4), 327–335.

[17] Rakha, M., Zekeya, N., Sevgan, S., Musembi, M., Ramasamy, S. and Hanson, P. (2017) Screening Recently Identified Whitefly/Spider Mite-Resistant Wild Tomato Accessions for Resistance to *Tuta absoluta*. Plant Breeding. 136(4), 562–568.

[18] Simmons, A.M., Wakil, W., Qayyum, M.A., Ramasamy, S., Kuhar, T.P. and Philips, C.R. (2018) Lepidopterous Pests: Biology, Ecology, and Management. In: Sustainable Management of Arthropod Pests of Tomato. (Wakil, W., Brust, G.E., Perring, T.M., ed-s.), Academic Press, Elsevier. 131–162.

[19] Cuthbeertson, A.G.S., Mathers, J.J., Blackburn, L.F., Korycinska, A., Luo, W., Jacobson, R.J. and Northing, P. (2013) Population Development of *Tuta absoluta* (Meyrick) (Lepidoptera:Gelechiidae) Under Simulated UK Greenhouse Conditions. Insects. 4(2), 185-197.

[20] Duarte, L., Martinez, M.A. and Bueno, V.H.P. (2015) Biology and Population Parameters of *Tuta absoluta* (Meyrick) Under Laboratory Conditions. Revista de Protección Vegetal. 30(1), 19-29.

[21] López, E. (1991) Tomato Moth: Critical Problem for the Profitability of the Summer Crop. Empresa y Avance Agricola. 1, 6-7 (in Spanish).

[22] Cocco, A, Deliperi, S. and Delrio, G. (2013) Control of *Tuta absoluta* (Meyrick) (Lepidoptera: Gelechiidae) in Greenhouse Tomato Crops Using the Mating Disruption Technique. Journal of Applied Entomology. 137(1-2), 16-28.

[23] Bayram, Y. (2019) Efficacy of Two Entomopathogenic Fungi and Their Combination with Summer Oil Against Tomato Moth, *Tuta Absoluta*. Fresen. Environ. Bull. 29(4A), 3453-3440.

[24] Begon, M., Harper, J.L. and Townsend, C.R. (1996) Ecology: Individuals, Populations, and Communities, 3rd edition. Blackwell Science Ltd. Cambridge, MA.

[25] Chi, H. and Liu, H. (1985) Two New Methods for the Study of Insect Population Ecology. Bulletin of the Institute of Zoology, Academia Sinica. 24(2), 225-240.

[26] Chi, H. (1988) Life Table Analysis Incorporating Both Sexes and Variable Development Rates Among Individuals. Environmental Entomology. 17(1), 26-34.

[27] Birch, L.C. (1948) The Intrinsic Rate of Natural Increase of an Insect Population. Journal of Animal Ecology. 17(1), 15-26.

[28] Kairo, M.T.K. and Murphy, S.T. (1995) The Life History of *Rodolia iceryae* Janson (Coleoptera:Coccinellidae) and the Potential for use in Innoculative Releases Against *Icerya pattersoni* Newstead (Homoptera: Margarodidae) on Coffee. Journal of Applied Entomology. 119(1-5), 487-491.

[29] Meyer, J.S., Ingersoll, C.G., McDonald, L.L. and Boyce, M.S. (1986) Estimating Uncertainty in Population Growth Rates: Jackknife vs. Bootstrap Techniques. Ecology. 67(5), 1156- 1166.

[30] Lawo, J.P. and Lawo, N.C. (2011) Misconceptions About the Comparison of Intrinsic Rates of Natural Increase. Journal of Applied Entomology. 135(10), 715-725.

[31] Huang, Y.B. and Chi, H. (2012) Assessing the Application of the Jackknife and Bootstrap Techniques to the Estimation of the Variability of the Net Reproductive Rate and Gross Reproductive Rate: A Case Study in *Bactrocera cucurbitae* (Coquillett) (Diptera: Tephritidae). Journal of Agriculture and Forest Entomology. 61(1), 37-45.

[32] Yu, J.Z., Chi, H. and Chen, B.H. (2013) Comparison of the Life Tables and Predation Rates of *Harmonia dimidiata* (F.) (Coleoptera: Coccinellidae) Fed on *Aphis gossypii* Glover (Hemiptera: Aphididae) at Different Temperatures. Biological Control. 64(1), 1-9.

[33] Yu, L.Y., Chen, Z.Z., Zheng, F.Q., Shi, A.J., Guo, T.T., Yeh, B.H., Chi H. and Xu, Y.Y. (2013) Demographic Analysis, a Comparison of the Jackknife and Bootstrap Methods, and Predation Projection: A Case Study of *Chrysopa pallens* (Neuroptera: Chrysopidae). Journal of Economical Entomology. 106(1), 1-9.

[34] Tukey, J.W. (1949) Comparing Individual Means in the Analyses of Variance. Biometrics. 5(1), 99-114.

[35] Deevey, E.S. (1947) Life Tables for Natural Populations of Animals. The Quarterly Review of Biology. 22(4), 283-314.

[36] Pinder, J.E., Wiener, J.G. and Smith, M.H. (1978) The Weibull distribution: A New Method of Summarizing Survivorship Data. Ecology. 59(1), 175-179.

[37] Tingle, C.C.D. and Copland, M.J.W. (1989) Progeny Production and Adult Longevity of the Mealybug Parasitoids *Anagyrus pseudococci*, *Leptomastix dactylopii* and *Leptomastidea abnormis* (Hymenoptera: Encyrtidae) in Relation to Temperature. Entomophaga. 34(1), 111-120.

[38] Wang, J.J., Tsai, J.H., Zhao, Z.M. and Li, L.S. (2000) Development and Reproduction of the Psocid *Liposcelis bostrychophila* (Psocoptera: Liposcelididae) as a Function of Temperature. Annals of the Entomological Society of America. 93(2), 261-270.

[39] Rostami, E., Madadi, H., Abbasipour, H., Allahyari, H. and Cutbertson, A.G.S. (2017) Life Table Parameters of the Tomato Leaf Miner *Tuta absoluta* (Lepidoptera: Gelechiidae) on Different Tomato Cultivars. Journal of Applied Entomology. 141(1), 88–96.

[40] Silva, G.A., Queiroz, E.A., Arcanjo, L.P., Lopes, M.C., Araújo, T.A., Galdino, T.S.V., Samuels, R.I., Rodrigues-Silva, N. and Picanço, M.C. (2021) Biological Performance and Oviposition Preference of Tomato Pinworm *Tuta absoluta* When Offered a Range of Solanaceous Host Plants. Scientific Reports. 11, 1153.

[41] Estay, P. (2000) Tomato Moth *Tuta absoluta* (Meyrick). INIA La Platina. 9(1), 1-4 (in Spanish).

[42] Torrest, J., Faria, C.A., Evangeliste, W.S. and Pratissoli, D. (2001) Within-Plant Distribution of the Tomato Leaf Miner, *Tuta absoluta* (Meyrick) Immature in Processing, with Notes on Plant Phenology. International Journal of Pest Management. 47(3), 173–178.

[43] Erdoğan, P. and Babaroğlu, N. (2014) Life Table of the Tomato Leaf Miner, *Tuta absoluta* (Meyrick) (Lepidoptera: Gelechiidae). Journal of Agricultural Faculty of Gaziosmanpasa University (JAFAG). 31(1), 80–89.

[44] Pereyra, P.C. and Sanchez, N.E. (2006) Effect of Two Solanaceous Plants on Developmental and Population Parameters of the Tomato Leaf Miner, *Tuta absoluta* (Meyrick) (Lepidoptera:Gelechiidae). Neotropical Entomology. 35(5), 671–676.

[45] Çekin, D. and Yaşar, B. (2015) The Life Table of *Tuta absoluta* (Meyrick, 1917) (Lepidoptera: Gelechiidae) on Different Tomato Varieties. Journal of Agricultural Science. 21(2), 199-206.

Received: **28.11.2021**
Accepted: **23.01.2022**

CORRESPONDING AUTHOR

Baran Aslan
Burdur Mehmet Akif Ersoy University,
Burdur Food Agriculture and Livestock
Vocational School
15030 Burdur – Turkey

e-mail: aslanb@mehmetakif.edu.tr

© by PSP Volume 31– No. 05/2022 pages 5024-5029 Fresenius Environmental Bulletin

EXPERIMENTAL STUDY ON SCR EMISSION DURING DPF ACTIVE REGENERATION

Jinliang Zhu[1], Zhentao Zhang[2], Zhiming Wang[1], Guihua Wang[1], Guoxiang Li[1,*], Shuzhan Bai[1]

[1]School of Energy and Power Engineering, Shandong University, Jinan 250061, China
[2]Shiwei Environmental Protection Co., Ltd. Weifang, 261000, China

ABSTRACT

Diesel particulate filter (DPF) active regeneration causes exhaust gas temperatures to be around 600°C, which not only affects the urea injections, but it also seriously affects the efficiency of the selective catalytic reduction (SCR), resulting in many difficulties in the control of tailpipe nitrogen oxides (NO_x) emission and ammonia leakage. In this research, the influence of DPF active regeneration on SCR was experimentally studied with a bench. The influence of the DPF active regeneration on the SCR temperature, ammonia storage, urea injection, tail exhaust NO_x, and ammonia leakage was quantitatively analyzed under the World Harmonized Transient Cycle (WHTC). The results showed that the average temperature of the SCR rose from 245°C to 502°C. The high temperature affected the SCR conversion efficiency, especially when the temperature exceeded 550°C. The SCR conversion efficiency decreased significantly, and the tail NO_x changed from 0.12 g/kw·h to 0.65 g/kw·h. The sensitivity of the SCR conversion efficiency to the temperature was reduced, and the sensitivity to the space velocity was increased. When the temperature rose sharply, the dynamic follow-up of the ammonia storage and the ammonia leakage of the tailpipe were difficult to control. The concentration of the ammonia leakage was positively correlated with the space velocity. The control research results could provide a reference for SCR size design, control, and diagnosis strategies.

KEYWORDS:
DPF, SCR, emission, active regeneration

INTRODUCTION

Euro VI emission regulations impose strict restrictions on nitrogen oxides (NO_x) and particulate matter (PM). To meet the requirements for regulations about PM and the particulate number (PN), diesel engine after-treatment is equipped with a diesel particulate filter (DPF). When the soot captured in the DPF reaches a certain amount, the engine will enter the DPF active regeneration mode from the normal mode so that the temperature upstream of the DPF is controlled at a high temperature (around 600°C) to burn the soot. To meet the regulatory requirements for NO_x and ammonia leakage, the after-treatment is equipped with selective catalytic reduction (SCR). Copper (Cu)-based SCR is considered to be a potential catalyst because it has good NO_x conversion efficiency at low temperature (< 350°C) [1-4].

Storing a large amount of ammonia at low temperatures can improve the conversion efficiency of Cu-based SCR. However, DPF active regeneration makes the temperature of after-treatment rise rapidly, which can easily lead to a large amount of ammonia leakage, and a temperature that is too high can reduce the efficiency of NO_x conversion. The large amounts of ammonia leakage and NO_x emission in the tailpipe caused by DPF active regeneration pose a challenge to the Euro VI engine. In particular, the requirements of the DPF and SCR for the exhaust gas temperature are contradictory. From the perspective of the soot load of the DPF, it is hoped that the exhaust temperature will quickly rise to the target temperature (550°C–600°C), but from the perspective of SCR ammonia leakage, it is hoped that the exhaust temperature will slowly rise to the target temperature, to reduce ammonia leakage.

For the DPF active regeneration mode, there are many studies on volatile organic compounds, PM, and PN in tail exhaust [5-10], but there are limited studies on SCR emission. This article describes the quantitative study of the influence of DPF active regeneration on the SCR factors under the WHTC cycle to provide data support for the size design, control, and diagnosis strategy of SCR.

MATERIALS AND METHODS

Experimental setup. The test engine in this study was an electronically controlled high-pressure common rail Euro VI engine. The air intake system was composed of a supercharged exhaust gas recirculation valve and an intake throttle valve. The after-treatment configuration was diesel oxidation catalyst (DOC)+DPF+ SCR. Temperature sensors were installed in the upstream of the DOC, DPF, and SCR and the downstream of the SCR. The DPF was

equipped with a differential pressure sensor for judging the soot load, and the analyzers for measuring the NO_x and ammonia were downstream of the SCR, as shown in Figure 1. Tables 1 and 2 show the related specifications and detailed information about the test bench, respectively.

Experimental method. The engine ran in the normal mode most of the time. In this mode, the engine had strong power and low fuel consumption. When the soot load in the DPF met certain conditions, the DPF active regeneration mode was triggered. The engine exhaust was used to increase the temperature of the DOC to oxidize the hydrocarbons, and then the DPF temperature was maintained at around 600°C through the engine's post-injection. Under the WHTC, the engine was run in normal mode and DPF active regeneration mode on the test bench, and the changes of the after-treatment temperatures, SCR ammonia storage, urea injection, and tail exhaust NO_x for the two cycles were quantitatively compared to analyze the impact of the DPF active regeneration on the SCR.

RESULTS AND DISCUSSION

Influence of the DPF active regeneration on the after-treatment temperatures. Many factors affect SCR conversion efficiency, including space velocity, ammonia storage, and urea injection, with the temperature being the core factor. In the appropriate temperature range, Cu-based SCR has high conversion efficiency, and temperatures that are too low or too high are not conducive to SCR conversion efficiency. In this research, the temperature of the soot combustion exceeded 550°C, which caused the temperature of the SCR to be in the high range. Under the WHTC, the DPF active regeneration was triggered at 350 s and it ended at 1,500 s. As can be seen from Figure 2，during the DPF active regeneration, the lowest temperature of the DPF was 218°C, the highest temperature was 600°C, and the average temperature was 514°C. The lowest temperature of the SCR was 220°C, the highest temperature was 596°C, and the average temperature was 502°C. In normal mode, the lowest temperature of the SCR was 203°C, the highest temperature was 300°C, and the average temperature was 245°C.

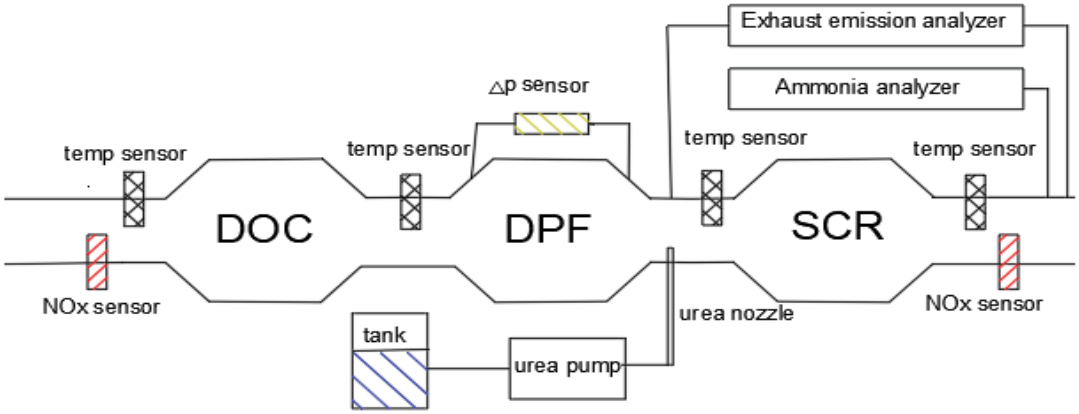

FIGURE 1
Schematic diagram of after-treatment layout

TABLE 1
Test engine specifications

Project	Specification
Engine type	6 Cylinder
Bore × stroke/mm × mm	108 × 130
Compression ratio	18
Swept volume/L	7.14
Rated power/kW	200
Rated speed/r/min	2100
Max torque/N/m	1100

TABLE 2
Catalyst specifications

	DOC	DPF	SCR
Volume (L)	6.6	13.0	15.1
Diameter (mm)	284	284	266.7
Length (mm)	105	205	270
Density *cpsi	400	300	600

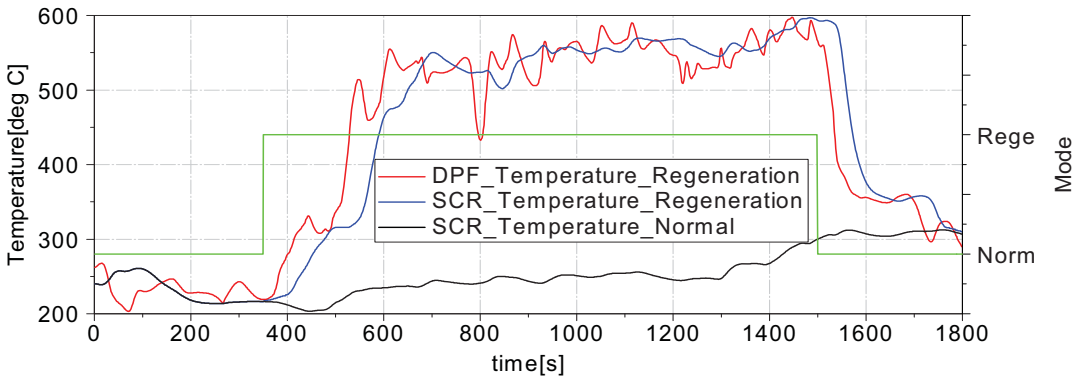

FIGURE 2
After-treatment temperature under WHTC

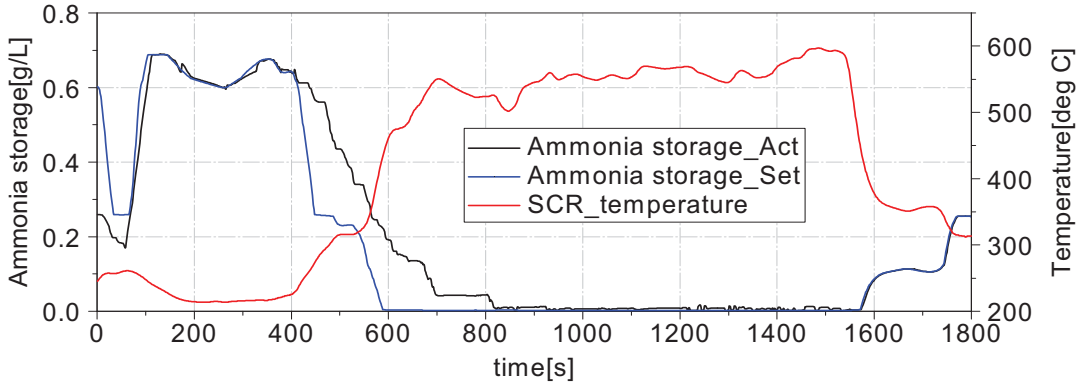

FIGURE 3
SCR ammonia storage during the active regeneration of the DPF

There was a huge difference in the SCR temperatures between the two modes. Compared with the normal mode, the average temperature of the SCR increased by 257°C and the highest temperature increased by 300°C. In the DPF active regeneration mode, temperatures that were too high affected the conversion efficiency of the SCR.

Influence of the DPF active regeneration on the ammonia storage. Proper ammonia storage was the key to the high NO_x conversion efficiency of the Cu-based SCR in the low-temperature region. Cu-based SCR could store a large amount of ammonia at low temperatures, and the ammonia storage capacity was reduced at high temperatures. In actual use, by injecting urea, the actual ammonia storage value will follow the change of the ammonia storage setting value, to achieve the desired SCR conversion efficiency. Setting different ammonia storage values according to the SCR temperature is a general method to reduce the tail NO_x.

As can be seen from Figure 3, there were two large deviations between the set values and the actual values of the ammonia storage. At the beginning of the WHTC, the deviation between the two was large. This was because the engine was stopped for 10 minutes between the cold start WHTC and the hot start WHTC, resulting in no change in the actual ammonia storage. Owing to the decrease of the SCR temperature, the set value of ammonia storage became larger, and the deviation between the two became larger. With the start of the urea injection of the hot start WHTC, the deviation between the two decreased. When the SCR temperature rose rapidly from 400 s to 700 s, the deviation between the two was large again. This was because the exhaust gas temperature rose sharply in the DPF active regeneration mode, resulting in a rapid drop in the ammonia storage setting. As can be seen from Figure 3, the deviation between the set value and the actual value of ammonia storage lasted for more than 400 s. When the SCR temperature did not change violently, the two coincided again.

Influence of the DPF active regeneration on the urea injection. Urea solution was used as the source of ammonia. Injecting urea into SCR is one of the main technical routes of Euro VI for controlling tail NO_x. The urea injection quantity was affected not only by the NO_x emission from the engine but also by the SCR conversion efficiency and the ammonia storage. When the set ammonia storage value was greater than the actual ammonia storage value, it led to more urea injection, so the actual ammonia storage value could quickly follow the set ammonia storage value.

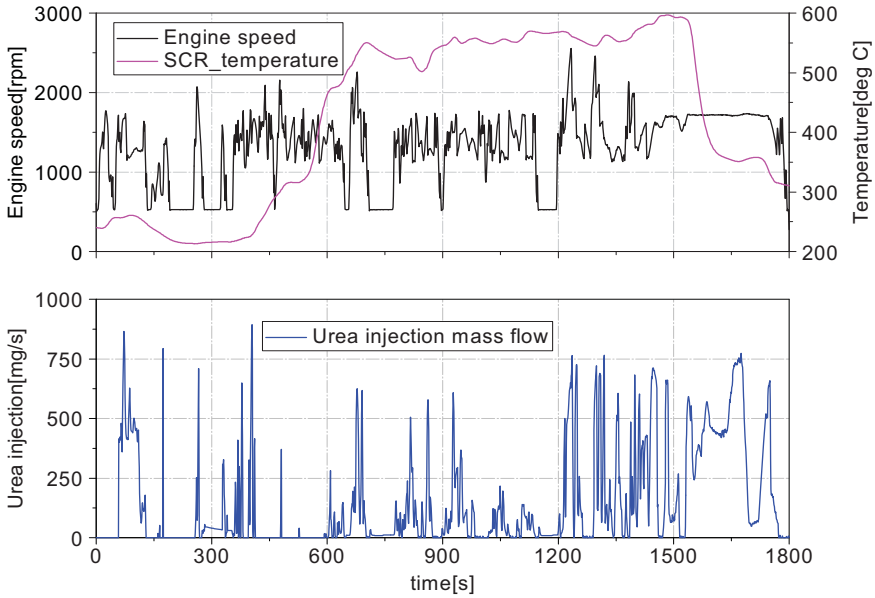

FIGURE 4
Urea injection during the active regeneration of the DPF

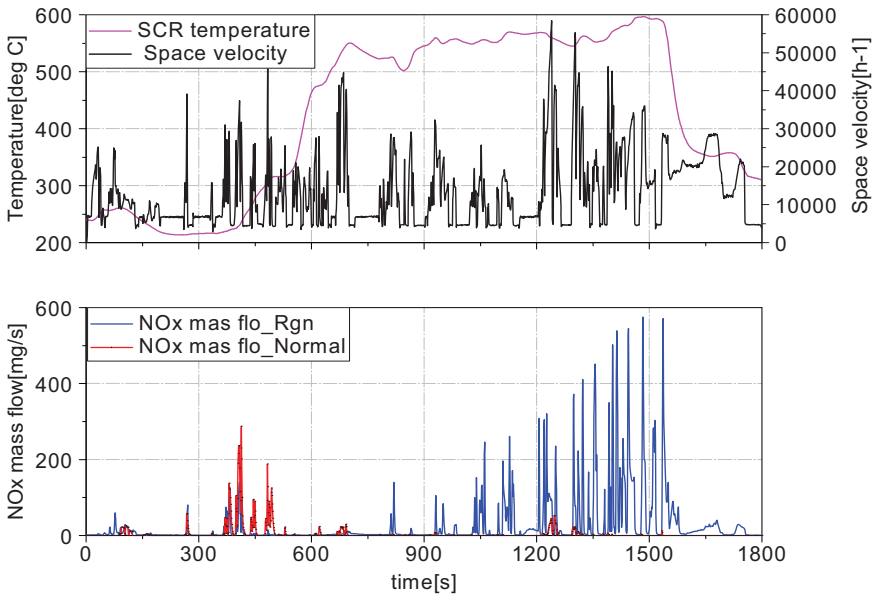

FIGURE 5
NO_x emission of DPF active regeneration

The urea injection consisted of two parts: feed-forward and ammonia storage deviation correction. The engine speed was positively correlated with the NO_x that was generated by combustion in the cylinder. As can be seen from Figure 4, the urea injection amount was positively correlated with the engine speed. When the engine was at idle speed, the urea injection amount was very small. When the engine speed was high, the urea injection was also large. When the set value of ammonia storage decreased rapidly due to the rapid rise of the SCR temperature, the urea injection corrected by the ammonia storage deviation was negative, resulting in less or no urea injection. The urea injection was very small from 400 s to 700 s. When the SCR temperature decreased rapidly from 1,500 s to 1,700 s, the set value of ammonia storage increased rapidly, and the urea injection corrected by the ammonia storage deviation was positive, resulting in excessive urea injection.

Influence of the DPF active regeneration on the tail exhaust NO_x. The tail exhaust NO_x was mainly related to the conversion efficiency of the SCR and NO_x emitted by the engine. At the appropriate temperature, the Cu-based SCR had high NO_x conversion efficiency. As shown in Figure 5, the DPF active regeneration caused the exhaust gas temperature to rise sharply. When the temperature exceeded 500°C, it significantly affected the conversion efficiency of the SCR. In normal mode, near 400

s of the WHTC, when the SCR temperatures were low, the tail exhaust NO_x reached the peak value of 290 ppm. Under other working conditions, the tail exhaust NO_x was relatively small, and the tail exhaust emission result was 0.12 g/kw·h. The calculation formula is as Eq 1 and Eq 2.

$$dm_{NOx}(mg/s) = NOx_{ppm} * dm_{EG}(kg/h) * \frac{NOx_{mol}}{EG_{mol}} * \frac{1}{3.6} * \frac{10^3}{10^6} \quad , \quad (1)$$

$$SE_{NO_x} = \frac{\int dm_{NO_x}}{CW_{Engine}} , \quad (2)$$

Where dm_{NOx} is the mass flow of the NO_x, $NO_{x\text{-}ppm}$ is the volume concentration of the NO_x, dm_{EG} is the mass flow of the exhaust gas, EG_{mol} is the molecular weight of the exhaust gas, $NO_{x\text{-}mol}$ is the molecular weight of the NO_x, SE_{NOx} is the specific emission, and CW_{Engine} is the engine cycle work.

It can be seen from Figure 5 that under the WHTC in the DPF active regeneration mode, a large amount of NO_x escaped from 1,000 s to 1,500 s, especially when the SCR temperature exceeded 550°C, and the escaped NO_x increased significantly and reached its peak value of 570 ppm. When the temperature was too high, the tail exhaust NO_x was positively correlated with the space velocity, and the NO_x emission value of the WHTC was 0.65 g/kw·h.

Influence of the DPF active regeneration on the NH_3 leakage. Ammonia is an environmentally unfriendly gas. The Euro VI regulations not only impose strict restrictions on NO_x tail emissions but also on NH_3. When the SCR conversion efficiency was reduced or the ammonia storage capacity was weakened, some ammonia leaked and escaped. The ammonia storage capacity was inversely related to the SCR temperature; that is, when the SCR temperature was low, the ammonia storage capacity was stronger. When a rapid temperature rise occurred, the ammonia storage capacity decreased rapidly, resulting in ammonia leakage due to the saturation of the ammonia storage in the SCR.

It can be seen from Figure 6 that under the WHTC in the DPF active regeneration mode, the SCR temperature rose sharply from 225°C to 550°C from 400 seconds to 700 seconds. At that time, there was a large amount of ammonia leakage, and its peak reached 400 ppm, resulting in an average ammonia leakage of 10.7 ppm. The leaked ammonia concentration was positively related to the space velocity. The calculation formula of the average ammonia leakage is shown in Formula (3). Under the WHTC in normal mode, the SCR temperature did not change dramatically, and the average ammonia leakage was 0.6 ppm.

$$NH_{3-Aver\_ppm} = \frac{\int NH_{3\_ppm}}{1800} \quad (3)$$

Where $NH_{3\_Aver\_ppm}$ is the average value of the ammonia leakage and NH_3 is ammonia leakage within 1800 seconds under the WHTC.

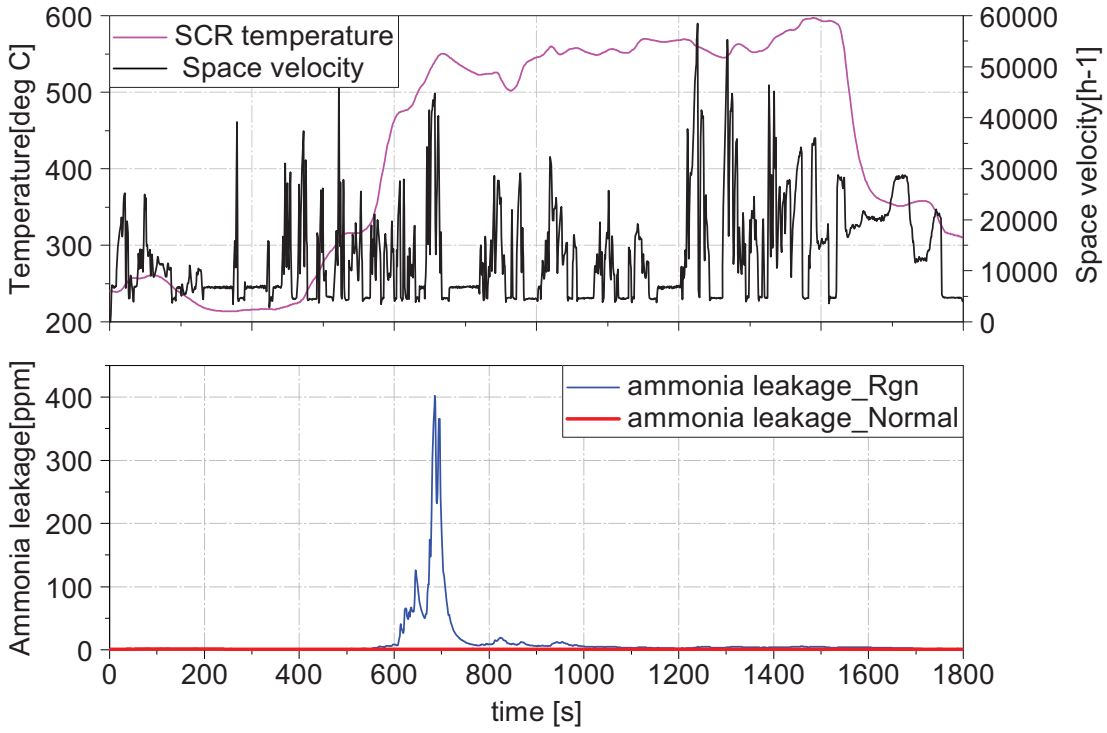

FIGURE 6
Ammonia leakage of DPF active regeneration

CONCLUSIONS

In this research, a quantitative analysis of the SCR temperature, ammonia storage, urea injection, tail exhaust NO_x, and ammonia leakage in the DPF active regeneration mode under the WHTC was performed. This research provided data support for the difficulties faced by SCR size design and tail exhaust NO_x control. The specific conclusions follow.

(1) The DPF active regeneration had a great influence on the temperature of the SCR, and the average temperature of the SCR increased from 245°C to 502°C.

(2) During the rapid rise of the SCR temperature, the dynamic follow-up between the set value and the actual value of the ammonia storage was poor.

(3) During the rapid rise of the SCR temperature, there was almost no urea injection. When the temperature dropped rapidly, the urea injection volume was large.

(4) The DPF active regeneration had a great impact on the tail exhaust NO_x. Under the hot start WHTC, the tail exhaust NO_x increased from 0.12 g/kw·h to 0.65 g/kw·h. When the temperature exceeded 550°C, the SCR conversion efficiency decreased further. At such a high temperature, the SCR was more sensitive to the space velocity than to the temperature.

(5) The SCR temperature rose rapidly, and even if urea was not injected, ammonia leakage could easily be caused, and the leaked ammonia concentration was positively correlated with the space velocity.

ACKNOWLEDGEMENTS

This work was supported by the Natural Science Foundation Project of Shandong Provincial (Grant No.ZR2019MEE041), and the open funds of National Engineering Laboratory of Mobile Source Emission Control Technology (Grant No.NELMS2019A01). The authors would like to thank the reviews whose constructive and detailed critique contributed to the quality of this paper.

REFERENCES

[1] Fickel, D.W., D'Addio, E., Lauterbach, J.A., Lobo, R.F. (2011) The ammonia selective catalytic reduction activity of copper-exchanged small-pore zeolites. Applied Catalysis B: Environmental. 102(3/4), 441-448.

[2] Sultana, A., Nanba, T., Haneda, M., Sasaki, M., Hamada, H. (2010) Influence of co-cations on the formation of Cu + species in Cu/ZSM-5 and its effect on selective catalytic reduction of NOx with NH3. Applied Catalysis B-Environmental. 101 (1-2), 61-67.

[3] Baik, J.H., Yim, S.D., Nam, I.S., Mok, Y.S., Lee, J.H., Cho, B.K., Oh, S.H. (2004) Control of NOxemissions from diesel engine by selective catalytic reduction (SCR) with urea.Topics in Catalysis.30 (1-4), 37-41.

[4] Andonova, S., Vovk, E., Sjöblom, J., Ozensoy, E., Olsson, L. (2014) Chemical deactivation by phosphorous under lean hydrothermal conditions over Cu/BEA NH3-SCR catalysts. Applied Catalysis B-Environmental. 147 (5), 251-263.

[5] Yamada, H., Inomata, S., Tanimoto, H. (2017) Mechanisms of Increased Particle and VOC Emissions during DPF Active Regeneration and Practical Emissions Considering Regeneration. Environmental Science & Technology. 51, 2914−2923.

[6] Yoon, S., Quiros, D.C., Dwyer, H.A., Collins, J.F., Burnitzki, M., Chernich, D., Herner, J.D. (2015) Characteristics of particle number and mass emissions during heavy-duty diesel truck parked active DPF regeneration in an ambient air dilution tunnel. Atmospheric Environment .122, 58-64.

[7] Qian, F., Xue, C.X., Xu, X., Ma, D., Li, P., Zhu, N. (2020) VOCs Emission Characteristics of DPF Regeneration in National VI Diesel Engine. Environmental Science. 41(2),674-681.

[8] Meng, Z., Chen, C., Qin, Y., Li, J., Du, Y., Jiang, Y. (2020) Experiment on Particulate Emissions During Diesel Particulate Filter Active Regeneration. Journal of Internal Combustion Engine. 38, 2.

[9] Quiros, D.C., Yoon, S., Dwyer, H.A., Collins, J.F., Zhu, Y., Huai, T. (2014) Measuring particulate matter emissions during parked active diesel particulate filter regeneration of heavy-duty diesel trucks. Journal of Aerosol Science. 73, 48-62.

[10] Meng, Z., Li, J., Qin, Y., Du, Y., Jiang, Y., Fang, J. (2019) Experimental on DPF Regeneration and Outlet Particle Concentration Emission. Journal of Internal Combustion Engine. 37, 4.

Received: **29.11.2021**
Accepted: **23.01.2022**

CORRESPONDING AUTHOR

Guoxiang Li
School of Energy and Power Engineering,
Shandong University,
Jinan 250061 – China

e-mail: liguox@sdu.edu.cn

© by PSP Volume 31– No. 05/2022 pages 5030-5037 Fresenius Environmental Bulletin

RESEARCH ON CASING FRACTURE DETECTION IN OIL DRILLING ENVIRONMENT BASED ON DEEP LEARNING METHOD

Hao Cui[1,2,*], Teng Fei[3]

[1]Department of Information Technology, Shandong Institute of Petroleum and Chemical Technology, Dongying 257000, China
[2]College of Computer Science and Technology, China University of Petroleum, Qingdao 266580, China
[3]Information and Service Center of Luming Oil & Gas Exploration & Development Co., Ltd., Shengli Oilfield, Dongying 257000, China

ABSTRACT

Drilling casing is an important device to ensure the safety of oil wells. Once a fracture problem occurs, it will directly affect oil extraction and transportation. To this end, a method of casing fracture detection in oil drilling environment based on deep learning is studied. The built-up crawling detection device is used to collect the casing sample image of the oil drilling environment, the sample image is grayed and denoised, and the convolutional neural network in deep learning is used to construct a fracture detection model to realize the casing fracture detection of the oil drilling environment. The results show that compared with the three detection methods of magnetic flux leakage method, ultrasonic detection method, and far-field eddy current method, different pipeline thickness, pipeline materials and pipeline smoothness conditions have little effect on the detection results. The detection accuracy of the method has been maintained above 90%, which proves the effectiveness and practicability of the method.

KEYWORDS:
Deep learning method, convolutional neural network, oil drilling environment casing, fracture detection

INTRODUCTION

Petroleum industry is an important part of a country's economic lifeline and an important pillar related to economic development. Oil is the main raw material for the production of fuel and gasoline. It is called "the blood of industry". Therefore, oil is one of the main energy resources. With the development of industry, the demand for oil is increasing year by year. Oil exploitation is an important project to meet the needs of. The casing in oil drilling environment can resist external forces and plays a key supporting role in oil exploitation. It is an important component to ensure the wellbore stability of oil and gas wells [1]. Due to pressure activities, it will cause borehole casing fracture and water bulging from the floor around the drilling site. Preventing casing fracture accident is not only a common well accident in drilling, but also a relatively difficult accident. If it is not handled properly, it is likely to lead to new accidents. Thus, casing fracture detection in oil drilling environment has important practical significance.

Casing fracture detection in oil drilling environment belongs to pipeline detection. Relevant experts have conducted relevant research on this kind of problem, and put forward many detection methods. There are three commonly used methods. The first method is magnetic flux leakage method, which carries out pipeline diagnosis through the change of magnetic field. When there are no defects, the magnetic lines of force are enclosed in the pipe wall and evenly distributed. When there is a defect problem, the magnetic field lines will be deformed, and some magnetic field lines will pass through the pipe wall to produce magnetic leakage, resulting in the fluctuation of the induced signal. Then, the existence of the problem can be judged by signal processing technology [2]. This kind of detection is applicable to the detection of material surface and near surface. When the pipe wall is too thick, the anti-interference ability becomes poor, the spatial resolution decreases and the detection error is large. The second ultrasonic testing method uses the characteristics that ultrasonic wave propagates at a uniform speed and can be partially reflected on the metal surface for pipeline flaw detection. This method has the advantages of large penetration capacity and is not limited by the thickness of the pipe wall, but the pipe surface is required to be smooth, otherwise it is easy to produce chaotic reflected waves and difficult to apply [3]. The third far-field eddy current method is a method to detect pipeline damage by using low-frequency eddy current that can penetrate the metal pipe wall. This method has a good effect on the detection of internal and external pipe wall defects, with high sensitivity and accuracy, with an accuracy of 2%-5%, but it is difficult to judge the type, shape and size of defects. There are many interference factors and special signal processing technology is required. In addition, it is only applicable to the detection of metal surface and near surface defects [4].

The problems of the mentioned three detection

methods are summarized, and a detection method based on deep learning is proposed to detect casing fracture in oil drilling environment. The research is carried out in the form of examples. Firstly, the object to be tested, that is, the casing sample of oil drilling environment, is selected, and then the in-depth learning testing methods and main equipment are introduced. Finally, the conclusion is discussed and the performance of the testing method is analyzed. The research is expected to provide reference and suggestions for casing fracture detection in drilling process.

MATERIALS AND METHODS

Materials. With the increase of well depth, the required mud density will increase, and the upper and lower layers will be in danger of pressure leakage. The role of casing is to prevent the pressure leakage of the upper formation when drilling the lower formation, which is to fix the wellbore, so as to ensure the progress of drilling process and the normal operation of the whole oil well after well completion [8].

Summarizing the previous research methods, there are three factors affecting the performance of detection methods, which consists of pipe thickness, pipe surface smoothness and pipe material. Therefore, taking these three factors as conditions, select the samples to be studied, as shown in Table 1.

Detection device. The equipment used in casing fracture detection consists of crawling structure, camera, image acquisition card, stepping motor, LED light source, central microcontroller and computer.

(1) Crawling structure. Crawling structure, also known as pipeline crawler, is mainly used for defect inspection and repair of natural gas pipeline, oil pipeline, urban water supply and drainage pipeline, tap water pipeline and other pipelines. At present, the crawling mechanism is divided into wheel crawling, crawler crawling, spiral crawling and creeping crawling according to different crawling modes [6]. Among them, the wheeled crawling mechanism is the most commonly used. The advantage of this form of crawling mechanism is that it can meet the requirements of stable speed during image acquisition, and the wheeled walking can be more suitable when the change range of pipe diameter is large. The wheel crawling mechanism selected in the study is DNC100 wheel crawler.

The features of the equipment are shown as:

1) The body meets the IP68 waterproof standard and can work under water for 10 meters.

2) Two high-resolution color cameras are installed at the front and rear respectively. The front camera can observe 360 °, auto focus and 100 times zoom system. The rear camera automatically opens when reversing and it is equipped with auxiliary lighting system.

3) Equipped with anti fog lens and laser ruler to make the image clearer and interpretation more accurate. Double motor drive is adopted, which can turn flexibly from front to back, left to right.

4) Mobile manipulator, flexible operation, can easily grasp all kinds of irregular foreign bodies.

5) The unique rear-view reversing system can prevent the vehicle from tipping and other dangers during reversing.

6) Independent high-power LED auxiliary lighting system can make the crawler obtain video effect in a large space.

7) The unique level sensor timely reminds the operator of the vehicle balance to prevent the crawler from tipping.

8) High strength fixing device for preventing vehicle body from slipping.

9) 12 inch large LCD.

10) The host controller using Windows XP operating system integrates functions such as photographing, video recording, Chinese character embedding, digital modeling, body pressure monitoring, body balance monitoring.

11) Equipped with portable remote control, the operation is more convenient.

12) The on-site take-up car is equipped with 100 m (or 120 m) high-strength detection line, brake and automatic wire arrangement device.

13) Equipped with 20 AH super large capacity field mobile power supply, the crawler can be used normally in any occasion. Field assembly is simple and easy to operate [7].

TABLE 1
Sample Selection of Casing in Oil Drilling Environment

Pipe thickness/ mm	Number/ group	fracture problem	pipeline material	Number/group	fracture problem	smoothness	Number/group	fracture problem
5.59	1	Yes	N80 casing	1	no	smooth surface	1	Yes
6.43	1	Yes	3Cr casing	1	Yes	Non-smooth surfaces	1	Yes
7.52	1	Yes	90SS casing	1	No	——	——	——
9.19	1	No	p110 casing	1	Yes	——	——	——
11.1	1	Yes	c90 casing	1	Yes	——	——	——

TABLE 2
DNC100 Technical parameters of wheeled crawlers

Qualification	Parameter	Qualification	Parameter
Applicable diameter	Φ323~Φ1200	Turning radius	≤6D
Positioning accuracy (mm)	±3	Climbing speed (m/min)	10~15
Crawling distance (m)	>1000	Radiation angle	360°×25°
Maximum gradeability	0°~36°	——	——

TABLE 3
Technical indicators for stepper motors

Qualification	Parameter	Qualification	Parameter
Step angle	1.8°±5%	Maximum axial force	60N
Number of phases	2	Rated current	4.3A
Moment of inertia	6000 （g.cm2）	Phase resistance	1Ω
Resistance accuracy	±（10%-15%）	Ambient temperature	-20℃~+50℃
Inductance accuracy	±20%	Environment humidity	90%Max
Maximum radial force	220N	——	——

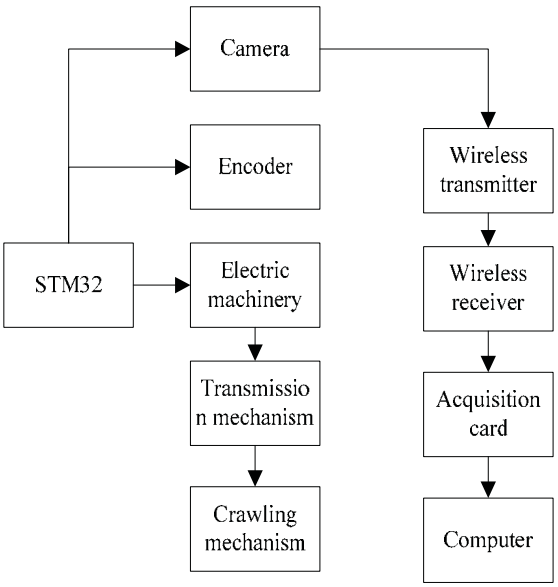

FIGURE 1
Structure diagram of casing fracture detection device.

The specific technical parameter settings of the equipment are shown in Table 2.

(2) Stepper motor. Stepping motor is an open-loop control motor that converts electric pulse signal into angular displacement or linear displacement. It is the main component to control the operation of crawling mechanism system [8]. When there is no overload, the speed and stop position of the motor only depend on the frequency and number of pulses of the pulse signal, and are not affected by the change of load. When the stepping driver receives the pulse signal, it drives the stepping motor to rotate in the set direction, that is, the so-called "step angle", which rotates step by step at a fixed angle. The angular displacement can be controlled by controlling the number of pulses, so as to realize accurate positioning. Controlling the frequency of pulse can control the speed and acceleration of motor rotation, so as to realize speed regulation. The stepping motor in the fracture detection system is a 60 HD stepping motor. The technical indexes of the stepping motor are shown in Table 3.

(3) Central microcontroller. The central microcontroller is the core control element of the whole device, which is mainly used to regulate the operation of the equipment [9]. The central microcontroller in the detection device is STM32 F100, which has an ARM Cortex M3 core with an operating frequency of up to 24 MHz, high processing performance and 16 bit timers, including motor control timers and a high speed 12 bit ADC with conversion time of 1.2 μs for efficient industrial control applications.

A set of casing fracture detection device for oil drilling environment is composed of the equipment, as shown in Figure 1.

Deep learning detection method. Casing fracture detection method is not only the core of research, but also the focus of research. The detection method in this chapter mainly constructs the detection model based on the deep learning algorithm. Deep learning is an important branch of machine learning. It refers to the neural network built by imitating the mechanism of human brain, which can learn, analyze and solve problems. It is the development and deepening of basic neural network. Therefore, deep learning and neural network have some similarities and differences. The same thing is that the optimal learning model is obtained through training parameters. The difference is that there are more hidden layers in deep learning. Therefore, the advantage of deep learning is that there is no need to manually select features, train weights, get sample images, and directly input them into the learning model to get the detection results [10].

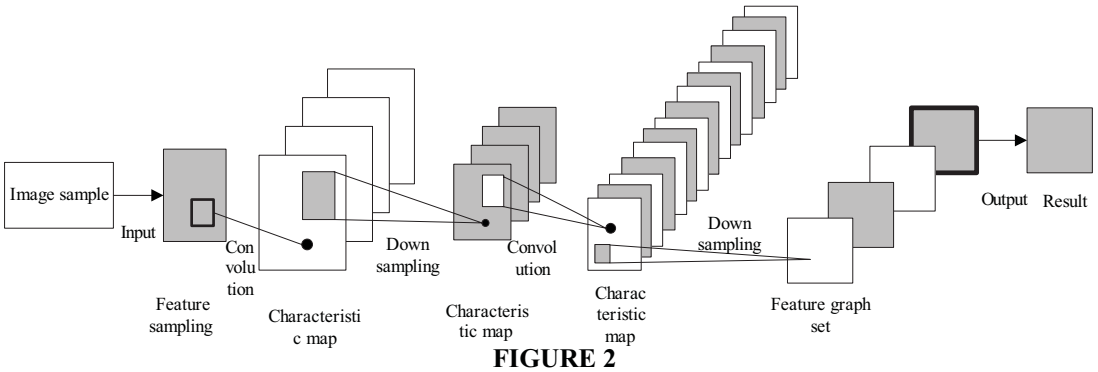

FIGURE 2
Structure of convolutional neural network.

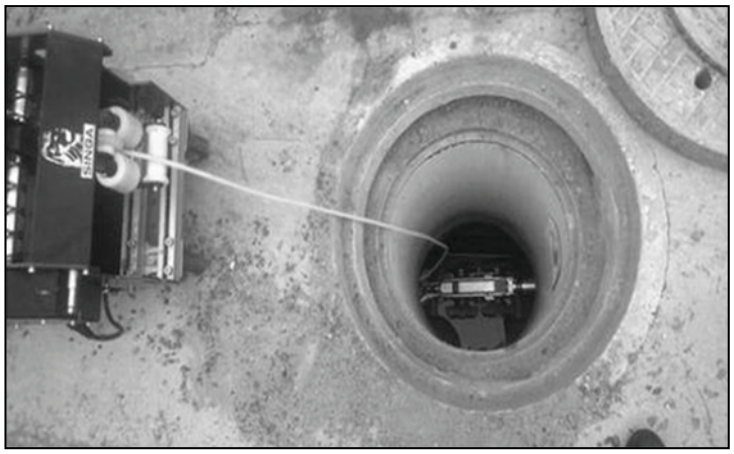

FIGURE 3
Sample collection of casing fracture.

At present, there are many kinds of deep learning models, such as convolutional neural network, deep confidence network, cyclic neural network, recursive neural network, Boltzmann machine and restricted Boltzmann machine. In this chapter, the convolutional neural network is selected to build the detection model [11].

Convolutional neural network is a feedforward neural network proposed by Hinton, which mainly includes input layer, convolution layer, lower sampling layer and full connection layer, which is shown in Figure 2 [12].

The working principle of convolution neural network was shown. Firstly, the sample image is input from the input layer into the convolution neural network structure, then the convolution layer is used for convolution, that is, weighted summation, and then after down sampling, the above convolution and down sampling operations are repeated repeatedly to extract the image sample features and reduce the image dimension. Finally, the extracted image features are input into the full connection layer to connect all features. The first stage of the convolutional neural network in the process is the forward propagation stage [13]. At this stage, similar to the basic neural network, it is necessary to judge whether the error between the actual output and the expected output is less than the set threshold. If it is less than the threshold, it proves that the training of convolutional neural network has been completed. If it is greater than the threshold, it will enter the second stage, namely the back propagation stage [14].

In the second stage, the error is input from the last layer of convolutional neural network, back propagated, and the weight of each layer is continuously adjusted until the requirements are met [15].

The basic flow of casing fracture detection based on convolutional neural network is shown as:

(1) Image sample acquisition of casing fracture. The built detection device is used to collect the image samples of casing fracture, and the acquisition diagram is shown in Figure 3.

In the process of image acquisition, the points should be noted:

1) The relevant parameters of the testing device shall be adjusted before testing.

2) The moving direction of the detection device shall be consistent with the oil transmission direction as far as possible.

3) In the process of image sample shooting, it is necessary to maintain slow and uniform operation, and the camera needs to remain relatively stationary all the time [16].

4) When the diameter is less than or equal to 200 mm, the speed of the crawler shall be less than 0.1 m/s. When it is greater than 200 mm, the speed of the crawler shall be less than 0.15 m/s [17].

TABLE 4
Image grayscale

Method	Definition	Principle formula
Component method	Use the pixel values of the three components (R, G, B) in the original image as the gray values of the three gray images	$\begin{cases} \text{Gray1}(i,j) = R(i,j) \\ \text{Gray2}(i,j) = G(i,j) \\ \text{Gray3}(i,j) = B(i,j) \end{cases}$ (1)
Maximum value method	Select the maximum value of the three-component pixel value in the original image as the gray value of the gray image	$\text{Gray}(i,j) = \max\left[R(i,j), G(i,j), B(i,j)\right]$ (2)
Average method	Calculate the average of the sum of the three-component pixel values in the original image, and use this as the gray value of the gray image	$\text{Gray}(i,j) = \frac{\left[R(i,j)+G(i,j)+B(i,j)\right]}{3}$ (3)
Weighted average method	According to the weight ratio, the pixel values of the three components (R, G, B) in the original image are multiplied, and then added, as the gray value of the gray image.	$\text{Gray}(i,j) = 0.299R(i,j) + 0.578G(i,j) + 0.114B(i,j)$ (4)
Annotation	R, G, B correspond to the three primary colors of red, green and blue respectively, $R(i,j)$, $G(i,j)$, $B(i,j)$ are the pixel values of the color image at point (i,j) respectively.	

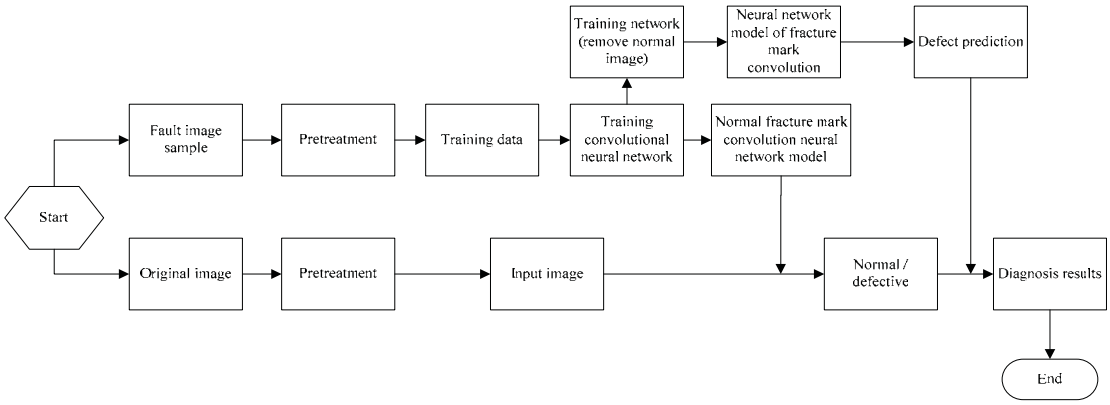

FIGURE 4
Fault Defects of Casing in Oil Drilling Environment.

(2) Image sample preprocessing. Although the collected image samples do not need image feature extraction, they need image preprocessing, including image graying and image denoising [18].

Image graying refers to converting a color image into a grayscale image. The specific method is shown in Table 4.

In the process of sample image acquisition, affected by various factors, the collected image quality is not good and is polluted by noise, so denoising is required [19]. Here, the mean filtering method is introduced. The specific process of mean filter denoising is shown:

Step 1: a template to the target pixel on the image should be given, that is, the filter template.

Step 2: Obtain all pixels of the current filter template.

Step 3: Calculate the sum of all pixels in the current filter template.

Step 4: Divide the result of step 3 by the total number of current filter template data to obtain the average value of all pixels.

Step 5: Replace the original pixel value with the average value of all pixels in the template.

Step 6: Slide the template and re assign the value to the currently traversed pixel until the entire image is traversed [20-21].

(3) Detection of casing fracture defects by convolution neural network detection model

The detection process of casing fracture defects based on convolution neural network detection model is shown in Figure 4.

TABLE 5
Analysis of overall test results

Working conditions 1			Working conditions 2			Working conditions 3		
Thick-ness/ mm	Facture problem	Results	Material	Fracture problem	Results	Smoothness	Fracture problem	Results
5.59	Yes	Existing problem	N80 casing	No	No	Smooth sur-face	Yes	Existing problem
6.43	Yes	Existing problem	3Cr cas-ing	Yes	Existing problem	Non-smooth surfaces	Yes	Existing problem
7.52	Yes	Existing problem	90SS casing	No	No	——	——	——
9.19	No	1	p110 casing	Yes	Existing problem	——	——	——
11.1	Yes	Existing problem	c90 cas-ing	Yes	Existing problem	——	——	——

TABLE 6
Analysis of Method Accuracy under Different Pipe Thickness (Unit: %)

Conditions		The proposed method	Magnetic Leakage Method	Ultrasonic testing	Far Field Eddy Method
Pipe thickness/ mm	5.59	95.32	90.255	93.58	90.56
	6.43	94.45	86.50	94.25	88.25
	7.52	96.55	84.02	93.22	87.69
	9.19	95.50	80.26	93.14	89.52
	11.1	95.47	77.30	92.25	88.50
Pipeline mate-rial	N80 casing	96.36	90.25	92.15	92.25
	3Cr casing	96.20	88.21	83.15	93.14
	90SS casing	96.54	91.36	90.20	85.98
	p110 casing	95.26	85.20	87.28	92.36
	c90 casing	96.30	87.66	90.63	80.47
Pipeline smoothness	Smooth surface	95.65	90.23	96.25	86.25
	Non-smooth surfaces	94.27	89.42	82.02	83.15

RESULTS AND DISCUSSIONS

Analysis of casing fracture detection results. The method based on deep learning is used to detect the casing fracture fault. The detection results are consistent with the actual situation of samples, which generally proves the effectiveness and feasibility of this method (Table 5). However, due to the small sample data, it can not strongly prove the detection accuracy of this method, so it needs to be further analyzed and studied.

Accuracy analysis of test results under different working conditions. In order to further prove the effectiveness of the proposed method, 470 groups of casing image samples are collected under each working condition, of which 20 groups of oil casing samples are interference samples for method accuracy test. There are three detection and comparison methods, which consists of magnetic flux leakage method, ultrasonic detection method and far-field eddy current method (Table 6).

It can be seen from Table 6 that although the working conditions are different, they have little impact on the casing fracture detection method in oil drilling environment based on in-depth learning, and the accuracy of the detection results has been maintained at more than 90%, while the three detection methods are affected by the working conditions to a certain extent [22]. As a result, the detection accuracy fluctuates greatly, which proves that the detection performance of this method is better than that of magnetic flux leakage method, ultrasonic detection method and far-field eddy current method.

CONCLUSIONS

To sum up, with the development of industry, the demand for oil resources is increasing. The environmental casing of oil drilling plays an important supporting role to ensure the safety of oil wells in the oil exploitation. Thus, the research on casing fracture detection is carried out, hoping to contribute to the continuous development of oil drilling industry. After research, the results are obtained.

(1) The proposed method can accurately detect

casing fracture, which proves the effectiveness and practical value of the method research.

(2) Compared with magnetic flux leakage method, ultrasonic testing method and far-field eddy current method, different working conditions have little impact on the detection accuracy of casing fracture detection method, and the accuracy is always maintained at more than 90%.

Although this study has made some achievements, there are also some problems, such as insufficient training sample size, limited defect classification and no quantification, which need to be further studied and analyzed.

ACKNOWLEDGEMENTS

This work was supported in part by Dongying Key Laboratory of Intelligent Information Processing.

REFERENCES

[1] Tom, Y., Devamanyu, H., Soujanya, P., Laboratories, T., Cambria, E. (2018) Recent Trends in Deep Learning Based Natural Language Processing. IEEE Computational Intelligence Magazine. 13(3), 55-75.

[2] Xu, Y., Wu, L., Xie, Z., Chen, Z.（2018） Building Extraction in Very High Resolution Remote Sensing Imagery Using Deep Learning and Guided Filters. Remote Sensing. 10(1), 144.

[3] Luo, B., Wang, H., Liu, H., Li, B., Peng, F. (2018) Early Fault Detection of Machine Tools Based on Deep Learning and Dynamic Identification. IEEE Transactions on Industrial Electronics. 66(1), 509-518.

[4] Jiang, Q., Yan, X., Huang, B. (2020) Deep Discriminative Representation Learning for Nonlinear Process Fault Detection. IEEE Transactions on Automation Science and Engineering. 17(3), 1410-1419.

[5] Li, Z., Gui, W., Zhu, J. (2019) Fault detection in flotation processes based on deep learning and support vector machine. Journal of Central South University. 26(9), 2504-2515.

[6] Yuan, Z., Huang, H., Jiang, Y., Tang, J., Li, J. (2019) An enhanced fault-detection method based on adaptive spectral decomposition and super-resolution deep learning. Interpretation. 7(3), 1-63.

[7] Zhao, H., Liu, H. (2018) Fault detection of wind turbine main bear based on deep learning network. Acta Energiae Solaris Sinica. 39(3), 588-595.

[8] Kalanidhi, K., Vinodkumar, D., Sridharan, P. (2019) Transmission power line fault detection based on deep leaning methods. Indian Journal of Power and River Valley Development. 69(3-4), 35-38.

[9] Ullah, I., Khan, R., Yang, F., Wuttisittikulkij, L. (2020) Deep Learning Image-Based Defect Detection in High Voltage Electrical Equipment. Energies. 13(2), 392.

[10] Iqbal, R., Maniak, T., Doctor, F., Karyotis, C. (2019) Fault Detection and Isolation in Industrial Processes Using Deep Learning Approaches. IEEE Transactions on Industrial Informatics. 15(5), 3077-3084.

[11] Chellamuthu, S., Sekaran, E. (2019) Fault detection in electrical equipment's images by using optimal features with deep learning classifier. Multimedia Tools and Applications. 78(19), 1-18.

[12] Zhang, L., Lin, J., Liu, B., Zhang, Z., Wei, M. (2019) A Review on Deep Learning Applications in Prognostics and Health Management. IEEE Access. 7(1), 162415-162438.

[13] Xiao, L., Miao, H., Shi, T., Hong, Y. (2020) LSTM-based deep learning for spatial–temporal software testing. Distributed and Parallel Databases. 38(3), 687-712.

[14] Hamadache, M., Jung, J., Park, J., Youn, B. (2019) A comprehensive review of artificial intelligence-based approaches for rolling element bearing PHM: shallow and deep learning. JMST Advances. 1(1), 125-151.

[15] Afrasiabi, S., Afrasiabi, M., Parang, B., Mohammadi, M. (2020) Integration of Accelerated Deep Neural Network Into Power Transformer Differential Protection. IEEE Transactions on Industrial Informatics. 16(2), 865-876.

[16] Liu, D., Deng, H., Zhang, Y. (2020) Research on the Wellbore Instability Mechanism of Air Drilling Technology in Conglomerate Formation. Fresen. Environ. Bull. 29(01), 600-606.

[17] Xu, G., Liu, M., Jiang, Z., Shen, W., Huang, C. (2020) Online Fault Diagnosis Method Based on Transfer Convolutional Neural Networks. IEEE Transactions on Instrumentation and Measurement. 69(2), 509-520.

[18] He, M., He, D. (2018) Simultaneous bearing fault diagnosis and severity detection using a LAMSTAR network-based approach. IET Science, Measurement & Technology. 12(7), 893-901.

[19] Li, L., Liu, G., Zhang, L., Li, Q. (2018) Deep learning-based sensor fault detection using S-Long Short Term Memory Networks. Structural Monitoring and Maintenance. 5(1), 51-65.

[20] Iyobosa, E., Fang, Z., Jun, N., Shang, J., Gang, M. (2021) Development of a robust bacterial consortium for petroleum hydrocarbon degradation. Fresen. Environ. Bull. 30(3), 2356-2367.

[21] Cheng, F., Wang, J., Qu, L., Qiao, W. (2018) Rotor-Current-Based Fault Diagnosis for DFIG Wind Turbine Drivetrain Gearboxes Using Frequency Analysis and a Deep Classifier. IEEE Transactions on Industry Applications. 54(2), 1062-1071.
[22] Mao, W., Chen, J., Liang, X., Zhang, X. (2020) A New Online Detection Approach for Rolling Bearing Incipient Fault via Self-Adaptive Deep Feature Matching. IEEE Transactions on Instrumentation and Measurement. 69(2), 443-456.

Received: **29.11.2021**
Accepted: **23.01.2022**

CORRESPONDING AUTHOR

Hao Cui
Department of Information Technology,
Shandong Institute of Petroleum and Chemical Technology,
Dongying 257000 – China

e-mail: 54037065@qq.com

© by PSP Volume 31– No. 05/2022 pages 5038-5047 Fresenius Environmental Bulletin

GEOLOGICAL CHARACTERISTICS OF WUFENG FORMATION AND LONGMAXI FORMATION IN BLOCK X OF CHANGNING SHALE GAS FIELD IN SOUTHERN SICHUAN CHINA

Yi Bai[1], Ying Guo[2,*], Jianning Liu[3], Xuan Deng[4], Yawei Liu[5], Wengang Ding[1]

[1]School of Geosciences, Yangtze University, Wuhan 430100, China
[2]CNOOC China Limited, Tianjin Branch, Tianjin 300459, China
[3]GuiZhou Communications Polytechnic, Guiyang 550000, China
[4]Zhanjiang Branch of China National off shore Oil Company Ltd., Zhanjiang 524057, China
[5]Drilling and Workover Engineering Operation Department of Downhole Services Company, Bohai Drilling Engineering Co., Ltd., CNPC, Cangzhou 062550, China

ABSTRACT

As a new clean natural gas energy, the exploration and development of shale gas resources has attracted worldwide attention. It is necessary to conduct in-depth study of the pilot demonstration area, analysis the geological characteristics of shale gas, and explore the main control factors in the process of accumulation. By taking the Block X of Changning shale gas field, Southern Sichuan, as the targeted area, we systematically evaluated the reservoir characteristics of Upper Ordovician Wufeng Formation-Lower Silurian Longmaxi Formation, based on the field outcrop sections, drilling coring and geophysical data. The results showed that the overall structure of the study area is well maintained, and the main production intervals of shale gas are located in the Wufeng Formation and Long-1 submember. Shale gas is mainly enriched in the middle and lower parts of Sq2. The content of brittle minerals (quartz + feldspar + calcite + dolomite) in shale gas production interval is high, with an average of 51.6%, and the fracturing ability is good. The reservoir space is dominated by inorganic pores, followed by organic pores, and the pore size is mostly between tens of nanometers and 200 nanometers. The physical property is good, and the average porosity is 4.58%.Overall, the physical properties of shale gas in Changning area are low porosity and low permeability.

KEYWORDS:
Geological characteristics, shale gas field, formation, sedimentary facies, reservoir

INTRODUCTION

With the growth of national economy and the improvement of people's living standards, the demand for clean energy increased rapidly. The contradiction between supply and demand has become increasingly prominent in recent years [1, 2]. Shale gas resources as a new clean natural gas energy, its exploration and development has attracted worldwide attention. Worldwide, the global shale accounts for about 60% of the total amount of sedimentary rocks. Among them, shale gas resources are very rich, with total resources of about 455.7×10^{12} m^3 and recoverable resources of 187×10^{12} m^3, which are roughly equivalent to conventional natural gas. They are mainly distributed in more than 40 countries and regions, including China, the United States, Argentina, Mexico, South Africa, Australia and others. Among them, shale gas resources in central Asia and China are nearly 100×10^{12} m^3 [3-5]. Therefore, shale gas is a very important unconventional natural gas resource in the world, and it is one of the main fields in the future for natural gas production and storage in countries and related regions [6-9].

According to the exploration and development process and symbolic results, it can be roughly divided into three stages: (1) shale gas geological conditions research, dessert area optimization and evaluation well drilling, preliminary exploration and development preparation stage. (2) Marine shale gas industrial exploitation test, marine-continental transition phase and continental shale gas exploration evaluation stage. (3) Marine shale gas large-scale exploitation, marine-continental transition phase-continental industrial exploitation test stage [10, 11]. To dates, the exploration and development of shale gas abroad has been carried out for nearly 200 years. In 1821, the world's first shale gas well was born in the Devonian system of the Appalachian basin in the eastern United States. Until the late 1970s, it entered commercial exploration and development [12, 13]. There are mainly five basins in the United States that focus on commercial exploitation of shale gas, namely, Ohio shale in Appalachian basin, Antrim shale in Michigan basin, Barnett shale in Fort worth basin, Lewis shale in San Juan basin and NewAlbany

shale in Illinois basin [14-17]. With the emergence of hydraulic fracturing stimulation technology, multiple fracturing stimulation technology, horizontal drilling technology and horizontal staged fracturing technology, shale gas production in the United States has increased rapidly from $1,800 \times 10^8$ m^3 to $4,620 \times 10^8$ m^3 [18-21]. According to the existing research data, its recoverable resources amount to 36×10^{12} m^3, ranking first in the world, mainly distributed in Sichuan, Ordos, Bohai Bay, Songliao, Jianghan, Tuha and Junggar basins. From the existing exploration and research results, Sichuan basin is the most promising area for shale gas exploration and development in China. The shale gas resources in the Upper Ordovician Wufeng Formation-Lower Silurian Longmaxi Formation are 12.4×10^{12} m^3, and the shale gas resource of Qiongzhusi Formation of Lower Cambrian reaches 6.17×10^{12} m^3 [22,23]. At present, several national shale gas exploration and development pilot demonstration area have been established in Sichuan basin, including Fuling of Sinopec, and Changning, Weiyuan and Zhaotong of CNPC. By the end of 2019, the proven reserves are nearly 2×10^{12} m^3, and the main production layer is the Upper Ordovician Wufeng Formation-Lower Silurian Longmaxi Formation. Many parameters are considered in basic geology, reservoir forming conditions, geological evaluation, selection and exploration and development of shale gas. Those mainly include mineral composition, physical properties, rock mechanical properties, reservoir pressure, organic matter maturity, organic matter content, effective reservoir thickness, total gas content, surface preservation conditions, burial depth, etc. Although the parameters selected in different areas and different intervals are different, the overall difference is not significant [24-26].

Domestic and foreign scholars and related oil companies have made great progress in basic geological research of shale gas through continuous exploration. However, strictly speaking, the unconventional geological theory of shale gas geological characteristics are still in further exploration and have not yet formed a complete system. Therefore, in the early stage of shale gas exploration and development, it is necessary to conduct in-depth analysis of the pilot demonstration area, and explore the main control factors in the process of accumulation. In this paper, the geological characteristics of the shale gas layer of the Upper Ordovician Wufeng Formation-Lower Silurian Longmaxi Formation in the key well area of Changning shale gas field in southern Sichuan, are studied to explore the accumulation conditions of shale gas, and provide useful geological data for the exploration and development of shale gas in the later stage of the area.

MATERIALS AND METHODS

Geological conditions of the targeted area. In terms of tectonic position, Sichuan Basin is located on the northwest edge of the upper Yangtze plate. From the perspective of regional structure, the study area is located in the southern margin of the low-steep structural belt in southern Sichuan basin, adjacent to the Loushan fold belt on the southern side, and the specific structural position is located in the southwest wing of the Changning structure [27,28]. According to the relevant seismic interpretation results and drilling data, Southwest Oil and Gas Field Company compiled the seismic reflection structure map of the basal boundary of the Upper Ordovician Wufeng Formation in the study area. The main body of the study area is located in the syncline area between Junlian buried structure and Changning structure. The southeast is Jianwu syncline and the west is Luochang syncline. Combined with the characteristics of seismic data section and plane structure, there are three kinds of structures in the area vertically. The middle and upper Cambrian and above strata are dominated by caprock detachment structure. The caprock detachment fault is characterized by plastic shale in the middle and upper Cambrian strata as the detachment surface. The fault generally does not pass through the middle unconformity surface. The faults above the middle and upper Cambrian are not developed, and the structure is a simple syncline slope. The middle and lower Cambrian and below strata are dominated by basement-involved structures, and the basement-involved faults generally does not cross the middle unconformity surface. The basal boundary strata of the Upper Ordovician Wufeng Formation in the whole area show a syncline structure with low in the middle east and high around. However, due to the limitation of the scope, the trap cannot be closed in the area.

The strata in the study area are flat, large faults are not developed, the structure is simple, and the stratum structure is stable. According to the drilling, logging and field profile data, the middle and upper Ordovician and above strata in the study area are well developed [29]. The sandstone and mudstone of Jurassic Shaximiao Formation are exposed on the surface from top to bottom, which are middle Ordovician Baota Formation, upper Ordovician Linxiang-Wufeng Formation, lower Silurian Longmaxi Formation-Shiniulan Formation, upper Silurian Hanjiadian Formation, Permian Liangshan Formation-Qixia Formation-Maokou Formation-Longtan Formation-Changxing Formation, Triassic Feixianguan Formation-Jialingjiang Formation-Leikoupo Formation- Xujiahe Formation and Jurassic Ziliujing Formation-Lianggaoshan Formation and Shaximiao Formation, lacking Carboniferous and Devonian systems. The study stratum belongs to the Upper Ordovician Wufeng Formation-Lower Silurian Longmaxi Formation, which is the main stratum of

shale gas production in Changning gas field in southern Sichuan.

Methods. In this study, porosity is evaluated according to compensated acoustic wave, long distance acoustic wave, compensated neutron and bulk density density. Based on the QFM model, the porosity of gas shale can be calculated by converting the element content measured by ECS to the skeleton parameters. Micro-resistivity scanning imaging logging and nuclear magnetic resonance logging have good resolution ability for natural fractures, induced fractures and faults. Well temperature logging, isotope logging or cross dipole shear wave logging can be used to identify and evaluate the fracture height and length after fracturing. The evaluation steps of reservoir characteristics are as follows: (1) The shale gas reservoir rock-electricity evaluation relationship parameters are analyzed and established, and the logging calculation model of rock physical parameters is established. (2) The effective matching series of shale gas logging are selected to establish the logging response characteristics and identification and evaluation methods of sensitive geophysical parameters of gas shale. (3) The calculation model of reservoir characteristic parameters such as porosity, pore pressure and permeability of gas shale and the evaluation method of reservoir effectiveness are established [30, 31]. (4) The shale mud, sand content, clay mineral composition and content of brittle minerals (quartz, calcite, feldspar,etc.) are calculated.

RESULTS AND DISCUSSION

Sequence strata division and characteristics. According to the identification marks of sequence interfaces such as lithology, paleontology, sequence, contact relationship, organic matter content and geophysics, three main sequence interfaces and two maximum flooding surfaces can be identified in the Wufeng Formation-Long 1 member of the main shale gas producing interval in Changning area, southern Sichuan, which can be traced and compared in the region. The first sequence interface is the lithologic transition surface between the Upper Ordovician Wufeng Formation and the Linxiang Formation. There are obvious differences in lithology and electrical properties between the upper and lower strata of the interface. The second sequence interface belongs to the lithofacies transition surface between the Lower Silurian Longmaxi Formation and the Upper Ordovician Wufeng Formation.The third sequence interface is the sequence interface between the Lower Silurian Longmaxi Formation 1 member and Long-2 member, which belongs to the transition surface of a secondary (fourth-order) sea-level fluctuation, and belongs to the continuous sedimentary sequence interface. According to the above main interfaces, three medium-term grade IV cycle sequences and six short-term base level cycles can be identified in the Wufeng Formation-Longmaxi Formation 1 member in the study area.

Grade IV sequence-Sq1, corresponding to Wufeng Formation, is well developed in Changning area, with good lateral contrast, similar lithology and similar thickness.The highstand system tract is carbonaceous argillaceous bioclastic limestone or carbonaceous limestone mudstone in Guanyinqiao Member, with thickness ranging from 0.09 to 0.70 m. The Long-1 member contains two grade IV sequences-Sq2 and Sq3. Sq2 corresponds to Long-1 sub-member-Long-2 sub-member lower part of Longmaxi Formation. Horizontally, Sq2 has good contrast and similar lithology, which are mainly composed of carbonaceous graptolite shale containing bone needle radiolarian and carbonaceous silt shale. Sq3 corresponds to the middle and upper part of Long-1 sub-member of Longmaxi Formation. Horizontally, the contrast is good, the lower lithology is mainly carbonaceous shale, the upper is silty mudstone, the thickness is similar.

Vertical and horizontal distribution of sedimentary facies. Combined with the corresponding environmental conditions, the shelf facies of Wufeng Formation-Longmaxi Formation in Changning shale gas field is divided into two subfacies, deep shelf and shallow shelf, and a variety of microfacies. Based on the study of sedimentary facies types, according to the corresponding characteristics, the sedimentary facies of Wufeng Formation-Longmaxi Formation of the main single well in the area can be longitudinally analyzed and well-connected comparative study. It can be seen from the results that the middle and lower part of Wufeng Formation - Long-1 member of Longmaxi Formation in Changning shale gas field in southern Sichuan (mainly Long-1 sub-member) is composed of deep shelf subfacies, and the microfacies gradually change from organic-rich siliceous shelf microfacies → organic-rich mud shed microfacies → deep-water silty mud shelf from the bottom to the top, reflecting the process of gradual shallowing and increasing oxygen content in water. The color of the corresponding lithology gradually becomes lighter, the grain size becomes coarser, and the organic matter content decreases. The upper part of Long-1 member (mainly Long-2 sub-member) - Long-2 member is mainly composed of shallow shelf subfacies, and the microfacies change from shallow water silty shelf microfacies → muddy silty shelf microfacies → silty shelf microfacies from the bottom to the top, reflecting the process of gradual shallowing and increasing oxygen content in water. The color of the corresponding lithology gradually becomes lighter, the grain size becomes coarser, the argillaceous content decreases and the organic matter content decreases. Overall, the layer from bottom to top, water gradually shallow, water energy gradu-

ally strengthened, oxygen content gradually increased, organic matter content gradually decreased.

When the Changning shale gas field in southern Sichuan was deposited in the Wufeng Formation-Long-1 member of Longmaxi Formation, the sedimentary facies belts of the same period were completely consistent in most wells, and the distribution was stable, and there was no obvious change in the horizontal facies. This also shows that the shale gas production intervals in Changning shale gas field in southern Sichuan are very stable, and they are concentrated in organic rich siliceous shelf microfacies and organic rich mud shelf microfacies of deep-water shelf subfacies in the lower part of Wufeng Formation - Long-1 member of Longmaxi Formation.

Mineral composition. The mineral composition can be determined by means of thin section, scanning electron microscope, cathode ray and X-ray diffraction.The results of X-ray diffraction analysis show that the main mineral components of the shale gas interval (Wufeng Formation- Long-1 of Longmaxi Formation) in the study area are quartz, feldspar, calcite, dolomite, pyrite and clay. The clay minerals are mainly illite, illite/smectite mixed layer and chlorite. Combined with the observation of microscope and scanning electron microscope, quartz minerals mainly include terrigenous clastic quartz, chemically precipitated siliceous, authigenic quartz and biogenic silica, and biogenic silica content is higher in some layers. Feldspar includes orthoclase and plagioclase, mainly terrigenous, with a small amount of authigenic origin. Calcite is mainly composed of biological calcareous bones and mud-powder crystal formed by chemical precipitation. Dolomite is mostly metasomatic, often automorphic-semiautomorphic. Pyrite is the product of syngenetic and quasi syngenetic stage, with tuberculous and moldy globular structure, and a small amount distributed along fractures. The statistics results are shown in Figure 1, it can be seen that the content of brittle minerals (quartz + feldspar + calcite + dolomite) in shale gas intervals in the area ranges from 32.4% to 92.8%, with an average of 67.3% and a median of 66.8%, among which the content of siliceous (quartz + feldspar) ranges from 14.7% to 81.6%, with an average of 52.0% and a median of 51.6%. The content of calcareous (calcite + dolomite) ranges from 1.8% to 62.8%, with an average of 15.3% and a median of 12.5%. The clay content ranges from 4.6% to 58.1%, with an average of 30.5% and a median of 31.0%.

Types and characteristics of reservoir space. Shale reservoir is mainly composed of clastic particles, matrix, cement, organic matter, pore and water. The first four components constitute the shale skeleton, which can be divided into inorganic components and organic components according to composition. The former includes quartz, clay, feldspar, calcite, dolomite, pyrite and barite minerals, and the latter is mainly kerogen and residual organic matter. The remaining skeleton is removed from the pores and their free water, as shown in Figure 2. In order to make pore classification simple and practical, according to the classification scheme of pore genesis and occurrence.The organic pores, organic fractures, inorganic pores and inorganic fractures are the four basic pore types, and the four basic pore types can be subdivided into subgroups. Among them, organic pores are subdivided into two sub-categories: organic evolution pores (internal pores of organic matter) and organic intergranular pores. Organic fractures are divided into two sub-categories: organic fracture and organic grain edge fracture. Inorganic pores can be subdivided into two sub-categories: mineral intragranular pores and mineral intergranular pores. Inorganic fractures are divided into inorganic fracture and mineral grain edge fracture.

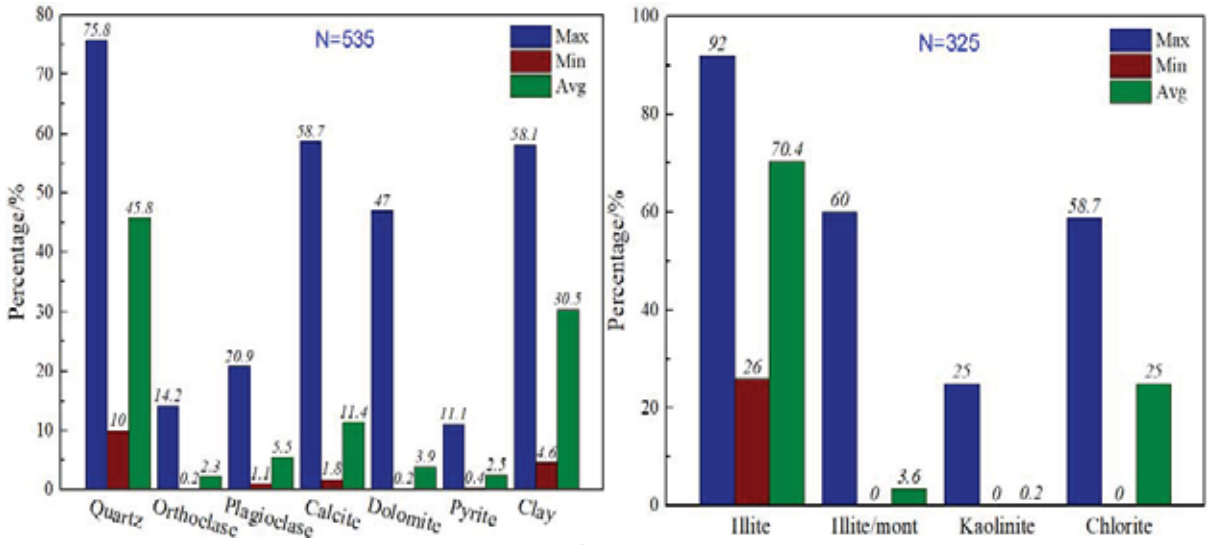

FIGURE 1
Mineral composition and of shale gas interval in study area

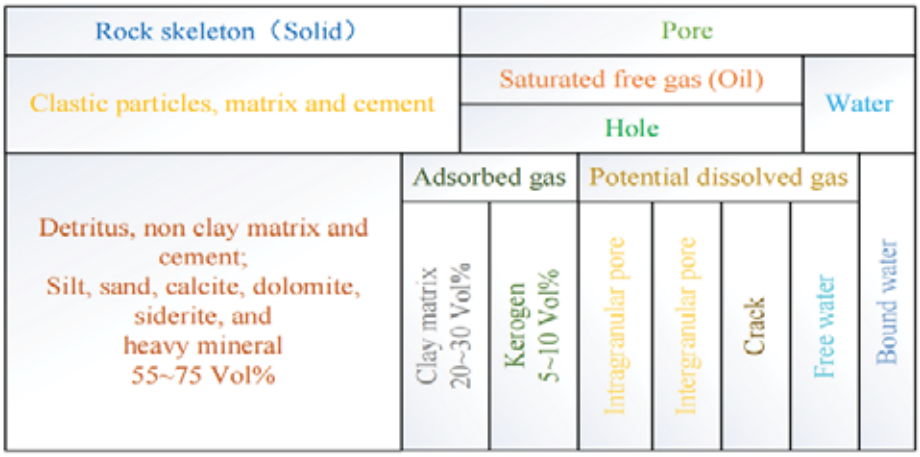

FIGURE 2
Conceptual model diagram of shale gas reservoir structure components

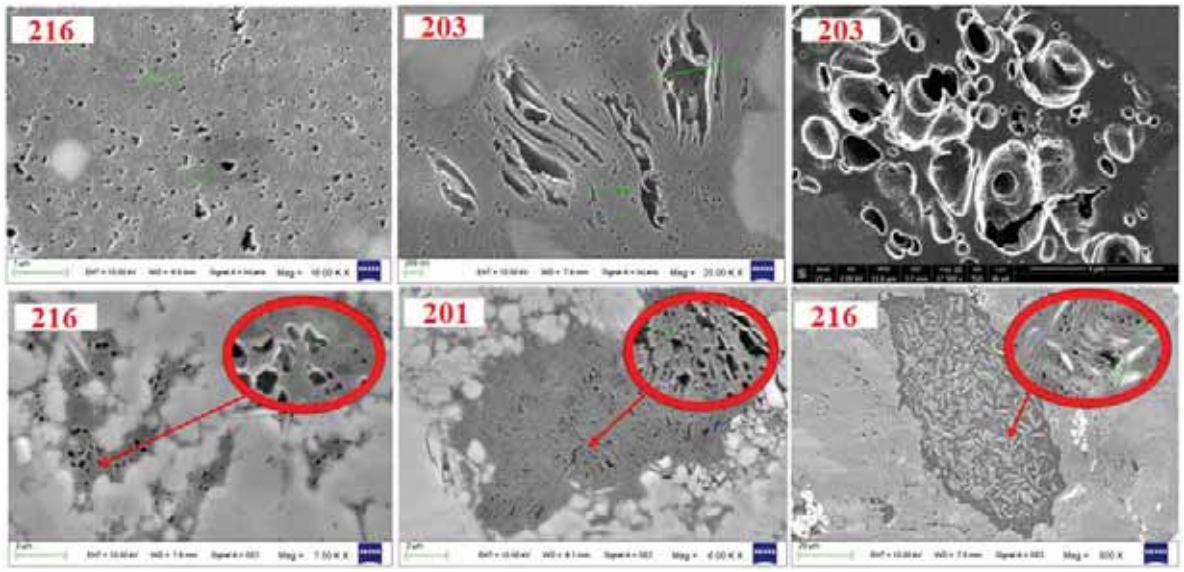

FIGURE 3
Organic pore characteristics of Wufeng Formation-Long-1 member in the study area

The organic matter maturity of Wufeng Formation-Longmaxi Formation in the study area has reached the over mature stage, and its kerogen and early oil cracking asphalt will produce organic matter evolution pores. Kerogen is often mixed with clay, quartz, feldspar, carbonate and other minerals to form honeycomb, spherical or stomatal pores in the process of thermal evolution, and honeycomb organic pores contaminated with quartz and clay minerals are the most common. In addition, the asphalt formed by oil cracking is filled in mineral intergranular pores and fractures. In the process of formation uplift, the decrease of temperature and pressure leads to shrinkage, and a small amount of organic matter internal pores can also be formed between asphalt and fracture wall or pore wall.

Organic pore. Organic pores can be formed in organic matter of different occurrence.The development of organic pores in isolated organic matter can be roughly divided into three types: one is the development of circular mesopores-macropores, and the organic matter between macropores develops mesopores. The second is the balanced development of micro-mesoporous-macropores, macropores are mainly large grooves. These three connectivity is different. The third type has the best connectivity, the first type has the worst connectivity, and the second type is between them. In terms of organic matter with the same occurrence, Changning far develops organic pores than Weiyuan, and the shape is mostly round, and the pore size is obviously larger than Weiyuan, which is almost mesoporous-macroporous scale, as shown in Figure 3.

Organic fracture. From the results, it can be seen that the asphalt formed by oil cracking will produce fractures during condensation or under force. According to its causes, organic matter fractures are formed under tension, organic matter shear fractures

are formed under shear force, organic matter shrinkage fractures and organic matter grain edge fractures are formed under condensation. Organic fractures are not common in Changning area, especially the grain edge fractures and shrinkage fractures. They are rarely developed in the middle and lower parts of Long-1 sub-member,only occasionally in the upper part. Relatively speaking, structural fractures are more common, and a small number of structural organic fractures can be seen in Long-1 sub-member.

Inorganic pore. Inorganic intragranular pores can be found in many minerals in black shale of Changning shale gas field in southern Sichuan, and unstable feldspar and carbonate minerals are more likely to form intragranular dissolved pores, as shown in Figure 5(a). These intragranular pores are generally diverse in shape, mainly isolated spherical and honeycomb. The pore size is different, generally tens of nanometers to tens of microns, resulting in poor connectivity. The pores between quartz particles are common in siliceous mudstone and siliceous rocks, generally less than 200nm, as shown in Figure 4(b). Intergranular pores can be seen in some feldspars. If the dissolution occurs at the edge, the intergranular pores are more obvious, mostly within 200nm, up to micron level. There are relatively more carbonate minerals in the upper Guanyinqiao and Long-2 sub-members of the study horizon in southern Sichuan, and intergranular pores are easily formed between particles. In addition, more intergranular pores are intergranular pores between multi-mineral combinations, which have large pore sizes and can reach the maximum micron level, as shown in Figure 4(c). Generally speaking, the quartz clastic grains of siliceous rocks are small and closely contacted with each other, and the intergranular pores are small and numerous. However, the total interparticle porosity or pore volume is not large, and the connectivity is not good.

Inorganic fracture. The formation of inorganic fractures is mainly related to tectonic stress and mineral properties. Firstly, structural fractures related to tectonic stress exist in local well areas and local intervals. Since Changning area is located at the wing of Changning anticline structural belt, affected by multi-stage uplift and superposition of different directions of tectonic movement, under the extrusion of multi-directional tectonic force, it is easy to form high-steep structural fractures, horizontal bedding fractures and mineral particles in different directions. For example, in Ning 203 and 216 wells, the microfractures are well developed, most of which are horizontal fractures and few of which are high angle fractures. The fracture width is large, common 1μm-2μm tensile micro-fractures, and most fractures are not filled, which provides a good transport channel for shale gas, as as shown in Figure 5. Secondly, there are a large number of mineral-related fractures, which are related to clay, siliceous, calcite, dolomite and feldspar, and are extremely rare in other minerals. This kind of fracture is usually manifested as grain edge fracture. The grain edge fractures related to brittle minerals such as quartz, feldspar and carbonate are mainly caused by the hardness difference between brittle minerals and surrounding materials, and formed in the process of uneven stress. The micro-fractures in clay minerals are mostly formed by dehydration of clay minerals or caused by uneven stress during diagenesis.

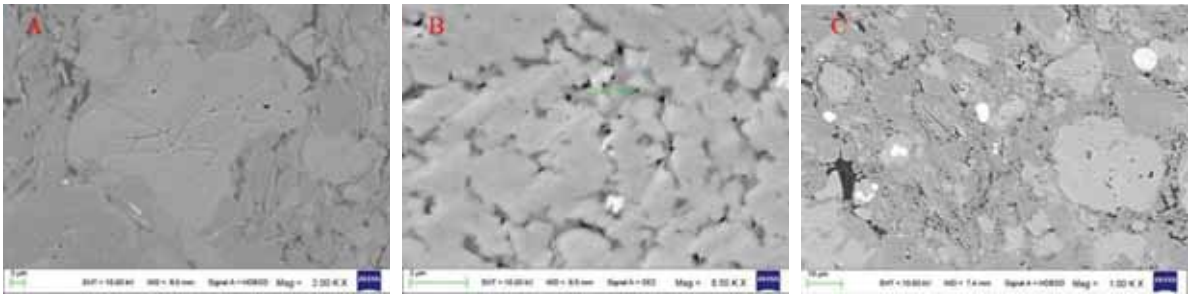

FIGURE 4
Characteristic diagram of inorganic pores in Long-1 member of the study area

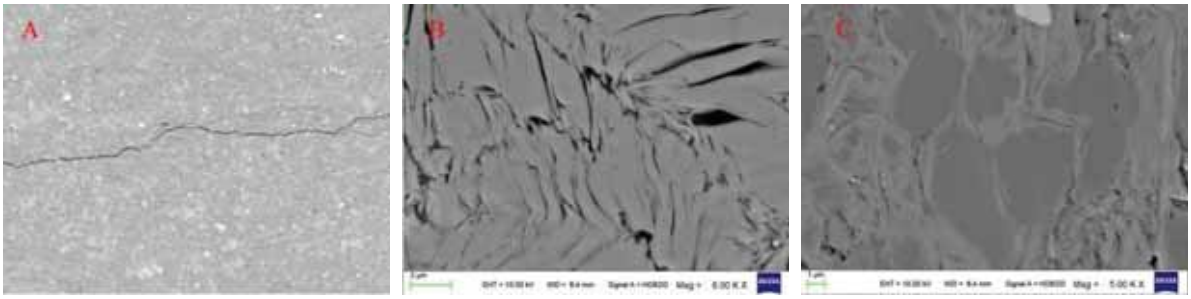

FIGURE 5
Characteristic diagram of inorganic fractures in Wufeng Formation-Long-1 member

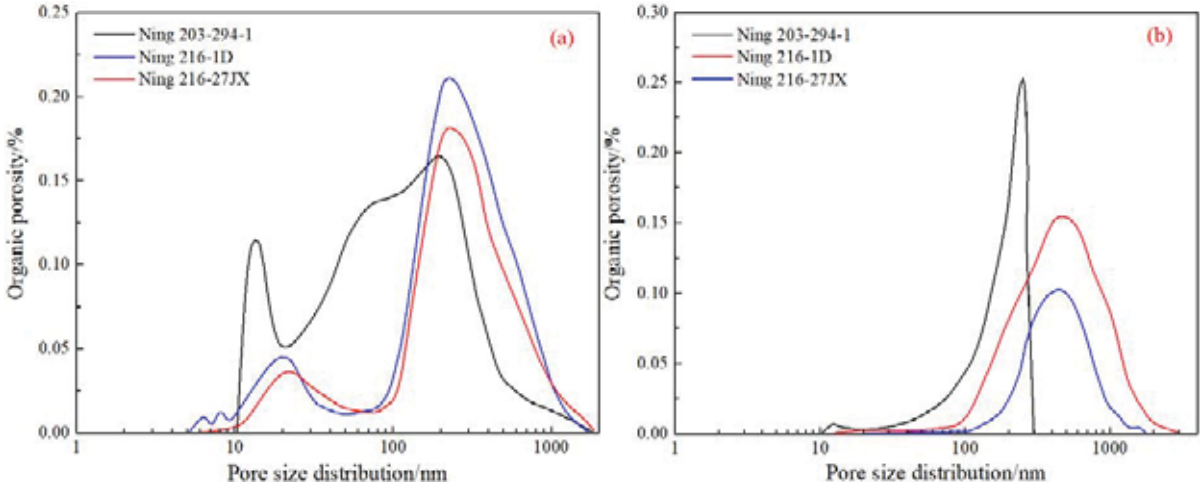

FIGURE 6
Distribution map of pore size in study area

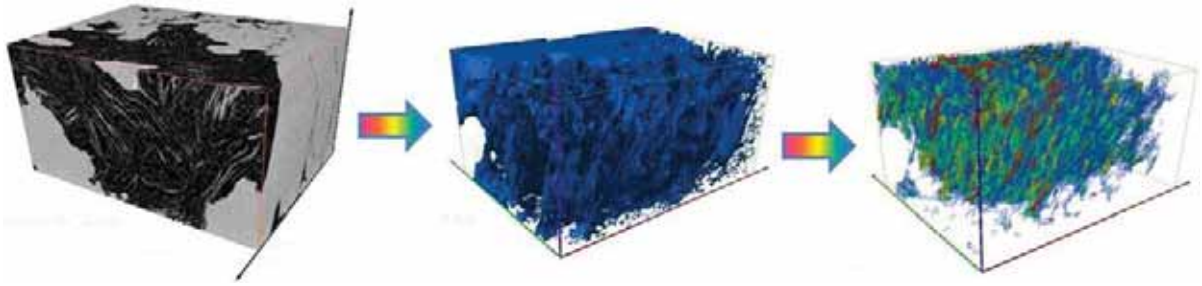

FIGURE 7
Distribution map of pore network in study area

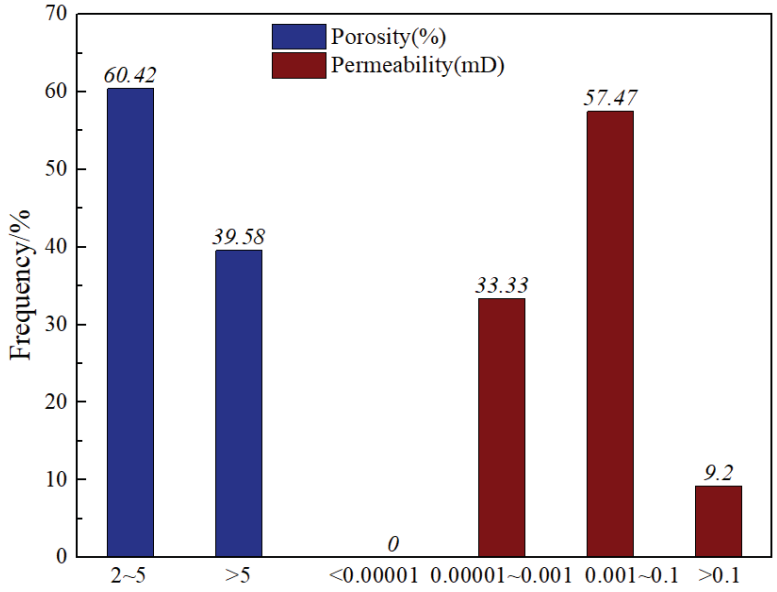

FIGURE 8
Distribution of porosity and permeability of core shale gas interval

Pore structure characteristics. The shale samples in the study area were polished by 0.4 mm × 0.4mm argon ion and analyzed by 4nm resolution secondary electron continuous scanning. A large area high resolution image was formed by multi-image stitching technology, and the porosity of different pore types was obtained by quantitative identification software. Through the analysis of typical well samples in the study area, the total pore, organic pore, organic fracture, inorganic pore and inorganic fracture were quantitatively characterized. The results show that the total porosity of the bottom sample of Longmaxi Formation in well Ning 216 (Sample

Ning 216-1D) is slightly better than that of well Ning 203 (Sample Ning 203-214-1), and the development degree of organic pores is equivalent, about 1.1%, accounting for about 60% of the total pores. From the comparison of the porosity of different samples in the vertical direction of well Ning 216, it is found that the bottom of Long-1 sub-member (Sample Ning 216-1D) is the largest, followed by the middle and upper parts (Sample Ning 216-29JX), and the middle and top parts (Sample Ning 216-21JX and 216-17JX) are smaller. The pore size of organic pores is mainly 100nm - 1μm macropores, and the pore size of inorganic pores is larger than that of well Ning 203, mainly 300nm - 600nm, as shown in Figure 6. Three-dimensional reconstruction of the obtained secondary electron images was carried out by scanning the slices of the organic matter under the focused ion beam scanning electron microscope, and the three-dimensional images of the organic matter and organic pores were extracted respectively. It can be seen that the pore network of the organic pores in the study area was developed, and the porosity in the organic matter was 33.8%, with good connectivity, as shown in Figure 7.

Physical characteristics. Through the porosity analysis and statistics of 480 samples from multiple coring wells in the study area (Figure 8), it is found that the porosity of shale gas layer is generally distributed between 2.03% and 7.78%, with an average of 4.58% and a median of 4.67%. The porosity between 2% and 5% accounted for 61.48% of the total samples, and the porosity between 5% and 10% accounted for 36.96% of the total samples. Based on the permeability analysis and statistics of 87 core samples from multiple wells, it is found that most of the samples are distributed between 1.95×10^{-5} mD and 9.08×10^{-1} mD, with an average of 3.14×10^{-3}mD and a median of 2.14×10^{-3} mD. The permeability of 1×10^{-5} mD ~ 1×10^{-3} mD accounted for 33.3% of the total sample, and greater than 1×10^{-3} mD accounted for 66.7% of the total sample. The average porosity of well Ning 216 - Ning 209 is 3.12% ~ 5.68%, and the permeability is $2.40\% \times 10^{-4}$ mD ~ 2.49×10^{-3} mD. The single well porosity of Changning H18-6 block is 4.44%, and the permeability is 9.98×10^{-3} mD, with no significant difference between the two. Compared with the main shale gas fields in North America, the physical properties are significantly lower. Therefore, the overall physical properties of shale gas in Changning area are low porosity and low permeability.

CONCLUSIONS

(1) The overall fault of the area is not developed and the structural preservation conditions are good. The top-bottom boundary and internal segment boundaries of the Upper Ordovician Wufeng Formation and the Lower Silurian Longmaxi Formation are relatively clear. Wufeng Formation can be divided into upper and lower sections. The lower section is mainly composed of black siliceous mudstone and shale, with high organic matter content. The upper section is the Guanyinqiao section, which is composed of dark gray argillaceous limestone.

(2) The strata belong to shelf facies deposition, which can be further divided into deep shelf and shallow shelf two subfacies and various microfacies. The organic-rich siliceous shelf microfacies and organic-rich mud shelf microfacies in deep shelf subfacies are most conducive to the accumulation and maintenance of organic matter, and are the best sedimentary facies belts for the formation and evolution of shale gas. They are mainly distributed in the middle and lower parts of the Wufeng Formation to the Long-1 sub-member of Longmaxi Formation. The second is the silty mud shelf microfacies in the deep shelf subfacies, which are mostly distributed in the upper part of Long-1 sub-member. Microfacies in shallow shelf subfacies are not conducive to the formation and evolution of shale gas, mainly distributed in the top of Long-1 sub-member and Long-2 formation.

(3) The content of brittle minerals in gas production section is high, with an average of 51.6%, and the content of clay minerals is about 30%. On the whole, the fracturing ability of the production interval is good. The reservoir space of gas layer is dominated by inorganic pores, followed by organic pores. The porosity of organic pores is generally about 30%, and the connectivity is good. The physical property the reservoir is good, and the average porosity is about 4.58%. The overall physical properties of shale gas in Changning area of southern Sichuan are low porosity and low permeability.

ACKNOWLEDGEMENTS

This work was no fund supported.

REFERENCES

[1] Nie, H.K., Chen, Q., Zhang, G.R., Sun, C.X., Wang, P.W., Lu, Z.Y. (2021) An overview of the characteristic of typical Wufeng-Longmaxi shale gas fields in the Sichuan Basin, China. Natural Gas Industry B. 8(3), 217-230.

[2] Kang, S., Lu, L., Tian, H., Yang, Y., Jiang, C., Ma, Q. (2021) Numerical simulation based on the canister test for shale gas content calculation. Energies. 14(6), 1011-1018.

[3] Simon, V., Moreau, L., Romdhana, M.H., Sablayrolles, C., Lecomte, D. (2017) Emissions of polycyclic aromatic hydrocarbon particulates from combustion of different fuels. Fresen. Environ. Bull. 21(4), 946-955.
[4] Pratiwi, S., Juerges, N. (2020) Review of the impact of renewable energy development on the environment and nature conservation in Southeast Asia. Energy Ecology and Environment. 5(2), 221-239.
[5] Shi, G.H., Jing, Y.Y., Wang, S.L., Zhang, X.T. (2010) Development status of liquefied natural gas industry in China. Energy Policy. 38(11), 7457-7465.
[6] Jiang, D., Zhan, Y.E. (2016) Analysis of the significance of gas development for energy conservation and emission reduction. Chemical Industry. 30(10), 81-86.
[7] Li, J., She, Y., Gao, Y., Li, M., Shi, Y. (2020) Natural gas industry in China: development situation and prospect. Natural Gas Industry B. 7(6), 604-613.
[8] Jia, A. (2018) Progress and prospects of natural gas development technologies in China. Natural Gas Industry B. 5(6), 547-557.
[9] Williams, L.B., Elliott, W.C., Hervig, R.L. (2015) Tracing hydrocarbons in gas shale using lithium and boron isotopes: Denver basin USA, Wattenberg gas field. Chemical Geology. 41(7), 404-413.
[10] Mendhe, V.A., Kamble, A.D., Bannerjee, M., Mishra, S., Mukherjee, S., Mishra, P. (2016) Evaluation of shale gas reservoir in barakar and barren measures formations of north and south Karanpura coalfields, Jharkhand. Journal of the Geological Society of India. 88(3), 305-316.
[11] Dong, D., Wang, Y., Li, X., Zou, C., Guan, Q., Zhang, C. (2016) Breakthrough and prospect of shale gas exploration and development in China. Natural Gas Industry B. 3(1), 12-26.
[12] Shar, A.M., Mahesar, A.A., Memon, K.R. (2017) Could shale gas meet energy deficit: its current status and future prospects. Journal of Petroleum Exploration & Production Technology. 8(4), 957-967.
[13] Paltsev, S., Jacoby, H.D., Reilly, J.M., Ejaz, Q.J., Morris, J. (2011) The future of U.S. natural gas production, use, and trade. Energy Policy. 39(9), 5309-5321.
[14] Mcglade, C., Speirs, J., Sorrell, S. (2013) Methods of estimating shale gas resources – comparison, evaluation and implications. Energy. 59(9), 116-125.
[15] Estrada, J.M., Bhamidimarri, R. (2016) A review of the issues and treatment options for wastewater from shale gas extraction by hydraulic fracturing. Fuel. 182(10), 292-303.
[16] Boruah, A., Hassan, D. (2013) Shale Gas an Unconventional Hydrocarbon Resource: Overview. Natural Gas Industry. 9(5), 201-206.
[17] Liu, W., Yuan, H., Fan, Z., Li, J., Sun, L. (2021) Using water-based drilling cuttings from shale gas development to manufacture sintered bricks: a case study in the southern Sichuan Basin, China. Environmental Science and Pollution Research. 40(5), 439-443.
[18] Tong, X., Zhang, G., Wang, Z., Wen, Z., Tian, Z., Wang, H. (2018) Distribution and potential of global oil and gas resources. Petroleum Exploration and Development. 21(3), 311-319.
[19] Abouelresh, M.O., Slatt, R.M. (2012) Lithofacies and sequence stratigraphy of the Barnett Shale in east-central Fort Worth Basin, Texas. AAPG Bulletin. 96(1), 111-122.
[20] Klett, T.R., Cook, T.A., Charpentier, R.R., Tennyson, M.E., Attanasi, E.D., Freeman, P.A. (2012) Assessment of potential additions to conventional oiland gas resources of the world from reserve growth. Earth Science Frontiers. 66(1), 441-443.
[21] Dilmore, R.M., Glosser, D., Carter, K.M., Bain, D.J. (2015) Spatial and temporal characteristics of historical oil and gas wells in pennsylvania: implications for new shale gas resources. Environmental Science & Technology. 49(20), 12015-23.
[22] Wilson, K.C., Durlofsky, L.J. (2013) Optimization of shale gas field development using direct search techniques and reduced-physics models. Journal of Petroleum Science & Engineering. 108(8), 304-315.
[23] Zou, C.N., Zhi, Y., Hou, L.H., Zhu, R.K., Cui, J.W., Wu, S.T. (2015) Geological characteristics and "sweet area" evaluation for tight oil. Petroleum Science. 12(4), 606-617.
[24] Zhao, X., Yang, F., Zhou, L., Xiugang, P.U., Jin, F., Han, W. (2018) Geological characteristics of shale rock system and shale oil exploration breakthrough in a lacustrine basin: a case study from the paleogene 1st sub-member of kong 2 member in Cangdong Sag, Bohai Bay Basin, China. Petroleum Exploration & Development. 45(3), 377-388.
[25] Li, H.S., Wang, H.G., Ji, G.D., Wen, H.Y. (2011) Key technologies for shale gas exploration and development in the United States. Petroleum Machinery. 11(9), 85-90.
[26] Guan, D.F. (2015) Comparative analysis and thinking on shale oil and gas resources in the United States and China. Sino-Foreign Energy. 20(12), 29-37.
[27] Goodwin, S., Carlson, K., Knox, K., Douglas, C., Rein, L. (2014) Water intensity assessment of shale gas resources in the Wattenberg field in northeastern Colorado. Environmental Science & Technology. 48(10), 5991-5.
[28] Wang, Z., Luo, D., Liu, L. (2018) Natural gas utilization in China: development trends and prospects. Energy Reports. 27(4), 351-356.

[29] Zou, C., Dong, D., Wang, Y., Li, X., Huang, J., Wang, S. (2015) Shale gas in China: characteristics, challenges and prospects (ii). Petroleum Exploration and Development. 43(6), 182-196.
[30] Xu, C., Zou, W., Yang, Y., Yong, D., Zhang, J. (2018) Status and prospects of deep oil and gas resources exploration and development onshore China. Journal of Natural Gas Geoscience. 3(1), 102-110.
[31] Guan, Q.Z., Dong, D.Z., Wang, S., Huang, J.L., Wang, Y.M. (2016) Preliminary study on shale gas microreservoir characteristics of the Lower Silurian Longmaxi Formation in the southern Sichuan Basin, China. Journal of Natural Gas Science and Engineering. 16(31), 382-395.

Received: **29.11.2021**
Accepted: **23.01.2022**

CORRESPONDING AUTHOR

Ying Guo
CNOOC China Limited,
Tianjin Branch,
Tianjin 300459 – China

e-mail: w2677408379@163.com

© by PSP Volume 31– No. 05/2022 pages 5048-5056 Fresenius Environmental Bulletin

EVALUATION OF VEGETATION CARBON STORAGE OF NATURAL FOREST PROTECTION PROJECT IN THE UPPER REACHES OF THE YANGTZE RIVER

Yalin Yang*, Yafeng He

General Graduate School, Kyonggi University, Suwon, Kyonggi-do 16227, Korea

ABSTRACT

Based on the continuous function method of biomass estimation and the regression function of biomass and stock volume, this paper analyzes the carbon storage of forest vegetation in the upper reaches of the Yangtze River in the Natural Forest Protection Project (NFPP) area (2000~2010). The density of forest vegetation is examined in the six provinces, autonomous regions, and municipalities of the upper reaches of the Yangtze River before and after the implementation of NFPP. Additionally, changes in carbon storage and the carbon sequestration capacity of forest vegetation are evaluated in the NFPP area of the upper reaches of the Yangtze River (2011~2020). The results show that the carbon storage of the first-stage forest ecosystem found in the protection project area of the upper reaches of the Yangtze River is 5,004.44 Tg C, of which the carbon storage of forest vegetation is 1,414.35 Tg C, and the carbon storage of forest soil is 3,525.74 Tg C. From 1988 to 1998, the carbon storage of forest vegetation increased by 290.65 Tg C. However, after the implementation of NFPP, the carbon storage of forest vegetation increased by 705.12 TgC. In addition, the carbon sequestration benefit of forest vegetation in the upper reaches of the Yangtze River was 80.92 Tg. C. The implementation of NFPP has also enabled forest soil erosion in the upper reaches of the Yangtze River to be controlled to a certain extent: from 1998 to 2008, the forest soil retention in this area reached 3,887.3 Tg, of which the forest soil carbon sequestration benefit was 7.23 Tg C.

KEYWORDS:
Yangtze River, Natural Forest Protection Project, forest vegetation, forest carbon storage, potential evaluation

INTRODUCTION

The Natural Forest Protection Project aims to fundamentally curb the deterioration of the ecological environment, protect biodiversity, and promote the sustainable development of society and the economy. It has reclassified the zoning of natural forests, adjusted the management direction of forest resources, and promoted the protection and cultivation of natural forest resources. Overall, the NFPP seeks to maintain and improve the ecological environment, and meeting the needs of society and allowing for the national economic development for forest products are seen as its fundamental purpose [1-5]. The NFPP not only plays an important role in the improvement of China's ecological environment, but also plays a huge role in carbon fixation in terrestrial ecosystems [6,7]. Therefore, clarifying the carbon sequestration capacity of the NFPP is an important topic in current regional carbon storage research.

The estimation of forest vegetation carbon storage is based on the estimation of forest vegetation biomass. This process involves multiplying the forest vegetation biomass by the carbon conversion rate (that is, the carbon content per gram of dry matter) to obtain the forest vegetation carbon storage. Dixon et al. [8] studied the carbon storage and carbon density of global forest vegetation, which were determined to be 359 Pg C and 86 Mg C/ha, respectively. Birdsey et al. [9] estimated the global carbon pool and carbon density as 510 Pg C and 106 Mg C/ha. Batjes et al. [10] discussed the forest carbon storage in tropical Southeast Asia, finding that Indonesia has the highest total carbon storage, while the Philippines has the highest average carbon sequestration, and Myanmar's overall carbon sequestration capacity is reduced. Birdsey et al. [11] studied forest carbon sinks in the northern hemisphere, and found that the annual carbon sinks in the northern hemisphere reached (1.7±0.05) Pg C. Bonan et al. [12] conducted a correlation analysis on the carbon storage of forest ecosystems in Central Asia, and determined that the amount of carbon sequestered was 3.07 Tg. Afforestation has a strong carbon sink function, with a total carbon sequestration of 12.97 Tg, while deforestation is the most important source of carbon release, with a total carbon release of 5.80 Tg. Forest land transfer shows strong carbon emission characteristics, with a total emission of 4.10 Tg. Fang et al. [13-15] established the regression equation between biomass and stock volume of different forest types, and analyzed the forest carbon storage and carbon density within China over the past 20 years. Wang et al. [16] used the third national set of forest resource inventory data (1984~1988) to examine the data of

561 survey plots of more than 160 pieces of forest biomass collected before 194, and classified the forests by type. The forests' ages were determined by 16 species, and the ratio of tree trunks to tree layer biomass of each forest type was established, from which the carbon storage and carbon density of China's forest vegetation were calculated as 3.75~4.20 Pg C and 38.7~43.1. Mg C/ha, respectively. Pan et al. [17] used different data to establish a fitting relationship between biomass and accumulation, estimating forest vegetation carbon storage to be 3.51~4.02 Pg C and forest vegetation carbon density to be 33.45~37.7 Mg C/ha. Comparing these two studies, the carbon storage estimations are relatively close, while the carbon density estimations are somewhat different. Zhao et al. [18] established a volume biomass model by collecting data on forest biomass and stock volume from nearly 300 surveyed sample plots to analyze China's forest carbon storage and carbon density. Xu et al. [19] collected the biomass data of 2,304 forest sample plots across the country, calculating the biomass-stock volume fitting relationship of tree species and age groups, and estimating the carbon storage and carbon density of China's forest vegetation from 1973 to 2003.

This paper takes the area of NFPP in the upper reaches of the Yangtze River as the research object, and uses the conversion factor continuous function method to estimate the carbon storage of the tree, shrub, litter, and soil layers of the forest ecosystem in this area. This is followed by the use of the biomass and stock volume regression function to evaluate the carbon sequestration benefits of the upper reaches of the Yangtze River, and finally to quantify this area's carbon sequestration contribution.

MATERIALS AND METHODS

The 7th National Forest Resources Inventory (2004~2008) was used to collect data about the study area. Both natural and artificial forests were included, and were sorted according to their age groups and dominant tree species. The Implementation Plan for Natural Forest Resources Protection Project in the Upper Yangtze River (Phase I 2000~2010) provided forest land area data for various provinces, autonomous regions, and municipalities, allowing for an estimation of the carbon storage of forest vegetation in the NFPP during its first phase. Five phases (1984~1988, 1989~1993, 1994~1998, 1999~2003, and 2004~2008) of National Forest Resources Inventory statistics were also used to determine the area and stock volume of each age group of arbor forests according to their dominant tree species, allowing for an estimation of forest vegetation in the six provinces, autonomous regions, and municipalities in the upper reaches of the Yangtze River 10 years before and after the implementation of NFPP. Changes in carbon storage were determined using data from the five phases. The forest area data in the Implementation Plan for Natural Forest Resources Protection Project in the Upper Yangtze River Region (Phase II 2011~2020) was then used to estimate the carbon sequestration capacity of forest vegetation during the second phase of NFPP.

In this study, the conversion factor continuous function method is used, and the reciprocal equation is used to express the relationship between BEF (biomass conversion factor) and stand accumulation. This method realizes this calculation from the actual measurement of the sample site, and its scale conversion has good adaptability. At the same time, this paper uses the main tree species biomass and stock volume regression functions, combined with the national forest resource inventory data, to calculate the regional forest vegetation biomass.

RESULTS AND DISCUSSION

Forest arbor carbon storage in NFPP. Assuming that the forest arbor carbon density in the NFPP area of each province, autonomous region, and municipality is equal to the forest arbor carbon density of each province, autonomous region, and municipality, the forest arbor carbon densities of the six provinces, autonomous regions, and municipalities in the upper reaches of the Yangtze River are 23.47 Mg C/ha (Hubei), 56.99 Mg C/ha (Sichuan), 28.94 Mg C/ha (Guizhou), 50.01 Mg C/ha (Yunnan), 105.24 Mg C/ha (Tibet), and 29.24 Mg C/ha (Chongqing). These results are shown in Figure 1.

We can see that the forest area of the six provinces, autonomous regions, and municipalities is calculated, and the forest arbor carbon storage in the natural protection engineering areas of the six provinces and cities in the upper reaches of the Yangtze River are respectively 58.39 Tg C, 664.1 Tg C, 108.26 Tg C, 441.9 Tg C, 44.26 Tg C, and 50.56 Tg C. From this, it can be determined that the forest arbor carbon storage in the first phase of the Yangtze River Natural Protection Project Area is 1367.47 Tg C. Among the six provinces, regions, and cities in the upper reaches of the Yangtze River, Sichuan Province has the highest forest arbor carbon storage, accounting for 48% of the natural protection project area in the upper reaches of the Yangtze River, while the forest arbor carbon density in Tibet is the highest, being 1.8~4.5 times that of the other five provinces and cities.

Carbon storage of shrubs, grasses, and litter in NFPP. SPSS was used to analyze the 372 data points in the distribution pattern of forest biomass. In order to unify the data categories, the shrub layer and the herb layer were merged into the shrub and grass layer. The analysis results are shown in Figure 2. This paper chooses the median as the representative value of the proportion of each layer. Among

these median values, the biomass proportions of the arbor layer, shrub layer, and litter layer are 93.92%, 3.22%, and 4.42%, respectively. The forest arbor carbon storage is 1367.47 Tg C, while the calculated forest shrub-grass layer carbon storage is 46.88 Tg C, and the forest litter layer carbon storage is 64.35 Tg C.

Forest soil carbon storage in NFPP. Using the 106 sets of data collected, the results was compiled and summarizes the soil carbon storage and soil carbon density of each forest type in the NFPP area of the upper reaches of the Yangtze River. The results are shown in Figure 3. The forest soil carbon storage of the six provinces in the upper reaches of the Yangtze River are 205.16 Tg C, 1946.54 Tg C, 351.38 Tg C, 780.7 Tg C, 49.96 Tg C, and 191.93 Tg C, respectively. The total forest soil carbon storage of the natural protection project area in the upper reaches of the Yangtze River is 3525.74 Tg C. Figure 5 shows that the forest soil carbon densities in the six provinces, autonomous regions, and municipalities in the upper reaches of the Yangtze River are 82.82 Mg C/ha, 166.08 Mg C/ha, 94.09 Mg C/ha, 88.85 Mg C/ha, 109.52 Mg C/ha, and 1,103 Mg C/ha, respectively, of which the forest soil reserves and carbon density are highest in the Sichuan NFPP area. Additionally, the forest soil carbon storage in the NFPP area of Tibet is the lowest, and the forest soil carbon density in the NFPP area of Hubei is the lowest.

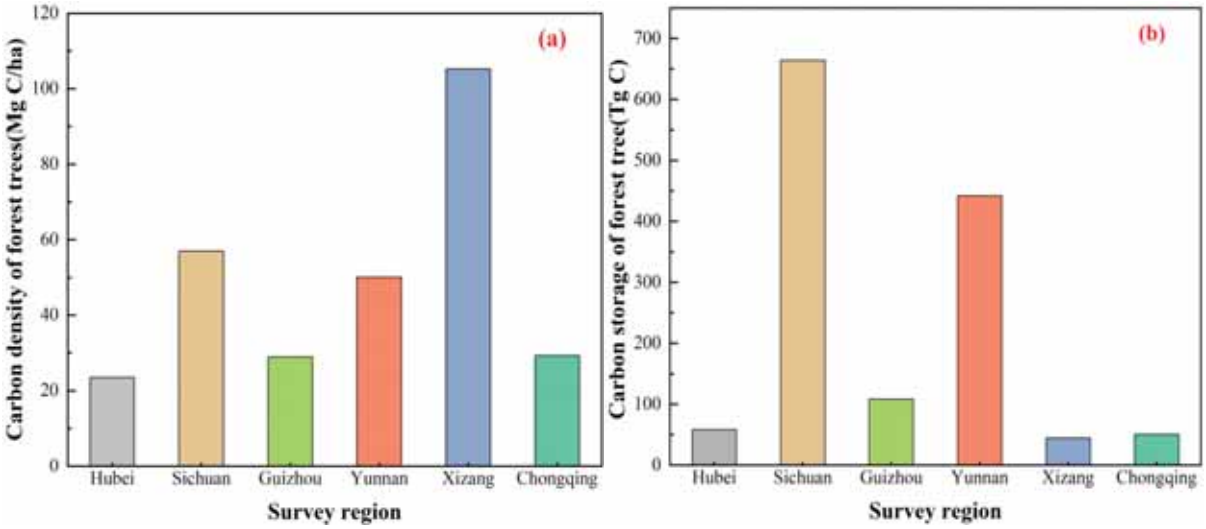

FIGURE 1
Carbon density and reserves of forest trees in NFPP area

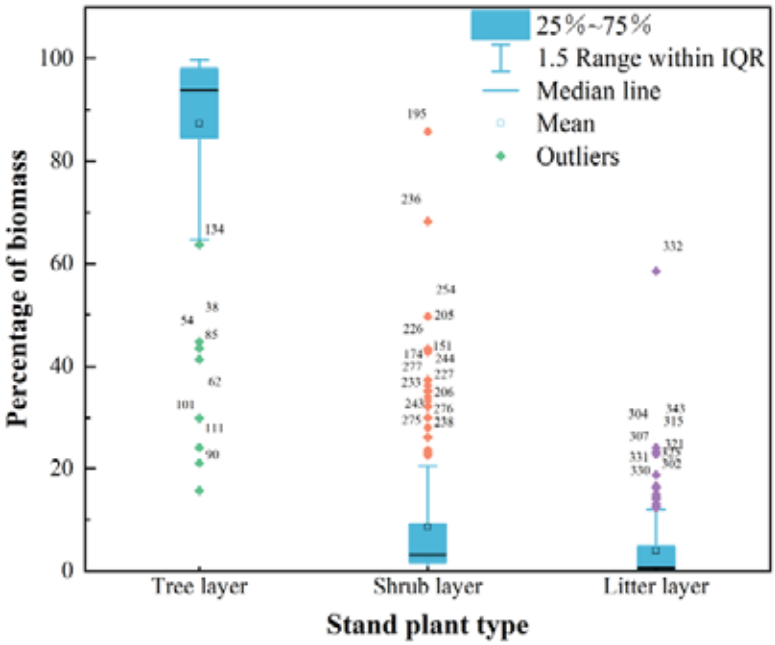

FIGURE 2
Stand plant distribution in the upper reaches of the Yangtze River

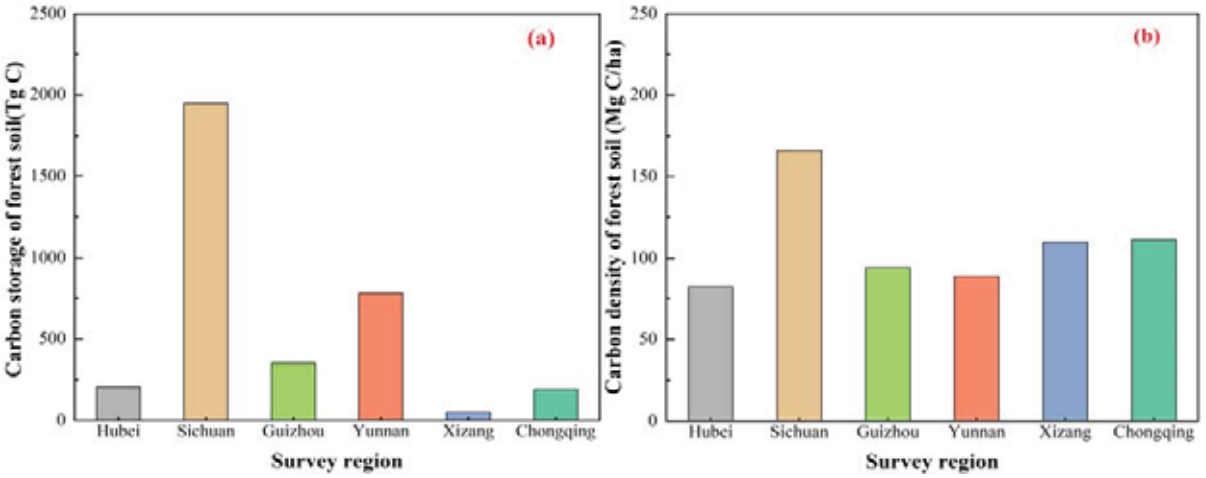

FIGURE 3
Stand plant distribution in the upper reaches of the Yangtze River

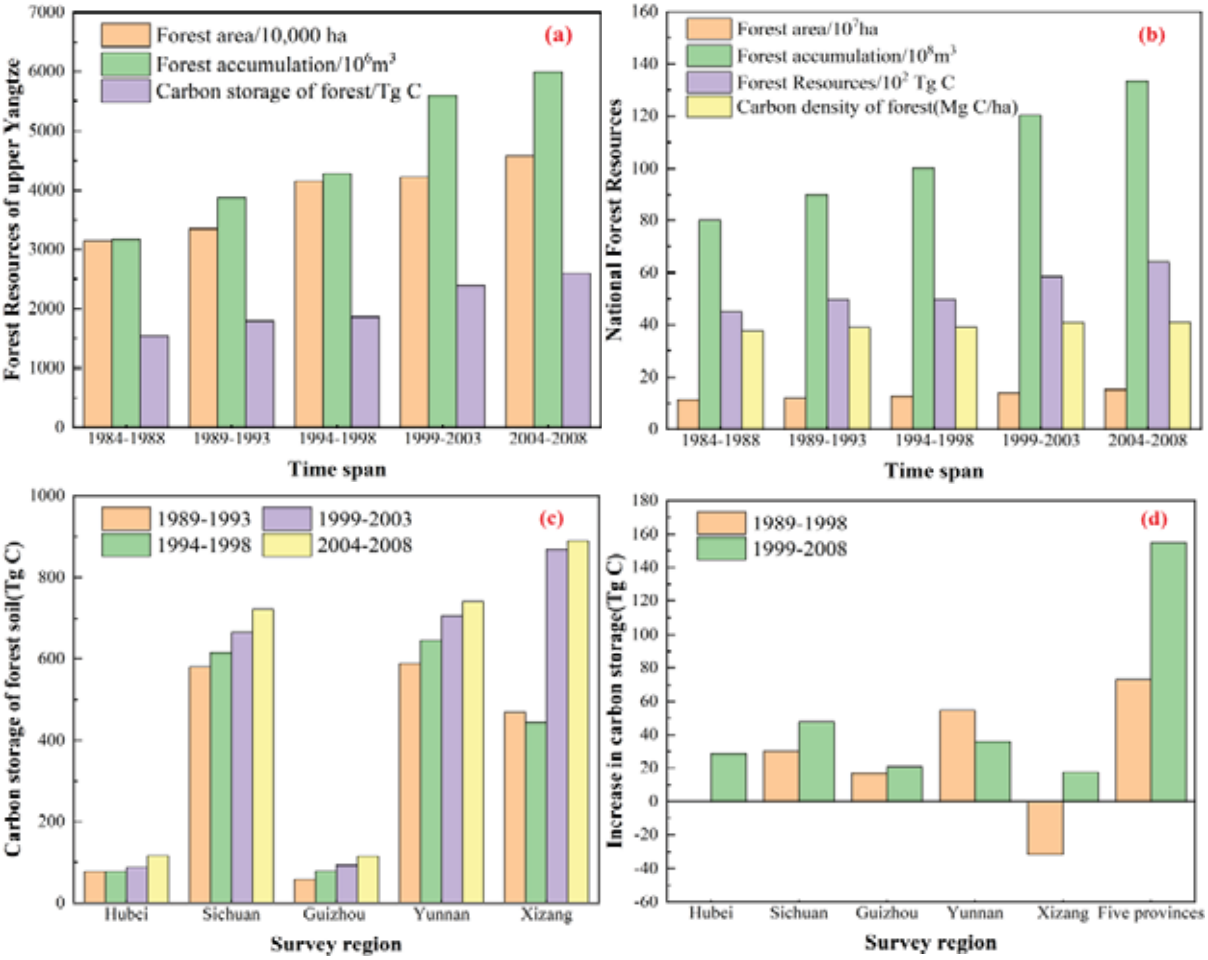

FIGURE 4
Forest resources and vegetation carbon storage

Carbon sequestration benefits of vegetation in NFPP. According to the data of five forest inspections, spanning periods from 1984~1988 to 2004~2008, the forest area of the six provinces, autonomous regions, and municipalities in the upper reaches of the Yangtze River increased from 31.7302 million hectares to 4,566.9 million hectares, and the forest stock increased from 3,162,452,700 cubic meters to 5,978,856,700 cubic meters. From 1984~1988 to 2004~2008, the carbon storage of forest vegetation in the six provinces, autonomous regions and municipalities in the upper reaches of the Yangtze River were 1,577.58 TgC, 1,795.05 TgC, 1,868.23 TgC, 2,419.25 TgC, and 2,573.35 TgC, respectively. These results are shown in Figure 4(a), and account

for 34.8%, 35.7%, 37.0%, 41.0%, and 39.9%, respectively, of vegetation carbon storage in national forests during the same period, as shown in Figure Figure 4(b). It can be seen from Figure 4(a) that the carbon storage of forest vegetation in the six provinces, autonomous regions, and municipalities in the upper reaches of the Yangtze River has increased relatively steadily. Figure 4(c) and (d) show that the carbon storage of forest vegetation increased by 290.65 Tg C in the six provinces, autonomous regions, and municipalities in the upper reaches of the Yangtze River 10 years before the implementation of the Natural Forest Protection Project (1988~1998), and the carbon storage of forest vegetation increased by 705.12 Tg C after 10 years of its implementation (1998~2008). In this paper, the two phases of forest vegetation carbon storage in Chongqing municipality and the corresponding two phases of forest vegetation carbon storage in Sichuan Province are added in order to compare the changes in carbon storage, and the increase in forest vegetation carbon storage, from 1999~2003 to 2004~2008. Compared with the increase in the period from 1989~1993 to 1994~1998, there was a decrease in carbon storage in Tibet during the 10 years prior to the implementation of the project, while Tibet's carbon storage in the 10 years after the project's implementation increased. The combined value of forest vegetation carbon storage in Sichuan, Guizhou, and Yunnan in the 10 years before the project's implementation was less than the combined value in the 10 years after the project's implementation, and the increase in carbon storage in the six upper reaches of the Yangtze River from 1999~2003 to 2004~2008 was 154.1 Tg C, which is 80.92 Tg C higher than the increase in carbon storage from 1989~1993 to 1994~1998 (73.18 Tg C). These changes reflect the project's impact on the carbon storage of forest vegetation in the upper reaches of the Yangtze River.

Benefits of carbon sequestration in forest soils of NFPP. In this paper, using the data of 40 typical forest plots in CERN and the general soil erosion equation, the soil conservation amount of different forest types and the fixed amount of carbon in the soil in the NFPP areas of the upper reaches of the Yangtze River are calculated. The results are shown in Figure 5. The forest soil conservation of the six provinces in the upper reaches of the Yangtze River are 42.24 Tg/a, 118.43 Tg/a, 137.93 Tg/a, 18.64 Tg/a, and 71.49 Tg/a, respectively, and the total forest soil conservation is 388.73 Tg/a. From Figure 5(b), it can be seen that the forest soil carbon sequestration for each of the six provinces in the natural forest protection project area is 88.01 Gg C/a, 224.70 Gg C/a, 250.84 Gg C/a, 30.58 Gg C/a, and 129.07 Gg C/a, respectively. The total forest soil carbon sequestration is 723.19 Gg C/a, of which the soil conservation and soil carbon conservation in the Yunnan NFPP area are both the largest, while those of the Tibet NFPP area are the smallest. After 10 years of the upper Yangtze River NFPP implementation (1998 to 2008), the forest soil holding capacity was 3,887.3 Tg C, of which the forest soil carbon sequestration benefit was 7.23 Tg C.

Forest biomass conversion of NFPP. The biomass transfer factor method is used to convert the stock volume of a forest species in the NFPP area in the upper reaches of the Yangtze River into biomass. The biomass transfer factor is a kind of biomass factor, and it aims to convert and expand the forest stock volume into target organisms to achieve the synchronization of conversion and expansion [20-22]. The biomass factor model is more flexible, and specific biomass factors are defined according to specific needs during research. The biomass factor is related to the forest age and will decrease as the forest age increases [23-26]. This paper divides the BCEF of different forest age groups for research, and defines that the BCEF in this paper is the conversion of a certain forest stand volume to a certain stand biomass, and its value is equal to the ratio of the forest stand biomass to the forest stand volume.

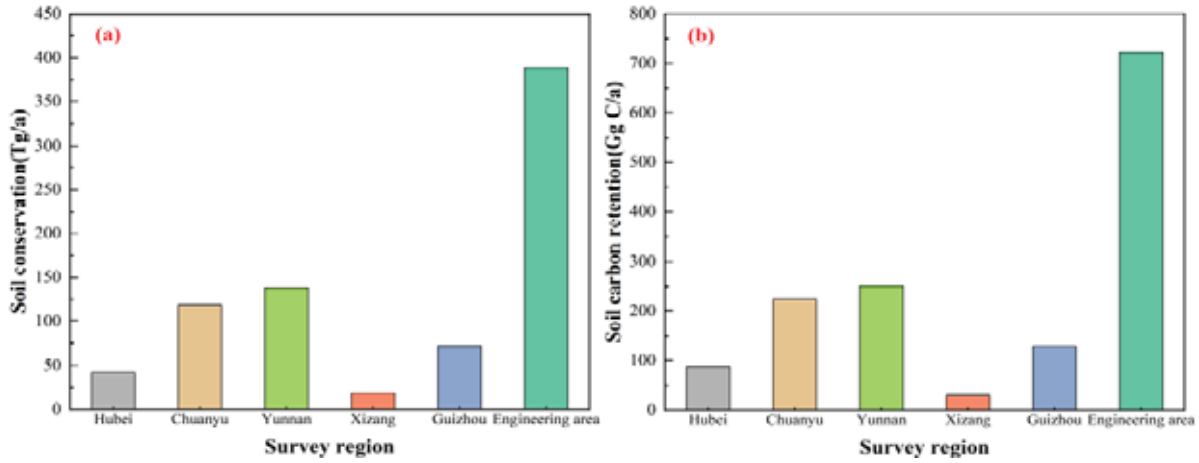

FIGURE 5
Soil and soil carbon retention in NFPP area

TABLE 1
BCEF factors of each age group of stand in the upper reaches of the Yangtze River

Province	Young		Middle aged		Near mature		Mature		Over mature	
	BCEF 1	BCEF 2	BCEF 1	BCEF 2	BCEF 1	BCEF 2	BCEF 1	BCEF 2	BCEF 1	BCEF 2
Guizhou	1.48	2.23	0.78	0.97	0.69	0.73	0.73	0.84	0.64	0.64
Hubei	2.81	1.90	1.05	1.12	0.89	1.00	0.88	0.91	0.70	0.70
Sichuan	2.59	2.47	1.06	1.15	0.83	0.89	0.79	0.75	0.71	0.62
Tibet	1.77	1.23	0.86	0.85	0.72	0.80	0.66	0.73	0.57	0.71
Yunnan	1.44	1.61	0.91	1.05	0.75	0.82	0.73	0.77	0.74	0.83
Chongqing	2.30	2.16	0.92	0.92	0.84	0.97	0.70	0.74	0.58	0.58

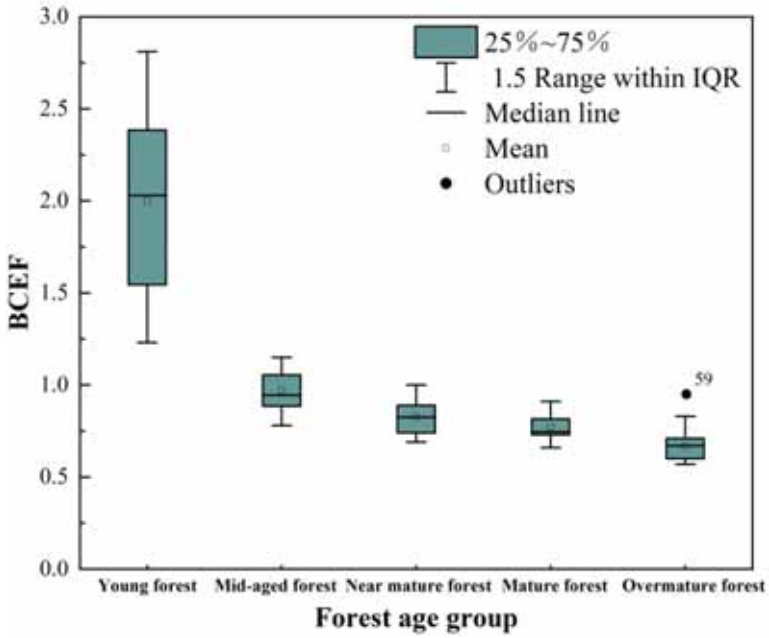

FIGURE 6
BCFF of each age group in the upper reaches of the Yangtze River

First, the BCEF of each forest age group is calculated in each province, region, and city in the upper reaches of the Yangtze River. The value range of the BCEF is calculated in each area, following which a representative value is selected. It can be assumed that the main tree species in the project area are the same as the dominant tree species of artificial arbor forests in each province in the national forest resource inventory. The natural protection project covers almost the entire scope of some provinces and cities. Secondly, the area accumulation data of major natural forest tree species is extracted from the national inventory data, assuming that the proportion of afforestation area in the project area is equivalent to the area proportion in the forest resource inventory. Making the tree species area equivalent to "1" allows for the calculation of BCEF2.

As can be seen from Table 1, BCEF has 5 age groups with 60 sample sizes. SPSS is used to analyze the 60 data to determine the range and representative value of BCEF for each age group, as shown in Figure 6. It should be noted that there is an abnormal value. Here, the median is selected as the representative value of each age group. Compared with the arithmetic mean, the median is not easily affected by extreme values, and the purpose of selecting the representative value is to reflect the general levels present in the region. According to the age division of each age group in the upper reaches of the Yangtze River, the forest age of each forest species from 200 to 2010 in the first phase of the natural conservation project area in the upper reaches of the Yangtze River is judged to be in the young forest stage. The BCEF representative value of young forest 2.03 was selected for biomass conversion. From Figure 7, we can see that the total carbon sequestration brought by the natural forest protection project in the upper reaches of the Yangtze River from 2000 to 2010 was 24.2 Tg C, of which the carbon sequestration of shelter forests was 21.49 Tg C, the carbon sequestration of special forests was 0.03 Tg C, and the carbon sequestration of timber forests was 2.68 Tg C. These numbers respectively account for 88.1%, 0.13%, and 11.06% of the total carbon sequestration. It shows that the protection forest has the strongest carbon sequestration ability in the protection project, and it is the backbone of the project's afforestation carbon sequestration [27, 28].

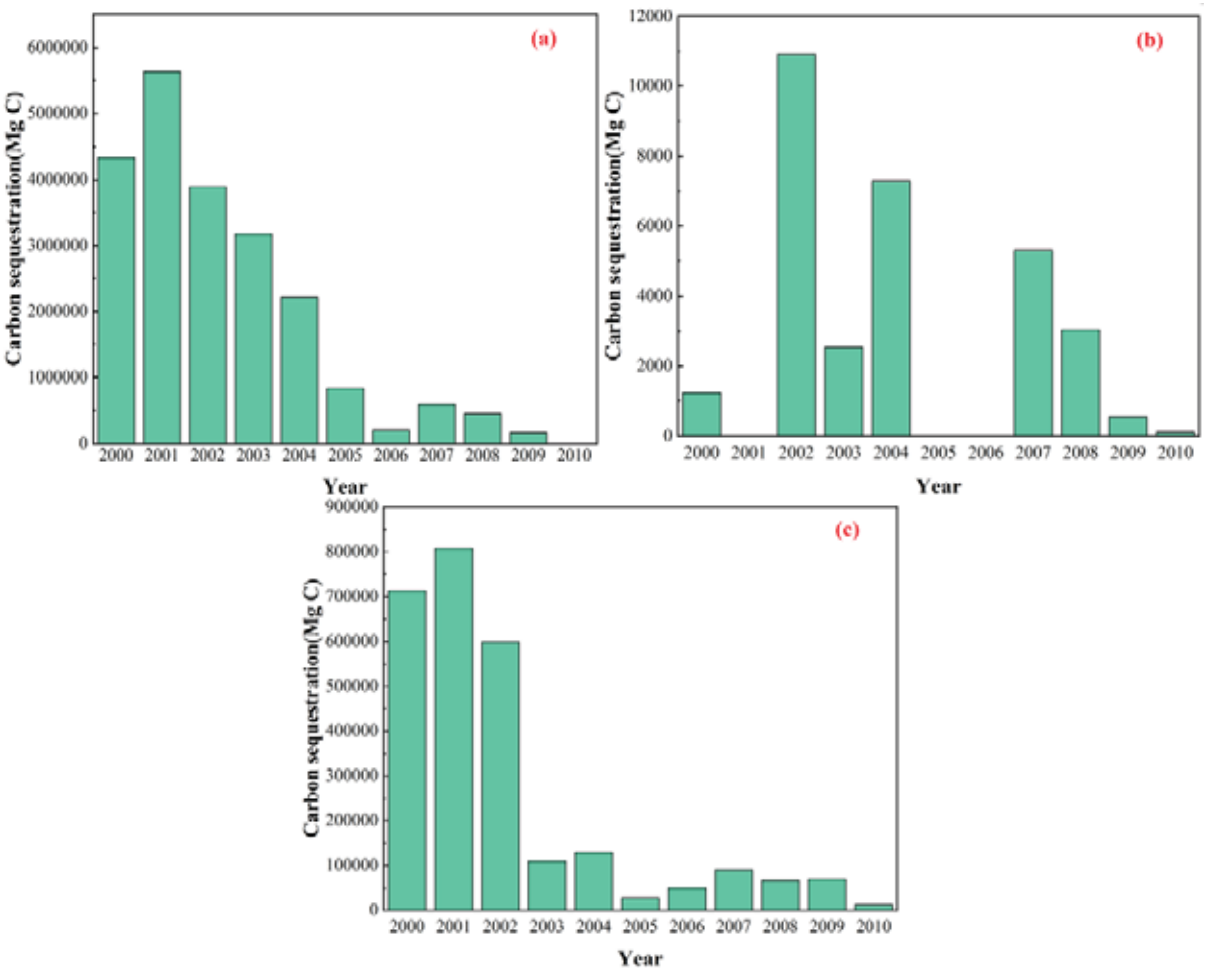

FIGURE 7
Afforestation and carbon sequestration of shelter forest, special forest and timber forest

CONCLUSIONS

(1) The carbon storage of the forest ecosystem in NFPP area in the upper reaches of the Yangtze River is 5,004.44 Tg C, of which the carbon storage of forest vegetation is 1,414.3 Tg C. Furthermore, the carbon storage of forest litter is 64.35 Tg C, and the carbon storage of forest soil is 3,525.74 Tg C, accounting for 28.26%, 1.29%, and 70.45% of forest ecosystem carbon storage, respectively.

(2) In the ten years before the implementation of NFPP, the carbon storage of forest vegetation increased by 290.65 Tg C, and in the ten years after its implementation, the carbon storage of forest vegetation increased by 705.12 Tg C. The increase in carbon storage of the six provinces in the upper reaches of the Yangtze River from 1999~2003 to 2004~2008 was 154.1 Tg C, which was 80.92 Tg C higher than the increase in carbon storage from 1989~1993 to 1994~1998 (73.18 Tg C). Therefore, the implementation of NFPP can improve the carbon storage of vegetation in the local area.

(3) The carbon sequestration benefit of forest vegetation in the upper reaches of the Yangtze River is 80.92 Tg C, within which the Tibet Autonomous Region has the highest carbon sequestration benefit of 48.96 Tg C. The forest soil carbon sequestration benefit of NFPP in the upper reaches of the Yangtze River is 7.23 Tg C, of which Guizhou Province's soil carbon sequestration benefit is the highest at 2.51 Tg C, indicating that the implementation of NFPP can further improve the capacity of forest carbon sinks.

ACKNOWLEDGEMENTS

This study was no funds supported.

REFERENCES

[1] Wei, Y., Yu, D., Lewis, B.J., Zhou, L.I., Zhou, W., Fang, X., Dai, L. (2014) Forest carbon storage and tree carbon pool dynamics under natural forest protection program in northeastern China. Geographical Science. 24(4), 397-405.

[2] Bremer, L.L., Wada, C.A., Medoff, S., Page, J., Burnett, K.M. (2019) Contributions of native forest protection to local water supplies in east Maui. The Science of the Total Environment. 688(10), 1422-1432.

[3] Zhou, W., Lewis, B.J., Wu, S., Yu, D., Zhou, L., Wei, Y., Dai, L. (2014) Biomass carbon storage and its sequestration potential of afforestation under natural forest protection program in China. Geographical Science. 24(4), 406-413.
[4] Yang, H. (2017) China's natural forest protection program: progress and impacts. The Forestry Chronicle. 93(2), 113-117.
[5] Wei, F.J., Xu, F. (2012) The focus and content of the natural forest resource protection project. Science and Technology Entrepreneur. 10(2), 243-250.
[6] Cao, S., Wang, X., Song, Y., Chen, L., Feng, Q. (2010) Impacts of the Natural Forest Conservation Program on the livelihoods of residents of Northwestern China: Perceptions of residents affected by the program. Ecological Economics. 69(7), 1454-1462.
[7] Ma, Z., Xia, C., Cao, S. (2020) Cost-Benefit Analysis of China's Natural Forest Conservation Program. Journal for Nature Conservation. 55(8), 1258-1268.
[8] Dixon, R.K., Solomon, A.M., Brown, S., Houghton, R.A., Trexier, M.C., Wisniewski, J. (1994) Carbon pools and flux of global forest ecosystems. Science. 263(5144), 185-190.
[9] Alexeyev, V., Birdsey, R., Stakanov, V., Korotkov, I. (1995) Carbon in vegetation of Russian forests: methods to estimate storage and geographical distribution. Water, Air, and Soil Pollution. 82(1), 271-282.
[10] Batjes, N.H. (1996) Total carbon and nitrogen in the soils of the world. Soil Science. 47(2), 151-163.
[11] Birdsey, R., Pregitzer, K., Lucier, A. (2006) Forest carbon management in the United States. Journal of Environmental Quality. 35(4), 1461-1469.
[12] Bonan, G.B. (2008) Forests and climate change: forcings, feedbacks, and the climate benefits of forests. Science. 320(5882), 1444-1449.
[13] Fang, J.Y., Chen, A.P. (2001) The dynamic changes of China's forest vegetation carbon pool and its significance. Bulletin of Botany. 43(9), 967-973.
[14] Fang, J.Y., Chen, A.P., Zhao, S.P., Ci, L.J. (2002) Estimation of forest biomass in China: A comparison. Journal of Plant Ecology. 26(2), 43-49.
[15] Fang, J.Y., Guo, Z.D., Piao, S.L., Chen, A.P. (2007) Estimation of China's terrestrial vegetation carbon sequestration from 1981 to 2000. Science in China Series D. 37(6), 804-804.
[16] Wang, X.K., Feng, Z.W., Ouyang, Z.Y. (2001) Plant carbon storage and carbon density of China's forest ecosystems. Journal of Applied Ecology. 12(1), 13-16.
[17] Pan, Y., Luo, T., Birdsey, R., Hom, J., Melillo, J. (2004) New estimates of carbon storage and sequestration in China's forests: effects of age-class and method on inventory-based carbon estimation. Climatic Change. 67(2), 211-236.
[18] Zhao, M., Zhou, G.S. (2004) Analysis of plant carbon storage and its influencing factors in China's forest ecosystem. Geographical Science. 24(1), 50-54.
[19] Xu, X.L., Cao, M.K., Li, K.R. (2007) Research on the temporal and spatial dynamics of vegetation carbon storage in China's forest ecosystems. Advances in Geographical Sciences. 1(6), 3-12.
[20] Ou, Q.X., Li, H.K., Lei, X.D., Yang, Y. (2018) Analysis of the difference in estimation of masson pine biomass conversion and expansion factor based on inventory data in Fujian Province-Comparison of three ensemble learning decision tree models. Application Acta Ecologica Sinica. 29(6), 2007-2016.
[21] Van Den Berge, S., Vangansbeke, P., Calders, K., Vanneste, T., Baeten, L., Verbeeck, H., Verheyen, K. (2021) Biomass expansion factors for hedgerow-grown trees derived from terrestrial LiDAR. BioEnergy Research. 14(2), 561-574.
[22] Ma, Z., Ma, Z. (2015) Evaluation method and application of theoretical resource potential of forestry residues based on biomass conversion factors. Forestry Inventory and Planning. 40(1), 1-8.
[23] Zhang, C., Wang, S.S., Li, Y.H., Kang, H., Mei, E.H., Chi, Y.C., Luo, Y.Y., Zhang, T., Meng, F.X., Nie, Q. (2018) Salix biomass and its relationship with growth factors based on different stubble times Relationship Research. Forestry Investigation and Design. 13(5), 98-104.
[24] Han, F.Y., Zhou, Q.Y., Chen, S.X., Chen, W.P., Li, T.H., Wu, Z.H., Jian, M. (2010) Study on the biomass and energy of two eucalyptus species at different ages. Forestry Science Research. 21(5), 690-696.
[25] Huang, Y.F., Liu, Y., Huang, S.Y., He, B.L., Chen, L.J., Li, Y.Q. (2015) Research on the growth and biomass allocation of Masson pine forests of different ages. Forestry Science and Technology. 36(4), 72-75.
[26] Ou, G.L., Xu, H. (2020) A review of forest biomass models. Journal of Southwest Forestry University. 40(1), 7-16.
[27] Puhlick, J.J., Fraver, S., Fernandez, I.J., Teets, A., Weiskittel, A.R., Kenefic, L.S. (2019) Site quality, disturbance, and vegetation effects on carbon storage and accumulation in old, mixed-species stands in central Maine, USA. Natural Areas Journal. 39(4), 429-441.
[28] Sohel, M., Alamgir, M., Akhter, S., Rahman, M. (2015) Carbon storage in a bamboo (Bambusa Vulgaris) plantation in the degraded tropical forests: implications for policy development. Land Use Policy. 49(6), 142-151.

Received: **29.11.2021**
Accepted: **23.01.2022**

CORRESPONDING AUTHOR

Yalin Yang
General Graduate School,
Kyonggi University,
Suwon Kyonggi-do 16227 – Korea

e-mail: khhkfo@163.com

© by PSP Volume 31– No. 05/2022 pages 5057-5063 Fresenius Environmental Bulletin

EFFECTS OF DIFFERENT SUPPLEMENTAL LIGHT MODES ON THE BIOCHEMICAL ELEMENTS SYNTHESIS AND QUALITY OF TOMATO SEEDLINGS IN GREENHOUSE

Xinying Liu[1,2,*], Man Zhang[1], Minzan Li[1]

[1]Key Laboratory of Modern Precision Agriculture System Integration, Ministry of Education, China Agricultural University, Beijing 100083, China
[2]Tarim University, Alar, Xinjiang, 843300, China

ABSTRACT

Improving crop light environment can not only increase crop biomass accumulation, but also affect crop yield and quality. Therefore, exploring the light environment requirements of different crops has always been a research hotspot in the field of facility horticulture. In this paper, taking a region with short light time in western China as an example, the effect of leaf back light supplementation on the quality of greenhouse tomatoes was systematically studied. The results of the study show that according to the light intensity in the western region and the growth habit of tomatoes, it is necessary to properly supplement the light of greenhouse tomatoes. The net photosynthetic rate (P_n) of tomato leaves under supplemental light treatment was significantly higher than that of the control. During the test time, the change trend of P_n-PPFD is the same as that of P_n. Under the E1 treatment, the maximum P_n of the leaves under the saturated light intensity was the highest, which increased by 63.4% compared with the control; followed by E2 and E3, with an increase of close to 42.8%. Foliar spraying of exogenous calcium can increase crop yield and improve quality. Calcium not only promotes the growth and development of crops, but also improves the quality of crops by improving the absorption of mineral nutrients by plants. There is an interaction effect between different light supplement modes and calcium, and the effect of low-concentration calcium fertilizer on fruit morphology and quality is better than that of high-concentration calcium fertilizer. Under different photoperiod conditions, exogenous Fe fertilizer has a promoting effect on the photosynthetic characteristics and fruit quality of tomato leaves, and the effect of spraying 145 μmol/L Fe fertilizer on leaves under 16h/8h photoperiod is the best. This research can provide technical support for the high-yield and high-quality production of vegetables in areas with short sunlight hours in western China.

KEYWORDS:
Greenhouse environment, supplemental light model, seedling stage tomato, biochemical element synthesis, exogenous calcium fertilizer, exogenous Fe fertilizer

INTRODUCTION

The growth of crops is significantly affected by light [1-3]. Light can affect the synthesis of photosensitizing pigments in plants [4-5]. Plants mainly perceive the external environment through the body's biological clock and light signals [6-7]. Artificial light environment regulation is a precise and effective way of regulation. The artificial facility environment often uses LED plant growth lights to supplement the light of the crops, thereby promoting the synthesis and transportation of the photosynthetic products of the crops [8-9]. Previous studies have shown that LED light supplementation can increase the yield and biomass of tomato fruits [9-10]. In addition, photoperiod is one of the main factors that affect the growth and development of plants, which affects the formation of photosynthetic pigments, mineral elements and nutritional quality [11-13].

Light provides energy for plant life activities and is also an important environmental factor that affects plant growth and development [14-15]. Improving crop light environment can not only increase crop biomass accumulation, but also affect yield and quality. Therefore, exploring the light environment requirements of different crops has always been a research hotspot in the field of facility horticulture [16-17]. In some parts of western China, the light hours are short in winter, spring and late autumn, especially in spring with dusty and continuous cloudy days. There is a serious lack of light in the facility greenhouses, and the normal growth of crops is severely restricted. Using artificial light sources to supplement light for crops in the greenhouse is an effective way to ensure the normal growth of plants, promote high yield and quality, and improve the economic benefits of facilities [18-19]. At present, a large number of studies have conducted research on facility supplement light from multiple perspectives such as light source selection, light intensity, and light period

[18-20].

Existing research on leaf back light supplementation pays more attention to the yield of greenhouse tomatoes, and there are relatively few systematic researches on tomato quality [21-23]. In this paper, taking a region with short light time in western China as an example, the effect of leaf back light supplementation on the quality of greenhouse tomatoes was systematically studied. This research can provide technical support for the high-yield and high-quality production of vegetables in areas with short sunlight hours in western China.

MATERIALS AND METHODS

The tomato from A region in western China was used as the test material. The experiment uses commercial substrate cultivation and LED lamps. The light source board is composed of red (R) LED lamp beads with a wavelength of 635 nm, blue (B) LED lamp beads with a wavelength of 480 nm, and full-wavelength white (W) LED lamp beads in a ratio of 1:2:3.

The photosynthetic parameters and chlorophyll fluorescence parameters were measured. During the supplemental light treatment, the Li-6400XT portable photosynthetic system (Li-Cor Inc., Lincoln, NE, USA) was used on the representative leaves of the bottom canopy every 6 d during 8:00~ 15:00, the photosynthetic parameters of the leaves were measured once, and a total of 20 measurements were carried out. For each measurement, 4 plants were selected for each treatment, and 5 sampling points of the same height were selected for each plant.

In addition, the experiment designed two factors of photoperiod and Fe (EDTA-Fe) concentration, among which, the photoperiod was set to 12h/12h (natural light) and 16h/8h (LED light supplement light 4 h). The distance between the LED light and the top of the plant can be adjusted to lock the growth height of the plant. The Fe concentration is set to 4 levels of 0 (CK), 100, 150, and 200 μmol/L.

RESULTS

Analysis of photosynthetically active radiation in the greenhouse. The light intensity required for plant growth is expressed by photosynthetically active radiation, so the total radiation exposure needs to be converted into photosynthetically active radiation for analysis. The conversion formula is shown in Formula (1).

$$PAR=Q\times A_1\times A_2 \quad (1)$$

In the formula, PAR represents photosynthetically active radiation, μmol/m^2•s, Q represents total radiation exposure, MJ/m^2, A_1 represents 0.01MJ/m^2=0.086 W/m^2, and A_2 is the light energy conversion coefficient.

Due to the influence of the maintenance structure of the greenhouse, the light intensity in the greenhouse is only 30% to 70% of the outdoor light intensity. Therefore, the light intensity in the greenhouse in this study is calculated as 60% of the outdoor light intensity. The photosynthetically active radiation required for tomato crop growth is above 300 μmol/(m^2·s) to satisfy its vegetative growth and fruit development. It can be seen from Figure 1 that the light intensity in the study area is relatively low from February to April in spring and September to October in autumn. Therefore, if long-season tomato cultivation is to be carried out in the greenhouse of the study area, it is necessary to formulate corresponding supplementary light strategies according to the natural light conditions in different seasons.

Studies have shown that the light environment at the seedling stage is very important for the growth of tomatoes [24-26]. Weak light in the seedling stage will cause the stems and leaves of the seedlings to be weak, and in severe cases, it will lead to the lengthening of the seedlings, resulting in weak growth of the tomato in the later stage, and ultimately affect the yield and quality. The photosynthetically active radiation required at the tomato seedling stage is about 200 μmol/(m^2·s). The long-season tomato seedling cultivation period in the study area is July, August, and September. The average photosynthetically active radiation in the greenhouse during these three months is about 189 μmol/(m^2·s). It can basically meet the light requirements of the tomato seedling stage, without additional artificial light supplementation.

When the seedling period of the tomato plants is over, the tomato plants begin to enter the vegetative growth and reproductive growth period. Because the requirements of the light intensity of the tomatoes in these two periods are similar, they are collectively referred to as the growth period here. During the growth period, tomato plants have an increased demand for light. The light environmental conditions at this stage will directly affect the growth of the tomato plant, the fruit setting rate, and the yield and quality of the fruit. It is an important stage that affects the yield of the tomato. Studies have shown that the photosynthetically active radiation required by tomatoes after entering the growth stage needs to be greater than 300 μmol/(m^2·s), and the light duration is 15h/d. After the beginning of October, the photosynthetically effective radiation in the greenhouse cannot reach the required light intensity, and artificial light supplementation is needed to adjust it.

The natural light in the study area is relatively sufficient, but there are obvious seasonal differences, in which summer and autumn have high light intensity and long sunshine hours. Moreover, the average daily radiation exposure outdoors in summer can reach 9.53 MJ/m^2, and the sunshine hours are 7.3 h/d. Due to the influence of the greenhouse maintenance

structure, the indoor light intensity is lower than the outdoor natural light. Assuming that 60% of the light enters the greenhouse, the conversion shows that the photosynthetic active radiation in the greenhouse is 184 μmol/(m^2·s). The average daily radiation exposure outdoors in autumn can reach 8.45 MJ/m^2, the sunshine duration is 6.4 h/d, and the photosynthetic active radiation in the greenhouse is 177 μmol/(m^2·s). The average daily radiation exposure outdoors in spring can reach 7.93 MJ/m^2, the sunshine duration is 4.5 h/d, and the photosynthetic active radiation in the greenhouse is 157 μmol/(m^2·s). The outdoor average daily radiation exposure in winter is the lowest 6.22 MJ/m^2, the sunshine duration is 4.2 h/d, and the photosynthetic active radiation in the greenhouse is 133 μmol/(m^2·s). According to the light conditions in the study area and the arrangement of the cultivation stubble, seedlings are grown in the greenhouse in July, August, and September. At this time, the light intensity in the greenhouse meets the needs of the tomato seedlings for light, so no additional artificial light is needed. However, when the tomato plant enters the period of vegetative growth and reproductive growth, the light intensity in the greenhouse cannot meet the normal growth needs of the tomato plant. It needs to be artificially supplemented with light to meet the growth requirements of tomato crops, so as to ensure the yield and quality of tomato plants in the greenhouse.

Analysis of photosynthetic parameters of tomato leaves with different supplementary light treatments. The light environment directly affects the growth and development of plants, and there is low light in the facility due to unfavorable weather conditions such as sand, rain, snow, and continuous shade [27-28]. It will not only inhibit plant growth and limit crop production potential, but it is more likely to cause disease to occur, which in turn will reduce the economic benefits of the facility. Usually, the amount of light in the middle and lower canopy of tomato is very low, and this part of the canopy is directly supplemented with light. And when the supplemental light intensity is 100~200 μmol·m^{-2}·s^{-1}, it can better promote the improvement of the photosynthetic parameters of tomato leaves and avoid excessive supplementary light. Based on this, combined with the cost of LED lamps, this experiment set up 100 μmol·m^{-2}·s^{-1} continuous fill light (E1, E3) and 200 μmol·m^{-2}·s^{-1} intermittent fill light (E2) fill light mode. The test results showed that the instantaneous P_n of the leaves under the supplementary light treatment (E1) of 100 μmol·m^{-2}·s^{-1} per day was significantly higher than that of other treatments. At the same time, the light response curve also shows that the response speed of the leaves to the light intensity under the E1 treatment is fast, and the maximum P_n under the saturated light intensity is also significantly higher than other supplementary light treatments. It shows that the photosynthetic potential of leaves is the best in this light supplement mode.

It can be seen from Figure 2 that the net photosynthetic rate (P_n) of tomato leaves under the supplemental light treatment was significantly increased compared with the control. The E1 treatment increased by 57.4% compared with the control, and the E2 and E3 treatments increased by about 44.6% and 44.0% compared with the control. There was no significant difference in the parameter values under the treatments of E1, E2 and E3, and they were all significantly higher than those of the control group. By drawing the light response curve, it can be seen that within the test time, the change trend of P_n-PPFD is the same as that of P_n (Figure 3). Under the E1 treatment, the maximum P_n of the leaves under the saturated light intensity was the highest, which increased by 63.4% compared with the control; the E2 and E3 treatments followed, and the increase was close to 42.8%.

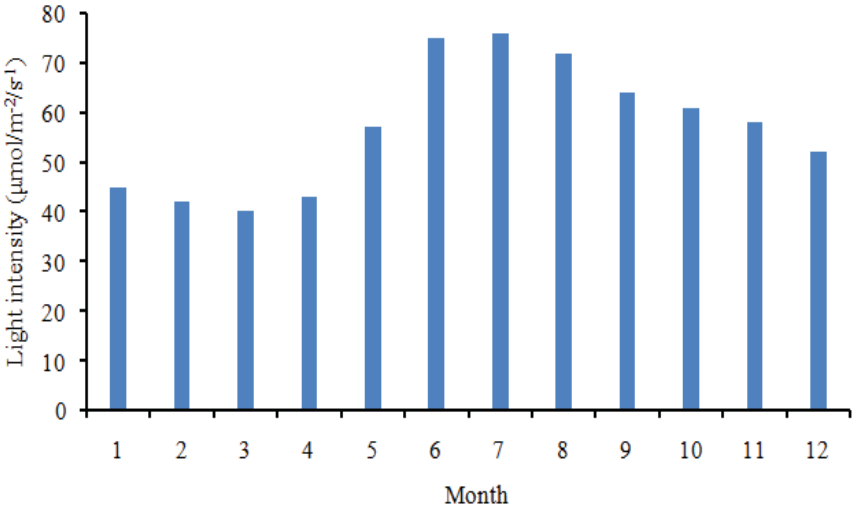

FIGURE 1
Distribution of light intensity in different months in A region of western China.

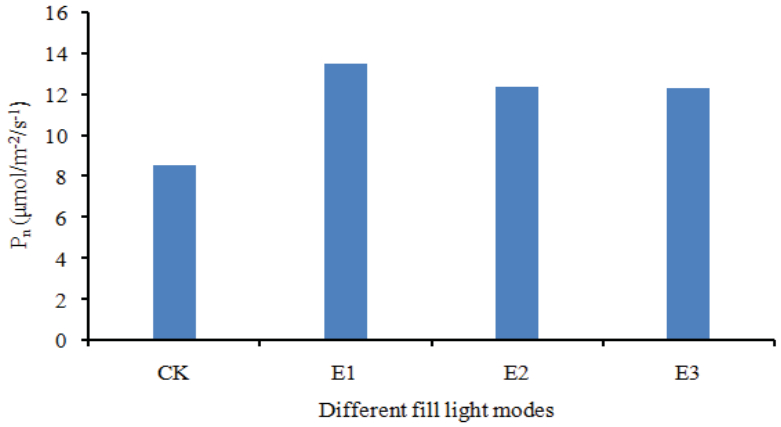

FIGURE 2
***P*n distribution characteristics under different fill light modes.**

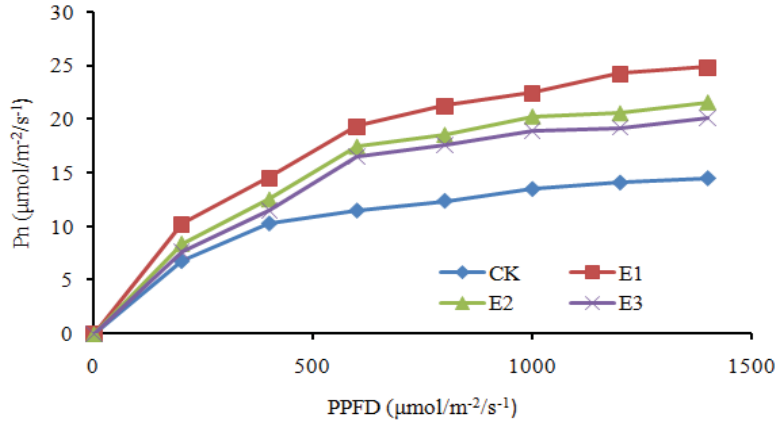

FIGURE 3
Relationship between Pn and PPFD in different fill light modes.

The maturation time of tomato fruits treated with supplemental light was significantly earlier, 28 days after planting, the plants treated with supplemental light began to bloom. 78 days after planting, the fruits of E1 treatment began to turn red, and the fruits of other treatments were still in the green maturity stage. The ripening time of the fruits of E2 treatment was second only to that of E1 treatment. After 81 days of planting, the fruits of E1 and E2 treatments had basically completed their color changes, and the E3 treatments began to change colors, while the control fruits were still in the green maturity stage, and the controls did not fully mature until 89 days after planting. The quality and yield of tomato single fruit of each supplemental light treatment were significantly improved, and the quality and yield of single fruit of E1 and E2 treatments were significantly higher than those of the control group.

Effects of different light supplement modes and calcium on morphological indexes of tomato fruits. Compared with CK, different light test conditions and calcium fertilizers can increase the quality, horizontal diameter, vertical diameter, and fruit hardness of the fruit to varying degrees. Compared with E2 and E3, E1 treatment tomato fruit single fruit quality, lateral diameter and longitudinal diameter were significantly improved, and the fruit hardness increased but the difference was not significant. The quality of single tomato fruit in E1 treatment was increased by 17.43% and 17.14% compared with E2 and E3 treatments, respectively [3,29].

It can be seen from Figure 4 that compared with CK, different light supplement modes and calcium fertilizers can significantly increase the soluble solid content of tomato fruits. Among them, the content of soluble solids in the fruits of E1 treatment was higher. Foliar spraying of exogenous substances such as calcium and silicon can increase crop yield and improve quality. Calcium not only promotes the growth and development of crops, but also improves the quality of crops by improving the absorption of mineral nutrients by plants. This study showed that, compared with the control, the individual fruit quality, horizontal diameter and vertical diameter of tomato fruits under different supplemental light modes and calcium coupling treatments were significantly higher than those of the control group. This indicates that there is an interaction effect between different light supplementation modes and calcium. It also showed that low-concentration calcium fertilizers had better effects on fruit morphology and quality than high-concentration calcium fertilizers.

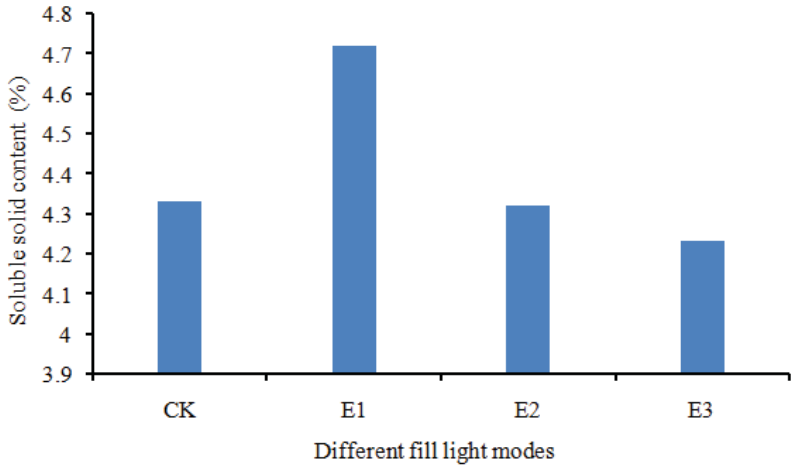

FIGURE 4
Effects of different light supplement modes and calcium fertilizer conditions on the soluble solid content of tomato fruits.

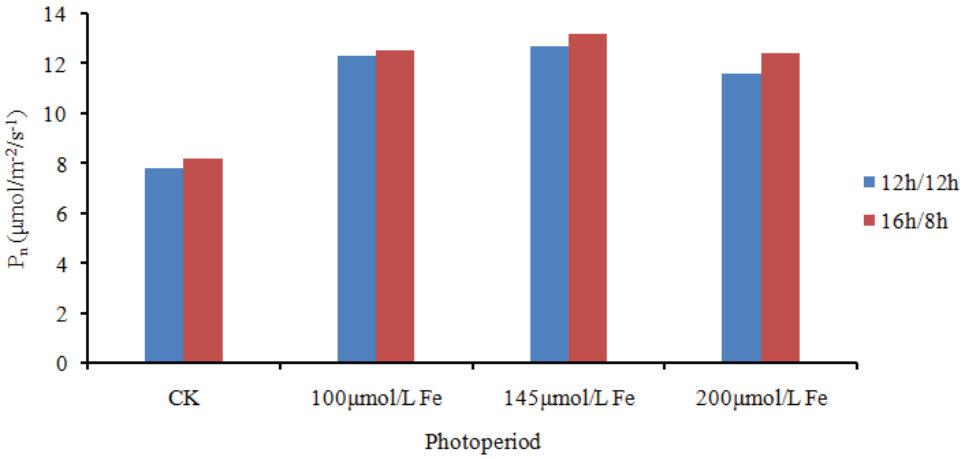

FIGURE 5
Effects of photoperiod and exogenous iron on photosynthetic characteristics of tomato leaves.

Effects of photoperiod and exogenous iron on photosynthetic characteristics of tomato leaves. The study found that with the increase of Fe concentration, the chlorophyll a (Chla), chlorophyll b (Chlb), carotenoid (Caro) and total chlorophyll content (Chla+b) of tomato leaves showed a trend of first increasing and then decreasing. Under the conditions of 12h/12h photoperiod, the content of Chla, Chlb, Caro, and Chla+b in tomato pages treated with 145 μmol/L Fe were the highest, which increased by 23.5%, 21.4%, 20.6 and 23.2% compared with CK, respectively. Compared with the 12h/12h photoperiod, the chlorophyll and carotenoid content of tomato leaves under the 16h/8h photoperiod increased to varying degrees. And when the Fe concentration is 145 μmol/L, the content of Chla, Chlb, Caro, and Chla+b is the highest.

As shown in Figure 5, under the two photoperiod conditions, with the increase of Fe concentration, the net photosynthetic rate (Pn) of tomato leaves showed a trend of first increasing and then decreasing. Compared with the 12h/12h photoperiod, the P_n of tomato leaves increased under the 16h/8h photoperiod, and the P_n of the leaves treated with Fe at 145 μmol/L was the highest for the above two photoperiods. Among them, the P_n of the 12h-145Fe leaves was significantly increased by 44.3% compared with the 16h-CK treatment, and the P_n of the 16h-145Fe pages was significantly increased by 35.2% compared with the 16h-CK treatment.

As an essential element for the synthesis of plant chlorophyll precursors, Fe participates in driving electron transfer. In this experiment, under the two photoperiod conditions, spraying Fe fertilizer on the page increased the total chlorophyll content and P_n of tomato leaves, and the effect of spraying 145 μmol/L Fe fertilizer on the leaves under the 16h/8h photoperiod was the most significant. This indicates that spraying Fe fertilizer with appropriate concentration on the page under long photoperiod is more conducive to leaf chlorophyll accumulation, light energy capture and electron transfer, thereby significantly enhancing the photosynthesis of tomato leaves. The results of this experiment also showed that under the two photoperiods, with the increase of

the concentration of exogenous Fe, the P_n of tomato leaves showed a trend of first increasing and then decreasing [30]. Under light conditions, plants synthesize CO_2 and H_2O into ATP through photoreactions, provide energy and reduction power for carbon assimilation, fix CO_2 and convert it into sugars, and starch organic matter to maintain plant growth and development. Soluble protein, lycopene and VC are important indicators to characterize the quality of horticultural crops. This study believes that spraying Fe fertilizer on the page can improve the nutritional quality of crops to a limited extent. In this experiment, compared with the same treatment under the 12h/12h photoperiod, the tomato soluble sugar, soluble protein, and lycopene content under the 16h/8h photoperiod all increased to varying degrees, and the overall sugar-acid ratio also increased. The effect of spraying 100, 145 μmol/L Fe fertilizer is the most obvious, which is consistent with previous conclusions. Therefore, under the two photoperiod conditions, the exogenous Fe fertilizer has a promoting effect on the photosynthetic characteristics and fruit quality of tomato leaves, and the effect of spraying 145 μmol/L Fe fertilizer on the leaves under the 16h/8h photoperiod is the best.

CONCLUSIONS

(1) In this paper, taking a region with short light time in western China as an example, the effect of leaf back light supplementation on the quality of greenhouse tomatoes was systematically studied.

(2) The results of the study show that according to the light intensity in the western region and the growth habit of tomatoes, it is necessary to properly supplement the light of greenhouse tomatoes. The net photosynthetic rate (P_n) of tomato leaves under supplemental light treatment was significantly higher than that of the control.

(3) During the test time, the change trend of P_n-PPFD is the same as that of P_n. Under the E1 treatment, the maximum P_n of the leaves under the saturated light intensity was the highest, which increased by 63.4% compared with the control; followed by E2 and E3, with an increase of close to 42.8%.

(4) Foliar spraying of exogenous calcium can increase crop yield and improve quality. Calcium not only promotes the growth and development of crops, but also improves the quality of crops by improving the absorption of mineral nutrients by plants. There is an interaction effect between different light supplement modes and calcium, and the effect of low-concentration calcium fertilizer on fruit morphology and quality is better than that of high-concentration calcium fertilizer.

(5) Under different photoperiod conditions, exogenous Fe fertilizer has a promoting effect on the photosynthetic characteristics and fruit quality of tomato leaves, and the effect of spraying 145 μmol/L Fe fertilizer on leaves under 16h/8h photoperiod is the best.

ACKNOWLEDGEMENTS

This work was not supported by any funds. The authors want to thank all the techniques who have contributed to this research and all the authors of the references.

REFERENCES

[1] Deans, R.M., Brodribb, T.J., Busch, F.A., Farquhar, G.D. (2019) Plant water-use strategy mediates stomatal effects on the light induction of photosynthesis. New Phytologist. 222(1), 382-395.

[2] Fan, X., Xu, Z., Liu, X., Tang, C., Wang, L., Han, X. (2013) Effects of light intensity on the growth and leaf development of young tomato plants grown under a combination of red and blue light. Scientia Horticulturae. 153, 50-55.

[3] Fischer, R.A., Rees, D., Sayre, K.D. (1998) Wheat yield progress associated with higher stomatal conductance and photosynthetic rates, and cooler canopies. Crop Science. 38, 1467-1475.

[4] Hernandez, R., Kubota, C. (2016) Physiological responses of cucumber seedlings under different blue and red photon flux ratios using LEDs. Environmental and Experimental Botany. 121, 66-74.

[5] Lu, N., Maruo, T., Johkan, M., Hohjo, M., Tsukagoshi, S., Ito, Y., Shinohara, Y. (2012) Effects of supplemental lighting with lightemitting diodes (LEDs) on tomato yield and quality of singletruss tomato plants grown at high planting density. Environmental Control in Biology. 50(1), 63-74.

[6] Singh, K.K., Goswami, T.K. (1998) Mechanical properties of cuminseed (Cuminumcyminum Linn) under compressive loading. Journal of Food Engineering. 36(3), 311-321.

[7] Fan, S., Yi, D. (2002) The effect of calcium on the nutrient absorption and growth of leaf lettuce. Acta Horticultural Sinica. 29(2), 149-152.

[8] Li, J., Zhang, M., Lin, Q. (2005) The interaction of potassium, calcium and magnesium on the growth and nutrient absorption of flue-cured tobacco. Journal of Anhui Agricultural University. 32(4), 529-533.

[9] Fu, R., Meng, X., Chai, S. (2019) Research progress on the relationship between plants and calcium environment. Northern Horticulture. 426(3), 167-172.

[10] Luo, X., Wang, S., Zhang, G. (2013) The effect of calcium ion concentration on photosynthesis of two ferns. Chinese Journal of Eco-environment. 22(2), 258-262.

[11] Zu, Y.G., Wei, X.X., Yu, J.H. (2011) Responses in the physiology and biochemistry of Korean pine (Pinuskoraiensis) under supplementary UV-B radiation. Photosynthetica. 49(3), 448-458.
[12] Ren, J., Duan, B., Zhang, X. (2010) Differences in growth and physiological traits of two poplars originating from different altitudes as affected by UV-B radiation and nutrient availability. Physiologia Plantarum. 138(3), 278-288.
[13] Mohammed, A.R., Tarpley, L. (2011) Morphological and physiological responses of nine southern US rice cultivars differing in their tolerance to enhanced ultraviolet-B radiation. Environmental and Experimental Botany. 70(2), 174-184.
[14] Lidon, F.C. (2012) UV-B irradiation in rice: interaction between micronutrients accumulation and the photosynthetic performance. Journal of Plant Interactions. 7(1), 19-28.
[15] Li, J., Tang, H., Chen, H. (2010) Effects of exogenous carbon monoxide on the antioxidant system of rice seedlings under drought stress. Northwestern Journal of Botany. 30(2), 330-335.
[16] Yang, Y., Yuan, H. (2001) Biological effects of ultraviolet UV-B irradiation on peanuts. Journal of Southwest Agricultural University. 23(4), 356-359.
[17] Gao, J. (2006) Plant Physiology Experiment Guide. Beijing: Higher Education Press. 67-69.
[18] Li, C., Zhong, Z. (2007) Simulating the photosynthetic physiological response of Pinustabulaeformis seedlings under the conditions of soil moisture changes in the hydro-fluctuating zone of the Three Gorges reservoir. Journal of Beijing Forestry University. 29(3), 23-28.
[19] Zhang, W., Wu, W. (2020) A novel spatial layout planning method of urban greening environment based on genetic algorithm. Fresen. Environ. Bull. 29(8), 6960-6968.
[20] Li, Y., Jin, Z. (2012) Diurnal changes of photosynthetic rate and chlorophyll fluorescence parameters of Magnolia leaves. Jiangsu Agricultural Sciences. 40(9), 164-168.
[21] Singh, A., Sarkar, A., Singh, S. (2010) Investigation of supplemental ultraviolet-B-induced changes in antioxidative defense system and leaf proteome in radish (Rophanussativus L. cv Truthful): an insight to plant response under high oxidative stress. Protoplasma. 245(1), 75-83.
[22] Wang, X., Liu, H., Han, R. (2008) Effects of He-Ne laser and enhanced UV-B radiation on protein metabolism of wheat seedlings. Acta Northwestern Botany. 28(1), 103-108.
[23] Wang, J., Li, Y., Liu, H. (2011) Research progress in chloroplast proteomics. Biotechnology Bulletin. 14(2), 1-6.
[24] Zhang, H., Wu, N., Hu, L. (2010) Effects of UV-B radiation stress of different intensities on the growth and chlorophyll fluorescence characteristics of broad bean seedlings. Journal of Southwest Normal University. 35(1), 105-111.
[25] Zhang, H., Wu, N., Hong, Y. (2008) The effects of UV-B radiation of different intensities on the germination and seedling growth of broad bean. Journal of Southwest University. 30(8), 132-136.
[26] Zi, X., Qiang, J., Chen, Z. (2006) The effect of UV-B radiation on the change of chlorophyll content of Yunnan Primula. Journal of Agricultural Environmental Sciences. 25(3), 587-591.
[27] Wang, C., Zheng, Y., He, D. (2003) Comparison of the sensitivity of different wheat indicators to the increase of ultraviolet radiation UV-B. Chinese Agricultural Science Bulletin. 19(6), 43-45.
[28] Li, J., Xu, Y. (2021) Impact of atmospheric fine particle pollution on the physical fitness of gymnasts in outdoor training based on the green environmental protection concept. Fresen. Environ. Bull. 30(1), 394-401.
[29] Zhang, F., He, Y., Zheng, Y. (2003) The effect of increased UV-B radiation on wheat. Journal of Nanjing Institute of Meteorology. 26(4), 545-551.
[30] Hu, L., Wu, N., Chen, F. (2010) Effects of salicylic acid on the fluorescence characteristics and antioxidant capacity of cucumber under UV-B stress. Journal of Southwest Normal University. 35(3), 191-96.

Received: **29.11.2021**
Accepted: **23.01.2022**

CORRESPONDING AUTHOR

Xinying Liu
Key Laboratory of Modern Precision Agriculture System Integration,
Ministry of Education,
China Agricultural University,
Beijing 100083 – China

e-mail: 2492402704@qq.com

© by PSP Volume 31– No. 05/2022 pages 5064-5070 Fresenius Environmental Bulletin

STRATIGRAPHIC DIVISION AND CORRELATION OF JURASSIC IN BAYAN HUSHU SAG HAILAR BASIN

Zhenzhen Jia*

Exploration and Development Research Institute, Daqing Oilfield Company Limited, Daqing Heilongjiang 163712, China

ABSTRACT

In order to determine the age and distribution characteristics of the Jurassic strata in the Bayanhushu Sag, Hailar Basin, by using core description, zircon U-Pb dating, geochemical analysis of rare earth elements, and logging characteristics, research on the division and correlation of Jurassic strata in Bayanhushu Sag has been carried out. The results show that the Jurassic of the Bayanhushu Sag in the Hailar Basin has developed the Triassic volcanic-sedimentary (coal-bearing) sequence from bottom to top, the Lower Jurassic Hongqi Wanbao Formation, the Middle-Upper Jurassic Tamulangou Formation, the second member of the Upper Jurassic Tamulangou Formation and the third member of the Lower Cretaceous Tamulangou Formation. Among them, the Triassic volcanic-sedimentary (coal-bearing) sequence is dominated by acidic volcanic rocks and sedimentary rocks, with a stratigraphic age ranging from 248 to 203 Ma. The Lower Jurassic Hongqi Wanbao Formation is dominated by intermediate acidic volcanic rocks and sedimentary rocks, with a stratigraphic age ranging from 197 to 181 Ma. The first member of the Middle-Upper Jurassic Tamulangou Formation is dominated by sedimentary rocks, intermediate-basic volcanic rocks and acidic volcanic rocks, with a stratigraphic age ranging from 171 to 156 Ma. The second member of the Upper Jurassic Tamulangou Formation is dominated by acidic volcanic rocks and sedimentary rocks and a small amount of intermediate-basic volcanic rocks, with a stratum age of 152-145 Ma. The third member of the Tamulangou Formation of the Lower Cretaceous is dominated by intermediate-basic volcanic rocks and sedimentary rocks, with undeveloped sedimentary rocks, and the stratum's age is 145-128 Ma. Finally, the Jurassic stratigraphic framework of Bayanhushu Sag is established, which provides guidance for understanding the development characteristics of Jurassic stratigraphy in Bayanhushu Sag, Hailar Basin.

KEYWORDS:
Bayan Hushu Sag, U-Pb dating, geochemistry, stratigraphic correlation, characteristics

INTRODUCTION

The Hailar Basin is a Mesozoic and Cenozoic continental faulted basin in the eastern part of the Inner Mongolia Autonomous Region. Due to its large area and rich oil and gas, the basin has attracted more and more attention [1-2]. The Bayan Hushu Sag is a secondary structural unit in the Zhalai Nuoer Depression in the west of the Hailar Basin. It covers an area of about 1500 km^2. It is a typical west-to-east ultra-single-fault-shaped sag (Figure 1) [3-5]. The exploration work in this depression began in the 1950s, with gravity, magnetic, seismic exploration and a large number of field geological surveys. In 2010, wells Shu 1 and Chu 5 located in the western steep slope zone successively obtained industrial oil flow, which proved that this depression has great exploration potential and is expected to become an important reserve replacement area in the Hailar Basin [6-9].

Stratigraphic division and comparison is the basic work in the geological work of oilfield development. The fineness and reliability of stratigraphic division and comparison are important for developing basin structure and analysis, determining the distribution of sedimentary systems, analyzing favorable reservoir-caprock combinations, understanding the distribution of oil and gas, and predicting favorable stratigraphic traps. The geological design of drilling is of great significance [10-13]. At present, the most used stratigraphic division methods include: lithostratigraphic division, which divides stratigraphic units based on one rock feature or a combination of several rock characteristics; biostratigraphic division, which divides stratigraphic units based on the same biological fossil content and its distribution range; chronostratigraphic division which is to divide stratigraphic units based on the geological time of formation of rock layers [14-18]. Different types of stratigraphic divisions can be superimposed on the same section, which is the concept of multiple stratigraphic divisions in modern stratigraphy.

The research foundation of Jurassic stratigraphy in Bayanhushu Sag of Hailar Basin is relatively weak. In addition, the Jurassic strata have the characteristics of large formation time span, large strata thickness, uneven distribution range, and complex

strata lithology. There is a lack of systematic and accurate understanding of whether large-scale Jurassic strata developed in the sag and the age, scale and distribution characteristics of the Jurassic strata. This study is planned to conduct systematic research on the Jurassic strata in Bayanhushu Sag, Hailar Basin in order to clarify the Jurassic stratigraphic sequence and correlation in the depression, and find favorable hydrocarbon generation and reservoir formation, providing direction and basis for oil and gas exploration in deep Jurassic strata in Hailar Basin.

MATERIALS AND METHODS

(1) Experimental materials and instruments. GeoLasPro excimer laser (Germany COMPEX company), PW1404/10 X-ray fluorescence spectrometer (Beijing Obotong Optical Technology Co., Ltd.), Aglient7500a plasma mass spectrometer (Agilent, USA), rock sample breaking machine, 91500 standard zircon samples, NIST630 synthetic silicate glass. The core samples are from Chu 8, Chu 4, Chu 3, Chu 5, Chu 1, Chu 10, Chu 15 and Chu 16 wells (Table 1).

(2) Experimental method. Zircon U-Pb chronological analysis method: He is used as the carrier gas of the denuding substance, and the instrument is optimized using the artificially synthesized silicate glass standard reference material NIST610 developed by the National Institute of Standards and Technology. 91500 standard zircon external calibration method is used for zircon in-situ U-Pb analysis; A laser beam spot with a diameter of 32μm and a frequency of 7Hz is used for sample analysis; GLITTER software is used to calculate the isotope ratio and $^{207}Pb/^{206}Pb$、$^{206}Pb/^{238}U$、$^{207}Pb/^{235}U$ age value; Andersen's method is used to correct the results for ordinary lead; The isoplot program is used to calculate its age.

Analysis methods of rare earth elements: A rock crusher is used to coarsely crush and select pure protolith samples; Acid foam treatment is carried out on samples where carbonate minerals can be observed. The acid is 10% hydrochloric acid, soaked for 24 hours; the acid is washed away with distilled water after the soaking is completed; the sample is dried in a drying oven at 60°C; the sample is crushed with an agate ball mill.

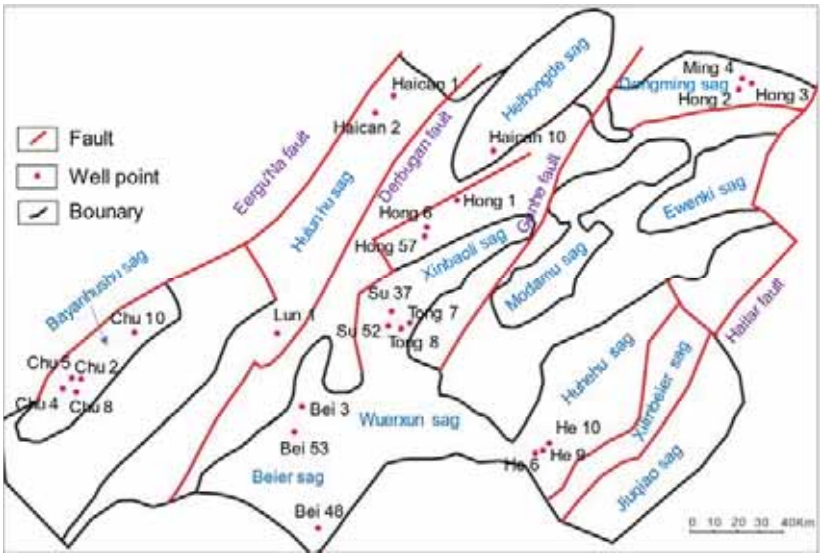

FIGURE 1
Tectonic unit diagram of Hailar Basin.

TABLE 1
Table of sampling locations of core samples

No.	Well name	Depth（m）	No.	Well name	Depth（m）	No.	Well name	Depth（m）
1	Chu 8	1655.5	6	Chu 4	2109.92-2119.2	11	Chu 15	1130.0m-1140.0
2	Chu 3	1413.2	7	Chu 4	2047.18-2056.46	12	Chu 15	The first core section 0.57-0073
3	Chu 3	1611.9	8	Chu 5	2260-2270	13	Chu 15	1330.0-1340.0
4	Chu 3	1616.5	9	Chu 10	1630.85	14	Chu 4	2999.75-3005.65
5	Chu 3	2178.8	10	Chu 8	1856.0-1866.0	15	Chu 16	2197.12

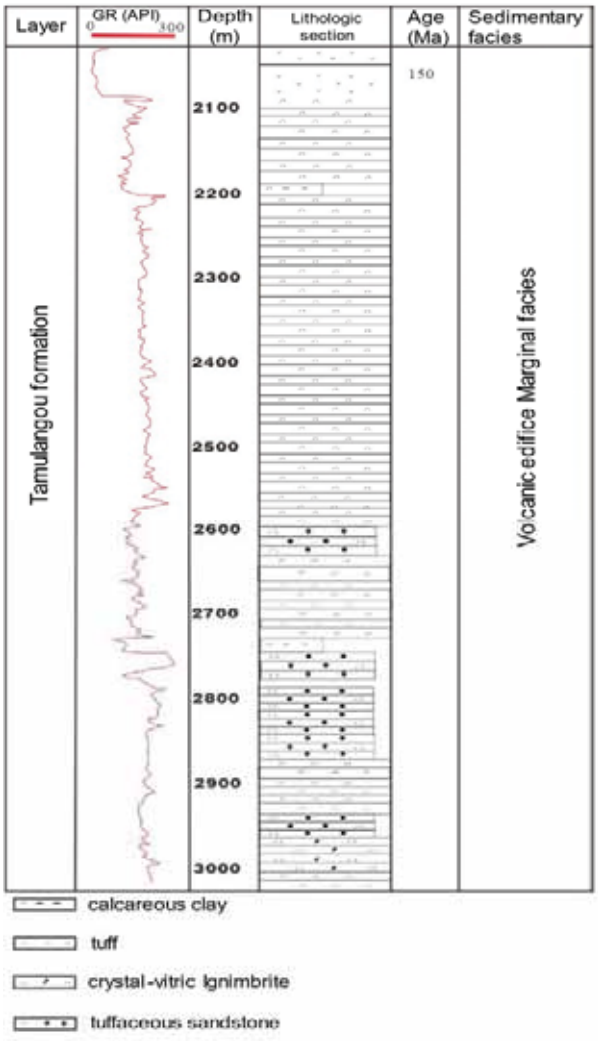

FIGURE 2
Comprehensive histogram of Jurassic strata in Well Chu 4 of Bayan Hushu Sag.

RESULTS

(1) Stratum comparison and division. 1) Drilling formation rock combination and logging characteristics. Chu 8, Chu 4, Chu 3, Chu 5, Chu 1, Chu 10, Chu 15, and Chu 16 were drilled into Jurassic strata in Bayan Hushu Sag. Taking Chu 4 as an example, the stratum below the T4 interface drilled in Well Chu 4 can be divided into 3 layers according to the difference in rock combination and logging characteristics. The lithology of the lower stratum is mainly acidic volcanic rock and thin layer of sedimentary rock. The rock type is mainly rhyolite tuff lava, rhyolite, rhyolite breccia tuff, tuffaceous mudstone, and tuffaceous sandstone. The lithology of the middle strata is mainly acidic volcanic rock with thin layers of sedimentary rock. The rock types are mainly rhyolite, Rhyolic tuff lava, rhyolitic tuff, tuffaceous siltstone, tuffaceous mudstone, etc. The upper strata are mainly intermediate-basic volcanic rocks, and the specific rock types are trachy andesitic aggregate breccia tuff lava.

The logging characteristics of each well section of the Ta-2 member in Well Chu 4 are as follows: the lowest stable rhyolite and rhyolite tuff lava section is from 3026 to 2783m. It has high natural gamma (GR) value, with the average value of 193API. The shape of each curve is straight and stable. The upper rhyolite with tuffaceous mudstone and rhyolite tuff section is 2783-2556m, the thick rhyolite section in the middle of each curve is straight and stable, and the top and bottom tuffaceous mudstone and rhyolite tuff section presents a strong jagged jitter. The upper rhyolite section is 2556-2202m thick, with high natural gamma (GR) value, ranging from 150-241 API, with an average of 186 API, and the shape of each curve is straight and stable. The uppermost section of rhyolite tuff, tuffaceous siltstone, and tuffaceous mudstone is 2202-2085 m, and each curve presents a strong jagged jitter. The logging characteristics of the Lower Cretaceous Baiyin Gaolao/Meiletu Formation in Well Chu 4 are as follows: Trachy andesitic agglomerated breccia tuff lava section is from 2085 to 2028m with medium and low natural gamma (GR) value, ranging from 63 to 91API. The shape of each curve is straight and stable (Figure 2).

2) Chronological characteristics of stratigraphy. The measured age of Well Chu 8 is 148±0.85 Ma, which is the Late Jurassic. The measured age of Well Chu 10 is 244.7±5.4 Ma, which is the Middle Jurassic. The measured age of Well Chu 15 is 246.9±2.9 Ma, which is Early and Middle Triassic. The measured ages of Well Chu 3 are 120±1Ma, 127±4Ma, 125±1Ma, 126±1Ma. The part below the T4 interface of Well Chu 8 is the Jurassic strata. The upper part of Well Chu 3 below T4 is the Cretaceous strata, and the part below T4 interface of Well Chu 15 and Chu 10 is the Triassic strata.

3) Division and comparison of well-seismic stratigraphic sequence. The cross-section of the Chu 8-Chu 3 seismic well in Bayan Hushu Sag shows that there are both Jurassic and Cretaceous strata in the stratum bounded by the T4-T5 interface. Among them, the Chu 8 encounters mainly the Upper Jurassic. The lower part of Chu 3 encounters the Jurassic strata, and the upper part encounters the Lower Cretaceous strata. The upper Jurassic strata and the Lower Cretaceous strata are in angular unconformity contact. The Upper Jurassic stratigraphic sequence encountered in Chu 8 is mainly a set of acidic volcanic rocks with acidic pyroclastic rocks and sedimentary rocks. The Upper Jurassic stratigraphic sequence encountered in the lower part of Chu 3 drill is mainly a set of acidic volcanic clastic rocks. The lower Cretaceous stratigraphic sequence drilled from the upper part encounters the middle basic rock sequence-acid rock sequence-middle basic rock sequence-acid rock sequence from bottom

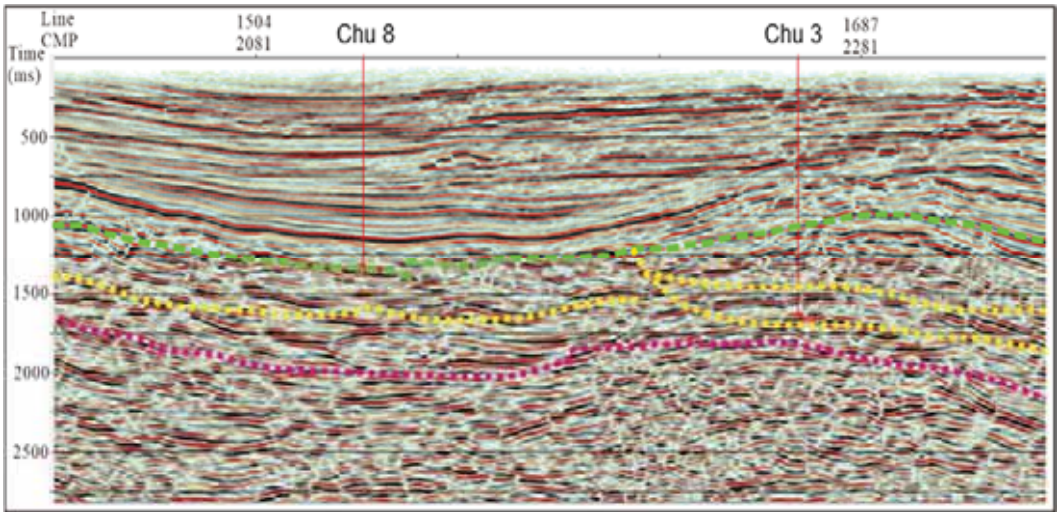

FIGURE 3
Jurassic seismic profile of Well Chu 8-Well Chu 3 in Bayan Hushu Sag.

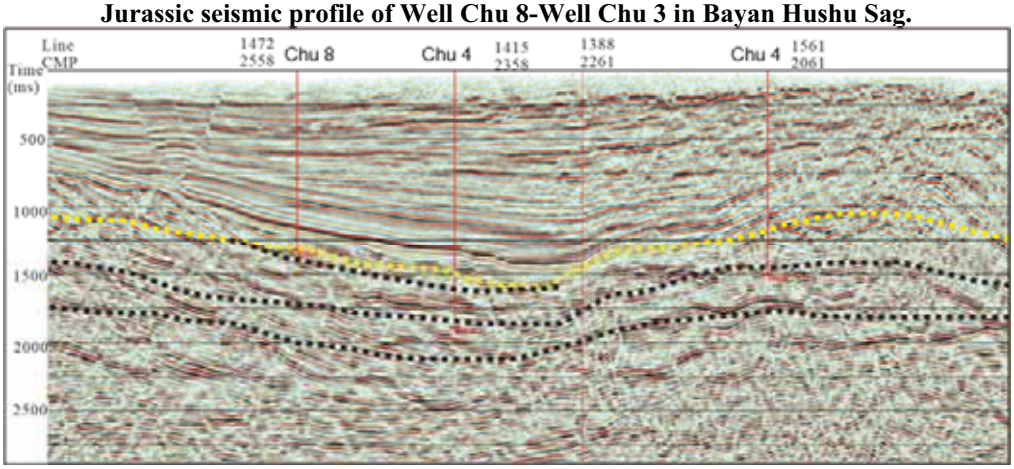

FIGURE 4
Jurassic seismic profile of Well Chu 8-Well Chu 4-Well Chu 5 in Bayan Hushu Sag.

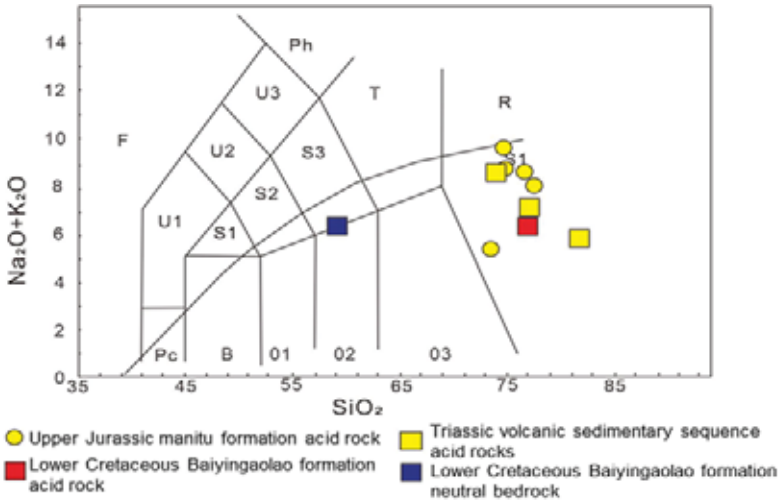

FIGURE 5
TAS diagram of volcanic rocks in Bayan Hushu Sag (base map according to Le Maritre, 1989).

to top. There are obvious lithology and logging interfaces on the wells of the boundaries of each layer, which can be continuously traced on the seismic section (Figure 3).

The comparison section of seismic strata and continuous well strata of Chu 8-Chu 4-Chu 5 in Bayan Hushu Sag shows that the confined strata at the T4-T5 interface of this section are mainly Jurassic strata, and there is also a small part of Cretaceous strata: among them, the main encounter of Chu 8 is

the Upper Jurassic formation (148Ma). The lower part of Chu 4 is the Middle-Upper Jurassic formation (161Ma), and the middle part is the Upper Jurassic formation (150Ma). It can be compared with the Upper Jurassic strata drilled in Chu 8. The two can be compared in rock assemblage, age, logging interface and seismic profile. The upper part drilled is the Cretaceous strata, which can be compared with the upper part of Chu 3. The strata of the Cretaceous strata drilled are compared, and the two can be compared in rock assemblage, age, logging interface and seismic profile (Figure 4).

4) Geochemical characteristics. The TAS diagram of volcanic rocks shows that the Triassic volcanic-sedimentary (coal-bearing) sequence acid rock, the acid rock of the second member of the Ta-2 member and the acid rock of the Ta-3 member mainly fall in the rhyolite area in the Bayanhushu sag of the Hailar Basin. In the trachytic andesite region, all samples in this depression are subalkaline series (Figure 5).

The REE distribution pattern of the basic volcanic rocks in the Bayan Hushu Sag of the Hailar Basin shows (Figure 6a) that the REE distribution pattern of the intermediate and basic rocks of the Ta-3 member is gentle to the right, with obvious differentiation of light and heavy rare earths, and enrichment of light rare earths. ∑LREE is 297.22 ppm, the heavy rare earth ∑HREE is 20.28 ppm, the light to heavy rare earth ratio ∑LREE/∑HREE is 14.66, the total rare earth ΣREE is 317.5 ppm, the Eu anomaly is not obvious, and the δEu value is 0.74 in acid volcanic rocks in Bayanhushu Sag, Hailar Basin. The distribution pattern diagram (Figure 6c) shows that the acidic volcanic rocks of the Triassic and the Ta-3 member have the same distribution pattern of rare earth elements, generally showing a gentle right-dipping pattern, with obvious differentiation of light and heavy rare earths, and enrichment of light rare earths. The ∑LREE is between 71.83-124.96 ppm, the heavy rare earth ∑HREE is between 6.09-15.57 ppm, the light and heavy rare earth ratio ∑LREE/∑HREE is between 8.03-11.79, the total rare earth ΣREE is between 77.92-140.53 ppm, and the Eu abnormality is not obvious. The δEu value is between 0.49-0.87. While the REE distribution pattern of acid volcanic rocks in the Ta-2 member is significantly different from that of the Triassic and Ta-3 member acid volcanic rocks. Type, light and heavy rare earths are distinctly differentiated, and light rare earths are enriched. ∑LREE is between 169.92-230.00 ppm, which is higher than the total amount of light rare earth elements in the acidic volcanic rocks of the Triassic and Ta-3 member. The total amount of heavy rare earths ∑HREE is between 11.08 -24.43ppm, which is higher than the total amount of heavy rare earth elements in the acidic volcanic rocks of the Triassic and the third member of the Tarim Basin. The light-heavy rare earth ratio ∑LREE/∑HREE is between 9.41 and 15.34, which is higher than that of the acid volcanic rocks of the Triassic and the Ta-3 member. The total amount of rare earth ΣREE is between 181.00-254.43 ppm, which is higher than the total amount of rare earths in the acidic volcanic rocks of the Triassic and the Ta-3 member. It has obvious negative Eu element anomalies, and the δEu value is between 0.12-0.43, which is significantly lower than the δEu value of the acidic volcanic rocks of the Triassic and the Ta-3 member.

The trace element spider web map of the basic rocks in the Bayan Hushu Sag of the Hailar Basin (Figure 6b) shows that the intermediate and basic volcanic rocks of Ta-3 member are generally right-dipping, with high field strength elements Pb enriched, and high field strength elements Nb, Ta, Sr, and Ti. The trace element spider map of acid rocks in the Bayan Hushu Sag of Hailar Basin shows (Figure 6d) that the Triassic acid volcanic rocks and the Ta-3 member acid volcanic rocks have relatively consistent trace element characteristics. Large ion lithophile elements Rb, K, high field strength elements Th, U, and Pb are enriched, large ion lithophile elements Ba, high field strength elements Nb, Ta, Sr, Ti, and element P are depleted. While the acid rocks of the second member of the tower are related to the Triassic and Tasan, the trace element characteristics of the acidic volcanic rocks of the second member are different. The specific manifestation is the large ion lithophile element K in the acid rock of the second member of the tower. The high field strength elements Th, U, Pb are more enriched than the latter two. The large ion lithophile element B, high field strength elements Sr and element P are also stronger than the Triassic and Ta-3 member, but the field strength elements Nb and Ta are less depleted than those of the Triassic and the Ta-3 member.

(2) Jurassic stratigraphic standard framework in Hailar Basin. There are 4 sets of strata developed from bottom to top in the T4-T5 confined strata in Bayanhushu Sag:

1) The lowermost part is the Triassic volcanic-sedimentary (coal-bearing) sequence, and the lithological characteristics are mainly composed of acidic volcanic rocks. The sedimentary rock has a coal line, and a small amount of intermediate-basic rocks are developed. The age is the Early Middle Triassic;

2) The Upper-Middle Jurassic strata are developed, and the lithological characteristics are mainly acidic volcanic rocks with thin layers of sedimentary rocks. The age and rock combination characteristics of this strata are similar to those of the Middle-Upper Jurassic Tamulangou Formation in the basin. Because the original strata (T4-T5 confined strata) were collectively referred as the Tamulangou Formation, we continue to use the original stratigraphic name. On this basis, it is divided into the first section of Tamulangou Formation, which can be compared with the Middle-Upper Jurassic Tamulangou Formation at the basin margin;

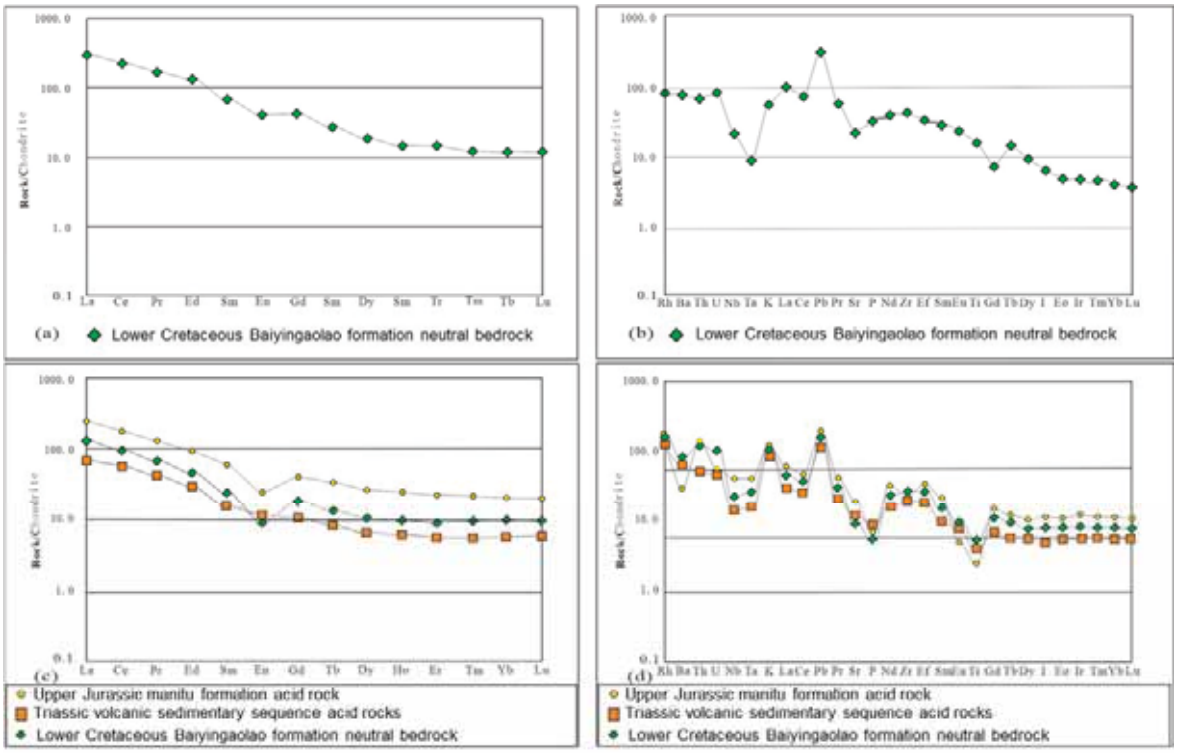

FIGURE 6
Standardized rare earth element formula diagram of volcanic chondrites in Bayan Hushu Sag.

3) Upper Jurassic strata is above the first member of the Middle-Upper Jurassic, and the lithological characteristics are mainly acidic volcanic rocks with thin layers of sedimentary rocks. Therefore, we named it the second member of Tamulangou Formation, and the age and rock combination of this strata are similar to those of the Upper Jurassic Manketo Obo/Manitu Formation at the basin margin;

4) A set of Lower Cretaceous strata developed above the second member of Tamulangou Formation. The lithology is characterized by the development of intermediate-basic and acidic volcanic rocks, but the sedimentary rocks are not developed. The age and lithological characteristics of this strata are obviously similar to those of the first and second members of the Tamulangou Formation. Therefore, it was named the third member of the Tamulangou Formation. The age and rock combination of this strata are similar to those of the Lower Cretaceous Baiyingolao/Meiletu Formation at the basin margin.

CONCLUSIONS

(1) Through the observation of cores from Jurassic wells drilled in the Hailar Basin, the identification of core cuttings under the microscope, logging feature analysis, geochemical analysis, zircon U-Pb chronology analysis, and seismic stratigraphic sequence division and comparison, the Jurassic and its upper and lower strata (below the T4 interface and above the Paleozoic basement) sequence, rock assemblage and chronological characteristics of the Hailar Basin are revealed. We identify the Jurassic in the study area from bottom to top, the Triassic volcanic-sedimentary (coal-bearing) sequence, the Jurassic (Hongqi Wanbao Formation, Mulangou 1st Member, Mulangou 2nd Member), and Lower Cretaceous Tamulangou Formation.

(2) During the period of the second member of the Upper Jurassic Tamulangou Formation (Upper Jurassic Manketou Obo/Manitu Formation), the Hailar Basin has the largest horizontal distribution of the Jurassic. The distribution patterns and identification signs of the various layers in the basin are: Triassic rock under the regional unconformity (T4) is composed of acidic rock, sedimentary rock (coal-containing), a small amount (<5%) of medium and basic rock and slight metamorphic rocks. The geological age is 248-203 Ma. The Lower Jurassic Hongqi Wanbao Formation is composed of acidic rock, intermediate basic rock, and sedimentary rock. The geological age is 197-178 Ma. The first member of the Middle-Upper Jurassic Tamulangou Formation is composed of intermediate basic rock, acid rock, sedimentary rock. The geological age is 174-156 Ma. The second member of the Middle-Upper Jurassic Tamulangou Formation (Corresponding area, the Upper Jurassic Manketou Obo/Manitu Formation) is distributed in various sags along various faults. The central and western sag groups (Bayanhushu, Hongqi, Hulunhu and other sags) are developed on a large scale which is composed of acidic rocks, sedimentary rocks, and a small amount (<5%) of intermediate and basic rocks, with a geological age of 156-145 Ma. The third member of the Tamulangou

Formation of the Lower Cretaceous, distributed in various sags along various faults is composed of basic and acid rock.

ACKNOWLEDGEMENTS

This work was not supported by any funds. The authors would like to show sincere thanks to those techniques who have contributed to this research.

REFERENCES

[1] Zhang, J.G. (2002) The formation of unconformity and its oil/gas geological significance in Hailar Basin. Petroleum Geology & Oilfield Development in Daqing. 21(5), 8-10.
[2] Li, P.P., Ge, W.C., Zhang, Y.L. (2010) Division of volcanic strata in the northwestern part of Hailar Basin: evidence from zircon U-Pb dating. Acta Petrologica Sinica. 26(8), 2482-2494.
[3] Dong, H. (2011) Oil-gas source and reservoir-forming mechanism of the damoguaihe formation in the southern Wuerxun Sag, Hailar Basin. Acta Petrolei Sinica. 32(1), 62-69.
[4] Cui, J.P., Ren, Z.L., Xiao, H. (2007) Relations between the thermal history and petroleum generation in the Huh Lake depression, Hailar Basin. Geology in China. 34(3), 522-527.
[5] Zhang, X.T., Li, L., Ren, Y.G., Shao, H.M. (2004) Lithology features and preliminary study of Budate Group hydro-fracturing in Beier sags, Hailar Basin. World Geology. 23(4), 343-347.
[6] Yang, Z.R., Zhang, Y.F., Yuan, Y. (2008) Potential analysis of coalbed gas resources in Huhehu depression, Hailar Basin. Coal Geology & Exploration. 36(2), 15-18.
[7] Song, L.I., Mao, X.P., Tang, D.Z., Tao, S., Yang, W.H. (2009) Resource assessment of coal-derived gas in Huhehu depression, Hailar Basin. Geology in China. 36(6), 1350-1358.
[8] Shuang, L.U., Shen, J.N., Wang, Z.P., Chun, L.I. (2003) Resource evaluation of coalbed gas and potential analysis in Hailar Basin. Coal Geology & Exploration. 31(6), 28-31.
[9] Shuqing, L.I., Wang, L. (2009) Reservoir characteristics of the Lower Cretaceous Nantun formation in Beier Sag of Hailar Basin. Journal of Palaeogeography. 11(2), 241-249.
[10] Ang, L.I., Zhang, L.Y., Song, Z.P., Pei, J.Y. (2013) The application of the method of joint inversion of PP and PS waves in Bei39 zone of Hailar Basin. Progress in Geophysics. 28(4), 1908-1918.
[11] Huang, M., Zhang, H., Zhang, J., Pei, S., Zhao, W. (2018) Zircon U-Pb ages of three episodes mesozoic granites in the Hailar Basin and its significance. Journal of Mineralogy and Petrology. 38(1), 35-41.
[12] Lin, S. (2008) Hailar basin reservoir block complex multidisciplinary reservoir technology application. Petroleum Instruments. 22(1), 75-77.
[13] Ping, G. (2012) The type of uplift zones and its control for hydrocarbon accumulation in the Wuerxun-Beier depression, Hailar Basin. Chinese Journal of Geology (Scientia Geologica Sinica). 47(1), 102-115.
[14] Niu, W. (2010) Progress of injection and production profile logging technology in Hailar Oilfield. Petroleum Instruments. 24(6), 54-56.
[15] Wang, H., Zhou, W., Qiu, Z.K., Li, T., Zhou, D.H., Yang, X., Zhai, Z.H., Tian, C. (2021) Comprehensive interpretation of seismic data of the Permian in the west slope of Mahu Sag in Junggar Basin based on the requirements of oil and gas exploration accuracy. Fresen. Environ. Bull. 30(7A), 8875-8885.
[16] Wei, S.Y., Liu, Z.B., Ren, D.W., Xiong, W., Wang, X.T. (2019) Reservoir study and sequence division of Shahezi formation in Songliao Basin, China. Fresen. Environ. Bull. 28(10), 7469-7476.
[17] Yu, Z.H. (2020) Study on sandstone distribution and sedimentary characteristics of the fourth member of Shahejie formation in Damintun Sag, China. Fresen. Environ. Bull. 29(3), 1813-1821.
[18] Liu, M.Y., Xiang, J.L., Yuan, X.H., Zhang, Y.B., Ma, H.N. (2021) Evaluation of Jurassic reservoir structure and trap in Sanquan Uplift based on fine seismic interpretation. Fresen. Environ. Bull. 30(2), 1215-1222.

Received: **30.11.2021**
Accepted: **23.01.2022**

CORRESPONDING AUTHOR

Zhenzhen Jia
Exploration and Development Research Institute,
Daqing Oilfield Company Limited,
Daqing Heilongjiang 163712 – China

e-mail: jzz669996@163.com

© by PSP Volume 31– No. 05/2022 pages 5071-5081 Fresenius Environmental Bulletin

UTILIZATION AND VALUE OF LOW-CARBON MATERIALS IN PRODUCT DESIGN BASED ON ENVIRONMENTAL PROTECTION CONCEPTS

Chunyan Cao*

School of Art, Taiyuan University of Science and Technology, Taiyuan Shanxi 030021, China

ABSTRACT

At present, people are not very aware of environmental protection, and the furniture materials used are a burden on the environment, and some materials threaten people's health. In addition, consumers' lack of environmental awareness in the way they dispose of old furniture has caused a waste of natural resources. The concept of green ecology is not connected with furniture design, the concept of green ecology design is weak and obsolete, and the manufacturing technology of the domestic furniture market is not perfect. Based on the analysis of these problems, the paper introduces the concept of green ecological design into people's daily life. In the selection of low-carbon material product design evaluation indicators, this study uses the Delphi method. Through face-to-face interviews, e-mails, etc., we collect experts' scores on the importance of low-carbon material product design low-carbon competitiveness evaluation indicators, and conduct statistical analysis on the survey results. After two rounds of expert review, the final evaluation index system was established. In the process of evaluating evaluation indicators at all levels, experts cannot communicate with each other and must make independent judgments. In the case that the low-carbon competitiveness evaluation index system of low-carbon material product design is initially determined, the analytic hierarchy process is used to layer multiple factors contained in the evaluation index system at all levels. We use the analytic hierarchy process to calculate and determine the importance and weight value of the evaluation indicators at all levels, so as to discover the degree of influence of each factor on the overall goal. We use new green ecological composite materials to manufacture furniture, expand the use of furniture, and design a novel green ecological combination furniture. Compared with traditional furniture, it is innovative in shape, convenient and simple to use, reasonable in area, and easy to store. Disassembly and assembly we make it more usable, adding lights and music to create a perfect and quiet private space, which can not only be used as indoor furniture but also transformed into public facilities, narrowing the distance between people. While giving full play to the renewable resource advantages of bamboo, this article makes household products more in line with modern aesthetic needs and enhances the added value of products, which will help promote the transformation of the bamboo industry from extensive resource consumption to high-level innovative design.

KEYWORDS:
Product design, low-carbon materials, environmental protection concept, fuzzy evaluation, evaluation system

INTRODUCTION

Affected by the global greenhouse effect and the uncontrolled and unlimited use of limited underground resources, various natural environmental disasters have been triggered [1]. People have to pay great attention to and deeply reflect on environmental issues. The low-carbon concept has not only become a hot spot in world economic development, but also provides people with a new direction for friendly solutions to economic and environmental problems [2-4]. The low-carbon concept of packaging has made green packaging a hot spot for development and a mainstream consciousness [5-6]. It has changed people's packaging production mode and inspired the packaging design thinking orientation led by the low-carbon concept [7]. Low-carbon is not only an attitude to life, but also a manifestation of social responsibility. To this end, on the basis of studying the local product packaging under the concept of low-carbon, we will use many other factors of industrial design and aesthetic principles, such as technology, art, aesthetics, psychology, materials, technology, market. In the context of today's low-carbon design, how to apply low-carbon design concepts to design ideas is the focus of this topic [8-10].

With the promotion of the concept of low-carbon economy, more and more consumers' requirements for products have shifted from simple realization of functions to the direction that can realize product functions while maintaining low energy consumption and low pollution requirements [11-12]. Relevant scholars believe that in the low-carbon economy era, there will be more and more regulations on product energy consumption and pollution

in the fields of trade and consumption, and companies that lack the concept of low-carbon and low-carbon materials will face increasing policy pressure and market pressure [13]. Researchers believe that the design, production, circulation, consumption, and recycling of low-carbon material products must take into account the environmental pollution of resource consumption [14]. Green design is to achieve low-carbon economy and resolve product requirements. Green design constitutes the core driving force for the sustainable development of enterprises in the era of low-carbon economy. Relevant scholars pointed out that green furniture has made significant development, and the product types have gradually become diversified [15-16]. The form and structure have also abandoned traditional styles and have begun to have a taste of innovation [17]. In terms of manufacturing and processing, they have vigorously absorbed the introduction of advanced processing from abroad. technology. But in general, the development of green furniture is still very one-sided and imperfect except for some furniture production companies with core strengths [18]. There are some problems, such as consumers' ignorance of green furniture, and whether green furniture conforms to the connotation of green ecology [19].

As the low-carbon economy belongs to a new type of economic development, there are few theoretical studies on the style of low-carbon material product design [20]. As the economy is developing rapidly today, people have realized the importance of the environment and energy. Therefore, adding the concept of low-carbon economy to the research of low-carbon material product design style and advocating environmental protection can deepen the theoretical research content of low-carbon material product design style, and can reflect the style characteristics of low-carbon material product design in the new era. For the development of low-carbon economy, it also has a certain role in broadening the field. There is a certain theoretical basis for the research of later scholars. Low-carbon material products are indispensable in people's daily life. Therefore, the design of low-carbon material products is getting more and more attention. Good low-carbon material product design can enrich people’s lives and make it easy for people to use. The concept of low-carbon economy is added to the design of low-carbon material products, and the environmental protection of low-carbon material products can be paid attention to when designing low-carbon material products.

MATERIALS AND METHODS

(1) Low-carbon bamboo materials. The longitudinal stiffness of bamboo is equivalent to that of wood, the longitudinal tensile strength is more than 200MPa, the along-grain tensile strength of bamboo is about twice that of wood, and the unit weight tensile strength is about 3-4 times that of steel; along-grain compressive strength is 84.6Mpa, about 3 times the compressive strength of wood. Bamboo material has small shrinkage, high degree of splitting, elasticity and toughness, along with grain tensile and high compressive strength.

There are many small holes in the bamboo, which can effectively absorb moisture and heat, and has a comfortable feeling of warm in winter and cool in summer. Bamboo has the function of absorbing ultraviolet rays, which can make the eyes more comfortable and prevent myopia to a certain extent. At the same time, the bamboo texture is straight and smooth, whether it is a longitudinal cut pattern or a string cut pattern, it is very vivid, smooth and natural. The natural color of bamboo is simple, easy to be bleached, dyed and carbonized, and it has strong modeling ability. Bamboo also has excellent performance in anti-static, absorbing radiation and formaldehyde. In addition, bamboo can completely return to nature after its use period without leaving pollution. It is a low-carbon, environmentally friendly and sustainable green material.

(2) The ecological value of bamboo. Bamboo is a natural and renewable resource. Because of its fast growth, large output, and annual harvestability, bamboo can effectively alleviate the problem of insufficient timber resources. In addition, the artificial bamboo has very little impact on the environment when it is adopted, manufactured and processed. It is non-polluting and non-toxic. It creates high economic value while minimizing the impact on the environment, which is beneficial to the path of sustainable development.

In terms of anti-corrosion and insect-prevention, because bamboo is easy to de-sugar and fat-removing treatment, after the sugar, fat, starch, and protein are removed, the eggs have no environment for growth and development, which effectively prevents the problem of bamboo infestation and uses it directly. Physical methods can be used to prevent insects. As wood cannot be treated with sugar and fat, it must be treated with preservatives. Bamboo products also have excellent performance in absorbing formaldehyde and radiation.

(3) Processing of bamboo. Bamboo laminated timber is a square bamboo board made by gluing horizontal or vertical pieces of bamboo strips (sheets) of a certain thickness and width. According to the arrangement order of the bamboo skins, it can be divided into flat-pressed bamboo boards and side-pressed bamboo boards. The size is no longer limited by the size of round bamboo, and at the same time it has the physical properties of bamboo. Processing methods such as sawing, planing, tenoning, drilling, sanding, assembling, various cladding and finishing decoration, have the characteristics of high strength,

large amplitude, and stable size. The new type of bamboo laminated timber furniture pays attention to the simple and bright shape and the smooth lines. It pursues the diversification of furniture functions. Through the multiple applications of materials and the rich color changes of low-carbon products, it forms a diversified style to meet different levels of consumption. Moreover, the new type of bamboo laminated furniture design can be integrated with the relationship between architectural design and interior design and has the function of carrying space integration.

(4) The application of noodles in the design of bamboo household products. The surface is formed by the movement trajectory of the line, can also be obtained by expanding the area of the point, and can also be regarded as the interface of the living space. Through the changes in the size, unit shape, texture, and quantity of the surface, people have different moods and feelings. The geometric surface gives people a sense of clarity, rationality, and order, and is easy to be monotonous and mechanical; the organic interview is a curved surface that cannot be obtained by geometric methods, giving flow and change, and at the same time, it does not violate the laws and order of nature. The edge detection and shape extraction of low-carbon bamboo in furniture product design are shown in Figure 1.

(5) Screening of initial evaluation indicators. The expert advisory group is composed of 10 low-carbon material product design experts, 6 low-carbon material product design students, and 4 low-carbon material product design company managers. The expert group is asked to give opinions by issuing questionnaires. A total of 20 questionnaires were distributed, and 20 were recovered, with a recovery rate of 100%. The number of approvals is greater than or equal to 12 as effective indicators (the number of questionnaires returned is 20, and the number of indicators approval rate reaches 60% is 12). The result shows that there are 34 effective indicators, which are not highly relevant to the research content of the paper. Subsequently, the evaluation indicators were adjusted and modified according to the recommendations given by the expert group. Therefore, after the first round of questionnaire survey, there were 34 qualified indicators, as shown in Table 1.

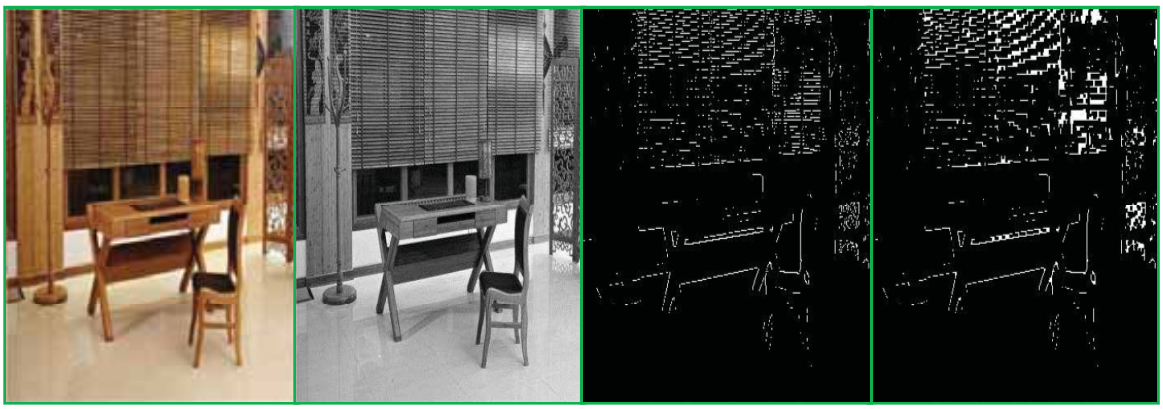

FIGURE 1
Edge detection and shape extraction of low-carbon bamboo in furniture product design.

TABLE 1
Revised indicators after the first round of questionnaires

Evaluation goal	First level indicator	Secondary indicators
Low-carbon competitiveness evaluation index system	Venue facilities	Environmental protection of venue building materials
		Utilization rate of smart energy-saving system in venues
		Venue utilization
	Economic factors	Gross value of tertiary industry
		Economic benefits of low-carbon exhibitions
		The proportion of tertiary industry in GDP
	Exhibition environment	Comprehensive index of environmental quality
		Green coverage
		Climate comfort
	Product enterprise	Enterprise's capital investment in low-carbon technology
		Utilization rate of low-carbon environmental protection technology
		Enterprise low-carbon design ratio

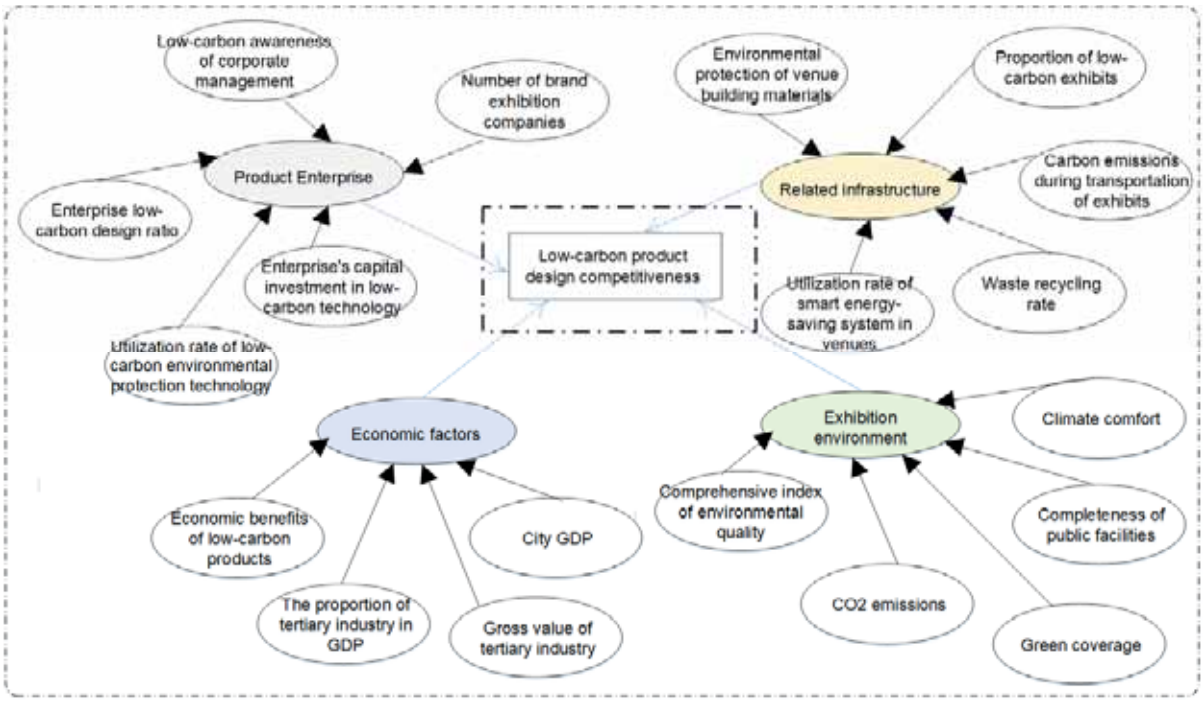

FIGURE 2
Evaluation model of factors affecting low-carbon competitiveness of product design.

After the first and second rounds of expert questionnaire surveys, after the first round of questionnaires, the indicators were adjusted and modified according to the suggestions given by the experts, and then the new indicator questionnaires were distributed to the experts. According to the second feedback information of the expert group, the final evaluation index is determined. According to the above analysis, the factors affecting the low-carbon competitiveness of low-carbon material product design are obtained, as shown in Figure 2.

(6) Final establishment of the evaluation index system. Through the collection of literature and the first and second rounds of experts' scoring of the indicators, and continuous revisions, and comprehensive consideration of each indicator, a complete set of low-carbon material product design low-carbon competitiveness evaluation indicator system is finally determined.

After the evaluation index system is determined, the opinion concentration, variability and variance are used to test the final evaluation index system. The index is divided by the level of "concentration of opinions", which is represented by the arithmetic mean Mj of each index. The higher the Mj, the greater the relative importance of the index that the expert believes; the index's coefficient of variation Vj is used to represent the group's "coordination of opinions" on the indicator. The smaller the indicator's Vj, the less controversy it receives from experts. Assuming that there are n experts and m indicators, Xij represents the score of the i-th expert on the j-th indicator, the calculation formula of opinion concentration as Eq. 1, Eq. 2:

$$M_j = \frac{1}{n-1}\prod_{i=0}^{n-1}\left(X_{ij} \bullet X_{(i+1)j}\right) \quad (1)$$

$$S_j = \left[\frac{1}{n-1}\prod (M_j - X_{ij} \bullet X_{(i+1)j})^2\right]^{1/2} \quad (2)$$

The calculation formula of the coefficient of variation as Eq. 3:

$$V_j = S_j \bullet S_{j+1} / M_j \quad (3)$$

We calculate the opinions of experts on the evaluation indicators according to the above three formulas, and calculate the "opinion coordination degree" and "opinion concentration degree" of each index. When the Mj>7.00 of the first-level index indicates that the experts have a high degree of concentration of opinions on the index, Vj<0.0547 indicates that the variation of the opinions of the experts on the index is small. Table 2 shows the concentration and variability of the first-level indicators.

It can be found from Table 2 that the concentration of the five first-level indicators is above 7.00, indicating that experts agree with the establishment of these five first-level indicators, indicating that these five indicators are representative. Especially for the two indicators of low-carbon material product design company A3 and venue facilities A4, the concentration of opinions of experts is above 6.00, indicating that these two indicators have a large impact on the low-carbon competitiveness of low-carbon material product design, and the consistency of the two indicators is also relatively good.

TABLE 2
Concentration and variability of primary indicators

First level indicator	Min	Max	Concentration	Standard deviation	Variability
Product enterprise	2	8	7.8	0.42	0.05
Economic factors	2	8	7.23	0.43	0.072
Product environment	2	8	7.77	0.32	0.048
Venue facilities	2	8	8.45	0.41	0.057

TABLE 3
Definition of importance scale

Scaling	Definition
1	Two factors are equally important
2,3	The former factor is slightly more important than the latter, and the intensity is lower
4	The former factor is more important than the latter, and the intensity is intermediate
5,6,7	The former factor is more important than the latter, and the intensity is higher
8	The former factor is absolutely more important than the latter, and the intensity is super high
9	Median value between two factors

TABLE 4
Judgment matrix of first-level indicators

/	A0	A1	A2	A3	A4
A0	2	0.8	0.5	0.4	0.9
A1	3	0.6	2	0.5	2
A2	1	1	1	0.9	2
A3	1	1	0.8	1	1
A4	3	4	0.9	0.8	0.7

(7) Determination of the weights of evaluation indicators. Although the evaluation index system involves many factors, the status and role of each factor in the overall evaluation goal are different. At this time, it is necessary to determine the proportion of each factor. The quantification of weight is the weight. This article uses a combination of subjective and objective methods to assign values to indicators. The subjective method is the expert scoring system, and the objective method is the analytic hierarchy process. The combination of these two methods ultimately determines the evaluation of this article. The specific steps of the analytic hierarchy process include: establishing a structural hierarchical model, constructing a pairwise comparison judgment matrix to calculate the eigenvector value and the largest eigenvalue, hierarchical single ordering and consistency testing, hierarchical total ordering and consistency testing. The definition of AHP importance scale is shown in Table 3.

After constructing the pairwise comparison matrix, we normalize each column of the judgment matrix, as Eq. 4:

$$\overline{b}_{ij} = b_{ij} \bullet \left(\prod_{k=0}^{n-1} b_{kj} \right)^{-1} \tag{4}$$

The normalized judgment matrix of each column is multiplied as Eq. 5:

$$\overline{W}_i = \prod_{j=0}^{n-1} \left[\overline{b}_{ij} \bullet \overline{b}_{i(j+1)} \right] \tag{5}$$

The formula for finding the largest characteristic root as Eq. 6:

$$\lambda_{Max} = \sum_{i=0}^{n-1} \left[\left(AW \right)_i \bullet \left(AW \right)_{i+1} / (n-1) W_i \right] \tag{6}$$

We test the consistency of the construction matrix by using the index CI, as Eq. 7:

$$CI = \frac{\lambda_{Max} - n}{(n-1) W_i} \tag{7}$$

The RI of the first-order and second-order judgment matrices is zero, that is, the judgment matrices are completely consistent. If the order is greater than 2, we use the ratio of CI and RI, CR, to judge whether the matrix has satisfactory consistency. When CR is less than 0.10, it indicates consistency, otherwise the judgment matrix must be adjusted.

This article uses analytic hierarchy process and Delphi method to assign evaluation indexes. The index weights are scored by experts in low-carbon material product design field according to the reference standard (1-9 points system). We use MATLAB software to process the data, and the judgment matrix is shown in Table 4.

RESULTS

(1) Results and analysis of product design. Products should be considered and constructed in terms of safety performance, user experience, and functional realization, and the concept of harmony and comfort should be incorporated into the design of the product. According to the actual needs of users, we decided to design a model that is beautiful and decorative in appearance, environmentally friendly and healthy in manufacturing materials, convenient and quick to use, combined and interesting in function, and added some high-efficiency functions and can make everything possible. In the early stage, some sketches were designed to explore functions, shapes and materials. This solution is a rectangular frame, with modules of different shapes placed in the frame, which can be stored and used for other purposes when needed.

We pay attention to the simplicity of the furniture shape design. Simplicity does not mean simplicity. According to the furniture structure style, choose the use of materials to fully demonstrate the characteristics of different materials and enhance the connotation of the use of furniture. "Freely" modular furniture is simple and generous in shape. The combination of materials allows it to show the charm of modern vitality. We pay attention to the modular design of the furniture form, classify according to the use function of the furniture, combine several independent module forms into an organic form, and each independent module has its own function. "Freely" modular furniture is composed of several different modules, each of which has its own different functions, which can be combined to form a multifunctional use space.

The meaning of furniture products is not to be a usable product, but to be sublimated into a work of art. We pay attention to the unity and change of form, symmetry and balance, rhythm and rhythm. "Freely" modular furniture is composed of two symmetrical modules on the base part, and the ceiling design is a slightly inclined changing module, with smooth appearance lines and obvious characteristics of the times.

Each piece of furniture has its own unique functionality. Through modular design, individual modules have their own independent functions. The base design can be used as a chair alone, and it can become a recliner after being pieced together. In order to achieve the efficiency of product use, a transparent top cover is added to the ceiling design. The top cover is designed with LED light distribution, and the top cover can be imaged to watch movies. The ceiling side wall is equipped with a playback button, surround sound, and freely play music.

In order to achieve the environmental protection of furniture materials, we choose natural materials with abundant materials, such as straw, bamboo, and paper materials. There are also metal and glass recyclable materials. The ceiling of the "Freely" modular furniture is made of stainless steel, and the ceiling and cover are made of fiber glass. Many materials will cause harm to the human body during use, such as very common materials containing PCB, PVC, PCT and lead elements. Try to use materials processed by new processes. The base part uses a new type. It is made of glued environmentally-friendly boards, and environmentally-friendly wood wax paint is applied to the surface. Each material has its own unique texture and texture. In the use of materials, the combined furniture has not undergone too much processing and decoration, which shows the original flavor of the materials, and the combination is very distinctive. The proportion of low-carbon materials used in furniture products is shown in Figure 3.

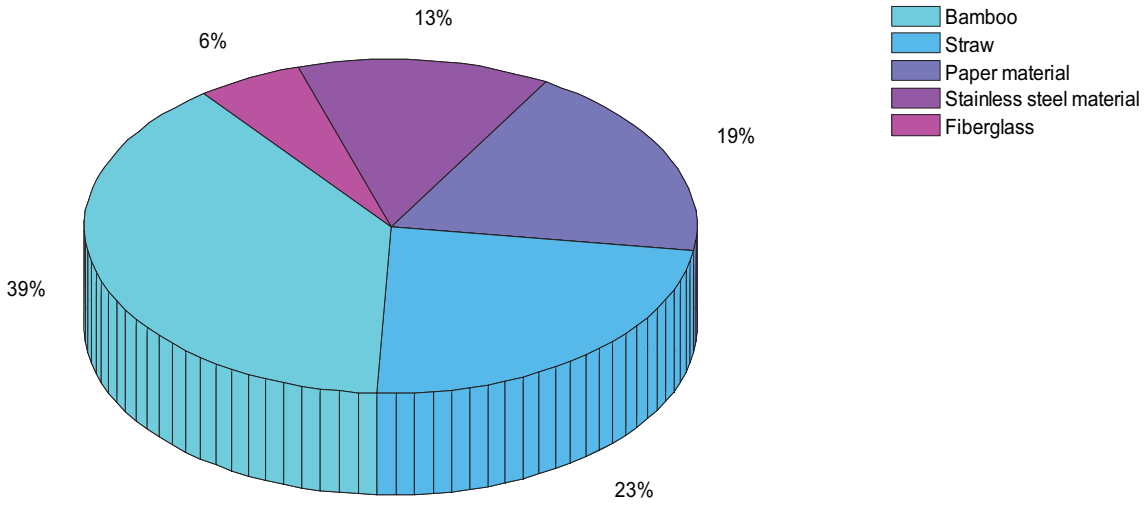

FIGURE 3
The proportion of low-carbon materials used in furniture products.

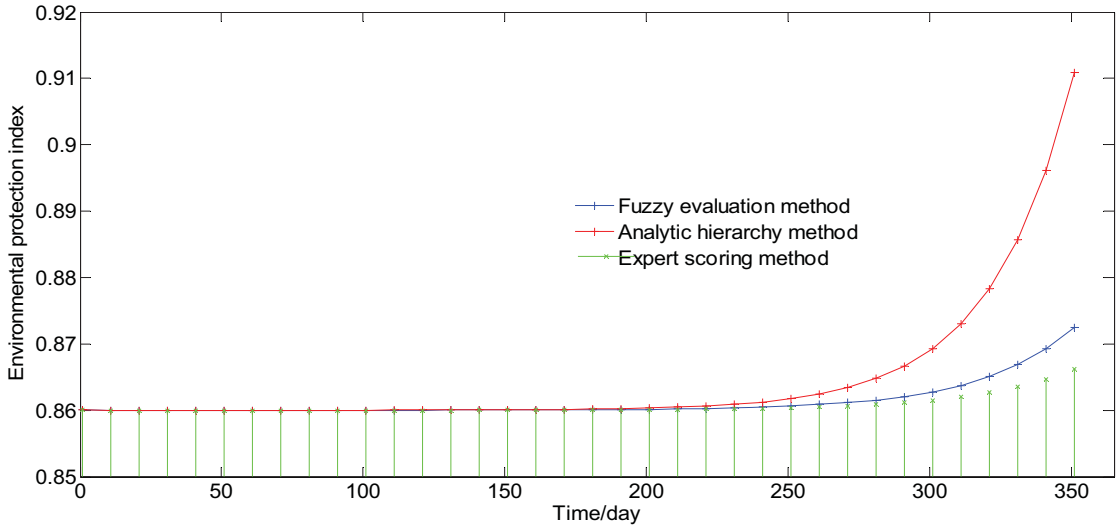

FIGURE 4
Environmental protection index of modular furniture over time.

(2) Results and analysis of product structure design. To test whether a piece of furniture is reasonable in structure, it is to see whether its structure can remain firm and stable during the use of the product. External forces will have an impact on the use of furniture, especially seating furniture. Therefore, the design of modular furniture should apply mechanical principles to it, and reasonably establish a furniture structural support system so that different modules can be firmly connected to ensure the normal and stable use of furniture.

Structurally, it is divided into upper and lower parts. The lower part is the seat part, which is formed by splicing two chair-like modules to form a reclining chair. The upper part is a roof-like structure, connected with the seat part, and the top part is a transparent glass structure with a number of LED lighting. In order to make people lie on it more comfortably, the design did not directly connect the backrest and the seat part like ordinary furniture, but added chamfers in the connecting part, which more closely fits the human back structure and makes the tail spine. And the spine is evenly stressed and more comfortable. This combination furniture has its own unique size. The length of the seat is set to 1.8M. Both adults and children are suitable for lying on it. The total height is 1,8M, so that people do not feel depressed when lying down. When looking at the transparent display on the top of the ceiling, it is a safe distance for eyesight and can protect the eyes. The width is 1.0M, a suitable width for private space, so you can freely turn over and change positions when lying down. The environmental protection index of modular furniture over time is shown in Figure 4.

(3) Results and analysis of product material design. The seat part of the "Freely" modular furniture is manufactured using environmentally friendly panels that have been compressed into modules. The environmental protection board is also called the reinforced resin board, which is a high-tech infrared photoelectric screening machine to extract the essence to strengthen the glass fiber resin, which can replace the use of wooden artificial board and natural wood on the market. The raw materials are recycled plant fiber materials such as straw, wood powder, bamboo powder, etc., added with a special non-formaldehyde environmentally friendly and safe grade mixture formula, which is compounded by high temperature and high pressure heavy equipment. The flat product has excellent processing performance and surface decoration performance, can facilitate rapid prototyping, and can be continuously recycled and reproduced. Using reinforced resin boards as raw materials, "Freely" modular furniture combines different modules to form through pre-design. The combined furniture produced by using environmentally-friendly panels is safe and harmless, has the characteristics of low pollution to nature, recyclable use, and abundant materials, which is a good alternative to natural resources.

Wood wax paint is made of linseed oil, sunflower oil, soybean oil, carnauba wax, candelilla wax, iron oxide and other environmentally friendly organic pigments as raw materials, adding plant waxes and fusion with other natural ingredients. The pigments used for color mixing It is an environmentally friendly organic pigment with a wide variety of colors. Therefore, the wood wax paint does not contain toxic and harmful ingredients such as triphenyl, formaldehyde and heavy metals, has no pungent odor, and has little harm to the human body. Modular furniture has a combination of different colors, which can be matched by consumers according to their own preferences, so that it is practical and decorative in indoor and office places with different decoration styles. The comparison of environmental protection value of environmentally friendly wood wax paint and ordinary paint is shown in Figure 5.

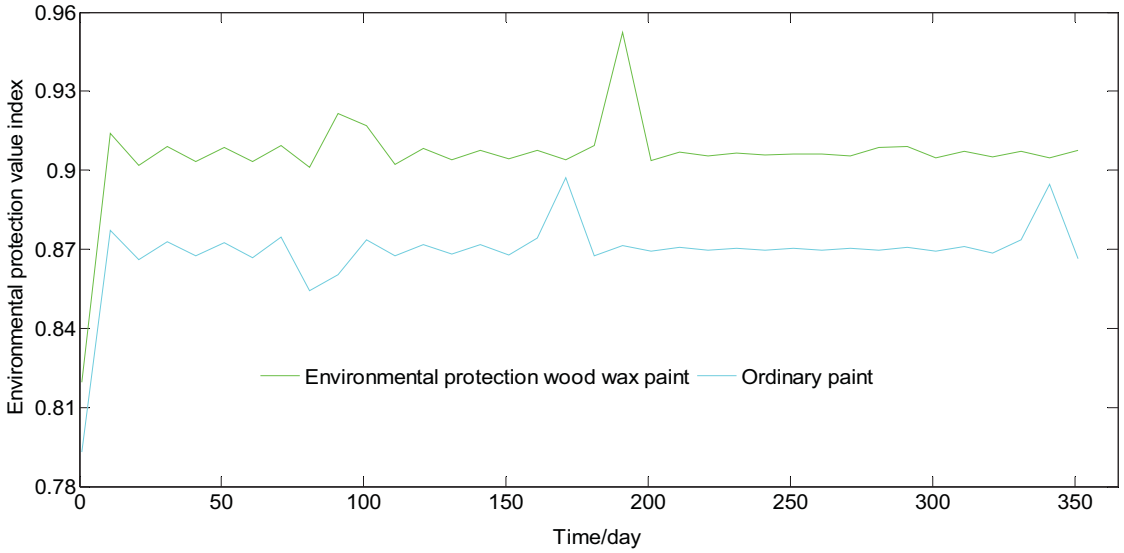

FIGURE 5
Comparison of environmental protection value of environmentally friendly wood wax paint and ordinary paint

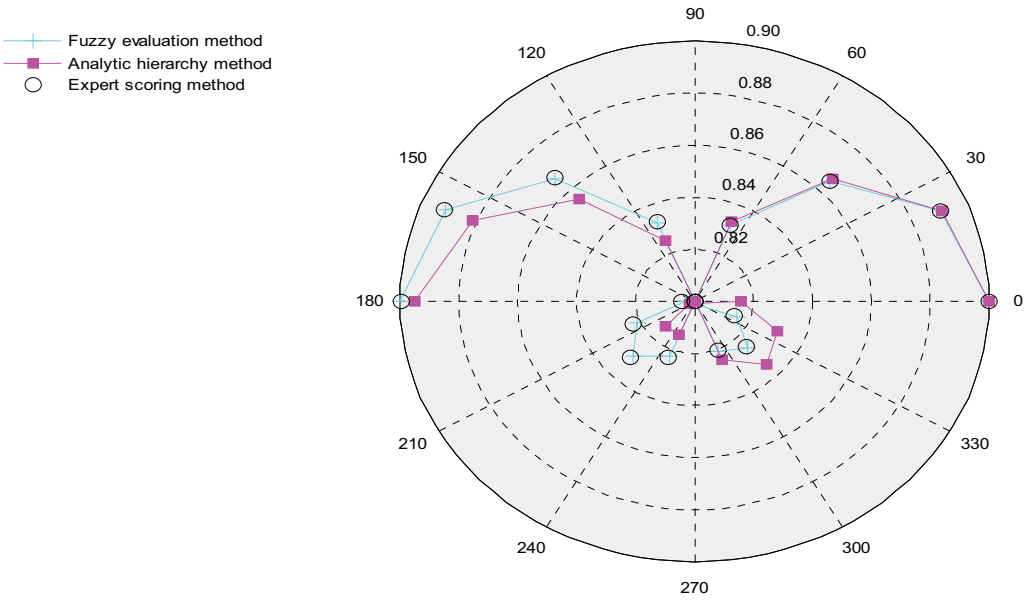

FIGURE 6
Scores of low-carbon bamboo furniture products under night use scenarios.

(4) Results and analysis of product functional design. "Freely" modular furniture itself can be regarded as a lounge chair, placed in the living room, study, balcony or yard leisure area, this modular furniture combination can be regarded as a lounge chair. There are buttons on the side of the ceiling to adjust the brightness of the light. At the same time, it is equipped with four external high-quality speakers to play music through Bluetooth connection, and surround stereo sound in all directions. Listening to the sound of cicadas and running water makes people feel like they have returned to nature, away from the hustle and bustle of the city. There is a USB interface beside the button, and you can play movies on the top of the screen through the mobile phone data cable for leisure and entertainment. Placed in the outdoor recreation area, when resting, you can look to the sky through the transparent display on the ceiling, which is very comfortable and comfortable. The seat part is composed of two modules, which can be split into two chairs and can be used alone. There is a drawer underneath, which can be used to place books, CDs, small objects, and materials and utensils. The ceiling part can be used as a table when it is inverted. use. At night, the LED lights can provide just the right amount of lighting to facilitate reading and learning. Figure 6 shows the scores of low-carbon bamboo furniture products under night use scenarios.

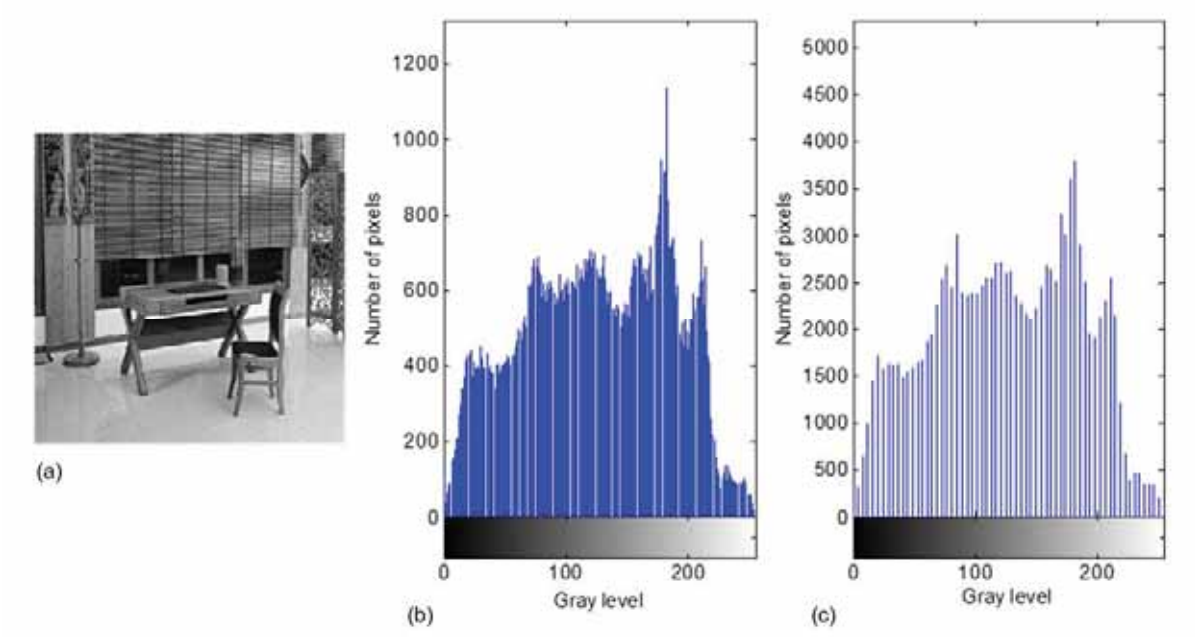

FIGURE 7
Grayscale distribution of low-carbon bamboo furniture products (a, a low-carbon bamboo furniture product; b, Histogram is not segmented; c, Histogram is divided into 64 segments).

(5) Results and analysis of product usage analysis. For humans, the color of low-carbon products is the richness of monotonous life, and it has a great stimulating effect on human psychology and spirit. "Freely" modular furniture is a green ecological furniture product with diverse combinations, novel shapes, and rich colors of low-carbon products. Its colors are colorful and can be used according to people of different ages. According to people's preferences, it can give different low-carbon products colors. There are different styles of light, lively, classic and sweet to provide options and then combine them, and place them in the study room.

Depending on the placement space, the color matching of its low-carbon products will have a different effect on the overall decoration of the home. Middle-aged and elderly people often choose atmospheric and classical colors, and they can choose dark and natural colors to match. The young people's choice of color is gorgeous and smart, and they can choose macarons and fresh colors to match. Children's color lies in their novel perception of the outside world, and they can choose a variety of seven-color colors to match. Figure 7 shows the gray distribution of low-carbon bamboo furniture products.

CONCLUSIONS

(1) Combining the traditional processing methods and modern processing methods of bamboo, it is proposed to use the three-dimensional composition design principle to design and transform bamboo household products, so that it can give full play to the advantages of renewable resources of bamboo, and make household products more powerful. The modern sense is more in line with modern aesthetic viewpoints. The design of bamboo home furnishing products protects the balance of the earth's ecological environment while designing a comfortable and convenient living and working environment for human beings. By enhancing the added value of bamboo products, the competitiveness of bamboo home furnishing products in the market has been strengthened, which will help promote the bamboo industry to take the path of sustainable development.

(2) The use of materials is environmentally friendly, which reduces the burden on the environment and does not harm people's health. The green and ecological materials are recycled to achieve the sustainable development of resources. The shape is novel and generous, and the colorful colors are in harmony with people's preferences and home decoration styles. We expand the function through design, realize the efficiency of furniture products, achieve the effect of multi-purpose and use the most of the things, increase the added value of furniture, and change the furniture into other ways while meeting people's needs for furniture. Functional products.

(3) In terms of furniture modeling and structure functions, the concept of green ecological design is applied to design furniture that can make the best use of, and modularity, recycling, and efficiency are used in design practice to make a shape that is popular with consumers. Under the premise of recognition, the function of furniture will be expanded to be more practical, so that consumers will have a better quality of life. Furniture products are no longer limited to the outdoors, but can also shine in outdoor leisure areas. Assembled furniture facilitates life, enriches

the connotation of life, allows people to build casually, get a better life experience, and satisfy people's emotional demands for private leisure space and shared space with others.

ACKNOWLEDGEMENTS

This work was supported by the Shanxi province philosophy and social science planning project (No. 2017); and the research on landscape ecological protection of tourist resort.

REFERENCES

[1] Tripathi, N., Hills, C.D., Singh, R.S., Atkinson, C.J. (2019) Biomass waste utilisation in low-carbon products: harnessing a major potential resource. NPJ Climate and Atmospheric Science. 2(1), 1-10.

[2] Shaharudin, M.S., Fernando, Y., Jabbour, C.J.C., Sroufe, R., Jasmi, M.F.A. (2019) Past, present, and future low carbon supply chain management: a content review using social network analysis. Journal of Cleaner Production. 218, 629-643.

[3] Kuo, T.C., Tseng, M.L., Chen, H.M., Chen, P.S., Chang, P.C. (2018) Design and analysis of supply chain networks with low carbon emissions. Computational Economics. 52(4), 1353-1374.

[4] Lu, Q., Zhou, G.H., Xiao, Z.D., Chang, F.T., Tian, C.L. (2018) A selection methodology of key parts based on the characteristic of carbon emissions for low-carbon design. The International Journal of Advanced Manufacturing Technology. 94(9), 3359-3373.

[5] Hildebrandt, J., Hagemann, N., Thrän, D. (2017) The contribution of wood-based construction materials for leveraging a low carbon building sector in Europe. Sustainable Cities and Society. 34, 405-418.

[6] Shubbar, A.A., Jafer, H., Dulaimi, A., Hashim, K., Atherton, W., Sadique, M. (2018) The development of a low carbon binder produced from the ternary blending of cement, ground granulated blast furnace slag and high calcium fly ash: an experimental and statistical approach. Construction and Building Materials. 187, 1051-1060.

[7] Mao, Z., Zhang, S., Li, X. (2017) Low carbon supply chain firm integration and firm performance in China. Journal of Cleaner Production. 153, 354-361.

[8] Baranova, P., Paterson, F. (2017) Environmental capabilities of small and medium sized enterprises: towards transition to a low carbon economy in the East Midlands. Local Economy. 32(8), 835-853.

[9] Zhang, L., Zhao, X., Ke, Q., Dong, W., Zhong, Y. (2021) Disassembly line balancing optimization method for high efficiency and low carbon emission. International Journal of Precision Engineering and Manufacturing-Green Technology. 8(1), 233-247.

[10] Zu, Y., Chen, L., Fan, Y. (2018) Research on low-carbon strategies in supply chain with environmental regulations based on differential game. Journal of Cleaner Production. 177, 527-546.

[11] Xiao, W., Du, G., Zhang, Y., Liu, X. (2018) Coordinated optimization of low-carbon product family and its manufacturing process design by a bilevel game-theoretic model. Journal of Cleaner Production. 184, 754-773.

[12] Li, Q., Long, R., Chen, H. (2017) Empirical study of the willingness of consumers to purchase low-carbon products by considering carbon labels: a case study. Journal of Cleaner Production. 161, 1237-1250.

[13] Cheng, J., Yi, J., Dai, S., Xiong, Y. (2019) Can low-carbon city construction facilitate green growth? Evidence from China's pilot low-carbon city initiative. Journal of Cleaner Production. 231, 1158-1170.

[14] He, B., Hua, Y. (2017) Feature-based integrated product model for low-carbon conceptual design. Journal of Engineering Design. 28(6), 408-432.

[15] Shuai, G., Li, Z., Zhang, D., Elhefnawey, M., Li, L. (2021) On rough set theory on achieving high quality cable material production by green low carbon technology. Ecological Chemistry and Engineering. 28(1), 49-59.

[16] Wang, D. (2011) Research on the current situation and strategy of packaging material in publications from the perspective of low-carbon economy. Packaging Engineering. 32(24), 127-129.

[17] Peng, T., Deng, H. (2021) Research on the sustainable development process of low-carbon pilot cities: The case study of Guiyang, a low-carbon pilot city in south-west China. Environment, Development and Sustainability. 23(2), 2382-2403.

[18] Zhang, X. (2020) Exploration of green packaging design based on ecology theory. Fresen. Environ. Bull. 29(8), 6657-6661.

[19] Gong, X.Q., Wu, B., Wu, F. (2021) Research on the impact of green product packaging design on ecological environment. Fresen. Environ. Bull. 30(4), 3228-3232.

[20] Xie, Q. (2020) Innovative design of product ecological packaging under the environment of big data based on ecological perspective. Fresen. Environ. Bull. 29(12), 10804-10810.

Received: **30.11.2021**
Accepted: **23.01.2022**

CORRESPONDING AUTHOR

Chunyan Cao
School of Art,
Taiyuan University of Science and Technology,
Taiyuan Shanxi 030021 – China

E-mail: cy13903517501@163.com

© by PSP Volume 31– No. 05/2022 pages 5082-5086 Fresenius Environmental Bulletin

NEW SOURCE FOR HIGH ANTHER CULTURE RESPONSE TURKISH LOCAL EGGPLANT (*Solanum melongena* L.) GENOTYPE

Vese Pakashtica[1,*], Merve A Yigit[2], Emrah Uysal[2], Cansu Bulbul[3], Duran Simsek[3], Hasan Pinar[2]

[1]Akdeniz University, Department of Agricultural Biotechnology, Antalya, Turkey
[2]Erciyes University, Department of Horticulture, Kayseri, Turkey
[3]Areo Seed Co., Antalya, Turkey

ABSTRACT

In this study, 28 local (Yamula) eggplant genotypes, 1 Manisa eggplant genotype and 3 Kemer eggplant genotypes commonly grown in Turkey were subjected to anther culture. While the genotypes ERU-3008, ERU-3011 and ERU-3016 did not have anther development, the others had anther developments at different ratios varied between 3.33% (ERU-3009 and ERU-3012) and 50% (ERU-961). Of the genotypes with anther development, 10 had embryo formation at different ratios varied between 6.25% (ERU-3015) 37.5% (ERU-952). Embryo formation was not observed in control group genotypes (Kemer and Manisa). It was observed in the present study that Yamula eggplant prominent especially with fruit flesh firmness yielded positive responses to anther culture.

KEYWORDS:
Turkish local eggplant, dihaploidization, anther culture

INTRODUCTION

In recent years, there is an accelerated transition from standard cultivars to F1 hybrid cultivars in eggplant cultivation practices of World. However, as it was in other vegetables, despite increasing yield levels, desired quality in eggplants is not achieved with F1 hybrids. Use of local seeds is encouraged, thus use of local cultivars for both standard seeds and F1 hybrid seeds accelerated. Yamula eggplant grown in Kayseri-Turkey province and surroundings is a local standard cultivar. Yamula eggplant has a specific striped peel texture and prominent with stiff flesh firmness. Purification in open-pollinating plants was used to be performed through individual selfing, in recent years, double-haploid methods have been introduced into purification processes. Anther culture has successfully applied in pepper and eggplant. Although pure-lines are achieved with conventional methods, such a process is a time-consuming process and takes about 10-12 years in foreign-pollinating plants and about 6-7 years in self-pollinating plants. Such a long durations can be reduced to 1-2 years with haploidy techniques. Haploid plants are obtained in couple of months with anther culture and homozygote double-haploid plants are obtained in a single generation through folding chromosomes of these plants. These fertile homozygote plants plant significant roles in acquisition of pure lines required to develop hybrid cultivars. Purification of mixed cultivars or populations in a short time is another advantage of haploidization [2].

Anther culture is defined as the process of separating anthers enclosing immature pollens from the buds, placing them into artificial growth media under in vitro conditions and obtaining haploid embryos from these immature pollens. Through anther culture, gamethopic development direction of pollen grains be turned into binucleate structure under normal conditions is directed to somatic development direction just at uninucleate stage and in this way, the process of "microspore endogenosis" or "endogenosis" is realized. Microspore structure and quality designate androgenetic potential of the plants. Sunderland [1] conducted the earliest studies on this issue and reported with cytological observations that within the cultures tobacco anthers, there were pollens stained at lighter colors and different in size. Such a case was called as pollen dimorphism. In this case, while some of the pollens maintain their development in gametophytic direction, the others tend to sporophytic development direction and gain embryo formation capability. Rashid [3] defined pollen dimorphism as the existence of pollen grains with two different morphologies with a potential to develop towards two different generation types in anthers. Pollens normally exhibit gametophytic development in angiosperms, but it was reported that sporophytic type of pollens had a chance to transform into a plant only under cultural conditions [4].

Several factors are effective in obtaining haploids through anther culture, such as donor plant-induced physiological factors, development stages of microspores, resultant anther separation times, physical factors during the culture, incubation conditions of the cultures, plant genotypic characteristics, pretreatments to buds, structure and composition of growth media.

This study was conducted to determine the responses of some Yamula eggplant genotypes locally grown in Kayseri province and surroundings and selected based on fruit and plant characteristics to anther culture. Another objective of the present study is to produce dihaploid plants from standard eggplant cultivars and to develop proper protocols for these plants.

MATERIALS AND METHODS

This study was conducted over the experimental fields and laboratories of Erciyes University Agricultural Faculty.

Plant Material. In this study, 28 Yamula eggplant genotypes were used as the plant material. A control group composed of 1 Manisa eggplant genotype and 3 Kemer eggplant genotypes was also used (Table 1).

Collection of flower buds. For anther culture, available mononuclear buds with a morphological development stage of microspores at 1stpollen mitosis stage were used. The buds at proper stages (with a bud length of 15-17 mm, anther color of greenish yellow, petals reached to sepal separation stage) were cultured (Figure 1).

Growth Media Composition. C (callus) and R (regeneration) growth media as recommended by [5] were used. All growth media were mixed with agar (0.8%). The anthers isolated from flower buds initially were placed into C medium; developed anthers were then transferred into R medium containing 0.1 mg/l kinetin.

Culture and Incubation. Flower buds at proper growth stage were sterilized in 70% ethanol for 1 minute and rinsed through distilled water. Buds were then placed into 10% commercial sodium hypochlorite with couple drops of Tween-20 for 15 minutes and passed through distilled water 3 times. Anthers were removed from the flower buds with a bistoury and pliers and immediately were placed into growth media as to have the dorsal surface in contact with the media and not to be immersed into the media (Figure 2). The petri dishes with planted anthers were subjected to heat shock at +35 ^{0}C at dark for 8 days. Then they were placed into climate chamber at +25±2 ^{o}C temperature and 16/8 light/dark photoperiods until the end of 12th day. Anthers were placed into R medium after 12th day and kept at +25±2 ^{0}C temperature and 16/8 photoperiod for development.

TABLE 1

Eggplant genotypes used in the study

	Genotype	Explanation
1	ERU3004	Yamula Eggplant
2	ERU3005	Yamula Eggplant
3	ERU3006	Yamula Eggplant
4	ERU3007	Yamula Eggplant
5	ERU3008	Yamula Eggplant
6	ERU3009	Yamula Eggplant
7	ERU3010	Yamula Eggplant
8	ERU3011	Yamula Eggplant
9	ERU3012	Yamula Eggplant
10	ERU3013	Yamula Eggplant
11	ERU3014	Yamula Eggplant
12	ERU3015	Yamula Eggplant
13	ERU3016	Yamula Eggplant
14	ERU3017	Yamula Eggplant
15	ERU3018	Yamula Eggplant
16	ERU949	Yamula Eggplant
17	ERU950	Kemer Eggplant
18	ERU951	Yamula Eggplant
19	ERU952	Yamula Eggplant
20	ERU953	Yamula Eggplant
21	ERU954	Yamula Eggplant
22	ERU955	Yamula Eggplant
23	ERU956	Yamula Eggplant
24	ERU957	Yamula Eggplant
25	ERU961	Yamula Eggplant
26	ERU964	Manisa Eggplant
27	ERU1255	Kemer Eggplant
28	ERU1256	Kemer Eggplant
29	ERU3000	Yamula Eggplant
30	ERU3001	Yamula Eggplant
31	ERU3002	Yamula Eggplant
32	ERU3003	Yamula Eggplant

FIGURE 1
Eggplant buds at proper stages for anther culture

FIGURE 2
Anther plantation to growth media

TABLE 2
Tissue culture results for the genotypes used in this study (GN: Genotype Number, NPA: Number of Planted Anthers, NDA: Number of developed anthers, GAO: Developed anther ratio, ES: Number of embryos, EFR: Embryo formation ratio).

GN	NPA	NDA	DAR (%)	NE	EFR (%)
ERÜ949	120	24	20	0	0
ERÜ950	120	12	10	0	0
ERÜ951	120	40	33.33	4	10
ERÜ952	120	24	20	9	37.5
ERÜ953	120	32	26.66	0	0
ERÜ954	120	48	40	5	10.41
ERÜ955	120	48	40	0	0
ERÜ956	120	52	43.33	0	0
ERÜ957	120	48	40	7	14.58
ERÜ961	120	60	50	5	8.33
ERÜ964	120	8	6.66	0	0
ERÜ1255	120	8	6.66	0	0
ERÜ1256	120	12	10	0	0
ERÜ3000	120	36	30	3	8.33
ERÜ3001	120	40	33.33	3	7.5
ERÜ3002	120	28	23.33	0	0
ERÜ3003	120	12	10	0	0
ERÜ3004	120	28	23.33	5	17.85
ERÜ3005	120	12	10	0	0
ERÜ3006	120	8	6.66	0	0
ERÜ3007	120	32	26.66	5	15.62
ERÜ3008	120	0	0	0	0
ERÜ3009	120	4	3.33	0	0
ERÜ3010	120	12	10	0	0
ERU3011	120	0	0	0	0
ERÜ3012	120	4	3.33	0	0
ERÜ3013	120	20	16.66	0	0
ERÜ3014	120	24	20	0	0
ERÜ3015	120	48	40	3	6.25
ERÜ3016	120	0	0	0	0
ERÜ3017	120	44	36.66	0	0
ERÜ3018	120	12	10	0	0

FIGURE 3
Transition of anthers into embryo and acclimatization of haploid plants

RESULTS AND DISCUSSION

In present experiments, 120 anthers of each genotype were planted into C media. Developed anthers were then transferred to R media. While anther development was observed in genotypes ERÜ-3008, ERÜ-3011 and ERÜ-3016, the others did not exhibited anther development. Therefore, the anther development ratios varied between 3.33% (ERÜ-3009 and ERÜ-3012) and 50% (ERÜ-961). Of the genotypes with anther development, anthers turned into embryo in 10 of them (Figure 3). Thus, embryo formation ratios varied between 6.25% (ERÜ-3015) and 37.5% (ERÜ-952). Embryo formation was not observed in genotypes of the control group (Table 2). All of the embryos obtained were achieved through direct embryo formation .

DISCUSSION AND CONCLUSION

Regeneration studies in eggplants initiated in 1960s. Previous studies revealed that both the genotypes and the growth regulators had significant effects on regeneration of eggplants. In present study,

in vitro dihaploidization efficiency of 32 eggplant genotypes (28 Yamula eggplants, 1 Manisa eggplant and 3 Kemer eggplants) was investigated. Present findings revealed both genotypic effects and cultivar-related effects. While 46 embryos were obtained from Yamula eggplant genotypes, Kemer and Manisa eggplant genotypes were not able to form any embryos. Doksöz [6] investigated *in vitro* embryo formation ability of 4 hybrids and 1 local eggplant genotypes and was not able to obtain embryos from Malkara F1, Çantalı F1 and Tatlıcan F1 genotypes. Callus formation was not also observed in these genotypes. Researcher observed embryo formation in Yamula and Karabaş F1 genotypes at different ratios based on treatments. A total of 161 embryos and 88 plants were obtained from all treatments of that study. The greatest embryo formation ratio (25.55%, 46 embryoids from 180 anthers) was observed in Yamula eggplant genotype. The lowest embryo formation ratio (6.66%, 12 embryoids from 180 anthers) was observed in Karabaş F1 genotype. Plant regeneration ratios from the anthers varied between 0.55 – 15.15%.

In another study, Başay and Ellialtıoğlu [7] tested androgenic responses of 5 eggplant genotypes and 12 hybrid lines with the aid of anther culture technique. In the first year, embryo formation ratio of Topan and Halepkarası genotypes was respectively observed as 2.49 and 4.49%. From the same genotypes, plant formation ratios were respectively observed as 1.55 and 2.42%. Embryo formation was not observed in the other 3 genotypes. In the second year, embryo formation was observed in Topan, Halep Karası and Teorem F1cultivars and Vd-1, Vd-2 lines and embryo formation ratio was 16% in Topan genotype and 2.63% in Halepkarası genotype. Embryo transformation was not observed in Vd-1 and Vd-2 breeding lines. In the same genotypes (Topan and Halep karası), plant regeneration ratio was respectively observed as 3.33 and 1.32%. Haploid embryo formation ratio in reciprocal hybrid individuals from the genotypes and lines used in that study was observed as 0,87% in Topan x Teorem F1 hybrid and 2,57% in Teorem F1 x Topan hybrid. In the same hybrid individuals, plant regeneration ratios were respectively observed as 0.69 and 2.57%.

Salas et al. [8] investigated anther culture reactions of 8 *S. melongena* genotypes, 1 *S. incanum*, 1 *S. incanum* X *S. Melongena* hybrid, 1 *S. macrocarpon* and 1 *S. aethioipicum* genotype. Reserachers observed callus formation ratios of between 12,5 – 45,8% in all genotypes, except for *S. incanum*. Contrary to callus formation, embryo formation was observed only in 5 of 12 genotypes. In these genotypes, embryo formation ratios varied between 0,7 – 60,9%. Embryo formation was observed only in the genotypes of *S. melongena*. In the other genotypes and hybrid genotypes, there was a tendency only for callus formation.

Considering the results of those studies and present findings, it was concluded that genotypic effect was among the most significant factors influencing the success in anther culture. It was observed in present study that Yamula eggplant prominent with fruit flesh firmness yielded positive responses to anther culture. Thus, growth media and plant growth regulators were recommended to improve *in vitro* dihaploidization efficiency in Yamula eggplants.

ACKNOWLEDGEMENTS

This work was supported by the 327 Scientific Research Projects Department 328 of Erciyes University (Project No. FCD-329 2016-6379).

REFERENCES

[1] Sunderland, N. (1971) Antherculture: a progress report. Sci. Prog. Oxf. 59, 527-549.

[2] Çömlekçioğlu, N., Büyükalaca, S. and Abak, K. (2001) Effect of silvernitrate on haploid embryo induction by anther culture in pepper (*Capsicum annuum* L.). XIth EUCARPIA Meeting on Genetics and Breeding of Capsicum & Eggplant. Antalya-Turkey.

[3] Rashid, A. (1983) Pollen dimorphismin relation to pollen plant formation. Physiol. Plant. 58, 544-548.

[4] Ellialtıoğlu, Ş., Başay, S., Kuşvuran, Ş. (2012) Investigation of the relationship between polymorphism and anther culture in eggplant. TABAD. 5, 149–152. (In Turkish).

[5] Dumas de Vaulx, R., Chambonnet, D. (1982) Stimulation of plant production in eggplant (*S. melongena* L.) anther culture by treatment at 8 +35ºC and low growth concentration. Agronomy. 2(10), 983-988. (In French).

[6] Doksöz, S. (2015) Obtaining Dihaploid Lines in Different Eggplant Genotypes by In Vitro Androgenesis Method, Gaziosmanpaşa University Institute of Science, Master's Thesis. (In Turkish).

[7] Başay, S., Ellialtıoğlu, Ş.Ş. (2013) Effect of genotypical factors on the effectiveness of anther culture in eggplant (*Solanum melongena* L.). Turk. J. Biol. 37, 499-505.

[8] Salas, P., Prohens, J. and Seguí-Simarro, J.M. (2011) Evaluation of androgenic competence through anther culture in common eggplant and related species. Euphytica. 182(2), 261-274.

Received: **30.11.2021**
Accepted: **23.01.2022**

CORRESPONDING AUTHOR

Vese Pakashtica
Department of Agricultural Biotechnology,
Akdeniz University,
Antalya – Turkey

e-mail: vesapakashtica@gmail.com

© by PSP Volume 31– No. 05/2022 pages 5087-5094 Fresenius Environmental Bulletin

ENVIRONMENTAL PRICES AND ENERGY EFFICIENCY OF MANDARIN (*Citrus reticulata*) PRODUCTION: A CASE STUDY OF HATAY PROVINCE TURKEY

Oktay Soyler[1], Omer Eren[2,*], Selcuk Ugurluay[2]

[1]Iskenderun Vocational School, Iskenderun Technical University, Iskenderun, Hatay, Turkey
[2]Department of Biosystem Engineering, Faculty of Agriculture, Hatay Mustafa Kemal University, 31060, Antakya, Hatay, Turkey

ABSTRACT

The main objective of this study was to determined environmental prices and energy efficiency for mandarin (*Citrus reticulata*) production in Hatay province of Turkey. This study was performed for 2019 production season in Arsuz, Erzin, Dörtyol and Samandağ towns in Hatay province of Turkey. The data provided from study were collected from 78 different mandarin productioner by using a face to face questionnaire method. Environmental prices were calculated depent with greenhouse gas (GHG) emission of agricultural inputs. Also, the agricultural input values, input energies and output values, output energies used in mandarin production were calculated to determine the energy efficiency. According to the study findings, the environmental prices in mandarin production was calculated as 430.11 € ha^{-1}. Total GHG emission was calculated as 7545.87 $kgCO_{2-eq}$ ha^{-1} for mandarin production with the greatest portions for electricity usage (39.42%). The electricity usage followed up nitrogen fertilizer (17.67%), water consumption of irrigation (14.49%), human labour (6.88%), diesel fuel consumption (4.96%), phosphate fertilizer usage (4.77%), machine usage (2.66%), farmyard manure usage (2.64%), potassium fertilizer usage (2.07%), herbicides usage (1.71%), fungicides usage (1.60%) and insecticides usage (1.14%), respectively. Additionally, GHG ratio value was calculated as 0.23 $kgCO_{2-eq}$ kg^{-1}. Energy efficiency, specific energy, energy productivity and net energy calculations were calculated respectively as 0.98, 1.73 MJ kg^{-1}, 0.58 kg MJ^{-1} and -1134.65 MJ ha^{-1}.

KEYWORDS:
Mandarin (*Citrus reticulata*), energy efficiency, environmental prices, Hatay, Turkey

INTRODUCTION

The homeland of citrus is Chinese, Southeastern Asia and India and nowadays, citrus can be cultivated in almost all countries which have subtropical climate. Citrus is a plant community including the fruit kinds such as bitter orange, orange, mandarin, grapefruit and lemon [1]. Citrus fruits, which contain plenty of vitamin C and have important benefits for human health, are used as jam, marmalade and fruit juice as well as for fresh consumption, and are also used as raw materials in the cosmetics industry [2].

Turkey is one of the most important citrus producer countries in the world. Mandarin has a fairly important place in citrus fruits production in Turkey. In 2019, 1.4 million tons of mandarin were produced in Turkey. 90% of mandarin production was realized in the Mediterranean region and 9% in the Aegean region. In this season, the province of Hatay had the largest share in Turkey's mandarin production with 38%. Hatay was followed by Adana with 37% and Mersin with 12% [3].

Mandarin production is a major source of income for Hatay province. However, currently there are no studies available with regards to the environmental prices and energy efficiency of mandarin production in the region. Hence, this study aims to measure and determine environmental prices and energy efficiency of mandarin.

Environmental prices are indices that are used to calculate the social marginal value of preventing emissions, or interventions like noise and land-use changes, expressing it in € per kg pollutant or per decibal, for example. They are implicit prices: the price of environmental quality cannot be determined directly in the marketplace and must therefore be calculated individually [4]. Calculating greenhouse gas (GHG) emissions is very important in determining environmental prices.

Energy use in agricultural production systems is an important issue in sustainable production systems as it is directly related to the stability of the whole system and environmental problems [5]. The management of the agricultural production system is provided with a comprehensive plan that determines the energy balance of production, such as input-output energy analysis. Various inputs such as human labour, electricity, seed, fertilizer, diesel fuel etc. are consumed in agricultural production sector. And it has also been reported in literature studies [6, 7, 8] that energy inputs are used inefficiently. At the

same time, agricultural practices form the part of the potential sources of GHG emissions with ~12% generated by Turkey [9], and ~9% in the world of all GHG emissions coming from this sector [10]. An increased awareness of environmental safety and cleaner agricultural system has been achieved globally through the years [11]. In accordance to this awareness, energy efficiency, as well as agricultural practices with an impact on the surrounding environment, must be addressed cautiously [12]. Hence, agricultural inputs need to be optimized to minimize the impact on environment and to save energy in agricultural production systems.

Several different researches have been performed on energy efficiency and GHG emissions in relation to different agricultural products. Some of these studies are on energy efficiency activities of mandarin [1, 13, 14, 15] and citrus [1, 16, 17, 18]. The studies on greenhouse gas emissions were performed agricultural crops such as mandarin [19] and fruits [20, 21, 22]. Even though several studies have been conducted on energy efficiency and GHG emissions in agricultural production, so far no studies have been conducted on the environmental prices. This current study has investigated (1) environmental prices, (2) GHG emissions and (3) energy efficiency of mandarin production system in Hatay province of Turkey.

MATERIALS AND METHODS

Determining the case study area and data collection. The study area is in the northeast part of Hatay province in the southern region of Turkey (Figure 1). The district is located at 36° 30' north latitude and 36° 20' eastern longitude. The Mediterranean climate is dominant in the region; hot and dry in summers, warm and rainy in winters.

This study has been conducted during the 2019 production season in the Arsuz, Dörtyol, Erzin and Samandağ towns in Hatay province of Turkey. Data used in this study have been obtained through face-to-face interviews with 78 different mandarin productioner in the year 2019. The 'simple random sampling' method was applied to determine the survey volume [23].

$$n = \frac{(\sum N_h S_h)^2}{N^2 D^2 + \sum N_h S_h{}^2} \quad (1)$$

To determine this, we used formulae given in Eq. 1, where n is the required sample size, N is the number of holding in a target population, so is the standard deviation, it is t value at 95% confidence limit (1.96), and d is the acceptable error (permissible error 5%).

A specific form of questionnaire has been designed to with the purpose of collecting the required information related to various agricultural input uses (human labour, diesel fuel, irrigation water, fertilizers, etc.), machinery use and crop yields.

Environmental prices. The environmental prices (EP) (€ ha^{-1}) were calculated as follows [4]:

$$EP = GHG_{ha} \times EPC \quad (2)$$

Where GHG_{ha} is the GHG emissions ($kgCO_{2\text{-eq}}$ ha^{-1}) and EPC is environmental prices coefficient as € per $kgCO_{2\text{-eq}}$. This value is 0.057 € $kgCO_{2\text{-eq}}^{-1}$ for climate change.

The greenhouse (GHG) emissions ($kgCO_{2\text{-eq}}$ ha^{-1}) associated with the inputs to growing 1 ha of mandarin were calculated as following adapted [24]:

$$GHG_{ha} = \sum_{i=1}^{n} R(i) \times EF(i) \quad (3)$$

$\sum$ where $R(i)$ is the application rate of input i ($unit_{input}$ ha^{-1}) and $EF(i)$ is the GHG emission coefficient of input i ($kgCO_{2\text{-eq}}$ $unit_{input}^{-1}$). Table 1 lists GHG emissions coefficients of agricultural inputs.

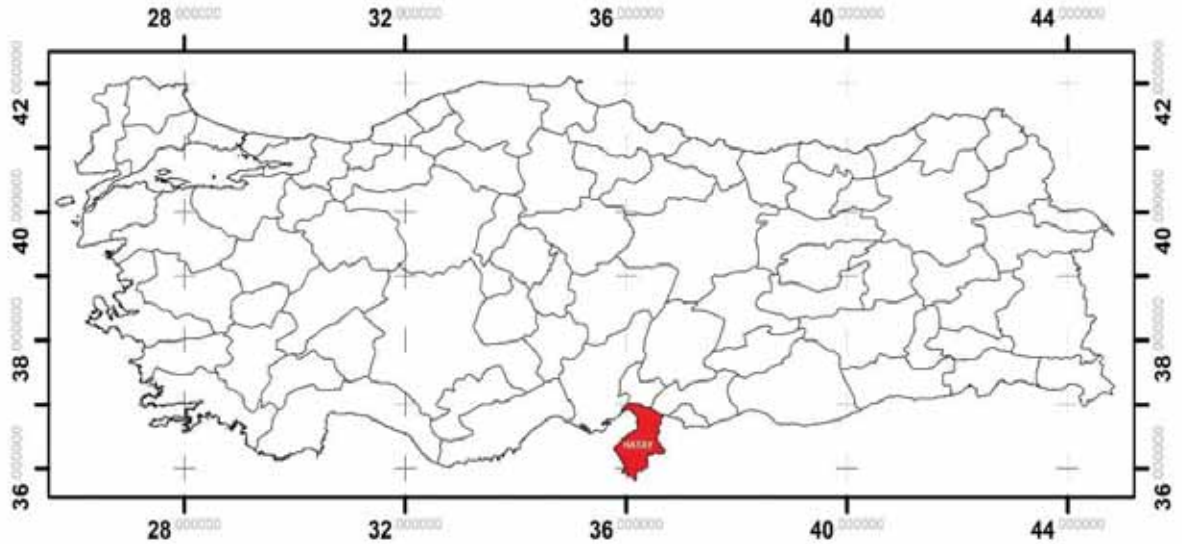

FIGURE 1
Location of the study area

TABLE 1
GHG emissions coefficients of agricultural inputs

Inputs	Unit	GHG coefficients ($kgCO_{2\text{-eq}}$ $unit^{-1}$)	References
Human labour	h	0.700	[25]
Machinery	MJ	0.071	[26]
Diesel fuel	L	2.760	[27]
Farmyard manure	kg	0.029	[28]
Chemical fertilizers			
Nitrogen (N)	kg	4.570	[29]
Phospate (P_2O_5)	kg	1.180	[29]
Potasium (K_2O)	kg	0.640	[29]
Chemical pesticides			
Insecticides	kg	18.700	[30]
Fungucides	kg	14.300	[30]
Herbicides	kg	10.970	[30]
Electricity (for Turkey)	MJ	0.167	[29]
Irrigation water	m^3	0.170	[31]

TABLE 2
Energy equivalents in mandarin production

Inputs and output	Unit	Energy equivalent (MJ $unit^{-1}$)	References
Human labour	h	1.96	[36]
Machinery	h	62.70	[37]
Diesel fuel	L	35.69	[38]
Farmyard manure	kg	0.30	[39]
Chemical fertilizers			
Nitrogen (N)	kg	45.00	[40]
Phospate (P_2O_5)	kg	8.00	[40]
Potasium (K_2O)	kg	2.00	[40]
Chemical pesticides			
Insecticides	kg	214.00	[41]
Fungicides	kg	156.70	[41]
Herbicides	kg	269.00	[41]
Electricity	kWh	11.93	[42]
Irrigation water	m^3	1.02	[43]
Output	**Unit**	**Energy equivalent (MJ $unit^{-1}$)**	**References**
Fruit	kg	1.70	[44]

Moreover, an index is defined to evaluate the amount of emitted kg $CO_{2\text{-eq}}$ per kg yield as following adapted [32] and [6]:

$$I_{GHG} = \frac{GHG_{ha}}{Y} \quad (4)$$

Where I_{GHG} is GHG ratio and Y is the yield as kg per ha.

Energy efficiency. Agricultural input energies and output energies in mandarin production have been calculated and used to determine the energy efficiency. Human labour energy, machinery energy, diesel fuel energy, farmyard manure energy, chemicals fertilizer energy, chemicals pesticides energy, electricity energy and irrigation water energy have been taken into consideration as inputs and mandarin yield has been taken into consideration as an output. Table 2 indicates the energy equivalents of the inputs of mandarin production. [33] Reported that "The input energy in crop production systems can be categorized as direct, indirect, renewable, and non-renewable energies". The direct energy sources involved in this study are human labour, diesel fuel, electricity and irrigation water. Indirect energy sources include machinery, farmyard manure, chemical fertilizers and chemical pesticides. Renewable energy sources in mandarin production system are human labour, farmyard manure and water for irrigation; while non-renewable energy sources are machinery, diesel fuel, chemical fertilizer, chemical pesticides and electricity.

The agricultural energy input (AEI) (MJ ha^{-1}) associated with the inputs to growing 1 ha of mandarin was calculated as following adapted [34]:

$$AEI = \sum_i^n R(i) \text{ x } E_{eq}(i) \quad (5)$$

$\sum$ where $R(i)$ is the application rate of input i ($unit_{input}$ ha^{-1}) and $E_{eq}(i)$ is the energy equivalent of input i (MJ $unit_{input}^{-1}$). The agricultural energy output (AEO) (MJ ha^{-1}) associated with the inputs to growing 1 ha of mandarin was calculated as following adapted [35]:

$$AEO = \sum_i^n Y(i) \text{ x } E_{eq}(i) \quad (6)$$

$\sum$ where $R(i)$ is the yield rate of output i ($unit_{input}$ ha^{-1}) and $E_{eq}(i)$ is the energy equivalent (often used lower heating values) of output i (MJ $unit_{input}^{-1}$).

In order to calculate the energy efficiency in mandarin production, "Energy ratio, specific energy, energy productivity and net energy have been calculated as follows, as adapted from [34]":

$$\text{Energy ratio (decimal)} = \frac{AEO}{AEI} \quad (7)$$

$$\text{Spesific energy (MJ kg}^{-1}) = \frac{AEI}{Y} \quad (8)$$

$$\text{Energy productivity (kg MJ}^{-1}) = \frac{Y}{AEI} \quad (9)$$

$$\text{Net energy (MJ ha}^{-1}) = AEO - AEI \quad (10)$$

RESULTS AND DISCUSSION

Environmental prices. The results of environmental prices and GHG emissions of agricultural inputs in mandarin production are shown in Table 3. The total environmental price of mandarin production has been determined as 430.11 € ha^{-1}.

The distribution of different agricultural inputs in environmental prices illustrated in Figure 2. The findings of this study indicates that the share of electricity used in total environmental prices was the highest (39.42%), followed by nitrogen fertilizer (17.67%) and irrigation water (14.49%) occupying second and third places. So, better agricultural management in terms of electricity used can lead to a mandarin production with lower environmental prices in the production area.

The total GHG emissions and ratio have been calculated as 7545.87 $kgCO_{2\text{-eq}}$ ha^{-1} and 0.23 $kgCO_{2\text{- eq}}$ kg^{-1} in this study. In similar a study [19], calculated the total GHG emission and GHG ratio of mandarin production in South East Spain as 4212. 00 $kgCO_{2\text{-eq}}$ ha^{-1} and 0.12 $kgCO_{2\text{-eq}}$ kg^{-1}. This study compared to literature study, the GHG emissions and ratio values was found to be higher.

TABLE 3
Environmental prices and GHG emissions of agricultural inputs in mandarin production

Inputs	Unit	Input used per area (unit ha^{-1})	GHG emissions (kg CO_{2eq} ha^{-1})	EP (€ ha^{-1})
Human labour	h	741.47	519.03	29.58
Machinery	MJ	2825.89	200.64	11.44
Diesel fuel	L	135.57	374.17	21.33
Farmyard manure	kg	6879.00	199.49	11.37
Nitrogen (N)	kg	291.76	1333.34	76.00
Phospate (P_2O_5)	kg	305.29	360.24	20.53
Potasium (K_2O)	kg	244.32	156.36	8.91
Insecticides	kg	4.58	85.65	4.88
Fungicides	kg	8.43	120.55	6.87
Herbicides	kg	11.76	129.01	7.35
Electricity	MJ	17809.84	2974.24	169.53
Irrigation water	m^3	6430.24	1093.14	62.31
Total	-	-	7545.87	430.11

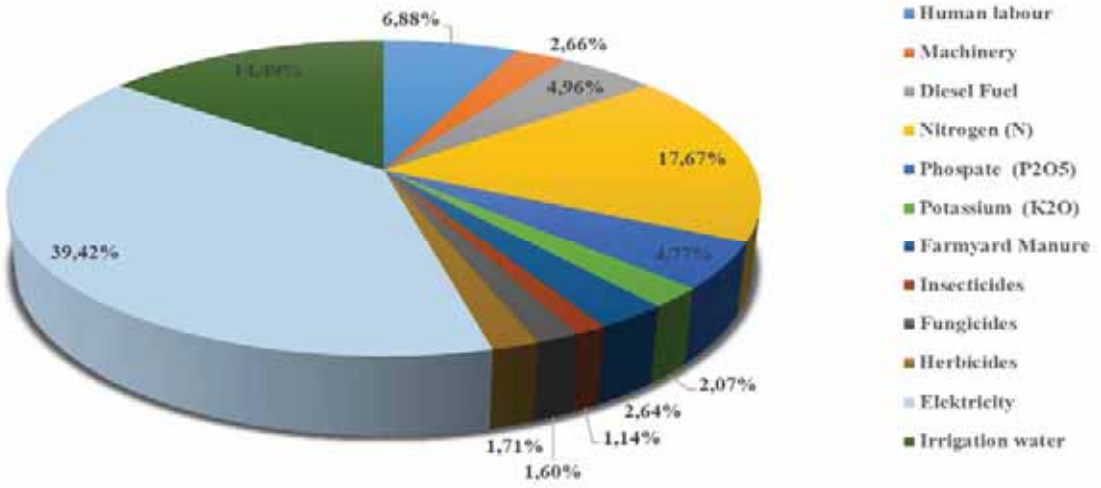

FIGURE 2
Distribution of environmental prices of agricultural inputs in mandarin production

TABLE 4
Agricultural energy inputs/outputs in mandarin production

Inputs	Unit	Input used per area (unit ha^{-1})	Energy value (MJ ha^{-1})
Human labour	h	741.47	1453.28
Machinery	h	45.07	2825.89
Diesel fuel	L	135.57	4838.49
Farmyard manure	kg	6879.00	2063.70
Nitrogen (N)	kg	291.76	13129.20
Phospate (P_2O_5)	kg	305.29	2442.32
Potasium (K_2O)	kg	244.32	488.64
Insecticides	kg	4.58	980.12
Fungicides	kg	8.43	1320.98
Herbicides	kg	11.76	3163.44
Electricity	kWh	1492.87	17809.94
Irrigation water	m^3	6430.24	6558.84
AEI	-	-	57074.85
Outputs	**Unit**	**Output per hectare (unit ha^{-1})**	**Energy value (MJ ha^{-1})**
Mandarin	kg	32906.00	55940.20
AEO	-	-	55940.20

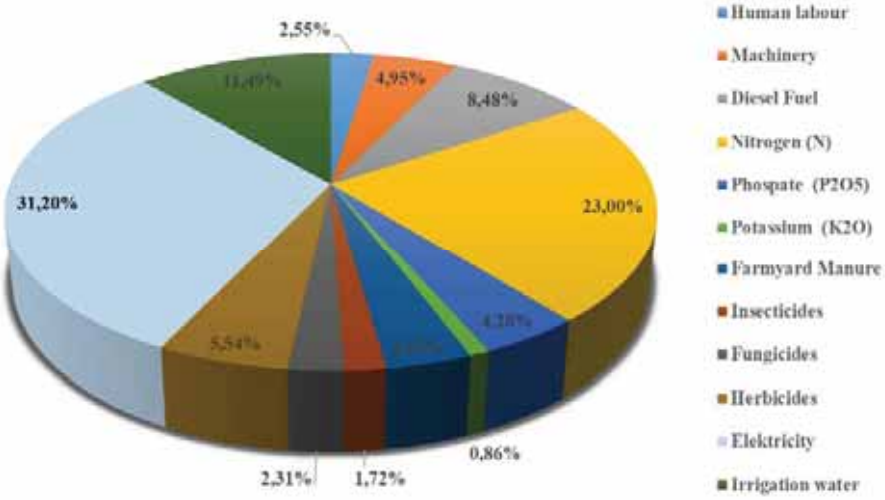

FIGURE 3
Distribution of energy inputs in mandarin production

Energy efficiency. The results of energy values of agricultural inputs and outputs in mandarin production are shown in Table 4. The average amount of mandarin produced per hectare for 2019 production season has been calculated as 32906.00 kg. Total agricultural energy input (AEI) and output (AEO) has been calculated as 57074.85 MJ ha^{-1}, 55940.20 MJ ha^{-1}, respectively.

The distribution of different agricultural energy inputs in total AEI illustrated in Figure 3. The findings of this study indicates that the share of electricity used energy in total AEI was the highest (31.20%), followed by nitrogen fertilizer energy (23.00%) and irrigation water energy (11.49%) occupying second and third places. So, better agricultural management in terms of electricity used energy would lead to a mandarin production with lower AEI in the production area.

The indicators of energy efficiency observed in the studied mandarin production units, including AEI, AEO, energy ratio, specific energy, energy productivity and net energy are given in Table 5. Indicator values in mandarin production have been calculated as 57074.85 MJ ha^{-1}, 55940.20 MJ ha^{-1}, 0.98, 1.73 MJ kg^{-1}, 0.58 kg MJ^{-1} and -1134.65 MJ ha^{-1}, respectively.

The energy ratio have been calculated as 0.98 in this study. In similar studies, energy ratio of mandarin production was reported to be 1.88 and 2.00 [1], 1.56 [13], 1.92 [14], 0.83 [15] and 1.17 [16]. This study compared to similar studies, the energy ratio value was found to be lower. Since the energy ratio value was calculated as lower than 1, a good result could not be obtained in terms of energy efficiency. It was determined to be better than the data obtained in the study of [15].

TABLE 5
Indicators and different forms of energy efficiency and inputs in mandarin production

	Units	Values	%
Indicators of energy efficiency			
AEI	MJ ha^{-1}	57074.85	
AEO	MJ ha^{-1}	55940.20	
Energy ratio	decimal	0.98	
Specific energy	MJ kg^{-1}	1.73	
Energy productivity	kg MJ^{-1}	0.58	
Net energy	MJ ha^{-1}	-1134.65	
Forms of energy inputs			
Directed energy	MJ ha^{-1}	30660.56	53.72
Indirected energy	MJ ha^{-1}	26414.29	46.28
Renewable energy	MJ ha^{-1}	10075.83	17.65
Non-renewable energy	MJ ha^{-1}	46999.02	82.35

At the same time, the different forms of AEI in the studied mandarin production season including direct energy, indirect energy, renewable energy and non-renewable energy are given in Table 5. Values of this forms in mandarin production have been calculated as 30660.56 MJ ha^{-1} (53.72%), 26414.29 MJ ha^{-1} (46.28%), 10075.83 MJ ha^{-1} (17.65%) and 46999.02 MJ ha^{-1} (82.35%), respectively.

CONCLUSIONS

Environmental prices and energy efficiency of mandarin production have been specified as a conclusion of this study. According to the current findings, mandarin production does not seem profitable in terms of energy ratio (0.98). The average amount of mandarin produced per hectare has been determineted as 32906.00 kg. Agricultural energy input and output has been calculated as 57074.85 MJ ha^{-1} and 55940.30 MJ ha^{-1}, respectively. The first three energy inputs with high values in mandarin production have been respectively electricity used energy, fertilizer energies and irrigation water energy. Net energy value have been calculated as -1134.65 MJ ha^{-1}. For this reason, a good result could not be obtained in terms of energy efficiency in cultivated mandarin production.

The total environmental prices have been calculated as 430.11 € ha^{-1} for mandarin production. Top three inputs with high values in terms of environmental prices in mandarin production have been respectively electicity, nitrogen fertilizer and irrigation water. Additionally, GHG emission and GHG ratio value have been calculated as 7545.87 $kgCO_{2\text{-eq}}$ ha^{-1} and 0.23 $kgCO_{2\text{-eq}}$ kg^{-1} in mandarin production in Hatay Province of Turkey.

As a result of this study, it has become apparent that reducing electricity usage, irrigation water usage and especially nitrogen fertilizer usage are needed with regards to the mandarin production in the study region. For this purpose (to reduce the high chemical fertilizer that causes GHG emissions), soil analysis is recommended in order to accurately determine the soil fertilizer needs.In addition, use of irrigation water and electricity should be made more efficient. Finally, greenhouse gas emissions during the production of other agricultural products in Turkey should be determined and studies related to environmental prices must be done.

REFERENCES

[1] Yılmaz, H., Aydın, B. (2020) Comparative input-output energy analysis of citrus production in Turkey: Case of Adana province. Erwerbs-Obstbau. 62, 29-36.

[2] Uysal, O., Polatöz, S. (2017) Citrus production and foreign trade in the world and in Turkey. Turkey Seed Growers Association (TURKTOB) Journal. 22, 6-11 (in Turkish).

[3] TUIK (2019) Turkish statistical institute datas. http://www.tuik.gov.tr (Accessed 08.10.2020).

[4] Bruyn, S.T., Ahdour, S., Bijleveld, M., De Graaff, L., Schep, E., Schroten, A., Vergeer, R. (2018) Environmental prices handbook. Methods and numbers for valuation of environmental impacts. CE Delft, Publication code: 18.7N54.057.

[5] Kehagias, M.C., Michos, M.C., Menexes, G.C., Mamolos, A.P., Tsatsarelis, C.A., Anagnostopoulos, C.D. and Kalburtji, K.L. (2015) Energy equilibrium and carbon dioxide, methane, and nitrous oxide-emissions in organic, integrated and conventional apple orchards related to natura 2000 site. Journal of Cleaner Production. 91, 89-95.

[6] Khoshnevisan, B., Shariati, H.M., Rafiee, S., Mousazadeh, H. (2014) Comparison of energy consumption and GHG emissions of open field and greenhouse strawberry production. Renewable and Sustainable Energy Reviews. 29, 316-324.

[7] Nassiri, S.M., Singh, S. (2009) Study on energy use efficiency for paddy crop using data envelopment analysis (DEA) technique. Applied Energy. 86(7-8), 1320-1325.

[8] Özkan, B., Akcaöz, H., Fert, C. (2004) Energy inpute-output analysis in Turkish agriculture. Renewable Energy. 29(1), 39-51.
[9] UNFCCC (2017) Summary of GHG emissions for Turkey. United nations framework convention on climate change. https://di.unfccc.int/ghg_profiles/annexOne/TUR/TUR_ghg_profile.pdf (Accessed 09.04 2020).
[10] UNFCCC (2017) Summary of GHG emissions for annex I. United Nations framework convention on climate change. https://di.unfccc.int/ghg_profiles/annexOne/ANI/ANI_ghg_profile.pdf (Accessed 09.04 2020).
[11] Khoshnevisan, B., Rafiee, S., Omid, M., Mousazadeh, H., Clark, S. (2014) Environmental impact assessment of tomato and cucumber cultivation in greenhouses using life cycle assessment and adaptive neuro-fuzzy inference system. Journal of Cleaner Production. 73, 183-192.
[12] Mohammadi-Barsari, A., Firouzi, S., Aminpanah, H. (2016) Energy-use pattern and carbon footprint of rain-fed watermelon production in Iran. Inf. Process. Agric. 3, 69-75.
[13] Bilgili, M.E. (2021) Energy use efficiency of mandarin production: A case study from Adana province. Erwerbs-Obstbau. 63, 61-64.
[14] Dağtekin, M., Bilgili, M.E., Beyaz, A. (2019) The effects of good agricultural practises on energy use effectiveness on mandarin production and environmental. Erwerbs-Obstbau. 61, 55-60.
[15] Mohammadshirazi, A., Akram, A., Rafiee, S., Avval, S.H.M., Kalhor, E.B. (2012) An analysis of energy use and relation between energy inputs and yield in tangerine production. Renew. Sustain. Energy Rev. 16, 4515-4521.
[16] Özkan, B., Akcaöz, H., Karadeniz, F. (2004) Energy requirement and economic analysis of citrus production in Turkey. Energy Convers and Management. 45, 1821-1830.
[17] Loghmanpor Zarini, R., Yaghoubi, H., Akram, A. (2013) Energy use in citrus production of Mazandaran province of Iran. African Crop Sci. J. 21(1), 61-65.
[18] Namdari, M., Kangarshahi, A.A., Amiri, N.A. (2011) Input-ouput energy analysis of citrus production in Mazandaran province of Iran. Afr. J. Agric. Res. 6(11), 2558-2564.
[19] Martin-Gorriz, B., Soto-García, M., Martínez-Alvarez, V. (2014) Energy and greenhouse-gas emissions in irrigated agriculture of SE (southeast) Spain. Effects of alternative water supply scenarios. Energy. 77, 478-488.
[20] Clune, S., Crossin, E., Verghese, K. (2017) Systematic review of greenhouse gas emissions for different fresh food categories. Journal of Cleaner Production. 140, 766-783.
[21] Stoessel, F., Juraske, R., Pfister, S., Hellweg, S. (2012) Life cycle inventory and carbon and water food print of fruits and vegetables: application to a Swiss retailer. Environ. Sci. Technol. 46, 3253-3262.
[22] Eren, Ö., Baran, M.F., Gökdoğan, O. (2019) Determination of greenhouse gas emissions (GHG) in the production of different fruits in Turkey. Fresen. Environ. Bull. 28(1), 464-472.
[23] Çicek, A., Erkan, O. (1996) Research and sampling methods in agricultural economics. Gaziosmanpaşa University Agricultural Faculty Publications. 12.
[24] Hughes, D.J., West, J.S., Atkins, S.D., Gladders, P., Jeger, M.J., Fitt, B.D. (2011) Effects of disease control by fungicides on greenhouse gas emissions by U.K. arable crop production. Pest Manag. Sci. 67, 1082-1092.
[25] Nguyen, T.L.T., Hermansen, J.E. (2012) System expansion for handling co-products in LCA of sugar cane bio-energy systems: GHG consequences of using molasses for ethanol production. Applied Energy. 89, 254-261.
[26] Pishgar-Komleh, S.H., Ghahderijani, M. and Sefeedpari, P. (2012) Energy consumption and CO2 emissions analysis of potato production based on different farm size levels in Iran. Journal of Cleaner Production. 33, 183-191.
[27] Clark, S., Khoshnevisan, B., Sefeedpari, P. (2016) Energy efficiency and greenhouse gas emissions during transition to organic and reduced-input practices: Student farm case study. Ecological Engineering. 88, 186-194.
[28] Houshyar, E., Mahmoodi-Eshkaftaki, M., Azadi, H. (2017) Impacts of technological change on energy use efficiency and GHG mitigation of pomegranate: Application of dynamic data envelopment analysis models. Journal of Cleaner Production. 162, 1180-1191.
[29] BioGrace-II (2015) Harmonised Calculations of Biofuel Greenhouse Gas Emissions in Europe. BioGrace, Utrecht, The Netherlands. http://www.biograce.net. (Accessed 09.04 2020).
[30] Maraseni, T.N., Cockfield, G., Maroulis, J., Chen, G. (2010) An assessment of greenhouse gas emissions from the Australian vegetables industry. Journal of Environmental Science and Health. 45(6), 578-588.
[31] Lal, R. (2004) Carbon emission from farm operations. Environment International. 30, 981-990.
[32] Houshyar, E., Dalgaard, T., Tarazgar, M.H., Jorgensen, U. (2015) Energy input for tomato production what economy says, and what is good for the environment. Journal of Cleaner Production. 89, 99-109.

[33] Mohammadzadeh, A., Damghani, A.M., Vafabakhsh, J., Deihimfard, R. (2017) Assessing energy efficiencies, economy and global warming potential (GWP) effects of major crop production systems in Iran: A case study in East Azerbaijan province. Environmental Science and Pollution Research. 24, 16971-16984.
[34] Farrell, A.E., Plevin, R.J., Turner, B.T., Jones, A.D., O'Hare, M., Kammen, D.M. (2006) Ethanol can contribute to energy and environmental goals. Science. 311, 506–508.
[35] Öztürk, H.H. (2010) Energy use in agricultural production. Hasad Yayınevi. ISBN 975-8377-78-7
[36] Mani, I., Kumar, P., Panwar, J.S., Kant, K. (2007) Variation in energy consumption in production of wheat-maize with varying altitudes in hill regions of Himachal Prades, India. Energy. 32, 2336-2339.
[37] Mardani, A., Taghavifar, H. (2016) An overview on energy inputs and environmental emissions of grape production in West Azerbayjan of Iran. Renewable and Sustainable Energy Reviews. 54, 918-924.
[38] Ejilah, I.R., Asere, A.A. (2008) A comparative performance and emission analysis of blended groundnut oil and mineral oil based lubricants using a spark ignition engine. Agricultural Engineering International. The CIGR E Journal Manuscript. 10, 07-11.
[39] Singh, J.M (2002) On garden energy use pattern in different cropping systems in Haryana, India. International Institute of Management University of Flensburg, Sustainable Energy Systems and Management. Master of Science, Germany.
[40] Ramirez, C.A., Worrell, E. (2006) Feeding fossil fuels to the soil an analysis of energy embedded and technological learning in the fertilizer industry. Resources, Conservation and Recycling. 46, 75-93.
[41] Ferraro, D.O. (2003) Energy cost/use in pesticide production. Encyclopedia of Pest Management, D. Pimentel. ISBN: 0-8247-0847-4. Marcel Dekker, Inc. New York. 1-4.
[42] De, D., Singh, R.S., Chandra, H. (2001) Technological impact on energy consumption in rainfed soybean cultivation in Madhya Pradesh. Applied Energy. 70 (3), 193-213.
[43] Rafiee, S., Mousavi Avval, S.H.M., Mohammadi, A. (2010) Modeling and sensitivity analysis of energy inputs for apple production in Iran. Energy. 35 (8), 3301-3306.
[44] Martin-Gorriz, B., Soto-García, M., Martínez-Alvarez, V. (2014) Energy and greenhouse-gas emissions in irrigated agriculture of SE (southeast) Spain. Effects of alternative water supply scenarios. Energy. 77, 478-488.

Received: **30.11.2021**
Accepted: **23.01.2022**

CORRESPONDING AUTHOR

Omer Eren
Department of Biosystem Engineering,
Faculty of Agriculture,
Hatay Mustafa Kemal University,
31060 Antakya Hatay – Turkey

e-mail: dromereren@gmail.com

© by PSP Volume 31– No. 05/2022 pages 5095-5104 Fresenius Environmental Bulletin

EFFECT OF SOIL SALINITY WIZARDS ON ION SELECTIVITY GROWTH AND PRODUCTIVITY OF RICE

Ayman A Mohamed[1], Yasser Mazrou[2,3], Bassiouni A Zayed[4], Shimaa A Badawy[1], Sameh A Nadier[4], Yaser Hafez[5], Khaled Abdelaal[5,*]

[1]Agronomy Department, Faculty of Agriculture Kafrelshiekh University, Egypt
[2]Business Administration Department, Community College, King Khalid University, Guraiger, Abha 62529, Saudi Arabia
[3]Faculty of Agriculture, Tanta University, Tanta 31512, Egypt
[4]Rice Research and Training Center, Sakha, Field Crop Research Institute, ARC, Egypt
[5]EPCRS Excellence Center, Plant Pathology and Biotechnology Lab., Agric. Botany Dept., Fac. Agric., Kafrelsheikh University, Egypt

ABSTRACT

Tow field experiments were conducted during 2019 and 2020 seasons to study the behavior of rice cultivars (Giza177, Sakha107 and Giza179) under three varying salinity wizards *Viz*, Salwax, Aquasal and Crop plus, whereas the first two materials were applied in soil before transplanting while, the third material was sprayed twice at rate 5 kg ha^{-1} for each one. The split plot design was used in this study whereas, salinity wizards were placed in the main plots but the sub plots were allocated to rice cultivars. The main obtained results in both seasons provided significant and positive effect was released by the used soil salinity chemicals treatments on behavior of rice cultivars as rice salinity tolerance, ion selectivity, growth parameters, yield attributes and grain yield. The most effective and beneficial treatment was SalWax followed by AquaSal and then crop plus regarding studied parameters. Applying these materials via soil was more efficient than those applied via foliage however, crop plus came in the last rank in this study. The studied three rice varieties significantly varied in their performance considering salinity tolerance, ion selectivity, rice growth, yield attributes and grain yield in both seasons. The results showed that Giza 179 cultivar gave apparent values of salinity tolerance were cleared in the lowest value of Na^+/K^+ ratio, high K^+ concentration, high growth, yield attributes and grain yield. The obtained result confirmed the superiority and tolerance of Giza179 rice variety under salt stresses. Sakha 107 rice variety is considered as salt moderately sensitive variety, while Giza177 was continued to be salt sensitive variety. The interaction effect brought the superiorly of the combination of Giza179 and Salwax under salt stress. It could be concluded that Salwax salinity wizards should apply in soil for rice growing under saline soil before transplanting at the rate of 5 kg ha^{-1}.

KEYWORDS:
Soil salinity, Rice, wizards, ion selectivity

INTRODUCTION

Rice is main diet for more than 80% of Egyptian population and the main crop during summer season in a northern part of Nile Delta. The most of rice cultivated area in Egypt is salt affected soil and the problem recently was magnified as a result of using poor quality water and climate change. Salinity stress is a chronic problem in Egypt which threats rice production sustainability, it is a harmful environmental issue that is considered one of the main causes of reductions in agricultural crop productivity through the dysfunction occurred in the plant physiological and biochemical processes in many plants [1-7], Salinity problem either from soil or water sharply hindered rice growth and yield, since rice is salt sensitive crop [8, 9]. The morphological and physiological characters of many plants were negatively affected with stress factors mainly salinity and drought [10-25]. Salt stress induces several adverse effects on growth development and physiological process and yield as well as quality of crop and soil degradation [26-28]. Rice is cultivated in Egypt under wide spectrum area affected by salt stress involving soil and water. Most of rice cultivated area is salt affected soil, whereas the great area of salt affected area is saline sodic soil. Maintaining and conservation of saline sodic soil is needed to improve its fertility by applied soil amendments to enhance rice productivity. In Egypt, rice is dominant summer crop cultivated under such soil that need relevant soil amendments to get reasonable rice yield [26]. Releasing of salt tolerant rice genotypes is one effective approaches for palliative the effects of salinity. Efforts now focus on breeding hybrid rice genotypes have main features such as long panicles, more productive tillers and high-yielding [29] as well as tolerant stress [26,30]. Varying rice genotypes are differentially influenced by salinity in their response regarding growth, yield attributes and grain yield as well as the salinity tolerance mechanism by minimizing the entry of salt into the plant, or reducing the concentration of salt in cytoplasm [31, 32]. Munns, [33] and Hossain et al. [34] stated that the salt-toler-

ant plants exhibited low Na^+ content, but accumulated high K^+ resulting in a lower Na^+/K^+ ratio, accumulation of excess Na^+ and Cl^- causes ionic imbalance that may impair the selectivity of root membranes and induce K^+ deficiency in plants. Zayed et al. [35] found that the Egyptians rice varieties,Giza177, Giza 178 and EHR1 as well as Giza 179 and Sakha 104 were significantly varied in their performance tolerance, ion selectivity, growth parameters, such leaf area index, dry mater, chlorophyll pigments, antioxidants, all yield attributes and yields under salt affected soil [36-38]. Applying soil amendments using compounds containing Ca^{+2} or S with acidity effect for saline sodic soil apparently improved yields as a result of soil reclamation and improving soil structure [39]. Application of wizards could mitigate some negative effects of salinity on grown plants and soil microorganisms, increases in soil organic carbon, result increase enhancement of water holding capacity, nutrient retention capacity and Improvement of structure and biology of soil [40]. Application of sulfur and gypsum significantly increased Ca^{2+} in the soil which probably replaced Na^+ from the exchange sites in the colloidal complex and consequently reduced pH, EC and SAR as well as increased rice growth, yield attributes and rice yield [41]. Sulfur as essential nutrient significantly increased growth parameters and yield of rice as well as water productivity under deficit irrigation and salinity condition up to 600 kg S ha^{-1} [26]. Under salinity condition, foliar spray with nutrients at critical growth stages will improve the emergence of panicle and reduce sterility. Due to numerous compensations of foliar application methods like a quick and capable response to needs have plants, more effective, less costly [42,43]. Spraying mixture of micronutrients involving Zn, Fe, Mn and B on rice was more efficient and benefit in enhancing rice salinity tolerance, rice growth development, yield attributes and yields comparing soil application [44, 45]. However, Shaban et al. [46] recorded the highest values of rice yield and its attributes as well as nutrients content by application of sulfur at a rate of 4.8 ton ha^{-1} or sulphuric acid at the rate of 1190 L ha^{-1}. Mohamed et al. [47] reported that Potassium foliar spray three times at certain rice growth was detected to be more beneficial than basal application at the rate of 48 kg K_2O regarding improving rice grain quality of Giza 179, yield components and grain yield. There for the current research aimed to study the behavior of some rice cultivars grown under salt affected soil by defining the difference in the morphological, physiological and yield traits among cultivars as well as determine proper and beneficial soil amendments for saline sodic conservation, keeping high soil fertility and quality that is ensuring high rice productivity.

MATERIALS AND METHODS

The experimental site: The experiments were performed at the Northern East of the Nile Delta, Egypt one kilometer from the boundary of El-Mansla lack at the Farm of Elsirw agriculture research station, Dammitta province.

The experimental design and treatments: The current attempt was designated to study the effect of applying some chemical wizards via soil or foliage on growth and yield of some rice varieties. The experimental design was split plot with four replications. The main plots included the four tested salinity wizards, control, Aquasal applied via soil, Salwax applied via foliage and Crop plus applied via foliage. The three varying varieties, Gza177, Sakha107 and Giza179 were distributed in the sub plots. The plots size was $10m^2$.

Composition of used chemicals and its approach application. 1-Salwax is also soil salinity treatment. The chemical gradients of Sal wax compound are15%, 14%, 4%, 5% and 50% of potassium, CaO, AmEC and carboxylic acids, respectively. It was applied as in the Aqua Sal.

2-Aquasal is salinity treatment material contained Calcium, Nitrogen and carboxylic acids at the concentration of 11, 9 and 50%, respectively. It was applied with first irrigation immediately before transplanting at the rate of 5kg ha^{-1}.

3-Crop plus is working as salinity effects alleviator via foliage application in the rate of 5 kg ha^{-1} at tillering and mid booting stages. The chemical composition of crop plus is 4.5%, 1.7% .3% 1.4 and 1.3% of sulfur, iron, zinc, manganese and cupper, respectively as nature growth stimulator with Mack technology.

The properties of experimental site: The representative soil sample of experimental site were taken in 0–30 cm soil depth, transferred to soil lab, prepared for some chemical and physical properties [48,49], the soil chemical and physical properties are listed in Table 1.

TABLE 1
Chemical and physical properties of experimental soil

season	Soil texture	pH	ECe dSm^{-1}	Cation meq l^{-1}				Anion meq l^{-1}		
				Ca^{++}	Mg^{++}	Na^+	K^+	SO_4	cl^{-1}	HCo_3
2019	clayey	8.23	8.0	18.8	16.8	40.0	0.30	32.0	40	11
2020	clayey	8.19	7.2	19.9	16.0	39.0	0.31	30.0	43	12

TABLE 2

Sodium% (Na+), potassium% (K+)and Na+ K+ ratio of rice leaf at heading stage affected by varieties and some of salinity wizards under saline soil in 2019 and 2020 seasons

Soil wizards	Na%		K%		Na/K ratio	
	2019	2020	2019	2020	2019	2020
control	1.76a	1.77a	1.30c	1.38d	1.38a	1.33a
Salwax	1.41c	1.45d	1.54a	1.61a	0.93c	0.92d
Aquasal	1.51b	1.55c	1.51ab	1.56b	1.01b	1.01c
Crop plus	1.56b	1.58b	1.45b	1.51c	1.09b	1.07b
F test	**	**	**	**	**	**
Rice varieties						
Giza177	1.90a	1.94a	1.34c	1.35c	1.43a	1.45a
Sakah107	1.55b	1.61b	1.42b	1.48b	1.09b	1.09b
Giza179	1.23c	1.20c	1.59a	1.71a	0.78c	0.70c
F test	**	**	**	**	**	**
Interaction	NS	**	NS	NS	NS	**

*, ** and Ns indicate P < 0.05, P < 0.01 and not significant, respectively. Means of each factor designated by the same latter are not significantly different at 5% level using Duncan's Multiple Range Test.

TABLE 3

Sodium (Na^+) % and Na^+/K^+ ratio of rice leaf as affected by the interactions between rice varieties and salinity wizards in 2020 season only.

Varieties	Na %				Na / K ratio			
	2020				2020			
	Salinity wizards							
	Control	Salwax	Aqua Sal	Crop plus	Control	Sal wax	Aqua Sal	Crop plus
Giza177	2.21a	1.76c	1.88b	1.93b	1.86a	1.22d	1.32c	1.42b
Sakha107	1.80c	1.46e	1.58d	1.60d	1.32c	0.93f	1.04e	1.08e
Giza179	1.29f	1.14g	1.19g	1.20g	0.80g	0.62i	0.68hi	0.70h
F. test	**				**			

TABLE 4

Growth parameters of rice affected by cultivars and some of salinity wizards under saline soil in 2019 and 2020 seasons

Soil wizards	Dry matter ghill^{-1}		LAI		Chlorophyll	
	2019	2020	2019	2020	2019	2020
control	30.00d	31.14d	3.76c	3.87c	30.16c	28.91c
Salwax	39.12a	41.19a	4.62a	4.77a	33.75a	34.41a
Aquasal	36.16b	37.65b	4.32b	4.48b	31.58b	32.58b
Crop plus	32.50c	34.58c	4.20b	4.39b	31.58b	32.08b
F test	**	**	**	**	**	**
Rice varieties						
Giza177	27.38c	29.34c	3.60c	3.76c	28.31c	27.68c
Sakha107	34.55b	36.36b	4.08b	4.26b	32.25b	31.87b
Giza179	41.41a	42.71a	5.00a	5.12a	34.75a	36.43a
F test	**	**	**	**	**	**
Interaction	NS	NS	NS	NS	**	**

*, ** and Ns indicate P < 0.05, P < 0.01 and not significant, respectively. Means of each factor designated by the same latter are not significantly different at 5% level using Duncan's Multiple Range Test.

TABLE 5

Chlorophyll content of rice as affected by varieties and some of salinity wizards under saline soil in 2019 and 2020 seasons.

Variety	2019				2020			
	Salinity wizards							
	Control	Sal wax	Aqua Sal	Crop plus	Control	Sal wax	Aqua Sal	Crop plus
Giza177	25.25g	32.00de	27.75f	28.25f	23.25h	31.25e	28.00g	28.25g
Sakha107	31.25e	33.25cd	32.00de	32.50de	29.75f	33.75c	32.50d	31.50de
Giza179	34.00bc	36.00a	35.00ab	34.00bc	33.75c	38.25a	37.25ab	36.50b
F. test	**				**			

The nursery was well fertilized with calcium super phosphate (15.5% P2O5) at the rate of 71.5 kg ha-1 on the dry soil before plaguing. After puddling nitrogen in form of urea (46%N) at the rate of 164.20 kg N ha-1 and zinc sulfate at the rate of 23.8 kg ha-1 were added. Rice seeds at the rate of 142.8 kg ha-1 were soaked, in running water, and incubated for 36 hours each to enhance germination and finally pre-germinated seeds were manually broadcasted. Weeds were chemically controlled using Saturn (50%) at the rate of 4.75 liters ha-1 dissolved in 200 liters of water which sprayed using Knapsack sprayer seven days after sowing. Cultivars were sown in separate nursery beds on April, 25th, in the two seasons of study. The previous crop was Egyptian clover (*Trifolium alexandrinum*, L) in the two seasons of study. In the permanent field, soil was well prepared. Calcium super phosphate (15.5% P2O5) and potassium sulfate (48% K2O) were applied in the dry soil before flooding. Thirty days old seedling was transplanted 20 cm row-to-row, 3-4 seedlings/hill with 20 cm hill to hill. Each plot included ten rows with five-meter length and 20 cm apart, (area 10 m2). The other usual agricultural practices of growing rice were performed as the recommendation of Ministry of Agricultural and Land Reclamation. At heading stage plant samples (five hills each), were randomly taken from each plot to estimate potassium and sodium leaf contents [50]. Leaf area index, dry matter weight (g m2), chlorophyll content, heading date and plant height (cm) was measured from the soil surface up to the tallest panicle tip for each plant. Total tillers (productive and non-productive tillers) of five hills were estimated and then converted to number of tillers/hill. At harvest, ten main panicles were randomly taken to determine the grain yield attributes, i.e., panicle length (cm), number of panicles hill-1, number of filled grains panicle-1, number of unfilled grains panicle-1, panicle weight (g) and 1000-grain weight (g). The grain and straw yields, of six inner rows for each sub plot, were determined and converted into t ha-1, based on 14% moisture content. All the data collected were subjected to analysis of variance [51]. Treatment means were compared by Duncan's multiple range tests [52]. All statistical analysis was performed using analysis of variance technique by means of "COSTAT" computer software package.

RESULTS AND DISCUSSIONS

Ion selectivity and rice growth parameters. The listed data in Table 2 being to confirm the ability and significant of applying varying salinity wizards to improve ion selectivity in rice plant grown under salt stress in both season via inducing clears K and Na balance. Interestingly applying the current salinity wizards significantly increased the concentration of K against Na of rice leaf in both seasons comparing to the control treatment. The most effective wizard one is being Sal wax compound followed by AquaSal and ultimately crop plus compound. The highest values of potassium leaf content were obtained when Salwax was applied to soil with irrigation water immediately before transplanting. At the same time the latter mentioned compound inhibited the lowest values of sodium and Na/K ratio in both seasons. On the opposite bank, the control treatment produced the lowest values of potassium and the maximum values of sodium and Na/K ratio in the two study seasons (Table 2).

The order of studied salinity wizards with respect to improve ion selectivity and rising K against Na uptake was as follows, Salwax, Aquasal, Crop plus and finally control treatment. The benefit action of current salinity wizards is mainly due to presence of calcium and potassium which eliminated more Na from soil and elevated K soil concentration induced high potassium uptake. Moreover, both compounds of Aquasal and Salwax had high concentration of carboxylic acid which might be reduced soil pH values under alkalinity soil that exhibited reasonable availability of K^+ and high K^+ plant uptake resulted in low Na^+/K^+ ratio as indication for improving ion selectivity criteria. Going back to crop plus role, as it indicated to its composition in the material chapter, it contains some of macro and micro elements that might be induced more early growth, more tillering and encouraged K uptake with reducing Na leaf content leading to low Na^+/K^+ ratio that is playing effective role in adjusting ion selectivity to strengthen rice plant salinity withstanding and improving rice growth under salt stresses. Regarding the behavior of the tested rice varieties concerning the ion selectivity criteria, the three tested rice varieties showed great variation in this concept. Giza177 rice varieties had the highest value of Na leaf content and subsequently higher Na^+/K^+ ratio indicating its poor ion selectivity and salinity sensitivity. On the other side, Giza179 showed the lowest mean of Na^+ leaf content and minimum mean of Na^+/K^+ ratio indicating its ion selectivity ability and its salinity tolerance. Sakha107 rice cultivar showed middle pattern regarding ion selectivity and it is considered as moderately sensitive for salinity. Regarding to the performance of rice cultivars consider K uptake that was completely opposite pattern of Na^+ in both seasons of study. The interaction effect between rice varieties and chemical wizards had significant effect of Na^+ and Na^+/K^+ ratio in 2020 season. Giza 179 gave the lowest values of both parameters when soil was treated by Salwax without significant differences with Aqua Sal under the same variety. The current obtained results confirmed the capability of Giza179 rice cultivar to select the benefit ion against Na^+ cation reducing its concentration in plant tissue. Furthermore, the vital role of salinity treatment wizard was found to be clear in declining Na^+ uptake and adjusting ion selectivity, since the

three used salinity wizards were effective in reducing both of Na^+ and Na^+/K^+ ratio, but the viability of Aqua Sal and Salwax exceeded the crop plus in the concern (Table 3).

Growth parameters. Considered studies were conducted on rice growth parameters as dry matter, leaf area index and chlorophyll content were significantly affected by salinity treatments material in both seasons. The data in Table 4 fixed the positive application of applied wizards on improving dry matter production, leaf area index and chlorophyll content of rice plants grown under salt stress during the current study. The chemical substance called Salwax prosper all over the tested treatments, it is being that keeping plant away from the hazard effect of salinity by reducing Na^+ uptake ensure proper growth under such stress. No significant differences was obtained between Aquasal and Crop plus regarding increasing leaf area index and chlorophyll content they are came in the second order. Leaf area and chlorophyll content considered the main component for photosynthesis processes which affected by salinity stress, salinity induce short leaf and oxidation for carotene pigments which protect chlorophyll. Applying the wizards substances mitigate the harmful effect of salinity on rice plant and furthered the photosynthesis component return in improve dry matter production. With respect to rice varieties the behavior of rice varieties were dissimilar under salt stress regarding leaf area index, chlorophyll content and dry matter, Giza179 was the best followed by Sakha107 and then Giza177 came in the last order [35,36]. The interaction between rice varieties and chemical substances had a significant effect on chlorophyll content. Giza177 and Sakha107 was improved by applying Salwax meanwhile Giza179 was improved by implemented Sal wax and Aqua Sal without significant difference between each other, both of the donated salinity withstanding (Table 5).

TABLE 6
Some yield component of rice as affected by varieties and some of salinity wizards under saline soil in 2019 and 2020 seasons

Soil wizards	Plant height (cm)		Number of panicle hill^{-1}		Panicle length cm	
	2019	2020	2019	2020	2019	2020
Control	84.89c	84.87b	14.60c	10.91c	17.05c	15.9c
SalWax	95. 53a	95.33a	17.99b	15.66b	18.85a	19.0a
AquaSal	93.45a	94.08a	18.61b	15.83b	18.51b	18.0b
Crop plus	91.39b	95.33a	19.70a	18.91a	18.50b	17.90b
F test	*	*	**	**	**	**
Varieties						
Giza177	92.51b	91.87b	13.40c	10.81c	16.66c	16.00c
Sakha107	88.78b	90.53b	17.23b	15.12b	17.81b	17.53b
Giza 179	94.2a	94.81a	22.55a	20.06a	20.21a	19.83a
F test	*	*	**	**	**	*
Interaction	**	**	*	*	NS	NS

*, ** and Ns indicate $P < 0.05$, $P < 0.01$ and not significant, respectively. Means of each factor designated by the same latter are not significantly different at 5% level using Duncan's Multiple Range Test.

TABLE 7
Plant height and panicle number of rice as affected by the interaction between rice varieties and some of salinity wizards in 2019 and 2020 seasons.

Factors	Plant height cm			Panicle number hill^{-1}		
	Giza177	Sakha107	Giza179	Giza177	Sakha107	Giza179
	2019					
Control	80.27d	86.60cd	87.80c	9.40f	14.20e	20.20c
Sal wax	97.45a	87.52c	98.00cd	14.00e	16.87d	23.10ab
Aqua Sal	97.20a	89.60bc	95.65bc	14.50e	18.77c	22.57b
Crop plus	95.12ab	91.40abc	88.05c	15.70de	19.07c	24.32a
Factors	2020					
Control	78.00e	86.62d	90.00c	7.50h	9.00gh	16.25cde
Sal wax	97.00a	92.75bc	96.25ab	11.75fg	15.00de	20.25b
Aqua Sal	95.75ab	91.25c	95.25ab	10.50fgh	17.50bcd	19.50bc
Crop plus	96.75a	91.50c	97.75a	13.50ef	19.00bc	24.25a

TABLE 8
Some yield component of rice as affected by varieties and some of salinity wizards under saline soil in 2019 and 2020 seasons

Soil wizards	Panicle weight (g)		Number of filled grains panicle^{-1}		Number of unfilled grains panicle^{-1}	
	2019	2020	2019	2020	2019	2020
control	2.25c	2.33c	89.20d	68.35c	22.78a	33.91a
SalWax	2.76a	2.78a	106.88a	109.37a	10.26b	21.41b
AquaSal	2.52b	2.61ab	103.33b	103.50b	12.25b	22.33b
Crop plus	2.44b	2.53b	98.51c	100.00b	12.81b	23.00b
F test	**	*	**	**	*	*
Rice varieties						
Giza177	2.32b	2.40b	88.16c	84.60c	19.03a	38.31a
Sakha107	2.40b	2.46b	97.13b	94.31b	12.73b	23.81b
Giza179	2.66a	2.79a	113.15a	122.00a	11.88b	13.37c
F test	**	**	**	**	**	**
Interaction	Ns	Ns	*	Ns	**	*

*, ** and Ns indicate P < 0.05, P < 0.01 and not significant, respectively. Means of each factor designated by the same latter are not significantly different at 5% level using Duncan's Multiple Range Test.

TABLE 9
1000-grain weight and yields of rice as affected by varieties and soil salinity wizard in 2019 and 2020 seasons.

Soil wizard	1000-grainweight		Grain yield t ha^{-1}		Biological yield t ha^{-1}		Harvest index	
	2019	2020	2019	2020	2019	2020	2019	2020
control	23.94c	25.45c	4.58d	4.03d	10.16d	9.34d	0.445a	0.429bc
SalWax	25.25a	26.24a	5.56a	5.10a	12.68a	11.40a	0.440a	0.445a
AquaSal	24.80b	25.96b	5.33b	4.86b	12.11b	11.07b	0.438a	0.436ab
Crop plus	24.49b	25.87b	4.98c	4.55c	11.74c	10.75c	0.422b	0.421c
F test	**	**	**	**	**	**	**	**
varieties								
Giza177	24.76a	25.85b	4.01c	3.57c	9.31c	8.49c	0.430b	0.420c
Sakha107	24.98a	26.42a	4.76b	4.32b	11.47b	10.05b	0.417b	0.430b
Giza179	24.11b	25.36c	6.57a	6.02a	14.25a	13.39a	0.462a	0.449a
F test	**	**	**	**	**	**	**	**
Interaction	NS	NS	**	**	**	NS	**	NS

*, ** and Ns indicate P < 0.05, P < 0.01 and not significant, respectively. Means of each factor designated by the same latter are not significantly different at 5% level using Duncan's Multiple Range Test

Yield Components. Data listed in Table 5 revealed that yield component parameters statically affected by applying chemical substances in 2019 and 2020 seasons. Implementation of chemical substances increased studied yield component parameters, expect unfilled grains in both season. Salinity induce short plant put applying chemical substances increase height of plant over control treatment no significant difference was obtained among the tested martial regarding increase plant height. Number of panicle and panicle length have a significantly effect by Salinity remediation material in the first season only. Cropplus encouraged plant to provide more panicle. On the other side, Salwax induced the tallest panicle in the first season only. The longest panicle and tallest plants were observed when Salwax was applied to rice plants in soil before transplanting. The spray of crop plus was found to have high efficiency to push rice plant healthy to produce more tillers with high capability to produce bearing tillers. Continuously, the crop plus compound spray produced the highest values of panicle number in both seasons. Both Salwax and Aquasal were a par regarding number of panicles hill^{-1} and plant height in both seasons. In other concern, both of Aquasal and salwax salinity wizard statistically were at the same level with respect to panicle length in bot season. As previously observed the applying both chemical salinity treatments of Salwax and Aquasal showed apparent role in improving ion selectivity which promoted rice plant salinity withstanding resulted in marked improvement of growth under such stresses which reflected on yield attributes. The same trend of panicle length was obtained with panicle weight and number of filled grain as well as was 1000-grain weight, grain and straw yields in both seasons. The latter mentioned yield component and yield reached their maximum values when soil was treatment by SalWax in both seasons. The AquaSal came directly behind Salwax salinity remediation material. Also, it was noticed that applying either soil salinity chemical remediation material or crop plus spray brought benefit effect in reliving the hazard effect on panicle fertility in the terms of filling progress resulted in high filled grain with low sterility comparing to the

control treatment in both seasons [25-28]. Therefore, the lowest numbers of unfilled grains were recognized when soil was treated by Salwax followed by AquaSal and then crop plus without significant differences in both seasons (Table 8).

Salwax salinity wizard recorded the heaviest panicle weight, heaviest 1000 grain weight, the maximum grain and biological yields and the highest values of harvest index in 2019 and 2020 seasons, respectively. Aqua Sal effect was in the second rank and crop plus was next to Aqua sal considering panicle weight, filled grain panicle^{-1}, 1000 grain weight which directly reflected on rice yields under such conditions. Only Crop plus spray surpassed the other two soil salinity wizards in the issue of panicle number since it had promotion action on tiller formation and subsequently bearing tillers in the terms of panicle numbers. Applying soil salinity chemical remediation material might be reclaimed soil by reducing Na and eliminated it away from soil particles by replacing both Ca^{+2} and K^{+} ions which increased K plant uptake against Na resulted in high salinity with standing, early and fast rice growth, high photosynthesis, high daily assimilate rate, high grain filling rate during the current photosynthesis and untimely higher grain yield. Regarding the benefit of crop plus spray, it might be due its high contain of some micronutrients such as Zn and Fe which improve plant development progress, metabolism, photosynthesis and enzyme activities lead to enhancing yield attributes producing high grain yield under such stresses. It was observed that applying salinity wizard early as possible through soil was more benefit and effective to improve rice early growth, rice salinity withstanding, root system formation and well plant development than applying correction material via foliage during growth stage that is mainly due to reducing Na uptake in the terms of ion toxicity and ameliorating osmotic stress from the beginning of life cycle of plant growth. The current results are in a good harmony with those reported by some authors [38-41]. As for, rice cultivars performance, pronounced variation was detected among the tested three rice varieties in both seasons regarding all yield attributes and yields (Tables 6, 8 and 9). Giza179 rice variety continues to fix its excellency under salt stress comparing two others varieties regarding the yield components. Giza179 rice variety gave the tallest plants, longest panicles, the highest values of panicle numbers hill^{-1}, the heaviest panicle ad 1000 grain weight and the lowest values of unfilled grains panicle^{-1}. As it was mentioned Giza179 showed the highest values of yield attributes that qualified it to bring the highest mean grain and biological yields under such salinity stress. Also, the ability of Giza179 rice variety to exert the highest values of harvest index as indication to its capability to produce more grain against straw and its higher affinity of dry matter partitioning toward economic yield under salt stress, since the salinity with salt sensitive variety hindered severely the conversion process of dry matter to grain yield. Giza 177 was the most affected variety under salt stress giving the least means of yield and yield components indicating its salt sensitivity. With respect to Sakha107 rice variety behavior, going back to the obtained data listed in Tables 6, 8&9, Sakha107 is considered as salt medium sensitive variety. Variation among rice varieties in their performance under salinity stress were also reported by [7, 8, 32-35].

The interaction between rice varieties and soil salinity wizards had significant effect on plant height and panicle number in both seasons, number of filled grains panicle-1 in 2019 season, number of unfilled grain panicle^{-1} in both seasons, rice grain yield in 2019 and 2020 seasons as well as biological yield and harvest index in 2019 season. All results related to the mentioned significant interaction came to provide a positive effect on yield attributes and rice grain yield under salt stress which was brought by applying tested salinity wizards and salt tolerant varieties. In this concern, the best combination was Giza179 with Salwax with all traits (Tables 7,). The worst combination was Giza177 and control treatment. Similar results were developed by [46]. It could be concluded that applying soil salinity with SalWax or AquaSal with salt tolerant variety such Giza179 ensure high yield under salt stress. The most efficient salinity wizard material was SalWax salinity remediation followed by AqauSal and then crop plus.

ACKNOWLEDGEMENTS

The authors would like to thank the Deanship of Scientific Research at King Khalid University, Saudi Arabia (RGP 2/67/43), and all members of PPB Lab., and EPCRS Excellence Centre (Certified according to ISO/9001, ISO/14001 and OHSAS/18001), Dept. of Agric. Botany, Fac. of Agric., Kafrelsheikh University, Kafr-Elsheikh, Egypt.

Funding. The authors acknowledge the Deanship of Scientific Research at King Khalid University for funding this work through the Program of Research Groups under grant number (RGP 2/67/43).

REFERENCES

[1] Abdelaal, K.A.A., EL-Maghraby, L.M., Elansary, H., Hafez, Y.M., Ibrahim, E.I., El-Banna, M., El-Esawi, M., Elkelish, A. (2020) Treatment of Sweet Pepper with Stress Tolerance-Inducing Compounds Alleviates Salinity Stress Oxidative Damage by Mediating the Physio-Biochemical Activities and Antioxidant Systems. Agronomy. 10, 26.

[2] Helaly, M.N., Mohammed, Z., El-Shaeery, N.I., Abdelaal, K.A.A., Nofal, I.E. (2017) Cucumber grafting onto pumpkin can represent an interesting tool to minimize salinity stress. Physiological and anatomical studies. Middle East J. Agric. Res. 6, 953–975.

[3] El-Shawa, G.M.R., Rashwan, E.M., Abdelaal, K.A.A. (2020) Mitigating salt stress effects by exogenous application of proline and yeast extract on morphophysiological, biochemical and anatomical characters of calendula plants. Sci. J. Flowers Ornam. Plants. 7, 461-482.

[4] ALKahtani, M.D.F., Kotb, A., Hafez, Y.M., Khan, N., Eid, A.M., Ali, M.A.M., Abdelaal, K.A.A. (2020) Chlorophyll Fluorescence Parameters and Antioxidant Defense System Can Display Salt Tolerance of Salt Acclimated Sweet Pepper Plants Treated with Chitosan and Plant Growth Promoting Rhizobacteria. Agronomy. 10, 1180.

[5] Abdelaal, K.A., Mazrou, Y.S., Hafez, Y.M. (2020) Silicon Foliar Application Mitigates Salt Stress in Sweet Pepper Plants by Enhancing Water Status, Photosynthesis, Antioxidant Enzyme Activity and Fruit Yield. Plants. 9, 733.

[6] Hasan, M.K., El Sabagh, A., Sikdar, M.S., Alam, M.J., Ratnasekera, D., Barutcular, C., Abdelaal, K.A., Islam, M.S. (2017) Comparative adaptable agronomic traits of blackgram and mungbean for saline lands. Plant Arch. 17, 589–593.

[7] El-Banna, M.F., Abdelaal, K.A.A. (2018) Response of Strawberry Plants Grown in the Hydroponic System to Pretreatment with H_2O_2 before Exposure to Salinity Stress. J. Plant Prot. Mansoura Univ. 9, 989–1001.

[8] Abdelaal, K.A.A., Attia, K.A., Alamery, S.F., El-Afry, M.M., Ghazy, A.I., Tantawy, D.S., Al-Doss, A.A., El-Shawy, E.S.E., AbuElsaoud, A.M., Hafez, Y.M. (2020) Exogenous Application of Proline and Salicylic Acid can Mitigate the Injurious Impacts of Drought Stress on Barley Plants Associated with Physiological and Histological Characters. Sustainability. 12, 1736.

[9] Hafez, Y., Elkohby, W., Mazrou, Y.S.A., Ghazy, M., Elgamal, A., Abdelaal, K.A. (2020) Alleviating the detrimental impacts of salt stress on morpho-hpysiological and yield characters of rice plants (*Oryza sativa* L.) using actosol, Nano-Zn and Nano-Si. Fresen. Environ. Bull. 29, 6882–6897.

[10] Badawy, S.A., Zayed, B.A., Sherif, M.A., Bassiouni, A.H.A., Mahdi, M.A., Seleiman, M.F.(2021) Influence of Nano Silicon and Nano Selenium on Root Characters, Growth, Ion Selectivity, Yield and Yield Components of Rice (*Oryza Sativa* L.) under Salinity Conditions. Plants. 10, 1657.

[11] Abdelaal, K.A. (2015) Effect of Salicylic acid and Abscisic acid on morpho-physiological and anatomical characters of faba bean plants (*Vicia faba* L.) under drought stress. J. Plant Prod. Mansoura Univ. 6, 1771–1788.

[12] Abdelaal, K.A., Hafez, Y.M., El-Afry, M., Tantawy, D.S., Alshaal, T. (2018) Effect of some osmoregulators on photosynthesis, lipid peroxidation, antioxidative capacity, and productivity of barley (*Hordeum vulgare* L.) under water deficit stress. Environ. Sci. Pollut. Res. 25, 30199–30211.

[13] Hafez, Y., Attia, K., Alamery, S., Ghazy, A., Al-Doss, A., Ibrahim, E., Rashwan, E., El-Maghraby, L., Awad, A., Abdelaal, K.A. (2020) Beneficial Effects of Biochar and Chitosan on Antioxidative Capacity, Osmolytes Accumulation, and Anatomical Characters of Water-Stressed Barley Plants. Agronomy. 10, 630.

[14] Abdelaal, K.A., Hafez, Y.M., El Sabagh, A., Saneoka, H. (2017) Ameliorative effects of Abscisic acid and yeast on morpho-physiological and yield characteristics of maize plant (*Zea mays* L.) under drought conditions. Fresen. Environ. Bull. 26, 7372–7383.

[15] Abdelaal, K.A.A., Rashed, S.H., Ragab, A., Hossian, A., El Sabagh, A. (2020) Yield and quality of two sugar beet (*Beta vulgaris* L. ssp. vulgaris var. altissima Doll) cultivars are influenced by foliar application of salicylic Acid, irrigation timing, and planting density. Acta Agric. Slov. 115, 239–248.

[16] Abdelaal, K.A.A., Elafry, M., Abdel-Latif, I., Elshamy, R., Hassan, M., Hafez, Y. (2021) Pivotal role of yeast and ascorbic acid in improvement the morpho-physiological characters of two wheat cultivars under water deficit stress in calcareous soil. Fresen. Environ. Bull. 30, 2554–2565.

[17] Elkelish, A., Qari, S.H., Mazrou, Y.M., Abdelaal, K.A., Hafez, Y.M., Abu-Elsaoud, A.M., Batiha, G., El-Esawi, M., El Nahhas, N. (2020) Exogenous Ascorbic Acid Induced Chilling Tolerance in Tomato Plants Through Modulating Metabolism, Osmolytes, Antioxidants, and Transcriptional Regulation of Catalase and Heat Shock Proteins. Plants. 10, 431.

[18] EL Sabagh, A., Hossain, A., Barutcular, C., Islam, M.S., Awan, S.I., Galal, A., Iqbal, A., Sytar, O., Yildirim, M., Meena, R.S. (2019) Wheat (*Triticum aestivum* L.) production under drought and heat stress-adverse effects, mechanisms and mitigation: A review. Appl. Ecol. Environ. Res. 17, 8307–8332.

[19] AlKahtani, M.D.F., Hafez, Y.M., Attia, K., Rashwan, E., Husnain, L.A., AlGwaiz, H.I.M., Abdelaal, K.A.A. (2021) Evaluation of Silicon and Proline Application on the Oxidative Machinery in Drought-Stressed Sugar Beet. Antioxidants. 10, 398.

[20] Alnusairi, G.S.H., Mazrou, Y.S.A., Qari, S.H., Elkelish, A.A., Soliman, M.H., Eweis, M., Abdelaal, Kh., El-Samad, G.A., Ibrahim, M.F.M., ElNahhas, N. (2021) Exogenous Nitric Oxide Reinforces Photosynthetic Efficiency, Osmolyte, Mineral Uptake, Antioxidant, Expression of Stress-Responsive Genes and Ameliorates the Effects of Salinity Stress in Wheat. Plants. 10 (8), 1693.

[21] El Nahhas, N., AlKahtani, M., Abdelaal, Kh. A.A., Al Husnain, L., AlGwaiz, H., Hafez, Y.M., Attia, K., El-Esawi, M., Ibrahim, M., Elkelish, A. (2021) Biochar and jasmonic acid application attenuates antioxidative systems and improves growth, physiology, nutrient uptake and productivity of faba bean (*Vicia faba* L.) irrigated with saline water. Plant Physiology and Biochemistry. 166, 807-817166

[22] Abdelaal, Kh.A.A., AlKahtani, M.D.F., Attia, K., Hafez, Y., Király, L., Künstler, A. (2021) The pivotal role of plant growth promoting bacteria in alleviating the adverse effects of drought and facilitating sustainable agriculture. Biology. 10(6), 520.

[23] Abdelaal, Kh., El-Okkiah, S., Metwaly, M., El-Afry, L. (2021) Impact of Ascorbic acid and proline application on the physiological machinery in soybean plants under salinity stress. Fresen. Environ. Bull. 30(11A), 12486-12497.

[24] Abdelaal, K.A., Mazrou, Y., Mohamed, A.A., Ghazy, M., Barakat, M., Hafez, Y., Gaballah, M. (2021). The different responses of rice genotypes to heat stress associated with morphological, chlorophyll and yield characteristics. Notulae Botanicae Horti Agrobotanici Cluj-Napoca. 49(4), 12550.

[25] Abdelaal, K.A., Attia, K.A., Niedbała, G., Wojciechowski, T., Hafez, Y., Alamery, S., Alateeq, T.K., Arafa, S.A. (2021) Mitigation of Drought Damages by Exogenous Chitosan and Yeast Extract with Modulating the Photosynthetic Pigments, Antioxidant Defense System and Improving the Productivity of Garlic Plants. Horticulturae. 7(11), 510.

[26] Arafa, S.A., Attia, K.A., Niedbała, G., Piekutowska, M., Alamery, S., Abdelaal, K., Alateeq, T.K., Ali, M.A.M., Elkelish, A. and Attallah, S.Y. (2021) Seed Priming Boost Adaptation in Pea Plants under Drought Stress. Plants. 10(10), 2201.

[27] Zayed, B.A., Okasha, A.M. Rashwan, E. (2019) Impact of different rates of phosphoric acid foliar spraying on rice growth and yield traits under normal and saline soils conditions. East African Scholars J. Agri. Life Sci. 2(2-February), 56-66.

[28] Chunthaburee, S., Dongsansuk, A., Sanitchon, J., Pattanagul, W., Theerakulpisut, P. (2016) Physiological and biochemical parameters for evaluation and clustering of rice cultivars differing in salt tolerance at seedling stage. Saudi J. of Biological Sciences. 23, 467–477.

[29] Zayed, B.A., Abdel-Aal, M.S.M., Deweedar, G.A. (2017). Response of rice yield and soil to sulfur application under water and salinity stresses. Egypt. J. Agron. 39(3), 239-249.

[30] Ding, Z., Kheir, A.M.S., Ali, M.G.M., Ali O.A.M., Abdelaal, A.I.N., Lin, X., Zhou, Z., Wang, B., Liu, B., He, Z. (2020) The integrated effect of salinity, organic amendments, phosphorus fertilizers, and deficit irrigation on soil properties, phosphorus fractionation and wheat productivity. Scientific Reports. 10, 2736.

[31] Zayed, B.A., Salem, A.K., Ali, O.A.M. (2014) Physiological characterization of Egyptian salt tolerant rice varieties under different salinity levels. Life Science J. 11(10), 1264-1272.

[32] Pongprayoon, W., Tisarum, R., Theerawittaya, C., Cha-um, S. (2019) Evaluation and clustering on salt-tolerant ability in rice genotypes (*Oryza sativa* L. subsp. indica) using multivariate physiological indices. Physiol. Mol. Biol. Plants. 25, 473-483.

[33] Zayed, B.A., El-Namaky, R.A., El–Refaee, Y.Z., Sedeek, S.E.M. (2012) Comparative study on hybrid and inbred rice under drought and saline stresses. Plant Production, Mansoura Univ. 3(1), 91–108.

[34] Zayed, B.A., Ali, O.A.M., Hammoud, S.A. (2016) Physiological and genetic performance of some rice genotypes grown in medium and high salinity soils. Menoufia J. Plant Prod. (1)October, 155-175.

[35] Munns, R. (2002) Comparative physiology of salt and water stress. Plant, Cell and Environment. 25, 239–250.

[36] Hossain, M.A., Hoque Burritt, M.A.D.J., Fujita, M. (2014) Proline protects plants against abiotic oxidative stress: biochemical and molecular mechanisms. In: Ahmad P (ed) Oxidative damage to plants. Elsevier Inc, San Diego.

[37] Zayed, B.A., Khedr, R.A., Hadifa, A.A., Okasha, A.M. (2017) Some Anti-oxidants, Phsysio-morphological, and Yield of Varying Rice Varieties Affected by Salinity Levels. J. Plant Production, Mansoura Univ. 8(7), 747–754.

[38] Abd El-Hamed, M.M. (2018) Effect of Potassium on productivity of some rice cultivars under various dates on saline soils. Proceeding of The Seventh Field Crops Conference, 18-19, Dec. 2018. Giza, Egypt.

[39] Abd El-Hamed, M.M. (2020) Comparative study of rice straw biochar and compost on rice growth and yield under saline sodic soil condition. J. of Plant Production, Mansoura Univ. 11(1), 79–84.

[40] Wichern, F., Islam, M.R., Hemkemeyer, M., Watson, C., Joergensen, R.G. (2020) Organic amendments alleviate salinity effects on soil microorganisms and mineralisation processes in aerobic and anaerobic paddy rice soils. Front. Sustain. Food Syst. 4, 1-14.
[41] Adugna, G. (2016) A review on impact of compost on soil properties, water use and crop productivity. Acad. Res. J. Agri. Sci. Res. 4(3), 93-104.
[42] Ahmed, K., Qadir, G., Jami, A.R., Saqib, A.I., Nawaz, M.Q., Kamal, M.A., Ehsan-Ul-Haq. (2017) Comparative reclamation efficiency of gypsum and sulfur for improvement of salt affected. Bulg. J. Agric. Sci. 23(1), 126–133.
[43] Rehman, A., Farooq, M., Cheema, Z.A., Wahid A. (2012) Seed priming with boron improve growth and yield of fine grain aromatic rice. Plant Growth Regulation. 68(2), 189-201.
[44] Rahman, I.U., Afzal, A., Iggbal, Z., Shah, H.A., Khan, M.A., Ijaz, F., Asmat Ullah, S., Nisar, A., Zainab, R. and Manan, S. (2015) Review of foliar feeding in various vegetables andcereal crops boosting growth and yield attributes. American-Eurasian J. Agric. Environ Sci. 15(1), 74-77.
[45] Zayed, B.A., Salem, A., Sharkawy, H.M. (2011) Effect ofdifferent micronutrient treatments on rice (*Oryza sativa* L.) growth and yield under saline soil conditions. World Journal of Agricultural Science. 7(2), 179-184.
[46] Phonglosa, A., Dalei, B.B., Senapati, N., Pattanayak, S.K., Saren, K.S., Ray, K. (2018) Effect of boron on growth, yield and economics of rice under eastern ghat high land zone of odisha. International Journal of Agriculture Sciences. 10(7), 5660-5662.
[47] Anand, S., Pavithra, R., Kamaraj, A., Satheeshkumar, P., Suganthi, S. and Padmavathi, S. (2020) Enhancing Crop Growth and seed yield in rice cv. ASD16 through foliar spray. Plant Archives. 20(1), 1137-1143.
[48] Shaban, S.K.H., Helmy, A.M., EL-Galad, M. (2013) Role of gypsum and sulphur application in ameliorating saline soil and enhancing rice productivity. Acta Agronomica Hungarica. 61(4), 303–316.
[49] Mohamed, A.A., Zayed, B., hafaz, E., Eltobgy, R., Hafez, Y. and Abdelaal, Kh. (2021) Effect of Potassium Fertilizer Treatments and Harvest Date on Rice Grain Yield and Quality of Rice Plants (Giza 179 Variety). Fresen. Environ. Bull. 30(2), 1010-1020.
[50] Black, C.A., Evans, D.D., Ensminger, L.E., Clark, F.E. (1965) Methods of Soil Analysis. Part 2- Chemical and microbiological properties. American Soc. of Agronomy, Inc., Publisher, Madison, Wisconsin, USA.
[51] Jackson, M.L. (1973) Soil Chemical Analysis. Prentice Hall of India, Ltd., New Delhi, India.
[52] Wolf (1982) A comprehensive system of leaf analysis and its use for diagnosing crop nutrient status. Communications in Soil Science and Plant Analysis. 13, 1035-1059.
[53] Gomez, K.A., Gomez, A.A. (1984) Statistical Procedures for Agricultural Research, IRRI. 2nd Ed. John Wily and Sons, New York, US. 680.
[54] Duncan, B. (1955) Multiple Range and Multiple F. test. Biometrics. 11, 1-42.

Received: **01.12.2021**
Accepted: **03.02.2022**

CORRESPONDING AUTHOR

Khaled Abdelaal
EPCRS Excellence Center,
Plant Pathology and Biotechnology Lab.,
Agric. Botany Dept., Fac. Agric.,
Kafrelsheikh University,
Egypt

e-mail: khaled.elhaies@gmail.com

© by PSP Volume 31– No. 05/2022 pages 5105-5112 Fresenius Environmental Bulletin

APPLICATION OF POLYMER FLOODING TECHNOLOGY IN LOW PERMEABILITY OILFIELD DEVELOPMENT: A CASE STUDY

Guanghui Rong[1], Honggang Zhang[2], Zhongbo Gu[3], Hao Hou[1], Chao Gao[4,*], Bo Wang[5], Wenjie Zhou[6]

[1]No.12 Oil Production Plant of Changqing Oilfield Company, CNPC, Xi'an, Shaanxi 710000, China
[2]No.3 Oil Production Plant of Changqing Oilfield Company, CNPC, Xi'an, Shaanxi 710000, China
[3]No.8 Oil Production Plant of Changqing Oilfield Company, CNPC, Xi'an, Shaanxi 710000, China
[4]Shaanxi Yanchang Petroleum (Group) Corp. Ltd., Xi'an, Shaanxi 710075, China
[5]Shaanxi Hongfeng Petroleum Engineering Technology Co., Ltd, Xi'an, Shaanxi 710016, China
[6]Dingbian Branch of Shaanxi Hongfeng Petroleum Engineering Technology Co., Ltd, Dingbian, Shaanxi 718699, China

ABSTRACT

In traditional polymer flooding technology, the flooding effect is affected by mechanical degradation, adsorption, dilution of polymer molecules during formation, and injection concentration variations. In the application of polymer flooding technology, how to optimize the polymer type and injection parameters to improve the oil displacement effect is very important. This paper conducts simulation experiments on polymer type, injection concentration, injection volume, etc., and evaluates the advantages of two polymers for flooding through the recovery factor and injection pressure. Studies have shown that when the concentration of ordinary intermediate polymer solution is 1200 mg/L and the concentration of salt-resistant polymer solution is 700 mg/L, the oil displacement effect for X low permeability reservoir is the most obvious. When the injection volume of two polymer solutions is 0.64 PV, the two polymers have the best increase in oil recover. When natural cores are used to study the oil displacement effect, salt-tolerant polymer floods the enhanced oil recovery value to 13.32%, which is higher 10.1% than that of ordinary middle-separation polymerization. Moreover, considering the polymer flooding effect and input cost, the pollution-distributed dilute salt-resistant polymer solution is used for flooding. The optimal injection concentration of the salt-resistant polymer solution is 700 mg/L and the optimal injection volume is 0.64 PV.

KEYWORDS:
Polymer flooding, low permeability, oilfield, oil displacement effect, recovery

INTRODUCTION

Low-permeability reservoirs are rich in oil and gas reserves and have great potential for development [1-3]. However, both have strong heterogeneity, poor permeability, and high salinity. With continuous adjustment of the well pattern, remaining oil distributions are becoming relatively scattered and most oil wells have problems such as high water cut, low productivity and a rapid productivity decline [4, 5]. Given the low permeability of the reservoir, high formation pressure, rapid rise in the oil field water cut and the presence of crude oil in the oil recovery, there is an urgent need to find effective methods to improve oil recovery.

Previously, Cai et al. [6] employed polymer flooding physical simulations to study the parameters of polymer injection and determined that the best injection time for the polymer is before the reservoir water content reaches 80%. Du et al. [7] studied the impact of polymer injection timing, injection concentration and slug size in low-permeability reservoirs on the oil displacement effect. Wang et al. [8] used core flow experiments to conduct polymer flooding experiments on cores with a permeability of 10-50 mD, the results of which showed that the pressure at the injection end increased with the increase of polymer concentration and relative molecular mass. Tan et al. [9] found that dendritic polymers can still have a viscosity retention rate of more than 80% after high-strength shearing by simulating the shearing effect of low-permeability formations. Zhang et al. [10] studied a silane coupling agent when modifying nano-SiO_2 by scanning electron microscopy to see the appearance of the surface hydroxyl groups. Modification by adsorption can improve the smoothness of the coupling agent in practical engineering applications. Samanta et al. [11] studied the influence of different types of nano-SiO_2 modification methods applied to the actual engineering of sealing. Tan et al. [12] successfully modified nano-SiO_2 by using a coupling agent ultrasonic method and achieved good diffusibility. This could be used without clumping and in full contact with the reacting substance. Eastmond et al. [13] found that two different types of polymers can react with the hydroxyl groups on the surface of nano-SiO_2 to achieve modification. Spange et al. [14] used monomers of many types of polymers to continuously react, allowing the

monomers to form polymers while grafting with the hydroxyl groups on the surface of nano-SiO_2 to form corresponding modifications. Ruan et al. [15] used gamma rays to promote the synthesis of nano-SiO_2 edges and the polymerisation of monomers to form modified compounds. Bachmann et al. [16] used nano-SiO_2 as a reactive monomer to finally initiate the polymerisation of polymer monomers to achieve modification. Bachmann et al. [17] synthesised a high molecular weight LH series polymer with a block structure by template polymerisation. In the sewage of the Gudao Oilfield, LH3500 produced by the optimised structure has good temperature and salt resistance. Zhou et al. [18] believed that the viscosity of polyacrylamide was the highest when the degree of hydrolysis was 20%. Yang et al. [19] believed that the arrangement of polyacrylamide groups affects the degree of the hydrolysis-viscosity relationship. That is, when the degree of hydrolysis is 33%, the regular triplet hydrogen bond form maximises the intramolecular hydrogen bond and thus the solution viscosity. Pan et al. [20, 21] introduced azo groups and vinyl monomers on the surface of nano-SiO_2 to undergo graft polymerisation and grafted hyperbranched polymers onto the surface of nano-SiO_2. Knobloch et al. [22] utilised nano-SiO_2 as reaction centres, allowing active hydroxyl groups on the surface and AB2 monomers to undergo a one-step polycondensation reaction to prepare nano-SiO_2 composite materials grafted with hyperbranched polymers. Zhao et al. [23] studied the effect of hyperbranched polyester amide on the dyeing ability of polypropylene fibres. Experiments show that adding 3% stearic acid-modified hyperbranched polyester amide has almost no effect on the physical properties of the fibre. Duan et al. [24] studied the effect of hyperbranched polyester amide grafted colloidal silicon on the curing behaviour of epoxy resins and found that a low grafting rate of hyperbranched polymers cannot cure epoxy resins. However, when the grafting rate reaches 60.4%, the curing reaction can proceed successfully. Chen et al. [25] used glycidol for anionic polymerisation and obtained hyperbranched polymers with relatively concentrated molecular weights. Wang et al. [26] found that the modified hyperbranched polyester has a good effect on the flocculation and decolourisation of dyes and the fixing performance of direct dyes. He et al. [27] prepared hyperbranched P inverse emulsion polymers by inverse emulsion polymerisation. The hyperbranched polymer has good viscosity, increasing the fluid loss reduction ability in freshwater, brine, and saturated brine base slurries. Sun et al. [28] synthesised an ammonium salt surfactant, which increased the recovery rate by more than 11%. Wang et al. [29] synthesised a petroleum naphthenic acid alkanolamide surfactant, which can reduce the oil/water interfacial tension to ultra-low interfacial tension.

In this paper, physical simulation flooding experiments were conducted by using artificial heterogeneous rectangular cores and natural cylindrical cores. Under certain permeability conditions, the optimal recovery factor, injection rate, pressure and other parameters were compared to study the flooding feasibility of different polymer solutions.

MATERIALS AND METHODS

In this study, the clean water and waste water are diluted, and the waste water and waste water are respectively taken from a combined station of X oilfield. The saturated model water is artificially synthesized brine with a salinity of 8230 mg/L, and the core flooding water is the advanced treatment sewage of the X oilfield A joint station. The constant speed condition is the injection rate of 0.9 mL/min, the constant pressure condition is the injection pressure of 0.016 MPa, and the experimental temperature is 47.5 ℃ [18, 20]. The experimental models are as follows: (1) Man-made three-layer heterogeneous rectangular core of dimension 45 mm×45 mm×300 mm, with air permeabilities of the upper, middle and lower layers of 100×10^{-3} μm^2, 300×10^{-3} μm^2, 500×10^{-3} μm^2 (for oil displacement experiment), respectively. (2) Man-made three-layer heterogeneous rectangular core of dimension 45 mm×45 mm×300 mm, with air permeabilities of the upper, middle and lower layers of 200×10^{-3} μm^2, 500×10^{-3} μm^2, 800×10^{-3} μm^2, 300×10^{-3} μm^2, 600×10^{-3} μm^2, 1000×10^{-3} μm^2 (for oil displacement experiment), respectively [8]. (3) Natural cylindrical core with a dimension of Φ25 mm×100 mm (used for oil displacement experiment). The used equipment includes SY71/QUINTIX224-1CN electronic balance, vernier caliper, ZJ-HK type special I type thermostat, HBS-S50-70 constant pressure and constant speed pump, Φ600×600 type high-pressure intermediate container, manual metering pump, vacuum pump, YB-150A, B-type pressure gauge, etc.

Prior to experiments, place the core in a holder, add 5 MPa ring pressure and evacuate for 6 h. Saturate the synthetic brine, then measure the porosity and pore volume. Place the core saturated with synthetic brine in a constant temperature box for more than 12 h (47.5 ℃). Perform the pore water permeability measurement. Saturated oil until there is no water at the core outlet and determine the original oil saturation. According to the displacement rate of 0.9 mL/min (rectangular core) and 0.3 mL/min (cylindrical core), when the water content reaches 96% at the outlet end of the core, calculate the waterflooding recovery factor. Inject a certain amount of polymer solution at the same injection rate to calculate the recovery during the polymer injection stage. Follow-up water flooding to the outlet end of the core with more than 98% water content, then calculate the final recovery factor.

RESULTS AND DISCUSSION

Effect of polymer concentration on oil displacement effect. Using man-made heterogeneous rectangular cores, the oil displacement experiments were carried out with different concentrations (800 mg/L, 1200 mg/L and 1400 mg/L) of clean and diluted ordinary intermediate polymer solution, and with different concentrations (600 mg/L, 700 mg/L and 800mg / L) of clean and diluted salt resistant polymer solution. In the flooding experiment of dilute salt-tolerant polymer solution, by analyzing the flooding effects of two polymer solutions with different concentrations, the concentrations of ordinary middle-part polymer and salt-resistant polymer suitable for polymer solution flooding in X oilfield could be screened out. It can be seen Figure 1 that, for the oil displacement effect curve of the ordinary intermediate polymer solution with different concentrations and the salt-resistant polymer solution, respectively. With the increase of the polymer solution concentration, increases in (i) the recovery factor during polymer injection, (ii) the water flooding recovery factor of polymer flooding and (iii) the oil recovery value of polymer flooding, are observed. At a polymer concentration of 800-1200 mg/L, the enhanced oil recovery value rises faster, while at a concentration of 1200-1400 mg/L, the enhanced oil recovery value rises slowly. Generally, the higher the concentration, the larger the enhanced oil recovery value. With the increase of the salt-tolerant polymer concentration, increases in (i) the recovery factor during polymer injection, (ii) the waterflooding recovery factor after polymer flooding and (iii) the oil recovery value of polymer flooding, are observed. At a concentration of 600～700 mg/L, the recovery factor shows a linear upward trend, while at a concentration of 700～800 mg/L, the recovery factor shows a slow upward trend. Generally speaking, the higher the concentration, the greater the value of the enhanced recovery factor. The oil displacement effect of low-concentration salt-resistant polymers is significantly higher than that of higher-concentration ordinary middle-separation polymers. EOR values of ordinary middle-separation polymer flooding and salt-tolerant polymer flooding are shown in Figure 1.

It can be seen that although the concentration of the salt-resistant polymer solution is low, the enhanced oil recovery value of the salt-resistant polymer flooding is significantly higher than that of the ordinary intermediate polymer with a higher concentration. The mineral solution has a significant effect on enhancing oil recovery. Figure 2 shows the comparison of the recovery efficiency of ordinary middle-separation polymer and salt-tolerant polymer flooding at each stage. Here, it can be seen that the recovery factor of the ordinary intermediate polymer solution during the polymer injection stage is significantly higher than the recovery factor of the subsequent water flooding stage. The recovery factor of the salt-tolerant polymer in the subsequent water flooding stage is similar to that of the polymer flooding stage and the yield is not much different. This shows that the recovery rate in the subsequent water flooding stage is the main reason that the recovery rate of salt-tolerant polymer flooding is higher than that of ordinary intermediate polymer. The reason for this is that the injectability of the ordinary middle-separation polymer solution and the salt-resistant polymer solution is relatively good. The injected polymer solution first enters the high permeability layer. In the polymer flooding stage, crude oil in the high permeability layer is more often driven. After the 0.48 PV polymer solution is injected, water flooding is carried out. Because the molecular structure of the salt-resistant polymer has better adaptability to the bottom layer, a large amount of retention can be

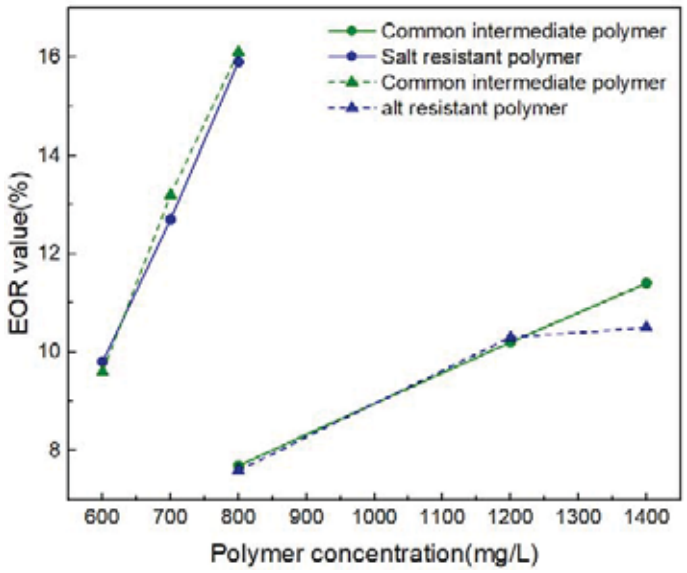

FIGURE 1
EOR effect of different polymer flooding

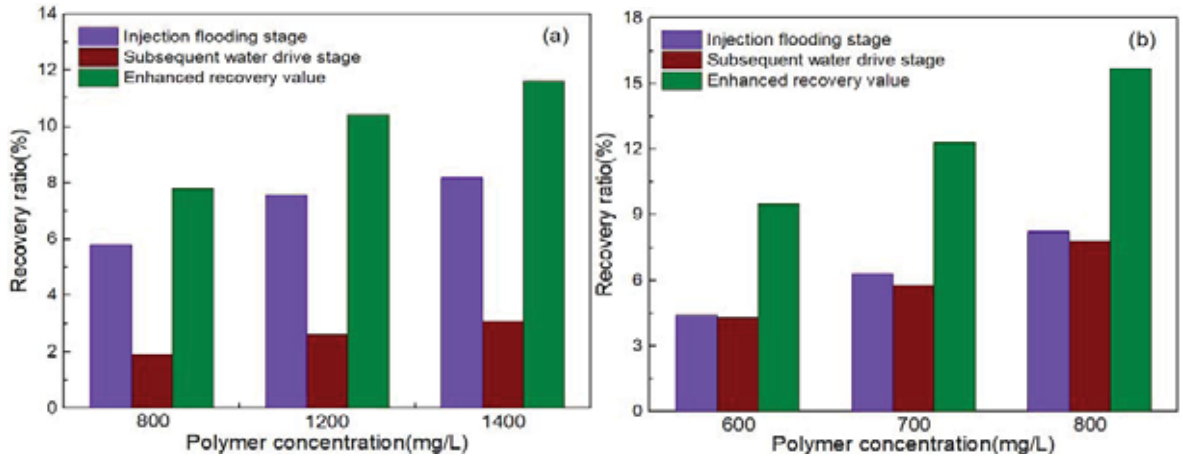

FIGURE 2
Recovery ratio of ordinary intermediate and salt resistant polymer in each stage

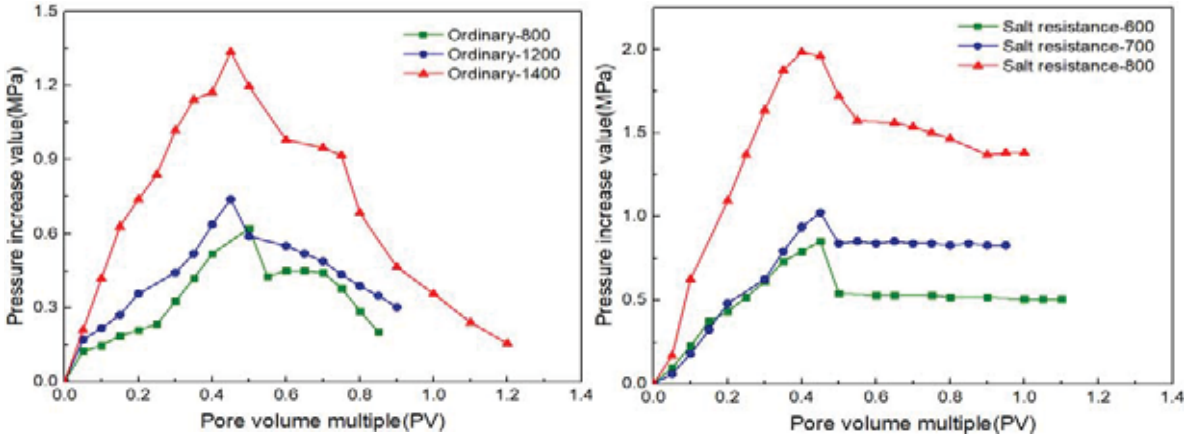

FIGURE 3
Pressure of oil displacement of ordinary intermediate and salt resistant polymer

formed in the high-permeability layer, which reduces the seepage of the high-permeability layer. Resistance adjusted the water absorption profile. Therefore, in the subsequent water flooding process of salt-resistant polymer flooding, the injected water can enter the low- and medium-permeability layers to drive crude oil out, thereby greatly improving the oil recovery.

Comparison of displacement pressure. Figure 3 shows the displacement pressure of polymer solution with different concentrations in the polymer flooding stage. It can be seen that the higher the polymer concentration, the higher the displacement pressure is and the higher the pressure in the subsequent water flooding stage is. For ordinary intermediate polymer, the displacement pressure of the polymer solution with a concentration of 1400 mg/L is much higher than the displacement pressures at 1200 mg/L and 800 mg/L. This is because as the polymer concentration and the hydrodynamic radius Dh of polymer molecules increases. When Dh is greater than the average diameter of the core throat, polymer injection becomes difficult and the pressure increases significantly. The increase in pressure will increase the swept volume, thereby increasing the oil displacement efficiency. For the salt-resistant polymer solution, the displacement pressure of the polymer solution with a concentration of 800 mg/L is also much higher than the displacement pressure of the polymer solution with the concentration of 700 mg/L and 600 mg/L. The difference is that in the subsequent water flooding stage of salt-tolerant polymer flooding, the displacement pressure does not decrease continuously but remains stable after a short period of decline. This helps to improve the oil recovery in the subsequent water flooding stage.

Comparison of crude oil recovery factor. Figure 4 shows the change curve of the enhanced oil recovery value in the polymer flooding stage with different concentrations of polymer solution. Regardless of whether it is a salt-tolerant polymer or an ordinary middle-separation polymer, larger concentrations of polymer for oil displacement lead to higher values of enhanced oil recovery under the same injection volume. Enhanced oil recovery values when the concentration of the ordinary intermediate polymer solution is 1400 mg/L and 1200 mg/L are not significantly different but are higher than when the concentration is 800 mg/L. Enhanced oil

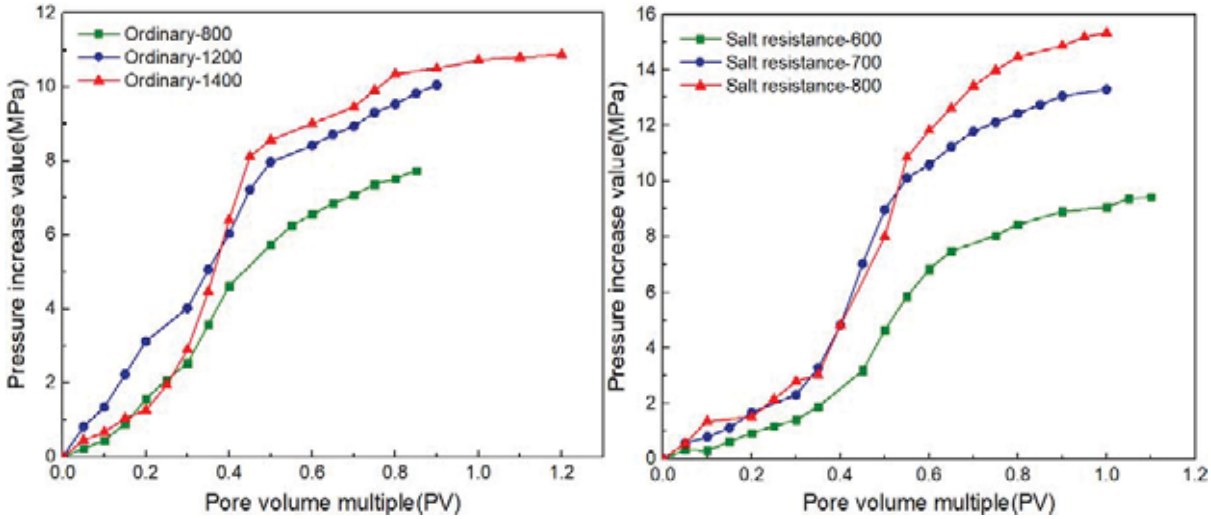

FIGURE 4
Recovery ratio of oil displacement of ordinary intermediate and salt resistant polymer

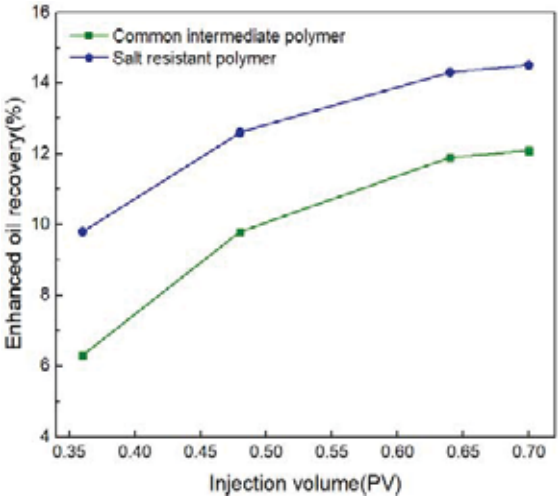

FIGURE 5
Relationship between EOR value and injection volume

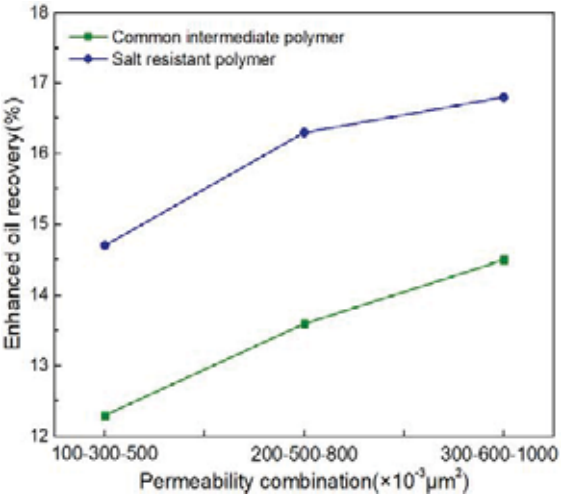

FIGURE 6
Relationship between EOR value and permeability combination

recovery values when the salt-tolerant polymer solution depth is 800 mg/L and 700 mg/L are also significantly higher than when the concentration is 600 mg/L. By comprehensively comparing the displacement pressure, water content and crude oil recovery factor of polymer solutions with different concentrations, it is determined that the optimal concentration of ordinary intermediate polymer solution is 1200 mg/L and the optimal concentration of salt-resistant polymer solution is 700 mg/L.

Influence of injection volume on oil displacement effect. In order to study the impact of different polymer injection rates on the oil displacement effect, three-layer heterogeneous man-made rectangular cores were used for different injection rates (0.36, 0.48, 0.64 and 0.7 PV) under the condition of pollution and dilute salt resistance. The oil displacement experiments were carried out with different injection amounts (0.36 PV, 0.48 PV, 0.64 PV, and 0.7 PV) of sewage diluted salt resistant polymer solution (concentration 700 mg/L) and sewage diluted ordinary intermediate polymer solution (concentration 1200 mg/L). From Figure 5, it can be seen that regardless of whether it is an ordinary middle polymer or a salt-tolerant polymer, as the injection volume increases, the enhanced oil recovery value increases. This is due to the increase in the injection volume of the polymer, which leads to an increase in the injection pressure and the swept volume, effectively displacing crude oil that has not been swept before. However, with the increase of the injection volume of polymer solution, the increasing effect of the two polymers to enhance the oil recovery value shows a slowing trend. When the injection volume is less than 0.64 PV, the slope of the curve is larger and the enhanced oil recovery value rises faster with the increase of the injection volume. On the other hand, when the injection volume exceeds 0.64 PV, the slope of the curve decreases significantly and the enhanced oil recovery value rises gently. This indicates

that when the injection volume is greater than 0.64 PV, as the injection volume increases, the recovery factor is not significantly improved. Considering the polymer solution flooding effect and the injection cost, it is considered that the optimal injection volume of the two polymer solutions is 0.64 PV.

Oil displacement effect of artificial core. Using different permeabilities to combine three layers of heterogeneous artificial rectangular cores (combination one: 100×10^{-3} μm^2, 300×10^{-3} μm^2, 500×10^{-3} μm^2, combination two: 200×10^{-3} μm^2, 500×10^{-3} μm^2, 800×10^{-3} μm^2, combination three: 300×10^{-3} μm^2, 600×10^{-3} μm^2, 1000×10^{-3} μm^2) under the same concentration, the oil displacement effect comparison experiment (injection volume 0.64 PV) of sewage mixed dilute ordinary intermediate polymer solution (concentration 1200 mg/L) and sewage mixed dilute salt resistant polymer solution (concentration 700 mg/L) was carried out, respectively. The oil displacement effect of cores with different permeability combinations is shown in Figure 6.

It can be seen that for the same injection agent, the enhanced oil recovery value increases with increasing average permeability of the core. This is because as the average permeability of the core increases, the distribution of pores and throats inside the core gradually improves and the area that is difficult to reach is reduced. This effectively takes advantage of the polymer's improved mobility ratio. Overall, the enhanced oil recovery value of salt-resistant polymer is higher than that of ordinary middle-separation polymer, especially for cores with lower average permeability. The oil displacement effect of salt-tolerant polymer is significantly higher than that of ordinary middle-separation polymer. The enhanced oil recovery value is about 2.757% higher than that of ordinary middle-separation polymers, indicating that the adaptability of salt-resistant polymers to low- and middle-permeability formations is significantly better than that of ordinary middle-separation polymers. Analyzing the reasons for this, it is believed that the salt-resistant polymer molecules have a strong ability to attract and entangle each other, forming a network structure that has certain rigidity and strong shear resistance. After entering the low permeability formation, the molecular structure cannot be easily destroyed. During the shearing process, the viscosity loss is not large and the high viscosity can be maintained to have a better oil displacement effect.

Oil displacement effect of natural core. Using natural cylindrical cores under the same viscosity (20 mPa·s), an oil displacement effect comparison experiment was carried out for the pollution-dissolving dilute ordinary intermediate polymer solution (1200 mg/L) and the salt-resistant polymer solution (700 mg/L). After water flooding to 96% water content, 0.64 PV ordinary middle-separation polymer solution and salt-resistant polymer solution were injected, followed by subsequent water flooding to above 98%. The flooding effects of different types of polymers under the same viscosity were compared, and the screened types of polymers applicable to X oilfield are listed.

Two natural cores were used to evaluate the oil displacement effect of common intermediate polymer and salt resistant polymer. The polymer flooding effect of natural core is shown in Figure 7. It can be seen that the oil displacement effect of salt resistant polymer is better than that of ordinary intermediate polymer with the same viscosity, and its EOR value is 3.21% higher than that of ordinary intermediate polymer, indicating that according to the characteristics of X oilfield reservoir, salt resistant polymer can give full play to its characteristics of good structural stability and viscosity retention ability, maintain high viscosity and improve oil displacement efficiency during displacement. It can be seen from Figure 7(b) that the subsequent water flooding EOR value of salt resistant polymer flooding experiment

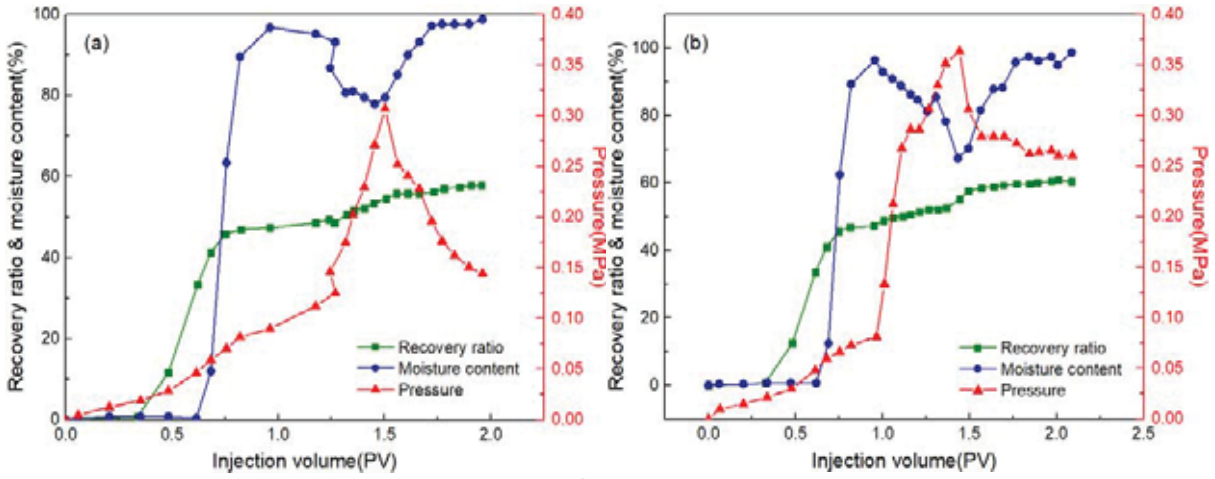

FIGURE 7
Oil displacement effect of ordinary intermediate and salt resistant polymer

is significantly higher than that of ordinary intermediate polymer at the same stage, indicating that salt resistant polymer can also play the role of profile control and flooding in low permeability reservoir. The reason is that the hydrodynamic radius DH of salt resistant polymer is large and evenly distributed [30, 31]. After selective injection into the high permeability layer, it can effectively block the high permeability layer, adjust the water absorption profile and improve the formation environment, so that it still has a good oil displacement effect in the subsequent water drive stage.

By comparing pressures, it can be found that in the process of injecting polymer solution for oil displacement, the displacement pressure of salt resistant polymer solution is slightly higher than that of ordinary intermediate polymer, but it is not obvious, indicating that after formation shear, the viscosity retention of salt resistant polymer solution is slightly higher than that of ordinary intermediate polymer, and the oil displacement effect is better. In the subsequent water drive stage, the subsequent water drive pressure of ordinary intermediate polymer decreased significantly, while the subsequent water drive pressure of salt resistant polymer decreased little and maintained at a high level, which also shows that salt resistant polymer has the effect of profile control. Considering the flooding effect of polymer solution and the input cost, it is recommended to choose salt-resistant polymer under the conditions of fouling for flooding. The optimal injection concentration of the salt-resistant polymer solution is 700 mg/L and the optimal injection volume is 0.64 PV.

CONCLUSIONS

In this paper, indoor physical simulation flooding experiments were conducted using artificial heterogeneous rectangular cores and natural cylindrical cores. The oil displacement effects of ordinary neutral and salt-resistant polymer solutions were compared from which the following conclusions were drawn: (1) Regardless of whether it is an ordinary middle-separation polymer or a salt-tolerant polymer, the greater the polymer solution concentration, the more obvious the oil displacement effect. Comprehensive comparisons of the displacement pressure, water cut and crude oil recovery factor of different concentrations of polymer were done to determine the ordinary middle. The optimal concentration of the polymer solution is 1200 mg/L and the optimal concentration of the salt-resistant polymer solution is 700 mg/L. (2) With increasing polymer solution injection rate, the enhanced oil recovery effect of the two polymers slows down. Considering the pressure change and the recovery rate increase degree of the polymer solution flooding process under different injection rates, it is believed that the optimal injection volume of the two polymer solutions is 0.64 PV. (3) Using natural cores to evaluate the oil displacement effect, the enhanced oil recovery value after the salt-resistant polymer flooding reaches 13.32%, which is higher than 10.1% of the ordinary middle-separation polymer. Considering the flooding effect and input cost of different polymers, it is recommended to use the pollution-resistant dilute salt-resistant polymer solution for flooding. The optimal injection concentration of the salt-resistant polymer solution is 700 mg/L and the optimal injection volume is 0.64 PV.

ACKNOWLEDGEMENTS

This study was no funds supported.

REFERENCES

[1] Liu, F., Wu, X., Zhou, W. (2020) Application of well pattern adjustment for offshore polymer flooding oilfield: a macro-scale and micro-scale study. Chemistry and Technology of Fuels and Oils. 56(3), 441-452.
[2] Mahat, S., Saaid, I.M., Lal, B. (2016) Green silica scale inhibitors for alkaline-surfactant-polymer flooding: a review. Journal of Petroleum Exploration and Production Technology. 6(3), 379-385.
[3] Su, B., Dou, M., Gao, X., Shang, Y., Gao, C. (2012) Study on seawater nanofiltration softening technology for offshore oilfield water and polymer flooding. Desalination. 297(5), 30-37.
[4] Douarche, F., Raille, M., Veiga, S.D. (2014) Sensitivity analysis and optimization of surfactant-polymer flooding under uncertainties. Oil & Gas Science and Technology. 22(8), 321-329.
[5] Yi, Z., Yang, F., Liu, X. (2015) Synthesis and properties of oil displacement copolymer P in low permeability, high temperature and high salt reservoirs. Applied Chemistry. 32(5), 519-526.
[6] Cai, C., Shen, Z., Xing, Y. (2017) Cases Studies on Polymer for Poor Reservoirs in Daqing Oilfield. Journal of Materials Research. 21(3), 261-266.
[7] Du, G. (2018) In situ surface modification of silane coupling agent for nanocrystalline silica. Functional Materials. 12(39), 2072-2074.
[8] Wang, Y., Li, G., Ren, S. (2014) Preparation of single-component polyurethane sealant by modified silica with silane coupling agent. Chemistry and Adhesion. 32(4), 65-67.
[9] Tan, X., Feng, A., Zhao, H. (2011) A Model for calculating polymer injectivity including the effects of sheared gradation. China Powder Technology. 17(1), 14-17.
[10] Zhang, M., Rong, M., Zhang, H. (2013) Mechanical properties of low nano-silica filled high density polyethylene composites. Polymer Engineering and Science. 43(2), 490-500.

[11] Samanta, A., Bera, A., Ojha, K., Mandal, A. (2012) Comparative studies on enhanced oil recovery by alkali-surfactant and polymer flooding. Journal of Petroleum Exploration & Production Technology. 2(2), 67-74.
[12] Tan, Y., Wang, D., Han, L. (2019) Preparation and characterization of polystyrene/Nano-SiO_2 composite particles. Materials Science and Technology. 17(4), 520-523.
[13] Eastmond, G., Nguyen, H., Piret, W. (2018) Graft polymerization from glass surfaces. Polymer. 21(6), 598-603.
[14] Spange, S. (2020) Silica surface modification by cationic polymerization and carbenium intermediates. Progress in Polymer Science. 25(6), 781-849.
[15] Rong, M., Zhang, M., Zheng, Y. (2011) Improvement of nano-SiO_2/PP composites in relation to percolation mechanism tensile properties of Polynner. Powder Technology. 42(7), 3301-3304.
[16] Ruan, W., Huang, X., Wang, X. (2016) Effect of drawing induced dispersion of nano-silica on performance improvement of poly-based nanocomposites. Macromolecular Rapid Communication. 27(8), 581-585.
[17] Bachmann, S., Wang, H., Albert, K. (2017) polymerization of styrene initiated by covalently bonded peroxide groups on silica. Journal of Colloid and Interface Science. 309(1), 169-175.
[18] Zhou, E., Li, H., Bo, S. (2011) Study on morphology and structure of polyacrylamide. Journal of Macromolecules. 12(1), 51-56.
[19] Yang, J., Li, H., Huang, P. (1997) Static adsorption of partially hydrolyzed polyacrylamide in porous media and influence of degree of hydrolysis on adsorption capacity. Journal of High Molecular Sciences. 33(5), 600-605.
[20] Pan, Y., Feng, J., Yang, S. (2018) Synthesis and prospect of hydrophobic associating polyacrylamide with temperature and salt resistance. Applied Chemistry. 47(8), 1773-1775.
[21] Jiang, Y., Lu, S., Zhang, C. (2017) Preparation and properties of epoxy resin/hypertropic polyester/nano-SiO2 composites. Polymer Materials Science and Engineering. 9(3), 134-137.
[22] Knobloch, L.O., Reina, R.E.H., Fdisch, H., Ganzer, L. (2018) Qualitative and quantitative evaluation of permeability changes during eor polymer flooding using micromodels. Engineering and Technology. 6(2), 18-28.
[23] Zhao, H., Luo, Y., Li, J. (2015) New method of grafting modification of Nano-SiO_2 surface hypertrophic polymer. Polymer Materials Science and Engineering. 21(3), 188-191.
[24] Duan, M., Ma, Y., Fang, S., Shi, P., Zhang, J., Jing, B. (2014) Treatment of wastewater produced from polymer flooding using polyoxyalkylated polyethyleneimine. Separation & Purification Technology. 13(3), 160-167.
[25] Chen, Q., Du, Y., Shen, L. (2010) Flocculation and decolorization of hyperhypertropic polyester derivatives. Printing and Dyeing. 36(17), 21-33.
[26] Wang, Z. (2014) Synthesis and properties of hyperhyperified reverse phase emulsion polymer for drilling fluid. Drilling Fluid & Completion Fluid. 31(3), 14-18.
[27] He, H., Chen, Y., Yu, Q., Wen, X., Liu, H. (2019) Optimization design of injection strategy for surfactant-polymer flooding process in heterogeneous reservoir under low oil prices. Energies. 12(19), 1-15.
[28] Sun, C., Hou, J., Pan, G., Xia, Z. (2016) Optimized polymer enhanced foam flooding for ordinary heavy oil reservoir after cross-linked polymer flooding. Journal of Petroleum Exploration & Production Technology. 6(4), 777-785.
[29] Wang, F., Lv, H., Wang, X., Jing, B., Fang, S. (2019) Preparation of a selective flocculant for treatment of oily wastewater produced from polymer flooding and its flocculant mechanism. Water Science & Technology. 79(3), 251-259.
[30] Thongsumrit, T.H., Trisarn, K. (2015) Comparison for oil recovery between water and polymer flooding in the u-thong oil field. Journal of Science & Technology. 22(2), 143-153.
[31] Tahir, M., Hincapie, R.E., Be, M., Ganzer, L. (2017) A comprehensive combination of apparent and shear viscoelastic data during polymer flooding for EOR evaluations. World Journal of Engineering & Technology. 5(4), 585-600.

Received: **01.12.2021**
Accepted: **23.01.2022**

CORRESPONDING AUTHOR

Chao Gao
Shaanxi Yanchang Petroleum (Group) Corp. Ltd.,
Xi'an Shaanxi 710075 – China

e-mail: haojie93@126.com

© by PSP Volume 31– No. 05/2022 pages 5113-5123 Fresenius Environmental Bulletin

LEAF STRUCTURE OF *Camellia weiningensis* AND ITS RELATIONSHIP WITH COLD RESISTANCE

Jie Qiu, Chao Gao*, Yang Hu, Biao Wang, Hongli Wei

Institute for Forest Resources and Environment of Guizhou, Key Laboratory of Forest Cultivation in Plateau Mountain of Guizhou Province, College of Forestry, Guizhou University, Guiyang 550025, China

ABSTRACT

This study investigated the relationship between the leaf structure of *Camellia weiningensis* and cold resistance. In July 2021, leaves were selected from 30 excellent trees and denoted wn-number. Paraffin sectioning was performed to observe 11 anatomical structural indices. Based on variance analysis, correlation analysis and cluster analysis, four typical indices were determined. A membership function was employed to comprehensively evaluate cold resistance. The leaves were composed of the cuticle, upper epidermis, palisade tissue, spongy tissue, stoma and lower epidermis and were bifacial. The upper and lower epidermis was composed of monolayer cells, and stomata were only observed in the lower epidermis. The palisade tissue was composed of densely arranged cells. The palisade tissue of most leaves contained three layers of cells, with a few leaves containing four layers. The main vein consisted of collenchyma, xylem, phloem and parenchyma. The trees differed greatly in terms of the 11 anatomical structural indices, where wn-4 had the thickest leaves. The average thickness of its upper and lower epidermis was 27.81 μm and 24.68 μm, respectively, with an average palisade tissue-spongy tissue ratio of 0.9 and a cuticle ranging from 9.46 μm to 17.71 μm in thickness. According to cluster analysis and correlation analysis, the indices most related to cold resistance included the thickness of the spongy tissue, the thickness of the lower epidermis, vein thickness and tissue structure tightness. According to the membership function values, the plants with strong cold resistance were wn-1, wn-3, wn-19, wn-22 and wn-28.

KEYWORDS:
Camellia weiningensis, leaf, anatomical structure, cold resistance

INTRODUCTION

Camellia weiningensis, a wild species belonging to the genus *Camellia* of Theaceae, is endemic to high-altitude regions (1800-2700 m) in Weining County, Northwest Guizhou Province, China [1]. *Camellia* is a high-quality oil tree species that originated in China, and it is distributed across 18 provinces of China. This species can grow in regions with annual average temperatures of 14-22 °C. *Camellia* oil contains a very high unsaturated fatty acid content, and its planting areas have expanded from merely tropical regions to subtropical and northern subtropical regions [2]. However, the damage caused by low temperature has seriously hindered the development of the *C. oleifera* industry on the northern edge of China's Dabie Mountains. Additionally, in 2008, an extended freeze occurred in southern China, which resulted in a sharp drop in the output of *C. oleifera* in the two main producing areas in Hunan and Jiangxi provinces, as well as a reduction in tea farmers' incomes. Therefore, the stress resistance of *C. oleifera* should be given more attention [3]. The flowering period of *C. oleifera* (from November to January of the next year) differs from that of most woody plants. Cold weather leads to flower and fruit drop; when the temperature drops below 8 °C, the release of *C. oleifera* pollen will be impeded, which will adversely affect pollination and fruit setting. Therefore, the damage caused by low temperature during flowering has become one of the factors limiting the yield of *C. oleifera* [4].

Plants are shaped by their natural environment and adapt to environmental changes to survive. The ability of plants to respond to environmental changes is positively correlated with their potential ability to adapt to local natural environmental conditions. Low temperature limits the geographical distribution and seasonal growth of plants. Plants living in alpine and low-temperature mountains for a long time will gradually adapt to low temperatures due to natural selection on genetic variations, resulting in survival under cold stress [5]. The response mechanism of plants to cold resistance is complex and can be reflected in morphological structure, physiological and biochemical indices and molecular changes. With changes in environmental conditions, plant physiological and biochemical indices tend to change; accordingly, the chlorophyll content will decrease with decreasing environmental temperature, and relative conductivity and soluble sugar will also vary with temperature [6, 7]. The morphological and anatomical structure of plants is the result of long-term adaptation to specific environmental conditions and

does not change due to temporary changes in the environment. Therefore, the characteristics of morphological and anatomical structures can be used as an important reference index for the study of plant cold resistance. Leaves are an important metabolic organ in plants and are the major organ for photosynthesis [8]. Due to their direct exposure, changes in the environment are more likely to lead to changes in the anatomical structure of leaves to ensure proper functioning. These changes can reflect the characteristics of plant adaptation to ecological conditions. With a variety of options for dealing with stress, plant responses can be classified into different types. Leaves are plant organs with strong plasticity; long-term low temperature stress often leads to changes in the anatomical structure indices of leaves, such as leaf thickness, palisade tissue thickness and spongy tissue thickness, to adapt to the damage caused by low temperature stress [9].

In recent years, research on plant cold resistance has gradually shifted to the molecular level, manifested by cold resistance gene labeling, isolation and identification, gene interactions, molecular mechanisms, and so on [10-14]. Nevertheless, studies using anatomical structural indices of *C. oleifera* leaves to evaluate cold resistance remain rare, with the exception of Zeng et al.'s comprehensive evaluation of cold resistance using nine indices of six *C. oleifera* cultivars [15] and Wu et al.'s [16] investigation into the effects of low temperature on the chlorophyll fluorescence, leaf anatomical structure and physiological and biochemical characteristics of two *C. oleifera* cultivars. No publications regarding the anatomical structure and cold resistance of *C weiningensis* leaves have been found in the literature.

Based on the aforementioned information, we conducted the current comparative analysis of the anatomical structures of the leaves from 30 excellent *C. weiningensis* plants. We aimed to clarify the anatomical characteristics of *C. weiningensis* leaves, evaluate the cold resistance of the plants, and explore the relationship between leaf anatomical structure and cold resistance. The results of this study might also provide reference data for selecting excellent *C. weiningensis* trees with strong cold resistance and provide basic biological data for studies on plant cold resistance.

MATERIALS AND METHODS

Experimental site. This study was conducted at the *Camellia oleifera* Research Station of Guizhou University, located in Tuijie Town, Weining County, Guizhou Province (Figure 1). The average altitude of Weining County is 2200 m. The annual temperature is 12.1 °C, with an average January temperature of 3.9 °C, an average July temperature of 17.0 °C and a total annual accumulated temperature of 4380 °C. The annual precipitation is 739 mm, and the annual frost-free period is 205 d. The county is a southwest monsoon-dominated area, and it contains a mountainous area with the highest terrain and the lowest temperature in Guizhou Province.

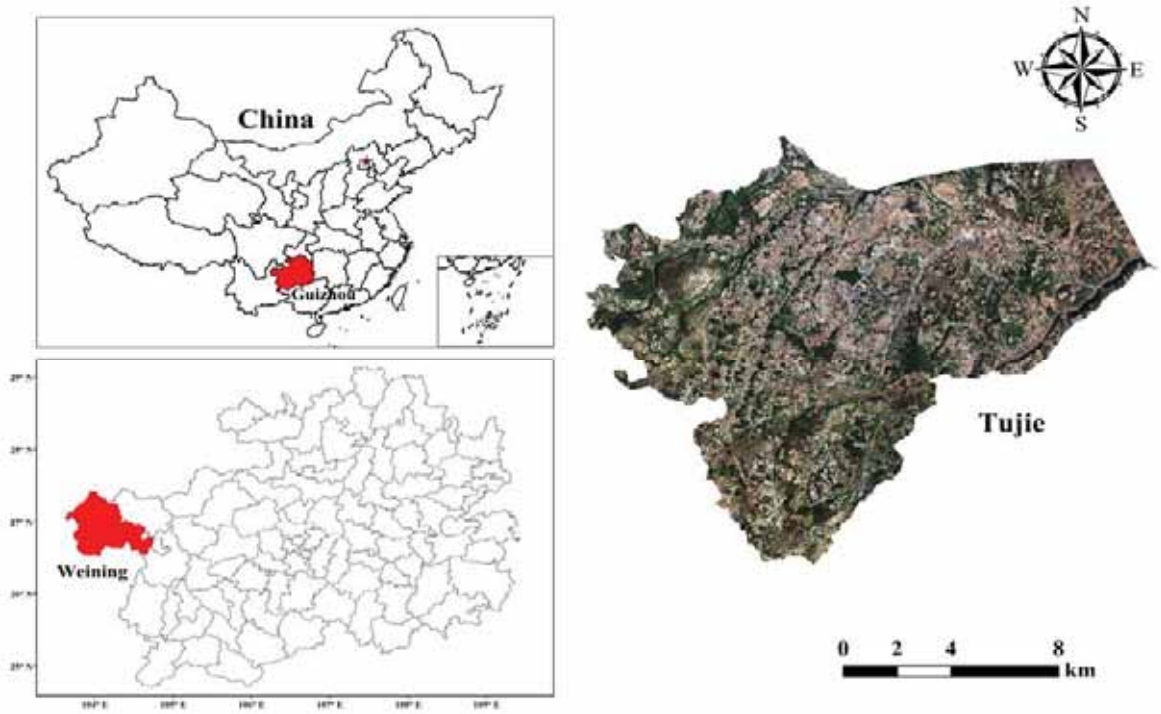

FIGURE 1
Overview map of the study area

Experimental materials. The *C. oleifera* cultivar used in this experiment was *C. weiningensis*. According to their fruit characteristics, 30 excellent individual plants were selected and numbered wn-1 to wn-30. Sampling was conducted from 8:00 a.m. to 10:00 a.m. on July 14, 2021, and three mature, disease-free leaves from the 5th to 7th nodes of each tree crown facing the sun were taken, with a total of 9 repetitions. The leaves were cut into 5 mm ×5 mm leaf blocks centered around the main vein, and then mesophyll tissue blocks of 5 mm × 5 mm were made (the main vein was avoided). The samples were immediately fixed in Carnoy solution (absolute ethanol (V): glacial acetic acid (V) = 3:1) for 12 h. Afterward, air was pumped out, and the samples were transferred into 70% alcohol and then stored at 4 °C.

Observational indices. The anatomical structure of the leaves was observed using paraffin sectioning. The samples underwent gradient alcohol dehydration and were treated with alcohol and xylene. The samples were then subjected to wax embedding [17]. Paraffin sectioning was performed (Leica RM2235, Germany), followed by drying, dewaxing, fast-green staining, sealing and drying. Images were collected under a microscope (Leica DM2500, Germany). ImageJ software was used to measure leaf thickness (LT), the thickness of the upper epidermis (TU), the thickness of the lower epidermis (TL), the thickness of palisade tissue (TP), the thickness of spongy tissue (TS), cuticle thickness (CT) and vein thickness (VT). The ratio of palisade tissue to spongy tissue (P/S), tissue structure tightness (CTR), tissue structure looseness (SR) and vein protuberant degree (VPD) were calculated as follows:

P/S = palisade tissue/spongy tissue;

CTR = the thickness of palisade tissue/that of the leaf,

SR = the thickness of spongy tissue/that of the leaf,

VPD = vein thickness/leaf thickness; and

Coefficient of variation (C/V) = (standard deviation/mean) ×100%.

Statistical analysis. Data were calculated and processed with Excel 2013. SPSS20.0 was used for descriptive analysis, variance analysis and Duncan's multiple comparison. Origin software was used for correlation analysis and cluster analysis, and Photoshop2019 was used for image processing. After cluster analysis, typical indices in each category were determined according to their values. The correlation index was positively related to its representativeness, which was calculated as follows:

$$R_i^2 = \sum \frac{r^2}{n-1} \quad (1)$$

Where R_i^2 represents the correlation index of the index in each category (i = 1, 2, …, n), n represents the number of indices in each category, and r represents the correlation coefficient of an index compared with other indices in the same category.

The membership function method was used to evaluate the cold resistance of the 30 individual plants as follows:

$$f(x_i) = (X_i - X_{imin})/(X_{imax} - X_{imin}) \quad (2)$$

Where $f(x_i)$ is the value of the cold resistance membership function, X_i is the determined value of a certain index, and X_{imin} and X_{imax} represent the maximum and minimum values of a certain determined index, respectively. If a certain index was negatively correlated with the cold resistance of the corresponding plant, inverse membership function transformation was performed [18], which was calculated as follows:

$$f(x_i) = 1 - (X_i - X_{imin})/(X_{imax} - X_{imin}) \quad (3)$$

Based on the abovementioned formulas, the average membership degrees of the cold resistance-related anatomical structural indices of each plant were determined. The membership value was used to evaluate the cold resistance of the plant. A higher average membership degree indicates stronger cold resistance.

RESULTS

Characteristics of the leaf anatomical structure. The leaves of *C. weiningensis* are composed of the upper epidermis, palisade tissue, spongy tissue, the lower epidermis, stomata (Figure 2-A) and leaf veins (Figure 2-C). Both the upper and lower epidermis are composed of a layer of arranged cells that are approximately rectangular in shape. The palisade tissue is attached to the lower part of the upper epidermis and is mostly composed of three layers of irregular long columnar cells (Figure 2-A). A few leaves contained four layers of palisade tissue (Figure 2-B). The cells in this tissue are closely arranged, and in most leaves, the thickness of the palisade tissue, located in the middle layer of the leaf, is large. However, a gradual decrease in the thickness of the palisade tissue was observed in some leaves, such as wn-21 (Figure 3-C1). Compared with palisade tissue, spongy tissue is loosely arranged and is composed of oval cells of different sizes and large cell gaps. Between the palisade tissue and sponge tissue, lateral veins are occasionally distributed. The main vein of the leaf is composed of collenchyma, xylem, phloem, parenchyma, and other structures (Figure 2-C).

The anatomical structures of the leaves and veins of the 30 excellent individual plants are shown in Figure 3 and Figure 4.

Comparison of the anatomical structure. LT is often used as one of the indicators of cold resistance as thicker leaves have slower water loss. In a severely cold growth environment, thick leaves can effectively delay the damage caused by low-temperature stress [19]. As shown in Table 1, the LT of *Camellia weiningensis* is 394.91-602.33 μm, with an

average of 498.71 μm. The leaves of wn-25 are the thinnest, and those of wn-4 are the thickest. The TU of wn-5 is the thinnest among all tested materials and is only 19.42 μm; the lower epidermis of wn-8 is the thinnest (19.34 μm). Both the TU and TL of wn-10 leaves are the thickest at 41.02 μm and 31.78 μm, respectively. The average TU and TL of all plant leaves are 27.81 μm and 24.68 μm, respectively. Overall, the lower epidermis is slightly thinner than the upper epidermis. The TP of all leaves ranges from 167.02 μm to 256.96 μm, with the thickest TP found for wn-7. The TS ranges from 157.75 μm to 292.44 μm. The average P/S is 0.9. The CT ranges from 9.46 μm to 17.71 μm, and the coefficient of variation of CT (19.64%) is the largest among all indices. A high CT value can help reduce the water loss on the surface of leaflets that do not have stomata [20]. The coefficient of variation of the upper epidermis is 19.37%. CTR ranges from 0.37 μm to 0.48 μm, and its coefficient of variation is the smallest among all considered indices. SR ranges from 0.38 μm to 0.53 μm. Among all plants, wn-14 shows the smallest looseness but the largest P/S ratio, while wn-16 has the largest looseness but the smallest P/S ratio. In addition, wn-16 has the thickest vein, whereas wn-5 has the thinnest vein and the lowest PVD.

Comprehensive evaluation of the cold resistance of the plants. Cold resistance-related anatomical index determination. The best way to evaluate cold resistance is to determine independent and representative indicators [9]. In this study, cluster analysis was performed on 11 anatomical structural indices for the leaves of the 30 plants (Figure 5). When the threshold was between 0.7-0.8, the indices could be divided into four categories. The first category included LT, TS and SR; the second included TU, TL and CT; the third included VT and VPD; and the fourth included TP, P/S and CTR.

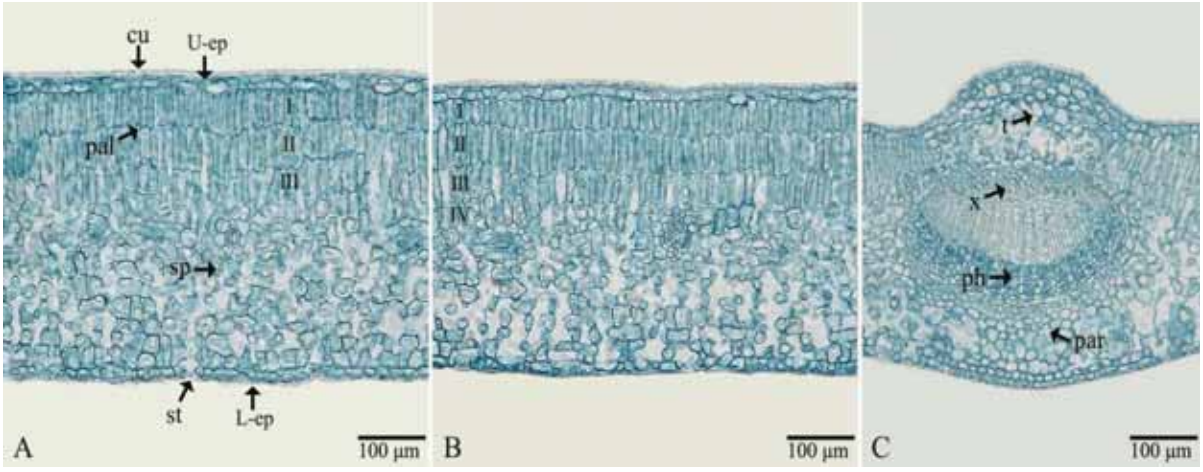

FIGURE 2

Structural characteristics of *Camellia weiningensis* leaves.

Notes: cu: cuticle; U-ep: upper epidermis cells; pal: palisade tissue; sp: spongy tissue; st: stomata; L-ep: lower epidermis cells; t: thick angle tissue; x: xylem; ph: phloem; and par: parenchyma. I, II, III, and IV represent the first layer of the palisade tissue, the second layer of the palisade tissue; the third layer of the palisade tissue, and the fourth layer of the palisade tissue. A. wn-2 leaves with three layers of palisade tissue; B. wn-1 leaves with four layers of palisade tissue; and C. wn-1 leaf veins. ×100.

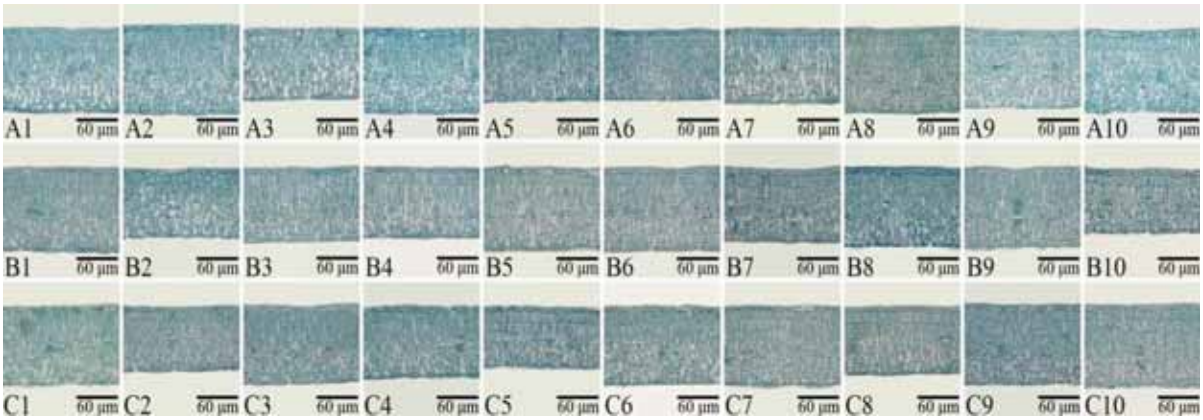

FIGURE 3

Leaf structure characteristics of 30 excellent *Camellia weiningensis* leaves

Notes: A1—A10 represent wn-1—wn-10 leaves; B1—B10 represent wn-11—wn-20 leaves; and C1—C10 represent wn-21—wn-30 leaves. ×100.

TABLE 1
Leaf anatomical structure characteristics of 30 excellent individual plants

Number	Leaf thickness	Thickness of upper epidermis	Thickness of lower epidermis	Thickness of palisade tissue	Thickness of spongy tissue	Cuticle thickness
wn-1	549.97±6.51cd	30.33±3.62bcd	29.82±3.81abc	216.78±7.61def	253.20±9.44fghi	12.96±1.97ghi
wn-2	532.51±3.69f	39.13±2.97a	29.57±3.15abc	197.51±4.97hi	265.71±5.03cdef	12.71±1.83hi
wn-3	442.26±4.50n	27.64±3.29cdef	23.42±2.02defghij	204.36±7.54gh	177.67±1.77o	13.47±1.11fghi
wn-4	602.33±6.55a	33.6±1.4b	27.56±3.59bcd	240.4±9.51b	292.44±8.65a	17.22±1.07ab
wn-5	490.94±12.31jk	19.42±2.43g	24.51±2.99defghi	197.38±6.76hi	242.07±10.02ijk	12.42±0.5hij
wn-6	461.53±4.17m	26.98±6cdef	25.24±2.15defgh	178.66±7.11kl	235.42±12.83jkl	11.75±1.47ijk
wn-7	557.97±7.92c	28.73±2.57bcdef	23.28±3.09defghij	256.96±5.22a	244.8±14.5ijk	15.67±1.56bcde
wn-8	531.78±1.88f	24.87±3.79def	19.34±2.5j	222.69±4.1cd	253.53±6.23fghi	11.86±0.78ijk
wn-9	517.67±6.81g	27.06±4.19cdef	24.29±1.32defghi	189.45±6.78ijk	272.09±8.22cde	15.84±1.65abcde
wn-10	543.56±10.31de	41.02±6.52a	31.78±1.81a	237.75±16.3b	232.4±10.45kl	14.8±0.93defg
wn-11	544.27±7.74de	29.67±4.28bcde	24.36±2.89defghi	207.44±4.63fgh	278.11±7.84bc	15.93±1.95abcde
wn-12	446.26±8.03n	24.07±4.04efg	24.66±2.7defghi	167.02±9.34m	225.67±12.92lm	15.09±1.66cdef
wn-13	482.33±3.69kl	24.29±3.15efg	20.8±4.26hij	204.8±8.67gh	217.75±10.05m	11.7±1.04ijk
wn-14	442.67±6.39n	25.33±3.41cdef	23.71±2.22defghij	210.62±8.21efg	168.87±6.39op	15.36±1.36bcde
wn-15	520±6.44g	30.95±4.66bc	23.86±1.66defghi	217.46±7.7def	246.91±9.56hij	12.09±1.28ijk
wn-16	537.45±5.32ef	29.09±2.67bcdef	21.53±3.27hij	197.93±7.38hi	285.67±6.56ab	14.22±0.9efgh
wn-17	479.42±5.38l	23.75±3.39fg	23.27±2.67defghij	229.38±5.6bc	196.44±4.18n	17.71±0.86a
wn-18	512±1.99gh	27.64±3.04cdef	24.67±1.2defghi	205.75±9.61fgh	258.33±11.35fgh	16.17±1.5abcde
wn-19	506.11±7.44h	29.6±2.67bcde	27.56±1.37bcd	195.31±5.76hi	264.69±8.64def	16.99±1.52abc
wn-20	409.38±4.21o	27.35±4.53cdef	21.38±3.12hij	177.45±9.27lm	174.26±11.23o	10.58±1.02jkl
wn-21	520.29±17.14g	24.44±4.84efg	21.96±3.27fghij	213.22±5.81defg	262.94±8.95efg	13.09±1.28ghi
wn-22	412.44±2.16o	26±2.08cdef	26.18±2.3cdefg	167.27±3.41m	191.86±3.79n	16.72±1.16abcd
wn-23	505.31±4.84hi	30.11±4.65bcd	26.91±2.3bcde	190.6±2.78ij	249.89±6.27ghi	15.42±2.07bcde
wn-24	467.2±5.81m	25.93±3.02cdef	26.47±2.28cdef	190.73±10.86ij	213.42±5m	9.78±0.92l
wn-25	394.91±5.65p	28.51±3.5bcdef	21.89±1.51ghij	183.2±10.99jkl	157.75±10.03p	10.29±0.9kl
wn-26	520.15±6.31g	27.37±3.26cdef	30.84±6.27ab	236.62±12.37b	226.11±9.83lm	15.52±0.97bcde
wn-27	496.66±3.4ij	26.91±1.87cdef	24.91±4.24defghi	198.84±6.58hi	241.45±5.93ijk	9.46±0.73l
wn-28	438.84±4.31n	23.57±3.03fg	20.58±2.64ij	191.95±7.15ij	193.97±11.95n	9.83±1l
wn-29	521.46±6.67g	24.73±2.86def	22.84±2.5efghij	221.24±7.06cde	248.58±5.55hij	13.18±1.96ghi
wn-30	573.6±9.11b	26.18±2.06cdef	23.27±3.41defghij	239.73±13.32b	277.12±18.69bcd	11.66±0.88ijk
Mean	498.71	27.81	24.68	206.28	234.97	13.65
Coefficient of Variation	10.12%	19.37%	16.30%	11.34%	15.75%	19.64%

TABLE 1
(Continued)

Number	Vein thickness	Ratio of palisade tissue to spongy tissue	Tissue structure tightness	Tissue structure looseness	Vein protuberant degree
wn-1	759.28±6.69n	0.86±0.05efg	0.39±0.02fghij	0.46±0.02efg	1.38±0.01no
wn-2	930.15±3.30d	0.74±0.03hi	0.37±0.01jk	0.50±0.01bcd	1.75±0.01g
wn-3	654.64±6.12t	1.15±0.05b	0.46±0.02ab	0.40±0.00kl	1.48±0.03kl
wn-4	854.71±2.48hi	0.82±0.05fgh	0.4±0.02efghi	0.49±0.01cde	1.42±0.02m
wn-5	570.87±3.78w	0.82±0.06fgh	0.4±0.02efgh	0.49±0.01cd	1.16±0.03r
wn-6	875.36±2.71g	0.76±0.05ghi	0.39±0.01ghijk	0.51±0.03abc	1.9±0.02d
wn-7	752.03±2.31o	1.05±0.08c	0.46±0.01ab	0.44±0.02ghi	1.35±0.02pq
wn-8	825.15±3.47k	0.88±0.03ef	0.42±0.01def	0.48±0.01def	1.55±0.01j
wn-9	718.48±3.71r	0.7±0.05i	0.37±0.01k	0.53±0.02ab	1.39±0.02n
wn-10	914.2±4.15e	1.03±0.12cd	0.44±0.03cd	0.43±0.02ij	1.68±0.02h
wn-11	989.28±6.37b	0.75±0.04hi	0.38±0.01hijk	0.51±0.01abc	1.82±0.03f
wn-12	970.94±2.18c	0.74±0.08hi	0.37±0.02jk	0.51±0.03abc	2.18±0.04a
wn-13	728.63±3.34q	0.94±0.08de	0.43±0.02de	0.45±0.02fghi	1.51±0.02k
wn-14	893.91±3.14f	1.25±0.09a	0.48±0.02ab	0.38±0.02l	2.02±0.03b
wn-15	848.04±4.99j	0.88±0.05ef	0.42±0.01def	0.47±0.01def	1.63±0.02i
wn-16	1016.81±3.34a	0.69±0.04i	0.37±0.01jk	0.53±0.02a	1.89±0.02d
wn-17	753.62±4.22o	1.17±0.05ab	0.48±0.01a	0.41±0.01jk	1.57±0.02j
wn-18	872.97±4.52g	0.8±0.07fgh	0.4±0.02efgh	0.51±0.02abc	1.71±0.01h
wn-19	857.97±4.91h	0.74±0.03hi	0.39±0.01ghijk	0.52±0.01ab	1.7±0.03h
wn-20	602.75±4.27v	1.02±0.12cd	0.44±0.03cd	0.42±0.03ijk	1.47±0.02l
wn-21	685.65±5.41s	0.81±0.03fgh	0.41±0.01efg	0.51±0.01abc	1.32±0.04q
wn-22	572.17±3.34w	0.87±0.03ef	0.4±0.01efgh	0.46±0.01efg	1.38±0.01no
wn-23	852.46±4.96ij	0.76±0.01ghi	0.38±0.01ijk	0.49±0.01cd	1.69±0.02h
wn-24	914.2±3.46e	0.89±0.07ef	0.41±0.03efg	0.46±0.02fgh	1.95±0.03c
wn-25	610.15±3.83u	1.17±0.14ab	0.46±0.03ab	0.4±0.03kl	1.55±0.02j
wn-26	967.25±3c	1.05±0.1c	0.45±0.02bc	0.43±0.03hij	1.86±0.02e
wn-27	736.09±2.68p	0.83±0.04fgh	0.4±0.01efghi	0.49±0.01cde	1.48±0.01l
wn-28	791.59±1.89l	0.99±0.08cd	0.44±0.02cd	0.44±0.03ghi	1.8±0.02f
wn-29	776.96±1.73m	0.89±0.04ef	0.42±0.01de	0.48±0.02def	1.49±0.02kl
wn-30	777.25±4.18m	0.87±0.1ef	0.42±0.03def	0.48±0.03cde	1.35±0.03op
Mean	802.45	0.9	0.41	0.47	1.61
Coefficient of Variation	15.34%	18.14%	8.71%	9.27%	14.65%

Note: The data in the table are the mean ± coefficient of variation; different letters in the same column indicate significant differences at the 0.01 level.

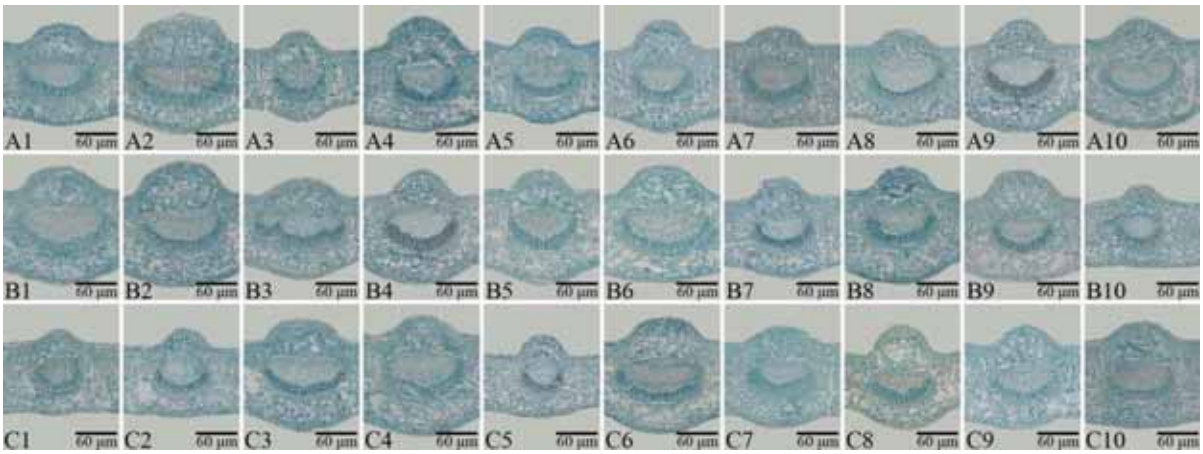

FIGURE 4

Leaf structure characteristics of 30 excellent *Camellia weiningensis* leaf veins.

Notes: A1—A10 represent wn-1—wn-10 leaf veins; B1—B10 represent wn-11—wn-20 leaf veins; and C1—C10 represent wn-21—wn-30 leaf veins. ×100.

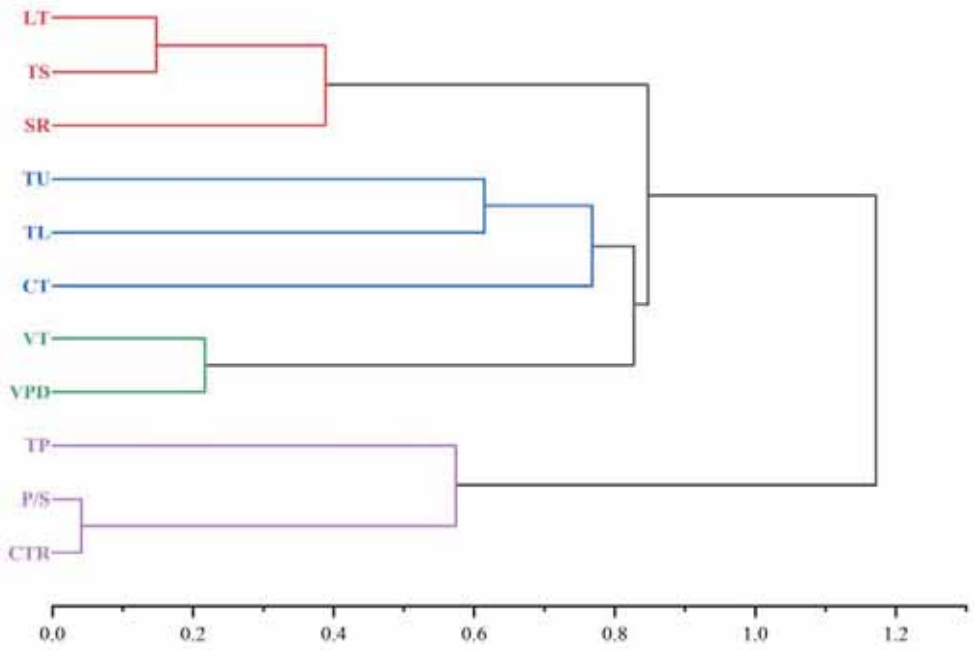

FIGURE 5

Cluster analysis result of 11 leaf anatomic structural indices.

Notes: LF, leaf thickness; TS, thickness of spongy tissue; SR, tissue structure looseness; TU, thickness of the upper epidermis; TL, thickness of the lower epidermis; CT, cuticle thickness; VT, vein thickness; VPD, vein protuberant degree; TP, thickness of palisade tissue; P/S, ratio of palisade tissue to spongy tissue; CTR, tissue structure tightness.

Correlation analysis was carried out on the 11 anatomical structural indices. The results showed that there are certain degrees of correlation among them (Figure 6). There are very significant correlations between LT and other indices, among which the correlations with P/S, CTR and VPD are very significantly negative and those with the remaining indices are very significantly positive.

TU has very significantly positive correlations with TL and VT and a significant negative correlation with CTR. TL has very significantly positive correlations with CT and VT. Both TP and TS exhibit correlations with the remaining indices. Among these correlations, TS is very significantly negatively correlated with P/S and CTR, VT is very significantly positively correlated with VPD and SR, and both VT and SR are very significantly negatively correlated with P/S and CTR. P/S is very significantly positively correlated with CTR. CT is very significantly positively correlated with VT but does not show significant correlations with the remaining indices.

FIGURE 6
Correlation matrix of 11 leaf structure indices.

Note: LF, leaf thickness; TS, thickness of spongy tissue; SR, tissue structure looseness; TU, thickness of the upper epidermis; TL, thickness of the lower epidermis; CT, cuticle thickness; VT, vein thickness; VPD, vein protuberant degree; TP, thickness of palisade tissue; P/S, ratio of palisade tissue to spongy tissue; CTR, tissue structure tightness.
*: significant correlation at the 0.05 level (P<0.05); **: significant correlation at the 0.01 level (P<0.01).

TABLE 2
Correlation indexes and rankings of four types of leaf anatomical structural indices

Index category no.	Leaf anatomic structural index	Correlation index	Order in category
1	Leaf thickness	0.445	3
1	Tissue structure looseness	0.418	2
1	Thickness of spongy tissue	0.700	1
2	Cuticle thickness	0.060	3
2	Thickness of upper epidermis	0.086	2
2	Thickness of lower epidermis	0.123	1
3	Vein thickness	0.613	1
3	Vein protuberant degree	0.613	1
4	Thickness of palisade tissue	0.185	3
4	Ratio of palisade tissue to spongy tissue	0.528	2
4	Tissue structure tightness	0.577	1

Based on the results of the correlation matrix and cluster analysis, the correlation index of each considered index in each category was calculated according to Eq. (1); then, the obtained results were ordered. A typical index is defined as one with the largest correlation index in the same category; if the correlation indices are the same, the coefficients of variation are compared, and the index with the largest coefficient of variation is considered the typical index [21]. As shown in Table 2, the correlation index of TS in category 1 is the largest at 0.700; therefore, it is selected as the typical index of this category. The correlation index of TL is the largest in category 2; thus, it is selected as the typical index of this category. For category 3, the correlation indices of VT and VPD are equal, but the coefficient of variation of the former (15.34%) is greater than that of the latter (14.65%). For category 4, the correlation index of CTR is 0.577, which ranks the first in this category; therefore, it is selected as the typical index.

TABLE 3
Comprehensive evaluation of the cold resistance of 30 excellent individual plants

Number	Thickness of spongy tissue	Thickness of lower epidermis	Vein thickness	Tissue structure tightness	Average value of membership function	Order of cold tolerance
wn-1	0.567	0.572	0.627	0.467	0.558	1
wn-3	0.492	0.457	0.654	0.600	0.551	2
wn-19	0.464	0.380	0.555	0.800	0.550	3
wn-22	0.767	0.500	0.460	0.467	0.549	4
wn-28	0.690	0.589	0.400	0.450	0.532	5
wn-17	0.556	0.400	0.500	0.667	0.531	6
wn-15	0.570	0.633	0.461	0.450	0.529	7
wn-23	0.470	0.625	0.400	0.600	0.524	8
wn-5	0.497	0.428	0.523	0.640	0.522	9
wn-13	0.635	0.431	0.479	0.520	0.516	10
wn-6	0.560	0.416	0.600	0.450	0.507	11
wn-24	0.427	0.567	0.466	0.560	0.505	12
wn-30	0.519	0.333	0.640	0.514	0.502	13
wn-21	0.660	0.420	0.590	0.333	0.501	14
wn-18	0.439	0.482	0.432	0.640	0.498	15
wn-4	0.563	0.548	0.470	0.400	0.495	16
wn-26	0.552	0.467	0.480	0.480	0.495	17
wn-9	0.429	0.599	0.536	0.400	0.491	18
wn-20	0.497	0.450	0.487	0.514	0.487	19
wn-27	0.316	0.481	0.480	0.667	0.486	20
wn-29	0.510	0.425	0.533	0.467	0.484	21
wn-12	0.542	0.390	0.520	0.480	0.483	22
wn-8	0.336	0.622	0.558	0.400	0.479	23
wn-16	0.467	0.467	0.600	0.333	0.467	24
wn-10	0.426	0.616	0.543	0.267	0.463	25
wn-7	0.425	0.546	0.475	0.400	0.462	26
wn-25	0.495	0.420	0.429	0.486	0.458	27
wn-2	0.450	0.513	0.467	0.333	0.441	28
wn-11	0.430	0.437	0.467	0.400	0.434	29
wn-14	0.590	0.228	0.360	0.400	0.395	30

Comprehensive assessment of cold resistance. Based on the four selected typical indices, as well as Eqs. (2) and (3), the membership function method was used to comprehensively assess the cold resistance of the 30 plants. The plants were ordered according to the average membership degree. A higher average membership degree indicates stronger cold resistance. The results are summarized in Table 3. The top five plants with the strongest cold resistance are wn-1, wn-3, wn-19, wn-22 and wn-28, and the five plants with the weakest cold resistance include wn-7, wn-25, wn-2, wn-11 and wn-14.

DISCUSSION

The growth and productivity of plants are influenced by biological and abiotic factors. Under the abiotic stress, plants will exhibit a series of morphological, physiological, biochemical and molecular changes; they will also show various adverse symptoms, such as chlorosis, necrosis and slow growth, which will eventually have an adverse impact on plant growth and yield [22, 23]. Low temperature is one of the abiotic factors that affects plants. Due to their different genetic characteristics and natural environments, different plants have different responses to low-temperature stress. One of the reactions of plants to low temperature is the inhibition of photosynthesis. This phenomenon is associated with changes in chloroplast ultrastructure and development as well as changes in the content and composition of photosynthetic pigments. These conditions often lead to leaf chlorosis. As the primary factor regulating the growth and development of *C. oleifera*, illumination plays a decisive role in the yield and quality of plants. Photosynthesis needs to strike a balance between the light energy absorbed by the light collection system and the energy consumed by the plant. Low temperature intensifies the imbalance between the energy source and metabolic pool, resulting in large changes in photosynthesis. As an important photosynthetic organ, leaves are the most sensitive to stress, and their structure and function change differently as the natural environment changes [24-27].

To date, numerous studies have reported the relationship between leaf anatomical structures and cold resistance. According to previous studies, under low temperature stress, the closer the arrangement of plant leaf palisade tissue is, the greater its thickness will be and the stronger the cold resistance of the plant will be. Thus, a thick cuticle is helpful for limiting the penetration of cold into mesophyll tissue

and thereby plays a role in enhancing boundary resistance. Furthermore, the upper and lower epidermis are significantly involved in plant tissue protection and build a barrier between the complex external environment and plant leaf tissue to reduce the damage caused by low temperature [28-30]. Palisade tissue contains chloroplasts, and the number of chloroplasts increases with the increase in cell layers. Additionally, increased palisade tissue can accelerate the transportation of water from the vascular bundle to the epidermis, thereby guaranteeing the supply of photosynthetic raw materials. In this study, leaves with four layers of palisade tissue (wn-1) ranked first in the comprehensive evaluation of cold resistance, which also confirmed the correlation between TP and cold resistance to a certain extent. Furthermore, this study showed that the degrees of cold resistance of the 30 excellent individual plants were consistent with the order of the thicknesses of their upper and lower epidermal layers but differed greatly from the order according to CT. Therefore, the resulting error based on a single index used to evaluate the cold resistance of *C. oleifera* will be large, and comprehensive evaluation based on multiple indices should be performed. CTR, LT and TS serve as the main indices used to evaluate the cold resistance of *Pyrus spp*. [31]. P/S and TS can be used as the main indices to evaluate the cold resistance of *Musa spp*. [16, 32]. Through index analysis, correlation analysis and cluster analysis of the 11 leaf anatomical structural indices, TS, TL, VT and CTR were selected as the typical indices of cold resistance in these plants. TS has been reported to be a typical index in Ma et al.'s study [33], and CTR has been reported to be a typical cold resistance index for *Musa spp.* [32]. However, according to Liu et al. [34], there is no correlation between CTR and SR with cold resistance in *Annonaceae*. Therefore, CTR may only reflect the basic distribution of palisade tissue. Leaf porosity and its proportion may more truly reflect the three-dimensional structure of leaves, and this index may be more reliable as a measurement index of CTR. Nevertheless, further studies in combination with physiological and biochemical indices should be conducted to support this presumption. LT has been proposed as one of the typical indices for the cold resistance of *Michelia* [33-35]. The results of this study were not completely consistent with those of previous studies. In *C. weiningensis*, we found a very significant positive correlation between TU and TL. VPD is the ratio of VT to LT. Lignin is the main component of the plant cell wall, which protects cells and tissues from adverse effects. Lignin content is positively correlated with plant stress resistance [36], while xylem, one component of the leaf veins, contains a large amount of lignin. Therefore, it may be of positive significance to select TL and VT to evaluate *C. weiningensis*. The typical indices in this study were completely consistent with those reported in Zhao et al.'s study on *C. gauchowensis* Chang [37]. Therefore, the selection of typical indices for plant stress resistance may vary according to the plant species, growth environment and development period [38]. The cold resistance of plants is a comprehensive characteristic composed of the interactions of a variety of factors. To avoid using a single morphological index to evaluate cold resistance, it is necessary to carry out a comprehensive analysis of multiple indices.

The membership function is a method based on measuring multiple indices that can comprehensively evaluate certain plant characteristics more accurately. Its operation is convenient and fast, and its results are reliable. This method has been widely used to study the cold resistance of *Cinnamomum camphora*, *Prunus persica*, *Juglans* and other plants [9, 21, 39]. The distribution, size, density, morphology and behavior of stomata in plant leaves are closely related to plant transpiration, as stomata are channels for gas and water exchange and loss. Plants with a higher stomatal density often have poorer cold resistance than plants with a lower stomatal density [40]. However, this study did not involve the observation of leaf stomata, which should be considered in the future. Most of the sugars produced by leaf photosynthesis are stored in various organs. These sugars can protect the cell membrane from low-temperature stress to a certain extent. High concentrations of sugar are likely to promote the vitrification of cell fluid to enhance cold resistance. However, this statement has not been analyzed in *C. oleifera* and thus needs to be further studied [41-44]. In this study, four indices were selected from 11 anatomical structural indices by the membership function method. According to the results, the plants with strong cold resistance were wn-1, wn-3, wn-19, wn-22 and wn-28. The selected excellent individual plants will provide data for the breeding of cold-resistant varieties of *C. oleifera*. Plant cold resistance is the result of many interactions. To further evaluate the cold resistance of *C. weiningensis*, comprehensive analysis in combination with physiological and biochemical indices should be considered in the future.

ACKNOWLEDGEMENTS

This work was supported by National Natural Science Foundation of China (32060331), Science and Technology Plan Project of Guizhou Province of China (Qian Ke He Zhi Cheng [2019]2310), Science and Technology Project of Guizhou Education Department (Qian jiao He KY[2018]097), Cultivation Project of Guizhou University([2019]35) and Research Project of Introducing Talents in Guizhou University([2017]41).

REFERENCES

[1] Li, Q., Guo, Q.Q., Gao, C., Li, H.E. (2020) Characterization of complete chloroplast genome of *Camellia weiningensis* in Weining, Guizhou Province. Acta Horticulturae Sinica. 47(04), 779-787 (in Chinese).

[2] Hu, J., Wu, W., Cao, Z., Wen, J., Shu, Q.L., Fu, S.L. (2016) Morphological, physiological and biochemical responses of *Camellia oleifera* to low-temperature stress. Pakistan J. Bot. 48(3), 899-905.

[3] Dou, T.X. (2013) The evaluation of cold resistance on ten *Camellia oleifera* cultivars. Dissertation. Huazhong Agricultural University. College of Horticulture & Forestry Sciences, Wu Han (In Chinese with an English Abstract).

[4] Wu, L., Li, J., Li, Z., Zhang, F.H., Tan, X.F. (2020). Transcriptomic analyses of *Camellia oleifera* 'Huaxin' leaf reveal candidate genes related to long-term cold stress. International Journal of Molecular Sciences. 21(3), 846.

[5] Miura, K., Furumoto, T. (2013) Cold signaling and cold response in plants. International Journal of Molecular Sciences. 14(3), 5312-5337.

[6] Liu, Y.M., Jin, L., Song, Z.Y. (2019) A study on cold resistance in five Sapotaceae fruit trees. Journal of Fruit Science. 36(2), 195-202.

[7] Meng, Y.Q., Zhang, L.F., Wang, L.H. (2009) Effects of low temperature stress on the cold-resistance physiological indexes of six leaf-colored climbing shrub species. Journal of Anhui Agricultural University. 36(2), 172-177.

[8] Boanares, D., Isaias, R., de Sousa, H.C., Kozovits, A.R. (2018) Strategies of leaf water uptake based on anatomical traits. Plant Biology. 20(5), 848-856.

[9] Wang, N., Yuan, M.L., Su, J.L. (2013) Relationship between leaf structure and cold resistance of several camphor tree species. Journal of Northwest Forestry University. 28(4), 43-49. (in Chinese with an English Abstract).

[10] Lu, Q., Guo, F., Xu, Q., Cang, J. (2020) LncRNA improves cold resistance of winter wheat by interacting with miR398. Functional Plant Biology. 47(6), 544-557.

[11] Huang, Z., Zhang, X., Jiang, S., Qin, M., Zhao, N.,Lang,L., Liu, Y., Tian,Z., Liu, X., Wang, Y., Zhang, B., Xu, A. (2017) Analysis of cold resistance and identification of SSR markers linked to cold resistance genes in *Brassica rapa* L. Breeding Science. 67(3), 213-220.

[12] Li, M.Y., Liu, J.X., Hao, J.N., Feng, K., Duan, A.Q., Yang, Q.Q., Xu, Z.S., Xiong, A.S. (2019) Genomic identification of AP2/ERF transcription factors and functional characterization of two cold resistance-related AP2/ERF genes in celery (*Apium graveolens* L.). Planta. 250(4), 1265-1280.

[13] Chen, J., Yang, X., Huang, X., Duan, S., Long, C., Cheng, J., Rong, J. (2017) Leaf transcriptome analysis of a subtropical evergreen broadleaf plant, wild oil-tea camellia (*Camellia oleifera*), revealing candidate genes for cold acclimation. BMC Genomics. 18(1), 1-14.

[14] Rihan, H.Z., Al-Issawi, M., Fuller, M.P. (2017) Advances in physiological and molecular aspects of plant cold tolerance. Journal of Plant Interactions. 12(1), 143-157.

[15] Zeng, J.L., Deng, Q.E., Li, J.A. (2020) Relationship between leaf anatomic structure and cold tolerance in six *Camellia oleifera* cultivars. Non-wood Forest Research. 38(01), 117-124. (in Chinese with an English Abstract).

[16] Wu, L.L., Li, J., Gu, Y.Y. (2020) Effect of chilling temperature on chlorophyll florescence, leaf anatomical structure, and physiological and biochemical characteristics of two *Camellia oleifera* cultivars. International Journal of Agriculture and Biology. 23(4), 777-785.

[17] Cao, L.Q., Zhong, Q.P., Luo, S., Yuan, T.T., Guo, H.Y., Yan, C., Yuan, Y. (2018) Variation in leaf structure of *Camellia oleifera* under drought stress. Forest Research. Beijing. 31(3), 136-143.

[18] Song, P., Ding, Y., Zhu, G., Han, L.I., Wang, Y. (2019) Evaluation of leaf anatomical structure and drought resistance evaluation of six species of Euonymus. Journal of Henan Agricultural University. 53(04), 574-580.

[19] Cui, G., Ma, C. (2007) Research on leaf morphology and cold resistance of *Alfalfa*. Acta Agrestia Sinica. 1,70-75.

[20] Lee, S.B., Suh, M.C. (2013) Recent advances in cuticular wax biosynthesis and its regulation in Arabidopsis. Molecular Plant. 6(2), 246-249.

[21] Guo, X., Liu, J., Zhai, J., Xiao, X., Lv, Y., Li, D., Pei, S., Zhang, L. (2015) Relationship between eaf anatomical structure and trunk cold resistance of 16 peach cultivars. J. Scientia Silvae Sinicae. 51(8), 33-43 (in Chinese with an English Abstract).

[22] Seki, M., Kamei, A., Yamaguchi-Shinozaki, K., Shinozaki, K. (2003) Molecular responses to drought, salinity and frost: common and different paths for plant protection. Current Opinion in Biotechnology. 14(2), 194-199.

[23] Sanghera, G.S., Wani, S.H., Hussain, W., Singh, N.B. (2011) Engineering cold stress tolerance in crop plants. Current Genomics. 12(1), 30.

[24] England, J.R., Attiwill, P.M. (2006) Changes in leaf morphology and anatomy with tree age and height in the broadleaved evergreen species, *Eucalyptus regnans* F. Muell. Trees. 20(1), 79.

[25] Ensminger, I., Busch, F., Huner, N.P.A. (2006) Photostasis and cold acclimation: sensing low temperature through photosynthesis. Physiologia Plantarum. 126(1), 28-44.

[26] Neuner, G., Bannister, P. (1995) Frost resistance and susceptibility to ice formation during natural hardening in relation to leaf anatomy in three evergreen tree species from New Zealand. Tree Physiology. 15(6), 371-377.
[27] Wu, Y., Yao, X., He, Z. (2021) Research progress of light effects on photosynthesis, growth and development of oil-tea (*Camellia oleifera*). Journal of Zhejiang University (Agriculture and Life Sciences). 47(2), 147-157.
[28] Marin, M., Koko, V., Duletić-Laušević, S., Koko, V. (2008) Micromorphology of trichomes of *Thymus malyi* (Lamiaceae). Journal of Microscopy. 232(3), 406-409.
[29] Bilska-Kos, A., Panek, P., Szulc-Głaz, A., Ochodzki, P., Cislo, A. (2018) Chilling-induced physiological, anatomical and biochemical responses in the leaves of *Miscanthus giganteus* and maize (*Zea mays* L.). Journal of Plant Physiology. 228, 178-188.
[30] Tian, J.H., Wang, H.X., Zhang, Z.H., Gao, Y. (2015) Effects of chilling stress on antioxidant system and ultrastructure of walnut cultivars. Yingyong Shengtai Xuebao. 26(5), 1320-1326.
[31] Wei, J., Zhang, Q., Lin, C.X. (2021) Relationship between cold tolerance and leaf tructure of different pear varieties (Strains). Journal of Henan Agricultural Sciences. 50(08), 103-112. (in Chinese with an English Abstract).
[32] He, H.W., Zhao, M., Wu, P., Long, F., Zou, Y. (2017) Cold resistance evaluation based on leaf anatomy structure of banana. Southwest China Journal of Agricultural Sciences. 30(1), 193-198.
[33] Ma, T., Xiao, L.J., He, N., Xu, T., Li, J., Ning, D.L. (2016) Analysis of anatomical leaf structure and cold resistance of 12 walnut cultivars in Yunnan Province. Guangdong Agricultural Sciences. 43(5), 55-59.
[34] Liu, S.B., Chen, Q., Hu, Z.H. (2004) Study on the relationship between leaf structure and cold resistance of 7 species of *Annonaceae* fruit trees. Journal of Fruit Science. 2004(03), 241-246. (In Chinese with an English abstract).
[35] Li, R.X., Jin, X.L., Hu, X.J., Chai, Y.X., Cai, M.Y., Luo, F., Zhang, F.J. (2017) Analysis and comprehensive evaluation on cold resistance of six varieties of Michelia. Ying yong sheng tai xue bao= The Journal of Applied Ecology. 28(5), 1464-1472.
[36] Zhang, J.B. (2009) The effect of the suddenly-decreased temperature on content of total phenols and lignin in leaves of Poplars. Forestry Sci. Technol. 34(6), 30-31.
[37] Zhao, J.R., Zhu, Z.J., Xiao, S.X. (2021) Study on Drought Resistance of Leaf Anatomical Structure of *Camellia gauchowensis* Chang Clone. Fenzi Zhiwu Yuzhong (Molecular Plant Breeding) (in Chinese with an English abstract).
[38] Li, G.H., Xu, T., Chen, G.Y. (2009) Comparative study on leaf anatomy of 10 varieties of Macadamia. Chinese Journal of Tropical Crops. 30(10), 1437-1441 (in Chinese with an English abstract).
[39] Liu, D., Zhang, B., Sun, H., Peng, S., Zhu, H. (2015) Comprehensive evaluation on cold resistance of early fruiting walnut cultivars. Acta Horticulturae Sinica. 42(3), 545. (In Chinese with an English abstract).
[40] Aasamaa, K., Sõber, A., Rahi, M. (2001) Leaf anatomical characteristics associated with shoot hydraulic conductance, stomatal conductance and stomatal sensitivity to changes of leaf water status in temperate deciduous trees. Functional Plant Biology. 28(8), 765-774.
[41] Shalaev, E.Y., Steponkus, P.L. (2001) Phase behavior and glass transition of 1, 2-dioleoylphosphatidylethanolamine (DOPE) dehydrated in the presence of sucrose. Biochimica et Biophysica Acta (BBA)-Biomembranes. 1514(1), 100-116.
[42] Senula, A., Nagel, M. (2021) Cryopreservation of plant shoot tips of potato, mint, garlic, and shallot using Plant Vitrification Solution 3. Cryopreservation and Freeze-Drying Protocols. Humana, New York, NY. 647-661.
[43] Vozovyk, K., Bobrova, O., Prystalov, A., Shevchenko, N., Kuleshova, L. (2020) Amorphous state stability of plant vitrification solutions. Biologija. 66(1).
[44] Wen, J., Zhang, C., Cao, Z., Wu, W., Hu, J., Shu, Q. (2014) Effects of Cold Stress on Cold Resistance of *Camellia oleifera* Seedling. Hubei Agricultural Sciences. 54(03), 609-612.

Received: **01.12.2021**
Accepted: **23.01.2022**

CORRESPONDING AUTHOR

Chao Gao
Institute for Forest Resources and Environment of Guizhou,
Key Laboratory of Forest Cultivation in Plateau Mountain of Guizhou Province,
College of Forestry,
Guizhou University,
Guiyang 550025 – China

e-mail: gaochao@gzu.edu.cn

© by PSP Volume 31– No. 05/2022 pages 5124-5131 Fresenius Environmental Bulletin

EVALUATION OF ECOLOGICAL RESTORATION EFFECT OF MARINE OIL SPILL POLLUTION BASED ON TM REMOTE SENSING

Jingjing Sha[1,2], Juan Li[1,2], Xiaoyu Li[1,2], Xiao Niu[3], Yaoru Li[1,2], Guoyi Wen[1,2], Xiaolin Zeng[1,2], Jimin Zhang[1,2,*]

[1]North China Sea Environmental Monitoring Center, State Oceanic Administration, Qingdao, Shandong 266033, China
[2]Key Laboratory of Ecological Prewarning and Protection of Bohai Sea, Ministry of Natural Resources, Qingdao, Shandong 266033, China
[3]School of Life Sciences, Tsinghua University, Beijing 100085, China

ABSTRACT

Marine oil spill pollution is one of the most serious marine ecological disasters. The current evaluation method of ecological restoration effect of marine oil spill pollution, has poor calculation ability of oil film thickness and image recognition ability of pollution area, resulting in a large number of abnormal evaluation results. In this study, the TM remote sensing is introduced into the evaluation method of ecological restoration effect of marine oil spill pollution. The TM remote sensing images are classified according to the image texture features and Bayesian classification method to determine the treatment area of marine oil spill. The nonlinear function of oil spill analysis is constructed by interpolation method combined with the radiation value of remote sensing sensor to determine the oil film thickness. The ecological restoration effect evaluation index is selected, and the remote sensing image data is substituted into it to construct the ecological restoration effect evaluation model of marine oil spill pollution. The experimental results show that the calculation ability of oil film thickness and the image recognition ability of pollution area of TM remote sensing method are better than the current method, and more accurate results can be obtained by using this method.

KEYWORDS:
TM remote sensing, marine oil spill, pollution, ecological restoration, evaluation, disaster

INTRODUCTION

With the rapid growth of energy demand for industrial development, the offshore oil exploitation industry and the offshore oil transportation industry have developed rapidly. Although modern technology provides more advanced technology for offshore oil exploitation, transportation and storage, there will still be marine oil spill accidents [1, 2]. A large number of coastal industries gather along the coast, the intensity of marine development and utilization is increasing, and the marine ecological environment is also facing unprecedented pressure. In particular, the exploitation of marine oil resources, coastal petrochemical industry, marine oil transportation and other industries are growing rapidly, which further increases the ecological environment risk [3-5]. The demand for oil and its products is growing, and the oil industry is more and more closely connected with the sea. Oil spills may occur in offshore oil exploitation, offshore oil transportation, port oil loading, unloading and storage and coastal oil product processing, resulting in marine oil pollution. In recent years, oil pollution accidents have occurred frequently, such as Tasman Helen oil spill and the grounding of Atigo oil tanker, especially the oil spill of ConocoPhillips drilling platform in 2011, resulting in a large number of crude oil leakage, serious economic losses and marine ecological damage [6-9]. Over the years, peoples are actively exploring and studying the fine detection method of oil spill pollution, and remote sensing oil spill detection technology is one of the research hotspots.

Currently, marine oil spill is mainly dominated by sea surface oil spill. The technology development that can be used for remote sensing detection of oil spill on the sea surface is relatively perfect. The multiple detection of oil film on the sea surface is mainly realized by carrying different types of sensors on aerial remote sensing platform, satellite remote sensing platform, and ship/sea-based/shore-based remote sensing platform [10-12]. The remote sensing platform includes the following: (1) aerial remote sensing: aerial remote sensing has the advantages of fast response, flexible mobility, high resolution, high timeliness, real-time image transmission, etc., which is the most widely used and the most effective technical means in oil spill accident monitoring [13,14]. (2) Satellite remote sensing: compared with aerial remote sensing, satellite remote sensing has the characteristics of large monitoring range, low cost, not affected by dangerous areas, and easy processing and interpretation of graphic data. It is a widely used oil spill remote sensing detection method [15]. (3)

Ship/sea-based/shore-based remote sensing: effective on-line monitoring of oil spills in high risk areas can be achieved by using sensors such as video and radar on shore-based/sea-based remote sensing platforms, which is an important technical supplement to aerial remote sensing and satellite remote sensing oil spill detection [16]. The sensors that can be used for oil spill detection on the sea surface include microwave sensors, optical sensors, laser sensors and laser-acoustic sensors.

After oil enters the ocean, it uses the driving force of wind to cause the oil film to spread greatly, forming a large area of marine pollution area and destroying the marine ecosystem. Due to the great harm of marine oil spill pollution, marine oil spill and marine pollution have become the hot issues in the marine field. According to the results of literature research, oil pollution is more harmful to the marine environment and marine resources. When marine oil spills occur, oil spills usually exist in three forms: oil film, adherents and dispersed solutes [17]. It has certain toxic effects on marine organisms and endangers marine ecosystems. In view of such a serious situation of marine oil spill pollution, systematic ecological restoration work has been carried out to alleviate the impact of oil pollution on the marine environment. Ecological restoration technology has the advantages of low cost and quick effect, and has been widely used in oil spill pollution area [18]. In the past few decades, a large number of experts and scholars have proposed a variety of ecological restoration effect evaluation methods, and there are a lot of problems when they are applied to the marine environment. For example, an evaluation method based on bird communities as reference was put forward to verify the resilience of ecological environment, but this method has low adaptability to marine pollution and poor application effect. An evaluation system of marine ecological environment governance was established based on the community of marine destiny [19, 20].

In this study, TM remote sensing technology is used to optimize the current evaluation method of ecological restoration effect. After the design is completed, the corresponding experimental links are constructed to analyze the recognition effect of marine pollution area, the calculation error of oil film thickness, the results of standardized index processing and adaptability of evaluation model. The experimental results show that the evaluation reliability of TM remote sensing method is high. At the same time, this technology can effectively improve the recognition ability of marine oil pollution areas, provide more reference data for the evaluation of ecological governance effect, promote the process of marine oil spill pollution control, and provide new technologies for marine oil spill pollution control.

MATERIALS AND METHODS

In this study, TM remote sensing technology is used as the core technology to design a new evaluation method of ecological restoration effect of marine oil spill pollution [21, 22]. A marine oil spill pollution area is selected as the research object, and the specific pollution area is shown in Figure 1. At the same time, the polluted area after treatment is drawn in the same image. Two commonly used evaluation methods and TM remote sensing evaluation method are selected to analyze the ecological restoration effect of the target sea area, and the experimental comparison process is completed. In order to make the experimental results more specific, the corresponding comparative indexes will be set in this experiment to analyze the difference between the TM remote sensing evaluation method and the current method.

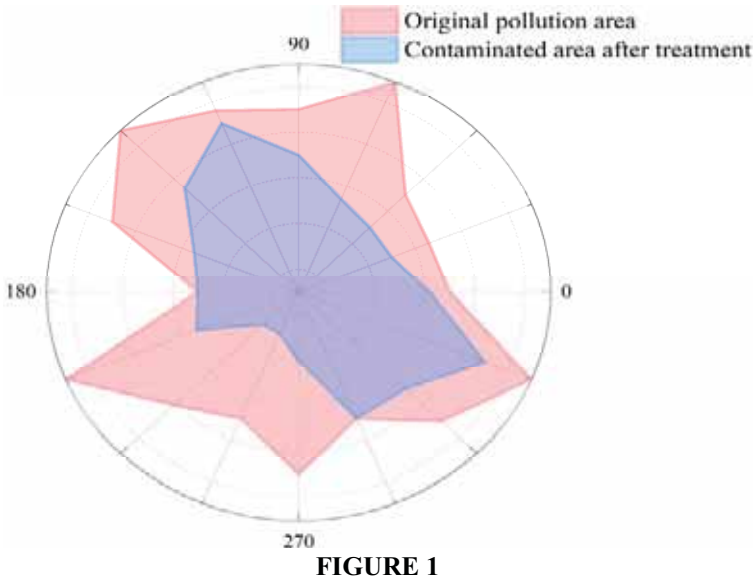

FIGURE 1
Pollution area of target sea area

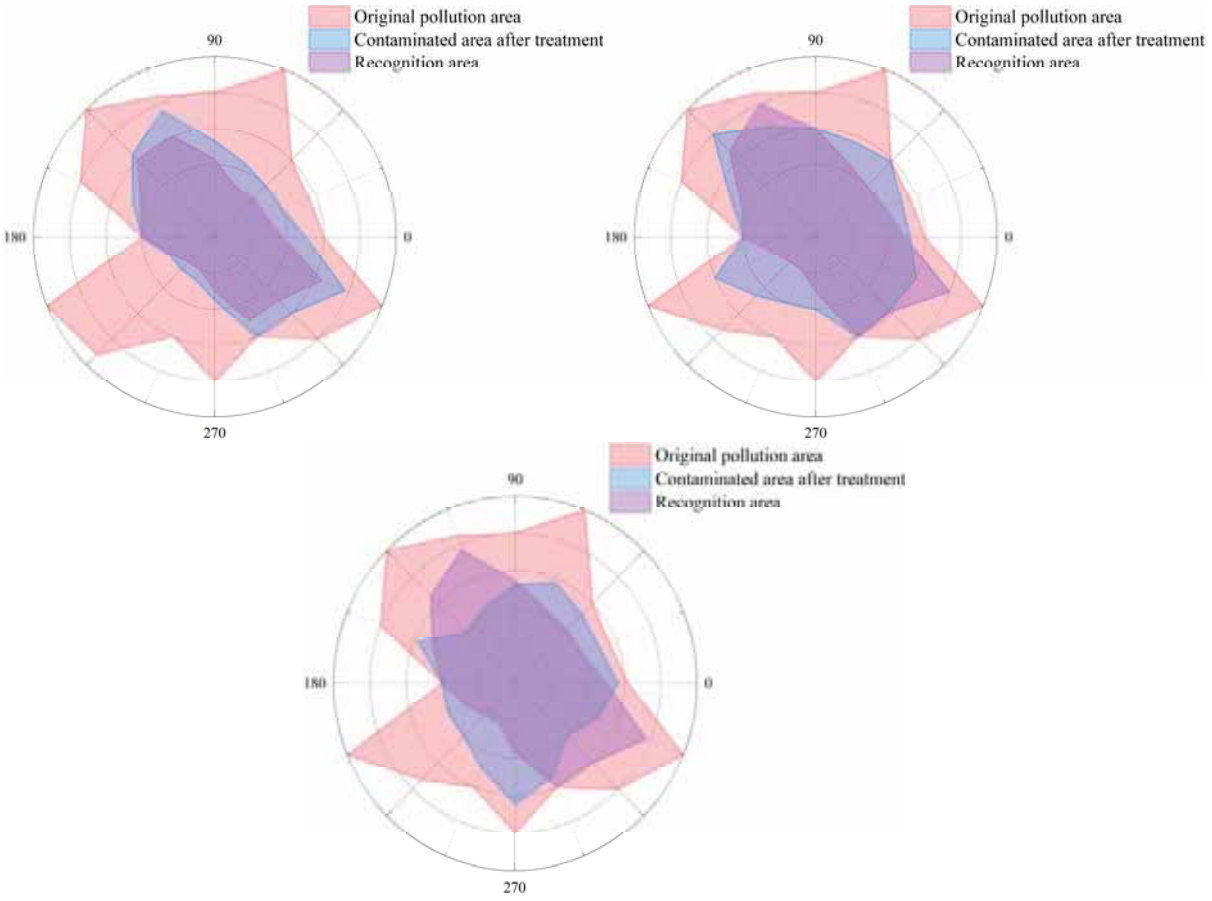

FIGURE 2
Recognition results of marine pollution area (TM remote sensing, method 1 and 2)

The extraction of oil spill information at sea is based on the characteristics of oil spill, using corresponding processing methods for different remote sensing data, excluding interference factors on satellite images, and extracting oil spill information [23-27]. The general processing methods are as follows: (1) Preprocessing remote sensing data to eliminate the influence of image geometric deformation and other factors. (2) The image information is enhanced by linear stretching and filtering to prepare for the interpretation and extraction of oil spill information. The seawater covered with oil film is quite different from ordinary seawater in texture. Oil spill information is extracted according to the texture characteristics and visual interpretation methods of oil spill, and the location of oil spill is determined and the corresponding area is calculated.

RESULTS AND DISCUSSION

Result of marine pollution area recognition effect. From the analysis of the image in Figure 2, it can be seen that the recognition result of TM remote sensing method for marine pollution area is close to the real area, and the authenticity of the evaluation result can be ensured by using this image. Compared with the TM remote sensing method, the image recognition effect of the current method is larger, and using this image for evaluation will cause the problem of abnormal evaluation results. Through literature research, it can be seen that the accuracy of image recognition has a direct relationship with the reliability of evaluation results. Therefore, TM remote sensing method is more reliable [28, 29].

Calculation error of oil film thickness. It can be seen from Table 1 that in the process of many experiments, the calculation error of TM remote sensing method is significantly lower than that of the current method. In the calculation process of oil film thickness, the calculation error of current method fluctuates greatly. According to this result, the data ability and reservoir recognition ability of the current method are poor, and this calculation result has a bad impact on the use of the evaluation method. In the follow-up research, the calculation part of the current method should be optimized. The marine oil spill information extraction module is set in the TM remote sensing method, which improves the application effect of the evaluation method and the calculation ability of the TM remote sensing method to a certain extent. The analysis of the above experimental results shows that the TM remote sensing method is better.

TABLE 1
Calculation error of oil film thickness

Number of experiments	TM remote sensing/cm	Method 1/cm	Method 2/cm
1	0.20	0.41	0.46
2	0.21	0.41	0.54
3	0.20	0.43	0.46
4	0.21	0.41	0.41
5	0.20	0.44	0.43
6	0.20	0.42	0.51
7	0.21	0.42	0.44
8	0.20	0.42	0.45
9	0.21	0.43	0.48
10	0.21	0.45	0.55

TABLE 2
Results of index standardization and adaptability of evaluation model

Number of experiments	TM remote sensing/%	Method 1/%	Method 2/%
1	86.12	84.21	84.15
2	85.24	83.68	82.24
3	86.95	82.11	80.51
4	85.81	83.26	81.93
5	86.74	82.53	80.06
6	85.74	84.83	81.35
7	85.01	84.17	82.66
8	85.25	84.05	84.73
9	85.24	82.94	83.85
10	86.63	82.39	83.31

Index standardization and adaptability of evaluation model. From the experimental results in Table 2, it can be seen that after the standardized processing of the index data, the method in the experiment has improved its adaptability to the evaluation model, but there are still subtle differences. The adaptability of TM remote sensing method and evaluation model is obviously higher than that of current methods. According to the experimental results, it can be determined that the index selection result of TM remote sensing method is more systematic and scientific. The above experimental results are summarized to determine that the use effect of TM remote sensing method is better [30]. In this experiment, three groups of experimental indexes are selected to analyze the application effect of TM remote sensing method in the current method. According to the experimental results, TM remote sensing method has better evaluation ability, and can obtain more accurate evaluation results.

Principal component analysis of TM image. Image principal component analysis (PCA) is a multi-dimensional orthogonal linear transformation based on statistical features. Through the transformation, the correlation between the original images can be eliminated, that is, the useful information of the original bands can be concentrated in the new variable-principal component image, so as to achieve the purpose of information extraction and compression. Table 3 is the statistical table of principal component analysis of TM image in a marine oil spill area.

Among the seven principal components obtained by principal component analysis, PC1 is brightness information, which reflects the contribution of each band to brightness value. TM_{+1} and TM_{+2} have the greatest contribution to PC1. The corresponding TM_{+2} and TM_{+4} bands of PC2 are the positive weight value (0.719%) and the negative weight value (-0.50%), respectively. It mainly reflects the red light absorption and near-infrared reflection of oil spill in the ocean, which is a photometric information. PC3 is the darkness information, which reflects the degree of refraction and induction of TM_{+} bands on the optical fiber of oil spill in the ocean. TM_{+3} and TM_{+4} contribute greatly to it. PC4 corresponding to TM_{+1} and TM_{+2} bands are negative weight (-0.74%) and positive weight (0.53%) respectively, which indicates that PC4 has a certain relationship with the absorption and reflection of oil spill in visible light. Therefore, it can be seen from the principal component that PC2 can be used as an important indicator of marine oil spill ecological restoration. The color transformation enhancement processing of image principal components can obtain effective anomalous hue information in the ocean. In addition, feature image principal component analysis method can be used, such as selecting TM_1, TM_2, TM_3 and TM_4 bands for feature KL transformation to obtain images with enhanced oil spill information, and selecting TM_1, TM_4, TM_5 and TM_6 bands for transformation to obtain images with enhanced

emulsion oil spill. Another method is to feature preprocessing of TM band, such as the ratio, then the image principal component analysis is carried out to enhance the required information such as marine oil spill pollution restoration.

Reflection spectral curve of marine oil spill. In this study, based on the analysis of the marine oil spill reflection spectrum curve, and it is sincere that each oil spill pollution area is affected. Therefore, the relevant information is extracted by looking at the special reflection peak of the reflection spectrum and calculating the index value related to the oil spill pollution area [31, 32]. These characteristic values include: maximum reflectance of green light, position of red absorption peak, maximum reflectance of near-infrared, greenness index, water effect index, etc. In order to make the size relationship of eigenvalues clear, the data is generated into the following histogram and line chart. Figure 3(a) is a comparison of the maximum reflectance of green light in some marine oil spill pollution areas. Figure 3(b) shows the positions of red light absorption peaks in the spectra of several marine oil spill pollution areas, usually between 0.68m-0.375m, from which we can see whether the waveform is blue shifted or not. When the oil spill part in the ocean is large, "red peak" will shift to the direction of wavelength increase, which is called "red shift". When the oil spill area decreases and "loses green" due to the ecological modification action, the "red peak" will move to the short wavelength, which is called "blue shift".

Figure 4 is the size of the seawater effect index in each observation, and its value is related to the degree of oil spill pollution, which can determine the repair of oil spill pollution. The results show that the larger the seawater effect index is, the better the ecological restoration effect of oil spill pollution is. As can be seen from the data, for block 1, the reflectivity of position D1 is the largest; for block 2, the reflectivity of position D2-D4 is higher than that of position D1. Whether block 1 or block 2, from the position of red light absorption peak, the position D2-D4 is less than the position D1, that is, the red light absorption peak is left, and the waveform appears blue shift. From Figure 4, block 2 has an effective restoration of marine oil spill pollution compared with block 1, and the location D3 in block 2 has the best restoration effect.

CONCLUSIONS

(1) TM remote sensing method for marine pollution area recognition results are close to the real area, using this image can ensure the authenticity of the evaluation results. In addition, the accuracy of image recognition has a direct relationship with the reliability of the evaluation results.The evaluation reliability of TM remote sensing method is higher.

TABLE 3
Statistical table of principal component analysis of TM image in a marine oil spill area

Band	PC1	PC2	PC3	PC4	PC5	PC6
Characteristic value	1022	216.8	95.53	10.88	9.404	2.257
Contribution rate /%	75.30	15.97	7.039	0.802	0.693	0.190
$TM+_1$	0.516	-0.286	-0.307	-0.743	-0.067	0.011
$TM+_2$	0.724	0.263	-0.333	0.525	0.145	-0.014
$TM+_3$	0.252	0.711	0.546	-0.312	-0.154	0.106
$TM+_4$	0.308	-0.498	0.455	0.274	-0.562	0.274
$TM+_5$	0.194	-0.207	0.418	0.006	0.270	-0.820
$TM+_6$	0.120	-0.228	0.339	-0.029	0.750	0.506

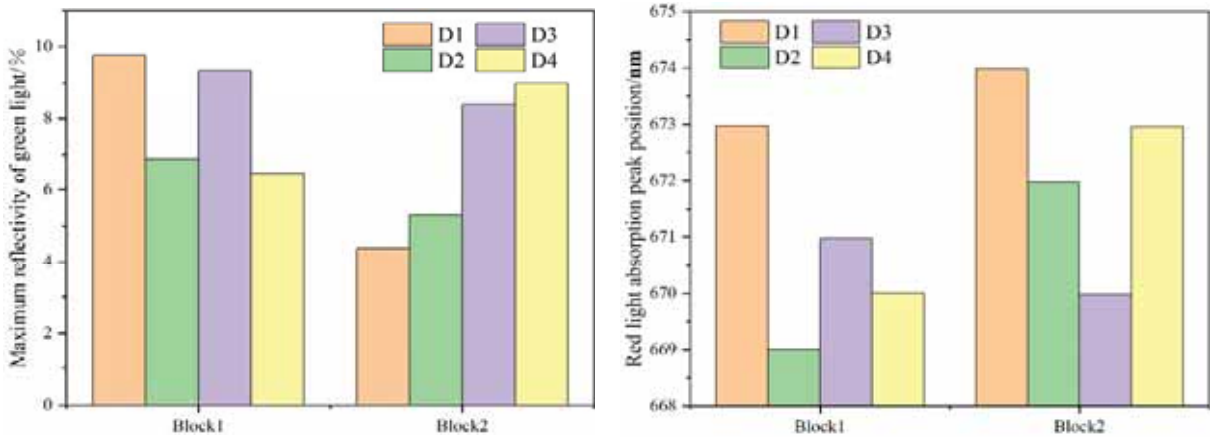

FIGURE 3
Maximum reflectance of green light and position of red light absorption peak in blocks

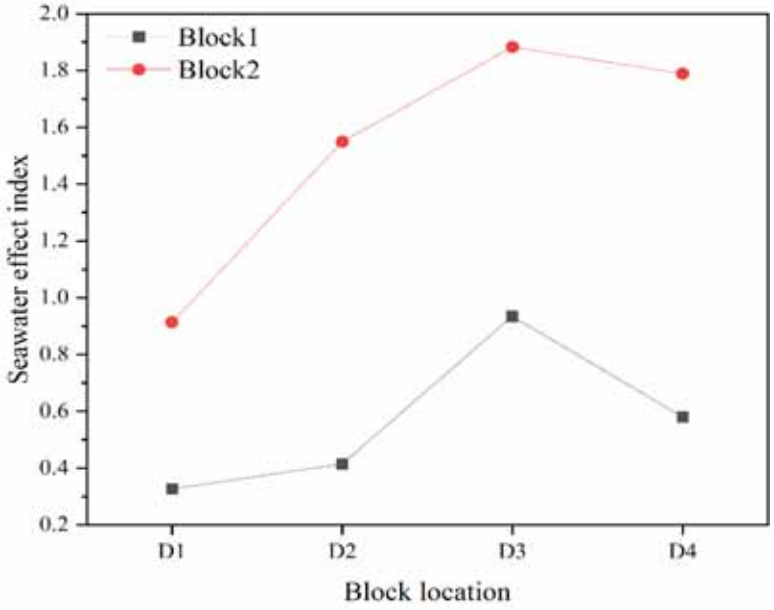

FIGURE 4
Seawater effect index in different blocks

(2) In the process of many experiments, the calculation error of TM remote sensing method is obviously lower than that of current methods. In the calculation process of oil film thickness, the calculation error of current method fluctuates greatly. The marine oil spill information extraction module is set in the TM remote sensing method, which improves the application effect of the evaluation method and the calculation ability of the TM remote sensing method to a certain extent. The use of TM remote sensing method is better.

(3) After the standardized processing of the index data, the method in the experiment has improved its adaptability to the evaluation model. The adaptability of TM remote sensing method and evaluation model is obviously higher than that of current methods. The results show that the index selection results of TM remote sensing method are more systematic and scientific.

ACKNOWLEDGEMENTS

This work was supported by Key Special Program on Marine Environmental Security Protection of National Research and Development Project of China (No. 2016YFC1402305).

REFERENCES

[1] Yan, Z.Y., Wang, J.Q., San, B., Fu, H.R., Ren, J. (2020) Assessment of oil spill damage to the sustainable carrying capacity of natural fisheries based on information entropy. Marine Sciences. 44(5), 71-75.

[2] Tong, Y.B., Deng, Z.G., Jiang, X.Y. (2020) Assessing the marine ecological risk of oil spill in Bohai Sea by oil spill model and SSD curve method. Marine Science Bulletin. 39(3), 390-400.

[3] Ning, J.L., Chen, Z.L., Wang, C.Y., Xie, W.J. (2018) Analysis of marine oil spill pollution monitoring based on satellite remote sensing technology. Materials Science and Engineering. 392(4), 4204-4215.

[4] Alexandrov, C., Kolev, N., Sivkov, Y., Hristov, A., Tsvetkov, M. (2020, June). Oil Spills Detection on Sea Surface by using Sentinel-1 SAR Images. Electrical Apparatus & Technologies. 32(6), 211-224

[5] Xu, L., Li, J., Brenning, A. (2014) A comparative study of different classification techniques for marine oil spill identification using RADARSAT-1 imagery. Remote Sensing of Environment. 14(1), 14-23.

[6] Han, Z.Z. (2015) Research progress of multi-sensor remote sensing detection technology for marine oil spill. Safety, Health and Environment. 11(15), 144-157.

[7] Ning, J.L., Chen, Z.L., Wang, C.Y., Xie, W.J. (2018) Analysis of marine oil spill pollution monitoring based on satellite remote sensing technology. Materials Science and Engineering. 392(4), 2045-2056.

[8] Song, W., Liu, S., Tong, X., Niu, C., Ye, Z., Jin, Y. (2021) Combined Geometric Positioning and Performance Analysis of Multi-Resolution Optical Imageries from Satellite and Aerial Platforms Based on Weighted RFM Bundle Adjustment. Remote Sensing. 13(4), 620-630.

[9] Fingas, M., Brown, C. (2014) Review of oil spill remote sensing. Marine Pollution Bulletin. 83(1), 9-23.

[10] Rajendran, S., Vethamony, P., Sadooni, F.N., Al-Kuwari, H.A.S., Al-Khayat, J.A., Seegobin, V.O., Nasir, S. (2021) Detection of Wakashio oil spill off Mauritius using Sentinel-1 and 2 data: Capability of sensors, image transformation methods and mapping. Environmental Pollution. 274(5), 1661-1668.
[11] Li, X., Xu, H., Zhang, F., Suo, A. (2018) Monitoring and Assessment of the Space Pattern of Ports Based on GF-1 Satellite Remote-Sensing Images. Pattern Recognition in Remote Sensing. 121(8), 241-247.
[12] Sun, M., Xie, J., Ji, Z., Cai, W. (2015) Remote sensing of ocean surface wind direction with shipborne high frequency surface wave radar. IEEE. 21(5), 39-44.
[13] Roberto, C., Chiara, M., Maria, C.R. (2019) Cadmium stress effects indicating marine pollution in different species of sea urchin employed as environmental bioindicators. Cell Stress and Chaperones. 24(4), 675-687.
[14] Leng, Y.B., Zhang, H. (2019) Assessment of Ecological Restoration Effect of Shenzhen River Phase IV Project Based on Bird Biodiversity. Water Power. 45(5), 221-227.
[15] Zhang, W.B., Zhu, Y.Q. (2020) Construction of Global Marine Environmental Governance System from the Perspective of a Maritime Community with a Shared Future. Pacific Journal. 28(5), 92-104.
[16] Rydgren, K., Auestad, I., Hamre, L.N., Hagen, D., Rosef, L., Skjerdal, G. (2016) Long-term persistence of seeded grass species: an unwanted side effect of ecological restoration. Environmental Science & Pollution Research. 23(14), 13591-13597.
[17] Lu, Y., Liu, J., Ding, J., Shi, J., Chen, J., Ye, X. (2019) Optical remote identification of spilled oils from the SANCHI oil tanker collision in the East China Sea. Science Bulletin. 64(31), 3213-3222.
[18] Ning, J.L., Chen, Z.L., Wang, C.Y., Xie, W.J. (2018) Analysis of marine oil spill pollution monitoring based on satellite remote sensing technology. Materials Science and Engineering. 392(4), 1204-1215.
[19] Fan, J., Zhang, F., Zhao, D., Wang, J. (2015) Oil spill monitoring based on SAR remote sensing imagery. Aquatic Procedia. 22(3), 112-118.
[20] Fu, Y.H., Li, Q.Y., Zhang, B.R. (2018) Marine oil spill spectral analysis and satellite information extraction. Journal of Remote Sensing. 12(6), 1010-1016.
[21] Yang, Y.J., Huang, Y., Tian, Q.J., Wang, L., Yang, R.R. (2015) The extraction model of paddy rice information based on gf-1 satellite wfv images. Spectroscopy & Spectral Analysis. 35(11), 3255-3266.
[22] Maiti, S.K., Maiti, D. (2015) Ecological restoration of waste dumps by topsoil blanketing, coir-matting and seeding with grass-legume mixture. Ecological Engineering. 77(4), 74-84.
[23] Chen, P., Fan, K.G., Gu, Y.Z., Xu, K. (2015) One operational visual method for oil spill detection by SAR image. Applied Mechanics & Materials. 74(2), 208-211.
[24] Sghaier, M.O., Foucher, S., Lepage, R. (2016) River extraction from high-resolution sar images combining a structural feature set and mathematical morphology. Applied Earth Observations & Remote Sensing. 156(9), 311-324.
[25] Wei, M., Qiao, B., Zhao, J., Zuo, X. (2019) The area extraction of winter wheat in mixed planting area based on sentinel-2 a remote sensing satellite images. International Journal of Parallel Emergent and Distributed Systems. 26(1), 1-12.
[26] Zou, Y.R., Lin, M.S., Ma, T.B., Zhu, H.T., Chen, G.M. (2017) Analysis of SAR oil spill texture characteristics based on GLCM. Ocean Bulletin. 29(4), 455-458.
[27] Chen, H., Xie, T., Fang, H., Meng, L., Zhao, L., Ai, R.B. (2019) Sea surface oil spill identification method based on sar polarization ratio and texture features. Acta Oceanologica Sinica. 41(9), 181-190.
[28] Gai, Y., Zhou, B., Sun, Y., Zhou, Y., Li, W. (2013) Study on extraction methods of ocean surface oil spill using HJ-CCD data. Environment and Transportation Engineering. 203(6), 756-759.
[29] Sajid, Z., Khan, F., Veitch, B. (2020) Dynamic ecological risk modelling of hydrocarbon release scenarios in arctic waters. Marine Pollution Bulletin. 153(12), 1001-1009.
[30] Liu, P., Li, X., Qu, J.J., Wang, W., Zhao, C., Pichel, W. (2011) Oil spill detection with fully polarimetric UAVSAR data. Marine Pollution Bulletin. 62(12), 2611-2618.
[31] Karaouzas, I., Smeti, E., Ourka, A., Vardakas, L., Mentzafou, A., Tornes, T. (2018) Assessing the ecological effects of water stress and pollution in a temporary river - implications for water management. Science of the Total Environment. 618(3), 1591-1604.
[32] Greening, H., Swann, R., Testroet-Bergeron, S., Allen, R., Alderson, M. (2018) Local implementation of a national program: the national estuary program response following the deep water horizon oil spill in the gulf of Mexico. Marine Policy. 87(1), 60-64.

Received: **02.12.2021**
Accepted: **23.01.2022**

CORRESPONDING AUTHOR

Jimin Zhang
North China Sea Environmental Monitoring Center,
State Oceanic Administration,
Qingdao, Shandong 266033 – China

e-mail: phnwsn@163.com

© by PSP Volume 31– No. 05/2022 pages 5132-5143 Fresenius Environmental Bulletin

EXPERIMENTAL RESEARCH AND ROAD PERFORMANCE ANALYSIS OF CONSTRUCTION WASTE RECYCLED MIXTURE

Suling Xue[1], Mei Zeng[2], Hui Sun[3,*]

[1]School of Civil Engineering, Jiaozuo University, Jiaozuo Henan 454000, China
[2]Department of Civil Engineering, Henan College of Industry & Information Technology, Jiaozuo Henan 454000, China
[3]School of Civil Engineering, Henan Polytechnic University, Jiaozuo Henan 454000, China

ABSTRACT

With the acceleration of the urbanization process in China, there are more and more demolition and renovation projects, and construction waste is also constantly produced. At the same time, the demand for sand and gravel materials in construction projects continues to increase. The resulting environmental damage and shortage of resources have caused great distress to people. If the construction waste is recycled and made into renewable materials, it can not only protect the environment, but also save construction materials and reduce project costs, which is of great significance to increase economic benefits and the sustainable development of various projects. This paper conducts research on the application of construction waste recycled materials in road engineering by way of experimental research. We study the influence of the content of glue and concrete particles on the mechanical properties of recycled aggregate inorganic mixtures, and determine the mix ratio that meets the requirements of the specification. In addition, we study the impact of debris content and concrete particle content on the road performance of recycled aggregate graded gravel. The results of the study show that: in combination with the actual project, when the cement content is 4% and the concrete particle content is 25%, the unconfined compressive strength of the water-stable mixture can meet the requirements of various pavement subbases. Increasing the cement content can achieve better High mechanical properties. The unconfined compressive strength of lime and fly ash stabilized mixtures with lime content of 6%, fly ash content of 14%, and concrete particle content of 25% can meet the requirements of various pavement subbases. Increasing the amount of fly ash can obtain higher mechanical properties. In this paper, the load-bearing ratio CBR of all recycled aggregate graded crushed stones tested in this paper is between 169% and 242%, which all meet the requirements of current specifications.

KEYWORDS:
Recycled aggregate, inorganic mixture, mechanical properties, frost resistance, graded crushed stone, strength prediction

INTRODUCTION

Recycling construction waste is an important link in the entire building life cycle, and it plays an important role in completing construction site resource conservation and energy reduction. After entering the 21st century, the development of construction waste processing technology has become a bottleneck, and the awareness of environmental protection in various countries has been continuously strengthened [1]. The investment in construction waste recycling technology has also increased in various countries around the world. China is strengthening research on material recycling. Developed countries such as Japan and the United States have conducted large-scale systematic research on the reuse of construction waste and conducted a comprehensive analysis [2]. Relying on strategic advantages, through formulating and improving national standards, we improve advanced technology, industry integration, and the development of related supporting industries to promote the integrated utilization of construction waste recycling resources [3].

China's research on the recycling of construction waste resources has just begun. The recycling and reuse of waste concrete has not attracted enough attention, but some scientific research institutions focusing on this field are conducting research and implementing targeted recycling and reuse. The physical and chemical properties of the aggregate are used for preliminary theoretical research [4-5]. The main research focuses on various performance indicators, such as compressive strength, apparent density, elastic modulus and related performance indicators of high-performance recycled concrete. Du Tinggou improves the surface of aggregates by using high-activity ultra-fine mineral mixture mortar and applies high-performance impermeable waterproof gold powder evenly on the surface of the particles, thereby improving the shortcomings of high water

absorption and many cracks of concrete recycled materials. Wu Bo suggested that after adding a certain amount of fly ash, the abrasion resistance of concrete recycled materials should be improved [6-7].

Some scholars believe that when 0.55 water ash is used, the compressive strength of recycled concrete during each curing period is lower than that of concrete without recycled materials. Although the 90d compressive strength is the lowest, it can still reach 91.5% of the concrete strength without added recycled aggregates [8-10]. Other scholars analyzed the changes in technical performance of cement stabilized crushed stone mixed with waste brick aggregate. In the test, 20%, 40%, 80% and 100% of brick aggregates were used instead of coarse aggregates and fine aggregates to prepare two sets of aggregates [11-12]. After adding 5% cement dosage to prepare specimens and test samples, the seven-day unconfined compressive strength, splitting strength, resilience modulus, shrinkage performance and frost resistance are measured. At the same time, the road performance of different grades of construction waste as the road foundation was studied. The results show that construction waste can be used as the foundation or subbase material of sidewalks, and a method of applying construction waste to the road base or subbase has been proposed [13-15].

Through research, it is found that the current recycling of construction waste recycled materials is mainly used as coarse aggregate instead of natural gravel, and construction waste has a large content of fine aggregate magazines, the processing process is not easy to screen, and the technology is not perfect, resulting in low strength. It cannot be guaranteed to have good performance in actual applications [16-17]. This paper mainly adopts the experiment of inorganic mixture (road base material) to study the influence of cementing material content and concrete particle content on its mechanical properties and study the effects content of debris and concrete particles on the bearing capacity, thereby effectively improving the application effect of recycled aggregate in road construction.

MATERIALS AND METHODS

(1) Experimental materials. The cement used in the test of this paper is composite slag Portland cement with strength number 32.5, and the lime used is the lime of Yida Mining Company (effective calcium content 73.5%, effective magnesium content 2.1%). The fly ash used in the experiment of this thesis is Grade I fly ash of Jintaicheng Building Materials Company (density 2.57 g/cm^3, water demand ratio of 93%, strength index of 91%). The recycled coarse aggregate used in the experiment of this paper comes from the recycled aggregate of Beijing Gaoqiang Road Concrete Co., Ltd. The main performance indicators and particle gradation of coarse aggregate are shown in Table 1. The recycled fine aggregate used comes from the recycled fine aggregate of Beijing Gaoqiang Road Concrete Co., Ltd. The main performance indexes and particle gradation of fine aggregate are shown in Table 2.

(2) Experiment method. 1) Material performance. The test is carried out in accordance with the requirements of the standard GB/T 14685-2001 "Pebbles and Crushed Stones for Construction", GB/T 17431.1-2010 "Lightweight Aggregates and Test Methods", and JTGE42-2005 "Highway Engineering Aggregate Test Regulations" [18-19].

2) Compaction test. The test was carried out in accordance with the requirements of JTGE51-2009 "Highway Engineering Inorganic Binder Stabilization Material Test Regulations". The test method is to use a 4.5kg hammer to hit the sample, the hammer hitting distance is 30cm.

3) Mechanical properties. The test and the production of test pieces are carried out in accordance with the standard JTGE51-2009 "Test Regulations for Inorganic Binder Stabilized Materials for Highway Engineering" [20-21].

RESULTS

(1) The influence of cement content on the performance of inorganic mixture. The experimental design of the experimental proportioning scheme is shown in Table 3.

TABLE 3
Experimental design

Mix ratio	Cement (%)	Aggregate grading
C-031	4	4:4:2
C-032	5	4:4:2
C-033	6	4:4:2
C-034	7	4:4:2
C-035	8	4:4:2

TABLE 1
Main performance indexes of coarse aggregate

Particle size(mm)	Crush index (%)	Bulk density (kg/m^3)	Apparent density (kg/m^3)	24h Water absorption (%)	Concrete content (%)
5~10	23	1213	2488	12.2	23
10~25	24	1303	2487	11.6	26

TABLE 2
Main performance indexes of coarse aggregate

Particle size (mm)	Fineness modulus	Bulk density (kg/m^3)	Apparent density(kg/m^3)	24h Water absorption (%)
0-5	2.6	1537	2457	11.8

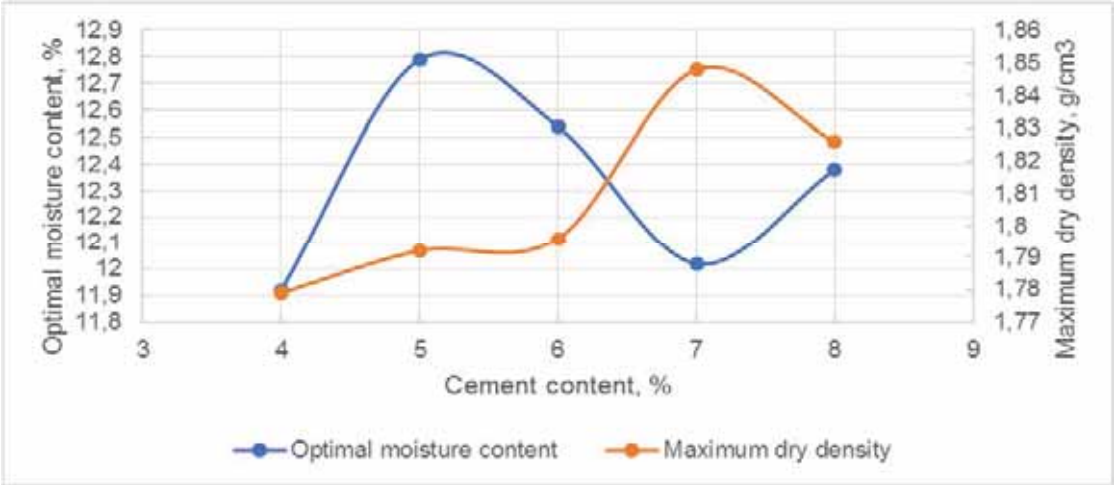

FIGURE 1
Relationship between maximum dry density, optimal moisture content and cement content.

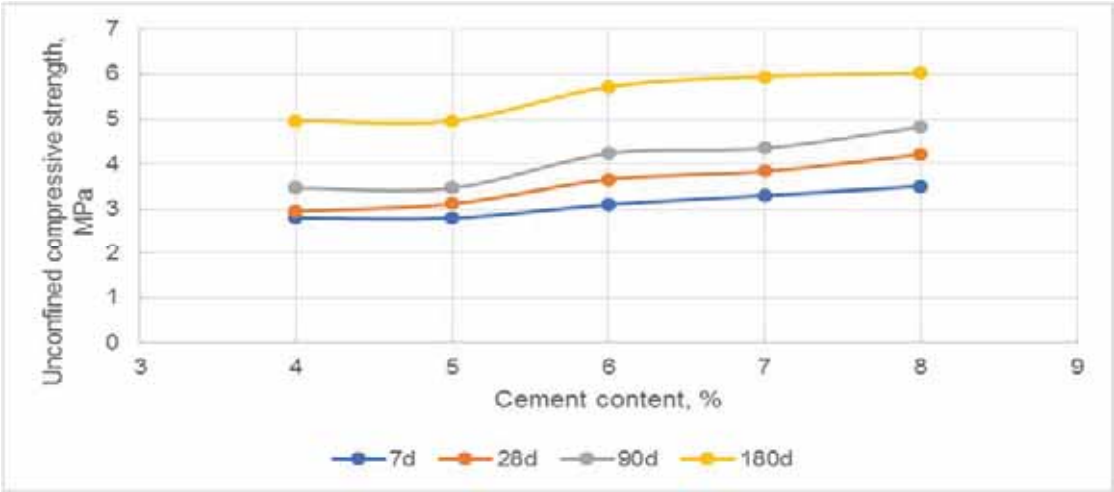

FIGURE 2
Relationship between unconfined compressive strength and cement content.

According to the data in Figure 1, it can be seen that as the cement content increases, the maximum dry density will increase. The optimal moisture content does not change with the cement content, but between 11.92-12.79% fluctuation. With the continuous increase of the cement content, the total amount of powder in the specimen is continuously increasing, which can better fill the gap between the aggregate particles, so that the compactness of the specimen is improved, and the maximum dry density continues to increase. When the cement content reaches 8%, the maximum dry density decreases. The analysis may be due to the fact that when the powder content in the test piece increases, it will occupy more volume, so that the aggregate particles become less, and the total mass becomes smaller, making the maximum dry density decreases.

According to Figure 2, when the cement content is 4%, the 7d unconfined compressive strength is 2.8MPa, the 28d strength is 2.95MPa, the 90d strength is 3.46MPa, and the 180d strength is 4.96MPa. When the cement content is 5 %, 7d unconfined compressive strength is 2.8MPa, 28d strength is 3.12MPa, 90d strength is 3.46MPa, and 180d strength is 4.96MPa. When cement content is 6%, 7d unconfined compressive strength is 3.1MPa, 28d strength is 3.65MPa, 90d strength is 4.23MPa, and 180d strength is 5.72MPa. When cement content is 7%, 7d unconfined compressive strength is 3.3MPa, 28d strength is 3.83MPa, 90d strength is 4.35MPa, and 180d strength is 5.95MPa.

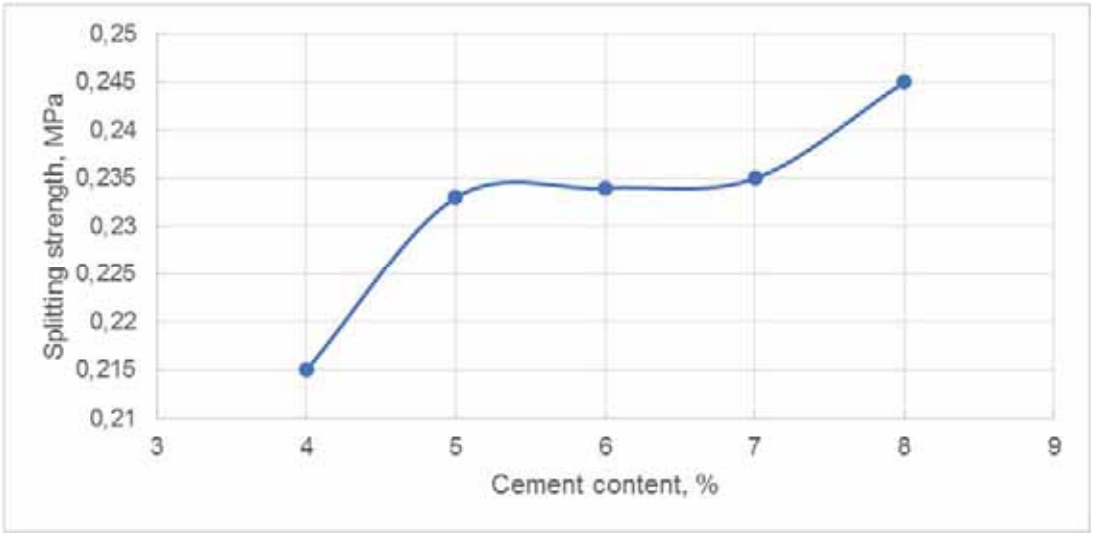

FIGURE 3
The relationship between splitting strength and cement content.

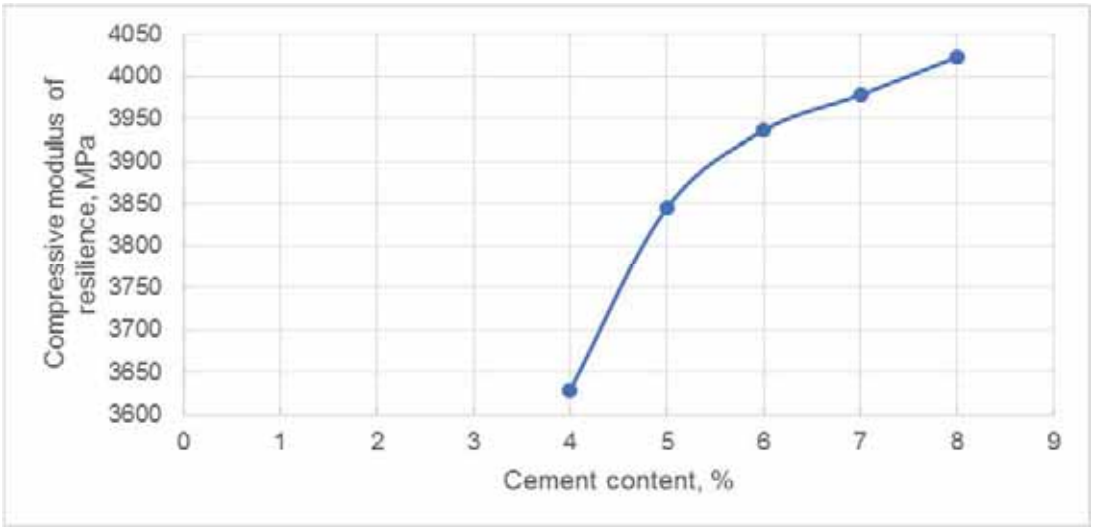

FIGURE 4
The relationship between compressive elastic modulus and cement content.

When the cement content is 8%, the 7d unconfined compressive strength is 3.5MPa, the 28d strength is 4.21MPa, the 90d strength is 4.82MPa, and the 180d strength is 6.03MPa. With the increase of cement content, the unconfined compressive strength increases. When the curing time is 7 days, the maximum gap between the various ratios is 0.7 MPa, and the gap between the ratios will increase with the increase of age. When the curing time is 180 days, the maximum gap between the various ratios is 1.26MPa. By comparing the curves of maximum dry density and unconfined compressive strength, it can be seen that the growth trend of unconfined compressive strength and maximum dry density is not completely consistent. When the cement content is 8%, the maximum dry density is lower than the value when the cement content is 7%. When the cement content is 8%, the unconfined compressive strength is the highest among the various test ratios. The reason could be that the strength effect provided by cement hydration is better than the strength provided by compaction.

According to Figure 3, it can be seen that when the cement content is 4%, the splitting strength is 0.215MPa. When the cement content is 5%, the splitting strength is 0.233MPa. When the cement content is 6%, the splitting strength is 0.234MPa. When the cement content is 7%, the splitting strength is 0.235MPa. When the cement content is 8%, the splitting strength is 0.245MPa. The maximum difference of splitting strength is 0.03MPa. With the increase of cement content, the splitting strength of specimens increases, and the effect of cement content on splitting strength is small.

According to Figure 4, it can be seen that when the cement content is 4%, the compressive resilience modulus is 3629MPa. When the cement content is 5%, the compressive resilience modulus is 3845MPa. When the cement content is 6%, the compressive

elastic modulus is 3936MPa. When the cement content is 7%, the compressive elastic modulus is 3978MPa. When the cement content is 8%, the compressive elastic modulus is 4023MPa. The value of the modulus of resilience of cement stabilized inorganic mixture is 3629MPa-4023MPa, and the maximum difference is 394MPa. Compared with ordinary aggregate inorganic mixture, the compressive resilience modulus of recycled aggregate inorganic mixture is obviously lower, which is beneficial to reduce the rigidity of the pavement base layer and improve the flexibility of the roadbed.

(2) Influence of lime and fly ash content on the performance of inorganic mixture. In order to explore the influence of lime and fly ash content on inorganic mixtures, related experiments were carried out in the modification of the base ratio of lime and fly ash content. The experiment design is shown in the Table 4.

According to Figure 5, it can be seen that when the lime content is 4%, the maximum dry density is 1.805g/cm^3. When the lime content is 5%, the maximum dry density is 1.769g/cm^3. When the lime content is 6%, the maximum dry density is 1.785g/cm^3. When the lime content is 7%, the maximum dry density is 1.747g/cm^3. When the lime content increases by 1%, the maximum dry density decrease is 0.038g/cm^3, but when the lime content is between 4% and 5%, there is a period of increase, and the increase rate is 0.016g/cm^3. Among them, when the lime content is 4%, the maximum dry density value is the largest. It can be seen that the maximum dry density decreases as the lime content increases. The optimal moisture content increases with the increase of lime content. With the increase of lime content, the water demand of the inorganic mixture increases, and the optimal moisture content increases correspondingly.

According to Figure 6, when the lime content is 4%, the 7d unconfined compressive strength is 2.25MPa, the 28d strength is 2.5MPa, the 90d strength is 3.05MPa, and the 180d strength is 3.4MPa. When the lime content is 5 %, 7d unconfined compressive strength is 2.25MPa, 28d strength is 2.6MPa, 90d strength is 3.1MPa, 180d strength is 3.7MPa. When lime content is 6%, 7d unconfined compressive strength is 2.46MPa, 28d strength is 2.7MPa, 90d strength is 3.15MPa, 180d strength is 3.85MPa. When lime content is 7%, 7d unconfined compressive strength is 2.32MPa, 28d strength is 2.95MPa, 90d strength is 3.39MPa, 180d strength is 3.95MPa.

With the increase of lime content, the unconfined compressive strength increases. When the curing time is 7 days, the maximum gap between the various ratios is 0.21 MPa, and the gap between the ratios will increase with the increase of age. When the curing time is 180 days, the maximum gap between the various ratios is 0.55MPa. When the content of lime increases and the content of fly ash decreases, the effect of improving the unconfined compressive strength is smaller than that of increasing the cement content, and the increase in the later strength is smaller than that of the water-stable type.

TABLE 4
Proportion of lime-ash stabilized inorganic mixture

Mix ratio	Lime (%)	Fly ash (%)	Aggregate grading
F-031	4	16	4:4:2
F-032	5	15	4:4:2
F-033	6	14	4:4:2
F-034	7	13	4:4:2

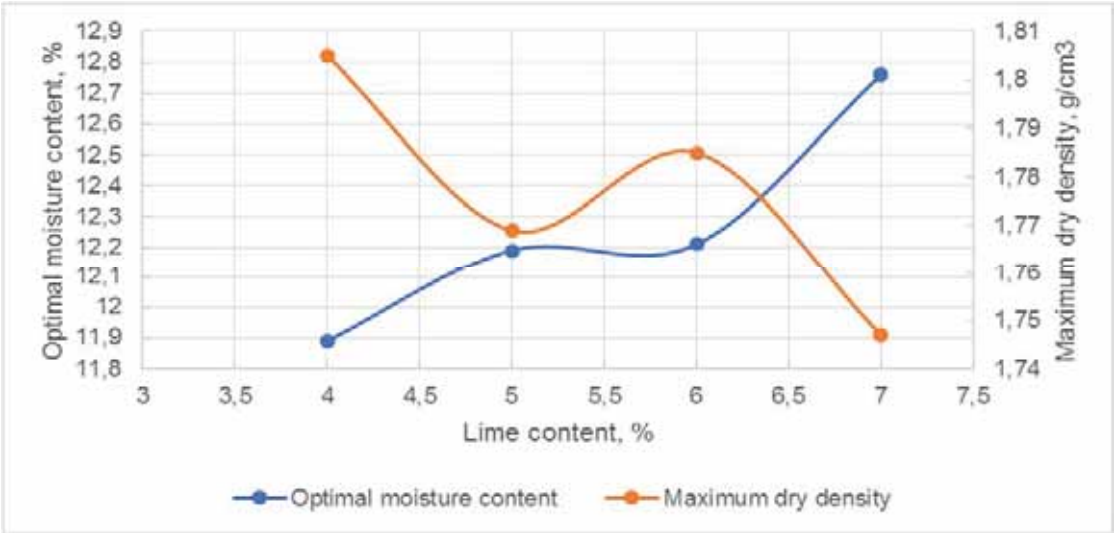

FIGURE 5
Relationship between maximum dry density, optimal moisture content and lime content.

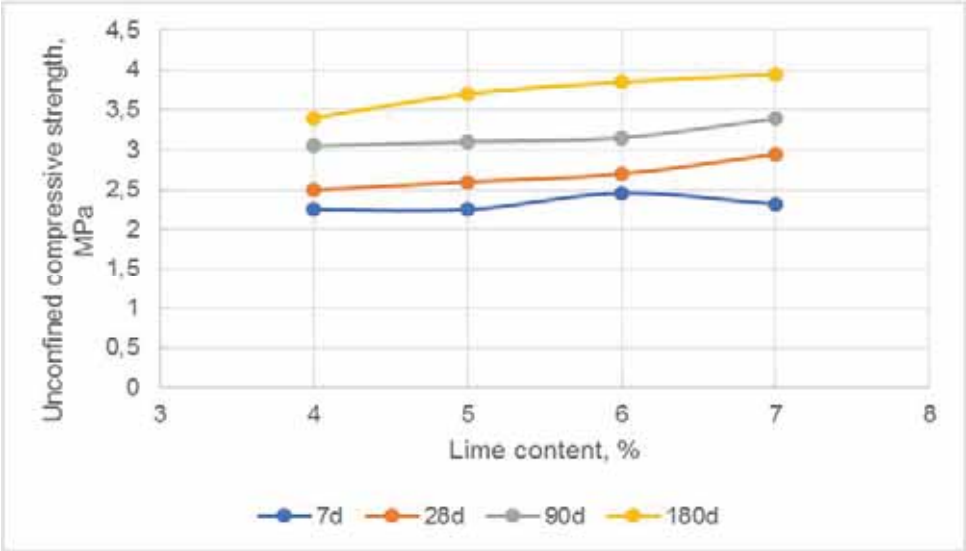

FIGURE 6
Relationship between unconfined compressive strength and lime content.

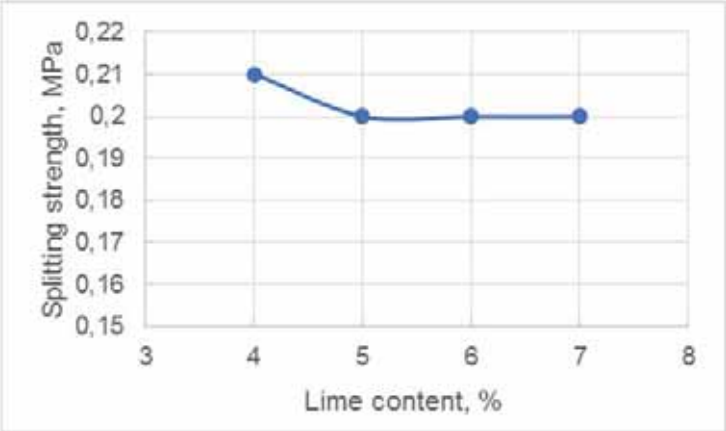

FIGURE 7
Relationship between splitting strength and lime content.

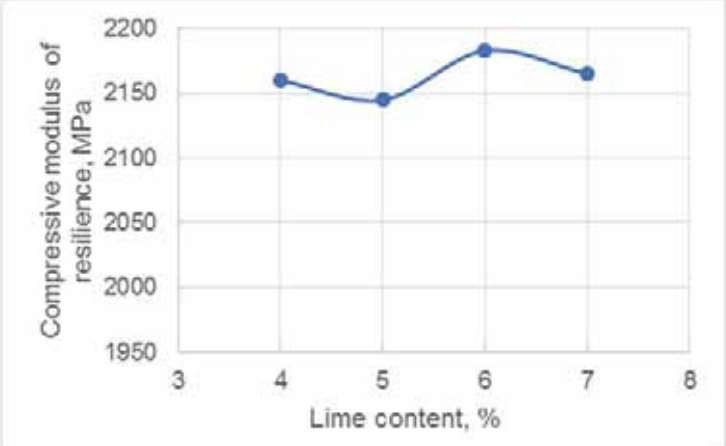

FIGURE 8
The relationship between compressive resilience modulus and lime content.

According to Figure 7, it can be seen that when the lime content is 4%, the splitting strength is 0.2 MPa. When the lime content is 5%, the splitting strength is 0.9 MPa. When the lime content is 6%, the splitting strength is 0.19MPa. When the lime content is 7%, the splitting strength is 0.19MPa. The maximum difference in splitting strength is 0.01MPa. With the increase of lime content, the splitting strength of the specimen decreases, and the influence of lime content on the splitting strength is small.

According to Figure 8 it can be seen that when the lime content is 4%, the compressive resilience modulus is 2160MPa. When the lime content is 5%, the compressive resilience modulus is 2145MPa. When the lime content is 6%, the compressive elastic modulus is 2183MPa. When the lime content is 7%, the compressive elastic modulus is 2165MPa. The resilience modulus of the lime-ash stabilized inorganic mixture is 2141MPa-2186MPa, and the maximum difference is 45MPa. The effect of changing the amount of lime on the resilience modulus is smaller than that of changing the amount of cement. Compared with ordinary aggregate inorganic mixtures, recycled aggregate inorganic mixtures have significantly lower compressive resilience modulus, which is beneficial to reduce the rigidity of the pavement base layer and improve the flexibility of the roadbed.

(3) Influence of concrete particle content on the performance of inorganic mixture. During the test, it was found that the recycled aggregate contains concrete particles, and the content of concrete particles is relatively high at about 25%. To explore the impact of concrete particles on the inorganic mixture, we increase the content of concrete particles on the basis of the cement content of 5%. The experimental design table is shown in Table 5.

According to Figure 9, it can be seen that when the concrete particle content is 25%, the maximum dry density is 1.779g/cm^3. When the concrete particle content is 40%, the maximum dry density is 1.872 g/cm^3. when the concrete particle content is 50%, the maximum dry density is 1.879g/cm^3. When the concrete particle content is 60%, the maximum dry density is 1.893g/cm^3, and when the concrete particle content is 60%, the maximum dry density value is the largest. The maximum dry density will increase with the increase of concrete particles. When 15% concrete particle content is increased on the basis of the original 25% concrete particle content, the maximum dry density increases by 0.093g/cm^3, and when 10% concrete particles are added, the maximum dry density increases again by 0.007 g/cm^3. When the concrete particles are increased by 10%, the maximum dry density will increase by 0.014 g/cm^3. The maximum dry density of the inorganic mixture will increase with the increase of the concrete particle content, but the increase will decrease with the increase of the concrete particle content. After the concrete particle content reaches 40%, the effect of increasing the concrete particle content on the maximum dry density becomes weaker and weaker.

TABLE 5
Proportion of concrete particle content change

Mix ratio	Cement (%)	Concrete particle content (%)	Aggregate grading
H-01	5	25	4:4:2
H-02	5	40	4:4:2
H-03	5	50	4:4:2
H-04	5	60	4:4:2

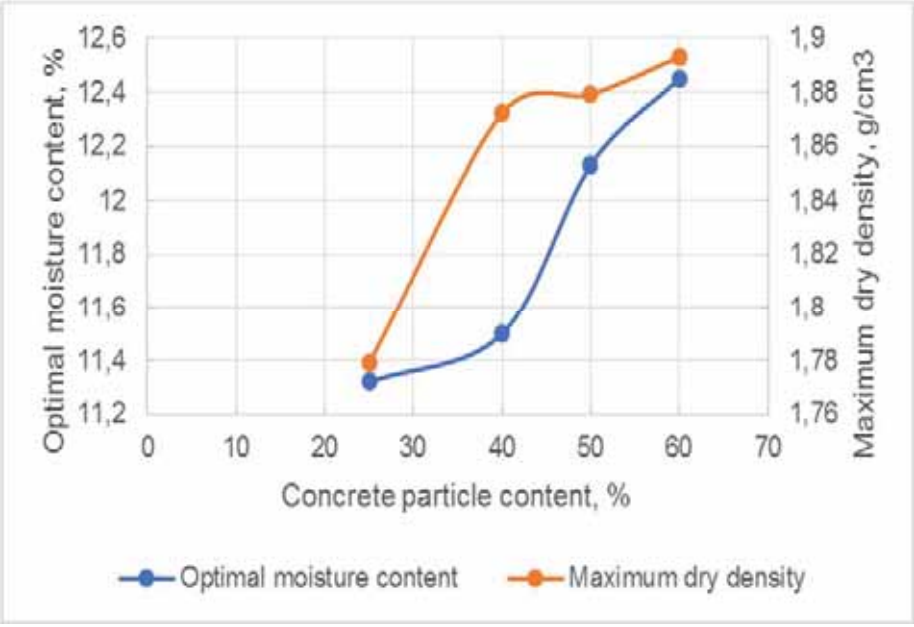

FIGURE 9
The relationship between maximum dry density, optimal moisture content and concrete particle content.

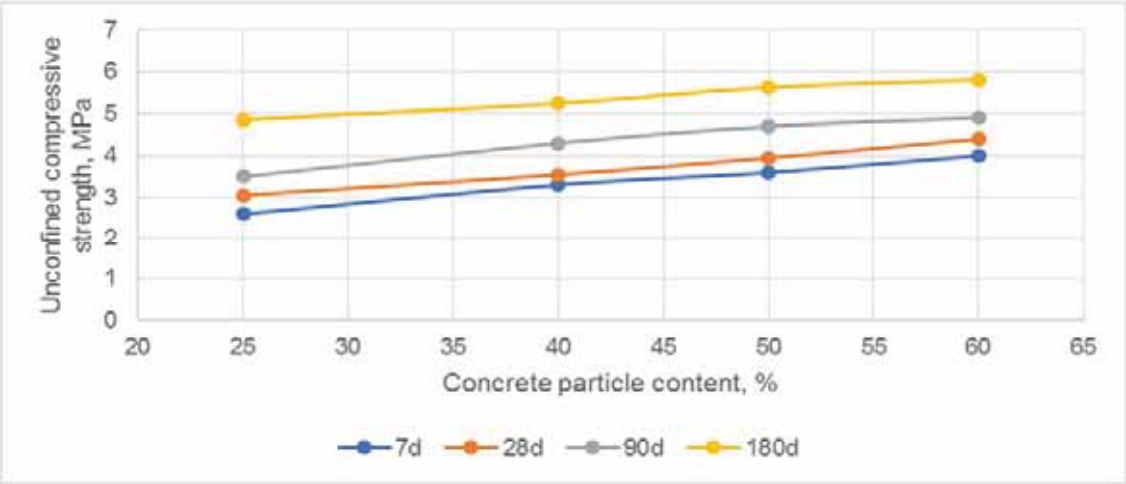

FIGURE 10
The relationship between unconfined compressive strength and concrete particle content.

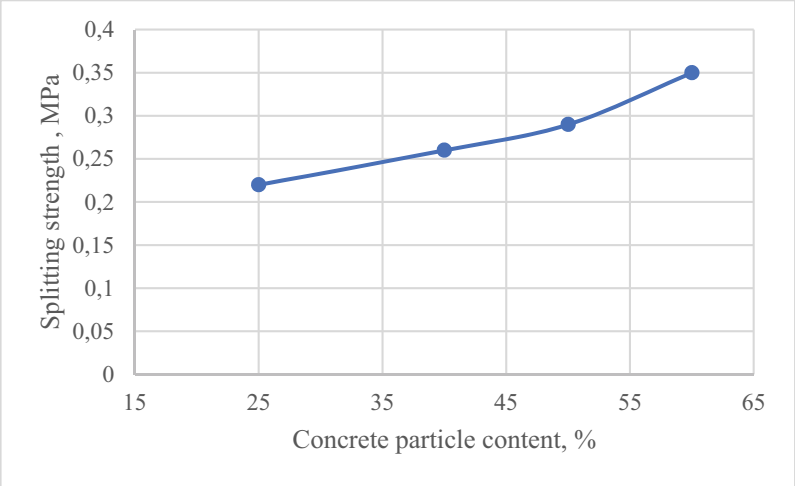

FIGURE 11
The relationship between splitting strength and concrete particle content.

According to Figure 10, when the concrete particle content is 25%, the 7d unconfined compressive strength is 2.6MPa, the 28d strength is 3.05MPa, the 90d strength is 3.5MPa, and the 180d strength is 4.85MPa. When the concrete particle content is 40%, the 7d unconfined compressive strength is 3.3MPa, the 28d strength is 3.55MPa, the 90d strength is 4.3MPa, and the 180d strength is 5.25MPa. When the concrete particle content is 50%, the 7d unconfined compressive strength is 3.6MPa, 28d strength is 3.95MPa, 90d strength is 4.7MPa, 180d strength is 5.63MPa. When concrete particle content is 60%, 7d unconfined compressive strength is 4MPa, 28d strength is 4.4MPa, 90d strength is 4.9MPa, 180d strength is 5.81MPa. When the curing time is 7d, the maximum gap between the various proportions is 1.4MPa. By comparing the graphs of the maximum dry density and unconfined compressive strength, it can be seen that the unconfined compressive strength and the maximum dry density increase in the same trend. With the increase of concrete particle content, the unconfined compressive strength of the inorganic mixture increases accordingly.

According to Figure 11, it can be seen that when the content of concrete particles is 25%, the splitting strength is 0.22MPa. When the content of concrete particles is 40%, the splitting strength is 0.26MPa. When the content of concrete particles is 50%, the splitting strength is 0.29MPa. When the concrete particle content is 60%, the splitting strength is 0.35MPa. The maximum difference in splitting strength is 0.13MPa. As the content of concrete particles increases, the splitting strength increases.

According to Figure 12, it can be seen that when the concrete particle content is 25%, the compressive elastic modulus is 3824MPa. When the concrete particle content is 40%, the compressive elastic modulus is 3963MPa. When the concrete particle content is 50%, the compressive elastic modulus is 4023MPa. When the concrete particle content is 60%, the compressive elastic modulus is 4095MPa. After increasing the content of concrete particles, the value of the rebound modulus of the cement stabilized inorganic mixture is 3824MPa-4095MPa, and the maximum difference is 271MPa. After increasing

the concrete particle content, the compressive resilience modulus will increase accordingly. Compared with ordinary aggregate inorganic mixtures, recycled aggregate inorganic mixtures have a significantly lower compressive resilience modulus, which is beneficial to reduce the rigidity of the pavement base layer and improve the flexibility of the roadbed.

(4) Road performance research. Recycled aggregates have good performance as pavement base materials. In order to make full use of recycled aggregates, consider using recycled aggregates as road base granular materials. In order to explore whether recycled aggregates can be used as roadbed aggregate materials, the compaction test of graded crushed stone and the CBR test of load-bearing ratio were carried out using recycled aggregates to verify the feasibility of its use as roadbed aggregate materials. In this paper, the main factors affecting the performance of graded crushed stone, concrete particle content and debris content are selected as variables to carry out research. The experimental design is shown in Table 6.

According to Figure 13, it can be seen that the maximum dry density value of J-01 is 1.785g/cm^3, the maximum dry density value of J-02 is 1.854g/cm^3, the maximum dry density value of J-03 is 1.889g/cm^3, the maximum dry density value of J-04 is 1.798g/cm^3, the maximum dry density value of J-05 is 1.776g/cm^3, and the maximum dry density value of J-06 is 1.781g/cm^3.

The maximum dry density value of graded crushed stone will increase significantly with the increase of concrete particle content. The density of concrete itself is much greater than that of bricks, which makes the maximum dry density increase significantly. The sundries will reduce the maximum dry density of graded crushed stone. Since most of the sundries are mainly rubber, wood chips, plastic and glass, the density of these sundries is low, which reduces the maximum dry density of graded crushed stone.

According to Figure 14, it can be seen that the load-bearing ratio value of J-01 is 186%, the load-bearing ratio value of J-02 is 217%, the load-bearing ratio value of J-03 is 242%, the load-bearing ratio value of J-04 is 209%, the load-bearing ratio value of J-05 is 175%, and the load-bearing ratio value of J-06 is 169%.

The load-bearing ratio value of graded crushed stone will increase with the increase of concrete particles. This trend is the same as the maximum dry density. The load-bearing ratio is related to the compactness of the specimen. The larger the maximum dry density, the greater the load-bearing ratio. The content of debris will reduce the load-bearing ratio value of the graded crushed stone. In the case of debris, the specimens are cured by soaking in water. Some debris will absorb water and expand, causing cracks in the specimens and reducing the compactness, which makes the load-bearing ratio drops.

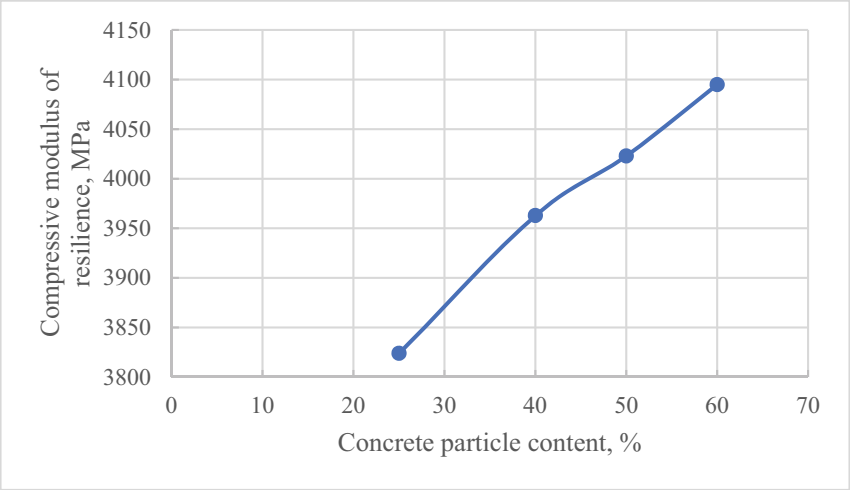

FIGURE 12
The relationship between compressive elastic modulus and concrete particle content.

TABLE 6
Test ratio of graded crushed stone

Mix ratio	Sundries content (%)	Concrete particle content (%)	Aggregate grading
J-01	0.5	25	4:4:2
J-02	0.5	35	4:4:2
J-03	0.5	45	4:4:2
J-04	0	25	4:4:2
J-05	1	25	4:4:2
J-06	1.5	25	4:4:2

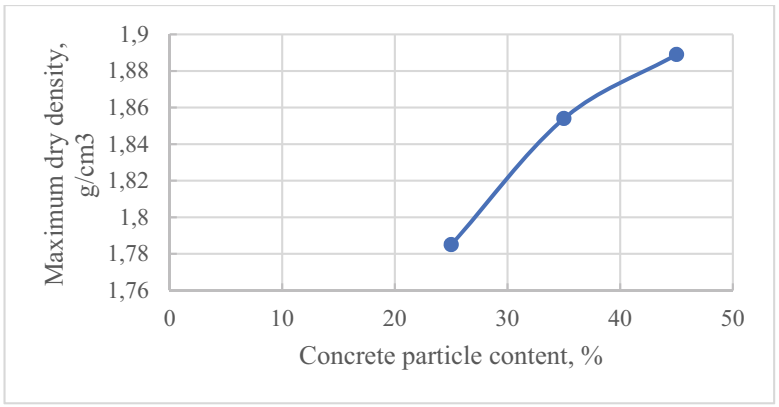

(a)

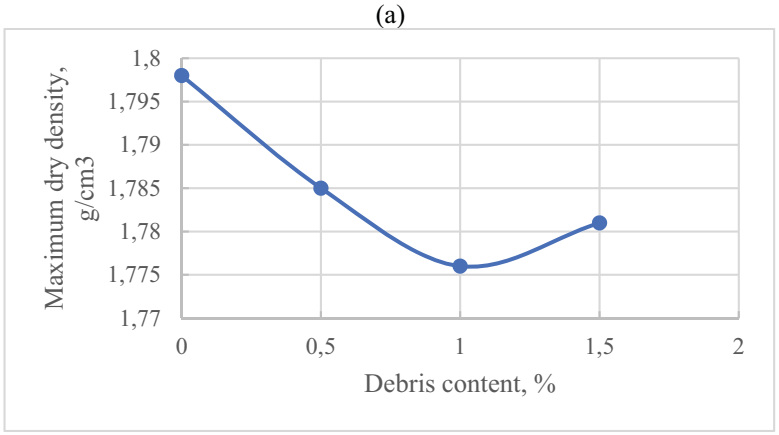

(b)

FIGURE 13

The relationship between maximum dry density and concrete particle content and debris content.

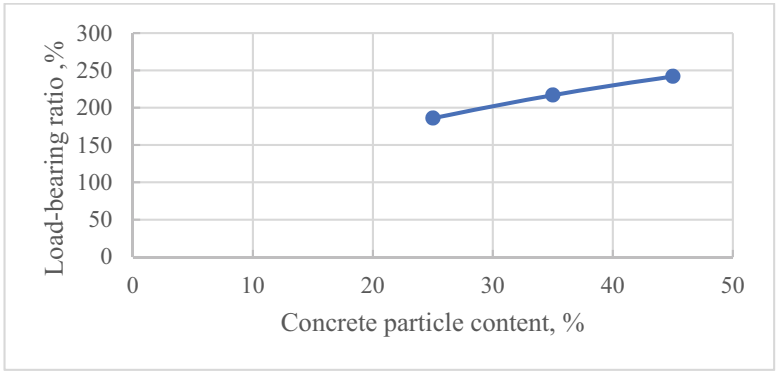

(a)

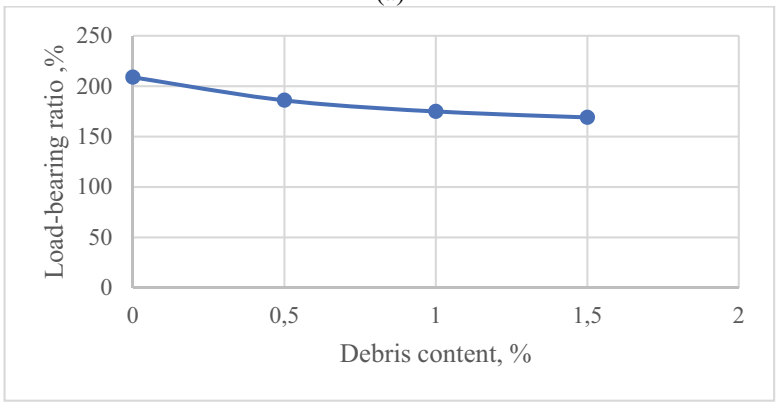

(b)

FIGURE 14

The relationship between maximum dry density and concrete particle content and debris content.

CONCLUSIONS

(1) With the increase of cement content, the maximum dry density of inorganic mixture increases. The optimal moisture content has no correlation with the change of cement content. With the increase of cement content, the maximum dry density can reach 1.848g/cm^3. The optimal moisture content value is between 11.92-12.79%. With the increase of cement content, the unconfined compressive strength increases. When the curing time is 7 days, the maximum gap between the various ratios is 0.7 MPa, and the gap between the ratios will increase as the age increases. With the increase of cement content, the splitting strength of the specimens also increases. The maximum difference of splitting strength is 0.03MPa, and the effect of cement content on splitting strength is small. The modulus of resilience of cement stabilized inorganic mixture is 3629MPa-4011MPa, and the maximum difference is 394MPa. Compared with ordinary aggregate inorganic mixtures, recycled aggregate inorganic mixtures have a significantly lower compressive resilience modulus, which is beneficial to reduce the rigidity of the pavement base layer and improve the flexibility of the roadbed.

(2) With the increase of lime content, the maximum dry density of the inorganic mixture decreases. With the increase of lime content, the optimal moisture content increases. With the increase of lime content, the maximum dry density is the largest, which can reach 1.803g/cm^3. The optimal water content is between 11.89-12.76% and the unconfined compressive strength increases with the increase of lime content. When the curing time is 7 days, the maximum gap between the various ratios is 0.21 MPa, and the gap between the ratios will increase as the age increases. When the content of lime increases and the content of fly ash decreases, the effect of improving the unconfined compressive strength is smaller than that of increasing the cement content, and the increase in the later strength is smaller than that of the cement stabilizer. With the increase of the lime content, the splitting strength of the specimens decreases, and the lime content has little effect on the splitting strength. The value of resilience modulus of lime-ash stabilized inorganic mixture is 2145MPa-2183MPa. The effect of changing lime content on resilience modulus is smaller than that of changing cement content. Compared with ordinary aggregate inorganic mixture, the compressive resilience modulus of recycled aggregate inorganic mixture is obviously lower, which is beneficial to reduce the rigidity of the pavement base layer and improve the flexibility of the roadbed.

(3) When the concrete particle content is 45%, the maximum dry density value is 1.889g/cm^3, the load-bearing ratio value is 242%. When the debris content is 1%, the maximum dry density value is 1.776g/cm^3, the load-bearing ratio value is 175%. The increase of the concrete particle content can effectively increase the maximum dry density and bearing ratio value of the graded crushed stone. Appropriately increasing the concrete particles in the brick-concrete recycled aggregate can improve the road performance of the brick-concrete recycled aggregate graded gravel. Increasing the content of impurities can significantly reduce the maximum dry density and load-bearing ratio of the graded crushed stone. The sundries can be sorted out as much as possible in the production process of recycled aggregates to reduce the sundries content. The quality of the debris itself is low, and the wood chips contained in the debris will cause damage to the CBR specimens after absorbing water and swelling. Impurities are between the aggregate and the aggregate, which affect the conduction of stress and make the inorganic mixture easier to be destroyed.

ACKNOWLEDGEMENTS

This work was supported by the Hubei key laboratory of disaster prevention and mitigation “China Three Gorges University” (2021KJZ04).

REFERENCES

[1] Villanova, D.L., Bergmann, C.P. (2007) Sinterability study of ceramic bodies made from a mixture of mineral coal bottom ash and soda-lime glass cullet. Waste Manag. Res. 25(1), 77-82.

[2] Kim, G.D., Kim, T.B. (2007) Development of recycling technology from waste aggregate and dust from waste concrete. Journal of Ceramic Processing Research. 8(1), 82-86.

[3] Batayneh, M.K., Marie, I., Asi, I. (2008) Promoting the use of crumb rubber concrete in developing countries. Waste Management. 28(11), 2171-2176.

[4] Tam, V., Tam, C.M. (2016) A review on the viable technology for construction waste recycling. Resources Conservation & Recycling. 47(3), 209-221.

[5] Yuan, F., Shen, L.Y., Li, Q.M. (2011) Emergy analysis of the recycling options for construction and demolition waste. Waste Manag. 31(12), 2503-2511.

[6] Lin, K.L., Wu, H.H., Shie, J.L., Hwang, C.L., Cheng, A. (2010) Recycling waste brick from construction and demolition of buildings as pozzolanic materials. Waste Manag. Res. 28(7), 653-659.

[7] Kumar, K.S., Baskar, K. (2014) Recycling of e-plastic waste as a construction material in developing countries. Journal of Material Cycles and Waste Management. 17(4), 718-724.

[8] Huang, W.L., Lin, D.H., Chang, N.B., Lin, K.S. (2002) Recycling of construction and demolition waste via a mechanical sorting process. Resources Conservation & Recycling. 37(1), 23-37.
[9] Rodrigues, F., Carvalho, M.T., Evangelista, L., Brito, J.D. (2013) Physical–chemical and mineralogical characterization of fine aggregates from construction and demolition waste recycling plants. Journal of Cleaner Production. 52(4), 438-445.
[10] Chong, W.K., Hermreck, C. (2010) Understanding transportation energy and technical metabolism of construction waste recycling. Resources Conservation & Recycling. 54(9), 579-590.
[11] Srour, I.M., Chehab, G.R., El-Fadel, M., Tamraz, A.S. (2013) Pilot-based assessment of the economics of recycling construction demolition waste. Waste Manag. Res. 31(11), 1170-1179.
[12] Jla, B., Yun, Y.A., Jian, Z., Jl, E. (2020) Key policies to the development of construction and demolition waste recycling industry in China. Waste Management. 108, 137-143.
[13] Islam, R., Nazifa, T.H., Yuniarto, A., Asm, S.U., Salmiati, S., Shahid, S. (2019) An empirical study of construction and demolition waste generation and implication of recycling. Waste Management. 95, 10-21.
[14] Hossain, S.S., Mathur, L., Majhi, M.R., Roy, P.K. (2019) Manufacturing of green building brick: recycling of waste for construction purpose. Journal of Material Cycles and Waste Management. 21(2), 281-292.
[15] Bains, M., Yang, H., Chen, J. (2019) International policy perspectives on construction waste minimization and recycling. Waste and Resource Management. 172(3), 1-23.
[16] Xuan, D.X., Houben, L., Molenaar, A., Shui, Z.H. (2012) Mixture optimization of cement treated demolition waste with recycled masonry and concrete. Materials & Structures. 45(1), 143-151.
[17] Mukharjee, B.B., Barai, S.V. (2015) Development of construction materials using nano-silica and aggregates recycled from construction and demolition waste. Waste Manag. Res. 33(6), 515-523.
[18] Bravo, M., Brito, J.D., Pontes, J., Evangelista, L. (2015) Durability performance of concrete with recycled aggregates from construction and demolition waste plants. Construction and Building Materials. 77, 357-369.
[19] Rafi, M.M., Qadir, A., Siddiqui, S.H. (2011) Experimental testing of hot mix asphalt mixture made of recycled aggregates. Waste Manag. Res. 29(12), 1316-1326.
[20] Yin, S., Kong, L.W., Yang, A.W., Mu, K. (2016) Indoor experimental study of road performance of granite residual soil for subgrade filling materials. Rock and Soil Mechanics. 37, 287-293.
[21] Wang, X., Yu, R., Shui, Z., Song, Q., Wu, S. (2019) Optimized treatment of recycled construction and demolition waste in developing sustainable ultra-high performance concrete. Journal of Cleaner Production. 221, 805-816.

Received: **02.12.2021**
Accepted: **08.02.2022**

CORRESPONDING AUTHOR

Hui Sun
School of Civil Engineering,
Henan Polytechnic University,
Jiaozuo Henan 454000 – China

e-mail: sunwei38478@163.com

© by PSP Volume 31– No. 05/2022 pages 5144-5151 Fresenius Environmental Bulletin

FORECAST METHOD OF TYPHOON EXTREME PRECIPITATION BASED ON SVM MODEL OPTIMIZATION

Jiahu Wang[1,*], Weigang Zhao[1], Jianzhong Wang[2], Cuijie Liu[2]

[1]College of Hydrology and Water Resources, Hohai University, Jiangsu Nanjing 210098, China
[2]Reclaimed water northeast survey, design and Research Co., Ltd, Jilin Changchun 130021, China

ABSTRACT

The frequent occurrence of extreme precipitation events has attracted widespread attention from all over the world, and it has a significant impact on the sustainable development of coastal cities. At present, the error in the prediction of heavy rainfall above the torrential rain level is relatively large. In this paper, taking the coastal areas of southeast China as an example, an optimized SVM model is used to quantitatively evaluate extreme precipitation under typhoon conditions. The research results show that the precipitation intensity in the study area is mainly distributed between 80 mm and 340 mm, which basically presents a normal distribution characteristic. The precipitation is scored using the ETS method proposed by the previous. The relationship between precipitation and score is a power exponential relationship. As the precipitation increases from 0 to 500 mm, the score decreases from 0.45 to about 0.05. This method has better forecasts of average precipitation in outer rain belts than in inner rain belts. For rain belts within the range of 0~80 km from the tropical cyclone center, the forecasted extreme precipitation threshold is 195 mm, which is very close to the actual extreme precipitation threshold of 205 mm. On the whole, this method has better forecasting ability of extreme precipitation in the inner rain belt of tropical cyclones than the outer rain belt. The actual measurement and prediction results of extreme precipitation based on the SVM model are very consistent, and the prediction results are slightly higher than the actual measurement results. This study shows that the extreme rainfall evaluation results based on the SVM model are reliable. This method can provide a reference for accurate prediction of extreme precipitation.

KEYWORDS:
Coastal city environment, extreme precipitation, tropical cyclone, SVM model, precipitation threshold

INTRODUCTION

Global warming has become a worldwide problem [1-3]. In this context, the frequent occurrence of extreme precipitation events has attracted widespread attention [4-6]. Extreme precipitation affects the sustainable development of cities [7-8]. Generally, extreme precipitation events mainly include the determination of extreme precipitation characterization values, extreme precipitation distribution and evolution trends, analysis of the causes of extreme precipitation, and model forecasts and evaluations [9-13].

Tropical cyclones often bring heavy rainfall, causing secondary disasters such as torrential rains, floods, and mudslides, causing serious casualties and property losses [14-15]. Therefore, improving the precipitation forecast of tropical cyclones is the direction of improvement in meteorological numerical models in recent years [16-18]. Although the tropical cyclone track forecast has been greatly improved, the improvement in the precipitation forecast is still small. The most important factor in determining the distribution of tropical cyclone precipitation is the tropical cyclone track [19-22]. Storms often occur near a narrow-band tropical cyclone track. Tropical cyclone precipitation is not only closely related to its path and intensity, but also related to other factors [23-25]. For example, topography is another important factor that affects the precipitation of tropical cyclones, and the difference in precipitation on the windward and leeward slopes is very obvious. Secondly, the vertical shear of ambient wind can produce asymmetry in the core of tropical cyclone precipitation field. In addition, the environmental humidity of tropical cyclones and the surface properties of the bottom layer will also affect the precipitation and distribution of landfall tropical cyclones.

With the development of numerical models, countries around the world carry out quantitative forecasts of extreme precipitation through numerical models [26-29]. Numerical models can describe the structural changes of tropical cyclones throughout the time, and can be used to reflect the cumulative precipitation of tropical cyclones within a region. But its shortcomings are limited by resolution and insufficient expression of the initial state of atmospheric physical processes [30-34].

At present, the ability to forecast heavy rainfall is still low. The absolute error of people's forecast of precipitation is too large, especially the score of precipitation deviation above the torrential rain level is

obviously too large. In this paper, taking the coastal areas of southeast China as an example, an optimized SVM model is used to quantitatively evaluate extreme precipitation under typhoon conditions. This method can provide a reference for accurate prediction of extreme precipitation.

MATERIALS AND METHODS

In this paper, data from 44 precipitation observation base stations along the coast of southeastern China are used to carry out quantitative evaluation studies of heavy precipitation. When the daily precipitation exceeds the 99% threshold, it is counted as an abnormally heavy precipitation day. In order to make it easier for forecasters to confirm the weather type, this article unified the classification according to the 500 hPa weather situation. In addition, combined with the characteristics of the extreme precipitation weather situation in the southeast region, two types of weather situations are summarized, namely the latitude type and the longitude type.

In order to investigate the extremes of various physical quantities in extreme heavy precipitation events, this paper uses NCEP data calculates physical quantities such as wind, temperature, sea level pressure, and atmospheric precipitation. And according to the standardized anomaly method to analyze the abnormal degree of the above physical quantity, the specific calculation method is shown in Formula 1~2:□□

$$N = (X - \mu) / \sigma \tag{1}$$

$$\sigma = \sqrt{\frac{\sum_{i-1}^{n} (X_i - \mu)^2}{n - 1}} \tag{2}$$

In the formula, σ is the mean value of the elements, the standard deviation, and N is the number of samples. N is the degree of deviation between the element value at a certain moment and the historical average value of the same period, that is, the degree of abnormality. The larger the absolute value of N, the higher the deviation of the element from the historical average value over the same period.

Support Vector Machine (SVM) is a machine learning method developed on the basis of statistical learning theory. SVM was originally used to solve the problem of pattern recognition, using its classification algorithm to achieve better generalization ability. With the introduction of ε-insensitive loss function, SVM has been extended to solve the problem of nonlinear regression estimation. The basic idea of SVM adopted in this paper is to transform the input space into a high-dimensional space through the nonlinear transformation defined by the inner product function, and then find a linear relationship between the input variable and the output variable in this high-dimensional space. The appropriate kernel function is selected to realize the conversion of the data from the input space to the corresponding nonlinear high-dimensional space.

The support vector regression machine can finally generate a sparse estimation function by selecting some training points (support vectors) to estimate the output according to the input data. Since the support vector regression machine selects a compromise between the risk error and the model complexity, it approximately implements Vapnik's principle of minimum structural risk. Therefore, compared with the neural network model based on the least empirical risk, the support vector regression machine achieves global optimization. SVR algorithm is used to realize the nonlinear fitting between input data and output data, and its fitting function f(x,w) can be expressed as formula 3.

$$f(x, w) = w \cdot \phi(x) + b = (w, \phi) + b \tag{3}$$

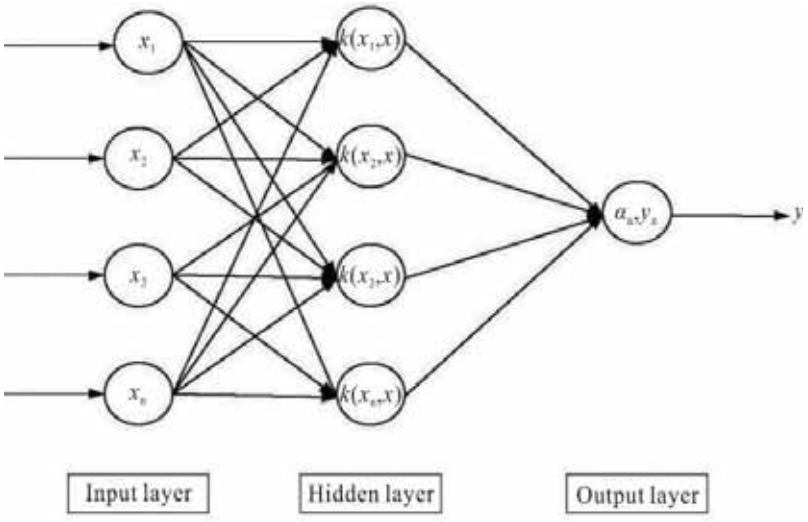

FIGURE 1
Support vector machine model.

In the formula, w is the weight vector; $\phi(x)$ is the nonlinear mapping, which generates a vector with the same dimension as the input vector x; b is the deviation; (w, ϕ) is the inner product of w and ϕ. The SVR optimization problem is to find a function that can estimate the output that is almost close to the target within the specified error, and at the same time minimize the w model parameters, so that it has a stronger generalization ability. The optimization goal is equivalent to a most basic convex quadratic programming problem (Equation 4).

$$\min \frac{1}{2}\|w\|^2 \tag{4}$$

The above formula is a function of the specified error ε and the target value y. Then we adopt the Lagrangian multiplier method and introduce the kernel function, so that we get an equivalent quadratic programming problem. Finally, the estimation function of the support vector regression machine is obtained, see formula 5.

$$f(x) = \sum_{i=1}^{1} (\alpha_i - \alpha_i^*) \exp\left(-\frac{\|x - x_i\|^2}{2\sigma^2}\right) + b \tag{5}$$

SVR's topology network structure is determined by support vectors, which overcomes the shortcomings of traditional neural network topology (weights and number of hidden layers) that rely heavily on empirical values. Practical problems such as linearity, high dimensionality and local minima have strong generalization ability. This SVR model is implemented using the structure shown in Figure 1. Among them, $\alpha_i y_i$ is the network weight, x_1, x_2,..., x_n is the input vector, y is the network output, and the number of hidden nodes is the number of support vector machines.

RESULTS

Analysis of the characteristics of extreme weather and precipitation. Table 1 shows the number of rainstorm stations and the statistical characteristics of extreme precipitation in two types of extreme precipitation cases. Two types of extreme precipitation have certain differences in precipitation characteristics. Type 1 (latitude type) corresponds to the rain belts mainly distributed in the south-central part of the southeast coast, and the rain belts are mostly northeast-southwest. Type 2 (longitude type) corresponds to the rain belt mainly in the north of the southeast coast. Rain belts are mostly distributed in short bands in northeast, southwest or north-south direction, and sometimes in northwest-southeast direction.

On the one hand, the cause of latitude extreme precipitation is due to the movement of the subtropical high and the northeast cold vortex, which is conducive to the formation of systemic rainbands and maintains them for a long time. The eastward movement of the cold vortex is blocked, and the airflow is guided to change direction at high altitude. Longitude extreme precipitation is caused by the increase in warm advection due to the blocking effect of the high pressure in front of the trough, which makes the low trough move slowly, and is conducive to the formation of longer-term precipitation. In addition, in the stable coordination between high and low pressure, the low pressure gradient is maintained or slightly enhanced. The southerly wind and easterly wind speed may increase slightly, which provides extremely favorable conditions for the transport of water vapor and the formation of instability. It is easy to produce heavy rainfall. The precipitation intensity in a certain 24 hours measured at the precipitation observation point in the study area A is shown in Figure 2. The precipitation intensity is mainly distributed between 80mm and 340mm, which basically presents a normal distribution characteristic.

Prediction of average precipitation based on SVM model. Due to the different dimensions of each parameter, in order to avoid the calculation difficulties in the inner product calculation of the kernel function, normalization preprocessing is required before use, so that each parameter is between [0,1].

$$X = \frac{x - x_{min}}{x_{max} - x_{min}} \tag{6}$$

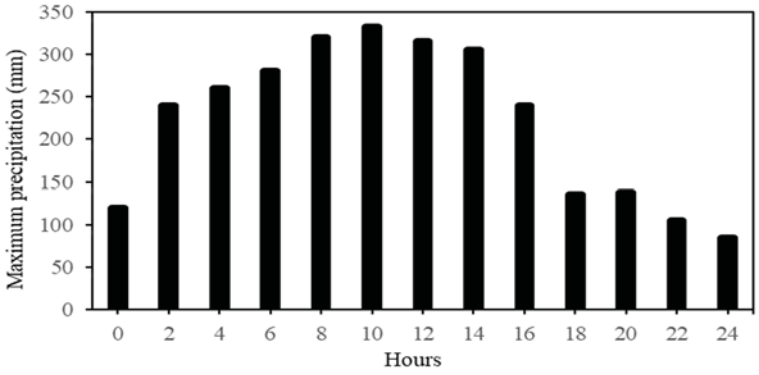

FIGURE 2
Distribution of maximum precipitation in 24 hours of extreme precipitation weather at base station A.

TABLE 1
Classification of two types of typical extreme precipitations.

Types of extreme rain weather	Proportion (%)	Number of observation base stations	Maximum precipitation (mm)
Latitude type	60	30	375
Longitude type	40	14	505

Among them, x, *X*-are the variable values before and after normalization; x_{min}, x_{max}-are the minimum and maximum values of the variable, respectively.

After the learning sample set is established, the determination of the productivity model is mainly to select the appropriate SVR parameters, namely the penalty parameter *C* and the kernel function base width γ. Their reasonable determination directly affects the accuracy and promotion ability of the model

In this paper, the cross-validation grid search method is used to determine the optimal parameters. The method is as follows: First, the sample data is divided into *n* subsets of the same size. First, use *n*-1 subsets as training samples to get a decision function, and use it to predict the subset that did not participate in the training, so that a total of *n* cycles are looped. Until all the subsets are used as test samples to be predicted again, the average of the accuracy of *n* predictions is taken as the final accuracy value. Therefore, it can avoid subjective errors caused by artificial selection of *C* and γ. The optimal parameter values selected in this case study were selected as *C*=100, γ=20, and ε=0.001.

The decision model constructs modeling data (X_i, Y_i) (i=1,2,...,k) according to the input and output parameters that have been determined. Then, the nonlinear mapping relationship between the input parameter (X) and the output capacity (Y) satisfies: $Y_i=f(X_i)[f:R_n \rightarrow R]$. According to the aforementioned SVR theory, select the appropriate accuracy parameters *C*, γ and ε, and substitute them into the RBF kernel function. After solving a quadratic programming problem to obtain α_i, α^*_i, b, we can get the decision model we need.

We adopt a more comprehensive evaluation method for the precipitation forecast of landing tropical cyclones, including model matching evaluation, average precipitation evaluation, and extreme precipitation evaluation, and quantify the three evaluation attributes. The value ranges from 0 to 1, where 0 means no skills, and 1 means most skills. The degree of matching between the 24h cumulative precipitation forecast and the actual situation is measured by the ETS score and the spatial correlation of the model. The average value of the two can measure the matching performance of the model. The value is between 0 and 1. The ETS calculation formula is as shown in Equation 7:

$$ETS = \frac{H - H_{\text{random}}}{H + M + FA - H_{\text{random}}} \quad (7)$$

In the formula, *H*, *M*, *FA*, H_{random} respectively represent the hit rate, false negative rate, false alarm rate, and the number of possible correct forecasts under random conditions. The numerator and denominator of the formula subtract the random precipitation rate at the same time, which can effectively eliminate the influence of the random precipitation rate on the precipitation score; the hit rate mainly refers to the matching degree of the forecast precipitation and the actual precipitation.

Figure 3 shows the ETS score of the 24-hour precipitation before the tropical cyclone that landed in the study area and the correlation coefficient between the 24-hour precipitation forecast and the actual situation. The relationship between precipitation and score is a power exponential relationship. As the precipitation increases from 0 to 500 mm, the score decreases from 0.45 to about 0.05.

This method has the highest ETS score for light rain forecasts, while the ETS scores for heavy rain and above model forecasts decline rapidly, all less than 0.1, and the average ETS scores for precipitation forecasts of different magnitudes are 0.17. For the different tropical cyclones that landed in the study area, the model performance was different, and the correlation coefficient between the forecast and the actual precipitation was 0.4 to 0.9.

Figure 4 shows the comparison between the precipitation observation results and the forecast results at Observation Station A within 24 hours. From the comparison of the forecast and the actual 24-hour average precipitation at different distances from the tropical cyclone center, it can be seen that the 24-hour average precipitation predicted by the model is 3-18 mm smaller than the actual 24-hour average. And the predicted maximum is located at 40 km from the center of the tropical cyclone, while the actual maximum is located at 80km. Forecast and actual conditions show the frequency of occurrence of all grid points in different precipitation levels within the range of tropical cyclone influence. The distribution trend of the forecast and the actual situation is roughly the same, which is manifested as the frequency of light rainfall is the most frequent, and the forecast is higher than the actual situation. However, the frequency forecast of heavy rain and above is less than the actual situation, and the corresponding median forecast with a cumulative precipitation frequency of 50% is nearly 3.5 mm smaller than the actual situation.

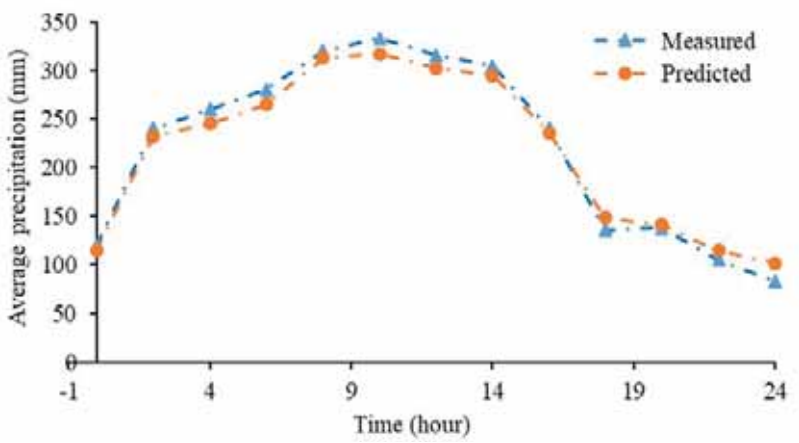

FIGURE 4
Comparison of precipitation observation results and forecast results in 24 hours at Observation Station A.

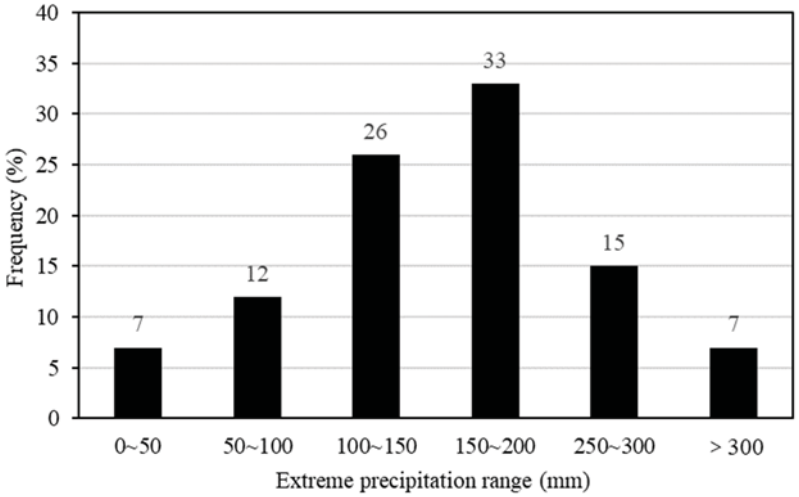

FIGURE 5
Distribution of extreme precipitation under extreme precipitation threshold in the study area.

In addition, comparing all grid point forecasts in different rain belts from the center of tropical cyclones and the median of the actual precipitation, it is found that within the 0-80km rain belt, the actual rainfall has the highest frequency of heavy rainfall, while the model forecast is the frequency of heavy rainfall. most. Moreover, the frequency of forecasts below heavy rain is higher than the actual situation. The opposite is true for heavy rain and above. The difference in the magnitude of the heavy rain is the most significant. The median forecasted rainfall is smaller than the actual situationIt can be seen that the average precipitation forecast of the outer rain belt is better than that of the inner rain belt in this model, and the median index of cumulative frequency of precipitation on different rain belts is 0.67 on average. In summary, the model's forecast performance for average precipitation does not depend on the model's forecast deviation of tropical cyclone paths, and it is more objective to evaluate the model's precipitation forecast performance.

Extreme precipitation assessment. Figure 5 shows the distribution of extreme precipitation under the extreme precipitation threshold conditions in the study area based on actual conditions and model forecasts under the influence of tropical cyclones. It can be seen that the threshold value corresponding to the 95 percentage of the observed cumulative precipitation within the influence of the tropical cyclone is about 200 mm, while the predicted extreme precipitation threshold is obviously smaller, around 85 mm. The extreme precipitation evaluation index is 0.96. For the rain belt within the range of 0~80 km from the tropical cyclone center, the forecast extreme precipitation threshold is 195 mm, which is very close to the actual extreme precipitation threshold of 205 mm. For the rain belt 100~200 km away from the tropical cyclone center, the actual extreme precipitation threshold is about 80 mm. The forecasted extreme precipitation threshold is too small, and the threshold quantile differs by 3.1%. It can be seen that this method is better than the outer rain belt in forecasting extreme precipitation in the inner rain belt of the tropical cyclone.

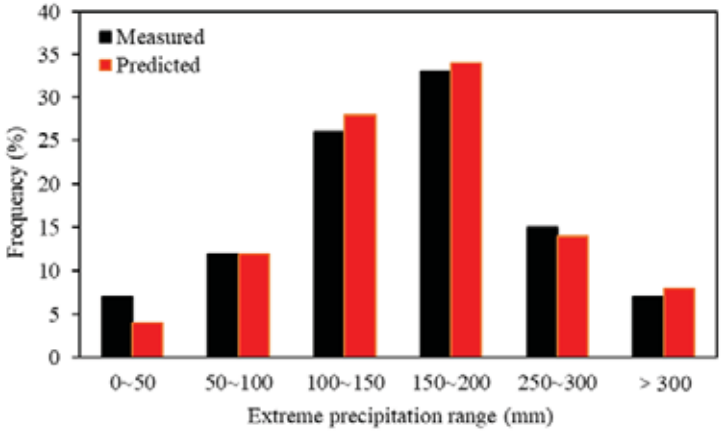

FIGURE 6
Comparison of the actual measurement and prediction results of extreme precipitation under extreme precipitation threshold conditions in the study area.

Figure 6 shows the comparison between the measured and predicted results of extreme precipitation under the extreme precipitation threshold conditions in the study area based on the SVM model. The predicted results are very consistent with the actual measured results, and the predicted results are slightly higher than the actual measured results. After calculation, the extreme precipitation evaluation index of grid points on different rain belts relative to the tropical cyclone path is on average 0.89, which is very close to the grid extreme precipitation index in the entire large area. Although the comprehensive evaluation index of extreme precipitation is relatively high, the evaluation index is obtained from the quantile of extreme precipitation. In fact, the forecasted and actual extreme precipitation thresholds are close to each other except for the inner rain zone (within 80km from the center of the tropical cyclone). The error gradually increases from the distance from the center of the tropical cyclone outward. This is because extreme precipitation mostly occurs in the inner rain belt of tropical cyclones. The occurrence of extreme precipitation in the outer rain belt is not only related to the structure of the tropical cyclone itself, but most of it is also related to the interaction of the surrounding weather system. Once the method has a deviation in the forecast of the peripheral weather system, it will inevitably affect the magnitude forecast of tropical cyclone precipitation. On the whole, the evaluation results of extreme rainfall based on the SVM model in this paper are reliable.

CONCLUSIONS

(1) In this paper, taking the coastal areas of southeast China as an example, an optimized SVM model is used to quantitatively evaluate extreme precipitation under typhoon conditions.

(2) The research results show that the precipitation intensity in the study area is mainly distributed between 80 mm and 340 mm, which basically presents a normal distribution characteristic. The precipitation is scored using the ETS method proposed by the previous. The relationship between precipitation and score is a power exponential relationship. As the precipitation increases from 0 to 500 mm, the score decreases from 0.45 to about 0.05.

(3) This method has better forecasts of average precipitation in outer rain belts than in inner rain belts. For rain belts within the range of 0~80 km from the tropical cyclone center, the forecasted extreme precipitation threshold is 195 mm, which is very close to the actual extreme precipitation threshold of 205 mm.

(4) On the whole, this method has better forecasting ability of extreme precipitation in the inner rain belt of tropical cyclones than the outer rain belt. The actual measurement and prediction results of extreme precipitation based on the SVM model are very consistent, and the prediction results are slightly higher than the actual measurement results.

(5) This study shows that the extreme rainfall evaluation results based on the SVM model are reliable. This method can provide a reference for accurate prediction of extreme precipitation.

ACKNOWLEDGEMENTS

This work was sponsored by the Key Project of Research and Development Plan (2018YFC1508006). The authors would like to show sincere thanks to all the techniques who have helped this research and all the authors of the references.

REFERENCES

[1] Jiao, K., Yao, S., Wu, H. (2014) Advances in characterization of pore system of gas shale. Geological Journal of China Universities. 20(1), 151–161.

[2] Lommatzsch, M., Exner, U., Gier, S. (2015) Dilatant shear band formation and diagenesis in calcareous, Arkosic sandstones, Vienna Basin (Austria). Marine and Petroleum Geology. 62, 144–160.
[3] Zhang, Y., Liu, Z., Huo, B. (2007) Power load combined forecasting model based on support vector machine. Power Demand Management. 9(2), 14-17.
[4] Yu, J., Tang, J., Dai, Y. (2012) Operational forecast error and cause analysis of typhoon tracks in my country. Meteorology. 38(6), 695-700.
[5] Ji, C., Xue, G., Zhao, F. (2007) Numerical simulation experiment of the influence of terrain on its precipitation and structure during the landing of Typhoon Rananim. Atmospheric Science. 31(2), 233-244.
[6] Huang, Y., Duan, Y., Yan, Y. (2009) Preliminary analysis of the influence of topography on precipitation of super typhoon Rosa. Meteorology. 35(9), 3-10.
[7] Zhu, H., Wang, D., Lou, S. (2015) Research on the influence of topography on the precipitation increase of typhoon "Sea Anemone". Heavy Rain Disaster. 34(2), 160-167.
[8] Yang, R., Min, J., Feng, W. (2013) Numerical experiment of the influence of Hainan Island topography on the precipitation of westward typhoon in the South China Sea. Journal of Tropical Meteorology. 29(3), 474-480.
[9] Dakos, V., Van, N., Donangelo, R. (2010) Spatial correlation as leading indicator of catastrophic shifts. Theoretical Ecology. 3(3), 163-174.
[10] Koochaki, A., Asadi, M., Mahmoodan, M. (2008) Optimal Overcurrent relays coordination using genetic algorithm/International Conference on Optimization of Electrical and Electronic Equipment. IEEE Xplore. 197-202.
[11] Carreras, B.A., Lynch, V., Dobson, I. (2002) Critical points and transitions in an electric power transmission model for cascading failure blackouts. Chaos: An interdisciplinary journal of nonlinear science. 12(4), 985-994.
[12] Gong, X., Zhao, S. (2007) Diagnosis of energy process and water vapor supply after Typhoon Maisha makes landfall. Climatic and Environmental Research. 12(3), 437-452.
[13] Huang, W., Yu, H., Liang, X. (2009) GRPES-TCM's prediction of landfall tropical cyclone precipitation and its performance evaluation. Acta Meteorologica Sinica. 67(5), 892-901.
[14] Shen, Y., Pan, Y., Yu, J. (2013) Quality assessment of fusion products of regional hourly precipitation in China. Journal of Atmospheric Sciences. 36(1), 37-46.
[15] Pan, Y., Shen, Y., Yu, J. (2012) Hourly precipitation fusion experiment in China based on the analysis of optimal interpolation method. Acta Meteorologica Sinica. 70(6), 131-1389.
[16] Chan, M., Donaldson, R. (1986) Attenuation of Communication Signals on Residential and Commercial Intrabuilding Power-Distribution Circuits. IEEE Trans. on Electromagnetic Compatibility. EMC-28(4), 44-47.
[17] Vines, R., Trussell, H., Gale, L. (1984) Noise on Residential Power Distribution Circuits. IEEE Trans. on Electromagnetic Compatibility. EMC-26(4), 31-33.
[18] Tian, Y., Feng, X. (2021) Analysis on the ecological performance management of operating enterprises in port city under the transitional economic environment. Fresen. Environ. Bull. 30(2), 943-948.
[19] Bai, X., Wang, Y., Su, D. (2015) Investigation on the fitness status of residents in Shijiazhuang City under the haze environment. Technological Innovation and Application. 23(35), 73-75.
[20] Mei, N., Shi, D., Li, Y. (2006) Optimization of relay protection setting based on improved particle swarm algorithm. Automation of Electric Power Systems. 30(16), 72-76.
[21] Donangelo, R., Fort, H., Dakos, V. (2010) Early warnings for catastrophic shifts in ecosystems: comparison between spatial and temporal indicators. International Journal of Bifurcation and Chaos. 20(2), 315-321.
[22] Ma, W., Zhou, S., Liu, S. (2021) Research on the environmental carrying capacity of ecotourism in Shijiazhuang city based on the pressure-state-response model. Fresen. Environ. Bull. 30(8), 10335-10340.
[23] Huo, M. (2016) How to exercise for the elderly in haze weather. Modern Health. 4(1), 32-76.
[24] Wang, Y., Yan, Z. (2007) Analysis of the impact of changes in precipitation inspection schemes on the effect of precipitation inspection and evaluation. Meteorology. 33(12), 53-61.
[25] Zheng, Z., Wang, Z., Gao, H. (2013) The characteristics of extreme precipitation changes in summer in Beijing and the impact of urbanization. Meteorology. 39(12), 1635-1641.
[26] Lu, G., Wang, W., Yu, H. (2014) Analysis of the impact of typhoon "Davi" on the 08.03 heavy rain weather process in Rizhao, Shandong. Arid Meteorology. 32(2), 256-262.
[27] Xu, H., Cheng, P., Wang, R. (2016) Numerical simulation of typhoon "Haiyan" passing through Hainan Island and diagnosis of the cause of rainstorm. Arid Meteorology, 34(3), 503-510.
[28] Shao, Y., Zhong, J., Zhou, Z. (1999) Summary of Centralized Meter Reading System for Low Voltage Users. Automation of Electric Power Systems. 23(17), 1-7.
[29] Xu, G., Zheng, R., Deng, M. (2021) Characteristic analysis of linear load leakage current in low-voltage power grid. Electrical Technology. 22(1), 33-36.

[30] Wang, K., Wu, Y. (2021) Impact of land use dynamic change on surface runoff - A case study on Zhengzhou City. Fresen. Environ. Bull. 30(8), 9850-9856.
[31] Sun, Y., Ma, M., Fu, C. (2021) On-line identification of load sensitivity of low-voltage microgrid based on power electronic transformer. Modern Electric Power. 38(1), 15-18.
[32] Xiao, Q., Zhu, S. (2014) Analysis and countermeasures of the environmental effects of haze in Shiyan City. Journal of Yunyang Teachers College. 12(3), 37-39.
[33] Wang, Q., Xiao, W., An, Y. (2014) Analysis of the causes and treatment methods of smog. Science and Technology Vision. 23(14), 256-257.
[34] Qian, Q., Zhang, C., Gao, S. (2014) Research on real-time correction technology of typhoon track ensemble forecast. Journal of Tropical Meteorology. 30(5), 905-910.

Received: **03.12.2021**
Accepted: **23.01.2022**

CORRESPONDING AUTHOR

Jiahu Wang
College of Hydrology and Water Resources,
Hohai University,
Jiangsu Nanjing 210098 – China

e-mail: TigerLLy@126.com

© by PSP Volume 31– No. 05/2022 pages 5152-5158 Fresenius Environmental Bulletin

ANALYSIS OF THE IMPACT OF URBAN TRAFFIC ENVIRONMENTAL ENERGY CONSUMPTION BASED ON EKC MODEL

Youqing Liu*

Faculty of Engineering, Imperial College London, London SW72AZ, UK

ABSTRACT

In recent years, with the continuous development of the economy and the continuous acceleration of the process of urbanization in China, the proportion of energy consumption in the transportation industry has shown a rising trend. The task of reducing transportation energy consumption is strategic and urgent. To comprehensively build a conservation-oriented society and promote the sustainable development of the transportation industry in China, it is necessary to explore decision support for reducing transportation energy consumption. Therefore, it is imperative to understand the current situation of energy consumption in the urban transportation industry in China, analyze and calculate and effectively predict transportation energy consumption, and decompose the main factors that affect this target variable. This study selects 10 representative cities in China as the research objects. Based on the Kuznets method in econometrics, through modeling analysis and example verification, the specific influencing factors of urban transportation energy consumption, urban transportation energy consumption and social economy and the relationship between development and consumption is studied. The research results show that per capita GDP and per capita transportation energy consumption are in an inverted U-shaped curve, but it has not reached the turning point of the curve. In other words, the current economic development cannot reduce per capita transportation energy consumption. At the same time, there is a weak decoupling between per capita transportation energy consumption and per capita GDP, and the elasticity of per capita transportation energy consumption relative to per capita GDP decreases as the economic level increases. In addition, population density, economic structure and intensity of traffic energy consumption have a negative impact on per capita traffic energy consumption. In contrast, urbanization rate has a positive impact on per capita traffic energy consumption, and the impact is greater than other factors.

KEYWORDS:
Urban traffic energy consumption, influencing factors, environmental Kuznets curve, modeling research

INTRODUCTION

After the outbreak of the global energy crisis in 1973, experts and scholars in various fields turned their attention to the influencing factors of energy consumption. The historical issues of energy and the sustainable development of the future have received the attention of the whole society, and they have begun to model energy consumption. The transportation industry is one of the core areas of energy consumption. The research of these models mainly focuses on the cost input, factor contribution analysis, consumption comparison analysis, etc. in the field of transportation [1-3]. Subsequently, several fields include the relationship between transportation energy consumption and economic development, the simulation of future energy consumption demand, and the feasibility study of related policies have emerged [4].

Some scholars have concluded that the energy consumption of road transportation in most countries accounts for 80% or more of the total energy consumption of transportation [5]. In terms of research on the impact factors of transportation energy consumption, some scholars believe that the consumption of transportation energy depends on the population of the city and will increase with the increase of the population. Some scholars believe that the irregular fluctuations of the impact of population factors on energy consumption depend on specific energy consumption sectors and other comprehensive considerations, while factors other than population have a greater impact, which is 1.9-4.5 times that of population factors [6]. Research based on relevant data shows that transportation energy consumption is affected by the way individuals go out, and the two are closely related, while the development of the country's economy affects and restricts the choices of personal going out behaviors [7]. Transportation energy consumption depends on people's transportation needs, and transportation demand increases with the increase in people's income. The increase in income makes people more inclined to use private cars to travel out. Transportation activities can significantly affect the energy consumption of transportation, and the reduction of energy consumption per unit of transportation is the key to the success of reducing energy consumption [8-9].

Some scholars have studied the relationship between land use and transportation and believe that the increase in urban density will lead to a decrease in transportation energy consumption, that is, there is a negative correlation between urban density and transportation energy consumption [10-11]. The research on transportation energy consumption in China started later than Western countries. It is mainly based on the following five research perspectives: urban passenger transportation, urban external transportation, transportation energy intensity, the relationship between transportation and economic development, and the relationship between transportation and energy consumption [12-15].

In view of the outstanding theoretical complexity and important practical significance, the issue of transportation energy consumption has long attracted extensive attention from the academic and engineering circles. Among many research methods, the environmental Kuznets curve (EKC) model can comprehensively and in-depth explain the quantitative relationship between economic development and environmental protection, so it has received more and more attention from scholars in recent years [16-18]. EKC theory believes that environmental pressure continues to increase with economic growth, until the economic level reaches a certain value, the environmental pressure has a turning point, and then the further increase in economic level will improve environmental quality [19-21]. This paper establishes an EKC theoretical measurement regression model. After that, this paper uses feasible generalized least squares (FGLS) to calibrate the parameters of the model. Finally, based on the theory of economic resilience, this article analyzes the impact of urban economic growth, urbanization development, and transportation energy intensity on urban per capita transportation energy consumption from the perspective of econometrics.

MATERIALS AND METHODS

(1) Research object. This question selects the 10 big in China as the research objects. These cities are basically in line with the future development trend of Chinese cities, so their research results can provide a reasonable reference for policy regulation in the process of urbanization. At the same time, problems such as traffic congestion, excessive energy consumption, and disorderly expansion of the city are relatively obvious, which directly restrict the sustainable development of the city. In addition, considering that the current statistical caliber of transportation energy consumption in Chinese cities is different from that of other countries and regions, that is, the transportation energy consumption statistics in China generally do not consider the energy consumption of private vehicles. In view of this shortcoming, the energy consumption of vehicles of operating organizations and energy consumption of private vehicles are firstly counted separately, and then the two are organically combined to obtain the required traffic energy consumption data. In addition, this article will obtain the original basic data of various factors affecting urban transportation energy consumption through official information such as statistical yearbooks.

(2) Research methods. 1) Model building. In the study of the relationship between economic growth and environmental pollution, EKC theory believes that the environmental degradation rate and economic growth show a trend of first growth and then decline, that is, the two show an inverted "U"-shaped relationship. In the analysis of two-dimensional variables, generally taking the level of economic development as the horizontal axis and the environmental degradation rate on the vertical axis, the environmental degradation rate presents an inverted U-shaped curve that first increases and then decreases with income growth. The related econometric model is shown as Eq. 1.

$$E_{it} = A_{it} + \beta_1 Y_{it} + \beta_2 {Y_{it}}^2 + \beta_3 {Y_{it}}^3 + \mu_{it} \quad (1)$$

In the formula, E_{it} means the environmental degradation rate of area i during t period; Y_{it} means the economic development level of city i during t period; A_{it}-time and individual effects; μ_{it}-random disturbance term; β_i-undetermined coefficient.

In this study, the environmental degradation rate and the level of economic development are expressed in terms of per capita transportation energy consumption and per capita GDP, respectively. In order to consider the impact of other variables on per capita transportation energy consumption, this study incorporates the control variables population density, economic structure, urbanization rate, and transportation energy consumption intensity into the model, and establishes an econometric regression model based on EKC theory, as shown Eq. 2.

$$E_{it} = A_{it} + \beta_1 Y_{it} + \beta_2 {Y_{it}}^2 + \beta_3 {Y_{it}}^3 + \delta_1 PD_{it} + \delta_2 ES_{it} + \delta_3 UR_{it} + \delta_4 EI_{it} + \mu_{it} \quad (2)$$

In the formula, E_{it}-the per capita traffic energy consumption of city/ in the t period which is expressed in natural logarithm; Y_{it} -the per capita GDP of city i in t period which is expressed in natural logarithm; PD_{it}-the population density of city i in t period, which is expressed in natural logarithm; ES_{it}- the economic structure of the city in t period, expressed in natural logarithm; UR_{it}- the urbanization rate of city i in period t, expressed in natural logarithm; EI_{it} - the intensity of traffic energy consumption in city i during t period which is expressed as a natural logarithm; A_{it}-time and individual effects; μ_{it}-random disturbance term; δ_i-control variable coefficient; β_i-per capita GDP coefficient.

TABLE 1
The relationship between per capita transportation energy consumption and per capita GDP

β	E and Y relationship description
$\beta_1 = \beta 2 = \beta 3 = 0$	E and Y do not have any relationship
$\beta_1 > 0$， $\beta 2 = \beta 3 = 0$	There is a monotonically increasing relationship between E and Y
$\beta_1 < 0$， $\beta 2 = \beta 3 = 0$	There is a monotonically decreasing relationship between E and Y
$\beta_1 < 0$， $\beta 2 > 0, \beta 3 = 0$	There is a U-shaped relationship between E and Y
$\beta_1 > 0$， $\beta 2 < 0, \beta 3 = 0$	There is an inverted U relationship between E and Y (EKC)
$\beta_1 > 0$， $\beta 2 > 0, \beta 3 > 0$	There is an N-shaped relationship between E and Y
$\beta_1 < 0$， $\beta 2 > 0, \beta 3 > 0$	There is an inverted N-shaped relationship between E and Y

TABLE 2
Values of related model parameters

ΔE	0.089	**0.173**$\Delta\overline{\boldsymbol{Y}}$	**-0.063**$\Delta\overline{\boldsymbol{Y}}^{\boldsymbol{2}}$	-0.512$\Delta\overline{PD}$	**-0.263**$\Delta\overline{\boldsymbol{ES}}$	0.765 $\Delta\overline{UR}$	0.351$\Delta\overline{EI}$
Std.err.	0.004***	**0.036*** **	**0.021*** **	0.039***	**0.039*** **	0.051***	0.026***
Groups=10		Wald chi2(10) = 15430.832***			Turing point:	Y=1.703	
Years=13		EKC existing			lnGDPpc=12.563		

The calibrated per capita GDP coefficient p value determines the relationship between per capita GDP and per capita transportation energy consumption. All possible relationships are listed item by item in Table 1.

In the specific modeling process, in order to fully study the relationship between per capita GDP and per capita transportation energy consumption, this paper considers the square term model and the cubic model, and carries out variable centering, first-order difference processing, and the introduction of dummy variables. The formula (2) is transformed into formulas (3) and (4). In formula (3) and formula (4), the time effect is the regression coefficient of the dummy variable in the formula. At the same time, the dummy variable in formula (3) and formula (4) is assigned a value of 1 in a given year, otherwise it is 0, to obtain a constant representing the time effect in the final regression result, as Eq. 3, 4:

$$\Delta\overline{E_{it}} = \alpha_0 + \sum_{\gamma=3}^{T} \alpha_r \, dr_t + \beta_1 \Delta\overline{Y_{it}} + \beta_2 \Delta\overline{Y_{it}}^2 + \beta_3 \Delta\overline{Y_{it}}^3 + \delta_1 \Delta\overline{PD_{it}} + \delta_2 \Delta\overline{ES_{it}} + \delta_3 \Delta\overline{UR_{it}} + \delta_4 \Delta\overline{EI_{it}} + \mu_{it} \quad (3)$$

$$\Delta\overline{E_{it}} = \alpha_0 + \sum_{\gamma=3}^{T} \alpha_r \, dr_t + \beta_1 \Delta\overline{Y_{it}} + \beta_2 \Delta\overline{Y_{it}}^2 + \delta_1 \Delta\overline{PD_{it}} + \delta_2 \Delta\overline{ES_{it}} + \delta_3 \Delta\overline{UR_{it}} + \delta_4 \Delta\overline{EI_{it}} + \mu_{it} \quad (4)$$

$\Delta\overline{E_{it}}$-first-order difference and centralized per capita transportation energy consumption; $\Delta\overline{Y_{it}}$—first-order difference and centralized GDP per capita; $\Delta\overline{PD_{it}}$-first-order difference and centralized Population density; $\Delta\overline{ES_{it}}$-first-order difference and the proportion of centralized tertiary industry; $\Delta\overline{UR_{it}}$-first-order difference and centralized urbanization rate; $\Delta\overline{EI_{it}}$ -the energy intensity of the first-order difference and centralization; μ_{it}-random error term; α_0-the beginning time effect; $\alpha_0 + \alpha_r$- the time effect of the γ period; dr- the time dummy variable of the γ period, $t = \gamma, \mathrm{dr} = 1, \mathrm{t} \neq \mathrm{r}, \mathrm{dr} = 0$.

2) Model calibration. When studying the situation of small sample size and heteroscedasticity and autocorrelation, the FGLS method, as a parameter calibration method based on generalized least squares (GLS), can effectively solve the problem of pseudo-regression. The GLS method satisfies the assumption of spherical perturbation terms by transforming the model and can effectively solve the error problems caused by autocorrelation and heteroscedasticity. In this study, the model was determined by the Wooldridge autocorrelation test, Wald homovariance test, and Pesaran's cross-sectional correlation test, and the formula (3) was calibrated using the FGLS method according to the test results. The calibration results show that the research data does not support the assumption of N-type or inverted N-type relationship, but the coefficient P of most of the square terms of GDP per capita is negative and significant. Therefore, there may be an inverted U-shaped curve between GDP per capita and energy consumption per capita. Relationship.

RESULTS

(1) The impact of urban economic growth on per capita transportation energy consumption. The regression model is applied to the case analysis of GDP per capita and economic structure factors, and the corresponding results are shown in Table 2.

The elasticity of per capita transportation energy consumption relative to per capita GDP explains the impact of per capita GDP changes on per capita transportation energy consumption, and these elastic values change with the year and the city. Therefore, the change in the elasticity value of per capita transportation energy consumption relative to per capita GDP can be used as a reference quantita-

tive basis for analyzing the EKC relationship and explaining related policies. If there is an EKC relationship between per capita GDP and per capita transportation energy consumption, the turning point can be calculated by making the elasticity of per capita transportation energy consumption relative to per capita GDP equal to 0. The value of coefficient 0 is the elastic value of per capita transportation energy consumption relative to GDP per capita at the center of the sample. It can be inferred that at the center of the sample, when the per capita GDP increases by 1.000%, the per capita transportation energy consumption increases by 0.173%. However, the elasticity value is not fixed, but depends on the time frame and the change of the data object. Therefore, in order to evaluate the change of elasticity value over time and the difference between cities, this study uses formula (5) to calculate the turning point and elasticity value of EKC, as Eq. 5:

$$ela_{it} = \beta_1 + 2\beta_2 \overline{Y_{it}} \quad (5)$$

In order to study the changes in the elasticity value of per capita transportation energy consumption relative to per capita GDP in different years and cities, this paper uses the coefficient P value obtained in Table 2 and uses the formula (5) to calculate the change trend of the elasticity value of each city during the entire study period. Figure 1 shows that although the elasticity value of each city is gradually decreasing, it is always positive, and the elasticity value of all cities is between 0.000-0.800, so the per capita transportation energy consumption is weakly decoupled from the per capita GDP. This means that the growth rate of per capita transportation energy consumption is less than the growth rate of per capita GDP. Although the vertical elasticity trend of the cities is generally similar, there are large differences in the horizontal view. For example, Xi'an and Chongqing have higher growth rates. Shenzhen and Guangzhou have lower elastic values. Cities with higher economic levels have relatively small elastic values, while cities with lower economic levels have larger elastic values.

By studying the relationship between the elasticity value and the economic level, it can be found that the elasticity value starts to decrease from a certain threshold, indicating that the growth of the economic level reduces the impact of per capita GDP on per capita transportation energy consumption. The higher the GDP per capita, the smaller the value of elasticity. The reason is that the application of efficient transportation methods improves the efficiency of transportation energy use. At the same time, per capita GDP has not reached the inflection point of EKC under any circumstances, that is, the elasticity value is never zero, so the growth of per capita GDP within the scope of the study will not reduce per capita transportation energy consumption.

(2) The impact of urbanization on per capita traffic energy consumption. Based on the calibrated model, a case study of the impact of urbanization on per capita traffic energy consumption is carried out, and the corresponding results are shown in Table 3. Among them, the impact of urbanization on per capita transportation energy consumption can be specifically divided into two aspects: urbanization rate and population density. The corresponding policy adjustments are mainly achieved by controlling the urbanization rate and optimizing the population structure. From the context of the case, the rapid economic development has accelerated the process of urbanization in China, a large number of people have entered the urban area, and the negative effects of urbanization have also appeared.

At the same time, urbanization is a phenomenon of modern social development and economic transformation, and a key factor influencing the level of urban transportation energy consumption. The research area selected in this paper is a city with a relatively good level of comprehensive development, so its urbanization rate is relatively high, and the corresponding problems are particularly significant. For the population density of selected urban objects, it has two main characteristics. On the one hand, although the population growth rate in China has slowed down in recent years, the total population has experienced a substantial growth process since the beginning of the 21st century; on the other hand, due to the relatively good overall development level of the cities selected in this study, the population density will increase accordingly.

In the results in Table 3, the coefficient of the control variable population density is rarely negative and significant, indicating that population density is negatively correlated with per capita traffic energy consumption. When other variables remain unchanged, an increase in urban population density by 1.000% will reduce per capita transportation energy consumption by 0.512%. Urban population density has a negative impact on transportation energy consumption. First, because the traffic energy consumption studied in this paper is expressed in terms of per capita value, although the total urban traffic energy consumption is increasing, it reflects that the value of per capita traffic energy consumption is getting smaller. Secondly, the theory of economic geography believes that in the process of population concentration, the urban economy has agglomeration effect, which can improve the efficiency of energy use. Therefore, higher population density is conducive to reducing per capita transportation energy consumption.

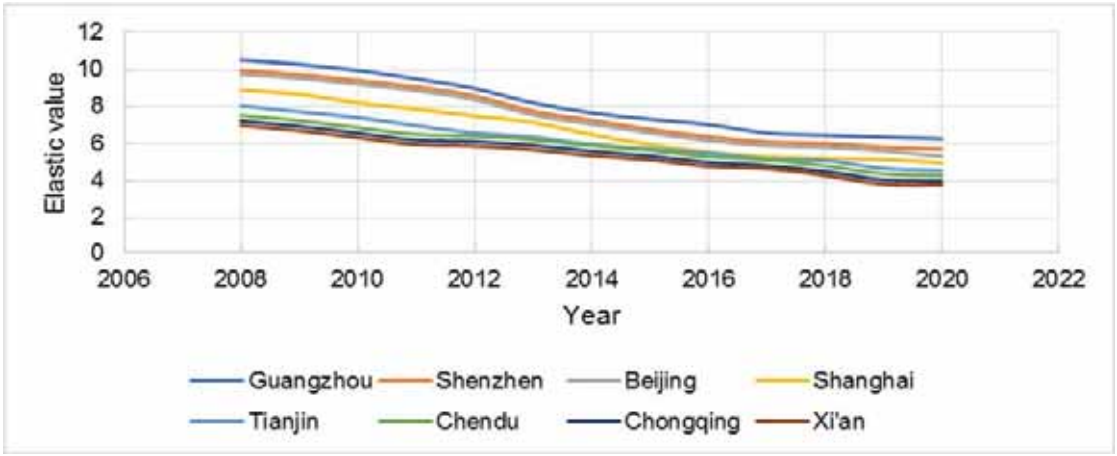

FIGURE 1
Elasticity of per capita transportation energy consumption in each city.

TABLE 3
Values of related model parameters

ΔE	0.089	$0.173\Delta\bar{Y}$	$-0.063\Delta\bar{Y}^2$	$\mathbf{-0.512\Delta\overline{PD}}$	$-0.263\Delta\overline{ES}$	$\mathbf{0.765}$ $\mathbf{\Delta\overline{UR}}$	$0.351\Delta\overline{EI}$
Std.err.	0.004***	0.036***	0.021***	**0.039*****	0.039***	**0.051*****	0.026***
Groups=10		Wald chi2(10) = 15430.832***			Turing point:	Y=1.703	
Years=13		EKC existing			lnGDPpc=12.563		

Third, in order to solve problems such as the rapid increase in the number of motor vehicles, cities have successively introduced policies such as purchase restrictions, traffic restrictions and foreign restrictions, which has gradually reduced the proportion of private car trips and shifted more to public transportation. Public transportation is more efficient than private cars, which reduces the energy consumption of transportation per capita. The coefficient Q of the control variable urbanization rate in the calculation results is positive and significant, indicating that the urbanization rate is positively correlated with per capita energy consumption. When other variables remain unchanged, an increase in urbanization rate of 1.000% will result in an increase in per capita transportation energy consumption by 0.765%.

As the urbanization rate increases, transportation energy consumption will increase accordingly. From the intuitive results, an increase in population density can reduce per capita energy consumption for transportation, while an increase in urbanization rate can increase per capita energy consumption for transportation. Combining the negative impact of population density on transportation energy consumption and the positive impact of urbanization rate on transportation energy consumption, the process of urbanization should be reasonably controlled in policy regulation, the population density in rural areas should be appropriately increased, and the overall transportation efficiency should be improved to reduce per capita traffic energy consumption. At the same time, the government should carry out regional industrial management to allow more urban populations to flow to marginal areas, and connect cities and rural areas through public transportation, so as to fully improve the utilization efficiency of transportation carriers.

(3) The impact of traffic energy intensity on per capita traffic energy consumption. This study uses the calibrated model to analyze the impact of traffic energy consumption intensity on per capita traffic energy consumption, as shown in Table 4. Corresponding policy regulation is achieved through the development of science and technology and the improvement of transportation energy efficiency. The intensity of transportation energy consumption is mainly affected by two aspects. On the one hand, advances in science and technology can improve the efficiency of transportation energy use which increases in consumption intensity. The traffic energy intensity of the cities studied in this paper has generally decreased in the sample time range, but the extent is not large. The degree of change in the traffic energy intensity of each city in the future still needs to be analyzed in conjunction with the policy and technical background. In the calculation results in Table 4, the coefficient of the intensity of traffic energy consumption is positive and significant, indicating that the intensity of traffic energy consumption is positively correlated with per capita traffic energy consumption. When other variables remain unchanged, for every 1.000% reduction in the intensity of traffic energy consumption, the per capita traffic energy consumption will also decrease by 0.351%.

TABLE 4
Values of related model parameters

ΔE	0.089	$0.173\Delta\overline{Y}$	$-0.063\Delta\overline{Y}^2$	$-0.512\Delta\overline{PD}$	$-0.263\Delta\overline{ES}$	$0.765\ \Delta\overline{UR}$	$\mathbf{0.351\Delta\overline{EI}}$
Std.err.	0.004***	0.036***	0.021***	0.039***	0.039***	0.051***	**0.026*****
Groups=10		Wald chi2(10) = 15430.832***			Turing point:	Y=1.703	
Years=13		EKC existing			lnGDPpc=12.563		

Improving energy efficiency is an inevitable general direction of industrial development, but its role in reducing transportation energy consumption is still limited. The energy efficiency of China's railway transportation and water transportation is higher than that of most countries in the world, and the road transportation is close to the standards of developed countries. However, the overall transportation energy consumption problem is still prominent. Considering the long-term economic development goals and expected population growth in the future, energy efficiency alone cannot offset the increase in transportation energy consumption. The reason lies in three aspects: first, road transportation is still the main source of energy consumption in the transportation in China, and its energy consumption is increasing year by year; second, with the updating of technology and the unification of equipment standards, the room for further improvement of fuel efficiency is smaller and smaller; third, the effect of policy control is often affected by market choices. The above-mentioned third point is particularly prominent in the auto market. The auto market in China is gradually shifting to a large-displacement type. Although the country has issued a number of policies aimed at reducing the purchase and use of heavy-duty private vehicles, more and more consumers in the market are focusing on comfort and driving experience requirements and tend to purchase large-displacement vehicles.

CONCLUSIONS

(1) Judging from the results of the overall law analysis, the urban GDP per capita and per capita transportation energy consumption are in line with the EKC relationship trend assumption. There is a weak decoupling between per capita transportation energy consumption and per capita GDP, that is, the growth rate of per capita transportation energy consumption is lower than the economic growth rate. At present, the value of per capita transportation energy consumption increases with the increase of per capita GDP, but this relationship will be reversed at a certain level of per capita GDP.

(2) From the perspective of sensitivity calculation and analysis, population density, economic structure, and traffic energy intensity are negatively correlated with urban per capita traffic energy consumption, while urbanization rate is positively correlated with per capita traffic energy intensity. When other variables remain unchanged, an increase in urban population density by 1.000% will reduce per capita transportation energy consumption by 0.512%. When other variables remain unchanged, for every 1.000% increase in the proportion of the tertiary industry, per capita transportation energy consumption will decrease by 0.263%. When other variables remain unchanged, for every 1.000% reduction in traffic energy intensity, per capita traffic energy consumption will decrease by 0.351%. When other variables remain unchanged, an increase in urbanization rate of 1.000% will result in an increase in per capita traffic energy consumption by 0.765%. Based on the sensitivity calculation results, the government can formulate relevant quantitative control policies to reduce urban per capita traffic energy consumption.

ACKNOWLEDGEMENTS

This work was not supported by any funds. The authors would like to show sincere thanks to those techniques who have contributed to this research.

REFERENCES

[1] Boerjesson, P.I.I. (1996) Energy analysis of biomass production and transportation. Biomass & Bioenergy. 11(4), 305-318.
[2] Bradley, M.J., Jones, B.M. (2002) Reducing global NOx emissions: developing advanced energy and transportation technologies. Ambio. 31(2), 141-149.
[3] Ma, Q., Luo, L., Wang, R.Z., Sauce, G. (2009) A review on transportation of heat energy over long distance: exploratory development. Renewable & Sustainable Energy Reviews. 13(6-7), 1532-1540.
[4] Zhang, M., Li, G., Mu, H.L., Ning, Y.D. (2011) Energy and exergy efficiencies in the Chinese transportation sector, 1980-2009. Energy. 36(2), 770-776.
[5] Holdren, J.P. (1991) Population and the energy problem. Population & Environment. 12(3), 231-255.
[6] Froling, M. (2011) Energy use, population and growth, 1800–1970. Journal of Population Economics. 24(3), 1133-1163.

[7] Paul, M., John, P. (2011) Estimating the energy consumption impact of casual carpooling. Energies. 4(1), 126-139.
[8] Ming, Z., Li, H., Min, Z., Mu, H. (2011) Decomposition analysis of energy consumption in Chinese transportation sector. Applied Energy. 88(6), 2279-2285.
[9] Kelly, J., Haider, W., Williams, P.W. (2007) A behavioral assessment of tourism transportation options for reducing energy consumption and greenhouse gases. Journal of Travel Research. 45(3), 297-309.
[10] Edwards, J.L., Schofer, J.L. (1977) Relationships between transportation energy consumption and urban structure: results of simulation studies. Transportation Research Record. 599, 52-59.
[11] Jia, S., Peng, H., Liu, S., Zhang, X. (2009) Review of transportation and energy consumption related research. Journal of Transportation Systems Engineering & Information Technology. 9(3), 6-16.
[12] Jia, S., Mao, B., Liu, S., Sun, Q. (2010) Calculation and analysis of transportation energy consumption level in China. Journal of Transportation Systems Engineering & Information Technology. 10(1), 22-27.
[13] Zhou, Q., Si, M.A., Luo, Y. (2012) Harmonious relations of transportation energy consumption in integrated transport development. Journal of Transportation Systems Engineering & Information Technology. 12(4), 11-16.
[14] Kim, C.K., Chung, K., Kim, Y., Lee, K.D. (2015) The effects of transportation energy policy on fuel consumption and transportation safety. Multimedia Tools and Applications. 74(7), 2535-2557.
[15] Sukarno, I., Matsumoto, H., Susanti, L. (2016) Transportation energy consumption and emissions - a view from city of Indonesia. Future Cities & Environment. 2(1), 1-11.
[16] Dinda, S. (2005) A theoretical basis for the environmental Kuznets curve. Ecological Economics. 53(3), 403-413.
[17] Luzzati, T., Orsini, M. (2009) Investigating the energy-environmental Kuznets curve. Energy. 34(3), 291-300.
[18] Agras, J., Chapman, D. (1999) A dynamic approach to the environmental Kuznets curve hypothesis. Ecological Economics. 28(2), 267-277.
[19] Meng, Y., Pu, J., Zhao, W.J., Sun, G.J., Chen, W.K. (2021) The relationship between air quality and economic growth based on the environmental Kuznets curve -taking Sichuan province as an example. Fresen. Environ. Bull. 30(7A), 9355-9362.
[20] Yue, Y., Ying, Y.R. (2021) Analysis of china's environmental Kuznets curve from the perspective of PM2.5 index. Fresen. Environ. Bull. 30(5), 5262-5269.
[21] Leng, J.F., Yuan, L.D. (2021) An empirical analysis of the environmental Kuznets curve in the Huaihe River Basin. Fresen. Environ. Bull. 30(7), 9355-9362.

Received: **04.12.2021**
Accepted: **23.01.2022**

CORRESPONDING AUTHOR

Youqing Liu
Faculty of Engineering,
Imperial College London,
London SW72AZ – UK

e-mail: mingshangxin89@126.com

© by PSP Volume 31– No. 05/2022 pages 5159-5166 Fresenius Environmental Bulletin

APPLICATION OF BP NEURAL NETWORK MODEL BASED ON SIMULINK IN REGIONAL WATER QUALITY PREDICTION

Yi Zhang*

Anhui Jianzhu University, Anhui, Hefe, Anhui 230601, P.R. China

ABSTRACT

River water quality simulation is an important technical means to inform decision-making processes and scientific management of the water environment. Based on the visualisation function of Simulink combined with the black-box learning mode of the BP network, after repeated training and verification, a BP neural network model based on Simulink was established in this paper. This model avoids the limitations and temporariness of BP network models in past research, expanding the application of this model. Based on the hydrological characteristics of the Moshui River, the water quality of the Moshui River's estuary was simulated and predicted. The study showed that when the pollutant discharge at the estuary is less than the predicted result (COD& S195.6 mg/L, ammonia nitrogen S45.5 mg/L), the water quality of the Moshui River will not be the main reason for changes in the water quality of Jiaozhou Bay. The water quality of the upper section of the Moshui River is relatively good. With changes to the functional area of each monitoring section, the downstream identification index is relatively large and the degree of pollution is aggravated. The main pollution factors are CODcr and ammonia nitrogen. The maximum allowable discharge of CODCr is 2639.74 t/a and that of ammonia nitrogen is 138.48 t/a. To protect the water quality of the river and mitigate damage and pollution, the area's pollutant discharge volume should be controlled below the maximum allowable discharge volume.

KEYWORDS:
BP neural network, Simulink, water quality prediction, pollutant discharge, river

INTRODUCTION

Water pollution control is one of the most serious and difficult problems currently faced by society. More than half of the rivers in the seven major water systems are polluted. 90% of urban waters are seriously polluted, 50% of urban water sources do not meet drinking water standards, and 40% of water sources are no longer drinkable [1-5]. The water environment is a complex ecosystem, and the quality of water is affected by many factors. Pollution is not reduced but increased in the long-term treatment, mainly due to the neglect of regional environmental capacity, the mutual promotion between water pollution and disasters, and the increase of domestic sewage [6, 7]. In the process of water pollution prevention and control, due to the limitations of single factor control and the mechanical shortcomings of water quality simulation tools, the simulation results can not objectively reflect the real situation of water environment system, resulting in the lack of pertinence of pollution prevention and control decisions. The computer software is the frontier of complex nonlinear science and artificial intelligence science [8-10].

BP networks are commonly used in the field of water environment research. They have been extensively applied and their application is relatively mature. However, research applying the Simulink toolbox in the field of water pollution control is still in its infancy [11]. Therefore, development of a water quality simulation model with strong adaptability and accurate prediction of river water quality has become a research priority. Zhang et al. [12] divided the development of water quality models into three stages based on model complexity: a simple oxygen balance model stage, a morphological model stage, and a multi-medium environment comprehensive ecological model stage. Hamarash et al. [13] analysed the sources of uncertainty in the simulation optimisation model and found that the discharge of pollutants and the background value of the river are random. Ran et al. [14] applied the fuzzy comprehensive evaluation method to the mainstream of the Huai River to evaluate the water environment quality. He et al. [15] established a model for comprehensive water quality evaluation, and tested the accuracy of the model with water quality data from the Fengzui River in Nanchuan, Chongqing as an example. Rosen et al. [16] divided water quality evaluation into three levels and then qualitatively judged which level of water quality it belongs to according to the proximity between the output value and the expected value. Xie et al. [17] used a five-layer BP network to qualitatively describe the water quality by level as serious pollution, medium pollution, clean, etc., and

quantified it numerically. 0 or 1 respectively indicates that it does not belong to or belongs to this pollution level, so as to comprehensively evaluate the water quality. Ni et al. [18] used the GA-BP model to evaluate groundwater quality and obtained good evaluation results. Tiwari et al. [19] used the grey prediction method to predict water quality, and the results show that the larger the grey level of the data, the lower the prediction accuracy. In order to improve the accuracy of water quality prediction, Wichelns et al. [20] proposed a water quality prediction model based on a weighted combination, a combination exponential smoothing method, and a GM (1,1) model. However, the researchers could not solve the problem of excessive errors. BP neural networks have several advantages, including a strong nonlinear prediction ability, self-learning capacity and fault tolerance, and these networks are widely used in water quality prediction. Gupta et al. [21, 22] applied a BP neural network to water quality evaluation and studied the spatiotemporal evolution trend in water quality. Some researchers compared this method with the comprehensive index evaluation method and found that the BP neural network evaluation process was more convenient, and the evaluation results were more objective. Aiming at the problems of low prediction accuracy and easy to fall into local optimization of small sample data of BP neural network, Sniders et al. [23] proposed a water quality prediction model based on the artificial bee colony algorithm with a double hidden layer BP neural network. Cox et al. [24] improved the cloud model theory based on the inertia weight of PSO and proposed a cloud model PSO algorithm (Cloud Particle Swarm Algorithm, CPSO) to optimise the water quality prediction of the BP neural network model. Li et al. [25] used the moments of random variables to represent the colour distribution characteristics of an image according to probability theory. In an image, the colour information has a certain probability distribution, and the colour information distribution can be described by the method of moments. However, Xie et al. [26] analysed the effectiveness of each order feature of the colour moment in their water quality evaluation research, and found that the water quality detection accuracy rate was less than 90%.

Based on the current research status of water quality simulation and the superiority of Simulink, this paper studied the BP network modelling method and applied it to water quality simulation. Based on the evaluation of the current water quality of the studied rivers, the findings indicated that the water quality models based on BP neural network model can simulate and predict the water quality of the Moshui River. These findings have certain theoretical significance and practical reference value.

MATERIALS AND METHODS

The process to establish the basic BP network model was as follows: the input layer neurons of the model network select the water quality monitoring data of Yanxia bridge (1# monitoring point), zhangjiaxicheng (2# monitoring point), Shiqiao (3# monitoring point) and sewage outlet (5# monitoring point) from 2011 to 2015, that is, the training samples of the network. The monitoring section data at the entrance to the sea (4# monitoring point) was used as the output of the network to simulate and predict the main pollutants. In order to verify the model, the water quality monitoring data in 2016 and 2017 were used as test samples to verify the accuracy of the network [27, 28]. The samples from 2011 to 2015 were selected to train the network and the known samples from 2016 to 2017 were used to test the network. The initial learning rate *Ti* was the default value of 0.01, the number of operations was 2000, and the allowable accuracy was 0.0001. Because the BP network is characterised by a black box, it can be applied to non-linear prediction and other fields, and can be used to establish the response relationship between input and output variables through internal learning and training [29-31]. Thus, it can be used for simulation and prediction of the main pollutants in the river. Separate training models for the main pollutants of CODCr and ammonia nitrogen were established. In the water quality monitoring data from 2011 to 20017, there were large differences in the magnitude of the multi-dimensional input sample number data, and due to this, the training samples and the monitoring data of each point were normalised using the Prestd function in Matlab. The data were normalised into unit mean and zero mean to unify the change range of an index, improve the training efficiency of the network, and avoid influences on the network recognition accuracy due to these differences in magnitude [32, 33]. Then, the Poststd function was used to achieve normalised data recovery.

RESULTS AND DISCUSSION

Training process. In the network training stage, the alternate method of training and testing was used for model learning. Based on the preliminary determination of the network model parameters, such as the learning rate, target error accuracy and learning times, the number of hidden layer nodes of the network model was selected. The training process was divided into four parts: network initialisation, network establishment, training and testing, and network operation results error analysis. (1) Network initialisation. First, the input samples of the network were selected, including the input vector p (p-test) of the training sample and the test sample and the target output vector t (t-test). Then, the sample data were

normalised using the prestd function in MATLAB. The network used random assignments for weights and thresholds. The training sample comprised the monitoring data from 2011 to 2015, and the test sample comprised the monitoring data from 2016 to 2017. The input was the index data (chemical oxygen demand and ammonia nitrogen) from the four sections of the river: Yanxia Bridge, Zhangjiaxicheng, Shiqiao and the sewage outlet. The output was the index value at the entrance to the sea. (2) Establish a network. The NewfF function was used to establish the network structure. The learning rate was the default value and the number of hidden layer nodes was [3, 16]. Through network training and testing, to the transfer function, display frequency (default value 25), training times (according to 2000 training times) and target accuracy (0.0001) of the network were determined, respectively. (3) Training and testing the network. According to the input training samples and test samples, the train function was used to train and test the network, respectively, and the results of the training and testing were normalised and restored using the Poststd function.

Error analysis of network operation results. 3 to 16 training and test results were obtained corresponding to each hidden layer node. Based on the network operation results, the relationship curve between the number of hidden layer units and error was established and the best number of hidden layer nodes and the weight and threshold of the network were determined. As can be seen from Figure 1, in the process of network training and testing, increasing the number of hidden layer nodes can reduce the number of training errors but after more than 10, the training error and testing error will fluctuate, that is, the generalization ability will change. By comprehensively comparing the change trend and relevant experience, it is determined that the number of hidden layer nodes of CODCr and NH_3-N network structure is 7 and l00 respectively. After network training, when the number of training times for the chemical oxygen demand network reached 100 and the number of training times for ammonia reached 91, the model best met the set requirements. The training process is shown in Figure 2.

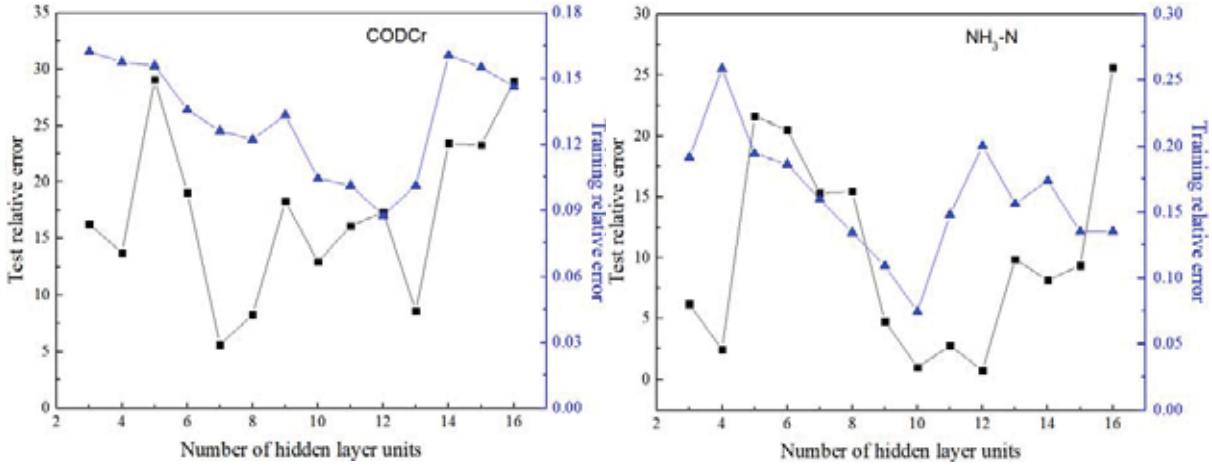

FIGURE 1
Relationship between CODCr/NH_3-N hidden layer node number and error

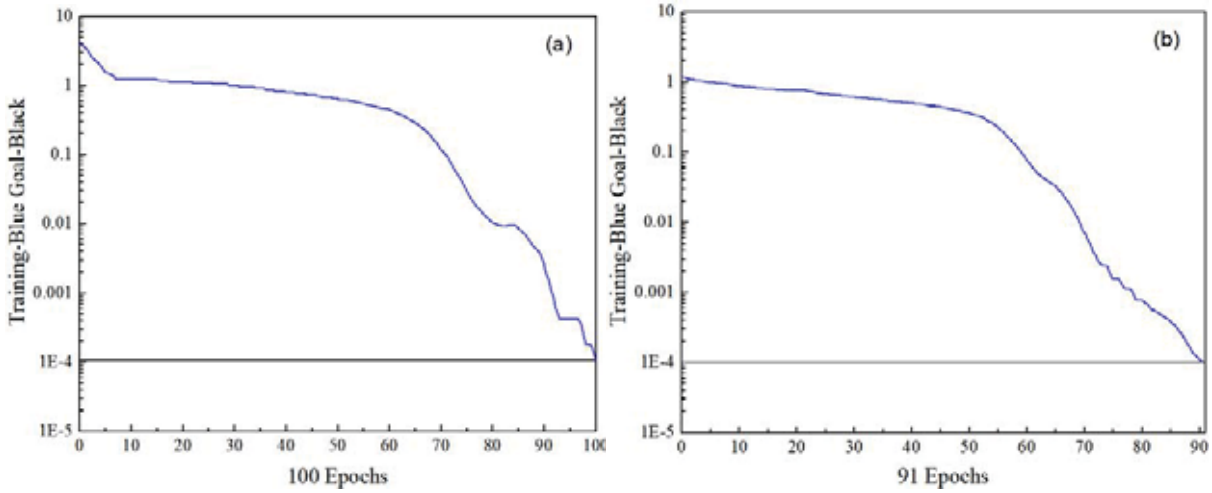

FIGURE 2
Training error of CODCr and NH_3-N in neural network model

It can be seen that when the number of hidden layer nodes for CODCr and ammonia nitrogen was 7 and 10, respectively, the training and test error performance were the best. The CODCr prediction value training error was 0.126% and the test error was 5.34%. For ammonia nitrogen prediction, the absolute training error value was 0.074% and the test error was 0.9%. From the training and test results of the network, it can be seen that the prediction error of the neural network for the training sample itself is very small, but for the untrained test sample, the prediction error is higher. This is because theoretically, the neural network method is based on the principle of empirical risk minimisation, which emphasises the minimisation of empirical risk; that is, it has good memory of learning and training samples. These results provide preliminary evidence suggesting that the network model may be suitable for water quality prediction. The applicability and reliability of this model must be verified by adjusting the relevant parameters of the existing input and output responses from 2016 to 2017 in order to find the best values of network weights and thresholds.

Verification of the BP network model. In order to demonstrate the suitability of this model for water quality prediction, the BP network model and Simulink model were utilised. First, the BP model was used for verification to obtain the optimal network weights and thresholds. The trained network was used to test and simulate the data in 2016 and 2017. The number of hidden layer nodes of the CODCr and ammonia nitrogen network models was 7 and 10, respectively, and the actual monitoring data of the Mozi River estuary in 2016 and 2017 were used as the test data for the network model. The Yanxia Bridge, Zhangjiaxicheng, Shiqiao and the sewage outlet data were used as the network input to predict the index concentration value at the entrance to the sea and to evaluate the relative error between the predicted output and the actual value. If the error accuracy meets the requirements, this would demonstrate that the model is applicable. Otherwise, the model structure would need to be re-adjusted to establish a new model. The prediction results are shown in Table 1 and Figure 3. The chemical oxygen demand verification results error values were 13.4% and 18.8%, respectively, and the ammonia nitrogen verification results error values were 1.88 % and 10.26%. When using computer simulation to simulate actual problems, the verification relative error should be less than 30%. Thus, the calculation results meet the research requirements, and the built model is suitable for river water quality prediction and simulation. Taking the sample data from 2016 to 2017 as the input, the consistency of the results was analysed under the operating conditions of the two modes. This was to verify the reliability and applicability of the Simulink model in the established BP network.

TABLE 1
Validation error of BP model

Index results	2016		2017	
	CODCr	NH_3-N	CODCr	NH_3-N
Measured value	167.17	20.367	138.00	17.041
Predictive value	189.62	20.75	163.94	18.79
Relative error (%)	13.4	1.88	18.8	10.26

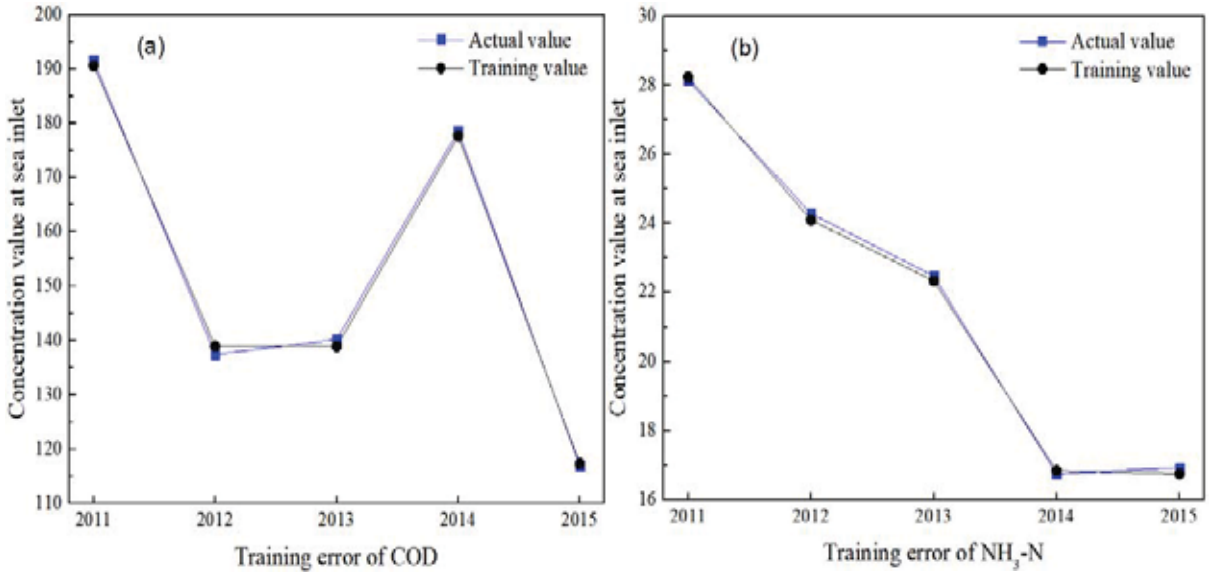

FIGURE 3
Training results of CODCr and NH_3-N

TABLE 2
Validation error of BP model

Index results		2016		2017	
		CODCr	NH_3-N	CODCr	NH_3-N
Automatically generated Simulink model	Measured value	167.17	20.367	138.00	17.041
	Predictive value	189.62	21.25	163.94	18.79
	Relative error (%)	13.4	4.35	18.8	10.26
Established Simulink model	Measured value	167.17	20.367	138.00	17.041
	Predictive value	192.25	21.39	105.29	18.92
	Relative error (%)	15	5.03	23.7	11.01

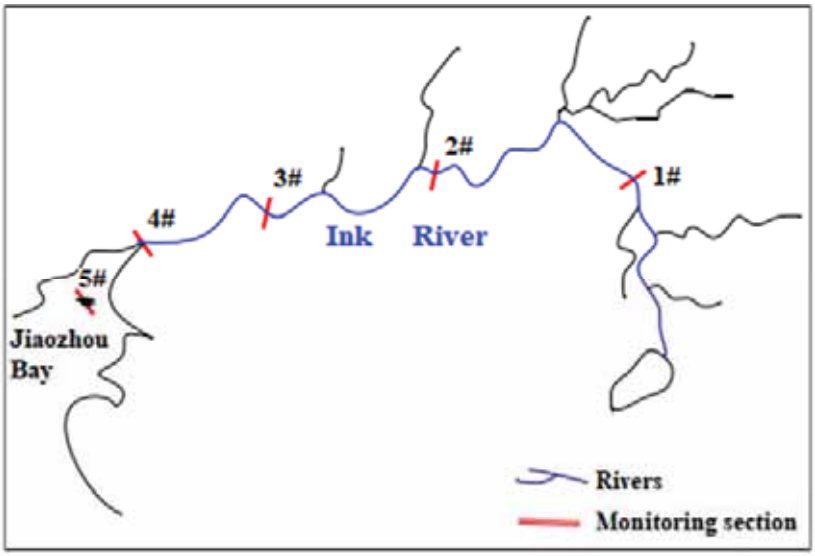

FIGURE 4
Sketch map of each monitoring section of Ink River

Applicability verification of Simulink model of BP network. After training the network, the connection weight matrix between each layer and the threshold value of each layer were determined simultaneously. However, in order to determine whether this model can be used in practice and will achieve the expected purpose, the model must be verified. The process of network verification involves the use of test samples instead of training samples as network input. Then, the network output is calculated and the error between the output and the test sample target are compared. If the test accuracy meets the requirements, it can be concluded that the model can be used for prediction. Otherwise, the model needs to be rebuilt. The BP network has been verified before and the obtained error accuracy was not large. Here, the Simulink model was used for visual simulation verification of the network. The water quality data from 2016 and 2017 were input into the established Simulink model for verification. The verification simulation results are shown in Table 2. It can be seen that the simulation results of the two methods have a certain degree of error, but the error is small. This is because the network is automatically generated by the network, its input is the data after normalization, while the input of the Simulink model is the data before normalization. Nonetheless, this error is within the allowable range. Thus, comparing this verification result with the verification result of the BP network model demonstrates that the BP network model based on Simulink established in this paper has certain applicability.

Application of water quality simulation prediction model. After training and verification of the Simulink-based BP network model, it is clear that the training and verification errors meet the design requirements. The input of this paper is the standard values of the functional areas of the four monitoring sections: Yanxia bridge 1# point, zhangjiaxicheng 2# point, Shiqiao 3# point and the 5# point at the outlet of the ink River into Jiaozhou Bay. The output was the pollutant discharge status at point 4# at the outlet of the Mohui River. The relative position of each monitoring point in Mok Hanoi is shown on a map of the river in Figure 4. Since each monitoring section of the Moshui River belongs to different functional areas, here, the water quality standards of each section were brought into the network and the main pollutants in the water pollution control area at the mouth of Moshui River were predicted. The standard values of the functional areas of each section were substituted into the model and predictive simulation was performed. The results are shown in Table 3.

TABLE 3
Prediction results of water quality at the mouth of ink River

Number	Monitoring function zoning	Category	CODCr	Ammonia nitrogen
1	Drinking water source area	III	20	1.0
2	Landscape entertainment water area	IV	30	1.5
3	Agricultural water area	V	40	2.0
5	Aquaculture area	II	3(CODMn)	0.3 (DIN)
4	Pollution mixing area at sea inlet		195.6	45.5

The standard values of the functional areas of monitoring points 1#, 2#, 3# and 5# were imported into the model as the input of the model; the water quality of the 4# point was predicted and simulated, and the above prediction results were used to determine pollutant discharge. It can be seen that when each functional area met the surface water environmental quality standards, the main pollutant prediction results of the pollution control area at the entrance to the sea were: CODCr ≤ 195.6 mg/L and ammonia nitrogen ≤ 45.5 mg/L. The results show that when the pollutant discharge at the mouth of the sea is less than the predicted result, the water quality of Moshui River will not be the main reason for the water quality change at Jiaozhou Bay.

CONCLUSIONS

In this study, the Moshui River Basin was employed as the study object and various calculation models and calculation parameters were evaluated in order to predict the concentration limit of the Moshui River's inlet to the sea under the assumption that the upstream functional areas and the sewage outlets in Jiaozhou Bay meet the required standards. The following main conclusions can be drawn: By using the comprehensive water quality labelling index method to evaluate and analyse the current water quality of the Moshui River, it can be seen that the water quality of the upper section of the Moshui River is relatively good. With changes to the functional area of each monitoring section, the downstream labelling index is relatively large and the degree of pollution is aggravated. The pollutant index was increased in 2017 and the overall pollution tended to increase. The main pollution factors were CODcr and ammonia nitrogen. Using the Simulink BP network model to simulate the water quality of the Moshui River, under the assumption that the sections of the upstream functional areas of the Moshui River and the sewage outlets in the bay meet the required standard of the functional areas, the following prediction results for the main pollutants in the inlet were obtained: CODcr ≤ 195.6 mg/L and ammonia nitrogen ≤ 45.5 mg/L. When the pollutant discharge at the entrance to the sea is less than the predicted result, the water quality of Moshui River will not be the main reason for the water quality change of Jiaozhou Bay. Based on the one-dimensional Simulink model, the water environment capacity of Moshui River was quantitatively calculated. The maximum allowable sewage discharge volume of the Moshui River was calculated to be 2639.74 t/a for CODCr and 138.48 t/a for ammonia nitrogen.

ACKNOWLEDGEMENTS

This study was no funds supported.

REFERENCES

[1] Jiang, T., Zhou, T.S., Han, L.Y. (2019) A nearest neighbor intrusion detection algorithm based on perceptual hash matrix. Acta Electronica Sinica. 47(7), 1538-1546.
[2] Gao, Y., Yan, P. (2016) Unified optimization based on multi-swarm PSO algorithm and cuckoosearch algorithm. Control and Decision. 31(4), 601-608.
[3] Su, C.H., Xiang, N., Chen, G.Y., Cai, K. (2012) Water quality evaluation model based on artificial bee colony algorithm and BP neural network. Journal of Environmental Engineering. 6(2), 699-704.
[4] Liu, D., Li, S., Fu, Q., Liu, J.Z., Long, C. (2018) Comprehensive evaluation method of groundwater quality based on BP network optimized by krill herd algorithm. Transactions of the Chinese Society of Agricultural Machinery. 224(9), 275-284.
[5] Liu, D.J., Zou, Z.H. (2012) Application of weighted combination model on forecasting water quality. Acta Scientiae Circumstantiae. 32(12), 3128-3132.
[6] Binayak, B., Shiva, R., Poudel, K. (2014) Mathematical modeling of hybrid renewable energy system: a review on small hydro-solar-wind power generation. International Journal of Precision Engineering and Manufacturing-Green Technology. 1(2), 157-173.
[7] Furlong, B.V., Riley, M.S., Herbert, A.W., Ingram, J.A., Mackay, R., Tellam, J.H. (2011) Using regional groundwater flow models for prediction of regional well water quality distributions. Journal of Hydrology. 398(2), 1-16.
[8] Kaur, M.N., Gupta, M.P., Saini, M.A. (2016) Assessment of water quality parameters for regional water samples. Journal of Environmental Engineering. 127(9), 1211-1219.

[9] Liu, D.J., Zou, Z.H. (2012) Simulation models for the river system recharged with reclaimed water based on Simulink. Systems Engineering. 30(5), 107-111.
[10] Pradhan, B., Abokharima, M.H., Jebur, M.N., Tehrany, M.S. (2014) Land subsidence susceptibility mapping at Kinta valley (Malaysia) using the evidential belief function model in GIS. Natural Hazards. 73(2), 1019-1042.
[11] Xu, M., Yan, F., Liu, Z.Z., Liu, M., Zou, S.W. (2016) Forecasting of water quality using grey GM (1,1)-Wavelet-GARCH hybrid method in Songhua River basin. Transactions of the Chinese Society of Agricultural Engineering. 32(10), 137-142.
[12] Zhang, C., Luo, Y., Liu, P. (2012) Application of grey metabolism GM (1, 1) in the quality prediction of water in main stream Yangtze River. Environmental Impact Assessment. 34(4), 11-14.
[13] Hamarash, I.I. (2018) Modeling and simulation of the perdawd ccgs connected to the kurdistan regional power system of Iraq using simulink. Lecture Notes in Engineering & Computer Science. 217(1), 1365-1378.
[14] Ran, Y.P., He, W.S., Lei, X.H. (2011) Application of GM (1,1) Model and Improved model to predict the water quality of Weihe river in Tianshui section. Journal of Water Resources and Water Engineering. 22(5), 88-91.
[15] He, Y., Tang, Y., Chen, L.Y., Pan, Y., Lu, M.Z. (2018) Evaluation of water quality based on BP neural network and study of the temporal and spatial evolution. Environmental Protection Science. 9(3), 17-22.
[16] Rosen, C., Vrecko, D., Gernaey, K.V., Pons, M.N., Jeppsson, U. (2016) Implementing adm1 for plant-wide benchmark simulations in Matlab/Simulink. Water Science & Technology. 54(4), 111-119.
[17] Xie, R., Huang, J., Qi, Z. (2018) Spatial sensitivity analysis of urban river water quality model for Nanfeihe river. Water Purification Technology. 21(8), 89-96.
[18] Ni, C., Yang, H., Pan, N., Lu, S., Ge, X., Jian, L. (2014) Discussion on strategy for water quality monitoring after regional water supply in Taihu region. Journal of Environmental Hygiene. 56(11), 651-659.
[19] Tiwari, K., Goyal, R., Sarkar, A. (2017) GIS-based spatial distribution of groundwater quality and regional suitability evaluation for drinking water. Environmental Processes. 336(7), 2251-2259.
[20] Wichelns, D. (2017) Volumetric water footprints, applied in a global context, do not provide insight regarding water scarcity or water quality degradation – science direct. Ecological Indicators. 74(9), 420-426.
[21] Gupta, S., Gandhar, A., Gandhar, S. (2018) Modelling and performance analysis of grid connected photovoltaic power systems. Journal of Water, Environment and Pollution. 15(3), 73-78.
[22] Hashem, R.A., Soliman, Y., Al-Sharm, S., Massoud, A. (2018) Design of an electric spring for power quality improvement in PV-based DC grid. 17(9), 156-161.
[23] Sniders, L., Komass, V.M. (2016) Invariant control of the technological plants to compensate an impact of main disturbances preemptively. Latvian Journal of Physics and Technical Sciences. 53(3), 34-44.
[24] Cox, W.E. (2015) Regional water-supply development and CWA section 404. Water resources planning and management and urban water resources. ASCE. 552(8), 2563-2572.
[25] Li, J., Yu, X., Wang, J., Huang, S. (2016) Coupling performance analysis of a solar aided coal-fired power plant. Applied Thermal Engineering. 106(5), 613-624.
[26] Xie, R., Huang, J., Qi, Z. (2018) Spatial sensitivity analysis of urban river water quality model for Nanfeihe river. Water Purification Technology. 22(7), 82-90.
[27] Ruan, M. (1997) Modelling sewer emission using Simulink. Water Science & Technology. 36(5), 185-192.
[28] Ye, C.M. (1993) Research progress in mathematical model of water environment. Advances in Environmental Science. 21(1), 74-80
[29] Xu, Z.X, Liao, Z. (2003) The development stage and spatial level of water quality mathematical model research. Environmental Science. 22(2), 79-85.
[30] AndrewsK, T., Babrara, J.L. (1999) Surface water quality management using a multiple-realization chance constrained method. Water Resources Research. 35(5), 1657-1669.
[31] Chuan, H.Y., Miao, Q., He, H. (2007) Application of fuzzy comprehensive evaluation in water environmental quality assessment. Journal of Qingdao University of Technology. 28(2), 68-71.
[32] Li, D., Wu, S., Liu, L., Liang, Z., Li, S. (2017) Evaluating regional water security through a freshwater ecosystem service flow model: a case study in Beijing-Tianjian-Hebei region, China. Ecological Indicators. 81(10), 159-170.
[33] Li, Z., Zhang, Q., Liao, H. (2018) Efficient-equitable-ecological evaluation of regional water resource coordination considering both visible and virtual water. Omega. 77(3), 562-573.

Received: **05.12.2021**
Accepted: **23.01.2022**

CORRESPONDING AUTHOR

Yi Zhang
Anhui Jianzhu University,
Anhui Hefe, Anhui 230601 – P.R. China

e-mail: jackzheng1@126.com

© by PSP Volume 31– No. 05/2022 pages 5167-5175 Fresenius Environmental Bulletin

APPLICATION OF Z-INDEX METHOD TO FLOOD DISASTER EARLY WARNING IN THE LOWER YELLOW RIVER

Jiahu Wang[1,*], Rongsheng Ying[1], Yan Feng[2], Abbos Yuldoshev[1]

[1]School of Hydrology and Water Resources, Hohai University, Nanjing, Jiangsu 210098, China
[2]Hydrology Bureau of Songliao Water Conservancy Commission (Information Center), Changchun, Jilin 130021, China

ABSTRACT

In this study, we collected the the daily precipitation data of 10 stations, and analyzed the sediment delivery pattern of 150 floods in the lower Yellow River from 1968 to 2007. Z-index method was innovatively applied to flood disaster early warning in the Lower Yellow River. The sediment delivery characteristics, flood time distribution characteristics and basin floods in the river was investigated respectively. The results showed that the sediment delivery ratio (SDR) decreases rapidly with the increase of average sediment concentration and average sediment coefficient, and there is an optimal flood level to maximize the sediment delivery rate. The sediment delivery ratio of the flood is negatively correlated with the maximum sediment concentration of the flood. When the maximum sediment concentration C_{max} is greater than 300 kg/m^3, the SDR is less than 0.50, indicating that the sediment delivery volume of high sediment concentration flood is relatively low. In terms of time distribution, the flood in the lower Yellow River mainly occurs from late June to early July and late August, and may also occur in mid-April and early October. From the perspective of basin flood index, each flood process can be reflected in the flood index, and its intensity can also be well matched. In addition, the flood index is reflected in the day before the occurrence of floods at all grades, which shows that the Z-index method has a certain prospect in predicting flood disasters.

KEYWORDS:
Yellow River, sediment delivery, Z-index method, flood disaster, early warning

INTRODUCTION

The lower Yellow River is a flood disaster prone area. Obvious flood disasters occur every 4 years, and severe flood disasters occur every 10 years on average [1-3]. Flood disasters occur frequently, which directly affects the safety of people's lives and property [4, 5]. Summer (June to August) is the most frequent period of floods in the lower Yellow River. Summer precipitation in most areas accounts for 35%-50% of annual precipitation [6]. Large scale rainfall is the direct cause of flood. In the study of flood disaster, the selection of flood index is very important. Z-index method is a kind of index used to characterize the grade of flood, which can objectively reflect the degree of flood disaster, and is widely used in the study of flood disaster [7-10].

It is necessary to determine the impact of precipitation on flood disaster through flood index. In order to analyze the flood situation and master the flood characteristics, many scholars have been studying the determination the index of flood. Zhou et al. [11] analyzed the common index of flood and proved that the flood year determined by Z-index can objectively reflect the historical flood situation. Wu et al. [12] used different methods such as Z-index and different time scales for comparative analysis. The results showed that Z-index has a good application effect on flood monitoring in China and can be used as a better method for flood monitoring. Yin et al. [13] optimized the Z-index method, and the optimized Z-index better reflected the actual flood situation in Yulin area of northern Shaanxi. Cheng et al. [14] analyzed the precipitation data of 58 years in the west of Jilin Province, selected Z-index as the flood evaluation index, obtained the drought and flood distribution types and occurrence probability of typical years in the west of Jilin Province by Monte Carlo simulation. Finally, the drought and flood years in the west of Jilin Province were predicted by using the combination model of Z-index method and wavelet-BP neural network. Agrawal et al. [15] studied the type differences of flood disasters, put forward three flood water level evaluation indexes: Chongqing single station flood index, zoning index and regional flood index Chongqing flood disaster causes, distribution and variation of in-depth research and analysis, and the temporal and spatial distribution characteristics of floods in Chongqing are systematically described. Meng et al. [16] analyzed the precipitation data of 53 meteorological stations in Liaoning Province from 1973 to 2002, selected the data of 8 typical representative stations, and compared the three drought and flood evaluation indexes of precipitation anomaly percentage, humidity index and Z-

index. Finally, an improved Z-index model is obtained and used as a flood evaluation index. Cao et al. [17] compared the standardized precipitation index (SPI), precipitation anomaly percentage and Z-index according to the monthly precipitation data of 83 meteorological stations in Huanghuai area from 1961 to 2013. On this basis, they reclassified the flood grade standard of Z-index, redetermined the flood index of the region, calculated the flood grade of Huanghuai area according to the new index, and reclassified the flood year. Jiang et al. [18] analyzed the precipitation data of Qingdao in the past 50 years with Z-index as the evaluation index, and pointed out that Z-index can better reflect the changes of flood in Qingdao. At the same time, they also pointed out that the drought and flood disasters in Qingdao have obvious stage and group characteristics.

Based on the precipitation data for 10 consecutive days, this study proposed to use it as the calculation object of flood Z-index in the lower Yellow River. Compared with conventional methods, the occurrence and development of flood disasters are analyzed, and the flood disaster index is discussed. Z-index method has a significant forward-looking effect on the flood forecasting of the lower Yellow River under the characteristics of flood and sediment delivery, and can play an important role in the warning of flood disasters in the lower Yellow River.

MATERIALS AND METHODS

According to the daily precipitation data of 10 stations in Hekou town and Jiahetan from April 1968 to October 2007. The forward recursive sliding calculation method is used to calculate the daily precipitation for 10 consecutive days (for example, the precipitation for 10 consecutive days on July 10 is the cumulative value from July 1 to 10), and then the long-term precipitation series of each month are constructed respectively. The above Z-index calculation method is used to calculate any Z-index with precipitation for 10 consecutive days. At the same time, the traditional monthly Z-index is calculated. When the precipitation flood index is obtained for 10 consecutive days, it can better reflect the monthly flood level. Compared with the traditional monthly data calculated Z-index is more convenient.

Yin et al. [19] proved that the fitting effect of Person Ⅲ precipitation distribution is good in a certain period. The Z-index assumes that the precipitation follows the Person III distribution. This also provides a theoretical basis for Z-index to calculate precipitation in any 10 days. By normalizing the precipitation data, the probability function Person III distribution can be transformed into standard normal distribution, where Z is the variable. The normal distribution curve of Z variable is divided into four grades (heavy, moderate, light, and normal), and determine the corresponding Z boundary value.

RESULTS AND DISCUSSION

Characteristics of water-sediment combination. Flood characteristics include water volume and its process and sediment volume and its process [20-22]. In order to describe the water-sediment combination characteristics of flood, it can be expressed by sediment concentration C_{mean}, average flow Q and incoming sediment coefficient R_c. According to the data of 150 floods, we draw the relationship between SDR, C_{mean} and R_c and sediment delivery ratio (sediment discharge ratio) in each flood, as shown in Figure 1. It can be seen that SDR increases and decreases rapidly with C_{mean} and R_C, which indicates that compared with water volume, the larger the amount of sand, the smaller the sediment delivery ratio of the river. The relationship is nonlinear, that is, the straight line is C_{mean} = 35 kg/m^3, R_C = 0.015 kg·s/m^3. The relationship in the figure can be represented and fitted by lines with different slopes. The above two turning points reflect some critical conditions in the relationship between sediment delivery rate and water-sediment combination. When C_{mean} is less than 35 kg/m^3 or R_C is less than 0.015 kg/m^3, the flood sediment delivery efficiency increases sharply, and the transmission ratio corresponding to this critical point is about 0.70.

Characteristics of flood flow. Figure 2 shows the relationship between the sediment delivery ratio and the total amount and average flow of flood runoff for 150 floods in the lower Yellow River. Although the points are scattered, there is still a certain trend. As can be seen from Figure 2(a), there is a maximum SDR, and the corresponding runoff is about 3 billion m^3. It can be seen from Figure 2(b) that when the flow is 4,000 m^3/s, the maximum value of SDR may appear. These two relationships show that there is an optimal flood discharge level to maximize the sediment delivery rate.

Sediment delivery characteristics of floods from different sources. According to the 150 flood data, the diagram of the relationship between the sediment discharge and the sediment delivery ratio of the flood is drawn, as shown in Figure 3. In order to reveal the difference of flood sediment delivery characteristics in different water and sediment source areas, different water and sediment sources are represented by different symbols. When the water in a water source area accounts for more than 40% of the total flood runoff, it is considered that the flood comes from that area. It can be seen that most of the points from the sandy coarse sand area are located below 0.60, indicating that the flood transmission ratio in the source area is less than 0.60. Most of the points in the clear water area above Hekou town are located above the straight line and on the left side of the straight line (Q_s is 300 million tons), indicating that the flood transmission ratio in the

clear water area above Hekou town is mostly greater than 0.60. It can also be seen from the figure that most points representing the flood in the sandy fine sand area are located on the straight line (SDR is 0.50) or higher, indicating that the transmission ratio of flood in this area is smaller than that in the clear water area above Hekou town and larger than that in the sandy coarse sand area.

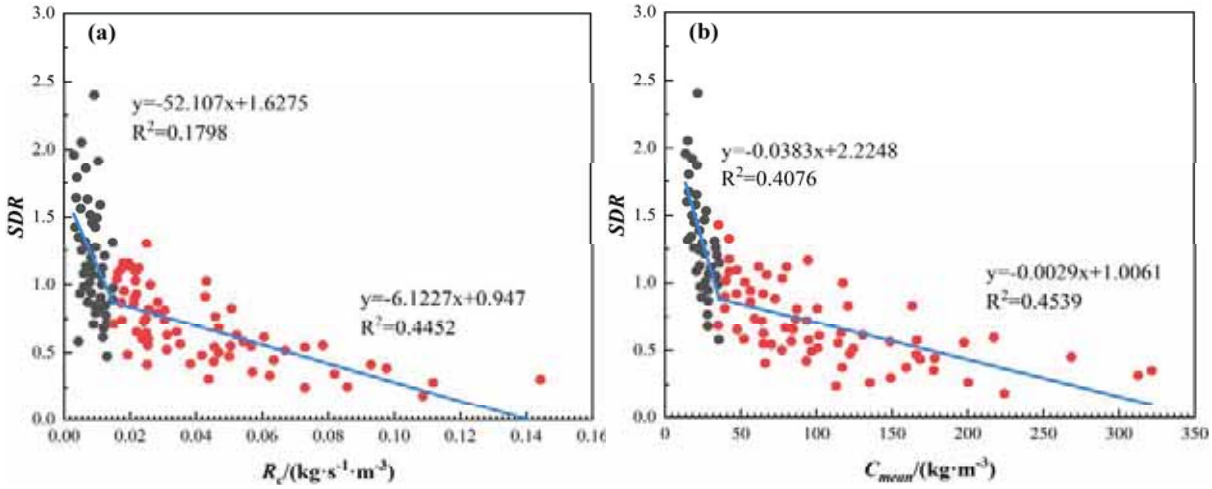

FIGURE 1
Relationship between SDR and R_C and C_{mean} for 150 floods in the lower Yellow River

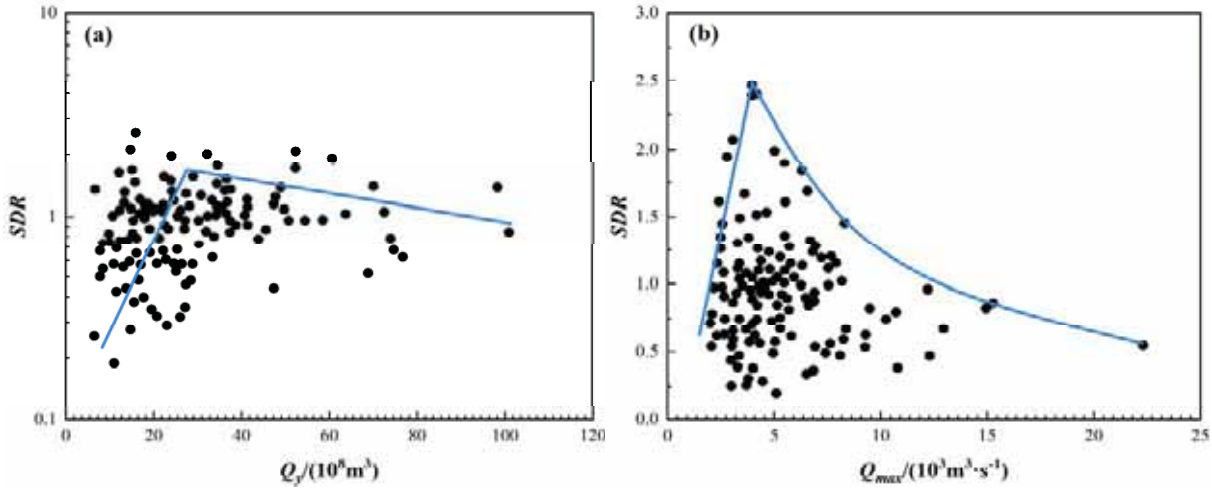

FIGURE 2
Relationship between SDR and Q_y and Q_{max} in then lower Yellow River

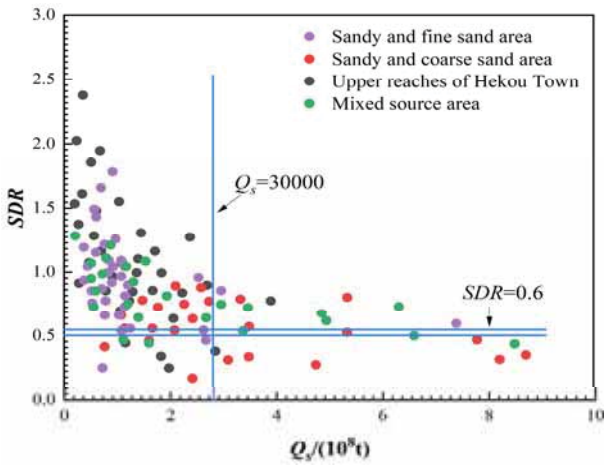

FIGURE 3
Relationship between SDRand Q_s of 150 floods

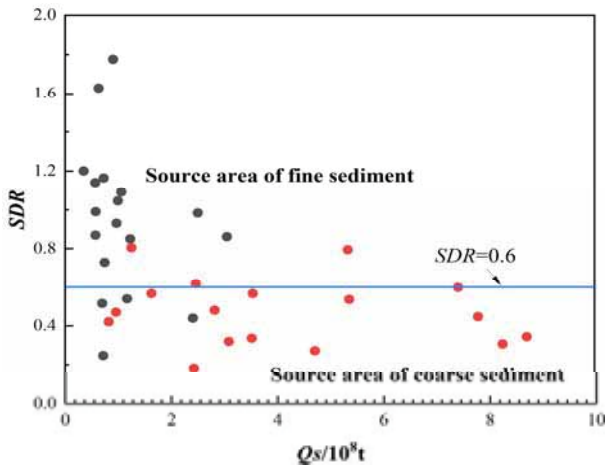

FIGURE 4
Relationship between SDR and Q_s from coarse and fine sand area

In order to further compare the flood delivery ratio in the sandy coarse sand area and sandy fine sand area, the relationship between the flood delivery ratio and the flood sediment volume in the two areas is drawn (Figure 4). It can be seen that, when SDR is 0.6, of the 18 floods in the sandy fine sand area, 13 were above and 5 below the water level line. Of the 17 floods in the sandy coarse sand area, 13 were below the water level line and 4 above the water level line. Figure 5 shows the relationship between sediment delivery ratio of previous floods and these two indexes. It can be seen that SDR increases with the increase of sediment proportion in coarse sediment area, reaching the peak, and the corresponding sediment percentage in coarse sediment area is 50%. For the sediment proportion of fine sediment area, the sediment proportion of fine sediment area corresponding to SDR peak is 40%. The two curves in Figure 5(a) and (b) show that there seems to be an optimal matching relationship between the source of the sediment in the flood, that is, 40% comes from the fine sediment area and 50% from the coarse sediment area, which makes the sediment delivery ratio of the flood is the largest. The physical and mechanical properties of suspended sediment flow with different particle sizes are different. Studies have shown that there is an optimal sediment particle size composition,which maximizes the sediment carrying capacity of two-phase flow [23-27]. The formation of the optimal relationship may be related to this mechanism. The sediment concentration of runoff in the clear water area above Hekou town is low, which can dilute the downstream flood. Therefore, when the proportion of runoff to total floods in the region increases, the flood of sediment delivery ratio will also increase. However, the relationship between the field flood delivery ratio drawn in Figure 5(c) and the proportion of runoff in the clear water area above Hekou town shows that when the percentage is greater than 60%, the SDR shows a slight downward trend. This is because when the water in the clear water area exceeds this percentage, the main stream is scoured, resulting in the increase of coarse sediment carried in the flow. This part of coarse sediment will be deposited in the downstream of the river, resulting in an increase in deposition rate and decrease in delivery ratio.

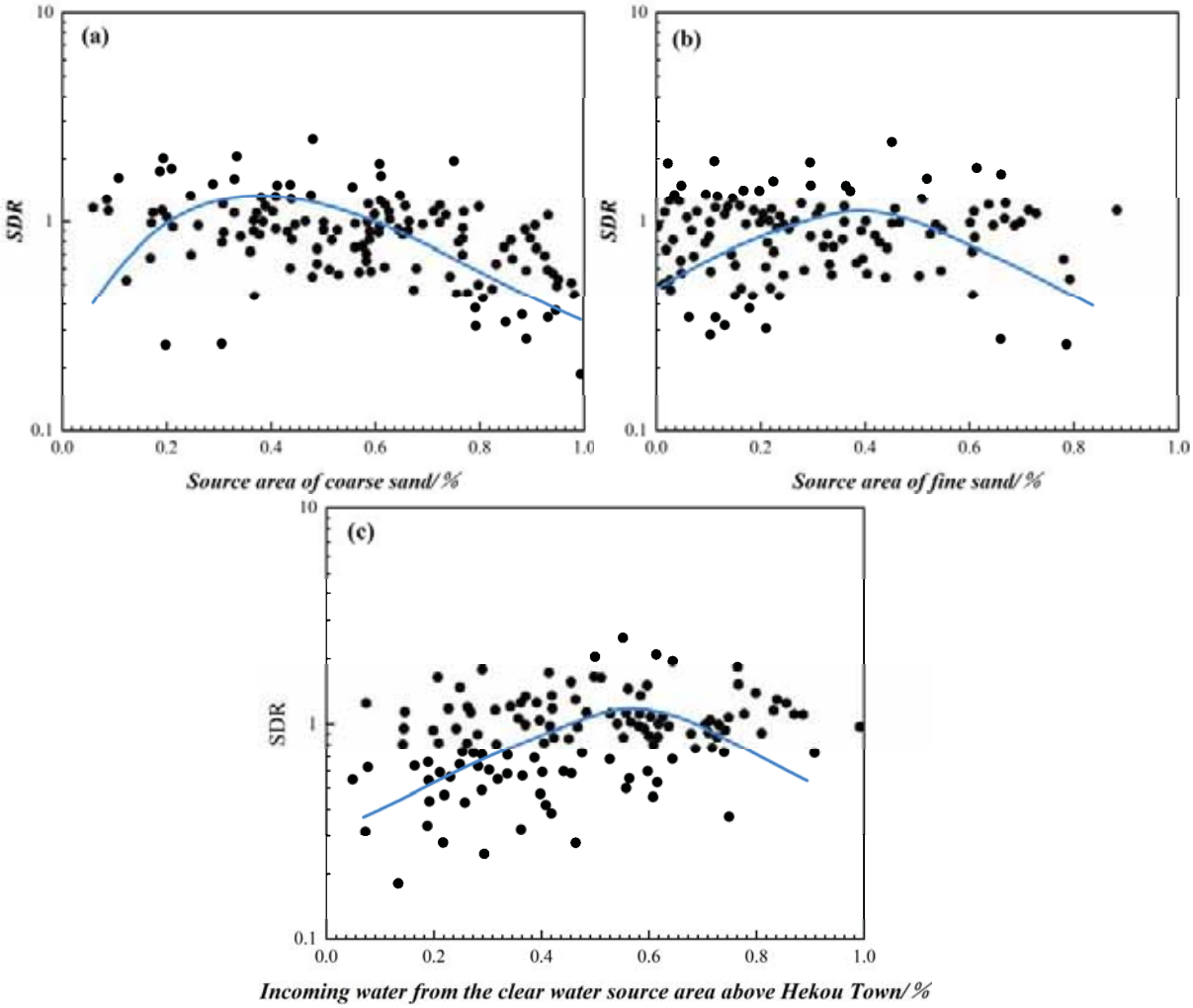

FIGURE 5
Relationship between SDR and the proportion of sand and water from different sources

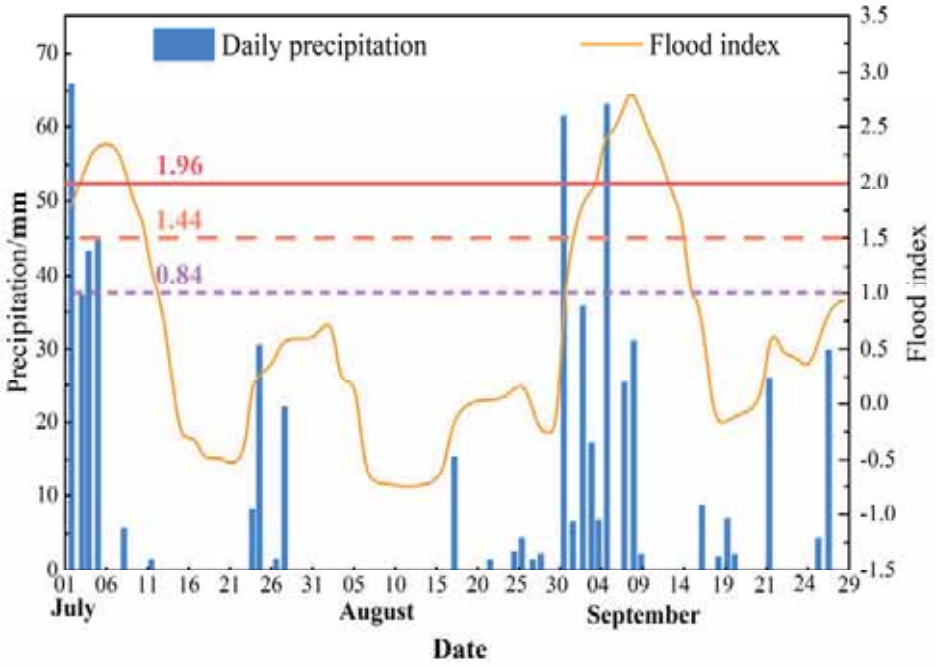

FIGURE 6
Distribution curve of daily flood index in the lower Yellow River

Comparison of The flood index of single station. The monthly flood index of the lower Yellow River is calculated according to the precipitation data for 10 consecutive days, and the weights of each flood grade in the flood degree are distinguished. Amplify the impact of heavy flood grading system. At the same time, the influence of the coexistence of drought and flood on the value of flood index is avoided. The calculated monthly flood index is compared with the traditional Z-index calculated by monthly precipitation. From the results, the latter is 10 months more than the former. The former had 9 months of medium-flood in the former. The increased months, although the total monthly precipitation is less than the traditional Z-value heavy flood months, it has the following characteristics: the calculation of L value takes into account the influence of artificial precipitation period division. The contribution of heavy rainfall at the end of last month to the flood index at the beginning of this month is considered. This will make this month's L value looks larger. When calculating L value, the weight of heavy flood grade is increased. If drought and flood coexist in this month, that is to say, precipitation anomaly concentrated in a period of time. However, there is no obvious precipitation in other periods, and this situation will also occur, which may reach the standard of severe flood in this month. But the total rainfall may not be large. In fact, this situation is more likely to cause serious disasters. The precipitation of this month is evenly distributed,but it is sustainable. In particular, the rainstorm for several days is scattered. Therefore, according to the precipitation statistics for 10 consecutive days, the frequency of moderate or mild flood is higher. According to the L method, it may reach the standard of heavy flood this month. The flood index is calculated based on any 10 day rainfall and time series. It not only improved the original Z-index, so that the flood index closer to reality. At the same time, it can better reflect the whole process of each flood. According to statistics, many floods occurred in the lower Yellow River in 1989, and the traditional flood index cannot reflect this situation. However, it can be reflected from the precipitation and flood index for any 10 consecutive days (Figure 6). Those meeting the criteria for heavy flood are: July 2-8 (the maximum total precipitation for 10 consecutive days is 323.7 mm), August 31-September 2 (192.6 mm), and September 4-9 (247.8 mm).

Distribution characteristics of flood. According to the monthly flood index obtained in the 20-year series of the lower Yellow River, 19 months flood index reached the heavy flood standard, and 40 months flood index reached the medium flood standard or above. Figure 7 shows the number of days that the lower Yellow River reach the flood standard within ten days. It can be seen from the average situation for many years that the floods in the lower Yellow River mainly occur from late June to early July and late August, and are more likely to occur in mid-April and early October. The occurrence probability increases gradually from heavy flood, medium flood to light flood. The occurrence probability of the three is high from late June to early July, and the occurrence probability of the three is low from early June to mid-June, late July and late September. Medium and light floods also have high value distribution from late August to early September.

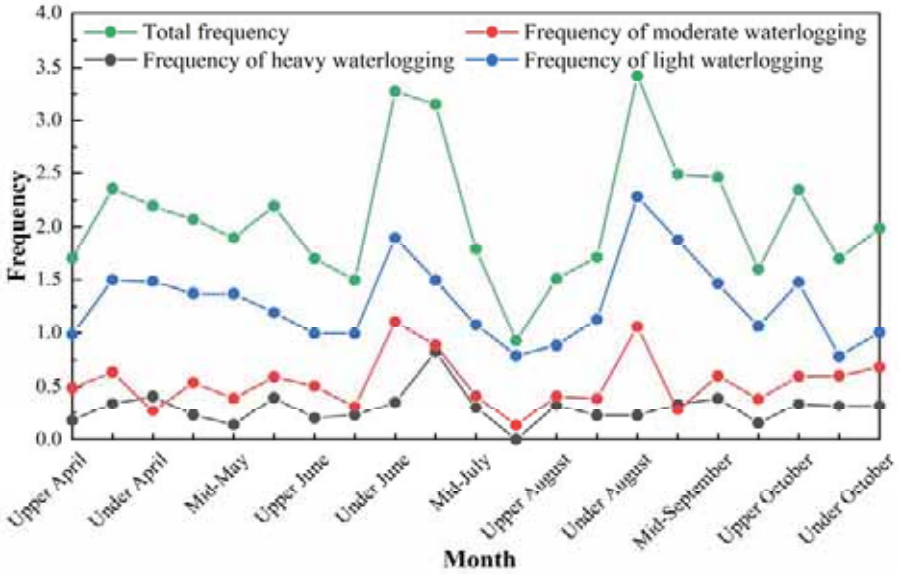

FIGURE 7
Distribution of average flood frequency in ten days in the lower Yellow River

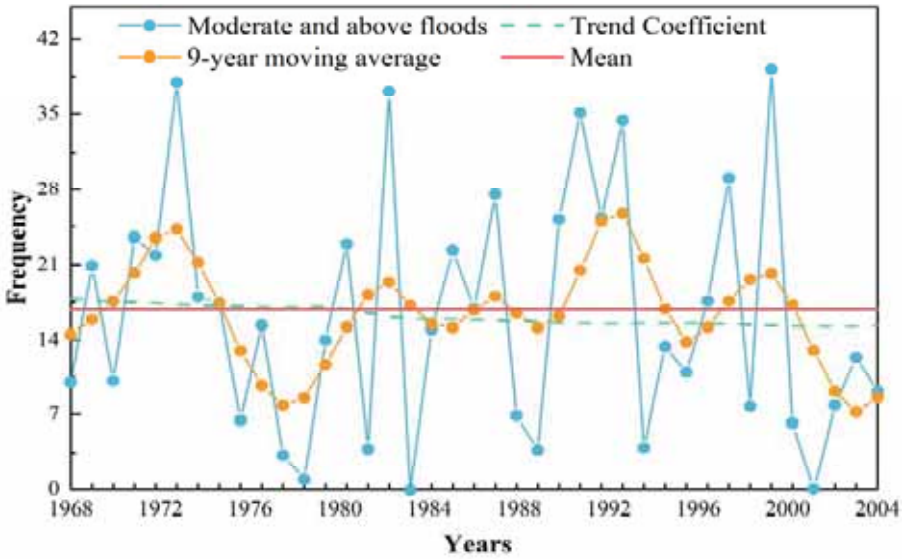

FIGURE 8
Distribution of flood frequency in the lower Yellow River over the years

The frequency distribution of medium and above floods in the lower Yellow River over the years, as shown in Figure 8, can better reflect the interannual and interdecadal characteristics of floods in the lower Yellow River. From the overall trend, it is basically stable and slightly decreased. Before the 1970s, it showed about 10 years of cyclical fluctuations. From the early 1980s to the early 1990s, it was a short-term fluctuation of 4-5 years. The period from the early 1990s to now is 7-8 years, the period from the late 1960s to the early 1970s is high incidence, and the period from the mid-1970s to the 1980s is low incidence. From the mid-1980s to the early 1990s, the overall stability. From the early 1990s to the late 1990s, this is a relatively frequent period. Since 2003, it has been in the low incidence period of flood disasters. Around 2010 is the transition period to the high incidence period.

Analysis of flood index in the lower Yellow River Basin. Starting from the flood index, the linear relationship between the flood grade of the basin and the flood index of the upper reaches is analyzed, so as to provide a basis for the flood grade prediction of the lower Yellow River Basin. There are 10 main stations in the upper reaches of the Yellow River. The contribution of each station to the flood grade of the basin is judged through experience, and the flood grade index Z_L of the lower Yellow River is calculated. According to the statistics of 42 flood processes in the lower Yellow River in the 1990s, and according to the water level height, 19 three-grade floods (light floods), 16 two-grade floods (severe floods) and 7 one-grade floods (extreme floods) are obtained, and the corresponding flood index of the day is fitted. It can be seen that each flood process

can be reflected in the flood index. As shown in Figure 9, the average flood index of three-grade flood case is 1.55, the average flood index of two-grade flood case is 1.92, and the average flood index of one-grade flood case is 2.1. The flood index is reflected before the occurrence of floods at all grades. The day before the one-grade flood basically meets the medium flood standard or even the heavy flood standard. The two-grade flood can reach the medium flood standard the day before, and some can reach the heavy flood standard. The day before the three-grade flood, it can basically meet the light flood standard and individual medium flood standard. The results show that the flood index analysis can predict the flood disaster, and its effect is significant and forward-looking.

Taking 2000 as the test object, the actual situation shows that there was a flood disaster in June. Figure 10 shows the distribution of flood index and daily precipitation in June. It can be seen that from April to September and from 23 to 29, the light flood standard was reached for several consecutive days, and the medium flood standard was reached on September 9. Although there was no flood record in this process at the beginning of this month, the timely regulation of reservoirs was not excluded. The height of water levels from 23 to 24 at the end of the month indicates that light flood standards have been met,

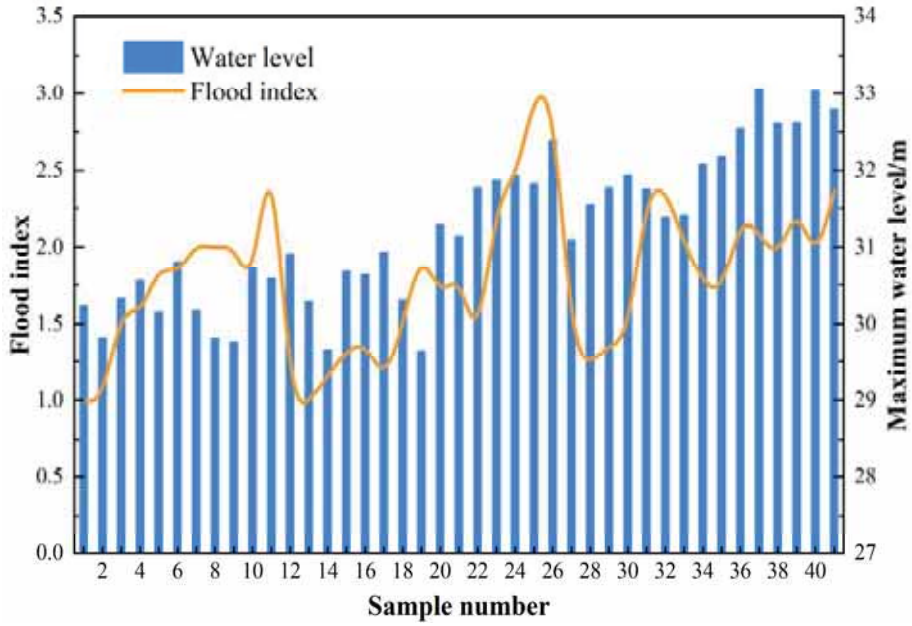

FIGURE 9
Comparison of water level and flood index in the flood process of the lower Yellow River

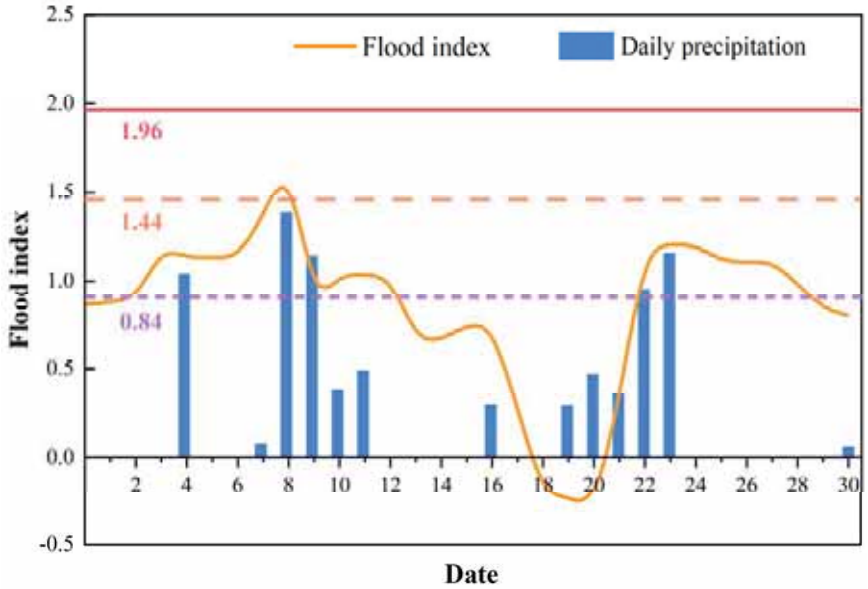

FIGURE 10
Flood index curve in June 2000

which corresponds to the flood index. After 24 days, without precipitation supplement, the flood index decreased gradually, and the disaster situation was gradually alleviated.

CONCLUSIONS

(1) SDR decreases rapidly with the increase of C_{mean} and R_C, which shows that compared with water volume, the larger the amount of sand, the smaller the sediment delivery ratio of the river. In addition, the relationship between them is nonlinear, the line turns at C_{mean} = 35kg/m^3 and R_C = 0.015 kg·s/m^3, which is a critical condition in the relationship between delivery ratio and water-sediment combination. When C_{mean} is less than 35 kg/m^3 or R_C is less than 0.015kg/m^3, the flood sediment delivery efficiency increases sharply. The delivery ratio corresponding to the critical point is about 0.70.

(2) Z-index has its unique advantages as the standard of flood classification.Using any continuous 10-day method to calculate the flood disaster, reducing the artificial time cut-off factor and overcoming the coexistence of drought and flood can better reflect the beginning and ending process of flood, and can more objectively reflect the intensity of flood disaster at the monthly scale, especially the flood disaster caused by concentrated precipitation.

(3) The occurrence probability of flood in the lower Yellow River gradually increases from heavy, medium to light floods. The probability of the three occurring from the late June to early July is very high. Late June to mid-June, late July and late September are the lowest periods of flooding. Medium and light floods also have high values from late August to early September. From the time distribution of flood frequency, a certain periodic law can be obtained. The comprehensive flood index of the lower Yellow River calculated by the single station flood index is in good agreement with the historical situation, which can be used as a basis for prediction and early warning.

ACKNOWLEDGEMENTS

This work was supported by the Key Project of Research and Development Plan (2018YFC1508006).

REFERENCES

[1] Zhang, X.P., Li, J.H., Wang, Y.J., Jiang, E.H. (2019) Analysis of physical exposure under major flood disaster scenarios in the broad beach area of the lower Yellow River. Flood Control and Drought Relief. 8(4), 22-28.

[2] Zhao, Z., Wang, H., Zhang, Y., Deng, C., Xie, Q., Wang, C. (2020) Problems and countermeasures of river management in the process of rapid urbanization in China. Water. 12(8), 2260-2269.

[3] Zhang, J., Shang, Y., Cui, M., Luo, Q., Zhang, R. (2021) Successful and sustainable governance of the lower Yellow River, China: A floodplain utilization approach for balancing ecological conservation and development. Environment, Development and Sustainability. 12(6), 1-15.

[4] Shao, H.W., Tao, P., Shan, F. H. (2012) Climate change risk research: a case study on flood disaster risk in China. Advances in Climate Change Research. 3(2), 92-98.

[5] Aerts, J.C., Botzen, W.J., Clarke, K.C., Cutter, S.L., Hall, J.W., Merz, B., Mysiak, J., Surminski, S., Kunreuther, H. (2018) Integrating human behaviour dynamics into flood disaster risk assessment. Nature Climate Change. 8(3), 193-199.

[6] Wang, L., Zhu, Q.K., Tong, X.L., Wang, Y., Chen, W.S., Lu, J.Y. (2016) Analysis on the characteristics of temporal and spatial changes of precipitation on the Loss Plateau in the past 50 years. Agricultural Research in Arid Areas. 34(3), 206-212.

[7] Li, X.X., Sang, Y.F., Xie, P., Liu, C.M. (2018) The randomness and spatial difference of the maximum rainfall in different chronological years in my country. Journal of Geo-Information Science. 132(8), 62-69.

[8] Zhou, L., Wu, X., Ji, Z., Gao, G. (2017) Characteristic analysis of rainstorm-induced catastrophe and the countermeasures of flood hazard mitigation about Shenzhen city. Geomatics, Natural Hazards and Risk. 8(2), 1886-1897.

[9] Jing, Y., Chen, C. (2016). Storm flood characteristics and identification of periodicity for flood-causing rainstorms in the second songhua river basin. Water. 8(12), 529-538.

[10] Kim, S., Zhang, R., Pham, H., Sharma, A. (2019) A review of satellite-derived soil moisture and its usage for flood estimation. Remote Sensing in Earth Systems Sciences. 12(4), 225-246.

[11] Zhou, J.H., Li, L.P., Qin, A.M. (2010) Determination of Meteorological Drought Index in Shanxi and Research on Arid Climate Change. Agricultural Research in Arid Areas. 21(3), 246-253.

[12] Wu, H., Hayes, M.J., Weiss, A., Hu, Q.I. (2001) An evaluation of the Standardized Precipitation Index, the China-Z Index and the statistical Z-Score. International Journal of Climatology: A Journal of the Royal Meteorological Society. 21(6), 745-758.

[13] Yin, Y., Zhang, L., Wang, X., Xu, W., Yu, W., & Zhu, Y. (2020). Meteorological Drought Changes and Related Circulation Characteristics in Yulin City of the Northern Shaanxi from 1961 to 2015. Atmosphere. 11(11), 1196-1208.

[14] Cheng, H.J. (2013) Using z index to determine drought and flood indicators and drought distribution characteristics in Jilin Province. Meteorology. 10(1), 5-8.
[15] Agrawal, S., Gopalakrishnan, T., Gorokhovich, Y., Doocy, S. (2013) Risk factors for injuries in landslide- and flood-affected populations in Uganda. Prehospital & Disaster Medicine. 28(4), 311-321.
[16] Meng, Y., Lu, J., Chen, C.L. (2004) Comparative analysis of three drought and flood indicators in Liaoning. Journal of Meteorology and Environment. 20(2), 22-23.
[17] Cao, Y.Q., Liu, J.J., Wang, X.F., Wang, Q. (2016) Analysis of drought and flood cycles, mutation points and trends in the Huanghuaihai Basin. Arid Zone Geography. 39(2), 275-284.
[18] Jiang, D.S., Wang, X.G., Mao, Z., Li, H. (2002) Analysis on the characteristics of drought and flood in Qingdao in the past 50 years. Marine Forecast. 8(4), 48-51.
[19] Yin, W.Y., Zheng, J., Wang, J.H., Cheng, L. (2011) Fitting and calculation of extreme value distribution of annual maximum daily rainfall. Meteorological Science and Technology. 114(2), 1137-1148.
[20] Yuan, S.L., Xie, T.M. (2018) Analysis of the characteristics of the storm flood and cement sand in Kuye River. Water Resources. 7(9), 108-117.
[21] Zhao, Y., Cao, W., Hu, C., Wang, Y., Wang, Z., Zhang, X., Xie, G. (2019) Analysis of changes in characteristics of flood and sediment yield in typical basins of the Yellow River under extreme rainfall events. Catena. 17(7), 31-40.
[22] Zhang, C.P., Qu, S.J., Shang, H.X., Chen, Z. (2018) Study on the sediment discharge characteristics of the flood with high sediment content in Sanmenxia Reservoir. Journal of Water Resources and Hydropower. 39(5), 11-14.
[23] Winterwerp, J.C. (2011) Fine sediment transport by tidal asymmetry in the high-concentrated Ems River: indications for a regime shift in response to channel deepening. Ocean Dynamics. 61(2), 203-215.
[24] Ma, L.C., Jiang, C.D., Li, D.F., Zhang, H.W., Li, Z. (2021) Sediment transport and diffusion in the Yellow River Estuary in 2018 based on numerical analysis. Earth and Environmental Science. 768(1), 2035-2049.
[25] Shu, A., Fei, X. (2008) Sediment transport capacity of hyperconcentrated flow. Physics, Mechanics and Astronomy. 51(8), 961-975.
[26] Liu, L.L., Yao, Q.F., Liu, W.J., Xu, J.H., Xu, N. (2007) Analysis of sediment carrying capacity and characteristics of coarse and fine sediments in the main canal and second canal in the Yellow River Diversion Irrigation District. Shandong Water Resources. 9(1), 31-35.
[27] Greco, S.E., Remier, A.K., Larsen, E.W., Plant, R.E. (2007). Sediment transport capacity-an improved Bagnold formula. International Journal of Sediment Research. 81(4), 354-363.

Received: **06.12.2021**
Accepted: **23.01.2022**

CORRESPONDING AUTHOR

Jiahu Wang
School of Hydrology and Water Resources,
Hohai University,
Nanjing, Jiangsu 210098 – China

e-mail: w2677408379@163.com

© by PSP Volume 31– No. 05/2022 pages 5176-5184 Fresenius Environmental Bulletin

SAFETY MINING GUARANTEE TECHNOLOGY FOR COAL FACE CROSSING COLLAPSE COLUMN BASED ON GROUTING REINFORCEMENT–A COMPARATIVE STUDY USING UDEC AND FLAC3D NUMERICAL SIMULATION

Cunjin Lu, Jinpeng Xu*, Tongming Wang

School of Resources and Geosciences, China University of Mining and Technology, Xuzhou, Jiangsu 221116, China

ABSTRACT

Safety mining technology is an important part of traditional mines to adapt to green and high-quality development. In the production process, the coal face crossing the collapse column is a typical important hazard, which may cause accidents such as collapse column activated water conduction. Through UDEC and FLAC3D numerical simulation, this paper compares the roof and floor overlying rock damage and hydraulic seepage caused by mining before and after the collapse column grouting, and provides a basis for the treatment and early warning of the activated water conduction hazard during the collapse column mining process. The results show that, compared with the non-grouting, grouting treatment measures can effectively reduce the risk of collapse column activated water conduction when the coal face passes through the collapse column.

KEYWORDS:
Safety mining, coal face, numerical simulation, collapse column

INTRODUCTION

In the process of coal mining, accidents that affect safety and economic benefits are prone to occur when the coal face crosses the collapse column, which has become an important factor in the safety production of coal mines [1-2]. The geological characteristics of China's coal mines are complex [3]. Coal mines in Shanxi, Henan and other areas often have collapse columns that affect the development of coal mines. They have caused types of accidents such as collapse column activated water conduction, and they have also accumulated rich management experience [4]. The geological changes caused by energy development are complex [5-6], and grouting treatment is an important technology to ensure the safety when the coal face crosses the collapse column. It can effectively improve the safety when the coal face crosses the collapse column. The simulation research of the grouting treatment effect when the coal face crosses the collapse column can provide a scientific basis for improving the safety production capacity of the coal mine, accumulating the experience of coping with the collapse column engineering. It also helps to build the green and safe development of the coal mine [7-8]. This paper is based on the example of Hemei 9th Mine 3103 coal face crossing 9-6 collapse column, and carries out the numerical simulation based on UDEC and FLAC3D. It compares the roof and floor overlying rock damage and hydraulic seepage caused by mining before and after the collapse column grouting, and evaluates and demonstrates the activation of the water conductivity during the mining process of the collapse column. It provides a basis for the next targeted research of its suitable treatment and early warning methods and measures.

MATERIALS AND METHODS

3103 coal face and 9-6 collapse column of Hemei 9th Mine. Hemei 9th Mine is located in the northern suburbs of Hebi City (Figure 1). From bottom to top, there are Middle Ordovician Majiagou Formation (O2m), Upper Carboniferous Benxi Formation (C2b) and Taiyuan Formation (C2t), Permian Lower Shanxi Formation (P1sh) and Lower Shihezi Formation (P1x), Upper Permian Upper Shihezi Formation (P2s), Neogene Pliocene Hebi Formation (N2h) and Quaternary (Q) strata. Among them, the Shanxi Formation is the main coal-bearing formation in the mining area. It is composed of sandstone, mudstone, sandy mudstone and coal seams. It contains 1 to 4 layers of coal. The two_1 coal seam is stable, widely developed and can be mined at present. The two_1 coal seam is the mineable coal seam in the whole area: the two_1 coal seam: the buried depth is 60~810 m, the elevation is 100~650 m. It occurs between the Beichagou sandstone and Dazhan sandstone in the lower part of Shanxi Formation, and the upper part is 0.69~19.65 m from Dazhan Sandstone (S10), with an average of 6.90 m. 51.89~93.83 m away from Shaguoyao sandstone (S12), 66.65 m on average. The distance from the bottom to Beichagou sandstone (S9) is 1.50~11.38 m, with an average of

4.63 m. It is 35.37~64.31 m away from L8 limestone, with an average of 48.78 m.

The outer section of 3103 coal face is located in the east of 3103 coal face of No. 31 mining area of Jiu Mine. The total length of the roadway is 642.6 m, and the net section of the roadway is 15.7 m^2. During the driving period, the distance between the top of the roadway and the two_1 coal seam is 10-21 m, and the geological conditions are relatively complicated.

In July 2019, the 9-6 collapse column was exposed during the driving of the outer section of the drainage roadway under the lower floor of the 3103 coal face. The collapse column in the two_1 coal seam has a short axis length of 47 m, a long axis length of 141m, and an area of about 4700 m^2. The current water level of the Ordovician karst fissure aquifer is about 135 m. The average distance between the aquifer and the above two1 coal is 183m, the seam floor elevation of the 9-6 collapse column is about -470m, and the Ordovician water pressure is about 7.88 MPa. According to the analysis of the previous drilling data, there are some water outlet points on the boundary of the collapsed column. The outlet points are mainly fissures within the collapsed column. The maximum water output is 10 m^3/h. The effluent water source is mainly sandstone water after the analysis of water samples taken, but there are limestone water components and the outlet channel is the fissure to conduct water.

In order to ensure that the 3103 coal face smoothly crosses the 9-6 collapse column during the mining process, it is necessary to carry out a systematic research on the 9-6 collapse column. According to the actual conditions of the mine, the discrete element numerical simulation software UDEC and the finite element numerical simulation software FLAC3D are used to establish two-dimensional and three-dimensional numerical simulation models for research.

Two_1 Lithology of coal roof and floor. The old roof of the two_1 coal seam is fine and medium-grained sandstone (Dazhan Sandstone). It is dark gray or gray-black, and thick layered. It is mainly composed of quartz, followed by feldspar, with a small amount of dark minerals. There are carbonaceous shales and a large amount of muscovite on the bedding plane. Siliceous and argillaceous cementation on the bedding plane is compact and hard, with oblique bedding and cross bedding. Its vertical fissures are developed, mostly filled by calcite veins, with thickness of 1.45~22.28 m, average thickness of 7.39 m

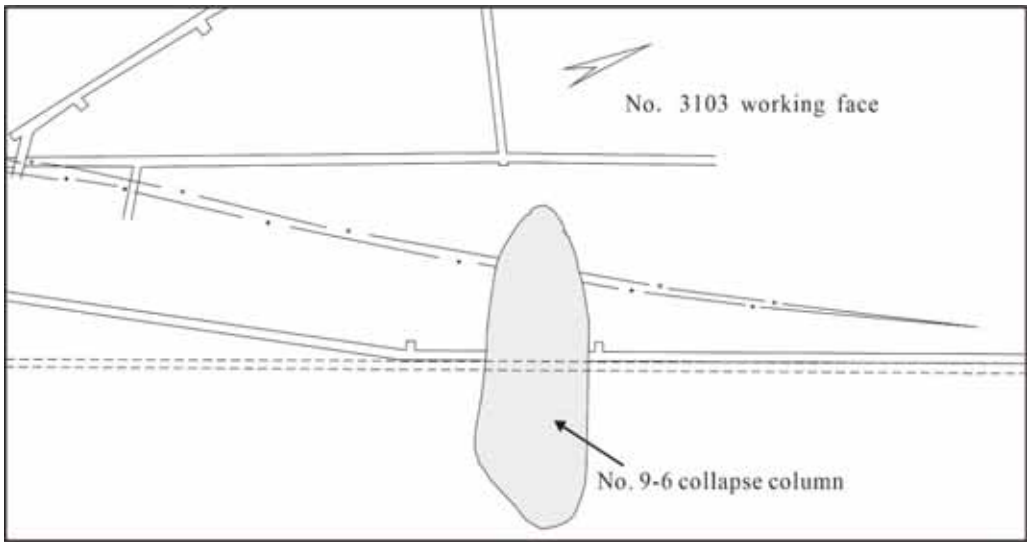

FIGURE 1
The location of the 9-6 collapse column and its relationship with the 3103 coal face in the Hemei 9th Mine.

TABLE 1
Rock mechanics characteristics of roof and floor of Shanxi Formation two_1 coal seam

Horizon	Rock name	Compressive strength (MPa)	Tensile strength (MPa)	Shear strength at 45° (MPa)	The angle of internal friction φ	Cohesion C
Roof	Medium Grained Sandstone	140.0	7.54~8.49	46.3	35.42	13.4
Floor	Coarse-grained Sandstone	81.7	3.84~4.05	28.5~30.1	38.08	6.9

The direct roof of the two_1 coal seam is mostly mudstone or sandy mudstone, and a very small amount is siltstone (Table 1). The thickness is 1.59~37.60 m, with an average of 6.90 m. When the lithology is mudstone, its strength is relatively low. The boreholes with a direct roof less than 3 m are mostly distributed near the fault zone. The boreholes with a direct roof above 10 m are mostly distributed in the zone with a width of about 300m in the northwest direction. The boreholes with a direct roof are within the range of 3~10 m is approximately evenly distributed throughout the area.

The direct floor of the two_1 coal seam is mudstone or sandy mudstone. The thickness is 0.65~18.43 m, with an average of 5.21 m. Only the direct floor of hole 910-09 is fine-grained sandstone (Beichagou Sandstone). Mudstone and sandy mudstone are easy to soften when exposed to water, and it is not easy to support during mining. The indirect floor of the two_1 coal seam is fine and medium-grained sandstone (Beichagou Sandstone). The thickness is 0.89-20.23 m, with an average of 9.54 m. The area is generally developed, with only 910-10 holes missing. The sandstone floor has high compressive strength and low softening degree. The interbedded structure of sandstone and mudstone can improve the engineering geological conditions of the floor to a certain extent. The roof and floor of the coal seam are relatively flat, with only partial unevenness. The roof is relatively complete, and the cracks are not well developed.

Stability of the roof and floor of the two_1 coal seam. The compressive strength of fine and medium grained sandstone (natural water content) of two_1 coal seam roof is 12.4~140.0 MPa. And the compressive strength after natural air drying is 30.4~43.7 MPa, and the softening coefficient is 0.49. It is a rock that is easy to soften, and its engineering geology is relatively poor. The tensile strength is 7.54~25 MPa under natural moisture conditions, and the tensile strength changes greatly, the shear strength at 45° is 46.3~217 MPa. According to "Gently Inclined Coal Seam Coal Face Roof Classification (MT 554-1996)", the roof of the two_1 coal seam belongs to Type II roof, which is a medium stable roof.

The compressive strength of mudstone and coarse-grained sandstone under the natural water-bearing state is 24.1~81.7, and the compressive strength of air-dry state is 49.4 MPa. Its one-week tensile strength is 3.84~9.00 MPa, and the shear strength at 45° is 28.5 ~30.1. The softening coefficient is 0.59. The rock is easy to soften. Therefore, the engineering geology of the coal seam floor is general, and some areas are prone to deformation such as bottom bulging. The direct floor of the two_1 coal seam is dominated by mudstone, with low strength. And the rock is easy to soften. Generally speaking, it should belong to the type I floor, which is an unstable floor.

Hydrogeological conditions. The mine field is located in the burial area of the Xiaonanhai Spring karst water system. It belongs to a weak runoff zone. The direction of groundwater runoff in the region is from west to east. After being blocked by faults, it diverges to the north and south. Affected by the structure of this area, groundwater will migrate to the deep. The water source of the two_1 coal seam is mainly the karst fissure water of the upper part of the Taiyuan Formation of the floor and the roof clastic fissure water, followed by loose rock pore water.

Simulation scheme design. The 3103 coal face of Hebi 9th Mine has a strike length of 1383 m, a leaning length of 194 m, and an area of 268302 m^2. The coal seam to be mined is the two_1 coal seam of Shanxi Formation, with an average coal seam thickness of 6.02 m and a coal seam inclination of 5°-20°. It is a gently inclined coal seam. The old roof of the coal seam is fine and medium grained sandstone (Dazhan Sandstone) with a thickness of 1.45-22.28 m and an average thickness of 7.39 m. The direct roof is mostly mudstone or sandy mudstone, with a very small amount of siltstone. The thickness is 1.59~37.60 m, with an average of 6.90 m. The direct floor of the coal seam is mudstone or sandy mudstone, with a thickness of 0.65-18.43 m and an average of 5.21 m. The indirect floor is a fine and medium grained sandstone (Beichagou Sandstone), with a thickness of 0.89-20.23 m and an average of 9.54 m. According to the design of the grouting reinforcement section of the collapse column, the thickness of the treatment section is 80 m, which is the depth section of 50~130 m below the two_1 coal seam floor. The simulated depth is required to reach an increase of 10m below the treatment section, that is, the two_1 coal seam floor is 140 m.

UDEC numerical simulation. UDEC (Universal Distinct Element Code) is a discrete element method program developed by ITASCA for researching discontinued. It can solve the mechanical problems of joints or block systems under dynamic or quasi-static conditions [9-10].

The length of the coal face is much greater than the width of the coal face, when the working face is advanced to a sufficient length, the stress field distribution of the surrounding rock of the coal face has little relationship with the length of the coal face. According to the related theories of elastic mechanics, this kind of problem can be applied to the plane strain problem. Moreover, the use of plane strain simulation can save computing resources. Therefore, the specific section in the coal face will be solved by the plane strain simulation. The UDEC numerical simulation software is used to simulate the change process of the coal roof and floor during the mining of the coal face and the influence of the mining on the activation of the collapse column, and to evaluate

the safety of the coal face crossing the collapse column.

Combining the needs of the research purpose, the model size is determined to be 400 m × 300 m. The width of the collapse column is 50 m inside the coal face, and the shape of the collapse column is large at the bottom and small at the top. The simulated height is about 2 times the calculated value of the water-conducting fracture zone of the normal formation, that is, 120m. The model basically includes the geological structure near the coal face and the main coal measure strata. The mechanical parameters of the model rock formation are shown in Table 2, and the model grid division is shown in Figure 2.

The rock mass and joint parameters are set as initial values. As the simulation progresses, the original rock stress field gradually balances. It is necessary to adjust the parameters according to the actual original rock stress field until the original rock stress field and the actual original rock stress field match. The surface contact model was selected as the constitutive model of the joints in the model.

The advancing direction of the simulated coal face is along the positive direction of the X axis, and the mining step pitch is dense at the front and sparse at the back. The reference material simulates the excavation process. Step-by-step analysis is performed during the model excavation process. First, the model stress change is analyzed. Then the displacement under the stress is analyzed. Finally, according to the results of stress and displacement, the disturbance of the collapse column in the mining process of the coal face is comprehensively analyzed.

There are 3 excavation schemes arranged in UDEC numerical simulation:

(1) Simulate the activated water conduction situation of the collapse column after the coal seam is excavated when the collapse column is not treated with grouting.

(2) Simulate the activated water conduction situation of the collapse column after the coal seam is excavated (the height is equal to the coal thickness of 6m) after the collapsed column is reinforced by grouting.

(3) Simulate the activated water conduction situation of the collapse column after the coal seam is excavated after grouting reinforcement (the height of the collapse column area is coal thickness of 3m).

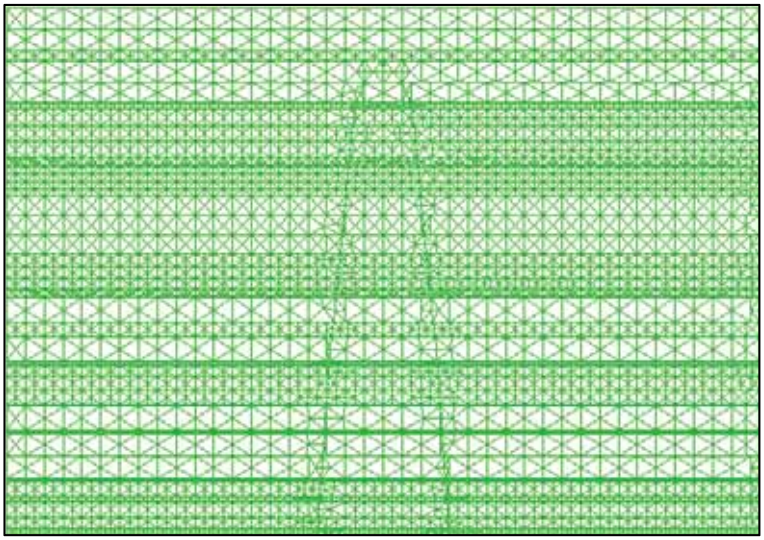

FIGURE 2
Model grid division.

TABLE 2
Mechanical parameters of the model rock formation

Number	Lithologic Map	Density (kg/m³)	Compressive Strength (MPa)	Tensile Strength (MPa)	Elastic Modulus (GPa)	Group Cohesiveness (MPa)	Angle of Internal Friction(°)	Poisson's Ratio
1	Mudstone	2200	61	2.2	22	2.5	33	0.2
2	Fine Sandstone	2400	64.3	2.6	25	2.8	32	0.3
3	Sandstone	2565	74.1	8.4	23	2.2	26	0.3
4	Limestone	2694	99.3	14.2	38	4	50	0.18
5	Two$_1$ coal seam	1378	21.6	1.1	10	1.5	19	0.32
6	Collapse column	2000	1.2	0.5	1.8	0.1	10	0.35

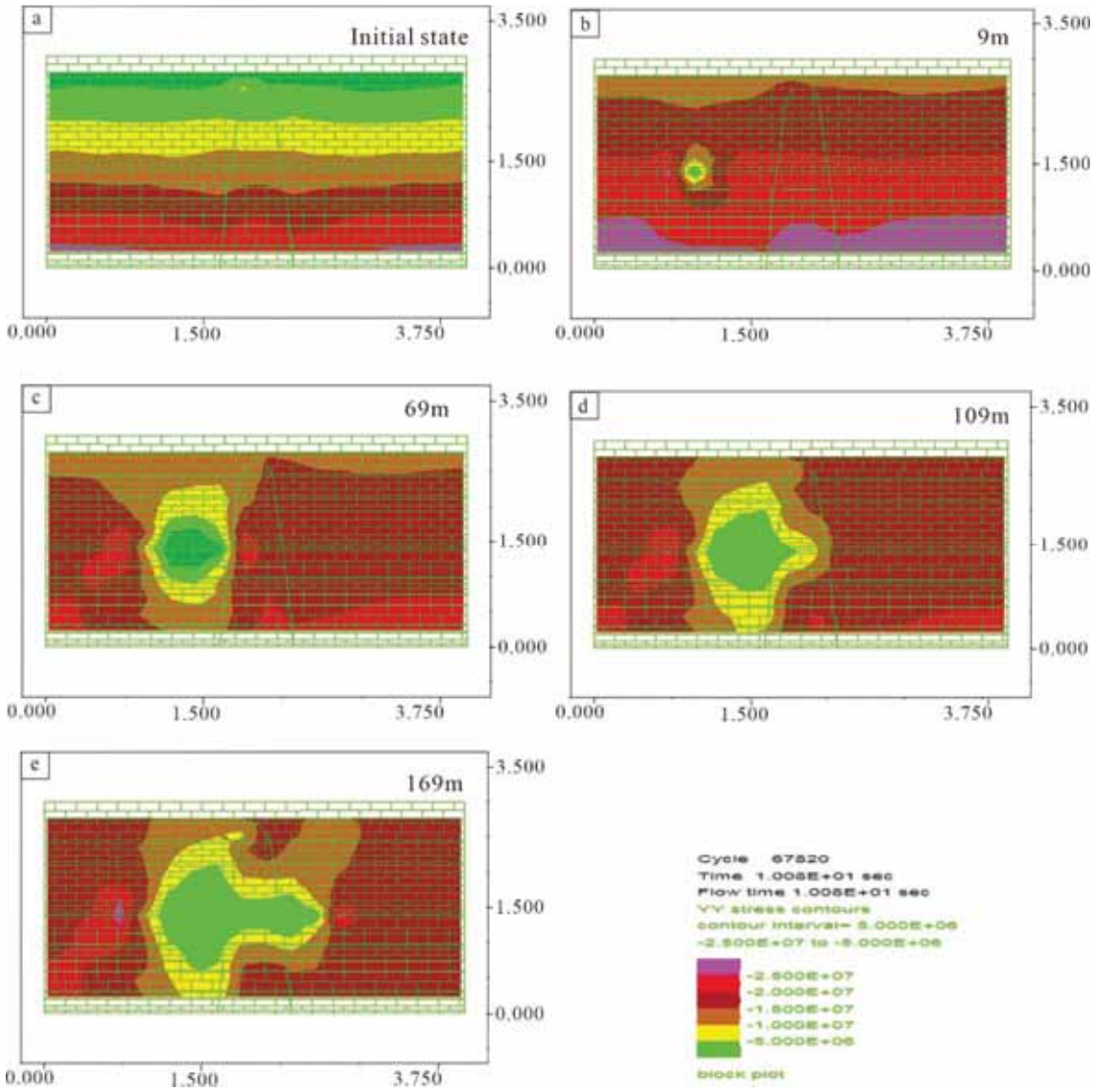

FIGURE 3
UDEC numerical simulation results without grouting.

FLAC3D numerical simulation. FLAC3D fits the actual structure by adjusting the polyhedral elements in the three-dimensional grid [11-12]. Refer to the UDEC numerical simulation to establish a three-dimensional numerical simulation model. The size of the model is determined to be 400m in length, 400m in width, and 300m in height. Refer to UDEC numerical simulation for strata division, strata mechanics parameters, boundary conditions, monitoring line layout, model excavation and result analysis plan. Two sets of simulations before and after grouting are carried out on the basis of UDEC numerical simulation results.

RESULTS

Analysis of UDEC numerical simulation results. When the coal face advanced from 5m to 9m, the impact on the collapsed column is small. After the coal seam is excavated, obvious rock damage has been formed on both sides of the goaf and the roof and floor areas, and the water pressure has risen upward. The water pressure in the weak area increases (the width of the red line represents the water pressure). When the coal face advanced to 69 m, the stability of the rock mass inside the collapse column has changed, and the boundary rock formation of the collapse column has been activated and shifted. Because the mining on the coal face affects the stability of the collapse column and surrounding rock formations, the collapse column is activated and conducts water. Water gushing also occurred on the bottom plate. When the coal face advanced to 109 m, the stress change area has affected the boundary on the opposite side of the collapse column, but the overall vertical stress has a tendency to reduce the vertical influence range, both sides of the goaf and the roof and floor areas have obvious rock failures. The plastic zone inside the collapse column has the largest height at the left boundary, and the water

level rose above the coal face. When the coal face advanced to 169 m, the coal face has crossed the collapse column. The vertical stress appeared the characteristics of "large on left and small on right" around the collapse column. The leading stress concentration appeared again in front of the coal face. To sum up, during the advancing process of the coal face, the hazard was greatest when it first touched the boundary of the collapse column. As the coal face continued to advance, the influence appears to decrease, and the stress, displacement and plastic zone all showed consistency. The simulation result is shown in Figure 3.

Result analysis of mining coal thickness of 3 m in the collapse column area after grouting. In order to evaluate the effect of grouting treatment, the rock mechanical properties of the grouting body are tested after grouting, and the parameters of the collapse column in the range of 0-90 m (grouting section) of the numerical simulation model are adjusted. And then the coal seam simulation excavation is carried out. The mining coal thickness is set to the actual coal thickness of 6 m, and the possibility of activated water conduction of the collapse column is analyzed. When the coal face is mined 5m, the stress change in the grouting section of the collapse column is smaller than that without grouting, indicating that the grouting has played a certain role in strengthening the rock mass inside the collapse column. The water pressure distribution in the floor aquifer is relatively even, and only slightly rises at the boundary of the collapse column. When the coal face advanced to 69 m, the damage area at the boundary of the floor collapse column after grouting is significantly smaller than before grouting. Moreover, the damage area is not connected. And the water pressure remains basically stable. There is only a certain rise inside the collapse column. But there was no water gushing on the coal face. This is in sharp contrast with the "activated" water conduction of the collapse column before grouting, which verifies the grouting effect. When the coal face advanced to 109 m, grouting section inside the collapse column has a stress change, but the value is relatively small. The grouting part of the lower section of the collapse column has no displacement, and the development range and damage degree of the plastic zone inside the collapse column is greater than that of the complete formation. The water level rose slowly but has not yet entered the coal surface. Under the combined effects of ground stress, floor water pressure and mining, the inside and boundary of the collapse column were not damaged after grouting treatment. When the coal face advanced to 169 m, after the plastic zone developed above the grouting section of the floor, it no longer continues to develop downwards. The grouting treatment has played a very good effect. However, at this time the cracks in the roof rock layer inside the collapse column developed to the top of the collapse column. The damage was relatively serious. It is necessary to consider corresponding preventive measures such as height restriction and optimized support during the mining process. The simulation result is shown in Figure 4.

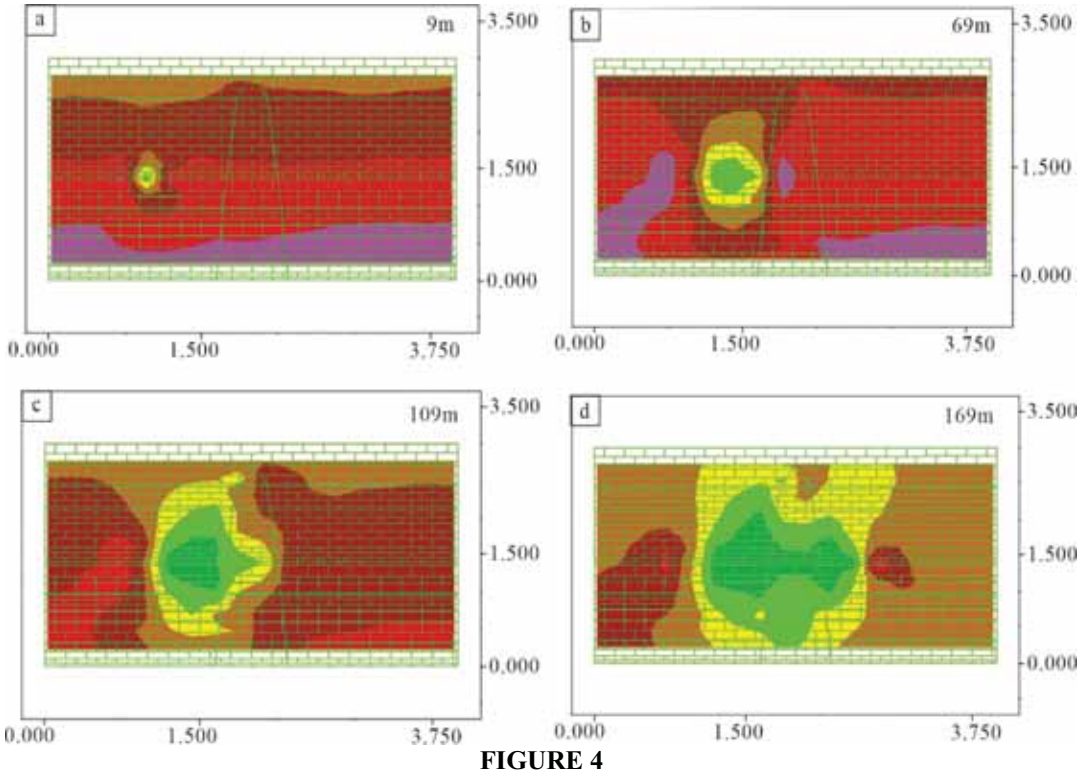

FIGURE 4
UDEC numerical simulation results under grouting conditions.

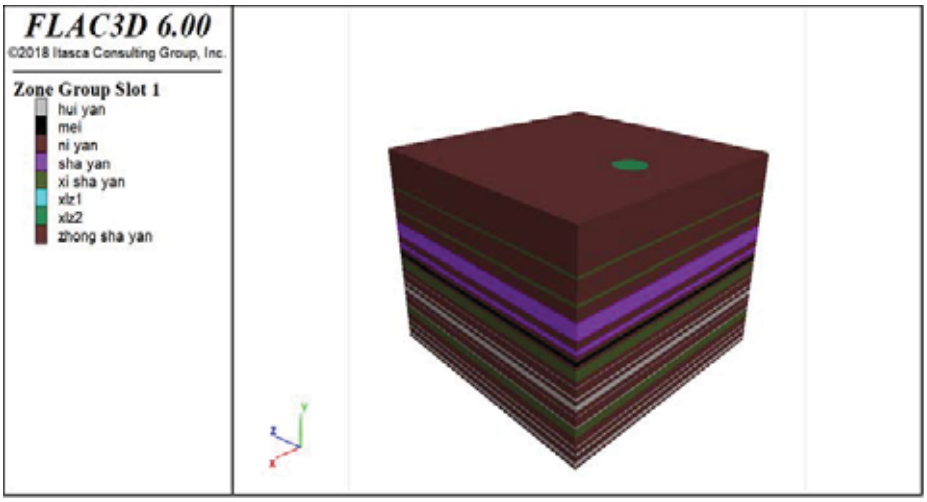

FIGURE 5
Model stratum division and collapse column setting.

FLAC3D numerical simulation. Based on the calculation results of the discrete element simulation software UDEC, three-dimensional numerical modeling of the actual project of the coal face crossing the collapse column is carried out. The development of the roof and floor rocks before and after the collapse column grouting treatment is simulated, and the risk of the activated water conduction of the collapse column is evaluated. The model is established with reference to the UDEC numerical simulation model, and a total of 32 strata are divided (Figure 5). The model length*width*height=400 m*400 m*300 m. The collapse column is located on the front side of the model with a diameter of 50m and the center is 100m away from the front of the model.

The understanding of small-scale laws can provide evidence for understanding the controlling factors of macroscopic characteristics [13]. The model was divided into 108,000 units. After setting the boundary conditions, original stress, boundary stress, etc., it ran to a balanced state, and then simulated coal seam excavation work was conducted. When the mining advanced to 9 m, the stress distribution in the collapse column area is significantly different from that of the surrounding complete stratum. The excavation of the coal seam has not yet affected the collapse column area. When the mining advanced to 69m, with the increase of the mining distance, the plastic zone expanded upward. When the mining advanced to 200 m, the excavation distance is equal to the width of the coal face. The stress in the collapse column area has changed greatly, and the range of change ran through the entire collapse column. The boundary on both sides of the collapse column is prone to longitudinal cracks due to displacement, which triggers the activation of the collapse column to conduct water there is no large-scale intersection between the failure zone and the upper failure area of the high-pressure aquifer of the floor, but there is a greater risk of conduction. Therefore, it is necessary to grouting and strengthening the floor rock of the collapse column. On the one hand, it can increase the strength of the rock mass and reduce the damage of the rock mass. On the other hand, the fissures in the collapse column area can be filled, compacted and sealed to avoid the seepage of the high pressure water of the floor through the fissures, causing the fissures to expand and triggering water damage in the collapse column [14-15].

The results of the mining after grouting. In order to verify the effect of grouting, after grouting reinforcement on the collapse column, a three-dimensional model was established to simulate the risk of activated water conduction of the collapse column after grouting reconstruction. When the coal seam was excavated to 49 m, the result was almost the same as that before grouting. However, when the mining advanced to 69 m, after the collapse column is grouted, the excavation of the coal seam to a distance of 50 m from the collapse column will not have a significant impact on the collapse column (Figure 6). When the mining advanced to 200 m, due to the collapse column floor 50-130 m has been grouted, this part was not damaged with the expansion of the mining distance, which fully verified the grouting effect. However, it is obvious that the stress has changed in the area above the grouting section and below the coal seam floor. And large displacements occurred on both sides of the collapse column, forming a plastic zone. The plastic zone inside and on the boundary of the collapse column is obviously larger than that of the surrounding complete stratum. This result verifies the conclusion drawn by the UDEC numerical simulation: in the process of advancing the coal face, it is the most harmful when it first touches the boundary of the collapse column. As the coal face continues to advance, the influence tends to decrease.

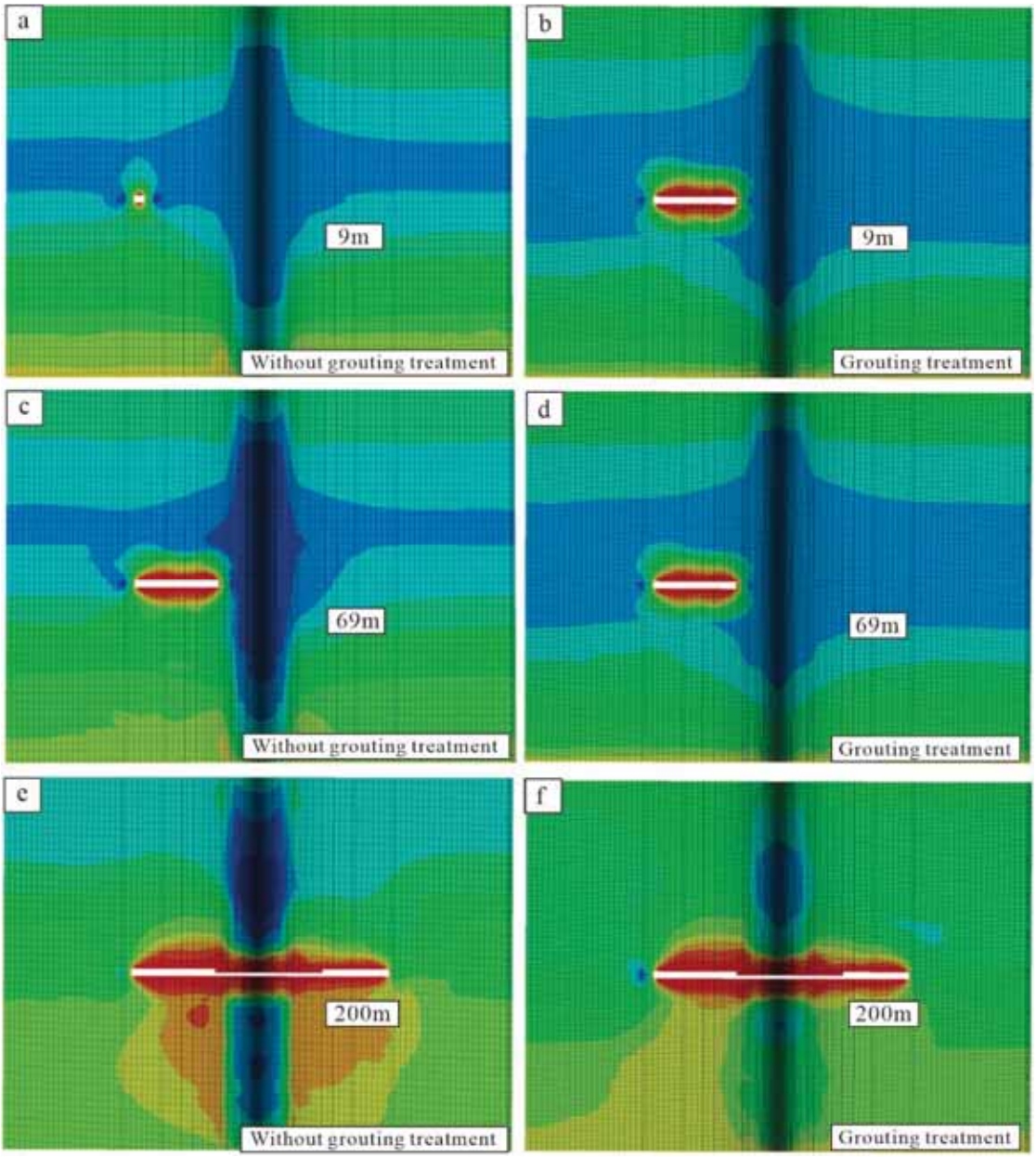

FIGURE 6
Results of FLAC3D numerical simulation.

CONCLUSIONS

Through numerical simulation, it is believed that the coal face crossing the collapse column before the grouting treatment will cause the collapse column activated water conduction. The water from the high-pressure aquifer of the floor is guided upwards to the coal face through the boundary of the collapse column and the internal superior channel, posing a serious threat to safety production. When the collapse column is treated with grouting, mining is carried out according to the coal thickness of 6 m and 3 m, respectively. Numerical simulation results show that there will be no adverse consequences of the collapse column activated water conduction, which verifies the effectiveness of the grouting treatment. Compared with before grouting, the vertical stress around the collapse column has the characteristics of "large on the boundary and small on the inside, large on the left and small on the right". The maximum displacement is in the middle of the collapse column. Mining in accordance with the 3 m height limit has a smaller damage area to the roof and floor, which is more beneficial to prevent roof drainage and water inrush from the floor.

ACKNOWLEDGEMENTS

The authors would like to show sincere thanks to all the techniques who have helped this research and all the authors of the references.

REFERENCES

[1] Zuo, J., Hong, Z., Peng, S., Shi, Y. and Zhang, Z. (2019) Investigation on failure behavior of collapse column in china's coal mine based on discontinuous deformation numerical method. PLoS One. 14, e0219733.

[2] Xu, Z., Sun, Y., Gao, S., Chen, H. and Li, X. (2021) Comprehensive exploration, safety evaluation and grouting of karst collapse columns in the Yangjian coalmine of the Shanxi province, China. Carbonates and Evaporites. 36, 1-12.

[3] Zhao, D., Guo, Y., Wang, G., Mao, X. (2019) Characteristizing nanoscale pores and its structure in coal–Experimental investigation. Energy Exploration & Exploitation. 37, 1-28.

[4] Zhang, H., Xu, G., Chen, X., Mabair, A., Zhou, J., Zhang, Y., Zhang, G., Zhu, L. (2020) Groundwater hydrogeochemical processes and the connectivity of multilayer aquifers in a coal mine with karst collapse columns. Mine Water and the Environment. 39, 356-368.

[5] Hou, X., Shi, W., Yang, T. (2018) A non-linear flow model for the flow behavior of water inrush induced by the karst collapse column. RSC Advances. 8, 1656-1665.

[6] Zhao, D., Guo, Y., Yin, S., Ren, C., Wang, Y. (2018) Prediction of geomechanical sweet spots in a tight gas sandstone reservoir: A case study of Lower Permian Strata in the Southern Qinshui basin, china. Interpretation. 7, 1-50.

[7] Chen, S., Yin, D., Cao, F., Liu, Y., Ren, K. (2016) An overview of integrated surface subsidence-reducing technology in mining areas of China. Natural Hazards. 81, 1129-1145.

[8] Li, H., Bai, H., Wu, J., Wang, C., Ma, Z. and Du, Y. (2017) Mechanism of water inrush driven by grouting and control measures—A case study of Chensilou Mine, China. Arabian Journal of Geosciences. 10, 468.

[9] Zhu, G., Sousa, R., He, M., Zhou, P., Yang, J. (2020) Stability analysis of a non-pillar-mining approach using a combination of discrete fracture network and discrete-element method modeling. Rock Mechanics and Rock Engineering. 53, 269-289.

[10] Gao, F., Stead, D., Kang, H. (2015) Numerical simulation of squeezing failure in a coal mine roadway due to mining-induced stresses. Rock Mechanics & Rock Engineering. 48, 1635-1645.

[11] Hang, L., Liu, T., Li, J., Ping, C. (2013) A simple generation technique of complex geotechnical computational model. Mathematical Problems in Engineering. 2013, 130-137.

[12] Emad, M., Mitri, H. and Kelly, C. (2018) Dynamic model validation using blast vibration monitoring in mine backfill. International Journal of Rock Mechanics and Mining Sciences. 107, 48-54.

[13] Zhao, D., Guo, Y., Wang, G., Jiao, W., Hui, Y. (2020) Quantitative characterization of nanoscale pores in shale reservoirs of Wufeng-Longmaxi Formation based on image processing. Fresen. Environ. Bull. 29(5), 3992-3999.

[14] Liu, S., Li, W., Wang, Q., Wu, Z., Yang, Z. (2017) Numerical simulation on crack propagation of rock mass with a single crack under seepage water pressure. Advances in Mechanical Engineering. 9(10), 168781401773289.

[15] Song, Z., Zhang, J. (2020) Progressive failure mechanical behaviour and response characteristics of sandstone under stress-seepage coupling. Journal of Geophysics and Engineering. 2, 200-218.

Received: **06.12.2021**
Accepted: **08.02.2022**

CORRESPONDING AUTHOR

Jinpeng Xu
School of Resources and Geosciences,
China University of Mining and Technology,
Xuzhou Jiangsu 221116 – China

e-mail: xu_jinpeng@126.com

© by PSP Volume 31– No. 05/2022 pages 5185-5191 Fresenius Environmental Bulletin

HETEROLOGOUS EXPRESSION OF LICHENASE GENE FROM *Streptococcus bovis* in *Escherichia coli* STRAIN XL1 BLUE MRF′

Makbule Baylan[1,*], Bahri Devrim Ozcan[2], Gamze Mazi[1]

[1]Cukurova University, Faculty of Fisheries, Department of Basic Science, Adana, Turkey
[2]Cukurova University, Faculty of Agriculture, Department of Animal Science, Adana, Turkey

ABSTRACT

In this study, *Streptococcus bovis* lichenase gene was cloned into recombinant vector pBR325SE2 (pBR325 plus *Spirulina platensis* serine esterase gene) and thus the integrative vector pBR325SLic was constructed. The pBR325SLic vector was transferred into the competent *E. coli* XL1 Blue MRF′ cells. Transformed bacteria *E.coli*/pBR325SLic grew in the selective medium containing chloramphenicol (Cm) while there were no non-transformant in the same medium. 1800 bp gene product using recombinant vector as template in PCR experiment was showed on the agarose gel. Lichenase production by recombinant *E. coli* cells cultivated in liquid media reached a maximum at 36 h, with levels of 192.8 μmol mg^{-1} protein/min. Optimum pH and temperature values for recombinant enzyme activity were 7.0 and 40 °C respectively. The recombinant enzyme lost most of its activity after pre-incubation at 50 °C for 15 min. However, the enzyme maintained its stability significantly in the pH range 4.0-10.0. The molecular weight of the enzyme was estimated to be 95.6 kDa by sodium dodecyl sulphate-polyacrylamide gel electrophoresis.

KEYWORDS:
Lichenase, *Streptococcus bovis*, *Escherichia coli*, Integrative vector, Cloning

INTRODUCTION

β-1,3-1,4-glucan is the major cell wall component of barley and other cereal endosperms. It consists of a polymer of glucose monomers joined by β-1,3- and β-1,4-glycosidic bonds in an irregular fashion [1, 2, 3]. 1,3-1,4-β-D-Glucan 4-glucanohydrolase (β-1,3-1,4-glucanase; lichenase) (EC 3.2.1.73) cleaves β-1,4 linkages adjacent to β-1,3 bonds in glucans, yielding cellobiosyltriose and cellotriosyltetraose [4, 5, 6]. Lichenases genes have been found in several microorganisms such as *B. subtilis* [7], *B. amyloliquefaciens* [8], *B. macerans* [9], *B. licheniformis* [10], *B. brevis* [11], *B. circulans* [12], *B. polymyxa* [13], *Clostridium thermocellum* [14], *Streptococcus bovis* [15], *Trichoderma reesei* [16] and *Orpinomyces* [6]. The β-(1,3-1,4)-glucanase gene from *Streptococcus bovis* was also cloned and expressed in *Lactococcus lactis* and *Enterococcus faecalis* [15].

Microbial lichenases used widely in animal feedstuff, especially for broiler chickens and piglets to improve digestibility and to reduce sanitary problems such as sticky droppings by enzymatic preparations containing bacterial β-glucanases [17, 18] and control of fungal pathogens and release of intracellular materials from microbial cells [19]. Therefore, the economic value of barley, oats, rye and even wheat can be improved by the addition of the appropriate preparation of β-glucanase and xylanase enzymes [20].

The serine esterase family includes enzymes responsible for the hydrolysis of a wide range of carboxyl ester substrates ranging from acetylcholine to long-chain fatty-acid esters of cholesterol or triacylglycerol and the juvenile hormones of insects. A particular serine residue at the active site of these enzymes is rendered reactive by the presence of histidine and a glutamate (or aspartate) residue, the components of the catalytic triad. Serine esterases catalyse hydrolysis of carboxylate esters [21].

In the present study, we aimed to construct the integrative vector pBR325SLic by cloning the *S. bovis* lichenase gene into pBR325SE2, and thus express the gene in *E. coli* XL1 Blue MRF' cells recombinantly.

MATERIALS AND METHODS

Bacterial Strains, Plasmids and Growth Conditions. *E. coli* XL1 Blue MRF' and pBR325 plasmid DNA were purchased from Stratagene and Sigma-Aldrich respectively. Recombinant plasmid DNA pBR325SE2 (pBR325 plus *S. platensis* serine esterase gene) was created in our laboratory [22]. pBR325SLic (pBR325SE2 plus lichenase gene) was created in this study. β-(1,3-1,4)-glucanase gene of *Streptococcus bovis* in host *E. coli* were obtained from culture collection of Prof. Dr.

Mehmet Sait Ekinci (University of Kahramanmaraş Sütçüimam, Kahramanmaraş, Turkey). *E. coli* XL1 Blue MRF' was cultured in LB (Luria-Bertani, 10 g/l tryptone, 5 g/l yeast extract, 10 g/l NaCl, the pH was adjusted to 7.5 with 1 M NaOH) and LB-Agar (1.5% wt/v agar) at 37 °C. For cultivation the bacteria *E. coli*/pBR325SE2 and *E. coli*/pBR325SLic, LB and LB-agar were supplemented with 25 μg mL^{-1} chloramphenicol (Cm).

DNA Modification and Cloning Procedures. The following modifying enzymes were purchased and used for DNA modifications; *Hind* III, *Bam* HI, and bacterial alkaline phosphatase, bacteriophage T4 DNA ligase as well as Pfu DNA polymerase (Fermentas, Vivantis and Promega Corporation). Restriction enzyme reactions were monitored by examining digestion by agarose gel electrophoresis using standard methods [23]. The lichenase gene was derived from the pL1Hc using *Hind* III and *Bam* HI restriction endonucleases. The lichenase gene was excised from gels and purified using the Genomic DNA Purification Kit (Fermentas). The shuttle vector pBR325SE2 was digested by *Hind* III and *Bam* HI and then dephosphorylated. The excised lichenase gene was cloned into the linearized pBR325SE2 and thus pBR322SLic was created. Recombinant plasmid pBR325SLic was transformed into the competent *E. coli* MRF' cells using the method as described previously [24].

PCR Analysis of Cloned Gene. For PCR analysis, recombinant plasmid pBR325SLic was subjected for isolation from recombinant *E. coli* cells according to [25]. The recombinant plasmid was used as a template in the PCR experiment to produce DNA fragment including gene sequence. Following primers were used for amplification of lichenase gene from the recombinant vector: Primer F: 5'-AAGTGAATTTAACTACGA-3', Primer R: 5'-GCTCTTCCATCAACATAC-3'. Amplification was performed on a Blue-Ray Biotech thermocycler and the PCR program was as follows: 95 °C for 3 min, 45 cycles of 94 °C for 40 s, 49 °C for 40 s, 72 °C for 40 s, and a final extension at 72 °C for 10 min [26]. The product (5 μL) was separated on a 0.8% agarose gel and analyzed for the yield of amplicons of expected sizes.

Enzymatic Properties of Recombinant Enzyme. β-(1,3-1,4) Glucanase (lichenase) activity was assayed by adding 1 mL enzyme (supernatant - extracellular proteins of 24 hours cultured recombinant *E. coli* cells) to 1 mL lichenan solution (2%, wt/v) in 0.1 M Na-phosphate buffer, pH 6.0 and incubating at 40°C for 30 min. After the reaction was stopped by the addition of 3 mL of 3,5-dinitrosalicylic acid reagent and incubating the sample tubes in boiling water for 5 min, A_{540} nm was measured in a Pharmacia spectrophotometer [27].

Temperature and pH effects on enzyme activity were assayed at different temperatures ranging from 20 to 100°C and at pH values ranging from 4 to 10 for 30 min. Following buffers were used in the reactions: 50 mM Na-acetate (pH 4-6), 50 mM Na-phosphate (pH 6-8) and 50 mM Tris (pH 8-10) [28]. Enzyme assay carried out as described previously.

For the measurement of thermal stability, the enzyme was pre-incubated at temperatures between 20 to 100°C for 30 min at optimum pH. The enzyme activity was determined under standard enzyme assay condition. Enzyme assay carried out as described previously.

The pH stability of lichenase was investigated over a pH range of 4–11 in 0.05 M buffers. Buffers used were Na-acetate (pH 4–6), Na-phosphate (pH 6–8), and tris (pH 8–11). Aliquots were taken after 30 min of incubation at 40°C and immediately assayed for residual lichenase activity [29].

Electrophoretic Analysis of Extracellular Proteins. To obtain the extracellular proteins of recombinant *E. coli* from culture supernatants, the overnight cultured cells were pelleted by centrifuge. The extracellular extracts (supernatants) were mixed with a 1:1 volume of 20% TCA for precipitation. After the incubation at room temperature overnight, protein pellets were obtained by centrifuge. Air-dried proteins were dissolved in 0.1 M Tris-HCL buffer (pH 8.0).

SDS-PAGE and SDS-Lichenan-PAGE (0.2% lichenan) were done as described previously [30] with slab gels (12% wt/v acrylamide). After the electrophoresis, the gel was stained for 1 h with Coomassie blue R 250 dye in methanol-acetic acid–water solution (4:1:5 by volume) and destained in the same solution without dye [31, 32]. For activity staining (zymogram analysis), SDS was removed by washing the gel at room temperature in solutions containing 50 mM Na_2HPO_4, 50 mM NaH_2PO_4 (pH 7.2), isopropanol 20% v/v for 1 h and 50 mM Na_2HPO_4, 50 mM NaH_2PO_4 (pH 7.2) for 1 h, respectively. Renaturation of enzyme proteins was carried out by keeping the gel overnight in a solution containing 50 mM Na_2HPO_4, 50 mM NaH_2PO_4 (pH 7.2), 5 mM β-mercaptoethanol and 1 mM EDTA at 4 °C. The gel was then transferred onto a glass plate, sealed with film, and incubated at 30°C for 4 h. The gel was stained in a solution of Congo-red (0.1% Congo-red, 0.2 M NaOH), for 1 h, and destained in 1 M NaCl for 30 min. Clear bands indicated the presence of lichenase activity [33, 34, 35].

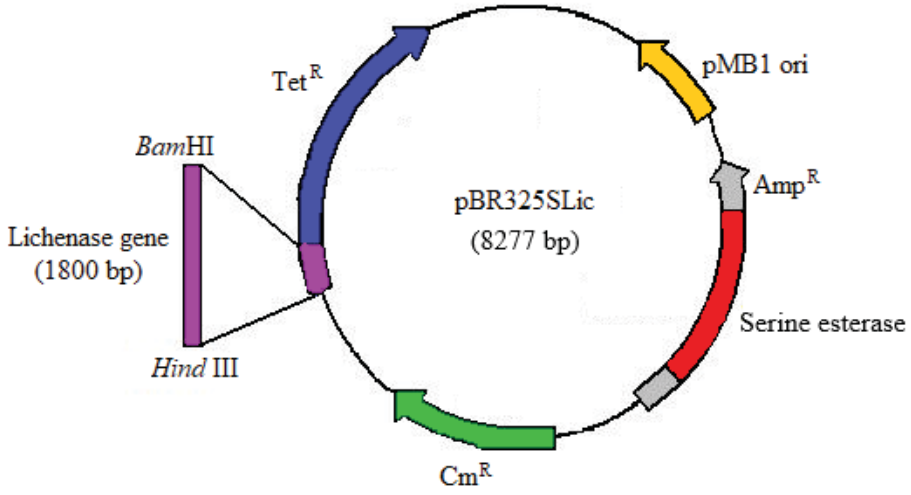

FIGURE 1
Structure of pBR325SLic (8277 bp; pBR325SE2 plus lichenase gene)

RESULTS AND DISCUSSION

In this study, the recombinant vector pBR325SLic (Figure 1) was created by ligating the lichenase gene into the *S. platensis*/*E. coli* integration vector pBR325SE2 [22] and transferred into the competent *E. coli* cells. *E. coli* colonies carrying the lichenase gene produced an activity zone as a result of Congo-red staining in the LB/Lichenan/Agar plate (Figure 2). PCR analysis using recombinant vector also produced a single band on agarose gel electrophoresis belonging to the lichenase gene of 1800 bp (Figure 3).

FIGURE 2
Congo-red staining of LB-lichenan-agar plate carrying recombinant and non-recombinant *E. coli* colonies (1: *E. coli* MRF′ strain as control (without any plasmid-no growth), 2: Recombinant *E. coli*/pBR325SLic colony showing clear lichenase activity)

Lichenase is one of the three distinct kinds of endoglucanases which active on lichenan and cereal glucans but not on carboxymethylcellulose and laminarin [36]. *Streptococcus bovis* JB1 lichenase gene cloned and characterized previously [15]. The 710 bps length gene is responsible for the production of 25 kDa protein. If plasmids carry sequences homologous to those of the host organism they could integrate into the chromosome [37]. Such an integrative vector had previously been developed cloning the cyanobacterium *Spirulina platensis* serine esterase gene into the plasmid pBR325 for *S. platensis* [22]. Although the *Streptococcus bovis* lichenase gene was previously cloned in *Escherichia coli* with different vectors [18], it was first cloned in this study using an integrative vector.

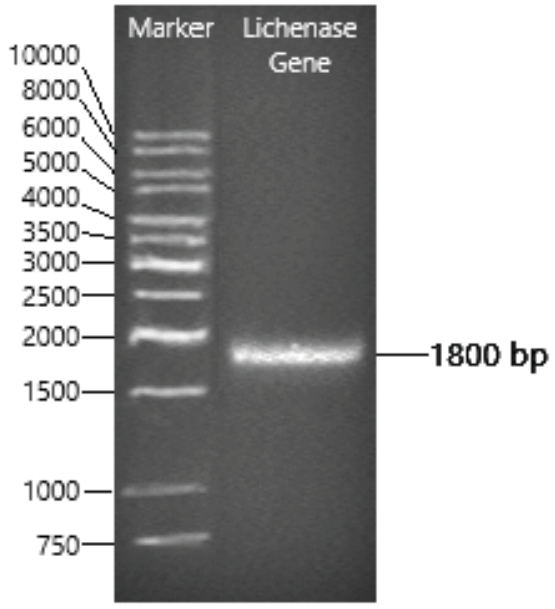

FIGURE 3
Agarose gel electrophoresis of lichenase gene amplified from recombinant vector via PCR

Temperatures between 20 and 100 ºC were used to test recombinant lichenase activity. Maximum lichenase activity was observed at 40 ºC (Figure 4A). The relative enzyme activities of the enzyme were 54, 94, 77 and 43% at 20, 30, 50, and 60 ºC respectively, after 30 min incubation. The enzyme lost most of its activity after incubation at 90 and 100 ºC. Besides,the relative enzyme activitiy between 20-60 ºC was calculated as 73.6%. Lichenase enzymes show a wide variation in pH and temperature optimum values. Teng et al [38] reported the optimum temperature of the *B. licheniformis* lichenase as 40 ºC. However, it was reported by other literature reviews that bacterial lichenases mostly show optimum activity above 40 ºC. Ekiz [39] and Kim et al [40] reported the optimum temperature of lichenase enzyme as 45 ºC, while Sun et al [41] and Furtado et al [42] 50 ºC, Afshin et al [43] and Yang et al [44]] 55 ºC, and Yang et al [45] 70 ºC. Optimum temperature of several lichenases from other studies were reported as 45 ºC [39, 40], 50 ºC [41, 42], 55 ºC [43, 44], and 70 ºC [45]. These reports indicated that optimum temperature of the recombinant lichenase is between normal values.

The thermal stability of the enzyme was determined by measuring its residual activity after preincubating at various temperatures. Enzyme activity remained relatively stable at 50 ºC and below after 30 min pre-incubation, but decreased rapidly beyond this temperature (Figure 4A). The stability of the enzyme at different pH levels was determined by preincubating the enzymes with the appropriate buffers. We found that the enzyme exhibited a significant amount of activity within the broader range of pH 4.0–10.0 (Figure 4B). Thermostability of enzymes is highly important in industrial applications, particularly in processes that require heat treatment. Recombinant lichenase may not show the expected thermal stability in heat treated industrial processes. This problem could be overcome by transferring the lichenase gene to a thermophilic bacterium, thereby increasing the thermostability of the enzyme. Aşan and Özcan [18] reported that the thermo-stability of the enzyme increased by cloning the *Streptococcus bovis* lichenase gene in a thermophilic bacterium *Streptococcus salivarius* subsp *thermophilus* FI8976. But this may not be enough for industrial production. This problem could be solved by transferring the gene into a non-pathogen thermophilic *Bacillus* strain suitable for industrial production. Such a genetic modification can increase the thermostability of enzymes, and a significant increase in enzyme production amounts depending on the copy numbers of the plasmid DNAs in the host microorganism.

Recombinant lichenase exhibited its maximum activity at pH 7.0 (Figure 4B). The average relative enzyme activity between pH 5.0 and 9.0 was 86%. Nevertheless, the average relative enzyme activity at pH 4.0–10.0 was 74%. The average enzyme activity at acidic (4.0-6.0) and alkaline (8.0-11.0) pH values were calculated as 65 and 61%, respectively. It has been reported that many bacterial lichenases show optimum activity around neutral pH values [44]. Although the recombinant lichenase enzyme showed its optimum activity at pH 7.0, it exhibited a wide pH activity range. Similar data were observed for the pH stability of the enzyme. The recombinant lichenase showed remarkable residual activity at pH 4.0-10.0. A similar result was reported by Yang et al [44] for the thermophilic fungus *M. cinnamomea* lichenase enzyme

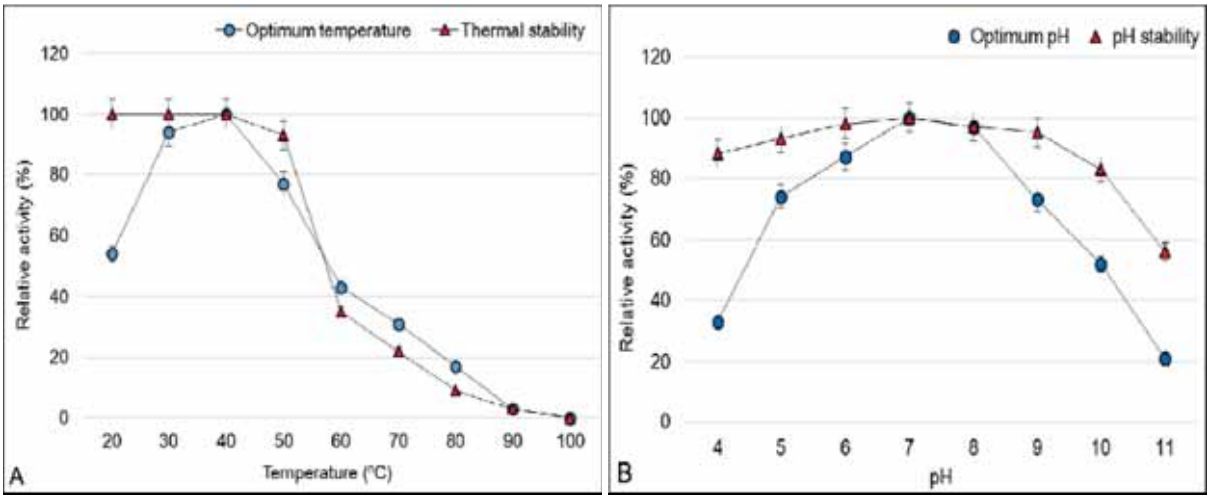

FIGURE 4
Enzymatic properties of recombinant lichenase. A) Effect of temperature on enzyme activity and stability, B) Effect of pH on enzyme activity and stability

with high activity values between 4.0-10.0 pH values. The high relative activity and stability of the lichenase enzyme at alkaline pH values make this enzyme a suitable candidate for use in areas such as detergent, paper and fruit juice industries where alkaline conditions are applied.

CONCLUSION

In the present study, *Streptococcus bovis* lichenase gene was cloned into *E. coli* XL1 Blue MRF′ via recombinant vector pBR325SE2. Research findings suggest that recombinant lichenase coud be used in industrial applications with current properties. However, the enzyme need to develop for thermal stability by cloning the gene into a thermostable bacterial strain.

REFERENCES

[1] Woodward, J.R., Phillips, D.R., Fincher, G.B. (1983) Water soluble (1-3), (1-4)-β-D-glucans from barley (Hordeum vulgare) endosperm. I. Physicochemical properties. Carbohydr. Polym. 3, 143–156.

[2] Edney, M.J., Marchylo, B.A., Macgregor, A.W. (1991) Structure of total barley-glucan. J. Inst. Brew. 97, 39–44.

[3] He, G., Zhang, X., Tang, X., Ruan, H. (2005) Partitioning and purification of extracellular β-1,3-1,4-glucanase in aqueous two-phase systems. Journal of Zhejiang University Science B. 6(8), 825–831.

[4] Anderson, M.A., and Stone, B.A. (1975) A new substrate for investigating the specificity of β-glucan hydrolases. FEBS Lett. 52, 202–207.

[5] Fleming, M., and Kawakami, K. (1977) Studies of the fine structure of b-D-glucans of barleys extracted at different temperatures. Carbohydr. Res. 57, 15–23.

[6] Chen, H., Li, X., Ljungdahl, L.G. (1997) Sequencing of a 1, 3-1,4-β-D-glucanase (Lichenase) from the anaerobic fungus *Orpinomyces* strain PC-2: Properties of the enzyme expressed in *Escherichia coli* and evidence that the gene has a bacterial origin. Journal of Bacteriology. 179(19), 6028-6034.

[7] Cantwell, B.A., McConnell, D.J. (1983) Molecular cloning and expression of a *Bacillus subtilis* β-glucanase gene in *Escherichia coli*. Gene. 23, 211-219.

[8] Hofemeister, J., Kurtz, A., Borriss, R., Knowles, J. (1986) The beta-glucanase gene from *Bacillus amyloliquefaciens* shows extensive homology with that of *Bacillus subtilis*. Gene. 49, 177-187.

[9] Borris, R., Manteuffel, R., Hofemeister, J. (1988) Molecular cloning of a gene coding for thermostable β-glucanase from Bacillus macerans. J. Basic Microbiol. 28, 1-10.

[10] Lloberas, J., Perez-Pons, J.A., Querol, E. (1991) Molecular cloning, expression and nucleotide sequence of the endo-β-1,3-1,4-D-glucanase gene from Bacillus licheniformis. Predictive structural analyses of the encoded polypeptide. Eur. J. Biochem. 197, 337-343.

[11] Louw, M.E., Reid, S.J., Watson, T.G. (1993) Characterization, cloning and sequencing of a thermostable endo-(1,3-1,4)-beta-glucanase encoding gene from an alkalophilic Bacillus brevis. Appl. Microbiol. Biotechnol. 38, 507-513.

[12] Bueno, A., Vazquez de Aldana, C.R., Correa, J., Villa, T.G., del Rey, F. (1990) Synthesis and secretion of a Bacillus circulans WL-12 1,3-1,4-β-D-glucanase in Escherichia coli. J. Bacteriol. 172, 2160-2167.

[13] Gosalbes, M.J., Pérez-González, J.A., González, R., Navarro, A. (1991) Two beta-glycanase genes are clustered in Bacillus polymyxa: molecular cloning, expression, and sequence analysis of genes encoding a xylanase and an endo-beta-(1,3)-(1,4)-glucanase. J. Bacteriol. 173, 7705-7710.

[14] Schimming, S., Schwarz, W.H., Staudenbauer, W.L. (1992) Structure of the *Clostridium thermocellum* gene licB and the encoded β-1,3-1,4-glucanase: a catalytic region homologous to *Bacillus* lichenases joined to the reiterated domain of clostridial cellulases. Eur. J. Biochem. 204, 13-19.

[15] Ekinci, M.S., McCrae, S.I,, Flint, H.J. (1997) Isolation and overexpression of a gene encoding an extracellular β-(1,3-1,4)-glucanase from *Streptococcus bovis* JB1. Appl. Environ. Microbiol. 63, 3752-3756.

[16] Saravanan, R., Pavani Devi, V., Shanmugam, A. (2007) Isolation and partial purification of extracellular enzyme (1,3)-β-D glucanase from *Trichoderma reesei* (3929). Biotech. 6, 440-443.

[17] Stone, B.A., and Clarke, A.E. (1992) Chemistry and biology of 1,3-β-glucans. La Trobe University Press, Bundoora, Australia.

[18] Aşan, M., Özcan, N. (2007) Expression of the β-(1,3-1,4)-glucanase gene in *Streptococcus salivarius* subsp. Thermophiles. Turkish Journal of Veterinary and Animal Science. 31(5), 319-324.

[19] Pitson, S.M., Seviour, R.J., McDougall, B.M. (1993) Noncellulolytic fungal β-glucanases: their physiology and regulation. Enzyme Microb. Technol. 15, 178-192.

[20] Zarghi, H. (2018) Application of xylanase and β-glucanase to improve nutrient utilization in poultry fed cereal base diets: Used of enzymes in poultry diet. Insights in Enzyme Research. 2(1), 11.
[21] Paul, G. (1999) Neuropathy target esterase. Biochemical Journal. 344, 625-631.
[22] Baylan, M. (2007) An investigation of gene transfer to *Spirulina platensis* (Cyanophyta). Ph.D. thesis, Institute of Natural and Applied Sciences, Çukurova University, Adana, Turkey.
[23] Sambrook, J, Fritsch, E.F., Maniatis, T. (1989) Molecular cloning: A laboratory manual. Cold Spring Harbor Laboratory.
[24] Hanahan, D. (1985) Techniques for transformation of *Escherichia coli*. In, Glover DM (Ed): DNA cloning: A practical approach. (1): 109-135, IRL. Press Inc., Oxford, United Kingdom.
[25] Birnboim, H.C., and Doly, J. (1979) A rapid alkaline extraction procedure for screening recombinant plasmid DNA. Nucleic Acids Research. 7, 1513-1523.
[26] Tekdal, D. (2009) Investigation facilities of gene transfer to *Spirulina platensis* (Cyanophyta) via electroporation. M.Sc. Thesis, Institute of Natural and Applied Sciences, University of Çukurova, Adana, Turkey.
[27] Miller, G.L. (1959) Use of dinitrosalicylic acid for determination of reducing sugar. Anal Chem. 31 (3), 424-426
[28] Özcan, N. (1992) Cloning and sequencing of a cellulase gene from *Fibrobacter succinogenes* SD35. PhD Thesis, Department of Molecular and Cell Biology, University of Aberdeen, Scotland, U.K.
[29] Elgharbi, F., Hmida-Sayari, A., Sahnoun, M., Kammoun, R., Jlaeil, L., Hassairi, H., Bejar, S. (2013) Purification and biochemical characterization of a novel thermostable lichenase from *Aspergillus niger* US368. Carbohydrate Polymers. 98, 967-975.
[30] Laemmli, U.K. (1970) Cleauage of structural proteins during the assembly of the head of the bacteriophage T4. Nature. 227 (5259), 680-685.
[31] Saul, D.J., Williams, L.C., Grayling, R.A., Chamley, L.W., Love, D.R., Bergquist, P.L. (1990) *celB*, a gene coding for a bifunctional cellulase from the extreme thermophile *Caldocellum saccharolyticum*. Appl. Environ. Microbiol. 56 (10), 3117-3124.
[32] Ozcan, N., Cunningham, C., Haris, W.J. (1996) Cloning of a cellulase gene from the rumen anaerobe *Fibrobacter succinogenes* SD35 and partial characterization of the gene product. Lett. Appl. Microbiol. 22 (1), 85-89.
[33] Lee, S.P., Morikawa, M., Takagi, M., Imanaka, T. (1994) Cloning of the *aapT* gene and characterization of its product, α-amylase-pullulanase (AapT), from thermophilic and alkaliphilic *Bacillus* sp. strain XAL601. Appl. Environ. Microbiol. 60 (10), 3764-3773.
[34] Ikeda, T., Yamazaki, H., Yamashita, K., Shinke, R. (1992) The tetracycline inducible expression of alpha-amylase in *Bacillus subtilis*. J. Ferment. Bioengineer. 74, 58-60.
[35] Coral, G., Arikan, B., Unaldi, M.N., Guvenmez, H. (2002) Some properties of crude carboxymethyl cellulase of *Aspergillus niger* Z10 wild-type strain. Turk. J. Biol. 26, 209-213.
[36] Khan, M.A.S., Akbar, M., Kitaoka, M., Hayashi, K. (2007) A unique thermostable lichenase from *Thermotoga maritime* MSB8 with divergent substrate specificity. Indian Journal of Biotechnology. 6, 315-320.
[37] Ekinci, M.S., Flint, H.J. (2002) Transformation and stability of cloned polysaccharidase genes in Gram-positive bacteria. Turkish Journal of Veterinary and Animal Science. 26, 303-308.
[38] Teng, D., Wang, J. H., Fan, Y., Yang, Y. L., Tian, Z. G., Luo, J., Yang, G.P., Zhang, F. (2006). Cloning of β-1,3-1,4-glucanase Gene from *Bacillus licheniformis* EGW039 (CGMCC 0635) and Its Expression in Escherichia coli BL21 (DE3). Applied Microbiology and Biotechnology. 72 (4), 705-712.
[39] Ekiz, D.Ö. (2017). Cloning of α-amylase and lichenase genes of bacteria isolated from rumen, molecular characterization of genes and enzymes. Ph.D. Thesis, Kahramanmaraş Sütçü İmam University, Graduate School of Natural and Applied Sciences, Kahramanmaraş, Turkey.
[40] Kim, J.Y., Kim, H.B., Lee, D.S. (2002). Cloning and expression of the Bacillus circulans endo-β-1,3-1,4-glucanase gene (bglBC1) in Escherichia coli. Biotechnology Letters. 24 (1), 53-57.
[41] Sun, J., Wang, H., Lv, W., Ma, C., Lou, Z., Yao, H., Dai, Y. 2012. Cloning and Expression of a Thermostable β-1,3-1,4-glucanase from Bacillus amyloliquefaciens ATCC 23350. Annals of Microbiology. 62 (3), 1235-1242.
[42] Furtado, G.P., Ribeiro, L.F., Santos, C.R., Tonoli, C.C., De Souza, A.R., Oliveira, R.R., Murakami, M.T., Ward, R.J. 2011. Biochemical and Structural Characterization of a β-1,3–1,4-Glucanase from Bacillus subtilis 168. Process Biochemistry. 46 (5), 1202-1206.
[43] Afshin, H., & Mirakhorli, N., and Saffar, B., and Khajali, F. (2020). Cloning and expression of β (1-3)(1-4) glucanase gene in *E. coli* for production as animal feed supplement. Journal of Molecular And Cellular Research (Iranian Journal of Biology). 33(1), 64-74.

[44] Yang, S., Xiong, H., Yan, Q., Yang, H., Jiang, Z. (2014). Purification and characterization of a novel alkaline β-1,3-1,4-glucanase (lichenase) from thermophilic fungus *Malbranchea cinnamomea*. J. Ind. Microbiol. Biotechnol. 41, 1487-1495.

[45] Yang, S., Qiaojuan, Y., Jiang, Z., Fan, G., Wang, L. (2008). Biochemical characterization of a novel thermostable β-1,3-1,4-glucanase (lichenase) from *Paecilomyces thermophile*. J. Agric. Food Chem. 56, 4345-5351.

Received: **07.12.2021**
Accepted: **08.02.2022**

CORRESPONDING AUTHOR

Makbule Baylan
Department of Basic Science,
Faculty of Fisheries
Cukurova University
Adana – Turkey

e-mail: makyan@cu.edu.tr

© by PSP Volume 31– No. 05/2022 pages 5192-5196 Fresenius Environmental Bulletin

CORRELATION BETWEEN DEVELOPMENT OF THE COUNTRY AND CONTRIBUTION TO AIR POLLUTION AN INDICATOR-BASED ANALYSIS FOR EU AND WBC

Zarko Vranjanac, Nenad Zivkovic, Amelija Djordjevic, Goran Janackovic, Dejan Vasovic*

University of Nis, Faculty of Occupational Safety in Nis, Carnojevica 10a Street, Nis, Republic of Serbia

ABSTRACT

Global climate changes are dominantly conditioned by the emission of greenhouse gases. With the aim of minimizing these impacts according to the Paris Climate Agreement, state parties oblige to limit the emission of greenhouse gases into the atmosphere. The present paper provides analysis of the contribution of CO_2 and nitrous oxide emissions as well as PM2.5 particles emission, in the function of air pollution in several developed EU countries (Germany, Austria and France) and Western Balkan countries (Serbia, Macedonia and Albania). The paper includes an in-debt analysis of the selected environmental indicators from the thematic area of air and climate change, according to the environmental indicators of the World Bank, EEA methodology and the applicable national methodology. Based on a conducted comparative analysis, the key findings show that in the observed countries there are significant differences with respect to the relative contribution to air pollution.

KEYWORDS:
Indicators-based analysis, emission of CO_2, nitrous oxide and PM2.5, development of a country

INTRODUCTION

Life on Earth is possible due to the existence of the natural greenhouse effect. The natural content of greenhouse gases (GHG) allows the Sun's energy to reach Earth, fall on it in the form of light, and then remain in the atmosphere in the form of infrared heat. This phenomenon keeps the planet warm enough, which ensures normal performance of the physiological functions of all living organisms.

CO_2 concentration, which is the most significant cause of the greenhouse effect, has increased by 35% (100 ppm) over the past 250 years. In the period 1995-2005, the concentration of anthropogenic CO_2 increased by 19 ppm, which represents the highest increase ever recorded. This sudden increase in CO_2 emissions has led to the global consensus on the need to reduce emissions in order to prevent and mitigate climate change. The basic document, based on which global efforts to reduce CO_2emissions are being implemented and coordinated, is the United Nations Framework Convention on Climate Change [1]. The Convention does not constitute a binding act, but it predicts the adoption of the protocols which introduce binding provisions for the state parties.

The most important such protocol is the Kyoto Protocol, according to which in the period 2008-2012, the most developed parties were obliged to reduce their emissions by 5% of those in 1990. The most important initiative of the EU is the obligation of the parties to reduce emissions by 20% of the 1990 level by 2020, to reach the level of energy production from renewable sources of 20%, and to reduce primary energy consumption by 20% by improving energy efficiency [2].

Regarding GHG emissions, it is evident that this represents a major responsibility of the developed countries, and therefore they should take the biggest burden of preventing and reducing GHG emissions. Annex II of the Convention suggests that the most developed countries assist developing countries in increasing their chances of meeting the Convention's goal through the implementation of the Convention measures and the preparation for their effective participation in the process of the Kyoto protocol implementation, as well as the relevant activities and actions implementation [3].

The Paris Climate Agreement distinguishes between developed and developing countries instead of Annex I and non-Annex I countries. It also did not introduce new ways of allocating emissions among countries to the notion of common but differentiated responsibilities and respective capabilities (CBDR-RC): as countries circumstances evolve, so too will their common but differentiated responsibilities [4, 5, 6].

The developing countries will be the earliest and most affected by climate change, although their contribution to these problems is relatively small. Their low incomes make it difficult to fund adjustments because the additional costs of developing countries adaptation to climate change can amount to several tens of billions of dollars. Furthermore, these countries face many difficulties in undertaking these actions, mainly due to the limited use of envi-

ronmentally friendly technologies, the lack of financial and human resources with adequate knowledge, and the lack of adequate efficient administrative structures [7]. Changes in energy technologies and the structure of economies have weakened the link between emissions and income growth, especially in some of the richest countries. By choosing the right policy it is possible to "decarbonize" both the developed and the developing economies to the extent necessary for climate stabilization while maintaining economic growth in both cases [8, 9, 10].

MATERIALS AND METHODS

The goal of the study is to analyse the contribution of annual emissions of direct and indirect GHGs and PM2.5 in developed EU countries (Germany, Austria, France) and Western Balkan countries (Serbia, Macedonia and Albania), throughout indicator-based analysis of global atmospheric pollution and climate stabilization of GHGs. Using the "DPSIR framework" as methodological basis, EEA indicators, as well as national indicators for environmental protection, the hybrid approach have been developed for the purpose of this paper [11,12]. Taking into account that paper considers the contribution to global atmospheric pollution, the following indicators from the WB thematic area of air and climate change have been considered and analysed, as follow: CO_2, nitrous oxide and PM2.5 particles emission [13].

CO_2 emission indicator shows the overall GHG emission, trend and sink. Direct greenhouse effect gases are gaseous atmospheric constituents that absorb and re-emit infrared radiation and they enter the atmosphere naturally or as a result of human activity. Indirect greenhouse effect gases are gaseous atmospheric constituents, which represent precursors of ozone, sulphate and aerosol, and they affect climate change [14].

The stabilization of direct and indirect GHGs, regardless of the level, requires annual emissions to be reduced to a level that balances the Earth's natural capacity to eliminate GHGs from the atmosphere. The longer the emissions are above this level, the higher the final stabilization level is. In the long term, global emissions should be reduced to below 5 Gt CO_2e annually - a level that a country can absorb without increasing the GHG concentration in the atmosphere. This is more than 80% below the absolute level of current annual emissions. The analysis is focused on the feasibility and costs of stabilizing GHG concentrations in the atmosphere in the range of 450-550 ppm CO_2e. Stabilizing to or below 550 ppm CO_2e would require global emissions to reach the maximum in the next 10-20 years, and then drop to a rate of at least 1-3% per year [15].

Nitrogen oxide emissions arise from energy processes, during the combustion of fossil fuels and biomass from agriculture, in the course of traffic, during industrial activities, and on animal farms. Nitrogen oxides are powerful (strong) greenhouse gases. Its estimated lifespan (114 years) is longer than the lifespan of methane (12 years). Nitrogen oxides have global warming capacities, about 310 times higher than CO_2 over a period of 100 years. Nitrogen oxide emissions are expressed in carbon dioxide equivalents using global warming potential, which makes it possible to compare the effective contribution of different gases. Each year of data shows the percentage change of that year from 1990 [16].

The impact of ambient air pollution with PM2.5 is defined by the average level of exposure of the nation's population to the concentrations of suspended particles of aerodynamic diameter less than 2.5 μm. Particles of this size have the ability to penetrate deeply into the respiratory tract of a person and cause severe health disorders. Population exposure is determined based on the mass of average annual concentrations of PM2.5 in ambient air in urban and rural areas. The guidelines set by the World Health Organization (WHO) for PM2.5 state that the annual mean concentrations should not exceed 10 $\mu g/m^3$, which represents a level lower than the one reported to have a negative effect on health [17].

It is clear that GHG emissions per capita are closely correlated with GDP. As a result, North America and Europe have so far produced about 70% of CO_2e emissions from energy generation, while developing countries account for less than a quarter. Most of future emissions will come from current developing countries due to a faster increase in population and GDP, as well as a growing share in energy-intensive industries. However, regardless of the historical pattern and common behaviour projections, the world should not choose between avoiding climate change and promoting growth and development [18].

RESULTS AND DISCUSSION

The study of the contribution of CO_2, nitrous oxide and PM2.5 aerosol emission to global atmospheric air pollution in the developed EU countries (Germany, Austria and France) and the developing Western Balkan countries (Serbia, Macedonia and Albania) was carried out from the indicator-based analysis to determinate impact of the GHG climate stabilization. The annual GHG emissions for the observed countries were taken from the IPPC report [18, 19]. The conducted analysis includes:

- the correlation of CO_2 emissions, expressed by the mass of the emitted gas expressed in kt, of the countries mentioned above;
- the nitrous oxide emission trend, expressed in %, relative to the reference year of 1990;
- PM2.5 air pollution, mean annual exposure to PM2.5 aerosol concentration levels in

micrograms per cubic meter.

The values of CO_2 emissions in Serbia, Macedonia and Albania, as well as in Germany, Austria and France, in the period 2006-2014, are shown in Figure 1. As expected, the most developed countries produce the greatest emissions.

Based on the analysed data, it can be concluded that the highest emission level of CO_2 is in Germany (Annual avg. 756473.5 kt), then in France (Annual avg. 346507.8 kt) and the smallest in Austria (Annual avg. 65516.6 kt). In Western Balkans countries the highest emission level of CO_2 is in Serbia (Annual avg. 47392.2 kt), significantly smaller in Macedonia (Annual avg. 8984.1 kt) and the smallest in Albania (Annual avg. 4678.6 kt).

The indicator of global atmospheric air pollution and climate change, the nitrous oxide emission trend for Serbia, Macedonia, Albania, Germany, Austria and France, from 2006 to 2012 in % change from 1990 is shown in Figure 2.

Based on the obtained results, it can be concluded that the average annual value of the nitrous oxide emission trend over the analysed period (for the reference year of 1990) in Serbia is higher than in Macedonia by 11.4% and by 14.6% than in Albania. The difference in the average annual value of the nitrous oxide emission trend between Macedonia and Albania is 3.2%. The percentage of the emission trend decrease in some Western Balkan countries reached the maximum in Serbia (100.0%) in 2006, 2007, 2011 and 2012, and in Macedonia in 2010 (37.4%), whereas the maximum was reached in Albania in 2007 (31.4%). The highest average annual decrease for the analysed period was achieved by Serbia (62%), while among the EU countries by France - 43.3%. Regarding Serbia, it can be observed that in 2008 it had a 15.4% and in 2010 50.4% increase in the nitrous oxide emission trend compared to 1990.

PM2.5 emissions, mean annual exposure in micrograms per cubic meter, as well as the indicator of global atmospheric air pollution and climate change in Serbia, Macedonia, and Albania, and the EU countries from 2010 to 2015 are shown in Table 1.

Based on the analysed data, it can be concluded that the average annual trend of exposure to PM2.5 aerosol emission over the analysed period was the highest in Macedonia and it amounted to 32%. In other words, it was 14.3% higher than in Serbia (17.7%), and 18.2% higher than in Albania (13.8%). In the EU countries, the value of this indicator was the highest in Austria (13.8%), which was 1.8% more than in Germany (12%) and 3.1% more than in France (10.7%). Based on this correlation, it can be concluded that there was less exposure to PM2.5 aerosols in Albania than in Serbia and Macedonia, and that in France, there was less exposure to PM2.5 aerosols than in Austria and Germany.

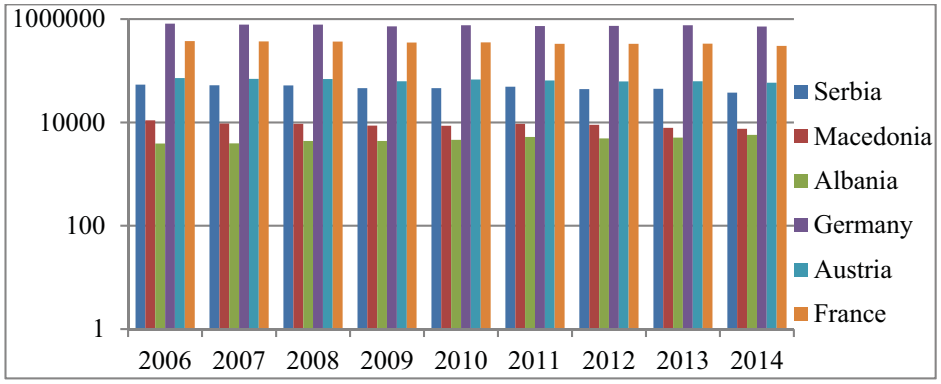

FIGURE 1
CO_2 emissions trend in kt in Serbia, Macedonia, Albania, and the EU countries from 2006 to 2014

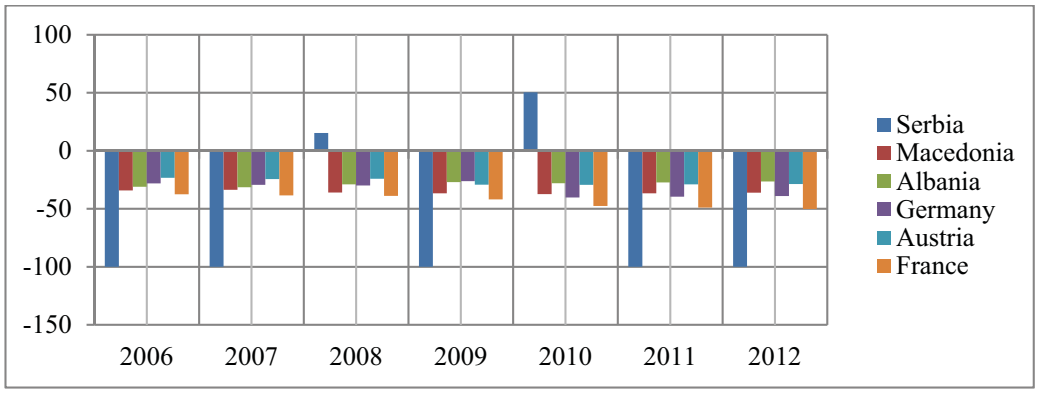

FIGURE 2
Nitrous oxide emission trend in Serbia, Macedonia, Albania, and selected EU countries from 2006 to 2012 in % change from 1990

TABLE 1
PM2.5 air pollution, mean annual exposure in Serbia, Macedonia, and Albania, and the EU countries from 2010 to 2015 in μg/m³

Year	Balkans			EU		
	Serbia	Macedonia	Albania	Germany	Austria	France
2010	20.1	34.9	15.3	13.7	15.1	12.2
2011	19.7	35.1	14.7	13.7	14.9	12.2
2012	19.2	34.2	14.5	13.3	15.2	12.3
2013	19.9	36.7	15.6	13.7	15.9	12.3
2014	20.6	38.6	16.7	13.9	16.5	12.3
2015	21.4	40.5	17.9	14.0	17.0	12.4
Total	120.9	220	94.7	82.3	94.6	73.7
Annual avg.	20.15	36.67	15.78	13.72	15.77	12.28
Country contribution (%)	17.7	32	13.8	12	13.8	10.7

By comparing the average annual trend of exposure to PM2.5 aerosol emission in Serbia, Macedonia and Albania with the EU countries (Germany, Austria, France) over the analysed period, correlations were determined. The average annual trend of exposure to PM2.5 aerosol emission in Germany was by 5.7% (6.43 μg/m³) lower than in Serbia, by 20% (22.95 μg/m³) lower than in Macedonia and by 1.8% (2.06 μg/m³) is lower than in Albania. The average annual trend of exposure to PM2.5 aerosol emission in Austria was by 3.9% (4.38 μg/m³) lower than in Serbia and by 10% (20.9 μg/m³) lower than in Macedonia, whereas the value was equivalent as in Albania. The average annual trend of exposure to PM2.5 aerosol emission in France was by 7% (7.87 μg/m³) lower than in Serbia, by 21.3% (24.39 μg/m³) lower than Macedonia, and by 3.1% (3.5 μg/m³) lower than in Albania.

CONCLUSIONS

The aim of this study was to carry out a comparative analysis of CO_2, nitrous oxide and PM2.5 aerosol emission in the EU countries (Germany, Austria and France) and the Western Balkan countries (Serbia, Macedonia and Albania). For the selected countries, the following values were determined: the value of the CO_2 emission indicator expressed by the mass of the emitted gas; the nitrous oxide emission trend relative to the reference year of 1990; PM2.5 air pollution, mean annual exposure trend expressed by the micrograms per cubic meter.

The comparative analysis of CO_2 emissions in Serbia, Macedonia and Albania in the period 2006-2014 indicated that there was a decrease in CO_2 emissions in Serbia and Macedonia, whereas an increase in CO_2 emissions was recorded in Albania. In EU countries, the highest level of CO_2 emissions is in Germany, then in France and the smallest in Austria. In addition, it can be concluded that all the above-mentioned EU countries have significantly reduced their emission levels in comparison with the base year 2006 over the last 4 years of the analysed period (2011-2014).

The nitrous oxide emission trend over the analysed period was higher in Serbia than in Macedonia and Albania, compared to the reference year of 1990. Serbia had the highest average decrease over the analysed period, and among the EU countries - France.

The annual trend of exposure to PM2.5 aerosol emission over the analysed period was the highest in Macedonia, followed by Serbia and Albania. In the EU countries, the value of this indicator was lower than in the Western Balkan countries.

It can be concluded that the use of innovative (green) technologies in the developed EU countries significantly reduces CO_2, nitrous oxide and PM2.5 aerosol emissions, while the use of conventional technologies in the Western Balkan countries contributes to a slower reduction of direct and indirect GHGs. Furthermore, the less developed countries should not be limited by reducing production, but rather supported by gradually introducing newer technologies which produce lower emissions of direct and indirect GHGs.

Environmental quality, global atmospheric pollution and climate change should therefore be tackled together using policies and measures that have been developed through an integrated approach. These integrated policies would avoid the negative feedback of climate on environmental quality, or vice versa, that has already been evidenced.

ACKNOWLEDGEMENTS

The published paper is the result of research funded by the Ministry of Education, Science and Technological Development of the Republic of Serbia.

REFERENCES

[1] United Nations. (1992) United Nations Framework Convention on Climate Change [online] https://unfccc.int/resource/docs/convkp/conv eng.pdf (Accessed May 2020).

[2] United Nations. (1998) Kyoto Protocol to the United Nations Framework Convention on Climate Change [online] https://unfccc.int/resource/docs/convkp/kpeng.pdf (Accessed May 2020).

[3] United Nations. (2015) Paris agreement [online] https://unfccc.int/sites/default/files/english_paris_agreement.pdf (Accessed May 2020).

[4] Kartha, S., Athanasiou, T., Caney, S., Cripps, E., Dooley, K., Dubash, N., Fei, T., Harris, P., Holz, C., Lahn, B., Moellendorf, D., Müller, B., Roberts, T., Sagar, A., Shue, H., Singer, P., Winkler, H. (2018) Cascading biases against poorer countries. Nat. Clim. Change. 8, 347–349.

[5] Rajamani, L. (2016) Ambition and differentiation in the 2015 Paris Agreement: Interpretative possibilities and underlying politics. Int. Comp. Law. Q. 65, 493–514.

[6] Pauw, P., Mbeva, K. and van Asselt, H. (2019) Subtle differentiation of countries responsibilities under the Paris Agreement. Palgrave Commun. 5, 86-87.

[7] Buccolieri, R., Cesari, R., Dinoi, A., Maurizi, A., Tampieri, F. and Di Sabatino, S. (2016) Impact of ship emissions on local air quality in a Mediterranean city's harbour after the European sulphur directive. Int. J. Environment and Pollution. 59(1), 30–42.

[8] IPCC. (2007) Fourth Assessment Report: Climate Change 2007 [online] https://www.ipcc.ch/pdf/assessmentreport/ar4/wg2/ar4_wg2_full_report.pdf (Accessed May 2018).

[9] IPCC. (2013) Climate Change 2013: The physical science basis. Contribution of working group I to the fifth assessment report of the intergovernmental panel on climate change. Cambridge University Press, Cambridge, UK and New York, USA.

[10] Li, D. (2021) Research on sustainable development planning of low-carbon city in Xi'an, China. Fresen. Environ. Bull. 30(1), 511-520.

[11] Vranjanac, Ž., Živković, N., Vasović, D., Janaćković, G., Dimitrovski D. (2018) Comparative Analysis of CO_2 Emissions Indicators in EU Countries and Western Balkan Countries – Assessment of Their Contribution to Climate Change. Journal of Environmental Protection and Ecology. 19(2), 453–461.

[12] Božnar, M., Grašič, B., Mlakar, P., Gradišar, D., Kocijan, J. (2017) The use of a new diagram for the analysis of the daily cycles in the air-pollution data. Int. J. Environment and Pollution. 62(2/3/4), 30–42.

[13] Dimitrovski, D., Djinlev, V. (2016) Calculating PM and NOx Emissions from Public Transportation: The Case of Skopje. Journal of Environmental Protection and Ecology. 17(3), 851-856.

[14] Živković, N., Mišić, N., Jovanović, M. (2015) Comparative analysis of the concentration of ambient air pollutants determined by measuring and modeling. Facta Universitatis, Series: Working and Living Environmental Protection. 11(2), 97-108.

[15] Vranjanac, Ž., Stojanović, J. (2015) The Impact of Traffic on Air Quality at the Intersection Streets in Nis. in IMKSM 15: Proceedings of the International May Conference of Strategic Management, Bor, Serbia. 887-895.

[16] Živković, N., Vranjanac Ž., Đorđević, A., Vasović, D., Dimitrovski, D. (2018) Contribution of CO_2, NO and PM2.5 particles emission to global atmospheric pollution: A comparative analysis of EU and Western Balkans countries. Paper presented at the 2nd GREDIT International Conference. Air, Water, Soil Pollution, Sustainable Development. 22-25 March 2018. Skopje, Macedonia.

[17] Popovic, D., Ostojic, G., Milincic, M., Dordevic, T., Sabic, D., Tatalovic, A. (2015) Climate Change and Regional Conflicts in the Southern Europe with an Emphasis on the Balkan Peninsula over the Past Two Millennia. Journal of Environmental Protection and Ecology. 16(2), 539-549.

[18] Carbon Dioxide Information Analysis Center (2016) Global Carbon Budget 2016. Environmental Sciences Division, Oak Ridge National Laboratory, Tennessee, United States. [online] http://cdiac.essdive.lbl.gov/GCP/carbonbudget/2016/ (Accessed May 2020).

[19] The World Bank. (2017) DataBank: World Development Indicators, Environment, emissions. [online] http://databank.worldbank.org/data/reports.aspx?source=2&series=EN.ATM.CO2E.KT&country=(Accessed May 2018).

Received: **11.12.2021**
Accepted: **08.02.2022**

CORRESPONDING AUTHOR

Dejan Vasovic
University of Nis,
Faculty of Occupational Safety in Nis,
Carnojevica 10a Street,
Nis – Republic of Serbia

e-mail: dejan.vasovic@znrfak.ni.ac.rs

© by PSP Volume 31– No. 05/2022 pages 5197-5203 Fresenius Environmental Bulletin

FERTILITY AND CHEMICAL COMPOSITION OF FOREST SOILS COVERED WITH *Allium ursinum* L. IN SERBIA

Zeljko Dzeletovic[1,*], Aleksandar Simic[2], Jordan Markovic[3], Gordana Andrejic[1], Tijana Denader[1], Snezana Babic[3]

[1]INEP Institute for the Application of Nuclear Energy, University of Belgrade, Banatska 31-b, 11080 Zemun Belgrade, Serbia
[2]Faculty of Agriculture, University of Belgrade, Nemanjina 6, 11080 Zemun - Belgrade, Serbia
[3]Institute for Forage Crops Kruševac, 37251 Globoder, Serbia

ABSTRACT

A. ursinum is a wild growing species, which is often found on various localities throughout Serbia, primarily within forest and occasionally on meadow. Fresh picked leaves and bulbs are used for preparing a salad or meals. For this research we have collected and analyzed soil and plant material from 12 different locations in Serbia. The analyses of basic fertility of soils have shown that *A. ursinum* grows mainly on acidic and soils containing high percentage of humus, with high total nitrogen content, low to medium supplies in available phosphorus and high supplies in available potassium. In those soils there is a very strong correlation between the total N content and total organic C (0.931). There is a relatively wide range of concentrations of overall Cd, Co, Cr, Cu, Ni, Pb and Zn in soils on which *A. ursinum* grows. The translocation factor for *A. ursinum* is TF ≥1 has been calculated for Cd, Pb and Zn.

KEYWORDS:
Wild garlic, soil fertility, trace elements, heavy metals

INTRODUCTION

Green leafy vegetables are an important ingredient in human nutrition, because they contain essential nutrients like vitamins, minerals, fibres and antioxidants. Among 920 onion species of the *Allium* genus there are many species appropriate for human nutrition like wild growing *Allium ursinum* L. [1]. It can be found in broadleaved forests or on forest glades, with dense stands, in moderate climatic conditions throughout Europe and in the north of Asia [2]. It is a perennial plant from which the aboveground part (leaves) is most frequently used by picking in the spring (Figure 1). New bulbs are also edible, and together with leaves are used for making salads. Because of its characteristic taste and nutrition value, *A. ursinum* has found its place in the cuisines of many nations as a seasoning or salad [3]. As a medicinal herb it is used in ethnomedicine [4, 5]; extracts and pure ingredients of *A. ursinum* represent a source of bioactive compounds [3, 4]. These compounds, in laboratory conditions, show antimicrobe and antioxidative activity [6].

The number of plant species, the structure and composition of plant communities depend on agrochemical characteristics of soil and managing the same [7]. The characteristics of soil substrate, on which *A. ursinum* grows, have not been specially analyzed, although some researchers consider that specific soil properties can have an effect on nectar characteristics in *A. ursinum* [8]. The goals of our research are (I) to establish the range of soil conditions on which this species grows in Serbia through basic analyses of soil fertility condition and (II) assess the impact of soil conditions on the concentrations of some heavy metals in individual *A. ursinum* organs.

FIGURE 1
Wild garlic (*Allium ursinum* L.)

TABLE 1
Basic soil fertility of locations covered by *Allium ursinum* in Serbia

Location	GPS N	GPS E	Elevation (m.s.l.)	pH_{H2O}	pH_{KCl}	N_{tot} (%)	Available (mg/100 g of soil) P_2O_5	Available (mg/100 g of soil) K_2O	Total organic C (%)	C/N
Taor	44,1094	19,8052	976	6.26	5.72	0.3523	5.12	20.14	5.435	15.43
Boždarevac	44,5508	20,3991	143	6.32	5.13	0.2732	3.41	29.23	2.099	7.68
Svileuva	44,4950	19,8110	181	6.02	4.72	0.3429	2.97	20.25	3.614	10.54
Bigrenica	44,0071	21,4704	282	6.97	5.99	0.4554	40.18	47.47	5.248	11.52
Petnica	44,2481	19,9551	272	6.62	5.54	0.3288	5.37	30.52	3.541	10.77
Bojčinska šuma	44,7456	20,1472	84	5.77	4.53	0.3081	8.75	38.11	3.228	10.48
Rudine	43,7150	19,7731	1029	6.89	6.25	0.2727	37.84	64.50	2.452	8.99
Kosmaj	44,4706	20,5748	509	5.71	4.97	0.2775	4.23	21.86	3.005	10.83
Rudnik	44,1288	20,5464	1105	5.46	4.42	0.4490	11.87	27.36	4.308	9.59
Ovčar	43,8982	20,1858	293	6.75	6.08	0.5780	4.45	21.32	7.526	13.02
Grabovica/Ždreban	44,0243	20,4871	497	6.25	5.20	0.2911	2.98	27.60	2.409	8.28
Lipovička šuma	44,6367	20,4122	277	5.34	4.04	0.1718	2.46	16.84	1.310	7.63
Average:			471	6.20	5.22	0.3417	10.80	30.43	3.681	10.40
SD:			364	0.55	0.71	0.1073	13.46	13.75	1.723	2.26

FIGURE 2
Underground (roots and bulb) and aboveground part (leaf) *A. ursinum* L.

MATERIALS AND METHODS

For this study we collected *A. ursinum* and soils from 12 locations in Serbia, Southeast Europe (Table 1). Sampling was carried out during April and May 2019. During the soil sample collection (from 0-20 cm depth), remnants of forest litter, fallen leaves, flattened grass, tree and shrub branches, mosses, etc., were removed. All research results relate to the features of the so-called fine soil, so that they are comparable with other authors' results. For the determination of basic soil fertility: pH, organic C content, total N (N_{tot}), available P_2O_5 and K_2O; and the analyses of total contents of Ca, Cd, Co, Cr, Cu, Mg, Ni, Pb and Zn, soil samples were air dried, ground in ceramic mortar and pestle and sieved through a 2 mm-sieve.

The plant material was washed with tap water, then rinsed with distilled water and air dried. The plant material (Figure 2) was then separated on the underground (roots and bulb) and aboveground part (leaf). The plant material was the ground for the analyses of total Cd, Co, Cr, Cu, Ni, Pb and Zn concentrations.

pH values were determined in water and 1M KCl, 1:2.5 w/v (ISO 10390:1994). Total organic C in the soil was determined by soil sample mineralization with boiling dichromate and sulphuric acid mixture and subsequent titration of excessive dichromate with Mohr salt solution [9]. N_{tot} in soil and plant samples was determined by semi-micro Kjeldahl method (ISO 11261:1995).

Available phosphorus (P_2O_5) and potassium (K_2O) were extracted according to Egner et al. [10], by extraction with AL solution (mixture of 0.1M ammonium lactate and 0.4M of acetic acid). P_2O_5 was determined by molybdenum blue method via spectrophotometer (580 nm, Shimadzu UV-1900i). The

K_2O concentrations have been determined by flame emission spectrophotometry on 766.5 nm, i.e. on the atomic absorption spectrophotometer Shimadzu AA-7000, according to calibration curve obtained after measuring the standard of known concentration.

The concentrations of metals (Cd, Co, Cr, Cu, Fe, Mn, Ni, Pb and Zn) in plant samples were determined by atomic absorption spectrophotometry (using a Shimadzu AA-7000 instrument), and their absorption values were compared with those of known standards. The translocation factor (TF) [11] has been calculated as follows:

$$TF = \frac{\text{Concentration of metals in leaves}}{\text{Concentration of metals in roots}} \quad (1)$$

The data presented in the tables represent arithmetic means and standard deviations (SD) of the results obtained from three analyses performed for each studied parameter. The correlation coefficients between the analysed parameters and statistical significance of correlation coefficients have been determined by Microsoft Excel 2010 for Windows.

RESULTS AND DISCUSSION

The soils on which *A. ursinum* grows are mostly acidic (Table 1), range of values from 5.34 to 6.97; 6.20 on the average; and from 4.04 to 6.25, average 5.22 for pH_{H2O} and pH_{KCl} respectively. The availability of metals in the soil has an increasing tendency at lower pH and decreasing at higher pH values [12].

These soils are characterized by relatively high N_{tot} content, 0.3417% on the average (Table 1). Due to relatively high N_{tot} content, soils with natural meadows and forests are characterized by relatively high intensities of mineralization and high indexes of N availability [13, 14].

The content of available K_2O is also relatively high, average 30.43 mg/100 g of soil (Table 1). However, although, according to content of available P_2O_5, these soils are medium supplied (average 10.80 mg/100 g of soil), they are mostly poor in P_2O_5. The contents of easily available P_2O_5 and K_2O in forest soils, are according to Nešić et al. [15], most frequently on optimal supply level.

The surface soil layer on which *A. ursinum* grows has predominantly a high percentage of humus, and contains 3.681% of organic C on the average (Table 1). This is considerably above the range of average values of the organic C content in forest soils in Serbia, 1.1-2.3% is noted by Nešić et al. [15]. Thereby, O-horizon in oak and beech forest soils, on which *A. ursinum* most often emerges, are characterized, relative to other types of forest trees, by medium content of soil organic C and N_{tot} and lower pH values [16]. According to Bodo et al. [8], the content of soil organic C negatively correlates with total quantity of nectar in *A. ursinum.*

The C/N ratio in analysed soils is in a wide range of values, from 7.63 to 15.43; average 10.40 (Table 1). Namely, in Serbia, according to Dželetović et al. [13], in forest soils, the values of C/N ratio are in the range of values from 10.31–12.79, and in natural meadow soils they are in the range from 9.04–10.52 [14]. Thereby, although the contents of total C and N in forest and meadow soils are in a relatively wider range of values, the correlation between these two parameters, according to Dželetović et al. [13] Dželetović and Mihailović [14], is very strong. Also, the results of our research confirm a very strong correlation ($r = 0.931$) between the total organic C and N_{tot} content in soils covered with *A. ursinum*.

The range of Ca and Mg concentrations is wide in the analysed soils, whereby average Mg concentrations are 10 times higher on the average from the average concentrations of Ca (Table 2). In most natural soils, the Ca concentration is usually higher relative to Mg [17]. According to Bodo et al. [8], the magnesium content in the soil positively correlates with total nectar quantity in *A. ursinum*.

TABLE 2
Concentrations of Ca, Cd, Co, Cr, Cu, Mg, Ni, Pb and Zn in soils covered by *A. ursinum* in Serbia (mg/kg)

Location	Ca	Cd	Co	Cr	Cu	Mg	Ni	Pb	Zn
Taor	906.55	0.15	12.02	45.55	18.66	7285.23	46.72	16.04	67.15
Boždarevac	257.88	0.16	8.91	23.38	12.69	4511.72	34.78	24.84	59.65
Svileuva	28.53	0.20	6.39	13.88	9.33	3917.43	13.65	14.36	54.72
Bigrenica	3229.89	0.09	10.76	25.53	22.15	7472.10	32.01	9.89	82.48
Petnica	262.44	0.20	8.29	20.71	11.80	5203.49	27.46	24.33	59.77
Bojčinska šuma	34.05	0.15	5.54	12.74	9.14	3973.32	13.71	22.04	47.78
Rudine	416.89	0.16	6.11	19.48	14.29	4585.24	25.08	21.91	62.11
Kosmaj	385.50	0.16	11.37	45.65	14.45	6375.57	49.51	52.40	70.52
Rudnik	22.14	0.33	12.52	26.15	20.62	6981.27	55.03	124.03	167.08
Ovčar	499.42	0.39	15.89	73.97	21.10	4889.58	208.90	35.05	69.11
Grabovica/Ždreban	43.92	0.18	8.17	11.33	6.14	4359.76	7.78	33.49	49.51
Lipovička šuma	18.37	0.04	7.49	12.85	8.08	3872.15	16.12	19.70	46.27
average	508.80	0.19	9.46	27.60	14.04	5285.57	44.23	33.17	69.68
SD	897.44	0.09	3.10	18.65	5.49	1366.64	54.05	30.75	32.43

TABLE 3
Strength of correlations between the analyzed soil parameters (r): (a) very strong (0.901 - 1.000); (b) strong (0.751 - 0.900); and (c) medium and weak (≤0.750)

Parameters	pH_{KCl}	$N_{tot.}$	P_2O_5	K_2O	Opr. C	Ca	Cd	Co	Cr	Cu	Mg	Ni	Pb
$N_{tot.}$	0.453 [c]												
P_2O_5	0.543 [c]	0.183 [c]											
K_2O	0.519 [c]	-0.011 [c]	0.884 [b]										
Organic C	0.523 [c]	0.931[a]	0.107 [c]	-0.113 [c]									
Ca	0.528 [c]	0.393 [c]	0.687 [c]	0.378 [c]	0.426 [c]								
Cd	0.196 [c]	0.750 [c]	-0.209 [c]	-0.182 [c]	0.623 [c]	-0.274 [c]							
Co	0.317 [c]	0.741 [c]	-0.105 [c]	-0.364 [c]	0.771 [b]	0.275 [c]	0.609 [c]						
Cr	0.469 [c]	0.652 [c]	-0.123 [c]	-0.281 [c]	0.776 [b]	0.171 [c]	0.577 [c]	0.879 [b]					
Cu	0.508 [c]	0.771 [b]	0.442 [c]	0.152 [c]	0.775 [b]	0.602 [c]	0.432 [c]	0.784 [b]	0.679 [c]				
Mg	0.309 [c]	0.446 [c]	0.345 [c]	0.041 [c]	0.504 [c]	0.628 [c]	0.089 [c]	0.619 [c]	0.406 [c]	0.793 [b]			
Ni	0.400 [c]	0.755 [b]	-0.122 [c]	-0.232 [c]	0.772 [b]	0.053 [c]	0.742 [c]	0.812 [b]	0.900 [b]	0.595 [c]	0.141 [c]		
Pb	-0.345 [c]	0.281 [c]	-0.119[c]	-0.165[c]	0.087 [c]	-0.299[c]	0.574 [c]	0.413 [c]	0.134 [c]	0.323 [c]	0.353 [c]	0.141 [c]	
Zn	-0.116[c]	0.490 [c]	0.194 [c]	0.011 [c]	0.313 [c]	0.095 [c]	0.511 [c]	0.499 [c]	0.173 [c]	0.633 [c]	0.624 [c]	0.193 [c]	0.884 [b]

TABLE 4
Average concentrations of Cd, Co, Cr, Cu, Ni, Pb and Zn in soils and in organs of *A. ursinum* (mg/kg ± SD) and translocation factors (TF) from all locations

	Cd	Co	Cr	Cu	Ni	Pb	Zn
soil	0.19 ± 0.09	9.46 ± 3.10	27.60 ± 18.65	14.04 ± 5.49	44.23 ± 54.05	33.17 ± 30.75	69.68 ± 32.43
root	0.30 ± 0.38	1.05 ± 1.17	11.02 ± 7.83	9.12 ± 10.01	5.91 ± 3.59	3.18 ± 3.30	12.64 ± 6.82
bulb	0.09 ± 0.21	0.59 ± 0.54	3.35 ± 2.74	0.00 ± 0.00	2.55 ± 1.77	1.42 ± 2.55	8.75 ± 2.63
leaf	0.32 ± 0.49	0.41 ± 0.58	3.23 ± 5.11	1.92 ± 2.50	3.51 ± 2.19	4.68 ± 7.34	12.17 ± 5.96
TF	1.07	0.40	0.29	0.21	0.59	1.47	0.96

Due to natural and antrophogenic causes, very diverse concentrations of trace metals appear in various habitats, from scarce to toxic [18]. A greater quantity of heavy metals in a soil can be manifested by increased accumulation in plants [19]. Various factors have an impact on biological accessibility, mobility, acceptance and toxicity of heavy metals in soil (soil pH, presence and nature of sorbents, inorganic and organic matter, root exudates and nutrients) [20]. Although the cadmium content in soil is low on all locations, 0.19 mg/kg on the average, it accumulated in plant material, i.e. in all parts. Cavanagh et al. [21] have established that the soil Cd and pH content correlate considerably with the Cd concentration in the onion, explaining the 38% variation, while the inclusion of the location as an additional variable, explained the 50% variation. The results of our research show slight correlation of Cd concentrations in soil with pH values (r = 0.196; Table 3). It is interesting that none of the analysed soil parameters correlate with pH value (Table 3). Although Cd concentrations in the root and leaf of *A. ursinum* are not phytotoxic, they are higher than in the soil, which resulted that TF is >1.0 (Table 4).

The Co concentrations in the examined soils range from 5.54 to 15.89 mg/kg, average 9.46 mg/kg (Table 2). According to Kabata-Pendias [22] the Co average value in the soil surface layer is approximately 10 mg/kg. Thereby, the Co concentrations in the examined soils show a strong correlation (r = 0.771) with the organic C concentration (Table 3).

The Cr concentrations in the examined soils range from 11.33 to 73.97 mg/kg, average 27.60 mg/kg (Table 2). This is somewhat lower than the average Cr content in the soil (60 mg/kg), stated by Kabata-Pendias [22]. The Cr concentrations in the examined soils show a strong correlation (r = 0,879) with Co (Table 3). The accumulation of this element showed certain regularity, i.e. considerably higher accumulation in the root or in the underground parts of the plant compared with the aboveground part (Table 4).

In soils covered with *A. ursinum* the Cu concentrations range from 6.14 to 22.15 mg/kg, average 14.04 mg/kg (Table 2), which is lower than the usual values for Cu concentrations in soils (14-109 mg/kg) [22]. Thereby, the Cu concentrations in the examined soils correlate with the contents of: N_{tot} (r = 0,771); organic C (r = 0,775); Co concentrations (r = 0,784); and Mg (r = 0,793) (Table 3). Copper is a necessary metal for higher plants and algae, especially for photosynthesis process. However, the accumulation of copper in the *A. ursinum* plant parts did not have certain regularity (Table 4).

The Ni concentrations in the examined soils are in a very broad range, from 7.78 to even 208.90 mg/kg (Table 2). It is considered that natural Ni concentration in soils is lower than 100 mg/kg [23]. A high Ni concentration in the soil from Ovčar is probably the result of natural Ni enrichment, because the lands in the area around the mountain Ovčar in Western Serbia are characterized by increased Ni concentrations [24]. Thereby, the Ni concentrations in the examined soils correlate with (Table 3): N_{tot} (r = 0.755); organic C (r = 0.772); Co concentrations (r = 0.812); and Cr (r = 0.900) (Table 3).

Nickel was not accumulated significantly in the plant material even on the locations with excess Ni

in the surface. Higher concentrations of Ni in underground parts is observed in almost all samples (Table 4). Plants cannot sustain their life cycle without adequate Ni supply, as it is a constituent part of several enzymes required for nitrogen metabolism in higher plants [25] and Ni supports plants in overcoming numerous biotic and abiotic stresses [26]. However, excessive Ni concentrations may lead to production of reactive oxygen species – ROS, and so affects numerous physiological and biochemical processes, such as photosynthesis, transpiration, as well as mineral nutrition, and it also causes phytotoxicity in plants [23]. Plants growing on metal contaminated surfaces show changed metabolism, reduced growth, and produce lower biomass and accumulate metals [27].

The Pb concentrations in the examined soils are within the range of concentrations usual for natural unpolluted soils, from 7.78-55.03 mg/kg. An exception is only the soil from mountain Rudnik, with 124.03 mg/kg. In the vicinity of this location is a Pb/Zn mine, which explains the naturally increased Pb concentrations in soil. Pb is present in a small quantity in almost all cultivated crops, and its concentration has been increasing considerably by growing these crops on soils contaminated with Pb [28]. The Pb concentrations in the examined soils more intensively correlate only with Zn concentrations ($r = 0.884$) (Table 3). Although detrimental effects of Pb are shown on sprouting, establishing stands, growth, uptake of nutrients and assimilation, ultra-structural and oxidative damages, carbon metabolism and enzymatic activities in plants [28], these symptoms have not been noticed in *A. ursinum* on Rudnik location (Figure 3). A high tolerance of some species of *Allium* genus to lead (Pb) is well known, in which the storage organ – bulb has the main role [29]. In addition, higher Pb concentrations that we have established in the leaf, not in the root and bulb, have resulted in relatively high TF (1.47).

Zinc is naturally present in all soils, most often in the concentrations ranging from 10-100 mg/kg [30]. In the examined soils only the sample of the soil from Rudnik location exceeds this range of concentration values, with 167 mg/kg, which has been expected, because in the environment (surroundings) nearby there is a Pb/Zn mine. Soils that are zinc contaminated with adverse effect on the soil ecosystem, are located around Zn smelting works, near Zn mine and under galvanized structures (e.g. high-voltage power-line poles) [30]. Toxic effects have been identified in overall Zn concentrations ranging from 100 to >1000 mg/kg, and toxicity is decreasing with an increase of exchangeable ion soil capacity [30]. Potentially detrimental Zn levels in soil from the mountain Rudnik (167 mg/kg), according to Kaur and Garg [31] may result in various changes in plants, such as: reduced growth, reduced photosynthesis and respiration, unbalanced mineral nutrition and intensified generation of ROS. These symptoms, as we have stated previously for Pb, have not been noticed. Zinc is quite uniformly accumulated in all the examined parts of the plant, without significant variations, so that TF is approximately 1.0 (Table 4).

In relation to similar research carried out in the region, Vučić et al. [32] have recorded considerably lower Cu concentrations in *A. ursinum*, from 1.56-1.93 mg/kg, Zn: 2.31-2.61 mg/kg, Ni: 0.36-0.39 mg/kg, Cr: 0.07-0.08 mg/kg and Co: 0.02-0.04 mg/kg, while Pb and Cd were below detection limit. On the contrary, Stojković [33] stated considerably higher Zn concentrations in *A. ursinum* (10.5-33.6

FIGURE 3
***A. ursinum* on location Rudnik.**

mg/kg). Increased content of organic matter in the soil reduces the availability of Cd, Pb and Zn. When examining *A. ursinum* in the conditions existing in Slovakia, in neutral (pH_{KCl} = 7.02) and in soil with high percentage of humus (3.47%), it as recorded somewhat higher metal concentrations: Zn 190 mg/kg, Cd 3.88 mg/kg, Cu 24.8 mg/kg, Ni 39.1 mg/kg, Pb 40.8 mg/kg [34].

CONCLUSION

The analyses of the basic soil fertility have shown that *A. ursinum* grows in Serbia mainly on acidic and soils with high percentage of humus, with high N_{tot} content, having low to medium percentage of available phosphorus, and high percentage of available potassium. In those soils there is a very strong correlation between the N_{tot} content and total organic C (r = 0.931). Therefore, *A. ursinum* grows on soils with wider range of concentrations of total Cd, Co, Cr, Cu, Ni, Pb and Zn. Potentially low detrimental Pb and Zn levels in the soil have not shown visible symptoms of toxicity in plants. In *A. ursinum* plants the translocation factor (TF) ≥1 for Cd, Pb and Zn has been calculated.

ACKNOWLEDGEMENTS

We acknowledge Ministry of Education, Science and Technological Advancement of Republic of Serbia, Agreement No: 451-03-9/2021-14/200019 (Ž. Dželetović and G. Andrejić); 451-03-9/2021-14/200116 (A. Simić); and 451-03-9/2021-14/200217 (J. Marković and S. Babić).

REFERENCES

[1] Radulović, N.S., Miltojević, A.B., Stojković, M.B., Blagojević, P.D. (2015) New volatile sulfur-containing compounds from wild garlic (*Allium ursinum* L., Liliaceae). Food Res. Int. 78, 1-10.

[2] Schmitt, B., Schulz, H., Storsberg, J., Keusgen, M. (2005) Chemical characterization of *Allium ursinum* L. depending on harvesting time. J. Agric. Food Chem. 53(18), 7288–7294.

[3] Demasi, S., Caser, M., Donno, D., Enri, S.R., Lonati, M., Scariot, V. (2021) Exploring wild edible flowers as a source of bioactive compounds: New perspectives in horticulture. Folia Hortic. 33(1), 27-48.

[4] Krivokapić, M. (2021) Assessment of antimicrobial, anti-inflammatory, antioxidant and cardioprotective effects of wild garlic extract, *Allium ursinum* L. PhD Thesis [in Serbian with English abstract], Faculty of Medical Sciences University of Kragujevac, Kragujevac.

[5] Živković, J., Ilić, M., Šavikin, K., Zdunić, G., Ilić, A., Stojković, D. (2021) Traditional Use of Medicinal Plants in South-Eastern Serbia (Pčinja District): Ethnopharmacological Investigation on the Current Status and Comparison With Half a Century Old Data. Front. Pharmacol. 118, 1020.

[6] Gođevac, D., Vujisić, L., Mojović, M., Ignjatović, A., Spasojević, I., Vajs, V. (2008) Evaluation of antioxidant capacity of *Allium ursinum* L. volatile oil and its effect on membrane fluidity. Food Chem. 107(4), 1692-1700.

[7] Skuodiene, R., Katutis, K., Nekrosiene, R., Repsiene, R., Karcauskiene, D. (2016) Effects of soil properties and humidity regimes on semi-natural meadow productivity. Acta Agr. Scand. B–S. P. 66(8), 653-663.

[8] Bodo, A., Farkas, A., Nagy, D.U., Rudolf, K., Hoffmann, R., Kocsis, M., Morschhauser, T. (2021) Soil humus, iron, sulphate and magnesium content affect nectar traits of wild garlic (*Allium ursinum* L.). Plants. 10(3), 597.

[9] Pansu, M., Gautheyrou, J. (2006) Handbook of Soil Analysis: Mineralogical, Organic and Inorganic Methods. Springer. Berlin. 1-993.

[10] Egner, H., Riehm, H., Domingo, W.R. (1960) Investigations of the chemical soil analysis as a basis for the evaluation of nutrient status in soil. II. chemical extraction methods for phosphorus and potassium determination. K Lantbruks Høgsk Ann, 26, 199-215. [in German].

[11] Baker A.J. (1981) Accumulators and excluders-strategies in the response of plants to heavy metals. J. Plant Nutr. 3(1-4), 643-654.

[12] Sanchez-Camazano, M., Sanchez-Martin, M.J., Lorenzo, L.F. (1994) The content and distribution of cadmium in soils as influenced by the soil properties. Sci. Total Environ. 156(3), 183-190.

[13] Dželetović, Ž.S., Pivić, R.N., Djurović, N.L.J. (2011) Available nitrogen in the surface mineral layer of Serbian forest soils. J. Forest Sci. 57(4), 131-140.

[14] Dželetović, Ž.S., Mihailović, N.L.J. (2017) Available nitrogen in the surface mineral layer of natural meadows. Acta Univ. Agric. et Silvic. Mendelianae Brun. 65(5), 1483-1492.

[15] Nešić, L.J., Pucarević, M., Sekulić, P., Belić, M., Vasin, J., Ćirić, V. (2008) Main chemical properties of Srem soils [in Serbian with English abstract]. Zbornik radova Instituta za ratarstvo i povrtarstvo. 45(2), 255-263.

[16] Oostra, S., Majdi, H., Olsson, M. (2006) Impact of tree species on soil carbon stocks and soil acidity in southern Sweden. Scand. J. Forest Res. 21(5), 364-371.
[17] Blume, HP., Brümmer, G.W., Fleige, H., Horn, R., Kandeler, E., Kögel-Knabner, I., Kretzschmar, R., Stahr, K., Wilke, B.M. (2016) Scheffer/Schachtschabel Soil Science. Springer-Verlag, Berlin Heidelberg. 1-618.
[18] Andresen, E., Peiter, E., Küpper, H. (2018) Trace metal metabolism in plants. J. Exp. Bot. 69(5), 909–954.
[19] Lidiková, J., Čeryová, N., Šnirc, M., Vollmannová, A., Musilová, J., Brindza, J., Grygorieva, O., Fehér, A. (2021) Comparison of Heavy Metal Intake by Different Species of the Genus *Allium* L. Biol. Trace Elem. Res. 199(11), 4360–4369
[20] Pinto, E., Aguiar, A.A., Ferreira, I.M. (2014) Influence of soil chemistry and plant physiology in the phytoremediation of Cu, Mn, and Zn. Crit. Rev. Plant Sci. 33(5), 351-373.
[21] Cavanagh, J.A.E., Yi, Z., Gray, C.W., Munir, K., Lehto, N., Robinson, B.H. (2019) Cadmium uptake by onions, lettuce and spinach in New Zealand: Implications for management to meet regulatory limits. Sci. Total Environ. 668, 780-789.
[22] Kabata-Pendias, A. (2011) Trace elements in soils and plants. 4th Edition. CRC Press, Boca Raton. 1-505.
[23] Shahzad, B., Tanveer, M., Rehman, A., Cheema, S. A., Fahad, S., Rehman, S., Sharma, A. (2018) Nickel; whether toxic or essential for plants and environment - A review. Plant Physiol. Biochem. 132, 641-651.
[24] Stajković-Srbinović, O., Delić, D., Rasulić, N., Kuzmanović, D.J., Houšková, B., Sikirić, B., Mrvić, V. (2017) Microorganisms in soils with high nickel and chromium concentrations in Western Serbia. Pol. J. Environ. Stud. 26(4), 1663–1671.
[25] Mustafiz, A., Ghosh, A., Tripathi, A.K., Kaur, C., Ganguly, A.K., Bhavesh, N.S. (2014) A unique Ni^{2+}-dependent and methylglyoxal-inducible rice glyoxalase I possesses a single active site and functions in abiotic stress response. Plant J. 78, 951-963.
[26] Sreekanth, T.V.M., Nagajyothi, P.C., Lee, K.D., Prasad, T.N.V.K.V. (2013) Occurrence, physiological responses and toxicity of nickel in plants. Int. J. Environ. Sci. Technol. 10(5), 1129-1140.
[27] Nagajyoti, P.C., Lee, K.D., Sreekanth, T.V.M. (2010) Heavy metals, occurrence and toxicity for plants: a review. Environ. Chem. Lett. 8(3), 199-216.
[28] Zulfiqar, U., Farooq, M., Hussain, S., Maqsood, M., Hussain, M., Ishfaq, M., Ahmad, M., Anjum, M.Z. (2019) Lead toxicity in plants: Impacts and remediation. J. Environ. Manage. 250, 109557.
[29] Wierzbicka, M. (1999) Comparison of lead tolerance in *Alium cepa* with other plant species. Environ. Pollut. 104(1), 41-52.
[30] Martens, J., Smolders, E. (2013) Zinc. In: Alloway B.J. (Ed.) Heavy metals in Soils - Trace Metals and Metalloids in Soils and their Bioavailability, Series: Environmental Pollution 22, Springer, Dordrecht. 465-493.
[31] Kaur, H., Garg, N. (2021) Zinc toxicity in plants: a review. Planta. 253(6), 129.
[32] Vučić, G., Vasilišin, L., Samelak, I., Kukrić, Z., Kukrić, N. (2018) Contents of Minerals in Sremus (*Allium ursinum*) from Different Locations of the Republic of Srpska [in Serbian with English abstract]. In: Miletić, N., Marković, D. (Eds.): 23rd International Symposium on Biotechnology, Faculty of Agronomy, Čačak, Serbia. 530-535.
[33] Stojković, M.B. (2014) Antioxidant activity, phenolic and mineral content of plant species: *Geranium macrorrhizum* L., *Allium ursinum* L., *Stachys germanica* L. and *Primula veris* L. PhD thesis [in Serbian with English abstract], University od Niš, Feculty of Science and Mathematics, Department of Chemistry, Niš.
[34] Lenková, M., Bystrická, J., Tóth, T., Hrstková, M. (2016) Evaluation and comparison of the content of total polyphenols and antioxidant activity of selected species of the genus *Allium*. J. Cent. Eur. Agric. 17(4), 1119-1133.

Received: **14.12.2021**
Accepted: **08.02.2022**

CORRESPONDING AUTHOR

Zeljko Dzeletovic
INEP Institute for the Application of Nuclear Energy,
University of Belgrade,
Banatska 31-b 11080
Zemun Belgrade – Serbia

e-mail: zdzeletovic@inep.co.rs

© by PSP Volume 31– No. 05/2022 pages 5204-5215 Fresenius Environmental Bulletin

UNFAVORABLE CLIMATIC FACTORS AND THEIR IMPACT ON THE DECLINE OF SPRUCE AT THE KOPAONIK NATIONAL PARK (CENTRAL SERBIA)

Goran Cesljar[1,*], Ljiljana Brasanac-Bosanac[1], Ilija Dordevic[1], Sasa Eremija[1], Marija Milosavljevic[1], Filip Jovanovic[1], Ljubinko Rakonjac[1], Srdan Simovic[2]

[1]Institute of Forestry, Kneza Višeslava 3, 11030 Belgrade, Serbia
[2]Kopaonik National Park, Suvo Rudište bb, 36354 Kopaonik, Serbia

ABSTRACT

The paper presents the results of research on the influence of natural (biotic and abiotic) factors on the decline of spruce [Picea abies (L.) Karst.] at the Kopaonik National Park (Republic of Serbia), in the period from 2010 to 2019. As an indicator of the influence of unfavorable climatic factors on the decline of forests in the Kopaonik National Park, the share of random yields of wood volume in the total allowable cut, resulting from the overpopulation of bark beetles, was determined. In order to understand the causes of decline, a sample plot, located in pure spruce stand older than 60 years in the northwest exposure and at the altitude of 1720 m, was used to monitor and assess the impact of air pollution and its effects on forest ecosystems. Furthermore, the data on temperatures and precipitation amounts during the year and in the vegetation period were analyzed in order to understand and connect the influence of unfavorable climatic factors with the decline of trees more clearly. A comparison was made between tree mortality, when occurred, with the Standardized Precipitation Index (SPI) and the Standardized Precipitation Evapotranspiration Index (SPEI) as the most commonly used indicators for monitoring drought. It was stated that the decline of trees was initiated by the influence of unfavorable climatic factors during three consecutive years (2011–2013), accompanied with snowstorms during the winter of 2012, which created favorable conditions for overpopulation of bark beetles as secondary pests. As a result, one of the largest deforestations was recorded on the territory of the Kopaonik National Park. These results indicate that changes in precipitation and air temperature, whose deviations from the decade long average have been occurring regularly for several years, have significantly weakened the vitality of trees, and thus increased their predisposition to the increase of already present bark beetles.

KEYWORDS:
Forest decline, climate factors, drought, bark beetle overpopulation, random yield of wood volume, Kopaonik National Park

INTRODUCTION

Decline of forests is one of the most recent problems in the world and in the Republic of Serbia, both from economic and ecological aspects. By observing only the last decade in Europe, the highest temperatures, without precipitation, have been recorded. It doesn't take long before a year or a season is characterized as the warmest and driest since the beginning of meteorological measurements in countries all over Europe [1, 2, 3]. The same observations are made globally [4]. These events greatly affect the resistance of different tree species. The research of Schuldt *et al.* [5] states that even species which are considered drought-resistant, such as pine (*Pinus nigra* J.F.Arnold) and beech (*Fagus sylvatica* L.), suffer long-term damage, with spruce (*Picea abies* /L./ Karst.) being most affected.

Decline of the forests is a result of number of factors. A numerous researchers deal with this issue. Some of them point out that unfavorable climate factors are dominant and primary in terms of forest mortality [6, 7, 8, 9, 10, 11, 12, 13, 14, 15, 16, 17, 18]. Climate change, at the local or regional level, increases the risk of extinction of certain plant species [19]. Droughts, accompanied by high temperatures, have a strong impact on forest ecosystems and are predisposed to outbreak of bark beetle in coniferous forests [20]. Some authors note that there may be a change in structure and composition of tree species in a particular area affected by drought, which is directly caused by drought [21], or insect attacks on trees weakened by drought [22], where the end result is the same. Unfavorable climate factors lead to decrease in stability of the entire ecosystem, which causes a disturbance of the biological balance and an increase in number of insects and phytopathogenic fungi, with the forest decline as a final outcome. If, in addition to all the

above, natural disasters such as snow, wind or ice occur, then the consequences in national parks are inevitable.

One of the main problems in national parks, as strictly protected areas, is that forest management is not allowed as in unprotected forests, where the amount of dead wood is much smaller, since sanitary feelings, removal of fallen trees after snowbrakes and windbrakes and other sanitary measures are allowed. In accordance with the previously presented approach of intensive protection of forest ecosystems, it is important to point out the fact that national parks are one of the highest forms of environmental protection and represent ideal areas for studying natural processes and their relations that are not affected by humans. Within national parks, especially in the first zones of protection, forests are left to run its own course, so it is only possible to monitor the development without any management.

Due to projected climate change [23], primarily considering the frequency of extreme climate events, there is a need for a strategy that will adapt existing forests to future conditions [24]. This scenario can be very important for forest ecosystems in which spruce is the main species because it is susceptible to many risks, such as windbreaks, snowbreaks, pathogens and pests (e.g., bark beetles). In the research of Neuner *et al.* [25], it is noted that spruce has less chances of survival if it is found in clean stands due to the warm climate. Also, Krupková *et al.* [26] and Bolte *et al.* [27] note that spruce is prone to both biotic and abiotic influences, where drought plays a crucial role, due to its shallow root. In fact, drought is a major cause of spruce decline [28], and bark beetles are one of the first insects to attack weakened spruce trees. Monitoring the changes in trees, affected by the decline process, is necessary in order to understand the cause itself, because it is known that several factors are linked. Vital spruce trees have several levels of defense system against bark beetle attacks. The first level of defense is the release of resin after the bark beetle penetrates the bark. Trees with a thicker bark and higher concentration of resin sacs are more successful in repelling attempted attacks. The second level of defense involves changes in metabolism near the entrance hole [29, 30], and the third is a systemic change in the complete metabolism of the host tree. The biology of most bark beetles is adapted to the physiological state of the host, which means that they burrow only into physiologically weakened trees (secondary pests). A small number of insect species is able to attack completely healthy, vital trees, under certain conditions, i.e., they become primary pests. Eight-toothed (*Ips typographus* L.) and six-toothed spruce bark beetle (*Pityogenes chalcographus* L.) are known to have the ability to dramatically multiply [31]. *I. typographus* and *P. chalcographus* are the most significant, economically harmful insect species in natural spruce stands in Europe. Research in 24 European countries confirmed this claim, where the eight-toothed spruce bark beetle is ranked first, and the six-toothed spruce is ranked third among the most important economically harmful spruce organisms [32]. Research has also confirmed that 8% of the total damage in Europe's forests, between 1850 and 2000, was caused mainly by *I. typographus* [33].

Continuous monitoring of the forests conditions is performed within the ICP Forests program [34] which is one of the most diverse approaches to researching the impact of various factors on forest ecosystems. Furthermore, it can gather information that is important in determining what happened in the previous period. Otherwise, by ascertaining decline of forests at a certain area, at a precise moment, without prior continuous monitoring of the condition, it is not possible to determine, with certainty, the reason for decline, due to various factors that may have influenced that condition.

Taking into account unfavorable climatic factors and random yields of wood volume, as their end result in interaction with bark beetles, the main goal of this paper is a better understanding of these impacts, primarily long-term drought and its effects on decline spruce forests in Kopaonik National Park. Thus, the impacts of spruce tree decline mentioned here combine the personal observations of teams collecting data from a sample plot, data from Kopaonik National Park on random yields of wood volume and data on temperatures and precipitation from the main meteorological station on Kopaonik by calculating a standardized precipitation index (SPI) and Standardized Precipitation Evapotranspiration Index (SPEI).

MATERIALS AND METHODS

Within the Kopaonik National Park, a permanent survey area was set up in 2010, i.e., Level II bioindication point as part of the ICP Forests program [35], whose main goal is to gain a better understanding of the cause-and-effect relation between forest ecosystems through intensive monitoring of natural (biotic and abiotic) stressors. This sample plot is located in a pure spruce stand older than 60 years, at the northwest exposure and at an altitude of 1720 m. During the years of research, the decline movement of all spruce trees was monitored in this sample plot. The basic method is based on monitoring defoliation according to the ICP Forests methodology [35] (Table 1).

TABLE 1
Assessment and categorization of defoliation according to the ICP Forests methodology

Classes of defoliation	Leaf/needle loss (%)	Degree of defoliation
0	0–10	None
1	>10–25	Slight (warning phase)
2	>25–60	Moderate
3	>60–100	Severe
4	100	Dead

In addition to the climatic characteristics of the research period (2010–2019), which relate to air temperature and precipitation data during the year and during the vegetation period, from the main meteorological station Kopaonik (RHSS) (coordinates: longitude 20°48'E, latitude 43°17'N; altitude 1710 m a.s.l.), which is located in the immediate vicinity of this sample plot, the problem of decline spruce forests is explained through the participation of random yield of wood volume in the total allowable cut gathered in all four forest management units of Kopaonik National Park, after extreme climatic events (2011–2013) in the period from 2014 to 2019.

In order to relate the drought period to the decline period of spruce trees, a standardized precipitation index (SPI) was calculated by McKee *et al.* [36] and Standardized Precipitation Evapotranspiration Index (SPEI) according to Vicente-Serrano *et al.* [37]. For the purposes of calculating the drought period according to the SPI, precipitation is the only input parameter, and to define the drought intensity, the categorization shown in Table 2 was used. We calculated the SPI for the six-month period (SPI-6), for the vegetation period (April–September), and the annual SPI (SPI-12) based on the data of the main meteorological station on Kopaonik. To calculate the SPEI, which in addition to precipitation is also based on temperature data, the global SPEI database was used [38]. For SPEI, we calculated time series at a single grid cell according to coordinates (43°25', 20°75'), which correspond to the research area. SPEI was also calculated for six and 12 months (SPEI-6 and SPEI-12), and categorization of humidity conditions was estimated based on the values shown in Table 3.

After obtaining SPI and SPEI results for dry periods, a comparison between dry period and tree mortality was performed.

For a total of 195 trees of spruce (analyzed in 13 groups, each consisting of 15 trees), annual mortality rates were calculated for two observation periods (2010–2014 and 2015–2019) based on monitoring data of defoliation according to the ICP Forests methodology [35] (trees with defoliation of 100% were considered dead). According to Sheil et al. [40], the true annual mortality is defined correctly by the following equation: $m = 1 - (N_1/N_0)^{1/t}$, where N_0 and N_1 are population counts at the beginning and end of the measurement interval – t. Given that *m* has been recommended as a standard quantity for comparing annual mortality rates in plant ecology [40], it was adopted as an annual mortality rate in this study. The variation in mortality rates was captured by using the mortality rate of each of the 13 groups of trees analyzed as a subpopulation. For calculating *m*, two 5-year intervals were used, because a 5-year interval is the most commonly used census interval length and it has been recommended by Lewis *et al.* [41] for maximizing the intercensus and intersite comparability. Before performing the statistical analysis, raw data on annual mortality rates were tested for normality. Since the assumption that these data come from normal distributions was not confirmed, the medians (M) were used for both intervals of observation, median absolute deviation (MAD) was determined

TABLE 2
Categorization of moisture conditions by SPI – Source: RHSS [39]

Category of moisture conditions	SPI values
Exceptional drought	SPI ≤ -2.326
Extreme drought	-2.326 < SPI ≤ -1.645
Severe drought	-1.645 < SPI ≤ -1.282
Moderate drought	-1.282 < SPI ≤ -0.935
Minor drought	-0.935 < SPI ≤ -0.524
Near normal	-0.524 < SPI< +0.524
Slightly increased moisture	+0.524 ≤SPI< +0.935
Moderately increased moisture	+0.935 ≤SPI< +1.282
Considerably increased moisture	+1.282 ≤SPI< +1.645
Extremely wet	+1.645 ≤SPI< +2.326
Exceptionally wet	SPI ≥ +2.326

TABLE 3
Categorization of moisture conditions by Standardized Precipitation Evapotranspiration Index (SPEI)

Category of moisture conditions	SPEI values
Extreme drought	≤ -2.0
Severe drought	-1.99 to -1.50
Moderate drought	-1.49 to -1.00
Near normal	-0.99 to 0.99
Moderate wet	1.00 to 1.49
Severely wet	1.50 to 1.99
Extremely wet	≥2.00

for each median, and the comparison and determination of the difference between the medians were carried out using the Kruskal-Wallis test (KWt). All statistical analyses were performed using the Statgraphics software (2009; Statpoint Technologies, Inc., Warrenton, VA).

RESULTS AND DISCUSSION

Influence of climatic factors on spruce decline. It is known that forest ecosystems can withstand a one-year drought without major impacts on them. However, repeated exposure to perennial droughts can have significant impacts on their functioning [42]. During these researches, on the entire territory of the Republic of Serbia between 2011 and 2013, the highest temperatures without precipitation, for a longer period of time, were recorded during the year and during the vegetation period, after which the decline of both individual trees and larger forest areas was observed. Particularly pronounced unfavorable climatic conditions, that affected the forest decline, were recorded during 2011 and in the vegetation period during 2012 [11, 18, 43]. Also, this dry period was recorded throughout a larger part of the European continent, which is confirmed by the data of the European Environment Agency – EEA [44]. Radulović *et al.* [45] cite drought as the main factor in the decline of coniferous forests in Serbia, while Spinoni *et al.* [46] emphasize that the frequency and severity of droughts increased especially in southern and eastern Europe during summer and autumn. Several studies, on the decline of spruce forests in Serbia in protected areas, such as Golija Nature Park [47], Tara National Park [48] and Kopaonik National Park [49], indicate that the decline was primarily caused by the influence of unfavorable climatic factors over a longer period of time, which preceded the mass decay of spruce stands. Drought is cited as the main trigger followed by parasitic fungi, windbreaks and snowbreaks (a pronounced problem in National parks), which led to the gradation of bark beetles as secondary pests.

In order to confirm previous research and better understand the consequences of the drought period, using new results on the spruce forest decline for the Kopaonik National Park, we calculated the deficit or surplus of precipitation based on SPI, with temperatures based on SPEI during the vegetation period (SPI-6, SPEI-6), which is shown in Figure 1, and on an annual basis (SPI-12, SPEI-12) in Figure 2.

The attached graphs show that the extremely dry period resulted in a deficit of precipitation, if we look at the whole year of 2011 (SPI-12), and especially the vegetation period of 2012 (SPI-6). These deficits actually show that the lack of precipitation was extremely low during these two years, i.e., it lasted for the whole year of 2011 and during the vegetation period of 2012.

In addition to precipitation, which is the only input data for SPI, we also included temperatures by calculating SPEI, which allows this index to calculate the impact of temperature on the development of drought. According to the presented methodology, SPEI values were calculated for a six-month (SPEI-6 – Figure 1) and twelve-month period (SPEI-12 – Figure 2). The attached Figure 1 shows the wet or dry events, over a six-month period, for the ten-year research interval in which the vegetation period was observed. It can be seen that 2012 was extremely dry, compared to previous and subsequent years, where it must be borne in mind that the presentation of SPEI 6 corresponds to September each year and represents a vegetation period. Also, it is noticed that some months, within this period, have the epithet of extreme drought. However, if we look at the periods a decade or two before this research [38], it can be clearly seen that 2012 is the driest year in the area of NP Kopaonik. Similar to the values of SPEI-6, the values of SPEI-12 also correspond to December of each monitored year and represent the annual SPEI (SPEI-12 – Figure 2). This review also highlights the drought period, which shows a prolonged drought during 2011 and 2012. It can be noticed that both indices (SPI and SPEI) show similar values during the years with an intensive drought.

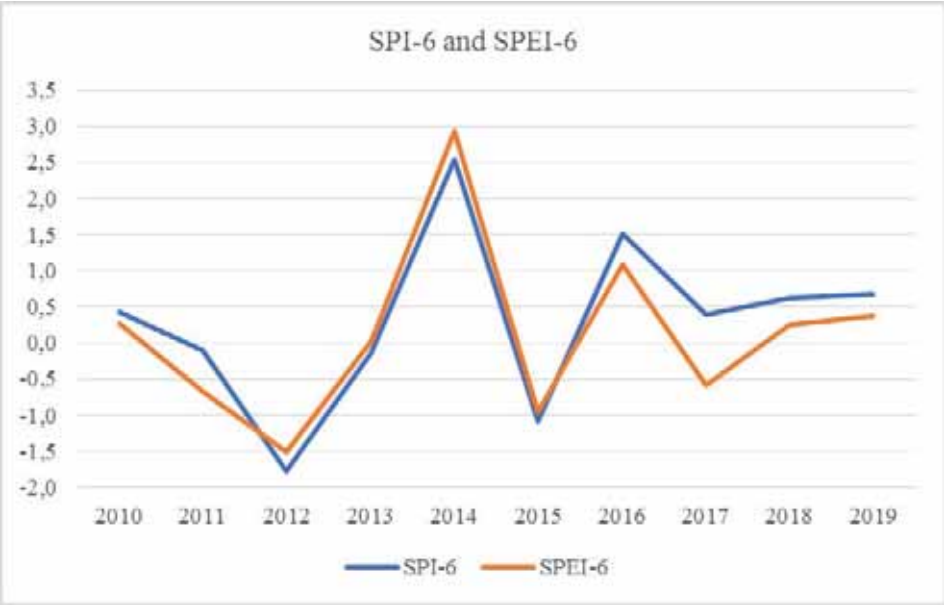

FIGURE 1
Moisture conditions in the growing season (April–September) in the Kopaonik National Park

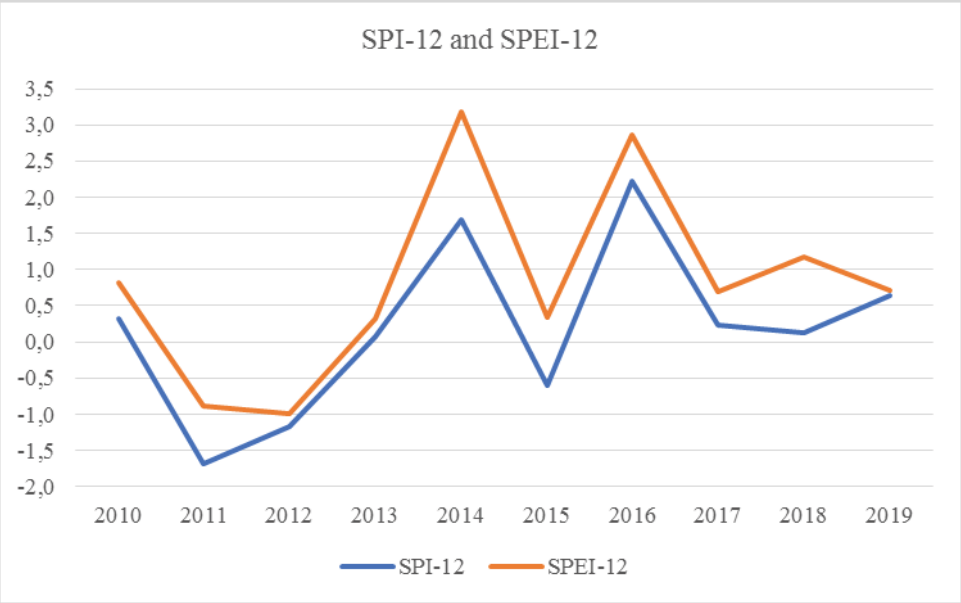

FIGURE 2
Moisture conditions on the annual level in the Kopaonik National Park

Spruce decline in the sample plot. Based on the ICP Forests methodology (part IV) [35], in the Level II sample plot – Kopaonik, within subfield 2, 30 trees were selected and condition of their crowns was assessed. However, in order to get a clearer picture and determine the cause of the possible tree decline, all trees within this sample plot (primarily defoliation) were observed. Since the Level II Kopaonik sample plot was set up, cases of individual trees, being attacked by the two most dominant species of spruce bark beetles, *Ips typographus* and *Pityogenes chalcographus*, have been registered. In the beginning, the attack was of low intensity and sporadic, and after extreme climate conditions, which were registered from 2011 to 2013, with snow and wind breaks in 2012, in 2013 the attack entered its culminating phase in some parts of the stand. Out of the total number of isolated trees (195), in the sample plot, 26 of them (or 13.4%) were attacked by these two most important species of spruce bark beetles, while in 2013 19 trees totally dried up [50]. Then, by 2015, the number of dry trees reached 35 (or 18% of the total sample plot). As an additional illustration of this phenomenon, a general overview of the condition of the spruce stand, in the sample plot of Level II Kopaonik is given (Figure 3), where the trees that dried in the period 2013–2015 are marked in red (Figure 3a and 3b). Also, Figure 3c shows a group of dried trees in the sample plot during 2013, while Figure 3d shows

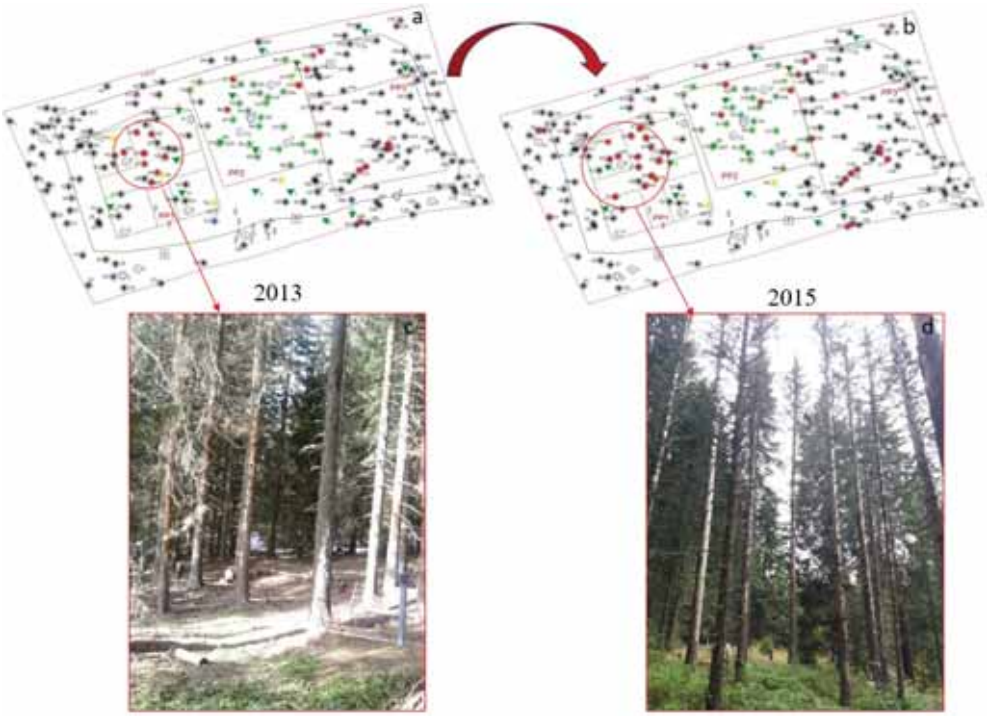

FIGURE 3
Spruce decline from 2013 to 2015 in the Level II sample plot – Kopaonik

the same group of dried trees that increased by 2015. A separate group of trees shows characteristic drying circles after bark beetle attack. Such phenomena of spreading of bark beetles and drying of trees are also detected in a large number of localities in the first protection zone of the Kopaonik National Park, for the same period.

In the same sample plot (total number of spruce trees 195), annual mortality rates were calculated for two observation periods (2010–2014 and 2015–2019) based on monitoring data of defoliation (trees with defoliation of 100% were considered dead). The results of the descriptive and non-parametric statistics for the annual mortality rates of spruce in the Kopaonik National Park for two observation periods are presented in Table 4. The medians of the annual mortality rates were 0.02 and 0.00 for the observation periods of 2010–2014 and 2015–2019, respectively. According to the KWt, there is a statistically significant difference at the 95% confidence level ($P = 0.04$) between the medians that represent the two observation periods. The Box and whisker plot (Figure 4) shows that the median of annual mortality rate for the first observation period (2010–2014), which was affected by drought, was higher than the median obtained for the second observation period (2015–2019).

Influence of spruce decline on the increase of random yield of wood volume. After the extreme climatic events were recorded, for the period 2011–2013 on the entire territory of the Republic of Serbia, forest areas affected by decline were easily observed. Despite the higher altitude, which is characterized by a humid climate (Kopaonik mountain), there was a deviation from the usual averages of precipitation and temperatures, for the mentioned years. According to the Forests Act of the Republic of Serbia (Article 45) [51], extraordinary measures for forest protection are adopted in case of significant disturbances of biological balance and serious damage to forest ecosystems caused by natural disasters. Natural disasters in forests are considered to be significant disturbances of the biological balance and the occurrence of serious damage to forest ecosystems. These damages can be caused by fires, decline, plant diseases and pests, windbreaks, snowstorms, floods, torrents, landslides and other unforeseen factors over the large areas of forests and forest land [51]. In this case, as a result of natural disasters, primarily prolonged droughts with snow and windbreaks, decline of forests occured, thus affecting the increase in yield (random yields) in the total felled wood volume. Random yield is defined as the amount of felled timber that is not intended for felling by regeneration felling and thinning plans, and the reason for its felling is accidental and is the result of natural disasters or other unforeseen circumstances, while irregular yield includes felled timber from trees which will be used for other purposes (roads, mines, etc.). Random yield for the entire area of the Kopaonik National Park, after the drought period (2014–2019), can be observed as the best indicator of tree decline. Table 5 shows the problem of decline spruce forests in all four forest management units of the Kopaonik National Park through the participation of random yield of wood volume in the total allowable cut

achieved in six years of management. Also, the problem of yield sustainability over a ten-year period is presented (Figure 5).

Table 5 shows that the volume of felling, in the first six years of the management in the area of NP Kopaonik, was significantly above the planned annual dynamics. The structure of the total allowable cut realized was very unfavorable, because the random yield dominated with 40%, while in 2017 the share of random yield was as high as 61%. If we look at the entire ten-year management period (2014–2023), the achieved allowable cut in the first six years was already at 72% of the planned, which implied significant reductions of all types of felling by the end of the period (Figure 5) and indicated the seriousness of tree decline when the aforementioned random yields occurred. It must be noted that the largest percentage of random yields was obtained from the first protection zones where the droughts were most intense and where it was necessary to "react", so that the scale of the drought would not take on the epithet of disaster.

TABLE 4
Descriptive and nonparametric statistics for the annual mortality rates of spruce in the Kopaonik National Park for two observation periods

Period of observation	Sample size	M	MAD	MIN	MAX	Range	Average rank in KWt	Test statistic	*P*-value
2010–2014	13	0.03	0.02	0.00	0.14	0.14	16.50	4.26385	0.0389283
2015–2019	13	0.00	0.00	0.00	0.05	0.05	10.50		

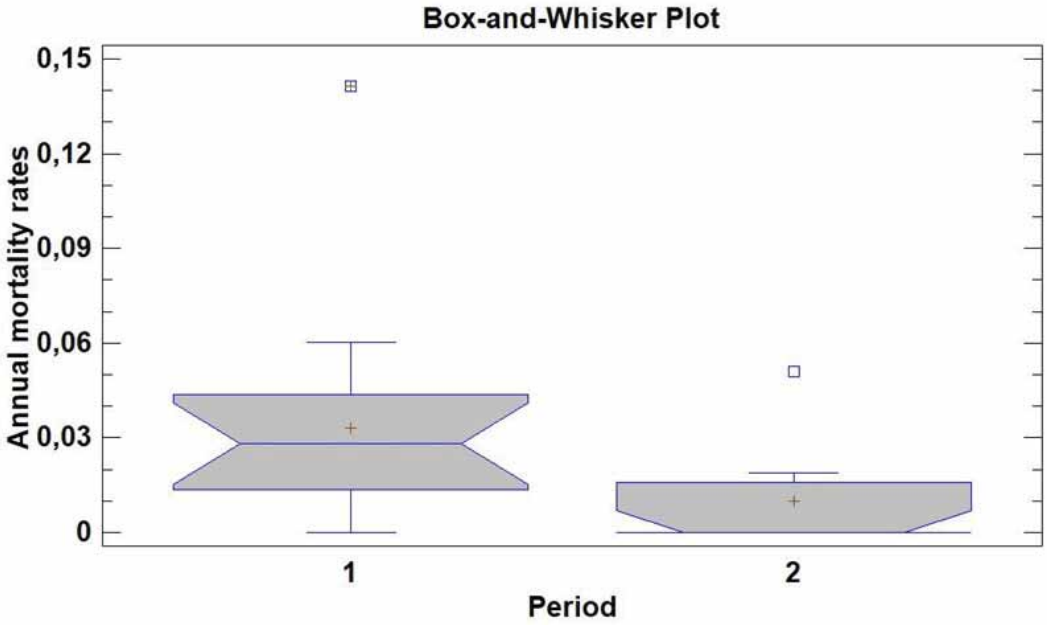

FIGURE 4
Box and whisker plot of basic statistical parameters of the annual mortality rates of spruce in the Kopaonik National Park for two observation periods: (1) 2010–2014, and (2) 2015–2019

TABLE 5
The structure of the felled spruce volume for the management period 2014–2019 in the Kopaonik National Park. Data source: NP Kopaonik

Year	Regular yield m^3 (1)	Random yield m^3 (2)	Irregular yield m^3 (3)	Total yield ($m^{3)}$ (1+2+3)	Proportion of random yield (%)
2014	18 311	11 494	1 142	30 947	37
2015	13 442	10 955	640	25 037	44
2016	20 489	11 584	204	32 276	36
2017	9 149	14 879	461	24 489	61
2018	10 672	7 419	1 621	19 712	38
2019	13 796	5 817	3 218	22 832	25
Total	85 859	62 148	7 286	155 293	40

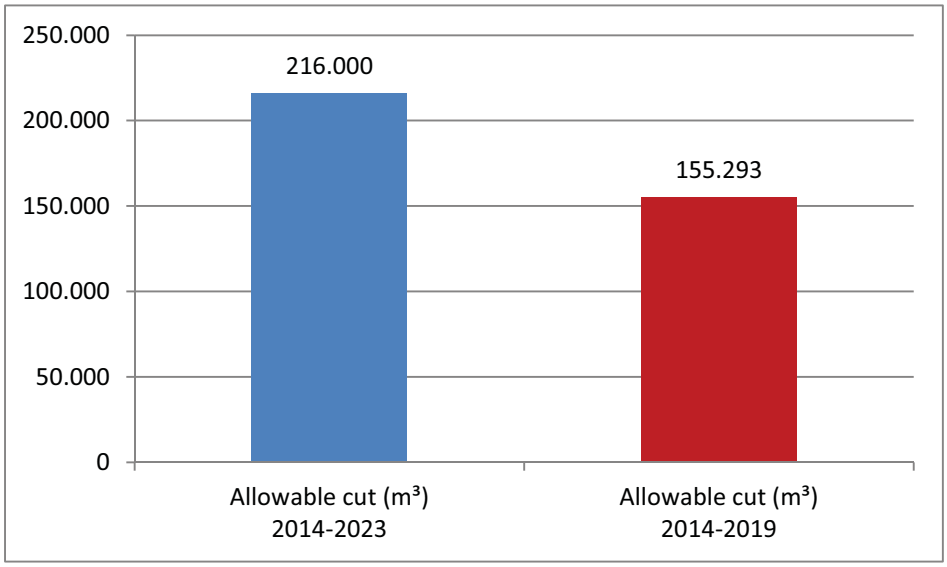

FIGURE 5
Allowable cut in the Kopaonik National Park. Data source: NP Kopaonik

Decline, which occurred on a large scale, where the random yield was a dominant part of the main yield, resulted in a serious violation of the principle of permanence (sustainability) of yield, which required urgent changes and amendments to forest management plans. The problem was further complicated by the fact that any change in the planning document had to be approved by the relevant Ministry.

Problems, from the planning aspect, caused by this phenomenon of strong intensity, are manifested in losses in production, structure and stability breaking of stands, uncertainty in achieving management goals, inability to realistically determine and respect the prescribed measures to achieve goals and jeopardizing the real purpose of management, as well.

CONCLUSION

National parks, as strictly protected areas in which every human activity is regulated by law, are not physically separated or detached parts of nature, but they are also affected by all kinds of biotic and abiotic factors present in the entire ecosystem. In this regard, national parks are ideal areas for monitoring the aforementioned factors.

Forest decline in the Kopaonik National Park can be attributed to the influence of three groups of factors – predisposing, stimulating and contributing. The stand and its age can be the predisposing factors. Incentive factors, and in this case the most influential, are physiological drought and extremely hot and dry three consecutive years (2011–2013), while contributing factors are damage from snow and wind in 2012, together with climatic factors and root rot fungi. The main factor in forest decline, which determines the total mortality of trees, can be considered the gradations of bark beetles, which accompanied all previously mentioned factors.

Very pronounced, and so far unnoticed, forest decline in the Kopaonik National Park, during several years (2014–2017), and certain circumstances related to the impact of very unfavorable climatic characteristics on the growth and development of vegetation in the period 2011–2013, as well as the overpopulation of bark beetles after these events, indicate their connection and contribution to the large-scale forest decline.

Looking at the whole area of Kopaonik, during the study period, it was found that the decline started from the first degree of protection due to impossibility to sanitate the areas that have been affected by wind and snowbreaks, especially after the winter of 2012, when a large amount of snow fell, just before and after a vegetation season, with an extremely low rainfall and extremely high temperatures. It caused favorable conditions for the attack and overgrowth of bark beetles. Due to the previously mentioned factors, there was a large percentage of the share of random yields of wood volume in the complete management of forests.

Decline, caused by unfavorable climatic factors such as high temperatures without precipitation over a long period of time, consumes and affects all forest ecosystems, both in protected (as is the case in national parks) and in forests that are not protected. However, a significant feature of the national park management is that adequate measures cannot be applied, at a given time, which can sometimes be key to mitigating decline progression due to secondary drying agents (e.g., bark beetles). On the other hand, a plus side of this kind of management is reflected through scientific research, because in national parks one can see the original influence of nature and its effect on forest ecosystems.

If we want to preserve forests, intensive monitoring can be a valuable tool in making timely decisions in the process of forest protection within national parks, where sanitary felling is not allowed and where administration is often an aggravating factor, when it is necessary to act quickly. It is obvious that humans have done a lot to upset nature's balance. Therefore, we are obligated to help nature, whenever possible, overcome the problems so it does not get out of control and could not be stopped later.

ACKNOWLEDGEMENTS

The research was supported by the Ministry of Education, Science and Technological Development and the Ministry of Agriculture, Forestry and Water Management of the Republic of Serbia – Forest Directorate (within the project: "Monitoring and Assessment of Air Pollution impacts and its Effects on Forest Ecosystems in Republic of Serbia – Forest Condition Monitoring").

REFERENCES

[1] Ciais, P., Reichstein, M., Viovy, N., Granier, A., Ogee, J., Allard, V., Aubinet, M., Buchmann, N., Bernhofer, C., Carrara, A., Chevallier, F., De Noblet, N., Friend, A.D., Friedlingstein, P., Grünwald, T., Heinesch, B., Keronen, P., Knohl, A., Krinner, G., Loustau, D., Manca, G., Matteucci, G., Miglietta, F., Ourcival, J.M., Papale, D., Pilegaard, K., Rambal, S., Seufert, G., Soussana, J.F., Sanz, M.J., Schulze, E.D., Vesala, T., Valentini, R. (2005) Europe-wide reduction in primary productivity caused by the heat and drought in 2003. Nature. 437, 529-533.

[2] Barriopedro, D., Fischer, E. M., Luterbacher, J., Trigo, R. M., García-Herrera, R. (2011) The hot summer of 2010: redrawing the temperature record map of Europe. Science. 332, 220-224.

[3] Hanel, M., Rakovec, O., Markonis, Y., Máca, P., Samaniego, L., Kyselý, J., Kumar, R. (2018) Revisiting the recent European droughts from a long-term perspective. Sci. Rep. 8, 9499.

[4] Levinson, D. H., Fettig, C. J. (2021) Climate Change: Updates on Recent Global and United States Temperature Anomalies and Impacts to Water, Forests, and Environmental Health. In: Pinkerton, K.E., Rom, W.N. (eds) Climate Change and Global Public Health. Respiratory Medicine. Humana Cham. 51-74.

[5] Schuldt, B., Buras, A., Arend, M., Vitasse, Y., Beierkuhnlein, C., Damm, A., Gharun, M., Grams, T. E. E., Hauck, M., Hajek, P., Hartmann, H., Hiltbrunner, E., Hoch, G., Holloway-Phillips, M., Körne,r C., Larysch, E., Lübbe, T., Nelson, D. B., Rammig, A., Rigling, A., Rose, L., Ruehr, N. K., Schumann, K., Weiser, F., Werner, C., Wohlgemuth, T., Zang, C. S., Kahmen, A. (2020) A first assessment of the impact of the extreme 2018 summer drought on Central European forests. Basic and Applied Ecology. 45, 86-103.

[6] Hansen, J., Sato, M., Ruedy, R., Lo, K., Lea, D. W., Medina-Elizade, M. (2006) Global temperature change. Proc. Natl. Acad. Sci. 103(39), 14288-14293.

[7] Seidling, W. (2007) Signals of summer drought in crown condition data from the German Level I network. Europian Journal of Forests Research. 126, 529-544.

[8] Kadović, R., Medarević, M. (2007) Forests and climate change. Proceedings, special edition. Ministry of Agriculture, Forestry and Water Management, Forest Administration, Faculty of Forestry, University of Belgrade, Belgrade. (In Serbian).

[9] Stanković, Z., Govedar, Z., Kapović, M., Hrkić, Z. (2010) Climate change impact on forest vegetation in Republic of Srpska. International Scientific Conference „Forest Ecosistems and Climate Changes" March 9-10. 2010. Belgrade, Serbia. Proceedings. 1, 21-25.

[10] Brašanac-Bosanac, Lj. (2013) Forest ecosystems of Serbia in the function of environmental protection from negative climate changes impact. Doctoral dissertation. University of Belgrade, Faculty of Geography. Belgrade 2013. (In Serbian).

[11] Češljar, G., Nevenić, R., Bilibajkić, S., Stefanović, T., Gagić- Serdar, R., Đorđević, I., Poduška, Z. (2013) Viability of trees on Bio-Indication plots Level 1 in Republic of Serbia in 2013. Sustainable of Forestry. Collection 67-68, 69-78.

[12] De la Cruz, A., Gil, P. M., Fernandez-Cancio, A., Minaya, M., Navaro-Cerrillo, R. M., Sanchez-Salguero, R., Grau, J. M. (2014) Defoliation triggered by climate induced effects in Spanish ICP Forests monitoring plots. Forests Ecology and Management. 331, 245-255.

[13] Sánchez-Salguero, R., Camarero, J. J., Carrer, M., Gutiérrez, E., Alla, Q. A., Hayles, L. A., Hevia, A., Koutavas, A., Sancho, E. M., Nola, P., Papadopoulos, A., Pasho, E., Toromani, E., Carreira, J. A., Linares, J. C., (2017) Climate extremes and predicted warming threaten Mediterranean Holocene firs forests refugia. Proceedings of the National Academy of Sciences of the United States of America. 114(47), E10142-E10150.

[14] Seidl, R., Thom, D., Kautz, M., Martin-Benito, D., Peltoniemi, M., Vacchiano, G., Wild, J., Ascoli, A., Petr, M., Honkaniemi, J., Lexer, M. J., Trotsiuk, V., Mairota, P., Svoboda, M., Fabrika, M., Nagel, T. A., Reyer, C.P.O. (2017) Forest disturbances under climate change. Nat. Clim. Change. 7, 395-402.

[15] Zhang, Q., Shao, M., Jia, X., Wei, X. (2017) Relationship of Climatic and Forest Factors to Drought- and Heat-Induced Tree Mortality. PLOS One 12(1), e0169770.

[16] Taccoen, A., Piedallu, C., Seynave, I., Perez, V., Gégout-Petit, A., Nageleisen, L. M., Bontemps, J. D., Gégout, J. C. (2019) Background mortality drivers of European tree species: climate change matters. Proc. Biol. Sci. 286(1900), 20190386.

[17] Senf, C., Buras, A., Zang, C.S., Ramming, A., Seidl, R. (2020) Excess forest mortality is consistently linked to drought across Europe. Nat. Commun. 11, 6200.

[18] Češljar, G., Đorđević, I., Brašanac-Bosanac, Lj., Eremija, S., Mitrović, S., Ćirković-Mitrović, T., Lučić, A. (2021) Determination of forest decline due to the action of dominant stress factor through monitoring of defoliation – case study of Maljen, Serbia. Agriculture and Forestry. 67(2), 211-226.

[19] Fischlin, A., Midgley, G. F., Price, J. T., Leemans, R., Gopal, B., Turley, C., Rounsevell, M. D. A., Dube, O. P., Tarazona, J., Velichko, A. A. (2007) Ecosystems, their properties, goods, and services, Climate Change 2007: Impacts, Adaptation and Vulnerability. Contribution of Working Group II to the Fourth Assessment Report of the Intergovernmental Panel on Climate Change. In: Parry, M. L., Canziani, O. F., Palutikof, J. P., van der Linden, P. J., Hanson, C. E. (eds.): Cambridge University Press, Cambridge. 211-272.

[20] Hrašovec, B., Krušić, I., Šilić, T., Franjević, M. (2012) Multilayer bark beetle population outbreak in the Northern Velebit nacional park and surrounding forests-management strategies and their implications on outbreak dynamics. 3rd European Congress of Conservation Biology, Glasgow, 28 August-1 September 2012. P17.6

[21] Allen, C. D., Breshears, D. D., McDowell, N. G. (2015) On underestimation of global vulnerability to tree mortality and forest die-off from hotter drought in the Anthropocene. Ecosphere. 6, 1-55.

[22] Anderegg, W. R., Hicke, J. A., Fisher, R. A., Allen C. D., Aukema, J., Bentz B., Hood, S., Lichstein, J.W., Macalady, A.K., McDowell, N., Pan, Y., Raffa, K., Sala, A., Shaw, J.D., Stephenson, N.L., Tague, C., Zeppel, M. (2015) Tree mortality from drought, insects, and their interactions in a changing climate. New Phytol. 208, 674-683.

[23] IPCC (2015) Climate Change 2014: Synthesis Report. Contribution of Working Groups I, II and III to the Fifth Assessment Report of the Intergovernmental Panel on Climate Change [Core Writing Team, R.K. Pachauri and L.A. Meyer (eds.)]. IPCC, Geneva, Switzerland. 1-151.

[24] Brang, P., Bugmann, H., Burgi, A., Muhlethaler, U., Rigling, A., Schwitter R. (2008) Climate change as a challenge for silviculture. Schweiz. Z. Forstwes. 159, 362-373.

[25] Neuner, S., Albrecht, A., Cullmann, D., Engels, F., Griess, V. C., Hahn, W. A., Hanewinkel, M., Härtl, F., Kölling, C., Staupendahl, K., Knoke, T. (2015) Survival of Norway Spruce Remains Higher in Mixed Stands under aDryer and Warmer Climate.Glob. Chang. Biol. 21, 935–946.

[26] Krupková, L., Havránková, K., Krejza, J., Sedlák, P., Marek, M. V. (2019) Impact of Water Scarcity on Spruce and Beech Forests. J. For. Res. 30, 899-909.

[27] Bolte, A., Hilbrig, L., Grundmann, B., Kampf, F., Brunet, J., Roloff, A. (2010) Climate Change Impacts on StandStructure and Competitive Interactions in a Southern Swedish Spruce-Beech Forest. Eur. J. For. Res. 129, 261–276.

[28] Hentschel, R., Rosner, S., Kayler, Z. E., Andreassen, K., Børja, I., Solberg, S., Tveito, O. E., Priesack, E. P., Gess-ler, A. (2014) Norway spruce physiological andanatomical predisposition to dieback. Forest Ecology and Management. 322, 27-36.

[29] Wermelinger, B. (2004) Ecology and management of the spruce bark beetle Ips typographus - a review of recent research. Forest Ecology and Management. 202(1-3), 67-82.

[30] Lieutier, F. (2007) Host resistance to bark beetles and its variations. In: Lieutier, F., Day, K. R., Battisti, A., Grégoire, J. C., Evans, H. F. (eds.): Bark and Wood Boring Insects in Living Trees in Europe: a Synthesis. 135-137.

[31] Tabaković-Tošić, M., Milosavljević, M. (2015) Impact of estreme weather conditions on the population dynamics of bark beetles in the forests of Eastern Serbia. Sustainable Forestry. 71-72, 27-38.

[32] Grégoire, J. C., Evans, H. F. (2007) Damage and control of BAWBILT organisms an overview. In: Lieutier, F., Day, K. R., Battisti, A., Grégoire, J. C., Evans, H. F. (eds.:) Bark and Wood Boring Insects in Living Trees in Europe, a Synthesis. 19-37.

[33] Jönsson, A. M., Susanne, H., Lars, B., Ravn, H. P. (2007) Impact of climate shange on the population dynimacs of Ips typographus in southern Sweden. Agricultural and Forest Meteorology. 146, 70-81.

[34] ICP Forests – International Co-operative Programme on Assessment and Monitoring of Air Pollution Effects on Forests. Available at: http://icp-forests.net/. (Accessed 25 April 2021)

[35] ICP Forests (2016) Manual, part IV: Visual assessment of crown condition and damaging agents. 5-54. Available at: https://www.icp-foests.org/pdf/manual/2016/ICP_Manual_2017_02_part04.pdf (Accessed 02 April 2021).

[36] McKee, T. B., Doesken, N. J., Kleist, J. (1993) The relationship of drought frequency and duration to time scales. Proceedings of the Eighth Conference on Applied Climatology. Boston MA: American Meteorological Society. 179-184.

[37] Vicente-Serrano, S. M., Beguería, S., López-Moreno, J. I. (2010) A Multi-scalar drought index sensitive to global warming: The Standardized Precipitation Evapotranspiration Index – SPEI. Journal of Climate. 23, 1696-1718.

[38] Global SPEI database. Available at: http://sac.csic.es/spei/database.html (Accessed 25 April 2021).

[39] Republic Hydrometeorological Service of Serbia (RHSS): Available at: http://www.hidmet.gov.rs/eng/meteorologija/uslovi_vlaznosti.php (Accessed 10 March 2021).

[40] Sheil, D., Burslem, D.F.R.P., Alder, D. (1995) The interpretation and misinterpretation of mortality rate measures. Journal of Ecology. 83, 331-333.

[41] Lewis, S. L., Phillips, O. L., Sheil, D., Vinceti, B., Baker, T. R., Brown, S., Graham, A. W., Higuchi, N., Hilbert, D. W., Laurance, W. F., Lejoly, J., Malhi, Y., Monteagudo, A., Vargas, P. N., Sonké, B., Supardi, N. M. N., Terborgh, J. W., Vásquez-Martínez, R. (2004) Tropical forest tree mortality, recruiting and turnover rates: calculation, interpretation and comparison when census intervals vary. Journal of Ecology. 92, 929-944.

[42] Moravec, V., Markonis, Y., Rakovec, O., Svoboda, M., Trnka, M., Kumar, R., Hanel, M. (2021) Europe under multi-year droughts: how severe was the 2014–2018 drought period? Environ. Res. Lett. 16, 034062.

[43] Češljar, G., Gagić-Serdar, R., Đorđević, I., Poduška, Z., Stefanović, T., Bilibajkić, S., Nevenić, R. (2014) Analysis of Types of Damages at the Sample Plots of Level 1 in 2013 at the Territory of the Republic of Serbia. Sustainable Forestry. Collection 69-70, 63-71.

[44] European Environment Agency – EEA (2012) Available at: https://www.eea.europa.eu/data-and-maps/figures/main-drought-events-in-europe (Accessed 10 April 2021).

[45] Radulović, Z., Karadžić, D., Milenković, I., Lučić, A., Rakonjac, Lj., Miletić, Z., Pižurica, R. (2014) Declining of forests - biotic and abiotic stress. Bulletin of the Faculty of Forestry. 71-88.

[46] Spinoni, J., Naumann, G., Vogt, V.V. (2017) Pan-European seasonal trends and recent changes of drought frequency and severity. Global and Planetary Change. 148, 113-130.

[47] Karadžić, D., Milanović, S., Golubović-Ćurguz, V. (2017) Project: Causes of spruce decline (Picea abies Karst.) in the area of the nature park "Golija". University of Belgrade, Faculty of Forestry. Ministry of Environmental Protection. 5-95.

[48] Danilović, M., Antonić, S., Stojnić, D., Vojvodić, P. (2016) Project: Selection of working methods and systems when using random yields, which resulted from forest decline, icebreak in Serbia. Ministry of Agriculture and Environmental Protection, Forest Administration. 1-127. (In Serbian).

[49] Matović, B., Orlović, S., Galić, Z., Marković, M., Poljaković-Pojnik, L., Pap, P., Drekić, M., Pilipović, A., Stojnić, S., Stojanović, D., Kebert, M., Trudić, B. (2016) Project: Multidisciplinary research of forest decline process. Ministry of Agriculture, Forestry and Water Management, Forest Administration. 1-63.

[50] Tabaković-Tošić, M., Nevenić, R., Češljar, G. (2014) Bark Beetle Outbreak in Spruce Communities Within a Sample Plot (Level II) in the Mountain Kopaonik in the Period 2010-2013. 3rd International Scientific Conference "Impact of nitrogen deposition and ozone on the climatic change mitigation potential and sustainability of European forests", 26-28 May 2014, Athens, Greece. 28.

[51] Forest Act of the Republic of Serbia (2010) Official Gazette of the Republic of Serbia, no. 30/2010, 93/2012, 89/2015 and 95/2018, Belgrade. (In Serbian).

Received: **16.12.2021**
Accepted: **11.02.2022**

CORRESPONDING AUTHOR

Goran Cesljar
Institute of Forestry
Kneza Višeslava 3
Belgrade 11030 – Serbia

e-mail: cesljargoran@gmail.com

© by PSP Volume 31– No. 05/2022 pages 5216-5222 Fresenius Environmental Bulletin

SYNTHESIS OF $Ag_5PMo_{10}V_2O_{40}$ MICRO / NANO MATERIALS BY AN INVERSE EMULSION ULTRASONIC METHOD USING AS GREEN CATALYST

Peixu Li[1,*], Peilun Li[2]

[1]School of Agronomy and Chemical Technology, Weifang University of Science and Technology, Shouguang 262700, China
[2]Zhongsheng Petroleum Development Co., Ltd, Shengli Oilfield, Dongying 257000, China

ABSTRACT

The research of polyoxometalates has been intensified with the continuous development of energy catalysis technology. $Ag_5PMo_{10}V_2O_{40}$ micro/nanomaterials were synthesized by inverse emulsion method with dichloromethane was used as the oil phase, combined with the characteristics of ultrasound that can generate local high temperature and high pressure, high-speed jets or shock. The structure, morphology and size distribution of micro/nano materials that were synthesized under different reaction conditions with varying the type of surfactant, the ratio of water/oil phase and the time of ultrasonic reaction were characterized by infrared (IR), scanning electron microscope (SEM) and dynamic light scattering (DLS). The results show that the $Ag_5PMo_{10}V_2O_{40}$ polyacid micro/nanomaterial has a stable structure, the morphology and size are controlled by the type of surfactant and the ratio of water/oil phase, and the reaction time has a significant effect on the size distribution of the material.

KEYWORDS:
Green catalysts, micro/nanomaterials, $Ag_5PMo_{10}V_2O_{40}$, inverse emulsion method, ultrasound

INTRODUCTION

Polyoxometalates (POMs) are the class of inorganic compounds with stable structure of metal oxygen clusters. According to the composition of different polyacids, they are mainly divided into heteropolyacids and homopolyacids [1-2]. Heteropolyacids are formed by dehydration and condensation of different inorganic oxo acid salts. The polyoxometalates have super strong acid catalysis, redox catalytic performance and unique "quasi-liquid phase" behavior are played the role of an efficient green dual-function catalyst in materials chemistry, biochemistry, electrochemistry, fine organic synthesis, petrochemicals and other fields [3-4]. With the continuous deepening of research on polyoxometallates, the use of different synthesis strategies to develop new polyoxometalate structures has become the focus, which is beneficial to tap its application value in the field of energy conversion and energy storage materials, and maximize the advantages of the physical and chemical properties of polyoxometalates.

Molybdenum heteropoly compound is a kind of polyoxometalate with the strongest oxidizing propert, and phosphomolybdic acid substituted with stronger oxidizing pentavalent vanadium (V^{5+}) can be used as an excellent catalyst for oxidation reaction [5]. The development of new multifunctional heteropolyacid micro/nanomaterials has become a hot spot in the current research of catalytic materials, and the preparation of heteropolyacid micro/nanomaterials by inverse emulsion ultrasonic method has the advantages of simplicity, high efficiency, and easy control.

In the inverse emulsion ultrasonic method, a microemulsion composed of a specific water/surfactant/hydrophobic organic solvent is placed in a high temperature and high pressure environment generated by ultrasonic cavitation [6-7], a microreactor with controllable material size and shape is formed that was adjusted by the concentration of each reaction material, ultrasonic frequency and reaction time and other reaction factors [8]. Among them, the high-temperature and high-pressure environment generated by ultrasonic cavitation not only provides energy for the formation of tiny particles, but also the shock wave and microjet crushing effect produced by the ultrasonic cavitation make the product homogenized, and finally obtain micro/nanomaterials with narrow particle size distribution and regular morphology [9].

In this article, the phosphomolybdovanadium heteropolyacid $Ag_5PMo_{10}V_2O_{40}$ micro/nanomaterials are prepared by inverse emulsion synthesis method with $Na_5PMo_{10}V_2O_{40}$ and $AgNO_3$ are used as synthetic raw materials, and combined with controllable and efficient ultrasound technology. The influence of different synthesis conditions with morphology and size of the product was studied by changing the type of surfactant, the ratio of water/oil phase and the ultrasonic reaction time in the reaction conditions. At the same time, this article analyzes the formation mechanism of the control product morphology, and provides a feasible reference for the preparation of

new functionalized polyoxometalate micro/nanomaterials.

MATERIALS AND METHODS

Materials. Tween 80, polyvinyl alcohol (PVA), sodium dodecyl sulfate (SDS), $AgNO_3$ and absolute ethanol were provided by Sinopharm Chemical Reagent Co., Ltd. in analytically pure; $Na_5PMo_{10}V_2O_{40}$ was synthesized by the synthesis method of reference [10], and it was confirmed by infrared spectroscopy that it is the Keggin structure type heteropolyacid salt.

Instruments. The FT-IR was measured by Nicolet NICOLET IS10 Fourier infrared spectrum analyzer in KBr tablet method with the scanning range 4000-500 cm^{-1}. The ultrasound was manufactured by KH-300 GDV Constant Temperature Chinese Display Ultrasound Apparatus with ultrasonic frequency 40kHz. The particle size distribution was measured by Brookhaven 90Plus dynamic light scattering instrument. The sample was centrifuged by TG16-WS desktop high-speed centrifuge at 8000r/min with 10 min. The sample was dried by Yaxing Yike LGJ-10NS laboratory freeze dryer at -50°C/9Pa for 24h. The TG was tested by Netzsch STA 449 F3 Jupiter thermal analyzer from room temperature to 800°C with 10°C/min.

Synthesis methods. (1) Preparation disperse phase. The 5mL of 0.02mol/L $Na_5PMo_{10}V_2O_{40}$ solution was add to 10mL deionized water and 0.0009 mol $AgNO_3$ solution in dropwise was slowly added. The mixture was stirred at 300 r/min and 20°C for 3 h. Thereafter, divide them into nine groups evenly.

(2) Preparation of emulsion. The emulsion was prepared by adding the disperse phase to dichloromethane under ultrasonic stirring.

(3) Synthesis reaction. According to the conditions provided in Table 1, different emulsions were prepared and the products were obtained. The synthesized product was freeze-dried by freeze dryer, and the obtained product was weighed, and then the yield of the synthesized product was calculated.

RESULTS AND DISCUSSION

FT-IR analysis. FT-IR analysis could better characterize the molecular structure characteristics of heteropoly acid salts. The three infrared curves in Figure 1 were the infrared curves of $Ag_5PMo_{10}V_2O_{40}$ micro/nanomaterials synthesized by experiments in the first group (red), the second group (blue), and the third group (green).

It can be seen from Figure 1 that in the wavenumber range of 700-1100 cm^{-1}, the three groups of phosphomolybdenum vanadium heteropolyacid $Ag_5PMo_{10}V_2O_{40}$ micro/nanomaterials synthesized under different experimental conditions have four obvious absorption peaks. The anti-symmetric stretching vibration absorption peak of P-O bond appears in the range of 1050-1080 cm^{-1}. The anti-symmetric stretching vibration absorption peak of coordination atom and terminal oxygen bond Mo=O appears in the range of 940-990 cm^{-1}. Mo-O-Mo antisymmetric stretching vibration absorption peaks of MoO_6 octahedrons with co-angular or co-edge bridging oxygen and metal coordination atoms appear in the range of 840-870 cm^{-1} and 730-770 cm^{-1}. These characteristic absorption peaks indicate that the synthesized heteropoly acid salt micro/nanomaterials all have the characteristic peaks of Keggin structure heteropoly acid, and the synthesized product is a Keggin type phosphomolybdovanadium heteropoly acid material. The micro/nanomaterials prepared under different synthesis conditions are affected by the reaction conditions, and the absorption frequency of the material skeleton will be slightly red-shifted or blue-shifted. This shows that the products of different sizes synthesized under different reaction conditions will affect the bond bonding force between atoms to a certain extent, resulting in the expansion of the bond vibration frequency distribution range, resulting in the reduction or broadening of the infrared characteristic absorption peak [11-13]. Therefore, based on the infrared characteristic map results, it is confirmed that the $Ag_5PMo_{10}V_2O_{40}$ micro/nanomaterials synthesized in this experiment are all Keggin structure heteropolyacid salts.

TABLE 1
Inverse emulsion synthesis conditions of each reaction system

Sample	Water-oil ratio	Surfactant	Surfactant dosage/mmol	Reaction time / h
Group 1	1:100	PVA	0.05	1.0
Group 2	1:100	Tween80	0.05	1.0
Group 3	1:100	SDS	0.05	1.0
Group 4	1:200	PVA	0.05	1.0
Group 5	1:200	Tween80	0.05	1.0
Group 6	1:200	SDS	0.05	1.0
Group 7	1:100	PVA	0.05	2.0
Group 8	1:100	Tween80	0.05	2.0
Group 9	1:100	SDS	0.	2.0

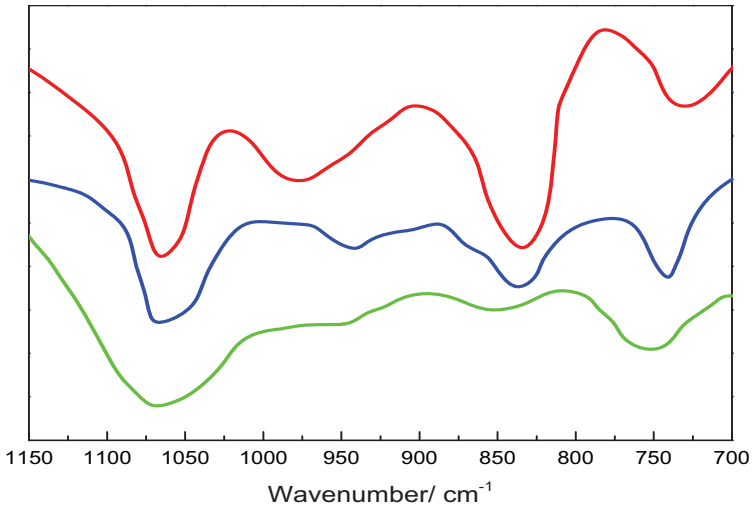

FIGURE 1
FTIR spectra of $Ag_5PMo_{10}V_2O_{40}$ micro/nanomaterials synthesized in Group 1 (red), Group 2 (blue) and Group 3 (green).

Shape analysis. Figure 2 is a scanning electron microscope microscopic image of $Ag_5PMo_{10}V_2O_{40}$ micro/nanomaterials prepared under 9 groups of different reaction conditions. It can be seen from Figure 2 that when the water-oil ratio and reaction time are the same in the reaction conditions, different surfactants have a significant effect on the morphology of the material. The reaction product of PVA as a surfactant is spherical, and Tween80 as a surfactant is lumpy, and the reaction product of SDS as a surfactant is rod-shaped. In the first, fourth, and seventh experiments of PVA as a surfactant, the product micro/nanomaterials showed a spherical structure. This is due to the internal hydrogen bonding of polyvinyl alcohol, which makes the cluster confined domain effect affected, and tends to form spherical objects. In the second, fifth, and eighth experiments of Tween80 as a surfactant, the product micro/nanomaterials showed a block structure. This is because non-ionic surfactants contain more hydrophilic polyoxyethylene, which can have a strong effect in the water phase and have a good emulsification effect, making the micro/nanomaterials form a relatively stable block morphology. In the third, sixth, and ninth group of experiments using SDS as a surfactant, the product micro/nanomaterials exhibited a rod-like shape with a certain longitudinal orientation, which is related to the longer alkyl chain in SDS [14-15]. The alkyl chain of SDS defines the spatial orientation of the material forming, so that the clustered heteropoly acid acts in a restricted domain in the long-range, and finally forms a rod.

When the surfactant and reaction time are the same, the water-to-oil ratio has an important influence on the size of the synthesized product. It can be seen from Figure 2 that the size of the micro/nanomaterials obtained in the 4th, 5th, and 6th experiments with a water-oil ratio of 1:200 is significantly smaller than the synthetic products obtained by other experimental groups with a water-oil ratio of 1:100, about It is about 50%, indicating that the lower the water-oil ratio, the smaller the concentration of the reaction monomer, and the smaller the size of the reaction product micro/nanomaterial particles obtained during the reaction. This may be because the less oil phase is contained, the same amount of surfactant can emulsify the oil phase into a smaller emulsion, which is conducive to the reaction of the reaction products at a smaller water-oil interface during the reaction [16]. Which make the size of the obtained micro/nanoparticles is smaller, and the final appearance is that the particle size of the lower oil and water is smaller than that of the synthesized reaction product, but the appearance does not change significantly.

In addition, it can also be seen from Figure 2 that during the formation process of the synthesized product, the ultrasonic reaction time is different, and the microenvironmental influence caused by the cavitation effect is different, resulting in a different final appearance of the synthesized product. Comparing the first group and the seventh group, it can be seen that the longer the reaction time, the larger the size of the reaction product obtained, and the wider the size distribution range. In the same way, the reaction conditions and product morphology of the second group and the eighth group, the third group and the ninth group are compared, and the same conclusion can be obtained. This is because chemical reactions are mainly affected by kinetic and thermodynamic reactions. Among them, reactions generally controlled by thermodynamics with a longer time and a higher temperature will produce materials with a relatively wide distribution and larger sizes [17]. This is because thermodynamics is a balanced and stable process. On the contrary, the kinetic controlled reaction is characterized by fast reaction, which is not conducive to the repair of the product morphology during the synthesis process.

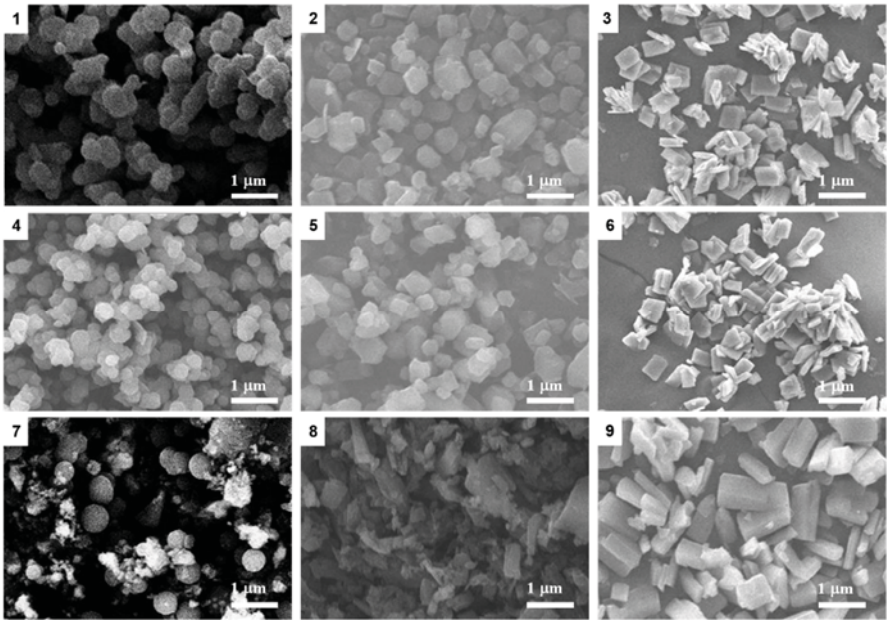

FIGURE 2
SEM images of $Ag_5PMo_{10}V_2O_{40}$ micro/nanomaterials synthesized in Group 1-9.

TABLE 2
Productivity of $Ag_5PMo_{10}V_2O_{40}$ micro/nanomaterials synthesized by the nine experiments

Group	1	2	3	4	5	6	7	8	9
Productivity/%	35.4	49.8	38.3	36.1	52.1	41.5	49.3	64.5	54.8

It can be seen from Figure 2 that in the experiment of preparing phosphomolybdenum vanadium heteropolyacid $Ag_5PMo_{10}V_2O_{40}$ micro/nanomaterials by the inverse emulsion ultrasonic method, the type of surfactant, the ratio of water/oil phase and the ultrasonic reaction time have an effect on the material morphology, size and distribution. The type of surfactant mainly affects the morphology of the material, while the water-oil ratio and ultrasonic time mainly affect the size and distribution of the material [18]. By adjusting the various factors of the reaction conditions, the morphology of the material can be prepared in a controllable manner, which provides the feasibility for further functional modification of the material.

Particle size distribution. The particle size and particle size distribution of micro/nanomaterials have an important impact on material properties. Figure 3 is the particle size distribution diagram of $Ag_5PMo_{10}V_2O_{40}$ micro/nanomaterials synthesized by the above nine sets of experiments.

It can be seen from Figure 3 that under the action of the same type of surfactant, the particle size and distribution range of the obtained heteropolyacid salt micro/nanomaterials are different when the water phase/oil ratio, the ultrasonic reaction time and the emulsifier are different. By comparing the particle size distribution diagrams of the products of the first group and the fourth group, the second and the fifth group, the third group and the sixth group, it can be seen that when the water ratio is larger, the reactant concentration is correspondingly larger, and the formed oil-in-water emulsion has a larger particle size, which is conducive to the formation of a spherical material with a larger particle size. By comparing the particle size distribution diagrams of the products of the first and seventh groups, the second and the eighth, the third and the ninth groups, it can be seen that as the ultrasonic reaction time increases, the interaction between the reactants becomes more sufficient, the formed oil-in-water emulsion particles are more uniform, which is conducive to obtaining micron-level materials with a longer length and larger distribution. In addition, when the water-oil ratio and the ultrasonic time are the same, and different surfactants are used as inverse emulsion emulsifiers, the particle size and distribution range of the obtained heteropolyacid salt micro/nanomaterials are different [19-20]. By comparing the particle size distribution diagrams of the products of the nine groups, it can be seen that the $Ag_5PMo_{10}V_2O_{40}$ micro/nanomaterials are significantly smaller than that of other groups, indicating that the nonionic surfactant Tween80 as an emulsifier is more conducive to the synthesis of $Ag_5PMo_{10}V_2O_{40}$ micro/nanomaterials with smaller particle size. Therefore, $Ag_5PMo_{10}V_2O_{40}$ micro/nanomaterials of different sizes and morphologies can be synthesized by adjusting the ratio of water/oil, selecting different emulsifiers, and optimizing different ultrasonic reaction times.

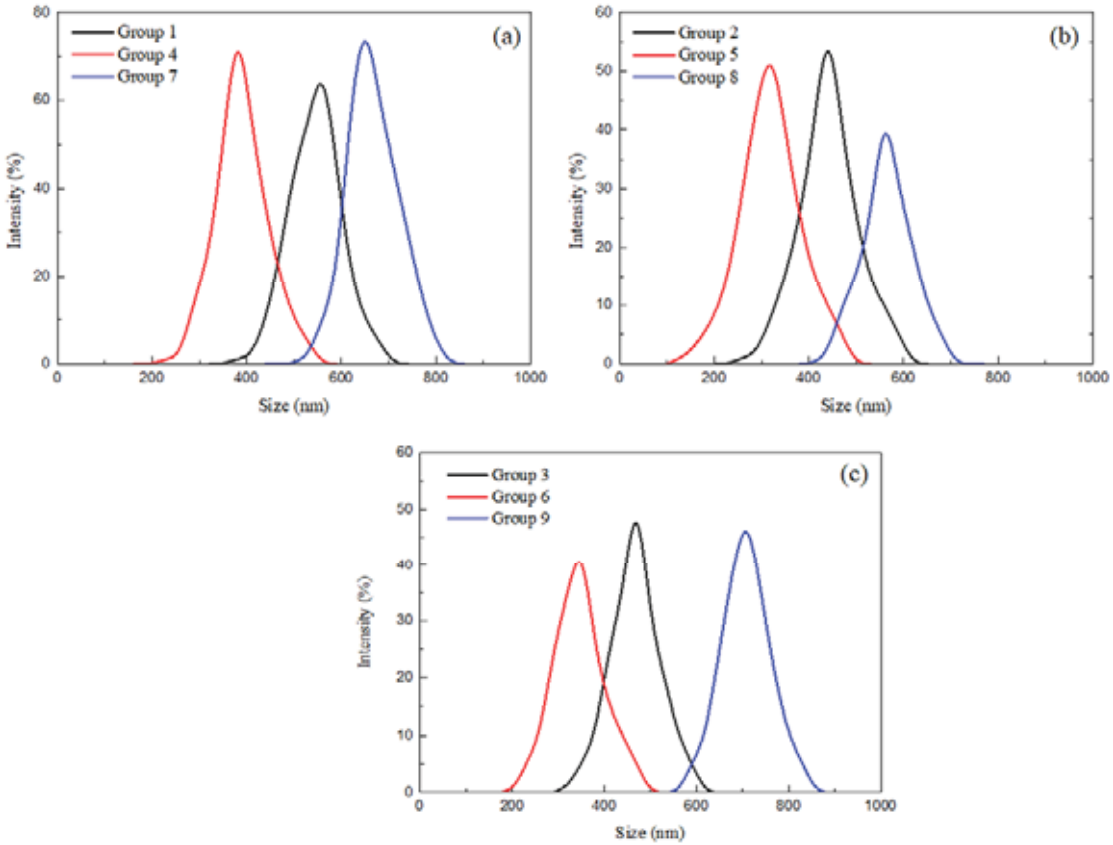

FIGURE 3
Diameter distributions of $Ag_5PMo_{10}V_2O_{40}$ micro/nanomaterials synthesized in Group 1~9

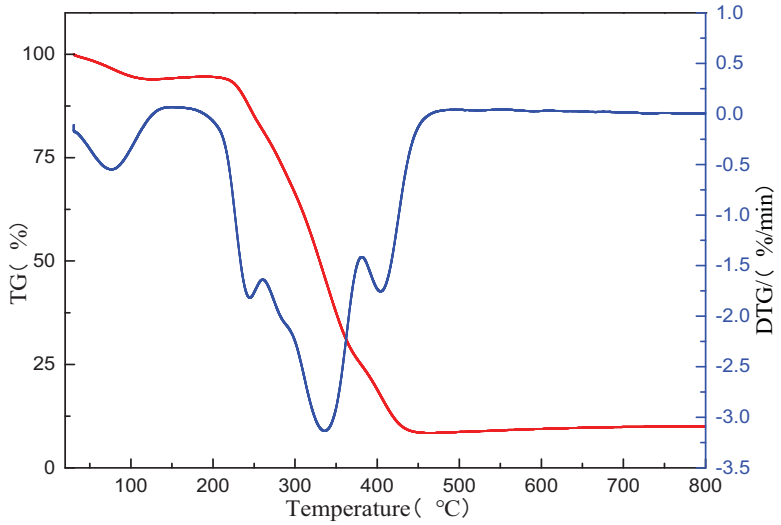

FIGURE 4
Thermogravimetric analysis curve of $Ag_5PMo_{10}V_2O_{40}$ micro/nanomaterials synthesized by the eighth group of experiments.

Productivity analysis. Table 2 shows that the yields of $Ag_5PMo_{10}V_2O_{40}$ micro/nanomaterials synthesized in groups 1-9. It can be seen from Table 2 that the reaction time of the 8th group with a reaction time of 2 h, a surfactant of Tween80 and an oil-water ratio of 1:100 has the highest yield, reaching 64.5%. The reaction conditions of this group are the best conditions to obtain high productivity of $Ag_5PMo_{10}V_2O_{40}$ micro/nanomaterial.

Thermogravimetric analysis. Figure 4 shows the thermogravimetric analysis curve of $Ag_5PMo_{10}V_2O_{40}$ micro/nanomaterials synthesized in the eighth group of experiments. The results showed that with the increase of temperature, after the free water of the product $Ag_5PMo_{10}V_2O_{40}$ micro/nanomaterials was lost, the thermal degradation loss occurred at about 270℃, and the degradation was completed at 390℃, the total thermal weight loss was

about 90%. During the thermal degradation at 268.6℃-390℃, the thermal weight loss rate changed three times, which were -1.88%/min at 250.0℃, -3.21%/min at 340.0℃ and -1.68%/min at 410.2℃. The analysis curve of TG-DTG shows that $Ag_5PMo_{10}V_2O_{40}$ micro/nanomaterials have good thermal stability.

CONCLUSIONS

Based on the needs of green environmental protection catalyst research, the $Ag_5PMo_{10}V_2O_{40}$ micro/nanomaterial was prepared by the inverse emulsion ultrasonic method in this article. At the same time, the influence of the surfactant, the ratio of water/oil phase and the ultrasonic reaction time in the reaction conditions on the morphology, size and distribution of micro/nanomaterials was explored, in order to prepare more new functionalized heteropoly acid salts nanomaterials provide a reference. Research indicates:

(1) The characteristic peaks of the FT-IR indicate that the phosphomolybdenum vanadium heteropolyacid material $Ag_5PMo_{10}V_2O_{40}$ with the Keggin structure was successfully synthesized by the inverse emulsion method. And the larger the water phase ratio and the longer the ultrasonic reaction time, the easier it is to form a larger size and wider distribution of micro/nanomaterials

(2) Different surfactants have a significant effect on the formation of material morphology. When the water-oil ratio and reaction time are the same in the reaction conditions, the reaction product $Ag_5PMo_{10}V_2O_{40}$ of PVA as a surfactant is spherical, the reaction product of Tween80 as a surfactant is a block, and the reaction product of SDS as a surfactant is a rod.

(3) When the reaction time is 2 h, the surfactant is Tween80 and the oil-water ratio is 1:100, the yield of Ag5PMo10V2O40 micro/nanomaterials is the highest (up to 64.5%), and has good thermal stability.

ACKNOWLEDGEMENTS

This work was not supported by any funds. The authors would like to show sincere thanks to all the techniques who have helped this research.

REFERENCES

[1] Xu, L., Hu, C.W., Wang, E. (1997) Research progress of heteropolyacid catalysts. Petrochemical Technology. 9, 632-638.

[2] Hu, C., Huang, R. (2003) The research progress and prospects in polyoxometalate chemistry. Chinese Journal of Inorganic Chemistry. 19(4), 337-344.

[3] Zhang, R., Chen, J., Zhu, L.X. (2004) Applied study of supported heteropoly acid catalysts. Chemical Industry Times. 18(2), 11-13.

[4] Li, W.Y., Liu, Y.Y., Zheng, H.Y., Li, Z. (2010) Molecular structure and application of heteropolyacid (salt) catalysts for organic synthesis. Chemical Industry and Engineering Progress. 29(02), 243-249.

[5] Wen, L.Y., Min, E.Z. (2000) Recent progress in heteropoly compound related solid acid catalysts. Petrochemical Technology. 29(1), 49-55.

[6] Zhang, Y., Lin, S.Y., Fang, Y. (2002) New developments in sonochemistry-preparation of nanomaterials by ultrasound. Physics. 31(2), 80-83.

[7] Qin, L.B., Zhang, L.J., Zhang, R., Lei, H., Zhou, Y. (2013) Ultrasonic synthesis of Ag/Ag3PW12O40 nanocubic crystals and photocatalytic degradation of rhodamine B. The Fifth National Polyacid Chemistry Symposium of the Chinese Chemical Society. 213.

[8] Eastoe, J., Hollamby, M.J., Hudson, L. (2006) Recent advances in nanoparticle synthesis with reversed micelles. Advances in Colloid and Interface Science. 128, 5-15.

[9] Cheng, X.F., Fu, Y.Z., Zhang, X.J. (2010) Research progress in preparation of nano-materials by ultrasonic methods. Inorganic Chemicals Industry. 42(11), 1-3.

[10] Nomiya, K., Matsuoka, S., Hasegawa, T., Nemoto, Y. (2000) Benzene hydroxylation with hydrogen peroxide catalyzed by vanadium(V)-substituted polyoxomolybdates. Journal of Molecular Catalysis A Chemical. 156(1), 143-152.

[11] Nawaz, S., Ahmad, M., Asif, S., Klemeš, J.J., Mubashir, M., Munir, M., Zafar, M., Bokhari, A., Mukhtar, A., Saqib, S., Khoo, K.S., Show, P.L. (2022) Phyllosilicate derived catalysts for efficient conversion of lignocellulosic derived biomass to biodiesel: A review. Bioresource Technology. 343, 126068.

[12] Ren, H., Meng, X., Lin, Y., Shao, Z. (2022) Structural stability of catalyst ink and its effects on the catalyst layer microstructure and fuel cell performance. Journal of Power Sources. 517, 230698.

[13] Lee, E., Seo, Y., Park, H., Kim, M., Yoon, D., Choung, J.W., Kim, C.H., Choi, J., Lee, K.Y. (2022) Development of etched SiO2@Pt@ZrO2 core-shell catalyst for CO and C_3H_6 oxidation at low temperature. Applied Surface Science. 575, 151582.

[14] Rokhum, S.L., Changmai, B., Kress, T., Wheatley, A. (2022) A one-pot route to tunable sugar-derived sulfonated carbon catalysts for sustainable production of biodiesel by fatty acid esterification. Renewable Energy. 184, 908-919.

[15] Mahara, Y., Ishikawa, H., Ohyama, J., Sawabe, K., Satsuma, A. (2016) Ag-M (M: Ni, Co, Cu, Fe) bimetal catalysts prepared by galvanic deposition method for CO oxidation. Catalysis Today. 265, 2-6.
[16] Kamari, Y., Ghiaci, M. (2016) Incorporation of TiO_2 coating on a palladium heterogeneous nanocatalyst. A new method to improve reusability of a catalyst. Catalysis Communications. 84, 16-20.
[17] Biswas, P., Woo, J., Guliants, V. (2010) Ruthenium and gold-doped M1 phase MoVNbTeO catalysts for propane ammoxidation to acrylonitrile. Catalysis Communications. 12(1), 58-63.
[18] Eijsbouts, S., van den Oetelaar, L.C.A., van Puijenbroek, R.R. (2005) MoS2 morphology and promoter segregation in commercial Type 2 Ni-Mo/Al_2O_3 and Co-Mo/Al_2O_3 hydroprocessing catalysts. Journal of Catalysis. 229(2), 352-364.
[19] Zabeti, M., Wan Daud, W., Aroua, M. (2009) Activity of solid catalysts for biodiesel production: A review. Fuel Processing Technology. 90(6), 770-777.
[20] Harada, M., Takanabe, K., Kubota, J., Domen, K., Goto, T., Akiyama, K., Inoue, Y. (2009) Hydrogen production by autothermal reforming of kerosene over MgAlOx-supported Rh catalysts. Applied Catalysis A: General. 371(1), 173-178.

Received: **16.12.2021**
Accepted: **11.02.2022**

CORRESPONDING AUTHOR

Peixu Li
School of Agronomy and Chemical Technology,
Weifang University of Science and Technology,
Shouguang 262700 – China

e-mail: Peixuli@163.com

© by PSP Volume 31– No. 05/2022 pages 5223-5228 Fresenius Environmental Bulletin

INFLUENCE OF PHYSICAL ACTIVITY, DIETARY HABITS AND MEDIA UTILIZATION PATTERNS ON EMERGENCY DEPARTMENT PATIENTS OUTCOMES IN WESTERN REGION OF SAUDI ARABIA

Khaled A Alswat[1,*], Thamer Almalki[1], Khalid Altalhi[1], Bader Almansouri[1], Abdulelah Almutairi[1], Abdullah Alharthi[1], Fatma Saffeyeldin Mohamed[1], Ahmed Gaber[2]

[1]Department of Internal Medicine, Taif University School of Medicine, P.O. Box 11099, Taif 21944, Saudi Arabia
[2]Department of Biology, College of Science, Taif University, P.O. Box 11099, Taif 21944, Saudi Arabia

ABSTRACT

Several studies showed tremendous benefits of physical activity on several health-related problems. The primary goal of this study is to evaluate the relation between the ER visit number and the physical activity. A cross-sectional study that was conducted in ER of the three General Hospitals ER. The International Physical Activity Questionnaire was used to evaluate the physical activity. A total of 322 participants were enrolled in the study with a mean age of 36.5±14.1 years. Compared to those who had ≥ 2 ER visit, those who has 1 ER visit were more likely to report low income (p 0.007), lower weight and BMI (p 0.024), less likely to have ≥ 2 chronic illness (p 0.022), and more likely to own television (p 0.045). Compared to inactive group, the active group was younger ($p< 0.05$), more likely to be smoker (p 0.5), have lower BMI ($p< 0.05$), and to own ≥ 2 devices ($p <0.05$). in conclusion, 30% of our cohort were physically active and interestingly, those were more likely to have a frequent ER visits which were likely due to the higher rate of smoking, energy drink, and media consumption which may offset the exercise benefits.

KEYWORDS:
Emergency, ER, media, energy, physical

INTRODUCTION

Physical activity is one of the main strategies to combat obesity. Several studies showed tremendous benefits of physical activity on several health-related problems which translated into lower mortality rate [1, 2]. The observed mortality benefits are dose dependent in the those who are physically active [3]. Also, evidence suggested that moving from been physically inactive to be active has been associated with health benefits [4]. Energy drinks commonly used by young individuals with variables health hazards mainly the cardiovascular one. A study suggested that energy drinks consumption cause tachycardia and hypertension [5]. Platelet dysfunction has been associated with energy drinks consumption [6]. Other study showed arterial aneurysmal formation and rupture has been reported with energy drinks [7]. Few case reports associated the energy drink consumptions with myocardial infarction and atrial fibrillation [8, 9].

Excessive media consumptions have been shown in previous studies to be associated with various health hazards. One study showed that media consumption in type I diabetes associated with worse glycemic control [10]. Another study showed excessive television viewing was associated with worse cardiovascular markers among adolescents [11]. Viewing video and or television for 4 hours or more daily was associated with an increased stroke risk as shown recently [12]. The primary goal of this study is to evaluate the Emergency Room (ER) patient's clinical characteristics. Also, we will evaluate the relation between the ER visit number and the physical activity, media and energy drinks consumptions, and BMI. We also will assess their impact on patient's ER disposition.

MATERIALS AND METHODS

A cross-sectional study that was conducted in ER of the three General Hospitals in Taif, Saudi Arabia. The study was conducted in accordance with the Declaration of Helsinki. The study protocol was reviewed and approved by The School of Medicine Research Unit at Taif University and was exempted given the non-intervention nature of the study (survey). The participants provided verbal informed consent. We invited the adult male patients who were admitted to the ER to participate in the study. We excluded pregnant women, bedridden patients, and those with altered mental status. Baseline characteristics were collected by researchers.

Each patient weight and height were measured by the researchers and body mass index (BMI) was

calculated. Data about dietary habits, media consumptions, and sleeping habits were also collected. We considered those who slept 6-8 hours per night to have optimal sleep. Those who reports monthly income of < 1335 USD were considered to have low income.

The International Physical Activity Questionnaire was used to evaluate the physical activity. Patients was active if they perform vigorous-moderate physical activity while were considered to be inactive if they perform walking only or no physical activity.

Data were entered into an excel sheet and analyzed using SPSS software, version 20.0. Multiple logistic regression analysis was used to determine the degree of association between the variables. The Chi squared test was used to study the relationship between variables and the T-test was used to compare between means.

RESULTS

A total of 322 participants were enrolled in the study with a mean age of 36.5±14.1 years, most Saudi and live in urban community, and mostly report low income and has low level of education. The baseline characteristics of all participants are shown in Table 1.

The mean BMI in the overweight range with more than 70% never self-weight at home. Around 75% of the participants were either overweight or normal weight (Figure 1).

TABLE 1
Baseline characteristics of the whole cohort.

Baseline characteristics (N=322)	
Mean age (yrs)	36.5±14.1
Urban residence (%)	91.2
High school or less (%)	79.4
Saudi nationality (%)	78.4
Married (%)	62.6
Low income (%)	66.3
Active job style (%)	60.4
Mean weight (Kg)	75.8±17.7
Mean BMI (Kg/m^2)	26.5±6.3
Pulse rate beat per minute (bpm)	88.1±15.0
Systolic blood pressure (mmHg)	137.8±23.6
Diastolic blood pressure (mmHg)	81.8±14.5
Never self-weight (%)	73
1 ER visit in the previous 12 months (%)	56.3
2 ER visit in the previous 12 months (%)	26.2
Patient discharged home (%)	30.8

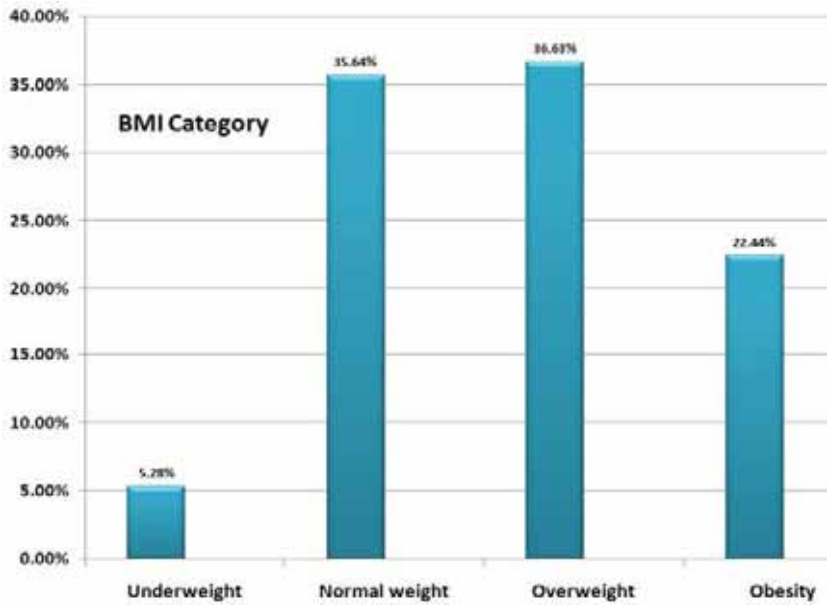

FIGURE 1
Weight distribution according to the body mass index (BMI) for the overall cohort.

TABLE 2
Chronic diseases history in all participants (N=322).

Chronic illness history	
No previous history of any chronic illness (%)	69.5
≥ 2 chronic illness (%)	4.7
Type 2 Diabetes (%)	14.0
Hypertension (%)	14.6
History of cardiovascular disease (%)	6.2
Asthma (%)	9.3
Osteoarthritis (%)	1.9

TABLE 3
Media consumption and lifestyle habits in all participants (N=322).

Media consumption	
Own personal computer (%)	44.6
Own tablet (%)	11.1
Own smart phone (%)	68.4
>3 hours of internet usage per day	44.8
Own television (%)	88.9
>3 hours of watching TV per day (%)	27.2
Own video games console (%)	19.3
>3 hours of video game playing (%)	18.2
Lifestyle habits	
Vigorous-moderate physical activity (Active group) (%)	31.4
Walking-inactive (Inactive group) (%)	68.6
Active smokers (%)	43.9
Passive smokers (%)	59.3
Daily fruits and vegetables eating (%)	41.8
Daily energy drink intake (%)	8.4
Never intake energy drink (%)	62.5
6-8 hours of sleeping per night (%)	43.8

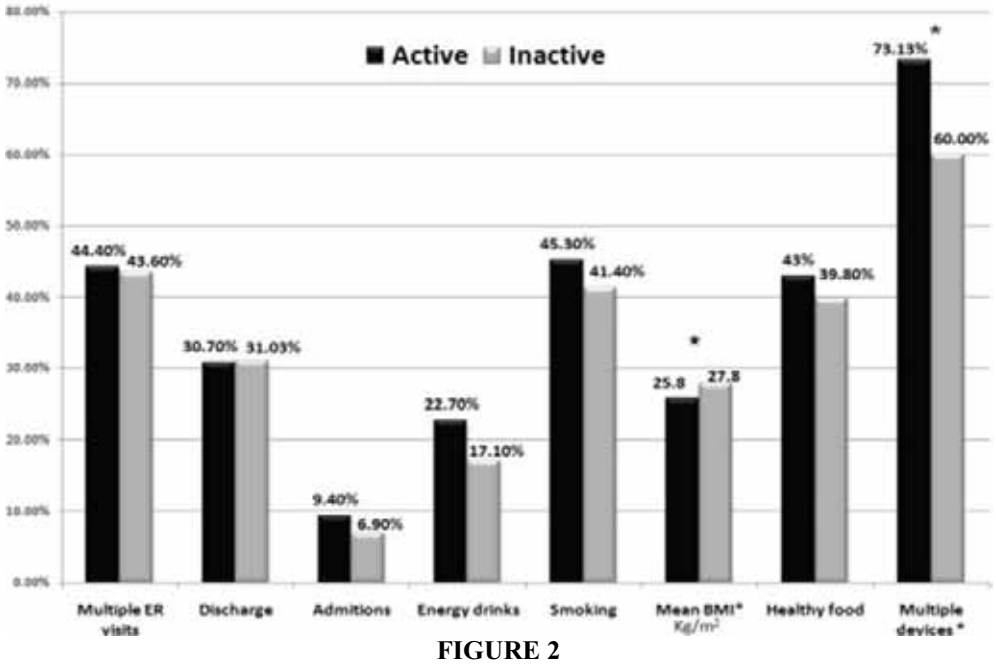

FIGURE 2
Comparison between active (vigorous and moderate) and inactive (walking and sedentary) groups.

More than half of the patients had one visit to the ER and almost 70% has no chronic illness. HTN followed by Type 2 Diabetes (T2D) were the most common 2 comorbidities in the patients presented to the ER (Table 2).

The most common used personal device was

smart phone followed by computer with almost half of them using internet > 3 hours per day. Most of them reports owning TV with majorities of them were watching it for < 3 hours per day (Table 3). Around two third of the whole sample were inactive, passive smokers and report no energy drink intake. About 40% of the sample report daily fruits and vegetable intake and optimal sleep duration (Table 3).

When groups were compared based on the number of the ER visit, 54% reports 1 ER visit in the past 12 months (Table 4). Compared to those who had ≥ 2 ER visit, those who has 1 ER visit were more likely to report low income (p 0.007), lower weight and BMI (p 0.024), less likely to have ≥ 2 chronic illness (p 0.022), less likely to have T2D (p 0.043), and more likely to own television (p 0.045).

68.6% of the participants was either inactive or reports minimal activity (walking) and 31.4% reports vigorous or moderate activity. When group compared based on their physical activity level as active (vigorous and moderate activity) compared to inactive (walking and inactive) (Figure 2).

Compared to inactive group, the active group were younger (p< 0.05), more likely to be active smokers (p 0.5), has lower mean BMI (p< 0.05), has higher mean SBP (p 0.071), has lower mean DBP (p 0.91), has lower mean pulse rate (p 0.34), more likely to reports healthy eating (p 0.62), more likely to report regular energy drinks consumptions (p 0.43), more likely to own ≥ 2 devices (p <0.05) but less likely to use them >3 hours daily (p 0.64), more likely to had ≥2 ER visit in the past year (p .31), and more likely to be admitted to the hospital (p .74).

TABLE 4
Groups characteristics based on the number of visits to the emergency room (ER) (N=322).

Variables	1 ER visit	≥ 2 ER visit	P value
Number of patients (%)	54	46	n/a
Mean number of ER visit (%)	1±0	3.26±2.5	< 0.001
Mean age (yrs)	35.5±13.3	36.9±14.9	0.361
Urban residence (%)	89.0	93.3	0.191
High school or less (%)	81.6	75.6	0.386
Saudi nationality (%)	76.2	81.5	0.260
Married (%)	60.1	64.7	0.696
Low income (%)	74.5	56.1	0.007
Active job style (%)	60.7	60.9	0.970
Mean weight (Kg)	73.0±15.9	77.6±17.8	0.023
Mean BMI (Kg/m^2)	25.5±5.1	27.1±6.8	0.024
Pulse rate beat per minute (bpm)	87.8±14.7	88.2±15.7	0.809
Systolic blood pressure (mmHg)	139.6±26.2	135.5±20.4	0.156
Diastolic blood pressure (mmHg)	81.4±14.5	82.5±14.8	0.554
Never self-weight (%)	76.9	66.9	0.259
Patient discharged home (%)	30.8	32.1	0.957
Chronic illness history			
No previous history of any chronic illness (%)	74.7	64.4	
≥ 2 chronic illness (%)	6.3	14.1	0.022
Type 2 Diabetes (%)	10.3	17.8	0.043
Hypertension (%)	10.9	17.9	0.060
History of cardiovascular disease (%)	4.6	8.9	0.099
Asthma (%)	9.2	8.1	0.455
Osteoarthritis (%)	0.6	3.7	0.059
Media consumption			
The mean number of the total of devices owned	2.3±1.3	2.4±1.2	0.898
Own personal computer (%)	46.8	42.1	0.243
Own tablet (%)	10.5	12.8	0.332
Own smart phone (%)	67.3	72.2	0.212
>3 hours of internet usage per day (%)	39.2	53.4	0.079
Own television (%)	92.4	85.7	0.045
>3 hours of watching TV per day (%)	27.8	25.2	0.558
Own video games console (%)	17.5	21.8	0.216
>3 hours of video game playing (%)	17.7	20.5	0.939
Lifestyle habits			
Vigorous-moderate physical activity (Active group) (%)	31.6	30.4	
Walking-inactive (Inactive group) (%)	68.4	69.6	0.815
Active smokers (%)	47.1	38.5	0.081
Passive smokers (%)	58.6	59.2	0.506
Daily fruits and vegetables eating (%)	44.2	38.4	0.198
Daily energy drink intake (%)	8.1	9.6	
Never intake energy drink (%)	61.3	64.4	0.746
6-8 hours of sleeping per night (%)	46.5	39.8	0.185

DISCUSSION

The study showed that majorities of the patients who visited the ER were overweight. Previous studies have shown that obese and overweight patients more likely to see primary care physicians compared to the general population [13-15]. Another study showed that the healthcare cost expenditures increased with weight and age [16].

Despite that only 1.9% of the patients have osteoarthritis and 69.5% had no chronic illness but only 68.6% reports no or minimal activity and we observed no difference in the ER visit numbers. Previous study of older adults showed that moderate physical activity correlated with lower ER visits and hospital stay [17]. However, in the present study, the mean age was 36.5$\pm$14.1 years and that is the likely reason behind the difference in the observation in both studies. The patients who had $\geq$ 2 ER visit were significantly less likely to reports low income and that might be because of the free health care system in Saudi and also given those with multiple ER visit were more likely to have chronic illnesses (Table 4). These finding concur with previously published study that showed providing free primary and specialty care resulted in lower hospitalization and ER visits [18].

Also, the present study showed that active group compared to the inactive group was non-significantly more likely to get admitted to the hospital possibly due to the higher rate of unhealthy habits (i.e. smoking and energy dink consumption) in the active group which may offset the good exercise effect. Recent study showed that the overall energy drink ER related visit increased in the recent years [19]. Also, active group in our study had non-significantly higher systolic blood pressure despite having lower BMI which may also be a reason for the observed higher hospital admission rate and could be explained by the higher energy drink consumption. A study in a healthy individual showed that energy drink consumption resulted in a higher systolic blood pressure [20].

The strength of the present study includes collecting data from the main hospital's ER in Taif, detailed history about the energy drink, physical activity, and media consumption. The weakness includes the limited sample size and no hospital stay data.

CONCLUSION

Only one third of our cohort were physically active and those were younger and has lower BMI when compared to the inactive group. Interestingly, those considered to be active were more likely to have a frequent ER visits and to be admitted to the hospital in the past year which were likely due to higher rate of smoking, energy drink consumption, and media consumption which may offset the exercise benefits.

ACKNOWLEDGEMENTS

The authors extend their appreciation to the Taif University Researches Supporting Project number (TURSP-2020/37), Taif University, Taif, Saudi Arabia.

Data Availability. The data supporting the findings of this study are available from the corresponding author upon reasonable request.

Author Contributions. All authors read and approved the final version of the manuscript. Khaled A. Alswat, Thamer Almalki and Ahmed Gaber participated in the design of the study, data analysis, wrote the original draft, review and edited the final version**.** Khalid Altalhi, Bader Almansouri, Abdulelah Almutairi, Abdullah Alharthi, participated in the design of the study, review and edited the final version. Fatma Saffeyeldin Mohamed, contributed in acquisition the data and data analysis.

Funding. The current work was funded by Taif University Researches Supporting Project number (TURSP-2020/37), Taif University, Taif, Saudi Arabia.

REFERENCES

[1] Kokkinos, P., Myers, J. (2010) Exercise and physical activity: clinical outcomes and applications. Circulation. 122(16), 1637-48.

[2] Woodcock, J., Franco, O.H., Orsini, N., Roberts, I. (2010) Non-vigorous physical activity and all-cause mortality: systematic review and meta-analysis of cohort studies. International J. Epidemiology. 40(1), 121-38.

[3] Wen, C.P., Wai, J.P., Tsai, M.K., Yang, Y.C., Cheng, T.Y., Lee, M.C., Chan, H.T., Tsao, C.K., Tsai, S.P., Wu, X. (2011) Minimum amount of physical activity for reduced mortality and extended life expectancy: a prospective cohort study. The Lancet. 378(9798), 1244-53.

[4] Arem, H., Moore, S.C., Patel, A., Hartge, P., De Gonzalez, A.B., Visvanathan, K., Campbell, P.T., Freedman, M., Weiderpass, E., Adami, H.O., Linet, M.S. (2015) Leisure time physical activity and mortality: a detailed pooled analysis of the dose-response relationship. JAMA Internal Medicine. 175(6), 959-67.

[5] Goldfarb, M., Tellier, C., Thanassoulis, G. (2014) Review of published cases of adverse cardiovascular events after ingestion of energy drinks. Am. J. Cardiol. 113(1), 168-72.

[6] Pommerening, M.J., Cardenas, J.C., Radwan, Z.A., Wade, C.E., Holcomb, J.B., Cotton, B.A. (2015) Hypercoagulability after energy drink consumption. J. Surg. Res. 199(2), 635-40.
[7] González, W., Altieri, P., Alvarado, E., Banchs, H., Colón, E., Escobales, N., Crespo, M. (2015) Celiac trunk and branches dissection due to energy drink consumption and heavy resistance exercise: case report and review of literature. Bol. Asoc. Med. P. R. 107(1), 38–40.
[8] Di Rocco, J.R., During, A., Morelli, P.J., Heyden, M., Biancaniello, T.A. (2011) Atrial fibrillation in healthy adolescents after highly caffeinated beverage consumption: two case reports. J. Med. Case Rep. 5(1), 18.
[9] Wilson, R.E., Kado, H.S., Samson, R., Miller, A.B. (2012) A case of caffeine-induced coronary artery vasospasm of a 17-year-old male. Cardiovasc. Toxicol. 12(2), 175-9.
[10] Galler, A., Lindau, M., Ernert, A., Thalemann, R., Raile, K. (2011) Associations between media consumption habits, physical activity, socioeconomic status, and glycemic control in children, adolescents, and young adults with type 1 diabetes. Diabetes Care. 34(11), 2356-9.
[11] Martinez-Gomez, D., Rey-López, J.P., Chillón, P., Gómez-Martínez, S., Vicente-Rodríguez, G., Martín-Matillas, M., Garcia-Fuentes, M., Delgado, M., Moreno, L.A., Veiga, O.L., Eisenmann, J.C. (2010) Excessive TV viewing and cardiovascular disease risk factors in adolescents. The AVENA cross-sectional study. BMC Public Health. 10(1), 274.
[12] McDonnell, M.N., Hillier, S.L., Judd, S.E., Yuan, Y., Hooker, S.P., Howard, V.J. (2016) Association between television viewing time and risk of incident stroke in a general population: results from the REGARDS study. Prev. Med. 87, 1-5.
[13] Noel, M., Hickner, J., Ettenhofer, T., Gauthier, B. (1998) The high prevalence of obesity in Michigan primary care practices. An UPRNet study. Upper Peninsula Research Network. J. Fam. Pract. 47(1), 39-43.
[14] Scott, J.G., Cohen, D., DiCicco-Bloom, B., Orzano, A.J., Gregory, P., Flocke, S.A., Maxwell, L., Crabtree, B. (2004) Speaking of weight: how patients and primary care clinicians initiate weight loss counseling. Prev. Med. 38(6), 819-27.
[15] Stecker, T., Sparks, S. (2006) Prevalence of obese patients in a primary care setting. Obesity (Silver Spring). 14(3), 373–6.
[16] Wee, C.C., Phillips, R.S., Legedza, A.T., Davis, R.B., Soukup, J.R., Colditz, G.A., Hamel, M.B. (2005) Health care expenditures associated with overweight and obesity among US adults: importance of age and race. Am. J. Public Health. 95(1), 159-165.
[17] Perkins, A.J., Daniel, O.C. (2001) Assessing the association of walking with health services use and costs among socioeconomically disadvantaged older adults. Prev. Med. 32(6), 492-501.
[18] MacKinney, T., Visotcky, A.M., Tarima, S., Whittle, J. (2013) Does providing care for uninsured patients decrease emergency room visits and hospitalizations? J. Prim. Care Community Health. 4(2), 135-142.
[19] Mattson, M.E. (2013) Update on Emergency Department Visits Involving Energy Drinks: A Continuing Public Health Concern. In: The CBHSQ Report. Rockville (MD): Substance Abuse and Mental Health Services Administration (US). PMID: 27606410.
[20] Kozik, T.M., Shah, S., Bhattacharyya, M., Franklin, T.T., Connolly, T.F., Chien, W., Pelter, M.M. (2016) Cardiovascular responses to energy drinks in a healthy population: The C-energy study. Am. J. Emerg. Med. 34(7), 1205-9.

Received: **16.12.2021**
Accepted: **11.02.2022**

CORRESPONDING AUTHOR

Khaled A Alswat
Professor of Medicine,
Department of Internal Medicine,
Taif University School of Medicine,
P.O. Box 11099,
Taif 21944 – Saudi Arabia

e-mail: k.alswat@tu.edu.sa

© by PSP Volume 31– No. 05/2022 pages 5229-5234 Fresenius Environmental Bulletin

PROTECTIVE EFFECTS OF L-ARGININE AGAINST AFB1-INDUCED RENAL OXIDATIVE STRESS AND HISTOLOGICAL CHANGES IN MICE

Eman A Al-Shahari[1,2], Attalla F El-Kott[3], Khaled Abdelaal[4,*], Abeer A Alm-Eldeen[5]

[1]Department of Biology, Faculty of Science and arts, King Khaled University, Saudi Arabia
[2]Department of Biology, Faculty of Science, Ibo University, Yemen
[3]Department of Biology, College of Science, King Khaled University, Saudi Arabia
[4]EPCRS Excellence Center, Plant Pathology and Biotechnology Lab., Agric. Botany Dept., Fac. Agric., Kafrelsheikh University, Egypt
[5]Zoology Department, Faculty of Science, Tanta University, Egypt

ABSTRACT

Aflatoxin B1 (AFB1) is a mycotoxin that causes toxic effects on some organs. It helps the formation of the reactive oxygen species (ROS) which in turn cause oxidative damage and lipid peroxidation. L. arginine is an essential amino acid that has the ability to decrease ROS production that resulted from the oxidative stress. Therefore, the present study was designed to examine the possible role of L. arginine against AFB1-induced renal oxidative stress and histolohical changes in male mice. Forty male mice were equally divided into four groups. Groups 1 contained mice that received normal saline, group 2 contained mice that received single nephroprotective dose of 300 mg/kg of L. arginine, group 3 contained mice that received a single dose of 50 mg/kg of AFB1 and group 4 contained mice that received AFB1 followed immediately by L-arginine at the same previous doses, respectively. After 2 weeks, the mice were anesthetized and the data were collected. The results showed that the mice that treated with AFB1 showed an increase in the levels of the urea, creatinine, total protein and globulin. A decrease in the kidney superoxide dismutase (SOD), catalase (CAT) and reduced glutathione (GSH) and an increase in the kidney malondialdehyde (MDA) and apoptotic cell levels were also determined. Furthermore, some deterioration changes in the renal glomerulei were observed. Interestingly, the mice that treated with AFB1 followed by L. arginine showed an improvement in the previous biochemical and histological parameters. This improvement may be related to the antioxidant properties of L. arginine that may reduce the oxidative stress and apoptotic cells levels in the kidney and as a result improve its histological structure.

KEYWORDS:
Kidney, AFB1, L. arginine, oxidative stress, apoptosis

INTRODUCTION

Aflatoxins are group of mycotoxins that cause several harms to human. It is derived from two different strains of fungi; *Aspergillus flavus* and *Aspergillus parasiticus.* They are found as contaminants in a great variety of crops like cereals, tree nuts and others due to the bad storage or transport when exposed to warm, humid or drought [1, 2]. There are several types of mycotoxcin, aflatoxin B1 (AFB1) considers the most hazardous to health according to the International Agency for Research on Cancer (IARC). The later reported AFB1 as the most carcinogenic agent to human. Generally, liver considers the main target of AFB1 toxicity. Furthermore, several previous studies documented the harmful effects of AFB1 to other organs like heart, kidneys and lungs [3, 4]. Generally, the most common route of the entry of the aflatoxin into the human body is the ingestion. AFB1 is metabolized in the liver to reactive epoxide intermediate (8, 9-epoxide) that is responsible for DNA mutation [5]. It can also bind to other macromolecules in different cells like RNA and proteins and consequently cause cellular dysregulation. It inhibits also the synthesis of the proteins, RNA and DNA [6]. It also may reduce the glutathione and as a result, toxicity is occurred from the reactive oxygen species (ROS). AFB1 could induce the oxidative stress and the apoptosis via mitochondrial pathway [7]. AFB1 could cause oxidative stress, apoptosis and histopathological lesions in many different organs [8]. Oxidative stress considers the main cause of the toxicity of AFB1. This is because it helps the formation of the free radicals which in turn causes the oxidative damage and lipid peroxidation that are behind the occurrence of the cellular damage that is responsible for the animals and human harms [9].

L-arginine is an essential amino acid that is catalyzed by nitric oxide synthase, arginine decarboxylase and arginase to synthesize the protein and other bioactive molecules like nitric oxide, proline, creatine and polyamines [10, 11]. It considers the source of the nitric oxide in the body [12]. Several previous

studies documented the ability of L. arginine to reduce the oxidative stress. It could protect ovine intestinal epithelial cells from the apoptosis via attenuating oxidative stress [13]. It could inhibit the inflammatory response and oxidative stress induced by lipopolysaccharide [14]. It could act as a prophylactic agent against hepatic carcinoma in mice by its ability to attenuate the oxidative stress [15]. Therefore, the present study was designed to examine the possible protective role of L. arginine against AFB1-induced renal oxidative stress and histological changes in male mice.

MATERIALS AND METHODS

Experimental animal groups. The experiment adhered to the guidelines of the ethical committee of the faculty of science, Tanta University, Tanta, Egypt. Forty male Swiss mice weighing 29 ± 2.5g were kept under balanced laboratory chow diet and water ad libitum at 22 ± 3℃ with 12h Light/dark cycles. After 2 weeks of acclimation, they were equally divided into four groups. Groups 1 (G1) contained mice that received normal saline, group 2 (G2) contained mice that received L. arginine, group 3 (G3) contained mice that received AFB1 and group 4 (G4) contained mice that received AFB1 followed immediately by L-arginine. AFB1 was purchased from Sigma Chemical Co. (St. Louis, MO, USA), dissolved in DMSO and received as a single dose of 50 mg/kg body weight [16]. L-arginine (Aldrich, UK) was dissolved in the saline and intraperitoneally injected in a single nephroprotective dose of 300 mg/kg [17]. After 2 weeks, the mice were anesthetized by diethyl ether and the blood was collected via retro-orbital bleeding. Some kidneys tissues were removed and homogenized a in phosphate buffer solution, pH 7.4, centrifuged at 3000 r/minutes for 10 minutes at 4 ℃, and the supernatant was stored. Other kidney tissues were fixed in 10% buffered formalin for histological observation.

Kidney functions. Serum creatinine was determined according to [18]. Blood urea nitrogen was estimated according to [19]. The concentration of the total protein, albumin and globulin were determined using commercial diagnostic kits (AMS, Italy).

Lipid peroxidation and antioxidant enzymes. Renal lipid peroxidation (MDA) content was calculated according [20]. The data was expressed as pmol/mL. Reduced glutathione (GSH) was calculated according to [21]. The data was expressed as μmol/g. Superoxide dismutase (SOD) activity was estimated according to [22]. The data was expressed as U/g. Catalase (CAT) activity was calculated according to the method of [23]. The data was expressed as U/mg.

Assessment of cell death level. One mg of the renal tissue was added to 100 µL lysis buffer in a microtube then vortexed, centrifuged at 1000 g for 10 min then washed by phosphate-buffered saline (PBS) 2 times. The cells were suspended in 20 µL of PBS then transferred to 96-well plate. 80 µL of immunoreagent was added to each well and covered by a foil for 2 hours at 20 °C under gently shaking then the absorbance was tested using ELIZA at 490 ± 10 nm.

Histological examination. Small pieces from the renal tissues which were fixed in the buffered formalin were washed, dehydrated and embedded in paraffin. 5 µm thick sections were cut and some sections were processed for hematoxylin and eosin staining [24].

Statistical analysis. The data were expressed as mean ± standard deviation (mean ± SD) in which they were the means of 4 replicates. One-way analysis of variance (ANOVA) was performed. This was followed by Tukey post hoc test. P values ≤ 0.05 was statistically significant. Statistical analysis was performed using Excel 2013 (Microsoft Corporation, USA), SPSS statistical version 22 software package (SPSS Inc., USA) and Minitab version 18).

RESULTS

The effect of L. arginine on AFB1-induced changes in the kidney functions. The results showed a non-significant ($p \geq 0.05$) change in the values of the urea, creatinine, albumin, globulin and total protein in the mice that treated with L. arginine comparing with the control mice, respectively. The levels of the urea and creatinine, total protein and globulin showed a significant ($p \leq 0.05$) increase while the level of the albumin showed a significant ($p \leq 0.05$) decrease in the mice that treated with AFB1 comparing with the control mice, respectively. Interestingly, the mice that treated with AFB1 followed by L. arginine showed a non-significant ($p \geq 0.05$) change in the urea, creatinine, albumin, globulin and total protein levels comparing with the control mice, respectively (Table 1).

The effect of L-arginine on AFB1-induced changes in the kidney antioxidant and oxidative parameters. The results showed a non-significant ($p \geq 0.05$) change in the values of the kidney SOD, CAT, catalase and GSH in the mice that treated with L. arginine comparing with the control mice, respectively. The mice that treated with AFB1 showed a significant ($p \leq 0.05$) decrease in the values of the kidney SOD, CAT and GSH while showed a significant increase in the value of the kidney MDA comparing with the control mice, respectively. The mice that treated with AFB1 followed by L. arginine showed a non-significant ($p \geq 0.05$) change in the values of the

TABLE 1
The effect of L. arginine on the urea and creatinine levels in the mice that treated with AFB1. The values represented as (mean ± SE& n= 4).

Groups	G1	G2	G3	G4
Urea (mg/ dl)	31.65 ± 1.00^{b}	33.93 ± 1.27^{b}	47.68 ± 1.27^{a}	37.48 ± 1.21^{b}
Creatinine (mg/ dL)	$0.82 \pm 0.01^{b, c}$	$0.83 \pm 0.03^{b,c}$	0.96 ± 0.03^{a}	$0.79 \pm 0.04^{b,c}$
Total protein (g/ dL)	5.2 ± 0.8^{b}	$5.4 + 1.1^{b}$	6.4 ± 0.9^{a}	$5.5 + 0.8^{b}$
Albumin (g/ dL)	$3.3 \pm 0.5^{b, c}$	$3.4 \pm 0.6^{b, c}$	2.6 ± 0.4^{a}	3.0 ± 0.6^{b}
Globulin (g/ dL)	$2.1 \pm 0.4^{b, c}$	$2.4 \pm 0.6^{b, c}$	4.1 ± 0.6^{a}	2.7 ± 0.3^{b}

(G1) control group, (G2), mice that received L. arginine, (G3) mice that received AFB1, (G4) mice that received AFB1 followed by L. arginine
Columns that do not share a letter are significantly different.
P values ≤ 0.05 were considered to be statistically significant.

TABLE 2
The effect of L. arginine on the kidney SOD, CAT, GSH and MDA in the mice that treated with AFB1. The values represented as (mean ± SE& n= 4).

Groups	G1	G2	G3	G4
SOD (U/g)	12.67 ± 0.22^{a}	12.57 ± 0.24^{a}	8.65 ± 0.34^{b}	12.02 ± 0.06^{a}
CAT (U/mg)	10.7 ± 0.24^{a}	10.8 ± 0.30^{a}	6.4 ± 0.57^{c}	10.8 ± 0.16^{a}
GSH (μmol/g)	4.37 ± 0.34^{a}	4.2 ± 0.15^{a}	2.9 ± 0.20^{b}	4.3 ± 0.15^{a}
MDA (pmol/mL)	4.4 ± 0.09^{b}	4.3 ± 0.08^{b}	8.12 ± 0.65^{a}	4.60 ± 0.13^{b}

(G1) control group, (G2) mice that received L. arginine, (G3) mice that received AFB1, (G4) mice that received AFB1 followed by L. arginine
Columns that do not share a letter are significantly different.
P values ≤ 0.05 were considered to be statistically significant.
SOD: superoxide dismutase, CAT: catalase, GSH: reduced glutathione and MDA: malondialdehyde activity

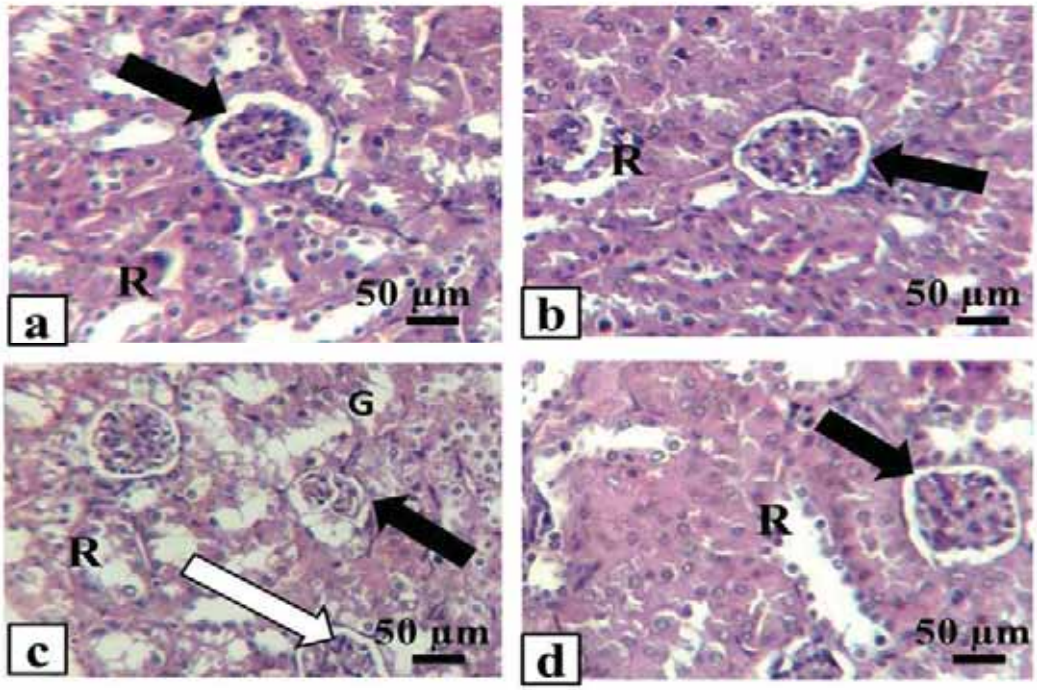

FIGURE 1
Light photomicrographs of the kidney tissue stained with hematoxylin and eosin.
(a, b): control mice (G1) and the mice that received L. arginine (G2), respectively sowing normal renal glomerulei with intact urinary spaces (black arrows) and intact renal tubules (R).
(c): mice that received AFB1 (G3) showed marked degeneration in some renal glomerulei (black arrow) and some apoptotic cells in other renal glomerulei (white arrow). Note the renal tubules with deteriorated lining epithelium (R)
(d): mice that received AFB1 followed by L. arginine (G4) showed almost normal renal glomerulei (black arrows) and Renal tubule (R)

kidney SOD, CAT, GSH and MDA comparing with the control mice, respectively (Table 2).

The effect of L-arginine on AFB1-induced change in the apoptotic cell levels in the renal tissue. The apoptotic cell levels in the mice that treated with L. arginine showed a non-significant ($p \geq 0.05$) change comparing with its level in the control mice. The apoptotic cell levels in the control mice and the mice that treated with L. arginine were 1.8 ± 0.9 U/g and 1.4 ± 0.7 U/g, respectively. However, the mice that treated with AFB1 showed a significant ($p \leq 0.05$) increase in the level of the apoptotic cells in the renal tissue comparing with its level in the control mice. The level of the apoptotic cells in the mice that treated with AFB1 was 4.9 ± 1.3 U/g. Interestingly, the level of the apoptotic cells in the renal tissue in the mice that treated with AFB1 followed by L. arginine showed a non-significant ($p \geq 0.05$) change comparing with the control mice as it reached 3.1 ± 0.8 U/g.

The effect of L-arginine on AFB1-induced change in the renal histological structure. The histological sections of the kidney from both the control mice and the mice that treated with L. arginine showed normal architectures. The renal glomerulei had oval to circular appearance with intact urinary spaces. The mean diameter of the renal glomerulei was about 70.3 ± 4.7 µm. Renal tubules were also intact and appeared with normal lining epithelium and tubular lumina (Figure 1a, b). The mice that treated with AFB1 revealed that the renal glomerulei had marked degeneration. Most of them lost their oval and circular appearance and appeared irregular in shape and in the same time lost their normal sizes. The mean diameter of the renal glumerulei was about 47.6 ± 4.9 µm.

The urinary spaces appeared much wider than what seen in the control mice. Some apoptotic cells appeared randomly in the renal glomerulei. Renal tubules appeared with deteriorated lining epithelium (Figure 1b). The mice that treated with AFB1 followed by L. arginine revealed that both of the renal glomerulei with their urinary spaces and the renal tubules appeared intact with their nearly normal structures and sizes. The mean diameter of the renal glomerulei was about 64.4 ± 4.2 µm. The apoptotic cells in the renal glomerulei were rarely detected (Figure 1c).

DISCUSSION

The present study was designed to study the effect of L. arginine on AFB1-induced changes in the functions and histological structures of the kidney in male mice. AFB1 treated mice showed alterations in the kidney functions as an increase in the levels of the urea, creatinine, total protein and globulin was recorded. With regard to the antioxidant and oxidant parameters, a decrease in the kidney SOD, CAT and GSH while an increase in the kidney MDA were determined. Furthermore, in addition to the histological deterioration in the structure of the renal glomerulei, an increase in the apoptotic cells level was recorded. These data was parallel with Liang et al. [25] who reported high levels of creatinine and urea after AFB1 administration due to its ability to induce toxicity [25]. Oxidative stress is the principle indicators of AFB1- induced toxicity [26]. Generally, aflatoxins are carcinogenic and genotoxic agents that cause toxic effects on many organs through DNA damage leading to oxidative damage. Oxidative stress considers a disturbance in the balance between the production of the radical and the defense of the antioxidant system. Exposure to AFB1 showed an increase in the lipid peroxidation and a decrease in the antioxidant enzyme activities such as SOD, GSH and CAT in many different organs like liver and kidney [27].

AFB1 is excreted mainly via biliary duct and urinary pathway. It could be also detected in the kidney tissue and urine samples. Generally, liver and the kidney are the main target organs of AFB1 toxicity [28]. With regard to the biochemical alterations that were recorded here in the present study, Liu et al. [29] documented that MDA is a product of lipid peroxidation and has a toxic effect to organ tissue. MDA content in any tissue reflects the degree of the oxidative damage. SOD is an antioxidant enzyme that has the ability to convert superoxide anion radicals to hydrogen peroxide and consequently protect against oxidative injury. Hydrogen peroxide is the main constituent of the ROS in redox sensing and redox signaling [30]. Therefore, an increase in the concentration of H_2O_2 causes extreme damage in the DNA, lipids and proteins and consequently SOD, CAT and GSH are good markers for antioxidant defense system.

The recorded increase in the apoptotic cell level and renal histological injury in the mice that treated with AFB1 in the current study were in parallel with other previous studies that reported a reduction in the renal glomerular filtration after AFB1 administration [26, 31]. Furthermore, Li el al. [28] documented that AFB1 could activate the pathways related to the oxidative stress leading to the increase in the cell apoptosis rate. The alteration of the histological structure of the kidney could be used as indicator for renal functions interruption [32]. AFB1 exposure causes serious kidney damage that leads to a disorder in AFB1 metabolites excretion that strength the occurrence of the renal injury [33].

The mice that treated with AFB1 followed by L. arginine showed a non-significant change in the renal functions comparing with the control mice. The situation of the antioxidant defense system represented by SOD, CAT and GSH and the MDA, and

the apoptotic cells levels were improved after L. arginine administration and showed also a non-significant difference with their levels in the control mice. The current data were in agreement with other previous studies with regard to the ability of L. arginine, a nitric oxide precursor, to ameliorate the toxic effects of different drugs on the renal functions and structures in acute and chronic renal injury. L. arginine could work against cyclosporine-induced nephrotoxicity [17], gentamycin-induced renal injury [34] and cisplatin-induced renal oxidative stress and toxicity [35]. L. arginine was recorded to have an indirect antioxidant effect via NO production [36]. NO could inhibit the oxidative stress in tissues via interrupting chain reaction of lipid peroxidation and as a result decrease the apoptotic level. This can be happened by developing non-radical novel nitrogen-containing lipid molecules. NO could induce the expression of antioxidant enzymes and activate the antioxidant capacity of GSH by forming S-nitrosoglutathione [37, 38]. NO has a direct effect in decreasing the renal damage via activating the microcirculation, organ blood flow and blood pressure regulation [39].

In conclusion, L-arginine could be used as an antioxidant agent against AFB1-induced renal oxidative stress and histological changes in mice due its ability to decline the oxidative stress.

ACKNOWLEDGEMENTS

The authors extend their appreciation to Scientific Research Deanship at King Khaled University for funding this work [general project under grant number (R.G.P.I/225/41).

REFERENCES

[1] World Health Organization. International Agency for Research on Cancer. (2002) IARC Monographs on the Evaluation of Carcinogenic Risks to Humans. IARC Press; Lyon, France. Aflatoxins. 82, 171–300.

[2] Marchese, S., Polo, A., Ariano, A., Velotto, S., Costantini, S., Severino. L. (2018) Aflatoxin B1 and M1: Biological Properties and Their Involvement in Cancer Development. Toxins (Basel). 10(6), 214- 332.

[3] Alm-Eldeen, A.A., Basyony, M.A., Elfiky, N.K. Ghalwash, M.M. (2017) Effect of the Egyptian propolis on the hepatic antioxidant defense and pro-apoptotic p53 and anti-apoptotic bcl2 expressions in aflatoxin B1 treated male mice. Biomedicine & Pharmacotherapy. 87, 247-255.

[4] Yan, H., Ge, J., Gao, H., Pan, Y., Hao, Y., Li, J. (2020): Melatonin attenuates AFB1-induced cardiotoxicity via the NLRP3 signalling pathway. J. Int. Med. Res. 48(9), 1-13.

[5] Wang, J.S., Groopman, J.D. (1999) DNA damage by mycotoxins. Mutation Res. 424,167–181.

[6] Gallagher, E.P., Kunze, K.L., Stapleton, P.L., Eaton, D.L. (1996) The kinetics of aflatoxin B1 oxidation by human cDNA-expressed and human liver microsomal cytochromes P450 1A2 and 3A4. Toxicol. Appl. Pharmacol. 141(2), 595-606.

[7] Rajput, S.A., Zhang, C., Feng, Y., Wei, X.T., Khalil, M.M., Rajput, I.R., Baloch, D.M., Shaukat, A., Rajput, N., Qamar, H., Hassan, M., Qi, D. (2019) Proanthocyanidins alleviates aflatoxinB1-induced oxidative stress and apoptosis through mitochondrial pathway in the bursa of fabricius of broilers. Toxins. 11(157), 1-13.

[8] Liu, T., Ma, Q., Zhao, L., Jia, R., Zhang, J., Ji, C., Wang, X. (2016) Protective effects of sporoderm-broken spores of ganderma lucidum on growth performance, antioxidant capacity and immune function of broiler chickens exposed to low level of aflatoxin B1. Toxins (Basel). 8(10), 278- 290.

[9] Alm-Eldeen, A.A., Mona, M.H., Shati, A.A., El-Mekkawy, H.I. (2015) Synergistic effect of black tea and curcumin in improving the hepatotoxicity induced by aflatoxin B1 in rats. Toxicology and Industrial Health. 31(12), 1269-1280.

[10] Bertrand, J., Goichon, A., Déchelotte, P., Coëffier, M. (2013) Regulation of intestinal protein metabolism by amino acids. Amino Acids. 45, 443–450.

[11] Tsikas, D., Wu, G. (2015) Homoarginine, arginine, and relatives: analysis, metabolism, transport, physiology, and pathology. Amino Acids. 47, 1697–1702.

[12] Moncada, S., Palmer, R.M.J., Higgs, E.A. (1991) Nitric oxide physiology, pathophysiology and pharmacology. Pharmacol. Rev. 43, 109–141.

[13] Zhang, H., Peng, A., Yu, Y., Guo, S. Wang, M.Z., Wang, H.R. (2019) L-Arginine protects ovine intestinal epithelial cells from lipopolysaccharides-induced apoptosis through alleviating oxidative stress. J. Agric. Food Chem. 67, 1683–1690.

[14] Qiu, Y., Yang, X., Wang, L., Gao, K., Jiang, Z. (2019) L-Arginine Inhibited Inflammatory Response and Oxidative Stress Induced by Lipopolysaccharide via Arginase-1 Signaling in IPEC-J2 Cells. Int. J. Mol. Sci., 20, 1-14

[15] Al-Shahari, E., El Barky, A., Mohamed, T., Alm-Eldeen, A. (2021) Doxorubicin, L-arginine, or their combination as a prophylactic agent against hepatic carcinoma in mice. Environ Sci Pollut Res., 28(28),37661-37671.

[16] Mulder, J., Turner, P., Massey, T. (2015) Effect of 8-oxoguanine glycosylase deficiency on aflatoxin B1 tumourigenicity in mice. Mutagenesis. 30(3), 401-409.

[17] Mansour, M., Daba, M.H., Gado, A., Al-Rikabi, A., Al-Majed, A. (2002) Protective effect of L-arginine against nephrotoxicity induced by cyclosporine in normal rats. Pharmacol. Res. 45(6), 441–446.
[18] Fabinay, D.L., Eringshausen, G. (1971) Automated reaction rate method for determination of serum creatinine with the Centrifi Chem. Clin. Chem. 17(8), 696–700.
[19] Patton, C.J., Crouch, S.R. (1977) Spectrophotometric and kinetics investigation of the Berthelot reaction for the determination of ammonia. Anal. Chem. 49(3), 464–469.
[20] Buege, J.A., Aust, S.D. (1978) Microsomal lipid peroxidation. Methods Enzymol. 52, 302-310.
[21] Beutler, E., Duron, O., Kelly, B.M. (1963) Improved method for the determination of blood glutathione. J. Lab. Clin. Med. 61, 882–888.
[22] Paoletti, F., Mocali, A. (1990) Determination of superoxide dismutase activity by purely chemical system based on NAD(P)H oxidation. Methods Enzymol. 186, 209-220.
[23] Aebi, H. (1984) Catalase in vitro. Methods Enzymol. 105, 121-126.
[24] Bancroft, J.D., Cook, H.C. and Stirling, R.W. (1994) Manual of histological techniques and their diagnostic application Edinburgh. New York. 457-458. Churchill Livingstone.
[25] Liang, N., Wang, F., Peng, X., Fang, J., Cui, H., Chen, Z., Lai, W., Yi Zhou, Y., Geng, Y. (2015) Effect of Sodium Selenite on Pathological Changes and Renal Functions in Broilers Fed a Diet Containing Aflatoxin B1. Int. J. Environ. Res. Public Health. Int J Environ Res Public Health. 12(9), 11196–11208.
[26] Yu, K., Zhang, J., Cao, Z., Ji, Q., Han, Y., Song, M., Shaoa, B. Li, Y. (2018) Lycopene attenuates AFB1-induced renal injury with the activation of the Nrf2 antioxidant signaling pathway in mice. Food Funct. 9(12), 6427–6434.
[27] Souza, M.F., Tome, A.R., Rao, V.S. (1999) Inhibition by the bioflavonoid termination of aflatoxin B1-induced lipid peroxidartion in rat liver. J. Pharm. Pharmacol. 51,125–129.
[28] Li, H., Li, S., Yang, H., Wang, Y., Wang, J., Zheng, N. (2019), L-proline alleviates kidney injury caused by AFB1 and AFM1 through regulating excessive apoptosis of kidney cells. Toxins. 11(4), 226-237.
[29] Liu, S.X., Li, C.G., Dai, D.L. (2010), Effect of Ligustrazine on MDA, SOD and T-AOC in Erythrocyte Membrane in Patients with Hemoglobin H Disease. Journal of Clinical Experimental Medicine. 11.
[30] Li, H., Xing, L., Zhang, M., Wang, J., Zheng, N. (2018) The Toxic Effects of Aflatoxin B1 and Aflatoxin M1 on Kidney through Regulating L-Proline and Downstream Apoptosis. Biomed. Res. Int. 1-11.
[31] Akinrinde, A.S., Adebiyi, O.E. (2019) Asekun, A. Amelioration of Aflatoxin B1-induced gastrointestinal injuries by Eucalyptus oil in rats. Journal of Complementary and Integrative Medicine. 17(1), 2019-2022.
[32] Francescato, H.D., Coimbra, T.M., Costa, R.S. and Bianchi Mde, L. (2004) Kidney Blood Pressure Res. 27, 148-158.
[33] Tang, L., Guan, H., Ding, X., Wang, J. S. (2007) Modulation of aflatoxin toxicity and biomarkers by lycopene in F344 rats. Toxicol. Appl. Pharmacol. 219(1), 10–17.
[34] Can, C., Sen, S., Boztok, N., Tuglular, I. (2000) Protective effect of oral L-arginine administration on gentamycin-induced renal failure in rats. Eur. J. Pharmacol. 390, 327–334.
[35] Saleh, S. and El-Demerdash, E. (2005) Protective effects of L-arginine against cisplatin-induced renal oxidative stress and toxicity: role of nitric oxide. Basic Clinical Pharmacology and Toxicology. 97, 91–97.
[36] Lass, A., Suessenbacher, A., Wolkart, G., Mayer, B., Brunner, F. (2002) Functional and analytical evidence for scavenging of oxygen radicals by L-arginine. Mol. Pharmacol. 61, 1081–1088.
[37] Rubbo, H., Radi, R., Trujillo, M., Telleri, R., Kalyanaraman, B., Barnes, S., Kirk, M., Freeman, B.A. (1994) Nitric oxide regulation of superoxide and peroxynitrite-dependent lipid peroxidation. Formation of novel nitrogen-containing oxidized lipid derivatives. J. Biol. Chem. 269, 26066–26075.
[38] Klatt, P., Lamas, S. (2000) Regulation of protein function by S-glutathiolation in response to oxidative and nitrosative stress. Eur. J. Biochem. 267, 4928–4944.
[39] Matsubara, A., Tamai, K., Matsuda, Y., Niwa, Y., Morita, H., Tomida, K., Armstrong, D., Ogura, Y. (2005) Protective effect of polyethylene glycol-superoxide dismutase on leukocyte dynamics in rat retinal microcirculation under lipid hydroperoxide-induced oxidative stress. Exp. Eye Res. 81, 193–199.

Received: **17.12.2021**
Accepted: **11.02.2022**

CORRESPONDING AUTHOR

Khaled Abdelaal
EPCRS Excellence Center, Plant Pathology and Biotechnology Lab., Agric. Botany Dept., Fac. Agric., Kafrelsheikh University, Egypt

e-mail: khaled.elhaies@gmail.com

© by PSP Volume 31– No. 05/2022 pages 5235-5242 Fresenius Environmental Bulletin

PREVALENCE AND RISK FACTORS OF INTESTINAL PROTOZOAN PARASITIC INFECTIONS AMONG DIARRHEIC HIV/AIDS PATIENTS ON ART IN SELECTED HOSPITALS IN ABUJA, NIGERIA

Abdulkadir Ademu[1,2], Umut Gazi[1,*], Ozgur Tosun[3], I Helen Inabo[4], Maryam Aminu[4], Aysegul Taylan Ozkan[5]

[1]Department of Medical Microbiology and Clinical Microbiology, Faculty of Medicine, Near East University, Nicosia, Cyprus
[2]Department of Applied Microbiology, School of Applied Science, Federal Polytechnic, Nasarawa, Nigeria
[3]Department of Biostatistics, Faculty of Medicine, Near East University, Nicosia, Cyprus
[4]Department of Microbiology, Faculty of Life Sciences, Ahmadu Bello University, Zaria, Nigeria
[5]Department of Medical Microbiology, Faculty of Medicine, TOBB University of Economics and Technology, Ankara, Turkey

ABSTRACT

Diarrhea is a common clinical condition associated with human immunodeficiency virus (HIV) infection. Our study aimed to determine the prevalence and risk factors of intestinal parasitic infections among diarrheic HIV patients by using volunteers from selected hospitals in Abuja, Nigeria. Information on socio-demographic factors from 100 diarrheic HIV-seropositive and 50 HIV-seronegative patients was obtained by using structured questionnaires. Freshly voided diarrheic stool samples were used for detection of intestinal parasites by direct microscopic examination. The association between different variables in the questionnaires and intestinal parasitic infection was determined using the Chi-square test of significance at $p<0.05$. The overall prevalence of intestinal parasitic infection was 18%, while it was 20% and 14% in HIV seropositive and seronegative subjects respectively. The most prevalent protozoa and helminth species were *Entamoeba histolytica/dispar* and *A. lumbricoides*, respectively in both study groups. Opportunistic protozoan parasites including *Cystoisospora belli, Cryptosporidium* spp and *Cyclospora* spp; and mixed infections of *E. histolytica*/*dispar* and *G. lamblia* and *Cryptosporidium* spp. and *S. stercoralis* were only detected in the seropositive group. While chronic diarrhea frequency was significantly higher in the seropositive group, none of the demographic characteristics was associated with enteric parasite infections among HIV seropositive volunteers. Our results highlight the importance of detailed examination of enteric parasites infection among diarrheic HIV subjects which would have a crucial impact on the therapeutic approach to improve the life quality of HIV/AIDS patients.

KEYWORDS:
HIV, AIDS, diarrhea, parasite, risk factors

INTRODUCTION

Since its discovery in 1980s human immunodeficiency virus (HIV), the aetiologic agent of Acquired Immune Deficiency Syndrome (AIDS), has been a major threat to global public health as it increases susceptibility to various infections and diseases by impairing host cellular immunity. While sub-Saharan Africa is the part of the world hardest hit by the virus, Nigeria has the world's second highest HIV/AIDS infection rate (~9% of global burden) after South Africa [1, 2].

Diarrhea is a common symptom of AIDS that contributes significantly to its morbidity and mortality rates [3]. Although it can be a direct consequence of anti-retroviral therapy (ART) and HIV infection, diarrhea can also be due to co-infection with different species of gastrointestinal parasites such as *Cryptosporidium parvum, Cystoisospora belli,* Microsporidium species*, Entamoeba histolytica* and *Giardia lamblia* [4-6]. Enteric parasites are among the most common opportunistic pathogens associated with AIDS and are responsible for about 80% of HIV-associated deaths [4, 5, 7-10]. Today, despite the data on significantly reduced rates of opportunistic infections after the introduction of ART, enteric parasites still continue to cause morbidity and mortality in HIV patients [11].

While previous studies estimated enteric parasite prevalence among HIV+ subjects in Nigeria between 8.2-60.7% [12, 13], there has not been any relevant data on HIV+ patients with diarrhea complains. Our study aims to fill this gap in the literature by using stool samples collected from five different state hospitals in Abuja, the capital city of Nigeria. The volunteers were also asked to fill a questionnaire to determine the risk factors associated with enteric parasitic infections. We believe that our results would provide guidance on the prevention and control/treatment of co-infections with enteric parasites to improve the life quality of HIV/AIDS patients.

MATERIALS AND METHODS

Study Area. The study was conducted at selected anti-retroviral treatment (ART) clinics/centers in Abuja, Nigeria. The centers provide comprehensive treatment and support to HIV/AIDS patients-children, pregnant women (Prevention of Mother to Child Transmission, PMTCT), and adults. They also provide laboratory services to monitor CD4 cell count and viral loads. The clinics served as referral centers for HIV/AIDS patients in the capital city and its environs. Here, patients were followed up regularly to monitor viral load and CD4 counts.

Study Design. Cross-sectional hospital-based research was performed in five secondary health facilities in Abuja, the Federal Capital Territory (FCT) of Nigeria.

Study Population. One hundred and fifty patients were enrolled in this study- 100 HIV-seropositive and 50 HIV-seronegative patients with diarrhea. Samples from the seronegative patients were used as control. Patients that were on anti-parasitic agents during sample collection were excluded from this study. The mean ages of participants were 37.0 ± 10.2 years and 38.0 ± 9.8 years in the seropositive and seronegative groups, respectively. The age range was 20-69 years for both groups, with median age of 35.8 years for the former group and 36.6 years for the latter group. The mode age group was 30-39 years for both study populations that corresponded to 40% of the seropositive and 48% of seronegative subjects.

The numbers of male and female subjects were 30 (30%) and 70 (70%) in the seropositive group while they were 14 (28%) and 36 (72%) in the latter group (Table 1).

Ethical Approval. The Federal Capital Development Authority's (FCDA) Hospital Management Boards and the FCT's Ministry of Health ethical committee both approved this research (06-09-2019, FHREC/2019/01/85). The essence of the study and its goals were explained to the participants in general terms. All participants gave informed consent before samples were collected and processed.

TABLE 1
Comparison of risk factors between diarrheic HIV-seropositive (n=100) and HIV-seronegative (n=50) patients, Abuja-Nigeria, 2021.

Sociodemographic variable	HIV-seropositive n (%)	HIV-seronegative n (%)	*p*-value
Age (Years)			
20-39	65 (65.0)	32 (64.0)	0.904
40-69	35 (35.0)	18 (36.0)	
Gender			
Male	30 (30.0)	14 (28.0)	0.780
Female	70 (70.0)	36 (72.0)	
Level of Education			
None/Primary	32 (32.0)	20 (40.0)	0.332
Secondary/Tertiary	68(68.0)	30 (60.0)	
Marital Status			
Married	52 (52.0)	22 (44.0)	0.356
Divorced/ Single/ Widowed	48 (48.0)	28 (56.0)	
Source of drinking water			
Tap	72 (72.0)	42 (84.0)	0.105
Well/River	28 (28.0)	8 (16.0)	
Type of Toilet Facility			
Water Cistern	80 (80.0)	35 (70.0)	0.172
Pit/Bush	20 (20.0)	15 (30.0)	
Occupation			
Unemployed/Student	45 (45.0)	22 (44.0)	0.908
Civil servant/ Business/ Artisan	55 (55.0)	28 (56.0)	
Crowded Homes			
Yes	17 (17.0)	10 (20.0)	0.652
No	83 (83.0)	40 (80.0)	
Hand Washing Habit			
Yes	78 (78.0)	35 (70.0)	0.284
No/Not always	22 (22.0)	15 (30.0)	
Contact with Animals			
Yes	25 (25.0)	16 (32.0)	0.365
No	75 (75.0)	34 (68.0)	
Diarrhea			
Acute	25 (25.0)	36 (72.0)	0.001
Chronic	75 (75.0)	14 (28.0)	

Socio-demographic Information. A structured questionnaire was used to obtain relevant socio-demographic information from individuals who consented to the study. The socio-demographic information were: age (20-39, 40-69), gender (male, female), level of education (none or primary and secondary or tertiary), sources of drinking water (tap, well or river), types of toilet facilities (water cistern, pit latrine or bush), occupation (unemployed or student, civil servant or business or artisan), crowded homes (yes, no), hand washing habits (yes, no or not always), contact with animals (yes, no), diarrhea (acute, chronic), and marital status (married, divorced or single or widowed).

Sample Collection and Parasite Detection. For parasitological analysis, diarrheic patients were requested to submit three (3) freshly voided stool samples collected on alternate days into wide-mouthed stool sample containers. Direct microscopic examination of the stool samples as wet and iodine mounts and trichrome staining were performed. The samples were further processed by using the formalin-ethyl acetate sedimentation technique. The direct smears and smears made from deposits of the sediment were stained using the Kinyoun's acid fast staining and then examined for coccidia using the oil immersion objectives.

Statistical Analysis. The IBM SPSS Processor was used to analyze the data collected from the questionnaires. The percentages were used to represent the data gathered from the questionnaires. The frequency and percentage of the results of the stool analysis were presented and the two sample T- test was used to compare parasites frequencies in diarrheic HIV seropositive and HIV seronegative groups. The association between different variables in the questionnaire and intestinal parasitic infection was determined using the Chi-square test of significance. If the *p*-value was less than 0.05, the results were statistically significant.

RESULTS

Characteristics of the subjects. All (100%) HIV seropositive and seronegative subjects included in our study had diarrhea. The numbers of volunteers with acute and chronic diarrhea were 25 (25%) and 75 (75%) among HIV- seropositive subjects, while the corresponding numbers for HIV-seronegative subjects were 36 (72%) and 14 (28%), respectively. According to the responses given in the questionnaires, the numbers of married people were 52 (52%) and 22 (44%) in HIV-seropositive and HIV-seronegative groups, respectively. Sixty-eight (68%) HIV seropositive and 30 (60%) HIV seronegative volunteers were with at least secondary education. More than half of the volunteers (55% for HIV seropositive; 56% for seronegative) were employed, while the unemployed/ student population was 45% and 44% in both HIV seropositive and HIV seronegative groups (Table 1). The majority of subjects from both groups used tap water as the main source of drinking water and had hand washing habit (72% and 84%; 78% and 70% in seropositive and seronegative group subjects, respectively). Moreover, 80% of seropositive and 70% of seronegative subjects had toilet tanks in their homes and 83% of seropositive and 80% of seronegative group members did not live in crowded conditions. The numbers of subjects without animal contact were 75 (75%) for the seropositive group, while it was 34 (68%) for the seronegative group (Table 1).

Prevalence of enteric parasites. The overall prevalence of intestinal parasitic infection among the 150 subjects studied was 18% (n=27). The parasites detected were *Entamoeba histolytica/dispar* (n=7; 4.7%), *Entamoeba coli* (n=5; 3.3%), *Ascaris lumbricoides* (n=3; 2.0%), *G. lamblia* (n=2; 1.3%), *Cryptosporidium* spp (n=2; 1.3%), *Cyclospora* spp (n=2; 1.3%), *Strongyloides stercoralis* (n=2; 1.3%), *Cystoisospora belli* (n=1; 0.7%), and *Hymenolepis nana* (n=1; 0.7%) (Table 2).

The numbers of volunteers with intestinal parasite co-infection were 20 (20%) and seven (14%) in the HIV seropositive and negative groups, respectively, among which two seropositive (2%) subjects were infected with more than one species of parasite. In the seropositive group, nine species of enteric parasites were identified that included *E. histolytica/dispar* (n = 5; 5%), *E. coli* (n = 4; 4%), *G. lamblia* (n = 1; 1%), *C. belli* (n = 1; 1%), *Cryptosporidium* spp (n = 2; 2%), *Cyclospora* spp (n = 2; 2%), *A. lumbricoides* (n = 1; 1%), *H. nana* (n = 1; 1%) and *S. stercoralis* (n =1; 1%). In contrast, the seronegative group had only five species which were *E. histolytica/dispar* (n = 2; 4%), *A. lumbricoides* (n = 2; 4%), *E. coli* (n = 1; 2%), *G. lamblia* (n = 1; 2%), and *S. stercoralis* (n = 1; 2%) (Table 2). While enteric parasites prevalence was lower in HIV-seronegative group, the difference was not statistically significant (p=0.370) (Table 3). The coccidian parasites such as *C. belli, Cryptosporidium* spp and *Cyclospora* spp were only observed in the HIV-seropositive group.

Effects of demographics on enteric parasite infections among HIV-positive and HIV- negative populations. In order to determine the risk factors associated with enteric parasite infections in diarrheic HIV patients, responses given to the questionnaires were compared between the 20 HIV-seropositive and seven HIV-seronegative subjects. When stratified by age and gender, the highest enteric parasite prevalence was reported among subjects aged 20-39 years and female volunteers in both groups (70% and 75.0%; and 71.4% and 85.7% in seropositive

and seronegative individuals, respectively). Both group members were also mostly with none/primary education (60.0% and 57.1%), use tap as source of drinking water (60.0% and 57.1%), not living in crowded homes (60.0% and 57.1%), have contact with animals (55.0% and 85.7%), and were married (55.0% and 57.1%). In contrast to the seronegative subjects, more than half of the volunteers in the seropositive group had water cistern as the type of toilet facility (42.9% vs. 55.0%), were unemployed/student (42.9% vs. 55.0%) and wash their hands regularly (14.3% vs. 55.0%). None of these factors displayed significant difference between the seropositive and seronegative groups (Table 4). However, when compared, the rate of chronic diarrhea was significantly higher in the seropositive group with enteric parasite co-infection ($p<0.05$) (Table 4).

DISCUSSION

Parasitic infections are among the most common causes of morbidity and mortality in HIV/AIDS patient. They pose a major public health concern especially in developing countries, such as Nigeria, which has the second-highest HIV/AIDS infection rate in the world [7, 13-15]. However, despite its importance, enteric parasite co-infection rate among HIV+ subjects in Nigeria are not yet clear due to results that ranged between 8.2% and 60.7% [12, 13]. Moreover, the prevalence is yet to be determined among HIV+ patients with diarrhea that is responsible for death of up to 100% of HIV/AIDS patients in developing countries [5, 7, 16-18]. Our study aimed to fill this gap in the literature using diarrheic HIV+ patients and determine associated risk factors in Nigeria. The results would contribute to the development of healthcare policies and practices aimed at improving the quality of life of HIV/AIDS patients in the country.

Our results suggest the overall prevalence of intestinal parasitic infection as 18%, which was in correlation with previous reports that estimated the range to be between 22% and 24% in Abuja, Nigeria [4, 19]. The prevalence for intestinal protozoan parasites (12.7%) was higher than that of helminths (4.0%). Similar trend was also reported by previous studies from the same region of Nigeria with prevalence range for intestinal protozoan and helminths parasites of 14-28% and 11-21%, respectively [4,11,19,20].

In our study, the prevalence of protozoan parasite infections was 15% and 8% in diarrheic HIV seropositive and seronegative subjects respectively, with *E. histolytica/dispar* as the most prevalent protozoa species which is in correlation with previous studies from Abuja city of Nigeria [4, 19].

TABLE 2
Prevalence of intestinal parasites among diarrheic HIV-seropositive (n=100) and HIV-seronegative (n=50) patients, Abuja-Nigeria, 2021

Organism	HIV-seropositive (n)%	HIV-seronegative (n)%	Total (n)%
Protozoa			
E. histolytica/dispar	5 (5.0)	2 (4.0)	7 (4.7)
E. coli	4 (4.0)	1 (2.0)	5 (3.3)
G. lamblia	1 (1.0)	1 (2.0)	2 (1.3)
Cystoisospora belli	1 (1.0)	0 (0.0)	1 (0.7)
***Cryptosporidium* spp**	2 (2.0)	0 (0.0)	2 (1.3)
***Cyclospora* spp**	2 (2.0)	0 (0.0)	2 (1.3)
Helminths			
A. lumbricoides	1 (1.0)	2 (4.0)	3 (2.0)
Hymenolepis nana	1 (1.0)	0 (0.0)	1 (0.7)
S. stercoralis	1 (1.0)	1 (2.0)	2 (1.3)
Mixed Infections			
E. histolytica* and *G. lamblia	1 (1.0)	0 (0.0)	1 (0.7)
Cryptosporidium* spp and *S. stercoralis	1 (1.0)	0 (0.0)	1 (0.7)
Total	**20 (20.0)**	**7 (14.0)**	**27 (18.0)**

TABLE 3
Distribution of intestinal parasites among diarrheic HIV-seropositive and HIV-seronegative patients, Abuja- Nigeria, 2021.

Group	Parasites +	Parasites -	Total	*p*-value
HIV +	20	80	100	0.370
HIV -	7	43	50	
Total	27	123	150	

TABLE 4
Prevalence and risk factors for intestinal parasites among diarrheic HIV-seropositive and HIV-seronegative patients, Abuja- Nigeria, 2021.

Sociodemographic variable	HIV-seropositive (n)%	HIV-seronegative (n)%	*p*-value
Age (Years)			
20-39	14 (70.0)	5 (71.4)	1.000
40-69	6 (30.0)	2 (28.6)	
Gender			
Male	5 (25.0)	1 (14.3)	1.000
Female	15 (75.0)	6 (85.7)	
Level of Education			
None/Primary	12 (60.0)	4 (57.1)	1.000
Secondary/Tertiary	8 (40.0)	3 (42.9)	
Marital Status			
Married	11 (55.0)	4 (57.1)	1.000
Divorced/ Single/ Widowed	9 (45.0)	3 (42.9)	
Source of drinking water			
Tap	12 (60.0)	4 (57.1)	1.000
Well/River	8 (40.0)	3 (42.9)	
Type of Toilet Facility			
Water Cistern	11 (55.0)	3 (42.9)	1.000
Pit/Bush	9 (45.0)	4 (57.1)	
Occupation			
Unemployed/Student	11 (55.0)	3 (42.9)	1.000
Civil servant/ Business/ Artisan	9 (45.0)	4 (57.1)	
Crowded Homes			
Yes	8 (40.0)	3 (42.9)	1.000
No	12 (60.0)	4 (57.1)	
Hand Washing Habit			
Yes	11 (55.0)	1 (14.3)	0.091
No/Not always	9 (45.0)	6 (85.7)	
Contact with Animals			
Yes	11 (55.0)	6 (85.7)	0.204
No	9 (45.0)	1 (14.3)	
Diarrhea			
Acute	3 (15.0)	5 (71.4)	0.011
Chronic	17 (85.0)	2 (28.6)	

On the other hand, mixed parasitosis was only detected among the diarrheic HIV-seropositive subjects, which is in agreement with the increased susceptibility of AIDS patients [6, 16, 20, 21]. Moreover, similar to previous studies [19], that compared prevalence of intestinal parasites infection among HIV-positive and HIV-negative patients in Abuja, *Cystoisospora belli* (1.0%), *Cryptosporidium spp* (2.0%) and *Cyclospora spp* (2.0%) were exclusively found in the HIV-seropositive group. These coccidian parasites are opportunistic protozoa causing emerging infections among HIV-seropositive patients [20]. It is important to treat or give preventive treatment for these opportunistic infections in diarrheic HIV-seropositive patients because cryptosporidiosis, cystoisosporiasis and cyclosporiasis lead to increase in morbidity and mortality.

The intestinal helminth prevalence was 3% and 6% for the HIV-seropositive and HIV-seronegative groups respectively which is in agreement with Abaver et al. (2011)[4] in Abuja that recorded low prevalence for HIV-positive patients and high prevalence for the HIV-negative patients. However, data reported by Abelau *et al.*(2011) [22] and Lar *et al.*(2015) [6] had the prevalence range between 33% and 59% among the HIV seropositive patients. The seronegative groups had lower prevalence of between 15% and 22% [20, 22]. The difference in rates between the two groups was not found to be statistically significant. The reason for this variation in prevalence could be environmental and behavioral patterns. This is because our study was conducted at the Federal Capital city, Abuja, with more urban dwellers while their studies were conducted in Jos with more rural ones [6, 11].

Similar to previous reports [20, 22], the most prevalent helminths parasite detected in both study groups, was *A. lumbricoides*. The helminth species that was detected in only HIV seropositive group was *H. nana*. Previous studies in Abuja did not record any prevalence for this parasite.

A number of factors were investigated in our

study to determine their association with intestinal parasites prevalence among the study participants. Subjects of the age group 20-39 years and female gender had higher prevalence of intestinal parasites infection in both HIV seropositive and seronegative subjects, which was in correlation with previous reports [6, 11, 23, 24]. Nevertheless, gender and age were not found to be risk factors associated with enteric parasites infection in HIV subjects with diarrhea. Similar lack of association was also reported for the level of education, source of drinking water, type of toilet, occupation, living in crowded homes, hand washing habits, contact with animals and marital status. On the other hand, the prevalence of chronic diarrhea among HIV-seropositive group with enteric parasite co- infection was statistically higher than that reported among HIV-seronegative counterparts. In conformity with similar reports by Gupta *et al*. (2008) [25] and Assefa *et al*. (2009) [26] the HIV-seropositive patients presented with more chronic diarrhea than the HIV-seronegative patients. This is thought to be due to the immunosuppressive state in the HIV seropositive subjects characterized by deficiency in cell-mediated immunity.

One main weakness of the study is the small sample size. Therefore, the results should be interpreted with caution. Our analysis included only diarrheic HIV-seropositive patients on ART and lacked any information about time since the subjects were diagnosed, both of which were previously shown to influence intestinal parasitic infection rates [23, 27, 28]. Moreover, our data could not be confirmed by molecular methods which have higher sensitivity and specificity than the conventional microscopy approach [29], due to financial restrictions. Therefore, future studies with alternative approaches and using higher numbers of subjects that are not on ART and with known diagnosis rates are recommended to further enrich the relevant literature on AIDS patients in the country and also contribute to the development of public health policies.

CONCLUSION

An overall prevalence of 18% intestinal parasitic infections was detected in our study while the corresponding rates in the diarrheic HIV seropositive and negative groups were 20% and 14%, respectively. The most prevalent protozoan and helminth parasites in both study groups were *E. histolytica/ dispar* and *A. lumbricoides*, respectively. While our results did not demonstrate increased rate of enteric parasites due to HIV infection, opportunistic and mixed parasitic infections were only reported in the seropositive volunteers. Seropositive subjects also displayed higher rates of chronic diarrhea. Further studies with advanced molecular techniques are required for more reliable data on the prevalence of intestinal parasitic infections among diarrheic HIV-positive patients. Our results also recommend the routine examination of enteric parasites in HIV subjects with diarrhea in order to improve the quality of life of HIV/AIDS patients by inclusion of anti-parasite treatment.

ACKNOWLEDGEMENTS

Our profound gratitude goes to the Federal Capital Development Authority's (FCDA) Hospital Management Boards and the FCT's Ministry of Health ethical committee for the approval of this research. We also wish to appreciate all the Hospital Laboratory staff for their support in the administration of questionnaires and sample collection.

REFERENCES

[1] Federal Ministry of Health. (2019) Nigeria HIV/AIDS Indicator and Impact Survey (NAIIS) - Fact Sheet. National Summary Fact Sheet, March, 1–5. https://naca.gov.ng/wp-content/uploads/2019/03/NAIIS-PA-NATIONAL-FACT-SHEET-FINAL.pdf. (25/02/2021)

[2] UNAIDS. (2020) 2020 Global AIDS report. 2020 Global AIDS Report. 1, 380.

[3] Jha, A.K., Uppal, B., Chadha, S., Bhalla, P., Ghosh, R., Aggarwal, P., Dewan, R. (2012) Clinical and microbiological profile of HIV/AIDS cases with diarrhea in North India. Journal of Pathogens. 1–7.

[4] Abaver, D.T., Nwobegahay, J.M., Goon, D.T., Iweriebor, B.C., Anye, D.N. (2011) Prevalence of intestinal parasitic infections among HIV/AIDS patients from two health institutions in Abuja, Nigeria. African Health Sciences. 11(Spec. Issue), 5–8.

[5] Sahoo, D., Baral, P., Mahapatra, S.R., Sarangi, A., Kiran Babu, K.K. (2018) Prevalence of enteric pathogens in HIV patients with chronic diarrhoea and their relationship with CD4 count. International Journal of Advances in Medicine. 5(6), 1491.

[6] Lar, P., Pam, V., Ayegba, J., Zumbes, H. (2015) Prevalence and distribution of intestinal parasite infections in HIV seropositive individuals on antiretroviral therapy in Vom, Plateau State Nigeria. African Journal of Clinical and Experimental Microbiology. 17(1), 18.

[7] Amoo, J.K., Akindele, A.A., Amoo, J.O.A., Efunshile, A.M., Ojurongbe, T.A., Fayemiwo, S.A., Thomas, N.B. and Ojurongbe, O. (2018) Prevalence of enteric parasitic infections among people living with HIV in Abeokuta, Nigeria. Pan African Medical Journal. 30, 66,1-9

[8] Nissapatorn, V. and Sawangjaroen, N. (2011) Parasitic infections in HIV infected individuals: Diagnostic & therapeutic challenges. Indian Journal of Medical Research. 134(12), 878–897.
[9] Nkenfou, C.N., Nana, C.T. and Payne, V.K. (2013) Intestinal parasitic infections in HIV infected and non-infected patients in a low HIV prevalence region, West-Cameroon. PLoS ONE. 8(2), 1–6.
[10] Wachamo, D., Bonja, F. (2019) Opportunistic infections and associated factors among HIV/AIDS patients taking ante-retroviral therapy Leku, Bona and Yirgalem Hospitals in Sidama Zone. Southern Ethiopia. 1–19.
[11] Ajayi, T.O., Makanjuola, B.O., Olayinka, A.T., Olorunkooba, A., Olofu, E.J., Nguku, P., Fawole, I.O. (2021) Predictors of intestinal parasite infection among HIV patients on ART in Jos, Plateau State, Nigeria. Pan African Medical Journal. 38, 306.
[12] Jegede, E.F., Ibijoke Oyeyi, E.T., Hamisu Bichi, A., Akwen Mbah, H., Torpey, K. (2014) Prevalence of intestinal parasites among HIV/AIDS patients attending Infectious Disease Hospital Kano, Nigeria. Pan African Medical Journal. 17, 2–8.
[13] Udeh, E.O., Obiezue, R., Okafor, F.C., Ikele, C.B., Okoye, I.C., Otuu, C.A. (2019) Gastro intestinal parasitic infections and immunological status of HIV/AIDS co-infected individuals in Nigeria. Annals of Global Health. 85(1), 99.
[14] Iroezindu, M.O., Ofondu, E.O., Hausler, H., Wyk, V.B. (2013) Prevalence and risk factors for opportunistic infections in HIV patients receiving antiretroviral therapy in a resource-limited setting in Nigeria. Journal of AIDS & Clinical Research. 01(S3), 1-9
[15] Machado, E.R., Santos, L.M.R., Almeira, L.G., Sales, I.M.P., Sousa, S.A., Eduardo, A.M.L.N., Chaves, P.L.G., Oliviera, L.B., Affonso, R.S. (2019) Correlation between parasitic infections in HIV patients. Biomedical Journal of Scientific and Technical Research. 15 (1), 11008-11013.
[16] Ihesiulor, U., Audu, A., Akande, A. (2016) Prevalence of intestinal parasitosis in chronic diarrhoea among ART naive HIV-infected patients in Kano, Northern Nigeria. International Journal of Science and Research (IJSR). 5(3), 2149-2157.
[17] Aminu, M., Ndaks, C.M. and Ella, E.E. (2014) Cryptosporidium infection and correlation with CD4+ T-Cell count among Human Immunodeficiency Virus seropositive patients within Kaduna Metropolis, Nigeria. The Open Conference Proceedings Journal. 5, 19-28.
[18] Joseph, A.A., Ano-Edward, G.H. (2016) Parasitic diarrhoea in treatment-naive HIV-positive patients attending the University of Ilorin Teaching Hospital (UITH) Highly Active Antiretroviral Treatment (HAART) Clinic. International Journal of Medicine and Biomedical Research. 5(3), 135-146.
[19] Udeh, E.O., Goselle, O.N., D-Papova, D.D., Abelau, M., Popov, T.V., Jean, N, David, J.S. (2008) The prevalence of intestinal protozoans in HIV/AIDS patients in Abuja. Nigeria Science World Journal. 3(3), 1-4.
[20] Inabo, H., Aminu, M., Muktar, H., Adeniran, S. (2012) Profile of intestinal parasitic infections associated with diarrhoea in HIV/AIDS patients in a tertiary hospital in Zaria, Nigeria. World Journal of Life Sciences and Medical Research. 2(2), 43.
[21] Obateru, O.A., Bojuwoye, B.J., Olokoba, A.B., Fadeyi, A., Fowotade, A., Olokoba, L.B. (2017) Prevalence of intestinal parasites in newly diagnosed HIV/AIDS patients in Ilorin, Nigeria. Alexandria Journal of Medicine. 53(2), 111–116.
[22] Abelau, M., Goselle, O.N., Udeh, E.O., D-Popova, D.D., Popov, T.V. (2011) Comparative study of the prevalence of helminth parasites in HIV seropositive and HIV seronegative individuals in Plateau state, Nigeria. Nigeria Annals of Natural Sciences. 11(1), 22-32.
[23] Chinwe, O.O., Sambo, E.O., Chibuzor, O.S., Sambo, E.D. and Ugoeze, E.S. (2020) Prevalence of opportunistic intestinal protozoan infection among HIV/AIDS patients in Jalingo Metropolis. Biomedical Sciences. 6(3), 74.
[24] Okafor-Elenwo, E.J., Izevbuwa, O.E., Akpoka, O.A. (2020) Prevalence of intestinal parasites amongst selected age groups within Okada, South-South Nigeria. International Journal of Applied Biology. 4(1), 44-51.
[25] Gupta, S., Narang, S., Nunavath, V. and Singh, S. (2008) Chronic Diarrhea in HIV Patients: Prevalence of Coccidian Parasites. Indian Journal of Medical Microbiology. 26(2), 172-5.
[26] Assefa, S., Erko, B., Medhin, G., Assefa, Z. and Shimelis, T. (2009) Intestinal Parasitic infections in relation to HIV/AIDS status, diarrhea and CD4 T-cell count. BMC Infectious Diseases. 9 (155), 1-6
[27] Akinbo, F.O., Okaka, C.E., Omoregie, R. (2010) Prevalence of intestinal parasitic infections among HIV patients in Benin City, Nigeria. Libyan Journal of Medicine. 5(1), 1-6
[28] Feasey, N.A., Healey, P., Gordon, M.A. (2011) Review Article: The aetiology, investigation and management of diarrhea in the HIV-positive patient. Alimentary Pharmacology and Therapeutics. 34(6), 587-603.

[29] Hartmeyer, G.N., Hoegh, S.V., Skov, M.N., Dessau, R.B., Kemp, M. (2017) Selecting PCR for the diagnosis of intestinal parasitosis; choice of targets, evaluation of in-house assays, and comparison with commercial kits. Journal of Parasitology Research. 2017, 620525.

Received: **18.12.2021**
Accepted: **11.02.2022**

CORRESPONDING AUTHOR

Umut Gazi
Department of Medical Microbiology and Clinical Microbiology,
Faculty of Medicine,
Near East University,
Nicosia – Cyprus.

e-mail: umut.gazi@neu.edu.tr

© by PSP Volume 31– No. 05/2022 pages 5243-5254 Fresenius Environmental Bulletin

THE EFFICIENCY OF SODIUM REMOVAL BY DECORATIVE PLANT SPECIES AND ALGAE IN THE FLOATING TREATMENT WETLAND

Nevena Cule[1,*], Aleksandar Lucic[2], Marija Nesic[3], Milorad Veselinovic[1], Suzana Mitrovic[1], Ljiljana Brasanac-Bosanac[1]

[1]Department of Environmental Protection and Improvement, Institute of Forestry, Belgrade, Serbia
[2]Department of Genetics, Plant Breeding, Seed and Nursery Production, Institute of Forestry, Belgrade, Serbia
[3]Department of Landscape Architecture and Horticulture, Faculty of Forestry, University of Belgrade, Belgrade, Serbia

ABSTRACT

The excess Na content in water can cause serious environmental and health problems. Most of the previous studies have indicated the potential of constructed wetlands (CW) in sodium (Na) removal from synthetic water in controlled conditions. To the best of our knowledge, this is the first study to investigate the efficiency of the floating treatment wetlands (FTW) for the removal of Na from the polluted urban river. The present study also expands our knowledge of phytoremediation potential of rarely or never used decorative terrestrial and aquatic plant species in CW or FTW. The results imply that proposed FTW model can ensure efficient Na removal. Even though the efficiency was negative or low during the first 3 treatment cycles, FTW was able to remove Na from polluted water by the end of water treatment. The highest Na removal efficiency of 44% had cell 1 with *Phragmites australis* followed by 43% in cell 4 with decorative macrophytes (*Iris pseudacorus*, *Iris sibirica* 'Perry's Blue', *Alisma plantago - aquatica*, *Lythrum salicaria*, *Menyanthes trifoliata*) and cell 3 with *P. australis* and *Canna indica* (25%). Cell 2 planted with *C. indica* showed the lowest efficiency of 5%. Species *A. plantago - aquatica* had good potential for Na accumulation from water. Also, it can be assumed that species *M. trifoliata* had a share in the Na removal. Translocation of accumulated Na from belowground biomass to shoots was very low in all species except *M. trifoliata*. Algae *Cladophora glomerata* enabled further water polishing with maximum Na removal efficiency of 23% in cell 5 at the end of water treatment. Further studies need to be done to investigate all mechanisms responsible for Na removal in FTW and to ensure proper species selection for Na removal in floating treatment wetlands.

KEYWORDS:
Floating treatment wetland (FTW), sodium, plants, algae, polluted urban river

INTRODUCTION

The wastewater discharge with elevated concentrations of sodium (Na) directly into rivers without prior treatment or even pre-treatment is a serious environmental problem. In larger settle-ments, municipal wastewater is often mixed with industrial wastewater, stormwater, and agricultural runoff. Deicing salts, artificial ferti-lizers, private septic system effluents, detergents, food, dyes, water softeners, brine, and other major contributors of Na can be found in this mixture of wastewaters [1,2]. The numerous adverse effects [3,4] are caused when this discharge reaches water bodies. The excess Na content in water can cause land degradation (salinization), reduction of water quality, as well as harmful effects to human health, aquatic flora and fauna, irrigation, and recreation [5]. The significance of this problem is further increased if it is known that rivers are often the main source of drinking water supply.

Over the past thirty years, multidisciplinary research has led to rapid advances in the potential use of various constructed aquatic systems for decentralised wastewater and polluted water treatment [6-9]. Although, most research was conducted within the constructed wetlands (CW) [4,6,10-13], floating treatment wetlands (FTW) have emerged as an innovative technology that can overcome some of the limitations of CW [14-16]. Floating islands usually consist of mesh platforms that support the substrate as well as aquatic and terrestrial vegetation with associated microorga-nisms [17]. These buoyant structures can be placed in premade or existing reservoirs and cells or directly on lake or river surface to facilitate the removal of organic compounds, nutrients, heavy metals, toxic substan-ces, pathogenic microorganisms, and other pollutants from water [7,15,18-21].

Extensive research has shown that FTWs are very efficient in the removal of mentioned pollutants [16,21-26]. However, there is a surprising paucity of scientific literature specifically related to Na removal efficiency in FTW. Previous studies of the excess Na concentration in water dealt mostly with salt

plant tolerance. So far, very few laboratory or greenhouse studies with synthetic water and halophytes or aquatic and terrestrial plants [5,11-13] have investigated the potential of CW in Na removal. Recognizing the stated knowledge gap, this paper evaluates the efficiency of the proposed FTW model for the removal of Na from the polluted urban river. To the best of our knowledge, this is the first study to investigate this topic. Additionally, this research will provide the opportunity to advance our knowledge in the potential use of *Iris pseudacorus* L., *Iris sibirica* 'Perry's Blue', *Alisma plantago - aquatica* L., *Lythrum salicaria* L., and *Menyanthes trifoliata* L. as these decorative species were rarely [17,27,28] or never used in CW or FTW.

MATERIALS AND METHODS

River Topciderka (Belgrade, Serbia) is used as a wastewater and rainwater collector of industries and settlements in its catchment. The floating treatment wetland (FTW) was constructed on the bank of this urban river to assess the possibility of it's revitalization in a completely natural way, that will be efficient, environmentally friendly, and economically viable. The water treatment was carried out over one vegetation period, from early May to mid-October. This FTW already showed high efficiency in the reduction of chromium, nickel, total phosphorus, total nitrogen, ammonium nitrate, nitrites, nitrates, biological and chemical oxygen demand, total organic carbon, and pathogen microorganisms [18,19]. In this paper, we argue that the proposed FTW model can be efficient in the Na removal from the polluted river.

Figure 1 illustrates the layout of modified FTW. The proposed model comprised of a pump for drawing water from the river, a collection tank (5.0 m^3), four cells with floating islands (surface area of 3.0 m^2 and volume of 3.0 m^3, each), and one cell with algae (surface area of 3.0 m^2 and volume of 1.5 m^3). The external metal railing and internal plastic bars were used to reinforce cells. All components of FTW were placed on the levelled ground and interconnected with plastic pipes. Each outlet branch of cells 1-4 had a water meter that precisely control the amount of water that came from cells 1-4 to cell 5. The equal amounts of water from each of the four cells with floating islands were introduced to cell 5 in this way. The positioning and construction of the inlet and outlet of the collection tank and cells provide the gravity flow of water through the whole FTW. To overcome the anaerobic conditions created in cells 1-4 (100% cell coverage), the inlet of cell 5 was placed on the upper edge of the cell, and water was fed into the cell from above. This facilitated introduction of more oxygen to FTW.

Three floating islands with 25 (cell 1-3) or 30 (cell 4) seedlings were placed in each of cells 1-4. The buoyant structures had handles and circular holes of 8.4 and 5.0 cm in diameter. The construction of the floating platform (light thermos-plastic material) allowed undisturbed roots and rhizomes growth in the water while keeping aerial plant parts above the water surface. Stone wool was used as a substrate. Non-invasive and plants suitable for rhizofiltration [19,29-31] were obtained from local nurseries. Species *Phragmites australis* (Cav.) Trin. ex Steud (PA) was planted in cell 1. The floating islands of cell 2 contained *Canna indica* L. (CI). A mix plantings of *P. australis* and *C. indica* seedlings (12:13) were established in cell 3. Each floating island of cell 4 was planted with mix plantings of *Iris pseudacorus* L. (IP; 8 seedlings), *Iris sibirica* 'Perry's

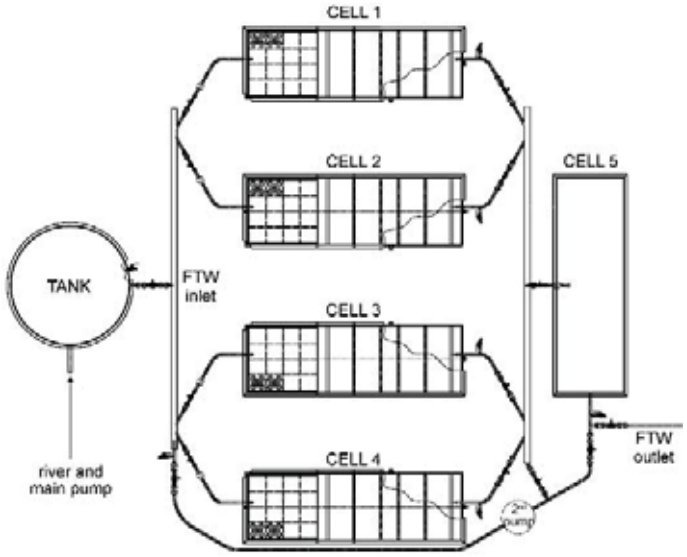

FIGURE 1
The scheme of the modified floating treatment wetland

Blue' (IS; 5), *Alisma plantago - aquatica* L. (APA; 5), *Lythrum salicaria* L. (LS; 5) and *Menyanthes trifoliata* L. (MT; 6). Algae were introduced to cell 5 directly from the river. Plastic containers (volume of 100 L) filled with tap water were used for growing plants in control (ø). No nutrients were added, and new water was fed each week. The stone wool was placed on the top of each container so that the substrate touched the surface of the water. Upon cutting hols (5.0 cm in diameter) in the stone wool first container was planted with 12 seedlings of *P. australis* while the second container contained 12 seedlings of *C. indica*. The third container was planted with 30 seedlings of decorative macrophytes, 6 seedlings of each species. Plants in FTW and control were grown for the same period and at the same locality.

The FTW start-up period lasted for one and a half months upon planting. The monitoring and maintenance of all FTW components were conducted during this period. New quantities of polluted water were pumped in from the river twice a week. The monitoring of FTW Na removal efficiency was performed after this period, during four identical treatment cycles (C1, C2, C3, C4). Each treatment cycle began with water pumping to the collection tank and its instantaneous transport by gravitation to cells 1-4. The water stayed in cells for 6 days. Treated water was moved to cell 5 for additional polishing (also 6-day HRT) and then it was released into the river. The treatment cycle was complete at the end of this period. The treatment cycles overlapped. The new treatment cycle started immediately after sampling of water, plants, and substrate in cells with floating islands after the first 6 days of treatment.

The polluted water samples were collected at the beginning of each treatment cycle at the FTW inlet. Treated water was sampled after every 6 days in cells 1-4 and at the end of each treatment cycle in cell 5. The composite water sample (1L) was collected from 5 spots within each cell (each angle and middle) at approximal 30 cm depth between 8:00 and 9:00 a.m. Water samples were stabilised with nitric acid and placed in a refrigerator until the analyses. To assess the initial Na concentration in plant and algal tissue sampling was done just before the beginning of water treatment (C0). The subsequent plant sampling was then done at the end of each 6-day treatment cycle in cells 1-4. Collected plants were divided into roots and above-ground biomass during the first 3 treatment cycles (C1, C2, C3). All plants were moved from FTW and divided into above-ground biomass, rhizomes, and roots at the end of the fourth treatment cycle (C4). Rhizomes were sampled only at the end of C4 so that the plants would not be damaged during the water treatment. Vegetative parts were washed with distilled water 3 times, dried at 80^{o}C for 24 hours [32], and subsequently milled to powder to pass a 40-mesh sieve. Composite samples were made and stored for chemical analysis. One composite plant sample represented one vegetative part of one plant species on one floating island within one cell. Algae were sampled at the end of each treatment cycle. The composite algal sample represented algae tissue collected from 5 spots within cell 5 (each angle and middle). The samples were prepared for analysis according to the same methodology as for plants. The substrate was sampled along with plant sampling. The composite substrate sample represented stone wool collected from 5 spots of one floating island (each angle and middle). Samples were air-dried, placed in plastic containers, and stored until analysis.

The extraction of Na from plant and algae tissue was done according to Şenilă et al. [33] in the microwave digestion unit (CEM MDS 2000, Berghof, Germany, Mod. Speedwave MWS3+). The extraction of Na from the substrate was done in aqua regia according to ISO 11466:1995 method. Samples were filtrated after dissolution and stored in closed sterile containers in the refrigerator for analysis. The concentrations of Na in water, plants, algae, and stone wool, were analysed using ICP-OES (Varian Vista-PRO, CCD Simultaneous ICP-OES) according to standard methodology (ISO 11885:2009).

The FTW Na removal efficiency was calculated as the removal rate (R) using the following equation: R(%) = (Co-Ct)/Co x 100; where Co (mg/l) is the Na concentration in polluted water and Ct (mg/l) is the Na concentration after 6-day of water treatment in cells 1-4 or at the end of water treatment in cell 5 [13,26]. Also, the translocation factor (TF) was determined to assess the ability of the selected plant species to translocate Na from root to shoot biomass [34]. Values of TF less than 1 indicate that the Na accumulates in roots to a greater extent and its translocation to the shoot biomass is poor [19].

When appropriate, statistical analysis was performed using Analyses of Variance (one-way and two-way ANOVA). Prior to ANOVA the normality of the data distribution was checked based on Chi-square test ($p > 0.05$) as well as equality of variances based on Cohran's C test ($p > 0.05$).

Significant differences between the groups were determined using Fischer's LSD test ($p < 0.05$). Data management and analysis were performed using Statgraphics Centurion XVI (Statpoint Technologies, Inc., Warrenton, VA, USA).

RESULTS

Table 1 provides the results of sodium concentration in polluted and treated water, as well as the efficiency of the floating treatment wetland. The inflow Na concentration was relatively constant during treatment cycles C1-C3 with values ranging from 2.135 mg/L to 2.755 mg/L. What stands out in Table 1 is the almost doubling of Na concentration

TABLE 1
Sodium concentration in polluted and treated water and the efficiency of the floating treatment wetland

Treatment cycle		C 1	C2	C3	C4
Influent to FTW (mg/L)	Inflow	2.755	2.695	2.135	4.428
Effluent of single cell (mg/L)	Cell 1	2.780	2.740	2.295	2.498
	Cell 2	2.614	2.720	2.222	4.196
	Cell 3	2.692	2.686	2.212	3.314
	Cell 4	2.856	2.719	2.213	2.539
Reduction of Na in single cell (mg/L)	Cell 1	-0.024	-0.044	-0.160	1.930
	Cell 2	0.141	-0.025	-0.087	0.231
	Cell 3	0.063	0.010	-0.077	1.114
	Cell 4	-0.101	-0.024	-0.078	1.889
Single cell efficiency (%)	Cell 1	-1	-2	-7	44
	Cell 2	5	-1	-4	5
	Cell 3	2	0	-4	25
	Cell 4	-4	-1	-4	43
Influent to Cell V (mg/L)	Cells 1-4	2.735	2.716	2.235	3.137
Effluent of single cell (mg/L)	Cell 5	2.845	2.521	2.349	2.417
Reduction of Na in single cell (mg/L)	Cell 5	-0.109	0.195	-0.113	0.720
Single cell efficiency (%)	Cell 5	-4	7	-5	23

Cells: 1 - *Phragmites australis* (Cav.) Trin. ex Steud., 2 - *Canna indica* L., 3 - *P.australis and C. indica,* 4 - *Iris pseudacorus* L., *Iris sibirica* 'Perry's Blue', *Alisma plantago - aquatica* L., *Lythrum salicaria* L., *Menyanthes trifoliata* L., 5 - algae; Treatment cycles: C1 - 1st treatment cycle, C2 - 2nd treatment cycle, C3 - 3rd treatment cycle, C4 - 4th treatment cycle. Each value represents the value of the composite sample of water taken from the tank or 5 spots in the cell.

in the inflow at the beginning of C4 (4.428 mg/L). A slight decrease of Na concentration was only noted in cell 2 and cell 3 in C1 after six days of water treatment thereby leading to a 5% and 2% Na efficiency reduction, respectively (Table 1). No evidence of Na concentration reduction was found in cells 1-4 at the end of C2 and C3. It is apparent that as Na concentration in the inflow increased, the efficiency of cells 1-4 improved after six days of water treatment in C4. The highest Na removal efficiency had cell 1 with *Phragmites australis* (44%) followed by cell 4 with decorative macrophytes (43%) and cell 3 with *P. australis* and *Canna indica* (25%). Cell 2 planted with *C. indica* showed the lowest efficiency with the value of 5% at the end of C4 (Table 1). The further water polishing in cell 5 with algae resulted in an additional 7% and 23% of Na concentration reduction in C2 and C4, respectively (Table 1).

A one-way ANOVA revealed that there were significant differences for Na concentration in shoots of species *P. australis*, *I. pseudacorus*, *I. sibirica* 'Perry's Blue', *A. plantago - aquatica*, and *L. salicaria* in relation to the length of their exposure to polluted water (Table 2). Shoots of *I. pseudacorus*, *I. sibirica* 'Perry's Blue', and *L. salicaria* contained significantly higher Na in the control (Ø) compared to initial Na concentrations (C0) as well as Na content at the end of each treatment cycle (C1-C4). Table 2 further reveals that shoot Na concentration increased significantly during water treatment (C1-C4) compared to initial Na concentrations (C0) in species *I. pseudacorus*, *I. sibirica* 'Perry's Blue', *A. plantago - aquatica,* and *L. salicaria*. The opposite trend was noted in *P. australis*. The concentrations of Na decreased significantly during C1-C3 compared to initial Na concentrations (C0). However, the shoot Na content of *P. australis* increased at the end of the last cycle (C4) and no significant difference was found compared to initial Na concentrations (C0). No significant differences were found for Na concentration in shoots of *C. indica* and *M. trifoliata* in relation to the length of their exposure to polluted water (Table 2). Also, no significant differences were found for Na concentration in rhizomes of *C. indica* and *I. sibirica* 'Perry's Blue' between control plants (Ø) and plants at the end of C4 (Table 2). *I. pseudacorus* rhizomes had significantly higher Na in the control (Ø) compared to C4. Conversely, species *A. plantago - aquatica* and *M. trifoliata* contained significantly higher rhizomes Na concentrations in C4 compared to the control (Ø). Further statistical analysis showed that there were significant differences for Na concentration in roots of species *C. indica*, *I. pseudacorus*, *I. sibirica* 'Perry's Blue', *A. plantago - aquatica*, and *L. salicaria* in relation to the length of their exposure to polluted water (Table 2). Species *C. indica*, *I. pseudacorus*, *I. sibirica* 'Perry's Blue', and *L. salicaria* contained significantly more Na in roots just

before the start of the water treatment (C0) compared to all cycles (C1-C4) and the control (Ø). Furthermore, there were no significant differences for Na content in roots of *C. indica*, *I. pseudacorus*, *I. sibirica* 'Perry's Blue' between plants in modified FTW (C1-C4) and the control (Ø). A similar trend was noted for *L. salicaria* (Table 2). Sodium concentration in roots of this species showed no significant differences in treatment cycles C2-C4 compared to the control (Ø). In contrast, Na content increased in *A. plantago - aquatica* roots over time while reaching a significant maximum in C3 and C4 (Table 2). No significant differences were found for Na concentration in roots of *P. australis* and *M. trifoliata* in relation to the length of their exposure to polluted water (Table 2).

A two-way ANOVA revealed that Na concentration in shoots and roots was significantly influenced by plant species, as well as the length of plants' exposure to polluted water (Table 3). However, no significant effect of the interaction of plant species and treatment cycles was observed. Further statistical analysis showed that Na content in rhizomes was significantly influenced by plant species (Table 3). What stands out in Table 3 is the significantly higher Na concentration in shoots of *A. plantago - aquatica* and *M. trifoliata* compared to other species in FTW. Species *A. plantago - aquatica* also had significantly higher Na content in rhizomes compared to other species while *C. indica* concentrated significantly more Na in the roots compared to all other species (Table 3). The Na content in shoots increased during the water treatment, and a significantly higher Na concentration was found at the end of C4 compared to all other cycles (Table 3). Surprisingly, the trend of change of Na concentration in roots in relation to the time of exposure of plants to polluted water was different (Table 3). Plants sampled just before the start of the water treatment (C0) contained significantly higher Na concentrations compared to all treatment cycles (C1-C4).

TABLE 2
Sodium concentration (g/kg) in shoots, rhizomes, and roots of selected plant species in relation to the treatment cycle

Shoots							
Level	PA	CI	IP	IS	APA	LS	MT
C0	[A]1.10±0.39[a]	5.61±2.13	2.84±0.71[c]	0.10±0.03[c]	7.48±0.82[bc]	0.80±0.28[c]	8.59±0.37
C1	0.43±0.14[b]	5.31±1.15	1.14±0.11[d]	0.14±0.03[c]	6.61±0.20[bc]	0.20±0.03[d]	6.89±0.41
C2	0.35±0.10[b]	4.31±1.43	2.24±0.04[c]	0.10±0.03[c]	8.47±2.43[ab]	0.33±0.09[cd]	7.02±2.19
C3	0.35±0.10[b]	3.85±1.27	2.07±0.17[c]	0.43±0.29[bc]	7.45±1.39[bc]	0.11±0.02[d]	8.72±0.81
C4	1.17±0.15[a]	5.42±1.46	4.12±0.39[b]	0.70±0.08[ab]	11.60±1.13[a]	1.58±0.34[b]	8.37±0.89
Ø		4.61±0.02	8.92±0.10[a]	0.84±0.01[a]	4.40±0.03[c]	3.24±0.02[a]	7.09±0.01
	[B]$F_{4.31}$=5.43*	ns	$F_{5.15}$=76.10*	$F_{5.12}$=7.03*	$F_{5.12}$=3.42*	$F_{5.12}$=43.35*	ns
Rhizomes							
C4	1.39±0.33	5.79±1.38	0.72±0.10[b]	0.64±0.23	9.76±0.95[a]		3.60±0.52[a]
Ø		1.92±0.01	1.75±0.01[a]	0.61±0.01	0.67±0.01[b]		2.12±0.02[b]
		ns	$F_{1.4}$=91.61*	ns	$F_{1.4}$=90.95*		$F_{1.4}$=18.11*
Roots							
C0	6.73±2.45	22.06±3.86[a]	7.67±0.49[a]	7.39±1.37[a]	5.14±1.15[bc]	8.50±1.04[a]	6.82±0.70
C1	5.61±0.62	12.99±2.73[b]	5.45±1.04[bc]	3.26±1.46[b]	3.11±0.34[cd]	6.18±0.74[b]	4.86±1.27
C2	3.55±0.55	11.72±1.65[b]	5.77±0.22[b]	2.15±0.60[b]	7.60±0.58[ab]	2.37±0.11[c]	3.51±0.07
C3	4.19±1.07	13.41±1.58[b]	4.45±0.30[c]	3.24±0.36[b]	8.85±1.56[a]	3.09±0.18[c]	3.61±1.03
C4	5.61±0.26	12.72±1.74[b]	5.75±0.29[b]	3.36±0.84[b]	10.76±1.77[a]	2.33±0.62[c]	4.50±0.24
Ø		6.07±0.04[b]	4.72±0.06[bc]	1.88±0.02[b]	1.51±0.02[d]	3.39±0.04[c]	3.58±0.01
	ns	$F_{5.27}$=3.69*	$F_{5.20}$=6.74*	$F_{5.12}$=4.52*	$F_{5.12}$=10.22*	$F_{5.12}$=17.98*	ns

Factor treatment cycle with 6 levels: C0 - just before the start of water treatment, C1 - 1st treatment cycle, C2 - 2nd treatment cycle, C3 - 3rd treatment cycle, C4 - 4th treatment cycle, Ø - control; plant species: PA - *Phragmites australis* (Cav.) Trin. ex Steud., CI - *Canna indica* L., IP - *Iris pseudacorus* L., IS - *Iris sibirica* 'Perry's Blue', APA - *Alisma plantago-aquatica* L., LS - *Lythrum salicaria* L., MT - *Menyanthes trifoliata* L.; [A]=each value represents the mean value ± SE with 95% CI; [B]= *F*-test indicator with a number of degrees of freedom; ns = not significantly different (p>0.05); Mean values followed by different lower-case letters in each series represent significant differences (*=p<0.05).

TABLE 3
Sodium concentration in shoots and roots (g/kg) in relation to plant species and treatment cycle and sodium concentration in rhizomes (g/kg) at the end of the water treatment in relation to plant species

Level	Shoots	Roots	Rhizomes
PA	0.68±0.10^{d}	5.14±0.58^{bc}	1.39±0.33^{cd}
CI	4.90±0.65^{b}	14.58±1.24^{a}	5.79±1.38^{b}
IP	2.48±0.25^{c}	5.82±0.27^{bc}	0.72±0.11^{d}
IS	0.29±0.08^{d}	3.88±0.62^{c}	0.65±0.23^{d}
APA	8.32±0.71^{a}	7.09±0.85^{b}	9.76±0.95^{a}
LS	0.60±0.16^{d}	4.49±0.70^{c}	
MT	7.92±0.48^{a}	4.66±0.44b^{c}	3.60±0.52^{bc}
	$F_{6,109}$=49,88*	$F_{6,107}$=30,28*	$F_{5,18}$=16,05*
C0	3.79±0.75^{ab}	9.19±1.57^{a}	
C1	2.96±0.60^{b}	5.92±0.93^{b}	
C2	3.26±0.72^{b}	5.24±0.73^{b}	
C3	3.28±0.57^{b}	5.83±0.80^{b}	
C4	4.71±0.71^{a}	6.43±0.81^{b}	
	$F_{4,109}$=2,80*	$F_{4,107}$=5,01*	
interaction (AXB)	ns	ns	

Factor plant species with 7 levels: PA - *Phragmites australis* (Cav.) Trin. ex Steud., CI - *Canna indica* L., IP - *Iris pseudacorus* L., IS - *Iris sibirica* 'Perry's Blue', APA - *Alisma plantago - aquatica* L., LS - *Lythrum salicaria* L., MT - *Menyanthes trifoliata* L.; Factor treatment cycle with 5 levels: C0 - just before the start of water treatment, C1 - 1st treatment cycle, C2 - 2nd treatment cycle, C3 - 3rd treatment cycle, C4 - 4th treatment cycle; [A]=each value represents the mean value ± SE with 95% CI; [B]= *F*-test indicator with a number of degrees of freedom; ns = not significantly different (p>0.05); Mean values followed by different lower-case letters in each series represent significant differences (*=p<0.05).

TABLE 4
Translocation factor (TF) of selected species at the end of the last treatment cycle (C4) in relation to plant species

Level	Na
PA	[A]0.18±0.02^{d}
CI	0.31±0.08^{cd}
IP	0.61±0.08^{bc}
IS	0.19±0.04^{d}
APA	0.56±0.01^{bc}
LS	0.83±0.30^{ab}
MT	1.04±0.10^{a}
	[B]$F_{6,20}$=9.13*

Factor plant species with 7 levels: PA - *Phragmites australis* (Cav.) Trin. ex Steud., CI - *Canna indica* L., IP - *Iris pseudacorus* L., IS - *Iris sibirica* 'Perry's Blue', APA - *Alisma plantago - aquatica* L., LS - *Lythrum salicaria* L., MT - *Menyanthes trifoliata* L.; [A]=each value represents the mean value ± SE with 95% CI; [B]= *F*-test indicator with a number of degrees of freedom; Mean values followed by different lower-case letters in each series represent significant differences (*=p<0.05).

Table 4 compares the ability of selected plant species to translocate Na from root to shoot biomass. As can be seen from the table, there was a significant difference between TF values in relation to plant species. However, all species except *M. trifoliata* had TF values below 1.

As it can be seen from Figure 2, Na concentration in algae tissue was 16.85 g/kg just before the start of water treatment. Although algae contained lower Na concentrations during water treatment (C1-C4) compared to initial concentrations (C0), Na content increased as time went by. The maximum Na concentration was reached in C4 with 8.04 g/kg, but it was still lower than the initial value (C0).

As Table 5 shows, no significant difference for Na concentration in stone wool was found between substrate sampled just before the start of water treatment in modified FTW (C0) and the control (Ø). Sodium concentrations then increased, so that significantly higher Na content had stone wool at the end of C1 compared to the other cycles (C3-C4). Table 5 further reveals that there has been a gradual decrease of Na concentration in stone wool as time went by. Significantly lower Na content was detected in the last two treatment cycles (C3-C4) compared to other cycles and control (Ø).

TABLE 5
Sodium concentration (g/kg) in the stone wool (substrate) in relation to the different treatment cycle

Level	Na
C0	16.37±0.44^{b}
C1	19.19±0.57^{a}
C2	17.23±0.70^{ab}
C3	12.92±0.99^{c}
C4	12.87±1.04^{c}
Ø	16.67±0.37^{b}
	$F_{5,64}$=11.82*

Factor treatment cycle with 6 levels: C0 - just before the start of water treatment, C1 - 1st treatment cycle, C2 - 2nd treatment cycle, C3 - 3rd treatment cycle, C4 - 4th treatment cycle, Ø - control; [A]=each value represents the mean value ± SE with 95% CI; [B]= *F*-test indicator with a number of degrees of freedom; ns = not significantly different (p>0.05); Mean values followed by different lower-case letters in each series represent significant differences (*=p<0.05).

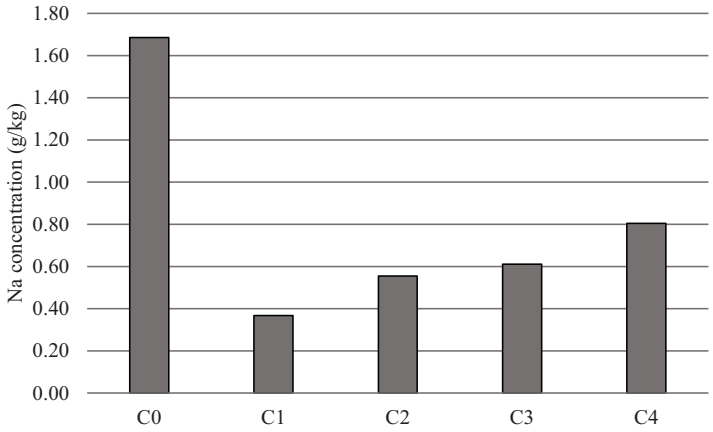

FIGURE 2
Sodium concentration (g/kg) in algae in relation to the treatment cycle. Factor treatment cycle with 5 levels: C0 - just before the start of water treatment, C1 - 1st treatment cycle, C2 - 2nd treatment cycle, C3 - 3rd treatment cycle, C4 - 4th treatment cycle; Each value represents the value of the composite sample of algae taken from 5 spots in the cell.

DISCUSSION

It has been reported that elevated concentrations of sodium (Na) in river water can cause numerous adverse effects on the environment and human health, as well as on aquatic flora and fauna [1-5]. However, far too little attention has been paid to the possible use of various constructed aquatic systems for the removal of excess amounts of Na from wastewater or polluted water. Very little can be found in the literature on this question. Prior studies that have noted the importance of Na removal in an environmentally friendly and cost-effective way were designed as laboratory or greenhouse experiments, mimicking the conditions in constructed wetlands [5,11-13,35]. While in most of these studies synthetic water with various concentrations of Na was treated with halophytes, Dipu et al. [11] and Moogouei and Chen [13] were the only ones that used aquatic macrophytes. Surprisingly and to the best of our knowledge, the efficiency of Na removal in FTW has not been assessed till now. This study evaluated the efficiency of the proposed FTW model with decorative plant species and algae for the removal of Na from the polluted urban river.

The results of this study indicated that Na removal efficiency ranged from negative to 44% in cells with floating islands and an additional negative to 23% in the cell with algae for the overall monitored period (Table 1). While the efficiency was negative or low in the first 3 treatment cycles (C1-C3), maximum Na removal was achieved in C4, in all cells. Several factors could explain this observation. Firstly, evaporation could cause the increase of salt concentration [12] and thus Na content in all cells. Maximum air temperatures ranged between 30-36°C during the treatment cycles C1-C3. Although evaporation was not monitored in this study, it is evident that high temperature induced the occurrence of this process. In accordance with this claim, a previous study by Freedman et al. [35] demonstrated that synthetic water had a higher Na concentration after 2 days treatment in CW due to enhanced evaporation. It is assumed that the evaporation decreased with the decrease of maximum air temperatures (16-25°C) during the treatment cycle C4. This can be a possible explanation of increased Na removal efficiency in FTW at the end of C4. These results further support the idea of Shelef et al. [5] who suggested that Na reduction in CW might not be caused by *Bassia indica* (Wight) A.J. Scott, but by reducing evaporation induced through shade effect. The second factor that could lead to increased Na removal efficiency in C4 compared to C1-C3 could be the almost doubling of Na concentration in the inflow at the beginning of C4. Higher Na concentrations could support interactions between Na and other nutrients (K, Ca, Mg, N, P) and thus promote their replacement by Na [36]. The current study found that significantly higher shoot Na concentrations were detected in C4 compared to C1-C3 (Table 3). Shelef et al. [5] also noticed that Na concentration in the shoot of annual halophyte increased with the higher salinity of the hydroponic solution and was 3.1 higher in the most hypersaline solution in comparison with the tap water. However, this outcome is contrary to that of Dipu et al. [11] who found that aquatic macrophytes were more efficient in Na removal from diluted dairy factory effluent compared to undiluted, under laboratory conditions in constructed wetlands. This disagreement is not surprising since Marschner [37] stated that the differences in the potential of sodium uptake are large between plant species. Consequently, future studies should concentrate on the investigation of Na accumulation by non-halophytes and interactions between salinity and nutrients as these interactions are complex and affected by numerous factors [36]. The plant and algae growth can be another factor influencing higher FTW efficiency

in C4. The efficiency of pollutant removal depends on the rate of plants growth [38] and biomass generation is often in a positive linear correlation with nutrient accumulation by plants [39]. It is assumed that algae can use the same mechanisms of nutrient accumulation as plants due to their close evolutionary relationship [40] and that they could absorb more pollutants per unit of biomass [41]. The results of this study are in accordance with this observation. Previous research [18] showed that the maximum biomass was generated in FTW at the end of C4. In addition, this study pointed out that the maximum Na content in plants and algae was detected in C4. All this led to the maximum achieved efficiency of FTW in the last treatment cycle (C4).

Cell 1 with *P. australis* and cell 4 with decorative macrophytes had the highest Na removal efficiency with values of 44% and 43%, respectively. The efficiency of cell 3 with *P. australis* and *C. indica* (25%) and cell 5 with algae (23%) could be also considered satisfactory. However, when the vegetation of floating islands comprised only of *C. indica*, the efficiency of Na removal was very low (5%). Unfortunately, comparing these results with the results of Na removal efficiency in other studies [5,11-13] would not have a meaning since these laboratory or greenhouse experiments treated synthetic water with higher Na content in constructed wetlands. Much higher Na concentrations in these experiments compared to Na content in the treated urban river as well as different construction characteristics of CW and FTW and presence of substrate could have a high impact on the obtained results of achieved efficiency. Still, the Na removal efficiency of laboratory CWs in these studies [5,11-13] ranged widely from 9.0% to 90.4%.

The precise status of sodium (Na) as a nutrient is a much-debated topic. Barker and Pilbeam [36] suggest that Na can be classified as a beneficiary nutrient as it fails to meet the criteria of an essential element for most plants. Authors further point that only some euhalophytes and some C_4 species struggle in completing their life cycle in the absence of Na. Several studies proposed term functional nutrient [37,42]. Nevertheless, selected decorative species were able to accumulate Na from polluted water. The differences in the potential of sodium uptake were evident between plant species. Most plants of species *P. australis* died in control thus it was not possible to compare Na concentration between plants in FTW and control. However, Na content in aboveground and belowground biomass did not differ significantly between initial (C0) and final (C4) Na concentrations. These findings are somewhat surprising given the fact that maximum Na removal efficiency was detected in cell 1 planted with this species. However, plants do not promote pollutant removal only by accumulation and concentration in their tissue. Plants in FTW facilitate other mechanisms responsible for pollutant removal by creating favourable conditions in their immediate proximity [10]. The large free root surface allows much rapid filtration of solid particles from the water column [8]. The root exudates can change water conditions and enhance rhizofiltration [43]. More oxygen is introduced into the water through stems, roots, and rhizomes [44] and thus micro-locations with aerobic conditions are created. Plant rhizosphere can be inhabited by beneficial microorganisms [45] to facilitate bioremediation of polluted water. This further highlights the fact that further research on the mechanisms of Na removal in FTV is needed. This outcome is also contrary to that of Moogouei and Chen [13] who found that Na accumulation in leaves of *P. australis* was 2.02 ± 0.4 mg/g when plants were grown in solution with 2000 mg/L NaCl for 14 days. A possible explanation of this might be a much lower Na concentration in FTW inflow (2.135-4.428 mg/L).

No previous studies have investigated the potential of selected decorative species to accumulate Na during water treatment in CW or FTW. Consequently, we are again unable to compare the obtained results with other studies. However, some general hypotheses can be made, and the results of this research can make a significant contribution and provide a basis for further studies of the phytoremediation potential of selected species. Species *C. indica* contained significantly higher Na concentration in the roots (14.58 g/kg) compared to other tested decorative species. However, significant differences in the concentration of this element in the root, rhizome, and shoot in the FTW and control were not found. These findings suggest that high Na concentration in *C. indica* is the consequence of naturally high Na content in this species [46] rather than accumulation of Na from polluted water or stone wool. Significantly higher Na concentration was found in shoots of *I. pseudacorus* and *I. sibirica* 'Perry's Blue' control plants compared to plants in FTW. Also, plants sampled just before the start of water treatment (C0) contained significantly higher Na concentrations in roots compared to plants in FTW and control. The same trend of Na concentration change in plant tissue was noted in species *L. salicaria*. It could be argued that roots of these species became saturated with Na during FTW start-up period. Since Na translocation to shoot was poor (TF<1) some Na was excreted resulting in the decrease of Na content in the root over time. Jesus et al. [12] also observed the occurrence of Na saturation in plants (halophytes) tested in their research. Species *A. plantago - aquatica* contained significantly higher Na concentration in the shoots (8.32 g/kg) and rhizomes (9.76 g/kg) compared to other tested species, save for *M. trifoliata* shoots. Considering that significantly higher concentrations of Na were found in the vegetative parts of plants in the FTW compared to control plants, as well as that the content of Na increased over time, it can be suggested that this species had

good potential for Na accumulation from water and stone wool. Like *A. plantago - aquatica*, species *M. trifoliata* had significantly higher Na concentration in the shoots (7.92 g/kg) compared to other tested species. Interestingly, *M. trifoliata* was the only tested species with TF value above 1 and thus the only one that was able to translocate accumulated Na from roots to shoots. Since the plants in FTW contained significantly more Na in the rhizome (3.60 g/kg) compared to the control plants, it can be assumed with caution that this species had a share in the removal of this nutrient from the polluted water.

Shelef et al. [5] showed that the annual halophyte *B. indica* accumulated over 80% of Na in shoots when grown in the hydroponic system. This differs from the findings presented here. Selected decorative species in the proposed model of FTW also showed very low translocation of accumulated Cr and Ni from belowground biomass to shoot [19]. These findings could have practical implications. Since all plants in FTW except *M. trifoliate* generated a considerable amount of biomass [18,19] it would be possible to use aboveground biomass upon harvesting as a resource and thus reduce the amount of secondary waste at the end of the rhizofiltration process.

The algae were introduced in cell 5 directly from the river to facilitate further water polishing. Species determination indicated that a monoculture of macroscopic algae *Cladophora glomerata* (Linnaeus) Kützing. developed in cell 5. The current study found that Na content in algae ranged within the reported limits for this species, 0.30–1.40 g/kg [41], during water treatment (C1-C4). Even though Na is a non-essential nutrient for algae, *C. glomerata* was able to accumulate Na from polluted water. The Na content in algae increased from cycle to cycle (C1-C4). However, Na removal efficiency was very variable and a maximum of 23% was reached in C4 when cells with floating islands also achieved their maximum.

The sodium concentration in stone wool varied during the water treatment. Unfortunately, this finding is rather difficult to interpret because no assumptions could be derived. However, it is possible that some Na was released from stone wool into the water or accumulated by plants since significantly lower Na content was detected at the end of water treatment (C4) compared to initial concentrations (C0) and control (Ø). It can thus be suggested that the stone wool did not act as an inert substrate in relation to Na.

CONCLUSION

This study set out to determine whether the proposed model of floating treatment wetland with decorative plant species and algae could be efficient in the removal of sodium from polluted urban river. To the best of our knowledge, this is the first research that assesses Na removal in FTW. Also, a key strength of the presented study is that it went beyond laboratory or greenhouse experiments treating synthetic wastewater. The present study expands our knowledge of rarely or never used decorative terrestrial and aquatic plant species in CW or FTW.

The findings indicate that FTWs can ensure efficient Na removal. Even though the efficiency was negative or low during the first 3 treatment cycles, after evaporation decrease and the inflow Na concentration and biomass increase the maximum efficiency of 44% and 43% was achieved in cell 1 with *P. australis* and cell 4 with decorative macrophytes, respectively. The second major finding was that only species *A. plantago - aquatica* had good potential for Na accumulation from water. Also, it can be assumed that species *M. trifoliata* had a share in the Na removal. Translocation of accumulated Na from belowground biomass to shoots was very low in all species except *M. trifoliata*. This can be a practical implication of this study since obtained aboveground biomass can be used as a potential resource for different industries. The results reported here suggest that *C. glomerata* enabled further water polishing as Na content in algae increased from cycle to cycle and maximum efficiency of 23% was reached at the end of water treatment (C4). Taken together, these results imply that Na removal was not caused only by plant and algal Na accumulation, but also other mechanisms affected water treatment. Consequently, further studies need to be done to investigate all the physical, chemical, and biological processes responsible for Na removal in FTW. Also, it would be interesting to test phytoremediation potential of other terrestrial plant species and aquatic macrophytes to ensure proper species selection for Na removal in floating treatment wetlands.

ACKNOWLEDGEMENTS

This research was supported by the City of Belgrade - Belgrade City Administration - Secretariat for Environmental protection, Serbia [contract number V-01 401.1-83] and Ministry of Education, Science and Technological Development, Republic of Serbia [grant numbers 200027, 200169].

REFERENCES

[1] -Steele, M.K., Aitkenhead-Peterson, J.A. (2011) Long-term sodium and chloride surface water exports from the Dallas/Fort Worth region. Sci. Total Environ. 409, 3021-3032.

[2] Yaseen, D.A., Scholz, M. (2019) Textile dye wastewater characteristics and constituents of synthetic effluents: a critical review. Int. J. Environ. Sci. Technol. 16, 1193-1226.

[3] Almasi, A., Mohammadi, M., Kazemitabar, Z., Hemati, L. (2021) Phytoremediation potential of Echinochloa crus galli and Hibiscus cannabinus in the stabilization of municipal wastewater sludge. Int. J. Environ. Sci. Technol. 18, 2137-2144.

[4] Almuktar, S., Abed, S.N., Scholz, M. (2018) Wetlands for wastewater treatment and subsequent recycling of treated effluent: a review. Environ. Sci. Pollut. Res. 25, 23595-23623.

[5] Shelef, O., Gross, A., Rachmilevitch, S. (2012) The use of Bassia indica for salt phytoremediation in constructed wetlands. Water Res. 46, 3967-3976.

[6] Benvenuti, T., Hamerski, F., Giacobbo, A., Bernardes, A.M., Zoppas-Ferreira, J., Rodrigues, MAS (2018) Constructed floating wetland for the treatment of domestic sewage: a real-scale study. J. Environ. Chem. Eng. 6, 5706-5711.

[7] Chen, Z., Costa, O.S., Jr. (2020) Artificial Floating Island System as a Sustainable Solution for Addressing Nutrient Pollution and Harmful Algal Blooms (HABs) in Ohio. pp. H116-0004.

[8] Van de Moortel, A.M.K., Meers, E., De Pauw, N., Tack, F.M.G. (2010) Effects of Vegetation, Season and Temperature on the Removal of Pollutants in Experimental Floating Treatment Wetlands. Water Air Soil Pollut 212, 281-297.

[9] Jenssen, F.D., Vatn, A. (1996) Ecologically sound wastewater treatment: Concepts and implementation. In: Etnier C, Guterstam B, editors. Ecological Engineering for Wastewater Treatment. 2nd ed. Boca Raton, CRC Press. 305-320.

[10] Brix, H. (1997) Do macrophytes play a role in constructed treatment wetlands? Water Sci. Technol. 35, 11-17.

[11] Dipu, S., Kumar, A.A., Thanga, V.S.G. (2011) Phytoremediation of dairy effluent by constructed wetland technology. Environmentalist 31, 263-278.

[12] Jesus, J.M., Cassoni, A.C., Danko, A.S., Fiúza, A., Borges, M.T. (2017) Role of three different plants on simultaneous salt and nutrient reduction from saline synthetic wastewater in lab-scale constructed wetlands. Sci. Total Environ. 579, 447-455.

[13] Moogouei, R., Chen, Y. (2020) Removal of cesium, lead, nitrate and sodium from wastewater using hydroponic constructed wetland. Int. J. Environ. Sci. Technol. 17, 3495-3502.

[14] Swansea University (2014) Report: Floating Treatment Wetlands (FTWs) in Water Treatment: Treatment efficiency and potential benefits of activated carbon. 1-44.

[15] Masters, B. (2012) The ability of vegetated floating Islands to improve water quality in natural and constructed wetlands: a review. Water Pract. Technol. 7.

[16] Stewart, F.M., Muholland, T., Cunningham, A.B., Kania, B.G., Osterlund, M.T. (2008) Floating islands as an alternative to constructed wetlands for treatment of excess nutrients from agricultural and municipal wastes–results of laboratory-scale tests. Land contam. Reclam. 16, 25-33.

[17] Pavlineri, N., Skoulikidis, N.T., Tsihrintzis, V.A. (2017) Constructed floating wetlands: a review of research, design, operation and management aspects, and data meta-analysis. Chem. Eng. Sci. 308, 1120-1132.

[18] Čule, N., Lučić, A., Dražić, D., Popović, V., Veselinović, M., Brašanac-Bosanac, L., Mitrović, S. (2017) Construction of floating treatment wetlands for remediation of polluted waters. Sustainable Forestry. 1-12.

[19] Cule, N., Lucic, A., Nesic, M., Veselinovic, M., Mitrovic, S., Sredojevic, Z., Brasanac-Bosanac, Lj. (2021) Accumulation of chromium and nickel by *Canna indica* and decorative macrophytes grown in floating treatment wetland. Fresen. Environ. Bull. 30, 7881-7890.

[20] Duncan, T. (2012) Floating reedbeds biofilter performance in urban stormwater treatment wetlands, National Conference Stormwater 2012. October 15-19, 2012, Melbourne, Australia. https://www.stormwater.asn.au/images/ Conference_Papers/Stormwater12/Duncan_Tom_-_Non_Refereed_Paper.pdf (accessed 10 October 2021)

[21] Keizer-Vlek, H.E., Verdonschot, P.F., Verdonschot, R.C., Dekkers, D. (2014) The contribution of plant uptake to nutrient removal by floating treatment wetlands. Ecol. Eng. 73, 684-690.

[22] Ali, S., Abbas, Z., Rizwan, M., Zaheer, I.E., Yavaş, İ., Ünay, A., Abdel-Daim, M., Bin-Jumah, M., Hasanuzzaman, M., Kalderis, D. (2020) Application of Floating Aquatic Plants in Phytoremediation of Heavy Metals Polluted Water: A Review. Sustainability 12, 1927 (1-33).

[23] Chance, L.M.G., Van Brunt, S.C., Majsztrik, J.C., White, S.A. (2019) Short-and long-term dynamics of nutrient removal in floating treatment wetlands. Water Res. 159, 153-163.

[24] Di Luca, G.A., Mufarrege, M., Hadad, H.R., Maine, M.A. (2019) Nitrogen and phosphorus removal and Typha domingensis tolerance in a floating treatment wetland. Sci. Total Environ. 650, 233-240.

[25] Jones, T.G., Willis, N., Gough, R., Freeman, C. (2017) An experimental use of floating treatment wetlands (FTWs) to reduce phyto-plankton growth in freshwaters. Ecol. Eng. 99, 316-323.
[26] Xian, Q., Hu, L., Chen, H., Chang, Z., Zou, H. (2010) Removal of nutrients and veterinary antibiotics from swine wastewater by a constructed macrophyte floating bed system. J. Environ. Manage. 91, 2657-2661.
[27] Caldelas, C., Araus, J.L., Febrero, A., Bort, J. (2012) Accumulation and toxic effects of chromium and zinc in *Iris pseudacorus* L. Acta Physiol. Plant 34, 1217-1228.
[28] Gao, J., Wang, W., Guo, X., Zhu, S., Chen, S., Zhang, R. (2014) Nutrient removal capability and growth characteristics of Iris sibirica in subsurface vertical flow constructed wetlands in winter. Ecol. Eng. 70, 351-361.
[29] Chen, C., Zhao, T., Liu, R., Luo, L. (2017) Performance of five plant species in removal of nitrogen and phosphorus from an experimental phytoremediation system in the Ningxia irrigation area. Environ. Monit. Assess. 189, 1-13.
[30] Cule, N., Vilotic, D., Nesic, M., Veselinovic, M., Drazic, D., Mitovic, S. (2016) Phytoremediation potential of *Canna indica* L. in water contaminated with lead. Fresen. Environ. Bull. 25, 3728-3733.
[31] Blaylock, M., Huang, J. (2000) Phytoextraction of metals. In: Phytoremediation of toxic metals: using plants to clean up the environment. Raskin I, Ensley DB (ed-s). New York, John Wiley and Sons, Inc. pp. 53-69.
[32] Campbell, C.R., Plank, C.O. (1998) Preparation of plant tissue for laboratory analysis. In: Handbook of reference methods for plant analysis. Yash, PK. (ed). Boca Raton, Taylor & Francis Group, CRC Press. 37-49.
[33] Şenilă, M., Şenilă, L., Roman, C. (2011) Evaluation of performance parameters for trace elements analysis in perennial plants using ICP-OES technique. J. Plant Dev. 8, 87-93.
[34] Marchiol, L., Assolari, S., Sacco, P., Zerbi, G. (2004) Phytoextraction of heavy metals by canola (*Brassica napus*) and radish (*Raphanus sativus*) grown on multicontaminated soil. Environ. Pollut. 132, 21-27.
[35] Freedman, A., Gross, A., Shelef, O., Rach-milevitch, S., Arnon, S. (2014) Salt uptake and evapotranspiration under arid conditions in horizontal subsurface flow constructed wetland planted with halophytes. Ecol. Eng. 70, 282-286.
[36] Barker, A.V., Pilbeam, D.J. (2006) Handbook of Plant Nutrition. CRC Press, Boca Raton, Florida, 1-632.
[37] Marschner, H. (1995) Mineral Nutrition of Higher Plants. Elsevier, Academic Press, 1-889.
[38] DeBusk, W.F. (1999) Wastewater treatment wetlands: Contaminant Removal Processes. Institute of Food and Agricultural Science, University of Florida, Gainesville, 1-4.
[39] Zhu, L., Li, Z., Ketola, T. (2011) Biomass accumulations and nutrient uptake of plants cultivated on artificial floating beds in China's rural area. Ecol. Eng. 37, 1460-1466.
[40] Phipps, S., Goodman, C.A., Delwiche, C.F., Bisson M.A. (2021) The role of ion-transporting proteins in the evolution of salt tolerance in charophyte algae. J. Phycol. 57, 1014-1025.
[41] Gerloff, G.C., Fitzgerald, G.P. (1976). The nutrition of great lakes Cladophora. U.S. Environmental Protection Agency, Environmental Research Laboratory; Center for Environmental Research Information, EPA/600-S3-84-016. 1-111.
[42] Subbarao, G.V., Ito O., Berry, W.L., Wheeler, R.M. (2003) Sodium—A Functional Plant Nutrient. CRC Crit Rev Plant Sci 22, 391-416.
[43] Tanner, C.C., Headley, T.R. (2011) Components of floating emergent macrophyte treatment wetlands influencing removal of stormwater pollutants. Ecol. Eng. 37, 474-486.
[44] Brix, H. (1993) Macrophyte-Mediated Oxygen Transfer in Wetlands: Transport Mechanisms and Rates. In: Constructed Wetlands for Water Quality Improvement. Moshiri GA (ed.). Lewis Publishers, CRC Press. pp. 391-398.
[45] Davis, L. (1995) A handbook of constructed wetlands: A guide to creating wetlands for: agricultural wastewater, domestic wastewater, coal mine drainage, stormwater. In the Mid-Atlantic Region. Volume 1: General considerations. USDA-Natural Resources Conservation Service, 1-53.
[46] Gaur, A. (2014) Nutritive value of rhizome of the *Canna indica* Linn. and characteristics of various extracted materials from the rhizome. Int. J. Pharma Bio Sci 5, 644-648.

Received: **19.12.2021**
Accepted: **11.02.2022**

CORRESPONDING AUTHOR

Nevena Cule
Department of Environmental Protection and Improvement,
Institute of Forestry,
Kneza Viseslava 3,
Belgrade – Serbia

e-mail: nevena.cule@yahoo.com

© by PSP Volume 31– No. 05/2022 pages 5255-5262 Fresenius Environmental Bulletin

EFFECTS OF ATMOSPHERIC SUSPENDED PARTICLE POLLUTION CONCENTRATION ON LUNG FUNCTION HEALTH OF LONG-DISTANCE RUNNERS

Yingjiao Xiang[1,2], Baishun Sun[1,2,*], Zhiqin Wang[1]

[1]Physical Education Teaching Research Department, Hunan Institute of Technology, Hengyang Hunan 421002, China
[2]Graduate School, Adamson University, Manila 1000, Philippines

ABSTRACT

Rapid economic development has made the problem of air pollution increasingly serious, and all sectors of society have begun to focus on air pollution. Throughout the world, there are air pollution problems in various countries, which have threatened the survival and healthy life of human beings, and the main factor leading to air pollution is suspended particulate matter in the air. It is of great significance to study the airflow characteristics of the alvear area of the lung alar region of ordinary adults, ordinary exercisers, and athletes, as well as the deposition of respirable particulate matter, to understand the transport mechanism of gas and particulate matter, and to evaluate the effect of enterable lung particulate matter on different types of people. Based on the Weibel-A model data, this paper establishes a normal alvear model by hypothetical simplification and reflects the kinetic mechanism of lung rhythm contraction/expansion by introducing dynamic wall boundary conditions. Numerical simulations are used to study the deposition characteristics of alveolar airflow and particles in ordinary adults, ordinary exercisers, and long-distance runners, as well as the effects of alveoli obstruction. By simulating the airflow and particle deposition characteristics of the alveoli in the lungs, it is found that compared with the fixed alveolar wall condition, the active alveolar wall condition can enhance the convection flow of the alveolar inflow field, more realistically reflect the gas flow in the alveoli, and the movement of the alveolar wall surface increases the particle deposition rate. In the range of 0.05-3 μm particle diameter, long-distance runners have the largest particle deposition rate, while the particle deposition rate of ordinary exercisers and ordinary adults is not much different. The results showed that under the same exposure environment, ordinary exercisers, ordinary adults, and long-distance runners are more likely to be invaded by atmospheric suspended particulate matter.

KEYWORDS:
Lung function, atmospheric particulate matter, pollution concentration, numerical simulation

INTRODUCTION

Atmospheric particulate matter, or atmospheric aerosols, is used to represent liquid and solid phase particulate matter floating in the atmospheric environment. Due to the different formation conditions and sources of the substance, and different chemical composition and particle size, the particulate matter is divided into various types [1-3]. Nowadays, PM10, PM2.5 is fully recognized as threatening human health of two kinds of solid atmospheric particles. The particles are small in volume. The aerodynamic particle size and large particles specific surface area is inversely proportional, which is easier to adsorb a large number of harmful, toxic substances [4,5]. Based on this property, the above two particles are easy to enter the human respiratory tract, and even some particles will go deep into the human lungs [6].

Through the investigation of epidemiology and related studies, people who work for a long time or in a polluted environment will reduce their cardiopulmonary function, increase the incidence of cardiopulmonary disease, and even the mortality rate will rise sharply [7,8]. If the exercise is in the atmosphere of serious air pollution, after strenuous exercise shortness of breath, the required oxygen also increases, solid particles will transition from the nasopharyngeal breathing mode to the nasopharynx, oropharynx mixed breathing mode, reducing the nasal filter air effect [9-11]. People increase the number of breathing during exercise. The human body inhales a large number of polluted substances in the atmospheric environment, which can be dispersed to the blood under the action of cardiopulmonary function, making the polluting substances further threaten human health [12-14].

The results of many foreign epidemiological studies have shown that atmospheric particulate matter can damage and threaten human health. According to relevant research results, the increase in the concentration of particulate matter in the atmosphere will induce some diseases, making them increase morbidity and mortality [15-17]. Increasing concentrations of atmospheric particulate matter can cause cardiovascular diseases, respiratory diseases, etc., especially for some people with low resistance, outdoor sports or athletes [18]. Atmospheric particulate

matter threatens the normal functioning of the human body and also produces economic losses to health. According to the results of the study on the economic loss of PM10 human health, from 2010 to 2020, the economic loss caused by PM10 particulate matter affecting human health has exceeded 1 billion yuan per year [19-21].

In this paper, based on the principle of the motion mechanism of particulate matter, a particulate matter deposition assessment model is constructed, the gas flow characteristics under different respiratory states and the influence of gravity and respiratory cycle on particle deposition are studied, and the numerical simulation of the deposition law and fluency of fine particulate matter in the alveoli region of the human body provides an important basis for exploring the influence of inhalable particulate matter on human health.

MATERIALS AND METHODS

(1) Experimental instruments and equipment. QDSphere polystyrene fluorescent microspheres manufactured by a biomedical technology company are selected as respirable particulates in six sizes, namely 0.05μm, 0.1μm, 0.5μm, 1μm, 3μm, and are listed in Table 1. Table 2 shows the instruments and specific models required for this experiment.

The function of the standard particle generation device in the experimental equipment is to generate a monodisperse polystyrene fluorescent microsphere aerosol, and the function of the breathing simulator is to simulate various breathing conditions. The function of the humidifier is to increase the humidity of the laboratory model, the function of the differential pressure instrument is to monitor the pressure of the alveoli in real time, the function of the air parameter multifunctional tester is to monitor the temperature and relative humidity in the alveoli in real time, the function of the portable particle counter is to detect the concentration of respirable particulate matter with a particle diameter of 0.3 μm to 5 μm in the experimental model, the function of the laser particle counter is to detect the concentration of respirable particulate matter with a particle diameter of less than 0.1 μm in the experimental model, and the function of the flow cytometer is to count the number of deposited particles.

(2) Experimental data collection. 1) Inhalable particulate matter alvear deposition. We immerse the joints, bronchi and alveoli at all levels in the deionized water, put the ultrasonic cleaner into it for five minutes, put it into the cryogenic dryer for drying after the cleaning, and place it on the ultraclean table to complete the assembly operation. After completing the assembly work, it is fixed in the airtight experimental chamber, connected with the sensor and pipeline, and the airtightness of the assembled experimental model is checked in depth. According to the experimental requirements, the respiratory flow, frequency and residual gas volume of the respiratory simulator are adjusted, and the humidifier humidity is adjusted to maintain the relative humidity in the laboratory model at a predetermined value. We open the particle counter and aerosol generator for deposition experiments, set the particle counter interval time of five minutes, and collect and save the aerosol concentration every five minutes.

TABLE 1
Basic parameters of polystyrene fluorescent microspheres

Product model	Average diameter (μm)	Polystyrene density wavelength coefficient	Emission wavelength (nm)	Solid content (%)
QDSF10100	0.102	1.03	535-585	2.5
QDSF10300	0.30	1.03	535-585	2.5
QDSF10500	0.50	1.03	535-585	2.5
QDSF11001	1.00	1.03	535-585	2.5
QDSF11003	3.15	1.03	535-585	2.5

TABLE 2
Experimental instruments and models of inhalable particulate matter deposited in the alveoli region of human lungs

Instrumentation	Type
Standard particle generator	F9631
Breathing simulator	—
Humidifier	SC-D052AE
Differential pressure gauge	MP100
Air parameter multifunctional tester	TSI8386
Portable particle counter	TSI Aero Trak9350
Laser particle counter	—
Flow cytometry	Attune NxT

Note: "—" indicates that there is no model number

2) Particle deposition count. In this paper, eluent eluate elution is selected to wash the particulate matter in the deposition model, and the amount of sedimented particulate matter is counted by flow cytometry. There are two types of commonly used flow cytometers, namely non-fluorescent and fluorescent particles, which can avoid non-fluorescent particles affecting the amount of sediment. After completing this deposition experiment, the alveoli model is disassembled and removed, and then 5 mL of deionized water is poured into the alveoli for one hour of soaking, and the shaking on the vortex shaker is continued for one minute. We place alveolar tubes and bronchial tubes in a small beaker, add deionized water with a capacity of 20 mL, use a vortex shaker to shake it for one minute, select a pipette to collect the cleaning solution for different parts separately, and place it in the corresponding EP tube. The sample added at a time is 50 μL, and the controlled injection speed is 12.5 μL/min per minute.

(3) Research methods. 1) Sedimentation experiment mode. The breathing mode is simulated by the breathing simulator, and the breathing state is described as a non-stationary sinusoidal function, with a breathing ratio of 1:1 the respiratory rate can be adjusted, and the residual gas volume of alveolar can be adjusted between 10% and 80%. Three breathing modes are set: (TV) Normal breathing mode, alveolar function residual gas volume of 30%, that is, the maximum alveolar deformation rate is 70%. (IC) Deep breathing mode, the alveolar function residual gas volume is 10%, that is, the maximum alveolar deformation rate is 90%/ (HFO) High-frequency breathing mode, the alveolar function residual gas volume is 50%, that is, the maximum deformation rate of the alveoli is 50%.

In this paper, the particle diameter (Dp) is 0.05 μm, 0.1 μm, 0.5 μm, 1 μm, 3 μm, and the deposition rate of particles of this particle size entering the human lung acinar experimental model is studied. T represents the respiratory cycle, its value is 4s, the experimental time is three to six hours, and the relative humidity of the air in the alveoli can reach 100%.

2) Mechanism of particulate matter motion. People will bring inhalable particulate matter into the human respiratory system during breathing, and particulate matter will be subjected to various forces during transmission, mainly gravity, drag force, electric field force and Brownian force. Thus, it can be concluded that the movement of respirable particulate matter in the human respiratory system is very complex, so it is necessary to simulate the deposition and transmission value of respirable particulate matter. It is assumed that all particles are the same diameter and do not rotate or deform. The heat transfer, air humidity and other factors affecting the movement of particles is not taken into account. The model avoids being deposited as particles after contact with particles and does not calculate the interaction forces between each particle.

This article focuses on the analysis of particles with a particle size of 0.05-3 μm, and the air density is small compared to the particle density, so the buoyancy effect on particles can be ignored. In addition, the fluency velocity gradient corresponding to the small particle size is also very small, and the model and the particle avoid sedimentation after colliding with each other, without rotation. Thus, there is no need to calculate the Magnus force and the Saffman force. However, for some particles with a diameter of less than 1 μm, the motion generated by Brownian diffusion to the particles is calculated, so the Brownian force is calculated for submicroparticles. In this paper, we will take an in-depth look at the particles affected by gravity, drag, and Brownian forces, and the following equations for controlling the motion of particulate matter are as Eq. 1:

$$m = \frac{du_p}{dt} = F_D + F_g + F_b \quad (1)$$

Among them, the mass of particulate matter is m, the speed of movement of particulate matter is U_p, and the drag force, gravity and Brownian force of particulate matter are represented by F_D, F_g, F_b, respectively.

3) Sedimentation assessment of particulate matter. In this paper, the collected data information is processed by COMSOL software, which can obtain the amount of particle deposition on different wall surfaces and all particulate matter released on the model. We select two macro parameters to analyze and evaluate the deposition results. The following details the macro parameters for measuring particle deposition rate:

The descriptive deposition efficiency can be described as Eq. 2:

$$DF_i = \frac{N_d}{N_i} \times 100\% \quad (2)$$

The descriptive deposition fractions as Eq. 3:

$$DE_i = \frac{N_d}{N_z} \times 100\% \quad (3)$$

where the amount of particulate matter deposited in the area i is represented by N_d, the number of particulate matter in the model is represented by N_z, and the amount of particulate matter flowing into the i area is represented by N_t.

Sedimentation efficiency is used to express the ability to acquire particulate matter per unit area, the amount of particulate matter deposited after entering the region, and the proportion of the region in the

sedimentation model by the sedimentation fraction. Sedimentation efficiency parameters are usually used when calculating the results of segregation of the respiratory system, and sedimentation fractions are used when studying the current status of sedimentation in the respiratory system. The core of this paper is the study and analysis of particle deposition in the alveoli region of the lung, so the sedimentation fraction is selected when calculating.

RESULTS

(1) Particle fractional deposition rate results of lung acinar alveoli. Figure 1 lists the fractional deposition rates of solid particles of different particle sizes in the 1st, 3rd, 5th, and 7th stages of the alveoli. After comparing the particles with different progressions, the sedimentation law is the same, that is, the trend of the hierarchical sedimentation rate after increasing the particle size diameter is to decrease first and then rise, and the corresponding sedimentation rate is the smallest when the particle size is 0.5 μm, which is in line with the particle deposition law of the human lung alar region given by the National Radiation Association. Areas with a high number of progressions at the site of the pulmonary acinars correspond to a greater amount of sediment, posing a more serious threat. In addition, under the premise of the same particle size, the particle sedimentation rate corresponding to the increase in particle size progression is increased, which is directly related to the particle movement time. When the alveoli progression is inversely proportional to the flow rate in the alveoli region, the lower the progression, the faster the flow rate. Therefore, the particles in the alveolar region have a relatively long residence time, providing sufficient movement time for the particles to stick to the wall.

(2) The effect of respiratory state on particle deposition. Figure 2 shows the sedimentation rate of particles of different particle sizes in three respiration states, and the particle density is all 1000 kg/m^3 per cubic meter. In three different respiration states, the development trend of the sedimentation rate after increasing the particle size is to decrease first and then increase, and the sedimentation rate is the smallest when the particle size is 0.5 μm.

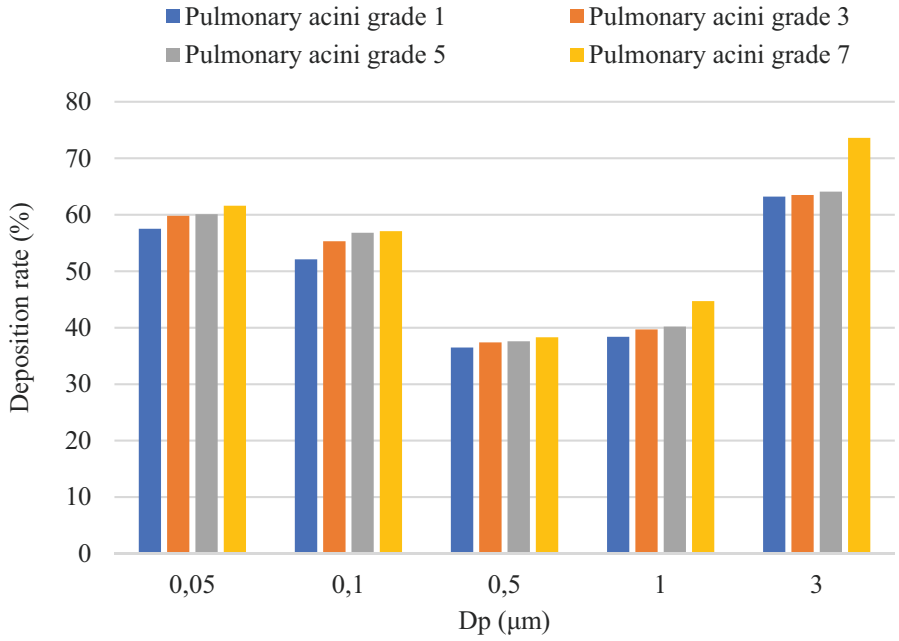

FIGURE 1
Trend of hierarchical deposition rate of different stage particles of lung acinar alveoli.

TABLE 3
Statistics of respiratory parameters in three respiratory states in adults

Breathing state	Respiratory cycle(s)	Minimum lung volume(L)	Maximum lung volume(L)	Coefficient of degree of change in alveolar volume (C)	Lung-scale coefficient of change(β)
TV	3.5	3.1	3.6	0.171	0.051
IC	6.5	3.1	3.6	0.835	0.226
HFO	2.5	3.1	3.6	0.166	0.055
HFO	2.5	3.1	3.6	0.166	0.055

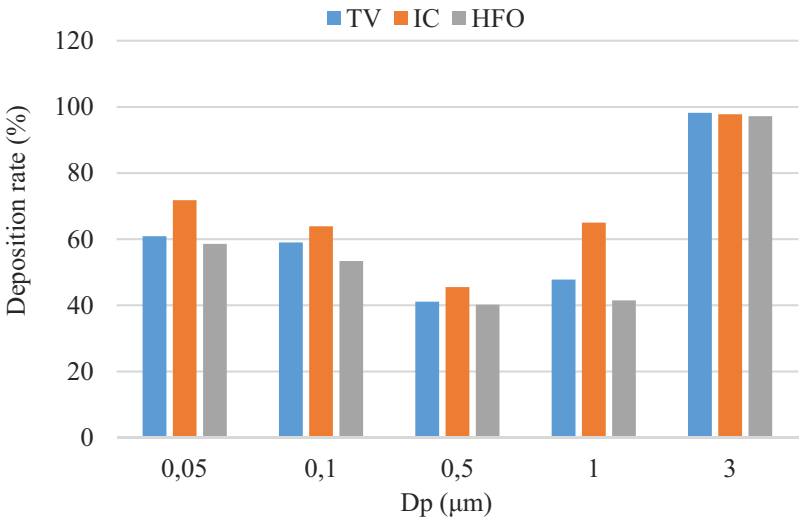

FIGURE 2
Trend of particle deposition rate in different respiratory states during the respiratory cycle.

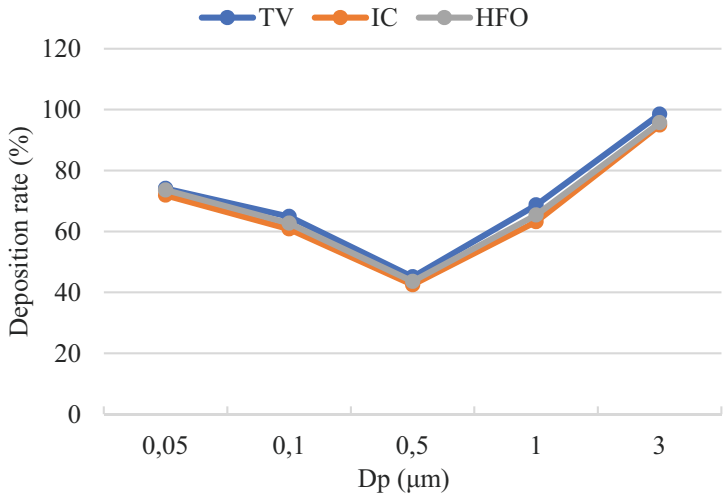

FIGURE 3
Trend of particle deposition rate under different respiratory conditions for the same breathing time.

A comparison of the sedimentation rates in three different respiratory states is obtainable, with the highest respiratory rate being deep breathing, then calm breathing, and finally high-frequency breathing. Table 3 below shows the respiratory parameters corresponding to the three respiratory states of adults. The particle deposition rate with long respiratory cycles in different respiratory states is higher. This result is due to the long period of breathing time in the granules in the alveoli of the lungs, and the effect of diffusion on particle production is also increased, resulting in an increase in the amount of particles deposited.

In this paper, by comparing the change of particle deposition rate in the above respiratory cycle, the length of breathing time affects the particle deposition effect problem, Figure 3 is the calculation time of 6s, the particles are released at the initial moment, and the sedimentation rate of particle size in three different respiratory states is analyzed. According to the figure, the figure shows that the corresponding particle deposition rate curves of the three different respiratory states are in the overlapping state, so it is concluded that the number of particles inhaled at different times in the respiratory state is equal, and the sedimentation rate of particles in the pulmonary acinar after 6s of respiration is basically the same. Compared with Figure 2, it can be obtained that respiration is an important factor affecting particle deposition in three respiratory states, and if the breathing time is equal, the sedimentation rate of particles in different particle states is generally the same.

(3) Comparison of particle deposition under the condition of moving alveolar wall and fixing alveolar wall. In order to make the simulation study closer to the respiration of real human lungs, the alveolar wall is given a speed to simulate the contraction and expansion of the real human alveoli, that is,

the dynamic alveolar wall condition. Figure 4 shows the deposition rate of various elapsed particles under the premise of fixing the alveolar wall and the active alveolar wall. The data in the analysis figure can be obtained. Based on the premise of moving alveolar wall, the sedimentation rate of particles is higher than that of fixed alveolar wall, and there is a unified deposition trend. The particle size is in the range of 0.05 μm to 0.5 μm, and the deposition rate decreases after increasing the particle diameter. When the particle size is in the range of 0.5 μm to 3 μm, the deposition rate corresponding to the increased particle size is increased, and the corresponding deposition rate is the largest when the particle size is 0.5 μm.

In order to compare the relative magnitude of the effects of different models on the sedimentation rate of particles of different particle sizes, the sedimentary growth rate is introduced here to characterize it, which is defined as Eq. 4:

$$\Delta DE(\%) = \frac{DE_{MW} - DE_{SW}}{DE_{SW}} \times 100\% \quad (4)$$

In the above formula, DE_{SW} represents the particle deposition rate corresponding to the fixed alveolar wall model, and DEM_W represents the particle deposition rate corresponding to the active alveolar wall model.

The sedimentation growth rates corresponding to the different particle diameters are listed in Table 4 below, the particle size range is 0.05 μm to 3 μm, and the sedimentation growth rate changes very significantly, in the range of 0.25% to 35.52%. For large particle sizes with a diameter of 3 μm and small particle size of 0.05 μm, the sedimentation growth rate is small. For particle sizes in the medium state, that is, particle size in the range of 0.1 μm to 1 μm, especially particles with a particle size of 0.5 μm have a higher sedimentary growth rate, the results show that compared with the fixed alveolar wall condition, the active alveolar wall condition directly affects particle deposition, but the impact on larger or smaller particles is smaller. The factors that lead to this result are that the deposition mechanism of larger particles and smaller particle sizes is gravitational sedimentation, Brown diffusion, and the convection field convection flow after moving the alveolar wall has a direct impact, so it will not directly affect larger and smaller particles.

(4) Comparison of particle deposits in the acinar vesicles of adults and long-distance runners. This simulation studies whether athletes are more severely affected by suspended particulate matter in the air under the same respiratory state (TV). The numerical simulation is used to calculate the particle deposition rate of ordinary adults, ordinary exercisers and long-distance runners at the same breathing time (6s). Figure 5 shows that the sedimentation rates of long-distance runners, ordinary exercisers, and ordinary adults are compared in the class 0-8 alveoli model of different particle sizes of species. According to this result, the sedimentation rate of particles in the alveoli of the lungs of ordinary adults, ordinary exercisers and athletes is basically not much different, indicating that different types of people do not have a large gap effect on the sedimentation law. When the particle size is 0.05 μm to 3 μm, the highest particle deposition rate is long-distance running, the lowest deposition rate is ordinary adults. When the particle size is 1 μm and 3 μm, the sedimentation rate is basically the same. Assuming that the breathing time is consistent, athletes have more deposited alveolar particles. It can be concluded that under the premise of the same environment and equal exposure time, long-distance runners are more affected by particulate matter in the air.

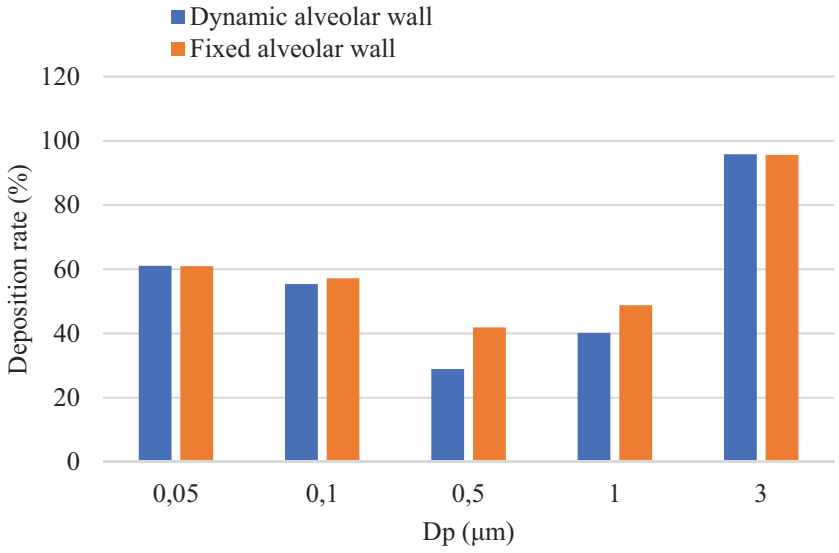

FIGURE 4
Trends in the sedimentation rate of particulate matter under the fixed alveolar wall and the active alveolar wall.

TABLE 4
Sedimentation growth rate of particulate matter of different diameters (%)

Particle diameter (μm)	0.05	0.1	0.5	1	3
ΔDE (%)	0.24	3.51	36.72	20.01	0.25

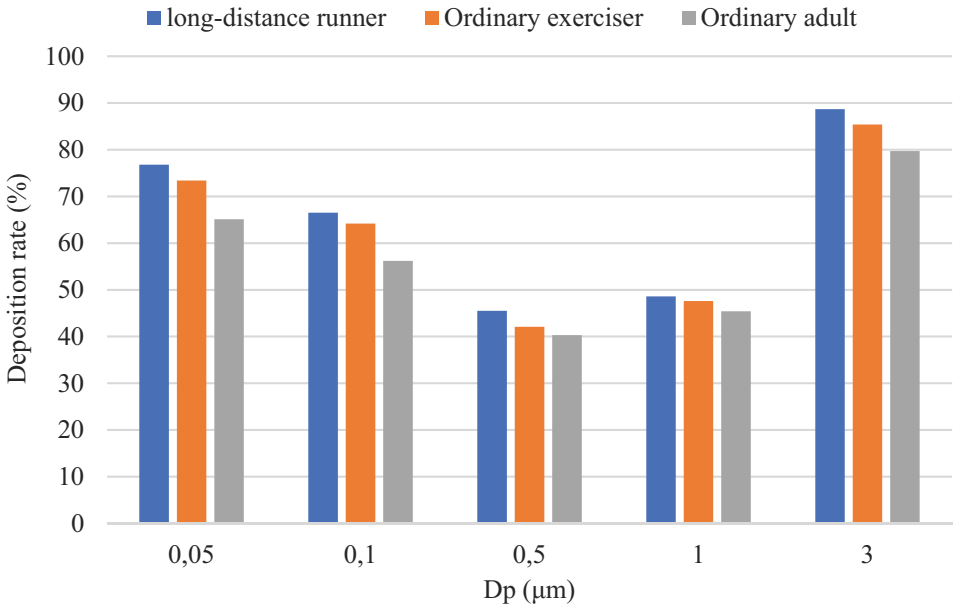

FIGURE 5
Trend of sedimentation rate change in different types of people under calm breathing.

Under the premise of equal movement time, the larger the movement speed of the particles, the longer the movement path, the higher the probability of contact with the wall of the lung alars, and the greater the deposition rate. According to the above, athletes corresponding to the alveoli of the various levels of air flow is larger, so when the breathing time is equal, the individual alveoli particles of long-distance runners have a longer movement length. Thus, the amount of sedimentation is larger. However, gravity directly affects the amount of particle deposition with large particle size, and adhesion deposition occurs in a short period of time, so increasing the respiration rate will directly affect the deposition rate.

CONCLUSIONS

(1) According to the particle classification experiment of the lung acinar, the fine bronchial tubes of the lungs have a limited role in intercepting fine particles, and most of the fine particles can still directly enter the alveoli area. The deposition rates of 0.05 μm, 0.1 μm and 3 μm particles are significantly higher than those of particle sizes of 0.5 μm and 1 μm, indicating that even in the fine bronchial region, it plays a major role in intercepting slightly larger particle size particles, making it difficult to reach the alveoli region. At the same time, the bronchial deposition rate of particulate matter of the same particle size is basically the same in grades 1-7, indicating that the size and physiological environment of the fine bronchial tubes are similar, and the hydrodynamic characteristics of the particles in the fine bronchi are also similar.

(2) Numerical simulation of normal alveoli results can be seen that the corresponding airflow velocity decreases, the pressure value increases, and the fractional sedimentation rate increases after increasing the number of alveoli. Comparing the fixed alveolar wall condition with the active alveolar wall condition, the latter can increase the convection flow rate of the alveolar flow field, which can increase the particle deposition rate in different respiratory states. The corresponding particle deposition is also different, which is directly related to the breathing time. The individual alveoli pressure value and airflow velocity of the individual alveoli of the athlete are large, and the corresponding particle deposition rate is high.

(3) We compare the sedimentation rates of long-distance runners, ordinary exercisers, and ordinary adults. According to this result, the particle deposition rate in the lung acinar vesicle of 0.05 to 3 μm ordinary adults and ordinary exercisers is basically not much different, and the particle deposition rate of long-distance runners is the largest. Therefore, in the case of exposure to the same environment for the same time, the remote mobilization individual is more harmful to airborne particles.

ACKNOWLEDGEMENTS

This work was not supported by any funds. The authors would like to show sincere thanks to those techniques who have contributed to this research.

REFERENCES

[1] Hueglin, C., Gehrig, R., Baltensperger, U., Gysel, M., Monn, C., Vonmont, H. (2005) Chemical characterisation of PM2.5, PM10 and coarse particles at urban, near-city and rural sites in Switzerland. Atmospheric Environment. 39(4), 637-651.

[2] Louie, P., Watson, J.G., Chow, J.C., Chen, A., Sin, D., Lau, A. (2005) Seasonal characteristics and regional transport of PM2.5 in Hong Kong. Atmospheric Environment. 39(9), 1695-1710.

[3] Huang, X.F., He, L.Y., Hu, M., Zhang, Y.H. (2006) Annual variation of particulate organic compounds in PM2.5 in the urban atmosphere of Beijing. Atmospheric Environment. 40(14), 2449-2458.

[4] Proias, G.T., Nastos, P.T., Paliatsos, A.G. (2002) PM10 concentrations in the urban area of Volos, Greece. Fresen. Environ. Bull. 11(8), 499-504.

[5] Kelessis, A.G., Petrakakis, M.J., Tzoumaka, P.N., Tsougas, M.A., Tzourelis, G.A., Zoumakis, N.M. (2006) PM2.5 concentration levels in urban Thessaloniki, Greece. Fresen. Environ. Bull. 15(8B), 853-858.

[6] Jimenez-Velez, B.D., Gioda, A., Perez, U., Rosa, Z. (2007) Particulate matter (PM10 and PM2.5) from different areas of Puerto Rico. Fresen. Environ. Bull. 16(8), 861-868.

[7] Meng, Z., Lu, B. (2007) Dust events as a risk factor for daily hospitalization for respiratory and cardiovascular diseases in Minqin, China. Atmospheric Environment. 41(33), 7048-7058.

[8] Brook, R.D., Rajagopalan, S., Pope, C.A., Brook, J.R., Kaufman, J.D. (2010) Particulate matter air pollution and cardiovascular disease: an update to the scientific statement from the American Heart Association. Circulation. 121(21), 2331-2378.

[9] Li, L., Lei, Y., Wu, S., Chen, J., Yan, D. (2017) The health economic loss of fine particulate matter (PM 2.5) in Beijing. Journal of Cleaner Production. 161(10), 1153-1161.

[10] Li, H.M. (2021) Experimental research on the recovery of early abnormal cardiopulmonary function of speed athletes under the atmospheric haze environment. Fresen. Environ. Bull. 30(1), 532-540.

[11] Couto, M., Kurowski, M., Moreira, A. (2018) Mechanisms of exercise-induced bronchoconstriction in athletes: current perspectives and future challenges. Allergy. 73(1), 8-16.

[12] Li, J., Xu, Y.J. (2021) Impact of atmospheric fine particle pollution on the physical fitness of gymnasts in outdoor training based on the green environmental protection concept. Fresen. Environ. Bull. 30(1), 394-401.

[13] He, Q.Y., Liu, X.M., Yao, R. (2021) Research on the influence of suspended particulate matter pollution on cardiopulmonary function of high intensity training basketball players. Fresen. Environ. Bull. 30(1), 577-584.

[14] Kong, X.K., Fan, C.H. (2021) The influence of atmospheric fine particles pollution on human skills during high intensity exercise. Fresen. Environ. Bull. 30(6B), 7939-7945.

[15] Pope, C.A., Dockery, D.W. (2006) 2006 critical review-health effects of fine particulate air pollution: lines that connect. Journal of the Air & Waste Management Association. 56(6), 709-742.

[16] Carlisle, A.J., Sharp, N.C.C. (2001) Exercise and outdoor ambient air pollution. British Journal of Sports Medicine. 35(4), 214-222.

[17] Wu, X., Chen, Y., Ji, G., Wang, G., Gong, Y. (2017) Spatial concentration, impact factors and prevention-control measures of PM2.5 pollution in China. Natural Hazards. 86(1), 1-18.

[18] Barman, S.C., Kumar, N., Singh, R., Kisku, G.C., Bhargava, S.K. (2010) Assessment of urban air pollution and it's probable health impact. Journal of Environmental Biology. 31(6), 913-920.

[19] Marcazzan, G.M., Vaccaro, S., Valli, G., Vecchi, R. (2001) Characterisation of PM10 and PM2.5 particulate matter in the ambient air of Milan (Italy). Atmospheric Environment. 35(27), 4639-4650.

[20] Polichetti, G., Cocco, S., Spinali, A., Trimarco, V., Nunziata, A. (2009) Effects of particulate matter (PM10, PM2.5 and PM1) on the cardiovascular system. Toxicology. 261(1-2), 1-8.

[21] Celis, J.E., Morales, J.R., Zaror, C.A., Inzunza, J.C. (2004) A study of the particulate matter PM10 composition in the atmosphere of Chillán, Chile. Chemosphere. 54(4), 541-550.

Received: **19.12.2021**
Accepted: **11.02.2022**

CORRESPONDING AUTHOR

Baishun Sun
Physical Education Teaching Research Department,
Hunan Institute of Technology,
Hengyang Hunan 421002 – China

E-mail: jojo46076793@163.com

© by PSP Volume 31– No. 05/2022 pages 5263-5270 Fresenius Environmental Bulletin

EVALUATION OF DOWNHOLE FLAME-RETARDANT OF FLY ASH GEL SYSTEM AND ITS DAMAGE TO COAL SEAM

Changji Dong[1,2,*], Yongli Liu[2]

[1]School of Safety Engineering, Heilongjiang University of Science and Technology, Harbin 150022, China
[2]School of Mining Engineering, Heilongjiang University of Science and Technology, Harbin 150022, China

ABSTRACT

As a subsidiary product of coal utilization, fly ash has extremely small particles. The emission of the fly ash into the atmosphere will have a great impact on the atmospheric environment. Collecting fly ash as a raw material for the production of building materials such as cement and bricks can not only solve the raw material problem, but also solve the environmental problem. For this reason, a new type of downhole flame retardant material, fly ash gel system, is prepared using fly ash as raw material. The downhole flame retardant properties are measured, and the characteristics of its damage to the coal seam are analyzed. The study found that with the development of the spontaneous combustion process, the ambient temperature continues to decrease, and the concentration of fly ash continues to increase. At the end of the experiment, the ambient temperature dropped to 101.34 °C and the fly ash concentration rises to 47.54 ug/m^3. At the same time, the study also finds that as the concentration of fly ash in the gel system increases, its flame retardant properties will be significantly improved. When the concentration of fly ash in the gel system is increased from 10 g/L to 40 g/L, the final ambient temperature will drop from 101.34 °C to 89.17 °C. In addition, the use of fly ash-based gel system can cause damage to the coal seam, which is manifested as a decrease in permeability and porosity. However, the use of the gel system has different effects on permeability and porosity. The increase in the concentration of fly ash in the gel system has a significant impact on the decrease in permeability, while the impact on porosity is small. Considering the flame-retardant properties of the fly ash-based gel system and the damage characteristics of the reservoir, it is recommended in engineering that the concentration of fly ash in the fly ash-based gel system should be higher than 20%.

KEYWORDS:
Atmospheric environment, fly ash, gel system, flame retardant properties, coal spontaneous combustion, coal seam damage

INTRODUCTION

At present, although a series of new energy development theories and technologies such as solar energy and geothermal energy are put on the agenda, it is believed that fossil fuels such as coal, oil and natural gas will continue to promote social development and maintain people's normal production and life for a long time [1-3]. According to statistics, in 2020, fossil fuel combustion and other energy sources account for 70% of global energy demand, and this data will only be reduced to about 60% by 2040 [4-5]. However, the combustion of fossil fuels not only produces a large amount of stable heat, but also produces by-products such as fly ash and carbon dioxide, which causes great environmental problems [6-7]. The capture and utilization of fly ash and carbon dioxide is an effective way to solve the by-products of fossil fuel combustion [8]. In addition, the spontaneous combustion of coal in the coal mining process is an accident that seriously affects the underground operating environment and the safety of coal miners [9]. Carrying out related research on coal combustion products (mainly fly ash) in coal spontaneous combustion can not only solve the technical problems of mining engineering, but also provide technical support for the secondary utilization and transformation of resources.

As we all know, the gel system injected into the coal and rock cracks and pores will make the underground formation have good flame retardant properties, and the fly ash-based gel system is a new green flame retardant. Figure 1 shows the microscopic mechanism of the fly ash-based gel system in mining flame retardant. As shown in Figure 1, in natural coal seams, gas is widely distributed in cracks and pore structures, and uncontrollable underground operations will have potential natural risks. However, with the continuous injection of the gel system, the gel system will drive out the gas in the coal seam cracks and pore structure while filling the coal seam cracks and pores [10]. As a result, the gas content in the coal seam is drastically reduced, which can reduce the risk of spontaneous combustion in the coal mining process. In addition, the gel system will melt during spontaneous combustion, and the melting process is obviously an endothermic process, which can greatly reduce the local temperature and reduce the hazard

range and extent of the coal seam after spontaneous combustion [11]. At the same time, the fly ash-based gel system will not only lower the temperature during the spontaneous combustion and melting process, but also control the release of a large amount of dust to cover the fire source to achieve the purpose of underground fire extinguishing.

At present, the analysis and research on spontaneous combustion in coal mining process has been relatively common and has made some progress. Wei et al. [12] used thermogravimetric analysis and differential scanning calorimetry analysis to optimize and analyze the spontaneous combustion index gases of coal samples and found that the depth and width of the goaf heat dissipation zone and the oxidation zone in the "Y" type ventilation are both greater than that of "U". "The ventilation system has good ventilation effect, and the goaf suffocation area can be extended to about 200m behind the working face, which can provide practical experience for adjacent mines or similar coal seams. Taking the Cuimu Coal Mine as an example, Zhai et al. [13] determined the spontaneous combustion risk area in the goaf through a combination of experimental research and numerical simulation, and found that nitrogen injection can effectively prolong the spontaneous combustion time and reduce the possibility of coal spontaneous combustion, which provides theoretical guidance and reference significance for the prevention and control of coal fires.

Wang et al. [14] proposed a comprehensive method that combines the pressure balance, grouting and filling cracks in the goaf to prevent the spontaneous combustion of coal in the goaf and the hazards caused by complicated air leakage. It shows that the concentration of oxygen and carbon monoxide in the goaf has decreased significantly, indicating that this method is very effective in eliminating the risk of spontaneous combustion of coal in the goaf. Chen et al. [15] used the beam tube method to monitor the ventilation effect of the "U" type ventilation system and the "Y" type ventilation system and analyzed the spontaneous combustion process in these three areas, and found that for the "U" type ventilation system, the width of the oxidation heating zone in the goaf is 68.5m, while the suffocation zone appears after 85.5m. The cutting roof pressure relief technology can be used to control the spontaneous combustion of the coal seam. It can be seen from the above experiments that the current deficiencies of related research on coal nature are concentrated in that the current research mainly focuses on the prediction and simulation of spontaneous combustion risk areas, and there is a lack of discussion on corresponding remedial measures. For this reason, it is of great significance to explore the disposal measures of coal spontaneous combustion for the gel system.

For this reason, the method of preparing fly ash-based gel system using fly ash is explored. At the same time, the flame retardant characteristics and mechanism of fly ash-based gel system are analyzed experimentally. Finally, the effect of fly ash-based gel system on the cracks and pore structure of coal seam is discussed. This research can provide technical support and reference for measures to control and reduce the risks and losses of underground operations caused by spontaneous combustion of coal.

MATERIALS AND METHODS

As mentioned above, the fly ash-based gel system has better flame retardant properties. On the one hand, the gel system melts when heated to lower the local temperature and flame retardant [16]. On the other hand, the gel system melted and dried to produce dust covering the surface of combustibles and flame retardant [17]. For this reason, the research on the preparation method of fly ash-based gel system and the analysis of its flame-retardant characteristics are of great significance to its flame-retardant field application.

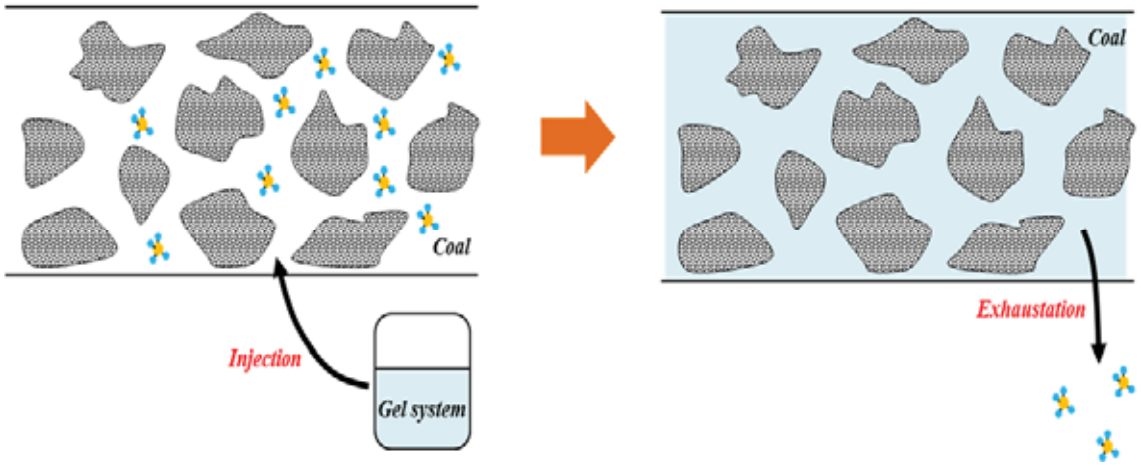

FIGURE 1
The microscopic mechanism of the flame retardant effect of the gel system.

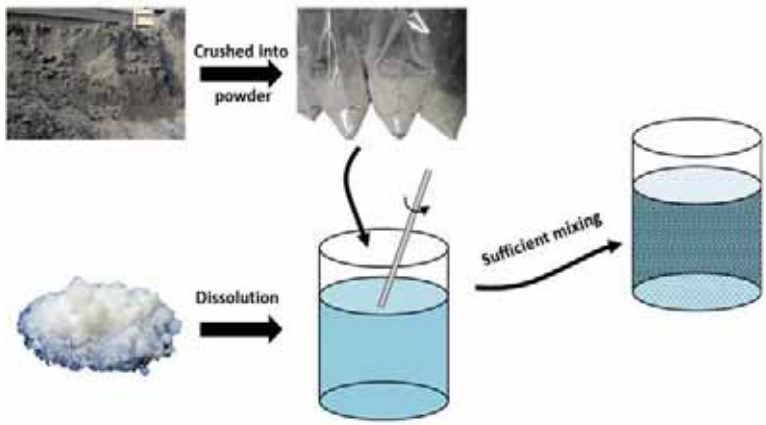

FIGURE 2
Schematic diagram of the preparation process of fly ash-based gel system.

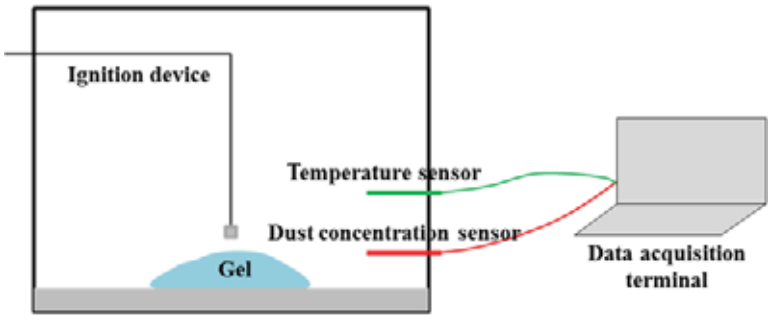

FIGURE 3
Experimental system for the flame-retardant properties of fly ash-based gel system.

Preparation of experimental materials and fly ash-based gel system. In the experiment, fly ash obtained from the power plant, sodium dodecyl sulfonate (SDS) purchased by Sinopharm Group and deionized water made by the laboratory are used. Figure 2 shows a schematic diagram of the preparation process of the fly ash-based gel system [18]. As shown in Figure 2, first, the power plant coal ash needs to be crushed into fly ash nanoparticles with a particle size of less than 50nm in a laboratory crusher, and vacuum packaged into bags to avoid agglomeration and affect subsequent use. Then, we add sodium dodecyl sulfate (SDS) crystals into a beaker containing 100 mL of water and dissolve with a glass rod until it becomes a gel. Finally, the prepared fly ash nanoparticles are slowly added to the beaker containing the gel and stirred evenly to form a fly ash-based flame-retardant gel system for subsequent flame-retardant characteristics and experiments.

Although the preparation of fly ash-based gel system in the laboratory requires high-precision molecular sieves to obtain nano-scale fly ash powder, it is necessary to go to a special powder processing laboratory to carry out the early grinding of nano-scale fly ash nanoparticles.

Experimental system and method of flame retardant properties of gel system. Figure 3 is an experimental system for developing the flame retardant properties of fly ash-based gel systems in this study. As shown in Figure 3, the experimental system is mainly composed of an ignition system, a temperature and concentration measurement system, and a data acquisition system. Among them, the function of the ignition system is to ignite the gel system and evaporate and melt the gel, and its response time is 0.25 ms. the main component of the temperature measurement system is a temperature sensor. The measurement range of the temperature sensor is 500 degrees Celsius, and the measurement accuracy is 0.5 degrees Celsius. The main component of the concentration measurement system is a dust concentration measurement sensor with a measurement accuracy of 500 ug/m^3 and a measurement accuracy of 0.25 ug/m^3. The data measurement system can collect temperature and concentration data according to the set time interval, and draw it into a dynamic curve for analysis and research.

During the experiment, a certain amount of fly ash-based gel needs to be placed first, and then the experimental system is turned on. Afterwards, it is ignited under the control of the main control system, and at the same time, the data measurement and acquisition system is turned on to collect experimental data (temperature and fly ash concentration data). Finally, after the end of the experiment, we remove the remaining experimental samples from the combustion, and clean up the gas in the container and pipeline.

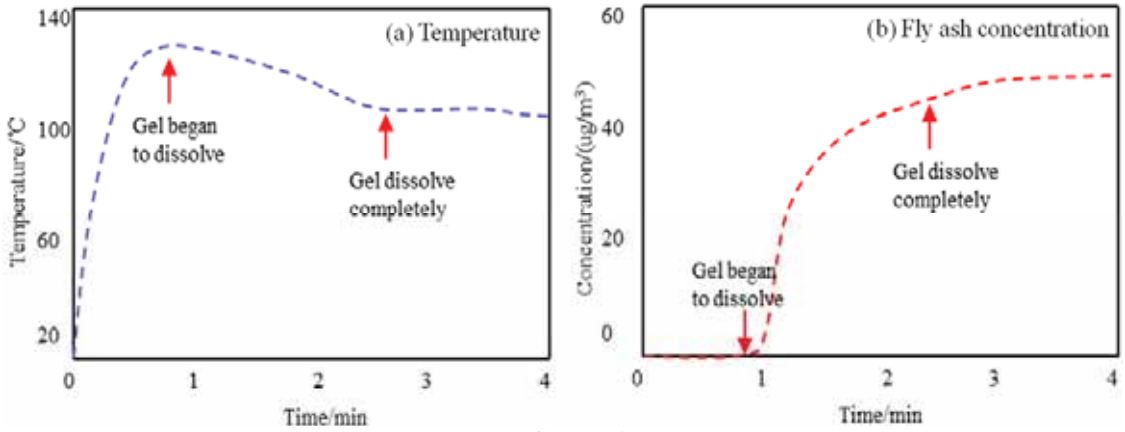

FIGURE 4
Evolution curve of temperature and fly ash concentration.

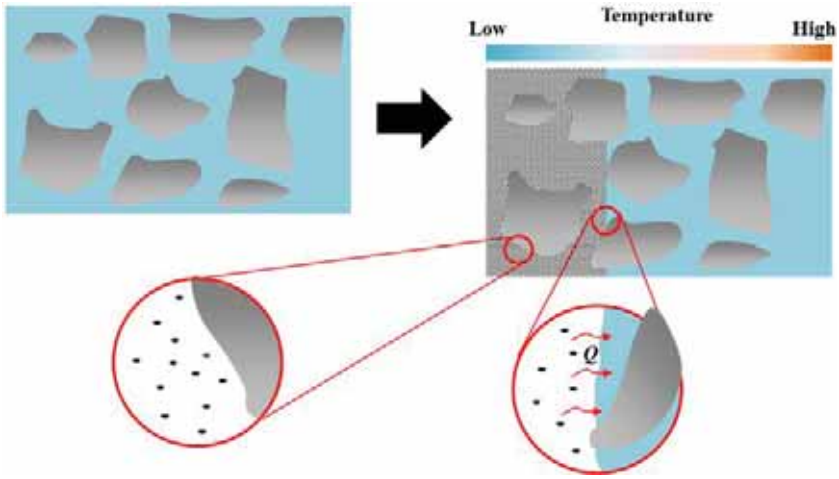

FIGURE 5
The mechanism of fly ash-based gel system in endothermic cooling and powder production to extinguish fire.

Flame retardant properties and mechanism of gel system. Figure 4 shows the relationship curve between temperature and fly ash concentration during the combustion test. Among them, Figure 4a is the temperature evolution curve, and Figure 4b is the fly ash concentration evolution curve. The concentration of fly ash in the gel system used in the experiment is 10 g/L. It can be found from Figure 4 that with the development of the experiment, the fly ash-based gel system burns and melts at 0.92 min after the start of the experiment. At this time, the temperature in the entire combustion chamber will decrease significantly, and the concentration of fly ash will also be reduced. At this time, the temperature in the chamber reaches the apex temperature of 134.65 degrees Celsius. As the experiment continues, the gel system will gradually undergo continuous dissolution and heat absorption, and the ambient temperature will further decrease. Correspondingly, the concentration of fly ash powder will gradually increase. By the end of the experiment, the temperature at the probe of the combustion chamber dropped to 101.34 degrees Celsius, and the fly ash concentration rose to 47.54 ug/m^3. It can be found that the fly ash-based gel system has better heat absorption, temperature reduction, powder production, and fire extinguishing capabilities.

Figure 5 shows the mechanism of the fly ash-based gel system in endothermic cooling and powder production to extinguish fire. It can be found from Figure 5 that when the coal seam is filled with a complete gel system, it is difficult to produce and mine coalbed methane. In this case, the gas concentration in the coal seam roadway will drastically decrease. In addition, even if a coal spontaneous combustion accident has occurred in the roadway or coal seam, the high temperature of combustion will cause the gel system in the cracks or pores to melt, and then absorb a large amount of heat in the surrounding coal seam to reduce the temperature below the ignition point [19-20]. At the same time, because the gel system contains a large number of nano-scale fly ash particles, the melting of the gel system will directly cover the surface of the coal seam in the non-spontaneous combustion area to prevent the aggravation and deterioration of spontaneous combustion accidents [21].

TABLE 1
Characteristic parameters of coal and rock samples

Concentration /(g/L)	Final temperature /℃	Fly ash concentration in the environment /(ug/m^3)
10	101.34	47.54
20	98.26	52.31
30	94.61	59.84
40	89.17	72.92

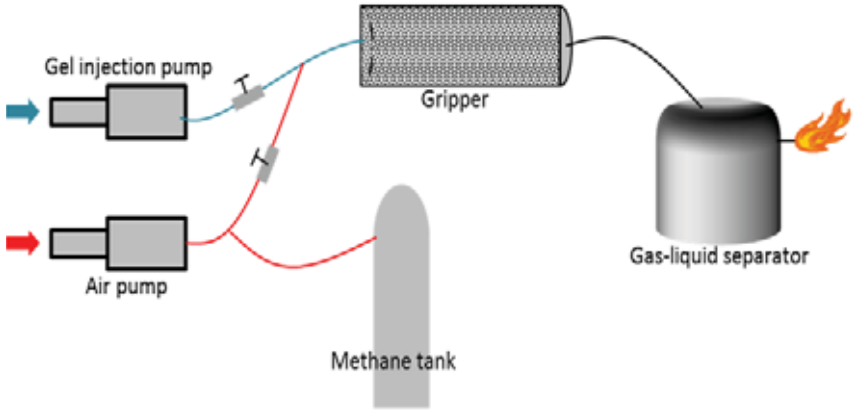

FIGURE 6
Experimental system for research on coal seam damage characteristics of gel system.

Table 1 shows the flame retardant effect of the gel system under different fly ash concentrations. It can be found from Table 1 that as the concentration of fly ash in the gel system increases, the final ambient temperature will decrease significantly. When the concentration of fly ash in the gel system is increased from 10 g/L to 40 g/L, the final ambient temperature will drop from 101.34 degrees Celsius to 89.17 degrees Celsius, a drop of 12.17 degrees Celsius. In addition, the experimental results in Table 1 also show that the increase in the concentration of fly ash in the gel system will significantly increase the concentration of fly ash in the environment of the burned area, thereby achieving excellent flame retardant conditions. When the concentration of fly ash in the gel system is increased from 10 g/L to 40 g/L, the concentration of fly ash in the final environment rises from 47.54 ug/m^3 to 72.92 ug/m^3, an increase of 53.39%. For this reason, the use of fly ash-based gel system to carry out flame retardant analysis and testing needs to consider the influence of fly ash concentration in the gel system.

RESULTS AND DISCUSSION

As the name implies, the gel system injected into the coal seam's cracks or pore structure will inevitably cause damage to the coal seam, resulting in deterioration of coal seam permeability and other physical properties, thereby affecting the mining of coalbed methane. These conclusions can be verified by related experimental studies in the early stage. For this reason, this article has carried out research on coal seam damage characteristics after analyzing the flame-retardant properties of fly ash gel system.

Experimental system and method of reservoir damage characteristics. Figure 6 is an experimental system used to carry out research on coal seam damage characteristics of gel system. This experimental system is mainly composed of gas injection system, gel injection system, coal rock holder, gas tank and gas-liquid separator. The gas injection system is connected with the holder and the gas tank, and the gas is injected from the gas tank into the coal holder during the experiment. The injection pressure limit of the air pump is 40MPa, the volume of the air tank is 30L, and the pressure is 50MPa. The main component of the gel injection system is the injection pump, which is used to inject the gel system into the coal holder. The gel injection pump needs to be treated with anticorrosion to avoid serious corrosion and damage to the fly ash-based gel system during the continuous experiment process. The role of the coal and rock holder is to carry the coal and rock and allow the gel system and gas to pass in to carry out the test. The volume is 3.0L. The function of the gas-liquid separator is to separate the gel system and methane gas generated at the end of the experiment, so as to realize the harmlessness of the experiment.

The entire experimental process can be briefly described as:

(1) Put the coal rock core column into the coal rock holder and fix the position to ensure that the subsequent injected gel system can be evenly distributed in the coal rock.

(2) The coal and rock physical properties (permeability and porosity) before injection into the gas gel system are determined;

(3) Turn on the gel system injection pump and inject the gel into the coal rock holder. After the injection is complete, close the gel system injection pump, and close the corresponding valve after 15.00 min;

(4) Turn on the corresponding valve and gas pump, and inject gas into the coal rock holder to displace the gas to measure the permeability and porosity;

(5) Ignite the gas separated by the gas-liquid separator, compare and analyze the permeability and porosity of coal before and after the gel system is injected.

Reservoir damage characteristics and mechanisms of the gel system. Figure 7 shows the porosity and permeability change curves of coal before and after the injection of the gel system when the fly ash concentration in the gel system is 10 g/L, 20 g/L, 30 g/L, and 40 g/L, respectively. From Figure 7a, we can find that as the concentration of fly ash increases, the permeability of coal rock will decrease significantly after the gel system is added. Before injecting any liquid, the permeability of coal rock is 11.54 mD, but when a gel system with a fly ash concentration of 10 g/L is injected into coal rock, the permeability of coal rock quickly drops to 9.87 mD. As the concentration of fly ash in the gel system increases, the degree of damage to coal permeability caused by the injection of the gel system will increase rapidly. When the gel system with a fly ash concentration of 40g/L is injected into the coal rock, the permeability of the coal rock has dropped to 2.43 mD, which is 78.94 % lower than that when the gel system is not injected. This is mainly because when the fly ash concentration in the injected gel system is low, its viscosity is low, and filling into the pores of the coal rock will not cause fatal damage to the flow of gas [23-24]. However, when the concentration of fly ash in the gel system is higher, its viscosity will be greatly increased, which will seriously hinder the effective permeation of gas [25-28].

From Figure 7b, we can also see that no matter how high the fly ash concentration in the gel system is, the injection of the gel system will seriously affect the porosity of the coal rock. Taking the fly ash concentration of 10 g/L as an example, the injection of fly ash-based gel system reduces the porosity of coal rock from 20.12% to 10.26%, a drop of 49.01%. However, changing the concentration of fly ash in the gel system will not affect the reduction of coal porosity to a large extent. The injection of the gel system with a fly ash concentration of 10 g/L will reduce the porosity of coal by 49.01%, while the injection of the gel system with a fly ash concentration of 20g/L, 30g/L and 40g/L will make the decrease the porosity by 52.03%, 53.26% and 54.05%, respectively. This is mainly because no matter how high the concentration of fly ash in the gel system is, the injection of the gel system will block almost all the effective pores, resulting in a sharp drop in the permeability of coal.

Discussion on flame retardant engineering strategy. After research, the following engineering suggestions are put forward to guide the natural prevention and control of coal in the coal mining process:

(1) A gel system with higher concentration of fly ash can be appropriately selected under the condition of ample cost, which can effectively prevent economic losses and environmental hazards caused by coal spontaneous combustion accidents. Under normal conditions, it is recommended that the concentration of fly ash in the gel system should not be less than 15% to prevent coal spontaneous combustion.

(2) Considering the flame-retardant characteristics of the fly ash-based gel system and the characteristics of reservoir damage (not conducive to the development of coalbed methane), it is recommended that the concentration of fly ash in the fly ash-based gel system should not be less than 20%.

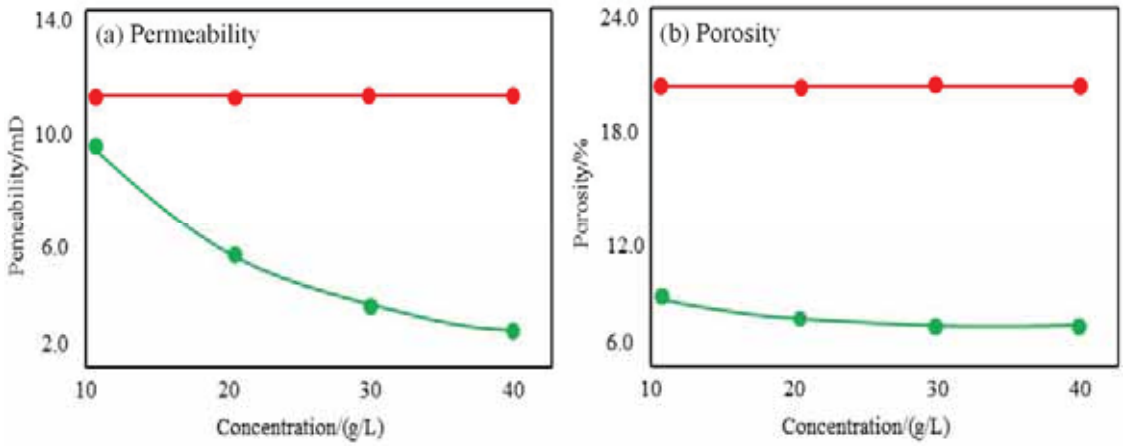

FIGURE 7
Research results of the damage characteristics of the gel system to the coal seam.

CONCLUSIONS

According to the problem of coal spontaneous combustion, the corresponding experimental analysis and discussion on the flame retardant and coal seam damage characteristics of the fly ash-based gel system are carried out, and the main conclusions are as follows:

(1) The melting and heat absorption of the gel system during the spontaneous combustion process will reduce the ambient temperature, and the released fly ash will cover the surface of the combustible material to achieve the purpose of flame retardancy. At the same time, with the development of the spontaneous combustion process, the ambient temperature will continue to decrease, and the concentration of fly ash will continue to increase. When the concentration of fly ash in the gel system used in the experiment is 10 g/L, at the end of the experiment, the temperature at the probe of the combustion chamber drops to 101.34 degrees Celsius, and the concentration of fly ash rises to 47.54 ug/m^3.

(2) As the concentration of fly ash in the gel system increases, its flame retardant properties will be significantly improved. When the concentration of fly ash in the gel system is increased from 10 g/L to 40 g/L, the final ambient temperature will drop from 101.34 degrees Celsius to 89.17 degrees Celsius, and the final environmental fly ash concentration will increase from 47.54 ug/m^3 to 72.92 ug/m^3.

(3) The use of fly ash-based gel system will cause coal seam damage, which is manifested as a decrease in permeability and porosity. However, the use of the gel system has different effects on permeability and porosity. The increase in the concentration of fly ash in the gel system has a significant impact on the decrease in permeability, while the impact on porosity is small. Before any liquid is injected, the coal rock permeability is 11.54 mD. When a gel system with a fly ash concentration of 10 g/L is injected into the coal rock, the coal rock permeability quickly drops to 9.87mD. When the fly ash concentration in the injected gel system is 40 g/L, the coal rock permeability will drop to 2.43 mD.

(4) Considering the flame-retardant properties of the fly ash-based gel system and the characteristics of reservoir damage (not conducive to the development of coalbed methane), it is recommended that the concentration of fly ash in the fly ash-based gel system should not be less than 20%.

ACKNOWLEDGEMENTS

This work was supported by the Major Special Projects of Engineering Science and Technology in Heilongjiang Province, China (No.2020ZX04A01).

REFERENCES

[1] Rastelli, E., Corinaldesi, C., Dell'Anno, A., Amaro, T., Queiros, A.M., Widdicombe, S., Danovaro R. (2015) Impact of CO2 leakage from sub-seabed carbon dioxide capture and storage (CCS) resevoirs on benthic virus-prokaryote interactions and functions. Front Microbiol. 6, 935.

[2] Jin, L. (2017) Experimental and numerical modeling of fluid injection into unconsolidated formations. Georgia: Georgia Institute of Technology. 72-78.

[3] Yan, M., Deng, J., Yu, B., Li, M., Zhang, B., Xiao, Q., Tian, D. (2020) Comparative study on sanding characteristics between weakly consolidated sandstones and unconsolidated sandstones. Journal of Natural Gas Science and Engineering. 76, 1-12.

[4] Lichtschlag, A., Haeckel, M., Olierook, D., Peel, K., Flohr, A., Pearce, C., Marieni, C., James, R., Connelly, D. (2021). Impact of CO2 leakage from sub-seabed carbon dioxide storage on sediment and porewater geochemistry. Int. J. Greenh. Gas Con. 109, 103352.

[5] St-Pierre, L., Hassani, F., Radziszewski, P., Ouellet, J. (2009) Development of a dynamic model for a cone bolt. International Journal of Rock Mechanics and Mining Sciences. 46(1), 107-114.

[6] Bazrafshan, E., Mostafapoor, F. (2011) Survey of medical waste characterization and management in Iran: a case study of Sistan and Baluchestan Province. Waste Management & Research. 29(4), 442-450.

[7] Lee, B., Moure-Ersaso, R. (2004) Alternatives for treatment and disposal cost reduction of regulated medical wastes. Waste Management. 24(2), 143-151.

[8] Chen, X., Li, L., Guo, Z., Chang, T. (2019) Evolution characteristics of spontaneous combustion in three zones of the goaf when using the cutting roof and release pressure technique. Energy Science & Engineering. 7(3), 710-720.

[9] Wang, H., Guan, Z., Shi, Y., Chen, W., Liu, Y., Zhang, B., Liang, D., Wang, X. (2018) Modeling and analyzing the motion state of bottom hole assembly in highly deviated wells. Journal of Petroleum Science and Engineering. 170, 763-771.

[10] Zhao, J., Zhou, L., Ma, J., Li, Y. (2016) Numerical simulation study of fracturing wells for shale gas with gas–water two-phase flow system under desorption and diffusion conditions. Journal of Natural Gas Geoscience. 1(3), 251-256.

[11] Chin, L. and Thomas, L. (1999) Fully Coupled Analysis of Improved Oil Recovery by Reservoir Compaction. In: Proceedings of SPE Annual Technical Conference and Exhibition, 3-6 October, Houston, Texas. 133-142.

[12] Wang, K., Tang, H., Wang, F., Miao, Y., Liu, D. (2019) Research on complex air leakage method to prevent coal spontaneous combustion in longwall goaf. Plos One. 14(3), e0213101.
[13] Chen, X., Li, L., Guo, Z., Chang, T. (2019) Evolution characteristics of spontaneous combustion in three zones of the goaf when using the cutting roof and release pressure technique. Energy Science & Engineering. 7(3), 710-720.
[14] Zhai, X., Wang, T., Li, H., Wang, K., Zubíček, V. (2019) Determination and predication on three zones of coal spontaneous combustion at fully-mechanised working face with nitrogen injection. International Journal of Oil Gas and Coal Technology. 22(3), 389-416.
[15] Wei, D., Du, C., Lei, B., Lin Y. (2020) Prediction and prevention of spontaneous combustion of coal from goafs in workface: A case study. Case Studies in Thermal Engineering. 21, 100668.
[16] Ghabraie, B., Ren, G., Zhang, X., Smith, J. (2015) Physical modelling of subsidence from sequential extraction of partially overlapping longwall panels and study of substrata movement characteristics. International Journal of Coal Geology. 140, 71-83.
[17] Ghabraie, B., Ren, G., Smith, J. (2017) Characterising the multi-seam subsidence due to varying mining configuration, insights from physical modelling. International Journal of Rock Mechanics and Mining Sciences. 93, 269-279.
[18] Li, Q., Zhou, L., Li, Z., Liu, Z., Fang, Y., Zhao, L., Han, Y. (2021) Factors affecting reorientation of hydraulically induced fracture during fracturing with oriented perforations in shale gas reservoirs. Frattura ed Integrità Strutturale. 15(58), 1-20.
[19] Yao, Y., Wei, M., Bai, B. (2022) Descriptive statistical analysis of experimental data for wettability alteration with surfactants in carbonate reservoirs. Fuel. 310, 122110.
[20] Punia, A. (2021) Carbon dioxide sequestration by mines: implications for climate change. Climatic Change. 165, 10.
[21] Chen, Y., Ding, Q., Yang, X., Peng, Z., Xu, D., Feng, Q. (2013) Application countermeasures of non-incineration technologies for medical waste treatment in China. Waste Management & Research. 31(12), 1237-1244.
[22] Yao, Y., Wei, M., Kang, W. (2021) A review of wettability alteration using surfactants in carbonate reservoirs. Advances in Colloid and Interface Science. 294, 102477.
[23] Abdul, R., Abdul, R., Munir, A., Abbas, A.C., Zhang, D.Y. (2019) The effect of carbon dioxide emission and the consumption of electrical energy, fossil fuel energy, and renewable energy, on economic performance: evidence from Pakistan. Environmental Science and Pollution Research. 26(21), 21760-21773.
[24] Gong, J., Caldas, C.H. (2010) Computer Vision-Based Video Interpretation Model for Automated Productivity Analysis of Construction Operations. Journal of Computing in Civil Engineering. 24, 252-263.
[25] Huang, X., Zhang, Y., He, M., Li, X., Yang, W., Lu, J. (2021) Asphaltene precipitation and reservoir damage characteristics of CO_2 flooding in different microscopic structure types in tight light oil reservoirs. Fuel. 122943.
[26] Huang, X., Gu, L., Li, S., Du, Y., Liu, Y. (2021) Absolute adsorption of light hydrocarbons on organic-rich shale: An efficient determination method. Fuel. 121998.
[27] Li, Q., Liu, L., Yu, B., Guo, L., Shi, S., Miao, L. (2021) Borehole enlargement rate as a measure of borehole instability in hydrate reservoir and its relationship with drilling mud density. Journal of Petroleum Exploration and Production. 11(3), 1185-1198.
[28] Cecati, C., Citro, C., Piccolo, A., Siano, P. (2011) Smart operation of wind turbines and diesel generators according to economic criteria. IEEE Transactions on Industrial Electronics. 58(10), 4514-4525.

Received: **19.12.2021**
Accepted: **11.02.2022**

CORRESPONDING AUTHOR

Changji Dong
School of Safety Engineering,
Heilongjiang University of Science and Technology,
Harbin 150022 – China

e-mail: 32408019@qq.com

© by PSP Volume 31– No. 05/2022 pages 5271-5280 Fresenius Environmental Bulletin

VITAL ROLE OF RECENT TECHNOLOGIES IN SORTING DIFFERENT SOLID WASTE MATERIALS IN RECYCLING PROCESS

Arun Vasantha Geethan Kathiresan[1], Godwin Barnabas Solomon[2,*], Valai Ganesh Sankararamasubramanian[3], VijayAnanth Suyamburajan[4]

[1]Department of Mechanical Engineering, St. Joseph's Institute of Technology, Chennai, India
[2,3]Department of Mechanical Engineering, Ramco Institute of Technology, Rajapalayam, India
[4]Department of Mechanical Engineering, VELS Institute of Science Technology and Advanced Studies, India

ABSTRACT

This paper aims to highlight the importance of recycling in the present situation. The need of recycling is carried out by analyzing the recycling rate in a globally in a statistical manner using Minitab 19.From the analysis the need to maximize the recycling rate with the support of computer vision approaches such as Pre-trained VGG-16 (VGG16), AlexNet, Support Vector Machine (SVM), K-Nearest Neighbor (KNN) and, Random Forest (RF) and other modern technologies are studied. From the real time studies it was observed that these trained models has accuracy more than 90% compared to the conventional .The computer vision approach is the most efficient way to sort out the recycled materials from the waste collected yard. These trained models and kits has around 400 images database to classify the waste such as plastic, rubber, metal. This sorting model is useful for the local government officials and in the recycling process. Similarly some of the decisions related to check the significance level from the mean values using Minitab 19 statistical software.

KEYWORDS:
Computer Vision, Models, Database, Sorting Model, Accuracy, Decision

INTRODUCTION

Recent study shows that 1.3 billion tons of waste generation s happening every year this would rather rise up by 2.2 billion by 2025.These numbers indicate the importance of addressing the Solid waste issues before it is affecting our environment and ecology system. Waste more it generated that will degrade the natural resources and affects the biological cycle. Due to this uncontrollable rate of solid waste generation that leads to air pollution results in bringing many pulmonary diseases such as asthma. Mainly for the peoples residing nearer to the trash bin areas. Nearly 250 million peoples are suffering from the respiratory and inhalation issues due to the improper solid waste management. Failure in addressing this solid waste issue it becomes the productive land for many flies, mosquitos will cause Dengue, Malaria like fatal diseases [1].

While planning for reducing the impact of solid waste generation it is mandatory to go for automation in waste management with a terminology called smart waste management. This involves closely monitoring the overflow of trash bins and disposing them in a safe manner. Recycling is an innovative method to provide dual benefit in reducing the level of waste generation as well as converting these wastes into useful products. Some sectors are using dumpster robots to sort out these wastes easily without the aid of human beings.

Most important task to be addressed is the waste management whether it is a most economical nation or not, technologically advanced nation or not. The most harmful effects of the solid waste management is the overflow of the trash bins.it leads to spreading of diseases especially during the pandemic season and also it makes the living environment unhealthy and ugly. The key factor is the urbanization and growing population both leads to more solid waste generation in the place where peoples are more accumulated compared to the normal population capacity. In order to eliminate these unhealthy issues and to prepare a clean environment it is mandatory to go for a smart waste management model instead of a conventional mode of waste management system. This smart waste management also paves way for the efficient recycling process in future and reduces the amount of solid waste dumped directly to the landfill site.

When the sorting process is initiated in the waste management using computer vision methods from the image set database to sort metals, plastics, and glass articles. Other biodegradable wastes can be used in other useful forms of fertilizers and manures for regular agricultural activities. On the other hand metal type materials can be recycled and plastics, rubber can be prevented from the dumping to the landfill site which can be clogged to the earth. Similarly glass materials can be melted to form a

decorative articles after thorough cleaning. This paper discusses the role of computer vision, machine learning and artificial intelligence in the efficient and smart waste management for the replacement of humans during the pandemic scenarios [2].

MATERIALS AND METHODS

Analysis of Solid Waste Generation throughout the Globe. In order to know the impact of solid waste generation it is necessary to know the impact of it worldwide that is shown in the Figure.1.This figure shows the waste generate per day throughout the globe across various nation by per capita. From this it is clear U.S, British stands tall among the per day waste generation compared to the Asian nations. Middle East countries contribute 1.5-2.0 Kg/day [3]. All the countries individual contribution in the solid waste generation per day by a citizen is tabulated in Table 1 and it is analyzed with the statistical software Minitab 19.

Analysis of Variance Method: One way ANOVA is used to check the equality in the mean of per capita waste generation in the world by assuming the following conditions

Null hypothesis: All means are equal, Alternative hypothesis: Not all means are equal, Significance level $\alpha = 0.05$.

Standard deviation of Global waste generation Kg/day = 1.32293

Composition of Different Wastes Generated by United States in the Year 2018. US is producing varying results in recycling rate which is higher for the materials like food containers batteries, cardboard and it is lower for the other mode of materials like clothing,food waste and small objects.Many of the recycling firms struggling in improving the recycling rate or simply they don't have any idea I improving or targeting the lower recycling rates. But, US has the chance to improve the recycling rates of lower rates as already discussed which is possible through education and flexible reuse policy [4].The composition of different solid wastes generated in US is shown in the Table 2 and Figure 3.

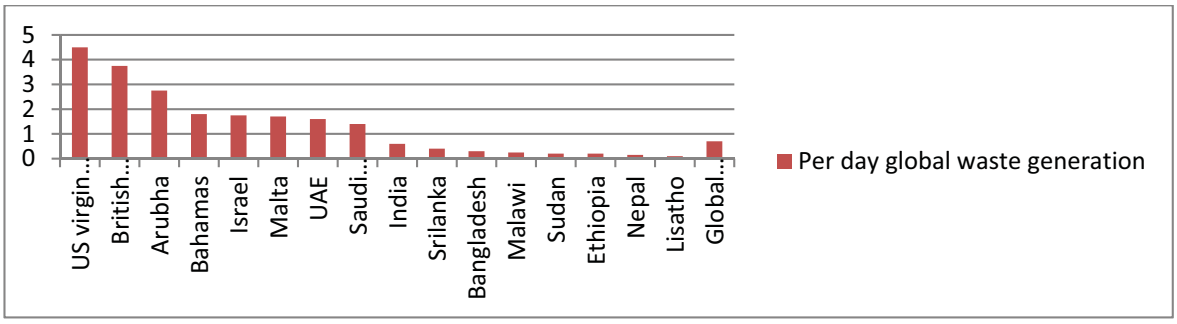

FIGURE 1
Comparison of global waste generation per capita per day in kg (source: http:// datatopics.worldbank.org

FIGURE 2
Interval plot of Global waste generation

TABLE 1
Analysis of Variance for per capita waste generation throughout the globe

Source	DF	Adj SS	Adj MS	F-Value	P-Value
Countries	16	28.00	1.750	*	*
Error	0	*	*		
Total	16	28.00			

Note: From the table 1 the percentage composition of different solid wastes can be calculated using the regression equation is framed

Regression Equation Percentage composition=21.59 + 0.0 Materials_ Food - 17.40 Materials_Glass- 12.83 Materials_ Metals - 20.20 Materials_ Miscellaneous organic wastes - 20.03 Materials_Others + 1.460 Materials_ Paper and paper board - 9.390 Materials_ Plastics - 18.46 Materials_ Rubber and Leather - 15.76 Materials_ Textiles - 15.40 Materials_ Wood - 9.480 Materials_ Yard trimmings (1)

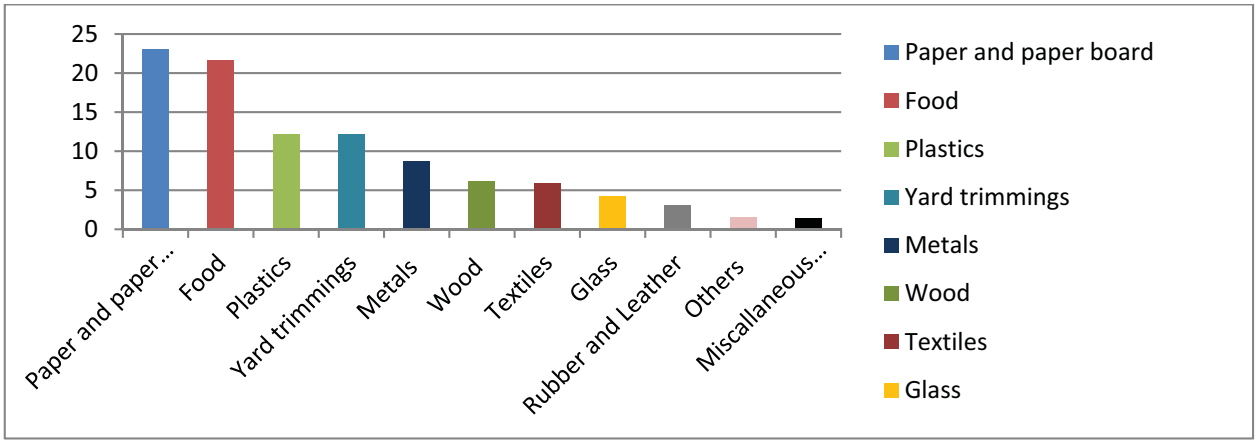

FIGURE 3
Composition of solid waste details

TABLE 2
Percentage composition of different wastes

Materials	Percentage composition
Paper and paper board	23.05
Food	21.59
Plastics	12.2
Yard trimmings	12.11
Metals	8.76
Wood	6.19
Textiles	5.83
Glass	4.19
Rubber and Leather	3.13
Others	1.56
Miscellaneous organic wastes	1.39

TABLE 3
Analysis of Variance for different solid wastes

Source	DF	Adj SS	Adj MS	F-Value	P-Value
Regression	10	564.593	56.46	*	*
Materials	10	564.593	56.46	*	*
Error	0	0.000	*		
Total	10	564.593			

MODERN METHODS AND TECHNOLOGIES USED IN THE SOLID WASTE MANAGEMENT

Use of artificial intelligence in waste management. As discussed earlier in order to increase the efficiency of cleaning process, various techniques such as artificial intelligence, IoT were effectively designed and implemented. Many developed and developing nation has the thought to integrate the smart cities. This approach is easily accessible with the integration of IoT and Data access networks, combinatorial optimization, Geographic Information Systems (GIS) [5].

The need of IoT integrated trash cans identify the trash volume and send it through the servers via internet. The collected data is analysed to develop an optimistic waste management. Developed model is simulated for the Copenhagen, by the analysed data. This innovative system attracted many 3rd parties and yields better results for many smart city plans. This approach needs sensor to send the trash volume in the garbage bins for immediate cleaning of the filled garbage cans and informs well before the garbage bin reaches the maximum volume. Data analysis process is carried out with the help of big data analytics enhanced with cyber systems [6].

Ultrasonic ranging module. This Ultrasonic ranging module senses the amount of garbage level wth the accuracy of 2 to 400mm so it clearly indicates the level of garbage level in the lid. The use of metal detector, temperature sensors and weight sensors to sort out the recyclable, non-recyclable and bio degradable wastes [5].Decision making process in this microcontroller is carried out by Arduino Uno. This set up is enough to transmit data over internet.

Role of AI, optimization techniques RFID tags, and smart dust bins and the loss of ocean creatures due to inefficient waste management: From the data collected through the server statistical analysis were conducted for regular cleaning of the trash cans on a proper timing interval is maintained. This system also prioritize based on the scenarios such as schools, houses, park, offices which has more human interaction compared to the open field areas. Based on the optimization techniques shortest routes for discharging the wastes will be identified which reduces the transportation cost and other expenses. The efficient result obtained from the optimization will be followed by the truck drivers with GPS location services [7,8].Genetic algorithm, travelling salesman problem, linear program are some optimization models used to minimized the transportation distance [9-11].

The other alternate source for the transfer of data is possible via RFID tags and readers. This is the combination of antenna and the embedded microchip with similar serial number to track the person, object. The purpose of the RFID tag is to receive the data and transfer the garbage details through RFID reader. There are two type of RFID tags active and passive tags the role of active tags is transmission of data for longer distance while passive tags is for transmission of data for few meters. The entire setup is to send an alert when the trash can is nearer to reach the maximum level. The role of RFID reader with microchip interface is to enhance the verification process. Every time RFID tag co-ordinates with RFID reader to measure the level of trash in trash can [12, 13].

The piston like structure is useful for the compression of garbage with leaf switch for upside movement by the side hole. Set up is carried out to make this leaf switch level lower than the maximum level. These measures are carried out in this smart bin as a precautionary to avoid the overflow of garbage. This can be avoided by the leaf switch [14].

Landfills are the major reason for the degradation of ocean life especially in the pacific region

TABLE 4
Percentage recycling rates in the United States for various materials.

S.no	Different materials	Percentage composition (%)
1.	Steel (cars)	100
2.	Steel (appliances)	88
3.	Steel (cans)	71
4.	Aluminum (Total)	50
5.	Aluminum (Cans)	67
6.	Paper & Paperboard	69
7.	Newspapers	71
8.	Corrugated cardboard	96.5
9.	Glass bottles & jars	33
10.	Rubber tires	81
11.	Car batteries	99.3
12.	Plastic bottles	28

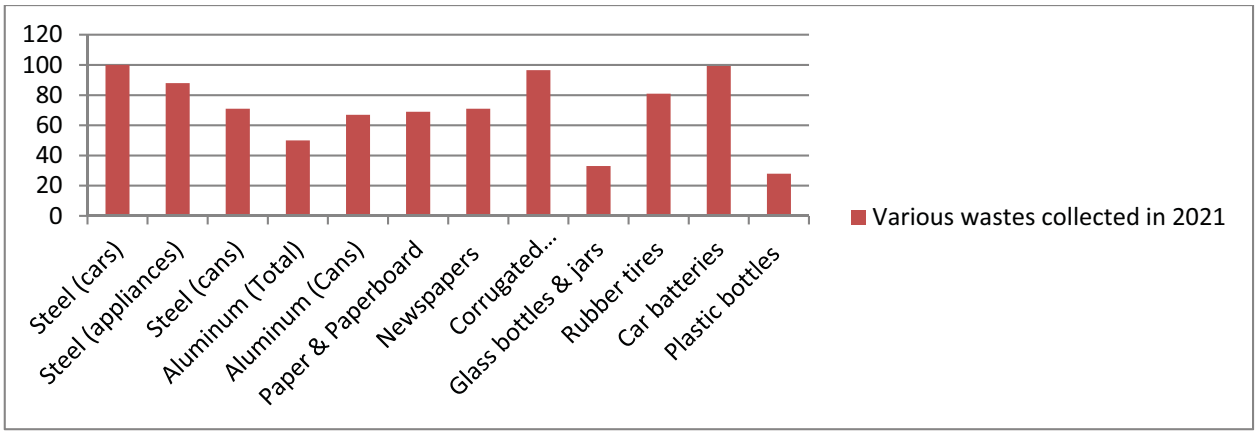

FIGURE 4
Percentage recycling rates in the United States for various materials

TABLE 5
Analysis of Variance for different solid waste materials collected

Source	DF	Adj SS	Adj MS	F-Value	P-Value
Regression	11	6434.87	585.0	*	*
Materials	11	6434.87	585.0	*	*
Error	0	0.00	*		
Total	11	6434.87			

Regression Equation for Percentage composition% =67.00 + 0.0 Materials_ Aluminum (Cans) - 17.00 Materials_ Aluminum(Total) + 32.30 Materials_ Car batteries + 29.50 Materials_ Corrugated cardboard - 34.00 Materials _Glass bottles & jars + 4.000 Materials_ Newspapers+ 2.000 Materials _ Paper & Paperboard - 39.00 Materials _Plastic bottles + 14.00 Materials_ Rubber tires + 21.00 Materials _Steel (appliances) + 4.000 Materials_ Steel (cans) + 33.00 Materials _Steel (cars)

affecting many of the turtle and other huge ocean creations .This dumping wastes play a vital role in the greenhouse gas emission. Many of the industries aims to reduce the wastes in their industry but only minimum amount of nearly 70-75% were reduced. Their measures of reducing these wastes are failed mainly due to the sorting issues. If the plastics are diverted properly from the landfill many millions of oil barrels used for plastic production will be saved. Mainly the sorting issues arise from plastic and glass materials and the there is only a minimum success rate in sorting these specific materials is achieved [15].

RESULTS

Analysis of Recycling Rates in 2021. Minitab19 software is used to analyzed the percentage composition of different solid waste materials to identify the future deposition of various wastes. These data's were provided by the United states for the year 2021[16].

ANALYSIS OF RECYCLING PERCENTAGE IN TOTAL SOLID WASTE PROCESSING IN SOME EUROPEAN COUNTRIES

The Table 6 shows the various waste handling scenarios of some of the European countries from the table it is clear that landfill composition is higher in Romania, Greek, and Slovakia. While the recycling composition is higher for the Germany, Belgium, Sweden, Austria. The incineration rate is found to be higher for Germany, Belgium, and Sweden. The mean and standard deviation of the recycling % is 21.467 and 11.987 which is very low compared to the mean and standard deviation of incineration and higher compared to composting. For incineration the mean and standard deviation is 22.385 and 15.169 whereas for composting the results are 14.929 and 10.344.The landfill composition is very higher compared to the other forms its mean and standard deviation are 45.200 and 32.411 [17].Table.6.shows the different waste treatment modules carried out by major European countries in solid waste management. The recycling rate with mean and standard deviation for the 15 countries is shown in the Figure 4.

TABLE 6
Various waste treatment methods in major European countries

S.no	Country	Landfill (%)	Incineration (%)	Recycling (%)	Composting (%)
1.	Germany	-	37	45	28
2.	Belgium	1	46	32	21
3.	Sweden	1	50	32	17
4.	Austria	3	28	32	37
5.	France	29	32	21	18
6.	United kingdom	37	20	25	18
7.	Italy	39	20	24	17
8.	Czech republic	58	17	22	3
9.	Spain	60	10	10	10
10.	Poland	62	9	7	22
11.	Hungary	63	8	25	4
12.	Bulgaria	70	2	25	3
13.	Slovakia	77	12	3	8
14.	Greek	80	-	17	3
15.	Romania	98	-	2	-

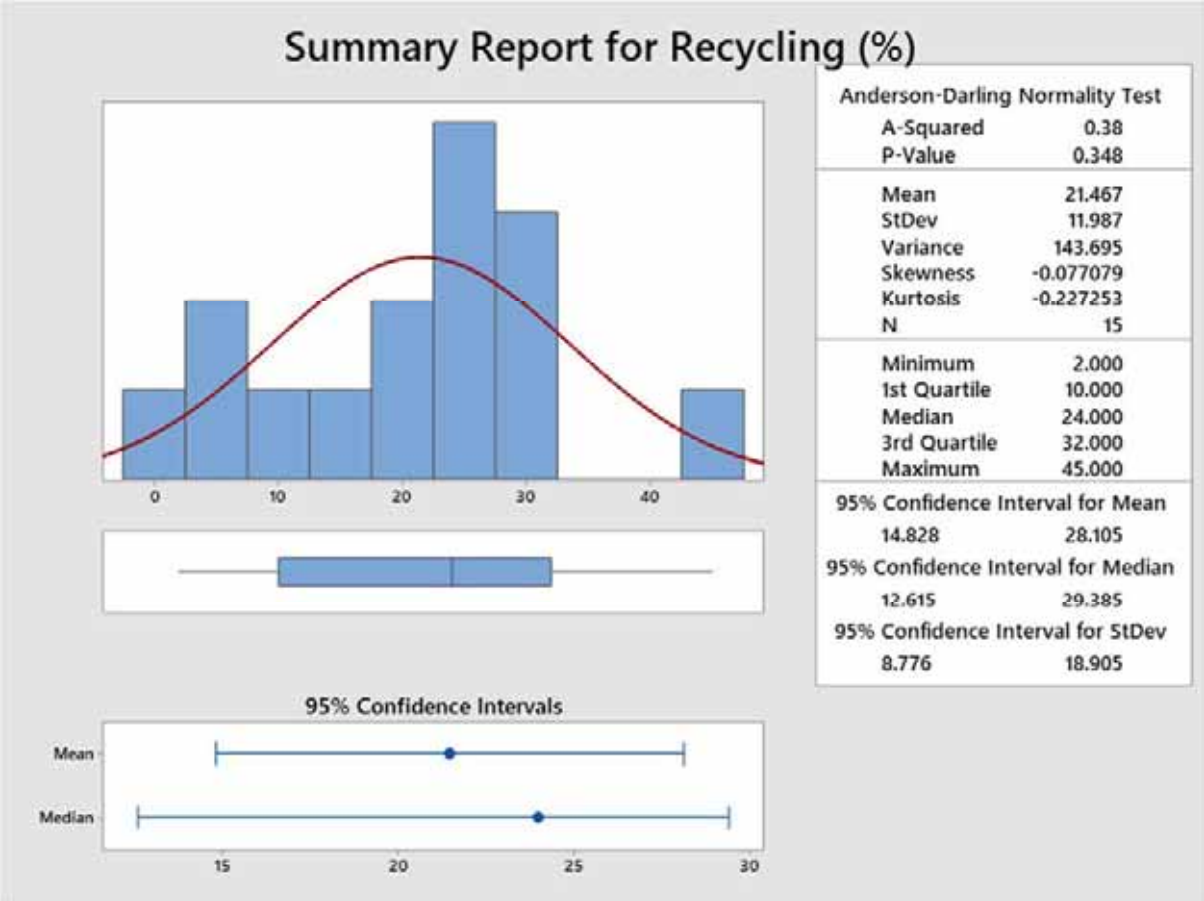

FIGURE 5
Recycling summary for the 15 countries

ANOVA to compare the recycling with landfill. As shown in the Table 6. The various waste treatments with their composition role play in the major European countries is displayed for that significance level from the mean level is verified using one way ANOVA with the following assumptions were carried out to check rate of recycling with the landfill and composting was made that is shown in the Tables 7,8 and Figures 5,6.

Null hypothesis All means are equal, Alternative hypothesis Not all means are equal, Significance levelα = 0.05, Equal variances were assumed for the analysis.

TABLE 7
Analysis of Variance for recycling v landfill

Source	DF	Adj SS	Adj MS	F-Value	P-Value
Landfill (%)	13	2011.73	154.749	*	*
Error	1	0.00	0.000		
Total	14	2011.73			

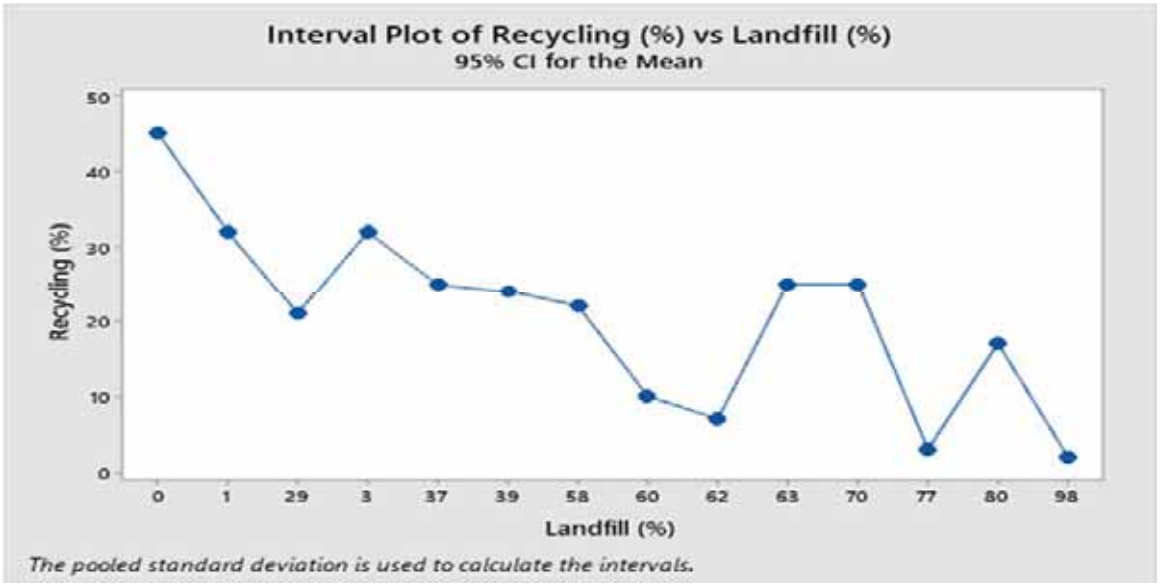

FIGURE 6
Interval plot of recycling (%) v landfill (%) in European countries

TABLE 8
Analysis of Variance for landfill v composting

Source	DF	Adj SS	Adj MS	F-Value	P-Value
Composting (%)	10	1939.07	193.91	10.67	0.018
Error	4	72.67	18.17		
Total	14	2011.73			

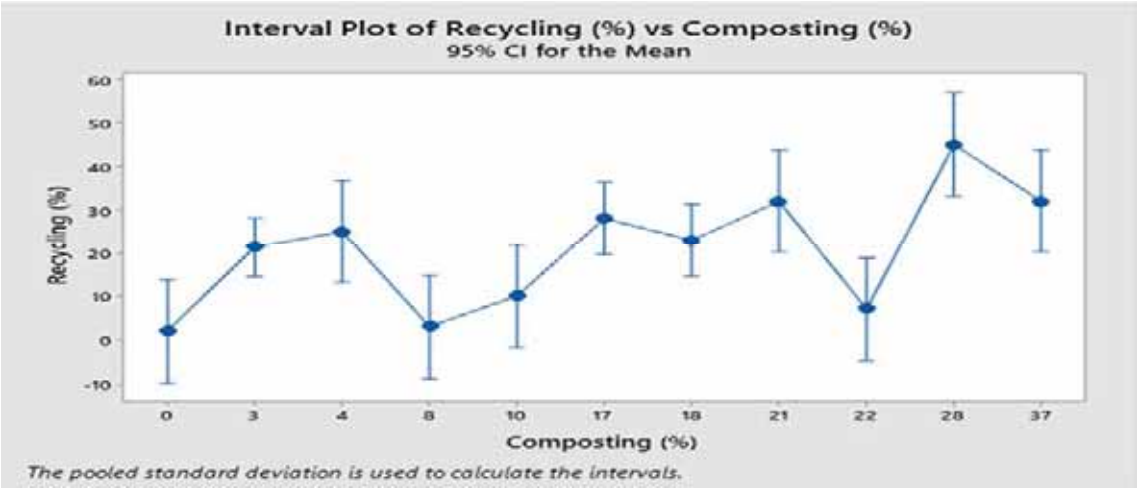

FIGURE 7
Interval plot of recycling v composting

FIGURE 8
Solid waste sorting plant with their key components [17]

ROLE OF AI, MACHINE LEARNING IN SORTING THE DIFFERENT TYPES OF WASTE

Efficient mode of waste management alone won't stop the problems faced by waste generation. That process prevents the people and animals from the harmful effects of waste management issues. Because many of the wastes are occupying the bare lands and oceans. By this process humans life quality and the entire ecosystem is affected. In order to solve this issue these wastes should be sorted out into biodegradable, recyclable and non-recyclable materials. This mode of sorting will improve the soil quality and improve the agriculture production activities. Also the demand for the recyclable materials like plastic, metal, rubber and paper is at its peak. Manual sorting of these unhygienic, unclean materials has serious impact on the human health so, this article discusses some of the cutting edge technologies in sorting out these waste materials for further use in the recycling market.Figure 5 shows solid waste sorting plant with their key components.

Sorting the materials like plastic, rubber, paper, glass and sheet metal will improve the recycling rate and at the same time it prevent dumping of these wastes in landfill. Recent studies shown that machine learning concept called Induction algorithm is useful in segregating different types of waste. This algorithm is helpful in detecting the plastic, glass and metal materials from the huge amount of garbage. It is carried out by high intelligence automation for sorting and recycling. While using these modern technologies it will improve the recycling potential.

Sorting of different types of wastes by trained robots. Robots were trained to recognize and sort out the different wastes. Once the feeding of the robot is over this robots are were trained to sort out different materials such as ferrous metals, non-ferrous materials, paper, cardboard, plastics etc. [18,19]. Feeding of the robot goes for 2 hours/day with the selected material and the test results of the sorting of the 13 different materials is shown in the Figure 8. Analysis of variance for the % purity v Materials with the following assumptions and their respective results are displayed in the Table.9.

Null hypothesis : All means are equal, Alternative hypothesis: Not all means are equal, Significance level $\alpha = 0.05$

Similarly robots are used to classify the HDPE color bottles in that the accuracy of the robot in classifying different bottles .In identifying the different HDPE color bottles the average accuracy of this robot is 85 % and their average precision level is 72.76%.While identifying the green color HDPE bottles its accuracy is 100%.This test run was carried out for 10 times to find out the identification rate of robots [20].

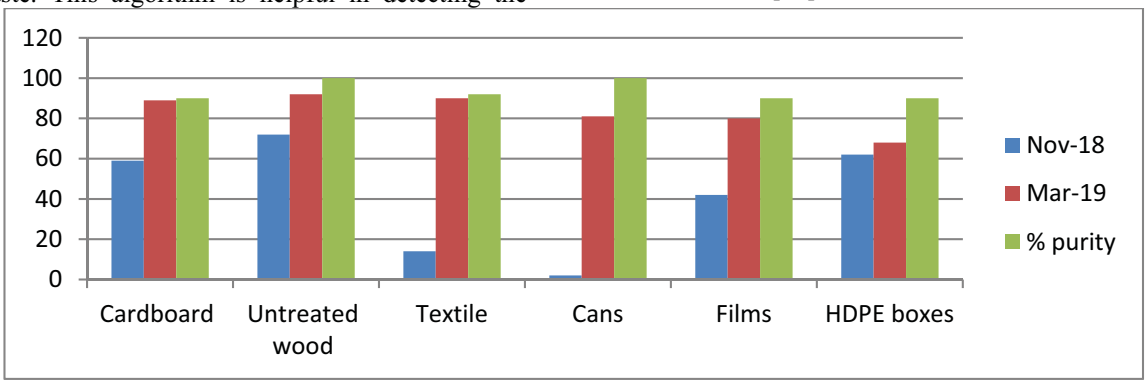

FIGURE 9
Materials sorting using robots during the period Nov-18& Mar-19

TABLE 9
Analysis of Variance for % purity v Materials

Source	DF	Adj SS	Adj MS	F-Value	P-Value
Materials	5	123.3	24.67	*	*
Error	0	*	*		
Total	5	123.3			

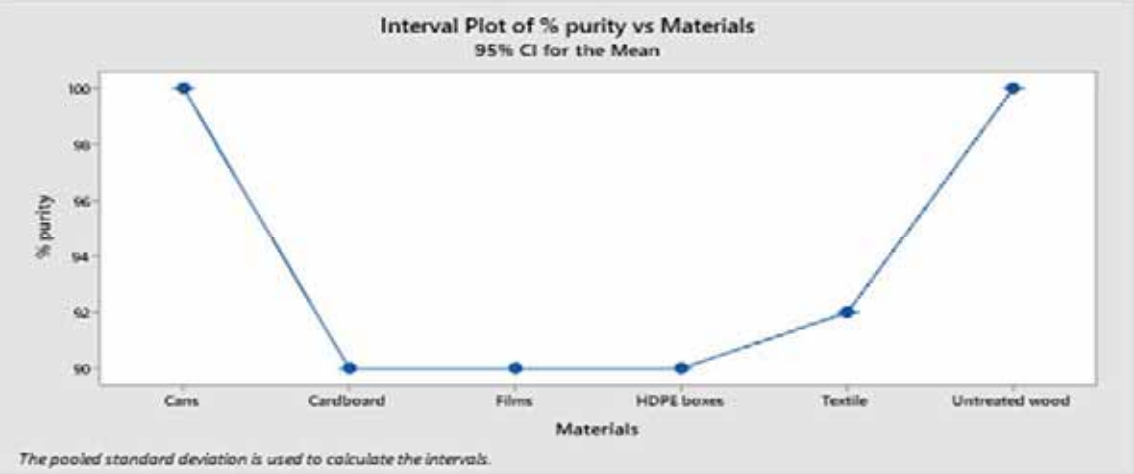

FIGURE 10
Interval plot mapping % purity by the robot v Materials.

CONCLUSION

This work discusses the need to focus on the recycling by reducing the traditional modes of solid waste management. But, without the support of modern methods and technology it is impossible to improve the recycling rate in future. Worldwide analysis about this recycling rate also confirms that only minimum countries are having the regular practice of recycling. The major problem in recycling is sorting out the different wastes during the recycling. Some, of the technologies which supports to the efficient solid waste management and improving the recycling rate in present and future were also discussed. Surely image trained kits, Machine learning (ML), artificial intelligence (AI), Internet of things (IoT) are going to play the key role in the recycling process in the upcoming decades.

REFERENCES

[1] Kumar, N.S., Vuayalakshmi, B., Prarthana, R.J., Shankar, A. (2017) IOT based smart garbage alert system using Arduino UNO. In: IEEE Region 10 Annual International Conference, Proceedings/TENCON.

[2] Gupta, P.K., Shree, V., Hiremath, L., and Rajendran, S. (2019) The Use of Modern Technology in Smart Waste Management and Recycling: Artificial Intelligence and Machine Learning Recent Advances in Computational Intelligence, Studies in Computational Intelligence 823.

[3] Atlas of Sustainable Development Goals (2020) available at http:// data topics. worldbank.org (Accessed date: 20.11.2021)

[4] The State of Recycling Today (2020) available at https://www.rts.com/resources/guides (Accessed date: 20.11.2021)

[5] Gutierrez, J.M., Jensen, M., Henius, M., Riaz, T. (2015) Smart waste collection system based on location intelligence. Procedia Comput. Sci. 61, 120-127

[6] Mitton, N., Papavassiliou, S., Puliafito, A., Trivedi, K.S. (2012) Combining cloud and sensors in a smart city environment. Eurasip. J. Wirel. Commun. Netw. 247, 1-10.

[7] Sinha, T., Kumar, K.M., Saisharan, P. (2015) Smart dustbin. Int. J. Ind. Electron. Electr. Eng. 3(5), 101-104.

[8] Kim, B.-I., Kim, S., Sahoo, S. (2006) Waste collection vehicle routing problem with time windows. Comput. Oper. Res. 33, 3624 – 3642

[9] Petit, J. (2003) Experiments on the minimum linear arrangement problem. J. Exp. Algorithmics (JEA). 8, 1-29.

[10] Rajesh Matai, Surya Singh and Murari Lal Mittal (2010). Traveling Salesman Problem: an Overview of Applications, Formulations, and Solution Approaches, Traveling Salesman Problem, Theory and Applications, Prof. Donald Davendra (Ed.), ISBN: 978-953-307-426-9
[11] López, J.G., Imine, M., Rumín, R.C., Pedersen, J.M., Madsen, O.B. (2008) Multilevel network characterization using regular topologies. Comput. Netw. 52(12), 2344–2359.
[12] Hunt, V.D., Puglia, A., Puglia, M. (2007) RFID-A Guide to Radio Frequency Identification. 978-0-470-10764-5, 1- 240
[13] Ali, M.L., Alam, M., Rahaman, M.A.N.R. (2012) RFID based e-monitoring system for municipal solid waste management. In: 2012 7th International Conference on Electrical and Computer Engineering, ICECE. 2012, 474-477.
[14] Hannan, M.A., Arebey, M., Basri, H., Begum, R.A. (2010) Intelligent solid waste bin monitoring and management system. Aust. J. Basic Appl. Sci. 4(10), 5314-5319.
[15] Torres-García, A., Rodea-Aragón, O., Longoria-Gandara, O., Sánchez-García, F., González-Jiménez, L.E. (2015) Intelligent waste separator. Computacion y Sistemas. 19(3), 487–500.
[16] Recycling (2021) available at https://www.explainthatstuff.com/recycling.html. (Accessed date: 22.11.2021)
[17] Nelles, M., Grünesa, J., Morscheck, G. (2016) International Conference on Solid Waste Management, 5IconSWM 2015 Waste Management in Germany – Development to a Sustainable Circular Economy? Procedia Environmental Sciences. 35 (2016), 6 – 14.
[18] Solid waste management (2020) available at https://www.akfer.com/en/detail-457-solid-waste-manegement. (Accessed date: 22.11. 2021)
[19] The Facts Plastics Europe (2021) available at-https://plasticseurope.org (Accessed date: 22.11.2021)
[20] Barrero, N., Galvis, D., and Martinez, C. (2018) The 9th International Conference on Production Research-Americas 2018 Industrial Robots for Waste Separation Tasks: An Approach to Industry 4.0 in Colombia.

Received: **19.12.2021**
Accepted: **11.02.2022**

CORRESPONDING AUTHOR

Godwin Barnabas Solomon
Department of Mechanical Engineering,
Ramco Institute of Technology,
Rajapalayam,India

e-mail: godwin@ritrjpm.ac.in

© by PSP Volume 31– No. 05/2022 pages 5281-5291 Fresenius Environmental Bulletin

RESEARCH PROGRESS ON THE APPLICATION OF RECEPTOR MODELS IN THE POLLUTION SOURCE APPORTIONMENT OF WATER ENVIRONMENT

Kai Chen[1,2], Yu Liu[1,*], Qimeng Liu[2], Tingting Yang[1,2], Weihua Peng[3], Zitao Wang[4]

[1]State Key Laboratory of Mining Response and Disaster Prevention and Control in Deep Coal Mines, Anhui University of Science & Technology, Anhui 232001, China
[2]School of Earth and Environment, Anhui University of Science & Technology, Anhui 232001, China
[3]Key Laboratory of Mine Water Resource Utilization of Anhui Higher Education Institutes, Anhui 232000, China
[4]Qinghai Institute of Salt Lakes, Chinese Academy of Sciences, Qinghai 810008, China

ABSTRACT

The deteriorating water quality seriously affects human health and social development, accurate identification and quantification of pollutant sources is an important scientific prerequisite for water pollution prevention and remediation. Based on the extensive literature analysis, the basic principles, development history and application characteristics of three major receptor models for water pollution source analysis are summarized, and their similarities and differences in the application of single and combined forms for source analysis of different pollution parameters in various water types (including atmospheric precipitation, river water, lake, reservoir, and groundwater) are analyzed. The results show that the three receptor models have their own advantages and limitations, and where the source discharge inventory is unknown, it is necessary to compare and discuss the apportionment results of multiple models to reduce the uncertainty of the data in order to obtain scientifically valid conclusions. Moreover, the development of hybrid/integrated models should be an important direction for future source apportionment research of water environment.

KEYWORDS:
Water environment, water pollution, source apportionment, APCS-MLR model, Unmix model

INTRODUCTION

Worldwide, the degradation of the water quality caused by human activities has received a great deal of attention from society and governments. Studies have shown that excessive discharges of waste from households, industry and agriculture are the main factors responsible for water pollution [1-2]. Determining the pollution sources in regional water bodies and their contributions is essential for regulators to rationalize the layout of industries and scientifically develop relevant regulations. However, there are many types pollutants in water and it is difficult to identify their sources, which often makes the results difficult to interpret when the research methods are not appropriate, thus the choice of reliable evaluation techniques is important for water resource protection and management [3-5].

The environmental pollution source assessment techniques include qualitative analysis and quantitative analysis, the former mainly uses statistical methods (principal component/factor analysis [3], cluster analysis [4], correlation analysis [5], network analysis [6], etc.) to identify source types, the latter can further quantify the contributions of emission sources. Quantitative methods also include diffusion model and receptor models. The diffusion model method requires detailed information on the emission inventories, meteorological conditions and chemical processes related to pollutants of the study area, and has a relatively limited application and target audience, while receptor models mainly include global optimal regression [7], chemical mass balance [8], absolute principal component score-multiple linear regression (APCS-MLR) [9], positive matrix factorization (PMF) [10] and Unmix [11] models, among which APCS-MLR, PMF and Unmix models do not require priority access to source component spectra and are therefore the most widely used in water body source The APCS-MLR, PMF and Unmix models has been widely applied in the study of pollution source apportionment in water bodies.

Currently, the research progress of receptor models in atmospheric particulate matter [2,12] and soil/sediment [13] source analysis has obtained a lot of attention, but there are relatively few reviews on the application of receptor models in water pollution source analysis. Therefore, this study introduces the technical principles of three receptor models, APCS-MLR, PMF and Unmix, and systematically collates the applications of each model in different water bodies over the past three decades. In addition, the applicability and limitations of each model are summarized, and future directions for the analysis of pollution sources in the water environment are proposed,

with a view to providing a guidance for the protection and management of water resources.

MATERIALS AND METHODS

APCS-MLR model. Since the data prior to principal component analysis/factor analysis are standardised by Z-score method, they could not be used directly to calculate the quantitative contributions of the factors. In 1985, Thurston and Spengler [9] proposed to introduce principal component/factor scores under zero-valued samples to eliminate the effect of standardization (i.e., to obtain absolute principal component/factor scores, APCS, for the samples) and then quantify the source contributions using multiple linear regression (MLR), with the following arithmetic procedure:

$$Z_{ik} = \left(C_{ik} - \overline{C}_i\right) / \sigma_i \quad (1)$$

$$\left(Z_0\right)_i = \left(0 - \overline{C}_l\right) / \sigma_i \quad (2)$$

Eq (1) ~ (2)：Z_{ik} is the standardized value of parameter i on sample k, C_{ik} is the measured concentration of parameter i on sample k, $\overline{C}$ is the mean concentration of parameter i for all samples, σ_i is the standard deviation of parameter i and $(Z_0)_i$ is the absolute zero concentration of parameter i.

$$\left(A_0\right)_j = \sum_{i=1}^{I} W_{ij} * \left(Z_0\right)_i \quad (3)$$

$$APCS_{jk} = \left(A_z\right)_{jk} - \left(A_0\right)_j \quad (4)$$

Eq (3) ~ (4): $(A_0)_j$, $(A_z)_{jk}$ and $(APCS)_{jk}$ are the absolute zero, raw and absolute principal component/factor scores of the samples, respectively.

$$C_i = \left(r_0\right)_i + \sum_{j=1}^{p} r_{ji} * APCS_{ji} \quad (5)$$

Eq (5): Ci is the measured concentration of parameter i，$(r_0)_i$ is the constant term of the equation (represent the total contribution of unknow sources), r_{ji} is the regression coefficient of source j on element i and r_{ji}*$APCS_{ji}$ represents the contribution of source j to the concentration of element i.

The prerequisites for the model are that the data are required to meet KMO and Bartlett's sphericity tests (KMO > 0.5 and p-value < 0.05) and that there should be sufficient degrees of freedom in the model (number of samples > 50 + number of parameters) [9]. In addition, the sources identified through the model may also have a negative contribution to the concentration of the elements, causing confusion when interpreting the source contribution. Therefore, Haji Gholizadeh [14] proposed a method of assigning source contributions by taking absolute values through negative contributions, and this theory was considered reasonable in subsequent applications of the model [15].

PMF model. The PMF model, developed by Paatero and Tapper [10] in the 1990s, first decomposes the sample component concentrations in a dataset into a source spectrum matrix and a source contribution matrix, and then determines the source type and average contribution by analyzing the characteristics of the variables in the different source composition spectra. The principle is as follows:

$$(X)_{n*m} = (G)_{n*p} * (F)_{p*m} + (E)_{n*m} \quad (6)$$

Eq (6): X is a matrix of n rows and m columns, G is the source contribution matrix, F is the source spectrum matrix, E is the residual matrix, and n, m and p represent the number of samples, the number of variables and the number of sources, respectively.

The model excludes the occurrence of negative source contributions under non-negative constraints, while the error is weighted for the uncertainty (U) at each data site, and the minimum value of the objective function Q_{Ture} is found by iterative operations, where information on the G and F matrices is obtained simultaneously, and U and Q_{Ture} can be calculated as:

$$\text{if } x_{ij} \le MDL, U = \frac{5}{6} * MDL \quad (7)$$

$$\text{if } x_{ij} > MDL, U = \sqrt{\left(EF * x_{ij}\right)^2 + (0.5 * MDL)^2} \quad (8)$$

$$Q_{\text{True}} = \sum_{i=1}^{n}\sum_{j=1}^{m}\left(e_{ij} / u_{ij}\right)^2 \quad (9)$$

$$e_{ij} = x_{ij} - \sum_{k=1}^{P} g_{ik} f_{kj} \quad (10)$$

Eq (7) ~ (8): x_{ij} represents the measured concentration of parameter j in sample i, MDL is the method detection limit and EF is the error fraction.

Eq (9) ~ (10): e_{ij} represents the error of the model for the parameter j measured on sample i, U_{ij} represents the uncertainty of the concentration of parameter j in sample i, g_{jk} represents the contribution of source k to sample j and f_{kj} represents the concentration of parameter j in source profile k.

It is important to note that the PMF model requires a subjective input of the number of sources by the researcher, which is dependent on the researcher's knowledge of the environmental conditions in the study area, as the number of sources input is not the same as the number of "actual sources", which can make interpretation of the results difficult. For example, too few sources will result in a mixture of different types of sources. In contrast, "too many sources" will result in a single source being divided into two or even more sources.

Unmix model. The Unmix model was proposed in 2003 by Henry [11], which uses a geometric technique of self-modelling curve resolution to place non-negative constraints on the source contribution, based on the following principle:

$$C_{ij} = \sum_{k}^{N} a_{ik} S_{kj} + E \quad (11)$$

Eq (11): C_{ij} represents the measured concentration of parameter j in sample i, a_{jk} is the mass fraction of parameter j in source k, S_{kj} represents the total amount of parameter j in source k and E is the error of the source composition.

The Unmix model is simple to use relative to other receptor models, but is more sensitive to the data and can fail to work if there are significant differences in concentration between species or too many missing values. In practice, the output information of model is considered reliable if the Min R^2 (the minimum correlation coefficient between the modelled and measured concentrations of the parameter) is above 0.8 and the Min Sig./Noise (the minimum noise to signal ratio) is above 2.

RESULTS AND DISCUSSION

APCS-MLR model. In 1985, Thurston and Spengler [9] proposed the APCS-MLR model for quantifying the contribution of soil, motor vehicle, coal combustion, salt and sulfate aerosols to atmospheric particulate matter in the Boston area of the U.S. Simeonov et al [16] were the first to apply the model to trace the pollution of nutrient indicators and heavy metal elements in the Aliakmon River in northern Greece. Thereafter, Zhou et al [17] quantified the effects of soil weathering, organic pollution, mineral pollution and agricultural runoff on offshore water quality in the eastern part of Hong Kong in different spatial and temporal scales through the APCS-MLR model, and the results were supported by cluster analysis and GIS method. Yang et al [18] showed that domestic sewage, industrial wastewater and agricultural activities were the main sources of surface water pollution in the urban, suburban and rural areas of the Wenrui River Basin, respectively.

TABLE 1
Summary of information for water source apportionment based on APCS- MLR model

Types	Indicated factors	Apportioned sources	Year [Ref]
A	PI, BOD_5, NH_3-N, COD, TP, Hg, Zn, Se, As and oil	domestic and industrial wastewater, agricultural non-point source, coal fired and vehicle emission	2016[19]
E	pH, EC, TH, TDS, F^-, NO_3^-, Fe and major ions	water-rock interactions, Industrial wastewater infiltration	2016[34]
B	pH, EC, COD, BOD_5, Trub, NH_3-N, NO_3^- and TN	agricultural non-point sources, water biochemical factors, organic pollution	2016[30]
D	TDS, Fe, Mn, NH_4^+, NO_3^-, NO_2^-, F^-, PO_43^-, COD, CN^- and major ions	leaching migration process, application of pesticide and fertilizer, geological environmental factors, industrial activities	2017[35]
D	TDS, TH, COD, NH_4^+, NO_3^-, NO_2^-, F^-, Fe, Mn and major ions	water-rock interactions, fertilizer, domestic and industrial wastewater	2018[37]
E	BOD, Chl-a, DO, E.coli, NO_3-N, NO_2-N, TN, PO_4-P, SiO_3-Si, SS, TP and UIA-N	domestic and industrial wastewater, agricultural and livestock pollution, surface runoff, river pollution inputs	2019[38]
C	pH, TW, DO, SDO, COD_{Mn}, COD_{Cr}, BOD_5, NH_3-N, TP, TN, TS and Chl-a	urban domestic source, agricultural and urban no-point sources	2020[32]
A	pH, EC, WT, DO, COD_{Mn}, BOD, NH_3-N, COD, TN, TP, AS and heavy metals	meteorological, mineral, natural, agricultural and grassland salt sources	2020[24]
A	T, DO, COD_{Mn}, COD, BOD_5, NH_3-N, TN, TP, F, As and F.coli	industrial wastewater, urban sewage sources, meteorological factors, atmospheric deposition and agricultural sources	2020[27]
A	pH, EC, TN, F^-, COD_{Mn}, SF, TP, BOD_5, DO, COD_{Cr}, WT, NH_3-N, Chl-a, LAS and E.coli	agricultural source, seasonal effect, septic tank leakage, industrial and domestic sewage	2020[26]
A&C	Phosphorus fractions	industrial and domestic sewage, pesticide and fertilizer, river input, biodegradation	2021[21]
A	pH, DO, EC, COD_{Mn}, BOD_5, COD, TW, F^-, LAS, NH_3-N, FC, TN and TP	urban runoff, environmental background, rural, livestock and planting sources	2021[28]
A	pH, DO, TP, NH_3-N, COD_{Mn}, BOD and oil	urban sewage discharge, meteorological and industrial production sources	2021[29]
D	TDS, TH, COD_{Mn}, FC, NH_3-N, F^-, NO_3^-, Fe, Mn and major ions	domestic and industrial pollution, geological environment and agricultural source	2021[36]

Note: A, B, C, D and E represent river water, reservoir water, lake water, groundwater, and sea water, respectively.

Recently, Yang et al [19] used heavy metals as indicators in the Xi'an-Xianyang section of the Weihe River and found that domestic sewage, industrial wastewater and atmospheric dust were the main factors of pollution, and then used APCS-MLR model to calculate the contributions of the factors to each water quality parameter during the wet and dry seasons, respectively. Ates et al [20] conducted a similar study in Lake Sabanka, Turkey, and the results showed that the model was an effective tool for pollution assessment of toxic metals and physicochemical indicators in lakes. In combination with correlation analysis and APCS-MLR model, Bay et al [21] identified that phosphorus in surface water and sediments in the Nanhai wetlands of Inner Mongolia originated from industrial wastewater and domestic sewage (29.07%), pesticides and fertilizers (29%) and degradation of plant and animal residues (18.49%). The APCS-MLR model has been widely applied for pollution assessment of surface waters (e.g. rivers [16,22-29], reservoirs [30] and lakes [31,32]) in different countries, as summarized in Table 1.

As for groundwater, Zhang et al [33] calculated the contribution of industrial wastewater to DO, NO_2^-, Mn and Fe concentrations in groundwater in the Hutuo River alluvial floodplain fan area in the range of 37.13% to 81.92% based on APCS-MLR model. After exclude the influence of agricultural factors, Gulgundi and Shetty [34] attributed high concentrations of NO_3^-, Cl^- and SO_4^{2-} in groundwater in the Bangalore region of India to recharge from septic tanks and industrial effluents, and further quantified their contributions to groundwater quality. In the Hun River floodplain fan area of Shenyang City, a typical industrial base in Northeast China, Meng et al [35] derived the contribution of dissolution-filtration process, agricultural activities, geological background and industrial activities to groundwater based on the APCS-MLR model to be 34.21%, 20.13%, 13.39% and 8.97%, respectively, with a cumulative contribution of 76.7%. Similarly, Zhang et al [36] identified four potential contamination factors for shallow groundwater in southwest

TABLE 2
Summary of information for water source apportionment based on PMF model

Types	Indicated factors	Apportioned sources	Year [Ref]
B	K^+, Ca^{2+}, heavy metals	Geological background, tanning, paint, municipal sewage, textiles, agricultural activities	2015[58]
B	COD, BOD_5, NO_3-N, NO_2-N, NH_3-N, As, Pb, oil and VPs	industrial (oil, ammonia, metals, coking and coal) and agricultural sources, composite wastewater	2015[59]
B	polycyclic aromatic hydrocarbons (PAHs)	biomass and coal combustion sources, petroleum, transportation, and coke sources	2016[45]
A	NH_4^+, NO_3^- and major ions	water splashing, weathering, fossil fuel burning, ocean release	2016[39]
A	NH_4^+, NO_3^-, Organic acids and major ions	biological, soil and marine sources, fossil fuels and wood burning, agricultural waste	2016[42]
A	F^-, NH_4^+, NO_3^- and major ions	coal combustion, soil, marine sources, secondary pollution sources	2017[40]
B	heavy metals	metal plating, plastic manufacturing and semiconductor packaging industry	2017[60]
B	PAHs	coke and coal burning, oil sources, vehicle emissions	2017[46]
A	heavy metals	iron and steel metallurgy, ground dust, coal burning, motor vehicles	2018[41]
B&C	PAHs	gasoline and coal combustion, coke source	2019[47]
B&D	As, Fe, Mn, O_2, P-tot, NH_4^+, NO_3^- and major ions	irrigation effects, reduction, water-rock interactions, agricultural activities	2019[61]
E	EDCs	industrial effluents, river inputs, domestic and farming effluents	2020[52]
B	pH, T, DO, COD_{Mn}, COD, BOD, Zn, TN, TP, F^-,NH_4^+-N	municipal and industrial wastewater, sewage non-point source, enterprise discharge	2021[53]
B&D	TDS, NO_3^-, Si and major ions	silicate weathering, halite and carbonate dissolution, agricultural input	2021[51]
B	DO, T, EC, TSS, BOD, COD, TP, TN and Chl-a	sewage input, agricultural and aquaculture non-point sources, organic pollution sources	2021[62]
C	PAHs	biomass burning, coal burning, vehicle emissions	2021[48]

Note: A, B, C, D and E represent rain water, river water, lake water, groundwater, and sea water, respectively.

China: leaching enrichment–infiltration of urban sewage, geological factor, industrial wastewater and agricultural input, with contributions of 42%, 17.83%, 13.74% and 6.78% in that order.

PMF model. Compared to the APCS-MLR model, the PMF model has been more widely applied to the sources of conventional ions [39,40], dissolved heavy metals [41] and many organic acids [42] in precipitation and water-soluble ions in atmospheric $PM_{2.5}$ [43] and PM_{10} [44] (Table 2). Meanwhile, a large number of studies have concluded that the PMF model is an effective tool of quantifying the sources of polycyclic aromatic hydrocarbons (PAHs) in different waterdodies, including river [45-47], lake [48] and groundwater [49,50]. Wang et al [45] quantified the sources of 16 PAHs in the Yangtze River basin, China based on the relationships of IcdP/(IcdP+BghiP), BaA/(BaA+Chr) and Flo/(Flo+Pyr), and further calculated the contributions of mixed biomass and coal combustion sources, coke source, petroleum source and transportation source in the order of 40.1%, 22.8%, 19.6% and 17.5% by PMF model, and similar studies were carried out in Jiangsu province [46], Ningxia Hui Autonomous Region [47], Anhui province [48] and Shanxi province [49], China.However, Liu and Han [51] compared the results of isotope inversion model and PMF model on the application of surface water pollution sources in a typical agricultural watershed in eastern Thailand and confirmed that PMF models are not applicable to the traceability of riverine sulphate. Lu et al. (2020) [52] first used PMF model to quantify the sources of endocrine disruptors (EDCs) in coastal waters of eastern China. Ma et al [53] analyzed pollutant concentrations in several rivers of the Qinhuai River basin using PMF model combined with stable isotopes mixing (SIAR) model, which better quantified the contribution of each source to the three sub-basin areas.

In the study of special pollutants in groundwater, Trinh et al [54] showed that 56% of poly brominated diphenyl ethers (PBDEs) in groundwater in Taiwan, China, were derived from anaerobic microbial debromination. Capozzi et al [55] systematically analysed the concentration of chlorinated benzene and its geochemical behaviour in groundwater of New Jersey, USA, and the results showed that the PMF model is a good indicator of the chlorinated benzene dechlorination process. In Indian, Pervez et al [56] analyzed the sources of toxic elements in groundwater in the Basta region based on the PMF model, and the results showed that the contributions of rock weathering, soil erosion and agricultural activities were 41.26%, 35.97% and 20.76% respectively, and This interpretation is consistent with earlier findings obtained by the team [57].

Unmix model. The Unmix model was developed later compared to the APCS-MLR model and PMF model, but has been applied more maturely for pollution assessment of $PM_{2.5}$ [63] and PM_{10} [64] in the atmosphere, and heavy elemental metals [65] and PAHs [66] in soil and sediment.

In respect of environmental pollution assessment in water (Table 3), an earlier approach based on factor analysis combined with the Unmix model by Huang et al (2007) [67] quantified the contributions of industrial wastewater, agricultural activities, and urban runoff to pollutants such as ammonia nitrogen, hexavalent chromium, petroleum species and lead in the Qiantang River, Zhejiang Province, China. Yin et al [68] used Unmix model for the first time to trace

TABLE 3
Summary of information for water source apportionment based on Unmix model

Types	Indicated factors	Apportioned sources	Year [Ref]
B	NH_3-N, F^-, COD_{Mn}, Cr^{6+}, BOD_5, TCd, TP, TPb and oil	geological sources, smelters and electroplating plants, urban runoff, agricultural and industrial effluents	2010[67]
A	NH_4^+, NO_3^- and major ions	coal and biomass burning sources, marine and secondary pollution sources	2016[68]
C	major ions and TDS	dissolution of carbonates, chlorates, sulfates and silicates	2016[69]
C	major ions	weathering and dissolution of feldspar and mafic minerals	2018[71]
C	major ions	silicate weathering, evaporative salts dissolution	2019[70]
C	NO_3^-,F^- and major ions	fertilizers and pesticides, weathering of silicate minerals, dissolution of chlorine salts and sulfates	2020[72]
B	PFASs	firefighting foam/fluoropolymer processing agent, electrolytic fluorination	2020[73]

Note: A, B and C represent rain water, river water and groundwater, respectively.

inorganic ions in rainfall in Los Angeles, USA, and the results showed that the contributions from secondary sources, marine transport sources and coal combustion and biomass burning sources were 50%, 43% and 7%, respectively, and this source apportionment result was similar to the sources of atmospheric particulate matter in the study area, indicating that the validity of the Unmix model. Sun [69-70] applied the Unmix model to explore the sources of major ions in groundwater from the Huabei coalfield, China, and further determined the source of mine inrush-water based on the differences in the contributions of different sources to each groundwater samples from different aquifers. Nagaraju et al [71] and Subba Rao et al [72] analyzed the driving mechanisms of major ios in groundwater with high fluoride concentrations in the Chittoor and Wanaparthy regions of southern India, and such studies showed that ion concentrations in deep groundwater are mainly controlled by water-rock interactions, such as weathering of silicate minerals and dissolution of carbonate and sulphate minerals.

In addition, Li et al [73] used Unmix and CBM models to discuss the sources of 26 emerging and legacy poly/perfluoroalkyl substances (PFASs) in surface waters of the Haihe River Basin, and their finding showed that fire-fighting foam/fluoropolymer processing aids (36.6%) were the dominant source. In recent years, although the Unmix model has been gradually introduced into pollution assessment studies of the water environment, more studies are still needed to further confirm its reliability.

Comparison of model applications. Generally, the three models have different computational processes, and therefore the source profiles of different models usually show some degree of variation for the same dataset (Table 4). In recent years, several scholars have applied two and more models to evaluate the pollution levels of different types of water bodies, and then compared in depth the similarities and differences in the results of the different models. Haji Gholizade et al [14] showed that although both APCS-MLR and PMF models obtained three major sources (discharge of agriculture waste and domestic and industrial wastewater) of river water contamination in southern Florida, USA, there were significant differences in source contributions, and for most parameters, the APCS-MLR had a better fit (R^2) compared to the PMF model, therefore this study concluded that the APCS-MLR approach to be more physically plausible. Chen et al [77] showed that the APCS-MLR and PMF models obtained approximately the same results when applied to quantify the contributions of groundwater pollution sources in the Lalin River basin, China. However, Liu et al [75] analyzed a variety of pollutants in Taihu Lake, Jiangsu Province, China, and calculated E/O values (Estimated/Observed value) ranging from 1.000 to 2.186 and 0.954 to 1.529 for the APCS-MLR and PMF models, respectively, based on the quasi-estimate that the closer the E/O value is to 1, the better the

TABLE 4
Summary of information for water source apportionment based on mixed model

Types	Indicated factors	Methods	Apportioned sources	Year [Ref]
A	Chl-, DO, TKN, TP, TN, AN, T, TSS, Turb and major cations	1 & 3	agriculture waste, domestic and industrial wastewater, seasonal factor	2016[14]
D	pH, TDS, SO_4^{2-}, Cl^-, NO_3^-, Fe, Mn, As, Ba and Ni	1 & 3	agriculture source, geological source, industrial source, natural source	2019[77]
D	pH, Turb, TDS, NO_3^-, F^-, TH, NH_3^-, S^-, major ions and heavy metals	2 & 3	electroplating, phosphating, sewage, industrial and nature source	2019[78]
B	BOD_5, COD, TSS, TP, TN, Cl^-, Cr, Cu and Pb	1 & 3	soil erosion, urban runoff, sewer leaking, vehicle emission	2019[74]
A	organophosphate esters (OPEs)	1 & 2 & 3	rigid and flexible polyurethane foam/coating, cellulosic/acrylic/vinyl polymer/unsaturated polyester, and polyvinyl chloride	2020[76]
D	TDS, Eh, NH_4^+, NO_2^-, NO_3^-, Fe, Mn and major ions	1 & 3	geogenic process, agricultural activities, natural source, domestic pollution, industrial source	2020[15]
C	pH, T, DO, SS, EC, TN, SO_4^{2-}, NO_3-N, NO_2-N, NH_3-N, TP, PO_4^{3-}, Chl-a, COD_{Mn}, BOD_5 and Cl^-	1 & 3	agriculture source, domestic sewage, industrial wastewater, atmospheric deposition, phytoplankton growth, rainfall or wind disturbance	2020[75]
D	pH, TDS, Eh, F^-, NO_3^-, NO_2^- and major ions	1 & 3	geogenic process, coal-fired, agriculture source, urbanization	2021[79]

Note: A, B, C and D represent river water, surface runoff water, lake water and groundwater, respectively. 1, 2 and 3 represent the APCS-MLR, Unmix and PMF models, respectively.

model resolution is. The study concluded that the PMF model is more suitable for water quality assessment in lakes. Similarly, Zhang et al [15] and Li et al [79] obtained similar conclusions in their quantification of the contribution of groundwater pollution sources in the Chengdu Plain and Tongchuan City, Shaanxi.

Gulgundi and Shetty [78] explained the differences in the application of the Unmix and PMF models in a groundwater pollution assessment study in southern India, where the PMF identified seven potential sources: natural factors, electroplating industry, phosphating, wastewater, geological factors, steel industry and paint industry. Although the strong sensitivity of the Unmix model makes it difficult to separate the industrial sources of steel and paint, the two models each have advantages and disadvantages in terms of E/O values and R^2 for different parameters, so this study suggests that a deeper understanding of the similarities and differences between the two models could lead to more scientific results. Qi et al [76] identified three sources of organophosphate esters (OPEs) in inflow rivers to the Bohai sea in eastern China based on three receptor models: polyurethane foam/coating, cellulose/acrylic/ethylene polymer/unsaturated polyester and polyvinyl chloride, but there were differences in the contribution rates obtained from different models for these three sources, but there were differences in the contribution rates obtained from different models for these three sources, with the APCS-MLR model calculated 49.9%, 29.7% and 20.5% for the three sources, while 57.9%, 28.6% and 13.5% obtained by PMF model and 47.9%, 30.8% and 22.4% obtained by Unmix model, respectively.

CONCLUSIONS

APCS-MLR, PMF and Unmix are the three commonly used receptor models for source apportionment of water pollution. This study systematically reviews the application of single and combined forms of the three models to the traceability of multiple contaminants in surface water or groundwater. The results show that the different receptor models have their own unique advantages, but also have their own limitations, mainly in the following aspects:

(1) The APCS-MLR model performs analysis directly on the dataset but does not consider the uncertainty of the data, resulting in a high contribution of unknown factors or sources.

(2) The PMF model improves analytical tolerance by introducing errors in parameter concentrations, but requires multiple runs to obtain the correct number of sources, while this model is prone to producing fingerprint spectral information that is difficult to interpret relative to the other two models.

(3) The Unmix model is more stable, but is sensitive to missing values and outliers in the dataset, sometimes requiring the elimination of one or even more variables to obtain valid parsing results, and it is often difficult to separate covariates and similar sources.

Therefore, there is no definitive answer as to which model is most appropriate for source analysis of water bodies, but it is certain that the results of each model vary depending on the parameters (or pollutants) chosen. In addition, each model relies on the source profile to infer the source types, which needs to be carefully analyzed in the context of the study area to make the results more reasonable and meaningful. In the study of source apportionment in the water environment, the analysis results of multiple models should be compared and discussed to reduce the uncertainty of the data and make the final interpretation fit the actual local situation. At the same time, referring to the pollutant quantification methods for atmospheric particulate matter and soil or sediment, combining the advantages of traditional receptor and dispersion models, and actively developing new hybrid and integrated models is an important development trend for future research on water pollution assessment.

ACKNOWLEDGEMENTS

This work was financially supported by the 2021 Graduate Science Research Projects in Anhui Higher Education Institutions (Grant No. YJS20210375); Natural Science Foundation of Anhui Province(1908085ME145); Natural Science Research Project of Universities in Anhui Province (KJ2020ZD64).

Declaration of Competing Interest. The authors declare that they have no known competing financial interests or personal relationships that could have appeared to influence the work reported in this paper.

REFERENCES

[1] Ministry of Ecological Environment of China (MEEC) (2021) State of the Ecological Environment Bulletin of China. Ministry of Ecological Environment of China, Beijing (In Chinese).
[2] Zhang, Y.J., Zheng, M., Cai, J., Yan, C., Hu, Y., Russell, A.G., Wang, X., Wang, S., Zhang, Y. (2015) Comparison and overview of $PM_{2.5}$ source apportionment methods. Chinese Science Bulletin. 60(2), 109-121.

[3] Hu, J., Long, Y., Zhou, W., Zhu, C., Yang, Q. (2020) Influence of different land use types on hydrochemistry and heavy metals in surface water in the lakeshore zone of the Caohai wetland, China. Environmental Pollution. 267, 115454.
[4] Yang, J., Holbach, A., Wilhelms, A., Krieg, J., Qin, Y., Zheng, B., Zou, H., Qin, B., Zhu, G., Wu, T., Norra, T. (2020) Identifying spatio-temporal dynamics of trace metals in shallow eutrophic lakes on the basis of a case study in Lake Taihu, China. Environmental Pollution. 264, 114802.
[5] Maitra, A., Keesari, T., Roy, A., Gupta, S. (2020) Fluoride contamination in and around selected geothermal sites in Odisha, Eastern India: assessment of ionic relations, fluoride exposure and remediation. Environmental Science and Pollution Research. 28, 18553–18566.
[6] Liu, L., Wang, Z., Ju, F., Zhang, T. (2015) Co-occurrence correlations of heavy metals in sediments revealed using network analysis. Chemosphere. 119, 1305–1313.
[7] Wu, W. (2016) Hydrochemistry of inland rivers in the north Tibetan Plateau: Constraints and weathering rate estimation. Science of The Total Environment. 541, 468–482.
[8] Liu, L., Zou, C. (2013) Research on source apportionment of atmospheric particulates by coupling the model of CBM and PMF. Journal of Chengdu University of Information Technology. 28(5), 557–562. (in Chinese)
[9] Thurston, G.D., Spengler, J.D. (1985) A quantitative assessment of source contributions to inhalable particulate matter pollution in metropolitan Boston. Atmospheric Environment. 19(1), 9–25.
[10] Paatero, P., Tapper, U. (1994) Positive matrix factorization: A non-negative factor model with optimal utilization of error estimates of data values. Environmetrics. 5(2), 111–126.
[11] Henry, R.C. (2003) Multivariate receptor modeling by N-dimensional edge detection. Chemometrics and Intelligent Laboratory Systems. 65(2), 179–189.
[12] Wang, Z., Li, Y.B., Guo, L., Song, Z., Xu, Y., Wang, F., Liang, W., Shi, G., Feng, Y. (2021) $PM_{2.5}$ source apportionment based on a variety of new receptor models. Environmental Science. 43(2), 608–618.
[13] Liu, C., Tian, F., Chen, J., Li, X., Qiao, X. (2010) A comparative study on source apportionment of polycyclic aromatic hydrocarbons in sediments of the Daliao River, China: Positive matrix factorization and factor analysis with non-negative constraints. Chinese Science Bulletin. 55, 915–920.
[14] Haji Gholizadeh, M., Melesse, A.M., Reddi, L. (2016) Water quality assessment and apportionment of pollution sources using APCS-MLR and PMF receptor modeling techniques in three major rivers of South Florida. Science of The Total Environment. 566–567, 1552–1567.
[15] Zhang, H., Cheng, S., Li, H., Fu, K., Xu, Y. (2020) Groundwater pollution source identification and apportionment using PMF and PCA-APCA-MLR receptor models in a typical mixed land-use area in Southwestern China. Science of The Total Environment. 741, 140383.
[16] Simeonov, V., Stratis, J.A., Samara, C., Zachariadis, G., Voutsa, D., Anthemidis, A., Sofoniou, M., Kouimtzis, T. (2003) Assessment of the surface water quality in Northern Greece. Water Research. 37(17), 4119–4124.
[17] Zhou, F., Huang, G.H., Guo, H., Zhang, W., Hao, Z. (2007) Spatio-temporal patterns and source apportionment of coastal water pollution in eastern Hong Kong. Water Research. 41(15), 3429–3439.
[18] Yang, L., Mei, K., Liu, X., Wu, L., Zhang, M., Xu, J., Wang, F. (2013) Spatial distribution and source apportionment of water pollution in different administrative zones of Wen-Rui-Tang (WRT) river watershed, China. Environmental Science and Pollution Research. 20(8), 5341–5352.
[19] Yang, X., Wang, L, Guan, J., Duan, J. (2016) Comprehensive assessment of water quality in Xi'an-Xianyang section of Weihe River based on multivariate analysis method. Chinese Journal of Environmental Engineering. 10(3), 1560–1565.
[20] Ateş, A., Demirel, H., Köklü, R., Dogruparmak, S.C., Altundag, H., Sengorur, B. (2020) Seasonal source apportionment of heavy metals and physicochemical parameters: A case study of Sapanca Lake watershed. Journal of Spectroscopy. 2020, 1–11.
[21] Bai, Y., Qian, C., Yuan, S., Xie, Z., Lai, L., Zhang, M., Liu, Y., Miao, C. (2021) Phosphorus fractions and quantitative identification of pollution sources in Nanhai wetland, Baotou. Environmental Science. 42(9), 4275–4286.
[22] Zhao, J., Xu, Z., Liu, X., Niu, C. (2013) Source apportionment in the Liao River Basin. China Environmental Science. 33(5), 838–842.
[23] Zheng, Q., Su, W., Yang, Z., Long, H., Zhou, F., Liu, Z. (2019) Assessment of water environmental quality and analysis of pollution source in Wujiang River Basin. Research of Soil and Water Conservation. 26(3), 204–212.
[24] Cheng, G., Wang, M., Chen, Y., Gao, W. (2020) Source apportionment of water pollutants in the upstream of Yangtze River using APCS–MLR. Environmental Geochemistry and Health. 42(11), 3795–3810.

[25] Fu, D., Wu, X., Chen, Y., Yi, Z. (2020) Spatial variation and source apportionment of surface water pollution in the Tuo River, China, using multivariate statistical techniques. Environmental Monitoring and Assessment. 192(12), 745.
[26] Zhang, H., Li, H., Yu, H., Cheng, S. (2020) Water quality assessment and pollution source apportionment using multi-statistic and APCS-MLR modeling techniques in Min River Basin, China. Environmental Science and Pollution Research. 27(33), 41987–42000.
[27] Qin, G., Liu, J., Xu, S., Wang, T. (2020) Water quality assessment and pollution source apportionment in a highly regulated river of Northeast China. Environmental Monitoring and Assessment. 192(7), 446.
[28] Hou, X., Zhang, K., Duan, P., Wang, X., Ta, L., Guo, Y., Xia, R. (2021) Pollution source apportionment of Tuohe River based on absolute principal component score-multiple linear regression. Research of Environmental Sciences. 34(10), 2350–2357.
[29] Li, Y., Liu, J., Qin, G., Tian, J. (2021) Water quality evolution characteristics and pollution source analysis in Huntai river basin. China Rural Water and Hydropower. 8, 14-17.
[30] Zeng, Q., Qin, L., Cheng, P., Li, X., Jia, D. (2016) Spatial and temporal distribution of main aquatic environment factors in Miyun Reservoir, Beijing since 1990s. Journal of Lake Sciences. 28(6), 1204–1216.
[31] Liu, Y., Guo, H., Yang, P. (2010) Exploring the influence of lake water chemistry on chlorophyll a: A multivariate statistical model analysis. Ecological Modelling. 221(4), 681–688.
[32] Du, Z., Wang, M., Yan, Z., Gao, W. (2020) Pollution source apportionment of Lake Dianchi based on absolute principal component score-multiple linear regression. Acta Scientiae Circumstantiae. 40(3), 1130-1137.
[33] Zhang, Q., Wang, H., Wang, Y., Yang, M., Zhu, L. (2017) Groundwater quality assessment and pollution source apportionment in an intensely exploited region of northern China. Environmental Science and Pollution Research. 24(20), 16639–16650.
[34] Gulgundi, M.S., Shetty, A. (2016) Identification and apportionment of pollution sources to groundwater quality. Environmental Processes. 3(2), 451–461.
[35] Meng, L., Zuo, R., Wang, J., Yang, J., Teng, Y., Zhai, Y., Shi, R. (2017) Quantitative source apportionment of groundwater pollution based on PCA-APCS-MLR. China Environmental Science. 37(10), 3773–3786.
[36] Zhang, H., Wei, X., Peng, M. (2021) Analysis of pollution sources and identification of environmental influencing factors of shallow groundwater in Chongqing, China. Research of Environmental Sciences. 34(12), 2896–2906.
[37] Meng, L., Zuo, R., Wang, J., Yang, J., Teng, Y., Shi, R., Zhai, Y. (2018) Apportionment and evolution of pollution sources in a typical riverside groundwater resource area using PCA-APCS-MLR model. Journal of Contaminant Hydrology. 218, 70–83.
[38] Liu, L., Tang, Z., Kong, M., Chen, X., Zhou, C., Haung, K., Wang Z. (2019) Tracing the potential pollution sources of the coastal water in Hong Kong with statistical models combining APCS-MLR. Journal of Environmental Management. 245, 143–150.
[39] Xiao, H, Xiao, H., Zhang, Z., Wang, Y., Long, A., Liu, C. (2016) Chemical characteristics and source apportionment of atmospheric precipitation in Yongxing Island. China Environmental Science. 36(11), 3237–3244.
[40] Sun, Q., Xiao, H., Xiao, H., Zhang, Z. (2017) Chemical characteristics and source apportionment of atmospheric precipitation in Nanchang City. Research of Environmental Sciences. 30(12), 1841–1848.
[41] Ye, A., Cheng, M., Zang, L., He, Q., Guo, L., Wang, X. (2018) Characteristics and sources of dissolved heavy metals in summer precipitation of Taiyuan City, China. Environmental Science. 39(7), 3075–3081.
[42] Sun, X., Wang, Y., Li, H., Yang, X., Sun, L., Wang, X., Wang, T., Wang, W. (2016) Organic acids in cloud water and rainwater at a mountain site in acid rain areas of South China. Environmental Science and Pollution Research. 23(10), 9529–9539.
[43] Shi, X., Palida, Y.H.F, Song, S. (2021) Characteristics and source analysis of water-soluble ions in $PM_{2.5}$ in Urumqi City. Journal of Environmental Engineering Technology. 11(6), 1049–1054.
[44] Jin, Z, Qian, L., Hu, Q., Shi, Y., Hu, J., Fu, G. (2021) Characteristics and source analysis of water-soluble ions in PM_{10} in Hangzhou. Journal of Zhejiang University of Technology. 49(1), 111–118. (in Chinese)
[45] Wang, C., Zou, X., Zhao Y., Li, B. (2016) Source apportionment and ecological risk assessment of polycyclic aromatic hydrocarbons in surface water from Yangtze River, China: Based on PMF model. Environmental Science. 37(10), 3789–3797.
[46] Wang, C., Zhou, S., Wu, S., Song, J., Shi, Y., Li, B., Chen, H. (2017) Surface water polycyclic aromatic hydrocarbons (PAHs) in urban areas of Nanjing, China. Water Science and Technology. 76(8), 2150–2157.
[47] Tian, D., Dang, H., Ding, R., Cai, Q., Zhang, P., Yang, H. (2019) Distribution, sources, and ecological risk assessment of polycyclic aromatic hydrocarbons in the surface waters of the Yinchuan Wetlands. Environmental Science. 40(7), 3068–3077.

[48] Qin, N., He, W., He, Q., Kong, X., Liu, W., Wang, Q., Xu, F. (2021) Multi-media exposure to polycyclic aromatic hydrocarbons at Lake Chaohu, the fifth largest fresh water lake in China: Residual levels, sources and carcinogenic risk. Atmosphere. 12(10), 1241.

[49] Shao, Y., Wang, Y., Xu, X., Wu, X., Jiang, Z., He, S., Qian, K. (2014) Occurrence and source apportionment of PAHs in highly vulnerable karst system. Science of The Total Environment. 490, 153–160.

[50] Ren, C., Zhang, Q., Wang, H., Wang, Y. (2021) Characteristics and source apportionment of polycyclic aromatic hydrocarbons of groundwater in Hutuo River alluvial-pluvial fan, China, based on PMF model. Environmental Science and Pollution Research. 28(8), 9647–9656.

[51] Liu, J., Han, G. (2021) Tracing riverine sulfate source in an agricultural watershed: Constraints from stable isotopes. Environmental Pollution. 288, 117740.

[52] Lu, J., Zhang, C., Wu, J., Zhang, Y., Lin, Y. (2020) Seasonal distribution, risks, and sources of endocrine disrupting chemicals in coastal waters: Will these emerging contaminants pose potential risks in marine environment at continental-scale?. Chemosphere. 247, 125907.

[53] Ma, X., Gong, C., Guo, J., Wang, L., Xu, Y., Zhao, C. (2021) Water pollution characteristics and source apportionment in rapid urbanization region of the lower Yangtze River: Considering the Qinhuai River Catchment. Environmental Science. 42(7), 3291–3303.

[54] Trinh, M.M., Tsai, C.L., Chang, M. (2019) Characterization of polybrominated diphenyl ethers (PBDEs) in various aqueous samples in Taiwan. Science of The Total Environment. 649, 388–395.

[55] Capozzi, S.L., Rodenburg, L.A., Krumins, V., Fennell, D.E., Mack, E.E. (2018) Using positive matrix factorization to investigate microbial dehalogenation of chlorinated benzenes in groundwater at a historically contaminated site. Chemosphere. 211, 515–523.

[56] Pervez, S., Dugga, P., Siddiqui, M.N., Dano, S., Verma, M., Candeias, C. (2021) Sources and health risk assessment of potentially toxic elements in groundwater in the mineral-rich tribal belt of Bastar, Central India. Groundwater for Sustainable Development. 14, 100628.

[57] Dugga, P., Pervez, S., Tripathi, M., Siddiqui, M.N. (2020) Spatiotemporal variability and source apportionment of the ionic components of groundwater of a mineral-rich tribal belt in Bastar, India. Groundwater for Sustainable Development. 10, 100356.

[58] Bhuiyan, M.A.H., Dampare, S.B., Islam, M.A., Suzuki, S. (2015) Source apportionment and pollution evaluation of heavy metals in water and sediments of Buriganga River, Bangladesh, using multivariate analysis and pollution evaluation indices. Environmental Monitoring and Assessment.187(1), 4075.

[59] Li, H., Hopke, P.K., Liu, X., Du, X., Li, F. (2015) Application of positive matrix factorization to source apportionment of surface water quality of the Daliao River basin, northeast China. Environmental Monitoring and Assessment. 187(3), 80.

[60] Vu, C.T., Lin, C., Shern, C.C., Yeh, G., Le, V.G., Tran, H.T. (2017) Contamination, ecological risk and source apportionment of heavy metals in sediments and water of a contaminated river in Taiwan. Ecological Indicators. 82, 32–42.

[61] Zanotti, C., Rotiroti, M., Fumagalli, L., Stefania, G.A., Canonaco, F., Stefenelli, G., Prevot, A.S.H. (2019) Groundwater and surface water quality characterization through positive matrix factorization combined with GIS approach. Water Research. 159, 122–134.

[62] Mamun, M., An, K.G. (2021) Application of multivariate statistical techniques and water quality index for the assessment of water quality and apportionment of pollution sources in the Yeongsan River, South Korea. International Journal of Environmental Research and Public Health. 18(16), 8268.

[63] Peter, A.E., Shiva Nagendra, S.M., Nambi, I.M. (2018) Comprehensive analysis of inhalable toxic particulate emissions from an old municipal solid waste dumpsite and neighborhood health risks. Atmospheric Pollution Research, 9(6), 1021–1031.

[64] Murari, V., Singh, N., Ranjan, R., Singh, R., Banerjee, T. (2020) Source apportionment and health risk assessment of airborne particulates over central Indo-Gangetic Plain. Chemosphere. 257, 127145.

[65] Ai, J.C., Wang, N., Yang J. (2014) Source apportionment of soil heavy metals in Jiapigou Goldmine based on the Unmix model. Environmental Science. 35(9), 3530–3536.

[66] Xu, J., Guo, J., Liu, G., Shi, G., Guo, C., Zhang, Y., Feng, Y. (2010) Historical trends of concentrations, source contributions and toxicities for PAHs in dated sediment cores from five lakes in western China. Science of The Total Environment. 470–471, 519–526.

[67] Huang, F., Wang, X., Lou, L., Zhou, Z., Wu, J. (2010) Spatial variation and source apportionment of water pollution in Qiantang River (China) using statistical techniques. Water Research. 44(5), 1562–1572.

[68] Yi, Y., Tang, W., Shao, S., Jiang, Y., Wang, B. (2016) Source apportionment of ions in atmospheric precipitation based on Unmix receptor model. Environmental Science and Management. 41(5), 150–153.
[69] Sun, L. (2016) Source quantification of major ions in groundwater from deep limestone aquifer system in northern Anhui Province, China based on Unmix model. Nature Environment and Pollution Technology. 15(1), 159–164.
[70] Chen, K., Sun, L. (2019) Source analysis of major ion quantification in groundwater of mine area. Safety in Coal Mines. 50(8), 173-178.
[71] Nagaraju, A., Balaji, E., Sun, L., Thejaswi, A. (2018) Processes controlling groundwater chemistry from Mulakalacheruvu area, Chittoor District, Andhra Pradesh, South India: A statistical approach based on hydrochemistry. Journal of the Geological Society of India. 91(4), 425–430.
[72] Subba, R.N., Sunitha, B., Sun, L., Spandana, B.D., Chaudhary, M. (2020) Mechanisms controlling groundwater chemistry and assessment of potential health risk: A case study from South India. Geochemistry. 80(4), 125568.
[73] Li, Y., Feng, X., Zhou, J., Zhu, L. (2020) Occurrence and source apportionment of novel and legacy poly/perfluoroalkyl substances in Hai River Basin in China using receptor models and isomeric fingerprints. Water Research. 168, 115145.
[74] Salim, I., Sajjad, R.U., Paule-Mercado, M.C., Memon, S.A., Lee, B.Y., Sukhaatar, C., Lee, C.H. (2019) Comparison of two receptor models PCA-MLR and PMF for source identification and apportionment of pollution carried by runoff from catchment and sub-watershed areas with mixed land cover in South Korea. Science of The Total Environment. 663, 764–775.
[75] Liu, L., Dong, Y., Kong, M., Zhou, J., Zhao, H., Tang, Z., Zhang, M. (2020) Insights into the long-term pollution trends and sources contributions in Lake Taihu, China using multi-statistic analyses models. Chemosphere. 242, 125272.
[76] Qi, Y., Liu, X., Wang, Z., Yao, Z., Yao, W. (2020) Comparison of receptor models for source identification of organophosphate esters in major inflow rivers to the Bohai Sea, China. Environmental Pollution. 265, 114970.
[77] Chen, R., Teng, Y., Chen, H., Hu, B., Yue, W. (2019) Groundwater pollution and risk assessment based on source apportionment in a typical cold agricultural region in Northeastern China. Science of The Total Environment. 696, 133972.
[78] Gulgundi, M.S., Shetty, A. (2019) Source apportionment of groundwater pollution using Unmix and positive matrix factorization. Environmental Processes. 6(2), 457–473.
[79] Li, W., Wu, J., Zhou, C., Nsabimana, A. (2021) Groundwater pollution source identification and apportionment using PMF and PCA-APCS-MLR receptor models in Tongchuan City, China. Archives of Environmental Contamination and Toxicology. 81, 397–413.

Received: **22.12.2021**
Accepted: **21.02.2022**

CORRESPONDING AUTHOR

Yu Liu
State Key Laboratory of Mining Response and Disaster Prevention and Control in Deep Coal Mines, Anhui University of Science & Technology, Anhui 232001 – China

e-mail: yliu@aust.edu.cn

© by PSP Volume 31– No. 05/2022 pages 5292-5296 Fresenius Environmental Bulletin

FIRE PERFORMANCE OF THERMALLY MODIFIED WOOD IMPREGNATED WITH CLAY NANOMATERIALS

Ali Ihsan Kaya*

Department of Design, Vocational School of Technical Sciences, Burdur Mehmet Akif Ersoy University, 15100 Burdur, Turkey

ABSTRACT

Wood is one of the most widely used traditional building materials. However, its thermal degradability and flammability pose serious safety concern regarding its use. In this research, the flammability behavior of cedar wood (Cedrus Libani A. Rich.) impregnated with inorganic based clay nanomaterials and thermally modified at 160, 180 and 210 ºC were investigated via thermal gravimetric analysis, cone calorimetry and limit oxygen index. The results showed that the unique combination of these two processes significantly decreased the overall heat release rate by up to 6%, total head release by up to 43% and the total mass loss by 66%. This study revealed that impregnation of thermal modified wood with nanoclay is a potential method to improve the fire retardancy of wood.

KEYWORDS:
Flammability, Impregnation, Thermal modification, Wood, Nanomaterials

INTRODUCTION

Wood material is a traditional material that is widely used in the furniture and construction industry. Its low resistance to biological pests such as fungus and insects, hydrophilicity, medium durability and low fire stability limit its use [1-4].

Through the development of technology, many methods are developed for to increase the durability of wood [5-8]. Thermal modification (TM) and impregnation with nano inorganic minerals are methods of preference for to improve the properties of wood since while the chemical structure of the cell wall can be improved via thermal processes through penetration of chemicals into the cell wall in the impregnation process the properties of the biopolymer wood may be improved [9-12].

Thermal modification changes the chemical structure of biopolymer wood significantly. Cellulose and hemicellulose are polysaccharides found in the cell walls of wood. Owing to its high degree of polymerization cellulose, which confers strength to wood fibers, is more resistant to heat [13-15]. However, hemicellulose is less resistant to heat. Degradation of hemicellulose against heat also reduces the mechanical properties of wood [16-17]. Lignin, which has aromatic structure, is resistant to heat and is confers rigidity to wood [18-20]. Aside from its effects on wood components, TM releases volatile components present from the wood. Hence, much less volatile combustible components would be left in wood after its thermal modification and thus the possibility of its ignition and subsequently combustion would be reduced [21-22].

The positive effects of modification of wood on improving its technological properties as well as fire resistance have already been shown [23-25]. In this study, the effect of impregnating nanoclay on thermally modified wood on its thermal stability and the fire performance were investigated in detail and the underlying flame reduction mechanism was discussed. It was observed that inorganic substance has positive impact on thermal stability of wood as it is incorporated into the cell walls and the interspaces inside the cell.

MATERIALS AND METHODS

Materials. The cedar tree samples (Cedrus libani A. Rich.) used in this study are randomly chosen from zones in the Elmalı and Finike districts of Antalya province. The nanoclay (montmorillonit) is purchased from Sigma-Aldrich, US.

Specimen Procurement. The cedar tree samples (Cedrus libani A. Rich.) were prepared in different dimensions: 130×13×3 mm^3 (L×R×T), 100×100×5 mm^3 and 127×10×10 mm^3. The test samples were chosen to have regular fibers, with no nodes, cracks and faults. These samples were conditioned against humidity under dry air and were dried in an oven at 103±2°C until complete dry humidity (oven dried) and then cooled to room temperature in a dessicator. The experiments related with the samples were carried out at three different temperatures, 160, 180 and 210°C and in all cases the thermal process period was 3 h. The modified wood samples were immersed in nanoclay (3%w/w) suspension under low vaccum (0.3 bars) for 2 h. Then the samples imbibed with wet clay were frozen in a freezer at -20 °C overnight. Then, they were freeze dried for 48

h. These steps were repeated for to prepare samples containing nanoclay (NC) at a ratio of 3% (w/w). While the samples, which were not thermally treated, were labeled as NW, the thermally treated ones were labeled as TMW1, TMW2 and TMW3 and those treated with nanoclay were labeled as NW-NC and the ones impregnated with nanoclay after thermal modification were labeled as TMW-NC1, TMW-NC2 and TMW-NC3.

Characterization. The TG/DTA analysis of wood samples was performed by a thermogravimetric analyzer (Seiko SII TG/DTA 7200, TA Instruments). The analyses were performed under nitrogen flow of 60.0 ml/min, and the samples were heated from room temperature to 800 °C at 10.00 °C/min. In the TGA analysis, initially (in the original state) the weight of each sample was approximately 5 mg. The flamability property of the wood samples was determined according to ISO 5660 standard via a cone calorimeter under a heat flux of 35 kW/m^2 via a Siemens Oxymat 6. The size of the sample wrapped in an aluminum foil was 100x100x5 mm^3. The limiting oxygen index (LOI) test of wood samples was performed via a YY 907 type oxygen index test instrument according to the ASTM D 2863 standard. The dimensions of the samples were 127x10x10 mm^3.

RESULTS AND DISCUSSION

Thermogravimetric Analysis (TG/DTA). Thermal stability of materials offer important clues regarding their flamability properties [26]. In this study, thermal stability of the wood samples, which were thermally modified and were impregnated with nanoclay, was investigated via thermogravimetric analysis. The results are presented in Figures 1a-1b.

In each step the temperatures when degradation started (T_{onset}) and the maximum temperature values (t_{max}) were indicated in the DTG curves. The T_{onset}, t_{max} and the mass losses for the samples and their comparative evaluation are given in Table 1. The TG-DTG thermograms showed that it is a single step process. In the TG-DTG curve, while dehydration of the lignocellulosic components was observed at 110-210 °C, a mass loss of 5-10% was observed due to hydration in the liquid structure. In this temperature range the water vapour and a small amount of CO_2 were found to bee free in the medium. The major mass loss was observed in the phase in the temperature range from 300 to 450 °C. At this stage the temperature depends on the ratio of the components of the structure of the hemicellulose affected from the thermal modification. A 20-40% mass loss was observed after degradtion of hemicellulose, cellulose and lignin. It is known that hemicellulose, cellulose and lignin degrade at 260-300 °C, 280-350 °C and 350-400 °C, respectively [27]. However, at 600-800 °C mass loss was observed due to carbonixation of the organic components and burning of the volatile components. While, for thermally modified samples, this loss was determined to be 12.66, 13.78, 16.41 and 22.52%, respectively, for thermally modified and impregnated wood samples this loss was 16.86, 18.89, 25.22 and 32.55%, respectively.

The data in Figures 2a-2b and in Table 1 showed that both the thermal modification and impregnation of nanoclay improved thermal stability. The TGA results showed that for the TMW- NC1 samples, the T_5, T_{10} and T_{max} were 159 °C, 225 °C and 380 °C, respectively. However, for the TMW-NC3 samples they were observed to be 188 °C, 301 °C and 388 °C, respectively. As can be seen in Table 1, the thermal degradation temperature were delayed in thermally modified and impregnated wood samples. When the results were taken into consideratiom, it was concluded that excellent thermal stability was achieved upon nanoclay impregnation and as the thermal application temperature increased.

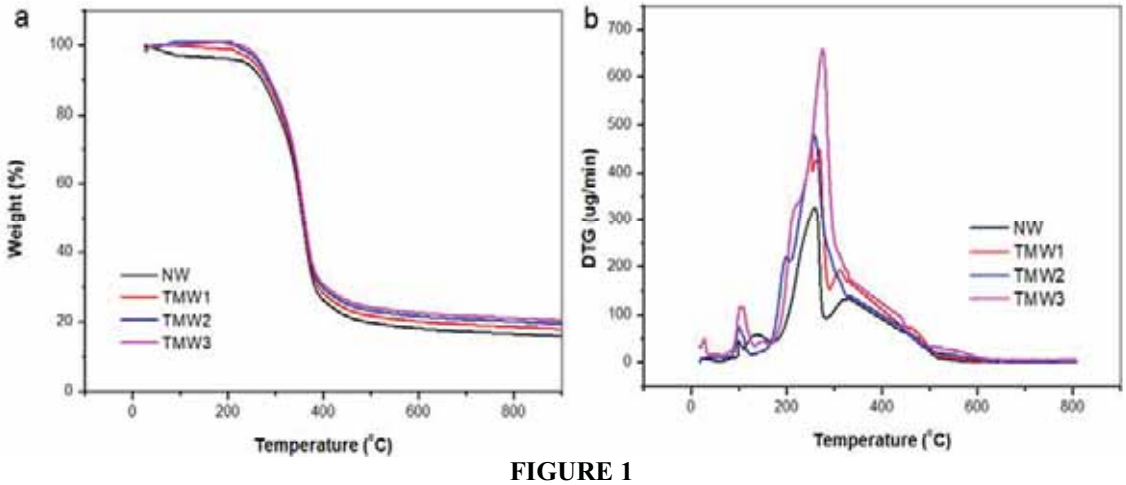

FIGURE 1
(a) TG, (b) derivative thermogravimetric weight loss of thermally modified wood (Cedrus libani A. Rich.) samples

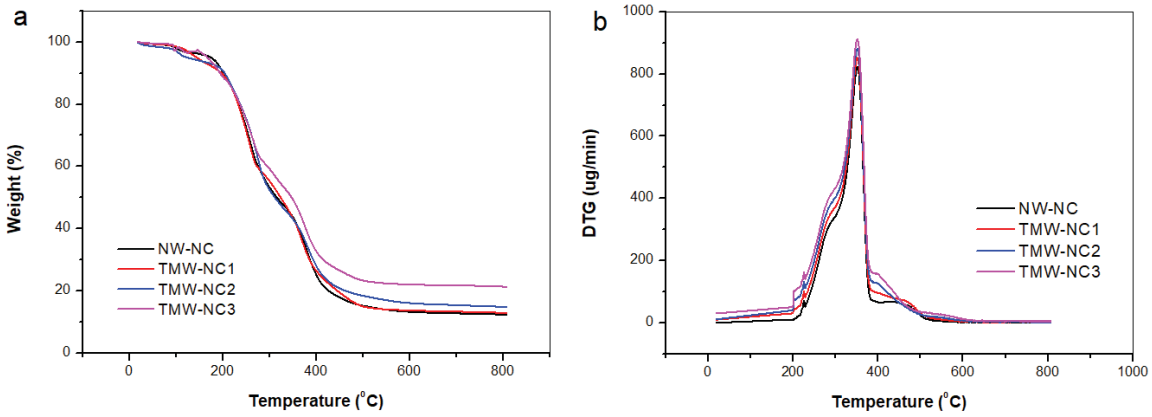

FIGURE 2
(a) TG, (b) derivative thermogravimetric weight loss of thermally modified and impregnated wood (Cedrus libani A. Rich.) samples

TABLE 1
TGA-DTA data for wood (Cedrus libani A. Rich.) samples

	$T_{5\ wt\%}$ (°C)	$T_{10\ wt\%}$ (°C)	$T_{50\ wt\%}$ (°C)	T_{max} (°C)	800 °C Residue (wt.%)
NW	150	194	275	365	12.66
TMW1	152	193	315	362	13.78
TMW2	158	194	317	363	16.41
TMW3	165	196	352	360	22.52
NW-NC	155	210	311	375	16.86
TMW-NC1	159	225	348	380	18.89
TMW-NC2	178	245	375	385	25.22
TMW-NC3	188	301	395	388	32.55

TABLE 2
Cone calorimeter data for wood (Cedrus libani A. Rich.) samples

	PHRR(1st) (kW/m^2)	PHRR(2nd) (kW/m^2)	AHRR (at 500 s) (kW/m^2)	AHRR (at 1500 s) (kW/m^2)	THR (for 300 s) (MJ/m^2)	İgnition time (s)
NW	167.90	254.10	110.40	55.29	44.29	32.30
TMW1	163.20	222.24	108.33	48.21	43.12	30.90
TMW2	135.32	165.21	106.44	45.72	42.94	30.10
TMW3	141.21	152.45	102.05	42.34	36.24	29.32
NW-NC	165.90	250.41	108.20	53.44	40.42	33.11
TMW-NC1	160.30	249.12	101.90	51.10	34.10	33.52
TMW-NC2	161.20	249.01	100.40	48.85	33.65	33.63
TMW-NC3	158.70	248.44	99.80	45.10	25.20	34.20

Cone Calorimeter. The most detailed information regarding flammability behavour can be obtained via cone calorimetry test. The heat release (HRR) and the total heat release (THR) are two important parameters that determine the combustion behavior. The cone calorimetry test results for the thermally modified and the impregnated wood samples are given in Table 2.

When the test results obtained for the thermally modified wood samples were compared with those of the thermally unmodified wood samples, it was observed that the PHRR values decreased by 2.30%, 19.10% and 15.51%, respectively. When a similar comparison was made for the thermally modified and impregnated wood samples, it was observed that the PHRR values decreased by 3.11%, 2.40% and 4.24%, respectively.

Thus, in the thermal modification and additional impregnation processes, it was observed that the flame retardancy increased as the temperature increased and the TMW-NC3 had the highest flame retardant property. This is due to the nanoclay particles that act as a barrier to prevent formation and transport of volatile products by filling the spaces, holes and cracks in the cell, and also by absorbing heat and preventing the transfer of heat to the inner layers. Hence, modification with the nanoclay decreases flammability and total heat.

TABLE 3
Limiting oxygen index test result of wood (Cedrus libani A. Rich.) samples

Content (%)	Limiting oxygen index (%)
NW	24.90
TMW1	25.10
TMW2	27.20
TMW3	29.09
NW-NC	25.30
TMW-NC1	32.20
TMW-NC2	38.70
TMW-NC3	42.90

The limiting oxygen index (LOI). The limiting oxygen index of the thermally modified and impregnated wood samples were determined according to the ASTM D 2863 standard. The LOI is the minimum amount of oxygen required to trigger ignition. This means that a substance with a higher LOI will require more oxygen for ignitation and it will not burn until this amount of oxygen is supplied. According to Table 3, the limiting oxygen index (LOI) scale is between 24.9% and 42.9%. It was determined that the highest flame retardant plate with an LOI of 42.9% was obtained with TMW-NC3, which increased the flame resistance by 72% as compared to pure NW.

CONCLUSION

In this study, the TM and the nanoclay impregnation were found to suppress combustion by forming a protective layer on the biopolymer during combustion and by minimizing oxygen. While the mass loss for the untreated wood was 87.34%, the mass loss for the TMW-NC3 was determined to be 21.54%. It was observed that the processes performed in the study reduced the mass loss by approximately 65.8%.

The fire behavior of the samples was investigated via the cone calorimetry test. It was observed that the HRR, AHRR and THR values decreased significantly as the temperature applied in the TM increased. According to the results of the cone calorimetry test, TMW-NC3 was found to be the strongest flame retardant. Wood is a material with low fire resistance. However, the flammability threshold can be increased by using suitable flame retardants. This would increase the usage area of wood especially in indoor applications. Our study showed that aside from TM nanoclay impregnation offers an alternative way for making designs with excellent performance that can meet the demands and needs of the furniture and construction industry.

ACKNOWLEDGEMENTS

This study was published as an abstract paper in International Conference on Science and Technology (ICONST 2021) hold from September 8 to 10, 2021, in Budva, MONTENEGRO.

REFERENCES

[1] Gaff, M., Čekovská, H., Bouček, J., Kačíková, D., Kubovský, I., Tribulová, T., Kačík, F. (2021) Flammability Characteristics of Thermally Modified Meranti Wood Treated with Natural and Synthetic Fire Retardants. Polymers. 13(13), 2160.

[2] Baral, S., Gaire, N.P., Aryal, S., Pandey, M., Rayamajhi, S., Vacik, H. (2019) Growth ring measurements of Shorea robusta reveal responses to climatic variation. Forests. 10(6), 466.

[3] Baral, S., Neumann, M., Basnyat, B., Gauli, K., Gautam, S., Bhandari, S.K., Vacik, H. (2020) Form Factors of an Economically Valuable Sal Tree (Shorea robusta) of Nepal. Forests. 11(7), 754.

[4] Zhuang, B.R., Zhan, Y.P., Huang, W.Y., Ye, H.L., Xie, Y.Q. (2018) Smoke suppression properties of Si-Al mesoporous structure on medium density fiberboard. Journal of Hazardous Materials. 357, 271-278.

[5] Gašparík, M., Osvaldová, L.M., Čekovská, H., Potůček, D. (2017) Flammability characteristics of thermally modified oak wood treated with a fire retardant. BioResources. 12(4), 8451-8467.

[6] Icel, B., Beram, A. (2017). Effects of industrial heat treatment on some physical and mechanical properties of iroko wood. Drvna Industrija: Znanstveni Časopis Za Pitanja Drvne Tehnologije. 68(3), 229-2369.

[7] Yaşar, S., Aytaç, U.Z., Beram, A. (2020) Some Properties of Boards Produced from Heat-Treated Brutian Pine (Pinus brutia Ten.) Particles. Bilge International Journal of Science and Technology Research. 4(1), 14-20.

[8] Beram, A., Yaşar, S., Aytaç, U.Z. (2016) Effects of Heat Treatment Applied to Brutian Pine (Pinus brutia Ten.) Particles on the Formaldehyde Emission and Burning Properties of Produced Boards. Bilge International Journal of Science and Technology Research. 5(1), 86-90.

[9] Icel, B., Guler, G., Isleyen, O., Beram, A., Mutlubas, M. (2015) Effects of industrial heat treatment on the properties of spruce and pine woods. BioResources. 10(3), 5159-5173.

[10] Kazan, B., Ozalp, M. (2021) Investigation of the Effects of Heat Treatment on Varnished Wood Material. Bilge International Journal of Science and Technology Research. 5(1), 22-33.

[11] Telesiński, A., Cybulska, K., Stręk, M., Płatkowski, M., Śnioszek, M., Biczak, R. (2017) Response of soil enzymes to volatile organic compounds emitted from creosote-treated wood. Fresen. Environ. Bull. 26(10), 6058-6063.
[12] Esmailpour, A., Taghiyari, H.R., Zolfaghari, H. (2017) Effects of heat treatment on sound absorption coefficients in nanosilver-impregnated and normal solid woods. IET Nanobiotechnology. 11(4), 365-369.
[13] Sivonen, H., Maunu, S.L., Sundholm, F., Jämsä, S., Viitaniemi, P. (2002) Magnetic resonance studies of thermally modified wood. Holzforschung, 56(6), 648-654.
[14] Pandey, K.K. (1999) A study of chemical structure of soft and hardwood and wood polymers by FTIR spectroscopy. Journal of Applied Polymer Science. 71(12), 1969-1975.
[15] Ozcan, S., Ozcifci, A., Hiziroglu, S., Toker, H. (2012) Effects of heat treatment and surface roughness on bonding strength. Construction and Building Materials. 33, 7-13.
[16] Osvald, A., Gaff, M. (2017) "Effect of thermal modification on flameless combustion of spruce wood." Wood Research. 62(4), 564-574.
[17] Sikora, A., Kačík, F., Gaff, M., Vondrová, V., Bubeníková, T., Kubovský, I. (2018) Impact of thermal modification on color and chemical changes of spruce and oak wood. Journal of Wood Science. 64(4), 406-416.
[18] Cademartori, P.H.G., dos Santos, P.S., Serrano, L., Labidi, J., Gatto, D.A. (2013) Effect of thermal treatment on physicochemical properties of Gympie messmate wood. Industrial Crops and Products. 45, 360-366.
[19] García, A., Toledano, A., Andrés, M.Á., Labidi, J. (2010) Study of the antioxidant capacity of Miscanthus sinensis lignins. Process Biochemistry. 45(6), 935-940.
[20] Lekounougou, S., Petrissans, M., Jacquot, J.P., Gelhaye, E., Gerardin, P. (2009) Effect of heat treatment on extracellular enzymatic activities involved in beech wood degradation by Trametes versicolor. Wood Science and Technology. 43(3-4), 331-341.
[21] Esteves, B., Pereira, H. (2009) Wood modification by heat treatment: A review. BioResources. 4(1), 370-404.
[22] Bal, B.C. (2013) Effects of heat treatment on the physical properties of heartwood and sapwood of Cedrus libani. Bioresources. 8(1), 211-219.
[23] Nabil, E., Mahmoud, N., Youssef, A., Saber, E., Kamel, S. (2018) Evaluation of physical, mechanical and chemical properties of Cedar and Sycamore woods after heat treatment. Egyptian Journal of Chemistry. 61(6), 1131-1149.
[24] Martinka, J., Chrebet, T., Král, J., Balog, K. (2013) An examination of the behaviour of thermally treated spruce wood under fire conditions. Wood Research. 58(4), 599-606.
[25] Babrauskas, V., Peacock, R.D. (1992) Heat release rate: the single most important variable in fire hazard. Fire Safety Journal. 18(3), 255-272.
[26] Chen, X., Huo, L., Jiao, C., Li, S. (2013) TG–FTIR characterization of volatile compounds from flame retardant polyurethane foams materials. Journal of Analytical and Applied Pyrolysis. 100, 186-191.
[27] Becidan, M., Skreiberg, Ø., Hustad, J.E. (2007) Products distribution and gas release in pyrolysis of thermally thick biomass residues samples. Journal of Analytical and Applied Pyrolysis. 78(1), 207-213.

Received: **08.10.2021**
Accepted: **06.02.2022**

CORRESPONDING AUTHOR

Ali Ihsan Kaya
Department of Design,
Vocational School of Technical Sciences,
Burdur Mehmet Akif Ersoy University,
15100 Burdur – Turkey

e-mail: aikaya@mehmetakif.edu.tr

© by PSP Volume 31– No. 05/2022 pages 5297-5306 Fresenius Environmental Bulletin

AGRICULTURAL LAND USE CHANGE AND ITS VULNERABILITY RESPONSE IN HEGANG COAL MINING AREA

Lei Wang[1,*], Jiarong Deng[2], Jiaxuan Wang[1], Jia Jia[1], Jing Ning[3], Yunlong Yao[1]

[1]Northeast Forestry University, Harbin 150040, China
[2]Huaian City Construction and Design Research Institute co., Ltd, Huaian 223021, China
[3]School of Public Administration and Law, Northeast Agricultural University, Harbin 150038, China

ABSTRACT

As a primary classification of land use, the study of land use change and vulnerability response of agricultural lands can help provide a scientific basis for improving agroecological security. Therefore, the analytic hierarchy process (AHP) method was used to establish an evaluation index system for the assessment of agricultural vulnerability in the coal mining area of Hegang City to analyze the existing problems and the evolution of agricultural vulnerability in this area from 1994 to 2014 and to identify feasible interventions. The results showed that (1) the overall vulnerability of agricultural land in Hegang City from 1994 to 2014 showed an upward trend, the vulnerability of the other agricultural land showed no significant change, whereas the vulnerability of farmland, woodland, and grassland showed an upward trend; (2) under the interference of human and coal mining environments, the adaptive capacity of agricultural land in the coal mining area in Hegang City decreased yearly, whereas the exposure and sensitivity increased continuously, and the mild vulnerability of agricultural land in the coal mining area evolved to severe vulnerability. The results of this study can provide a scientific basis for the rational development and ecological protection of agricultural land in the coal mining area of Hegang City.

KEYWORDS:
Coal mining area, Agricultural land, Land use, Ecological vulnerability

INTRODUCTION

China's coal resources are abundant; coal mines were rapidly developed to meet the increased economic demand [1].This caused the surrounding agricultural land cover and ecological patterns to suffer drastic changes and has triggered a severe ecological vulnerability crisis in these areas[2]. There is no complete, unified, conceptual definition of agricultural land vulnerability owing to the lack of systematic research on the ecological vulnerability of agricultural land in coal mining areas. Therefore, a vulnerability evaluation study on the current situation of agricultural land can complement the concept of agricultural land vulnerability and related theories[3, 4] and provide an accurate understanding and evaluation of the rational use of agricultural land resources[5,6]. It is beneficial to solve the current problems with this type of land and maintain ecological balance while predicting and preventing future risks[7].

Vulnerability is a measure of the degree of ecological degradation [8, 9]. Economic development has created environmental and social benefits, but the changes in climatic environment and the impact of human activity have caused drastic changes in the global ecological environment, highlighting the issue of ecological vulnerability. Vulnerability research has become a key area of concern in related fields [10, 11]. A vulnerability assessment involves evaluating an object's tolerance for disturbances by monitoring its structure and function under the influence of external factors [12, 13]. This research has received extensive attention from the International Human Dimensions Programme on Global Environmental Change, the United Nations Intergovernmental Panel on Climate Change, the International Geosphere Biosphere Programme, and other institutions and related researchers, with a trend of disciplinary synthesis in its application area [14-17]. The combination of geographic information systems (GIS) and remote sensing improves the accuracy of vulnerability evaluation and is widely used in various fields[18,19], such as land use and mining vulnerability research. This research includes assessing land use, land cover[5,20,21], regional disaster[22], and ecological vulnerability change[23,24] and evaluating mining pollutability and ecological vulnerability [25, 26]. Many precise and effective research methods have been proposed and applied, such as principal component analysis, analytic hierarchy process, layer superposition, and functional model evaluation [27]. The fields involved in ecological vulnerability research are gradually becoming more comprehensive, and the results help deepen the understanding

of ecological vulnerability and solve practical problems effectively.

Hegang City, Heilongjiang Province, Northeast China was selected as the study area. With ecological vulnerability as a theoretical guide and GIS, remote sensing, and GPS (3S) as technical support [13, 28], the study of the vulnerability of agricultural land in the coal mining area of Hegang City from 1994 to 2014 was conducted. This study aimed to establish a vulnerability evaluation index system for agricultural land in the coal mining area; analyze the reasons for the vulnerability of the study area, the development trend, and the degree of influence of each evaluation factor; and understand the features, formation, and evolution mechanism of the vulnerable environment to realize the coordinated development of agriculture and economy in the coal mining area [29], provide scientific evidence for the ecological restoration and reconstruction of the area, and promote the sustainable development of the ecological environment of agricultural land in Hegang City.

MATERIALS AND METHODS

Data source. Hegang City is located in the plain buffer zone (129°4E to 132°3E, 47°4N to 48°9N) between the Sanjiang plain, the Xiaoxing'an Mountains, and the Heilongjiang Province. It has a temperate, continental, monsoon climate, with an average annual temperature of approximately 3 °C, an average frost-free period of approximately 152 days, an average precipitation of approximately 640 mm, and a transitional terrain from northwest to southeast with distinct undulations. The concentrated coal mining area in Hegang City, shown in Figure 1, has a long history of mining because of its abundant mineral resources and is an important national coal base and energy supply in northeast China. However, due to the high degree of coal mining and the complex natural and human interference factors, the ecological environment within the research area has been damaged.

The data was obtained from the Landsat series ETM/TM/OIL remote sensing image data on the geospatial data cloud in 1994, 2001, 2006, 2010, and 2014. The remote sensing image data of the study area were stitched and synthesized from 1 to 2 remote sensing images, with the resulting 5-period remote sensing image cloud covering less area and having a high image resolution. The acquisition time was September every year, and the remote sensing images were pre-processed with image geometry correction, radiation correction, image fusion, mosaic, and cropping. Other data sources included Google maps or Baidu maps as reference images, Hegang City coal mine area vector boundaries, Heilongjiang Province Statistical Yearbook, China City Statistical Yearbook, Hegang City Statistical Yearbook, and field sampling data, other statistical data, and literature.

Land use classification. Support vector machines are supervised classification methods that can be used to process segmented raster inputs or standard images with good generalizability and high classification accuracy.

The formula is as follows.

$$\phi(\omega, \xi) = \frac{1}{2}\omega^{T}\omega + C\sum_{i=1}^{N}\xi \quad (1)$$

xi∈Rn denotes the target input and yi∈{-1,1} denotes the target output. ξ denotes the degree of deviation from the classification result in the ideal linear case.

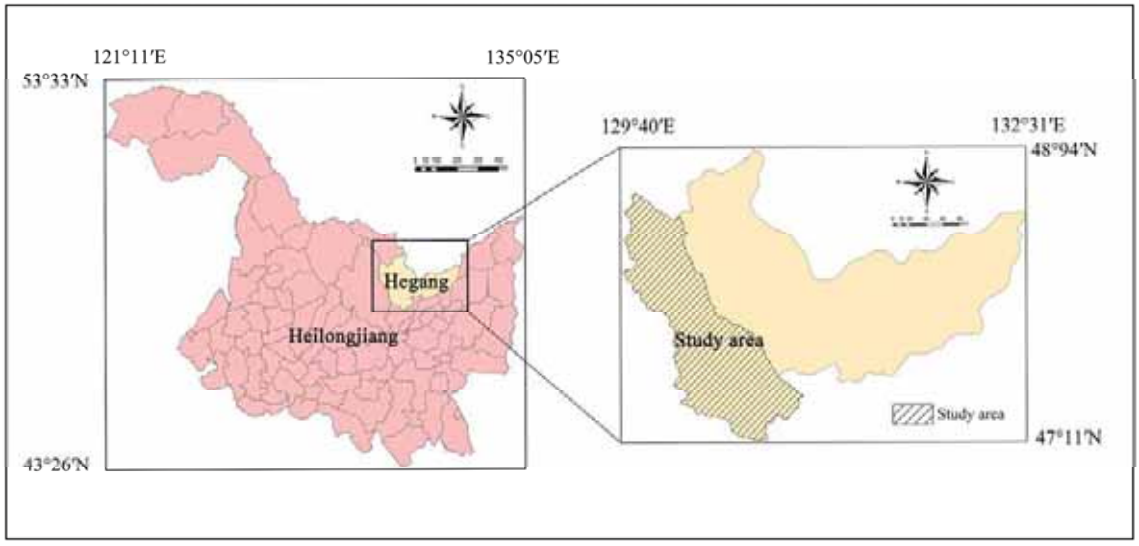

FIGURE 1
Studies the district bitmap

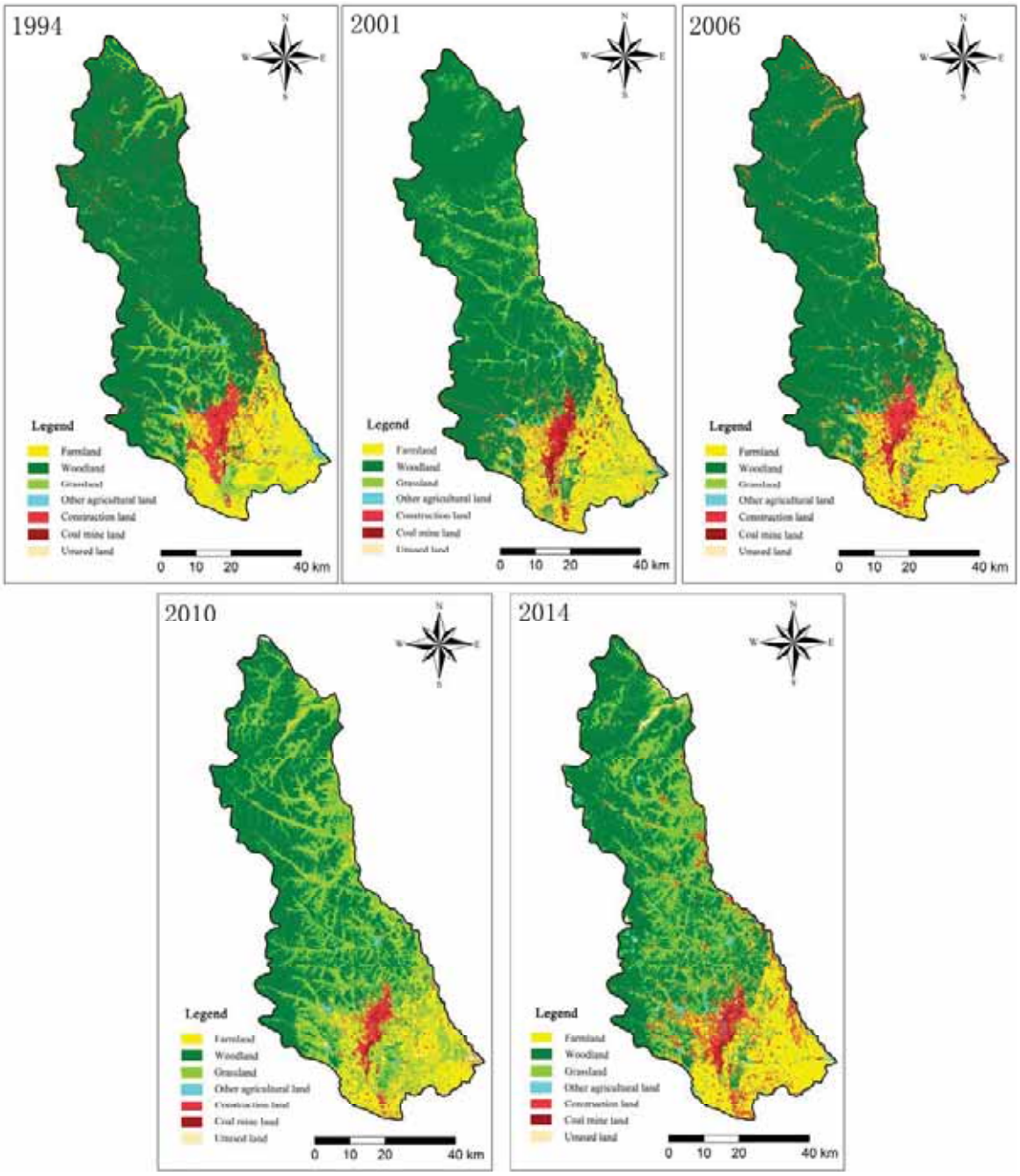

FIGURE 2
Land use classification of Hegang Study area from 1994 to 2014

Using a support vector machine, the land use types in Hegang City were divided into seven categories: farmland, woodland, grassland, other agricultural land, coal mine land, construction land, and unused land, as shown in Figure 2. Using spatial superposition analysis, the agricultural land in the coal mining area of Hegang City was divided into four categories, farmland, woodland, grassland, and other agricultural land, as shown in Figure 3.

Determination of evaluation index weights. AHP is often applied to decision-making problems under uncertainty and with multiple assessment criteria [30]. From the three attributes of environmental exposure, sensitivity, and adaptive capacity, an index system for assessing the ecological vulnerability of agricultural land in the study area was established. The evaluation factors of these three aspects were selected, and the AHP method was used to analyze the correlations and weights of each factor to develop the evaluation index system.

The vulnerability evaluation index system of agricultural land in the coal mining area of Hegang City was analyzed using the Yaahp software platform. After standardization, the assessment matrix was tested for consistency, and the weight values were found to be reasonable. The final weights of 22 individual indicators were obtained and are listed in

Table 1.

Data standardization. Before conducting the vulnerability analysis of the study area, the related data were normalized to ensure the evaluation indicators remained in the same range, between 0 and 1 and all the indicators were grouped using the same criteria. When the selected evaluation indicators were positively correlated with vulnerability, they were calculated using equation (2); when the selected indicators were negatively correlated with vulnerability, equation (3) was used.

$$R_i = S_i - Min(S_i) / Max(S_i) - Min(S_i) \quad (2)$$

$$R_i = Max(S_i) - S_i / Max(S_i) - Min(S_i) \quad (3)$$

R_i represents the value of the i^{th} indicator after normalization, S_i is the initial value of the i^{th} indicator, Min (S_i) is the minimum value of the i^{th} indicator in the layer, and Max (S_i) indicates the maximum value of the i^{th} indicator in the layer.

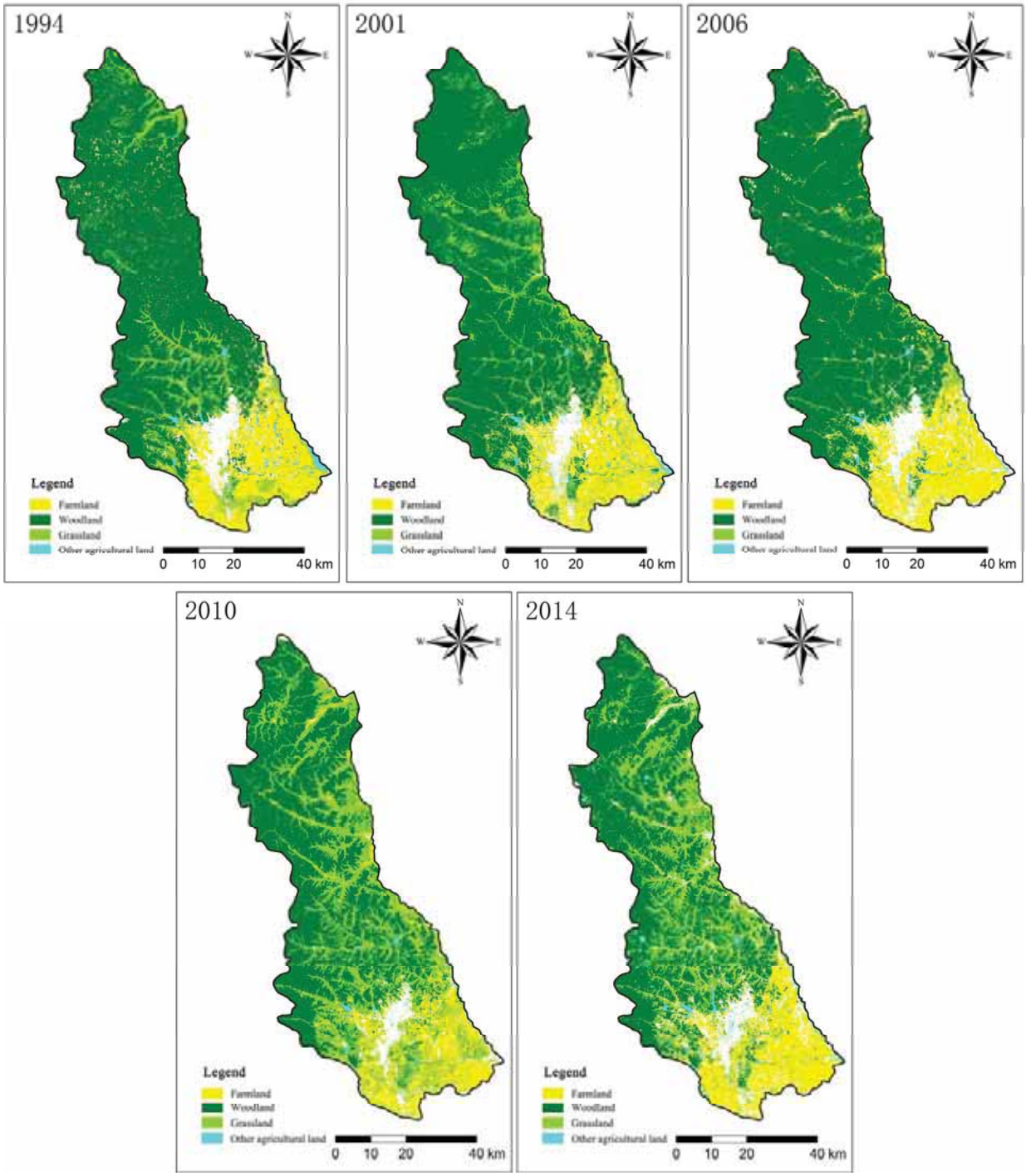

FIGURE 3
Agricultural land classification map of Hegang Coal Mine District from 1994 to 2014

TABLE 1
Weight of vulnerability evaluation index of agricultural land in the study area

Target layers	Guideline layers	Sub-criteria layers	Indicator layers	Weights
Agricultural land Vulnerability (V)	Exposure(E) 0.1429	Natural conditions exposure E_1 0.0109	Average annual temperature E_{11}	0.0024
			Average annual rainfall E_{12}	0.0073
			Average annual sunshine hours E_{13}	0.0012
		Population development exposure E_2 0.0196	Population density E_{21}	0.0112
			Natural population growth E_{22}	0.0028
			Agricultural population share E_{23}	0.0056
		Socio-economic development exposed E_3 0.0365	Per capita GDP E_{31}	0.0033
			Engel's coefficient E_{32}	0.0044
			Share of total agricultural output in total regional output E_{33}	0.0127
			Annual raw coal production E_{34}	0.0117
			Net income per farmer E_{35}	0.0043
		Agricultural land use exposure E_4 0.0758	Per capita food production E_{41}	0.0076
			Cultivated land per capita E_{42}	0.0227
			Agricultural fertilizer use intensity E_{43}	0.0455
	Sensitivity(S) 0.2587	Agricultural land use sensitivity S_1 0.0114	Soil erosion S_{11}	0.0078
			Slope S_{12}	0.0036
		Landscape type sensitivity S_2 0.2743	Crushability S_{21}	0.1007
			Dimensional S_{22}	0.1736
	Adaptability(AC) 0.5714	Environmental governance capacity AC_1 0.1905	Industrial wastewater discharge compliance rate AC_{11}	0.0476
			Comprehensive utilization rate of industrial solid waste AC_{12}	0.1429
		Vegetation regulating capacity AC_2 0.3810	Ratio of agricultural to forestry land AC_{21}	0.0762
			NDVI AC_{22}	0.3048

Calculation of evaluation model. By normalizing the evaluation indices of the vulnerability of agricultural land in the coal mining area of Hegang City, the ecological vulnerability of the region was quantitatively reflected [31]. The evaluation model was constructed from three aspects, exposure, sensitivity, and adaptive capacity, and the equations used are as follows:

$$E=\sum_{i=1}^{n} W_i X_{ei} \quad (4)$$

$$S=\sum_{j=1}^{m} W_j X_{sj} \quad (5)$$

$$AC=\sum_{p=1}^{k} W_p X_{acp} \quad (6)$$

$$V=(E+S)/AC \quad (7)$$

where V represents agricultural land vulnerability; E is agricultural land vulnerability exposure; S is agricultural land vulnerability sensitivity; AC is agricultural land vulnerability adaptive capacity; n, m, and k represent the number of rating indicators for agricultural land vulnerability exposure, sensitivity, and adaptive capacity; W_i, W_j, and W_p are the weights of each evaluation indicator; and X_{ei}, X_{sj}, and X_{acp} are the values of evaluation indicators.

In Equation (7), when V is greater than 1, it indicates that the vulnerability of agricultural land is more prominent and that the ecosystem is severely damaged. Conversely, when V is less than 1, it indicates that the vulnerability is recessive and that the ecosystem tends to be repairable.

Calculation of ecological vulnerability index. The analysis of different landscape types in the agri-

cultural land classification was integrated using multiple evaluation indicators. The vulnerability of different landscape patterns was combined with the vulnerability of the study area to construct an ecological vulnerability index of the study area, which was calculated using equation (8).

$$EVI = \sum_{i=1}^{n} \frac{A_i}{A_t} V_i \quad (8)$$

Where EVI is the ecological vulnerability index of the study area, A_i is the area of landscape type i, A_t is the total area of the study area, and V_i is the vulnerability index of landscape type i.

RESULTS AND DISCUSSION

Overall vulnerability analysis. The overall vulnerability index of the study area from 1994 to 2014 was calculated and the total vulnerability index of agricultural land as a proportion of total vulnerability was analyzed. Further analysis of the changing dynamics of the vulnerability of agricultural land in the study area was conducted, and the results are shown in Table 2.

The results showed that the overall change in vulnerability in the study area from 1994 to 2014 was positive, indicating that the vulnerability was in an aggravated state. The agricultural land vulnerability index was calculated according to the percentage of agricultural land, and it was clear that the vulnerability of agricultural land was prominent in 2001, while it had improved in 2006, indicating that environmental management measures and artificial protection measures we implemented. However, it was greater than 1 in both 2010 and 2014, which indicated that the vulnerability of agricultural land was trending downward.

Exposure evaluation and analysis. Based on the results of the analysis, the weights of the vulnerability exposure indicators, and the standardized values of each indicator shown in Table 3, the exposure index and vulnerability index of different landscape types in the agricultural land from 1994 to 2014 were calculated using equations (4) and (8).

From the table, it can be seen that the vulnerability exposure index of agricultural land in Hegang City from 1994 to 2014 was positive, which indicated that the vulnerability exposure of agricultural land in the study area was aggravated. Woodland had the highest degree of exposure yearly and showed the most change, followed by farmland and grassland.

Sensitivity evaluation and analysis. The sensitivity of agricultural land plays an important role in the study of agricultural land vulnerability; the stronger the sensitivity, the greater the impact on the agricultural land ecosystem, and the more severely the agricultural land vulnerability is impacted. Using equations (5) and (8), the exposure and vulnerability indices of different landscape types of agricultural land from 1994 to 2014 were calculated, with results listed in Table 4.

The results indicated that the overall sensitivity of agricultural land vulnerability in the coal mining area of Hegang City from 1994 to 2014 showed a weakening trend. The sensitivity indices of woodland and farmland were the highest, followed by grassland, indicating that woodland, grassland, and farmland were significantly disturbed by external influences.

TABLE 2
Comprehensive index of land use vulnerability in the study area from 1994 to 2014

	1994	2001	2006	2010	2014	Annual change
Agricultural land share	0.8846	0.8789	0.8773	0.8754	0.8887	0.0041
Total vulnerability Index	0.8296	2.0801	1.0029	2.2695	1.4584	0.6288
Agricultural land Vulnerability Index	0.7339	1.8281	0.8798	1.9867	1.2961	0.5623

TABLE 3
Vulnerability exposure index of agricultural land in the study area from 1994 to 2014

Landscape types		1994	2001	2006	2010	2014	Annual change
Agricultural land	Farmland	0.00964	0.00855	0.00824	0.01055	0.01410	0.00446
	Woodland	0.04225	0.03881	0.03590	0.04726	0.05943	0.01717
	Grassland	0.00566	0.00384	0.00469	0.00569	0.00884	0.00317
	Other land	0.00100	0.00091	0.00090	0.00114	0.00160	0.00060
Total exposure		0.05856	0.05211	0.04973	0.06463	0.08396	0.02540

TABLE 4
Vulnerability sensitivity index of agricultural land in the study area from 1994 to 2014

Landscape types		1994	2001	2006	2010	2014	Annual change
Agricultural land	Farmland	0.01418	0.04500	0.00272	0.00102	0.00456	-0.00962
	Woodland	0.06217	0.20429	0.01184	0.00456	0.01923	-0.04294
	Grassland	0.00833	0.02022	0.00155	0.00055	0.00286	-0.00547
	Other land	0.00147	0.00478	0.00030	0.00011	0.00052	-0.00095
Total sensitivity		0.08616	0.27430	0.01640	0.00624	0.02717	-0.05899

TABLE 5
Index of vulnerability and adaptability of agricultural land in the study area from 1994 to 2014

Landscape types		1994	2001	2006	2010	2014	Annual change
Agricultural land	Farmland	0.02872	0.02574	0.01093	0.00509	0.01279	-0.01593
	Woodland	0.12587	0.11687	0.04760	0.02283	0.05393	-0.07194
	Grassland	0.01687	0.01157	0.00622	0.00275	0.00802	-0.00885
	Other land	0.00298	0.00274	0.00119	0.00055	0.00145	-0.00153
Total adaptive capacity		0.17445	0.15692	0.06594	0.03123	0.07620	-0.09825

Adaptation evaluation and analysis. The trend of adaptability with exposure and sensitivity was prominent. The four most representative indicators were used to evaluate and analyze the adaptive capacity of agricultural land vulnerability based on environmental management capacity and vegetation regulation capacity, using equations (6) and (8), and the results are shown in Table 5.

The vulnerability adaptive capacity of agricultural land in the study area from 1994 to 2014 was in a weakened state; the adaptive capacity of woodland had the fastest decreasing trend, followed by farmland, grassland, and other agricultural land. Form the vulnerability adaptive capacity index, it was found that the total adaptive capacity of the agricultural land reduced overall throughout the study period. This could be due to coal mining or anthropogenic disturbance in the mining area.

In general, both the amount of annual change in adaptive capacity and the rate of weakening are greater than the sensitivity. While the exposure is in an enhanced state, the vulnerability of agricultural land in the study area is threatened.

Comprehensive analysis and grading of agricultural land vulnerability. Using the calculation model of the agricultural land vulnerability index, the comprehensive vulnerability index of agricultural land use in the study area was calculated, with results shown in Table 6.

Combining the data in the table and the ecological vulnerability index values of the agricultural land, which ranged between 0.734 and 1.987, the vulnerability index of agricultural land was classified as slight, medium, heavy, or extreme, as shown in Table 7. The total vulnerability values of the agricultural land were classified, and the results are listed in Table 8.

TABLE 6
Comprehensive vulnerability index of agricultural land in the study area from 1994 to 2014

Landscape types		1994	2001	2006	2010	2014	Annual change
Agricultural land	Farmland	0.121	0.300	0.146	0.324	0.218	0.097
	Woodland	0.530	1.362	0.635	1.453	0.917	0.388
	Grassland	0.071	0.135	0.083	0.175	0.136	0.065
	Other land	0.013	0.032	0.016	0.035	0.025	0.012
Total vulnerability Index		0.734	1.828	0.880	1.987	1.296	0.562

TABLE 7
Vulnerability level table of agricultural land in Hegang Coal mining area

Vulnerability levels	Slight	Medium	Heavy	Extreme
Vulnerability Index	≤0.8	0.8-1.0	1.0-1.3	≥1.3

TABLE 8
Vulnerability classification results of agricultural land in Hegang Coal mining area

Landscape type	1994	2001	2006	2010	2014
Agricultural land	Slight	Extreme	Medium	Extreme	Heavy

TABLE 9
Vulnerability hierarchy of different landscape types in the study area

Vulnerability level	Level 1	Level 2	Level 3	Level 4	Level 5
Vulnerability Index	≤0.1	0.1-0.2	0.2-0.4	0.4-0.8	≥0.8

TABLE 10
Vulnerability classification results of different landscape types in the study area

Landscape types	1994	2001	2006	2010	2014
Farmland	Level 2	Level 3	Level 2	Level 3	Level 3
Woodland	Level 4	Level 5	Level 4	Level 5	Level 5
Grassland	Level 1	Level 2	Level 1	Level 2	Level 2
Other land	Level 1	Level 1	Level 1	Level 1	Level 1

From Table 8, it can be seen that there were significant changes in the vulnerability of agricultural land in the coal mining area of Hegang City from 1994 to 2014, caused by changes in the spatial and temporal dimensions. The agricultural land in the study area in 1994 was mildly vulnerable and the ecosystem was slightly affected. In 2001, the agricultural land was extremely vulnerable, indicating that between 1994 and 2001, the ecosystem of the study area was severely damaged by external disturbances. However, by the end of 2006, the vulnerability had reduced to medium vulnerability, indicating that some environmental management measures were taken between 2001 and 2006 with significant results. By 2010, the vulnerability had increased to an extreme level, indicating that, between 2006 and 2010, the ecological environment was once again subjected to anthropogenic disturbances, leading to an increase in vulnerability. Some treatment measures were also taken between 2010 and 2014; however, they were not effective in restoring the ecological environment, resulting in the land being heavily vulnerable in 2014.

Vulnerability ranking of different landscape types. Based on the statistical results of the vulnerability indices of the different landscape types in the study area from 1994 to 2014, the vulnerabilities of the different landscape types of agricultural land in the coal mining area of Hegang City were divided into five levels: primary, secondary, tertiary, quaternary, and quinary vulnerability (Table 9). The vulnerability values of the agricultural land types were classified according to these levels, and are listed in Table 10.

The study showed that different landscape types of the agricultural land in the study area had varying levels of vulnerability from 1994 to 2014, whereas the other agricultural land remained at the primary level of vulnerability throughout the 20 years. In 1994, the farmland, woodland, and grassland were in the secondary, quaternary, and primary levels of vulnerability, respectively, and were all severely damaged in 2001, which increased their vulnerability. By 2006, their vulnerabilities had returned to their original levels, indicating that, during this five-year period, some environmental management and protection measures had been implemented locally for agricultural land. Vulnerability continued to deteriorate from 2010 to 2014; the trend of change in forest land was the most severe, and was in the quinary level of vulnerability in 2010 and 2014.

CONCLUSIONS

In this study, the vulnerability of different landscape types in agricultural land from 1994 to 2014 was assessed from three perspectives, vulnerability exposure, sensitivity, and adaptive capacity. AHP was used to determine the influence factor weights from various aspects, construct a vulnerability evaluation model for agricultural land, and calculate the vulnerability indices for different landscape types in the temporal and spatial dimensions. The following conclusions were drawn:

The vulnerability of agricultural land in the coal mining area of Hegang City showed an overall increase between 1994 and 2014, but the increase was not large, indicating that the vulnerability of agricultural land showed a weak upward trend. Woodland and farmland were most affected by human activities and external interferences, whereas the vulnerability of grassland and other agricultural land evolved more slowly. The sensitivity of woodland and farmland were the highest among the different landscape types, indicating that woodland and farmland were subjected to the greatest degree of natural environmental factors and human interferences The adaptive capacity of woodland declined significantly,

followed by that of farmland, grassland, and other agricultural land.

The vulnerability of agricultural land in coal mining areas continuously changes, and its performance characteristics are different depending on the disturbance factors. The development of agricultural land in coal mining areas has been constrained, the overall structure and carrying capacity of this agricultural land has been damaged, and its vulnerability has been revealed. More research efforts on agricultural land in coal mining areas is required to alleviate the problems faced by sustainable agricultural development. Future work should focus on the harmonious relationship between the environment and economy, consider the factors affecting the vulnerability of agricultural land in coal mining areas comprehensively, and strive to improve the strategies for restoring and maintaining agricultural land ecosystems in coal mining areas. The existing resources should be used effectively to carry out reasonable environmental protection and achieve sustainable development of such areas [32, 33].

REFERENCES

[1] Tang, Y.N., Zhou, W.Q. (2020) Resource reuse valuation of ecological restoration in abandoned mining areas: A case study of Xuzhou City, Jiangsu Province, China. Chinese Journal of Ecology. 39(10), 3430-3441.

[2] Ma, L., Tian, H.Z., Kang, L. (2020) Eco-environmental impact and spatial control of mineral resources exploitation in the Yellow River Basin. Resources Science. 42(01), 137-149.

[3] Yan, J.Y., Zhao, Y. (2020) Research Hotspot and Prospect of Ecologically Vulnerable Area in China in the Past Three Decades. Journal of Nanjing Normal University (Natural Science Edition). 43(04), 74-85.

[4] Tang, Q., Wang, J.M., Jing, Z.R. (2020) Ecological Vulnerability of Mining Resource-based Cities: A Review. Journal of Ecology and Rural Environment. 36(07), 825-832.

[5] Jordaan, A., Bahta, Y.T, Phatudi-Mphahlele, B. (2019) Ecological vulnerability indicators to drought: Case of communal farmers in Eastern Cape, South Africa. Jamba (Potchefstroom, South Africa). 11(1), 591.

[6] Shu, Y.G., Peng, W.J., Zhou, P.P. (2020) Vulnerbility assessment of agro-ecological environment in Karst mountain based on set pair analysis model of grey trigonometrically whitening weight. Chinese Journal of Applied Ecology. 31(08), 2680-2686.

[7] Li, S., Nie, X., Zhang, A.L. (2020) Research progress on farmland ecological compensation mechanism based on ecosystem service evaluation. Resources Science. 42(11), 2251-2260.

[8] Wang, R.Y., Zhao, G.X., Zhou, W., Zhu, X.C., Wang, J.R., Qin, Y.W. (2008) Assessment of the impacts of land use on regional ecological environmental vulnerability. Transactions of the Chinese Society of Agricultural Engineering. 24(12), 215-220.

[9] Qu, Z.Q., Shen, T.T., Xu, S.L., Liu, Y., Han, G.D. (2020) Review of ecological vulnerability evaluation. Grassland and Prataculture. 32(03), 1-4+42.

[10] Turner, B.L., Kasperson, R.E., Matson, P.A., McCarthy, J.J., Corell, R.W., Christensen, L., Eckley, N., Kasperson, JX., Luers, A., Martello, ML., Polsky, C., Pulsipher, A., Schiller, A. (2003) A framework for vulnerability analysis in sustainability science. Proceedings of the National Academy of Sciences. 100(14), 8074-8079.

[11] He, G., Bao, K.Y., Wang, W.W., Zhu, Y.N., Li, S.Z., Jin, L. (2021) Assessment of ecological vulnerability of resource-based cities based on entropy-set pair analysis. Environmental Technology. 42(12), 1874-1884.

[12] Fu, G., Bai, J.D., Qi, Y., Yan, B., He, J., Xiao, N.W., Li, J.S. (2018) Ecological Vulnerability Assessment in Beijing Based on GIS Spatial Analysis. Journal of Ecology and Rural Environment. 34(09), 830-839.

[13] Wang, J., Hu, B.Q. (2018) GIS-based Vulnerability Assessment and Comprehensive Treatment of Xi jiang River Drainage Basin in Guangxi. Journal of Yangtze River Scientific Research Institute. 35(09), 48-53.

[14] Bohle, H.G. (2001) Vulnerability and Criticality: Perspectives from Social Geography. IHDP Update. 2, 1-7.

[15] Chen, R.S., Guo, X.N., Xiong, B., Wang, Y., Chen, Q. (2021) Climate change, land degradation and food insecurity: linkages and potential solutions. Acta Ecologica Sinica. 41(07), 2918-2929.

[16] Moran, E., Ojima, DS., Buchmann, B., Canadell, JG., Coomes, O., Graumlich, L., Jackson, R., Jaramillo, V., Lavorel, S., Leadley, P. (2005) Global Land Project: science plan and implementation strategy. Environmental Policy Collection.

[17] Timmerman, P. (1981) Vulnerability, Resilience and the Collapse of Society: A Review of Models and Possible Climatic Applications. Institute for Environmental Studies, University of Toronto.

[18] Al-Nasrawi, A.K.M., Jones, B.G., Hamylton, S.M. (2016) GIS-based modelling of vulnerability of coastal wetland ecosystems to environmental changes: Comerong Island, southeastern Australia. Journal of Coastal Research. 75(10075), 33-37.

[19] Zhao, L., Wang, W., Zhang, Y.S., Li, R., Wu, D.T. (2014) The Spatio-Temporal Evolution about Urban Vulnerability on the Northeast Region since Northeast Revitalization. Economic Geography. 34(12), 69-77.
[20] Malaviya, S., Munsi, M., Oinam, G., Joshi, PK. (2010) Landscape approach for quantifying land use land cover change (1972–2006) and habitat diversity in a mining area in Central India (Bokaro, Jharkhand). Environmental Monitoring and Assessment. 170(1), 215-229.
[21] Xiang, J., Li, X., Xiao, R., Wang, Y. (2021) Effects of land use transition on ecological vulnerability in poverty-stricken mountainous areas of China: A complex network approach. J. Environ. Manage. 297, 113206.
[22] Jiang, W.J., Cheng, C.M., Zhang, Y.B., Zhao, H. (2019) Risk assessment of flood disasters in Zhejiang province based on GIS/AHP integration method. Bulletin of Surveying and Mapping. (02), 125-130.
[23] Hou, K., Li, X., Zhang, J. (2015) GIS analysis of changes in ecological vulnerability using a SPCA model in the Loess plateau of Northern Shaanxi, China. International Journal of Environmental Research and Public Health. 12(4), 4292-4305.
[24] Qian, D.W., Yan, C.Z., Xiu, L.N. (2020) Land cover change and landscape pattern vulnerability response in Mu li mining and its surrounding areas in the Qinghai-Tibet Plateau. Journal of Glaciology and Geocryology. 42(04), 1334-1343.
[25] Khalil, A., Hanich, L., Hakkou, R., Lepage, M. (2014) GIS-based environmental database for assessing the mine pollution: A case study of an abandoned mine site in Morocco. Journal of Geochemical Exploration. 144, 468-477.
[26] Dai, X.A., Gao, Y., He, X.W., Yao, Y. (2021) Spatial-temporal pattern evolution and driving force analysis of ecological environment vulnerability in Panzhihua City. Environmental Science and Pollution Research. 28(6), 7151-7166.
[27] Li, H., Zhang, Y.P., Cheng, Y.Q. (2008) Concepts and Assessment Methods of Vulnerability. Progress in Geography. 27(2), 18-25.
[28] Xu, J., Li, G.F., Wang, Y.H. (2015) Review and prospect of resource-based city vulnerability in China and Abroad. Resources Science. 37(06), 1266-1278.
[29] Jia, H., Chen, H., Mao, N.Z., Nie, X. (2018) Landscape sustainable development in highly sensitive ecological fragile areas. Resources Science. 40(06), 1277-1286.
[30] Sahoo, S., Dhar, A., Kar, A. (2016) Environmental vulnerability assessment using Grey Analytic Hierarchy Process based model. Environmental Impact Assessment Review. 56, 145-154.
[31] Ma, J., Li, C.X., Wei, H., Ma, P., Yang, Y.J., Ren, Q.S., Zhang, W. (2015) Dynamic evaluation of ecological vulnerability in the Three Gorges Reservoir Region in Chongqing Municipality, China. Acta Ecologica Sinica. 35(21), 7117-7129.
[32] Tai, X.L., Xiao, W., Tang, Y.X. (2020) A quantitative assessment of vulnerability using social-economic-natural compound ecosystem framework in coal mining cities. Journal of Cleaner Production. 258.
[33] Yang, Z.Q., Lu, Z.H., Liu, D., Yuan, M.Y., Wang, F., Rong, Z.Y., Huang, Y.K. (2021) Ecological security evaluation on the coal resource-based city: a case study of Xilinhot City. Acta Ecologica Sinica. (01), 1-10.

Received: **09.11.2021**
Accepted: **03.12.2021**

CORRESPONDING AUTHOR

Lei Wang
Landscape Architecture,
School of Landscape Architecture,
Northeast Forestry University,
Harbin 150040 Heilongjiang – China

e-mail: wanglei@nefu.edu.cn

© by PSP Volume 31– No. 05/2022 pages 5307-5314 Fresenius Environmental Bulletin

MODELING OF SEAWATER INTRUSION IN THE COASTAL AQUIFER A CASE STUDY OF BOSASO PLAIN SOMALIA

Abdullahi Ali Said*, Recep Yurtal

Department of Civil Engineering, Faculty of Engineering, Cukurova University, Adana, Turkey

ABSTRACT

Seawater intrusion is one of the most important processes that damage groundwater quality in the coastal regions. Groundwater overexploitation in the coastal aquifer of the Bosaso Plain has resulted in seawater intrusion problem. In this study we present a two-dimensional density-dependent numerical model developed with the SEAWAT code, which is aimed to predict the extent of seawater intrusion by different groundwater pumping scenarios. After model development the SEAWAT model was calibrated using both average value of heads and total dissolved solids (TDS) concentration for the 2013 field data. Three scenarios were simulated to understand the effects of pumping to the extent of seawater intrusion for a period 27 years. The model results show that seawater intrusion significantly affects the groundwater concentrations near the coastline and demonstrated high levels of TDS. The predicted results reveal that increasing pump rate will move the seawater intrusion about 6.2 km inland by the year 2040. Results also revealed that a 50% reduction in the pump rate will bring relief to the aquifer by protecting fresh groundwater and preventing any further seawater intrusion. This study is a beneficial tool for decision makers to develop a management strategy for efficient groundwater exploitation in Bosaso plain.

KEYWORDS:
Groundwater modeling, Seawater intrusion, coastal aquifer, Bosaso Plain,Puntland, Somalia

INTRODUCTION

Groundwater is most important water resource all over the world [1]. More than 98% of the available fresh water is groundwater [2]. Coastal plains characterize the most populated areas of the word and coastal aquifers become main water resource in arid and semi-arid regions specially Somalia. Somalia is located in horn of Africa and its coastline is more than 3,333 kilometers in length, the longest of coastline in Africa and the Middle East.

Seawater intrusion is one of the most important processes that damages groundwater quality in the coastal zones by raising salinity levels where water become unsuitable for drinking and irrigation water [3]. High salinity concentration of groundwater is considered as main sources of pollution in coastal aquifers. Seawater intrusion is an unavoidable process that happens over a long period of time due to natural conditions and overexploitation of coastal aquifers. Uninterrupted coastal systems are normally less vulnerable to this phenomenon. Over pumping activities accelerate intrusion rates. Most of the time, the problem is not recognized at the time it occurs. Seawater intrusion problem has become well spread around the word. Such as Palestine ([4], Nigeria [5], Tunisia [6], Libya [7], Turkey [8] and Italy [9]. The simulation of seawater intrusion is a complicated because the intrusion can vary from one aquifer to another. A common approach of seawater intrusion modelling is based on the sharp interface and the Ghyben– Herzberg relation [10].

The Bosaso is largest city in Puntland state of Somalia the rapid development in the city and its population is increasing very fast it is expected to increase the clean water required and thus it brings intensive groundwater abstraction from the coastal aquifer of Bosaso Plain, which will cause severe seawater intrusion problem. Currently the city is experience water quality degradation problems due to seawater intrusion. Thus, the need arises to clearly understand and estimate the groundwater flow and seawater intrusion into Bosaso coastal aquifer as result of excessive pumping in the area. The developed model of seawater intrusion will help authorities to an effective management tool in order to take appropriate decisions to avoid further decline of water quality.

The main objective of this study is to model the potential effect of seawater intrusion into the coastal aquifer in Bosaso Plain and to investigate the effects of different sceneries of pumping on seawater intrusion by utilizing the SEAWAT, which is a variable density solute transport computer code.

MATERIALS AND METHODS

Study area. Bosaso is a coastal town and major city of Puntland state of Somalia, situated on the southern coast of the Gulf of Aden, in large plain surrounded by mountains from west, east and south and

the Gulf of Aden from the north, the city (Figure 1). The study area covers an area of 48 km^2 between 49°6′0″–49°13′30″ longitudes and 11°10′0″–11°19′0″ latitudes. The vegetation is more or less absence in the area. The area is generally slopping towards the sea Gulf of Aden. According to Köppen-Geiger the climate of the study area is the arid type [11].its characterized by very scarce rainfall, generally less than 30mm/year, very high temperature, which reach peaks of about 45 degrees centigrade in July and August, a high evaporation rate, estimated at more than 300mm/year, and relative humidity of about 70%. During the winter however, the temperature drops and the climate becomes pleasant.

Geological and Hydrogeological of Bosaso Plain. The Bosaso Plain is covered alluvial fanglomerates and alluvial deposits as shown in the Figure 2. All the boreholes in the study area are located in alluvial deposits. The alluvial deposits consisting of calcrete soil, gravel and conglomerates underlain by cemented very hard limestone boulders. The very hard limestone boulders are followed by layers of clay light colored, Tertiary sediments comprising loose, unconsolidated alluvial sediments, sandy soils, erosional and depositional sandy clayey materials. The main water source is located southeast of the town in Biyo Kulule. There, 11 boreholes were drilled in alluvial sediments with an average depth of 60 m. The average pumping rate is around 10 l/s which enable a total groundwater extraction of ca. 100 l/s.

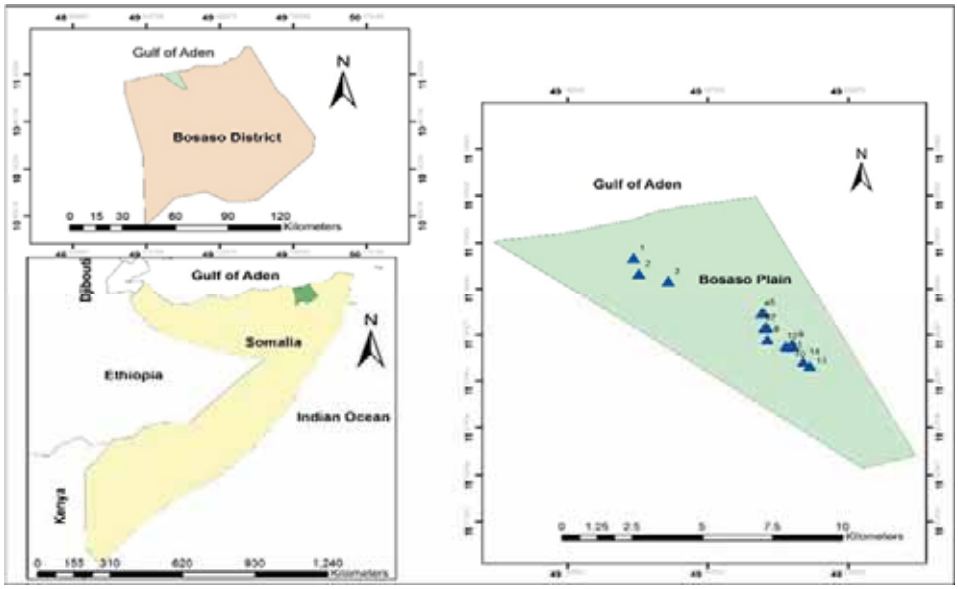

FIGURE 1
Location map of the study area

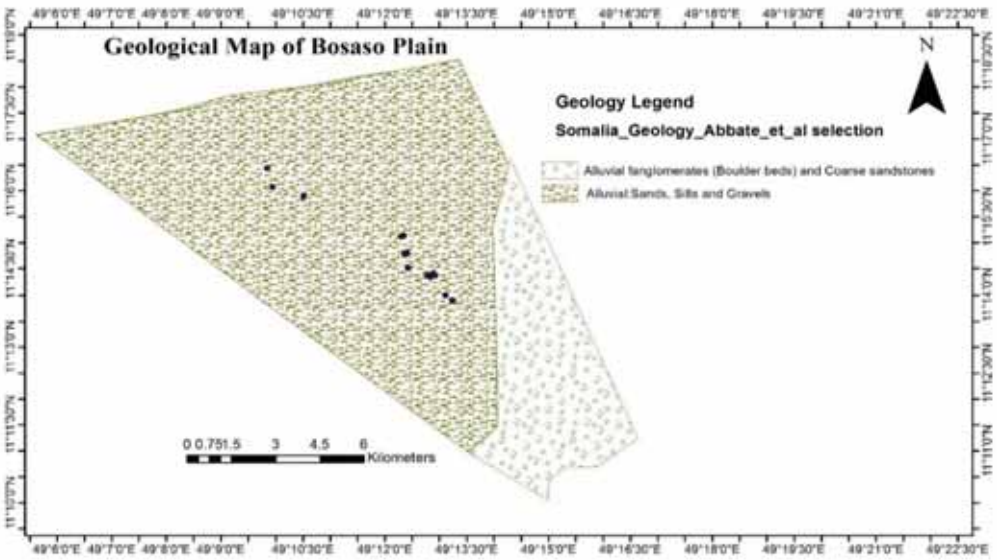

FIGURE 2
Geological map of study area Abbate et al [12].

Numerical Methods of Groundwater Modelling. Groundwater modelling has become an important tool for groundwater resources monitoring, quality assessment and managing. Groundwater modelling is considered to be an excellent way of presenting the hydrogeological situation of the groundwater system and predicting future scenarios of groundwater withdrawal and their effect of socio-economic impacts [13]. The groundwater flow with combination solute transport models can be used to assess the effect of current or future activities on groundwater quantity and quality [14]. Numerical models are mathematical models that use the numerical time-stepping procedure to solve the groundwater flow equations with combination solute transport over time. In contrast to analytical solutions, numerical solution the head is calculated at discrete points (nodes) and is not continuous in space or time. Finite Difference Method (FDM) and Finite Element Method (FEM) are the most common methods used in groundwater modelling

RESULTS AND DISCUSSION

Model Conceptualization and Boundary Conditions. In this research, we utilized Visual MODFLOW Flex 5.1 which is graphical user interface for MODFLOW to model groundwater flow and simulate the seawater intrusion. Flow chart showing the groundwater modelling procedure of the Bosaso Plain is given in Figure 3.

The modeling process began with the definition of the conceptual model representing the area of study. Conceptual of model is a process in which data describing subsurface hydrology are systematically gathered to define groundwater flow and solute transport processes. Since the aquifer's lower layer is impermeable, consideration has been given to one-layer model containing alluvial material (sand and gravel). The eastern and western boundary along were assumed to be no flow boundary condition (Neumann boundary). The Digital Elevation Model (DEM) obtained directly from SRTM data (NASA Shuttle Radar Topography Mission) with 30m-resolution was used to define the top surface of the model. The bottom elevation of the aquifer was assigned by interpolating the depth of wells. Afterwards, finite difference grid consisting 1 layer, 92 rows and 107 columns was generated with active area covers $48.25km^2$.

The Hydraulic conductivity were assigned into the model by diving model into 4 zones, each zone was assigned its specific value in a unit of meter per a day. All nodes along the northern side representing the coastline of the Gulf of Aden (6.5 km) was assigned to a constant head (Dirichlet boundary) condition with 0.0 m elevation and constant concentration of 35000 mgl^{-1}**.** The recharge of the aquifer is characterized as Mountain front recharge (MFR). Therefore, 85000 m3/day estimated by TS [15] was assigned along the mountain front in the south of the plain with applies specified flux stresses applied to the aquifer system. The total groundwater extraction form study area was estimated 8000 m3/d this volume was distributed equally to all 14 municipal wells in the model. To simulate seawater intrusion in Bosaso plain. SEAWAT program was utilized under a transient condition. SEAWAT parameter was assigned as shown in Table 1.

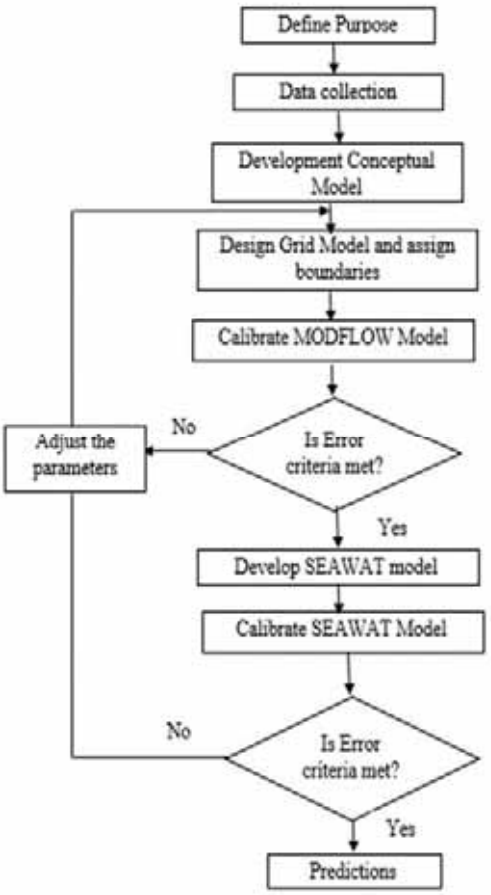

FIGURE 3
Groundwater modelling procedure

TABLE 1
SEAWAT model input parameters for the study area

Parameter	value
Freshwater density	1000 kg/m^3
Seawater density	1025 kg/m^3
Seawater concentration	35000 mgl^{-1}
Total porosity	0.3
Specific storage	0.30
Specific yield	0.20
Longitudinal dispersion	60m
Horizontal transverse dispersion	0.6m
Vertical transverse dispersion	0.1m
Density/Concentration slope	0.7143
Recharge concentration	0 mgl^{-1}

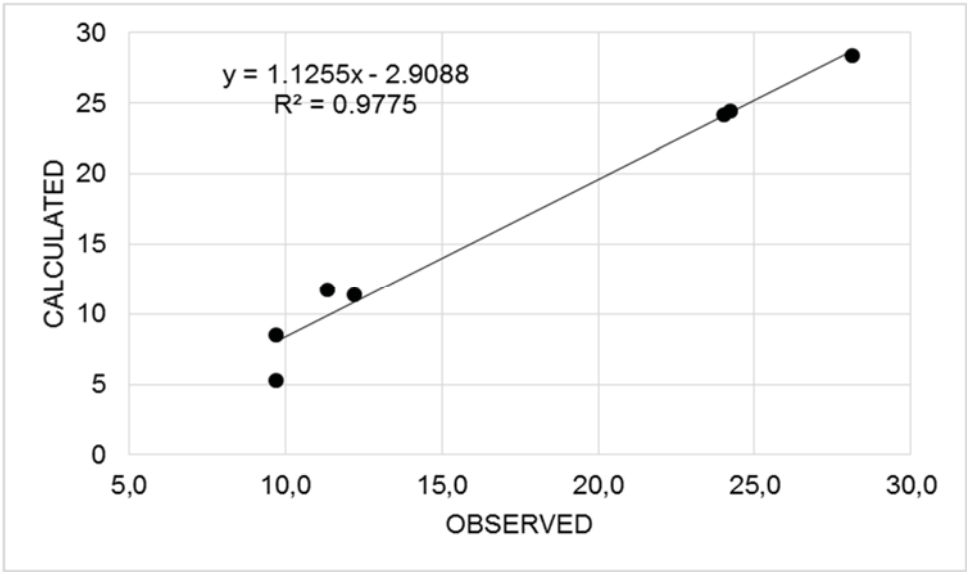

FIGURE 4
Calculated versus observed head

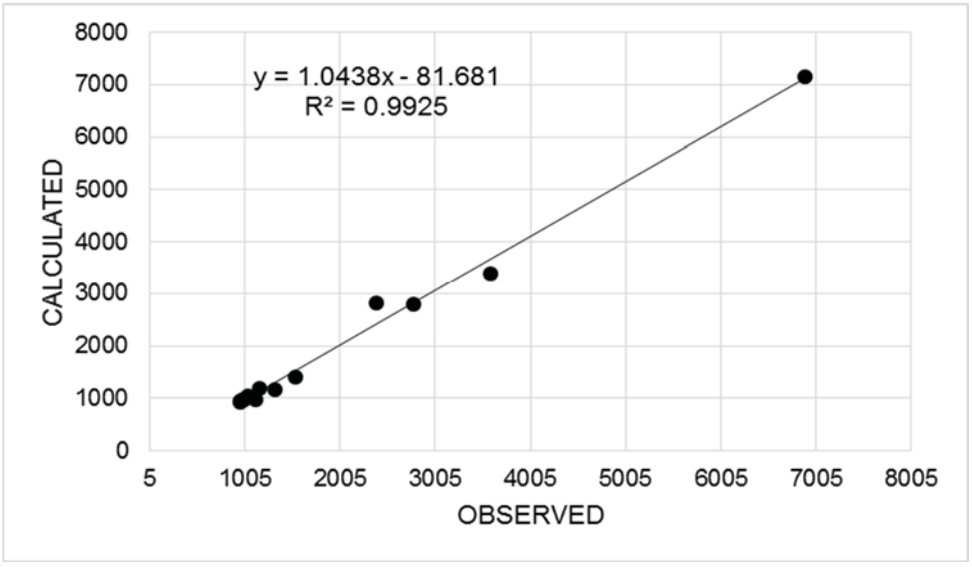

FIGURE 5
Calculated versus observed concentration of TDS (mgl-1)

Calibration of the model. Model calibration is the process to adjust the model's input parameters in order to match the reality of field conditions to attain the best representation of the aquifer system under certain acceptable criteria. The model calibration involved a trial and error adjustment procedure of the model inputs data, observed heads were compared to simulated heads in steady state condition [16]. The calibration of steady state simulation was carried by using automated parameter estimation code (PEST). The average static water level and concentration measured in 2013 were taken as the target of calibration. Hydraulic conductivity values estimated by pumping test results was used as the initial values for calibration. The hydraulic conductivity values were adjusted by sequential trial and error until the reasonable match between the observed and simulated heads was obtained.

The root mean square (RMS) and the correlation coefficient (r^2) error between observed and simulated heads, were used to evaluate how the observed compared to the model simulated targets. To this date there is no established standard to evaluate the calibration process. A common thumb rule is that the RMS should be less than 10% for well calibrated model according to Anderson [16]. Figure 4 shows the steady state calibration matching between observed and calculated heads. A calibration with the RMS of 7.6 % m and r^2 of 0.97 m was achieved, which indicated a good match between the observed and calculated heads. TDS was used as the calibration parameter for solute transport (SEAWAT) model. A total of 14 observed TDS values were using during the calibration. A correlation coefficient of 0.99 and RMS of 2.64 % were obtained (Figure 5).

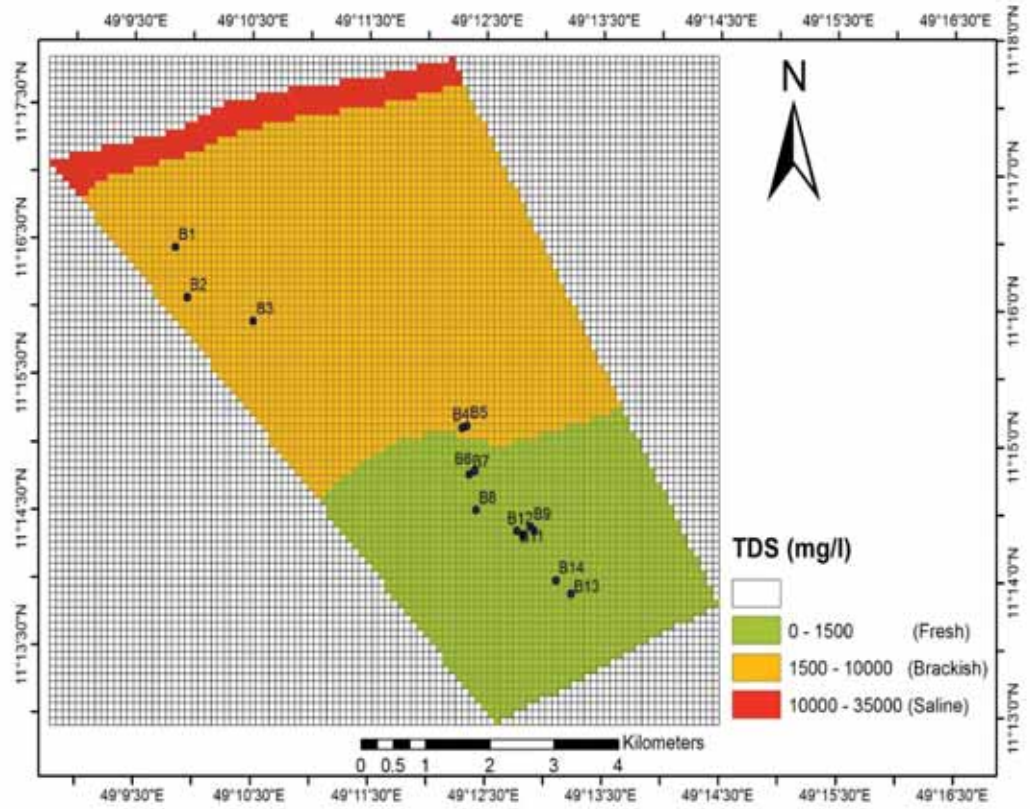

FIGURE 6
Simulated groundwater TDS concentration for year 2013

After model was successfully calibrated seawater intrusion was simulated. Figure 6 shows the simulated TDS concentrations distribution of groundwater in the year 2013. It can be seen that the aquifer is already affected by seawater intrusion and it extended into 5700 m inland. It is clear that seawater intrusion reaches first five wells with high salinity between 1500- 6000 mgl-1. TDS concentration of the rest of the wells reached less than 1500 mgl-1. The relatively high seawater intrusion is attributed due to over pumping and aquifer geometry.

Prediction of Seawater Intrusion under Different Scenarios. The calibrated of SEAWAT model was used to predict various management scenarios to identify the effects of excessive groundwater withdrawal from the coastal aquifer. The recharge rate has been taken in all scenarios as it was in 2013. Four different scenarios were carried out to simulate the extent of seawater intrusion in Bosaso plain for the years 2013-2040.

1. The first scenario : the present pumping rates was maintained. The exploitation volume 2920000 m^3/day till 2040.
2. The second scenario: to satisfy maximum water demands for Bosaso city 8176000 m^3/year till 2040.
3. The third scenario: the groundwater pumping rate is reduced by 50% 5840000 m^3/year till 2040

Groundwater which contains TDS up to 1500 mgl-1 can be considered as freshwater and can be used for water supply. It should be noted that the extent of seawater intrusion in the Bosaso aquifer changes from scenario to scenario. The model result of the first scenario indicate that the concentration is increasing as it approaches the shoreline as expected as shown in Figure 7. When compared to the simulated concentration in 2013 the result indicated that the saline water and brackish water will move further 300m and 500m inland respectively in 2040. In this scenario the seawater intrusion would not reach new wells, but shows gradually increasing of salinities until 2040 if the current extraction rates are maintained.

Predicted model results of the second scenario indicated that the simulated seawater intrusion will continue to spread further inland by reaching two new municipal wells which will make the total of 7 affected municipal wells as shown in Figure 8. The wells were affected by first scenerio their TDS concentration were increased. For instance, well B3 had TDS concentration 3286 mgl^{-1} in the first scenario and an increased 3377 mgl-1 in the second scenerio. Furthermore the width of saline water was moved from 500m to 700m where the width of brackish water moved from 5700 m to 6200 m in 2013 to 2040, respectively. The results of third scenario, by reduced 50% pumping rate shows slow progress of groundwater quality recovery as shown in Figure 9. The predicted results revealed that the two wells will become freshwater.

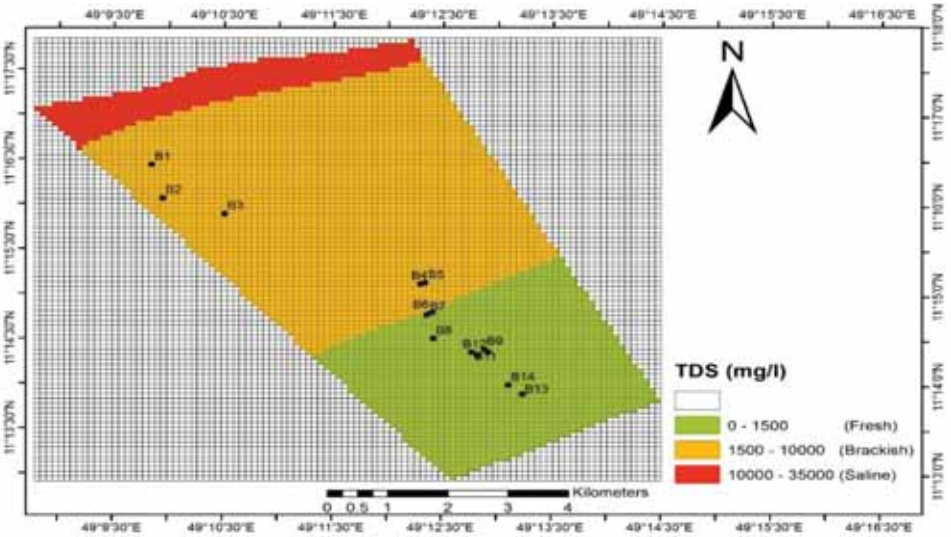

FIGURE 7
Predicted groundwater TDS concentration for year 2040 under scenario 1

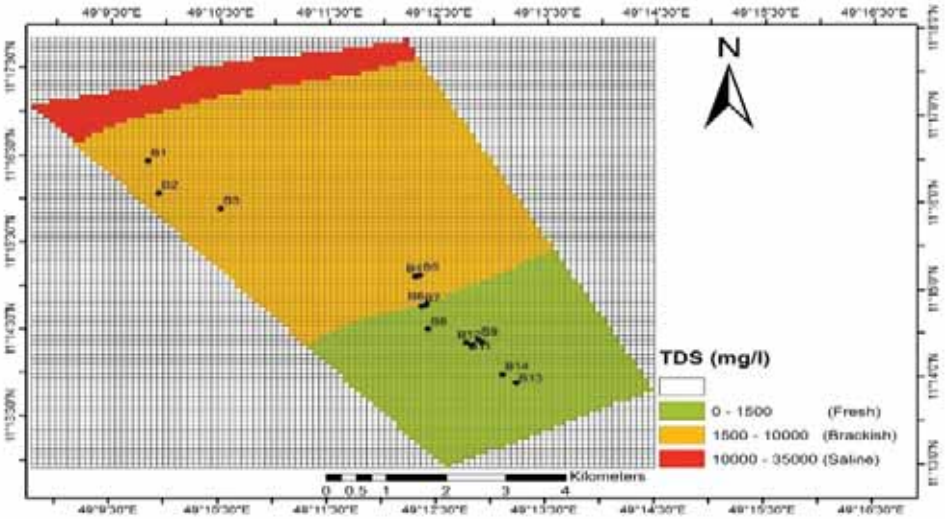

FIGURE 8
Predicted groundwater TDS concentration for year 2040 under scenario 2

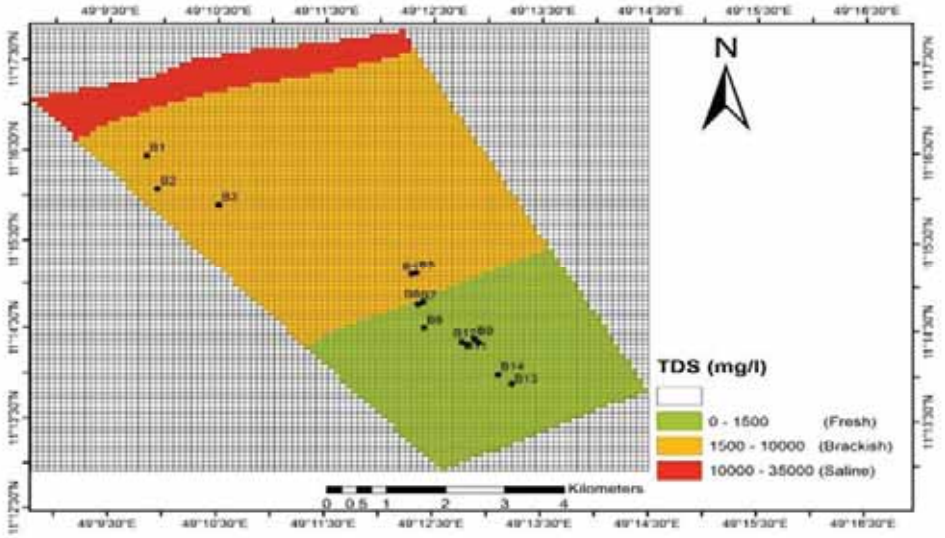

FIGURE 9
Predicted groundwater TDS concentration for year 2040 under scenario 3

CONCLUSIONS

Bosaso plain aquifer is more vulnerable to the seawater intrusion due to deficiency of rainfall and over withdrawal to meet the city water demand. The objective of this study was to model the potential effect of seawater intrusion into the coastal aquifer of Bosaso Plain. The variable density flow code (SEAWAT) was used to determine how far inland seawater intrusion has moved and to predict the future extend. The conceptual model was developed by using geological and hydrogeological information in the Bosaso Plain then the conceptual model was converted into a numerical model using finite difference method. Afterwards, the Model was calibrated using automated parameter estimation code (PEST) by adjusting hydraulic conductivity until the reasonable match between the observed and simulated heads and concentration were obtained. Statistical error criteria such as root mean square (RMS) have been used to evaluate the calibrations. Good match between the observed and simulated head and concentration values was achieved. The model prediction was carried out of 27 years until 2040 based on calibrated model.To evaluate the effects of groundwater pumping on seawater intrusion in the Bosaso plain, the simulations in the three management scenarios was conducted. The first scenario will induce further seawater intrusion into aquifer. The simulation results revealed the interface will move about 6 km inland and that concentration of TDS in municipal wells will continue to increase until 2040. The second scenario was the worst case and will accelerate the seawater intrusion by affecting 7 municipal wells and extending seawater interface further 6.2 km inland. Furthermore, the third scenario by reducing 50% of pumping rate shows positive impact into aquifer by preventing any further seawater intrusion and slowly reducing salinity. Overall, based on model predictions, it is evident that increased pumping rate will lead to further seawater movement into Bosaso Plain aquifer.

Recommendations. The following recommendation can be made of this study.

- This study is a useful example of modelling seawater intrusion in the coastal aquifers. The SEAWAT model reveals to be an effective and robust simulation tool for variable-density flow and transport in porous media
- There should be adequate investment to ensure continues groundwater monitoring in the study area.
- The excessive pumping of groundwater lead to further intrusion of seawater intrusion in to the aquifer. Therefore, it is necessary to stop the continuous deterioration of water quality of the aquifer by finding alternative sources such as seawater desalination plants or artificial recharge.
- All wells located in the contaminated area must be closed to avoid further seawater intrusion or can used as injection wells.
- Bosaso water authority must pursue strategic plan to use additional water resource to meet future water demand as increasing water demand leads deterioration in the quality of groundwater.
- The model should be updated to increase its simulation accuracy as new data become available.

ACKNOWLEDGEMENTS

The authors would like to acknowledge Puntland State Agency for Water Energy and Natural Resources (PSAWEN), Bossaso Water Supply (GUMCO) in Somalia for providing data utilized in this research. This work was supported by Research Projects Center of Cukurova University (Project number: FYL-2018-11190). This manuscript was extracted from MSc thesis submitted by Abdullahi Ali Said in the Institute of Natural and Applied Sciences of Çukurova University, Adana, Turkey, in 2019.

REFERENCES

[1] Bear, J. (1979) Hydraulics of groundwater. McGraw-Hill International Book, New York.
[2] Fetter, C. (2001) Applied hydrogeology - 4th edition. Upper Saddle River, N.J.: Pearson, 4 pp.
[3] Bear, J., Cheng, A.H., Sorek, S., Quazar, D. and Herrera, I. (1999) Seawater intrusion in coastal aquifers, concepts, methods and practices", Kluwer Academic publisher, Dordrecht, The Netherlands. ISBN 0-7923-5573-3.
[4] Qahman, K., Larabi, A. (2006) Evaluation and numerical modeling of seawater intrusion in the Gaza aquifer (Palestine). Hydrogeology Journal. 14(5), 713-728.
[5] Oteri, A.U., Atolagbe, F.P. (2003) Seawater Intrusion into Coastal Aquifers in Nigeria. The Second International Conference on Saltwater Intrusion and Coastal Aquifers Monitoring, Modelling, and Management. Mérida, Yucatán, México.
[6] Gaaloul, N., Pliakas, F., Kallioras, A., Schuth, C., Marinos, P. (2012) Simulation of seawater intrusion in coastal aquifers: Forty five-years exploitation in an eastern coast aquifer in NE Tunisia. Open Hydrol. J. 6, 31-44.
[7] Alfarrah, N., Walraevens, K. (2018) Groundwater overexploitation and seawater intrusion in coastal areas of arid and semi-arid regions. [online] Biblio.ugent.be. Available at: https://biblio.ugent.be/publication/8547673. (Accessed 19.01. 2019)

[8] Cobaner, M., Yurtal, R., Dogan, A., Motz, L.H. (2012) Three dimensional simulation of seawater intrusion in coastal aquifers: A case study in the Goksu Deltaic Plain. Journal of Hydrology. 464, 262-280.
[9] Felisa, G., Ciriello, V., Di Federico, V. (2013) Saltwater intrusion in coastal aquifers: a primary case study along the Adriatic Coast investigated within a probabilistic framework. Water. 5, 1830–1847.
[10] Badon Ghyben, W. (1889) Notes on the probable results of the proposed well drilling near Amsterdam. Inet. Ing. Tijdschr. 1888-89,21, The Hague. (Nora in verband met de voorgenomen put boring nabij Amsterdam Koninkl. Inst. Ing. Tijdschr.).
[11] Rubel, F., Kottek, M. (2010) Observed and projected climate shifts 1901-2100 depicted by world maps of the Köppen-Geiger climate classification. Meteorologische Zeitschrift. 19, 135-141.
[12] Abbate. E., Sagri, M., Sassi, F.P., Aden, I.H., Arush, M.A., Yusuf, O.S. (1994) The geological map of Somalia 1:1.500.000. University of Florence, SELCA, Florence.
[13] Himmelsbach, T., Buter, R. (2001) Conceptual hydrogeological model to assess groundwater resources of the heterogeneous fractured aquifers at Tsumeb (Northern Namibia), In: NewApproaches Characterizing Groundwater flow, Seiler and Wohnlich (eds), Balkema Publication. 1, 245-249.
[14] Istok, J.D. (1989) Groundwater modelling by the finite element. American geophysical union, USA.
[15] Terre Solidali, T.S. (2013) Bosaso Groundwater Resources Puntland Report No. FED/2012/298-778.
[16] Herzberg, A. (1901) The water supply on parts of the north sea cost. J. Gasbeleucht. u. Wasserversorg. Jahrg. 44, Munich. (in German).

Received: **14.05.2020**
Accepted: **15.03.2022**

CORRESPONDING AUTHOR

Abdullahi Ali Said
Department of Civil Engineering,
Faculty of Engineering,
Cukurova University,
Adana – Turkey

e-mail: abdulahi.said01@gmail.com

© by PSP Volume 31– No. 05/2022 pages 5315-5322 Fresenius Environmental Bulletin

ASSESSMENT AND VALUATION OF SOIL LOSS: A CASE STUDY IN BELGRADE SUBURBAN AREA

Mirjana Todosijevic*, Sinisa Polovina, Katarina Lazarevic

University of Belgrade, Faculty of Forestry, Belgrade, Republic of Serbia

ABSTRACT

Soil degradation process reduce the ability of the land to perform its primary function – food production. The most aggressive process being soil erosion, endangers the environment and affects the quality of life. The constant loss of arable land by soil sealing, due to urban expansion, is affecting agricultural production. As a result, the conditions for food production are limited, and the economic prosperity of that area is disputable. This paper represents an analysis of the land use and its change detected by Corine Land Cover (CLC) and the assessment of soil erosion rate and its spatial distribution using Revised Universal Soil Loss Equation (RUSLE) model through a GIS-based approach, for two periods (2000, 2018) in Belgrade suburban area. This study area, characterized by many agricultural areas concentrated around the capital of the Republic of Serbia, is attractive from the economic point of view due to the proximity of the market. The results indicate that with the constant increase of inhabitants, agricultural areas have been reduced due to urban sprawl. The average annual soil loss decreased from 5.85 to 1.95 t/ha·year. Analysis shows that the high medium erosion rate that was detected in the study area in 2000, decreased by 65% compared to the results from 2018, while the processes of low erosion rate has increased by 20%. Despite all the soil loss detected in the study area, soil sealing is the most harmful process of soil degradation due to its often implication of the complete loss of biological functions.

KEYWORDS:
Land use change, soil erosion, RUSLE, soil sealing, cost-benefit analysis

INTRODUCTION

Soil is the primary medium for basic ecosystem function. It provides goods and services that are necessary for the satisfaction of human needs (ecosystem services). Soil is the natural medium for plant growth (food production) and habitat for billions of organisms. Through carbon storage and a reduction of GHG emissions, soil regulates the global climate. The soil security is defined by McBratney, Field, and Koch (2014) as "maintaining and improving the world's soil resources to produce food, fibre, and freshwater, to contribute to energy and climate sustainability, and to maintain the biodiversity and the overall protection of the ecosystem" [1].

Soil degradation process reduce the ability of soil to perform its primary function - food production. Therefore, the conditions for food production are limited, and the economic prosperity of that area is uncertain. The speed of soil degradation (decrease in physical, chemical, and biological soil's quality and productivity) depends on natural, and anthropogenic factors [2]. Soil erosion is a natural process influenced by the magnitude of rainfall intensity, land cover, slope, soil type and is often accelerated by human activities (improper cultivation of agricultural land, urban sprawl) [3].

To preserve soil resources (non-renewable), it is necessary to identify the causes that lead to degradation so that appropriate measures can be implemented to prevent or slow down the process of degradation [4]. As the base of our food production, the soil is damaged by erosion (poor land management), compaction, sealing, contamination, acidification, salinization (by poor irrigation management), desertification, flooding and landslides, decline in soil organic matter, and decline in soil biodiversity [5].

Agriculture, as the world's largest industry, is putting soil under great pressure. Driven by the need to produce food for a growing population, agriculture continues to have a tremendous impact on our ecosystems and resources. According to the United Nations report from 2017, the world population is expected to reach 9.7 billion in 2050 [6], indicating that it would require raising overall food production by 70%. The growing population is stressing Earth's resources and is putting food security under mass pressure. Minimizing further degradation and restoring the productivity of soils that are already degraded using principles of sustainable soil management, we can ensure food security and soil conservation. UN Sustainability Goal (SDG) 2, aims to ensure sustainable food production systems and implement resilient

agricultural practices that increase productivity and production, and that progressively improve land and soil quality through sustainable agriculture by 2030.

Furthermore, agriculture indirectly contributes to economic growth by improving the caloric nutrient intake of the poor and providing food price stability. Economic growth in developing economies, especially broadly-based growth in the rural economy, is essential for reducing poverty and hunger, meeting the Millennium Development Goals (MDGs), and ensuring sustainable development. Unsustainable practices encourage soil degradation, while sustainable practices such as conservation agriculture and adequate land use (contour tillage, contour planting, application of anti-erosion crops) may in the future have a positive impact on microbiological activity and soil fertility, as well as yield of planted crops [7,8].

Soil sealing driven by urban sprawl is characteristic of numerous cities nowadays. It was estimated that 19 EU countries lost approximately 0.81% of their potential agricultural production capacity due to soil sealing between 1990 and 2006, with large variability between regions [9]. Polovina et al. (2021) using the G2 model on the territory of the Master Plan of Belgrade, showed that urbanization processes cause the distribution of soil loss and sediment production in such a way that classes of natural and nature-related elements stand out as particularly fragile categories [10].

MATERIALS AND METHODS

Study area. Belgrade (44° 48' 14.44" N; 20° 27' 54.47" E) is the capital of the Republic of Serbia, and its administrative territory is divided into 17 municipalities. Study area Jajinci - Kumodraž, is located in the north part of the Voždovac municipality (Figure 1). Belgrade area is characterrized by a moderate continental climate. The average annual air temperature is 11.7 °C, the average annual rainfall is 669.5 mm. The dominant soil type is eutric cambisol (pH 5.5-6.5; humus 4-7%), mostly in its typical form [7]. Large areas of these soils, especially variants formed on flat terrains and deep loose substrates, are used as agricultural lands. In those soils, due to degradation, exists a reduction of humus to 2-3% and depletion of nutrients.

In Serbia, the extreme population concentration in Belgrade leads to illegal and unplanned construction, resulting in the loss of arable land due to soil sealing. From data shown in Table 1, it is apparent that in 2019 almost ¼ of the total Serbian population is concentrated in Belgrade (as opposed to only 9% in 1948) [11]. The primary reasons for the population concentration in Belgrade's metropolitan area have been a result of an intensive in-migration process due to the disintegration of the former Yugoslavia, change of the state borders, wars, and political changes [12].

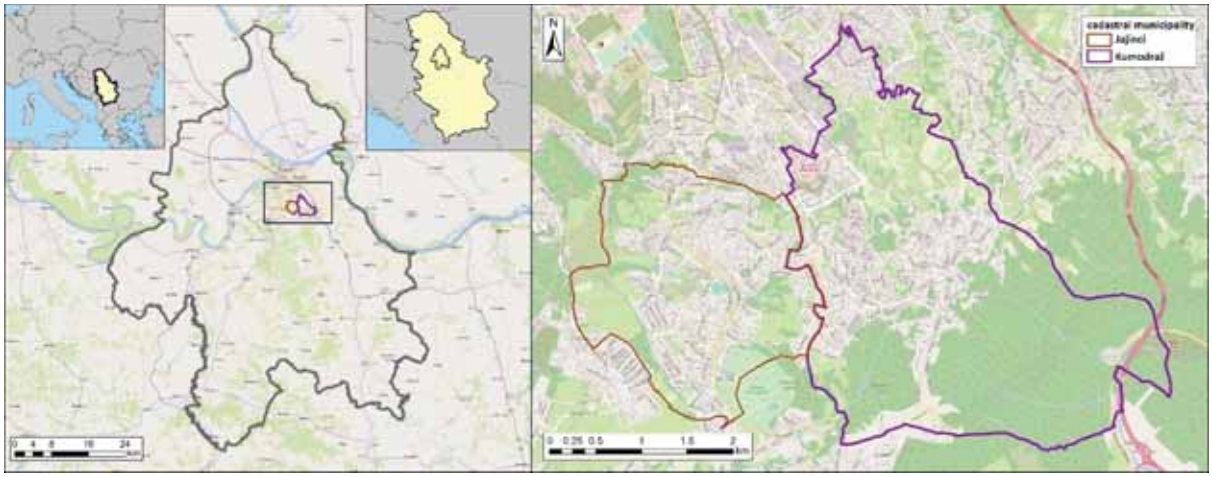

FIGURE 1
Study area

TABLE 1
Comparative overview of the number of population in 1948, 1953, 1961, 1971, 1981, 1991, 2002 and 2011 [11]

	1948	1953	1961	1971	1981	1991	2002	2011	2019
Republic of Serbia	6527583	6978119	7641962	8446726	9313686	7822795	7498001	7186862	6963764
Belgrade	634003	731837	942190	1209360	1470073	1602226	1576124	1659440	1694056
Voždovac	52338	61200	85458	134206	159364	161376	151768	158213	169495
Agriculturists	/	/	/	5137	3187	1276	743	303	152

RUSLE

Revised Universal Soil Loss Equation (RUSLE) is widely used to estimate rates of soil erosion caused by rainfall and associated with overland flow [13]. This well-known method can be expressed as:

A=R·K·L·S·C·P

where: A - estimated average soil loss rate (t/ha·year); R - rainfall-runoff erosivity factor (MJ·mm/ha·h·y); K - soil erodibility factor (t·ha·h/ha·MJ·mm); LS – topographic factor (L - slope length factor and S - slope steepness factor; dimensionless), C – crop management factor (dimensionless), and P – conservation supporting practice factor (dimensionless).

Each factor of RUSLE was described in the GIS as a specific thematic layer with spatial resolution of 30m. By overlaying these layers, and applying appropriate map algebra functions, a spatial distribution map of soil loss was generated.

Rainfall erosivity factor (R) represents the erosivity of rainfall i.e., defines the interdependence of precipitation and production of erosion material [13, 14, 15]. For this paper, due to the lack of data on thirty-minute precipitation values, average annual precipitations data were used, using a mathematical relation [16, 17]:

$$R = b_0 \cdot P_m$$

where: R – Rainfall erosivity (MJ·mm/h·ha·month); b0 – empirical coefficient (MJ/h·month); Pm – average monthly precipitation (mm/month).

The value of the empirical coefficient has a range of values from 1.1 to 1.5 [16], for this paper, the value of the coefficient was adopted to be 1.1. This value has been successfully applied in the territory of the Republic of Serbia [18]. For the needs of the first period of research (2000), climatic data have been obtained empirically from meteorological stations for the observation period 1971-2000; as well as for the second period (2018) from 2001 to 2018. Factor R is presented in the form of a raster using the IDW (Inverse Distance Weighting) deterministic interpolation method.

Soil erodibility factor (K) represents the soil response to the erosive power associated with rainfall and runoff. For this paper, a digital pedological map of 1:20 000 scale has been used and the relevant data on soil characteristics were taken based on relevant literature sources [19] as well as soil samples used in projects of the Faculty of Forestry, University of Belgrade [20, 21].

Topographic Factor (LS) represents the effect of slope length and slope steepness on water erosion. Today, there are different methods and algorithms for the calculation of the topographic factor LS [22]. In this paper, the formula Desmet, Govers, (1996) was applied [23], which was also applied for the area of the European Union [24] using EU-DEM.

$$L_{i,j} = \frac{(A_{i,j} - in + D^2)^{m+1} - A_{i,j-in}^{m+1}}{D^{m+2} \times x_{i,j}^{m} \times 22.13^{m}}$$

$$S = \begin{cases} 10.8sin\theta + 0.03, & \theta < 9\% \\ 16.8sin\theta - 0.5, & \theta \geq 9\% \end{cases}$$

Vegetation cover-management practice factor (C) represents the ratio of the soil loss from land under a specific crop and management system to the corresponding loss from the standard plot, i.e., according to the conditions under which factor K is determined [14]. Factor C for this paper was obtained based on the Corine Land Cover (CLC) vector database for 2000 and 2018. Factor C values are assigned in the form of attributes concerning surveys applied in the territory of EU member states [25].

Conservation supporting practice factor (P) represents the ratio of soil loss on slopes that are protected by certain conservation measures about soil loss on slopes that are under arable land and cultivation in the direction of terrain slope [13, 26]. For purposes of this study, P factor values were obtained according to Panagos et al. (2015) [27] and assigned in the form of attributes to the CLC vector database for 2000 and 2018.

COST-BENEFIT ANALYSIS

The cost-benefit analysis involves comparing the costs to the benefits of a project, quantified in monetary terms, for the purpose of deciding whether the investment is justified. There are two popular models of carrying out cost-benefit analysis calculations – Net Present Value (NPV) and benefit-cost ratio.

The formula for Net Present Value (NPV):

NPV = ∑ Present Value of Future Benefits – ∑ Present Value of Future Costs

The formula for benefit-cost ratio (B/C):

B/C = ∑ Present Value of Future Benefits / ∑ Present Value of Future Costs.

The cost-benefit analysis was used to assess the economic value of crops (orchards, grains) in the study area, including an assessment of the situation for the period 2000-2018, the real rate of return (RRR) of 12%. Calculations are based on the establishment of orchards, production of certain crops, revenues, and costs that are in line with current market prices.

RESULTS AND DISCUSSION

The erosion process has changed over two analysed periods, which are separately explained and presented through each factor of the RUSLE model.

CORINA 2000 and CORINA 2018 changes. An analysis of the change in land cover according to the CLC database for 2000 (Figure 2A) and 2018 (Figure 2B) was performed. According to Table 2, the changes of each category of land cover for the observed periods have been shown. The largest negative changes, i.e., soil loss, were recorded under different categories from the group of agricultural lands, such as non-irrigated arable land (211), Complex cultivation patterns (242), and Land principally occupied by agriculture, with significant areas of natural vegetation (243). Positive changes in surfaces were recorded under the category Discontinuous urban fabric (112) and the category Transitional woodland-shrub (324). The constant increase in the number of inhabitants has increased the demand for housing, which has put great pressure on agricultural and "arable, but uncultivated" land in peripheral urban areas [28, 29].

Change of factor R from 2000 to 2018. The average value for the first period (2000) of factor R is 743.90 MJ·mm/ha·h·y, and for the second period (2018) of 750.72 MJ·mm/ha·h·y (Figure 3). Compared to both periods, the average value of factor R increased by 0.92%.

Factor K. The average value of the factor K is 0.052 t·ha·h/ha·MJ·mm, which classifies it in the group of highly erodible soils. The obtained values of the coefficient K were used for both periods (Figure 3).

Factor LS. According to the described algorithm [23] the range of topographic impact values goes from 0.03 up to 26.11 with an average value of 2.56 (Figure 3).

Vegetation cover-management practice factor (C). According to the described methodology, the values are presented in the form of attributes based on the CLC database for 2000 and 2018 and converted to raster database. For the first period (2000), the value of factor C has a range of values from 0 up to 0.3 with an average value of 0.048 (Figure 3). Compared to the second observed period (2018), the average value of factor C is 0.014 with a range of values from 0 up to 0.2 (Figure 3).

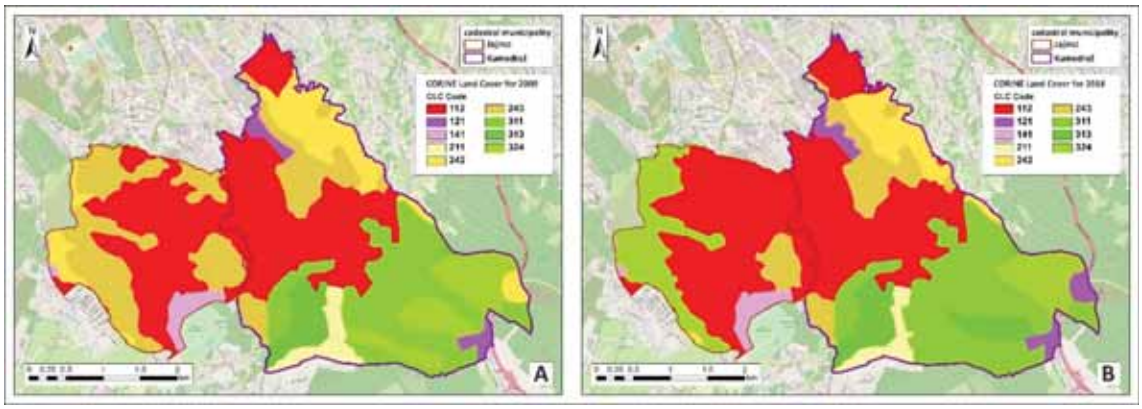

FIGURE 2
Change in land cover according to the CLC database for 2000 (A) and for 2018 (B)

TABLE 2
Change of land cover for 2000 and 2018 according to CLC database

CLC code and name	2000	2018	2000-2018
	ha	ha	variation ha
(112) Discontinuous urban fabric	558.35	641.00	82.66
(121)Industrial or commercial units	26.52	40.73	14.21
(141) Green urban areas	28.28	28.38	0.10
(211)Non-irrigated arable land	42.76	35.12	-7.64
(242)Complex cultivation patterns	140.46	81.89	-58.57
(243) Land principally occupied by agriculture, with significant areas of natural vegetation	317.33	137.44	-179.89
(311) Broad-leaved forest	250.04	299.29	49.24
(313) Mixed forest	53.70	84.21	30.51
(324) Transitional woodland-shrub	123.62	193.01	69.39
Total	**1541.06**	**1541.06**	**0.00**

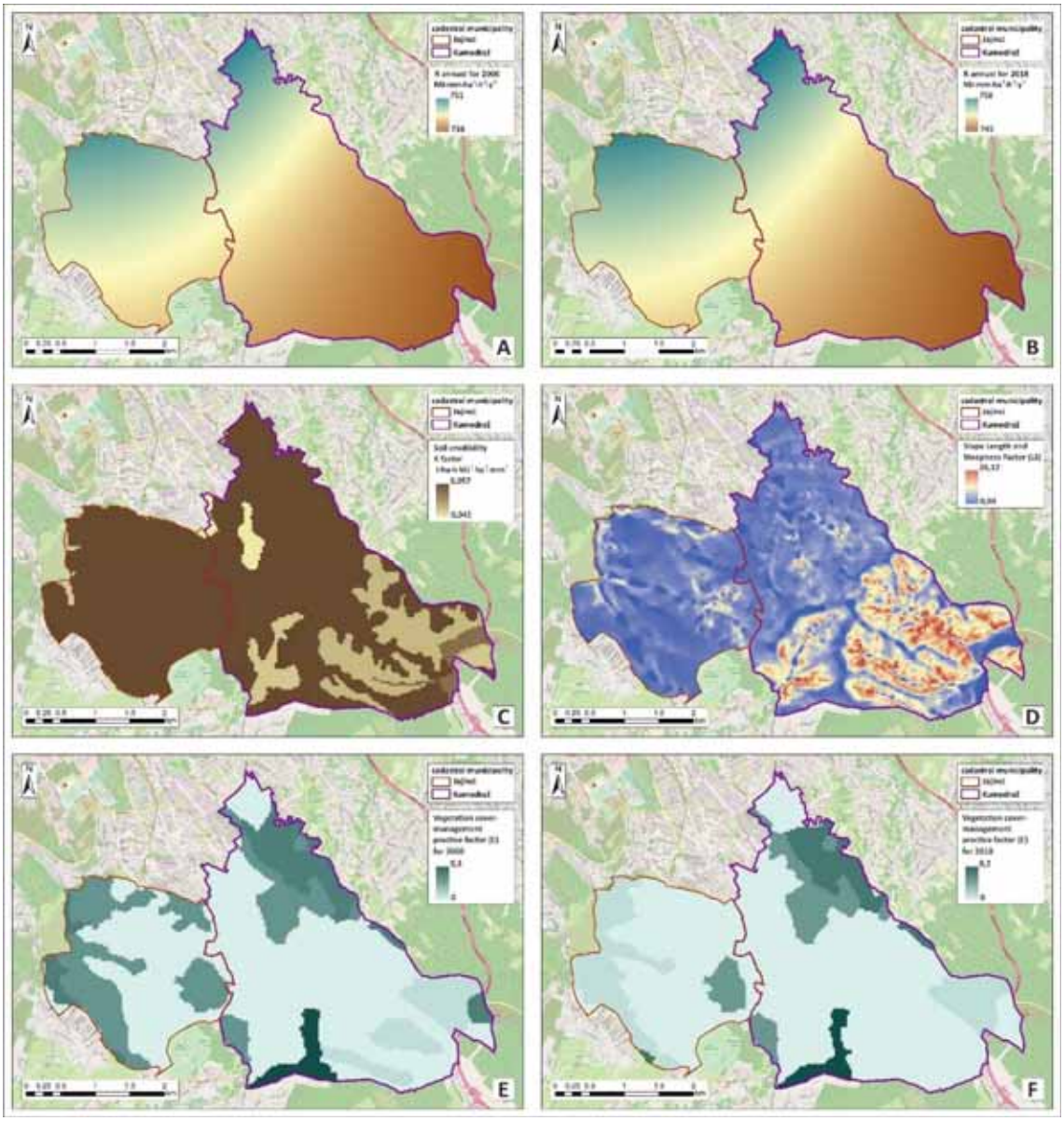

FIGURE 3
RUSLE parameters: Spatial distribution of rainfall erosivity factor for 2000 (A) and 2018 (B); soil erodibility coefficient (C); topographic influence factors (D); vegetation cover-management practice factor for 2000 (E) and 2018 (F).

Factor P. For this paper, P factor values were obtained according to the authors [24] and assigned in the form of attributes to the CLC vector database for 2000 and 2018.

RUSLE 2000 and 2018. The defined parameters (R, K, LS, C, P) represent starting points for the calculation of soil loss according to the RUSLE model. Potential soil loss for both periods is shown in the form of raster databases. In Figure 4, the spatial distribution of soil loss for the year 2000 is shown. The average value in the research area is 5.85 t/ha·year, with a range of values from 0 up to 73.92 t/ha·year. According to the second period (2018), the average value for the researched area is 1.95 t/ha·year, with a range of values from 0 up to 49.67 t/ha·year (Figure 4). Assessment of soil loss was done only in areas that are susceptible to the intensities of erosion processes (agricultural areas, semi-natural, and forest areas).

According to the first period (2000), the study area belongs to the category of high medium soil erosion. After the application of conservation works, as well as the process of urbanization, the average value decreased, hence why the investigated area belongs to the category of low medium soil erosion. According to the spatial distribution in the study area, all forms of destructive categories are represented. The categories of Artificial Surfaces, which have a high degree of non-porous surfaces, are excluded from the analysis of soil loss and comparison.

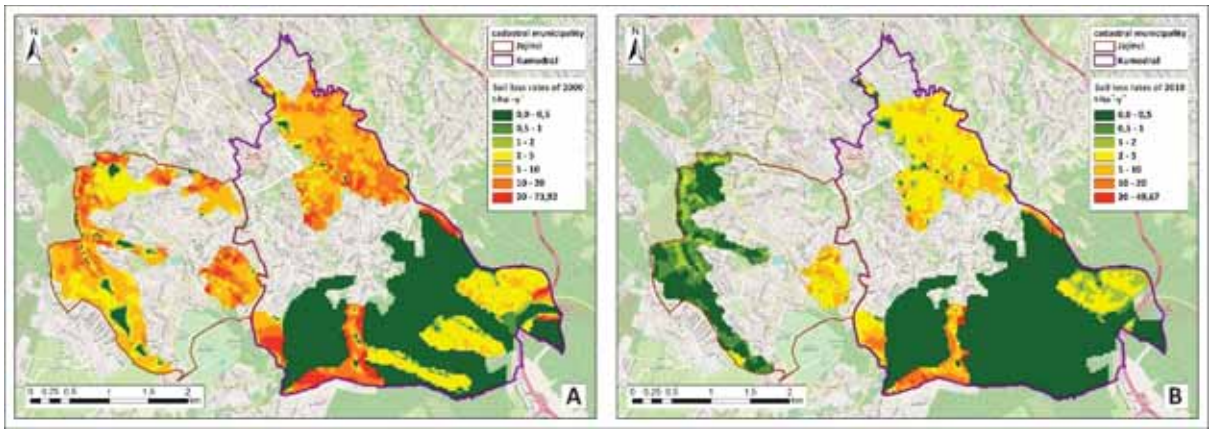

FIGURE 4
Spatial distribution of soil loss using the RUSLE model for 2000 (A) and 2018 (B)

In the previous 20 years, the Jajinci - Kumodraž area played a dominant role in the production and supply of food of the Belgrade area. As the population grew, Belgrade expanded to the detriment of agriculture. Thus, agricultural areas decreased from 317.33 ha to 137.44 ha (56.69%), while urban areas increased significantly. Unfavourable natural characteristics and inadequate land use, especially on sloping terrain, are contributing to soil erosion which is one of the main causes of environmental degradation [30]. The population benefited economically from agriculture given the proximity of a large market, due to the pressures of urbanization.

In the study area, basic crops such as sunflower, wheat, soybeans, and oats are grown, with a large area being occupied by orchards (peach, apricot, plum, cherry, apple, pear, blackberry, raspberry) [31]. This situation was noted in the field and was recognized within the CLC database. The land under the orchard plantations shows a reduction of soil loss, but also a large economic profit, which was also influenced by the proximity of the market [32]. Economic analysis of orchards and grains for period 2000 – 2018 shows the economic justification of investing in the mentioned cultures. Analysis was done only for the above-mentioned cultures. Using economic analysis, calculations of orchards and grains for plant production cycle of 15 years, with a discount rate of 12%. Results show established NPV being 13.89, and B/C 1.055 (Figure 5). The gain value greater than 1, points to the cost-effectiveness of an investment.

Comparative analysis of erosion (2000 – 2018) show that even though the process of soil erosion decreased, a significant % of the land has permanently lost its function. The number of inhabitants has increased significantly, which is characteristic of the suburban municipalities of Belgrade. With the construction, the man was given a place to live, but the land as a natural resource is permanently damaged and lost. This is a result of abandoning agricultural production and altering agricultural land into construction land.

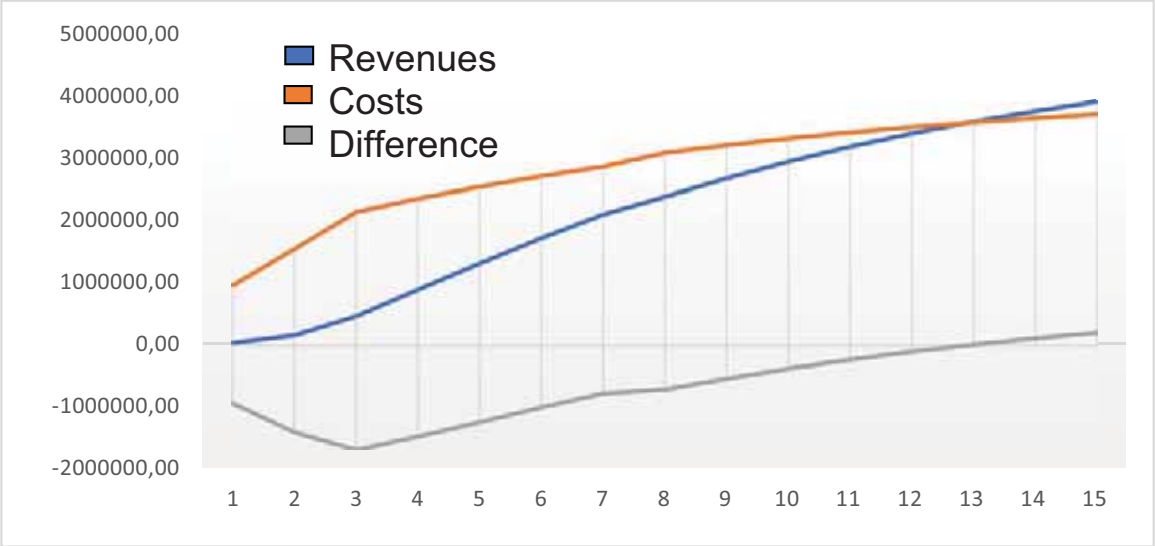

FIGURE 5
Graphical representation of the revenues and costs ratio for plant production cycle of 15 years

CONCLUSION

In the suburban area of Belgrade, due to intensive land use and in addition to the economic benefits from plant crops, the erosion process was intensive. The population in the suburban area of Belgrade increased significantly. Urban sprawl conditioned inhabitants to abandon the former way of life, agricultural areas decreased significantly, as well as erosion processes. But the bigger and more aggressive problem arose. The problem of permanent loss of all soil functions - soil sealing. This raises some questions that demand an answer… What is going to happen with the environment? Are the people's basic needs for life satisfied? Is this in favour of development?

REFERENCES

[1] McBratney, A., Field, D.J., Koch, A. (2014) The dimensions of soil security. Geoderma. 213, (January), 203-213.

[2] Dragović, N., Vulević, T. (2020) Soil Degradation Processes, Causes, and Assessment Approaches - Springer Nature Switzerland AG 2020, W. Leal Filho et al. (eds.), Life on Land, Encyclopedia of the UN Sustainable Development Goals. (Accessed date: 29.01.2019.)

[3] Putrantoa, D.D.A., Sarinob, Yuonoc, A.L. (2017) Spatial Distribution Level of Land Erosion Disposition Based on the Analysis of Slope on Central Lematang sub-Basin). AIP Conference Proceedings. 1903, 100016.

[4] Momirović, N., Kadović, R., Perović, V., Marjanović, M., Baumgertel, A. (2019) Spatial assessment of the areas sensitive to degradation in the rural area of the municipality Čukarica, International Soil and Water Conservation Research. 7(1), 71-80.

[5] Adhikari, B., Nadella, K. (2011): Ecological economics of soil erosion: a review of the current state of knowledge in "Ecological Economics Reviews". Robert Costanza, Karin Limburg & Ida Kubiszewski, Eds. Ann. N.Y. Acad. Sci. 1219, 134–152.

[6] United Nations, Department of Economic and Social Affairs, Population Division (2017) Probabilistic Population Projections based on the World Population Prospects: The 2017 Revision. Population Division, DESA. http://esa.un.org/unpd/wpp/ (Accessed date: 30.01.2019.)

[7] Lazarević, K., Zlatić, M., Kostadinov, S. (2016) Influence of socio-demographic factors on erosion processes in the rural part of the municipality of Voždovac. Bulletin of the Faculty of Forestry. 114, 75-102.

[8] Todosijević, M., Čakmak, D., Belanović Simić, S., Zlatić, M., Kadović, R., Lazarević, K., Perović, V. (2018) Raspberry Production on Sustainable Principles in Western Serbia. Soil and water resources protection in the changing environment, Catena, Soil Science, Advanced in GeoEcology 45, 120-132.

[9] Gardi, C., Panagos, P., Van Liedekerke, M., Bosco, C., De Brogniez, D. (2015) Land take and food security: assessment of land take on the agricultural production in Europe. Journal of Environmental Planning and Management. 58(5), 898–912.

[10] Polovina, S., Radić, B., Ristić, R., Kovačević, J., Milčanović, V., Živanović, N. (2021): Soil Erosion Assessment and Prediction in Urban Landscapes: A New G2 Model Approach. Appl. Sci. 11, 4154.

[11] Census of Population, Households and Dwellings in the Republic of Serbia 2011 (2014): comparative overview of the number of population in 1948, 1953, 1961, 1971, 1981, 1991, 2002 and 2011; Data by settlements, Book 20. Published by: Statistical Office of the Republic of Serbia, 198pp.

[12] Živanović, Z., Tošić, B., Nikolić, T., Gatarić, D. (2019): Urban System in Serbia—The Factor in the Planning of Balanced Regional Development. Sustainability. 11, 4168.

[13] Renard, K., Foster, G., Weesies, G., McCool, D., Yoder, D. (1997): Predicting soil erosion by water: a guide to conservation planning with the Revised Universal Soil Loss Equation (RUSLE). Agricultural Handbook No. 703. 404 pp.

[14] Wischmeier, W.H., Smith, D.D. (1978): Predicting rainfall erosion losses: a guide to conservation planning. Agriculture Handbook No. 537. USDA/Science and Education Administration, US. Govt. Printing Office, Washington, DC. 58 pp.

[15] Morgan, R. P. C (2005) Soil Erosion and Conservation. National Soil Resources Institute, Cranfield University. 304pp.

[16] Van der Knijff, J.M., Jones, R.J., Montanarella, L. (2000) Assessment in Italy Soil Erosion Risk. EUR 19044 EN; The Official Publications Office of the European Communities: Luxembourg, 1-34.

[17] Grimm, M., Jones, R.J., Rusco, E., Montanarella, L. (2003) Soil erosion risk in Italy: A revised USLE approach. Eur. Soil Bur. Res. Rep. 11, 23.

[18] Perović, V., Kadović, R., Djurdjević, V., Braunović, S., Čakmak, D., Mitrović, M., Pavlović, P. (2019) Effects of changes in climate and land use on soil erosion: A case study of the Vranjska Valley, Serbia. Reg. Environ. Chang. 19, 1035–1046.

[19] Antonović, G., Živanović, Ž., Bogdanović, M., Ćorović, R., Trifunović, M. (1976): Soils in the area of Belgrade south of the Sava and Danube; City of Belgrade – City Geodetic Authority.
[20] Ristić, R., Radić, B., Miljanović, V., Trivan, G., Ljujić, M., Letić, L., Savić, R. (2013) Blue-green corridors as a tool for mitigation of natural hazards and restoration of urbanized areas: A case study of Belgrade city. Spatium. 504, 18–22.
[21] Ristić, R., Radić, B., Trivan, G., Malušević, I. (2014): "Blue-green" corridors as a tool for erosion and stream control in highly urbanized areas - A case study of Belgrade city. IAHS-AISH Proc. Reports 2014. 363, 315–320.
[22] Brychta, J., Brychtová, M. (2020): Possibilities of including surface runoff barriers in the slope-length factor calculation in the GIS environment and its integration in the user-friendly LS-RUSLE tool. Soil and Water Research. 15, 2020 (4): 246–257.
[23] Desmet, P.J., Govers, G. (1996): A GIS procedure for automatically calculating the USLE LS factor on topographically complex landscape units, Journal of Soil and Water Conservation. 51 (5), 427–433.
[24] Panagos, P., Borrelli, P., and Meusburger, K. (2015): A new European slope length and steepness factor (LS-factor) for modeling soil erosion by water, Geosciences, 5 (2): 117–126.
[25] Panagos, P., Borrelli, P., Meusburger, C., Alewell, C., Lugato, E., Montanarella, L. (2015): Estimating the soil erosion cover-management factor at European scale. Land Use Policy Journal. 48C, 38-50.
[26] López-García, E.M., Torres-Trejo, E., López-Reyes, L., Flores-Domínguez, Á.D., Peña-Moreno, R.D., López-Olguín, J.F. (2020) Estimation of soil erosion using USLE and GIS in the locality of Tzicatlacoyan, Puebla, México. Soil & Water Res. 15, 9−17.
[27] Panagos, P., Borrelli, P., Meusburger, K., van der Zanden, E.H., Poesen, J., Alewell, C. (2015): Modelling the effect of support practices (P-factor) on the reduction of soil erosion by water at European scale, Environmental Science & Policy. 51, 23-34. ISSN 1462-9011.
[28] Shikangalah, R.N., Jeltsch, F., Blaum, N., Mueller, E.N. (2016) A Review on Urban Water Erosion. J. Stud. Humanit. Soc. Sci. 5, 163 - 178.
[29] Pribadi, D.O, Vollmer, D., Pauleit, S. (2018) Impact of peri-urban agriculture on runoff and soil erosion in the rapidly developing metropolitan area of Jakarta, Indonesia, Regional Environmental Change, Springer-Verlag GmbH Germany 18: 2129-2143.
[30] Vulević, T., Todosijević, M., Dragović, N., Zlatić, M. (2018): Land use optimization for sustainable development of mountain regions of western Serbia, Journal of Mountain Science. 15, 1471-1480.
[31] Zlatić, M. (1994): Evaluation of antierosion works from the aspect of technical and economic justification in the endangered area of the city of Belgrade, doctoral dissertation, University of Belgrade, Faculty of Forestry, Belgrade.
[32] Rončević, V., Zlatić, M., Todosijević, M. (2019): Environmental and economic effects of investments in sustainable land management in the basin of Šutilovac stream. Bulletin of the Faculty of Forestry. 119, 213-232.

Received: **20.10.2021**
Accepted: **20.03.2022**

CORRESPONDING AUTHOR

Mirjana Todosijevic
University of Belgrade, Faculty of Forestry,
Kneza Višeslava 1,
11030 Belgrade – Republic of Serbia

e-mail: mirjana.todosijevic@sfb.bg.ac.rs

© by PSP Volume 31– No. 05/2022 pages 5323-5329 Fresenius Environmental Bulletin

NOTICE

THE STATISTICAL STUDY ON GREEN ECONOMY EFFICIENCY IN ECO-ECONOMIC BELT

Ru Guo*

Mathematics Department of Science College, XiJing University, Xi'an 710123, China

ABSTRACT

The construction of the Hanjiang Eco-economic Belt has been included in China's development plan. The region has significant location advantages and huge development potential. Adhering to the concept of green development, realizing the coordinated development and organic unity of economic and social development and ecological environmental protection is important for promoting the economic and social development of the region. Sustained development plays an important role. Based on the existing research results, this paper focuses on the three industrial wastes, and considers environmental pollution as an undesired output into the calculation of economic efficiency. Construct a comprehensive index reflecting the impact of environmental pollution on the economic efficiency of the Hanjiang River Eco-economic Zone. Based on the analysis characteristics of the DEA model, measure the traditional economic efficiency and green economic efficiency of the Hanjiang Eco-economic Zone, and analyze its trend change level. The research results show that the green economic efficiency of most cities in the Hanjiang River Ecological Economic Zone shows an upward trend, and the fluctuation range is smaller than that of the traditional economic efficiency. The unevenness of the green economy efficiency of the cities in the Hanjiang Eco-economic Belt is more prominent, and the green economy efficiency of upstream cities is higher than that of downstream and midstream cities. There is a U-shaped relationship between the green economic efficiency of the Hanjiang Eco-economic Zone and the level of economic development.

KEYWORDS:
Han River, Ecological economic zone, Green, efficiency

INTRODUCTION

The basis of human survival and development is the material exchange between man and nature, in which ecological problems have been accompanied by all stages of economic and social development. From the perspective of the structure of ecology and economics, the two are derived from the same root, eco, so many scholars believe that "ecology is natural economics" [1-3]. From the perspective of ecological and economic benefits, it is believed that the essence of the ecological environment is an economic issue, ecology and economic development are closely linked, and both aim at maximizing benefits. During the industrial revolution, the ecological environment resources were considered as exogenous variables of economic growth. They were valueless and infinite, and could be used and obtained freely. The growth of the traditional economy could increase indefinitely [4]. However, with the explosive population growth, insufficient food supply, ecological degradation, increased environmental pollution, energy resource crisis and many other alarm bells sounded, the contradiction between environmental problems and human survival and development has become increasingly prominent, and people have begun to question the traditional economic growth model. And criticism, and gradually realized that the ecological development of economic ecologicalization and ecological economicalization is a long-term strategy for coordinating economic development and ecological environmental protection. It is the inevitable choice to get out of the predicament and achieve balanced development and sustainable development of economic and ecological benefits [5-7]. In addition, the economic system and the ecosystem interact, interweave, and penetrate each other to form a closely-connected composite system, which means that the ecosystem is a place for storing various material resources in nature, and the economic system is based on the resources in the ecosystem. There is a close relationship between the two places where production activities are carried out, and both are indispensable [8-11]. The operation of ecological economy is the process of human development and utilization of natural resources and the ecological environment. Humans are required to follow the following three basic principles in the process of economic development: First, the basic principles of saving resources and protecting the environment. The economic system is using the ecosystem. When developing material resources, we must always remember to protect the environment and save resources, and leave enough natural resources and a good ecological environment for future development;

the second is the principle of resource sharing, which must be realized during the development of ecosystems in different regions and economic systems in different regions Resource sharing, to be specific, is to jointly realize the sustainable development of the economy while meeting its own needs without harming the development of other regions; the third is the principle of effectiveness, through the introduction of advanced technologies and optimizing resource allocation to achieve maximum unit resources Output, reduce unit energy consumption and increase the effective output rate of resource utilization. Therefore, studying ecosystems and ecological economic systems and applying their principles to production practices can achieve rapid and effective economic and social development [12-14].

Green economy is a new type of economic development model. It is a knowledge-based economy and a green economy that creates green wealth. Based on the traditional industrial economy, it is market-oriented and a new stage of development that meets the needs of human environmental protection and health. It is an organic combination of material civilization and non-material civilization [15]. From the perspective of political economy, the green economy is the greening of every link in the economic system of production, processing, circulation, distribution, and consumption. On the one hand, the green economy uses technology industries as the main means to promote the marketization of green products and devote themselves to human welfare. On the other hand, within the scope of the limited resources and energy carrying capacity, the green economy introduces high technology into every link of ecological protection and economic development through human capital to achieve economic, social and ecological benefits. Highly unified [16-18]. The British Green Economic Research Institute (GRI) is currently the only international research institution with the theme of "Green Economics". It publishes the "Journal of Green Economy" and holds academic seminars every year. According to GRI's definition of green economy, green economy is the harmonious interaction between man and nature, and it is an economic way to improve human well-being and achieve a fairer society. Green economists generally believe that all factors that determine the economic foundation should be related to the ecosystem in some way. The green economy is a challenge to the orthodox mainstream economics of the green movement, and it has gradually been recognized as a climate change issue in the world. The current mainstream view is that green economy theory is a new economic development model described from the perspective of green and economy; among them, "green" not only includes the content of ecological economy, circular economy and low-carbon economy, but also covers the concept of people-oriented and comprehensive development. Thereby enhancing human well-being, promoting social progress, and ensuring the harmonious coexistence between man-nature-environment [19-21]. The "green economy" is also different from the traditional economy. It is based on a green, healthy, and effective foundation, introducing technological progress into the economic development track, and maximizing economic benefits through technological innovation with minimal investment in resources and energy. Green economy theory is the idea of dealing with the internal relationship between man and the environment. On the one hand, it emphasizes the role of green productivity. Through the introduction of knowledge and technology-based high-tech industries, it meets the needs of people's production and life within the scope of limited resource carrying capacity. Protect the environment and achieve sustainable development; on the other hand, natural resources are the energy input for economic growth, while environmental pollution is the price paid for economic growth. Green economic theory regards the efficient use of natural resources and the effective treatment of environmental pollution as impacts An important endogenous variable for the development of a green economy, with efficiency, harmony, and sustainable development as the fundamental purpose, low-energy, high-yield, high-tech, and high-efficiency recycling as the characteristics, and comprehensive coordination of economic, social and environmental aspects in the development of a green economy , And strive to improve the quality of the economy, accelerate the construction of ecological civilization and promote the harmonious development of society.

MATERIALS AND METHODS

Overview of the research area. Han River Ecological Economic Zone. The Han River is the largest tributary of the Yangtze River. The northern section of the Han River covers the upper, middle and lower reaches of the Han River. Its basin covers 10 cities (forest areas) and 39 counties (cities, districts) in the province, covering an area of 63,000 square kilometers. The basin area occupies the entire province's territory. 33.89% of the area.

The Hanjiang River Basin is rich in natural resources, strong economic foundation, and superior ecological conditions. It is an important food production area and an important ecological function area in China. Historically, it was one of the five major corridors from my country's western plateau to the central basin and eastern plain. It is now A strategic channel connecting the Yangtze River Economic Belt and the New Silk Road Economic Belt.

Model selection. Entropy Method to Calculate Comprehensive Index of Environmental Pollution. Due to the limitation of the number of indicators in the DEA model, this article first treats the

undesired output with entropy weighting. Entropy was originally the quantity of the state of matter derived from the laws of thermodynamics. It was introduced by C.E. Shannon in information theory, called information entropy. Now it is widely used in various fields such as biology, finance, social economics and so on. The principle of information theory believes that information can be used to objectively measure the degree of order of a system, and entropy can be used to objectively measure the degree of disorder of a system; information entropy has an inverse relationship with storage capacity, that is, information entropy is small, and the amount of information provided is large. The role played in the comprehensive evaluation is greater, and the weight given to it is higher. Entropy weight method is an objective weighting method, based on the original data information, through the amount of information between indicators and the degree of correlation and variability between indicators, the entropy weight of each indicator is calculated using information entropy, and the indicators are assigned scientifically and objectively. Weight, reduce the influence of subjective factors.

Data processing. The data mainly comes from the "China City Statistical Yearbook", "Hubei Province Statistical Yearbook", "Shaanxi Province Statistical Yearbook", "Henan Province Statistical Yearbook" and the websites of the municipal statistical bureaus, mainly using statistical software such as word2010, Excel 2010, SPSS, Minitab, etc. Perform data processing.

RESULTS AND DISCUSSION

Environmental Pollution Index Measurement. Since the DEA model has a certain quantitative relationship between input and output and decision-making units when measuring efficiency, environmental pollution indicators are now processed with entropy weight, and the results are shown in Figure 1.

According to Figure 1, it can be seen that Nanyang, Yichang, and Hanzhong are dominated by high-energy-consuming industries, with high environmental pollution indexes. The environmental pollution indexes of Yichang and Hanzhong are in the range of 0.7 to 0.8, and the value of Nanyang's environmental pollution index is hovering around 0.7. The pollution index of these cities has shown a significant downward trend. The environmental indexes of cities such as Ankang, Jingmen, and Shiyan were the second place and fluctuated slightly in the range of 0.6 to 0.7. Although the environmental indexes of Jingmen and Shiyan increased during 2006-2009, the environmental pollution index tended to decrease throughout the study period. Although Ankang's environmental pollution index plummeted to 0.5653 in 2013, the overall level showed an upward trend. The environmental indices of Xiangyang, Xiaogan, and Xianyang fluctuate in the range of 0.4 to 0.7; the degree of fluctuation is in order of Xianyang, Xiaogan, and Xiangyang. The environmental pollution index of cities such as Shangluo and Suizhou is relatively low, but the environmental pollution index shows an overall upward trend, and pollution is relatively aggravated. The environmental pollution index of cities such as Qianjiang and Tianmen fluctuates the most, and it gradually rises to the highest point during 2006-2010, and the environmental pollution index gradually decreases during the "Twelfth Five-Year Plan" period. The environmental pollution index of Xiantao is the lowest, but the pollution index is rising in the later period.

Analysis of Trend Changes in Economic Efficiency Level. The super-efficiency SBM model that comprehensively considers expected output and undesired output, uses Max DEA software to measure the green economic efficiency of major cities in the Hanjiang Ecological Economic Zone, and compares it with the traditional economic efficiency that does not consider environmental pollution and resource input. Analyze the difference between traditional economic efficiency and green economic efficiency and their respective impacts on economic development. Due to the differences in the economic basis and related policies of the cities and regions in the Hanjiang Eco-economic Belt, the production technology constraints with variable returns to scale are selected. The results of the calculation are shown in Figure 2. An efficiency value greater than 1 indicates that the output efficiency of the city is effective, and an efficiency value less than 1 indicates that the output efficiency of the city is lacking.

City economic efficiency analysis. The traditional economic efficiency of cities in the upper reaches of the ecological economic belt has obvious interannual changes, especially in 2013, the fluctuation range of each city is relatively large (Figure 3). The traditional economic efficiency of Qianjiang has changed relatively smoothly, and the efficiency value has stabilized at around 0.9443 with small changes. The traditional economic efficiency of Xiantao has the most effective value, but the fluctuation range is also the largest. The maximum efficiency value is 2.6 times the minimum efficiency value. The traditional economic efficiency of Tianmen, Ankang, and Jingmen has a similar trend. They all show a circular change of first decline and then rise. Among them, the traditional economic efficiency of Tianmen and Jingmen is greater than the traditional economic efficiency of Ankang. The minimum value of Nanyang's traditional economic efficiency is 0.4706, and the maximum value is 0.7219. The economic efficiency value is the smallest among the upstream cities. Looking at the upper reaches of

the Hanjiang Eco-economic Belt, the traditional economic efficiency plummeted in 2013 due to weather and other reasons, fluctuating around 0.9 as a whole, and the economic efficiency value was higher than that of cities with low resource utilization such as Ankang and Nanyang.

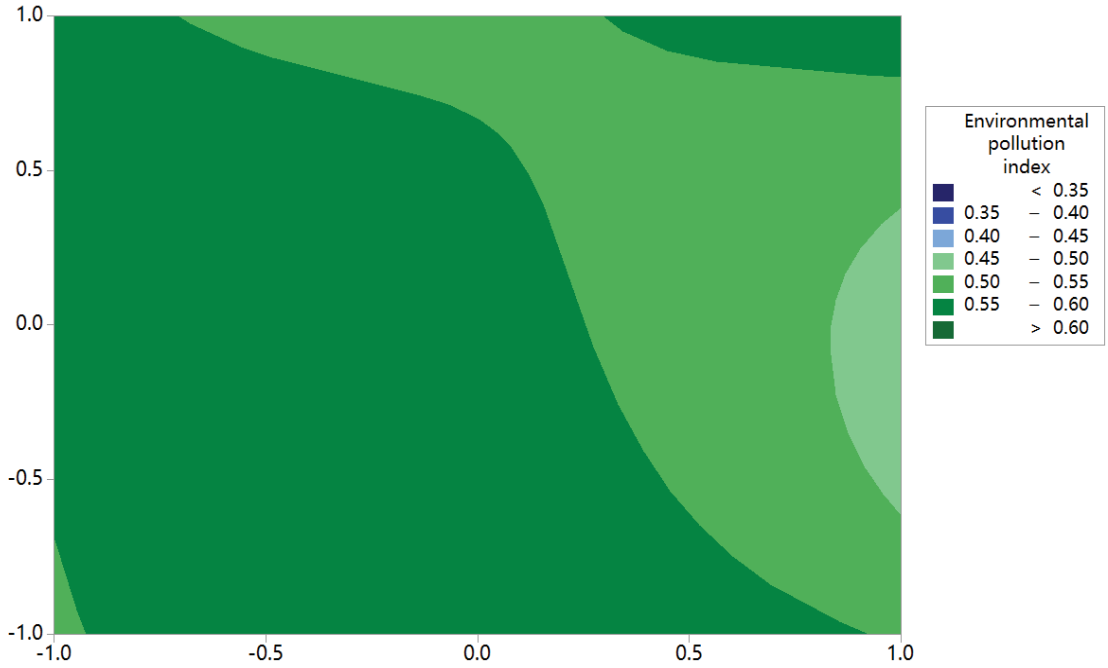

FIGURE 1
Contour Plot of Environmental pollution index

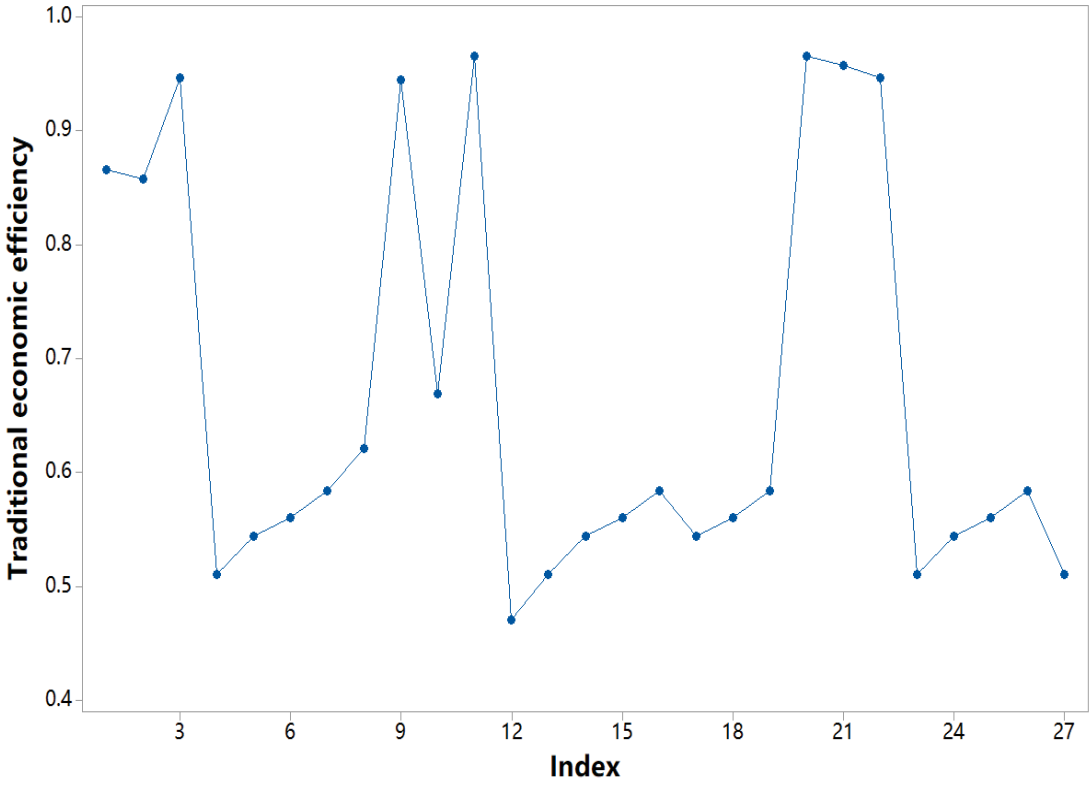

FIGURE 2
Time Series Plot of Traditional economic efficiency

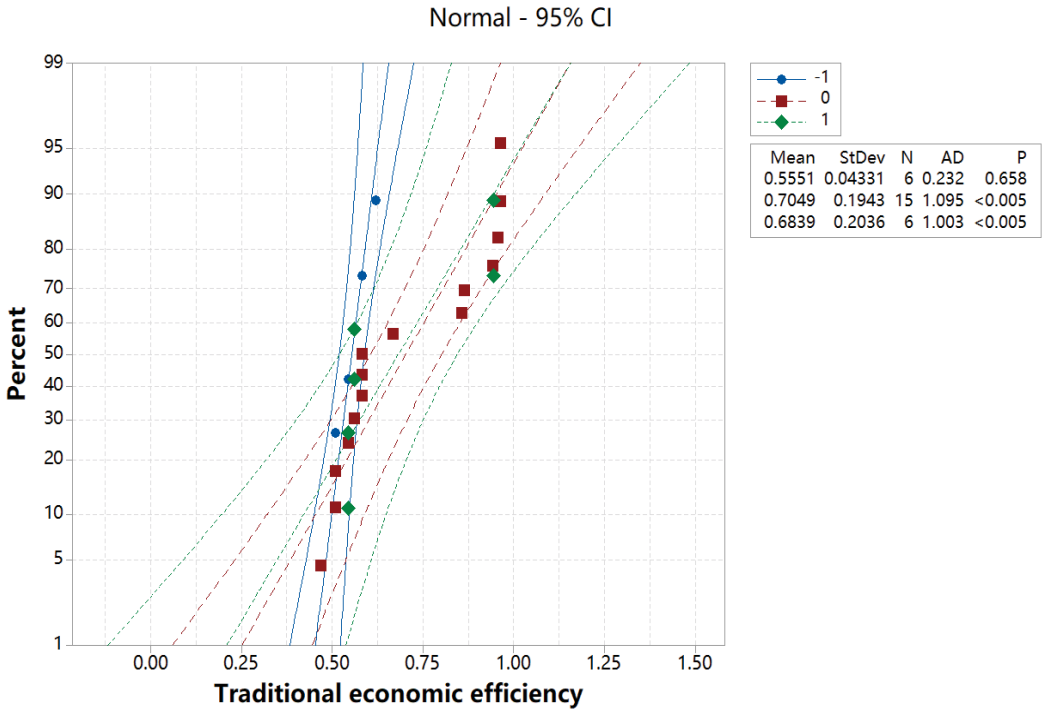

FIGURE 3
Probability Plot of Traditional economic efficiency

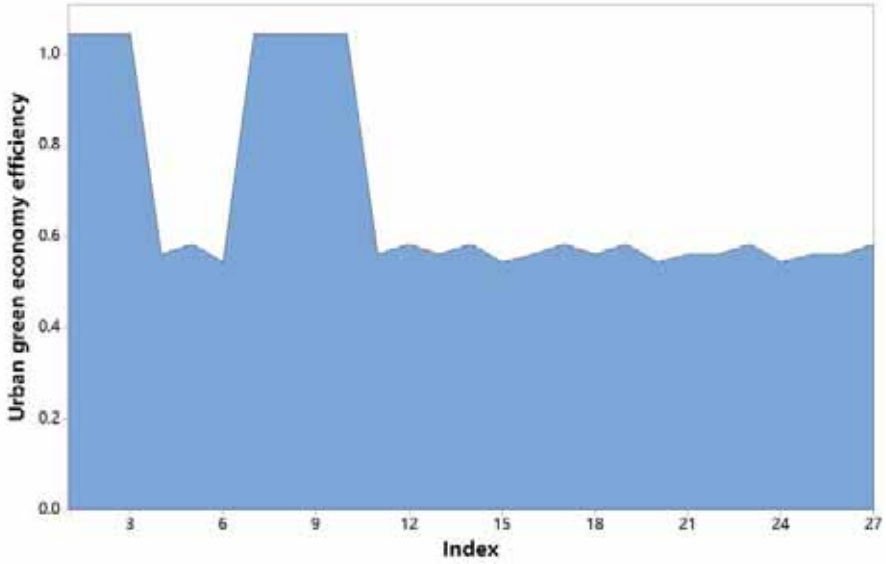

FIGURE 4
Area Graph of Urban green economy efficiency

Urban green economy efficiency. As shown in Figure 4, the average value of Qianjiang's green economy efficiency is 0.8405, with a small fluctuation range. In 2013, the fluctuation range was the largest and the green economy efficiency increased by 61.2%. However, the effective years of green economy efficiency are more than invalid years, indicating that resources and environment are considered After the factors, the economic quality of Qianjiang has been improved. Xiantao's green economic efficiency remained stable from 2003 to 2010. In 2011, the green economic efficiency dropped by 9%, but with the "Twelfth Five-Year Plan" proposed, the green economic efficiency increased at a rate of more than 15% every year. The average green economic efficiency of Ankang and Tianmen are relatively small at 0.4236 and 0.5260, respectively. Among them, Ankang's green economic efficiency is the most stable among upstream cities, and Tianmen fluctuates more than Ankang, but the green economic efficiency of the two cities has a steady upward trend, indicating that Ankang and Tianmen at the same time of economic development, we have al-

ways paid attention to the protection of the environment and the conservation of resources. The average value of Jingmen's green economic efficiency is greater than 1, and the green economic efficiency is the most effective. It shows that while promoting economic growth, Jingmen is consistent with the concept of green development promulgated by the national government. It not only seeks to increase the economic quantity, but also pays more attention to the improvement of environmental quality. Tianmen is consistent with its changing trend.

From the perspective of the upper reaches of the Hanjiang Eco-economic Belt, the rate of change in the efficiency of the urban green economy is smaller than that of the traditional economy, indicating that there are differences in resources and environmental protection in the development of the economy. The urban traditional economic efficiency reached the minimum value of 0.5833 in 2013 and the maximum value of 0.9323 in 2008. Except for the decline of the agricultural economy caused by waterlogging, the traditional economic efficiency suddenly dropped to the lowest point. In other years, the traditional economic efficiency remained at around 0.8460 and fluctuated slightly. Although the efficiency of the green economy has increased and decreased during the "Tenth Five-Year Plan" and "Eleventh Five-Year Plan" period, it has basically remained at around 0.84. With the "Twelfth Five-Year Plan" proposed, the government attaches great importance to industrial structure adjustment, resource conservation, and pollution control, coordinating regional common development and development, after integrating economic growth and resource environment, the green economic efficiency of the upper reaches of the Hanjiang Ecological Economic Belt has an upward trend, but the overall fluctuation range is smaller than the traditional economic efficiency. In addition, with the exception of Jingmen's green economic efficiency, the average green economic efficiency of other cities is lower than the traditional economic efficiency.

CONCLUSION

Based on the existing research results, this paper focuses on the three industrial wastes, and considers environmental pollution as an undesired output into the calculation of economic efficiency. Construct a comprehensive index reflecting the impact of environmental pollution on the economic efficiency of the Hanjiang River Eco-economic Zone. Based on the analysis characteristics of the DEA model, measure the traditional economic efficiency and green economic efficiency of the Hanjiang Eco-economic Zone, and analyze its trend change level. The research results show that the green economic efficiency of most cities in the Hanjiang River Ecological Economic Zone shows an upward trend, and the fluctuation range is smaller than that of the traditional economic efficiency. The unevenness of the green economy efficiency of the cities in the Hanjiang Eco-economic Belt is more prominent, and the green economy efficiency of upstream cities is higher than that of downstream and midstream cities. There is a U-shaped relationship between the green economic efficiency of the Hanjiang Eco-economic Zone and the level of economic development.

ACKNOWLEDGEMENTS

This paper is supported by the first school funds of Xijing University in 2019 "Thinking on the Transformation and Development of City Commercial Bank in Shaanxi Province in the New Economic era" (XJ190109).

REFERENCES

[1] Dong, Q.Y., Futawatari, T. (2015) A review of the progress in China's renewable energy generation, and its links with energy conservation, environmental degradation and economic growth. Fresen. Environ. Bull. 24, 405-411.
[2] Gultekin, U. (2019) Renewable electricity generation for sustainable development and environmental management in Turkey. Fresen. Environ. Bull. 28, 8171-8174.
[3] Zhou, H.Y. (2020) Incentive mechanism of low carbon economic growth quality based on fuzzy cluster analysis. Fresen. Environ. Bull. 29(4), 2350-2356.
[4] He, Y., Lin, K., Zhang, F., Wang, Y., Chen, X. (2018) Coordination degree of the exploitation of water resources and its spatial differences in China. Sci. Total Environ. 644, 1117-1127.
[5] Xu, Y.P., Wang, M., Qin, M., Shi, H.X., Sui, B.W., Jia, X.Z., Lu, D.L. (2018) Study of the relationship between economic growth and environmental quality with the Kuznets curve in Guangxi, China. Fresen. Environ. Bull. 27, 2818-2828.
[6] Xiong, S., Tian, Y., Ji, J., Ma, X. (2017) Allocation of energy consumption among provinces in China: a weighted ZSG-DEA model. Sustainability. 9(12), 2115-2116.
[7] Zhou, H.Y. (2020) Incentive mechanism of low carbon economic growth quality based on fuzzy cluster analysis. Fresen. Environ. Bull. 29(4), 2350-2356.
[8] Pao, H., Chen, H.A., Li, Y. (2015) Competitive dynamics of energy, environment, and economy in the U.S. Energy. 89, 449-460.
[9] Tang, X., McLellan, B.C., Snowden, S., Zhang, B., Hook, M. (2015) Dilemmas for China: Energy, economy and environment. Sustainability. 7, 5508-5520.

[10] Han, S., Zhu, J. (2011) Research on the dynamic relationship of the Energy-Economy-Environment (3E) system-based on an empirical analysis of China. Energy Procedia. 5, 2397-2404.
[11] Gozgor, G., Chi, K.M.L., Lu, Z. (2018) Energy consumption and economic growth: New evidence from the OECD countries. Energy. 153, 27-34.
[12] Price, J., Keppo, I. (2017) Modelling to generate alternatives: A technique to explore uncertainty in energy-environment-economy models. Appl. Energy. 195, 356-369.
[13] Salehi, M., Jalalian, M., Siar, M.M.V. (2017) Green transportation scheduling with speed control: trade-off between total transportation cost and carbon emission. Comput. Ind. Eng. 113, 392-404.
[14] Liu, M., Yang, S.S., Zhang, K.X., Li, J.J., Liu, H.Y., Dai, Y.J. (2018) The study of smart growth of salt lake city and Nottingham city using the entropy method to explore the social, environment and economic changes. Fresen. Environ. Bull. 27, 4631-4636.
[15] Meng, X.Z., Venkatesan, A.K., Ni, Y.L., Steele, J.C., Wu, L.L., Bignert, A., Bergman, A., Halden, R.U. (2016) Organic Contaminants in Chinese Sewage Sludge: A Meta-Analysis of Literature of the Past 30 Years. Environmental Science & Technology. 50(11), 5454-5466.
[16] Yang, X.W. (2015) Study on the Effect of Foreign Direct Investment and Foreign Trade on Energy Efficiency in the Yangtze Delta Region Using Stochastic Frontier Analysis Approach. Advanced Materials Research. 1070-1072, 383-387.
[17] Patterson, M.C. (1996) What is Energy Efficiency? Concepts, Indicators and Methodological Issues. Energy Policy. 24(5), 377-390.
[18] Bosseboeuf, D., Chateau, B., Lapillonne, B. (1997) Cross-County Comparison on Energy Efficiency Indicators: the On-Going European Effort towards a Common Methodology. Energy Policy. 25(7-9), 673-682.
[19] Yuan, Y.Q., Jin, M.Z., Ren, J.F., Hu, M.M., Ren, P.Y. (2014) The dynamic coordinated development of a regional environment-tourism-economy system: a case study from western Hunan Province, China. Sustainability. 6(8), 5231-5251.
[20] Chen, J.Y., Ni, X.B., Liu, M.L., Chen, J.F., Mao, Z.H., Jin, H.Y., Pan, D.L. (2015) Monitoring the occurrence of seasonal low-oxygen events off the Changjiang Estuary through integration of remote sensing, buoy observations, and modeling. Journal of Geophysical Research Oceans. 119(8), 5311-5322.
[21] Liu, Z. (2016) The energy-environment efficiency of road and railway sectors in China: Evidence from the provincial level. Ecological Indicators. 69, 559-570.

Received: **01.06.2021**
Accepted: **03.12.2021**

CORRESPONDING AUTHOR

Ru Guo
Mathematics Department of Science College,
XiJing University,
Xi'an 710123 – China

e-mail: guoru898@hotmail.com

ERRATUM

SEROPREVALENCE OF TOXOCARIASIS IN CRYPTOGENIC EPILEPSY PATIENTS

Abdurrahman Ekici[1,*], Zeynep Tas Cengiz[1], Aydin Cagac[2], Hasan Yilmaz[1], Yunus Emre Beyhan[1], Abdullah Yilgor[2]

[1]Department of Parasitology, Faculty of Medicine, Van Yuzuncu Yil University, Van, Turkey
[2]Department of Neurology, Dursun Odabas Medical Center, Van Yuzuncu Yil University, Van, Turkey

We request that the following correction be made in our previous article "Ekici, A., Cengiz, Z. T., Cagac, A., Yilmaz, H., Beyhan, Y. E., & Yilgor, A. (2021). Seroprevalence Of Toxocariasis In Cryptogenic Epilepsy Pati ents. Fresenius Environmental Bulletin, 30(6 A), 6371-6375"

Correction: The funding statement should be added to the article as shown below; Funding statement: This study was supported by BAP project number: 2015-TF-B171

CORRESPONDING AUTHOR

Abdurrahman Ekici
Department of Parasitology,
Faculty of Medicine,
Van Yuzuncu Yil University,
Van – Turkey

e-mail: abdurrahman2400@gmail.com

AUTHOR INDEX

Z

SUBJECT INDEX

FEB – GUIDE FOR AUTHORS

General

FEB accepts original papers, review articles, short communications, research abstracts from the entire sphere of environmental-chemistry,-biology,-microbiology,- technology, -biotechnology and-management, furthermore, about residue analysis/ and ecotoxicology of contaminants.

Acceptance or no acceptance of a contribution will be decided, as in the case of other scientific journals, by a board of reviewers. Papers are processed with the understanding that they have not been published before (except in form of an abstract or as a part of a published lecture, review or thesis);that they are not under consideration for publication elsewhere; that their publication has been approved by all co-authors, if any, as well as- tacitly or explicitly- by the responsible authorities at the institute where the work has been carried out and that, if accepted, it will not be published elsewhere in the same form, in either the same or another language, without the consent of the copyright holders.

Language

Papers must be written in English. Spelling may either follow American (Webster) or British (Oxford) usage but must be consistent. Authors who are less familiar with the English language should seek assistance from proficient colleagues in order to produce manuscripts that are grammatically and linguistically correct.

Size of manuscript

Review articles should not exceed 30 typewritten pages. In addition up to 5 figures may be included.

Original papers must not exceed 14 typewritten pages. In addition up to 5 figures may be included.

Short-Communications should be limited to 4 typewritten pages plus not more than 1 illustration.

Short descriptions of the authors, presentation of their groups and their research activities (with photo) should together not exceed I typewritten page. Short research abstracts should report in a few brief sentences (one-fourth to one page) particularly significant findings. Short articles by relative newcomers to the chemical innovation arena highlight the key elements of their Master and PhD-works in about I page.

Book Reviews are normally written in-house, but suggestions for books to review are welcome.

Preparation of manuscript

Dear authors,

FEB is available both as printed journal and as online journal on the web. You can now e-mail your manuscripts with an attached file. Save both time and money. To avoid any problems handling your text please follow the instructions given below:

When preparing your manuscripts have the formula K/SS (Keep It Simple and Stupid) in mind. Most word processing programs such as MS-Word offer a lot of features. Some of them can do serious harm to our layout. So please do not insert hyperlinks and/or automatic cross-references, tables of contents, references, footnotes, etc.

1. Please use the standard format features of your word processor (such as standard.dot for MS Word).
2. Please do not insert automatisms or secret link-ups between your text and your figures or tables. These features will drive our graphic department sometimes mad.
3. Please only use two fonts for text or tables "Times New Roman" and for graphical presentations "Arial".
4. Stylesheets, text, tables and graphics in shade of grey
5. Turn on the automatic language detection in English (American or British)
6. Please - check your files for viruses before you send them to us!!

Manuscripts should be uploaded on our website prt-parlar.de

Thank you very much!

STRUCTURE OF THE MANUSCRIPT

Title page: The first page of the manuscript should contain the following items in the sequence given: A concise title of the paper (no abbreviations). The names of all authors with at least one first name spelled out for every author. The names of Universities with Faculty, City and Country of all authors.

Abstracts: The second page of the manuscript should start with an abstract that summarizes briefly the contents of the paper (except short communications). Its length should not exceed 150-200 words. The abstract should be as informative as possible. An extended repetition of the paper's title is not considered to be an abstract.

Keywords: Below the Summary up to 6 key words have to be provided which will assist indexers in cross-indexing your article.

Introduction: This should define the problem and, if possible, the frame of existing knowledge. Please ensure that people not working in that particular field will be able to understand the intention. The word length of the introduction should be 150 to 300 words.

Materials and methods:
Please be as precise as possible to enable other scientists to repeat the work.

Results: Only material pertinent to the subject must be included. Data must not be repeated in figures and tables.

Acknowledgements: Acknowledgements of financial support, advice or other kind of assistance should be given at the end of the text under the heading "Acknowledgements". The names of funding organisations should be written in full.

References: Responsibility for the accuracy of references rests with the authors. References are to be limited in number to those absolutely necessary. References should appear in numerical order in brackets and in order of their citation in the text. They should be grouped at the end of the paper in numerical order of appearance. Abbreviated titles of periodicals are to be used according to Chemical or Biological Abstracts, but names of lesser known journals should be typed in full. References should be styled and punctuated according to the following examples:

ORIGINAL PAPERS:
l. Author, N.N. and Author, N.N. (Year) Full title of the article. Journal and Volume, first and last page.

BOOK OR PROCEEDING:
2. Surname, N., Surname, N.N., Surname, N.N., Surname, N. (Year) Title of the contribution. In: Title of the book or proceeding. Volume, Publisher, City, first and last page

DOCTORAL THESIS:
3. Author, N.N. (Year) Title of the thesis, University and Faculty, City

UNPUBLISHED WORK:
Papers that are unpublished but have been submitted to a journal may be cited with the journal's name followed by "in press". However, this practice is acceptable only if the author has at least received galley proofs of his paper. In all other cases reference must be made to “unpublished work" or "personal communication".

Discussion and Conclusion: This part should interpret the results in reference to the problem outlined in the introduction and of related observations by the author/s or others. Implications for further studies or application may be discussed. A conclusion should be added if results and discussion are combined.

Corresponding author: The name of the corresponding author with complete postal address